Ibrahim Dincer · Can Ozgur Colpan
Fethi Kadioglu *Editors*

Causes, Impacts and Solutions to Global Warming

Springer

Causes, Impacts and Solutions to Global Warming

Ibrahim Dincer
Can Ozgur Colpan
Fethi Kadioglu

Editors

Causes, Impacts and Solutions to Global Warming

Springer

Editors
Ibrahim Dincer
Faculty of Engineering
  and Applied Science
University of Ontario
Institute of Technology
Oshawa, ON, Canada

Can Ozgur Colpan
Makina Muhendisligi Bolumu
Dokuz Eylul University
Buca, Izmir, Turkey

Fethi Kadioglu
Faculty of Civil Engineering
Istanbul Technical University
Maslak, Istanbul, Turkey

Preface

Global warming is considered an average increase in the Earth's temperature due to greenhouse effect as a result of both natural and human activities. In common usage, "global warming" often refers to the warming that can occur as a result of increased emissions of greenhouse gases from human activities, e.g., carbon dioxide, methane, water vapor, and fluorinated gases, which act like a greenhouse around the earth, trapping the heat from the sun into the earth's atmosphere and increasing the Earth's temperature.

Catastrophic events around the world have brought a desperate picture to the forefront! The Global Conference on Global Warming 2012 (GCGW-12) brought all disciplines together for local and global solutions to combat global warming. This conference is a multidisciplinary global conference on global warming (and climate change), not only in engineering and science but also in all other disciplines (e.g., ecology, education, social sciences, economics, management, political sciences, and information technology). It covers a broad range of topics on energy and environment policies, energy resources, energy conversion technologies, energy management and conservation, energy security, renewables, green technologies, emission reduction and abatement, carbon tax, sustainable development, pollution control and measures, policy development, etc. Intensifying global environmental problems require internationally coordinated responses, which must balance the goals of energy security, environmental protection, and economic growth. The adoption of a comprehensive approach to energy and environment issues and the integration of energy and environment policies have become central activities of several countries. National and global solutions to reduce pollutants and greenhouse gas emissions have implications for energy security, energy trade, economic growth, etc. The issue that global climate change poses for energy policymakers is the focus of continuing international debate. For example, despite the policy measures taken to date, unless the rapid establishment and implementation of further effective policies and programs to reduce emissions are conducted, greenhouse gas emissions would continue increasing unless the right cure is underway. Of course, this requires the full range of possible areas for action and policy instruments.

This book is a unique collection of 62 selected papers out of the papers presented in the GCGW-12 in Istanbul, Turkey, on July 8–12, 2012, to cover a wide variety of topics on the causes, impacts, and solutions to global warming. There is a diverse coverage of global warming in this book from climate change modeling to forecasting weather events, from sustainable energy technologies and resources to waste management, and many more to serve as a sustainable source of knowledge and information for researchers, scientists, engineers, practitioners, etc.

As mentioned above, global warming is one of the major concerns of the human beings in this century. A significant part of global warming comes from the human activities, such as consuming fossil energy sources, e.g., oil, coal, and natural gas. In the solution of global warming, engineering approaches play a key role. These approaches are linked to many areas including energy and environment policies, energy conversion technologies, energy management and conservation, energy saving, energy security, renewable and sustainable energy technologies, emission reduction, sustainable development, pollution control and measures, policy development, global energy stability and sustainability, carbon tax, and waste management. Innovative engineering solutions are needed to reduce the effects of global warming and also to obtain better efficiency, better cost-effectiveness, better use of energy and resources, better energy security, better environment, and better sustainability. In this book, several engineering approaches and potential solutions from renewables to hydrogen, including data analysis, modeling, simulation, assessment, optimization studies, that reduce the effects of global warming are discussed in detail. Incorporated through this book are many wide-ranging practical examples, case studies, and policy and strategy development which provide useful information for practical applications. Complete references are included with each chapter to direct the curious and interested reader to further information.

We hope this edited book provides a unique source of potential solutions for combating global warming to be more widely applied and the benefits of such efforts more broadly derived, so that the future can be made more efficient, clean, and sustainable. We sincerely appreciate the help and assistance provided by various individuals who deserve a clear acknowledgement. Dr. Dincer acknowledges the support provided by the Turkish Academy of Sciences.

Oshawa, ON, Canada   Ibrahim Dincer
Buca, Izmir, Turkey   Can Ozgur Colpan
Maslak, Istanbul, Turkey   Fethi Kadioglu

Contents

Contributors

Mawada Abdellatif Liverpool John Moores University, Liverpool, UK

Ayad K.M. Aboderheeba Dublin City University, Dublin, Ireland

Aysegul Abusoglu University of Gaziantep, Gaziantep, Turkey

Canan Acar University of Ontario Institute of Technology, Oshawa, ON, Canada

Dragan Adamović University of Novi Sad, Novi Sad, Serbia

Abdelhamid Addoun USTHB, Algiers, Algeria

Seyedali Aghahosseini University of Ontario Institute of Technology, Oshawa, ON, Canada

Pouria Ahmadi University of Ontario Institute of Technology, Oshawa, ON, Canada

Saif A. Ahmed Higher Colleges of Technology, Dubai, United Arab Emirates

Bertuğ Akıntuğ Middle East Technical University Northern Cyprus Campus, Mersin, Turkey

Saoud Al-Abdooli Higher Colleges of Technology, Dubai, United Arab Emirates

Fatma Alfarjani Dublin City University, Dublin, Ireland

Rafid Alkhaddar Liverpool John Moores University, Liverpool, UK

Mohamed K. Al-Radhi Higher Colleges of Technology, Dubai, United Arab Emirates

Nesrin Altinsoy Istanbul Technical University, Istanbul, Turkey

Onder Altuntas Anadolu University, Tepebaşı, Turkey

Ali H. Assi Lebanese International University, Beirut, Lebanon

William Atherton Liverpool John Moores University, Liverpool, UK

Aysel Atımtay Middle East Technical University, Ankara, Turkey

Hakan Aydın TEI, Eskisehir, Turkey

Faruk Aydın Blacksea Technical University, Trabzon, Turkey

M. Tolga Balta Aksaray University, Aksaray, Turkey

Ehsan Baniasadi University of Ontario Institute of Technology, Oshawa, ON, Canada

Nilgun Baydogan Istanbul Technical University, Istanbul, Turkey

A. Filiz Baytas Istanbul Technical University, Istanbul, Turkey

Khaled Benyounis Dublin City University, Dublin, Ireland

Levent Bilgili Yildiz Technical University, İstanbul, Turkey

Onur Birdal Istanbul Technical University, Istanbul, Turkey

Bryan Brooker Amgen Inc., Longmont, CO, USA

Bulent Buyuk Istanbul Technical University, Istanbul, Turkey

Aligul Buyukaksoy Missouri University of Science and Technology, Rolla, MO, USA

Hakan Caliskan Usak University, Usak, Turkey

Uğur Buğra Çelebi Yildiz Technical University, İstanbul, Turkey

Serdar Celik Southern Illinois University, Edwardsville, IL, USA

Filiz Dadaser-Celik Erciyes University, Kayseri, Turkey

Can Coskun Recep Tayyip Erdoğan University, Rize, Turkey

Ertugrul Demir Istanbul Technical University, Istanbul, Turkey

Sinan Demir University of Gaziantep, Gaziantep, Turkey

Ibrahim Dincer University of Ontario Institute of Technology, Oshawa, ON, Canada

Aleksandra Djukić-Vuković University of Belgrade, Belgrade, Serbia

Fatih Dogan Missouri University of Science and Technology, Rolla, MO, USA

Jovan Dorić University of Novi Sad, Novi Sad, Serbia

Savas Durduran Selçuk University, Konya, Turkey

Ertan Durmusoglu Kocaeli University, Kocaeli, Turkey

Semih Ekercin Aksaray University, Aksaray, Turkey

Leonard E.N. Ekpeni Dublin City University, Dublin, Ireland

Abbas El-Zein University of Sydney, Darlington, NSW, Australia

Sema Akyıl Erenturk Istanbul Technical University, Istanbul, Turkey

Mustafa Ertürk Balikesir University, Balikesir, Turkey

Mohamed Fenni University Ferhat Abbas, Setif, Algeria

Mohamed A. Gadalla American University of Sharjah, Sharjah, United Arab Emirates

Abdulla Galadari Higher Colleges of Technology, Dubai, United Arab Emirates

Hadi Ganjehsarabi Ege University, İzmir, Turkey

Abdulwahab Giwa Ankara University, Ankara, Turkey

Jale Gülen Yildiz Technical University, İstanbul, Turkey

Ali Gungor Ege University, İzmir, Turkey

Kevork Hacatoglu University of Ontario Institute of Technology, Oshawa, ON, Canada

Sevilay Haciyakupoglu Istanbul Technical University, Istanbul, Turkey

Michael Hall Kyushu University, Fukuoka, Japan

Halil S. Hamut University of Ontario Institute of Technology, Oshawa, ON, Canada

Hassan A.N. Hejase United Arab Emirates University, Al Ain, United Arab Emirates

Arif Hepbasli Yaşar University, Izmir, Turkey

Nilufer Durmaz Hilmioglu Kocaeli University, Kocaeli, Turkey

Mehdi Hosseini University of Ontario Institute of Technology, Oshawa, ON, Canada

Fadi Abraham University of Ontario Institute of Technology, Oshawa, ON, Canada

Go Iwahana The University of Alaska, Fairbanks, AL, USA

Mohammad bin Jarsh Higher Colleges of Technology, Dubai, United Arab Emirates

Nader Javani University of Ontario Institute of Technology, Oshawa, ON, Canada

Mehmet Kanoglu University of Gaziantep, Gaziantep, Turkey

Suleyman Karacan Ankara University, Ankara, Turkey

Aykan Karademir Kocaeli University, Kocaeli, Turkey

T. Hikmet Karakoc Anadolu University, Eskişehir, Turkey

Harisha Karanam Southern Illinois University, Edwardsville, IL, USA

Nilgun Karatepe Istanbul Technical University, Istanbul, Turkey

Kari Taulavuori University of Oulu, Oulu, Finland

Mohammadali Khalvati TDMT & Associates, Thornhill, ON, Canada

Muhammad A.A. Khan Middle East Technical University Northern Cyprus Campus, TRNC, Mersin, Turkey

Aissa Khelifi USTHB, Algiers, Algeria

Seda Aslan Kilavuz Kocaeli University, Kocaeli, Turkey

Emre Kiyak Anadolu University, Eskisehir, Turkey

Urszula Kossowska-Cezak Warsaw University, Warsaw, Poland

Stanislav M. Ksenofontov The Siberian Branch of the Russian Academy of Science, Yakutsk, Russia

Sule Kusdogan Anadolu University, Tepebaşı, Turkey

Joshua Lowrey Dalhousie University, Truro-Bible Hill, NS, Canada

Luciano Massetti Institute of Biometeorology of the National Research Council, Florence, Italy

Trofim Ch. Maximov The Siberian Branch of the Russian Academy of Science, Yakutsk, Russia

Thomas Mehlitz Solar Millennium AG, Köln, Germany

Adnan Midilli Recep Tayyip Erdoğan University, Rize, Turkey

Ljiljana Mojović University of Belgrade, Belgrade, Serbia

Susan Morgan Southern Illinois University, Edwardsville, IL, USA

Ali Muhtaroğlu Middle East Technical University Northern Cyprus Campus, Mersin, Turkey

Greg F. Naterer Memorial University, St John's, NL, Canada

Tri Nguyen-Quang Dalhousie University, Truro-Bible Hill, NS, Canada

Filiz Ugur Nigiz Kocaeli University, Kocaeli, Turkey

Svetlana Nikolić University of Belgrade, Belgrade, Serbia

Muhd Yunus Muhd Noor Malaysian Nuclear Agency, Bangi, Malaysia

Othman Nor'azizi Universiti Teknologi, Johor Bahru, Malaysia

Othman Norazli Universiti Teknologi, Johor Bahru, Malaysia

A.B. Noor Ezlin Universiti Kebangsaan, Bangi, Malaysia

Zuhal Oktay Recep Tayyip Erdoğan University, Rize, Turkey

Abdul-Ghani Olabi Dublin City University, Dublin, Ireland

Ahmet Ozbilen University of Ontario Institute of Technology, Oshawa, ON, Canada

Hasan Ozcan University of Ontario Institute of Technology, Oshawa, ON, Canada

Betül Özer Ardahan University, Ardahan, Turkey

Necat Ozgur General Directorate of the Protection of Natural Assets, Ankara, Turkey

Sinan Ozlu University of Ontario Institute of Technology, Oshawa, ON, Canada

Ahmet Öztopal Istanbul Technical University, Istanbul, Turkey

Jelena Radonić University of Novi Sad, Novi Sad, Serbia

Tahir A.H. Ratlamwala University of Ontario Institute of Technology, Oshawa, ON, Canada

Bale V. Reddy University of Ontario Institute of Technology, Oshawa, ON, Canada

William Retzlaff Southern Illinois University, Edwardsville, IL, USA

Marc A. Rosen University of Ontario Institute of Technology, Oshawa, ON, Canada

Ayhan Sarikaya Missouri University of Science and Technology, Rolla, MO, USA

Zekâi Şen Istanbul Technical University, Istanbul, Turkey

Elif Sertel Istanbul Technical University, Istanbul, Turkey

Mine Sertsoz Anadolu University, Tepebaşı, Turkey

Rahme Seyhun Middle East Technical University Northern Cyprus Campus, Mersin, Turkey

Maitha H. Al Shamisi United Arab Emirates University, Dubai, United Arab Emirates

Chelliapan Shreeshivadasan Universiti Teknologi, Johor Bahru, Malaysia

Sevinc Sirdas Istanbul Technical University, Istanbul, Turkey

Atsuko Sugimoto Hokkaido University, Sapporo, Japan

Svend Svendsen Technical University of Denmark, Kongens Lyngby, Denmark

Larbi Temdrara Université de Chlef, Chlef, Algeria

Hakan İbrahim Tol Technical University of Denmark, Kongens Lyngby, Denmark

Fahim N. Tonmoy University of Sydney, Darlington, NSW, Australia

A. Beril Tugrul Istanbul Technical University, Istanbul, Turkey

Onder Turan Anadolu University, Eskişehir, Turkey

Maja Turk-Sekulić University of Novi Sad, Novi Sad, Serbia

Robert Twardosz Jagiellonian University, Krakow, Poland

Francesca Ugolini Institute of Biometeorology-National Reseach Council, Florence, Italy

Kaan Ünlügençoğlu Yildiz Technical University, İstanbul, Turkey

Mirjana Vojinović-Miloradov University of Novi Sad, Novi Sad, Serbia

Isil Yazar Eskisehir Osmangazi University, Eskisehir, Turkey

Ilhami Yildiz Dalhousie University, Truro-Bible Hill, NS, Canada

Asena Cansu Yildiz University of British Columbia, Vancouver, BC, Canada

Jin Yue Dalhousie University, Truro-Bible Hill, NS, Canada

Sema Yurdakul Middle East Technical University, Ankara, Turkey

Calin Zamfirescu University of Ontario Institute of Technology, Oshawa, ON, Canada

Yury I. Zhegusov The Siberian Branch of the Russian Academy of Science, Yakutsk, Russia

Part I
Causes and Impacts

Chapter 1
Vegetation at Northern High Latitudes Under Global Warming

Kari Taulavuori

Abstract Northern areas are warming at a rapid rate. Global warming may disturb plant overwintering in the northern hemisphere in several ways: (1) Preparation for winter may be delayed, (2) warm spells in winter may prematurely interrupt dormancy, (3) extreme changes in temperature may result in lethal freezing, as well as (4) activity beginning too early in spring at high temperatures. In addition, (5) some species may be damaged due to thinning or lack of snow cover. Patterns predicted for global warming will undoubtedly extend the growing season, thus increasing plant biomass and productivity, but incidence of forest fires and pathogen attacks will reduce the significance of any positive impacts. In addition, invasion of aggressive alien species is one potential threat for northern biodiversity.

Temperature is the most important ecological filter for range shifts in species and populations towards northern areas. Thus, under a warmer climate, temperate vegetation may replace parts of boreal vegetation, with boreal vegetation shifting partly to tundra, although summer droughts may cause confounding effects on these expectations. In addition, photoperiod and other light related factors (light quality and quantity), may modify the adaptation of a given species or population to the new environment. Thus, the overall prediction on a vegetation community level is unpredictable without experimental studies. Understanding of the mechanisms behind vegetation range shifts is important from the biodiversity, forestry, and agricultural points of view.

K. Taulavuori (✉)
Department of Biology, University of Oulu, PO Box 3000, 90014 Oulu, Finland
e-mail: kari.taulavuori@oulu.fi

Nomenclature

Common garden experiment	An experiment where populations from different latitudes are reciprocally collected into same garden.
Deacclimation (dehardening)	Opposite process to autumn cold hardening process; refers to loss of hardening against low temperatures due to physiological readiness and high temperature exposure.
Drought	Extended period without water supply or precipitation.
Ecodormancy	Plant resting stage during which physiology is ready for break of dormancy, but exogenous factors (low temperature) prevent from it.
Ecological filter	Ecological filter is an environmental factor that determines distribution of species and populations.
Endodormancy	Plant resting stage during which endogenous factors (physiology) maintain dormancy irrespective of the high temperatures.
Freezing tolerance (frost hardiness)	Ability of plant to withstand temperatures below 0 °C.
Light saturation point	Irradiance level to reach maximum photosynthesis; increase in irradiance cannot increase photosynthesis after saturation point.
Morphogenic response	Light mediated response to shape of growth.
Perennial species	Species living longer than 2 years.
Supercooling	Cooling below freezing point without becoming solid form (crystallization).
Winter dormancy	Plant resting stage over the cold season.

1.1   Introduction

Northern high latitudes make for a harsh environment from the plant perspective. Soil pH is low and precipitation is relatively high, resulting in leaching of nutrients from the soil [1]. Fungal-based decomposition is slow in cool soils, which in turn slows down nutrient cycling [2]. Plant life and performance in the north thus often occurs in suboptimal nutrient concentrations. The growing season is short being only 1.5–3.5 months, depending on the latitude and other geographical aspects (altitude, oceanity or continentality, etc.). Besides the short growing season, the accumulation of temperature sum is low, meaning cool conditions during growing season. The Arctic is defined as an isotherm that excludes areas where the mean temperature of the warmest summer month (July) exceeds +10 to +12 °C [3].

Light conditions at northern high latitudes are unique during the growing season. Day length begins to extend from the vernal equinox onwards at an exponential rate, being 12 h on the 20th March, but reaching 24 h at the beginning of June, from

the Arctic Circle (66.56°N) northwards. Thus, there is no sunset above the Arctic circle before 10th July due to the high solar elevation, while nights without any dark break continue much longer at higher latitudes (e.g., end of July at 70°N) [4, 5]. The light environment of the polar summer is associated not only with the day length, but also light quantity and quality. Light quantity (irradiance) is much lower in polar areas compared to mid or low latitudes. For example, vegetation around the Arctic Circle in Scandinavia receives only about 55 % of the irradiance of that in the Alps (47°N) [6]. Light quality (spectral composition) is also different since the polar summer nights are enriched with a relatively high proportion of diffuse blue [5].

Winter, in turn, is characterized by the polar night during which the sun is below the horizon for a month or longer. The darkness of the polar night does not interfere with vegetation, since plants in northern high latitudes are dormant over the winter [7]. However, temperatures during winter may be pernicious if vegetation is not well protected against them (e.g., [8]). In addition, frost-bite is increased by high wind speeds. Stress on plants is increased if weather conditions are variable, ranging from extreme frost to above zero temperatures in the daytime during late winter. In late winter, excess light may also be a problem, since albedo (i.e., reflectance) from snow cover may double the irradiance of some vegetation [7]. Snow, indeed, is an effective insulator against both light and temperature in northern high latitudes, and therefore is an important ecological determinant of northern nature.

While the northern environment sounds barren, the fact is that the vegetation existing there is adapted to these conditions. The local species can survive and produce offspring in these conditions, where other vegetation is noncompetitive. The climate at northern high latitudes is now warming rapidly and much larger changes are projected, which may result in a significant shift in vegetation zones towards the North [3]. This chapter summarizes first (Sect. 1.2) the environmental changes at northern high latitudes projected by the Arctic Climate Impact Assessment [3]. Then, Sect. 1.3 introduces the basic adaptations of plants to the northern environment in order to understand the significance of possible responses to global warming. Plant responses at northern high latitudes, mainly from an individual perspective, are then discussed in relation to warming winters and growing seasons (Sects. 1.4 and 1.5, respectively). The perspective is broadened from individual to vegetation level in Sects. 1.6 and 1.7. Importance of temperature as an ecological filter to control species' and populations' geographical ranges is highlighted, especially since global warming may effectively move this ecological filter northward. Finally, in Sect. 1.8, it is demonstrated that unpredictable competition between local and invading vegetation in the Arctic will occur under the projected vegetation range shifts. This is due to different adaptations to light quantity and quality, and photoperiod.

1.2 Changing Environment at Northern High Latitudes Due to Global Warming

Annual Arctic temperatures have increased significantly during the past decades, and increases in Alaska and Western Canada have been as much as 3–4 °C [3]. According to the Arctic Climate Impact Assessment [3] the following trends in the Arctic climate will be seen within the next 100 years. (1) The temperatures will increase significantly, by 3–5 °C on the land areas and up to 7 °C over the oceans. Winter temperatures are projected to increase much more, i.e., 4–7 °C and 7–10 °C over the land areas and oceans, respectively. This increase in temperature is predicted to cause the following consequences: (2) declining snow cover, (3) diminishing lake and river ice, (4) melting ice sheet in Greenland, (6) melting glaciers, (7) increasing precipitation, and (8) river flows. These all contribute to the (9) rising sea level, which (9) subsequently decreases the salinity of oceans. Reduced salinity would cause, in turn, (10) changes to global ocean circulations, bringing heat from the tropics to polar areas, and thus (11) boosting the warming effect. Finally, (12) an additional driving effect could be caused by the ground, which would be more visible as the snow and ice sheets melt. The Earth's ground and oceans absorb the heat energy much more effectively than ice and snow. Thus, the global warming changes predicted in the Arctic concern the whole globe.

1.3 Plant Adaptations to Northern High Latitudes

Plant life in the northern latitudes is traditionally thought as an ambivalent existence between survival and capacity adaptations [9, and references therein]. Survival adaptation refers to the survival over long and harsh winters, while the capacity adaptation deals with the adequate acquisition of resources during a short, cool growing season. There is a trade-off between these two adaptations, since long winter dormancy is favorable for survival adaptation, while long a growing season is favorable for capacity adaptation. The environmental control behind both adaptations is temperature. In spring, it would be a great advantage to start growth processes early enough to extend the growing season and thus acquire resources for as long as possible at elevating temperatures, while at the same time it would be useful to continue dormancy for a while, to avoid lethal freezing during late frosts.

Good examples demonstrating these adaptations are the Ericaceous dwarf shrub species. In northern Finland (66°N) the deciduous *Vaccinium myrtillus* starts flowering at a 100 dd temperature sum, while the relatively evergreen species *V. vitis-idaea* activates later, at a 250 dd [10] (for calculation of dd, see Appendix). Before any growth process can start, however, the plant must stir from the deepest rest stage called endodormancy. During endodormancy, which is deepest in autumn, plant growth is arrested irrespective of warm temperatures. But as soon

as the plant has accumulated chilling temperature (0–5 °C) over sufficient time, it enters ecodormancy, which means that the plant is able to begin growth processes, given that the temperature is high enough (>5 °C). And the higher the temperature, the sooner the effective temperature for growth sum will be obtained [11]. The switch from endodormancy to ecodormancy occurs in mid-winter, and therefore the plants at northern high latitudes remain in the ecodormant stage for months to guarantee survival over winter.

Once growth has started, many important processes need to be accomplished during the short summers of the north. The annual species must emerge from seeds, grow, flower, and store resources in its own seeds for offspring in the next growing season. Perennial herb species have overwintered partly or entirely below ground and may rapidly produce new shoots, but their life is less hectic than an annual species, since it is not necessary to produce new seeds each year because of their long-lived below-ground organs. Even so, a cold growing season is not necessarily a catastrophe for the annual species, due to the rich seed bank below ground. This is also an effective strategy from the survival adaptation point of view, since the seeds do not have to meet the low temperature-driven challenges of winter.

Species such as trees, which are too tall to overwinter below snow cover, have to cope with changes in ambient air temperature in winter. Temperature −40 °C is a physical limit for supercooling [12], acting as a filter for species using this mechanism to avoid lethal freezing, into lower latitudes [13]. In those areas where winter temperatures may drop below −40 °C, only trees with extracellular freezing tolerance mechanisms can survive. In supercooling species, the plant escapes from lethal intracellular freezing by preventing freezing process, as a result of cooling of the intercellular fluid. However, cooling is not an endless continuum, and finally, at around −40 °C, a spontaneous freezing event takes place. In extracellular freezing, the plant cell dehydrates its intracellular water outside the cells where harmless freezing occurs [8]. Once frozen, the ice crystals enhance the osmotic pressure that draws out more of the internal water.

In terms of survival adaptation, it is important to notice that the environmental signal that triggers preparation of perennial species for winter is photoperiod, instead of temperature [14]. Shortening days/extending nights are a signal that provides a fixed calendar for the plants' seasonality.

1.4 Plant Responses to Winter Warming

The temperature increases predicted by climate change models may threaten overwintering of northern vegetation in various ways. Basically, temperatures may be too warm or fluctuate too much. In addition, snow cover may be thinned, lacking, or present for too short a time.

1.4.1   Ineffective Cold Hardening in Autumn
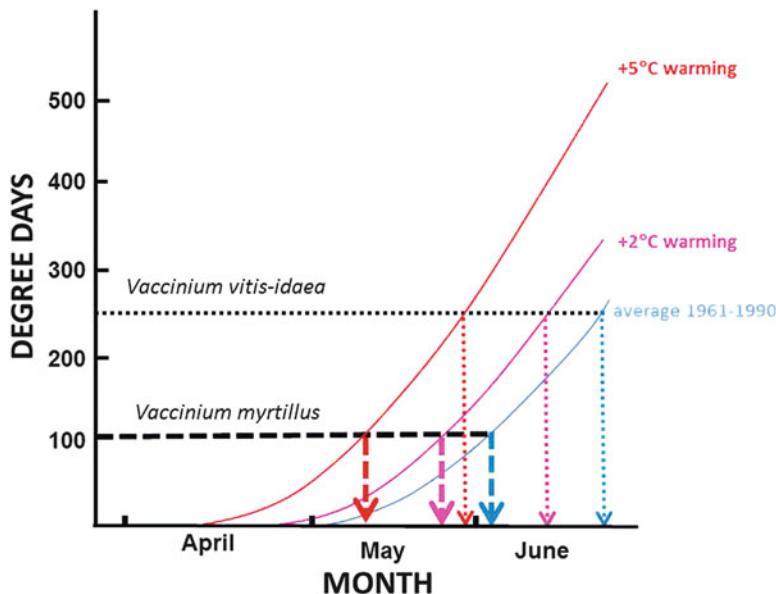
While the signal to start cold hardening process is photoperiod, the lowering temperatures in autumn interact to enhance frost tolerance. Indeed, the wintertime frost hardiness fluctuates with a delay with ambient air minimum temperatures. In cases of an abnormally warm autumn followed by extreme frost, some freezing injuries may occur [15]. However, the margin between frost tolerance and ambient temperatures is generally so great, in locally adapted species or populations, that incidence of frost damage in autumn remains rare. So far, no significant delays in frost hardening processes have been reported in response to warm autumns.

1.4.2   Loss of Frost Hardiness During Warm Spells in Mid-Winter

Climate change increases climatic variability, and the direction of prevailing winds may change abruptly. Change from continental to oceanic winds may warm the winter weather significantly. Temperature elevation of daily mean values up to +10 °C for a couple weeks in mid-winter accumulates the temperature sum to 70 dd. This is 70 % of the temperature sum necessary (see Sect. 1.3) for the requirement of growth initiation in *Vaccinium myrtillus* species. It has been shown experimentally that this species markedly loses its frost hardiness, and also displays visible signs of growth when exposed to +10 °C for 2 weeks in January [16]. It also indicates that the switch from endodormancy to ecodormancy had had occurred, and plants had started to deacclimate towards summer conditions.

1.4.3   Injuries Due to Sudden Winter Extreme Events

Winter injuries do not necessarily require any deacclimation process driven by an accumulation of temperature sum. Experimental studies have shown that artificial snowmelt prior to a few days' exposure to temperatures around zero, and followed by ambient winter temperatures below zero, may cause significant injuries in subarctic dwarf shrub species [17–19]. The reason behind the damage might be the initial level of frost hardiness in plants overwintered below snow. A 50 cm layer of snow insulates very well against ambient frost, resulting in exposure to temperatures not lower than around −5 to 0 °C. Thus it is understandable that the actual frost hardiness level cannot increase significantly, and frost experienced by plants after the treatment, without protecting snow may be fatal.
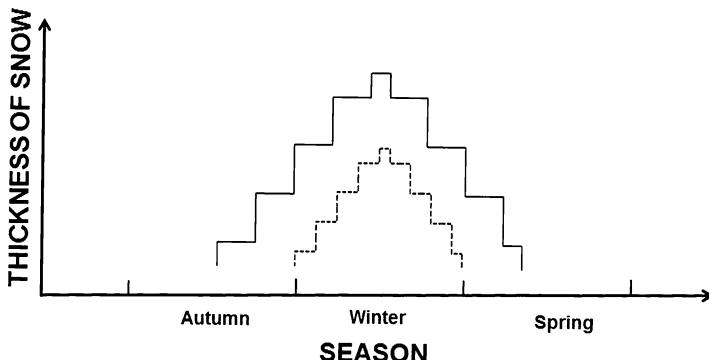
Fig. 1.1 Onset of growth in two *Vaccinium* species under long-term mean temperatures (*blue*), and projected temperature elevations of +2 °C (*pink*) and +5 °C (*red*) in Oulu (65°N). The long-term mean temperatures supplied by the Finnish Meteorological Institute [23] (figure is modified after Havas [10])

1.4.4 Injuries Due to Hastened Spring with Late (Night) Frosts

Global warming may hasten spring in northern high latitudes significantly. Once snow has melted, the plants may experience unusually high temperatures, especially during sunny days. As soon as the effective temperature sums have accumulated and new growth has sprouted from buds, there is no way back to winter dormancy—deacclimation is irreversible. The warming temperatures decrease plant frost hardiness gradually close to summer conditions [20, 21]. The higher the temperature, the sooner the bud break occurs [22]. Based on the temperature sum of 100 dd required for growth in *Vaccinium myrtillus*, a 5 °C elevation in the mean temperature has been found to accelerate the onset of growth by 3 weeks (Fig. 1.1). Even in a warm and early spring, frosts, especially during night hours, cannot be excluded, bringing obvious risks to plants showing early activity.

1.4.5 Injuries in the Absence of Snow Cover

Decline in snow cover may be realized in two ways, either through thinner cover, or by a shorter duration (Fig. 1.2). This is an important aspect since many of the subarctic species are chamaephytes, i.e., those adapted to overwinter below snow

Fig. 1.2 Schematic presentation on the projected changes in snow cover in northern areas under warming climate. *Solid line*, current duration and thickness of snow cover; *dashed line*, snow cover in the future

cover, and thereby protected against harsh winter conditions or excess light in late winter and spring. Havas (1971) [24] proposed, for example, that *Vaccinium myrtillus* from a latitude of 69°N cannot develop as high a degree of frost hardiness as ecotypes from 60°N latitude, since the latter have adapted to overwinter without or with relatively thin snow cover. Therefore, evolutionary pressure has favored clones that are able to develop a deep state of frost hardiness. So, here the big question deals with phenotypic plasticity of northern populations in relation to snow cover. In addition, the dependence on snow cover changes from species to species. A related species *Vaccinium vitis-idaea* is probably not as sensitive to freezing temperatures compared to *V. myrtillus*. However, it also needs snow cover to prevent winter desiccation caused by solar heat [25]. Thus the thickness of snow cover is probably less important in this species than the duration of snow.

1.5 Plant Responses to Warming Growing Season

The growing season is currently cool and short at high latitudes. Global warming effects are predicted to extend the growing season, and increase the temperature sum received by vegetation. Increasing temperature in northern areas leads to an increase in plant biomass and productivity through enhanced photosynthesis. However, not all species benefit from rising temperatures, especially due to increased periods of drought. For example, a 4 °C rise in summer temperature would result in the elimination of white spruce trees at the tree line in Alaska, and tree line movement towards the south in Siberia is caused by the same reason, in addition to air pollution and forest fires [3]. According to ACIA [3], the number of forest fires is predicted to increase by as much as 80 % in North America, and a

temperature elevation in Siberia of 5.5 °C is likely to double the number of years with several fires during this century. Nevertheless, positive impacts could be seen in agriculture, forestry, and wild plants. Flowering and consequent seed and berry production of plant species may benefit under higher temperatures. This may further modify the existing tree line. For example, Mountain birch is the Arctic tree line species in Scandinavia, because its seed maturation occurs in lower summer temperatures compared to coniferous trees. It is worth noting that birch trees are rare at lower (68°N) latitudes, where temperature is not yet a barrier against seed formation of conifers (i.e., Scots pine and Norway spruce), and the taller-growing conifers there are the winners in competition for light.

Northern agriculture may benefit from some new species as plants using C4 photosynthesis may be cultivated in more northern areas. Longer and warmer growing seasons increase the potential number of harvests and thereby the seasonal yields of forage crops, and warming is projected to advance commercial crop production northward throughout this century [3]. However, the incidence of pathogen attacks and insect outbreaks are obvious negative consequences of a warming climate. In addition, invasion of weeds and aggressive alien species (for example in Finland: *Fallopia japonica, Lupinus polyphyllos, Rosa rugosa*; [26]) is one potential threat to northern biodiversity. Alien species are those exotic species that are introduced outside their normal distribution. They may be called "aggressive" if depriving dominance from native species.

1.6 Temperature as an Ecological Filter for Vegetation

Temperature is obviously the most important ecological filter for species' and populations' range shifts towards the northern areas. It affects the formation of biomes and vegetation zones through two determinants, growing season [27] and cold winter period [8]. For example, the tree line ecotone exists at around 4,000 m altitude around equator and at only 400 m altitude on the fells of Finnish Lapland. According to the "Climate Hazard Hypothesis" [28–30], temperature is the major component affecting the formation of the Arctic tree line in Scandinavia. According to the hypothesis, temperature controls formation of the tree line in three ways: Through (1) adequate resource acquirement, (2) seed maturation (3) and winter survival. The first two refer to growing season temperature, and the latter refers to the cold period in winter. The temperature of the growing season should be high enough to ensure that photosynthetic yield exceeds maintenance respiration, and thereby avoid stunted growth. It is required also to guarantee seed production for future generations. A good example for the role of temperature as an ecological filter is the occurrence of the boreal zone in Europe about 10°N polarward compared to the boreal zone in North America. This is, of course, due to the proximity of the Gulf Stream in Europe.

1.7 Global Warming Moves the Temperature Filter
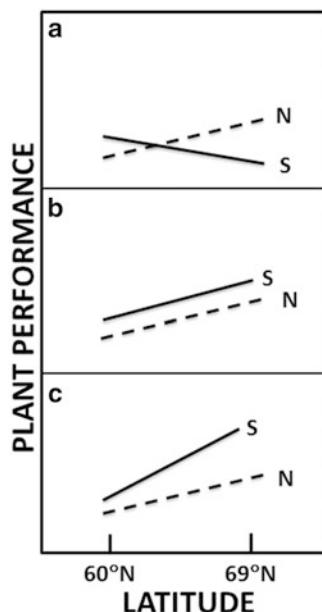
According to the ACIA [3], vegetation zones are likely to shift by as much as 1,000 km northward in the scenario of +7 °C for annual warming. Principally, temperate vegetation may replace parts of boreal vegetation, and the boreal forest shifts partly to tundra. Low shrub tundra vegetation in turn would expand to polar deserts, as long as the Arctic Ocean prevents the shifts onwards. The invading species thus displace some the Arctic species such as lichens and mosses, the diversity of which in the Arctic is higher than anywhere else. Forests are generally thought to move into current tundra areas, but the process seldom occurs in a straightforward manner. Lack of suitable soil may prevent or hinder the movement of tree species. The existing tundra mat is not the best substrate for seeds to germinate. Also, summer droughts and water logging may cause confounding effects on these expectations. Tree establishment in new areas may be prevented by human activity such as air pollution in some areas in Russia [3].

Species invasion in northern high latitudes under a warming climate is thus not a straightforward process. In the authors' opinion, there are aspects that are almost totally forgotten from the models and projected scenarios for vegetation dynamics, and thus their value as prediction tools. In particular, attention should be paid to light environment. Poleward invasion changes the light environment experienced by plants, at least through changes in irradiance, spectral composition and photoperiod due to a lower solar angle in the North [5]. The reduced irradiance of the northern light spectrum may be inadequate to reach the light saturation of photosynthesis in some species adapted to high light. Spectral composition, having an increased proportion of blue light during night hours, may reduce growth through photomorphogenic responses. High annual variation in day length may also result in mistiming of phenological stages (e.g., growth, reproduction, dormancy). It has been recently proposed that climate change-driven species' range shifts may be filtered by photoperiodism [31].

1.8 Modeling the Future Vegetation in Northern High Latitudes: A Mission Impossible?

The main question is: Do southern and northern plant species or populations differ from each other when exposed to equal southern temperature in the northern light environment? The null hypothesis is that southern plants suffer from the change to northern light conditions (Fig. 1.3a). This is based on assumptions generalized from common garden experiments (e.g., [32]). The following examples could result: (1) Southern plants cannot get an environmental cue to start the cold hardening process in time, in the northern photoperiod [5]. (2) Species with high light saturation point (e.g., Scots pine) suffer from the lower irradiance of the northern light environment [5].

Fig. 1.3 Sketch of the possible performances (reaction norms) (i.e., latitudes have equal temperature, but different light climate). *S* southern plant, *N* northern plant (modified from Kawecki and Ebert [33]; Savolainen et al. [32]). See text for more details

However, the use of results from common garden experiments may be questioned in species range shift forecasts, since these do not deal with the situation where southern plants exist in their current temperature climate combined with northern light conditions. The basic concept to be remembered, given that the temperature is the most efficient ecological filter against invasions, is that the temperature experienced by plants does not change if range shifts occur. In this case, the situation indicated in Fig. 1.3b might be the most likely: The southern plants can compete well in the northern light environment. Indeed, the risk of delayed winter dormancy of southern plants is decreased under locally adapted temperature, especially since the day length decreases in the north at much more faster rate from August to September. There is evidence that south-to-north transplanted Scots pine seedlings did not delay in frost hardening in a 3 year experiment [34]. There is also evidence that some trees from the *Rosaceae* family do not follow photoperiodic patterns in their growth cessation in autumn [35], for example.

It could be also hypothesized that southern species may exhibit higher plasticity towards range shifts (as in Fig. 1.3c), since the seasonal variation in day length is insignificant at lower latitudes (e.g., [31]), and thus the dependence on the photoperiod is presumably minor in plants from lower latitudes. Taulavuori et al. [36] proposed that if vegetation adapted to high UV-A radiation (i.e., species from the South) invades to lower UV-A radiation environment to the North, they may benefit in competition between the native vegetation, as less resources are required for protection against UV-A radiation.

Once there are multiple light actions, and plant responses are dependent on species and populations, modeling process without comprehensive light response

data is irrelevant. Therefore, true response data should be acquired from experimental studies. It is proposed that an experiment, where species and populations can compete under the northern light environment along with temperatures reflecting predicted future scenarios, could reveal the reaction norms required for modeling the vegetation dynamics for future conditions.

1.9 Concluding Remarks

- Warming may cause delay in frost hardening in autumn, loss of frost hardiness during warm spells in winter, injuries due to sudden winter extreme events, injuries due to hastened spring activity, and injuries due to declining snow cover.
- Vegetation may benefit from the warmer growing seasons, while increase in pathogen attacks and insect outbreaks has negative impacts.
- The role of temperature as an ecological filter is reduced, resulting in species and population range shifts northward.
- Photoperiod and other light conditions (quantity, quality), however, may form another filter which buffers against vegetation shifts. Therefore, future vegetation dynamics may be difficult to predict without experimental simulations.

References

1. Lundsrtöm US, van Breemen N, Bain D (2000) The podsolization process. A review. Geoderma 94:91–107
2. Rosslining A, Roose T, Herrmann AM, Davidson FA, Finlay RD, Gadd GF (2009) Approaches to modeling mineral weathering by fungi. Fung Biol Rev 23:138–144
3. ACIA (2005) Arctic climate impact assessment. University Press, Cambridge
4. Nilsen J (1985) Light climate in northern areas. In: Junttila O, Kaurin Å (eds) Plant production in the north. Norwegian University Press, Oslo
5. Taulavuori K, Sarala M, Taulavuori E (2010) Growth responses of trees to arctic light environment. Progress Bot 71:157–168
6. Körner C (2003) Alpine plant life: functional plant ecology of high mountain ecosystems. Springer, Berlin
7. Marchand PJ (1996) Life in the cold: an introduction to winter ecology, 3rd edn. Hanover, University Press, New England
8. Sakai A, Larcher W (1987) Frost survival of plants. Springer, Berlin
9. Hänninen H, Kramer K (2007) A framework for modelling the annual cycle of trees in boreal and temperate regions. Silva Fenn 41:167–205
10. Website 1: http://www.oulu.fi/northnature/english/englanti/ajankohtkesa.html

11. Lang GA, Early JD, Martin GC, Darnell RL (1987) Endo-, para-, and ecodormancy: physiological terminology and classification for dormancy research. HortScience 22:371–377
12. Wisniewski M, Bassett C, Gusta LV (2003) An overview of cold hardiness in woody plants: seeing the forest through the trees. HortScience 38:952–959
13. Quamme HA (1985) Avoidance of freezing injury in woody plants by deep supercooling. Acta Horticulturae 168:11–30
14. Taulavuori K, Niinimaa A, Laine K, Taulavuori E, Lähdesmäki P (1997) Modelling frost resistance of Scots pine seedlings using temperature, daylength and pH of cell effusate. Plant Ecol 133:181–189
15. Colombo SJ (1998) Plant physiological responses to a changing environment. In: Colombo SJ, Buse LJ (eds) Impacts of climate change in Ontario's Forests, Ontario Forest Research Information Paper No. 143: 25–28
16. Taulavuori K, Laine K, Taulavuori E (2002) Artificial deacclimation response of *Vaccinium myrtillus* in mid-winter. Ann Bot Fennici 39:143–147
17. Bokhorst SF, Bjerke JW, Tømmervik H, Callaghan TV, Phoenix GK (2009) Winter warming events damage sub-Arctic vegetation: consistent evidence from an experimental manipulation and a natural event. J Ecol 97:1408–1415
18. Bokhorst S, Bjerke JW, Davey M, Taulavuori K, Taulavuori E, Laine K, Callaghan TV, Phoenix GK (2010) Impacts of extreme winter warming events on plant physiology in a sub-Arctic heath community. Physiol Plant 140:128–1404
19. Bokhorst S, Bjerke JW, Street LE, Callaghan TV, Phoenix GK (2011) Impacts of multiple extreme winter warming events on sub-Arctic heathland: phenology, reproduction, growth, and CO_2 flux responses. Glob Chang Biol 17:2817–2830
20. Taulavuori K, Laine K, Taulavuori E, Pakonen T, Saari E (1997) Accelerated dehardening in the bilberry (Vaccinium myrtillus L.) induced by a small elevation in air temperature. Environ Pollut 98:91–95
21. Taulavuori K, Taulavuori E, Skre O, Nilsen J, Igeland B, Laine K (2004) Dehardening of mountain birch (*Betula pubescens* ssp. czerepanovii) ecotypes at elevated winter temperatures. New Phytol 162:427–436
22. Skre O, Taulavuori K, Taulavuori E, Nilsen J, Igeland B, Laine K (2008) The importance of hardening and winter temperature for growth in mountain birch populations. Environ Exp Bot 62:254–266
23. FMI (1991) Climatological statistics in Finland 1961-1990. Supplement to the meteorological yearbook of Finland, vol 90. Helsinki, The Finnish Meteorological Institute
24. Havas P (1971) The water economy of the bilberry (*Vaccinium myrtillus*) under winter conditions. Rep Kevo Subarctic Res Stat 8:41–52
25. Taulavuori K, Bauer E, Taulavuori E (2011) Overwintering stress of Vaccinium vitis-idaea in the absence of snow cover. Environ Exp Bot 72:397–403
26. Website 2: http://www.mmm.fi/attachments/mmm/julkaisut/esitteet/esitteet/65fVxzOt1/Vieraslajiesite.pdf
27. Dahl E (1951) On the relationship between summer temperature and the distribution of alpine vascular plants in the lowlands of Fennoscandinavia. Oikos 3:22–52
28. Karlsson PS, Nordell KO (1987) Growth of *Betula pubescens* and *Pinus sylvestris* seedlings in a subarctic environment. Func Ecol 1:37–44
29. Skre O (1993) Growth of mountain birch (*Betula pubescens* Ehrh.) in response to changing temperature. In: Alden J, Mastrantonio JL, Ødum S (eds) Forest development in cold climates New York. Plenum Press, London
30. Weih M, Karlsson PS (2001) The nitrogen economy of mountain birch seedlings, implications for winter survival. J Ecol 87:211–219
31. Saikkonen K, Taulavuori K, Hyvönen T, Gundel PE, Hamilton CE, Vänninen I, Nissinen A, Helander M (2012) Climate change-driven species' range shifts filtered by photoperiodism. Nat Clim Chang 2:239–242

32. Savolainen O, Pyhäjärvi T, Knürr T (2007) Gene flow and local adaptation in trees. Annu Rev Ecol Evol Syst 38:595–619
33. Kawecki TJ, Ebert D (2004) Conceptual issues in local adaptation. Ecol Lett 7:1225–1241
34. Taulavuori E, Taulavuori K, Niinimaa A, Laine K (2010) Effect of ecotype and latitude on growth, frost hardiness, and oxidative stress of south to north transplanted Scots pine seedlings. Int J Res 2010:16. doi:10.1155/2010/162084
35. Heide OM (2011) Temperature rather than photoperiod controls growth cessation and dormancy in *Sorbus* species. J Exp Bot 62:5397–5404
36. Taulavuori K, Keränen J, Suokanerva H, Lakkala K, Huttunen S, Laine K, Taulavuori E (2012) Decreased frost hardiness of *Vaccinium vitis-idaea* in reponse to UV-A radiation. Physiol Plant 145:516–552

Chapter 2
Exceptionally Hot Summers Months in Central and Eastern Europe During the Years 1951–2010

Robert Twardosz and Urszula Kossowska-Cezak

Abstract This chapter reports a study of extremely hot months (EHMs) during the period 1951–2010. Input data includes average, maximum and minimum monthly air temperatures, the number of days with $t_{max} > 25$, 30, 35 °C and the number of days with $t_{min} > 20$ °C, as recorded during three summer months (June–August) at 59 weather stations in Central and Eastern Europe. This body of data was used to identify and characterise EHMs, which were defined as months with an average monthly temperature exceeding the long-term average by two or more standard deviations ($t \geq t_{av.} + 2\sigma$). The frequency and geographical coverage of EHMs were also identified.

Over the 60-year study period a total of 47 EHMs of various sizes and location were identified of which 15 occurred at only 1–2 stations and another 15 at 3–6 stations. The remaining 17 EHMs, which occurred at more than 6 stations (i.e. more than 10 % of all stations), were selected for an in depth analysis. Their distribution during the study period was found to be uneven with just 6 EHMs during the first 50 years and 11 during the final decade. The EHMs with the greatest geographical extent occurred in Russia in June (36 stations) and August (34) 2010, in August 2007 (25), August 1972 (19), June 1999 (19) and August 1992 (17). The average temperature in a typical EHM was 3–5 °C greater than the long-term average (scale of anomaly), but sometimes it reached 5–6 °C greater.

R. Twardosz (✉)
Department of Climatology, Jagiellonian University, ul. Gronostajowa 7,
30-387 Kraków, Poland
e-mail: r.twardosz@uj.edu.pl

U. Kossowska-Cezak
Department of Climatology, Faculty of Geography and Regional Studies,
Warsaw University, ul. Krakowskie Przedmieście 30, 00-927 Warszawa, Poland

2.1   Introduction

An increased frequency of extreme meteorological phenomena and exceptional weather conditions, including exceptionally hot summers and summer heat waves, is often quoted as a symptom of contemporary climate change. Considerable fluctuation of thermal conditions from year to year is particularly characteristic of the temperate geographical zone covering much of the European continent. Nonetheless, the last decade of the twentieth century and the first decade of the twenty-first century stand out with particularly frequent occurrences of hot summer months and even entire summer seasons. Examples of this phenomenon include extremely hot summer seasons of 2003 in Western Europe and of 2010 in the European part of Russia characterised by an enormous extent of both the scale of thermal anomalies and their spatial coverage [1].

Such intensive and persistent heat waves are classified as extreme climatic phenomena and are known to have multiple adverse consequences. Overheating has severely adverse effects on the human health and well-being and may increase the risk of death [2–7]. Droughts that accompany heat spells damage the agriculture and increase the risk of wide spread forest fires. High air temperatures cause the melting of mountain glaciers, which cannot recover during the subsequent winter. Modelling research shows that the tendency for such adverse weather conditions to increase in frequency is likely to continue leading to more frequent, lasting and intense hot spells [8–12]. The exceptional heat waves of 2003 and 2010 constitute particularly strong manifestations of the contemporary warming of the European climate and abound in proofs of the effects mentioned before. Sources of such anomalies are still to be fully understood. In the temperate zone of Europe the direct causes include stationary high-pressure systems, which normally involve tropical advection and, additionally, strong insolation on long summer days due to the lack of cloud cover typical of high-pressure systems. Various scholars pointed to different primary causes of these anomalies, including ocean thermal conditions [13], especially their surface temperature [14–17], but also a growing concentration of greenhouse gases in the atmosphere [18–20].

This chapter focuses primarily on the frequency of exceptionally hot summer months in Central and Eastern Europe, their spatial extent and the thermal characteristic of the months. Most of the study area is relatively flat and only the south-western part features uplands and two large mountain ranges, i.e. the Carpathian Mts. and Sudety Mts., running predominantly along an east–west axis. This morphology contributes to a great variation in the frequency, intensity, duration and timing of hot spells within a relatively small area [21–23].

This chapter builds on the authors' earlier research on whole summer seasons [1].

2.2 Data and Method

The input to the study involved monthly average, maximum and minimum air temperatures; the number of days with t_{max} >25, 30 and 35 °C (defined respectively as summer days, hot and very hot days); and days with t_{min} >20 °C (tropical nights), as recorded in the summer months (June–August) at 59 weather stations in Central and Eastern Europe in 1951–2010 (Table 2.1). The study area spans 45–60°N and 15–65°E, excluding the Scandinavian Peninsula. The weather records were sourced from an on-line database *European Climate Assessment & Dataset* (ECA&D).

An EHM was defined as a month, in which the average air temperature was higher by at least two standard deviations ($t \geq t_{av.} + 2\sigma$) than the long-term average (1951–2010). The same definition had been applied for extremely hot summers [1, 22].

The study area is predominantly lowland. Indeed, 49 of the 59 weather stations are located below 200 m a.s.l., 7 stations are between 200 and 300 m and only 3 stations are above 300 m a.s.l. (L'viv at 323 m, Praha at 365 m and Cluj at 413 m). Astrachan' lies in a depression at −23 m.

The central and eastern sections of the area, which form the majority, have a moderate continental climate, while a transitional maritime to continental climate

Table 2.1 List of weather stations included in the study (station names after CLINO) [24]

Station			Station			Station		
No.	Name	WMO no.	No.	Name	WMO no.	No.	Name	WMO no.
1	Vaasa	02911	21	Ekaterinburg	28440	41	Orenburg	35121
2	Jyväskyla	02935	22	Berlin	10381	42	Ufa	28722
3	Petrozavodsk	22820	23	Praha	11518	43	Aktobe	35229
4	Arhangel'sk	22550	24	Poznan	12330	44	Zagreb	14236
5	Kotlas	22887	25	Krakow	12566	45	Wien	11035
6	Syktyvar	23804	26	Kaliningrad	26702	46	Budapest	12843
7	Pecora	23418	27	Warszawa	12375	47	Beograd	12840
8	Ivdel'	23921	28	Brest	33008	48	Debrecen	12882
9	Riga	26422	29	Kaunas	26629	49	Cluj	15120
10	Tallinn	26038	30	Minsk	26850	50	L'viv	33393
11	Daugavpils	26544	31	Vasilevici	33038	51	Chernivtsi	33658
12	Tartu	26242	32	Kyiv	33345	52	Bucuresti	15420
13	St. Petersburg	26063	33	Smolensk	26781	53	Chrisinau	33815
14	Moskva	27612	34	Kursk	34009	54	Sulina	15360
15	Vologda	27037	35	Voronez	34122	55	Odesa	33837
16	Kostroma	27333	36	Tambov	27947	56	Kharkiv	34300
17	Niznij Novgorod	27553	37	Saratov	34172	57	Luhans'k	34523
18	Kazan'	27595	38	Aleksandrov-Gaj	34391	58	Astrachan'	34880
19	Kirov	27199	39	Samara	27995	59	Atyrau	35700
20	Perm	28224	40	Ural'sk	35108			

prevails over the western part. The average long-term temperature of the warmest month, i.e. July, ranges from ca. 15 °C in the extreme north of the area to 25 °C and more in the southeast. This is evidence of a wide range of thermal characteristics within the study area. In this context it is important to note that the definition of an EHM is relative, which means that in each case it is related to the average long-term temperature in a given month at a given station. The adoption of this method has two specific consequences:

1. The average air temperature of an EHM ranges widely. For example, in July it may even fall short of 20 °C in the north-east, while in the southeast it must be 10 °C higher to meet the criterion ($t \geq t_{av.} +2\sigma$). This means that an EHM may mean very different thermal conditions in different sections of the same climatic zone.
2. Subsequent summer months with similar average temperatures may or may not qualify as EHMs. For example, in 1972 in Moscow, the average temperature of July was 22.4 °C and 20.6 °C in August, but only the cooler August cleared the threshold ($t \geq t_{av.} +2\sigma$).

2.3   General Characteristic of EHM Occurrence in the Summer Season

During the 60-year period, 326 months met the condition $t \geq t_{av.} +2\sigma$ (3.1 % of all months in the period) at 59 weather stations. These EHMs occurred in 47 calendar months in 33 years of the study period, as shown in Table 2.2. The table also specifies the number of stations where a given EHM occurred and offers the calendar of extremely hot summer seasons (EHS). Interestingly, for statistical purposes there were several EHSs without a single EHM.

The study revealed that EHMs varied very widely in terms of their geographical extent, ranging from one or two stations (13 and 2 EHMs) to more than a half of all stations (one EHM each at 36 and 34 stations).

The EHM count at all stations ranged from 3 to 10, but at a clear majority (41) it was 4–6. There was no clear spatial pattern, as even neighbouring stations differed greatly in the number of occurrences, e.g. Chernivtsi 3, Kyiv 8. Generally, however, they were less numerous (3–4) in the west of the area (from Lithuania to Poland, the Czech Republic, Slovakia to Romania) and at some stations in Russia within the belt 50–55°N, than in Belarus, north-eastern Ukraine and Russia between the Black and Caspian Seas and on the Caspian coast of Kazakhstan (7–10). They were also surprisingly frequent (8) in Pecora, the farthest station to the north-east.

The likelihood of an EHM in June, July and August is virtually identical (15, 16 and 16 cases), but the geographical extent of EHMs clearly increases as the summer progresses from 87 station-months in June to 98 in July and 141 in August (Table 2.2). This would suggest that the gradually warming ground plays a role as a factor in levels of air temperature.

Table 2.2 Calendar of exceptionally hot months (EHM) and summers (EHS) and number of station at which EHM and EHS occurred in Central and Eastern Europe

Year	EHM			EHS	Year	EHM			EHS	Year	EHM			EHS
	Jun	Jul	Aug	Jun–Aug		Jun	Jul	Aug	Jun–Aug		Jun	Jul	Aug	Jun–Aug
1951			2		1971					1991	5			
1952			3		1972		4	19	16	1992	1		17	7
1953			4		1973					1993	1			
1954	2	4		1	1974		1		1	1994		3		
1955					1975	3				1995	1			
1956					1976					1996				
1957			1		1977					1997			3	3
1958					1978					1998	7			3
1959					1979	4				1999	19	1		3
1960		1			1980					2000			1	1
1961					1981			5	8	2001		15		
1962					1982					2002		9	9	10
1963					1983		1			2003	7	3	9	7
1964	11				1984		1	1		2004				
1965					1985					2005				
1966					1986					2006	1	9	5	3
1967					1987					2007	9	3	25	8
1968			3		1988		6		5	2008				
1969					1989	9	1			2009				
1970					1990					2010	7	36	34	39
										Totals	87	98	141	115
													326	

Table 2.3 Years, months and occurrences with EHMs in individual decades of the period 1951–2010 in Central and Eastern Europe

10-years	No. of years	No. of months	No. of occurrences	EHM with the highest extend (number of stations)
1951–1960	6	7	17	4 each in Aug 53 and Jul 54
1961–1970	2	2	14	11 in Jun 64
1971–1980	4	5	31	19 in Aug 72
1981–1990	6	7	24	9 in Jun 89
1991–2000	9	11	59	19 in Jun 99, 17 in Aug 92
2001–2010	6	15	181	34 and 36 in Jul and Aug 10, 25 in Aug 07
1951–2010	33	47	326	36 in Aug 10; 34 in Jul 10

EHMs were distributed highly unevenly during the study period, and increased in frequency after 1990 (Tables 2.2 and 2.3). Until that year, their occurrence was similar at 5–7 per decade, with an exception of just 2 EHMs during the period 1961–1970. In the last decade of the twentieth century, this number increased to 11 EHMs (including 5 at a single station), which trend continued in the first decade of the twenty-first century with 15 EHMs. These latter EHMs occurred simultaneously over large areas, the record of which was in 2010. Also EHMs in the twenty-first century tended to be more concentrated in the same year at 2–3 each.

Individual EHMs spanned different parts of the study area and while they showed no temporal pattern, there was a general increase in their occurrence in European Russia.

2.4 Location, Extent and Thermal Characteristic of Extremely Hot Months

As has already been mentioned, 15 of the 47 EHMs occurred in areas with just 1 or 2 meteorological stations (Table 2.2). Some of these represent an interesting case of EHMs around the edges of the study area (Berlin, Bucuresti, Astrachan'), which may suggest that the EHMs recorded there could have covered a wider territory that fell outside the study area boundaries. These 15 cases will be omitted from an examination of the detailed thermal characteristics of EHMs that follows, as will 15 other EHMs which occurred at only 3–6 stations.

Indeed, only the 17 remaining EHMs which occurred at more than 6 stations (more than 10 % of all stations) are included in the discussion, as they represent the greatest geographical extent and/or greatest temperature increase. All 47 EHMs, however, are included in Table 2.3 and in a summary of all EHMs (Table 2.4).

Table 2.4 Exceptionally hot months (EHM) in Central and Eastern Europe (1951–2010)

Year	Month	No. of stations	Stations (no. according to Table 2.1)
1951	Aug	2	4, 5
1952	Aug	3	47, 49, 52
1953	Aug	4	7, 8, 20, 42
1954	Jun	2	56, 57
	Jul	4	4, 38, 40, 58
1957	Aug	1	7
1960	Jul	1	4
1964	Jun	11	25, 27, 28, 30, 31, 32, 48, 49, **50**, 51, 53
1967	Aug	3	4, 5, 6
1972	Jul	4	2, 13, 15, 16
	Aug	19	3, 4, 5, 6, 13, 14, **15**, **16**, **17**, **18**, 19, 34, **35**, **36**, 37, 38, 39, 56, 57
1974	Jul	1	7
1975	Jun	3	56, 57, 59
1979	Jun	4	26, 27, 28, 48
1981	Aug	5	7, 8, 19, 20, 21
1983	Jul	1	45
1984	Jul	1	43
1985	Aug	1	15
1988	Jul	6	5, 6, 8, 18, 19, 20
1989	Jun	9	4, 5, 6, 7, 8, 16, 19, 20, 21
	Jul	1	21
1991	Jun	5	6, 7, 8, 20, 21
1992	Jun	1	22
	Aug	17	23, 24, **25**, 27, 28, 30, 31, 32, 44, **45**, **46**, 47, **48**, 49, 50, 51, 53
1993	Jun	1	7
1994	Jul	3	22, 23, 45
1995	Jun	1	12
1997	Aug	3	9, 10, 22
1998	Jun	7	38, 39, 40, 41, 43, 58, 59
1999	Jun	19	1, 2, 3, 9, 10, 11, 12, 13, 14, 15, 16, 28, 29, 30, 31, 32, 33, 54, 55
	Jul	1	56
2000	Aug	1	47
2001	Jul	15	3, 9, 11, 12, 14, 30, 31, 32, 33, 34, 35, 54, 55, 56, 57
2002	Jul	9	14, 30, 31, 32, 33, 50, 54, 55, 56
	Aug	9	1, 2, 9, 22, 24, 26, 27, 28, 29
2003	Jun	7	23, 25, **44**, **45**, 46, 47, 49
	Jul	3	1, 2, 9
	Aug	9	7, 8, 21, 22, 23, 44, 45, 46, 47
2006	Jun	1	58
	Jul	9	22, 23, 24, 25, 26, 27, 28, 44, 45
	Aug	5	1, 2, 57, 58, 59

Table 2.4 (continued)

Year	Month	No. of stations	Stations (no. according to Table 2.1)
2007	Jun	9	44, 45, 46, 47, 48, 52, 53, 54, 55
	Jul	3	47, **52**, 53
	Aug	25	3, 10, 12, 13, 14, 15, 16, 17, 18, 19, 30, 34, 35, 36, 37, 38, 39, 40, 41, 42, 55, 56, 57, 58, 59
2010	Jun	7	32, 34, 35, 43, 56, 58, 59
	Jul	36	1, **2**, **3**, 9, **10**, 11, **12**, **13**, **14**, **15**, **16**, **17**, 18, 19, 22, 24, 26, 28, 29, 30, 31, 32, **33**, **34**, **35**, **36**, 37, 38, **39**, 40, 41, 44, 56, 57, 58, 59
	Aug	34	11, 12, 13, **14**, 15, 16, 17, 18, 21, 28, 29, 30, **31**, **32**, **33**, **34**, **35**, **36**, **37**, 38, **39**, 40, 41, 42, 43, 50, 51, 53, 54, **55**, **56**, 57, 58, 59

Notes: Station numbers printed in bold mean that the average temperature met the formula $t \geq t_{av.}+3\sigma$

2.5 EHMs During 1951–2000
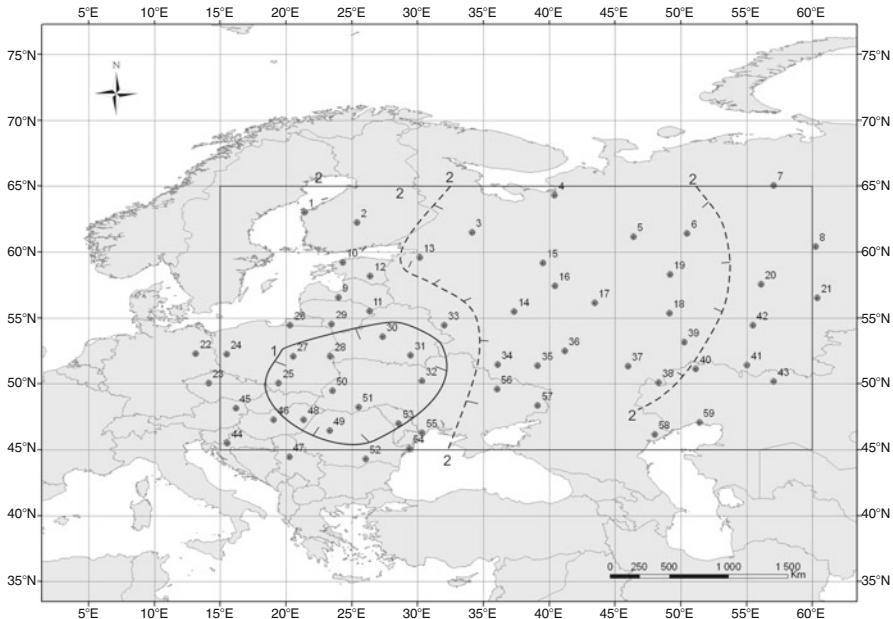
During the first 50 years of the study period, only six EHMs extended to more than 10 % of the stations (Table 2.2).

June 1964 (Fig. 2.1, Table 2.5) was an EHM in the south-western part of the area covering sections of Poland, Belarus, Slovakia, Hungary, western Ukraine and northern Romania (Fig. 2.1). The EHM centred on L'viv where the temperature reached $t \geq t_{av.}+3\sigma$ (the anomaly, or Δt, in L'viv was 4.2 °C, and outside L'viv it ranged from 2.5 to 4.0 °C). At most of the stations this was the hottest June in the study period. Hot days were recorded across the area.

August 1972 (Fig. 2.1, Table 2.5) was the first EHM of the period, which covered nearly all of the European part of Russia (Δt from 3.0 to 6.5 °C). In its central section the anomaly reached three standard deviations from the long-term average, or more than 5 °C, including 6.1 °C in Voronez and 6.5 °C in Tambov. (There were only 13 cases where the long-term average temperature was exceeded by more than 6.0 °C). At some of the stations this was the hottest August of the study period. Hot days were recorded across the area (e.g. 7 in St. Petersburg compared to an average of once in 3 years and ca. 20 in the south compared with ca. 5 on average). In the southern half of the EHM area there were cases of the very rare tropical nights (e.g. 8 in Kharkiv, 1–2 on average). The summer of 1972 proved an EHS and the month was the hottest in Finland and northern Russia and the second most expansive EHS during the study period [28].

June 1989 (Table 2.5). The EHM covered the entire north-eastern part of the European Russia (Δt from 4.2 to 5.5 °C). At a majority of the stations it was the warmest EHM of the study period. Hot days were observed at all stations.

August 1992 (Fig. 2.2, Table 2.5) The EHM covered a south-western part of the area, including the larger part of Poland in the south. In most of the area the average

Fig. 2.1 Geographic coverage of the exceptionally hot month of June 1964 (1) and August 1972 (2)

temperature exceeded the long-term average by more than 3 °C (Δt from 2.9 °C in Poznan to 5.0 °C in Wien; in Wien, Budapest, Debrecen and Krakow the anomaly exceeded three standard deviations). At nearly all stations (excluding those located at the edge of the area) this was the hottest August of the period. The maximum temperatures were very high, hot days were recorded at all stations and there were also some very hot days. Krakow had the highest frequency of very hot days (t_{max}>35 °C; 13 cf an average of 1 day every 2 years). These exceptionally high temperatures in Krakow could be explained both by the foehn effect and a vast forest fire at Kuźnia Raciborska 120 km to the west [25]. In the south of the area there were many instances of tropical nights (t_{min}>20 °C = ca. 20, cf an average of ca. 4).

In Poland, Slovakia, Czech Republic and Hungary the summer of 1992 was classified as an EHS. It was also the hottest summer of the period in southern Poland and Krakow's only EHS [28].

June 1998 (Table 2.5) was the first EHM to cover the southeast of the study area starting from the latitude of Samara to the Caspian Sea. It was the hottest June in this territory in the study period (Δt from 3.5 to 4.7 °C). Both the maximum and minimum temperatures were very high and all stations recorded both hot and very hot days (e.g. 20 hot and 9 very hot days at Orenburg, cf 9 and 2 on average; 26 and 12 at Atyrau, cf 17 and 5 on average) and tropical nights (e.g. 8 in Orenburg, cf 1 on average and 19 at Atyrau, cf 8 on average).
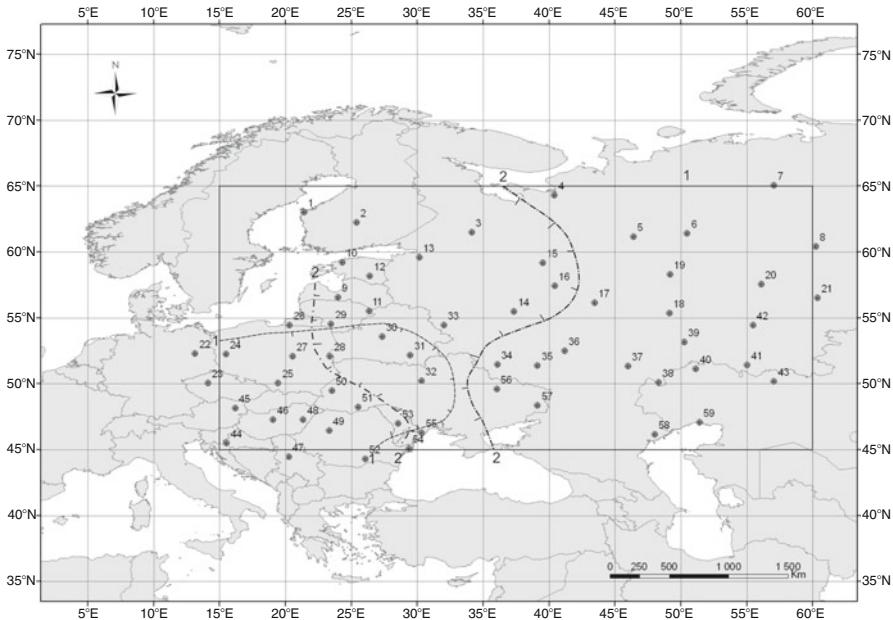
Table 2.5 Thermal characteristic of the EHM: June 1964, August 1972

Station		Temperature (°C)			Number of days with temperature			
					T_{max}		T_{min}	
No.	Name	Average	Max	Min	>25 °C	>30 °C	>35 °C	>20 °C
June 1964								
27	Warszawa	20.0	25.7	13.6	17	6	–	–
32	Kyiv	22.3	28.1[a]	16.9	26[a]	9	–	1
50	L'viv	**20,6**[a]	**26,6**[a]	14.1	21[a]	3[a]	–	–
August 1972								
4	Arhangel'sk	17.1	23.3[a]	11.9	12[a]	1	–	–
13	St. Petersburg	19.9[a]	24.7[a]	15.8	16[a]	7[a]	–	4
14	Moskva	20.6	**27.6**[a]	14.1	21[a]	13	–	–
17	Niznij Novgorod	**22.7**[a]	27.1	17.2[a]	20	10	–	8
35	Voronez	**25.0**	**31.9**	**18.1**[a]	27[a]	22[a]	8	8
56	Kharkiv	23.9	30.2	17.6	26[a]	19	3	8
June 1989								
4	Arhangel'sk	17.6[a]	24.0[a]	11.5	16[a]	1	–	–
7	Pecora	17.2	24.6[a]	10.7	17[a]	4	–	1
20	Perm	21.0[a]	27.2[a]	14.5[a]	23[a]	5	–	–
21	Ekaterinburg	23.1[a]	28.0[a]	15.3[a]	27[a]	6	–	–
August 1992								
25	Krakow	**22.0**[a]	**30.2**[a]	15.4	27[a]	16[a]	13[a]	1
32	Kyiv	22.9	30.0	17.4	27	12	–	2
45	Wien	**25.1**[a]	**31.5**[a]	**18.7**[a]	30[a]	21[a]	3[a]	9[a]
47	Beograd	26.8[a]	33.6[a]	20.6[a]	31[a]	28[a]	11[a]	20[a]
June 1998								
41	Orenburg	24.8[a]	31.9	16.8[a]	27[a]	20[a]	9	8
58	Astrachan'	26.6[a]	33.3[a]	20.2[a]	30[a]	23	10[a]	16[a]
June 1999								
2	Jyväskyla	17.7[a]	23.5[a]	11.8[a]	10	–	–	–
13	St. Petersburg	20.5[a]	25.9[a]	15.7[a]	18[a]	4	–	3[a]
14	Moskva	21.4[a]	27.2[a]	14.4	22[a]	6	–	–
30	Minsk	21.1[a]	26.9[a]	15.4[a]	22[a]	5[a]	–	–
32	Kyiv	22.6[a]	28.1[a]	17.1[a]	23	11[a]	–	3
55	Odesa	22.8	27.6[a]	18.4	24	5	–	7

Notes: a value in bold means that the temperature meets the criterion t $\geq$ t$_{av.}$+3σ
[a]Highest in 60 years

June 1999 (Fig. 2.2, Table 2.5) was one of the most extensive EHMs, ranging from Finland to north-western Russia, the Baltic states (but not Poland), Belarus, and central Ukraine to the Black Sea. Across its territory it was the hottest June in the study period (Δt from 2.4 to 3.0 °C in the south, to 4.3–5.0 °C in the centre to 3.3–3.9 °C in the far north). The maximum temperatures were particularly high with hot days at all stations, especially in Kyiv (11, cf. 2 on average), but no very hot days.

Fig. 2.2 Geographic coverage of the exceptionally hot month of August 1992 (1) and June 1999 (2)
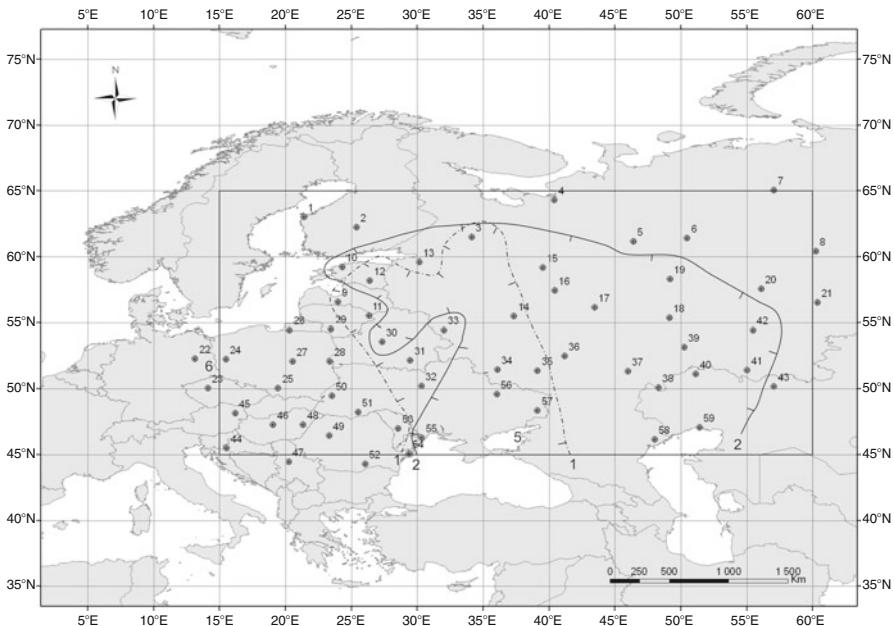
2.5.1 EHMs During 2000–2010

There were nearly twice as many EHMs (11) during the last decade of the study period, which were observed at more than 10 % of the stations than during the previous 50 years (Table 2.2).

July 2001 (Fig. 2.3, Table 2.6). The EHM covered an area stretching from Estonia, Latvia, eastern Lithuania, Belarus and the Ukraine without its western part and the western edge of Russia. In the centre of the area, the average temperature was more than 4 °C higher than the long-term average (Δt across the area from 3.1 to 4.9 °C). Hot days were recorded at all the stations, very hot days in the south (e.g. 16 hot and 4 very hot days in Kharkiv, on average every 4 and 5 years) and also tropical nights at nearly all stations, especially on the Black Sea coast (13 in Kharkiv, 26 in Odesa; cf averages of 2 and 7 respectively).

July 2002 (Table 2.6). The EHM covered more or less the same area as the year before, apart from the far north, but including the whole of the Ukraine (Δt from 3.0 to 3.9 °C). Just as in the previous year, hot days were recorded across the board, but very hot days only in the far south. Tropical nights occurred everywhere.

August 2002 (Table 2.6). This was the second consecutive EHM that year, but this time only at the north-western end of the study area stretching from Finland to the northern half of Poland (Δt from 2.7 to 4.0 °C). At certain stations (Jyvaskyla,

Fig. 2.3 Geographic coverage of the EHM of July 2001 (1) and August 2007 (2)

Riga, Kaliningrad, Poznan) this was the hottest August of the study period. There were isolated hot days.

In addition the entire summer season of 2002 was classified as an EHS at a few stations in the western part of the study area.

In 2003, all summer the months qualified as EHMs, but only in June and August were more than 10 % of the stations involved (Table 2.2). In these months, the EHM area covered a south-western section of the study area (Δt from 2.3 to 3.3 °C), which was on the periphery of an EHS observed throughout Western Europe. There the exceptional heat wave contributed to higher death rates and to an increased rate of melting of Alpine glaciers noted in several studies [e.g. 4, 18, 19, 23, 26–29].

June 2003 (Table 2.6) was an EHM in Western Europe, which only covered the south-western edge of the study area from Praha and Krakow to Beograd (Δt from 2.8 to 4.6 °C). At nearly all of the stations it was the hottest June of the study period. In Wien and Zagreb the average temperature climbed to $t \geq t_{av.}+3\sigma$. Hot days were recorded at all stations, but there were only sporadic cases of very hot days.

August 2003 (Table 2.6) was the second case, 49 years after July 1954, of a dual-area EHM: one in the foreland of the Ural Mountains to the east of the area (Δt from 4.2 to 5.1 °C, the hottest August of the study period) and the other in the far south-west stretching from Berlin to Beograd (Δt from 2.7 to 4.6 °C). Again, like in June, this latter area was on the periphery of a powerful EHM that covered Western Europe and featured the greatest temperature increase rate during the study period. The single largest temperature anomaly was recorded in the south-western

Table 2.6 Thermal characteristics of the EHM: July 2001, July and August 2002

Station		Temperature (°C)			Number of days with temperature			
					T_{max}		T_{min}	
No.	Name	Average	Max	Min	>25 °C	>30 °C	>35 °C	>20 °C
July 2001								
9	Riga	21.7	26.8	13.0?	20	5	–	–
14	Moskva	23.0	28.4	17.8	27	10	–	5
30	Minsk	22.1	27.5	17.5	24	7	–	6
32	Kyiv	24.6	30.3[a]	19.5	31[a]	16	–	10
35	Voronez	24.1	30.6	18.2	31[a]	15	3	6
55	Odesa	26.0[a]	30.6[a]	21.7[a]	31[a]	20[a]	1	26[a]
July 2002								
14	Moskva	22.6	28.3	16.3	26	8	–	2
30	Minsk	22.0	27.9[a]	16.5	25[a]	7	–	2
32	Kyiv	23.9	29.7	18.7	28	20[a]	–	11
50	L'viv	21.0[a]	26.6	15.8[a]	20	5	–	1[a]
55	Odesa	25.6	30.4	21.1	30	17	3[a]	20
August 2002								
2	Jyväskyla	17.0[a]	23.5[a]	10.3	11[a]	–	–	–
9	Riga	20.9[a]	26.1[a]	13.6	28[a]	2	–	–
22	Berlin	20.6	26.2	15.9[a]	25[a]	1	–	–
27	Waszawa	20.7	26.8	15.0	25	2	–	–
June 2003								
25	Krakow	19.1[a]	25.9[a]	14.3	17	3	–	–
45	Wien	**22.6**[a]	**28.1**[a]	**17.0**[a]	25[a]	9	–	3
47	Beograd	25.0[a]	30.8[a]	**19.2**[a]	28[a]	18[a]	2	12[a]
August 2003								
7	Pecora	17.4[a]	22.5	13.5[a]	9	2[a]	–	–
21	Ekaterinburg	20.4[a]	26.1	15.7[a]	20	6	–	1
22	Berlin	20.5	26.9	14.3	19	9[a]	–	–
45	Wien	24.4	**30.8**	17.9	30[a]	18	2	5
47	Beograd	25.6	32.2	19.3	31[a]	24	4	9
July 2006								
22	Berlin	23.2[a]	29.8[a]	16.3[a]	29[a]	15[a]	1	2[a]
25	Krakow	21.3[a]	29.7[a]	15.7	26	18[a]	3	–
27	Warszawa	23.1[a]	30.0[a]	16.2	29[a]	18[a]	1	2
45	Wien	24.1[a]	29.8[a]	18.3[a]	26	17[a]	–	6[a]
June 2007								
45	Wien	21.5	27.0	15.8	22	3	–	–
52	Bucuresti	23.3[a]	31.4[a]	15.0	29	20[a]	1	1
55	Odesa	23.4[a]	27.0	18.9[a]	28[a]	7	–	8
August 2007								
13	St. Petersburg	19.7	24.1	15.4	16[a]	3	–	1
14	Moskva	20.2	25.7	14.7	18	9	–	1
34	Kursk	21.8	27.6	16.1	21	12	1	2
39	Samara	24.0	28.9	17.5[a]	28[a]	14	–	10[a]
41	Orenburg	24.3	32.0[a]	16.1	29[a]	25[a]	6	5

Table 2.6 (continued)

Station		Temperature (°C)			Number of days with temperature			
					T_{max}		T_{min}	
No.	Name	Average	Max	Min	>25 °C	>30 °C	>35 °C	>20 °C
55	Odesa	24.7	28.7	20.6[a]	28	10	3	17
58	Astrachan'	27.4	35.1	20.4[a]	31[a]	30[a]	19[a]	16

Notes: a value in bold means that the temperature meets the criterion $t \geq t_{av.}+3\sigma$
[a]Highest in 60 years

part of the Massif Central, France (Gordon weather station) [12]. In the western part of the study area the summer of 2003 also qualified as an EHS.

July 2006 (Table 2.6) was an EHM in the west and stretched from Poland to western Hungary and Croatia and, just as in 2003, it was part of an EHM centred on Western Europe. Throughout the area affected it was the hottest July in the study period (Δt from 2.8° in Zagreb to 5.2 °C in Poznan). Hot days occurred very frequently at all stations (e.g. 18 each in Warszawa and Krakow, cf 3–4 on average), while very hot days were sporadic.
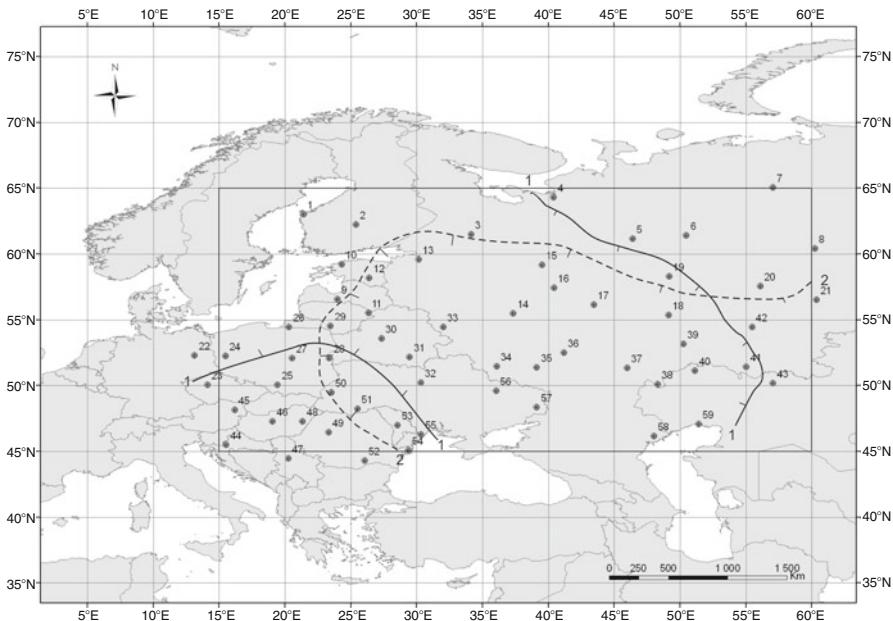
The summer of 2007 again involved three EHMs, even if July only covered 5 % of the stations. In the south-western part of the area the season qualified as EHS.

June 2007 (Table 2.6). The EHM covered a small area in the south-west to the south of the line Vienna-Odessa and was part of a larger EHM in the Balkan Peninsula. In the east of the affected area, Bucuresti to Odesa, this was the hottest June during the study period (Δt from 2.7 to 3.7 °C, except Sulina 2.2 °C). Throughout the area hot days and tropical nights were commonly recorded, but very hot days were only recorded sporadically.

August 2007 (Fig. 2.3, Table 2.6) covered the largest area to that date, including a larger south-eastern part of European Russia, parts of Estonia, Latvia and Belarus, eastern Ukraine and western Kazakhstan. The long-term average was exceeded by ca. 3 °C in the north, by 3.5–4.5 °C in the south and by ca. 5 °C in the centre (Δt from 2.8 to 5.3 °C). Hot days were recorded throughout the area, from 2 to 3 in the north (cf an average of once every few years) to 30–31 on the Caspian coast (cf an average of 18–20), where very hot days peaked in frequency (19–22, cf an average of 3–6). Tropical nights were also observed throughout the area with the record numbers on the Black Sea and Caspian coasts (Odesa 17, cf an average of 7; Atyrau 25, cf an average of 10).

The most intense heat wave of 2007 was recorded in the Balkan Peninsula [30].

All three summer months of 2010 qualified as EHMs, but for the first time their coverage was similar, especially in July and August (Fig. 2.4). The latter two were also the EHMs with the largest territorial extent during the study period. Both had a similar coverage to August 2007, including a western part of the European Russia, Belarus, the Ukraine and western Kazakhstan. In an earlier study the authors [28]

Fig. 2.4 Geographic coverage of the EHM of July (1) and August (2) 2010

found that the average temperature at certain Russian stations exceeded the long-term averages by up to 4σ.

June 2010 (Table 2.7). The EHM was split into two relatively small areas: one from Kyiv to Voronez along the border between Russia and the Ukraine (Δt from 3.4 to 4.0 °C) and the other in the southeast from Astrachan' to Aktobe (Δt from 3.1 to 4.9 °C). At most of these stations this was the hottest June during the study period. Tropical nights were recorded at all stations and very hot days at nearly all of them.

July 2010 (Fig. 2.4, Table 2.7). The EHM covered an area of record size stretching from the Baltic coast to the eastern part of the Black Sea and the Caspian Sea. At all stations, except Berlin and Poznan, it was the hottest July during the study period. Everywhere the average long-term temperature was exceeded by more than 3.5 °C and in the central part of the area affected by more than 5 °C, including by more than 6 °C at 8 stations (record Δt values: 6.9 °C at Kursk and 6.8 °C in Moscow and Tambov). At 14 stations from Jyvaskyla to Samara the average monthly temperature equalled $t \geq t_{av.}+3\sigma$. Hot days were observed throughout the area; from 5 at Jyvaskyla (an average of once in 3 years), 14 at St. Petersburg (on average 1) to 23–25 at Kursk and Voronez (on average 3–6) and 31 (on all days of the month) on the Caspian Sea (on average 21–24). In the central and south-eastern part of the area there were also very hot days (e.g. 7–9 at Kursk and Voronez, on average once in a few years; 24 at Atyrau, on average 9). Tropical nights were also recorded at all stations and at most of them at record levels,

Table 2.7 Thermal characteristics of the EHM in 2010

Station		Temperature (°C)			Number of days with temperature			
					T_{max}			T_{min}
No.	Name	Average	Max	Min	>25 °C	>30 °C	>35 °C	>20 °C
June 2010								
32	Kyiv	22.0	27.3	16.6	22	8	–	3
34	Kursk	21.9[a]	27.4	16.5	21	8	1	1
58	Astrachan'	26.2	32.5	19.0	30[a]	25	7	14
July 2010								
2	Jyväskyla	**20.9**[a]	26.8[a]	14.9[a]	22[a]	5[a]	–	1
9	Riga	22.1[a]	27.3[a]	12.7?	21[a]	11[a]	–	3
13	St. Petersburg	**24.5**[a]	**28.9**[a]	**20.1**[a]	26[a]	14[a]	1[a]	16[a]
14	Moskva	**25.6**[a]	**32.1**[a]	**19.1**[a]	31[a]	22[a]	9[a]	16[a]
22	Berlin	22.2	28.4	15.4	22	11	3[a]	2[a]
32	Kyiv	25.0[a]	30.3[a]	19.6	31[a]	17	1[a]	13[a]
34	Kursk	**26.1**[a]	**32.1**[a]	**20.3**[a]	31[a]	23[a]	7[a]	17[a]
39	Samara	**26.8**[a]	**33.2**[a]	17.5	30[a]	25[a]	15[a]	6
41	Orenburg	25.9[a]	33.4	18.4[a]	30	25[a]	15[a]	11[a]
58	Astrachan'	29.1[a]	36.1[a]	21.5[a]	31[a]	31[a]	20[a]	26[a]
August 2010								
13	St. Petersburg	19.8	23.6	16.1[a]	14	5	1[a]	6[a]
14	Moskva	**21.5**[a]	27.4	**15.6**[a]	19	16	7[a]	8[a]
21	Ekaterinburg	19.5	24.5	14.4	15	10[a]	2[a]	8[a]
32	Kyiv	**25.2**[a]	**31.2**[a]	**19.1**[a]	23	19[a]	13[a]	18[a]
34	Kursk	**25.2**[a]	**31.2**[a]	**19.3**[a]	23	20[a]	13[a]	19[a]
39	Samara	**25.0**[a]	30.2[a]	14.6?	25	17	12[a]	9?
41	Orenburg	24.7[a]	32.0[a]	17.0[a]	26	21	14[a]	6
55	Odesa	**26.4**[a]	31.1[a]	20.5	28	17[a]	7[a]	21[a]
58	Astrachan'	27.7[a]	35.5[a]	19.0?	30	27	16	16

Notes: a value in bold means that the temperature meets the criterion $t \geq t_{av.}+3\sigma$
[a]Highest in 60 years

including the only occurrence during the study period at Jyvaskyla, 16 each in St. Petersburg and Moscow (less than one on average) and 26–27 at Astrachan' and Atyrau (on average 13–14).

August 2010 (Fig. 2.4, Table 2.7) This EHM by-and-large overlapped with the territory of the July EHM, but included a shift to the east into the southern Ural Mts., at the cost of northern and western coverage (Δt from 2.7 to 7.0 °C). In its central section it was the hottest August during the study period. Here, in the central part of European Russia and the neighbouring part of Ukraine, the average monthly temperature reached $t \geq t_{av.}+3\sigma$, which in absolute terms typically meant 5 °C. In the town of Kursk, which recorded the greatest anomaly at $t \geq t_{av.}+3.9\sigma$, or 7.0 °C, as well as in Kiev, Kharkiv and Voronez, this was the third consecutive EHM, a sole event of the type during the study period. All the stations within the EHM area recorded hot days, ranging from 5 in St. Petersburg (on average once in

3 years), to 16 in Moscow (on average 1), 20 at Kursk (on average 2) to 27 at Astrachan' (on average 18). Very hot days were also recorded by most stations where they typically reached the highest frequency during the study period. Moscow with its 7 very hot days (after 9 such days in July) stood out particularly, as they included the sole case of a maximum temperature above 35 °C during the study period. On the Caspian coast the incidence of very hot days, common in the area, was 3–5 times greater than the average. Tropical nights were noted almost at all stations, including 19 at Kursk (on average less than 1) and 8 in Moscow (on average once in 5 years), while in the far south of the territory affected they were 2–3 times more frequent than on average.

The final year of the study period was unique within its decade with two consecutive EHMs with the greatest spatial scale and greatest temperature increase. This long spell of exceptionally high temperatures caused a considerable deterioration in living conditions and highly adverse economic effects as it contributed to the development of vast wildfires, which, in turn, caused the levels of air pollution in Moscow to rise by 2–3 times [31]. The wildfires may have also made a considerable contribution to the scale of the temperature increase [1]. This proposition is supported by a study on an EHS of 1992 in Poland [25].

2.6   Conclusions

During the period 1951–1960, 47 exceptionally hot summer months (EHMs) of varying territorial extent occurred in Central and Eastern Europe. In total 22 EHMs covered areas represented by 1–3 out of the total 59 stations (5 %), 30 EHM were recorded by 6 stations (10 %) and only 7 EHMs occurred in areas with more than 15 stations (more than 25 %).

The EHMs with small station coverage must be seen in the context of the boundaries of the study area, beyond which many EHMs might indeed have continued.

A vast majority of the EHMs occurred in a single area and there were only three EHMs, which had two separate locations during the study period (July 1954, August 2003 and August 2006).

EHMs did not display any specific spatial or temporal patterns of occurrence, although there were temporary trends when they concentrated in a similar area, including 4 EHMs in the far north-west (1981–1991), 5 EHMs in the far south-west (twenty-first century), and a series of EHMs in European Russia (2007 and 2010). During the study period, the frequency of EHMs increased after 1990 and further still after 2000.

These latest EHMs grew in size and frequency to 2 or even 3 in the same year, sometimes in the same area. The persistence of exceptionally hot spells increased while the deviation of the average temperature from the long-term average was often greater than ever before. This constitutes an unquestionable example of the contemporary global warming.

The most intense and vast EHMs in the area included: August 1972 (Russia), August 1992 (the south-west), June 1999 (broad belt from Finland to the Black Sea), August 2007 (Russia) and July and August 2010 (Russia). The persistence of exceptionally hot spells increased while the deviation of the average temperature from the long-term average was often greater than ever before. This constitutes an unquestionable example of the contemporary global warming.

References

1. Twardosz R, Kossowska-Cezak U (2012) Exceptionally hot summers in central and eastern Europe (1951–2010), Theor Appl Climatol 112:617–628. doi:10.1007/s00704-012-0757-0
2. Błażejczyk K, McGregor G (2007) Warunki biotermiczne a umieralność w wybranych aglomeracjach europejskich. Przegląd Geograficzny 3–4:401–423
3. Hutter HP, Moshammer H, Wallner P, Leitner B, Kundi M (2007) Heatwaves in Vienna: effects on mortality. Wien Klin Wochenschr 119(7–8):223–227
4. Twardosz R (2009) Fale niezwykłych upałów w Europie na początku XXI wieku. Przegląd Geofizyczny 3–4:193–204
5. Muthers S, Matzarakis A, Koch E (2010) Climate change and mortality in Vienna—a human biometeorological analysis based on regional climate modeling. Int J Environ Res Public Health 7:2965–2977
6. Barriopedro D, Fischer EM, Luterbacher J, Trigo RM, García-Herrera R (2011) The Hot summer of 2010: redrawing the temperature record map of Europe. Science 332 (6026):220–224
7. Revich BA, Shaposhnikov DA (2012) Climate change, heat waves, and cold spells as risk factors for increased mortality in some regions of Russia. Stud Russ Econ Dev 23(2):195–207
8. Meehl GA, Tebaldi C (2004) More intense, more frequent, and longer lasting heat waves in the 21st century. Science 305:994–997
9. Révész A (2008) Stochastic behaviour of heat waves and temperature in Hungary. Appl Ecol Environ Res 6(4):85–100
10. Kürbis K, Mudelsee M, Tetzlaff G, Brázdil R (2009) Trends in extremes of temperature, dew point, and precipitation from long instrumental series from central Europe. Theor Appl Climatol 98:187–195
11. Bardin MY (2011) Scenary forecasts of air temperature variations for the regions of the Russian Federation up to 2030 using the empirical stochastic climate models. Russ Meteorol Hydrol 36(4):217–228
12. Fischer EM, Schär C (2010) Consistent geographical patterns of changes in high-impact European heat waves. Nat Geosci 3:398–403
13. Black E, Sutton R (2007) The influence of oceanic conditions on the hot European summer of 2003. Clim Dyn 28:53–66
14. Della-Marta PM, Luterbacher J, von Weissenfluh H, Xoplaki E, Brunet M, Wanner H (2007) Summer heat waves over western Europe 1880–2003, their relationship to large-scale forcings and predictability. Clim Dyn 29:251–275
15. Feudale L, Shukla J (2011) Influence of sea surface temperature on the European heat wave of 2003 summer. Part I: an observational study. Clim Dyn 36(9–10):1691–1703
16. Dole R, Hoerling M, Perlwitz J, Eischeid J, Pegion P, Zhang T, Quan XW, Xu T, Murray D (2011) Was there a basis for anticipating the 2010 Russian heat wave? Geophys Res Lett 38, L06702. doi:10.1029/2010GL046582

17. Zveryaev I, Zyulyaeva Yu, Gulev S, Koltermann P (2012) Intercomparison of the Russian Summer HeatWaves of 2010 and 1972. Geophysical Research Abstracts, 14: EGU2012-9714, 2012, EGU General Assembly 2012

18. Schär C, Vidale PL, Lüthi D, Frei C, Häberli C, Liniger MA, Appenzeller C (2004) The role of increasing temperature variability in European summer heatwaves. Nature 427:332–336

19. Stott DA, Stone DA, Allen MR (2004) Human contribution to the European heatwave of 2003. Nature 432:610–614

20. Gruza GV, Ran'kova EYA (2011) Estimation of probable contribution of global warming to the genesis of abnormally hot summers in the European part of Russia. Izvestiya, Atmospheric Oceanic Physics 47(6):661–664

21. Gerstengarbe FW, Werner PC (1992) The time structure of extreme summers in central Europe between 1901 and 1980. Meteorol Zeitschrift NF 1:285–289

22. Filipiuk E, Kaszewski BM (2000) Hot and cold summer in Central Europe (1871–1990). Prace Geograficzne 108:149–154

23. Twardosz R, Batko A (2012) Heat waves in Central Europe (1991–2006). Int J Global Warming 4:261–272, Nos 3/4

24. WMO (1996) Climatological normals (CLINO) for the period 1961–1990. WMO, Geneva

25. Kossowska-Cezak U (1993) Lato roku 1992 w Polsce na tle sezonów letnich ostatnich 120 lat. Przegląd Geofizyczny 1:67–74

26. Auswirkungen des Hitzesommer 2003 auf die Gewässer. Dokumentation. 2004, Schriftenreiche Umwelt, Nr 369. Gewässerschutz, Bern

27. Fink AH, Brücher T, Krüger A, Leckebusch GC, Pinto JG, Ulbrich U (2004) The 2003 European summer heatwaves and drought—synoptic diagnosis and impacts. Weather 59 (8):209–216

28. Chase TN, Wolter RA, Pielke SR, Rasool I (2006) Was the 2003 European summer heat wave unusual in a global context? Geophys Res Lett 33:L23709

29. D'Ippoliti D, Michelozzi P, Marino C, de'Donato F, Menne B, Katsouyanni K, Kirchmayer U, Analitis A, Medina-Ramón M, Paldy A, Atkinson R, Kovats S, Bisanti L, Schneider A, Lefranc A, Iñiguez C, Peruccilet CA (2010) The impact of heat waves on mortality in 9 European cities: results from the EuroHEAT project. Environ Health 9(37):1–9

30. Founda D, Giannakopoulos C (2009) The exceptionally hot summer of 2007 in Athens, Greece—A typical summer in the future climate? Global Planet Change 67(3–4):227–236

31. Zvyagintsev AM, Blum OB, Glazkova AA, Kotel'nikov SN, Kuznetsova IN, Lapchenko VA, Lezina EA, Miller EA, Milyaev VA, Popikov AP (2011) Air pollution over European Russia and ukraine under the hot summer conditions of 2010. Izvestiya, Atmospheric Oceanic Physics 47(6):699–707

Chapter 3
Spatial Correlations and Distributions of Heating and Cooling Degree-Day Normals in Turkey

Ilhami Yildiz, Jin Yue, Tri Nguyen-Quang, Joshua Lowrey, and Asena Cansu Yildiz

Abstract This study provides knowledge and basic information concerning the spatial correlations and distribution characteristics of heating and cooling degree-day normals in Turkey at the base temperatures of 5, 10, 15, and 20 °C, and 18 and 24 °C, respectively. The heating and cooling degree-day data are analyzed by multiple regression and spatial correlations developed using as regressors altitude, latitude, and longitude. With other variables held constant, heating degree-day values are positively related to altitude and latitude. The effects of regressors altitude and latitude are both significant, but not that of longitude. Altitude is determined to be the most influential regressor on the heating degree-day distributions. With other variables held constant, cooling degree-day values are negatively related to altitude and latitude while positively related to longitude. The effects of regressors altitude, latitude, and longitude are all significant. Latitude is determined to be the most influential regressor.

Keywords Heating degree-day • Cooling degree-day • Spatial correlations • Climatic normals • Spatial distributions • Multiple regressions • Turkey

I. Yildiz (✉) • J. Yue • T. Nguyen-Quang • J. Lowrey
Department of Engineering, Dalhousie University, Faculty of Agriculture,
Truro-Bible Hill, NS B2N 5E3, Canada
e-mail: iyildiz@dal.ca

A.C. Yildiz
Department of Political Science, and Department of Geography
(Environment and Sustainability Program), The University of British Columbia,
Vancouver, BC V6T 1Z4, Canada

Nomenclature

D   Degree-day
N   Period of time
T   Temperature, °C
Alt   Altitude, m
Lat   Latitude, degrees
Long   Longitude, degrees

Greek Letters

Σ   Total

Subscriptions

b   Base
c   Cooling
d   Mean daily
h   Heating
j   Variable
max   Daily maximum
min   Daily minimum

3.1   Introduction

Reliable methods to estimate a building's seasonal energy use are needed to evaluate expected operating costs and possible savings from energy conservation methods. For instance, the value of additional insulation or preheated ventilating air depends on the expected reduction in energy use during the heating season [1]. Methods to predict energy use during the heating season include the degree-day method, the bin or temperature frequency method, and more complex simulation methods. This chapter presents the heating and cooling degree-day data (normals) development in Turkey, but not bin method or simulation. Degree-day method is commonly used to estimate energy consumption for heating and cooling in residential, commercial, and industrial buildings, as well as in greenhouses, storages, and warehouses [2–4]. This approach is also used for plant and insect growth, and freezing and thawing of soil and water surfaces [2, 5–15]. Estimating energy requirements and fuel consumption of heating, ventilating, and air conditioning (HVAC) systems for any period of time can be a difficult task due to the many dynamic factors which influence energy requirements. Therefore, the most reliable method for estimating future energy requirements of a building is the past

operating experience. If such records do not exist, then calculations for estimating energy requirements are often necessary, especially for new buildings.

Tests conducted in the 1930s and 1940s showed that fuel consumption for heating in residences and public buildings varied directly with the difference between average daily outside temperature and 18 °C [1]. When the outside temperature was 18 °C, essentially no heat was required and fuel consumption approached zero. The difference between 18 °C and the average daily outside temperature is an index of heating requirements and is the basis for the heating degree-day method.

Degree-days vary greatly from place to place and also slightly from year to year. A normal heating or cooling season also varies from country to country, or from city to city depending on local climate and regulations. It should be kept in mind that the degree-day procedure is simple, but gives only a rough estimate. Inaccuracies result from minor variations in degree-days from year to year, local wind conditions, unusual exposures, and wide variations in internal heat sources. Degree-day energy estimates are much more accurate if past operating expenses are known. The degree-day procedure is not a recommended method for animal buildings, which have large internal heat production and low balance point temperatures [1].

As discussed above, the degree-day base for most residences was set at 18 °C in the 1930s and 1940s. However, residences today have much higher insulation levels and sensible heat production inside has increased tremendously. Balance point temperatures for residences are now substantially below the original heating degree-day baseline temperature of 18 °C. There are two ways to adjust for this difference. The first is to determine the number of degree-days with a base temperature equal to the balance point temperature of the building in hand. However, it would be a difficult task to accurately calculate the balance point temperature for a residence. The second is to use an empirical correction factor, which roughly accounts for internal and solar heat gains and varies with the severity of the climate. Typical values for this correction factor are provided by [1].

Climatic zones in Europe have been defined on the basis of the amount of heating and cooling degree days, working with selected European cities (including three major Turkish cities) [16]. The approach is orientated mainly towards the assessment of building energy performance; therefore, the outcomes are evaluated with regard to the actual heating and cooling energy needs of a reference building (office use) located in the representative cities of the proposed climatic zones, and facing the four cardinal orientations.

In a recent study, using a time period of 1900–2008, the variability and trends of heating degree-days in Argentina have been studied [17]. Spatial variations are driven by latitude and altitude. The analysis of temporal distribution of heating degree-days reveals that the center of the mean heating season varies from mid-June to mid-July, which corresponds to mid-winter, the temporal center of the heating season. Cold season are longer, and the length of the cold season extends with increasing latitude and westward with increasing altitude. Heating seasons are

longer due to delayed beginning of summer. And in the high Andes, the heating season extends all year around.

In another study, the impacts of climate change in the Northern Pacific Coast on related regional scale energy demands have been studied [18]. Cooling degree-days at 237 stations in the State of California are studied for the 1970–2007 period, and most of the locations show an increase in cooling degree-days over this period possibly as a consequence of global warming. However, most sites located near the coast have a decrease in cooling degree-days for the same period and this effect is attributed to intensified sea breeze flows, which suggests increases in cold marine air intrusions over coastal land masses due possibly to an increased regional sea breeze potential, which ventilates coastal areas, helps reduce maximum temperatures, and contributes to decrease in cooling degree-day accumulations [19]. It has been shown that coastal cooling is present along the entire California coast. This effect takes place in a narrow strip line roughly 100 km from the coast and extends from north to south along the California coast. On the other hand, locations with increasing temperatures are mostly located away from the coast or at high elevations where marine influences are no longer important and the global warming effects are more relevant.

The spatial and temporal characteristics of Turkish seasonal cooling degree-days and heating degree-days in the context of climate change have also been studied by [20], and it is observed that spatially coherent and statistically significant trends of both heating and cooling degree-days appear in some regions of Turkey. In general, the sign of the trends is inconsistent with general circulation model (GCM) predictions.

Using the Mann–Kendall trend test and linear regression techniques, the annual and seasonal variations of heating and cooling degree-days in Xinjiang, China, from 1959 to 2004, have been studied by [21]. Their findings indicate that autumn, winter, and annual heating degree-days show significant decreasing trends (particularly true for the northern Xinjiang). Annual cooling degree-days at 23 out of 51 stations, however, present significant increasing trends (particularly true for the western parts of northern Xinjiang), while no remarkable positive trends are observed at the other stations. Also, no fixed spatial patterns have been identified in the variations of annual and summer cooling degree-days.

In another study, the annual and seasonal trends of heating, cooling, and industrial degree-days from 1970 to 2006 in five coastal cities in Saudi Arabia have been studied by [22]. Increasing trends are observed in case of annual cooling degree-days and industrial degree-days. Their heating degree-days analysis indicates a slight heating during January to March and in December, and shows a decreasing trend.

In the context of climate change, another study [23] assesses the potential development of energy use for future residential heating and air conditioning. In a reference scenario global energy demand for heating is projected to increase until 2030 and then stabilize. In contrast, energy demand for air conditioning is projected to increase rapidly over the whole 2000–2100 period mostly driven by income growth. The net effect of climate change on global energy use and emissions is
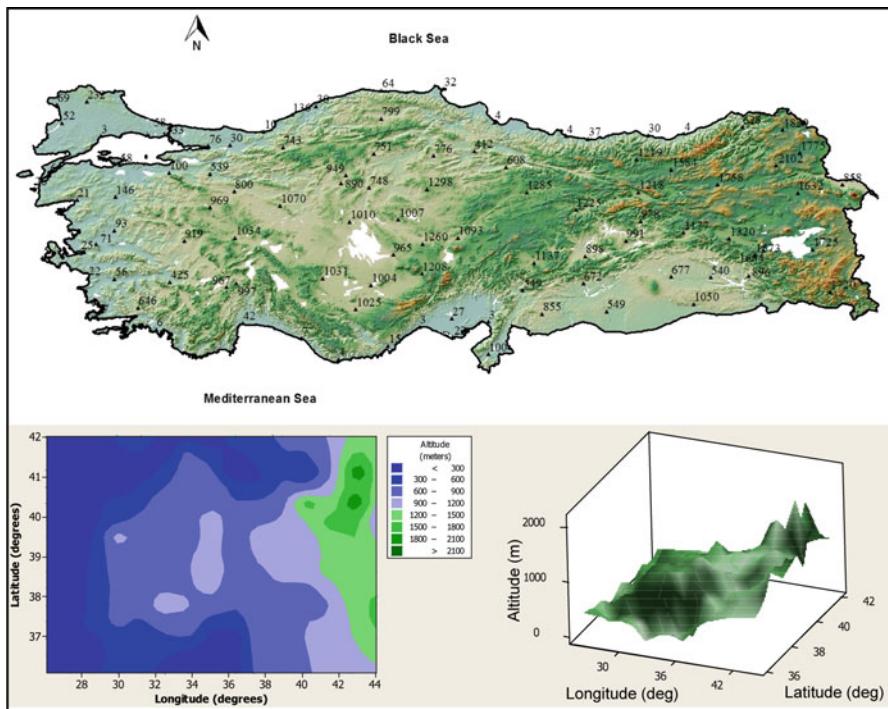
relatively small as decreases in heating are compensated for by increases in cooling. However, impacts on heating and cooling individually are considerable in this scenario, with heating energy demand decreased by 34 % worldwide by 2100 as a result of climate change, and air conditioning energy demand increased by 72 %. At the regional scale, considerable impacts are observed, particularly in South Asia, where energy demand for residential air conditioning could increase by about 50 % due to climate change, compared to the situation without climate change.

A comprehensive study [24] provides monthly and annual distributions and corresponding number of days of heating, cooling, and industrial degree-days for Turkey. Due to the fact that climate is changing, updating climatic design parameters becomes vital. As a complementary effort to the abovementioned study, and for providing further analysis and insights, the study presented in this chapter is performed to develop updated heating and cooling degree-day spatial distributions at different base temperatures, and spatial correlations and distributions for all over Turkey. The findings presented in this chapter will enable the designers to estimate annual heating and cooling energy consumptions in residential, commercial, and industrial buildings. It will also make it possible to make comparisons and designs of alternative building systems in terms of energy efficiencies. Utility companies and manufacturing and marketing companies of HVAC systems will be able to easily determine the demand, marketing strategies, and policies based on the information presented in this chapter.

3.2 Materials and Methods

In this study, 30-year annual averages of heating and cooling degree-days are determined and presented for 100 different locations providing a spatial distribution of the degree-days for the country (Fig. 3.1). The raw weather data for the locations are provided by the State Meteorological Service of Turkey (DMI). The dry-bulb temperature values (minimum and maximum temperatures) observed daily for a 30-year period of record (1976–2005) are used.

If the data for any location are not sufficient, reliable, or ready to process on a digital environment, then the location is not included in the study. The heating and cooling degree-day data are analyzed by multiple regression and spatial correlations are developed using as regressors altitude, latitude, and longitude. With other variables held constant, the relationships and significance between the heating and cooling degree-day values and each of the regressors are analyzed. How well did the regressors, taken together, explain the variation in the dependent variable is assessed by the value of R^2_{adj}. Whether the regressors, taken together, are significantly associated with the dependent variable is assessed by the statistic F in the "analysis of variance." What relationship each regressor has with the dependent variable when all other regressors are held constant is assessed by looking at the regression coefficients. And whether the relationship of each regressor with the dependent variable is statistically significant or not, with all other regressors taken

Fig. 3.1 Station locations and corresponding elevations (in meters, *top*), contour graph (*bottom left*), and 3-D elevation distributions (*bottom right*) of stations with respect to latitude and longitude

into account, is answered by looking at the *t* values in the table of regression coefficients. Which regressor has the most effect on the dependent variable is addressed by using the *beta weights* (*standardized regression coefficients*). *Minitab 15* is used to perform the abovementioned statistical analyses. Spatial distribution maps are generated using *ArcGIS 10*.

3.2.1   Degree-Day Method

Since many factors, which influence energy requirements of buildings, are dynamic and vary in time, the calculations that take all variations into account are quite complex. Therefore, estimating energy requirements and fuel consumption of HVAC systems for either short- or long-term operation can be a difficult task. As a result, the records of past energy requirements and/or fuel consumption for a particular residence are the best basis for estimating future energy use. However, when past records are not available, data from similar local dwellings can be used with caution. Since people have different living habits, even identical residences

can have very different energy use patterns. Therefore, energy consumption must often be estimated from computed heating or cooling loads [24]. Any estimating method produces a much more reliable result over a long period of operation than over a short period. Almost all the methods give sort of a reasonable result over a full annual heating and/or cooling season, but estimates for shorter periods, for instance, a month, can be quite different. The degree-day method for estimating heating energy requirements is based on the assumption that, on a long-term average, energy consumption will be proportional to the difference between the mean daily temperature and a heating base temperature (for example, 18 °C). For estimating cooling energy requirements, it is based on the assumption that energy consumption will be proportional to the difference between the mean daily temperature and a cooling base temperature of 18 or 24 °C [25]. The difference between the mean daily temperature and the base temperature is called as "degree-day" [3]. In determining the heating and cooling base temperatures for buildings, solar and internal heat gains for buildings are taken into account. For example, if the inside temperature is to be maintained at 21 °C in a residential building, it is assumed that it is the solar and internal gains which maintain inside temperature at 21 °C until the outside temperature drops below 18 °C [3]. Therefore, the most commonly used base temperature for residential heating is 18 °C [3, 26, 27]. In other words, on a day, when the mean outside temperature is 10 °C below 18 °C, twice as much energy is consumed as on days when the mean temperature is 5 °C below 18 °C. An equation has been developed for this concept stating that energy consumption is directly proportional to the number of degree-days in the estimation period [3].
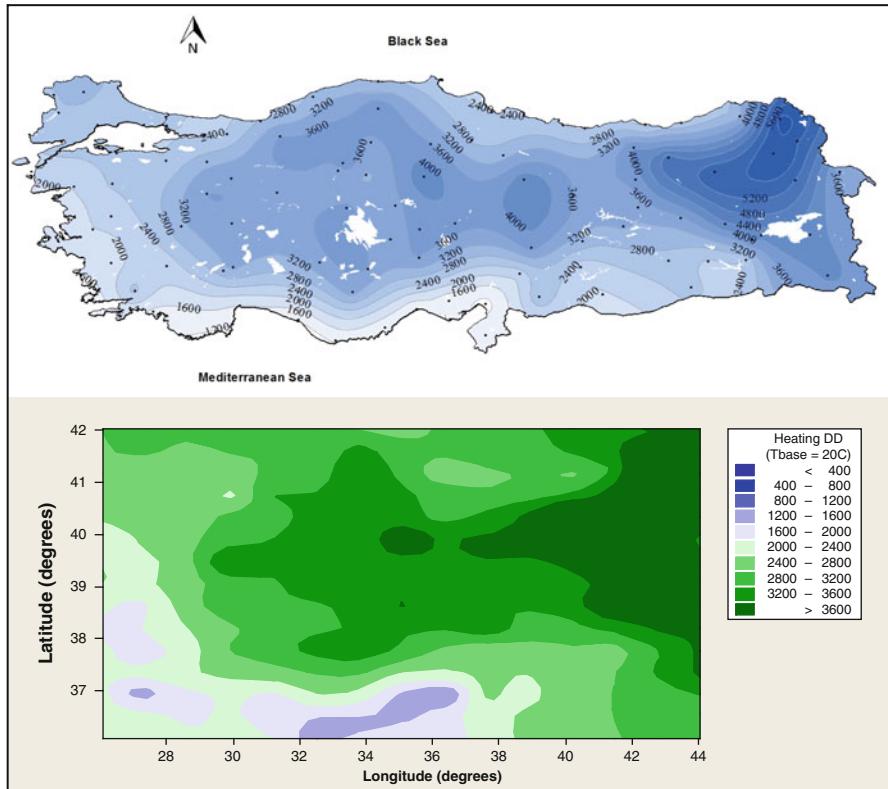
Heating Degree-Days

As mentioned earlier, degree-day method is commonly used to estimate energy consumption for heating and cooling in residential, commercial, and industrial buildings, as well as in greenhouses, storages, and warehouses. This procedure is also used for plant and insect growth, and freezing and thawing of soil and water surfaces. According to the procedure, daily heating degree-day accumulation (T_h) is defined as the deviation of the mean temperature from a heating base temperature (Eq. 3.1) and has the same unit as temperature. When the mean temperature is equal to or above the base temperature, then the heating degree-day for the day is zero:

$$T_h = T_b - T_d \qquad (3.1)$$

where T_b is the base temperature (five different base temperatures, 0, 5, 10, 15, and 20 °C, are used in this study), and T_d is the mean daily air temperature. The mean daily air temperature, T_d, is defined as

$$T_d = \frac{(T_{max}\, T_{min})}{2} \qquad (3.2)$$

Fig. 3.2 Spatial distributions (*top*) and contour graph (*bottom*) of heating degree-days with respect to latitude and longitude at the base temperature of 20 °C
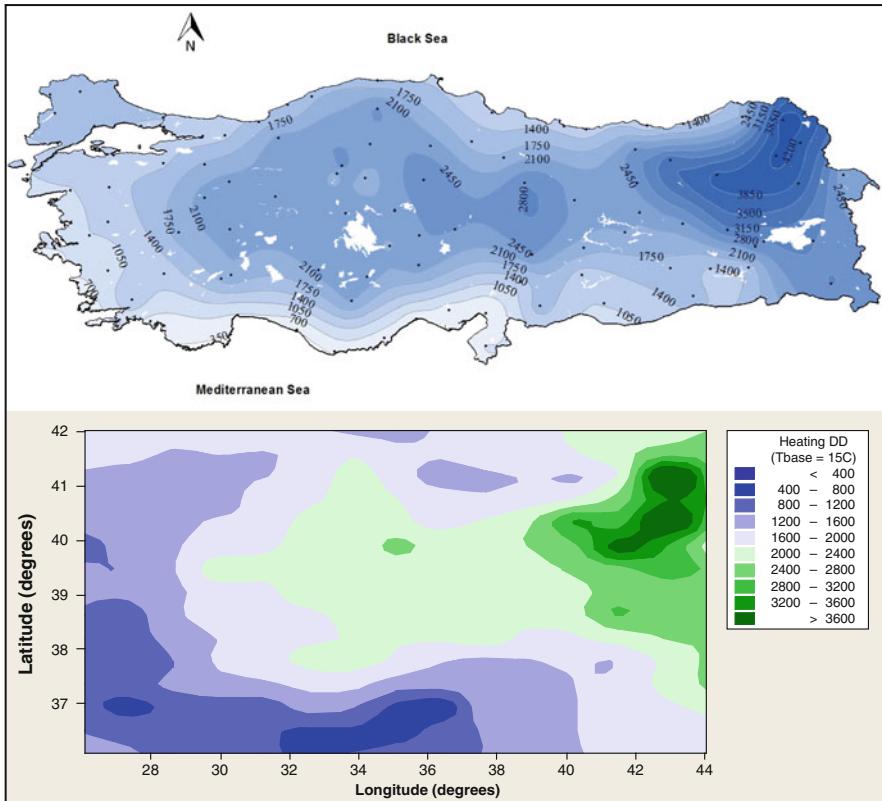
where T_{max} is the daily maximum temperature, and T_{min} is the daily minimum temperature, both in °C.

For a certain period of time (weekly, monthly, seasonal, annual, etc.), accumulated heating degree-day (D_h) is defined as

$$D_h = \sum_{j=1}^{N} (T_h)_j \begin{Bmatrix} \text{If} & T_d < T_b & \text{then} & T_h = T_b - T_d \\ & & \text{else} & T_h = 0 \end{Bmatrix} \qquad (3.3)$$
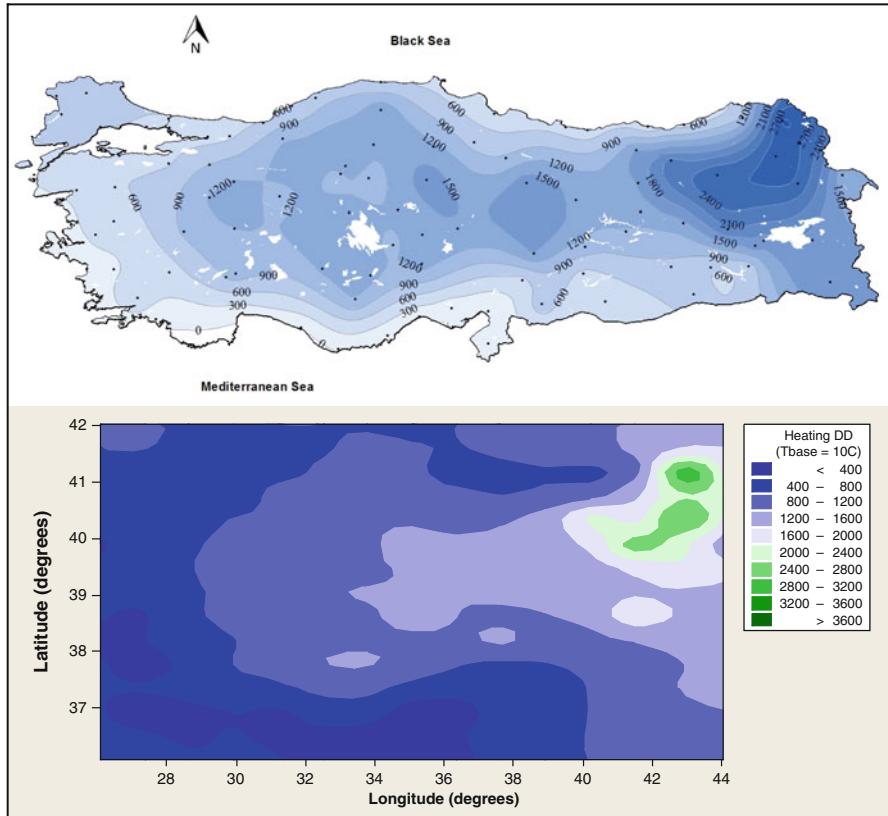
where N is defined as the period of time (number of days).

Using *ArcGIS 10*, the spatial distributions of the D_h for the base temperatures of 5, 10, 15, and 20 °C are mapped and presented in Figs. 3.2, 3.3, 3.4, and 3.5. Approximate corresponding number of days to estimate the length of the heating season is reported by [24]. If desired, using the generated spatial distribution maps and contour graphs for different base temperatures, heating regions for each can easily be established. However, special attention must be paid with respect to the

Fig. 3.3 Spatial distributions (*top*) and contour graph (*bottom*) of heating degree-days with respect to latitude and longitude at the base temperature of 15 °C

North Anatolian Mountains paralleling the Black Sea coast and the Taurus Mountains paralleling the Mediterranean coast where the number of stations is not always enough to generate reliable contour maps. In several other studies, heating degree-days for the country are determined at different base temperatures for different locations [28, 29]. In another study, the degree-hours method is used to estimate the residential heating energy requirement and fuel consumption in Istanbul, Turkey [30]. In this particular study, the heating season in Istanbul starts on October 19th and ends on May 7th lasting 201 days. In the studies mentioned above, either only a couple of years' weather data are used or no information is provided for the period of weather data used. Even though these studies provide quite useful information, they are limited in terms of the base temperatures and set point temperatures investigated, and lack the visual presentation of spatial distributions and relevant statistical analyses. In another study, even though the study does not have any design intentions or goals, seasonal heating and cooling degree-days in Turkey are determined and analyzed in the context of climate
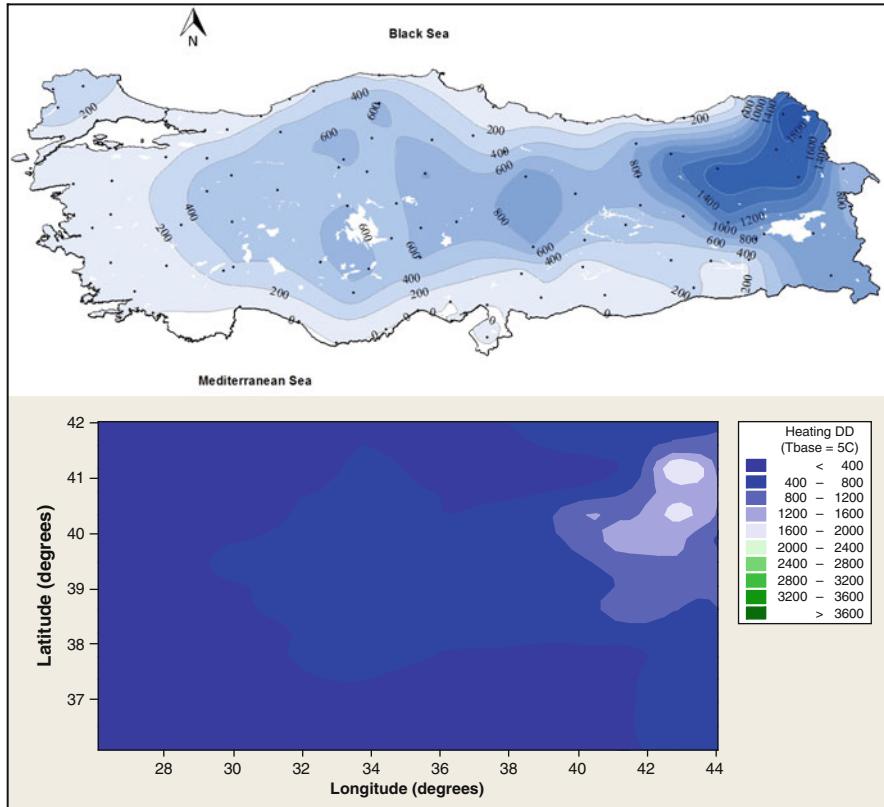
Fig. 3.4 Spatial distributions (*top*) and contour graph (*bottom*) of heating degree-days with respect to latitude and longitude at the base temperature of 10 °C

change [20]. Therefore, it is one of the main objectives of this study to determine up-to-date heating degree-day information for different base temperatures and spatial correlations and their significance for all over the country using reliable long-term and up-to-date weather data.

Cooling Degree-Days

According to the procedure, daily cooling degree-day (T_c) value is defined as the deviation of the mean temperature from a cooling base temperature of 18 or 24 °C (Eq. 3.4), and has the same unit as temperature. When the mean temperature is below the base temperature, then the cooling degree-day for the day is zero:

$$T_c = T_d - T_b \tag{3.4}$$

Fig. 3.5 Spatial distributions (*top*) and contour graph (*bottom*) of heating degree-days with respect to latitude and longitude at the base temperature of 5 °C
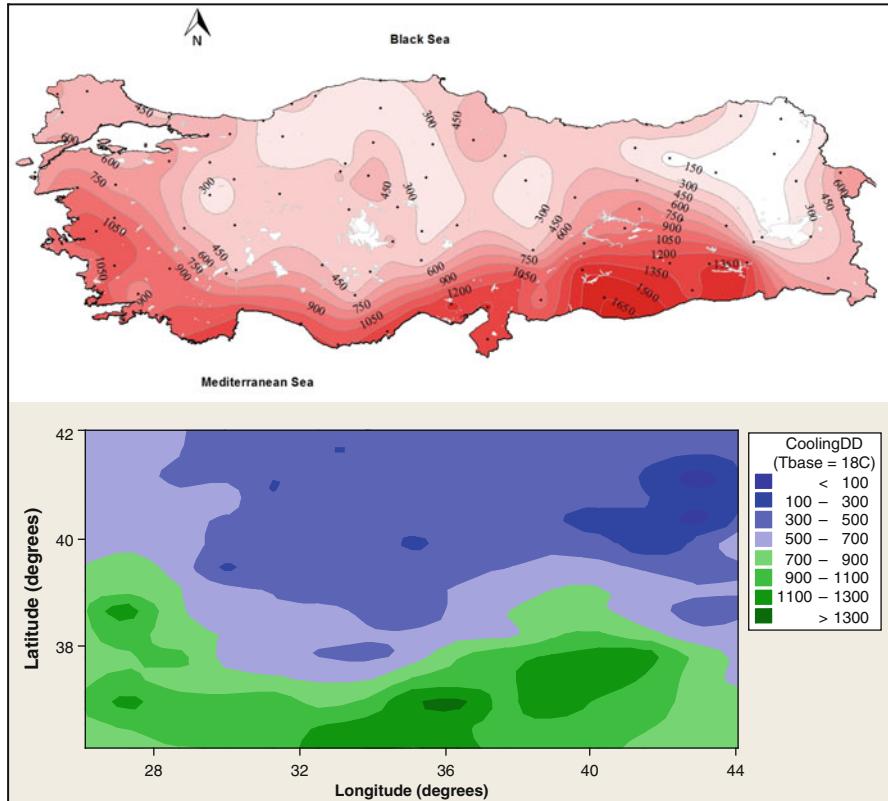
where T_b is the base temperature (18 or 24 °C), and T_d is the mean daily air temperature. The mean temperature, T_d, is defined earlier in Eq. 3.2.

For a certain period of time (weekly, monthly, seasonal, annual, etc.), then, accumulated cooling degree-day (D_c) is defined as

$$D_c = \sum_{j=1}^{N} (T_c)_j \left\{ \begin{array}{llll} \text{If} & T_d > T_b & \text{then} & T_c = T_d - T_b \\ & & \text{else} & T_c = 0 \end{array} \right\} \tag{3.5}$$

where N is defined as the period of time (number of days).

Using *ArcGIS 10*, the spatial distributions of the D_c for the base temperatures of 18 and 24 °C are mapped and presented in Figs. 3.6 and 3.7. Approximate corresponding number of days to estimate the length of the cooling season is reported by [24]. If desired, using the generated spatial distribution maps and contour graphs for different base temperatures, cooling regions for each can easily be established. However, as in the case of heating degree-days, special attention
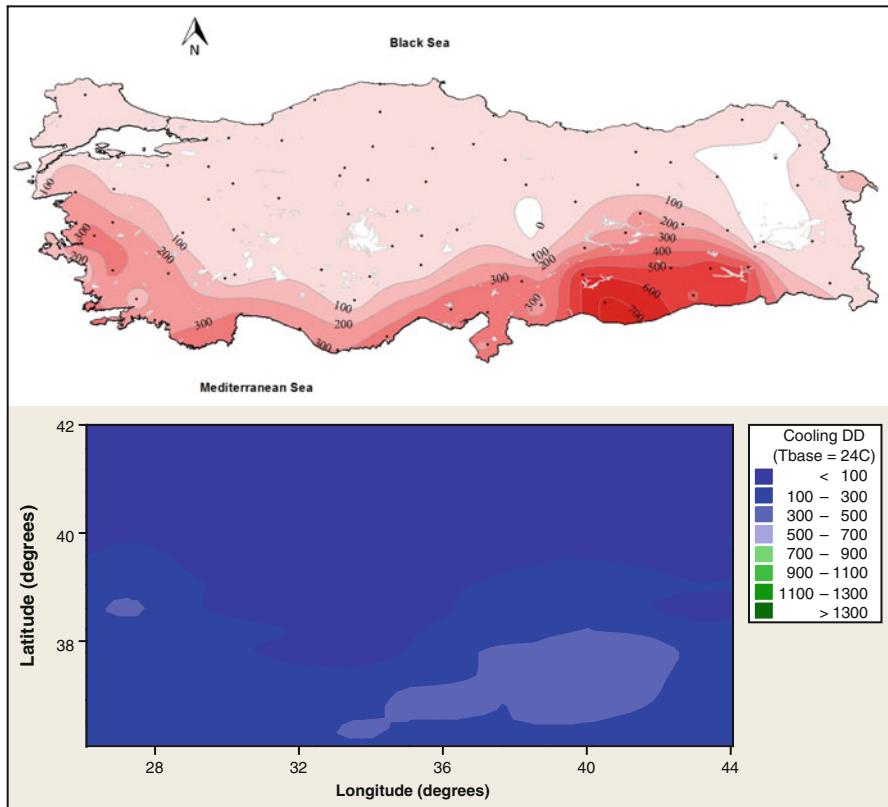
Fig. 3.6 Spatial distributions (*top*) and contour graph (*bottom*) of cooling degree-days with respect to latitude and longitude at the base temperature of 18 °C

must be paid with respect to the North Anatolian Mountains paralleling the Black Sea coast and the Taurus Mountains paralleling the Mediterranean coast where the number of stations is not always enough to generate reliable contour maps.

3.3 Results and Discussion

3.3.1 Heating Degree-Days

Spatial distributions of annual average heating degree-days (D_h) are determined for 100 different locations at the base temperatures of 20 °C (Fig. 3.2), 15 °C (Fig. 3.3), 10 °C (Fig. 3.4), and 5 °C (Fig. 3.5). The findings show that, at all base temperatures, comparably high D_h values are observed in the northeastern part of

Fig. 3.7 Spatial distributions (*top*) and contour graph (*bottom*) of cooling degree-days with respect to latitude and longitude at the base temperature of 24 °C

the country, especially at Ardahan, Sarikamis, Kars, Erzurum, and Agri (Figs. 3.2, 3.3, 3.4, and 3.5). It is not the objective of this chapter; however, another study [24] reports that intensive monthly D_h accumulations are generally observed in the winter months of December, January, and February. Regardless of what base temperature is used, relatively speaking, very small monthly D_h accumulations are observed along the Mediterranean coastal strip at low altitudes and latitudes (Iskenderun, Alanya, Anamur, Mersin, and Bodrum). Figures. 3.2, 3.3, 3.4, and 3.5 clearly show the same distribution here with respect to the spatial distributions of climatic normals.

Based on the findings, the lowest energy consumption for heating would take place in the coastal Aegean (especially in the southwestern corner) and the Mediterranean coast, while the highest energy consumption would be observed in the regions which have severe winter conditions, such as the northeastern corner of the country and high altitudes of the Central Anatolia (Figs. 3.2, 3.3, 3.4, and 3.5). For instance, a building in the northeastern corner of the country would have about five

times more heating energy consumption than the very same building would have at the low altitude and latitudes of the Mediterranean coastal strip. This is an extremely important piece of information for the utility companies and manufacturing and marketing companies of HVAC systems for them to easily determine the demand and associated logistics for distribution and their marketing strategies and policies.

Figure 3.2 shows that at 20 °C base temperature, highest D_h values are observed in the northeastern corner of the country (Ardahan, Sarikamis, Kars, Erzurum, and Agri) and high altitudes of the Central Anatolia, while the lowest are observed in the coastal Mediterranean (Iskenderun, Alanya, Anamur, Mersin) and coastal southwestern corner (Bodrum, Kusadasi, Aydin). The D_h data are analyzed by multiple regression using as regressors altitude, latitude, and longitude (Fig. 3.2). The regression (Eq. 3.6) is a very good fit ($R^2_{adj} = 96$ %) and the overall relationship is significant ($F_{3,96} = 713$, $p < 0.0005$). With other variables held constant, D_h values are positively related to altitude and latitude, increasing by 171 degree-days for every extra 100 m of altitude, and by 282 degree-days for every extra degree of latitude. D_h values are negatively related to longitude, decreasing by 13.1 degree-days for every extra degree of longitude. The effects of both regressors altitude and latitude are significant, except that of longitude ($t = 34.50$, $p < 0.0005$; $t = 19.89$, $p < 0.0005$; $t = 2.35$, $p = 0.021$, respectively). Altitude is determined to be the most influential regressor on the D_h and Figs. 3.1 and 3.2 clearly show this relationship. Which regressor has the most effect on the D_h is addressed by using the *beta weights* (*standardized regression coefficients*). The beta weights are determined as 0.940, 0.421, and 0.006 for altitude, latitude, and longitude, respectively. If the data are analyzed by simple regression or visually using a contour map or graph without determining the beta weights, one could conclude that longitude is a very influential regressor on the D_h. However, this is not the case in reality. The D_h increases with the increased longitudes; however, altitude also increases, and hence it is the most influential regressor as the beta weights support. Same trend is observed at the other base temperatures:

$$D_{h(TB=20°C)} = -8736 + 1.71^*(Alt) + 282^*(Lat) - 13.1^*(Long) \qquad (3.6)$$

where altitude (alt) is in meters, and latitude (lat) and longitude (long) are both in degrees.

Figure 3.3 shows that at 15 °C base temperature, highest D_h values start to retreat towards the northeastern corner of the country (Ardahan, Sarikamis, Kars, Erzurum, and Agri), while the low region starts to expand and covers almost all the coastal Mediterranean and Aegean. The D_h data are also analyzed by multiple regression using as regressors altitude, latitude, and longitude (Fig. 3.3). The regression (Eq. 3.7) is a very good fit ($R^2_{adj} = 95$ %) and the overall relationship is significant ($F_{3,96} = 669$, $p < 0.0005$). With other variables held constant, D_h values are positively related to altitude and latitude, increasing by 141 degree-days for every extra 100 m of altitude, and by 205 degree-days for every extra degree of latitude. D_h values are negatively related to longitude, decreasing by 6.6 degree-days for

every extra degree of longitude. The effects of both regressors altitude and latitude are significant, except that of longitude (t = 33.60, p < 0.0005; t = 17.00, p < 0.0005; t = 1.40, p = 0.164, respectively). Altitude is determined to be the most influential regressor on the D_h and Figs. 3.1 and 3.3 clearly show this relationship. And again, Figs. 3.1 and 3.3 support this relationship clearly. The beta weights are determined as 0.944, 0.371, and 0.040 for altitude, latitude, and longitude, respectively:

$$D_{h\,(Tb=15°C)} = -6910 + 1.41^*(Alt) + 205^*(Lat) - 6.62^*(Long) \qquad (3.7)$$

where altitude is in meters, and latitude and longitude are both in degrees.

Figure 3.4 shows that at 10 °C base temperature, highest D_h values concentrate in the northeastern corner of the country, while the low and lowest regions expand and cover all the coastal Mediterranean, Aegean, and Black Sea. The D_h data are analyzed by multiple regression using as regressors altitude, latitude, and longitude (Fig. 3.4). The regression (Eq. 3.8) is a very good fit (R^2_{adj} = 93 %) and the overall relationship is significant ($F_{3,96}$ = 436, p < 0.0005). With other variables held constant, D_h values are positively related to altitude and latitude, increasing by 106 degree-days for every extra 100 m of altitude, and by 132 degree-days for every extra degree of latitude. D_h values are negatively related to longitude, decreasing by 1 degree-day for every extra degree of longitude. The effects of both regressors altitude and latitude are significant, except that of longitude (t = 27.11, p < 0.0005; t = 11.78, p < 0.0005; t = 0.26, p = 0.796, respectively). Altitude is determined to be the most influential regressor on the D_h and Figs. 3.1 and 3.4 support this. The beta weights are determined as 0.932, 0.315, and 0.009 for altitude, latitude, and longitude, respectively:

$$D_{h\,(Tb=10°C)} = -4865 + 1.06^*(Alt) + 132^*(Lat) - 1.14^*(Long) \qquad (3.8)$$

where altitude is in meters, and latitude and longitude are both in degrees.

Figure 3.5 shows that at 5 °C base temperature, highest D_h values concentrate only in the northeastern corner of the country, while the low region expands and covers all the coastal Mediterranean, Aegean, and Black Sea and inlands except for the Central Anatolia. The D_h data are analyzed by multiple regression using as regressors altitude, latitude, and longitude (Fig. 3.5). The regression (Eq. 3.9) is a very good fit (R^2_{adj} = 84 %) and the overall relationship is significant ($F_{3,96}$ = 175, p < 0.0005).

With other variables held constant, D_h values are positively related to altitude, latitude, and longitude, increasing by 66 degree-days for every extra 100 m of altitude, by 65 degree-days for every extra degree of latitude, and by 3.5 degree-days for every extra degree of longitude. The effects of both regressors altitude and latitude are significant, except that of longitude (t = 16.89, p < 0.0005; t = 5.85, p < 0.0005; t = 0.80, p = 0.427, respectively). Beta weights suggest that altitude is the most influential regressor on the D_h, and this is supported by the distributions

shown in Figs. 3.1 and 3.5. The beta weights are determined as 0.873, 0.235, and 0.041 for altitude, latitude, and longitude, respectively:

$$D_{h\,(Tb=5°C)} = -2676 + 0.66^*(Alt) + 65.1^*(Lat) + 3.47^*(Long) \qquad (3.9)$$

where altitude is in meters, and latitude and longitude are both in degrees.

Even though the maps are not presented here, high D_h values at the base temperature of 0 °C concentrate fully in the high altitudes of northeastern corner, while the low region expands and covers the whole country. The D_h data are also analyzed by multiple regression using as regressors altitude, latitude, and longitude. The regression (Eq. 3.10) is a good fit ($R^2_{adj} = 66$ %) and the overall relationship is significant ($F_{3,96} = 65$, p < 0.0005). With other variables held constant, D_h values are positively related to altitude, latitude, and longitude, increasing by 31 degree-days for every extra 100 m of altitude, by 30 degree-days for every extra degree of latitude, and by 4.6 degree-days for every extra degree of longitude. The effects of both regressors altitude and latitude are significant, except that of longitude (t = 9.76, p < 0.0005; t = 3.25, p < 0.0005; t = 1.29, p = 0.199, respectively). Altitude is still the most influential regressor on the D_h. The beta weights are determined as 0.739, 0.191, and 0.098 for altitude, latitude, and longitude, respectively:

$$D_{h\,(Tb=0°C)} = -1363 + 0.31^*(Alt) + 29.6^*(Lat) + 4.62^*(Long) \qquad (3.10)$$

where altitude is in meters, and latitude and longitude are both in degrees.

3.3.2 Cooling Degree-Days

The D_c maps for the base temperatures of 18 and 24 °C are generated and their spatial distributions are presented in Figs. 3.6 and 3.7. The highest D_c accumulations are observed in the southeastern region of the country. This region is followed by the low altitudes of Mediterranean and Aegean coastal strips. On the other hand, the northeastern corner of the country and several other high-altitude locations have very low, essentially close to zero, accumulations of cooling degree-days. Figure 3.7 also shows that, even though the magnitudes vary, the cooling degree-day accumulations at 24 °C basically follow the same trends throughout the country. An earlier study [24] reports that the highest accumulations of cooling degree-days at different locations are generally observed in the month of July. However, it is important to note that it is observed in the month of August instead with some delay, at the locations in the Black Sea and Marmara regions. The study attributes the findings to the effects of ocean and latitude. It is also reported that the cooling season covers the months of June, July, August, and September; however, in some regions, the season includes the months of May and October, and even the

month of April in some cases. Throughout the country, it is concluded that no cooling is necessary for the five-month period from November through March.

Figure 3.6 shows that at 18 °C base temperature, highest D_c values are observed in the southeastern corner of the country (Sanliurfa, Adiyaman, Adana, Iskenderun, Batman, Siirt, Mardin, Diyarbakir) and the coastal Mediterranean, while the lowest are observed in the northeastern corner (Sarikamis, Ardahan, Kars, Bayburt, Erzurum) and at high altitudes of the Central Anatolia (Yozgat and Sivas, for instance). The D_c data are analyzed by multiple regression using as regressors altitude, latitude, and longitude (Fig. 3.6).

The regression (Eq. 3.11) is a very good fit ($R^2_{adj} = 78$ %) and the overall relationship is significant ($F_{3,96} = 119$, $p < 0.0005$). With other variables held constant, D_c values are negatively related to altitude and latitude decreasing by 47 degree-days for every extra 100 m of altitude, and by 177 degree-days for every extra degree of latitude. D_c values are positively related to longitude, increasing by 21.6 degree-days for every extra degree of longitude. The effects of regressors altitude, latitude, and longitude are all significant ($t = 11.46$, $p < 0.0005$; $t = 15.08$, $p < 0.0005$; $t = 4.71$, $p < 0.0005$, respectively). Latitude is determined to be the most influential regressor on the D_c; however, altitude is also as influential as latitude. The beta weights are determined as 0.694, 0.709, and 0.285 for altitude, latitude, and longitude, respectively:

$$D_{c\ (Tb=18°C)} = 7106 - 0.47^*(Alt) - 177^*(Lat) + 21.6^*(Long) \qquad (3.11)$$

where altitude is in meters, and latitude and longitude are both in degrees.

Figure 3.7 shows that at 24 °C base temperature, highest D_c values are still observed in the southeastern corner of the country, and the coastal Mediterranean and Aegean regions, while the rest of the country at higher latitudes (above approximately 39 °N) has comparably low cooling degree-day normals. The D_c data for base temperature of 24 °C are analyzed by multiple regression using as regressors altitude, latitude, and longitude (Fig. 3.7). The regression (Eq. 3.12) is a good fit ($R^2_{adj} = 61$ %) and the overall relationship is significant ($F_{3,96} = 52$, $p < 0.0005$). With other variables held constant, D_c values are negatively related to altitude and latitude decreasing by 15 degree-days for every extra 100 m of altitude, and by 68 degree-days for every extra degree of latitude. D_c values are positively related to longitude, increasing by 12 degree-days for every extra degree of longitude. The effects of regressors altitude, latitude, and longitude are all significant ($t = 6.71$, $p < 0.0005$; $t = 10.68$, $p < 0.0005$; $t = 4.73$, $p < 0.0005$, respectively). Just like for the base temperature of 18 °C, latitude is determined to be the most influential regressor on the D_c. The beta weights are determined as 0.544, 0.672, and 0.383 for altitude, latitude, and longitude, respectively:

$$D_{c\ (Tb=24°C)} = 2493 - 0.150^*(Alt) - 68.4^*(Lat) + 11.9^*(Long) \qquad (3.12)$$

where altitude is in meters, and latitude and longitude are both in degrees.

3.4   Conclusions

The heating and cooling degree-day data are analyzed by multiple regression and
spatial correlations developed using as regressors altitude, latitude, and longitude.
Highest D_h normals are observed in the northeastern corner of the country and
high altitudes of the Central Anatolia, while the lowest are observed in the coastal
Mediterranean and coastal southwestern corner of the country. With other
variables held constant, heating degree-day values are positively related to altitude
and latitude, while negatively related to longitude. The effects of regressors
altitude and latitude are both significant, but not that of longitude. Altitude is
determined to be the most influential regressor on the heating degree-day
distributions. Highest D_c normals are observed in the southeastern corner of the
country, and the coastal Mediterranean and Aegean regions, while the rest of the
country at higher latitudes (above approximately 39 °N) has comparably low
cooling degree-day normals. With other variables held constant, cooling degree-
day values are negatively related to altitude and latitude while positively related to
longitude. The effects of regressors altitude, latitude, and longitude on cooling
degree-day distribution are all significant. Latitude is determined to be the most
influential regressor.

   The developed spatial correlations and data generated are useful and needed
in various endeavors, such as estimating annual figures for locations having no
data at all, and estimating the annual heating and cooling energy consumptions for
any residential, commercial, and industrial buildings in Turkey. It will also be
possible to make comparisons and designs of alternative building systems in terms
of energy efficiencies. Utility companies and manufacturing and marketing
companies of HVAC systems will be able to easily determine the demand, market-
ing strategies, and policies based on the findings of this study.

Appendix

This section presents the details of heating and cooling degree-day multiple regres-
sion analyses and spatial correlations with respect to altitude, latitude, and
longitude.

Table 3.1 Regression analysis: Heating degree-days with respect to altitude, latitude, and longitude at the base temperature of 20 °C

```
The regression equation is
Heating DD (Tbase=20C) = - 8736 + 1.71 Altitude (meters)
        + 282 Latitude (degrees) - 13.1 Longitude (degrees)


Predictor                Coef  SE Coef       T      P
Constant              -8736.3    586.1  -14.91  0.000
Altitude (meters)     1.70816  0.04951   34.50  0.000
Latitude (degrees)     282.07    14.18   19.89  0.000
Longitude (degrees)   -13.074    5.557   -2.35  0.021


S = 221.579   R-Sq = 95.7%   R-Sq(adj) = 95.6%


Analysis of Variance


Source           DF         SS        MS        F      P
Regression        3  105035280  35011760   713.11  0.000
Residual Error   96    4713331     49097
Total            99  109748611


Beta Weights (standardized regression coefficients)
The regression equation is
Heating DD (Tbase=20C) = - 0.0001 + 0.940 Altitude (meters)
        + 0.421 Latitude (degrees) - 0.0641 Longitude (degrees)
```

Table 3.2 Regression analysis: Heating degree-days with respect to altitude, latitude, and longitude at the base temperature of 15 °C

```
The regression equation is
Heating DD (Tbase=15C) = - 6910 + 1.41 Altitude (meters)
        + 205 Latitude (degrees) - 6.62 Longitude (degrees)


Predictor                Coef  SE Coef       T      P
Constant              -6909.7    497.6  -13.89  0.000
Altitude (meters)     1.41223  0.04204   33.60  0.000
Latitude (degrees)     204.67    12.04   17.00  0.000
Longitude (degrees)    -6.625    4.718   -1.40  0.164


S = 188.133   R-Sq = 95.4%   R-Sq(adj) = 95.3%


Analysis of Variance


Source           DF        SS        MS        F      P
Regression        3  70999535  23666512   668.66  0.000
Residual Error   96   3397818     35394
Total            99  74397353


Beta Weights (standardized regression coefficients)
The regression equation is
Heating DD (Tbase=15C) = - 0.0001 + 0.944 Altitude (meters)
        + 0.371 Latitude (degrees) - 0.0395 Longitude (degrees)
```

Table 3.3 Regression analysis: Heating degree-days with respect to altitude, latitude, and longitude at the base temperature of 10 °C

```
The regression equation is
Heating DD (Tbase=10C) = - 4865 + 1.06 Altitude (meters)
        + 132 Latitude (degrees) - 1.14 Longitude (degrees)


Predictor               Coef  SE Coef       T      P
Constant             -4865.1    462.5  -10.52  0.000
Altitude (meters)    1.05942  0.03908   27.11  0.000
Latitude (degrees)    131.86    11.19   11.78  0.000
Longitude (degrees)   -1.139    4.386   -0.26  0.796


S = 174.880   R-Sq = 93.2%   R-Sq(adj) = 93.0%


Analysis of Variance

Source          DF        SS        MS       F      P
Regression       3  40040522  13346841  436.41  0.000
Residual Error  96   2935974     30583
Total           99  42976496


Beta Weights (standardized regression coefficients)
The regression equation is
Heating DD (Tbase=10C) = 0.0000 + 0.932 Altitude (meters)
        + 0.315 Latitude (degrees) - 0.0089 Longitude (degrees)
```

Table 3.4 Regression analysis: Heating degree-days with respect to altitude, latitude, and longitude at the base temperature of 5 °C

```
The regression equation is
Heating DD (Tbase=5C) = - 2676 + 0.656 Altitude (meters)
        + 65.1 Latitude (degrees) + 3.47 Longitude (degrees)


Predictor               Coef  SE Coef       T      P
Constant             -2676.5    459.6   -5.82  0.000
Altitude (meters)    0.65590  0.03883   16.89  0.000
Latitude (degrees)     65.10    11.12    5.85  0.000
Longitude (degrees)    3.474    4.358    0.80  0.427


S = 173.784   R-Sq = 84.6%   R-Sq(adj) = 84.1%


Analysis of Variance

Source          DF        SS       MS       F      P
Regression       3  15876694  5292231  175.24  0.000
Residual Error  96   2899269    30201
Total           99  18775963


Beta Weights (standardized regression coefficients)

The regression equation is
Heating DD (Tbase=5C) = - 0.0000 + 0.873 Altitude (meters)
        + 0.235 Latitude (degrees) + 0.0412 Longitude (degrees)
```

Table 3.5 Regression analysis: Heating degree-days with respect to altitude, latitude, and longitude at the base temperature of $0\,^\circ$C

```
The regression equation is
Heating DD (Tbase=0C) = - 1363 + 0.310 Altitude (meters)
        + 29.6 Latitude (degrees) + 4.62 Longitude (degrees)


Predictor                Coef  SE Coef       T      P
Constant              -1363.4    376.5   -3.62  0.000
Altitude (meters)     0.31035  0.03181    9.76  0.000
Latitude (degrees)     29.565    9.110    3.25  0.002
Longitude (degrees)     4.615    3.570    1.29  0.199

S = 142.341   R-Sq = 66.9%   R-Sq(adj) = 65.8%


Analysis of Variance

Source          DF       SS       MS       F      P
Regression       3  3927728  1309243   64.62  0.000
Residual Error  96  1945064    20261
Total           99  5872791


Beta Weights (standardized regression coefficients)
The regression equation is
Heating DD (Tbase=0C) = - 0.0001 + 0.739 Altitude (meters)
        + 0.191 Latitude (degrees) + 0.0978 Longitude (degrees)
```

Table 3.6 Regression analysis: Cooling degree-days with respect to altitude, latitude, and longitude at the base temperature of $24\,^\circ$C

```
The regression equation is
Cooling DD (Tbase=24C) = 2493 - 0.150 Altitude (meters)
        - 68.4 Latitude (degrees) + 11.9 Longitude (degrees)


Predictor                Coef  SE Coef        T      P
Constant               2493.0    264.7     9.42  0.000
Altitude (meters)    -0.15004  0.02236    -6.71  0.000
Latitude (degrees)    -68.418    6.405   -10.68  0.000
Longitude (degrees)    11.874    2.510     4.73  0.000

S = 100.075   R-Sq = 62.0%   R-Sq(adj) = 60.9%


Analysis of Variance

Source          DF       SS       MS       F      P
Regression       3  1571405   523802   52.30  0.000
Residual Error  96   961450    10015
Total           99  2532855


Beta Weights (standardized regression coefficients)
The regression equation is
Cooling DD (Tbase=24C) = 0.0000 - 0.544 Altitude (meters)
        - 0.672 Latitude (degrees) + 0.383 Longitude (degrees)
```

Table 3.7 Regression analysis: Cooling degree-days with respect to altitude, latitude, and longitude at the base temperature of 18 °C

```
The regression equation is
Cooling DD (Tbase=18C) = 7106 - 0.469 Altitude (meters)
        - 177 Latitude (degrees) + 21.6 Longitude (degrees)


Predictor                  Coef  SE Coef        T      P
Constant                 7105.6    484.1    14.68  0.000
Altitude (meters)      -0.46860  0.04090   -11.46  0.000
Latitude (degrees)     -176.63     11.71   -15.08  0.000
Longitude (degrees)      21.632     4.591     4.71  0.000


S = 183.047   R-Sq = 78.8%   R-Sq(adj) = 78.2%


Analysis of Variance


Source          DF        SS        MS        F      P
Regression       3  11972442   3990814   119.11  0.000
Residual Error  96   3216581     33506
Total           99  15189023


Beta Weights (standardized regression coefficients)
The regression equation is
Cooling DD (Tbase=18C) = 0.0002 - 0.694 Altitude (meters)
        - 0.709 Latitude (degrees) + 0.285 Longitude (degrees)
```

References

1. Midwest Plan Service (1983) Structures and Environment Handbook. Eleventh Edition. Revised 1987. Iowa State University, Ames, Iowa 50011. ISBN 0-89373-057-2
2. Environment Canada (1978) The climates of Canada for agriculture. The Canada Land Inventory Report No. 3, Ottawa, Canada
3. ASHRAE (2009) Handbook of Fundamentals, ASHRAE, Inc. Atlanta, GA 30329, U.S.A. 28.1-28.9
4. Yesilirmak E, Yildiz I (2001) Monthly and annual averages of growing degree-days at different base temperatures for Turkiye. GAP 2nd Agricultural Congress: October 24-26, Harran University, Sanliurfa, Turkey
5. Thomas MK (1953) Climatological Atlas of Canada. National Research Council Canada, Ottawa, Canada
6. Ramirez JM (1964) The agro-climatology of North Dakota. Part 1-Air temperature and growing degree days. North Dakota State University, Extension Bulletin No. 15. Fargo, North Dakota, U.S.A
7. McKay GA, Mooney OR, Maybank J, Pelton WL (1967) The agricultural climate of Saskatchewan. Canada Department of Transport, Climatological Studies No. 10. Toronto, Canada
8. Neild RE, Seeley MW (1976) Applications of growing degree days in field corn production. In: Agrometeorology of the Maize (Corn) Crop. Geneva, Switzerland. WMO-No. 481:426–436
9. Edey SN (1980) Degres-jours de croissance et production des cultures au Canada. Agriculture Canada Publication No. 1635, Ottawa, Canada
10. Environment Canada (1990) Eastern Canadian boreal and sub-arctic wetlands. In: A Resource Document. Ottawa, Canada

11. Agriculture Canada (1993) Risk analyses of growing degree-days in Atlantic Canada. Research Branch Technical Bulletin 1993-5E, Ottawa, Canada
12. Bootsma A (1994) Long term (100 Yr) climatic trends for agriculture at selected locations in Canada. Clim Change 26:65–88
13. Lenihan JM, Neilson RP (1995) Canadian vegetation sensitivity to projected climatic change at three organizational levels. Clim Change 38:51–86
14. Sykes MT, Prentice IC (1996) Climate change, tree species distributions and forest dynamics: a case study in the mixed conifer/northern hardwoods zone of northern Europe. Clim Change 34:161–177
15. Singh B, Maayar ME, Andre P, Bryant CR, Thouez JP (1988) Impacts of a GHG-induced climate change on crop yields: effects of acceleration in maturation, moisture stress and optimal temperature. Clim Change 38:51–86
16. Tsikaloudaki K, Laskos K, Bikas D (2012) On the establishment of climatic zones in Europe with regard to the energy performance of buildings. Energies 5(1):32–44
17. Castenada ME, Claus, F (2012) Variability and trends of heating degree-days in Argentina. Int J Climatol (2012). Published online in Wiley Online Library. DOI: 10.1002/joc.3583
18. Sequera P, Rhona O, Gonzalez JE, Ghebreegziabher AT, Bornstein R, Lebassi B (2011) Impacts of climate changes in the Northern Pacific Coast on related regional scale energy demands. Proceedings of the ASME 2011 5th International Conference on Energy Sustainability. ES2011-54. August 7-10, 2011, Washington, DC, USA
19. Lebassi BH, Gonzalez JE, Fabris D, Maurer E, Miller NL, Milesi J, Switzer P, Bornstein R (2009) Observed 1970-2005 cooling of summer daytime temperatures in coastal California. J Climate 22:3558–3573. doi:10.1175/2008JCLI2111.1
20. Kadioglu M, Sen Z, Gultekin L (2001) Variations and trends in Turkish seasonal heating and cooling Degree-Days. Clim Change 49(1–2):209–223
21. Jiang F, Li X, Wei B, Li Z (2009) Observed trends of heating and cooling degree-days in Xinjiang Province. China Theor Appl Climatol 97(3–4):349–360
22. Rehman S, Al-Hadhrami LM, Khan S (2011) Annual and seasonal trends of cooling, heating, and industrial degree-days in coastal regions of Saudi Arabia. Theor Appl Climatol 104 (3–4):479–488
23. Isaac M, van Vuuren D (2009) Modeling global residential sector energy demand for heating and air conditioning in the context of climate change. Energy Policy 37:507–521
24. Yildiz I, Sosaoglu B (2007) Spatial distributions of heating, cooling, and industrial degree-days in Turkey. Theor Appl Climatol 90(3–4):249–261
25. Environment Canada (1982) Canadian climate normals, 1951–1980. Vol. 4–Degree Days, Atmospheric Environment Service, Ottawa, Canada
26. Williams GDV, MacKay KH (1970) Tables of daily degree-days above or below any base temperature. Canadian Department of Agriculture, Publication No: 1409, Ottawa, Canada.
27. Wilson CW (1973) the Climate of Quebec—the application of climatic information—Part two. Environment Canada, Atmospheric Environment, Ottawa, Canada
28. Yener C, Gurdil F (1987) Türkiye derece-gün değerlerinin belirlenmesi ve derece-gün yöntemi, TÜBİTAK Yapı Araştırma Enstitüsü. Rapor No: H139, Ankara, Turkey
29. Dagsoz KA (1995) Türkiye'de Derece-Gün Sayıları, Ulusal Enerji Tasarruf Politikası, Yapılarda Isı Yalıtımı. İzocam A.Ş., Istanbul, Turkey
30. Durmayaz A, Kadioglu M, Sen Z (2000) An application of the degree-hours method to estimate the residential heating energy requirement and fuel consumption in Istanbul. Energy 25:1245–1256

Chapter 4
Use of Empirical Regression and Artificial Neural Network Models for Estimation of Global Solar Radiation in Dubai, UAE

Hassan A.N. Hejase, Ali H. Assi, and Maitha H. Al Shamisi

Abstract The geographical location of the United Arab Emirates (UAE) (latitude between 26° and 32° North and longitude between 51° and 56° East) favors the development and utilization of solar energy. This chapter presents estimation models for the global solar radiation (GSR) in Dubai, UAE. It compares between six empirical regression models and the best of 11 different configurations of artificial neural network (ANN) models. The models have been developed using measured average daily GSR data for 7 years (2002–2008) while the measured data for the years 2009–2010 are used for testing the models. Results of monthly average daily GSR data of all the empirical models for the test period 2009–2010 yield low statistical error parameters and coefficients of determination (R^2) better than 96 %. Comparison with ANN models and Solar Radiation (SoDa) Web site data shows that the optimal multilayer perceptron (MLP) ANN model is the best with $R^2 = 98$ %, and with the lowest statistical error parameters. The results also confirm that a simple linear regression model provides a very good estimation for monthly and daily average GSR data.

Keywords Global solar radiation • Empirical regression • Artificial neural networks

H.A.N. Hejase (✉) • M.H. Al Shamisi
College of Engineering, United Arab Emirates University,
P.O. Box 15551, Al-Ain, UAE
e-mail: hhejase@uaeu.ac.ae; maitha.h.alshamisi@gmail.com

A.H. Assi
Department of Electrical and Electronic Engineering,
Lebanese International University, Beirut, Lebanon
e-mail: ali.assi@liu.edu.lb

Nomenclature

x_j	Inputs of ANN
w_{ij}	Weights of ANN
y_j	Outputs of ANN
f	Activation function
net_j	Total weighted sum of input signals to neuron j
$y_j^{(t)}$	Target output for neuron j
xc_j	Center of the radial basis function

Greek Symbols

Σ	Summation function
ω_s	Mean sunrise hour angle in radians
ϕ	Latitude in radians
δ	Declination angle in radians
η	Learning rate
σ_j	A factor that depends on whether neuron j is an output/hidden neuron
μ	Momentum coefficient
$\varphi_j(x)$	Hidden layer output (activation function) for RBF ANN

Acronyms

ANN	Artificial Neural Network
G_0	Extraterrestrial solar radiation on a horizontal surface (kWh/m^2)
GIS	Geographical Information System
GSR	Mean daily Global Solar Radiation (kWh/m^2)
MABE	Mean Absolute Bias Error (kWh/m^2)
MAPE	Mean Absolute Percent Error
MBE	Mean Bias Error (kWh/m^2)
MLP	Multilayer Perceptron
NASA	National Aeronautics and Space Administration
R^2	Coefficient of Determination
RBF	Radial Basis Function
RGSR	Clearness coefficient
RH	Relative Humidity (%)
RMSE	Root-Mean-Square Error (kWh/m^2)

RSSH   Sunshine duration ratio
RREX   Renewable energy Resource EXplorer
S_0 Theoretical maximum sunshine hours
SoDa   Solar radiation Data
SSE   Solar meteorology and Solar Energy
SSH   Mean daily Sunshine Hours
SWERA   Solar and Wind Energy Resource Assessment
T   Maximum air Temperature (degrees Celsius)
UAE   United Arab Emirates
W   Average Wind Speed (knots)

4.1   Introduction

Most of our energy is produced from fossil fuels which are the main contributor to
the emission of greenhouse gases and global warming. Gulf corporation countries
that include the United Arab Emirates (UAE) are seeking to make better use of their
abundant sustainable energy sources and specifically solar energy. New sources of
clean energy are essential to help reduce carbon dioxide levels and protect the
endangered ozone layer and avoid future climate changes. New policies are now in
place in many countries to encourage the use of renewable energy sources such as
solar, wind, tidal waves, geothermal, and biofuels.

The UAE has experienced a rapid increase in electricity consumption between
1980 and 2000 according to a 2010 World Bank report [1]; this consumption
continues today. Electricity consumption has increased from 5.865 billion kWh in
1980 to about 38.593 billion kWh in 2000 and 79.544 billion kWh in 2009
(11,463.63 kWh per capita in 2009) with an annual growth rate of nearly 10 %
compared to a world average of 3 % [1].

Power generation capacity in the UAE has grown at a compounded rate of 12 %
annually during the last 5 years and current capacity stands at about 30 GW while
the annual power consumption grew at a slightly less than 8 % during the same
period, according to a UAE Gulf news article [2].

The UAE has initiated many ambitious investment projects in alternate energy
sources. Abu Dhabi's Economic Vision-2030 aims at generating 7 % of its energy
needs from renewable sources. In Dubai, UAE, the Mohammed bin Rashid Al
Maktoum Solar Park has been established in early 2012 as part of a strategy to
diversify Dubai's energy sources so that 1 % of its power will be renewable by 2020
and 5 % by 2030. In parallel to these efforts, the UAE utility companies are running
energy saving campaigns to raise awareness among the population of the
consequences of increased energy consumption on the global warming.

The UAE initiatives fall short of the existing projects around the world and in
particular Germany and Japan who both lack the solar energy abundance that UAE
enjoys (over 330 sunny days a year).

The global solar radiation received at the surface of the Earth is of utmost importance for scientists working on ecological and crop models, building thermal performance, hydrology, and meteorology. Solar radiation data are typically obtained through measurements from stations scattered at different locations of a particular region. However, it is difficult to obtain at all locations because of the high cost of equipment, operation, and maintenance. This demands the development of prediction models that can be used in locations where measurement data are not available.

The potential of solar energy harvesting in the UAE is significant, with an average annual sunshine hours of 3,568 h (i.e., 9.7 h/day). This corresponds to an average annual solar radiation of approximately 2,285 kWh/m^2, i.e., 6.3 kWh/m^2 per day [3]. The abundance of solar energy in the UAE, in particular, and Arabian Gulf region, in general, has triggered the interest of numerous researchers to develop solar models.

In earlier work, the authors have developed global solar radiation (GSR) models for the cities of Abu Dhabi and Al-Ain in the UAE using several approaches that include classical empirical regression [3–5], artificial neural networks (ANN) [6–8], and autoregressive moving-average (ARMA) time-series regression techniques [5, 9]. The classical regression models include the linear Angström–Prescott model and its derivations, namely, the second and third order correlations, in addition to the single term exponential model, logarithmic model, and linear logarithmic model [3].

Numerous authors, to count a few [3–5, 11–24], have developed empirical regression models to estimate the monthly average daily global solar radiation (GSR) in their region using various parameters. The mean daily sunshine duration is the most commonly used and available parameter. The most popular model is the linear model by Angström–Prescott [3, 4, 21] which establishes a linear relationship between GSR and sunshine duration with knowledge of extraterrestrial solar radiation and the theoretical maximum daily solar hours. Many studies with empirical regression models are available for diverse regions around the world [5].

Menges et al. [19] compare 50 GSR empirical models available in the literature for computing the monthly average daily GSR on a horizontal surface. The models are tested and verified using data recorded in Konya, Turkey. They use linear, logarithmic, quadratic, third order polynomial, logarithmic-linear, exponential, and power models that correlate the normalized GSR (clearness index) to normalized sunshine hours (sunshine duration ratio) data [5]. Menges [19] also includes direct regression models involving various weather parameters such as precipitation, cloud cover, etc., in addition to geographical data (altitude, latitude) [5].

Şahin [22] presents a novel method for estimating the solar irradiation and sunshine duration by incorporating the atmospheric effects due to extraterrestrial solar irradiation and length of day. The author compares the developed model to Angström's equation with favorable advantages as the suggested method does not use the Least Square Method, in addition to having no procedural restrictions or assumptions [9].

Ulgen and Hepbasli [24] introduce two empirical correlations to estimate the monthly average daily GSR on a horizontal surface for Izmir, Turkey. Their models resemble Angström type equations [5]. The authors compare the developed models with 25 other models previously reported in the literature on the basis of statistical error tests, i.e., mean bias error (MBE), root-mean-square error (RMSE), mean percentage error (MPE), and coefficient of determination (R^2), with favorable results.

Other authors use estimation models based on artificial neural network techniques and, most specifically, multilayer perceptron (MLP) and radial-basis function (RBF) methods [6–8, 25–36].

Alawi and Hinai [25] have used ANN models to estimate solar irradiation in areas not covered by direct measurement instrumentation. The input data to the network are the location, month, mean pressure, mean temperature, mean vapor pressure, mean relative humidity, mean wind speed, and mean duration of sunshine [6, 8]. The corresponding ANN model estimated solar irradiation with an accuracy of 93 % and mean absolute percentage error of 7.3 %. Elminir et al. [29] have developed an ANN model for solar radiation in different spectrum bands with data collected between 2001 and 2002 at an urban area in Helwan, Egypt. The input data to the ANN model included daily values of wind direction, wind velocity, ambient temperature, relative humidity, and cloud cover. The back propagation algorithm is used with one-hidden layer and a sigmoid transfer function. The corresponding prediction accuracy is approximately 94.5 %. Krishnaiah et al. [31] have used ANN for estimating hourly GSR (HGSR) in India. The ANN models are implemented based on real meteorological data taken in India. Solar radiation data from seven stations were used for training the ANN while data from two stations were used for testing the prediction models. The resulting mean MBE, RMSE, and R^2 values are found to be 0.3133, 4.61, and 0.999954 respectively for the locations tested. The estimated values are in excellent agreement with the actual values.

Mohandes et al. [33] apply ANN techniques to estimate GSR using weather data collected from 41 stations in Saudi Arabia. The input variables in the network include: latitude, longitude, altitude and sunshine duration. The authors use data from 31 stations for training the network and data from the remaining 10 stations for testing. The accuracy of their results is within 16.4 % because the available sample data is not large enough to allow a credible comparison between the ANN and empirical regression models.

ANN-based estimation models of GSR for Abha, Saudi Arabia have been developed by Rehman and Mohandes [34] using different combinations of data including measured air temperature and relative humidity. Their results show that neural networks are well capable of estimating global solar radiation from temperature and relative humidity.

Lam et al. [35] use ANN models to estimate daily GSR using measured sunshine duration for 40 cities covering 9 major thermal climatic zones and subzones in China. The resulting coefficients of determination (R^2) are 0.82 or higher,

indicating reasonably strong correlation between daily solar radiation and the corresponding sunshine hours.

Mubiru [36] employs ANN models to estimate monthly average GSR on a horizontal surface for locations in Uganda based on weather station data: sunshine duration, maximum temperature, cloud cover, and location parameters: latitude, longitude, altitude. His results show good agreement between the computed and measured values of global solar radiation. An R^2 of 0.974 is obtained with MBE of 0.059 and RMSE of 0.385. Mubiru [36] also presents an extensive literature review of ANN-based GSR estimation techniques. He emphasizes the superiority of the proposed ANN model. The review highlights the popularity of ANNs in analyzing and processing solar radiation data and the considerable attention ANNs have received in this area.

The advantage of the ANN techniques is their ability to handle complex, dynamic and nonlinear systems with noisy and incomplete data. ANNs mimic the human brain in the way they learn the process and correlate between input and output data. ANN models can, therefore, easily cope with missing data and outliers in contrary to empirical models that are seriously affected by these abnormalities [10].

This chapter employs classical empirical regression techniques to estimate the monthly average daily GSR data in Dubai, UAE. The model data are compared to data from the optimal MLP and RBF ANN techniques, as well as to monthly average daily GSR data obtained from the Solar Radiation (SoDa) Web site [37] for the years 2002–2005.

The current work on the solar radiation data in the city of Dubai, UAE will be correlated with other models developed by authors for the UAE cities of Abu Dhabi and Al-Ain. The final objective is to come up with a common solar radiation model for the UAE that is capable of estimating the mean monthly GSR with good accuracy.

4.2 Background

This section presents a brief review of the used empirical regression models and the MLP and RBF ANN techniques. It addresses the available databases and Web sites for solar radiation data. The section also includes formulas of the main statistical error parameters used in building and testing the GSR models.

4.2.1 Empirical Regression Modeling Approach

Mean daily values of GSR data are calculated from the knowledge of latitude and longitude in the city of Dubai (latitude $= 25°\ 16'$ north and longitude $= 55°\ 16'$ east). The daily mean extraterrestrial solar radiation on a horizontal surface

Table 4.1 Nonlinear empirical regression models for Dubai weather data (y = RGSR; x = RSSH) [5]

Model reference	Type	Equation
[21]	Linear	$y = b_1 + b_2 * x$
[12]	Quadratic	$y = b_1 + b_2 * x + b_3 * x^2$
[23]	Cubic	$y = b_1 + b_2 * x + b_3 * x^2 + b_4 * x^3$
[14]	Logarithmic	$y = b_1 + b_2 * \log_e(x)$
[20]	Log-Linear	$y = b_1 + b_2 * x + b_3 * \log_e(x)$
[15]	Exponential	$y = b_1 * \exp(b_2 * x)$

in kWh/m^2 (G_0) and theoretical maximum daily sun hours (S_0) are calculated from the equations [5]:

$$G_0 = \frac{24 G_{sc}}{\pi} \left[1 + 0.033 \cos\left(\frac{360\,n}{365}\right) \right] \left[\cos(\phi) \cos(\delta) \sin(\omega_s) + \omega_s \sin(\phi) \sin(\delta) \right]$$

(4.1)

$$S_0 = \frac{2}{15} \left(\frac{180}{\pi}\right) \omega_s,$$

(4.2)

where n is the day index, ω_s is the mean sunrise hour angle in radians, ϕ is the latitude in radians, and δ is the declination angle in radians. G_{SC} is a constant representing the daily extraterrestrial solar radiation on a horizontal surface and is equal to 1.367 kWh/m^2. The declination angle (δ) is defined by the equation [5]:
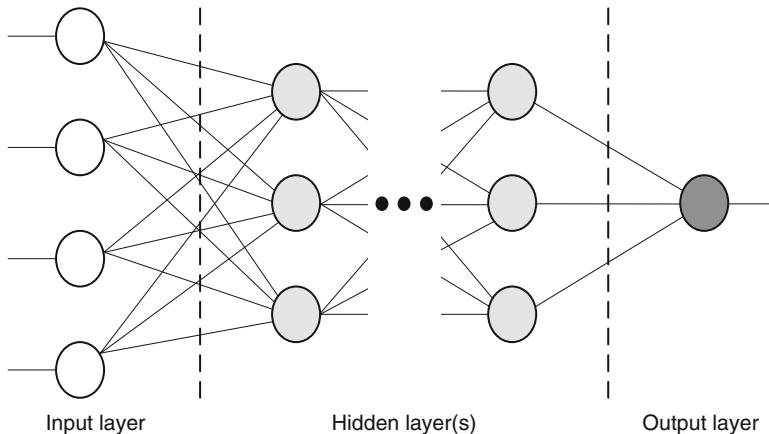
$$\delta = \sin^{-1}\left[\sin\left(\frac{23.45\pi}{180}\right) \sin\left(\frac{2\pi[n + 284]}{365}\right) \right].$$

(4.3)

The empirical models used in this chapter require knowledge of the mean daily GSR and daily sunshine hours (SSH). The discussion of available weather data is addressed in Sect. 4.3.

The available measured GSR and SSH data are next normalized to the extraterrestrial values G_0 and S_0 described in Eqs. (4.1) and (4.2), resulting in the normalized data arrays of clearness index (RSSH = GSR/G_0) and sunshine duration ratio (RSSH = SSH/S_0). The RGSR-RSSH data are finally fitted to different nonlinear regression models as per Table 4.1.

4.2.2   Artificial Neural Networks (ANN) Modeling Approach

A neural network is a massively parallel distributed processor made up of simple processing units that have a natural propensity for storing experiential knowledge and making it available for use. The artificial neural network (ANN) is an artificial intelligence technique that mimics the behavior of the human brain [6, 38].

Fig. 4.1 A multilayer perceptron (MLP) network (Source: modified from [6])

ANNs have the ability to model linear and nonlinear systems without the need to make assumptions implicitly as in more traditional statistical approaches. They have been applied in various aspects of science and engineering [6, 39, 40].

ANNs can be grouped into two major categories: feed-forward and feedback (recurrent) networks. In the former network, no loops are formed by network connections while one or more loop may exist in the latter. The most common family of feed-forward networks is a layered network in which neurons are organized into layers with connections strictly in one direction from one layer to another [6, 41].
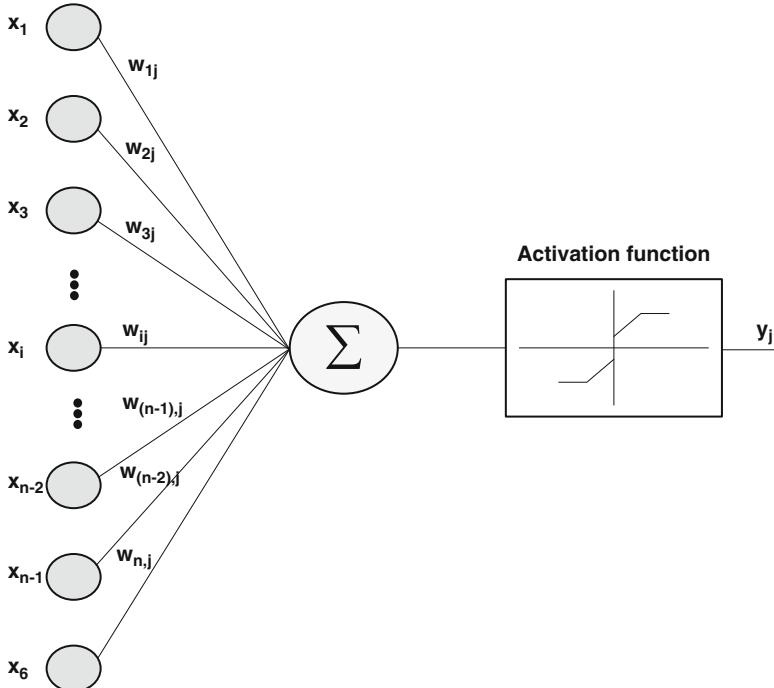
Multilayer Perceptron (MLP) Technique

The MLP ANN technique is the most popular type of feed-forward networks. Figure 4.1 shows an MLP network which has three types of layers: an input layer, an output layer and a hidden layer.

The diagram for the perceptron process is depicted in Fig. 4.2. Neurons in the input layer only act as buffers for distributing the input signals x_i to neurons in the hidden layer. Each neuron j in the hidden layer sums up its input signals x_i after weighting them with the strengths of the respective connections w_{ij} from the input layer and computes its output y_j as a function f of the sum [6]:

$$y_j = f\left(\Sigma x_i w_{ij}\right) \tag{4.4}$$

where f is the activation function which can be a simple threshold function or a sigmoidal, hyperbolic tangent, or radial basis function. The output of neurons in the output layer is computed similarly. The back-propagation algorithm, a gradient

Fig. 4.2 Details of the perceptron process (Source: modified from [6])

descent algorithm, is the most commonly adopted MLP training algorithm. It computes
the change Δw_{ij}, the weight of a connection between neurons i and j, in the form [6]

$$\Delta w_{ij} = \eta \sigma_j x_i, \tag{4.5}$$
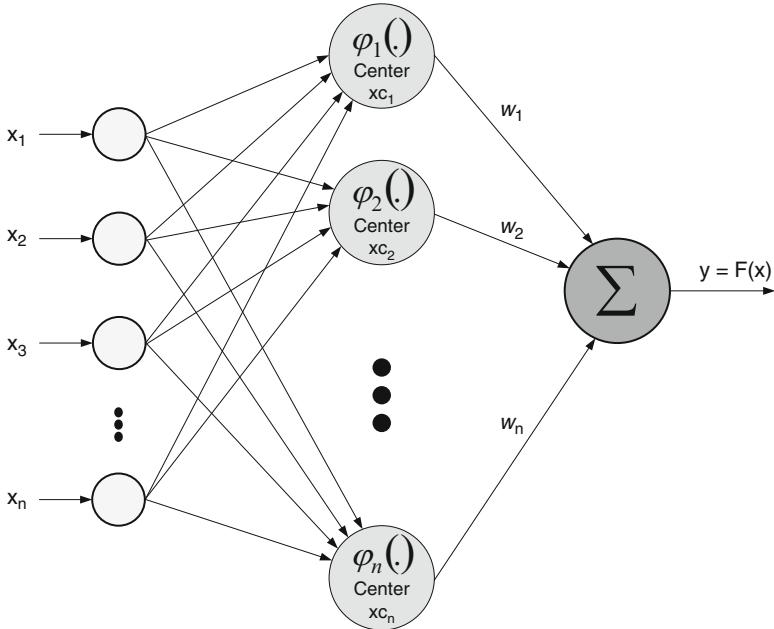
where η denotes the learning rate and σ_j is a factor that depends on whether neuron
j is an output neuron or a hidden neuron. For output neurons [6],

$$\sigma_j = \left(\frac{\partial f}{\partial net_j}\right)\left(y_j^{(t)} - y_j\right) \tag{4.6}$$

and for hidden neurons

$$\sigma_j = \left(\frac{\partial f}{\partial net_j}\right)\sum_q \sigma_q w_{qj}. \tag{4.7}$$

In Eq. (4.6), net_j is the total weighted sum of input signals to neuron j and $y_j^{(t)}$ is
the target output for neuron j. Since there is no target output of the hidden neurons
in Eq. (4.7), the difference between the target and actual output of a hidden neuron
j is replaced by the weighted sum of the σ_q- terms already obtained for neuron q

Fig. 4.3 Radial Basis Function network (Source: modified from [6])

connected to the output of neuron j. The process begins with the output layer; the σ term is computed for neurons in all layers with weight updates determined for all connections, iteratively. The weight updating process occurs after the presentation of each training pattern (pattern-based training) or after the presentation of the whole set of training patterns (batch training). The training epoch is completed when all training patterns have been presented once to the MLP [6].

A commonly adopted method to speed up the training process is to add a momentum term to Eq. (4.5) which allows the previous weight change to, effectively, influence the new weight change:

$$\Delta w_{ij}(I+1) = \eta \sigma_j x_i + \mu \Delta w_{ij}(I), \tag{4.8}$$

where μ is the momentum coefficient, and $\Delta w_{ij}(I)$ is the weight change in epoch I [26].

Radial Basis Function (RBF) Technique

The radial basis function network consists of three layers as shown in Fig. 4.3. The input layer has neurons with a linear function that simply feeds the input signals to the hidden layer. Moreover, the connections between input and hidden layers are

not weighted. The hidden neurons are processing units that perform the radial basis function. Each unit is mathematically described by [6]

$$\varphi_j(x) = \varphi(||x - xc_j||), j = 1, 2, \ldots, n, \tag{4.9}$$

where xc_j denotes the center of the radial basis function and vector x is the pattern applied to the input layer. The selection of the basis function is not crucial to the network performance; the most common being the Gaussian basis (activation) function which is used in this study [42] and is defined by

$$\varphi_j(x) = \exp(-\beta||x - xc_j||^2)j = 1, 2, \ldots, n. \tag{4.10}$$

The output neuron is a summing unit to produce the output as a weighted sum of the hidden layer outputs in the form [38, 42]

$$F(x) = \sum_{j=1}^{n} w_j \varphi_j(x), \tag{4.11}$$

where w_j denotes the weight between the jth hidden layer and the output $y = F(x)$.

4.2.3 Available Databases and Web-Based Sites for Solar Radiation Data

The development of Web-based and database systems have been encouraged due to the increased demand for GSR information from industry and research communities. Such systems offer GSR information derived from satellites. In the next paragraphs of this section, we provide a general review of available Web services and applications [43].

The Solar Radiation Data (SoDa) Web site [37] is an effort to consolidate different databases through the WWW server. The databases used for renewable energy are very diverse, and the useful parameters are sunshine duration, cloudiness, global irradiation with its diffuse and direct components, spectral distribution, atmospheric turbidity, atmospheric aerosol optical thickness, etc. The support of the information is also diverse: long time-series are available for a few hundreds of measuring stations (pin-point measurements) while shorter time-series are available for pixels. These pixels have various sizes: from 5 to 250 km. Moreover, SoDa provides many different average solar radiation maps (i.e., worldwide map). This Web service is available for free to everyone [37].

Surface meteorology and Solar Energy (SSE) [44] is a data-delivery web that was made available to the public in 1997. It provides easy access to parameters needed in the renewable energy industry (e.g., solar and wind energy). It is sponsored by NASA's Applied Sciences Program in the Science Mission Directorate developed by POWER: Prediction of Worldwide Energy Resource Project.

SSE displays the solar radiation, wind speed, atmospheric pressure, air temperature and humidity for a given location around the globe based on latitude and longitude data. It provides the following services: over 200 satellite-derived meteorology and solar energy parameters, monthly averaged from 22 years of data, data tables for a particular location, color plots on both global and regional scales and global solar energy data for 1,195 ground sites [44].

SWERA Renewable energy Resource EXplorer (RREX) [45] is an online Geographic Information System (GIS) tool for viewing renewable resource data. It encompasses a range of solar and wind data sets and maps. It relies on satellite and terrestrial measurements, numerical models, and empirical and analytical mapping methods. Through this interactive system, users can view several renewable resource data sets available through SWERA. RREX reports annual data when you click on the map. Users can view monthly data values from all available data sets at a given site by clicking on the desired location on the map [45].

Meteonorm [46] is a comprehensive meteorological reference. It gives access to meteorological data for solar applications, system design, and a wide range of other applications at any location in the world. It is designed for engineers, architects, teachers, planners, and anyone interested in solar energy and climatology.

SolarGIS [47] is a Web based system that includes high-resolution climate databases, maps and software for solar energy applications. It consists of four map-based applications:

- IMaps—interactive maps
- ClimData—access to solar radiation and air temperature data
- PvPlanner—high-performance PV simulator with extensive reporting capabilities
- PvSpot—sensor-less monitoring of the PV systems; the PV output for the defined time periods (daily, weekly, monthly, yearly, or other) is estimated according SolarGIS data in 15-min time steps.

In a previous work, the authors [43] have compared solar data from the three database services, namely, SoDa, SSE, and RREX, with ground station measurements provided by the NCMS center. Comparisons show that the SSE and SWERA Web sites outperform the other databases in predicting daily and monthly average GSR, respectively. This work can be extended by investigating more systems and the reasons behind the observed differences in GSR data for a given region in the UAE.

4.2.4   Statistical Error Parameters

This section defines formulas used to compute the statistical error parameters in MATLAB [5, 48]. These parameters attest to the accuracy of the models used for estimating the mean daily global solar radiation (GSR). The error parameters are also computed using SPSS [49] and values agree very well with MATLAB results.

The statistical analysis involves the computation of the coefficient of determination (R^2), the root mean square error (RMSE), the mean bias error (MBE), the mean absolute bias error (MABE), and the mean absolute percentage error (MAPE). The RMSE parameter provides information on the short term performance and measures the variation of predicted values around measured data. The lower the RMSE, the better is the estimation. The MBE parameter indicates the average deviation of predicted values from the corresponding measured data. It provides information on the long term performance of the models; the lower MBE the better is the long term model prediction. A positive (negative) MBE value indicates the amount of overestimation (underestimation) of the estimated GSR. The MAPE parameter estimates the percent deviation of the predicted values from the objective function [5].

The calculation of the aforementioned statistical parameters for monthly or daily average GSR data is done through the equations [5]:

$$\text{MAPE} = 100 \times \frac{1}{N} \sum_{i=1}^{N} \left| \frac{\text{GSR}_m^i - \text{GSR}_e^i}{\text{GSR}_m^i} \right| \tag{4.12}$$

$$\text{MBE} = \frac{1}{N} \sum_{i=1}^{N} \left(\text{GSR}_m^i - \text{GSR}_e^i \right) \tag{4.13}$$

$$\text{MABE} = \frac{1}{N} \sum_{i=1}^{N} \left| \text{GSR}_m^i - \text{GSR}_e^i \right| \tag{4.14}$$

$$\text{RMSE} = \sqrt{\frac{1}{N} \sum_{i=1}^{N} \left(\text{GSR}_m^i - \text{GSR}_e^i \right)^2} \tag{4.15}$$

$$R^2 = 1 - \frac{\sum_{i=1}^{N} \left(\text{GSR}_m^i - \text{GSR}_e^i \right)^2}{\sum_{i=1}^{N} \left(\text{GSR}_m^i - \overline{\text{GSR}}_m \right)^2}, \tag{4.16}$$

where $\text{GSR}_m{}^i$ and $\text{GSR}_e{}^i$ denote the ith measured and estimated values from the regression/ANN model in kWh/m^2, respectively, and N is the total number of data points. $\overline{\text{GSR}}_m$ is the mean measured value (in kWh/m^2) defined by

$$\overline{\text{GSR}}_m = \frac{1}{N} \sum_{i=1}^{N} \text{GSR}_m^i \tag{4.17}$$

The units of RMSE, MBE and MABE error parameters used in the comparisons of GSR data are in kWh/m^2.

4.3   Methodology

The weather database for Dubai, UAE is provided by the National Center for Meteorology and Seismology (NCMS) in Abu Dhabi, UAE. The available Dubai model data for the years 2002–2010 includes the maximum air temperature (T in $^\circ$C),

mean wind speed (W in knots), daily sunshine hours (SSH), mean percent relative humidity (RH) and mean daily global solar radiation (GSR in kWh/m^2). The GSR estimation models are produced using empirical regression methods and ANN MLP and RBF models.

4.3.1 Data Preparation and Rehabilitation

The weather dataset for the years 2002–2010 is first examined for any missing values and outliers. The missing data points are replaced with the mean of measured values for the same week. Long arrays of missing data (a month for example) are substituted with the corresponding average of the same days over the remaining model years. The total number of missing SSH or GSR data for Dubai does not exceed 2 % of the total data points. Two leap year days are also removed (February 29 for years 2004 and 2008) to ensure uniformity of month comparison over the 9-year model period.

The weather data is next divided into two groups: one data group from 2002 to 2008 for the estimation models and the remaining data set (2009–2010) for testing and validating the resulting regression and ANN models. The 7-year daily mean for the five available weather parameters (T, W, SSH, RH, GSR) is computed yielding a data set of size N = 365 for each variable.

The procedure used in the development of the MLP and RBF models starts with input data normalization (i.e., target values) in the range of 0 to 1, followed by the dataset matrix size identification [6, 10]. The normalized sub-datasets are then created and prepared for training and testing. First, the training set is randomized before creating and training the ANN. The output values are generated and denormalized, and finally the performance of the ANN model is verified through comparison of output and target values. All these steps are carried out using MATLAB tools [48].

4.3.2 Results and Discussion of Empirical Regression Models

This section focuses on the development of the empirical regression models and their validation. It also discusses the corresponding statistical error parameters which reflect the adequacy of these models for long-term estimation of GSR data.

GSR Estimation Models Using Empirical Regression

The empirical regression models defined in Table 4.1 are generated using MATLAB [48] and SPSS [49]. The regression models use the 7-year average

Table 4.2 Monthly average daily values of sunshine-hours in Dubai during 2002–2008

Month	Sunshine Hours (SSH)	Maximum sunshine hours (S_0)	RSSH = SSH/S_0
January	8.49	10.63	0.80
February	9.06	11.16	0.81
March	9.73	11.85	0.83
April	10.50	12.59	0.84
May	11.15	13.22	0.85
June	11.35	13.55	0.84
July	11.06	13.39	0.83
August	10.66	12.84	0.84
September	10.11	12.12	0.84
October	9.48	11.39	0.84
November	8.84	10.76	0.82
December	8.28	10.45	0.79
Annual	*9.89*	*12.00*	*0.83*

Table 4.3 Monthly average daily GSR values in Dubai during 2002–2008

Month	GSR (kWh/m^2)	G_0 (kWh/m^2)	RGSR = GSR/G_0
January	3.322	6.491	0.512
February	4.200	7.666	0.548
March	5.417	9.136	0.593
April	6.775	10.451	0.648
May	7.708	11.286	0.683
June	7.743	11.618	0.666
July	7.028	11.470	0.613
August	6.559	10.817	0.606
September	5.890	9.648	0.610
October	4.653	8.159	0.570
November	3.683	6.797	0.542
December	2.993	6.120	0.489
Annual	**5.498**	**9.138**	**0.590**
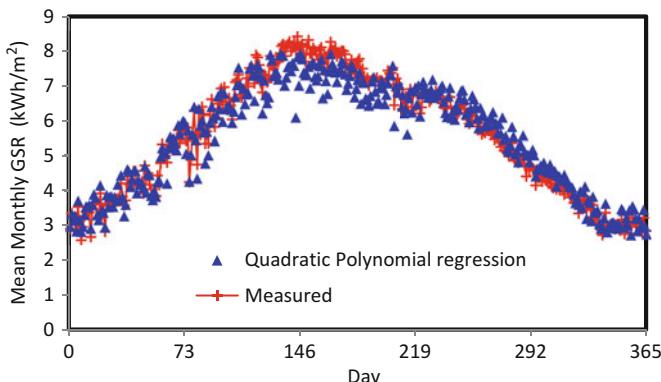
daily GSR and SSH data and the computed extraterrestrial G_0 and S_0 parameters as discussed in Sect. 4.2.1.

Table 4.2 shows the measured monthly average daily SSH values, the computed maximum daily hours of sunshine (S_0), and the corresponding ratio (RSSH = SSH/S_0) in Dubai for the years 2002–2008. The highest value of sunshine hours is observed during the month of May, and with an annual average of 12 h as seen in Table 4.2. The measured monthly average daily GSR along with the computed G_0 and clearness index values (RGSR = GSR/G_0) for Dubai during 2002–2008 are displayed in Table 4.3. The annual average GSR and clearness index are 5.498 kWh/m^2 and 0.59, respectively.
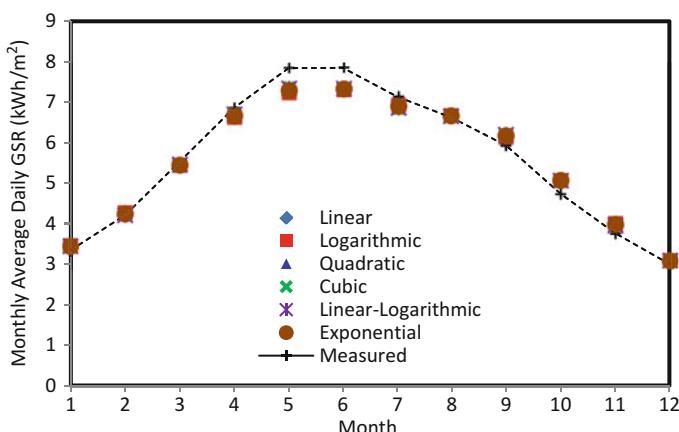
Table 4.4 shows the coefficients obtained for each regression model shown in Table 4.1. The statistical error parameters resulting from each regression model can be computed using SPSS or MATLAB. The best regression model must yield the lowest value of RMSE, MBE, MABE, MAPE, and R^2 (Figs. 4.4 and 4.5).

Table 4.4 Estimated
coefficients for empirical
regression models for years
2002–2008 in Dubai
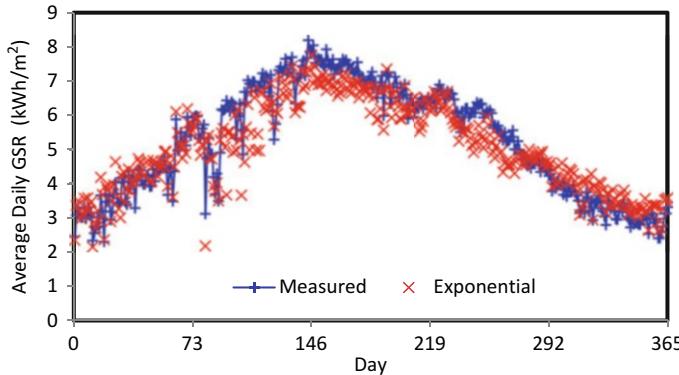
| Type	b_1	b_2	b_3	b_4
Linear	−1.2956	2.2878		
Quadratic	8.3306	−21.5662	14.7551	
Cubic	−30.9546	126.0446	−169.8774	76.8809
Logarithmic	0.9461	1.8365		
Log-Linear	−24.0210	25.4591	−18.7077	
Exponential	1.7667E-2	4.2489		

Fig. 4.4 Average daily GSR data comparison between the empirical quadratic regression model and the measured data in Dubai, UAE for the years 2002–2008


Fig. 4.5 Monthly average daily GSR data comparison between the empirical regression models and the measured data in Dubai, UAE for the years 2002–2008

Fig. 4.6 Comparison of daily average GSR data for the exponential regression model with measured data for the test period 2009–2010
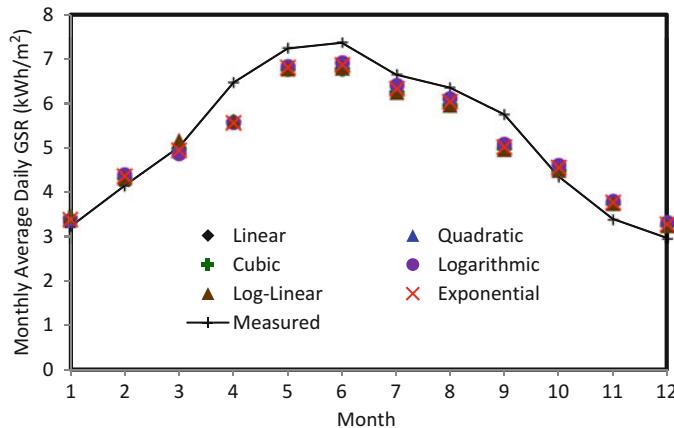
Validation and Testing of the Empirical Regression Models

The six selected empirical regression models are validated by computing the estimated daily average GSR data from these models using the test data set of the years 2009–2010. The empirical models compare very well with measured data for the test data period. All models yield coefficients of determination values R^2 better than 89 %. The estimation models also result in low values for RMSE, MBE, MABE, and MAPE indicating their adequacy as weather prediction models for Dubai, UAE. The exponential regression model outperforms the other five empirical models as shown in Fig. 4.6, with the lowest error statistics, i.e., $R^2 = 91.16$ %, RMSE $= 0.5502$ kWh/m^2, MABE $= 0.4298$ kWh/m^2, MBE $= -0.1623$ kWh/m^2, and MAPE $= 8.31$ %.

Figure 4.7 shows the comparison of monthly average daily GSR data between regression models and test data for the years 2009–2010. The data are also depicted in Table 4.5 along with the annual averages. The annual average GSR during the period 2009–2010 is slightly higher than 5 kWh/m^2 as evidenced in Table 4.5.

Table 4.6 shows the statistical error parameters for the six empirical regression models. The lowest values in regression models favor the logarithmic model, but all models yield high R^2 values (>96 %) and low values of RMSE, MBE, MABE, and MAPE. For the logarithmic model, the error parameters are RMSE $= 0.4297$ kWh/m^2, MABE $= 0.3756$ kWh/m^2, MBE $= -0.1333$ kWh/m^2, MAPE $= 7.42$ %, and $R^2 = 96.44$ %. Hence, the logarithmic model provides the best long term prediction. In addition, Table 4.6 confirms that the use of the simple linear regression model will also yield very good prediction results for daily and monthly average GSR data in Dubai.

The monthly average daily SSH and GSR values for the years 2009–2010 are shown in Tables 4.7 and 4.8, respectively. The same annual averages are maintained for clearness index (0.564 versus 0.59 for years 2002–2008), maximum sunshine hours (12), and monthly average GSR (5.247 kWh/m^2 versus 5.498 kWh/m^2 for years 2002–2008).

Fig. 4.7 Comparison of monthly average daily GSR values from regression models with measured data for the test period 2009–2010

Table 4.5 Monthly average daily GSR values (kWh/m^2) for Dubai during test period 2009–2010

Month	Measured	Linear	Quadratic	Cubic	Log	Log-Linear	Expo
Jan	3.2307	3.3911	3.4658	3.4411	3.3861	3.4696	3.4012
Feb	4.1532	4.4009	4.3315	4.3288	4.4086	4.3325	4.3730
Mar	5.0219	4.8998	5.1450	4.9738	4.8760	5.1757	4.9527
Apr	6.4694	5.5742	5.6023	5.5826	5.5749	5.6055	5.5648
May	7.2392	6.8247	6.7732	6.7639	6.8291	6.7751	6.8082
Jun	7.3676	6.9029	6.7903	6.7691	6.9137	6.7946	6.8625
Jul	6.6490	6.3898	6.2497	6.2520	6.4062	6.2506	6.3323
Aug	6.3547	6.0946	5.9636	5.9614	6.1095	5.9650	6.0419
Sep	5.7519	5.0767	4.9744	4.9961	5.0909	4.9718	5.0280
Oct	4.3559	4.6064	4.5028	4.4991	4.6180	4.5043	4.5653
Nov	3.3981	3.8074	3.7622	3.7595	3.8132	3.7630	3.7859
Dec	2.9688	3.3269	3.2664	3.2709	3.3347	3.2662	3.2991
Average	*5.2467*	*5.1079*	*5.0689*	*5.0499*	*5.1134*	*5.0728*	*5.0846*

Table 4.6 Error parameters for monthly average daily GSR estimation models for 2009–2010

Parameter	Linear	Quad	Cubic	Log	Log-Linear	Expo
RMSE	0.4321	0.4623	0.4631	0.4297	0.4624	0.4441
MABE	0.3764	0.4019	0.3956	0.3756	0.4043	0.3817
MBE	−0.1388	−0.1778	−0.1969	−0.1333	−0.1739	−0.1621
MAPE (%)	7.40	7.62	7.46	7.42	7.68	7.36
R^2 (%)	96.51	96.71	97.12	96.44	96.60	96.61

RMSE, MABE, and MBE values in kWh/m^2

Table 4.7   Monthly average daily values of sunshine hours for Dubai in 2009–2010

Month	Sunshine hours (SSH)	Maximum sunshine hours (S_0)	RSSH $=$ SSH/S_0
January	8.45	10.63	0.79
February	9.12	11.16	0.82
March	9.50	11.85	0.80
April	10.07	12.59	0.80
May	10.98	13.22	0.83
June	11.19	13.55	0.83
July	10.84	13.39	0.81
August	10.43	12.84	0.81
September	9.65	12.12	0.80
October	9.26	11.38	0.81
November	8.73	10.76	0.81
December	8.40	10.45	0.80
Annual	**9.72**	**12.00**	**0.81**

Table 4.8   Monthly average daily values of global solar radiation on a horizontal surface for Dubai during 2009–2010

Month	GSR (kWh/m$^{2)}$	G_0 (kWh/m^2)	RGSR $=$ GSR/G_0
January	3.231	6.488	0.497
February	4.153	7.675	0.542
March	5.022	9.143	0.552
April	6.469	10.448	0.619
May	7.239	11.286	0.641
June	7.368	11.621	0.634
July	6.649	11.476	0.580
August	6.355	10.827	0.587
September	5.752	9.648	0.596
October	4.356	8.156	0.534
November	3.398	6.793	0.501
December	2.969	6.125	0.484
Annual	**5.247**	**9.141**	**0.564**

4.3.3   Results and Discussion of ANN Models

Both the MLP and RBF neural network methods (Sect. 4.2.2) are applied for estimation of GSR in Dubai using the available data for the years 2002–2010. The ANN training models consider 11 different combinations of the four available weather variables (T, W, SSH, RH) as depicted in Table 4.9. Each of these models is used based on the availability of the weather parameters in the region where the solar energy system is being investigated [6, 10].

Table 4.9 Models based on different combinations of input weather parameters [6, 10]

Model No.	Input parameters
1	T–W–SSH–RH
2	T–W–SSH
3	T–W–RH
4	T–SSH–RH
5	W–SSH–RH
6	T–Wind
7	T–SSH
8	T–RH
9	W–SSH
10	W–RH
11	SSH–RH

Table 4.10 ANN toolbox training back-propagation algorithms in MATLAB [48]

No.	Function	Algorithm
1	Trainlm	Levenberg–Marquardt
2	Trainer	Bayesian Regulation
3	Trainbfg	BFGS Quasi-Newton
4	Trainrp	Resilient
5	Trainscg	Scaled conjugate gradient
6	Traincgb	Conjugate gradient with Powell–Beale Restarts
7	Traincgf	Conjugate gradient with Fletcher–Reeves updates
8	Traincgp	Conjugate gradient with Polak–Ribiére updates
9	Trainoss	One Step Secant
10	Traingdx	Gradient descent with momentum and adaptive learning rate
11	Traingdm	Gradient descent with momentum
12	Traingd	Gradient descent
13	Traingda	Gradient descent with adaptive learning rate
14	Trainscg	Scaled conjugate gradient

For the MLP models, the authors have investigated various network architectures in order to determine the optimal MLP architecture (i.e., the highest R^2, and the lowest RMSE, MBE, and MAPE) for each combination of input variables [6, 10]. Fourteen back-propagation training algorithms, described in Table 4.10, are tested with changes made in the number of neurons, hidden layers, and transfer functions in order to obtain the most appropriate algorithm for the training process [48].

The structure of MLP network is initially simple, but its complexity gradually increases as the number of hidden layer(s) and neurons in the hidden layer(s) increase. The model starts with one hidden layer and five neurons, and then the number of neurons is augmented in increments of five until a stable performance is reached (i.e., no more improvement). Next, a second hidden layer is added, and the gradual increase of neurons in the hidden layers is repeated. The same procedure is followed when a new hidden layer is added [6, 7, 10]. Different transfer functions in the hidden layer/

Table 4.11 Statistical error parameters of the developed MLP models for different network structures in Dubai for 2002–2008 [50]

Model	Network structure	Training algorithm	R^2	RMSE	MBE	MAPE (%)
1	4–105–1	Traingdx	0.97	0.268	−0.00255	4.33
2	3–20–1	Traincgb	0.96	0.299	0.00043	4.46
3	3–405–1	Traingdx	0.86	0.636	−0.00028	10.97
4	3–10–15–10–1	Traingda	0.98	0.220	0.04826	3.85
5	3–85–90–95–1	Traingda	0.96	0.280	0.00610	4.08
6	2–380–385–1	Trainrp	0.86	0.617	−0.09365	11.07
7	2–105–1	Trainb	0.80	0.746	−0.00500	13.41
8	2–280–285–1	Traingdx	0.80	0.757	0.05536	11.00
9	2–5 -10–1	Trainr	0.87	0.699	−0.09932	13.76
10	2–15–20–1	Trainr	0.88	0.620	0.19303	9.64
11	2–10–1	Trainb	0.97	0.255	0.02925	3.98

Units of RMSE and MBE are kWh/m^2

output layer are investigated including the tangent sigmoid, log sigmoid and linear functions. Generally, the ANN training algorithms (Table 4.10) used in MATLAB outperformed the other investigated training algorithms [6, 7, 10].

For the RBF models, the function's radius value (known as the spread) and the number of neurons are varied for the best performance of the RBF network. Basically, the larger the value of the spread, the smoother the function approximation will be. However, if the spread value is too large, many neurons may be required to fit the rapidly changing function. On the other hand, very small spread values may require many neurons for a smooth function fit and networks cannot be well generalized [48]. In this chapter, the spread varies between 1 and 60 whereas the number of neurons changes between 5 and 600 in order to come up with the best ANN models.

Table 4.11 shows the statistical error parameters resulting from a comparison of the developed MLP models for the 11 different configurations with the measured GSR data [50]. The best MLP ANN training model for long performance prediction is MLP model "four" with three hidden layers (10-15-10 neurons) and three input parameters (T, SSH, RH). Model "four" is the best among all the investigated MLP models as it yields the lowest error parameter values (MBE = 0.0483 kWh/m^2, RMSE = 0.22 kWh/m^2, MAPE = 3.85 %) and a coefficient of determination R^2 = 98 %.

Table 4.12 shows that the model "two" is the best among all the investigated RBF models [50]. RBF model "two" requires three input parameters (T, W, SSH) with one hidden layer (205 neurons), and yields MBE = −0.00001 kWh/m^2, RMSE = 0.318 kWh/m^2, MAPE = 4.09 %, and R^2 = 95 %.

The R^2 values for all models (MLP and RBF), shown in Tables 4.11 and 4.12, are higher than 75 %, indicating a reasonably good correlation between the estimated and measured values of average daily GSR. The RMSE values of all models vary between 0.220 and 1.142 kWh/m^2. All models are adequate for long-term prediction as attested by the low MBE error parameters. The MAPE values

Table 4.12 Statistical error parameters of the developed RBF models for different network structures in Dubai for 2002–2008 [50]

Model	Network structure	R^2	RMSE	MBE	MAPE (%)
1	4–105–1	0.95	0.318	0.00025	4.71
2	3–205–1	0.95	0.318	−0.00001	4.09
3	3–365–1	0.84	0.681	−0.00062	12.04
4	3–25–1	0.95	0.319	−0.00003	4.64
5	3–60–1	0.95	0.339	0.00909	3.97
6	2–70–1	0.78	0.766	−0.00224	13.38
7	2–245–1	0.75	0.806	−0.00506	14.25
8	2–210–1	0.75	0.803	−0.0078	14.64
9	2–10–1	0.86	1.142	0.00242	22.56
10	2–80–1	0.82	1.105	0.02964	21.25
11	2–50–1	0.95	0.339	0.00878	4.52

Units of RMSE and MBE are in kWh/m^2
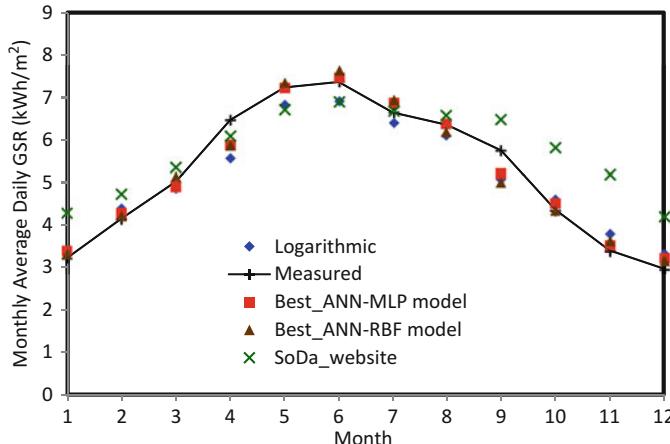
Table 4.13 Monthly average daily GSR (kWh/m^2) for Dubai during test period 2009–2010

Month	Measured	Log	MLP	RBF	SoDa
Jan	3.2307	3.3861	3.4106	3.3374	4.3000
Feb	4.1532	4.4086	4.3005	4.2330	4.7473
Mar	5.0219	4.8760	4.9146	5.1546	5.3625
Apr	6.4694	5.5749	5.8872	5.8819	6.0940
May	7.2392	6.8291	7.2259	7.3482	6.7160
Jun	7.3676	6.9137	7.4639	7.6403	6.8990
Jul	6.6490	6.4062	6.8752	6.9485	6.6815
Aug	6.3547	6.1095	6.3806	6.1954	6.5793
Sep	5.7519	5.0909	5.2240	5.0240	6.4820
Oct	4.3559	4.6180	4.5260	4.3636	5.8253
Nov	3.3981	3.8132	3.5413	3.6495	5.1983
Dec	2.9688	3.3347	3.2413	3.1811	4.2150
Average	**5.2467**	**5.1134**	**5.2493**	**5.2464**	**5.7583**

vary between 3.85 % and 22.56 %. In all models except RBF model "two", the MLP models yield better accuracy for estimating the average daily GSR as compared to RBF models.

4.3.4 Comparison Between the Best Empirical Regression, the Best MLP and RBF ANN Models, and SoDa Web site

Table 4.13 and Fig. 4.8 compare the estimated monthly average daily GSR from the best empirical regression model (logarithmic) and the two best ANN models (MLP model 4 and RBF model 2), with the measured data for the years 2009–2010. For comparison, we include in Fig. 4.8 and Table 4.13 the monthly average daily

Fig. 4.8 Comparison of monthly average daily GSR data from the best regression model (Logarithmic), the best MLP and RBF ANN models, and satellite Web site data (So-Da) with measured data for test period of 2009–2010

Table 4.14 Statistical error parameters for monthly average daily GSR from the best regression and ANN estimation models in Dubai

Parameter	Log	MLP	RBF	SoDa
RMSE	0.4297	0.2690	0.3189	0.8760
MABE	0.3756	0.2077	0.2455	0.7734
MBE	−0.1333	0.0026	−0.0003	0.1890
MAPE (%)	7.42	4.34	4.71	16.63
R^2 (%)	96.44	98.54	97.81	87.46

Units of RMSE, MABE, and MBE are in kWh/m^2

GSR data for Dubai (years 2002–2005) from the Solar Radiation data (SoDa) Web site [37].

Table 4.14 shows the statistical error parameters for the estimation models shown in Fig. 4.8. Better performance in all statistical error parameters is observed for the best ANN MLP and RBF models. The SoDa Web site gives a relatively good estimation for monthly GSR data but is less accurate than other models discussed. It does not, however, provide a good estimation for daily average GSR data [43]. The resulting low error parameter values (RMSE, MBE, MABE, MBE, and MAPE) for the MLP-ANN model clearly confirms the potential of ANN techniques for long term GSR data prediction. The negative MBE values for the logarithmic and RBF-ANN models imply that these models overestimate the GSR values, especially in the months of May-July (Fig. 4.8).

The Dubai measured data for 2009–2010 have some outliers which may negatively affect the regression models; however, the ANN models are more capable of handling data randomness. The implementation of ANN models requires expertise and computer time for training, in contrast to the empirical regression models that

can be implemented with the least effort and time. In addition, the regression models make use only of the sunshine-hour data and geographical location of Dubai. It is worth mentioning that the results of this chapter confirm that the use of even the simplest linear regression model will yield very good estimation results for daily and monthly average GSR data in Dubai. These simple models are indispensable prediction tools for scientists requiring GSR information in the absence of weather monitoring devices in their region.

4.4 Conclusions

Six different empirical regression models are developed for the estimation of the monthly and daily average global solar radiation in Dubai, UAE. The models require data for one weather parameter (sunshine hours), in addition to the geographical location (latitude, longitude) of Dubai. The estimated monthly average daily GSR data are compared with data from the best two MLP and RBF ANN models and SoDa Web site data (available for 2002–2005) with very good agreement. All models yield coefficients of determination that exceed 90 % for daily average GSR and 96 % for monthly average GSR, in addition to low MBE, MABE, MAPE, and RMSE error statistics that attest to the suitability of these models for long-term weather data prediction. The optimal MLP ANN model using three weather variables (temperature, sunshine hours, and relative humidity) yields the lowest error parameter values (MBE = 0.0483 kWh/m^2, RMSE = 0.22 kWh/m^2, MAPE = 3.85 %) and a 98 % coefficient of determination (R^2). The results confirm that the use of even the simplest linear regression model will yield very good estimation for daily and monthly average GSR data in Dubai. These simple models are indispensable tools for scientists requiring GSR information in the absence of weather monitoring devices in their region.

References

1. International Energy Agency (IEA Statistics © OECD/IEA, http://www.iea.org/stats/index.asp), Energy Statistics and Balances of Non-OECD Countries and Energy Statistics of OECD Countries (http://www.indexmundi.com/facts/united-arab-emirates/electric-power-consumption#EG.USE.ELEC.KH)
2. Rahman S (2012) UAE power capacity outpaces demand. http://gulfnews.com/business/economy/uae-power-capacity-outpaces-demand-1.1068506, August 31
3. Assi A, Jama M (2010) Estimating global solar radiation on horizontal from sunshine hours in Abu Dhabi—UAE. In: Proceedings of the 4th International conference on renewable energy sources (RES'10), 101–108, Sousse, Tunisia, 03–06 May 2010

4. Assi A, Jama M, Al-Shamisi M (2012) Prediction of Global Solar Radiation in Abu Dhabi. ISRN Renew Energy, 2012: 10, doi:10.5402/2012/328237

5. Hejase HAN, Assi AH (2011) MATLAB-assisted regression modeling of mean daily global solar radiation in Al-Ain, UAE. In: Assi AH (ed) Engineering education and research using MATLAB. Intech, New York, pp 195–218

6. Al-Shamisi MH, Assi AH, Hejase HAN (2011) Using MATLAB to develop artificial neural network models for predicting global solar radiation in Al Ain City—UAE. In: Assi AH (ed) Engineering education and research using MATLAB. Intech, New York, pp 219–238

7. Assi A, Al-Shamisi M (2010) Prediction of monthly average daily global solar radiation in Al Ain City–UAE using artificial neural networks. In: Proceedings of the 25th European photovoltaic solar energy conference, 508–512, Valencia, Spain, 06–10 September 2010

8. Assi A, Al-Shamisi M, Jama M (2010) Prediction of monthly average daily global solar radiation in Al Ain City–UAE using artificial neural networks. In: Proceedings of the 4th International conference on renewable energy sources (RES'10), 109–113, Sousse, Tunisia, 03–06 May 2010

9. Hejase HAN, Assi AH (2012) Time-series regression model for prediction of mean daily global solar radiation in Al-Ain, UAE. ISRN Renew Energy, 2012:11 2012. doi:10.5402/2012/412471

10. Al Shamisi MH, Assi AH, Hejase HAN (2012) Artificial Neural Network Modeling of Global Solar Radiation. Accepted for publication, Int J Green Energy, Taylor and Francis publisher, posted online Feb, 22, 2012. doi:10.1080/15435075.2011.641187

11. Abdalla YAG, Feregh GM (1988) Contribution to the study of solar radiation in Abu Dhabi. Energy Convers Manag 28(1):63–67

12. Akinoglu BG, Ecevit A (1990) A further comparison and discussion of sunshine based models to estimate global solar radiation. Energy 15:865–872

13. Al Mahdi N, Al Baharna NS, Zaki FF (1992) Assessment of solar radiation models for Gulf Arabian countries. Renew Energy 2(1):65–71

14. Ampratwum DB, Dorvlo ASS (1999) Estimation of solar radiation from the number of sunshine hours. Appl Energy 63:161–167

15. Elagib N, Mansell MG (2000) New approaches for estimating global solar radiation across Sudan. Energy Convers Manag 41:419–434

16. Falayi EO, Adepitan JO, Rabiu AB (2008) Empirical models for the correlation of global solar radiation with meteorological data for Iseyin, Nigeria. Int J Phys Sci 3:210–216

17. Fortin J, Anctil F, Parent L, Bolinder M (2008) Comparison of empirical daily surface incoming solar radiation models. Agric For Meteorol 148:1332–1340

18. Khalil A, Alnajjar A (1995) Experimental and theoretical investigation of global and diffuse solar radiation in the United Arab Emirates. Renew Energy 6(5–6):537–543

19. Menges HO, Ertekin C, Sonmete MH (2006) Evaluation of solar radiation models for Konya, Turkey. Energy Convers Manag 47:3149–3173

20. Newland FJ (1988) A study of solar radiation models for the coastal region of south China. Sol Energy 31:227–235

21. Podestá G, Núñez L, Villanueva C, Skanski M (2004) Estimating daily solar radiation in the Argentine Pampas. Agric For Meteorol 123:41–53

22. Şahin AD (2007) A new formulation for solar irradiation and sunshine duration estimation. Int J Energy Res 31:109–118

23. Samuel T (1991) Estimation of solar radiation for Sri Lanka. Sol Energy 47:333–337

24. Ulgen K, Hepbasli A (2002) Comparison of solar radiation correlations for Izmir, Turkey. Int J Energy Res 26:413–430

25. Al-Alawi S, Al-Hinai H (1998) An ANN-based Approach for Predicting Global Solar Radiation in Locations with no Measurements. Renew Energy 14:199–204

26. Behrang MA, Assareh E, Ghanbarzadeh A, Noghrehabadi AR (2010) The potential of different artificial neural network (ANN) techniques in daily global solar radiation modeling based on meteorological data. Sol Energy 84:1468–1480

27. Benghanem M, Mellit A, Alamri SN (2009) ANN-based modeling and estimation of daily global solar radiation data: a case study. Energy Convers Manag 50:1644–1655

28. Boccol M, Willington E, Arias M (2010) Comparison of regression and neural networks models to estimate solar radiation. Chilean J Agri Res 70:428–435

29. Elminir H, Areed F, Elsayed T (2005) Estimation of solar radiation components incident on Helwan site using neural networks. Sol Energy 79:270–279

30. Kassem AS, Aboukarima AM, El Ashmawy NM (2009) Development of neural network model to estimate hourly total and diffuse solar radiation on horizontal surface at Alexandria city (Egypt). J Appl Sci Res 5:2006–2015

31. Krishnaiah T, Srinivasa S, Madhumurthy K, Reddy KS (2007) A neural network approach for modelling global solar radiation. J Appl Sci Res 3(10):1105–1111

32. Mohandes M, Balghonaim A, Kassas M, Rehman S, Halawani TO (2000) Use of radial basis functions for estimating monthly mean daily solar radiation. Sol Energy 68(2):161–168

33. Mohandes M, Rehman S, Halawani TO (1998) Estimation of global solar radiation using artificial neural networks. Renew Energy 14:179–184

34. Rehman S, Mohandes M (2008) Artificial neural network estimation of global solar radiation using air temperature and relative humidity. Energy Policy 36:571–576

35. Lam JC, Wan KKW, Liu Y (2008) Solar radiation modeling using ANNs for different climates in China. Energy Convers Manag 49:1080–1090

36. Mubiru J (2008) Predicting total solar irradiation values using artificial neural networks. Renew Energy 33(10):2329–2332

37. SoDa: a Web service on solar radiation, http://www.soda-is.com/eng/index.html. Accessed 10 June 2012

38. Haykin S (2009) Neural networks and learning machines. Pearson Education, Inc., New Jersey

39. Yang J, Rivard H, Zmeureanu R (2005) Building Energy Predication with Adaptive Artificial Neural Networks. Ninth International IBPSA Conference Montréal 15–18

40. Chantasut N, Charoenjit C, Tanprasert C (2004) Predictive mining of rainfall predictions using artificial neural networks for Chao Phraya River. In: 4th International conference of the asian federation of information technology in agriculture and the 2nd world congress on computers in agriculture and natural resources 9–12.

41. Jain A, Mao J, Mohiuddin K (1996) Artificial neural networks: a tutorial. Computer 29(3):31–44

42. Jayawardena AW, Fernando DAK (1998) Use of radial basis function type artificial neural networks for runoff simulation. Computer-Aided Civil Infrastruct Eng 13:91–99. doi:10.1111/0885-9507.00089

43. Assi AH, Al-Shamisi MH, Hejase HAN (2012) Solar radiation in UAE—a comparison between ground station measurements and satellite estimation. In: Proceedings of the global conference on global warming 2012 (GCGW-2012), CD-ROM, Istanbul, Turkey, July 8–12

44. Surface meteorology and Solar Energy (SSE) Release 6.0, http://eosweb.larc.nasa.gov/sse/. Accessed on 13 Oct 2012

45. Solar and Wind Energy Resource Assessment (SWERA)—A United Nations environment programme facilitated effort. http://en.openei.org/apps/SWERA/. Accessed 10 June 2012

46. http://meteonorm.com/.

47. SolarGIS: http://geomodelsolar.eu/solar-radiation-data.

48. MATLAB (2010), version 7.10.0.499 (R 2010 a). The MathWorks Inc.

49. IBM SPSS Statistics for Windows (2010), Version 19.0.0, SPSS Inc.

50. Al-Shamisi MH, Assi AH, Hejase HAN (2012) Using artificial neural networks to predict global solar radiation in Dubai City (UAE). In: Proceedings of the 2nd International conference on renewable energy: generation and applications (ICREGA 2012), CD-ROM, Al-Ain, UAE, March 4–7

Chapter 5
Turkish Water Foundation Climate Change Downscaling Model Principles

Zekâi Şen and Ahmet Öztopal

Abstract Even though the atmosphere is modeled analytically, solutions are valid only if they are in good agreement with the necessary ground data within certain error bands. Available models provide basic information on the average behavior of the phenomenon concerned based on a set of simplifying assumptions. However, the natural phenomena temporal or spatial behavior shows unexpected deviations from the average. A set of assumptions such as the homogeneity, isotropy, uniformity, first order approximation, and alike cannot be valid at fine resolutions. In practice, simple but effective methods help to facilitate forecasting.

The global circulation (climate) model (GCM) is functional mainly due to extraterrestrial solar irradiation and terrestrial free water bodies as rivers, lakes, seas, and oceans at coarse resolutions. The end products of such models are available at several centers. The main problem is to develop a local model, which renders the coarse resolution into a practically finer local resolution by taking into consideration the combined effects of GCM outputs with the available ground measurements such as radiation, temperature, precipitation, humidity, wind speed, etc. It is the main purpose of this paper to develop a local downscaling methodology based on a set of statistical temporal and spatial pattern description techniques. Among such techniques are the spatial dependence function (SDF) for spatial downscaling and the White Markov (WM) process for temporal downscaling in addition to their combination in an effective manner over Turkey as a regional downscaling model.

Z. Şen (✉)
Hydraulics and Water Resources Division, Civil Engineering Faculty,
Istanbul Technical University, Sarıyer, 34469 Istanbul, Turkey
e-mail: zsen@itu.edu.tr

A. Öztopal
Department of Meterological Engineering, Faculty of Aeronautics
and Astronautics, Sarıyer, 34469 Istanbul, Turkey
e-mail: oztopal@itu.edu.tr

Nomenclature

S	Standard deviation
V	Cumulative semi-variogram
W	Weight coefficients
X	Observation time series value
x	Standard observation time series value
$\overline{X}$	The average value of the original time series
Z	Meteorological variable

Acronyms

AOGCMs	Coupled Atmosphere–Ocean General Circulation Models
ARIMA	Autoregressive Integrated Moving Average
ENSO	El-Nino Southern Oscillation
GCM	Global Circulation Model
IPCC	International Climate Change Panel
NAO	North Atlantic Oscillation
PCSV	Point cumulative semi-variogram
RegCM	Regional Climate Model
SDF	Spatial Dependence Function
SUAÖY	Su Vakfı Altölçekleme Yazılımı (Water Foundation Downscaling Software)
WMP	White Markov Process

5.1 Introduction

Various analyses related to the observations prove that rapid transitional climate changes are possible [1]. Model simulations show that such changes are expected more frequently in this century if the greenhouse gas emissions continue to increase. According to IPCC reports [2–5] there is a growing change in the global climate due to anthropogenic effects, which cause changes in the chemical

composition of the atmosphere. It is, therefore, necessary to improve understanding of the global climate system to assess the possible impacts of climate change on meteorological processes. General Circulation Models (GCMs) have mathematical bases of dynamic meteorology, atmosphere and ocean physics and state equation of gases. The outputs of such models are improved recently by coupled atmosphere–ocean GCMs (AOGCMs) along with transient procedures of forcing the greenhouse gases. Presently, GCMs resolution is coarser than $2°$ for latitudes and longitudes, which corresponds to about 300 km between grid points. These models provide meteorological scenario outputs up to 2,100 at nodes of quadrangle grids, which are tens of thousands of km^2 in size. However, in hydrometeorological studies the interested scale is about few hundred km^2. Hence, it is necessary to develop downscaling procedures in order to bring the scenario data to practically applicable scales with combination of past local meteorological records [6–8].

All regional studies for future climate change use m GCMs outputs of the atmosphere coupled with oceanic effects. In these models, the physical laws and empirical relationships that describe atmospheric and oceanic systems are represented by mathematical equations. It is possible to assess greenhouse gases effect the climate change system by changing input variables to GCMs. These models cannot depict adequately different geographical and spatial variability due to insensitive atmospheric, ocean, and the land surface affects. Furthermore, land-use changes such as deforestation and desertification are among the major local climate effective factors, which are not taken into account in the GCM, but they affect substantially local climates.

Despite of these limitations, researchers depend rather confidently on GCM outputs in their local downscaling works for local predictions. Such confidences may cause rather questionable local downscaling predictions on small scales. However, according to Wilks [9] "in spite of the problems that plague current GCMs, they are the best tool one has for projecting future changes in climate at a regional level." Nevertheless he suggests that the model results "should be treated strictly as scenarios of possible future climate and not as predictions."

Northern hemisphere atmospheric circulation shows different regimes related to North Atlantic Oscillation (NAO). However, understanding of the processes that generate NAO is not adequate for trust or not. The NAO effect extends up to Turkey and additionally ENSO (El-Nino Southern Oscillation) causes variability, which is obvious from unusually frequent El Nino transitions that have occurred in and around 1976. Changes in large-scale atmospheric circulation as represented by the ENSO and the NAO would further affect the occurrence of extreme events. The early 1990s were notable for recurrent droughts and periods of intense rainfall in the western Mediterranean and for extreme cold events and rainfall in the east. Recent climatic extremes are linked with the exceptional behaviors of ENSO and NAO. Record-breaking NAO values occurred in 1983, 1989, and 1990, while the prolonged 1990–1995 ENSO event was the longest on record.

The outlook for precipitation is much less certain, but most projections point to more precipitation in winter months and less in summer months over Turkey

as a whole. A common feature of many projections shows a declining annual precipitation over much of the Mediterranean region south of 40°N or 45°N. Even areas with more precipitation may get drier than today due to increased evaporation and changes in the seasonal distribution of rainfall and its intensity. On the other hand, it is expected that the frequency and severity of droughts could increase across Turkey. Changes in large-scale atmospheric circulation, as represented by the ENSO and NAO could further affect the occurrence of extreme events.
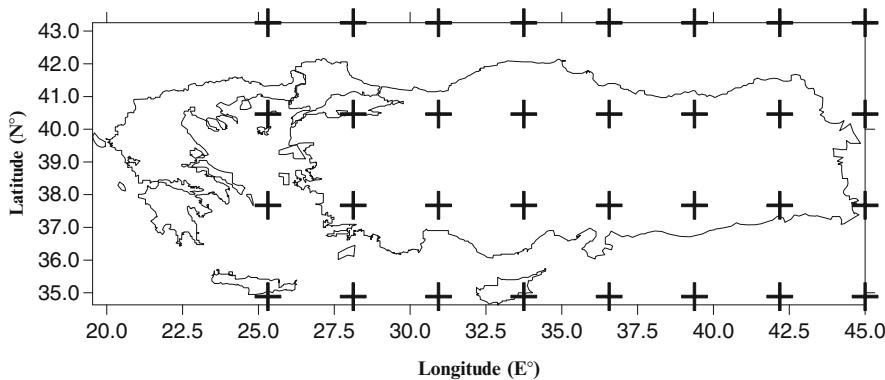
Many climate periods are nonlinear due to their nature and they cannot be predicted by linear models. One of the major reasons that they are not linear is due to the minor and sudden changes in the climate. This may show itself as a transition in the form of rapid climate change. In order to differentiate such events from the "extreme cases," change should be continuous to a certain extent. Among the conventional samples, there are transitions from one characteristic to another either naturally or forcibly that are triggered by enforcements. This happens in the nonlinear systems that have multiple balances [10]. Findings related to such possibility of transitions are founded in the paleo-climate records [11]. They can also be found in air patterns in today's observations [12]. Mediterranean region and Turkey are not intact from rising concentrations of greenhouse gases, which cause warming similar in magnitude to the global increase.

GCMs are particularly weak in determining moisture and hence precipitation availability. This is partly is due to the fact that potential evapotranspiration is not properly assessed by GCMs as a result of crude treatment of the hydrological cycle and partly because of the huge uncertainties over future precipitation. Despite of the weakness of the GCM in determining moisture content, there is a high level of consistency in model results for Turkey, with models showing an overall reduction in summer moisture availability in response to rising concentrations of greenhouse gases.

The main purpose of this research is to present a simple but effective downscaling model that functions locally by translating the GCM outputs over Turkey into local points. In the development of this downscaling model the spatial characteristics are modeled by the spatial dependence function and the time scale through the white Markov process.

5.2 Study Area and Data

Monthly precipitation data are used in this study from 1960 to 2006 in 299 stations over Turkey as an observation data and GCM data of National Centre for Atmospheric Research (NCAR). Figure 5.1 shows that the study area covers all Turkey, which is located between 36°–42°N and 26°–45°E.
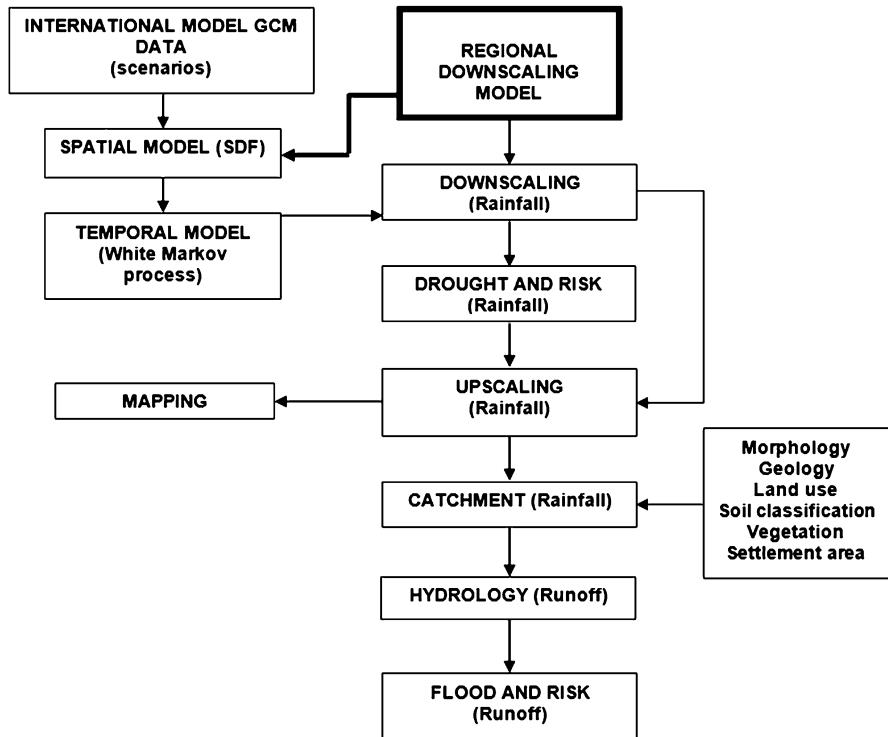
Fig. 5.1 Study area and National Centre for Atmospheric Research (NCAR)—node distribution [13]

5.3 Methodology

The structure of the proposed model is given through a set of short steps as follows.

1. *Global circulation model* (*GCM*): It constitutes dynamics base of the work and the analytic formulations are given by Trenbert [14].
2. *SRES scenarios*: They take into consideration social, cultural, features in addition to economy, technology, energy variety demography, agriculture, and environmental issues in local and global scales [4].
3. *Downscaling model*: GCM data are available at seven different centers (USA, Canada, UK, Germany, Italy, Japan and Australia). These centers run global modeling based on the previous two steps and the outputs are referred to as the GCM results. The relevant outputs from GCM for Turkey are then treated with the local statistical downscaling model by considering point cumulative semi-variogram (PCSV) principles for spatial resolution as developed by Şen [15] and the white Markov process (WMP) [16] is used for refining the serial dependence function of the scenario data so as to match them with the historical data structure.
4. *Field models*: Spatial transfer models have been used to make predictions at any point in Turkey. These models are generated with the use of spatial dependence function (SDF) [17].

The local model development and its joint operation with the GCM are presented in Fig. 5.2.
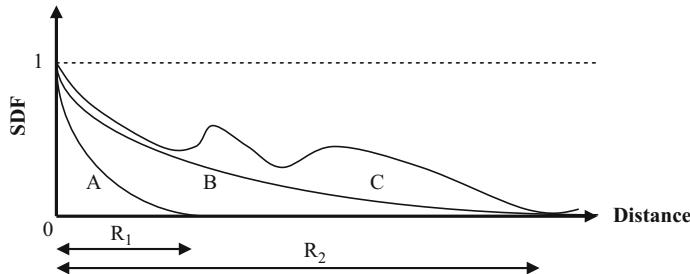
Fig. 5.2 Model flow diagram [13]

5.3.1 Spatial Dependence Function (SDF)

Space variability is a basic feature and very important in the physical sciences [18]. Field variability theory is developed by Matheron [19, 20] and the basics of this theory are suggested by a South African engineer, Krige [21]. The SDF is graph shows the spatial dependence value that varies between 0 and 1 with distance on the horizontal axis (see Fig. 5.3).

The distance between the starting point and the point closest to SDF is called the "radius of influence" (R_1 and R_2). If the meteorological variable has small spatial dependence then the radius of influence is also small. A circle with the radius of influence is considered around any station and then the effect of each station that remain within this area has weight coefficient, which can be obtained according to distances of each station to the center pint. Finally, estimation is obtained according to the Eq. (5.1) by multiplying the weight percentage with the recorded values at respective station.

Fig. 5.3 Theoretical SDFs [13]

$$V_E = \frac{1}{n} \sum_{i=1}^{n} (Z_T - Z_i)^2 \tag{5.1}$$
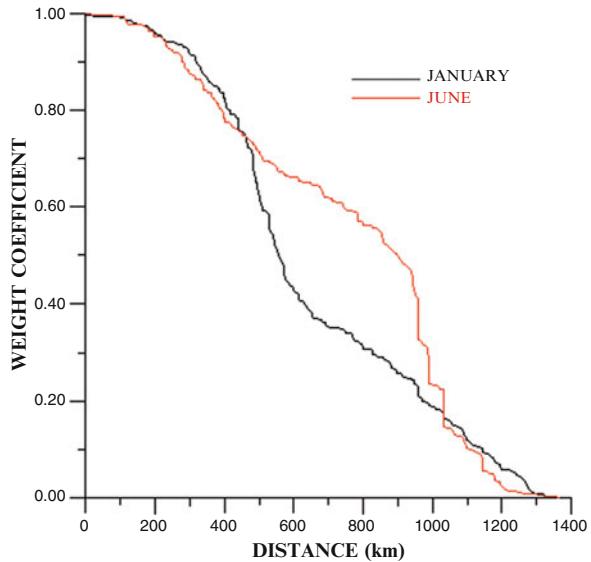
Various functions are claimed by scientists in relation to the above mentioned SDFs, but none of them is used in this work, because—they do not depend on actual data. For instance, Gilchrist and Cressman [22] assumed that the SDFs of each station should be in parabolic shape, so they have used a SDF, which is not obtained from the data. Bergthorsson and Döös [23] tried to find a result by using the best interpolation method following the initial estimations by Şen and Habib [24]. Cressman [25] reduced the radius of influence from 1,500–750 km and then to 500 km in order to obtain the best regional estimation. Unfortunately this method is used in the dynamic downscaling software (such as RegCM) in order to facilitate the spatial behavior process in downscaling. Barnes [26] has discovered a SDF, which he claimed it to be similar to the Gauss curve and used it without making references to actual data. All these methods are explained by Şen [27]. Goodin et al. [28] and Koch et al. [29] have applied spatial methods for wind fields and satellite image modeling and interpretations, respectively. However, deterministically proposed spatial dependence functions are suggested by Gandin [30, 31] without consideration any data but on logical and rational bases.

The main idea in most of the optimization analysis is to assess the estimation in a specific range as the weighted average of the randomly distributed fields. SDF methodology suggested by Şen [27] is applied to 299 meteorology stations in Turkey and different SDFs are obtained for each month and for each meteorology variable at any given station. Figure 5.4 shows the SDFs for the months January and June at one of the rainfall stations in Istanbul, Turkey.

For the calculation of SDF, a set of assumptions have been issued by Şen and Öztopal [15, 32, 33]. Let, Z_p represent the forecast variable and Z_i, the meteorological variables at location, i, with weight, W_i. In this case, the weighted average of forecast can be written as follows.

$$Z_P = \sum_{i=1}^{n} \left(\frac{W_i}{W_T} \right) Z_i \tag{5.2}$$

Where the sum of the weight averages is,

$$W_T = W_1 + W_2 + \cdots + W_n \tag{5.3}$$

W_i's can be obtained from SDFs, as values between 0 and 1 according to the distance.

5.3.2 White Markov Process (WMP)

There are many hydrological processes that have been used in order to make the observed data as similar as possible to the artificial data (synthetic data in stochastic hydrology or scenario data in climate change works). WMP differentiates from classical temporal stochastic modeling works due to its two important features [16]. It is simple and fast in terms of calculations and preserves the correlation coefficient, ρ, which is the criteria of the short term dependency and the Hurst coefficient, h, which is the criterion of the long-term dependency in the artificial series. The WMP complies with the simple, fast and Gaussian processes developed by Mandelbrot [34] to preserve the Hurst event.

WMP has two processes embedded to its structure, namely, first order Markov process in addition to an independent (white noise) process. Hence, temporal autocorrelation function can be formed freely with the combination of a process with high level first degree correlation coefficient coupled with an independent process.

Generally, to obtain the WMP, Z_t, a white independent process, η_t, is added at β level to the first degree Markov Process, X_t, as,

$$Z_t = X_t + \beta\eta_t \qquad (5.4)$$

The statistical structure of this process has been identified by Şen [16]. Particularly the k-th degree dependency coefficient ρ_k can be expressed as,

$$\rho_k = \alpha\rho_M{}^k \qquad (5.5)$$

Here, α represents the ratio of the standard deviation of white (independent) process and first degree Markov processes, which leads to,

$$\alpha = 1/\left(1 + \beta^2/\sigma_M{}^2\right) \qquad (5.6)$$

With substitution of the first order Markov process autocorrelation function as, $\rho_M{}^{k-1}$ at k-th lag in the correlation coefficient of the WMP the previous equation turns into,

$$\rho_k = \rho\rho_M{}^{k-1} \qquad (5.7)$$

If short term synthetic data are generated then it is possible to preserve the Hurst coefficient as greater than 0.5. So the WMP shows a simple, but effective approach of the ARIMA (1, 0, 1) processes frequently used in hydrological studies [35]. In order to determine this, many simulation works have been done by Şen [16] on digital computers.

WMP has been employed in this paper as a regulator in the adaptation of the GCM results to the observed data pattern. Left side of the Eq. (5.4) represents the scaled (regulated) scenario data, Z_t, the first term on the right side, X_t, is the scenario data transferred to the measuring points with the downscaling through the SDFs. Second term on the right includes the adjustments that can be made for the adaptation of the downscaled scenario data in the same location. It is observed that the inner dependencies of the scenario data are scaled but not regulated more than observed data. Empirical auto-correlation functions are observed to be similar to each other as the white noise (independent) process (second term on the right side) is added to the scenario data in order to obtain downscaled scenario data. Through the WMP, it is possible to reduce the serial (temporal) dependency structure of the downscaled scenario data. Hence, it is necessary to determine α (one of the parameters of WMP) in such a way that it provides the harmony between the historical and downscaled scenario series.

5.4 Application
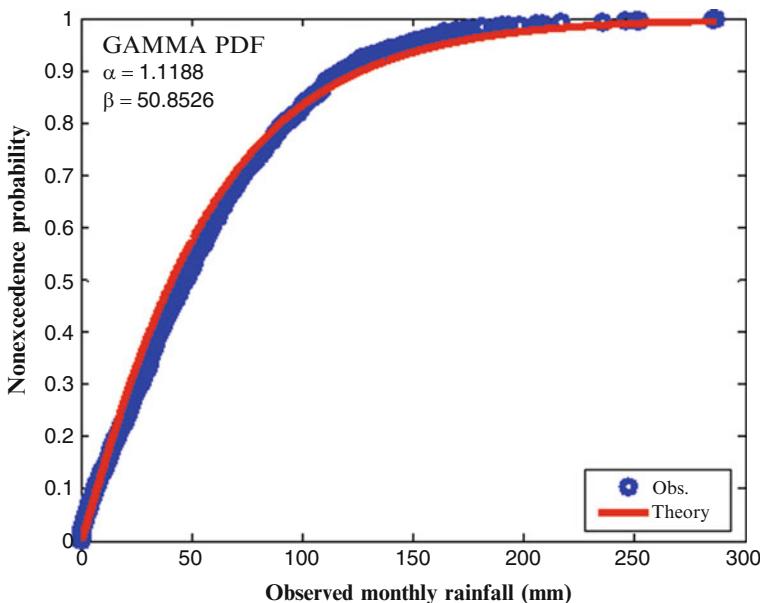
All of the aforementioned methodologies are gathered under the umbrella of a local software and the necessary calculations are obtained numerically and in the graphical forms for interpretations over Turkey. Similar downscaling structure can be used in any part of the world provided that the basic GCM and local data sets are available.

The prospects for precipitation over Turkey in a globally warming world are highly uncertain due to the general weakness of GCMs in predicting regional precipitation. Models offer conflicting evidence over how precipitation may change on the average over Turkey.
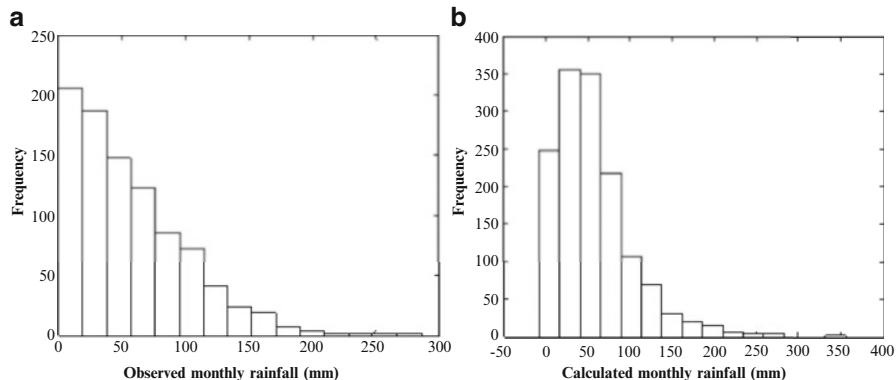
Reliability analysis of the observed data has been performed for each station in Turkey, and some of the past unreliable data is modified. In Fig. 5.5, probability distribution function (PDF) of İstanbul station is given and it confirms with the Gamma PDF.

In Fig. 5.6 frequency diagrams are given for observed and calculated monthly rainfalls. It is seen that frequency diagrams resemble each other in terms of degree, but details can be observed after comparisons.

1. While the distribution of the observation data is exponential (low rainfalls are always larger) (Fig. 5.6a), it is understood that the rainfall distribution until 2050 confirms with the Gamma (Fig. 5.6b).


**Fig. 5.5** Frequency distribution functions of theoretical and calculated rainfall [13]

Fig. 5.6 Frequency diagrams of the monthly rainfall data (**a**) Observation, (**b**) Scenario data [13]

2. Combination of the observation and scenario distributions helps to identify drought rainfall in the downscale model scenario outputs and there is expected increase in the next 50 years. The most dry seasons will not be the most frequent one, but an increase in the frequency of the 50 mm monthly rainfall is expected to occur.
3. While it is expected that the higher rainfall may occur more frequently (200 mm and more).
4. According to the extractions from the previous graphs, it is estimated that the rainfall in Turkey may not decrease dramatically, but the frequencies of the drought and extreme rainfall may increase.
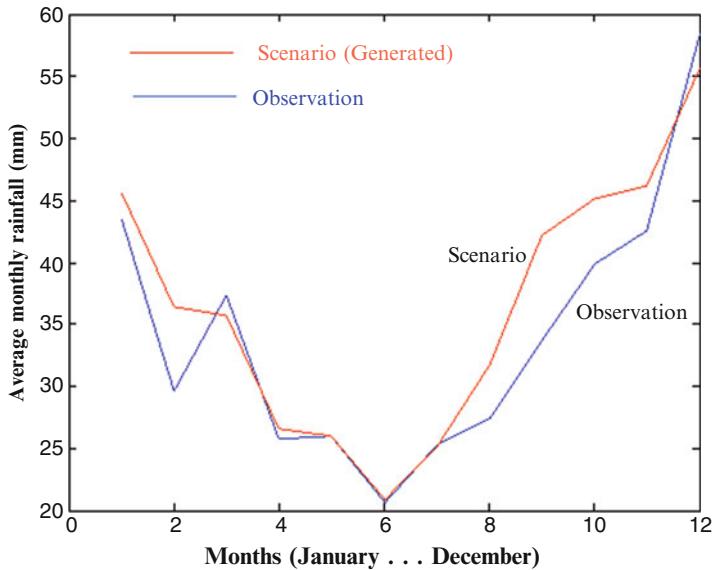
In Fig. 5.7, it has been checked if the scenario data up to 2050 confirm each other on monthly basis in terms of the rainfall amounts.

Tendency of the observation and scenario monthly average rainfalls resembles each other, although in winter season there is not a significance difference, but in the summer season monthly averages of the scenario data are more frequent.
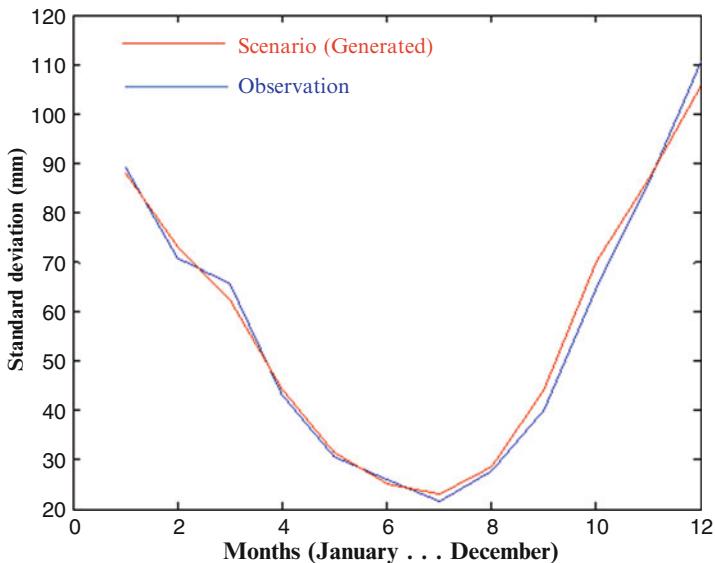
Figure 5.8 shows the monthly average standard deviation values obtained from the observation and scenario data.

The most important feature of this model is that the correlations of the observation and scenario data should be similar to each other. In this study, after the adaptation of the abovementioned monthly averages and standard deviations, standard values are obtained from scenario and observation data. If the given observation time series value is X_i, then the standard series x_i is obtained by calculating the average value of the original time series is $\overline{X}$, and standard deviation is S_X,
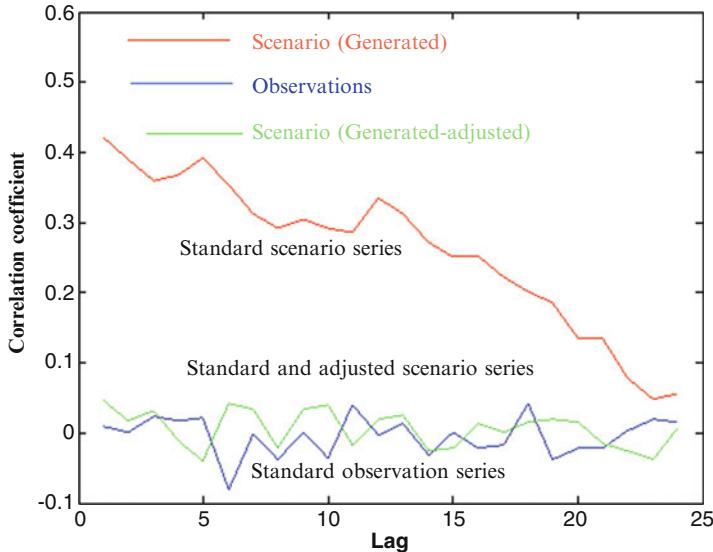
$$x_i = \frac{X_i - \overline{X}}{S_X} \tag{5.8}$$

**Fig. 5.7** Observation and scenario monthly average rainfalls [13]

Fig. 5.8 Observation and scenario monthly average rainfall standard deviations [13]

Fig. 5.9 Observation and scenario [13]

When the monthly changes of the time and dependency coefficient of the observation and scenario (generated) rainfall data in Fig. 5.9 are reviewed, it is understood that those data are never in a harmony and the scenario data have always more dependency coefficients than the observation data.

Physical meaning of this can be explained as when the variability over the distances (such as 300 km) is accepted as constant then it causes a more dependent result. In fact, past data records are affected even from the changes within the 5–10 km distances on the earth. Convective flows have also a role on that. For this reason, it is expected that the observation-time dependency has less dependency, and the results already confirm this. However, it is necessary that the scenario and observation correlation functions should be adapted as to be close to each other. To do this, "whitening" process is needed, which means that random compounds should be added to the scenario data in order to get the scenario data closer to the observation data correlation function. As the most important parameter of a random variable is its standard deviation, random compounds with various standard deviations should be added to the scenario data and this should be continued until the sum of the squares of the errors of the differences between the correlation functions is minimized.

After these settings, time correlation functions of the real data obtained from the calculation of the observation and scenario data with regards to the Eq. (5.8) are shown in Fig. 5.9. It is clearly seen that 12 month recurrent repetitions exist in the monthly rainfall.

5.5 Conclusions

Climate change studies are in progress towards better modeling directions so as to predict future meteorological and consequent hydrological events in the future. This paper presents an effective downscaling model for climate change impact scenario expectations. The model has two distinctive parts that are integrated in a harmonic manner for adjusting the estimations with local ground meteorology records. The first part concentrates on spatial behavior of the meteorological variables through an innovative spatial dependence function (SDF), which helps to make predictions on point basis from Atmospheric Circulation Model grid points to any desired point as spatial downscaling procedure. The second component is for temporal adjustment through the white Markov process, which helps to adjust the serial structure of scenario values indistinguishably from the measurements. The couple of spatial downscaling and temporal adjustment provide the climate change estimation procedure that is applied to precipitation data for replicates up to 2050 on monthly basis. Among the main findings are the possibilities of effective spatial dependence preservation together with temporal structure according to observed monthly precipitation series. It is found that the monthly values abide with the Gamma probability distribution functions and the first order serial correlation coefficient is sufficient for the downscaling methodology of this work. For Turkey, the percentage of error between the climate change impact replicates and the observations remain within the practically acceptable error limits of $\pm 10\ \%$ during the same time period from 1970 to 2000.

References

1. Appenzeller C, Stocker TF, Anklin M (1998) North Atlantic oscillation dynamics recorded in Greenland Ice Cores. Science 282(5388):446–449. doi:10.1126/science.282.5388.446
2. IPCC (International Climate Change Panel) – SAR (1995) Second assessment report. http://www.ipcc.ch/publications_and_data/publications_and_data_reports.shtml#.UNJNSeS6cl8
3. IPCC– TAR (2001) Third assessment report: climate change 2001. http://www.ipcc.ch/publications_and_data/publications_and_data_reports.shtml#.UNJNSeS6cl8
4. IPCC – SRES (2007) Special report on emissions scenarios. http://www.ipcc.ch/publications_and_data/publications_and_data_reports.shtml#.UNJNSeS6cl8
5. IPCC – AR4 (2007) Fourth assessment report. http://www.ipcc.ch/publications_and_data/publications_and_data_reports.shtml#.UNJNSeS6cl8
6. Goyal MK, Ojha CSP (2011) Evaluation of linear regression methods as downscaling tools in temperature projections over the Pichola Lake Basin in India. Hydrolog Processes 25:1453–1465. doi:10.1002/hyp.7911
7. Goyal MK, Ojha CSP (2012) Downscaling of surface temperature for lake catchment in an arid region in India using linear multiple regression and neural networks. Int J Climatol 32:552–566. doi:10.1002/joc.2286
8. Goyal MK, Burn DH, Ojha CSP (2012) Evaluation of machine learning tools as a statistical downscaling tool: temperatures projections for multi-stations for Thames River Basin, Canada. Theor Appl Climatol 108:519–534. doi:10.1007/s00704-011-0546-1

9. Wilks DS (1992) Adapting stochastic weather generation algorithms for climate change studies. Clim Change 22:67–84. doi:10.1007/BF00143344

10. Lorenz E (1993) The essence of chaos. University of Washington Press, Seattle, 224 pp

11. Stocker TF, Wright DG (1996) Rapid changes in ocean circulation and atmospheric radiocarbon. Paleoceanography 11:773–796. doi:10.1029/96PA02640

12. Corti S, Molteni F, Palmer TN (1999) Signature of recent climate change in frequencies of natural atmospheric regimes. Nature 398(6730):799–802

13. Şen Z, Uyumaz A, Öztopal A, Cebeci M, Küçükmehmetoğlu M, Erdik T, Sırdaş S, Şahin AD, Geymen A, Ceylan V, Oğuz S, Karsavran Y (2010) Final report on the impacts of climate change on İstanbul and Turkey water resources. İSKİ Project, 552 pp.

14. Trenbert KE (1993) Climate system modeling. Cambridge University Press, Cambridge, 818 pp

15. Şen Z (1989) Cumulative semivariogram model of regionalized variables. Math Geol 21(8):891–903. doi:10.1007/BF00894454

16. Şen Z (1974) Small sample properties of stationary stochastic processes and the hurst phenomenon in hydrology. Unpublished Ph.D. Thesis, Imperial College of Science and Technology, 256 pp

17. Şen Z (2008) Wadi hydrology. Taylor and Francis Group, Boca Raton, FL, 347 pp

18. Cressie NAC (1993) Statistics for spatial data revised edition. Wiley, New York, NY, p 900

19. Matheron G (1971) The theory of regionalized variables and its applications. Ecole de Mines, Fontainbleau, France, 211 pp

20. Matheron G (1963) Principles of geostatistics. Econ Geol 58:1246–1266

21. Krige DG, Magri EJ (1982) Geostatistical case studies of the advantages of log-normal, De Wijsian Kriging with mean for a base metal mine and a gold mine. J Int Assoc Math Geol 14(6):547–555. doi:10.1007/BF01033878

22. Gilchrist B, Cressman GP (1954) An experiment in objective analysis. Tellus 6:309–318

23. Bergthorsson P, Döös BR (1955) Numerical weather map analysis. Tellus 7:329–340

24. Şen Z, Habib Z (2000) Spatial precipitation assessment with elevation by using point cumulative semivariogram technique. Water Resour Manag 14(4):311–325. doi:10.1023/A:1008191012044

25. Cressman GP (1959) An operational objective analysis system. Mon Weather Rev 87:367–374

26. Barnes SL (1964) A technique for maximizing details in numerical weather map analysis. J Appl Meteorol 3:396–409

27. Şen Z (2009) Spatial modeling principles in earth sciences. Springer, Dordrecht, The Netherlands, p 351pp

28. Goodin WR, McRea GJ, Seinfeld JH (1979) A comparison of interpolation methods for sparse data: application to wind and concentration fields. J Appl Meteorol 18(6):761–771, 10.1175/1520-0450(1979)018 < 0761:ACOIMF > 2.0.CO;2

29. Koch SE, Desjardins M, Kocin PJ (1983) An iterative Barnes objective map analysis scheme for use with satellite and conventional data. J Appl Meteorol 22(9):1487–1503, 10.1175/1520-0450(1983)022 < 1487:AIBOMA > 2.0.CO;2

30. Gandin LS (1965) Objective analysis of meteorological fields, Leningrad, Gidromet. Israel Program for Scientific Translations, Jerusalem, p 242, Translated from Russian

31. Gandin LS (1965) Objective analysis, lectures on numerical short-range weather prediction, WMO, Regional Training Seminar, 633–677

32. Öztopal A (1998) Meteorological applications of genetic algorithms. Unpublished M.Sc. Thesis, İstanbul Technical University, Turkey, 66 pp

33. Şen Z, Öztopal A (2001) Genetic algorithms for the classification and prediction of precipitation occurrences. Hydrolog Sci J 46(2):255–267. doi:10.1080/02626660109492820

34. Mandelbrot BB (1971) A fast fractional Gaussian noise generator. Water Resour Res 7(3):543–553

35. Box GEP, Jenkins GM, Gregory CR (2008) Time series analysis: forecasting and control. Holden-Day, San Francisco, CA, 784 pp

Chapter 6
Climate Change Expectations in the Next Half Century of Turkey

Sevinc Sirdas, Zekâi Şen, and Ahmet Öztopal

Abstract Turkey as one of the mid-latitude countries in sub-tropical climate belt of the world has a special location meteoro-hydrologically. Various air mass movements display their impacts over Turkey's air, weather, and climate situations on a daily, monthly, or yearly base. Such a meteorologically interactive region is expected to have climate change signature variations as a result of various air movements in the future. A set of values from over three decades of observed temperatures, records from two overlapping periods 1960–1990 and 1970–2000 based on the records from the 30 years in the past, are taken. The basic time duration between 1960 and 1990 displays the actions as observed in the regular time period in the world. This time is considered as a base to determine the state of future temp changes. This study avoids statistical comparisons based on arithmetic averages and standard deviations; instead it adopts a method of interpreting the changes over the last three decades based on Special Report on Emissions Scenarios for different time intervals (5-, 10-, and 50-year). In this work, after establishing a special downscaling methodology, different General Climate Model results are coupled with local variables and following the verification and validation with measured data from almost 300 spatially distributed monthly temperature data, the significance of climate change impact is presented with relevant interpretations. The above explanations note that the greatest change in the last 40 years in terms of temperature is more visible in the highest temperatures rather than the average and lowest temperatures. Generally speaking, because the highest heats are observed in

S. Sirdas (✉) • A. Öztopal
Department of Meteorological Engineering, Faculty of Aeronautics and Astronautics,
Istanbul Technical University, Maslak, 34469 Istanbul, Turkiye
e-mail: sirdas@itu.edu.tr; oztopal@itu.edu.tr

Z. Şen
Hydraulics and Water Resources Division, Civil Engineering Faculty, Istanbul Technical
University, Maslak, 34469 Istanbul, Turkiye
e-mail: zsen@itu.edu.tr

summer times (less rainfall month), one may conclude that there is rise in the number of drought incidents in these times in Istanbul and different cities of Turkey.

Nomenclature

Z_P	The meteorological variable to be estimated in the station
Z_i	The adjacent meteorological variable values
W_i	The weight of the i-th station
W_T	The sum of the weight coefficients of all stations
V_E	The mean square errors
Z_T	Any estimate of the random distribution of a point

Greek Symbols

Σ	Summation function
α_i	The weight coefficients

Acronyms

GCM	General Circulation Model
SRES	Special Report on Emissions Scenarios
IPCC	Intergovernmental Panel on Climate Change
WMO	World Meteorological Organization
UNESCO	United Nations Educational, Scientific and Cultural Organization
IPCC-AR4	Intergovernmental Panel for Climate Change Assessment Report 4
EEA	European Environment Agency
UNFCCC	United Nations Framework Convention on Climate Change
CCIS	Canadian Institute for Climate Studies
EH40PYC	Max-Planck-Institute for Meteorology
HadCM	Hadley Centre Coupled Model
NCAR	National Center for Atmospheric Research
CCCMA	Canadian Coupled Climate Model and Analysis
RDF	Regional Dependence Function
CSV	Cumulative Semi-Variogram
PCSV	Point Cumulative Semi-Variogram
TAR WG3	Third Assessment Report Working Group 3
SCM	Successive Corrections Method

6.1 Introduction

Not only does climate play a role on present-day human activities, but also more significantly and scientifically its future predictions are among the most desirable elements so as to mitigate and to provide adaptive decisions, projects, plans, necessary structures, and their right as well as adjusted operations in order to reduce expected climate change impacts down to a safety minimal level. Water and food security plans, human health improvements, environmental protections, and social and economic affair are all related to climate change in the long run, but on the present day weather effects in the short run. Climate changes as the long-run average of weather patterns digest and refrain oscillation characteristics of weather events, and hence extremes in terms of floods, droughts, and consistent decreases or cuts disturb aforementioned activities more severely than weather events. It is, therefore, necessary to care for climate change possibilities in the future in order to sustain supportive agricultural products, water resource distribution and management, and vegetative life, all of which support human life on the earth.

Intergovernmental Panel on Climate Change (IPCC) with Special Report on Emissions Scenarios (SRES) [1 and 2] expresses the importance of future climate change expectations on different regions and sectors and definite role of anthropogenic atmospheric pollution by increase of greenhouse gases in an unprecedented rate, which must be offset for prosperous and sustainable future expectancies in various walks of life.

Researchers on climate change may be classified broadly into two categories depending on their data and material uses in their researches based on either past meteorology records or future meteorological variabilities which are statistically indistinguishable from the past records not only in stochastic sense but also and more significantly in climate change aspect sense also. Herein, stochastic similarity is the reflective pattern of future records in the future with the same characteristics in terms of extreme events, floods, droughts, heat waves, etc. On the other hand, future climate change replicates are not based on the past measurements stochastically only, but additionally climate change scenarios including population growth, energy types, agriculture, environmental, and socio-economical expectations. Hence, a climate change replicate of any future meteorology variable is not a sole extension of meteorology time series into future.

Since 1900, precipitation decreased by over 5 % over much of the land bordering the Mediterranean Sea, with the exception of the stretch from Tunisia through to Libya where it increased slightly [3]. Within these overall trends, regular alternations between wetter and drier periods are discernible. Records for both the western Mediterranean and the Balkans indicate major moist periods sometime during the periods1900–1920, 1930–1956, and 1968–1980 with intervening dry periods [4].

IPCC Technical Paper on Climate Change and Water [5] has mentioned some global warming effect on water resources of Turkey that is quoted here: "Increase in annual runoff in the North by up to 30 % and decrease by up to 36 % in the South.

Decrease in summer low flow by up to 80 %. Moreover decreasing drought risk in N. Europe, increasing drought risk in W. and S. Europe. By 2070s, today's 100-year droughts are studied to return, on average, every 10 (or fewer) years in parts of Spain and Portugal, western France, the Vistula Basin in Poland, and western Turkey" [6–10].

According to research of Solomon et al. [11], the range of climate sensitivities in climate models used for Intergovernmental Panel for Climate Change Assessment Report 4 (IPCC-AR4) is suggested to be 2.1–4.4 K per CO_2 doubling, or a warming of 0.6–1.2 K/W m^2 of forcing. However Knutti and Hegerl [12] showed that observational studies have not pointed this range and the upper limit is particularly challenging to estimate. Hannart et al. [13] and Baker and Roe [14] gave emphasis to quote here that all feedbacks, and thus the calculated climate sensitivity, may depend in a—largely unknown—nonlinear method on the state of the system before perturbation (the "background climate state") and on the type of forcing.

Jarvis et al. [15] mentioned in their paper that to avoid dangerous climate change, the feedback links need to exist between climate change and societal actions. They show that the global growth of new renewable sources of energy post 1990 represents a climate–society feedback of ~0.25 % $year^{-1}$ per degree increase in global mean temperature. As they resulted that to achieve the outcomes negotiated in Durban in 2011, society will have to become ~50 times more responsive to global mean temperature change than it has been since 1990. In addition Rohling et al. [16] find overlap in the 68 % probability envelopes that implies equilibrium warming of 3.1–3.7 K for 2XCO2, equivalent to a fast feedback (Charney) climate sensitivity between 0.8 and 1.0 K/W m^2 even though the known uncertainties associate with paleoclimate sensitivity calculations, and comparing with two previous approaches. However they point out that "for longer, multi-centennial projections, some of the slow feedbacks (namely vegetation-albedo and aerosol feedbacks) may need further consideration." According to their new approach a broad selection of previously published estimates for the past 65 Myra agrees on a best general estimate of 0.6–1.3 K/W m^2, which agrees with IPCC-AR4 estimates for equilibrium climate sensitivity.

Recent research done by European Environment Agency (EEA) cited here that the United Nations Framework Convention on Climate Change (UNFCCC) has agreed to limit the increase in global mean temperature since preindustrial times to less than 2 °C, in order to prevent the most severe impacts of climate change. Current global actions to reduce greenhouse gas emissions ("mitigation") are insufficient to constrain the temperature increase to 2 °C, and global warming could be well above 2 °C by 2100. Even if the 2 °C limit is kept, substantial impacts on society, human health, and ecosystems are projected to occur. Adaptation to and mitigation of climate change are therefore both needed. EEA's report [17] confirms that precipitation changes across Europe show more spatial and temporal variability than temperature. Since the mid-twentieth century, annual precipitation has been generally increasing across most of northern Europe, most notably in winter, but decreasing in parts of southern Europe. Furthermore in Western Europe intense

precipitation events have significantly contributed to the increase. There are no widespread significant trends in the number of either consecutive dry or wet days across Europe [17].

Turkey is self-sufficient as for the water resources and their future behavior under different climate change scenarios must be assessed for sustainable development. It is, therefore, necessary to develop local models for downscaling from the General Circulation (Climate) Model (GCM) outputs down to local scales so as to see what may happen in the future. For this purpose, a specific statistical downscaling approach is developed and the results are presented in this chapter.

6.2 Background: Atmospheric Modeling and Downscaling

Atmospheric environment is crucial for designing the livable world for next generation. Starting point of numerical weather prediction is related to forecasting weather in advance at wartime. Long-term and medium-range weather forecasting is parallel to the development of computers and subsequently around 10^7 calculations should be done at each grid point. Atmospheric models are mainly classified hydrostatic and non-hydrostatic which are solving dynamic and physical nonlinear partial differential equations by using numerical methods.

Model simulations cover a range of possibilities for future including idealized emission or concentration assumptions. These include SRES illustrative marker scenarios for the 2000–2100 period and model experiments with greenhouse gases and aerosol concentrations held constant after year 2000 or 2100. Global Climate Models used these scenarios to reveal significant impacts on food, water, energy, terrestrial biodiversity and ecosystem, agriculture, forests and forestry, and human health. Non-hydrostatic climate and medium-range numerical weather prediction models solve dynamical and physical equations by using numerical methods at each grid point. Downscaling methodology supplies derived atmospheric variables for every grid and station point as well. Objective analysis transfers values from gridded points to stations or inverse. Successive corrections methods (SCM) such as Cressman or Barnes schemes calculate variables depending on the distance between grid and station. In the SCM, the field variables are modified by the observations in an iterative manner. A pass is made through every grid point, updating the variable at each grid point based on first guess field and the observations surrounding that grid point. After one pass is made through the domain, another pass is made, again modifying the field at each grid point based on the observations surrounding the grid point [18]. The most common least squares method of data assimilation has been optimal interpolation (OI). Least squares methods differ from successive correction methods and nudging methods in that the observations are weighted according to some known or estimated statistics regarding their errors, rather than just by empirical values. Thus, observations from different sources can be weighted differently based on known instrument and

other errors [18]. In SCM the influence of the observations is determined empirically, without considering the error statistics of the observations or the background. In optimal interpolation, the influence of the observations on the analysis is related to how large or small the errors in the observations are likely to be.
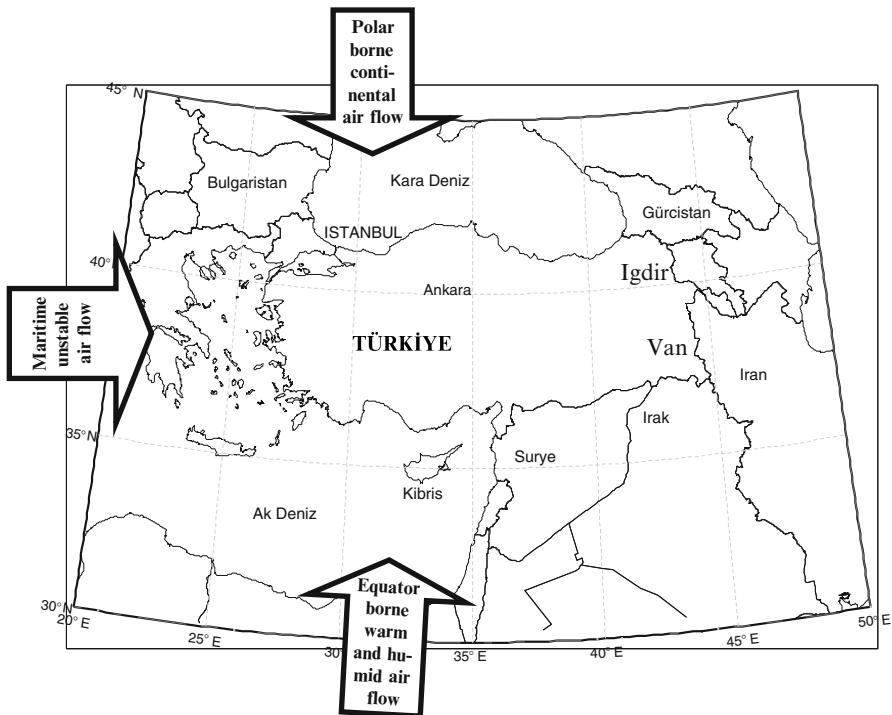
Modelers and researchers need to calculate the effect of global climate as to how it is going to shape the local environment. Having available information at grid and station level can show very apparent future climate expectations.

6.3 Study Area and Climate

Turkey, including rugged mountains of Anatolian Peninsula in southeastern Asia and east Thrace Peninsula in the southeastern Europe, is subject to different air mass movements from North Atlantic through Europe, Sahara reservoir extension from Africa, Siberian cold reservoir from north and Central Asia, and Arabian Peninsula air movement through Basra depending on seasons (Fig. 6.1).

The impacts may also be in long terms such as within a decade. In general, considering that the climate situation is of two options—summer and winter—Turkey experiences hot and moderate equator-originated climate in summer and is affected by cold and continental air circulations originated in the Arctic pole in winter. The continental air from the Siberian direction in winter is cold and dry and for this reason, it causes fog and cool weather. When it arrives at the Black Sea region, the dry air is replaced by humid air and for this reason, it elevates after hitting the Northern Mountains along the Black Sea terrain; this is why altitude-difference (orographic) rainfalls occur in West and East Black Sea regions. Different climatic types rule in Turkey, which is surrounded by sea in three parts and located between the warm climatic line in the south (below 38°N latitude) and sub-tropical lines (above 38°N latitude) in the north. It is possible to classify these in four items as three are of the climatic types over the Black Sea, Aegean, and Mediterranean Seas under the influence of the sea weather. The other is the continental climatic region affecting the East, Southeast, and Central Anatolia on the Asian side as well as the internal parts of Thrace on the European part of Turkey.

Atlantic Ocean-borne continental weather arrives in Turkey over Europe and Balkan Peninsula and it causes unstable rainfalls and snow in the inlands of Thrace and rainfall in shores in winter. The same air movement slides to the south, where it becomes more influential in terms of rainfall due to greater humidity. Consequently, increase in the rainfalls is observed in Toros Mountains behind the Mediterranean coastal line. The continental weather movements from Northern Africa in summer and the air movements from the north create frontal rainfall occurrences that collide around Turkey. The movement of dusts from the Sahara deserts of Africa leads to greater amount of rainfalls. On the other hand, typical

Fig. 6.1 Air circulations coming to Turkey [43]

December–February cyclones also affect Turkey. The cyclones in central latitudes are not frequent in June–October period. However, a strong upward-level line may lead to abnormal rainfalls in Turkey and Northern Iran.

The primary cyclone direction passes through the East Mediterranean. The two cyclone directions are related to the cold fronts of Cyprus and South Europe. This applies to the cyclones passing through Basra Gulf and the Fertile Crescent (Mesopotamia) [19]. Central and southeast Anatolian regions are drought areas because of the influence of the dry air movements. The main physical geographical impacts affecting Turkey in terms of rainfall are as follows:

- Black Sea and Mediterranean basins
- High mountainous terrains in west–east direction in the north and south
- High Anatolian Plato that exceeds 1,100 m altitude
- Air movements carrying humid that causes fertile rainfalls from Atlas Ocean to Turkey

Deep valleys in the southern edges of the Black Sea Mountains and small and low plateau on the Toros Mountains are dry and semidry areas. It is known that the

maritime-polar air movements carried by the northern and northwestern air movements cause strong rainfalls in the northern and western parts of Turkey in winters and early springs. Places with slight amount of rainfalls emerge in the southern parts and mountainous terrains of the West Black Sea region.

The emergence, magnitude, and ending of the dry conditions in Turkey display some differences from one region to another. In terms of the dry cycle time, it is possible to make the following statements on the aspects of different regions [20, 21]:

- The duration of the dry cycle is the longest with 6–7 months in Southeast Anatolia, Mediterranean, and Aegean shores as well as in the central parts of Central Anatolia. This is also the case with the low-altitude places including Igdir and Van (see Fig. 6.1).
- The Central Anatolian region, Marmara, and the southern parts of East Anatolia display a 5 or 6 months long dry period.
- The dry cycle in the northern side of Eastern Anatolia, the slight rainy parts of East Black Sea, and the shores of the Western Black Sea is 2–4 months.
- The only place with no dry period is the rainy parts of East Black Sea [22].

The gravity and duration of the need for irrigation in various regions in Turkey depend on the amount of water shortage and dry cycle periods as outlined above. The previous paragraph reviews the need for water, water shortage, and the gravity and duration of the drought with reference to the average values. However, they display significant differences from one year to another. Rainfall impact is closely related to the correlation between the need for water and the amount of rainfall. Essentially, need for water is a function of the heat. The rainfall effect varies depending on the heat and the annual changes in the rainfall. The monthly changes in the rainfalls are rare in our country. The monthly change between the periods April and December never exceeds 0.7–0.8 °C. This becomes 1.5–2.5 °C in the period between December and April. The winter period is relatively shorter. The deviations in this period do not cause any significant change in the amount of water needed. The impact of the positive deviations remains limited. Under these conditions, the greatest role in terms of water shortage in Turkey should be sought in the deviations in the distribution of these depending on time and place. In general, in years where the rainfall amounts significantly decline, the entire country suffers from a shortage of water or drought. Such a case took place in 1928 and 1932. In these years, the water shortage was deeply felt in the country but the rainfall effect lost impact. As a result of this, Central Anatolia and partially Çukurova fell into the domination of a desert climate. During this time, Southeast Anatolia became natural part of Syrian Desert. At the same time, dry conditions have become influential in Trachea, Southern Aegean, and East Anatolia. Only Black Sea and southwest Mediterranean remained outside of the dry conditions. Hydrological and meteorological drought analysis of Turkey's overall are presented and also the aim of this study is presented in the drought management plan for Ankara [23].

6.4 Methodology and Data

6.4.1 SRES Scenario Models

Scenario modeling methods established jointly by the World Meteorological Organization (WMO) and the United Nations Educational, Scientific and Cultural Organization (UNESCO) and IPCC, as defined in the various SRES are used all over the world. Especially in the form of suspension in 2000 [24], the IPCC emissions of greenhouse gases on the basis of production and to explore future developments in the SRES scenarios may be developed in the atmospheric environment. In doing so, the following terminology had taken on global climate models besides summarized in Table 6.1.

1. Story line: A set of verbal scenarios describing designs. The main scenario characteristics and dynamics with different effective relationship between the variables explain in detail.
2. Scenario: In open story lines of logic and potential prediction of the future.
3. Scenario team: The same population (demographic), the political, socioeconomic, and technological history appears by bringing together the lines.

These scenarios are taking into consideration the effects of climate change for demographic, economic growth, industry developments, and technologies of Turkey used in the next 50 years. The climate change scenario simulation data centers were found to be reliable around the world. It has been agreed upon that utilizing scenario data sets obtained from four scenario simulation data centers, which were selected according to distance from Turkey (ranged from closest to farthest), would be more favorable than making use of only one model center. For this reason, studies have been made using the data of the following four centers producing that scenarios:

(a) EH40PYC (Max-Planck-Institute for Meteorology, Germany)
(b) HadCM (Hadley Centre Coupled Model, England)

Table 6.1 The four SRES scenario families[a]

Fourth assessment report	More economic focus	More environmental focus
Globalization (homogeneous world)	A1	B1
	Rapid economic growth (groups: A1T; A1B; A1Fl)	Global environmental sustainability
	1.4–6.4 °C	*1.1–2.9 °C*
Regionalization (heterogeneous world)	A2	B2
	Regionally oriented economic development	Local environmental sustainability
	2.0–5.4 °C	*1.4–3.8 °C*

[a]Standard Reports on Emission Scenarios (SRES) [1, 2 and 24, 25] have studied global average surface warming until 2100 (according to Canadian Institute for Climate Studies, CCIS study)

Table 6.2 Climate centers and their scenario types used in the study

Scenarios					
Centers	A1B	A2	A2B	A2C	B2
NCAR	X	X	–	–	X
EH40PYC	–	X	–	–	X
HadCM	–	X	X	X	X
CCCMA	–	X	–	–	X

(c) NCAR (National Center for Atmospheric Research, USA)
(d) CCCMA (Canadian Coupled Climate Model and Analysis, Canada)
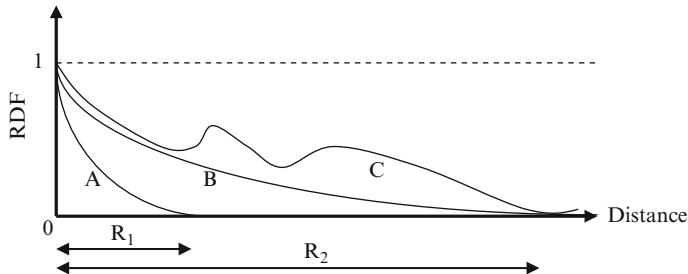
In the following Table 6.2, it is possible to obtain from each of the SRES scenario places the data indicated with "X." Here it is concluded that each SRES scenario was not found in all centers.

According to the given list 11 scenarios are selected in this study. Their http address and web site are listed here [44–47]:

(a) Max Planck Institute fur Meteorologie
    http://www.mpimet.mpg.de/en/home.html
(b) Hadley Centre for Climate Prediction and Research
    http://www.metoffice.gov.uk/research/hadleycentre/
(c) National Centre for Atmospheric Research
    http://www.ncar.ucar.edu/
(d) Canadian Center for Climate Modeling and Analysis
    http://www.cccma.ec.gc.ca/eng_index.shtml

6.4.2 Downscaling Method

As for the methodology statistical downscaling procedure is employed as developed specially for the climate change over Turkey [26, 27]. In order to determine rainfall amount of the each meteorological station two stages are required. The first of these involves the calculation of *R*egional *D*ependence *F*unction (*RDF*). Such a function is an indication of regional dependence which displays connection between the fixed station and all station records. It gives the relationship between distance and regional autocorrelation coefficient [26]. Logically, the distance decreases are expected to decrease regional dependency. Each meteorological variable and every month (time period) are different for RDF. The used approaches for calculation are developed by Sen [27–30]. In general, any downscaling process according to the average weighted scaling is done with the following equation. Here Z_P is the meteorological variable to be estimated in the station, Z_i, i = 1, 2, n, which shows adjacent meteorological variable values, and α_i also displays the weight coefficients:

Fig. 6.2 Theoretical RDF functions [43]

$$Z_P = \sum_{i=1}^{n} \alpha_i Z_i \qquad (6.1)$$

The weight percentages decreased with increasing distance, and the general behavior of each station is based on time period (day, month, and year) and weather condition variable. With the following expression it is possible to specify explicitly in terms of the percentage of weights:

$$Z_P = \sum_{i=1}^{n} \left(\frac{W_i}{W_T}\right) Z_i \qquad (6.2)$$

where W_i is the weight of the i-th station to indicate that the sum of the weight coefficients of all stations written in the below form:

$$W_T = W_1 + W_2 + \cdots + W_n \qquad (6.3)$$

W_i values are obtained by RDF in this study. RDF is the value in the range of 0–1. Thus, the general state of RDF will be resembled within the curves shown in Fig. 6.2 wherein A, B, and C are shown in different RDF. In practice, the forms of A or B are the most frequent.

The distance between the start point and the value of RDF very close to zero is called the radius of influence. These variables are independent of direction (isotropic), and the radius of influence is equal in all directions. Thus, the distance of the radius of influence affects the area that accepts this circular. The number of stations used in this study is 299.

RDFs are obtained for the weight coefficients similar to Fig. 6.7. With this weight percentages of the values recorded in each station by multiplying the estimated value are obtained according to Eq. (6.2).

Gilchrist and Cressman [31] assumed that RDF of each station needs to be in the form of a parabola function, and thus has not been obtained from the data used in an RDF. After the initial guess values are refreshed using the interpolation method recursively to obtain the best result [32, 33]. Cressman [34] tried to capture the best

regional forecasts by reducing the radii of influence to 1,500, 750, and 500 km successively. In addition, until 1979, all existing methods of rational mutual comparative reviews were provided by Goodin et al. [35]. Besides, some studies are done by using Barnes method in software such as that of Koch et al. [36].

According to studies made by [32] and [37] "the problem of RDF based on simple inverse distance is the recordings made according to each other's regional dependence not to be considered." For example, the two points at the same distance from a node have given the same weight value from where they have been ignored even if the records are not close to each other.

6.4.3 Point Cumulative Semi-variogram Models

Data that is received from various centers of approximately equal intervals of 250–400 km built a regular network node points (Figs. 6.3, 6.4, 6.5, and 6.6). However, it is not rational to use coarse scale for water- related studies. First of all this data must be downscaled to dense grid networks. In this study, RDF obtained from available data will be used. The fundamental of regional dependence function is developed by Sen [27, 29] as cumulative semi-variogram (CSV) and point cumulative semi-variogram (PCSV) methods.

The average of squares of errors can be reduced minimum value easily such as the best least square method with following equation:

$$V_E = \frac{1}{n} \sum_{i=1}^{n} (Z_T - Z_i)^2 \tag{6.4}$$

The main idea of most optimization analysis is estimate of any point which scattered randomly considered as the weighted average of the values in the forecast fields. The RDF calculation method described in detail by Sen [26] is applied to 299 meteorological stations. Here, for each station weather variables are obtained separately from the RDFs. Accordingly, a total number of 17,940 RDFs were obtained from 299 (station) $\times$ 12 (months) $\times$ 5 (variable). The sample of RDF is given in Fig. 6.7.

In this way, the RDFs are obtained for the best curve by applying the genetic algorithm methods in Fig. 6.8.

If we look at the graph in Fig. 6.8, while blue (diamond shape) refers to PSV values, the pink (square) shows Barnes [38] function trained with the genetic algorithm (x-axis is the standardized distance and y-axis is the weight coefficient). The fixed station has the distance "0" and weight coefficient "1" from PCSV; thus the graph shows the RDF of that station. As a result, the climate change data of each station are obtained with the node points value moved to the stations by using Barnes function trained with the genetic algorithms.
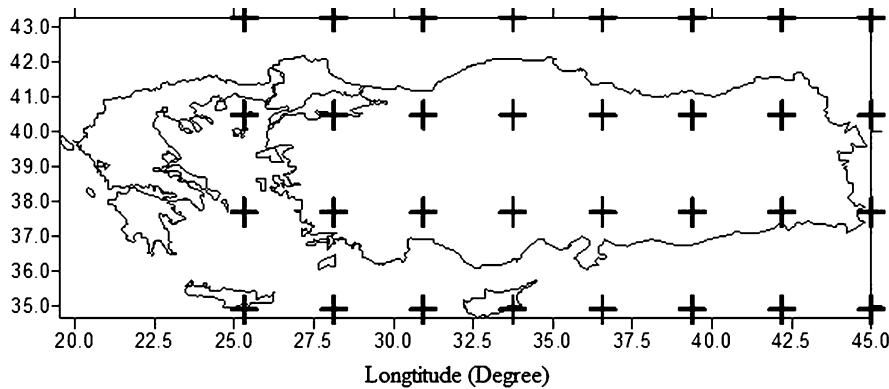
Fig. 6.3 National Center for Atmospheric Research—NCAR distribution of nodes [43]
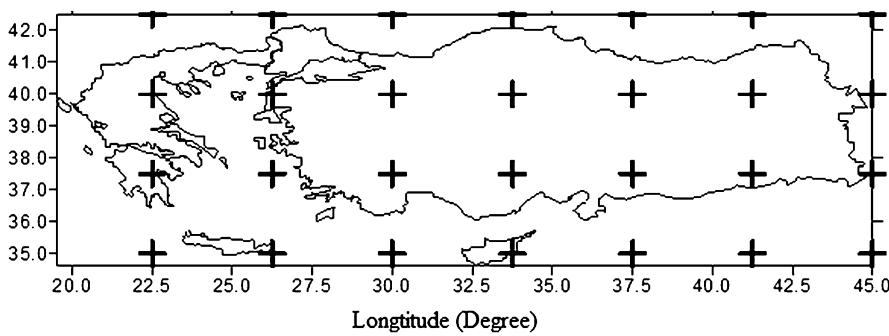

**Fig. 6.4** Hadley Centre for Climate Prediction and Research—HADCM3 distribution of nodes [43]
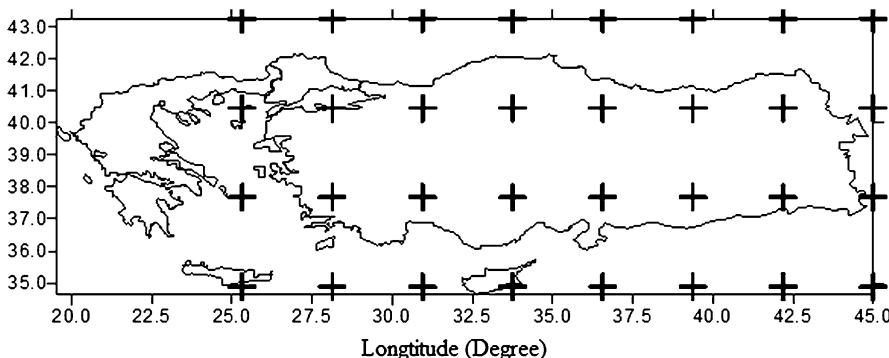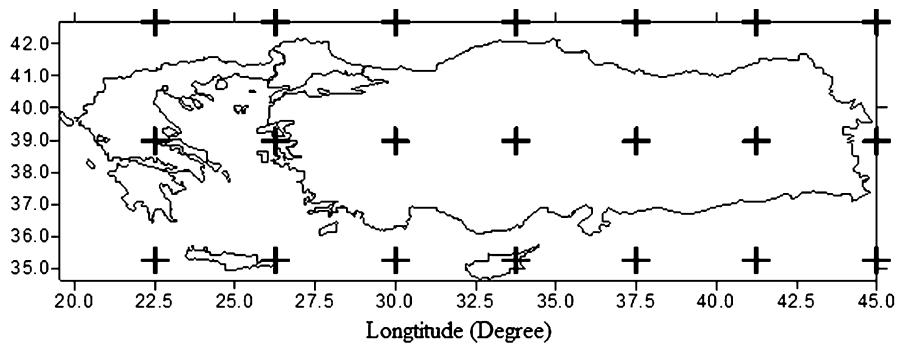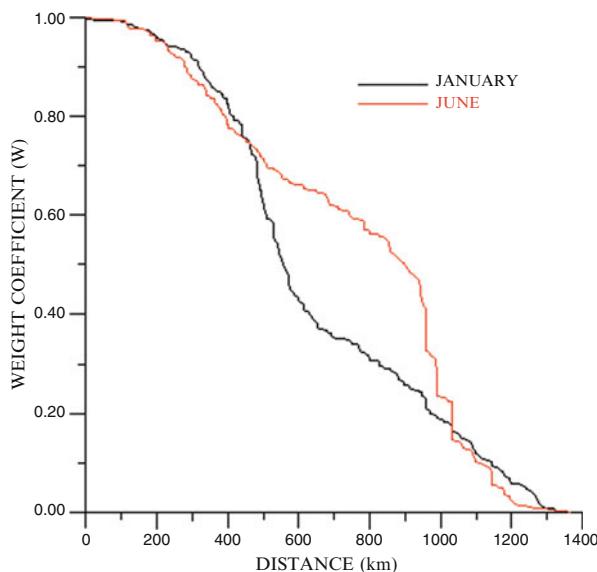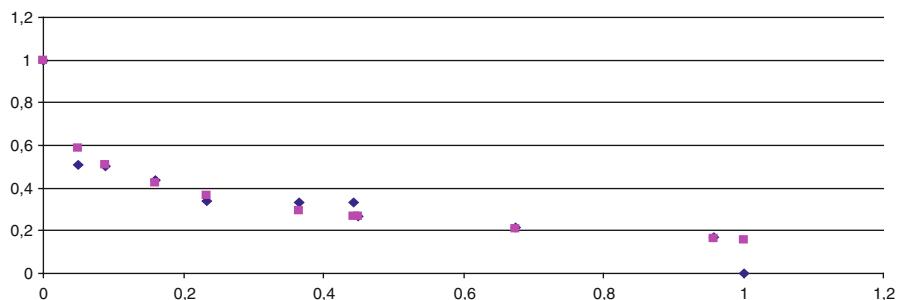
**Fig. 6.5** Max Planck Institut fur Meteorologie—EH4OPYC distribution of nodes [43]

**Fig. 6.6** Canadian Center for Climate Modeling and Analysis—CCCMA distribution of nodes [43]

**Fig. 6.7** Regional dependence function [43]

Fig. 6.8 Raw and genetic algorithm-applied RDF values [43]

6.5 Results and Discussions

6.5.1 Future Temperature Prediction Data

To obtain a set of values from over three decades of observed temperatures, records from two overlapping periods 1960–1990 and 1970–2000 based on the records from the 30 years in the past are taken. The arithmetic average based on these values, standard deviations, and trend values provide insights into the way of actions of the temperature climate component. The basic time duration between 1960 and 1990 displays the actions as observed in the regular time period in the world. This time is considered as a base to determine the state of future temp changes.

Before comparison with the scenario forecasts, it is useful to investigate the forms of changes and trends in terms of time and location in climate by reliance on comparison with the temperature actions as observed in the four decades between 1960 and 2000. Figure 6.9 shows the form of temperature changes in 30 years from the period between 1960 and 1990. Here, the upward triangles refer to increases, whereas the downward triangles point to declines. Accordingly, in terms of largest monthly temperatures, the temperature increases in Istanbul and nearby towns have been observed.

Before comparison with the scenario predictions to be given here, by comparison of the situations observed in the temperature actions in the last 40 years of the twentieth century, it is useful to locate the trends in terms of time and location. Figure 6.9a provides information on the declines in the temperatures in terms of highest monthly temperatures in Istanbul between 1960 and 1990.

In terms of average temps, at the same regular time period, despite declines in Asian part of Istanbul, European part displays some increase (Fig. 6.9b). There is no significant change in interior parts. The changes appeared in shores of Turkey. In Ankara, temperature trends show some increases, whereas the lake regions (the city of Isparta and the nearby towns) appear to have shown some declines in temps.

Figure 6.9c shows that the temperature trends of lowest temperatures in regular period of time appear in the coastal regions in Turkey, also confirming that there has been no significant change in interior parts. In face of increased trends in European parts, the Asian part (Kocaeli peninsula) of the city showed some decline trend in the lowest temperatures.

Based on the past observations, a second regular period of time is defined between 1970 and 2000 (Fig. 6.10). Internationally insignificant, this period is important as it shows the type of the change in temperature actions. During this regular period, it becomes evident that greater temperatures have become widespread in Turkey after comparison with the situation in Fig. 6.9a. Except in the entire Black Sea and Central Anatolia temperature increases are observed in all others. The points to be underlined include the following:
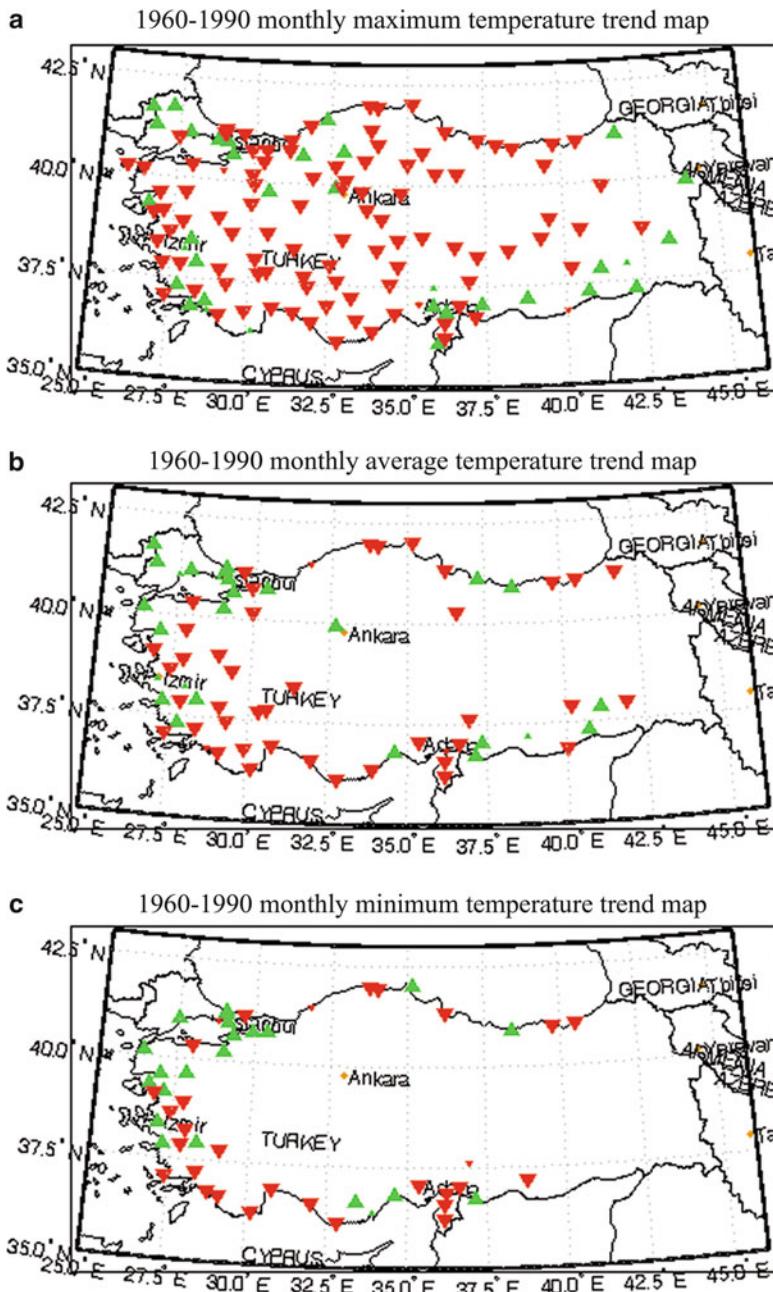
Fig. 6.9 Temperature trends 1960–1990: (**a**) highest, (**b**) average, (**c**) lowest [43]
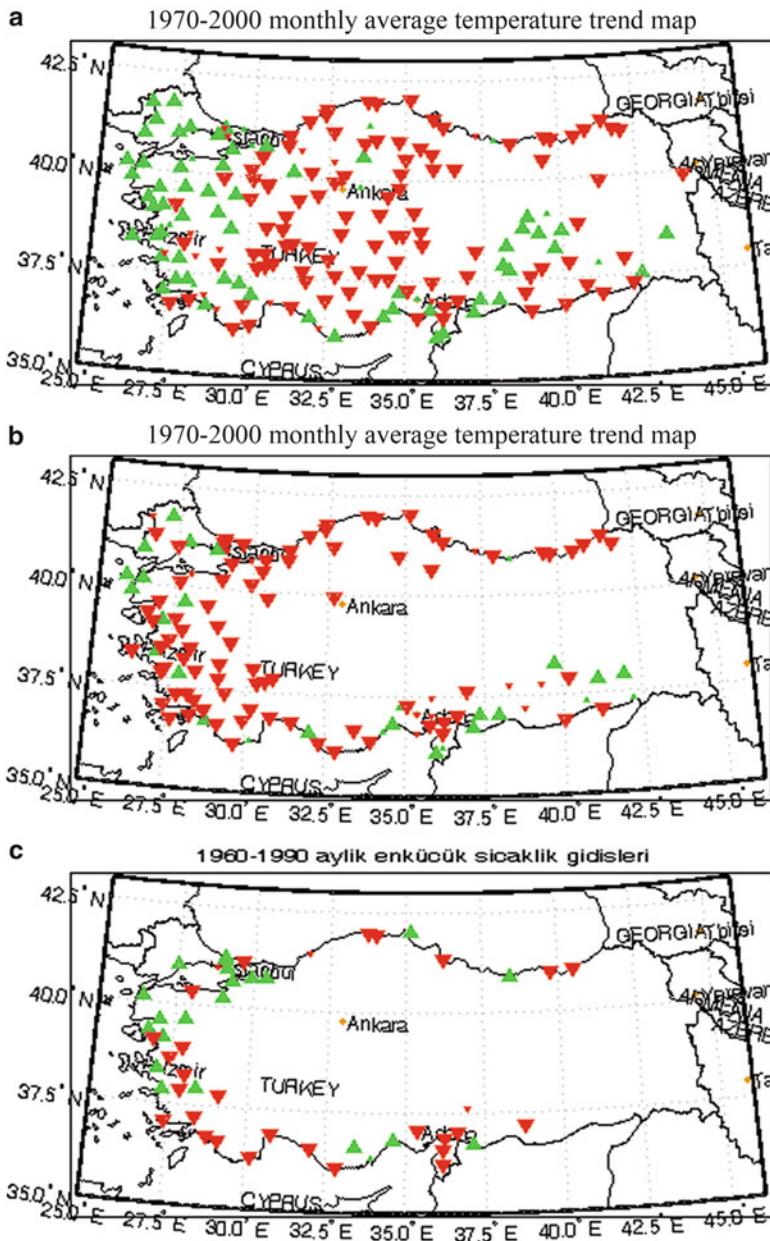
Fig. 6.10 (**a**) Largest, (**b**) average, (**c**) smallest temperature trends between 1970 and 2000 [43]

- Between 1970 and 2000, Thrace, Aegean, Mediterranean, and Southern Anatolia have become hotter.
- Temperature increases have become more influential in Istanbul and its surrounding.
- The Euphrates River region has become hotter in terms of highest temps. This means that the snows in this region will melt down earlier than usual.

Figure 6.10 shows that declines are observed in shores in terms of average temperatures. It appears that the declines are greater than those observed in 1960–1990 period. The temperatures declined further in Istanbul as depicted in Fig. 6.10c that gives details for the change in the entire Turkey in terms of lowest temperatures in 1970–2000 period compared to the values and figures from Fig. 6.9c.

The above explanations note that the greatest change in the last 40 years in terms of temperature is more visible in the highest temperatures rather than the average and lowest temperatures. Generally speaking, because the highest heats are observed in summer times (less rainfall month), one may conclude that there is rise in the number of drought incidents in these times in Istanbul.
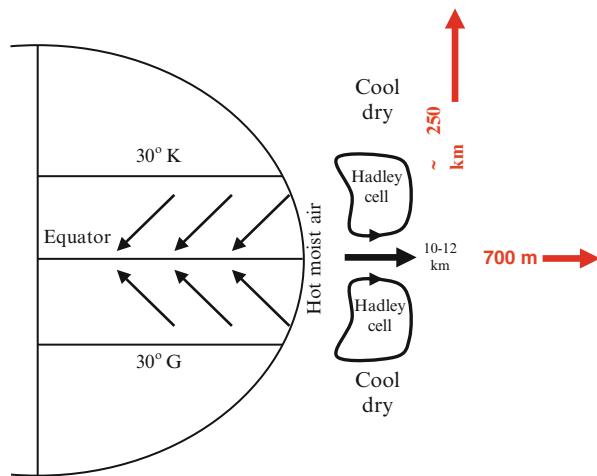
6.5.2 Impact of Global Warming on Turkey

It is extremely useful to consider the proper measures to be taken to effectively address the issue of climate change with particular reference to its impacts upon the water resources of the city of Istanbul and devise an action plan based on the relevant findings. Planning studies based on proper assessments may be done by relying on scientific methods considering the global and local climate-hydrology and -meteorology models. The modeling studies focusing on the city of Istanbul will serve as a general model for the entire Turkey.

Continental and water ecosystems as well as socioeconomic systems (agriculture, forestry, and fishery and water resources) are key to the human development and prosperity and responsive to the climatic changes. A 1 °C increase in global warmth may lead to serious changes that could affect the ability of the forests in regional climates to expand and rejuvenate. In many cases, these changes may destroy the functions and biological diversity of the forests in moderate and subtropical lines where Turkey is located. Depending on the doubling of the equal CO_2 amounts in the atmosphere, as a result of the probable changes in temperature and water amounts, a substantial part of the forests in the world and the plant habitats will be seriously affected due to growing impact of wildfires. A 1–3.5 °C increase in the global warmth will take the current temperature lines to the polar areas of the world in the next century by 200–250 km and increase the level of equal temperature curves by 700–750 m [27].

Geographically speaking, Turkey has relatively hot regions in the south; this means that in case of a 1 °C increase in the overall warmth of the globe, these parts

Fig. 6.11 The shifts in the climate lines after 1 °C increase in global warmth [43]
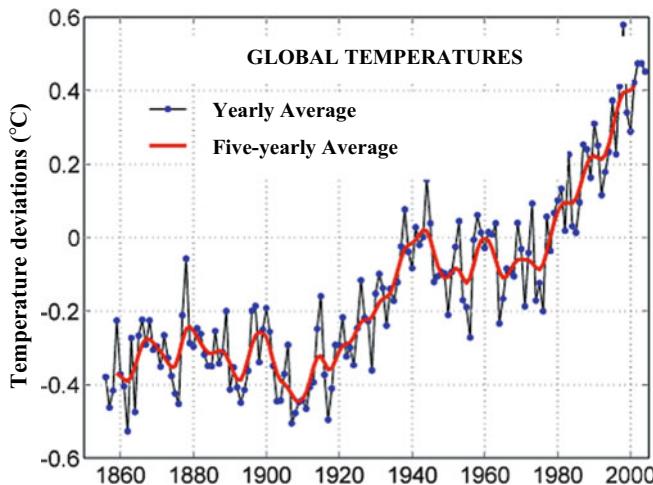
will be most affected. The probable repercussion of this will be the spread of drought and arid lands through the north of Turkey (Fig. 6.11).

In the aftermath of such a possibility, Turkey will have to deal with a number of problems including excessive rainfall, leakages, humidity, evaporation, and changes in the storage capacity and hydrologic cycle. Such a shift will also decrease the amount of snowfall, causing visible decline in the amount of water resources in the country. In light of these approaching dangers, it is essential to consider proper measures and devise comprehensive scenarios that consider these possibilities and that enable us to think about joint operation of artificial water resources including dams. Devising such measures will also entail social and economic benefits in the long term.

Global warming impacts are becoming more visible in the atmosphere and that which is created by the greenhouse effect has become more visible since 1980s and made a peak in 1990s (Fig. 6.12). During the period since 1860 when the reliable observation tools and devices were first used, in 1998, for both northern and southern hemispheres, the temperatures became the highest in terms of annual average surface heats. This is the case with the globe and the hemispheres.

In other words, a record of the highest temperature was broken in 1998 in terms of both global and hemispheric results. Compared to the 1961–1990 climatologic normal values, the period itself becomes the hottest. It was concluded that the annual average surface temperature was 0.57 °C hotter than the normal in the globe in 1998 [39]. The hottest year before this was 1997 [40, 41].

Turkey will particularly suffer from lack of water resources, wildfires, droughts, and desertification due to the climate change and global warming as well as ecological deterioration in connection with such incidents. The targeted amount of water consumption based on the studies developed by the relevant public offices and institutions responsible for water affairs and use of water resources by the end of 2000 is 39.3 billion cubic meters. Moreover 29.3 billion cubic meter (75 %) is

Fig. 6.12 Global average temperature differences between 1856 and 2004 based on the data between 1960 and 1990 for the global average temperatures [2]

Table 6.3 The actual water usage up to 2000 in Turkey and the development of probable water usage by 2030

Year	Total water use ($\times 10^6$ m^3)	Development (%)	Water use					
			Irrigation		Drinking-domestic use		Industry	
			($\times 10^3$ m^3)	(%)	($\times 10^3$ m^3)	(%)	($\times 10^3$ m^3)	(%)
1990	30,600	28	22,016	72	5,141	17	3,443	11
1999	38,900	35	29,200	75	5,700	10	4,000	11
2000	39,300	36	29,300	75	5,800	15	4,200	10
2030	110,000	100	71,500	65	25,300	23	13,200	12

used for irrigation whereas 5.8 billion cubic meter (15 %) for potable water and 4.2 billion cubic meter (10 %) for industrial water usages. 2.1 billion cubic meter out of the underground waters in this amount is used in irrigation whereas 1.9 billion cubic meter as potable water and 2.0 billion cubic meter for industrial purposes (Table 6.3). For this reason, it is among the countries under risk [2].

Depending on the increased amount of greenhouse gases in the atmosphere, a climate change in the years to come will have the following impacts upon Turkey's environment and socioeconomic structure given below to emphasize significant expectations which are defined by Türkeş [42].

- Depending on the duration and magnitude of the hot and dry cycle, the wildfires will become a more eminent problem.

- The agricultural product potential may be changed (this change may vary according to the regional and seasonal differences).
- Climate lines will move from the Ecuador line to the poles by hundreds of kilometers. As a result of this, Turkey will be affected by a drier and hotter climate line dominant in the Middle East and Northern Africa. The plants and insects unable to adapt to these changes will be eliminated.
- Natural continental ecosystems and agricultural production systems will be negatively affected by the changes in the number of harmful diseases.
- The human pressure over vulnerable mountains, valleys, and canyons will become more visible.
- The problems in the dry and semidry areas as well as the water resources of Turkey will become more imminent. The need for agricultural and potable water will become graver.
- In terms of the climate self-natural changeability, the greatest pressure over water resources in Turkey will be felt in the seasons where weather anomalies cause further rainfalls of the Mediterranean climate. For this reason, a negative change in drought risk will increase the impact of the climate change over agriculture.
- In addition to the expansion of the dry and semidry lands, the gravity of the summer drought will be more visible; desertification and greater saltiness will deteriorate the erosion.
- The increases in the statistical distribution and the growing number of hot days (for instance, the tropical days) will affect negatively the human health and biological productivity.
- Due to the contribution of the urban temperature, particularly in the metropolitan cities, night temperature will significantly increase, leading to greater amount of energy consumption for cooling purposes.
- Infections to be caused by changes in the water availability as well as heat stress will deteriorate the overall state of human health in urban cities.
- While the impacts of the climate change over wind and sun and other renewable energy sources will vary from one region to another, the wind frequency and strength will be subjected to remarkable changes.
- In sea flows and sea ecosystems as well as fishery zones, some changes will occur to cause socioeconomic problems in terms of their consequences.
- Depending on the increase in sea level, densely populated areas of Turkey may be subjected to floods and excessive water inflow.
- Changes in the abilities of the forests and seas to hold CO_2 will weaken the natural houses and sinks.
- The lands covered by seasonal snow and permanent snow and ice as well as the duration of icing may shrink.
- The change in the timing and volume of the flow due to melting of the snow may negatively affect the water resources, agriculture, transportation, and tourism (recreation) sectors.

6.6   Conclusions

This study has shown that climate change may lead to some negative impacts in Turkey's vulnerable areas in terms of desertification from Central Anatolia, Southeast Anatolia, and Aegean to Mediterranean regions in terms of forestry and water resources. In recent years, the primary reason for the collective elimination of trees and deforestation in Turkey as well as spread of harmful insects has been drought, air pollution, and acid rains. During the period between 1993 and 1994, two millions trees were cut down due to insect influence. In addition, depending on the dry conditions influential over the Mediterranean Basin starting from 1970s, the trees are turned into dry in massive scale in Aegean and Mediterranean regions. In addition, the weakening of the trees affects the resistance of the forests against the storms, snow, hurricane, avalanche, and other similar natural disasters; as a result of this, the amount of cut and hurt trees increases, and this makes the forest more vulnerable to other harms and dangers. These negative impacts also affect the forest biological diversity, gene reserves, and carbon holding capacities.

Heavy rains are observed in the Black Sea parts of the study area. The air movement moving from the North Adriatic Sea to Black Sea causes a drop in the pressure and inclement weather in fall and winter times. This area is under the influence of the Mediterranean climate type modified under the conditions of the Black Sea and Marmara Sea effects in summer times. As a natural outcome of this, summer times are not heavily hot nor are the winter times severely cold. In addition, the impact of the seawater mass as well as the land is visibly observed. For instance, starting from the Black Sea shores through some certain hills in the south, the rainfall amounts became visibly higher and heavier due to altitude difference. As a result of this, the springs in the Black Sea carry surface flows to the sea. The sequence of the high hills along the shores hinders the contact with the inlands. For this reason, local and occasional rainfalls are frequently observed as a result of the elevation of the humid air to the sides of these hills.

In the work site, the average air temperature is 14 °C. The number of days experiencing subzero temperatures is pretty small. Starting from March, the average monthly temperatures rise up whereas they start to decline after August. The humidity changes in the region range between 50 and 85 %. The average relative humidity is 73 %. The average humidity amount in different seasons displays a uniform situation and offers an emission of 75 %.

The dominant wind direction in the west side of the study site is north and northeast. During the period between November and April, the number of winding from the south increases. Significant increase is observed in the number of southwest winds in December and January.

The solar time is greater in summer times in this area. The average daily sunning time in July and August is 11–12 h where evaporation is also visibly higher. In winter times, however, this declines to 3–4 h and for this reason, it ends without

causing evaporation of the water. In general, it has been found out that regions such as the Mediterranean region are more sensitive and vulnerable to climate change. As a country in the aforementioned region, Turkey needs to be prepared for inevitable severe weather and extreme climate conditions.

References

1. IPCC (2001) Climate change 2001: the scientific basis. Contribution of Working Group I to the third assessment report of the intergovernmental panel on climate change
2. IPCC (2007) Climate change: the physical science basis. In: Solomon S, Qin D, Manning M, Chen Z, Marquis M, Averyt KB, Tignor M, Miller HL (eds) Contribution of working group I to the fourth assessment report of the intergovernmental panel on climate change. Cambridge University Press, Cambridge
3. Nicholls N, Gruza GV, Jouzel J, Karl TR, Ogallo LA, Parker DE (1996) Observed climate variability and change. In: Houghton JT, Filho LGM, Callander BA, Harris N, Kattenberg A, Maskell K (eds) Climate change 1995: the science of climate change. Cambridge University Press, Cambridge, pp 133–192
4. Maheras P, Kolyva-Machera F (1990) Temporal and spatial characteristics of annual precipitation over Balkans in the twentieth century. J Climatol 10:495–504
5. Bates BC, Kundzewicz ZW, Wu S, Palutikof JP (eds) (2008) IPCC technical paper VI - June. Geneva, IPCC Secretariat, 210 pp
6. Alcamo J, Florke M, Marker M (2007) Future long-term changes in global water resources driven by socioeconomic and climatic change. Hydrolog Sci J 52:247–275
7. Arnell NW (2004) Climate change and global water resources: SRES emissions and socio economic scenarios. Glob Environ Chang 14:31–52
8. Lehner B, Czisch G, Vassolo S (2005) The impact of global change on the hydropower potential of Europe:a model-based analysis. Energy Policy 33:839–855
9. Lehner B, Döll P, Alcamo J, Henrichs H, Kaspar F (2006) Estimating the impact of global change on flood and drought risks in Europe: a continental, integrated analysis. Clim Change 75:273–299
10. Santos FD, Forbes K, Moita R (2002) Climate change in Portugal: scenarios, impacts and adaptation measures. SIAM study report. Gradiva, Lisbon, Portugal, 456 pp
11. Solomon S, Qin D, Manning M, Chen Z, Marquis M, Averyt KB, Tignor M, Miller HL (2007) Contribution of working group I to the fourth assessment report of the intergovernmental panel on climate change. Cambridge University Press, Cambridge, 996 pp
12. Knutti R, Hegerl GC (2008) The equilibrium sensitivity of the Earth's temperature to radiation changes. Nat Geosci 1:735–743
13. Hannart A, Dufresne JL, Naveau P (2009) Why climate sensitivity may not be so unpredictable. Geophys Res Lett 36, L16707
14. Baker MB, Roe GH (2009) The shape of things to come: why is climate change so predictable? J Climatol 22:4574–4589
15. Jarvis AJ, Leeda DT, Hewitt CN (2012) Climate–society feedbacks and the avoidance of dangerous climate change. Nat Clim Change 2:668–671
16. Rohling EJ, Rohling EJ, Sluijs A, Dijkstra HA, Köhler P, van de Wal RSW, von der Heydt AS, Beerling DJ, Berger A, Bijl PK, Crucifix M, DeConto R, Drijfhout SS, Fedorov A, Foster GL, Ganopolski A, Hansen J, Hönisch B, Hooghiemstra H, Huber M, Huybers P, Knutti R, Lea DW, Lourens LJ, Lunt D, Masson-Demotte V, Medina-Elizalde M, Otto-Bliesner B, Pagani M, Pälike H, Renssen H, Royer DL, Siddall M, Valdes P, Zachos JC, Zeebe RE (2012) Making sense of palaeoclimate sensitivity. Nature 491(7426):683

17. EEA (2012) Climate change, impacts and vulnerability in Europe 2012. (EEA Report No 12/2012). European Environment Agency, Copenhagen. http://www.eea.europa.eu/
18. Lynch P (2007) The origins of computer weather prediction and climate modeling. J Comput Phys 227(2008):3431–3444
19. Bayraktar H, Turaliglu FS, Sen Z (2005) The estimation of average areal rainfall by percentage weighting polygon method in tn Southeastern Anatolia Region, Turkey. Atmos Res 73 (1–2):149–160
20. Sirdas S (2002) Meteorological drought modeling and application to Turkey. Ph.D. Dissertation, İstanbul Technical University
21. Sirdas S, Sen Z (2003) Spatio-temporal drought analysis to the Trakya region, Turkey. Hydrolog Sci J 28:809–821
22. Erinc S (1957) Tatbiki Klimatoloji ve Türkiye İklimi. İ.T.Ü. Hidrojeoloji Enstitüsü, Istanbul
23. Ceylan A (2009) Drought management plan for Ankara, Turkey. WMO Newsletter MeteoWorld June 2009
24. Nakićenović N, Swart R (eds) (2000) Special report on emissions scenarios: a special report of working group III of the intergovernmental panel on climate change. Cambridge University Press, Cambridge. ISBN 0-521-80081-1
25. IPCC TAR WG3 (2001) Climate change 2001: mitigation. In: Metz B, Davidson O, Swart R, Pan J (eds) contribution of working group III to the third assessment report of the intergovernmental panel on climate change. Cambridge University Press, Cambridge. ISBN 0-521-80769-7
26. Şen Z (2009) Spatial modeling principles in earth sciences. Springer, Dordrecht, 351 pp
27. Sen Z (2009) Precipitation downscaling in climate modeling using a spatial dependence function. Int J Glob Warm 1(1–3):29–42
28. Şen Z (1974) Small sample properties of stationary stochastic processes and the Hurst phenomenon in hydrology. Unpublished Ph.D. Thesis, Imperial College of Science and Technology, 256 pp
29. Şen Z (1989) Cumulative semivariogram model of regionalized variables. Int J Math Geol 21:891
30. Şen Z, Öztopal A (2001) Genetic algorithms for the classification and prediction of precipitation occurreces. Hydrolog Sci J 46(2):255–267
31. Gilchrist B, Cressman GP (1954) An experiment in objective analysis. Tellus 6:309–318
32. Bergthorsson P, Döös BR (1955) Numerical weather map analysis. Tellus 7:329–340
33. Şen Z, Habib Z (2000) Spatial analysis of monthly precipitation in Turkey. Theor Appl Climatol 67:81–96
34. Cressman GP (1959) An operational objective analysis system. Mon Weather Rev 87:367–374
35. Goodin WR, McRea GJ, Seinfeld JH (1979) A comparison of interpolation methods for sparse data: application to wind and concentration fields. J Appl Meteor 18:761–771
36. Koch SE, DesJardins M, Kocin PJ (1983) An iterative Barnes objective map analysis scheme for use with satellite and conventional data. J Appl Meteor 22:1487–1503
37. Thiebaux HJ, Pedder MA (1987) Spatial objective analysis. Academic, San Diego, CA, 299 pp
38. Barnes SL (1964) A technique for maximizing details in numerical weather map analysis. J Appl Meteor 3:396–409
39. World Meteorological Organization (2011) WMO statement on the status of the global climate in 2010, World Meteorological Organization (WMO).
40. Tayanç M, Im U, Dogruel M, Karaca M (2009) Climate change in Turkey for the last half century. Clim Change 94:483–502. doi:10.1007/s10584-008-9511-0
41. Türkeş M (1998) Influence of geopotential heights, cyclone frequency and Southern Oscillation on rainfall variations in Turkey. Int J Climatol 18:649–680
42. Türkeş M (1999) Vulnerability of Turkey to desertification with respect to precipitation and aridity conditions. Turk J Eng Environ Sci 23:363–380

43. Şen Z, Uyumaz A, Öztopal A, Cebeci M, Küçükmehmetoğlu M, Erdik T, SirdaS S, Şahin AD, Geymen A, Ceylan V, Oğuz S, Karsavran Y (2010) Final report on the impacts of climate change on İstanbul and Turkey water resources. İSKİ Project, 552 pp.
44. http://www.mpimet.mpg.de/en/home.html
45. http://www.metoffice.gov.uk/research/hadleycentre/
46. http://www.ncar.ucar.edu/
47. http://www.cccma.ec.gc.ca/eng_index.shtml

Chapter 7
Environmental Pollution by Organic Contaminants as the Contributors of the Global Warming

Jelena Radonić, Maja Turk-Sekulić, and Mirjana Vojinović-Miloradov

Abstract Because they contain black carbon as the UV-absorbing component, soot particles are regarded as contributing significantly to global warming. They are released to ambient air during the burning of solid, liquid, and gaseous fuels—coal and petroleum in particular. Concurrently with soot, polycyclic aromatic hydrocarbons (PAHs) are formed as the by-products of the incomplete combustion of organic matter. A correlation between concentration levels of PAHs in atmospheric particles and soot content is detected, given PAHs' high affinity for carbonaceous materials and strong sorption to soot particles. Therefore, it can be assumed that sorption to the soot particles governs the gas–particle partition process of polycyclic aromatic hydrocarbons in ambient air. The main objective of the chapter is to estimate the gas–particle partition of PAHs using the soot–air partition coefficient (K_{SA}) within the model proposed by Dachs–Eisenreich and to compare the modeled values with results obtained from the field measurements. Air sampling campaign is performed during the early summer period at six selected urban and industrial localities in Vojvodina (Serbia), using the high-volume ambient air samplers. For each sampling period, one quartz fiber filter (GF) and two polyurethane foam filters are used. Contemporary usage of both types of sampling medium has enabled the simultaneous collection of suspended particles and gaseous phase of PAHs. Samples are analyzed using GC-MS instrument (HP 6890–HP 5972) supplied with a J&W Scientific fused silica column DB-5MS. The statistical analysis is performed using Statistica 10. The modeled values obtained using the Dachs–Eisenreich approach are in reasonable agreement with results from the field measurement and, consequently, confirm that soot–air partition coefficient can be used as prediction parameter of the gas–particle partitioning processes for PAHs.

Keywords Global warming • Soot • Polycyclic aromatic hydrocarbons

J. Radonić (✉) • M. Turk-Sekulić • M. Vojinović-Miloradov
University of Novi Sad, Trg Dositeja Obradovica 6, 21000 Novi Sad, Serbia
e-mail: jelenaradonic@uns.ac.rs; majaturk@uns.ac.rs; miloradov@uns.ac.rs

Nomenclature

ϕ	Particle-bound fraction (%)
ΔH_{vap}	Heat of evaporation (kJ·mol^{-1})
ρ_{oct}	Octanol density (kg/dm^3)
ΔS_{vap}	Evaporation entropy (kJ·mol^{-1}·K^{-1})
a_{AC}	Specific surface area of the activated carbon (m^2·g^{-1})
a_{EC}	Specific surface area of the elemental carbon (m^2·g^{-1})
c	Constant depending on the substance's molecular weight and heat of condensation (Pa·cm)
C_G	The gas-phase concentration (ng·m^{-3} of air)
C_P	Concentration of the compound on particles (ng/μg of particles)
f_{EC}	Fractions of elemental carbon in aerosol (g$_{EC}$/g$_{TSP}$)
f_{OM}	Organic fraction of the aerosol (g$_{OM}$/g$_{TSP}$)
H'	Henry constant (−)
K_{OA}	Octanol/air partition coefficient (−)
K_p	Gas–particle partition coefficient (m^3·μg^{-1})
K_{SA}	Soot/air partition coefficient (dm^3·kg^{-1})
K_{SW}	Soot/water partition coefficient (dm^3·kg^{-1})
M_{OM}	Molecular weight of the organic matter (g·mol^{-1})
$p_L{}^0$	Sub-cooled liquid vapor pressure (Pa)
T	Absolute temperature (K)
TSP	Concentration of suspended particles in the ambient air (μg·m^{-3})
γ_{OM}	The activity coefficient of the organic film (−)
θ	Particles' surface (m^2·m^{-3})

Acronyms

BC	Black carbon
GC-MS	Gas chromatography-mass spectroscopy
LRT	Long-range transport
NATO	North Atlantic Treaty Organization
OC	Organic carbon
PAHs	Polycyclic aromatic hydrocarbons
PUF	Polyurethane foam filters
SVOCs	Semivolatile organic carbon species
UNEP	United Nations Environment Programme
UV	Ultraviolet
VOCs	Volatile organic carbon species

7.1   Introduction

Soot aerosols are released to atmosphere during the biomass burning and incomplete combustion of solid, liquid, and gaseous fuels—coal and petroleum, in particular. After getting into the air, they coagulate into larger clusters, get coated by other chemicals, and react with surrounding particles and gases in the atmosphere [1, 2]. Warming the atmosphere, darkening snow when it is deposited, and influencing cloud formation, ubiquitous soot particles—because they contain black carbon (BC) as the UV-absorbing component—have significant climate impact. BC-containing atmospheric particles can have a warming or a cooling effect on climate, depending on the albedo of the underlying surface relative to the albedo of the BC haze itself. The albedo of the haze depends on what other chemical species are present in the particles, their relative amounts, and whether they primarily scatter or absorb light [2]. The composition of soot particles predominantly depends on the type of combustion material. For example, combustion of fossil fuel results in emissions of BC and organic carbon, OC, with a relatively high ratio of BC mass concentration to mass concentration of OC. On the other hand, combustion of biomass also results in the emission of BC and OC, but with a lower ratio of BC to OC [2]. Combustion of fossil fuel and biomass also emits other particulate and gas-phase species including potassium, SO_2, NO_x, CO_2, as well as volatile (VOCs) and semivolatile organic carbon species (SVOCs).

As the by-products during the processes of incomplete combustion of all types of organic matter (including biomass and fossil fuels), polycyclic aromatic hydrocarbons (PAHs) are formed concurrently with soot particles. The highest concentrations of PAHs are detected in the vicinity of large industrial sites, busy roads, and areas heated by domestically burning coal and wood. Primarily, PAHs are emitted into the atmosphere and are mostly sorbed to particulate matter. However, PAHs are also present in the gaseous phase. PAHs that have two or three rings (naphthalene, acenaphthene, anthracene, fluorene, and phenanthrene) are present in air, predominantly in the vapor phase. By contrast, PAHs that have four rings (fluoranthene, pyrene, benz(a)anthracene, chrysene) exist both in the vapor and in the particulate phases, while PAHs with five or more rings (benz(a) pyrene, benzo(g,h,i)perylene) are found predominantly in the particulate phase [3]. As PAHs have high affinity for carbonaceous materials, strong sorption of PAHs to atmospheric soot particles is expected.

Atmospheric partition of semivolatile organic compounds (including PAHs) between gas and particulate phases directly determines long-range transport (LRT) and transformation processes of pollutants in the ambient air and atmosphere while influencing indirectly compounds' fate in other environmental medium. Previous researches in this area detect correlation between concentration levels of PAHs in atmospheric particles and soot content, so it can be assumed that sorption to the soot particles governs the gas–particle partition process of PAHs in ambient air [4, 5]. A number of recent studies are focused on estimating, modeling, and

predicting the gas–particle partitioning of SVOCs/PAHs [6–12]. The literature also identifies several approaches for describing their atmospheric distribution.

The main objective of the chapter is to estimate the gas–particle partition of PAHs using the soot–air partition coefficient K_{SA} within the model proposed by Dachs–Eisenreich and to compare the modeled values with results obtained from the field measurements in the Vojvodina region, Serbia. Localities selected within the research are the cities of Novi Sad and Pančevo. They are located in the Pannonian Plain and have similar characteristics: developed industrial activity, the River Danube runs through both cities, and both have oil refineries in the industrial zones that were heavily damaged by explosions and fires during the NATO operation "Alien force" in 1999. The cities of Novi Sad and Pančevo are defined as hot spots by UNEP, as the most jeopardized cities during the conflict period in Serbia [13].

7.2 Background: Modeling the Gas–Particle Partitioning of Polycyclic Aromatic Hydrocarbons

7.2.1 Junge–Pankow Adsorption Model

The most common method for estimating adsorption of SVOCs to aerosols is Junge–Pankow adsorption model, which assumes that chemicals adsorb to the active sites on the surface of particles, and is represented by Eq. (7.1) [14]:

$$\phi = \frac{C_P}{C_G + C_P} = \frac{c\theta}{(p_L^0 + c\theta)} \tag{7.1}$$

where θ is the particles' surface ($m^2 \cdot m^{-3}$), p_L^0 is sub-cooled liquid vapor pressure (Pa), and constant c (Pa·cm) depends on the substance's molecular weight and heat of condensation.

7.2.2 Pankow Absorption Model

The absorption of gas-phase compounds into an organic film coating the particle, which makes an important contribution to the overall particle–gas partitioning process, is described by Pankow absorption model [15]:

$$K_P = \frac{RTf_{OM}}{10^6 M_{OM}\gamma_{OM}p_L^0} \tag{7.2}$$

where f_{OM} is the organic fraction of the aerosol, M_{OM} is molecular weight of the organic matter ($g \cdot mol^{-1}$), and γ_{OM} is the activity coefficient of the organic film.

7.2.3 K_{OA} Absorption Model

Assuming that the entire organic matter of the aerosol is available to absorb gaseous compounds, the K_{OA} absorption model, given by Eq. (7.3), can be used to predict the values of partition coefficient K_P, knowing the coefficient K_{OA} and the organic fraction of the aerosol, f_{OM} [16]:

$$\log K_P = \log K_{OA} + \log f_{OM} - 11.91 \tag{7.3}$$

where K_{OA} is octanol–air partition coefficient (octanol is used as a surrogate for the aerosol organic matter).

7.2.4 Dachs–Eisenreich Dual Model

In order to extend the partitioning model between water and sedimentary soot carbon suggested by Gustafsson [17] to air–soot partitioning, and to assess the potential role of adsorption onto soot carbon and absorption into the organic matter as mechanisms driving the gas–particle partitioning of PAHs, Dachs–Eisenreich dual model is developed [4].

Soot particles are by-products of the combustion of liquid and gaseous fuels and their production depends strongly on the carbon-to-oxygen ratio during the combustion. PAHs are formed concurrently with soot particles and also play an important role in soot formation and particle growth [18]. PAHs have a high affinity for carbonaceous materials and a correlation between PAH aerosol concentrations and soot content is observed [19]. Therefore, adsorption of PAHs onto the soot fraction of atmospheric aerosols, or primary aerosol carbon with which it is highly correlated, may be an important mechanism affecting the gas–particle partitioning of PAHs [4].

To quantify the PAH content in the soot phase, a soot/air partition coefficient is needed. The soot/water partition coefficient K_{SW} is assumed to be equal to the activated carbon/water partitioning coefficients reported in literature [20]. The soot carbon and activated carbon have similar specific surface areas, but they are not exactly structurally the same and may have different sorptive properties. In reality, soot carbon is also composed by a fraction of organic carbon that may be coating the elemental carbon [4].

Soot–air partition coefficient, K_{SA} ($dm^3\ kg^{-1}$), at temperature T, is described by the equation

$$K_{SA} = \frac{K_{SW}}{H'} \tag{7.4}$$

where K_{SW} is partition coefficient between soot and water ($dm^3\ kg^{-1}$) and H' is dimensionless Henry constant.

The effect of temperature on Henry's constant H′ is expressed in the following equation:

$$\log H' = -\frac{\Delta H_{vap}}{RT} + \frac{\Delta S_{vap}}{R} \tag{7.5}$$

where ΔH_{vap} is heat of evaporation (kJ mol^{-1}) and ΔS_{vap} is evaporation entropy (kJ mol^{-1} K^{-1}).

Coefficients K_{SW} and K_{SA} can be obtained from the adsorption experiments on activated carbon. To describe the distribution of organic pollutants between the gaseous and particulate phases, assuming that elemental carbon is a surrogate for the soot phase, the overall gas–particle partition coefficient that accounts for both the organic matter and the soot phases is given by the equation [4]:

$$K_P = 10^{-12}[(f_{OM}M_{oct}\gamma_{oct}/\rho_{oct}M_{OM}\gamma_{OM})K_{OA} + f_{EC}(a_{EC}/a_{AC})K_{SA}] \tag{7.6}$$

where f_{OM} and f_{EC} are fractions of organic matter and elemental carbon in aerosol, respectively; ρ_{oct} is octanol density, 0.82 kg/dm^3; and a_{EC} and a_{AC} are specific surface areas (m$^2 \cdot$g^{-1}) of the elemental carbon and the activated carbon used for the experimental determination of the coefficient K_{SA} ($10^{-12} = 10^{-9}$ kg/μg $\times$ 10^{-3} m^3/dm^3). The results of Dachs and Eisenreich dual model are expressed in Eq. (7.7) [4]:

$$K_P = 10^{-12}\left[\frac{f_{OM}}{\rho_{oct}}K_{OA} + f_{EC}K_{SA}\right] \tag{7.7}$$

To estimate the value of K_{SA}, Dachs proposes the use of the thermodynamic model described by Eq. (7.8) [21]:

$$\log K_{SA} = -0.85 \log p_L + 8.94 - \log\left(\frac{998}{a_{EC}}\right) \tag{7.8}$$

where p_L is sub-cooled liquid vapor pressure (Pa).

Within the calculations, commonly used value for the a_{EC} is 62.7 m^2/g [22].

7.3 Material and Methods

7.3.1 Collection of Air Samples

Air sampling campaign is performed during early summer (median air temperature was 19 °C) at six selected urban and industrial localities in Vojvodina (region of Serbia). Sampling spots are located in Novi Sad and Pancevo, the two cities with significant industrial activities. Three samples are collected at an industrial zone, in the yard of the Novi Sad Oil Refinery (N_1). Additional three samples are taken at the residential zone of Novi Sad, in the proximity and downwind of the oil refinery (N_2).

Three air samples are provided from the third, heavy traffic-contaminated, urban sampling spot—the Novi Sad city center (N_3). Two sampling spots in Pancevo are placed at industrial area—the Pancevo Oil Refinery (P_1) and Pancevo Chemical Industry (P_2). The Pancevo city center is chosen as the third, urban locality (P_3). Four samples of ambient air are provided from the localities P_1 and P_3 and three air samples are obtained at sampling spot P_2.

Three high-volume ambient air samplers are used (one GV2360 Thermoandersen TSP sampler, and two samplers that are made of stainless steel boxes equipped with an 8×10 in. filter holder and a 9 cm-in-diameter/30 cm long polyurethane foam (PUF) filter holder). The total air sampled is 1,600 m^3/24 h for the GV2360 Thermoandersen TSP sampler and 900 m^3/24 h for the other two samplers. One glass fiber filter (Whatman, fraction $d_{ae} < 50$ μm) and two polyurethane foam filters (GumotexBřeclav, density 0.03 $g \cdot m^{-3}$) are used for each sampling period. Glass fiber filters are burned in 450 °C for 5 h, and PUF filters are Soxhlet extracted by 1:1 acetone/hexane (Merck suprasolv) by a Foss TecatorSoxtec 1045 HT-2 apparatus for 4 h to 120 °C, prior to the sampling campaign. Glass fiber filters and PUF filters are placed in a zipped plastic bag after being wrapped in aluminum foil. Contemporary usage of both types of sampling medium enables the simultaneous collection of suspended particles and gaseous phase of pollutants. All samples are taken over the period of 24 h [3].

7.3.2 Analysis of Samples

Samples are analyzed using GC-MS instrument (HP 6890–HP 5972) supplied with a J&W Scientific fused silica column DB-5MS. Analytical details and quality assurance/quality control measures are published earlier [23, 24]. All analytical procedures are done within the laboratories of the Research Centre for Environmental Chemistry and Ecotoxicology (RECETOX), Masaryk University, Brno, the Czech Republic.

The statistical analysis is performed using Statistica 10.

7.4 Results and Discussion

7.4.1 Gas–Particle Partitioning

Based on the obtained measured data, the experimental values of the PAHs' particle-bound fraction, ϕ [%], are determined using the following equation:

$$\phi = \frac{C_P}{C_G + C_P} \tag{7.9}$$

Table 7.1 Median particle-bound fractions, ϕ [%], of PAHs at all sampling sites (modified from [3])

	N_1	N_2	N_3	P_1	P_2	P_3
Nap	2.315	5.890	3.365	0.939	1.754	1.576
Acy	10.714	10.870	1.724	2.778	0.000	0.000
Ace	2.804	5.660	5.714	8.771	10.811	4.952
Flo	0.993	1.818	1.439	0.062	0.390	0.829
Phe	0.395	0.631	0.789	0.153	0.094	0.435
Ant	1.245	1.237	2.264	0.000	0.304	0.639
Flu	4.762	3.807	2.921	1.150	0.852	3.430
Pyr	5.665	6.480	3.173	1.072	1.995	4.802
B(a)A	41.176	66.138	43.529	27.390	53.846	33.561
Chr	33.065	30.369	35.357	8.563	28.205	33.996
B(b)F	97.388	98.022	94.211	36.614	93.500	91.905
B(k)F	96.685	96.284	95.149	42.006	95.050	92.922
B(a)P	100.000	100.000	100.000	23.333	100.000	100.000
I(123 cd)P	100.000	100.000	100.000	48.589	100.000	100.000
D(ah)A	100.000	100.000	100.000	100.000	100.000	100.000
B(ghi)P	100.000	100.000	100.000	49.560	100.000	100.000

where C_P is the concentration of the compound on particles (ng/µg of particles) and C_G is the gas-phase concentration (ng·m^{-3} of air). The results are presented in Table 7.1.

7.4.2   Modeled Values of Distribution of PAHs

In order to estimate the extent to which dual Dachs–Eisenreich distribution model fits the experimental data, measured and modeled values for the particle-bound fraction ϕ of individual PAHs are compared. The modeled values of the particle-bound fraction, ϕ, are calculated according to Eq. (7.10), using the modeled partition coefficient values and the measured concentration of suspended particles in the ambient air, TSP:

$$\phi = \frac{K_P \cdot TSP}{1 + K_P \cdot TSP} \tag{7.10}$$

Based on the available experimental data, the following experimental values are used for calculation of the gas–particle partition coefficient (K_P) and particle-bound fraction (ϕ):

– *TSP = 114 µg m^{-3}* (sites P_1, P_2, and P_3).
– *TSP = 187 µg m^{-3}* (sites N_1 and N_2).
– *TSP = 205 µg m^{-3}* (site N_3).

- $f_{EC} = 0.0298\ g_{EC}/g_{TSP}$ (sites P_1, P_2, and P_3).
- $f_{EC} = 0.0267\ g_{EC}/g_{TSP}$ (sites N_1 and N_2).
- $f_{EC} = 0.0195\ g_{EC}/g_{TSP}$ (site N_3).

In order to simulate three different scenarios, three different values of the organic fraction of the aerosol are used: $f_{OM} = 20$, 25, and 40 %. Table 7.2 shows modeled values of K_p and ϕ for the three scenarios at the location N_3.

The model calculation is performed for the temperature of 25 °C.

The ratios of measured and modeled ϕ values at the sampling location N_3 are shown in Fig. 7.1a. Figure 7.1b presents comparison of measured and modeled values of ϕ for the three different scenarios at the location N_3.

For the observed group of pollutants, all three model scenarios give almost identical values for particle-bound fractions of PAHs, which may indicate a minor contribution of the absorption process in the overall distribution of atmospheric PAHs.

Figure 7.2 presents the variability of the ratios of measured ϕ values at six investigated sites and the values predicted using the Dachs–Eisenreich dual model for the urban scenario ($f_{OM} = 0.40\ g_{OM}/g_{TSP}$).

Significant deviations between the measured and modeled ϕ values for the low-molecular-weight PAHs can be observed at all investigated sites. The ratio between measured and modeled ϕ for Flo, Phe, Ant, Flu, Pyr, B(a)A, and Chr are less than one order of magnitude. The dual model provides very accurate estimates of atmospheric distribution for high-molecular-weight PAHs (B(b)F, B(k)F, B(a)P, I(1,2,3-cd)P, D(ah)A, and B(ghiP)).

Previous studies confirm that Dachs–Eisenreich model provides acceptable estimates of the atmospheric distribution for urban sites, while for rural conditions, modeled values are one order of magnitude lower than the experimental ones [8, 10, 12].

The observed differences between the modeled and measured values of ϕ could be the result of variations in the chemical composition of atmospheric particles, which is not taken into account when using the uniform value for the f_{OM}.
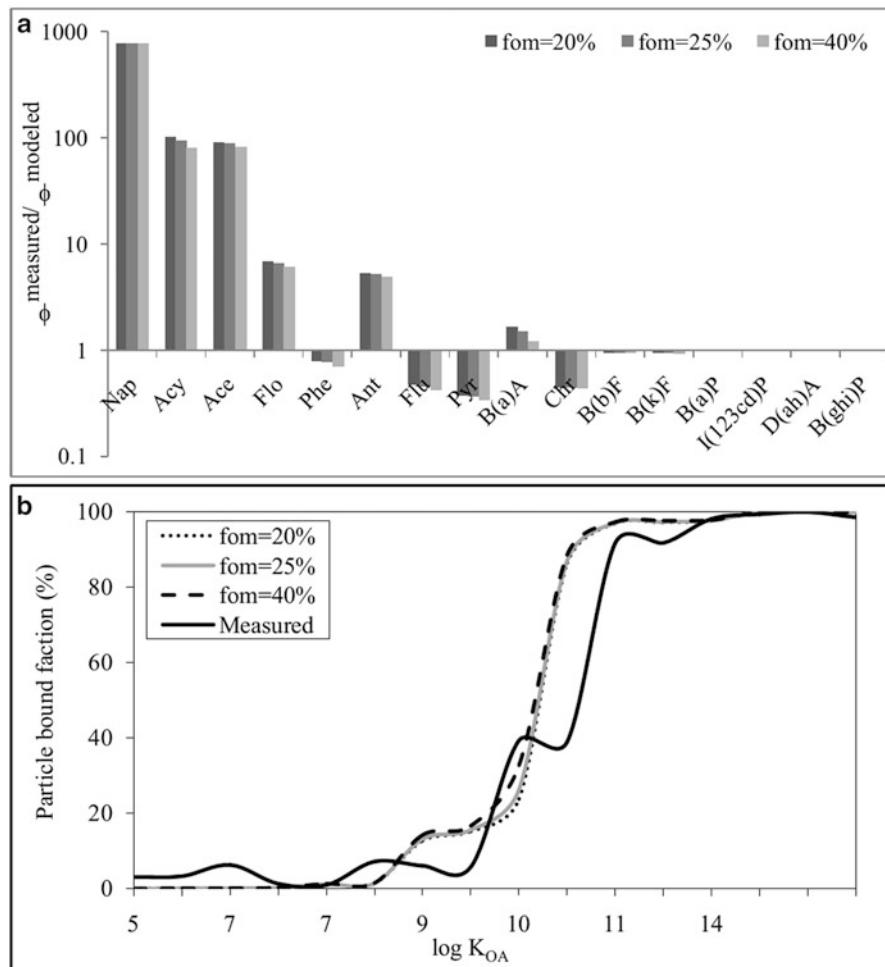
Urban sites are often characterized by multiple sources of PAH (motor vehicles, various branches of industry), contributing to the complexity of the PAH distribution processes. The processes of adsorption and desorption of PAHs are very slow due to the presence of liquid films of organic matter. This makes the phase of elemental carbon less available to the PAHs. The diffusion through the liquid film inside the particles containing elemental carbon could be a limiting step for mass transfer. The deviation between measured and modeled ϕ values in urban sites could be a result of slow reaching the equilibrium state between the gaseous and particulate phases. Underestimation of experimental ϕ values could also be caused by the presence of inert fractions of PAHs in particles.

Deviations between the measured and the modeled values of low-molecular-weight PAHs could also be due to the presence of PAHs in the aqueous phase of the particles. This was not taken into account by the dual Dachs–Eisenreich model of atmospheric distribution.

Table 7.2 Modeled values of distribution coefficients and particle-bound fractions of PAHs (locality N_3)

PAH	log K_{OA}	log K_{SA}	K_p (f_{om} = 20 %)	K_p (f_{om} = 25 %)	K_p (f_{om} = 40 %)	Φ (f_{om} = 20 %)	Φ (f_{om} = 25 %)	Φ (f_{om} = 40 %)
Nap	5.13[a]	6.89[b]	$4.20 \cdot 10^{-7}$	$4.30 \cdot 10^{-7}$	$4.50 \cdot 10^{-7}$	0.004	0.004	0.004
Acy	6.23[c]	7.78[b]	$3.41 \cdot 10^{-6}$	$3.51 \cdot 10^{-6}$	$3.82 \cdot 10^{-6}$	0.032	0.035	0.041
Ace	6.22[a]	8.18[b]	$8.00 \cdot 10^{-6}$	$8.11 \cdot 10^{-6}$	$8.41 \cdot 10^{-6}$	0.069	0.071	0.077
Flo	6.68[a]	8.60[d]	$2.11 \cdot 10^{-5}$	$2.14 \cdot 10^{-5}$	$2.22 \cdot 10^{-5}$	0.183	0.189	0.207
Phe	7.45[a]	9.40[d]	$1.32 \cdot 10^{-4}$	$1.34 \cdot 10^{-4}$	$1.39 \cdot 10^{-4}$	1.132	1.167	1.27
Ant	7.34[a]	9.50[d]	$1.63 \cdot 10^{-4}$	$1.65 \cdot 10^{-4}$	$1.69 \cdot 10^{-4}$	1.355	1.382	1.461
Flu	8.6[a]	10.50[d]	$1.68 \cdot 10^{-3}$	$1.70 \cdot 10^{-3}$	$1.77 \cdot 10^{-3}$	12.764	13.141	14.253
Pyr	8.61[a]	10.60[d]	$2.09 \cdot 10^{-3}$	$2.11 \cdot 10^{-3}$	$2.19 \cdot 10^{-3}$	15.219	15.584	16.658
B(a)A	9.54[a]	10.54[b]	$2.60 \cdot 10^{-3}$	$2.81 \cdot 10^{-3}$	$3.44 \cdot 10^{-3}$	23.855	26.288	32.735
Chr	10.44[a]	12.10[d]	$6.97 \cdot 10^{-2}$	$7.13 \cdot 10^{-2}$	$7.64 \cdot 10^{-2}$	86.504	87.103	88.619
B(b)F	10.98[a]	12.84[b]	$3.68 \cdot 10^{-1}$	$3.74 \cdot 10^{-1}$	$3.91 \cdot 10^{-1}$	96.999	97.102	97.375
B(k)F	11.19[a]	12.84[b]	$3.82 \cdot 10^{-1}$	$3.92 \cdot 10^{-1}$	$4.20 \cdot 10^{-1}$	97.244	97.384	97.729
B(a)P	10.77[a]	13.00[d]	$5.14 \cdot 10^{-1}$	$5.18 \cdot 10^{-1}$	$5.29 \cdot 10^{-1}$	97.723	97.761	97.866
I(123cd)P	11.56[e]	15.39[b]	122.09	122.11	122.18	99.99	99.99	99.99
D(ah)A	13.9[a]	14.54[b]	36.62	41.47	56.00	99.981	99.984	99.989
B(ghi)P	11.01[a]	14.54[b]	17.27	17.28	17.30	99.928	99.928	99.928

[a][25], [b][21], [c][26], [d][5], [e][27]
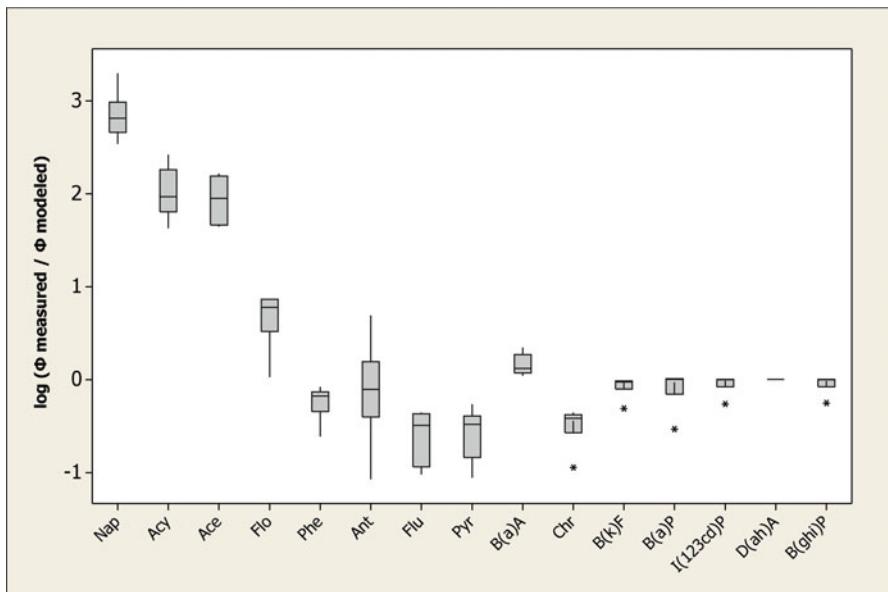
Fig. 7.1 Measured and modeled ϕ values at sampling location N_3: (**a**) The ratios of measured and modeled ϕ values. (**b**) Comparison of measured and modeled ϕ values for the three scenarios

7.5 Conclusions

PAHs have high affinity for carbonaceous materials and strongly sorb to soot particles.

Correlation between the concentration levels of PAHs in atmospheric particles and soot content is detected and it can be assumed that the sorption potential of PAHs to the soot particles governs the gas–particle partition process of PAHs in ambient air.

Fig. 7.2 The ratios of measured and modeled ϕ values for individual PAH at six investigated sites

The modeled values obtained using the Dachs–Eisenreich model are in reasonable agreement with results from the field measurement and soot–air partition coefficients are confirmed to be proper prediction parameter of the gas–particle partitioning processes for high-molecular-weight PAHs.

The observed differences between modeled and measured ϕ values of the low-molecular-weight PAHs could be a result of the variations in the chemical composition of atmospheric particles, slow reaching the equilibrium state between the gaseous and particulate phases, and presence of PAHs in the aqueous phase of the particles.

References

1. Karcher B, Mohler O, DeMott PJ, Pechtl S, Yu F (2007) Insights into the role of soot aerosols in cirrus cloud formation. Atmos Chem Phys 7:4203–4227
2. AMAP (2011) The impact of black carbon on arctic climate (2011). In: Quinn PK, Stohl A, Arneth A, Berntsen T, Burkhart JF, Christensen J, Flanner M, Kupiainen K, Lihavainen H,

Quinn PK, Stohl A, Arneth A, Berntsen T, Burkhart JF, Christensen J, Flanner M, Kupiainen K, Lihavainen H, Shepherd M, Shevchenko V, Skov H, Vestreng V (2011) The impact of black carbon on arctic climate. AMAP Technical Report No. 4, Oslo, Norway

3. Radonic J, Vojinović-Miloradov M, Turk SM, Kiurski J, Djogo M, Milovanovic D (2011) The octanol–air partition coefficient, K_{OA}, as a predictor of gas–particle partitioning of polycyclic aromatic hydrocarbons and polychlorinated biphenyls at industrial and urban sites. J Serb Chem Soc 76(3):447–458

4. Dachs J, Eisenreich SJ (2000) Adsorption onto aerosol soot carbon dominates gas-particle partitioning of polycyclic aromatic hydrocarbons. Environ Sci Technol 34:3690–3697

5. Dachs J, Ribes S, van Drooge B, Grimalt J, Eisenreich SJ, Gustafsson O (2004) Response to the comment on influence of soot carbon on the soil-air partitioning of polycyclic aromatic hydrocarbons. Environ Sci Technol 38:1624–1625

6. Arp HPH, Schwarzenbach RP, Goss KU (2008) Ambient gas/particle partitioning. 1. Sorption mechanisms of apolar, polar, and ionizable organic compounds. Environ Sci Technol 42 (15):5541–5547

7. Arp HPH, Schwarzenbach RP, Goss KU (2008) Ambient gas/particle partitioning. 2: the influence of particle source and temperature on sorption to dry terrestrial aerosols. Environ Sci Technol 42(16):5951–5957

8. Galarneau E, Bidleman TF, Blanchard P (2006) Seasonality and interspecies differences in particle/gas partitioning of PAHs observed by the Integrated Atmospheric Deposition Network (IADN). Atmos Environ 40:182–197

9. Lohmann R, Lammel G (2004) Adsorptive and absorptive contributions to the gas-particle partitioning of polycyclic aromatic hydrocarbons: state of knowledge and recommended parametrization for modeling. Environ Sci Technol 38(14):3793–3803

10. Odabasi M, Cetin E, Sofuoglu A (2006) Determination of octanol–air partition coefficients and supercooled liquid vapor pressures of PAHs as a function of temperature: application to gas–particle partitioning in an urban atmosphere. Atmos Environ 40:6615–6625

11. Radonic J, Turk SM, Vojinovic MM, Čupr P, Klánová J (2009) Gas-particle partitioning of persistent organic pollutants in the Western Balkan countries affected by war conflicts. Environ Sci Pollut Res 16(1):65–72

12. Vardar N, Tasdemir Y, Odabasi M, Noll KE (2004) Characterization of atmospheric concentrations and partitioning of PAHs in the Chicago atmosphere. Sci Total Environ 327 (1–3):163–174

13. UNEP (1999) The Kosovo conflict—consequences for the environment and human settlements. http://www.grid.unep.ch/btf/final/finalreport.pdf

14. Junge C (1977) Basic considerations about trace constituents in the atmosphere as related to the fate of global pollutants. In: Ss IH (ed) Fate of pollutants in the air and water environments. Wiley, New York, USA

15. Pankow JF (1994) An absorption model of gas/particle partitioning of organic compounds in the atmosphere. Atmos Environ 21:185–188

16. Harner T, Bidleman TF (1998) Octanol-air partition coefficient for describing particle/gas partitioning of aromatic compounds in Urban air. Environ Sci Technol 32:1494–1502

17. Gustafsson O, Haghseta F, Chan C, Macfarlane J, Gschwend PM (1997) Quantification of the dilute sedimentary soot phase: implication for PAH speciation and bioavailability. Environ Sci Technol 31:203–209

18. Seinfeld JH, Pandis SN (1998) Atmospheric chemistry and physics. Wiley-Interscience, New York, USA, p 1326

19. Simo R, Grimalt JO, Albaiges J (1997) Loss of unburned-fuel hydrocarbons from combustion aerosols during atmospheric transport. Environ Sci Technolog 31:2697–2700

20. Walters RW, Luthy RG (1984) Equilibrium adsorption of polycyclic aromatic hydrocarbons from water onto activated carbon. Environ Sci Technol 18:395–403

21. van Noort PCM (2003) A thermodynamics-based estimation model for adsorption of organic compounds by carbonaceous materials in environmental sorbents. Environ Toxicol Chem 22:1179–1188
22. Jonker MTO, Koelmans AA (2002) Sorption of polycyclic aromatic hydrocarbons and polychlorinated biphenyls to soot and soot-like materials in the aqueous environment: mechanistic considerations. Environ Sci Technol 36:3725–3734
23. Turk M, Jakšić J, Vojinović MM, Klanova J (2007) Post-war levels of persistent organic pollutants (POPs) in air from Serbia determined by active and passive sampling methods. Environ Chem Lett J 5:109–113
24. Klanova J, Kohoutek J, Kostrhounova R, Holoubek I (2007) Are the residents of former Yugoslavia still exposed to elevated PCB levels due to the Balkan wars? Part 1: air sampling in Croatia, Serbia, Bosnia and Herzegovina. Environ Int 33:719–726
25. Mackay D, Shiu WY, Ma KC, Lee SC (2006) Handbook of physical-chemical properties and environmental fate for organic chemicals, volume I, introduction and hydrocarbons, 2nd edn. CRC Press Taylor & Francis Group, Boca Raton, Florida, USA
26. Virtual Computational Chemistry Laboratory (VCCL) (2004) (http://146.107.217.178/lab/alogps/start.html)
27. National Library of Medicine (NLM), Specialized Information Services (SIS) (2004) (http://toxnet.nlm.nih.gov/)

Chapter 8
Assessment of Vulnerability to Climate Change Using Indicators: Methodological Challenges

Fahim N. Tonmoy and Abbas El-Zein

Abstract Climate change vulnerability assessment (CCVA) can help policy makers incorporate climate futures in planning. We discuss some of the most important methodological challenges facing CCVA, including geographical and temporal scales, aggregation, and nonlinearity. CCVA literature is large and multi-disciplinary and appears to stem from a number of different paradigms (risk assessment, natural disaster management, urban planning, etc.). It is therefore difficult to elicit major directions, findings, and methodologies from this body of work. We study a sample of peer-reviewed CCVA publications and investigate the extent to which the CCVA literature is foregrounding and engaging with these methodological problems. We find that:

1. Critical scrutiny of prevalent assessment methodologies and development of new ones remain limited since only 10 % of the studies focus on such issues. This is despite the fact that many scholars have raised questions about the methodological aspects of vulnerability assessment.
2. Among the studies that aggregate indicators and consider both the biophysical and socioeconomic processes generating vulnerability, 59 % use methods based on multiple attribute utility theory (MAUT) such as arithmetic mean, geometric mean, or GIS-based MAUT, approaches that have strict theoretical requirements which are hardly met in the context of CCVA.
3. Although a number of theoretical papers have argued that indicator-based vulnerability assessment is likely to be most valid at smaller rather than larger geographical scales, only 17 % of studies are conducted at local scale.

We argue that, at this stage of development of vulnerability assessment, methodological concerns ought to receive more attention in the literature, lacking which the scientific validity of assessments will remain doubtful.

F.N. Tonmoy (✉) • A. El-Zein
University of Sydney, Darlington, NSW, Australia
e-mail: fahim.tonmoy@sydney.edu.au; abbas.elzein@sydney.edu.au

Acronyms

ATEAM   Advanced terrestrial ecosystem analysis and modeling
CCVA   Climate change vulnerability assessment
GIS   Geographic information system
IBVA   Indicator-based vulnerability assessment
IPCC   Intergovernmental panel on climate change
MAUT   Multiple attribute utility theory
SES   Socio-ecological system

8.1 Introduction

Anthropogenic climate change is one of the most complex challenges of this century. Climate scientists around the world are providing evidence that anthropogenic climate change is almost certainly causing increases in average temperatures, shorter cycles of drought and rainfall, as well as more frequent extreme events such as heat waves and cyclones. These events present both threats and opportunities to our cities and urban infrastructure. Therefore, local and national governments around the world are developing mitigation and adaptation strategies in order to secure communities against the loss of life, well-being, investment, and heritage.

Effective adaptation to climate change is dependent on the identification and proper understanding of the vulnerable system in question, the stressors it is exposed to, as well as the processes generating its vulnerability. In the literature, this exercise is generally termed "climate change vulnerability assessment" (CCVA). Although CCVA can take many forms, it consists, either implicitly or explicitly, of assessing the vulnerability of a valued attribute (e.g., health, shelter, security, economic prosperity) of a socio-ecological system (SES) (e.g., locality, community, economic sector, infrastructure and its users) to one or more climate-related hazards (e.g., heat waves, flood events, rise in sea levels). CCVA can help in identifying vulnerable "hot spots," better allocating adaptation resources, better understanding systemic weaknesses which make the system vulnerable, monitoring the effects of adaptation measures, or better communicating the risk and justifying policy to the public [1–3]. Demand for CCVA has increased over the last few years among policymakers, engineers, and planners, particularly in relation to the potential vulnerability of major development projects and infrastructure [4]. In this chapter, we discuss some of the most important methodological challenges and assess the extent to which the CCVA literature is engaging with them.

8.2   Challenges of Climate Change Vulnerability Assessment
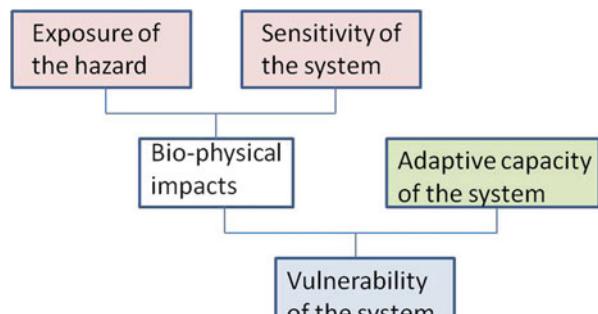
In the following sections, we discuss some of the key conceptual and theoretical as well as methodological challenges of CCVA.

8.2.1   Conceptual and Theoretical Challenges of Climate Change Vulnerability Assessment

There is no single accepted definition of vulnerability in the literature and a number of authors have attempted to pinpoint the concept. However, one commonly used definition (illustrated in Fig. 8.1) has been presented by the IPCC in its Third Assessment Report [5].

"... the degree to which a system is susceptible to, or unable to cope with, adverse effects of climate change, including climate variability and extremes. Vulnerability is a function of the character, magnitude, and rate of climate variation to which a system is exposed, its sensitivity, and its adaptive capacity" [5].

This definition of vulnerability recognizes both the external, geophysical determinants of risk, called exposure to climate stressors, AND the internal, socioeconomic and institutional processes generating vulnerability, usually referred to as the system's sensitivity to the stress and its adaptive capacity [1, 2, 6]. These are sometimes referred to in the literature as the three dimensions of vulnerability and are seen as the outcome of the interaction of two traditions of vulnerability research in physical and social science—a synthesis that provides a better account of the contextual and social dynamics of climate hazards and the multiple linkages that govern their impacts [3, 7]. However, some scholars have described this definition of vulnerability as vague and argued that vulnerability and related concepts such as adaptive capacity and sensitivity are themselves vague and inconsistently defined in the literature [8, 9]. From a practical point of view, quantification or measurement of that concept remains critical. Some authors

Fig. 8.1 Components of vulnerability (adapted from IPCC, 2001)

argue that vulnerability cannot, in principle, be measured as it is not an observable phenomenon such as the mass of an object, energy, or temperature [10].

Alongside those criticisms, another body of literature has evolved concentrating on the development of various theoretical aspects of vulnerability such as building a conceptual model of vulnerability and development of assessment methods. Broadly, three conceptual models can be found in the literature. One is a risk-hazard framework, which conceptualizes vulnerability as a dose–response relationship between an exogenous hazard to a system and its adverse effects [11, 12]. We call this approach "biophysical approach." The second approach is a social constructivist framework which regards social vulnerability as a preexisting condition of a household or a community that is mainly determined by socioeconomic and political factors [8, 13, 14]. We call this approach the "socioeconomic approach." The third stream, referred to as "integrated approach," conceptualizes vulnerability as the differential abilities of communities to cope with external stress [8, 15]. It is the "biophysical" and "integrated" approaches that have been used mostly in the climate change vulnerability literature. Füssel and Klein [8] present a reading of the evolution of the "integrated approach": first generation of vulnerability assessment, and second generation of vulnerability assessment and adaptation policy assessment. The move from the biophysical approach to the first-generation vulnerability assessment is characterized primarily by the evaluation of climate impacts in terms of their relevance to society and by the consideration of potential adaptation. On the other hand, second-generation vulnerability assessment acknowledges that it is not the mere availability of adaptation options but the capacity of communities and institutions to actually implement them that determines their vulnerability to climate change [8]. Luers [16] has developed a three-dimensional vulnerability framework in which "vulnerability" and "sensitivity/exposure" are the main two dimensions while "threshold" acts as the third dimension, highlighting the fact that change in the sensitivity and exposure with respect to thresholds drives the state of vulnerability. For more discussion of frameworks readers are referred to [3, 15, 17–20].

8.2.2 Methodological Challenges of CCVA

For the sake of clarity, we call CCVA any attempt at assessing vulnerability to climate change stresses be it quantitative or qualitative, based on indicators, mechanistic models, or a mix of both. On the other hand, we refer to vulnerability assessments that are based exclusively or ultimately on indicators as indicator-based vulnerability assessment (IBVA). "Ultimately" in the previous sentence is a reference to some studies that present the outcome of mechanistic models in the form of indicators, so the vulnerability model will carry a mechanistic component, the outcome of which is subsequently expressed by indicators.

As discussed in the previous sections, there is an extensive literature of vulnerability research available in the context of social and global change. However, the

application of these concepts in policy-driven assessments has been limited by a lack of robust metrics to model and measure vulnerability within and across systems [21]. Therefore, how to measure vulnerability remains an important question, and a methodological challenge. The strict answer to this question is that vulnerability is a social construct and cannot be measured. Another question therefore is how to make the concept operational. In IBVA, making the concept operational consists of three steps: (a) definition of vulnerability framework, (b) selection of indicators, and (c) modeling or aggregation of indicators [9].

Definition of Vulnerability Framework

The first step in building the most basic vulnerability model is to define the problem at hand by answering the following three questions:

1. Which SES is the object of study (e.g., locality, community, industrial sector)?
2. The vulnerabilities of which valued attributes of this SES are to be assessed?
3. The vulnerabilities to which climate-related stress(es) are to be assessed?

Selection of Indicators

The selection of indicators is usually governed by the choice of valued attributes and SES of concern. However, this selection is not straightforward and involves a degree of subjectivity and uncertainty. Adger [7] points to the different possible processes generating vulnerability and cautions against approaches that implicitly preselect one and discard others. Therefore, indicator selection aims to represent all of the important processes generating vulnerability [9].

Modeling or Aggregation of Indicators

Once the domain of SES, valued attribute of concern, and indicating system variables have been defined, the next step of IBVA is to combine those system variables or indicators by way of modeling or aggregation. Some scholars argue that aggregation of indicators is not essential and that information about vulnerability should be gleaned from individual indicators. However, aggregation allows better comparability and communicability. It is through comparability that hot spots and policy direction on resource allocation can be identified and better communicated. While it is true that aggregation can hide complexity, policy makers can have access to both aggregated and individual indicators for a better understanding of vulnerability.

Modeling is useful when the exact relationships between the system variables (indicators) are known in a mechanistic sense, via simple closed-form equations or more complex relationships implemented in a simulation model. Modeling is

mostly used in the domain of ecosystem vulnerability (e.g., vulnerability of fisheries or crops due to change in temperature and/or hydrologic cycle), and is closely associated with the impact assessment domain ("biophysical approach"). This is because it is usually possible to simulate the exogenous climatic impacts and the system's (ecosystem) sensitivity to those impacts. The vulnerability of anthropogenic systems, on the other hand, is much more difficult to model in a mechanistic sense, not least because of the complexity of processes determining adaptive capacity, and the necessarily qualitative nature of the research generating knowledge about it. Adaptive capacity is a critical system property which describes the ability to cope or mobilize scarce resources to anticipate or respond to perceived or current stresses [22]. Therefore, researchers pursuing the "integrated approach" (which usually includes the three dimensions, exposure, sensitivity, and adaptive capacity) tend to use the IBVA and forms of aggregation other than modeling. In the following section, we present a brief description of some of the methodological challenges pertaining specifically to IBVA. For a more detailed discussion of these challenges, the reader is referred to El-Zein and Tonmoy [23].

8.2.3 Challenges in Indicator-Based Vulnerability Assessment

In the following sections, we discuss some of the key methodological challenges of IBVA.

Aggregation of Indicators in IBVA

As the exact relationships between indicators are not known, IBVA uses a form of aggregation sometimes called vulnerability mapping, especially although not always, when the systems in question are spatially defined communities. Mapping is most commonly performed by combining multiple indicators into single indices of vulnerability for a given stressor under a given dimension, and then combining multiple indices in order to build an overall, relative estimate of vulnerability [24, 25]. These "combinations" are usually simple arithmetic or geometric means, based on multiple attribute utility theory (MAUT) widely used in economics, engineering, decision science, development studies, and, to a lesser extent, social science [26–29]. Some studies also use empirical equations for aggregation in order to develop a vulnerability index [30–32]. However, use of such methods of aggregation in IBVA face some theoretical and practical challenges which have been recognized by many authors [3, 33–35]. MAUT requirements for additive independence and complete knowledge of system interactions by analyst are rarely if ever satisfied in IBVA. IBVA studies using MAUT assume complete compensation between different indicators, convert nonlinear relationships into linear, monotonic ones, and allocate a weight to each indicator often, without recourse to solid scientific evidence [24, 36–38].

Incommensurability and Compensation

Analysts using MAUT for aggregation of indicators in IBVA build a utility-value function usually without providing an objective basis for its construction, especially in relation to the weights applied to indicators. In IBVA, one indicator is not generally convertible into another and deductive arguments to guide such a conversion cannot be easily built. Therefore, aggregation through a summative or a multiplicative procedure is problematic, forcing commensurability and compensation, i.e., the well-known problem of "comparing apples and oranges."

Nonlinearity

The second difficulty with MAUT procedures is that they assume a linear association between indicator and vulnerability and do not usually allow the simulation of thresholds and nonlinear relationships. For example, a widely documented effect in the literature on heat stress is the "comfort temperature" which yields minimum daily or monthly mortality counts in a city, beyond which there is a steep rise in the number of deaths [39], particularly in cold climates, a phenomenon represented by parabolic or bilinear relationships in time-series analysis of mortality counts. In fact, nonlinearity is prominent in the literature on vulnerability with at least one framework defining vulnerability as a degree of departure from a threshold [16].

Uncertainty

Various sources of uncertainty characterize IBVA. First, while individual indicators hold a relationship to a process generating vulnerability, a quantitative description of this relationship is often lacking. This is due to the inductive and/or normative nature of indicator selection, as opposed to deductive, theory-driven approaches [40]. Second, random and nonrandom fluctuations of indicators, especially if they are averaged over spatial or temporal scales and/or projected into the future, can generate a high level of imprecision. Third, indicators and the weights attached to them are sometimes evaluated by interviewing stakeholders or experts and the process inevitably carries a level of subjectivity, as well as possible variances between the opinions of different informants.

Scale

Processes generating vulnerability can be fundamentally different at different scales. As an example, access to resources, diversity of income sources, as well as social status of individuals play a vital role in determining vulnerability at a household level. On the other hand, vulnerability at a larger scale such as of a

nation, region, or community is determined more strongly by institutional and market structures, such as prevalence of informal and formal social security and insurance, infrastructure, and income [9, 14]. A number of scholars have argued that, at local compared to larger scales, it is easier to define systems, identify socioeconomic and biophysical processes that determine vulnerability, and build inductive arguments to characterize them, and hence IBVAs should be conducted at smaller rather than larger scales [9, 14].
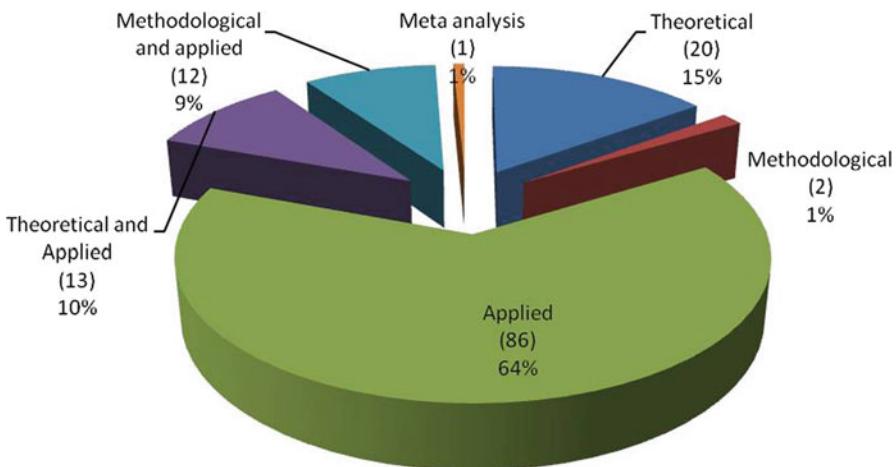
Temporal Framework

Vulnerability frameworks generally view it as possible future harm, referring to a value judgment: "How bad is the system under a specific hazard?" A proxy indicator of "badness" is then sought, such as the number of people who might die during a flood event or the losses to ecosystem due to ocean acidification. Hinkel [9] argues that such possible future highlights the forward-looking aspect of vulnerability. However, the question remains as to whether the framework is referring to today's vulnerability (determined in part by past adaptation) or to one which might unfold in the future depending on prior adaptation. The answer to this question should in turn dictate the point in time at which indicators are measured and provide a level of temporal consistency to the analysis. Unfortunately, IBVA studies, especially those carrying a significant socioeconomic component, often combine indicators at different points in time (e.g., mixture of current socioeconomic data with future climate projection) and associate them with what is rather ambiguously termed as "climate change vulnerability," without any reference to time (present or future). A consistent approach, in the case of the above example, would combine projections of future adaptive capacity with future climate data. Such an effort has been made, for example, in the Advanced Terrestrial Ecosystem Analysis and Modeling (ATEAM) project in Europe to assess ecosystem vulnerability due to future climate change [41, 42]. However, attempts at temporal consistency remain very limited in the literature.

8.3   Methodological Scope of the CCVA Literature

To what extent has the literature on vulnerability engaged with these methodological challenges? As part of a larger meta-analysis of the literature we are presently conducting, we report here some preliminary findings in relation to the question raised above. Scrutinizing a sample of 134 peer-reviewed papers, selected on criteria of relevance and citation, we investigated the focus of the peer-reviewed CCVA literature in relation to:

1. Broad content (theoretical, methodological, applied, or a combination of these).
2. Physical hazard(s) under consideration (e.g., sea level rise, heat waves, floods).

Fig. 8.2 Distribution of papers according to their broad content (number of papers in brackets)
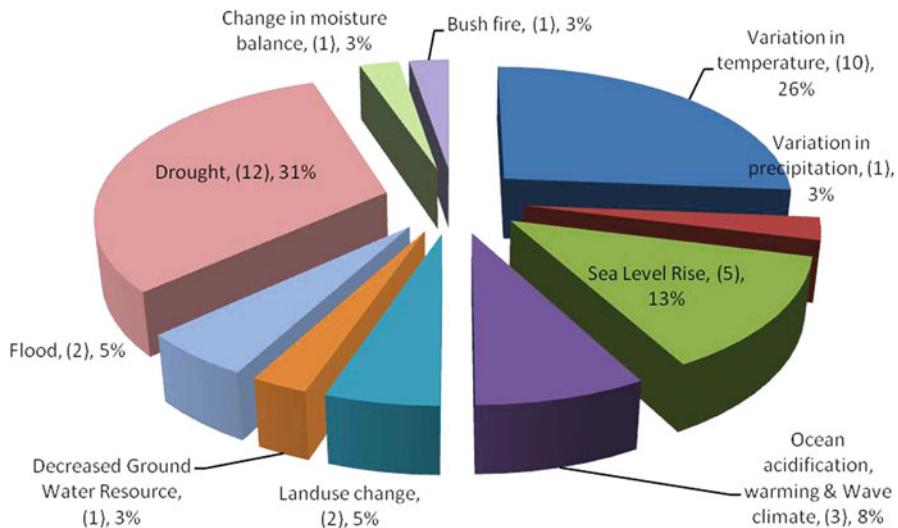
3. Geographical scale (e.g., local, municipal, regional, national).
4. Aggregation methods employed (e.g., multi-attribute utility theory, GIS overlaying).

8.3.1   Broad Content

64 % of papers in our sample consist of vulnerability assessment studies applied to a specific setting (see Fig. 8.2). 15 % of papers are dedicated to theoretical issues around vulnerability assessment (definitions, conceptual frameworks, measurability, and so on), with another 10 % engaging with theoretical aspects of vulnerability assessment and reporting an assessment study. Most methodological papers (9 % of total) also contain an applied component, while another 1 % are dedicated exclusively to methodological issues. Given the significant methodological challenges facing vulnerability assessment, it appears that this area of climate change adaptation is under-researched.

8.3.2   Physical Hazard Under Consideration

70 % of the studies in our sample consider multiple stresses, with the remaining 30 % studying a single stress. This is consistent with the fact that SESs are usually subject to multiple climate change-related stresses. Focusing on single-stress papers, we find that the impacts of increased frequency of droughts and temperature extremes are considered in more than 50 % of the studies, and around 75 %, if sea
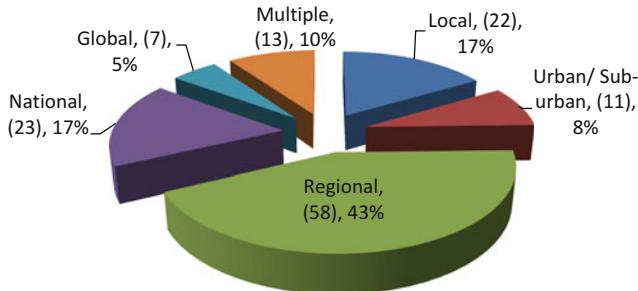
Fig. 8.3 Distribution of papers according to the physical hazard under consideration
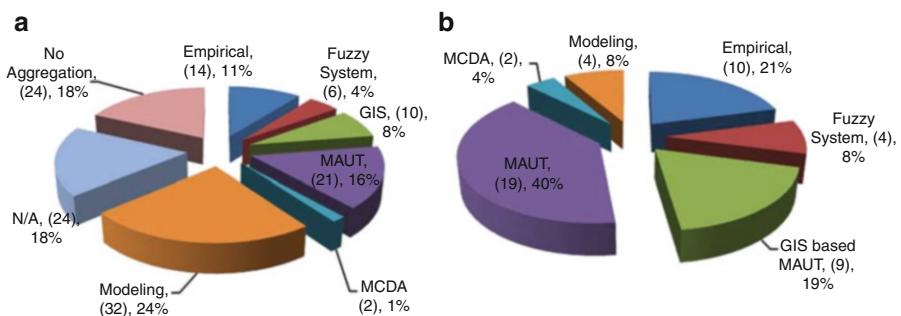
level rise and ocean acidification and warming are included (see Fig. 8.3). This distribution seems to match the most important biophysical climate stressors identified by the IPCC working group 1 [43].

8.3.3   Geographical Scale

Geographical scale plays a dominant role in determining relevant processes generating vulnerability. Here, studies termed "global" generally assess the impact of a specific hazard on the whole world, at least nominally. Studies grouped under "national" compare vulnerabilities of different nations. "Regional" scale refers to studies conducted at a subnational level that is typically larger than a city. "Urban/ suburban" refers to studies conducted at city scale or smaller geographical unit. Finally, studies that consider the vulnerability of a specific community, usually defined by a given locality (a specific suburb, a group of neighboring villages, etc.) down to a household level, are termed "local." Figure 8.4 shows that most studies (65 %) are conducted at regional or higher levels. Only 17 % of vulnerability studies have been conducted at a truly local level which is, arguably, the scale at which processes generating vulnerability are most well defined and the scientific validity of the assessment is at its highest.

Fig. 8.4 Distribution of papers according to the geographical scale of studies

Fig. 8.5 Distribution of papers by aggregation methods employed: (**a**) for the whole study sample (134 papers) and (**b**) studies that consider both biophysical and socioeconomic domains, excluding 23 % of studies with no aggregation (48 papers)

8.3.4 Aggregation Methods Employed

It can be seen from Fig. 8.5a that MAUT, and GIS-based MAUT, accounts for 24 % of aggregation methods employed in our study sample. However, when we exclude studies that do not aggregate indicators as well as those that do not consider socioeconomic processes generating vulnerability (i.e., those focusing exclusively on natural ecosystems), we find that MAUT and GIS-based MAUT forms of aggregation are employed in 59 % of publications (Fig. 8.5b). This is due to the fact, discussed earlier, that mechanistic simulation models accounting for socioeconomic and institutional factors are much more difficult to build, with researchers resorting instead to the simplicity of MAUT aggregation. A number of agricultural studies use empirical equations to calculate such indicators as crop vulnerability index and crop sensitivity index. However, little justification is usually given for these indices in the studies themselves. On the other hand, only 12 % of studies in the reduced sample use more sophisticated methods such as multi-criteria decision analysis or fuzzy logic. These methods are usually better suited for the mix of quantitative and qualitative data that characterizes indicator-based vulnerability models.

8.4　　Conclusions

In light of the methodological challenges facing CCVA, our preliminary reading of the literature on vulnerability assessment allows us to draw the following conclusions:

1. Critical scrutiny of prevalent assessment methodologies and development of new ones remain limited in the literature since only 10 % of the studies focus on such issues. This is despite the fact that many scholars have raised questions about a number of methodological aspects of vulnerability assessment.
2. Although a number of theoretical papers have argued that IBVA is likely to be most valid at smaller rather than larger geographical scales, only 17 % of studies are conducted at local scales.
3. Among the studies that aggregate indicators and consider both biophysical and socioeconomic processes generating vulnerability, 59 % use methods based on MAUT such as arithmetic mean, geometric mean, or GIS-based MAUT, approaches whose scientific validity is in question when applied in the context of IBVA.

At this stage of development of vulnerability assessment, we believe that the methodological challenges we discussed above ought to receive more attention in the literature, lacking which the scientific validity of assessments will remain doubtful.

References

1. Klein RJT (2003) Adaptation to climate variability and change: what is optimal and appropriate? In: Giupponi C, Schechter M (eds) Climate change in the mediterranean: socio-economic perspectives of impacts, vulnerability and adaptation. Edward Elgar, Cheltenham
2. Eriksen S, Kelly P (2007) Developing credible vulnerability indicators for climate adaptation policy assessment. Mitigation and Adaptation Strategies for Global Change 12:495–524
3. Füssel H-M (2007) Vulnerability: a generally applicable conceptual framework for climate change research. Global Environmental Change 17:155–167
4. Mclaughlin S, Cooper JAG (2010) A multi-scale coastal vulnerability index: A tool for coastal managers? Environmental Hazards-Human and Policy Dimensions 9:233–248
5. IPCC, Mccarthy JJ, Canziani OF, Leary NA, Dokken DJ, White KS (eds.) (2001) Climate change 2001: impacts, adaptation and vulnerability. Contribution of Working Group II to the fourth assessment report of the intergovernmental panel on climate change. Cambridge University Press, Cambridge, UK
6. Parry ML, Canziani OF, Palutikof JP, Van Der Linden PJ, Hanson CE (2007) Climate change 2007: impacts, adaptation and vulnerability. Contribution of Working Group II to the Fourth

Assessment Report of the Intergovernmental Panel on Climate Change. Cambridge University Press, Cambridge, UK

7. Adger WN (2006) Vulnerability. Global Environmental Change 16:268–281
8. Füssel H-M, Klein R (2006) Climate change vulnerability assessments: an evolution of conceptual thinking. Climatic Change 75:301–329
9. Hinkel J (2011) "Indicators of vulnerability and adaptive capacity": towards a clarification of the science-policy interface. Global Environmental Change 21:198–208
10. Moss RH, Brenkert AL, Malon EL (2001) Vulnerability to climate change: a quantitative approach: Pacific Northwest National Laboratory PNNL-SA-33642. Prepared for the US Department of Energy. Washington, DC
11. Dilley M, Boudreau TE (2001) Coming to terms with vulnerability: a critique of the food security definition. Food Policy 26:229–247
12. Downing TE, Patwardhan A (2004) Assessing vulnerability for climate adaptation. In: UNDP Adaptation Policy Framework: United Nations Development Program. http://www.undp.org/cc/apf.htm. Accessed at [Online]
13. Blaikie P, Cannon T, Davis I, Wisner B (1994) At risk: natural hazards, people's vulnerability and disasters. Available. http://books.google.co.in/books?id = _j3gw8Cz0pMC
14. Adger WN, Kelly PM (1999) Social vulnerability to climate change and the architecture of entitlements. Mitigation and Adaptation Strategies for Global Change 4:253–266
15. Turner BL, Kasperson RE, Matson PA, Mccarthy JJ, Corell RW, Christensen L, Eckley N, Kasperson JX, Luers A, Martello ML, Polsky C, Pulsipher A, Schiller A (2003) A framework for vulnerability analysis in sustainability science. Proceedings of the National Academy of Sciences 100:8074–8079
16. Luers AL (2005) The surface of vulnerability: an analytical framework for examining environmental change. Global Environmental Change 15:214–223
17. Watts MJ, Bohle HG (1993) The space of vulnerability: the causal structure of hunger and famine. Progress in Human Geography 17:43–67
18. Bohle HG (2001) International human dimensions programme (IHDP). Update 2:1
19. Kasperson JX, Kasperson RE, Turner BL II, Schiller A, Hsieh W-H (2003) Vulnerability to global environmental change. In: Diekmann A, Dietz T, Jaeger C, Rosa ES (eds) The human dimensions of global environmental change. MIT Press, Cambridge
20. Adger WN (2001) Scales of governance and environmental justice for adaptation and mitigation of climate change. Journal of International Development 13:921–931
21. Luers AL, Lobell DB, Sklar LS, Addams CL, Matson PA (2003) A method for quantifying vulnerability, applied to the agricultural system of the Yaqui Valley, Mexico. Global Environmental Change 13:255–267
22. Nathan E (2011) Adaptive capacity and its assessment. Global Environmental Change 21:647–656
23. EL-Zein A, Tonmoy FN (2013) Assessment of Vulnerability to Climate Change using a Multi-Criteria Outranking Approach with Application to Heat Stress in Sydney. Ecological Economics (Under review)
24. Bernier E, Gosselin P, Badard T, Bedard Y (2009) Easier surveillance of climate-related health vulnerabilities through a Web-based spatial OLAP application. International Journal of Health Geographics 8:18
25. Yoo G, Hwang JH, Choongik C (2011) Development and application of a methodology for vulnerability assessment of climate change in coastal cities. Royaume-Uni, Elsevier, Kidlington
26. Alessa L, Kliskey A, Lammers R, Arp C, White D, Hinzman L, Busey R (2008) The arctic water resource vulnerability index: an integrated assessment tool for community resilience and vulnerability with respect to freshwater. Environmental Management 42:523–541
27. Brenkert AL, Malone EL (2005) Modeling vulnerability and resilience to climate change: a case study of India and Indian states. Climatic Change 72:57–102
28. Lexer MJ, Seidl R (2009) Addressing biodiversity in a stakeholder-driven climate change vulnerability assessment of forest management. Forest Ecology and Management 258:S158–S167

29. Malone E, Brenkert A (2008) Uncertainty in resilience to climate change in India and Indian states. Climatic Change 91:451–476
30. Aguilar MY, Pacheco TR, Tobar JM, Quinonez JC (2009) Vulnerability and adaptation to climate change of rural inhabitants in the central coastal plain of El Salvador. Climate Research 40:187–198
31. Abuodha PAO, Woodroffe CD (2010) Assessing vulnerability to sea-level rise using a coastal sensitivity index: a case study from southeast Australia. Journal of Coastal Conservation 14:189–205
32. Duriyapong F, Nakhapakorn K (2011) Coastal vulnerability assessment: a case study of Samut Sakhon coastal zone. Songklanakarin Journal of Science and Technology 33:469–476
33. Ebert U, Welsch H (2004) Meaningful environmental indices: a social choice approach. Journal of Environmental Economics and Management 47:270–283
34. Böhringer C, Jochem PEP (2007) Measuring the immeasurable—a survey of sustainability indices. Ecological Economics 63:1–8
35. Klein RJT (2009) Identifying countries that are particularly vulnerable to the adverse effects of climate change: an academic or a political challenge? The Carbon and Climate Law Review 3:284–291
36. Preston BL, Brooke C, Measham TG, Smith TF, Gorddard R (2009) Igniting change in local government: lessons learned from a bushfire vulnerability assessment. Mitigation and Adaptation Strategies for Global Change 14:251–283
37. Tran LT, O'neill RV, Smith ER (2010) Spatial pattern of environmental vulnerability in the Mid-Atlantic region, USA. Applied Geography 30:191–202
38. Rinner C, Patychuk D, Bassil K, Nasr S, Gower S, Campbell M (2010) The role of maps in neighborhood-level heat vulnerability assessment for the City of Toronto. Cartography and Geographic Information Science 37:31–44
39. Mcmichael AJ, Wilkinson P, Kovats RS, Pattenden S, Hajat S, Armstrong B, Vajanapoom N, Niciu EM, Mahomed H, Kingkeow C, Kosnik M, O'neill MS, Romieu I, Ramirez-Aguilar M, Barreto ML, Gouveia N, Nikiforov B (2008) International study of temperature, heat and urban mortality: the 'ISOTHURM' project. International Journal of Epidemiology 37:1121–1131
40. Vincent K (2007) Uncertainty in adaptive capacity and the importance of scale. Global Environmental Change 17:12–24
41. Metzger MJ, Rounsevell MDA, Acosta-Michlik L, Leemans R, Schrotere D (2006) The vulnerability of ecosystem services to land use change. Agriculture Ecosystems & Environment 114:69–85
42. Metzger M, Schröter D, Leemans R, Cramer W (2008) A spatially explicit and quantitative vulnerability assessment of ecosystem service change in Europe. Regional Environmental Change 8:91–107
43. IPCC, Parry ML, Canziani OF, Palutikof JP, Van Der Linden PJ, Hanson CE (eds) (2007) Climate change 2007: impacts, adaptation and vulnerability. Contribution of Working Group II to the fourth assessment report of the intergovernmental panel on climate change. Cambridge University Press, Cambridge, UK

Chapter 9
Investigating the Climate Change Impacts on the Water Resources of the Konya Closed Basin Area (Turkey) Using Satellite Remote Sensing Data

Semih Ekercin, Elif Sertel, Filiz Dadaser-Celik, and Savas Durduran

Abstract This chapter presents the pre-results from an ongoing study that mainly focuses on the use of remote sensing data to investigate the climate change effects on water resources in the Konya Closed Basin Area (KCBA), Turkey. In this study, multitemporal Landsat images along with climatic data were used to explore the dimension of drought effects on water lands and lakes located in the basin area. Image processing procedure includes both normalized difference vegetation index (NDVI) image interpretation and pre-processing stages (geometric and atmospheric correction). Our results suggest that in addition to socioeconomic profits of the use of groundwater for agricultural purposes, its effects on the ecological balance and water reserves in the KCBA should be analyzed in detail. Also, management strategies and plans should be developed to protect and/or rehabilitate current conditions in terms of drought in the KCBA. Furthermore, the region should regularly be monitored by up-to-date remote sensing data (at least annually) for better management of the water resources in the basin.

S. Ekercin (✉)
Dept. of Geomatics Engineering, Aksaray University, 68100 Aksaray, Turkey
e-mail: ekercin@gmail.com

E. Sertel
Dept. of Geomatics Engineering, Istanbul Technical University, Istanbul, Turkey

F. Dadaser-Celik
Dept. of Environmental Engineering, Erciyes University, Kayseri, Turkey

S. Durduran
Dept. of Geomatics Engineering, Selçuk University, Konya, Turkey

9.1   Introduction

The climate system of the earth, globally and locally, obviously has been changed from preindustrial period to present. Some of the changes are due to natural phenomena and some due to human activities where the vital role has been played by the emission of the so-called greenhouse gasses. The annual mean temperature in the temperate zones in Northern Hemisphere has increased by 1.4 °C due to the changes in climate and it is expected that this increase will reach 2.5 °C in the near future. At present, the mean annual temperature increase of 1.4 °C leads to a net increase of around 2.0–2.5 °C during the hot months of summer, resulting in increased evaporation from the water and soil surfaces while amplifying the transpiration from the plant leaves. Atmospheric CO_2 has reached 376 ppm as of year 2000 leading to a greenhouse effect and meltdown of glaciers and increased frequency and magnitude of hurricanes in oceans [1, 2].

Remote sensing has been used to investigate the impacts of climate change studies for many years at local and global scale [3–7]. Remote sensing provides information about land surface conditions, including snow cover, vegetation characteristics, and soil freezing, and their role in the exchange of moisture and energy between the land surface and atmosphere. Sensors deployed on platforms in the air and space can acquire data about the Earth's surface and atmosphere. Satellite observations are particularly useful to modellers because they provide repetitive, broad regional views of good spatial resolution, in a digital format [8].
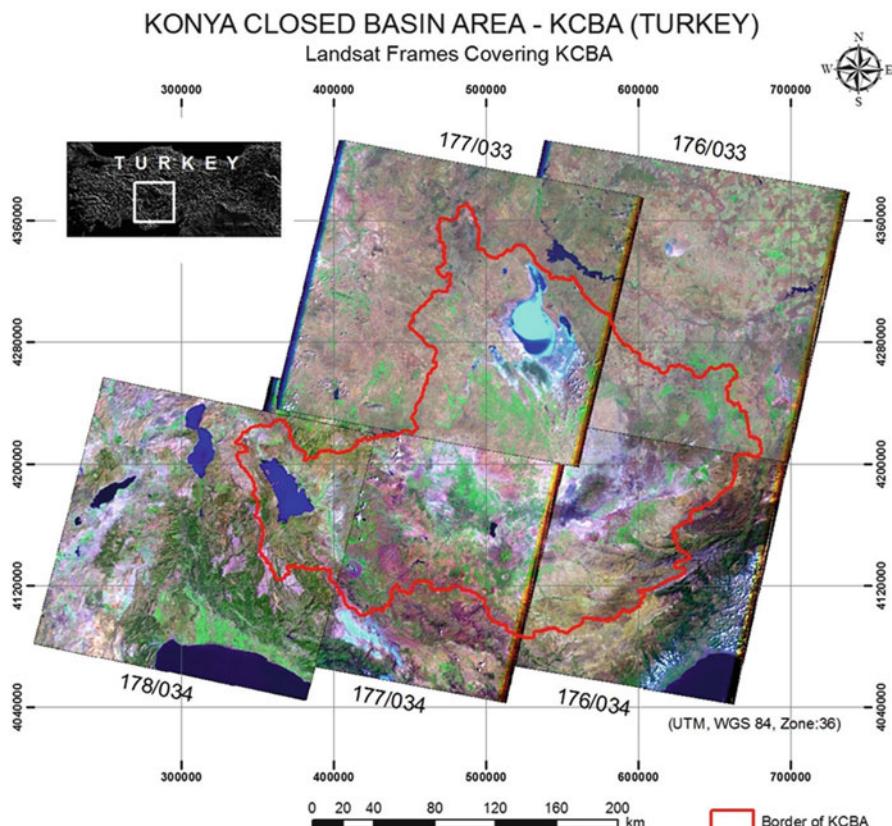
Remote sensing of the water regions became increasingly important over the recent decades because of both the problem of global climate change and worsening ecology. This technology has application, for instance, in identifying and quantifying areas experiencing drought which is one of the most important problems in the world. In practice, using multitemporal satellite data registrated properly, comparisons can be made between and among years for specific months [9]. On the other hand, remote sensing data can be integrated with geographic information system (GIS) which is an essential tool for analyzing and extracting more reliable and consistent information [10–12].

This study presents the pre-results of ongoing project supported by The Scientific and Technological Research Council of Turkey—TUBITAK (Grant Number: 110Y303). The project focuses mainly on the investigation of drought impact on Konya Closed Basin Area (KCBA), Turkey, by examining multitemporal satellite remote sensing data. The region has been experiencing drought over the last two decades resulting from two main phenomenons: (1) uncontrolled use of groundwater resources for agricultural purposes and (2) lack of precipitation (or natural drought). The first stage of the study includes evaluation of the multitemporal climatic data on the Salt Lake Basin Area for a period of 35 years (1970–2005). The changes in mean temperature and precipitation are evaluated for the study area by comparing two periods: 1970–1992 and 1993–2005. In the second stage, the effects of climate changes in the region were investigated by evaluating water reserve changes through multitemporal Landsat image data.

9.2   Methodology

9.2.1   Study Area

The KCBA is located in the Central Anatolian Plateau (Turkey) at latitude 36°
51′–39° 29′N and longitude 31° 36′–34° 52′E and at an altitude of about 1,000 m
(Fig. 9.1). KCBA covers a 5,426,480-ha surface area (nearly 7 % of Turkey's total
area) larger than that of the Netherlands. Within the basin, there are 11 watery
regions (lakes, reed beds) named as Lakes Samsam, Kozanlı, Kulu, Beyşehir,
Suğla, Bolluk, Tersakan, Tuz, and Reed Beds Ereğli, Reed Bed, and Hotamış.
A smooth plane at 900–1,050 m altitude has formed the main part of the Central
Anatolia Plateau in KCBA, Turkey's largest closed basin in which three million
people live, 45 % in rural areas and 55 % in urban areas. The agricultural revenue
provided by KCBA was due to grains (9.2 %), beans (6.2 %), and industrial crops
including sugar beet (8.5 %). As a result of insufficient drainage, the soils of the

Fig. 9.1 Location of the study area

region usually have the alluvial and salty characteristics due to high groundwater level, watering, and terrestrial semiarid mild climate conditions dominant in the basin. The water of the basin comes to an end in stagnant water, marshy places, or semimarshy places. The lack of a river in this wide basin, limited rainfall, and high evaporation ratios have formed a favorable water balance that is rarely met in closed basins. The shallow lake and reed beds at the center of the basin are fed by many rivers flowing to the region. The climate characteristics of the basin present the Mediterranean climate (mild and rainy winters, hot and dry summers) at the south, the terrestrial climate (cold winters, hot and dry summers) at the center and north of the basin, and the desert climate in Karapınar and its vicinity. The rainfalls were mostly observed in winter and spring seasons. The natural richness and the lakes of the basin provide significant living places for the migratory birds [13, 14].

9.3   Satellite Remote Sensing Data and Image Processing

The Landsat-5 TM image data set listed in Table 9.1 and covering the KCBA were converted to the UTM coordinate system (Zone 36) using approximately 45 control points (for each full-frame Landsat-5 TM image) both extracted from 1:25,000-scale topographic maps and recorded by GPS during the fieldwork. A second-order polynomial transformation method was performed to create the output images with 30 m ground resolution. The root-mean-square error of the polynomial transformation is less than half a pixel for all the data set (Table 9.1). In order to preserve radiometric integrity, a nearest neighbor resampling method was used [15]. Checkpoints were measured on the geometrically corrected image set and compared with the topographic sheets to evaluate the quality of the geometric correction [16].

After the geometric correction procedure, preparation of a Landsat-5 TM mosaic image is started (Table 9.2) which will be used to base data covering KCBA. Many techniques have been developed to create image mosaics of satellite images over large areas [17, 18]. In this study, image mosaicing algorithm of the Erdas Imagine© software was used to produce high-resolution Landsat-5 TM image mosaics.

9.4   Climatic Data

In this study aiming to investigate the effects of climate change on the water resources of the KCBA, temperature and precipitation records collected by nine meteorological stations located in the KCBA were used as climatic data (Figs. 9.2 and 9.3). The measurements of monthly raw data of temperature and precipitation collected between 1970 and 2005 were captured from the stations, namely, Aksaray, Cihanbeyli, Çumra, Ereğli, Karaman, Karapınar, Konya, Kulu, and Şereflikoçhisar.

Table 9.1 Satellite remote sensing data used in the study and the details of geometric correction process

Sensor	Date	Spectral band	Spatial resolution (m)	Number of control points	RMS (pixel)
Landsat-5 TM	21.08.2011	7 (VNIR-SWIR, TIR)	30, 120	43	0.48
	29.07.2011			40	0.40
	17.05.2011			48	0.34
	17.05.2011			41	0.45
	10.05.2011			42	0.39
	10.05.2011			49	0.45
	10.08.2007			49	0.47
	25.07.2007			52	0.48
	17.08.2007			45	0.36
	23.06.2007			52	0.49
	23.06.2007			45	0.45
	16.06.2007			45	0.42
	15.08.2003			53	0.45
	08.08.2003			40	0.40
	08.08.2003			38	0.45
	10.06.2002			43	0.43
	10.06.2002			42	0.39
	09.06.2002			45	0.46
	09.06.2002			46	0.42
	26.08.1998			48	0.45
	01.08.1998			50	0.49
	01.08.1998			42	0.43
	16.06.1993			46	0.47
	16.06.1993			49	0.39
	09.06.1993			41	0.42
	09.06.1993			40	0.43
	16.08.1989			41	0.48
	16.08.1989			45	0.44
	09.08.1989			44	0.48
	26.08.1984			39	0.41
	26.08.1984			46	0.43
	03.08.1984			54	0.45
	16.07.1984			45	0.48
	16.06.1984			41	0.47
	16.06.1984			48	0.49

Atmospheric warming has led to significant effects in Turkey especially after 1993 after which the changes were more notably measurable. The obvious results of the warming could be seen in glaciers in high mountains and lakes at low lands [19]. Therefore, 1970–1992 and 1993–2005 periods were compared to examine the temporal changes in temperature and precipitation values. Annual, five summer-month (May, June, July, August, and September) and July values of climate records were

Table 9.2 Presentation of mosaic image dates for Konya Closed Basin Area—KCBA

Mosaic image date	1984 (August)	1989 (August)	1998 (August)	2003 (August)	2007 (August)	2011 (August)
Full-frame dates	03.08.1984	09.08.1989	26.08.1998	08.08.2003	19.08.2007	30.08.2011
Full-frame dates	03.08.1984	09.08.1989	26.08.1998	08.08.2003	19.08.2007	29.07.2011
Full-frame dates	26.08.1984	16.08.1989	01.08.1998	15.08.2003	10.08.2007	21.08.2011
Full-frame dates	26.08.1984	16.08.1989	01.08.1998	15.08.2003	25.07.2007	21.08.2011
Full-frame dates	16.07.1984	*Unavailable*	08.08.1998	22.08.2003	17.08.2007	28.08.2011

selected as indicator for the detection of changes in temperature. Taking into account snowing season, precipitation records collected in January were used for the detection of changes in precipitation. Climate records were received from the Turkish State Meteorological Service as monthly raw data. The values of climate records used for annual, January, July, and five summer months in this study were calculated for a 35-year period.

9.5   Results and Discussion
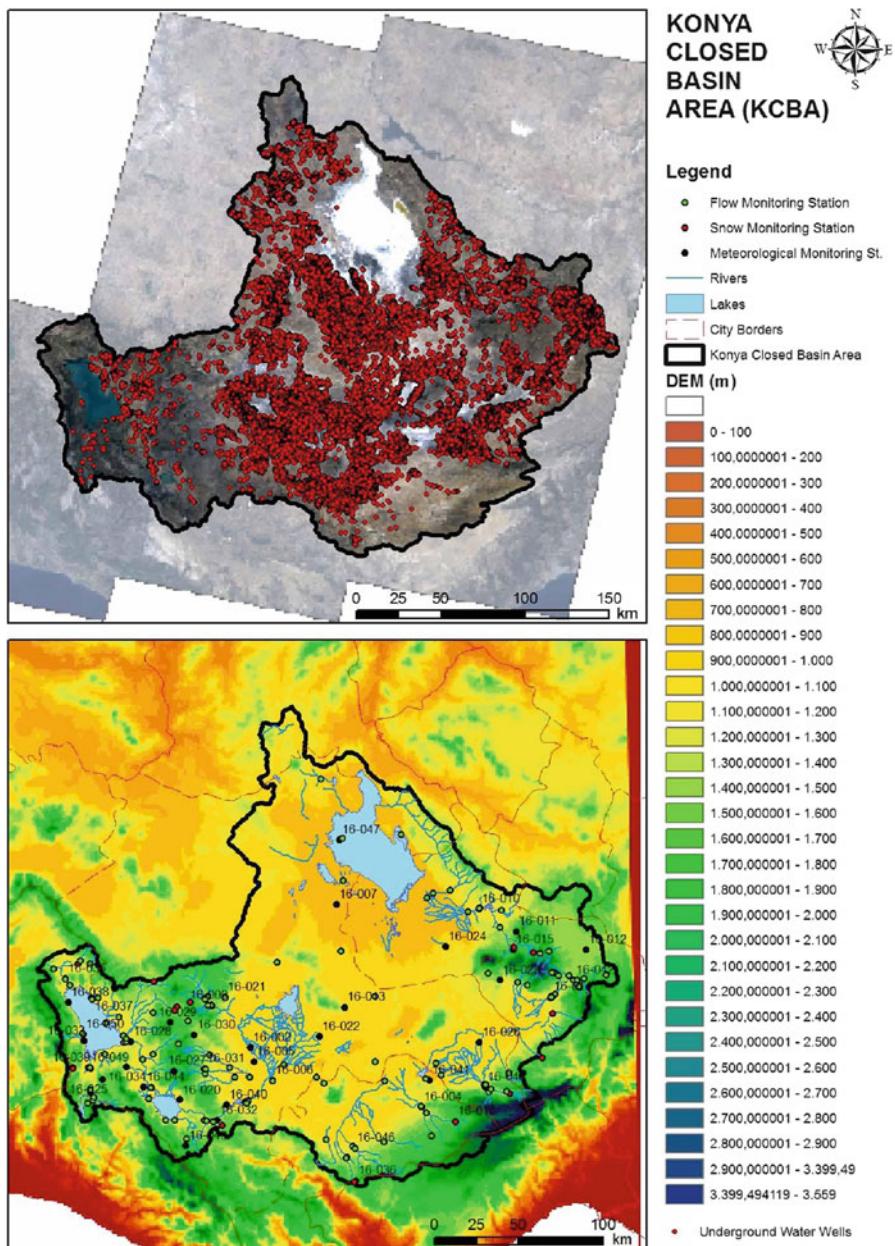
9.5.1   Evaluating Climatic Data

The analysis of the meteorological data for 1993–2005 period has shown that the annual increase in temperature over the 12 years was between 0.2 and 1.3 °C compared to the means between 1970 and 1992 (Fig. 9.3). The increase in mean annual temperature in the basin was in Aksaray +1.0 °C, in Cihanbeyli +1.1 °C, in Çumra +0.8 °C, in Ereğli +1.3 °C, in Karaman +0.6 °C, in Karapınar +0.7 °C, in Konya +0.2 °C, and in Kulu +0.8 °C.
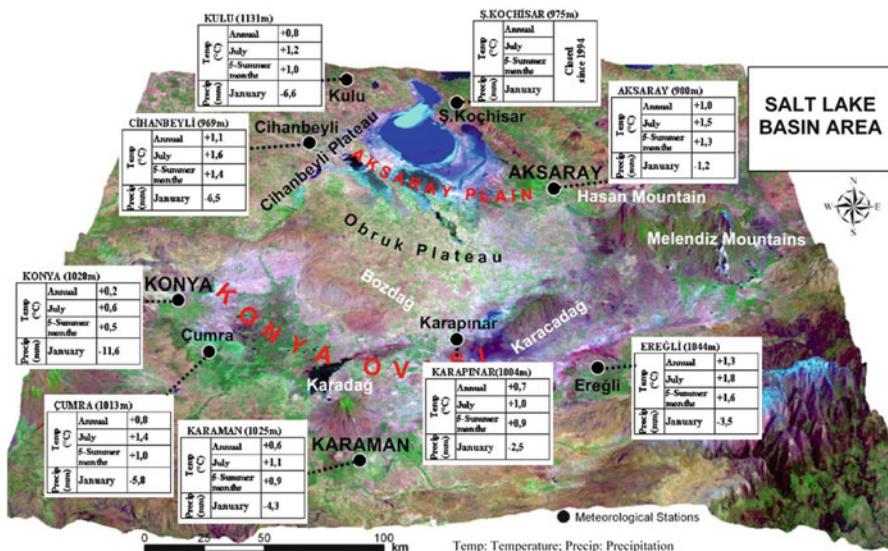
On the other hand, the changes in warming for the means of five summer months for the same period in the basin was in Aksaray +1.3 °C, in Cihanbeyli +1.4 °C, in Çumra +1.0 °C, in Ereğli +1.6 °C, in Karaman +0.9 °C, in Karapınar +0.9 °C, in Konya +0.5 °C, and in Kulu +1.0 °C.

The most important result of the study attracting attention is that all stations showed much pronounced changes in warming for July with an increase of more than 1.0 °C between 1993 and 2005 compared to 1970 and 1992 (Fig. 9.3). At this point, it can be mentioned that dry summer season has extremely affected the region for the last two decades.

In order to calculate the impact of warming in Salt Lake Basin, in addition to temperature, precipitation records obtained from nine meteorological stations in

Fig. 9.2 Distribution of groundwater wells and monitoring stations in the KCBA
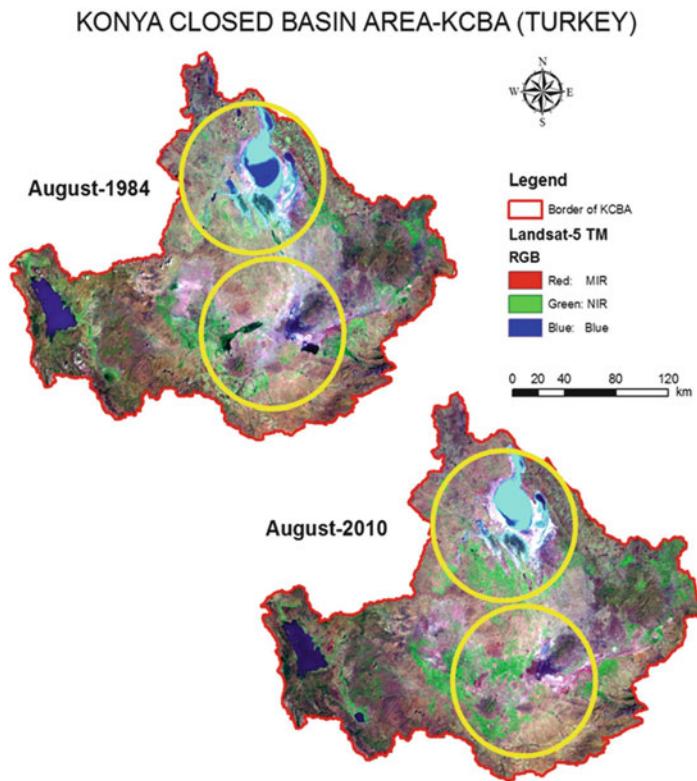
Fig. 9.3 Evaluation of climatic data (mean temperature and precipitation) by comparing 1970–1992 and 1993–2005 periods according to the nine meteorological stations located in the Salt Lake Basin Area

1970–1992 period were compared to the period between 1993 and 2005. For this process, taking into account snowing season, January (mean) precipitation records were used to detect the changes in snow which feeds groundwater which is the most important component among the water resources in the Salt Lake Basin Area. The analysis of the meteorological data for 1993–2005 period showed a simultaneous decrease in mean precipitation between 1.2 and 11.6 mm. January precipitation changes for these nine stations were recorded as 1.2 mm (from 38.0 to 34.8 mm; −8.4 %) for Aksaray, 6.5 mm (from 35.2 to 28.7 mm; −18.5 %) for Cihanbeyli, 5.8 mm (from 37.2 to 31.4 mm; −15.6 %) for Çumra, 3.5 mm (from 30.4 to 26.9 mm; −11.5 %) for Ereğli, 4.3 mm (from 40.6 to 36.3 mm; −10.6 %) for Karaman, 2.5 mm (from 29.8 to 27.3 mm; −8.4 %) for Karapınar, 11.6 mm (from 37.0 to 25.4 mm; −31.4 %) for Konya, and 6.6 mm (from 43.9 to 37.3 mm; −15.0 %) for Kulu (Fig. 9.3).

9.6 Regional Effects of Climate Change on Water and Salt Resources
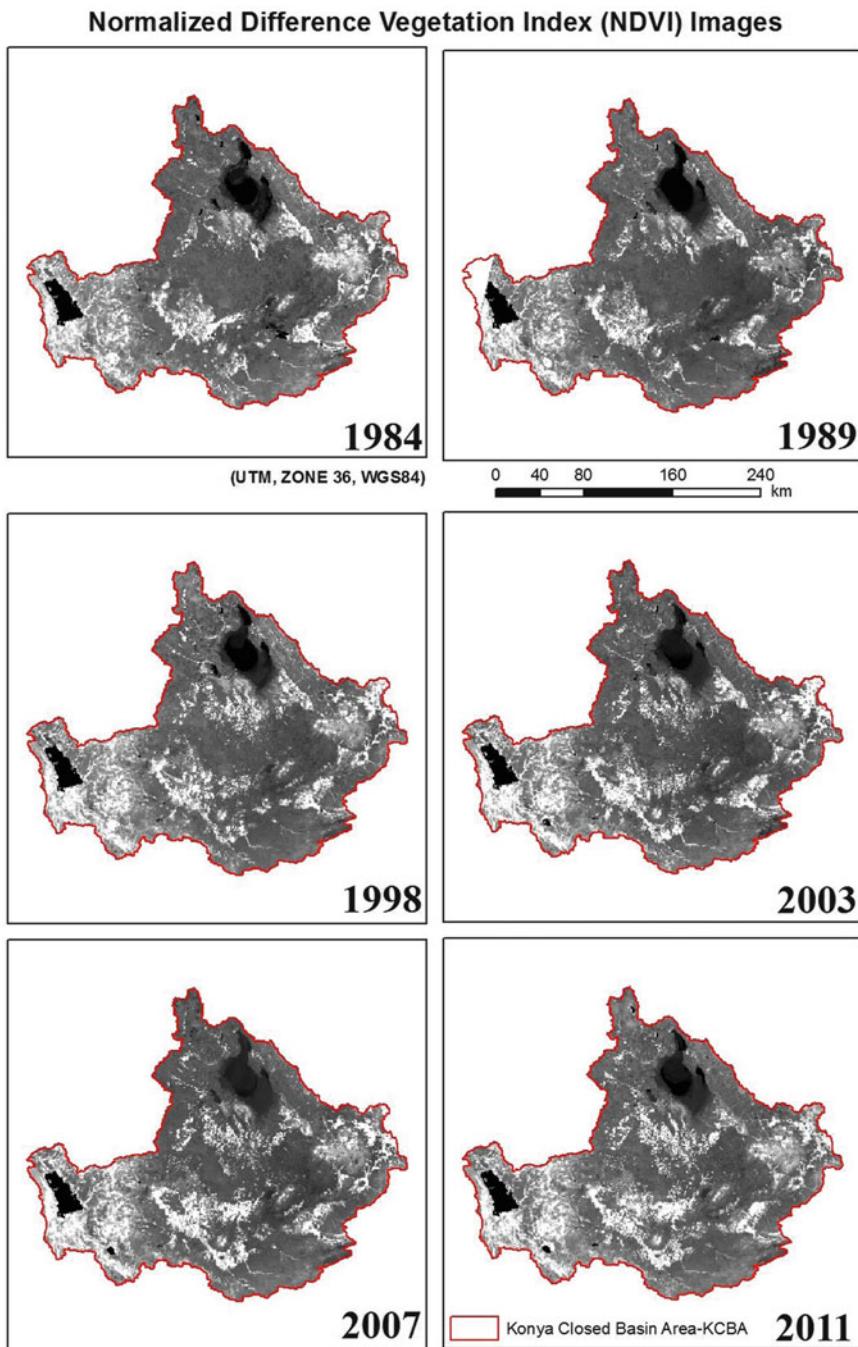
Analysis of climatic data showed that significant changes in precipitation and air temperature in KCBA have occurred during the recent decades. These changes could also be responsible for the changes in land cover; Fig. 9.4 provides two views

Fig. 9.4 Visual presentation of changes in water reserves located in the basin area through multitemporal Landsat-5 TM data

of the KCBA obtained from Landsat images acquired in August 1984 and August 2010.

Visual examination of Fig. 9.4 shows that there is a significant reduction in the area covered by lakes and marshes from 1984 to 2010. The Salt Lake and small lakes and marshes located to the south of the basin were almost dry in 2010. This is most probably not only due to the decrease in precipitation but also due to the decrease in groundwater input to the lakes and marshes. Groundwater is used excessively in irrigation in the Konya Closed Basin. From Figs. 9.4 and 9.5, we notice that agricultural areas have expanded in the basin, which put an extra pressure to groundwater resources that have already been affected by the adverse climatic conditions.

Normalized Difference Vegetation Index (NDVI) Images

Fig. 9.5 NDVI images of the KCBA for summer season (August)

9.7   Conclusions

In this study which presents the pre-results of ongoing project supported by TUBITAK, we have investigated the dimension of climate change effects in KCBA (Turkey) using multitemporal satellite remote sensing data.

The most important result of the study attracting attention is that all stations located in the KCBA showed much pronounced changes in warming for July with an increase of more than 1.0 °C between 1993 and 2005 compared to 1970 and 1992. At this point, it can be mentioned that dry summer season has extremely affected the region for the last two decades. Additionally, the analysis of the meteorological data for 1993–2005 period showed a simultaneous decrease in mean precipitation between 1.2 and 11.6 mm.

On the other hand, groundwater of Konya Closed Basin has been exhausted because of the climate changes and agricultural watering and planning mistakes experienced in the basin. In addition to this, the contamination due to merging event of the aquifers with different groundwater characteristics and the formations of arid and ponor regions due to sudden level changes still continue.

The use of satellite imagery and other data sources manipulated and integrated in a GIS environment provides an essential and valuable information base. Additionally, this study shows that satellite imagery provides an essential tool in determining drought impact due to the operational acquisition of satellite imagery.

References

1. Kantarcı MD (2006) Effects of climate change and aridity on Ergene river basin water productivity. In: International conference on climate change and middle East: past, present and future. Istanbul, Turkey, 20–23 Nov 2006, p 246–258
2. Tokgöz N, Kantarcı MD (2001) The effect of SO2 pollution on forest in Turkey originated from coal consumption at East-Central-South European Countries. J Environ Prot Ecol 2:402–406
3. Dube O (2001) Remote sensing, climate change and land-use impacts in semi-aridlands of Southern Africa. In: Geoscience and remote sensing symposium, 2001. IGARSS apos;01. IEEE 2001 International vol 6, pp 2686–2688
4. Latifovic R, Pouliot D (2006) Analysis of climate change impacts on lake ice phenology in Canada using the historical satellite data record. Remote Sens Environ 106:492–507
5. Nagai S, Ichii K, Morimoto H (2007) Interannual variations in vegetation activities and climate variability caused by ENSO in tropical rainforests. Int J Remote Sens 28:1285–1297
6. Piwowar JM, Ledrew EF (2002) ARMA time series modelling of remote sensing imagery: a new approach for climate change studies. Int J Remote Sens 23:5225–5248
7. Vianna ML, Cabral AP, Gherardi DFM (1993) TM-Landsat imagery applied to the study of the impact of global climate change on a tropical coastal environment during the last deglaciation. Int J Remote Sens 14:2971–2983

8. http://www.uwpcc.washington.edu. Accessed 30 May 2012
9. Pozdnyakov D, Korosov A, Grassl H, Pettersson L (2005) An advanced algorithm for operational retrieval of water quality from satellite data in the visible. Int J Remote Sens 26:2669–2687
10. Bausmith JM, Leinhardth G (1997) Middle school students' map construction: understanding complex spatial displays. J Geogr 97:93–107
11. Goodchild MF (2001) Metrics of scale in remote sensing and GIS. Int J Appl Earth Obs Geoinf 3:114–120
12. Jaiswal RK, Mukherjee S, Raju KD, Saxena R (2002) Forest fire risk zone mapping from satellite imagery and GIS. Int J Appl Earth Obs Geoinf 4:1–10
13. Doğdu MS, Toklu MM, Sağnak C (2007) Konya Kapalı Havzasında Yağış ve Yeraltısuyu Seviye Değerlerinin İrdelenmesi. I. Türkiye İklim Değişikliği Kongresi. pp 394–401
14. Durduran SS (2010) Coastline change assessment on water reservoirs located in the Konya Basin Area, Turkey, using multitemporal landsat imagery. Environ Monit Assess 164:453–461
15. Almeida-Filho R, Shimabukuro YE (2002) Digital processing of a Landsat-TM time series for mapping and monitoring degraded areas caused by independent gold miners, Roraima State, Brazilian. Remote Sens Environ 79:42–50
16. Metternicht GI, Zinck JA (1998) Evaluating the information content of JERS-1 SAR and Landsat TM data for discrimination of soil erosion features. Int J Photogramm Remote Sens 53:143–153
17. Du Y, Cihlar J, Beaubien J, Latifovic R (2001) Radiometric normalization, compositing, and quality control for satellite high resolution image mosaics over large areas. IEEE Trans Geosci Remote Sens 39:623–634
18. Kim K, Jezek KC, Liu H (2007) Orthorectified image mosaic of Antarctica from 1963 Argon satellite photography: image processing and glaciological applications. Int J Remote Sens 28:5357–5373
19. Kantarcı MD (2006) Effects of climate change and aridity on Ergene River basin water productivity. In: International conference on climate change and middle East: past, present and future. Istanbul, Turkey, 20–23 Nov 2006, pp 246–258

Chapter 10
Trend Analysis of Rainfall in North Cyprus

Rahme Seyhun and Bertuğ Akıntuğ

Abstract Cyprus, as the third largest island in the Mediterranean Sea, is located at the South of Turkey and the West of Syria and Lebanon. With a semiarid climate, rainfall is the only source of water in the island. Therefore, changes in rainfall regime directly affect the water resource management and ecosystem in the island. In order to improve water management strategies, it is vital to investigate the changes in the rainfall pattern. In this study, a nonparametric Mann–Kendall rank correlation method is employed to identify the existence of a linear trend in annual and monthly rainfall series. After application of homogeneity test and filling in missing data, this method is applied to the observed rainfall data from 20 rain-gauge stations that are located in the northern part of the island for the period of 1978–2009. The results show that there is no significant trend in the annual rainfall; however, upward trends in September rainfall and downward trends in March rainfall have been observed in most of the stations. This indicates that there are no significant changes in annual total rainfall; however, there is a shift in monthly rainfall regime.

Keywords Rainfall trend analysis • Mann–Kendall test • North Cyprus

Nomenclature

a	Most probable time point of change or the last time point of the sub-series with mean $\overline{z_1}$
d	Distance from the location of gauged station to the ungauged station
H_o	Null hypotheses
H_1	Alternative hypotheses

R. Seyhun • B. Akıntuğ (✉)
Middle East Technical University, Northern Cyprus Campus,
Kalkanlı, Güzelyurt, Mersin 10, Turkey
e-mail: rahme.seyhun@gmail.com; bertug@metu.edu.tr

k	Total number of reference stations
n	Length of the data set
N	Number of surrounding stations
P_x	Estimate of rainfall for the ungauged station
p	Rainfall values of rain gauges used for estimation
Q_i	Difference and ratio between the candidate and reference series at time step i
Q	Mean values of Q_i series
S	Mann–Kendall test statistic
T	Standard normal homogeneity test statistic
t	Number of ties of extent
V_j	Square of the correlation coefficient between the candidate and a reference station
X_{ji}	Reference series (the *jth* of a total of k)
$\overline{X_j}$	Mean values of the X series
x_i	Data values at times i
x_j	Data values at times j
Y_i	Candidate series at year i (or other time unit)
$\overline{Y}$	Mean values of Y series
Z_i	Standardized series with zero mean and unit standard deviation
$\overline{z_1}$	Averages of the Z_i sequences before the shift
$\overline{z_2}$	Averages of the Z_i sequences after the shift
Z	Standardized test statistic

Greek Symbols

Σ	Summation function
μ_1	Theoretical mean level of standardized differences (or ratios) before a possible shift or trend
μ_2	Theoretical mean level of standardized differences (or ratios) after a possible shift or trend
σ_Q	Standard deviation of the Q_i series

Acronyms

SNHT	Standard normal homogeneity test
$Var_{(s)}$	Variance of s

10.1   Introduction

The effects of climate change, which is formed as a result of the increased greenhouse gases in the atmosphere over the twentieth century, have been analyzed by many researchers. As several extreme events in recent years have caused large losses of life and property, the alarm over the possibility that these events were due to climate change is increased [1]. It has been documented that increased greenhouse gas concentration in the atmosphere has resulted in the increase of the global average surface temperature by about 0.74 °C from 1906 to 2005 [2]. It has further been documented that significantly increased precipitation has been observed in eastern parts of North and South America, northern Europe, and northern and central Asia. There is a possibility that increased atmospheric temperature is related with an increase in heavy precipitation due to an increase in atmospheric water vapor and the warmer air [2]. The effects of climate change have been analyzed in many studies with focusing on precipitation and surface air temperature [3–9].

The main objective of this study is to identify whether there is an evidence of significant trends in annual, seasonal, and monthly total precipitation over Northern Cyprus. The chapter is organized as follows. Selected previous trend analysis studies in meteorological and hydrological variables are given in the next section. The explanation of meteorological data is given in Sect. 3. Following this section the methodology is presented in Sect. 4 and the results and the discussion of results are given in Sect. 5. Finally the conclusions are given in the last section.

10.2   Background: Previous Trend Analysis Studies

The number of trend analysis of meteorological and hydrological variables over the Mediterranean region is available in the literature. For example, Feidas et al. [3] studied trends in the annual and seasonal surface air temperature for 20 stations in Greece from 1955 to 2001, and for satellite data from 1980 to 2001. It is found that there are no significant trends for annual values. However, results for satellite data indicated that there is a remarkable warming trend in mean annual, winter, and summer in Greece. Kostopoulou and Jones [4] analyzed trends over the eastern Mediterranean region for precipitation- and temperature-related climate extremes. The study period is from 1958 to 2000. It was found that there were significant warming trends during summer in temperature indices. Significant positive precipitation trends were also seen for central Mediterranean region, while eastern half of the study region shows negative trends in all precipitation indices. Alpert et al. [10] examined 265 stations for 6 different daily rainfall categories in the Mediterranean region. Spain, Cyprus, Italy, and Israel were examined in the region for the period of 1951–1995. It was indicated that there is a paradoxical increase in the extreme daily rainfall, although there is a

decrease in the total rainfall. The study of Yosef et al. [11] examined 6 daily rainfall categories for 32 stations across Israel from January 1950 to April 2003. Some of the stations show a significant increase in the heavy to torrential daily rainfall. On the other hand, any significant change in the annual rainfall is not seen.

There are also many studies in Turkey about the trends in hydroclimatologic variables. For example, Kadıoğlu [12] studied trends in the surface air temperature for 18 stations across Turkey. It is indicated that there was an increasing trend in mean annual temperatures over the period of 1939–1989 but a decreasing trend from 1955 to 1989. However, it is also indicated that these trends were not statistically significant. Kahya and Kalaycı [13] analyzed trends in monthly streamflows over Turkey from 1964 to 1994. According to their results the river basins located in western Turkey demonstrated downward trends for streamflow variable, while there were no significant trends in the basins located in eastern Turkey. In another study, Partal and Kahya [6] performed trend tests for 13 hydrologic variables (annual mean precipitation and monthly total precipitation) across Turkey for a period covering 1929–1993. It is found that there are strong downward trends in annual mean, January, February, and September precipitation. The other variables show both decreasing and increasing trends, and most of the decreasing trends are in western and southern part of Turkey. According to the studies of Kahya and Kalaycı [13], and Partal and Kahya [6], it can be said that the reason for decreasing streamflow in western Turkey is most likely due to the decreasing precipitation in the same region.

The trends in hydroclimatologic variables are also analyzed in the other parts of the world. For example, Luterbacher et al. [5] studied the trends, variability, and extremes of the seasonal and annual temperature since 1500 for Europe. It is found that there is a warming trend in the climate of Europe in the late twentieth and early twenty-first century over the past 500 years. There is a 0.5 °C increase in the winter average temperatures for the period of 1500–1900 compared to the twentieth century. In addition to these findings, it is also indicated that the coldest winter and hottest summer were in 1708/1709 and 2003, respectively. Burn and Elnur [14] stated the similarities in trends and patterns in the hydrological and meteorological variables at selected locations in Canada. They studied 18 hydrological variables for 248 Canadian catchments for a period of 1940–1997. The study implies that there is a relationship between the hydrological and meteorological variables. In the study of Vincent et al. [15], scientists from eight South American countries undertook a study with daily climatological data from their region. The study is about the examination of the trends in the indices of daily temperature extremes from 1960 to 2000. Although it was found that there are no significant changes in the indices of daily maximum temperature, there are significant trends in the indices of daily minimum temperature. Significant increasing and decreasing trends are observed in the percentage of warm nights and cold nights, respectively, at many stations. Tabari et al. [16] examined the trends of the annual maximum, minimum, and mean air temperature and

precipitation time series from 1966 to 2005 in the west, south, and southwest of Iran. The results indicated that there are warming trends in annual maximum, minimum, and mean air temperature. The results for precipitation series show various patterns (increasing and decreasing trends).

10.3   Meteorological Data

The meteorological data records that are used in this study consist of 20 precipitation stations across North Cyprus. It is assumed that these selected stations reflect the regional hydroclimatic conditions of North Cyprus. The distribution of selected meteorological stations is given in Fig. 10.1. In this study, monthly, seasonal, and annual total rainfall data that are obtained from the daily total rainfall observations are analyzed. Except two stations, all 18 stations have continuous 33 years of data ranging from 1978 to 2009. The missing data of these two stations are filled in by using the available data of neighboring stations corresponding to the same time period.

10.4   Methodology

There might be lack of continuous data due to natural hazards (floods, hurricanes, etc.), human-related problems (mistake in handling data, etc.), and others [17]. The gaps in the data should be filled in using suitable methods. Although there are different methods to fill in missing data gaps, inverse distance method is employed in this study.

Fig. 10.1 Precipitation stations across North Cyprus

In addition, climatological records are often limited by degree of inhomogeneity of the data. The reason of this is logistic problems, such as station relocations and equipment drift. In addition, changes in measuring techniques and changes in the surroundings of a station, such as urbanization, may also cause inhomogeneity in the recorded data [18, 19]. Therefore, the first stage of the trend test studies should be the determination of the non-homogeneities in the data to develop homogenized records. For this purpose, standard normal homogeneity test (SNHT) is employed in this study.

With increasing attention to climate change, trend tests of climatologic variables have become popular during the final quarter of the last century in environmental sciences. Among various trend analysis techniques, a nonparametric Mann–Kendall trend test is employed in this study. This method was commonly used in the trend test studies in literature [6, 12–14, 20, 21].

The brief description of these three methods, namely, inverse distance method, SNHT, and Mann–Kendall Trend Test, is presented below.

10.4.1 Inverse Distance Method

Inverse distance method is selected in this study to fill in the missing data because of its simplicity and applicability to North Cyprus. In this method, weights for each sample are inversely proportionate to its distance from the point being estimated [22]. Given the observed rainfall values of nearby rain gauges and the distance from the gauged stations to the ungauged station, the estimate of missing rainfall at ungauged station is possible by Eq. (10.1) as

$$P_x = \frac{\sum\limits_{i=1}^{N} \frac{1}{d_i^2} p_i}{\sum\limits_{i=1}^{N} \frac{1}{d_i^2}} \tag{10.1}$$

where P_x is the estimate of rainfall for the ungauged station, p_i is the rainfall values of rain gauges used for estimation, d_i is the distance from the location of gauged station to the ungauged station, and N is the number of surrounding stations.

10.4.2 Standard Normal Homogeneity Test

Several methods have been developed for homogenization. Among those tests, the SNHT is developed by Alexandersson [23], and applied to precipitation data set from southwestern Sweden. While the test is examining inhomogeneities in the form of abrupt shifts in the mean value of the observations, it is then modified to

have the ability to test inhomogeneities in the form of linear time trends [24]. SNHT is used commonly in the past studies, such as Wijngaard et al. [19] and Tuomenvirta [25].

The first step of the test is to develop and document nearly true critical values of the SNHT statistics. The aim of this is to make correct conclusion with simplified usage of the test in practice [18]. Therefore, large sets of random normal numbers are used to simulate critical values. According to this test, $Y_i (i = 1, \ldots, n)$ denotes a candidate series at year i (or other time unit). X_j denotes one of the reference series (the *jth* of a total of *k*), which are developed from a group of surroundings. In addition to these series, Q_i $(i = 1, \ldots, n)$ is developed to denote the difference and ratio between the candidate and reference series at time step *i*. The ratio and difference terms are formed as in Eq. (10.2) and Eq. (10.3), respectively:

$$Q_i = \frac{Y_i}{\left[\sum_{j=1}^{k} V_j X_{ji} \overline{Y}/\overline{X_j}\right] \Big/ \sum_{j=1}^{k} V_j} \qquad (10.2)$$

$$Q_i = Y_i - \left\{\sum_{j=1}^{k} V_j \left[X_{ji} - \overline{X_j} + \overline{Y}\right] \Big/ \sum_{j=1}^{k} V_j\right\} \qquad (10.3)$$

where V_j denotes the square of the correlation coefficient between the candidate and a reference station. Bar denotes mean values, which is for X_j and Y series.

Standardized series are essential in the SNHT. Thus, standardization (Eq. (10.4)) of the Q_i series is performed to obtain a series Z_i (with zero mean and unit standard deviation):

$$Z_i = \left(Q_i - \overline{Q}\right)/\sigma_Q \qquad (10.4)$$

where $\overline{Q}$ and σ_Q are the mean and standard deviation of the Q_i series, respectively.

The null and alternative hypotheses which are used to test whether there is a single shift in the mean level of the candidate series are expressed in Eq. (10.5):

$$H_o : Z_i \tilde{\ } N(0,1) \quad \text{for} \quad i = 1, \ldots \ldots, n$$

$$H_1 : \begin{cases} Z_i \tilde{\ } N(\mu_1, 1) \\ Z_i \tilde{\ } N(\mu_2, 1) \end{cases} \quad \text{for} \quad \begin{array}{l} i = 1, \ldots .. a \\ i = a+1, \ldots .., n \end{array} \qquad (10.5)$$

Alexandersson and Moberg [24] generated a test statistic based on the principle of likelihood ratio to test the validity of H_1 against H_o. This test statistic is given in Eq. (10.6):

$$T = \max\left\{a(\overline{z_1})^2 + (n-a)(\overline{z_2})^2\right\}, \quad 1 \le a \le n-1 \qquad (10.6)$$

where $\overline{z_1}$ and $\overline{z_2}$ are the averages of the Z_i sequences before and after the shift. The value of a corresponding to T is the most probable time point of change or the last time point of the sub-series with mean $\overline{z_1}$. If T is above the critical value of a certain critical level (e.g., 95 %), then the null hypothesis of homogeneity can be rejected at the corresponding significance level (i.e., 5 %) [18].

10.4.3 Mann–Kendall Trend Test

The Mann–Kendall test is widely used to test for randomness against trend in hydrological and climatological time series [13]. It has two parameters which are essential to detect trends. First of these parameters is significance level that indicates the trend's strength, and the second is the slope magnitude which indicates the direction and magnitude of the trend. First step of the test is the calculation of the Mann–Kendall test statistic, S. This value is used to determine whether there is a trend or not, and also to determine the direction of the trends according to the sign of the S value [26]. If there is a trend, the significance of it should be examined. Because of that, standardized test statistic, Z, is computed with using variance and S values, which is then used in two-sided test [20]. According to the significance level, Z values give information about the null hypothesis, H_o, and alternative hypothesis, H_1. The null hypothesis, H_o, indicates that there is no trend, while alternative hypothesis, H_1, indicates that there is a trend in the analyzed data set. Each step of the Mann–Kendall Test is presented below from Eqs. (10.7) to (10.10).

Mann–Kendall test statistic, S, is calculated using Eqs. (10.7) and (10.8):

$$S = \sum_{i=1}^{n-1} \sum_{j=i-1}^{n} Sgn(x_j - x_i) \qquad (10.7)$$

where x are data values at times i and j, and n is the length of the data set.

$$Sgn(\theta) = \begin{cases} +1 & \text{if} \quad \theta > 0 \\ 0 & \text{if} \quad \theta = 0 \\ -1 & \text{if} \quad \theta < 0 \end{cases} \qquad (10.8)$$

A positive value of S shows an upward trend, while negative value indicates a downward trend.

The test statistic S, which is approximately normally distributed, has mean zero and a variance which is calculated by

$$Var(s) = \frac{\left[n(n-1)(2n+5) - \sum_{t} t(t-1)(2t+5) \right]}{18} \qquad (10.9)$$

where t denotes the number of ties of extent. For the sample size n larger than 10, the standardized test statistic Z is computed as

$$Z = \begin{cases} \frac{S-1}{\sqrt{\text{var}(S)}} & \text{if} & S > 0 \\ 0 & \text{if} & S = 0 \\ \frac{S+1}{\sqrt{\text{var}(S)}} & \text{if} & S < 0 \end{cases} \qquad (10.10)$$

Following this, two-sided test for trend is applied using the Z values, and if $|Z| \le Z_{\alpha/2}$, H_o should thus be accepted. This means that there is no trend.

10.5   Results and Discussion

First of all, filling in missing rainfall data is performed. Three years' (1995, 1996, and 1997) missing monthly values of two gauge stations, namely, Akdeniz and Yeşilırmak, are filled in using inverse distance method. The name of the reference stations and their distance to stations with missing data are given in Table 10.1.

Mann–Kendall trend test method assumes that the data is homogeneous. In order to check the homogeneity of observed rainfall data, the SNHT is applied to the records of each precipitation stations. While the test statistics are calculated, the values are compared with critical levels at 90, 95, and 97.5 % confidence intervals. The results show that the rainfall time series that are selected to be used in this study are all homogenous.

Mann–Kendall test is used to identify trends in total annual and monthly time series of all 20 stations for the period of 1978–2009 at the 10 % significance level. Mann–Kendall trend test results of annual and monthly total rainfall of all stations are given in Table 10.2. Although the results show that there is no trend in the annual rainfall time series in all stations, upward trends in September and downward trends in March rainfall have been observed in most of the stations. The distribution of September and March trend analysis results are given in Figs. 10.2 and 10.3. During summer months, Cyprus takes very low or no rainfall. The average July and August rainfall in North Cyprus is 1.5 and 1.8 mm, respectively. The rainfall season usually starts in September. According to trend test results, one can say that there is an
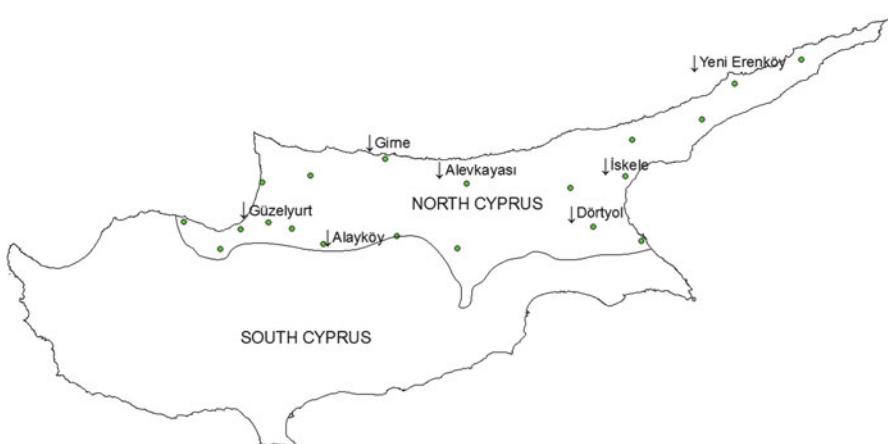
Table 10.1 Missing data stations, reference stations, and distance between these stations

Missing data station	Reference stations	Distance to missing data station (km)
Yeşilırmak	Lefke	12.1
	Yeşilyurt	13.3
	Gaziveren	16.1
Akdeniz	Çamlıbel	10.3
	Kozanköy	16.1
	Güzelyurt	12.0

Table 10.2 The significant monthly and annual precipitation trends at the 10 % significance level

Station	Jan.	Feb.	Mar.	Apr.	May	Jun.	Jul.	Aug.	Sep.	Oct.	Nov.	Dec.	Ann.
North Coast and Girne Mountains Region													
Çamlibel	—	—	—	—	—	—	—	—	↑	—	↑	—	—
Akdeniz	—	—	—	—	—	—	—	—	—	—	—	—	—
Girne	—	—	↓	—	—	—	—	—	↑	—	—	—	—
Alevkayası	—	—	↓	—	—	—	↑	↑	↑	—	—	—	—
Kantara	—	—	—	—	—	—	—	—	—	—	—	—	—
West Mesaoria Plain Region													
Zümrütköy	—	—	—	—	—	—	—	—	↑	—	—	—	—
Lefke	—	—	—	—	—	—	—	—	—	—	—	—	—
Güzelyurt	—	—	↓	—	—	—	—	—	↑	—	—	—	—
Yeşilırmak	—	—	—	—	—	—	—	—	—	—	—	—	—
Gaziveren	—	—	—	—	—	—	—	—	↑	—	—	—	—
Middle Mesaoria Plain Region													
Alayköy	—	—	↓	—	—	—	—	—	↑	—	—	—	—
Lefkoşa	—	—	—	—	↑	—	↑	—	↑	—	—	—	—
Ercan	—	—	—	—	—	—	—	—	↑	—	—	—	—
East Mesaoria Plain Region													
Geçitkale	—	—	—	—	—	—	—	—	↑	—	—	—	—
Dörtyol	—	—	↓	—	—	—	—	—	↑	—	—	—	—
East Coast Region													
Mağusa	—	—	—	↑	—	—	—	—	↑	—	—	—	—
İskele	—	—	↓	—	—	—	—	—	↑	—	—	—	—
Karpass Peninsula Region													
Mehmetçik	—	—	—	—	—	—	—	—	—	—	—	—	—
Yenierenköy	—	—	↓	—	—	—	—	—	—	—	—	—	—
Dipkarpaz	—	—	—	—	—	—	—	—	—	—	—	—	—

Downward, upward, and no trends were marked by "↓," "↑," and "—," respectively

Fig. 10.2 Spatial distribution of decreasing trend in March rainfall

Fig. 10.3 Spatial distribution of increasing trend in September rainfall

increase in September rainfall while on the other hand a decrease in March rainfall across the north of the island. In addition to the trends in September and March, increasing trends are also obtained in April (Mağusa), May (Lefkoşa), July (Lefkoşa and Alevkayası), August (Alevkayası), and November (Çamlıbel) in some of the stations. On the other hand, half of the stations (Zümrütköy, Gaziveren, Lefkoşa, Ercan, Geçitkale, and Mağusa) show increasing trends in September but no trends in March.

In addition to the trend studies for annual and monthly rainfall data, seasonal total rainfall data are also studied. The results show a few trends for some of the stations. The decreasing trends are seen in spring rainfall at Girne and Yenierenköy stations, while two increasing trends in fall rainfall at Çamlıbel and Lefke and one in summer at Alevkayası station are indicated. The seasonal trend analysis results are given in Table 10.3.

10.6 Conclusions

In this study, trend analysis of monthly, seasonal, and annual total precipitation at 20 stations in North Cyprus has been carried out using Mann–Kendall nonparametric test. It has been observed in most of the stations that there is no trend in the annual total rainfall; however, upward trends in September rainfall and downward trends in March rainfall in most of the stations are observed. In other words, after long summer months with no or very low rainfall, there is an increasing trend in September rainfall. On the other hand, there is a decreasing trend in March rainfalls. It can be said that there is an evidence of a shift in monthly rainfall regimes in North Cyprus.

Table 10.3 The significant
seasonal precipitation trends
at the 10 % significance level

Geographical region/station	Spring	Summer	Fall	Winter
North Coast and Kyrenia Mountains Region				
Çamlibel	—	—	↑	—
Akdeniz	—	—	—	—
Girne	↓	—	—	—
Alevkayası	—	↑	—	—
Kantara	—	—	—	—
West Mesaoria Plain Region				
Zümrütköy	—	—	—	—
Lefke	—	—	↑	—
Güzelyurt	—	—	—	—
Yeşilırmak	—	—	—	—
Gaziveren	—	—	—	—
Middle Mesaoria Plain Region				
Alayköy	—	—	—	—
Lefkoşa	—	—	—	—
Ercan	—	—	—	—
East Mesaoria Plain Region				
Geçitkale	—	—	—	—
Dörtyol	—	—	—	—
East Coast Region				
Mağusa	—	—	—	—
İskele	—	—	—	—
Karpass Peninsula Region				
Mehmetçik	—	—	—	—
Yenierenköy	↓	—	—	—
Dipkarpaz	—	—	—	—

Downward, upward, and no trends were marked by "↓," "↑," and
"—," respectively

The trend results obtained in this study are not sufficient to approve climate
change in North Cyprus. However, this study will contribute to the researches about
the effects of climate change in the Mediterranean region.

References

1. Easterling DR, Meehl GA, Parmesan C, Changnon SA, Karl TR, Mearns LO (2000) Climate
   extremes: observations, modeling, and impacts. Science 289:2068–2074
2. Intergovernmental Panel on Climate Change (2007) The physical science basis, summary for
   policymakers. Cambridge University Press, New York, Cambridge
3. Feidas H, Makrogiannis T, Bora-Senta E (2004) Trend analysis of air temperature time series
   in Greece and their relationship with circulation using surface and satellite data: 1955–2001.
   Theor Appl Climatol 79:185–208
4. Kostopoulou E, Jones PD (2005) Assessment of climate extremes in the Eastern Mediterra-
   nean. Meteorol Atmos Phys 89:69–85

5. Luterbacher J, Dietrich D, Xoplaki E, Grosjen M, Wanner H (2004) European seasonal and annual temperature variability, trends, and extremes since 1500. Science 303:1499–1503

6. Partal T, Kahya E (2006) Trend analysis in Turkish precipitation data. Hydrol Process 20:2011–2026

7. Kysely J (2009) Trends in heavy precipitation in the Czech Republic over 1951–2005. Int J Climatol 29:1745–1758

8. Clark JS, Yiridoe EK, Burns ND, Astatkie T (2000) Regional climate change: trend analysis of temperature and precipitation series at selected Canadian sites. Can J Agric Econ 48:27–38

9. Giannakopoulos C, Hadjinicolaou P, Kostopoulou E, Varotsos KV, Zerefos C (2010) Precipitation and temperature regime over Cyprus as a result of global climate change. Adv Geosci 23:17–24

10. Alpert P, Ben-gai T, Baharad A (2002) The paradoxical increase of Mediterranean extreme daily rainfall in spite of decrease in total values. Geophys Res Lett 29:31-1–31-4

11. Yosef Y, Saaroni H, Alpert P (2009) Trends in daily rainfall intensity over Israel 1950/1–2003/4. Open Atmos Sci J 3:196–203

12. Kadıoglu M (1997) Trends in surface air temperature data over Turkey. Int J Climatol 17:511–520

13. Kahya E, Kalaycı S (2004) Trend analysis of stream flow in Turley. J Hydrol 289:128–144

14. Burn DH, Elnur HMA (2002) Detection of hydrologic trends and variability. J Hydrol 225:107–122

15. Vincent LA, Peterson TC, Barros VR, Marino MB, Rusticucci M, Carrasco G, Ramirez E, Alves LM, Ambrizzi T, Berlato MA, Grimm AM, Marengo JA, Molion L, Moncunill DF, Rebello E, Anunciaçao YMT, Quintana J, Santos JL, Baez J, Coronel G, Garcia J, Trebejo I, Bidegain M, Haylock MR, Karoly D (2005) Observed trends in indices of daily temperature extremes in South America 1960–2000. Am Meteorol Soc 18:5011–5023

16. Tabari H, Somee BS, Zadeh MR (2011) Testing for long-term trends in climatic variables in Iran. Atmos Res 100:132–140

17. Elshorbagy AA (2000) Group-based estimation of missing hydrological data: Approach and general methodology. Hydrol Sci J 45(6):849

18. Khaliq MN, Quarda TBMJ (2007) On the critical values of the standard normal homogeneity test (SNHT). Int J Climatol 27:681–687

19. Wijngaard JB, Klein Tank AMG, Können GP (2003) Homogeneity of 20th century European daily temperature and precipitation series. Int J Climatol 23:679–692

20. Douglas EM, Vogel RM, Kroll CN (2000) Trends in floods and low flows in the United States: impacts of spatial correlation. J Hydrol 240:90–105

21. Cannarozzo M, Noto LV, Viola F (2006) Spatial distribution of rainfall trends in Sicily (1921–2000). Phys Chem Earth 31:1201–1211

22. Silva RPD, Dayawansa NDK, Ratnasiri MD (2007) A comparison of methods used in estimating missing rainfall data. J Agric Sci 3(2):101–108

23. Alexandersson H (1986) A homogeneity test applied to precipitation data. J Climatol 6:661–675

24. Alexandersson H, Moberg A (1997) Homogenization of Swedish temperature data. Part I. Homogenization test for linear trends. Int J Climatol 17:25–34

25. Tuomenvirta H (2002) Homogeneity testing and adjustment of climatic time series in Finland. Geophysical 38(1–2):15–41

26. Hirsch RM, Slack JR (1984) A nonparametric trend test for seasonal data with serial dependence. Water Resour Res 20(6):727–732

Chapter 11
Forecasting Tropical Storms in the Eastern Region of the United Arab Emirates: Lessons Learnt from Gonu

Saif A. Ahmed, Mohammad bin Jarsh, Saoud Al-Abdooli, Mohamed K. Al-Radhi, and Abdulla Galadari

Abstract In 2007, a strong tropical storm in the Arabian Sea, Cyclone Gonu, caused major damages when it made landfall on the coast of the Sultanate of Oman. The Category 5 tropical storm moved north along the coast in the Gulf of Oman and reached the Eastern Coastline of the United Arab Emirates (UAE), causing loss of life and damage to property and infrastructure. It is therefore imperative to understand the probability of such storms hitting the region in the future, to take necessary measures and preparations to reduce the impact. This study is important for understanding the feasibility of developing infrastructure to withstand tropical storms, managing the coast, and also evaluating risks of the damages. This study looks at meteorological statistical data from past decades in the region to understand the probability of strong tropical storms causing damage in the Eastern Coast of the UAE. It uses statistical analysis to predict tropical storms that are strong enough to reach the Eastern Coast of the UAE, which is situated along the Gulf of Oman, to the north of the Arabian Sea, which is not usually affected by tropical storms coming from the Indian Ocean. The study looks into historical meteorological data of the region, from temperatures, wind speed, and direction, and then compares them during the time Cyclone Gonu hit the region.

Keywords Climate change • Storm forecasting • Gonu • Storm surges • Tropical storms • The United Arab Emirates • Peninsula • Probability • Cyclone • Phytoplankton • Bloom • Oceanographic

S.A. Ahmed (✉) • M. bin Jarsh • S. Al-Abdooli • M.K. Al-Radhi • A. Galadari
Higher Colleges of Technology, Dubai, UAE
e-mail: saif14413@gmail.com; mohammad.binjarsh@hotmail.com; abdooli1112@hotmail.com; mohdnet88@hotmail.com; aigaladari@gmail.com

11.1   Introduction

In June 2007, Gonu developed as a severe tropical storm in the Indian Ocean. It had been described as the most powerful storm ever recorded in the Arabian Sea [1, 2]. It had a great socioeconomic impact when it made landfall along the coast of Oman and to a much lesser extent in the eastern coast of the United Arab Emirates (UAE) and Iran. Since the region has not been affected by a similar storm in the past, the region was not ready to alleviate the impact of the storm. Nonetheless, it is important to forecast the probability of similar storms in the future to allow policymakers in the region to be equipped, if necessary, with the means to curtail the impact of the storm.

The Indian Ocean experiences tropical storms prior to and after the monsoon season. The monsoon season typically starts in June and ends by September. The range of tropical storm seasons in the Indian Ocean is in May, as well as October and early November [3]. Other storms may develop during June and September, when the monsoon season starts and ends [4]. Nonetheless, it has been statistically shown that the frequency of tropical storms in the Bay of Bengal surpasses four times that in the Arabian Sea [5]. Although severe cyclones making landfall on the Arabian Peninsula are very rare, they have been historically reported [6].

It is important for people to understand and learn how the world works from a natural point of view in which sudden changes on earth can affect its behavior. Natural disasters are dangerous due to the fact it is unpredictable causing damages and fatalities, as people and governments are unprepared. Learning from past disasters is a step closer to understanding how to avoid them or at least respond to them.

In June 2007, when cyclone Gonu made landfall in the Sultanate of Oman, it has made devastating loss of life and destruction of infrastructure. As the storm moved northwards along the Gulf of Oman, its intensity was reduced, but nonetheless, it has also caused loss of life and destruction in the eastern coast of the UAE, typically in the areas of Kalba and Fujairah, until the storm dissipated as it crossed through Iran. Since it was not typical for the area to experience severe tropical storms that make landfall on the Arabian Peninsula, emergency response and preparations were insufficient to deal with the strength of a cyclone such as Gonu.

This study focuses mainly on the eastern coast of the UAE, and not Oman, to forecast the probable frequency of such severe storms to make landfall in the area. It uses statistical climatic data of the region to identify the difference in the climate during Gonu's landfall in the area compared to other years during the same period. This is important to consider if it would be feasible for the UAE to invest in coastal developments to reduce the impact of similar storms, such as building levees or having warning systems in place for climatic or oceanographic disturbances in the area.

11.2   Background

There have been few tropical storms that are categorized as cyclones to have hit the Arabian Peninsula. Most tropical storms make landfall in the Bay of Bengal, but few move northwesterly to make landfall on the Arabian Peninsula. There have been several observations of cyclones that make landfall on the Arabian Peninsula and all of them have been statistically seen to be recorded during pre-monsoon and post-monsoon seasons [7]. It has been recorded that Oman had been struck by tropical storms of similar strength to Gonu on June 4 and 5, 1890, and May 2, 1895 [8]. The storm of 1890 seems to have made landfall further north of the Arabian Sea towards the Gulf of Oman (Sea of Oman). However, this data is based on historical documents that may not be of great reliability, as the reports on the region were very limited at the time. The historical storms have occurred, but the strength of such storms could be questioned. Although they have been reported to have damaged the area, it is difficult to categorize the strength of these storms.

Eight intense cyclones have been recorded to strike the eastern region of the Arabian Peninsula in the past 60 years, as can be seen from Table 11.1. However, only Gonu made landfall in the east coast of the UAE. It might have been possible that the storm that hit Oman in 1890 might have also affected the east coast of the UAE based on logical deductions of the track record of the storm from historical documents. Nonetheless, the reliability of those records and the exact coordinates where the storm had made landfall remain questionable, but it is still reasonable to conclude that the effects of the 1890 storm would have reached the east coast of the UAE.

If from the past 60 years, only one cyclone made landfall in the east coast of the UAE, and possibly the storm of 1890 might have also, then it may be concluded that the frequency of such storms to occur may be once in every 60 years. Therefore, the probability of a cyclone to hit the east coast of the UAE is less than 2 % every year.

Table 11.1 Severe cyclones making landfall on the Arabian Peninsula since 1959

Cyclone	History
Cyclones crossed Salalah region in Oman	May 1959, May 1963, and November 1966
A cyclone crossed Masirah Island in Oman with high wind speeds reaching 120 knots with 430 mm rainfall	June 1977
A cyclone hit Ras Madraka (south of Masirah Island) in Oman resulting in a 200 mm rainfall	June 1996
A storm affected Salalah in Oman with 58 mm of rainfall in the city and 150 mm in the mountains	June 2002
Gonu, affecting Oman, the UAE, Pakistan, and Iran	June 2007
Phet, affecting Masirah and Ras al-Hadd, in Oman	June 2010

11.3   Gonu

Cyclone Gonu is the biggest tropical cyclone that hit the Arabian Sea. It is impera-
tive to learn from Gonu and try to prepare for the worst if a cyclone as strong ever
hit the region again. To do so, gathering information about the cyclone, how it
originated, and the climatic conditions that moved the cyclone towards the coast of
Oman is important to forecast future storms.

Gonu started as a small storm categorized as level one and then it got stronger as
it moved towards Oman reaching a Category 5 storm with wind speeds exceeding
240 kph. It then weakened as it lost moisture moving towards land.

Gonu was detected as a low-category thunderstorm in south of Mumbai in India.
Northwesterly winds caught up with the storm along with low pressure coming
from Pakistan. Gonu started moving north and northeast, and later turning on a
westward track. Due to the low amount of vertical wind shear the storm got stronger
until it reached southeast of Oman near Masirah Island with a wind speed of
315 kph. The storm maintained its strength for about 6 h. As it moved closer to
the Arabian Peninsula, the dry air and cool waters reduced vapor, weakening the
storm as it made landfall in Oman.

As Gonu made landfall in Oman, it caused many fatalities and destroyed many
facilities along the coastline. In the cities, such as Muscat, the wind speeds reached
100 kph leaving residents without power. Due to the nature of the area, which is
mountainous, the heavy rainfall caused the valleys (*wadis*) to be flooded,
contributing as the major cause of the destruction. Parts of Oman have reported
over 150 mm of rain. As Gonu travelled further north in the Gulf of Oman (Sea of
Oman), it initiated problems in the towns of Kalba and Fujairah along the east coast
of the UAE, causing damages due to high waves and heavy rainfall.

Gonu caused about $4 billion of damages and at least 49 deaths in the Sultanate
of Oman while causing $215 million of damages and 23 deaths in Iran, where it
dissipated [9]. Although the damages to the east coast of the UAE were minimal
compared to those in Oman and Iran, there was an extended damage to the fisheries
industry in the east coast of the UAE for an extended period of time due to
phytoplankton bloom (also known as the red tide) that has occurred in the area in
the years after Gonu. The phytoplankton bloom that emerged between 2007 and
2008 in the Arabian Sea had been attributed to Gonu [10, 11].

11.4   Methodology

Meteorological statistical data was collected from two authorities in the UAE. The
first phase was distributing the data for the past decade and taking the average mean
of each month for the decade, for data that includes temperature, wind speed, wind
direction, and rainfall were distributed for the past decade, taking the average
monthly mean. The data gathered were assumed to be normally distributed.

Probability analysis such as means of the maximum temperature and the minimum temperature was collected and gathered in a graph for the probability of cyclone in the region.

Historical data for cyclones reported to hit the Arabian Peninsula was also gathered to determine the probability of such phenomenon to occur. Statistical data is not high enough to produce a good trend due to rarity of the event and the lack of historical records. In the past, storms of lesser forces than cyclones might have produced severe destruction in agriculture and homes due to the vulnerability of the infrastructure at the time. Due to the lack of objective measurements, the reliability of the data may be questionable, which further provides comfort to the rarity of cyclones hitting the Arabian Peninsula.

11.5   Interpretation of Data

The climate and weather, such as temperatures, wind speed, and direction, are analyzed to understand the cyclone phenomenon in the region and how it may impact coastal areas. Statistical data have been used showing each month's weather data to relate that information to the Gonu cyclone incident in June 2007. The study looks at the climatic trend for the decade 2000–2010 to determine if there are any unusual changes to the climate that might have triggered the intensity of cyclone Gonu.

Gonu started to form on May 31, 2007, and dissipated by June 7, 2007, as it crossed through Makran. In the city of Fujairah, along the UAE's east coast affected by Gonu, the average maximum temperature in June 2007 was 37 °C and the average minimum temperature was 31 °C. For the decade, the average maximum temperature in June is 39.75 °C with a standard deviation of 3.077 and the average minimum temperature is 31.35 °C with a standard deviation of 0.9. As a result, the average maximum temperature recorded in June 2007 is significantly different than the rest of the decade, as it is significantly cooler.

Wind direction information was gathered for the past decade, as shown in Table 11.2. It was noticeable that there were two major directions that the wind takes shape along the different months in the years. In winter months (November, December, January, February) the wind direction percentages are westerly and northwesterly direction, while in summer months (June, July, August) the wind direction is easterly and southeasterly. Gonu was formed in the Bay of Bengal area and moved towards the Gulf of Oman in which the Bay of Bengal is just southeast of the Gulf of Oman. This is one of the reasons that moved the cyclone towards the Gulf of Oman.

Compared to the whole decade (2000–2010), June 2007 had the highest percentages of easterly winds at 38.6 %. With a decade average of 30.68 % of easterly wind during the month of June and a standard deviation of 5.052, the percentages of easterly winds during June 2007 are significantly different than the average of the remaining years. Similarly, southeasterly winds in June 2007 were at

Table 11.2 Average percentage of monthly wind directions in the UAE's east coast (2000–2010)

	N	NE	E	SE	S	SW	W	NW	Calm
Jan	4.19	7.69	14.72	5.43	1.78	3.16	27.27	29.55	4.88
Feb	2.95	12.85	18.82	6.02	2.33	4.28	24.97	25.61	6.69
Mar	5.95	13.14	18.86	5.98	2.27	3.98	17.43	22.39	9.46
Apr	4.82	14.98	19.14	4.97	2.25	3.05	17.22	22.48	7.46
May	5.47	19.64	21.04	6.18	2.59	3.30	17.75	17.35	5.93
Jun	6.38	18.15	30.68	11.97	4.41	3.18	9.05	10.72	5.64
Jul	3.84	9.80	38.51	23.79	4.75	1.98	5.18	4.59	7.32
Aug	4.30	7.72	40.05	26.19	7.30	3.79	3.72	2.31	6.44
Sep	5.03	9.79	34.86	18.03	5.87	4.88	8.55	5.87	8.84
Oct	4.61	10.01	27.48	8.31	3.75	5.95	15.44	16.65	7.67
Nov	5.20	9.02	18.67	5.94	2.13	6.05	24.27	25.18	5.11
Dec	4.62	11.70	23.88	9.91	3.25	3.95	17.32	19.15	6.37

Table 11.3 Mean wind speeds in the UAE's east coast (2000–2010)

	2000	2001	2002	2003	2004	2005	2006	2007	2008	2009	2010
Jan	7.2	6.8	6.5	6.4	5.8	7.1	7.5	7.9	6.9	7.9	7.8
Feb	8.9	7.5	7.2	6.7	4.6	7.8	6.1	7.9	8	6.5	6.4
Mar	9.8	7.1	6.9	7.3	8	8.5	6.1	10	7.1	8.5	7.7
Apr	8.1	7.5	6.9	7.8	11.6	7.7	7.8	8.2	8.4	6.9	10.1
May	7.9	8.3	8.1	6.7	9.2	7	7.8	6.9	9.3	9.1	9.4
Jun	6.2	5.9	7.6	5.8	7.9	6.1	5.6	6.3	7.1	7.7	6.9
Jul	5.4	5.7	6	5.4	5.5	6.9	7.5	6.2	5.8	7	6.5
Aug	5.1	5.5	5.7	5.5	5.5	6.1	5.3	6.9	5.8	7.1	5.3
Sep	5.8	5.1	5.3	5.3	5.7	8.1	5	5	5.5	5.9	4.5
Oct	3.9	5.3	4.9	5.2	4.7	5.2	5.7	5.2	6.1	5.5	5.5
Nov	5.4	5.1	4.7	6.7	6	6	6.1	6.1	5.9	5.7	5.6
Dec	5.8	4.9	6.4	6.2	7.6	6.1	7.1	7.4	7.2	6.5	6.5

19.9 % of the time, while the average for the month of June is 11.97 % with a standard deviation of 4.47. This means that June 2007 had statistically significant more easterly and southeasterly winds than the average for that month, and it also was the record highest for the whole decade. This information suggests that Gonu had significantly affected the wind direction making it more prominently in the easterly and southeasterly directions. This is substantial, because the east coast of the UAE is aligned such that during the pre-monsoon cyclone season it fits perfectly with the direction of the wind, making the impact to the coast at almost heads on. This may cause the most severe type of tidal waves from the tropical storms. This of course does not suggest that those winds caused the storm, but that the storm had caused these winds (Table 11.4).
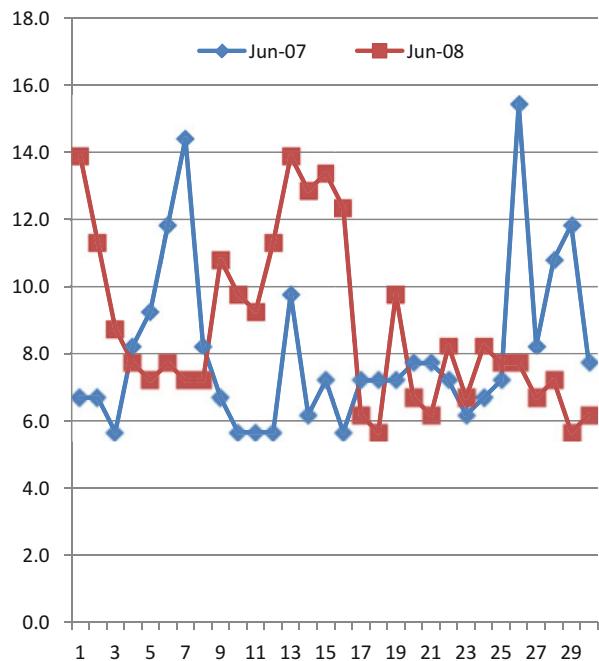
Although the data shows that the direction of the wind was more prominently easterly and southeasterly in direction compared to the norm for that period in June 2007, the wind speeds were not significantly different. In actuality, June 2007 had the lowest average gust speeds for the same period between 2006 and 2010. Also,

	Jun-06	Jun-07	Jun-08	Jun-09	Jun-10
1	6.2	6.7	13.9	11.8	7.2
2	6.7	6.7	11.3	7.2	0.0
3	5.7	5.7	8.7	12.3	8.7
4	6.2	8.2	7.7	10.3	8.7
5	6.7	9.3	7.2	8.7	7.7
6	6.2	11.8	7.7	6.7	7.2
7	7.2	14.4	7.2	9.8	7.2
8	6.7	8.2	7.2	17.0	8.2
9	7.2	6.7	10.8	17.5	7.2
10	8.2	5.7	9.8	7.7	8.2
11	11.3	5.7	9.3	7.2	7.7
12	8.2	5.7	11.3	6.2	7.7
13	7.2	9.8	13.9	6.2	8.7
14	7.7	6.2	12.9	18.0	9.3
15	6.7	7.2	13.4	17.0	8.2
16	9.8	5.7	12.3	13.4	7.7
17	6.7	7.2	6.2	10.3	6.7
18	7.7	7.2	5.7	8.2	7.7
19	7.7	7.2	9.8	12.9	6.2
20	7.2	7.7	6.7	10.3	6.2
21	7.2	7.7	6.2	7.2	7.7
22	8.7	7.2	8.2	6.7	9.3
23	7.2	6.2	6.7	5.1	8.7
24	6.7	6.7	8.2	10.3	11.3
25	7.7	7.2	7.7	8.2	8.7
26	7.2	15.4	7.7	9.3	7.2
27	7.2	8.2	6.7	10.3	7.2
28	9.3	10.8	7.2	12.9	8.2
29	7.2	11.8	5.7	8.7	14.9
30	15.4	7.7	6.2	8.7	17.0

Table 11.4 Highest gust speeds recorded for the month of June in the UAE's east coast (2006–2010)

the highest gust of wind recorded when Gonu made landfall on the eastern coast of the UAE on 6th and 7th of June was 14.4 m/s (52 kph). The wind speed that hit the eastern coast when Gonu made landfall is insignificant to the average highs achieved, as shown in Table 11.3. In other words, the region does experience significantly more wind speeds, even when it is not due to a tropical storm. Therefore, the damages in the area done by Gonu are not due to the wind speeds. However, it would be more correct to state that it was due to the waves that had caused seawater levels flood the affected areas as well as the heavy rainfall. The actual change and difference between low and high tide in June 2007 were not at all different than the norm. As it would be typical to cyclones, it would not usually affect the tidal difference, as expected. It can be clearly conclusive that the damages done during Gonu's landfall on the eastern region of the UAE were mainly due to the height of waves without concerns from wind speeds. Nonetheless, since the east

Fig. 11.1 Highest gust
speeds recorded for the
month of June in the UAE's
east coast (2007–2008)
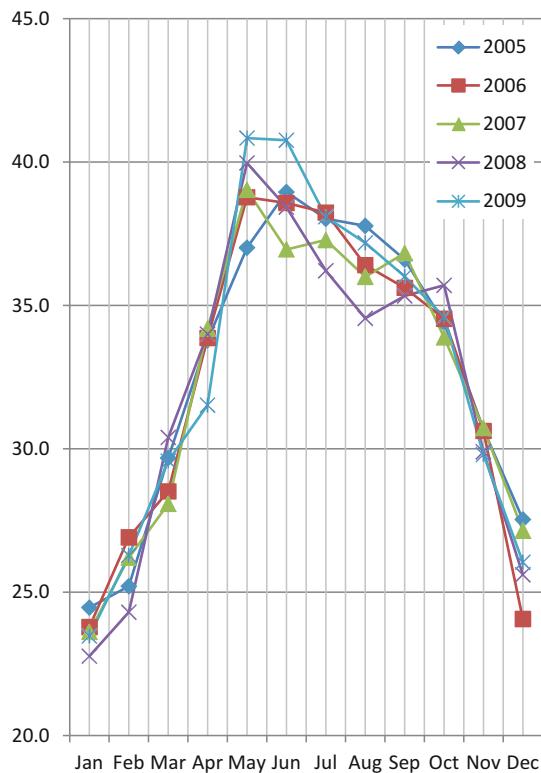
coast of the UAE is a mountainous region, then the flooding of valleys (*wadis*) due
to the heavy rainfall is also partly blamed for the destructive nature of severe
tropical storms and not the actual wind speeds.

As derived from the records, Fig. 11.1 shows that the wind gusts experienced
during Gonu in the first week of June 2007 are not unusual when compared to the
second week of June 2008. Hence the damages from floods are the most important
factor of the storm and not the winds.

The average temperatures of the eastern coast of the UAE in the past decade can
be seen in Fig. 11.2. It shows that the trend is not changing, whether pre-Gonu or
post-Gonu. There seems to be no significant changes in the overall trend line,
although in months of specific years, there were statistically significant changes
to the trend. Nonetheless, it is not a permanent change in the trend, as the years later
show an adjustment back to the average trend line.

The climate is not proven to have changed and cannot be blamed for the
development of Gonu in the Arabian Sea, which is a rare occurrence with a
probability of at most once in 60 years from the historic data since 1867. Saying
that, the results do not define climate dynamics of the region further in the future, as
climate changes have been detected in generality from sedimentary deposits along
the Arabian Sea [12]. Nonetheless, the effects of cyclone Gonu to the marine
ecology and the fisheries industry after it has crossed path in the area have shown
to be of long term, especially with the phytoplankton bloom that the region has
experienced.

Fig. 11.2 Average monthly temperatures in degree Celsius in the UAE's east coast (2005–2009)

11.6   Limitations of the Study

Even though the study does not prove that there is an occurrence of climate change to be blamed for Gonu, this research has its pitfalls, in such that the recorded historical data of the climate in the region is very limited to provide conclusive evidence for or against climatic changes in the region. Nonetheless, there are theories that show that anthropogenic air pollution, though not causing higher intensities of cyclones, could cause more damage in the form of acid rain [13], which is another issue that needs to be addressed from the outcomes of tropical storms in the region. This is especially important in the Arabian Sea due to its close proximity to oil-producing nations that emit significant amounts of pollution into the atmosphere during oil extraction, as well as significant air pollution emitted in various parts of the Indian subcontinent along the Bay of Bengal.

As the majority of the Arabian Peninsula is a dry desert, it may actually be a blessing in such a way that the effects of anthropogenic air pollution may not cause damages in the form of acid rain in the region, and that the air pollution is more

likely dispersed without being heavily concentrated in the area. In addition to that, the climate of the Arabian Peninsula helps in weakening tropical storms as they approach the region. This has been observed also with Gonu, which provides the necessary reasons why tropical storms in the north of the Indian Ocean do not affect the Arabian Sea as it would the Bay of Bengal.

More evidence of climate change increasing the frequency of intense tropical storms in the north of the Indian Ocean is also being reported in one study [14]. Therefore, there could be reason to consider climate changes as a cause of these storms, although our study can neither prove nor disprove this theory. The data used in our study is mainly from the eastern region of the UAE. Nonetheless, tropical storms in the region develop and intensify further to the southeast of the Arabian Peninsula, and such data was not analyzed to consider the climatic dynamics of the area. More studies on the climate trends in the Arabian Sea, as well as oceanographic data in the temperatures of the water and evaporation, are important to conclude the effects of climate change in the region, if any. The conclusion of this study, in which the intensity of Gonu in the Arabian Sea in 2007 can neither be associated nor disassociated with global warming or climate change, is similar to the conclusion reached in one study [15], where it is also asserted that the evidence from single events or the oscillations of the climate dynamics are inconclusive in either its association or disassociation with global warming. It is important to note that major critiques on the attribution of global warming with tropical storms are still a heated debate in various scientific forums [16].

In our study, we have no conclusive evidence whether global warming increases the intensities and frequencies of tropical storms or the other way around. The thing we know for sure, however, is that climate change is inevitable, regardless of its causes and dynamics. Nonetheless, the scope of this study is neither to associate nor to disassociate global warming to the increase of frequency and intensity of tropical storms in the region, but merely to forecast future impacts of intense tropical storms on the eastern coast of the UAE.

Although this study is limited, from a statistical perspective, there seems to be adequate evidence to conclude a very low probability for intense cyclones to affect the east coast of the UAE. However, this may be true for the next century, but in this world only one thing is guaranteed, and that is change. As the earth is dynamic, change is inevitable and future studies are required to further understand and forecast intense cyclones in the region beyond a century from today.

11.7   Conclusions

Severe tropical storms making landfall in the Arabian Peninsula are very rare. Tropical storms surging farther north of the Arabian Sea into the Gulf of Oman (Sea of Oman) have also a lesser probability of occurrence. Severe storms making landfall in the east coast of the UAE would also have a much lower probability of occurrence, especially since the length of UAE's east coast is minimal when

compared to that of Sultanate of Oman, and farther to the north of the Gulf of Oman. From the statistical analysis, there does not seem to be a trend of significant climatic changes occurring in the east coast of the UAE. It is safe to say that Gonu was a rare occurrence in such a way that the frequency of occurrence of similar storms to hit the east coast of the UAE would be at most once every 60 years.

The interpretation of the data shows that there were insignificant changes to the normal weather patterns in the region during the days preceding the cyclone and in its aftermath. While forecasting the data using different regression patterns, it is also found that a strong cyclone with damages similar to Gonu making landfall in the east coast of the UAE causing damages would occur at most once every 60 years. Although the data shows that weather patterns prior to the storm are not significantly different from the average, it would be difficult to predict a storm making landfall in the UAE. Nonetheless, since the UAE's east coast lies in the northern tip of the Gulf of Oman, the strength of cyclones would usually drastically decrease, since there is high probability to lose its strength en route while making landfall in the eastern part of the Sultanate of Oman. Although the meteorological data acquired for the study is limited due to inadequate historical recording accuracy in the region, the findings provide a confidence in the rarity of the event with a recurrence of once every 60 years at the most.

There is a lack of instrumentation and measurement for early detections of tropical storms to make landfall in the east coast of the UAE. Due to the low probability of the impact of cyclones compared to the investments made for such measurement systems, it may not necessarily be feasible to have an independent system for the UAE. Instead, cooperating with systems from the Sultanate of Oman would be the most economical solution for any risk assessments and emergency response for UAE's east coast.

References

1. Dibajnia M, Soltanpour M, Nairn R, Allahyar M (2010) Cyclone Gonu: the most intense tropical cyclone on record in the Arabian Sea. In: Charabi Y (ed) Indian Ocean tropical cyclones and climate change. Springer, New York, NY, pp 149–157
2. Najar KA, Salvekar PS (2010) "Understanding the tropical cyclone Gonu," Indian Ocean tropical cyclones and climate change, vol 6. Springer, New York, NY, pp 359–369
3. Webster PJ, Holland GJ, Curry JA, Chang HR (2005) Changes in tropical cyclone number, duration, and intensity in a warming environment. Science 309(5742):1844–1846
4. Murty TS (1984) Storm surges – meteorological ocean tides. Bull Fish Res Board Can 212:898
5. Singh OP, Khan TMA, Rahman MS (2001) Has the frequency of intense tropical cyclones increased in the North Indian Ocean? Curr Sci 80(4):575–580

6. Staubasser M, Sirocko F, Grootes PM, Erlenkeuser H (2002) South Asian monsoon climate change and radiocarbon in the Arabian Sea during early and middle Holocene. Paleoceanography 17(4):1063–1075
7. Murty TS, El-Sabh MI (1984) Cyclones and storm surges in the Arabian Sea: a brief review. Deep Sea Res 31(6–8):665–670
8. Bailey RW (1988) Records of Oman: 1867–1947. Archive Editions, Buckinghamshire, England
9. Fritz HM, Blount CD, Albusaidi FB, Al-Harthy AHM (2010) Cyclone Gonu storm surge in Oman. Estuar Coast Shelf Sci 86:102–106
10. Wang D, Zhao H (2008) Estimation of phytoplankton responses to hurricane Gonu over the Arabian Sea based on ocean color data. Sensors 8:4878–4893
11. Piontkovski S, Al-Azri A (2010) "Influence of a tropical cyclone Gonu on phytoplankton biomass (chlorophyll A) in the Arabian Sea," Indian Ocean tropical cyclones and climate change, vol 6. Springer, New York, NY, pp 339–347
12. von Rad U, Schaaf M, Michels KH, Schulz H, Berger WH, Sirocko F (1999) A 5000-yr record of climate change in Varved sediments from the oxygen minimum zone off Pakistan, Northeaster Arabian Sea. Quatern Res 51(1):39–53
13. Sriver RL (2011) Climate change: man-made cyclones. Nature 479:50–51
14. Singh OP (2010) Recent trends in tropical cyclone activity in the North Indian Ocean. In: Charabi Y (ed) Indian Ocean tropical cyclones and climate change. Springer, Dordrecht, Netherlands, pp 51–54
15. Anthes RA, Corell RW, Holland G, Hurrell JW, MacCracken MC, Trenberth KE (2006) Hurricanes and global warming – potential linkages and consequences. Bull Am Meteorol Soc 87:623–627
16. Pielke R, Landsea C, Mayfield M, Laver J, Pasch R (2006) Reply to "Hurricanes and Global Warming – Potential Linkages and Consequences". Bull Am Meteorol Soc 8:628–631

Chapter 12
Future Challenges in Urban Drainage Systems Under Global Warming

Mawada Abdellatif, William Atherton, and Rafid Alkhaddar

Abstract The increase of extreme rainfall intensity and frequency as a result of climate change are predicted to put heavier pressures on existing sewer systems, which could result in urban flooding. By considering different possible levels of greenhouse gas emissions and through the development of sophisticated climate models, it is possible to predict what climate change might look like during the coming century. The broad objective of this chapter is to improve engineers, planners and designers' appreciation of the potential risks associated with urban drainage systems. This work is applied to a selected site in the North West of England to predict future rainfall using a downscaling model of HadCM3 outputs. The methodology employs the estimated uplift for the future design storm to the existing combined drainage system which is designed according to the current UK standards. Thus the system should sustain rainfalls with a specific return period without detriment to the level of services. Results obtained from InfoWorks CS used in the simulation of the drainage system demonstrated that there is considerable change in the number of flooded manholes together with surcharge in some sewers for winter and summer seasons during the 2080s.

M. Abdellatif (✉) • W. Atherton • R. Alkhaddar
Peter Jost Centre, School of the Built Environment, Liverpool John Moores University, Byrom Street, Liverpool L3 3AF, UK
e-mail: mawadaabdellatif@yahoo.co.uk; w.atherton@ljmu.ac.uk; r.m.alkhaddar@ljmu.ac.uk

Nomenclature

ANN	Artificial Neural Network
A1FI	High emissions scenario of greenhouse
A2	Medium-high emissions scenario of greenhouse
B2	Medium-low emissions scenario of greenhouse
B1	Low emissions scenario of greenhouse
CSO	Combined sewers over flow
DWF	Dry weather flow
GPD	Generalised Pareto Distribution
GLM	Generalised Linear Model
HadCM3	Hadley Centre Coupled Model, version 3
HI	High impact
IPCC	Intergovernmental Panel on Climate Change
MI	Medium impact
NI	No impact
UKWIR	United Kingdom Water Industry Research
UU	United Utilities
VHI	Very high impact
WwTW	Wastewater Treatment Works

12.1 Introduction

Drainage systems are needed in developed urban areas because of interaction between human activity and natural water cycle. This interaction has two main forms: the abstraction of water from natural water cycle to provide water supply for human life, and covering of land with impermeable surfaces that divert rainwater away from the local natural system of drainage. These two types of interaction give rise to two types of water that required drainage [1].

The first type, wastewater (dry weather flow, DWF) is constituted of population generated flows from residential properties within the network, trade and commercial flows, and infiltration from groundwater into the sewerage system networks. After use, if not drained properly, wastewater could cause pollution and create risk to health.

The second type of water requiring drainage is storm water, which is rainwater that is fallen on a built-up area. If the storm water is not drained properly, it will cause inconvenience, damage, flooding and further health risks.

There are basically two types of conventional sewerage system, a combined system in which wastewater and storm water flow together in the same pipe, and a separate system in which wastewater and storm water are kept in separate pipes. Some towns include hybrid systems, for example a "partially separated" system, in which waste water is mixed with some storm water, while the majority of storm water is conveyed by separate pipes. In the UK, most of the older sewerage systems

are combined which accounts to about 70 % of the total length of sewerage pipes in the country and only 30 % are separate system [1].

In dry weather, the system carries wastewater flow only. During rainfall event, the flow in the sewers increases as a result of addition of storm water and in heavy rainfalls the storm water could be 50 or even 100 times the average wastewater flow. It is simply not economical to provide capacity for this flow; therefore the solution is to provide structures in the sewers network system, which diverts flows above certain level out of the system and into a natural watercourse. These structures are called combined sewers overflows or CSOs

In the UK, some cities have sewers with more than 150 years old and replacement/renewal rates of these sewers are very low. Although the annual average replacement/renewal rate for the UK is currently 0.4 %, however under current investment in sewer renewal, replacement of the existing assets, by some estimate, would take more than 1,000 years [2]. This means that the existing urban drainage systems have been designed for the past climate conditions, but maybe not for the situation occurring today or for the future.

The chapter focuses on examining possible impacts of climate change on storm water systems, whether as a separate surface water system or combined with sewerage system. Specifically the chapter is concerned with change in generation of storm waters due to change in rainfall pattern in future and its implications on performance of existing urban drainage infrastructures.

12.2 Urban Drainage and Climate Change

The evidence for global warming is compelling, with records showing that global-average surface air temperature has risen by 0.60 °C since the beginning of the twentieth century, with about 0.40 °C of this warming occurring since the 1970s [1, 3]. The main clue to the cause of these rises is the significant increase in the concentration of greenhouse gases (e.g. carbon dioxide, methane) observed over the past 200 years.

An emerging challenge in the field of urban drainage is global warming which potentially leads to climate change. Storms and floods are now the most frequent and costly extreme weather events occurring in Europe, with floods causing around €15bn of economic damage in 2002 [4, 5]. Practitioners will hence need guidance on adapting input data to account for the anticipated effects of climate change [6].

The main findings of climate change studies, of relevance to urban drainage, are an increase in total rainfall (and hence runoff) and increased storm intensities. The potential implications [1] are as follows:

- Increased flows that may exceed the capacity of existing sewer systems leading to more frequent surcharging and surface flooding.
- Greater deterioration of sewers due to more frequent surcharging.
- More frequent Combined Sewer Overflow (CSO) spills.

- Greater build-up and mobilisation of surface pollutants in summer.
- Poorer water quality in rivers due to extra CSO spills and reduced base flows in summer.
- Increased flows of dilute wastewater at treatment plants due to higher rainfall and infiltration, potentially leading to poorer treatment by biological processes.

The Intergovernmental Panel on Climate Change (IPCC) released four scenarios for greenhouse gases based on different views of how the world might develop over the coming years (e.g. high emissions (A1FI), medium-high (A2), medium-low (B2) and low (B1) emission scenarios), for prediction of future trends in climate. They assist in climate change analysis, including climate modelling and the assessment of impacts, adaptation and mitigation [7].

The wide range of predictions from climate change scenarios, based on different assumptions, result in uncertainty, which limits the value of these predictions to storm water management, policy definition and planning [8]. Despite this [9] concluded that studies using different climate change and urban drainage scenarios can be used as an indication of possible impacts resulting from climate change.

There are numerous studies that have investigated the impact of climate change on urban flooding. However, most of them were focused on the impacts from rivers and coastal sources, as they are the most apparent and catastrophic ones. Few of these studies in the UK have considered the urban flooding on combined sewers systems. One of the latest studies, which have considered flooding on combined sewers systems, is the work carried out by the United Kingdom Water Industry Research (UKWIR), which used the Weather Generator method for generating future rainfall [10]. The study by [11] found that an increase of 40 % in rainfall intensity will lead to an increase in flooding volume of 100 % and an increase in number of damaged buildings of 130 %; the value of flood damage will increase by 200 % as stated in [12].

This chapter presents the outcome of a study to assess how climate change on inter-annual to multi-decadal timescale, the far future (or 2080s), will affect design standards of wastewater network due to the presumed increase in rainfall intensity and frequency in the Northwest England. Moreover, results from the study could possibly lead to improvement management and design of the sewer network system. However if the impact is severe and costive, it is probable that the impact cannot be prevented and thus adaptation will be necessary.
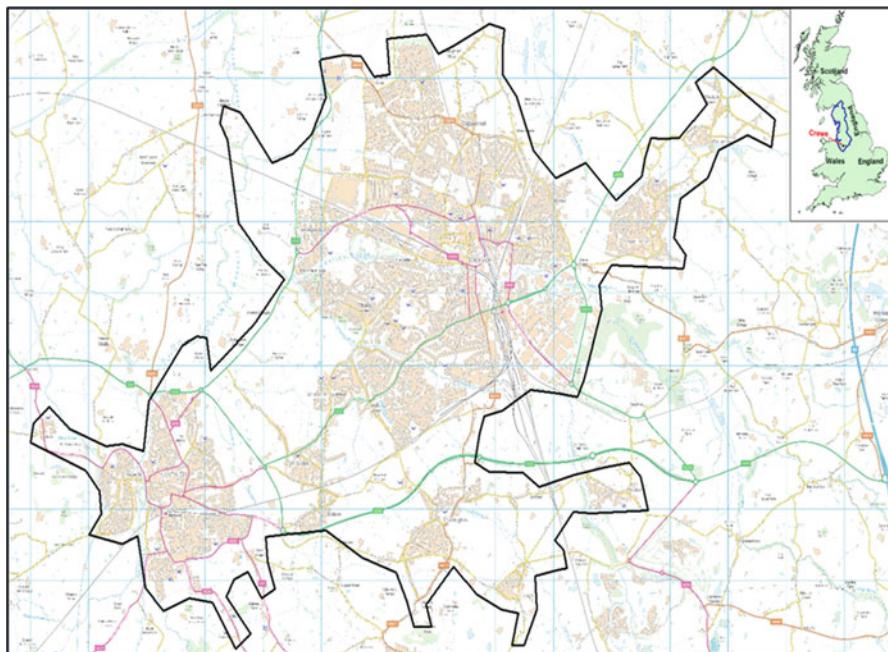
These objectives are achieved here by applying the downscaled future rainfall from global climate model (HadCM3) during winter and summer seasons (for more information see [13]) to hydraulic model (a sewer network model) employing InfoWorks CS software. The results have been analysed using a risk assessment model (Data Manager, or DM) developed by MWH UK.

12.3   Description of the Catchment

The Crewe study area is located in the south east of Cheshire County in North-western England (see Fig. 12.1). It consists predominantly of residential housing interspersed with areas of retail, commercial and industrial developments, covering a total area of approximately 32 km^2. The main concentration of the retail, commercial and industrial developments is in the central parts of Crewe [14]. Population figures derived from occupancy rates and address seed points obtained from UU, indicate a current residential population in the study area of approximately 90,484. The main river within the Crewe drainage area is the River Weaver which lies just outside the study area boundary and receives discharges from Crewe Wastewater Treatment Works (WwTW) which is about 5 km to the north west of Crewe town centre.

The sewer system in the study area is largely combined although some areas of more recent development, around the periphery of the town are drained by separate systems. The catchment sewer model consists of 1,655 sub-catchments, 1,830 nodes and 1,797 sewers with a total length of 94.64 km and sewer sizes ranging between 100 and 4,500 mm.

There are 23 combined sewer overflows (CSO) within the catchment area. Eighteen of these discharge into Leighton Brook, Valley Brook, Wistaston Brook or their tributaries and one, at the Crewe WwTW storm tank, spills to the River Weaver. The remaining four spill into watercourses outside the study area [14].

Fig. 12.1 Location of Crewe Catchment

12.4 Future Rainfall Predictions

Evaluating regional impacts from possible climate change in the future requires a methodology to estimate certain meteorological variables (e.g. rainfall) for the time period and geographical region of interest. In general two physical systems are involved: the climate system in which the effect of greenhouse gases emissions can be simulated by General Circulation Models, GCMs (from which rainfall is downscaled due to coarse resolution of the GCMs) and the hydrological system such as urban drainage systems [15].

A hybrid Generalised Linear Model (GLM) and Artificial Neural Network (ANN) approach is introduced in a previous work [13] by the same authors as part of a study to downscale coarse global climate model (HadCM3) outputs to finer spatial scales, as the coarse resolution limits its use for impact study. The outputs of this model are used to explore the possible future changes in rainfall pattern in the Crewe area of the North West of England under A1FI and B1 emission scenarios for winter and summer seasons. Subsequently, forecasters can use this future downscaled rainfall for impact assessment.

The downscale model developed used a two stage process to model rainfall. The first stage is the rainfall occurrence process, which is modelled with logistic regression to represent wet and dry sequences of rainfall and given by [16] as follows.

$$\ln\left(\frac{p_i}{1 - p_i}\right) = X_i\beta \tag{12.1}$$

where P_i is the probability of rain for the ith case in the data set, X_i is covariate vector (climate predictors), B is model coefficients

The second stage is rainfall amount which is modelled with a multilayer feed forward artificial neural network (MLF-ANN) technique to represent the non-linear relationship between the observed rainfall amount series and the same selected set of climatic variables (predictors) used to model the rainfall occurrence process.

Then frequency analysis with Generalised Pareto Distribution (GPD) introduced by [17], is carried out to obtain the return level—return period relationship of the extreme rainfall event during the present (1961–1990) and future periods (2080s) under high (A1FI) and low (B1) emission scenarios for winter and summer seasons. The cumulative distribution function, $F(x)$, for GPD, where $k \neq 0$ is:

$$F(x) = 1 - \left(1 + \frac{k}{\sigma}(x - u)\right)^{-\frac{1}{k}} \tag{12.2}$$

where k is shape parameter, σ is scale parameter, x is the random variable $(x > u \ (mm))$

12.5   Rainfall Runoff Volume Model

For purposes of modelling Crewe urban drainage system, all the components of the system (storm water and DWF) are considered in the simulation, in addition to other inflows in the catchment. Two antecedent conditions are considered, in-depth wetness of the catchment which governs the infiltration into the ground and is represented by UCWI and NAPI values, and surface wetness of the catchment which governs initial losses of rainfall in wetting the surface and forming puddles. Other loses such as evapotranspiration during the storm should also be considered, however it is generally viewed as unimportant in the Northwest of England as its value is not significant. Areal reduction factor is also used to reduce the depth of rainfall in synthetic storms to represent the average loss across the catchment.

The runoff volume model determines how much of the rainfall runs off the catchment into the drainage system after accounting for initial losses. In the current study InfoWork CS Software Version 12 is used to model dry and wet weather flows in Crewe Catchment. The model was built, calibrated and verified in 2007 by water authority in Northwest of England. It incorporates numerous runoff volume models; however, in practice only three are generally used in UK wastewater network modelling and in the current study [1, 18]. These are:

- Wallingford Procedure (fixed PR) Runoff Model: The Wallingford model is applicable to typical urban catchments in the UK. It uses a regression equation to predict the runoff depending on the percentage impermeability, the soil type and antecedent wetness of each sub-catchment. The model predicts total runoff from all surfaces in the sub-catchment, both pervious and impervious. Therefore this model should not be mixed with another model within one catchment. It is used to represent continuing losses with an initial losses model. In this model, runoff losses are assumed to be constant throughout a rainfall event and are defined by the relationship:

$$PR = 0.829 \, PIMP + 25.0 \, SOIL + 0.078 \, UCWI - 20.7 \qquad (12.3)$$

  where PR is the percentage runoff, PIMP is the percentage impervious area (roads and roofs) by total contribution area, SOIL is an index of the water holding capacity of the soil, UCWI is the urban catchment wetness Index
- New UK (Variable PR) Runoff Model: This model is applicable to all catchments with all surface types, but particularly those which show significant delayed response from pervious areas. It calculates the runoff from paved and permeable surfaces separately and calculates the increase in runoff during an event as the catchment wetness increases. Percentage runoff is calculated using:

$$PR = IF^*PIMP + (100 - IF^*PIMP) * API30/PF \qquad (12.4)$$

where PR the percentage runoff, IF Effective impervious area factor, PIMP the percentage impervious area (roads and roofs) by total contribution area, PF Soil storage depth (0.2 m), API_{30} 30-day antecedent precipitation index

$$API_{30} = \sum_{n=1,30}(P - E)n\ Cp^{n-0.5} \qquad (12.5)$$

where n number of days prior to the event (P-E)n Net Rainfall on day n, Pn Total rainfall depth on day n, En Effective evaporation on day n, Cp Decay factor depending on the soil index

- Fixed Percentage Runoff Model: This is applied to one surface type in the sub-catchment (impervious) with the percentage of rainfall that actually runs off into the system.

12.6 Assessing the Drainage System Performance

Possible consequences caused by climate change in urban drainage systems include flooding (surface flooding, internal flooding in house basements or flooding in low laying properties), sewer surcharges and additional spills from combined sewer overflows (CSOs). Three indicator sets are therefore selected in this chapter to represent the possible consequences: (1) number of flooding manholes and total volume of flood water spilling from the manholes; (2) number of surcharging sewers and the pressure head above the top of the sewers (3) number of buildings and house basements in danger of flooding.

In order to predict a development trend of possible consequences in different climate change scenarios, simulations for A1FI (high emission) and B1 (low emission) scenarios in 2080s (2070–2099) are used to represent the far future. The runs employed an uplift percentage of extreme rainfall (design storm) in future from the present rainfall of the existing system of Crew catchment using Info-Work CS, version 12.

Present rainfall for the period (1961–1990) is used as a baseline against future conditions induced by climate change during winter and summer. Each simulation runs for 7 days for the design storm of 5 years return period with durations of 60, 120, 180, 360, 480 and 1,440 min, as the system is designed to hold a current 5 years storm without CSO spilling.

The uplift percentages are obtained from extremes frequency analysis carried out in previous work by the same authors. The uplift percentages are found to be between 35–42 and 16–33 % in 5 year of future extremes rainfall in winter for scenario A1FI and B1, respectively, in all durations. In summer the 5 year future extremes values are predicted to reduce by 16–28 % for scenario A1FI and 27–39 % for scenario B1.

Flood risk to properties is a function of the level of water (energy grade line) adjacent to a property. This can manifest in two forms, the water level in the sewer (surcharge flood) and the water level on the ground (surface or overland flood), when caused by flooding from sewers.

Table 12.1 Surface flooding for the base period (1961–1990) and future 2080s under A1FI and B1 scenarios

	Winter			Summer		
	Base period	A1FI.80s	B1.80s	Base period	A1FI.80s	B1.80s
Duration	No. of flooding manholes	No. of flooding manholes	No. of flooding manholes	No. of flooding manholes	No. of flooding manholes	No. of flooding manholes
60	132	244	185	119	22	49
120	96	179	155	100	62	50
180	79	134	109	85	38	32
360	42	93	73	54	31	23
480	37	75	70	38	26	13
1,440	15	34	23	16	2	13

Table 12.2 Surcharge in sewers for the base period (1961–1990) and future 2080s under A1FI and B1 scenarios

	Winter			Summer		
	Base period	A1FI.80s	B1.80s	Base period	A1FI.80s	B1.80s
Duration	No. of flooding manholes	No. of flooding manholes	No. of flooding manholes	No. of flooding manholes	No. of flooding manholes	No. of flooding manholes
60	536	659	592	512	400	352
120	436	564	530	459	377	326
180	386	497	441	403	285	262
360	270	384	349	302	239	185
480	215	335	322	258	186	150
1,440	112	178	134	131	195	120

Table 12.1 shows results of surface flooding during winter and summer, obtained with use of the aforementioned uplift percentages. Results in Table 12.1 clearly show a significant increase in number of flooding manholes in winter in the Crewe area; and a reduction during summer for all durations. The worst condition is associated with the 60 min duration, which gives a maximum number of 244 manholes and a total flood volume of 14,545.3 m^3 (this is more than twice the flood volume in the present of 5,960.2 m^3).

Table 12.2 shows the sewer surcharge results, evaluated by the number of surcharging sewers nodes when the simulated water level is above the top of the sewers. The worst conditions are for a 5 year return period storm when the duration is 60 min in winter, under scenario A1FI, which results in 659 flooding manholes. In summer there is a considerable drop in numbers of surcharged pipes under both scenarios.

Table 12.3 Building at very high risk of flooding for the base period (1961–1990) and future under A1FI and B1 Scenarios

	Winter			Summer		
	Base period	A1FI.80s	B1.80s	Base period	A1FI.80s	B1.80s
Duration	No. of flooding manholes	No. of flooding manholes	No. of flooding manholes	No. of flooding manholes	No. of flooding manholes	No. of flooding manholes
60	1,225	1,672	1,429	1,132	910	730
120	1,100	1,412	1,342	1,063	839	744
180	999	1,297	1,179	992	700	649
360	741	1,073	887	710	661	591
480	675	857	828	702	596	533
1,440	495	589	529	504	467	480

Similarly, Table 12.3 shows a quantitative analysis of future flood risk which provides another impression of how the risk might change in the future affecting basements and properties in low laying ground levels due to sewer surcharge.
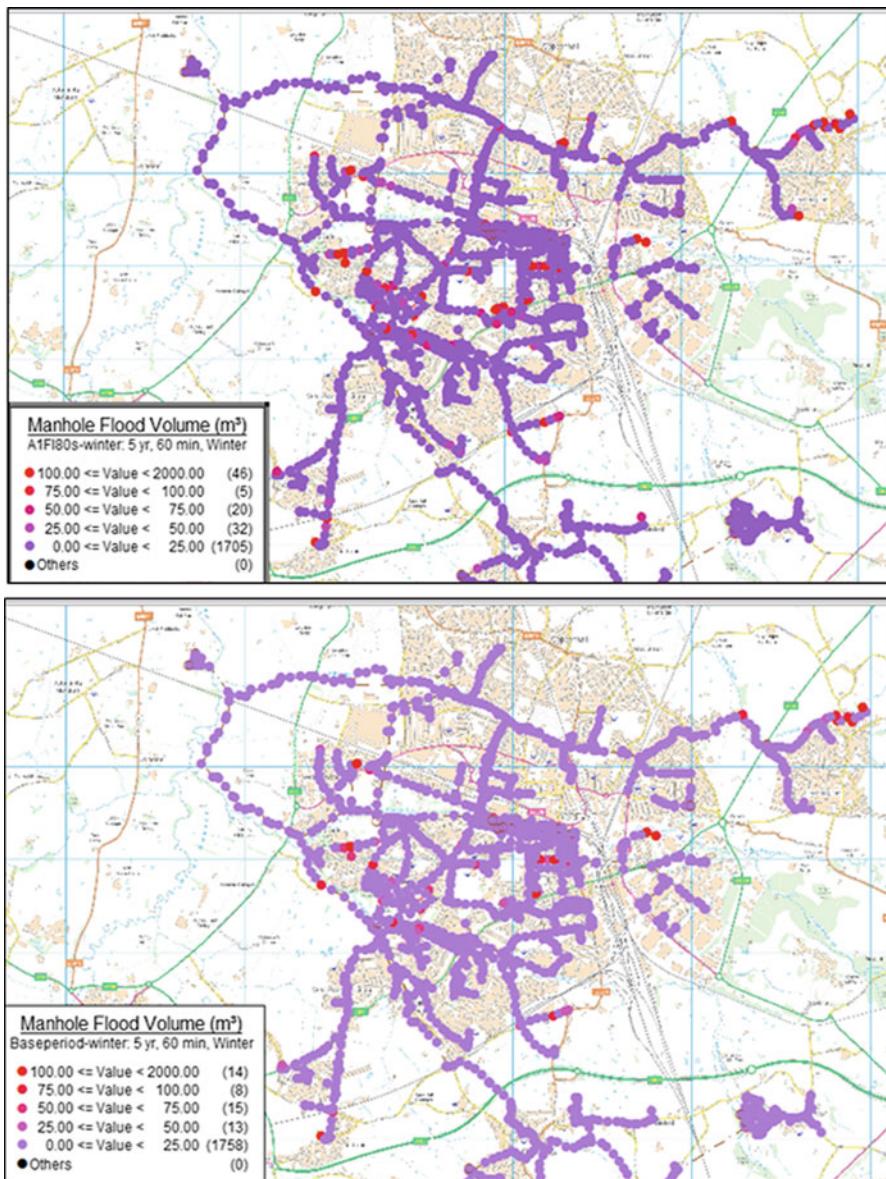
The assessment of flood risk for surcharged sewers is based on a comparison between the predicted top water level at the upstream end of the sewer (taken from the InfoWorksCS simulation package) and individual property levels using DM software.

It could be observed from the results in Table 12.3, that the number of properties at very high risk of flooding reaches its maximum with storm durations of 60 min in winter. The risk of surcharged sewers on a building are categorised as very high impact (VHI) when the difference between basement or property and sewer surcharge levels is greater than 200 mm, as medium impact (MI) if the difference is between 200 and 100 mm, and as no impact (NI) if it is less than 100 mm [19].

In summer the risk is projected to decrease, especially under the low scenario (B1), due to the assumption inherited in this scenario of reduction in greenhouse concentration as a result of the use of clean energy.
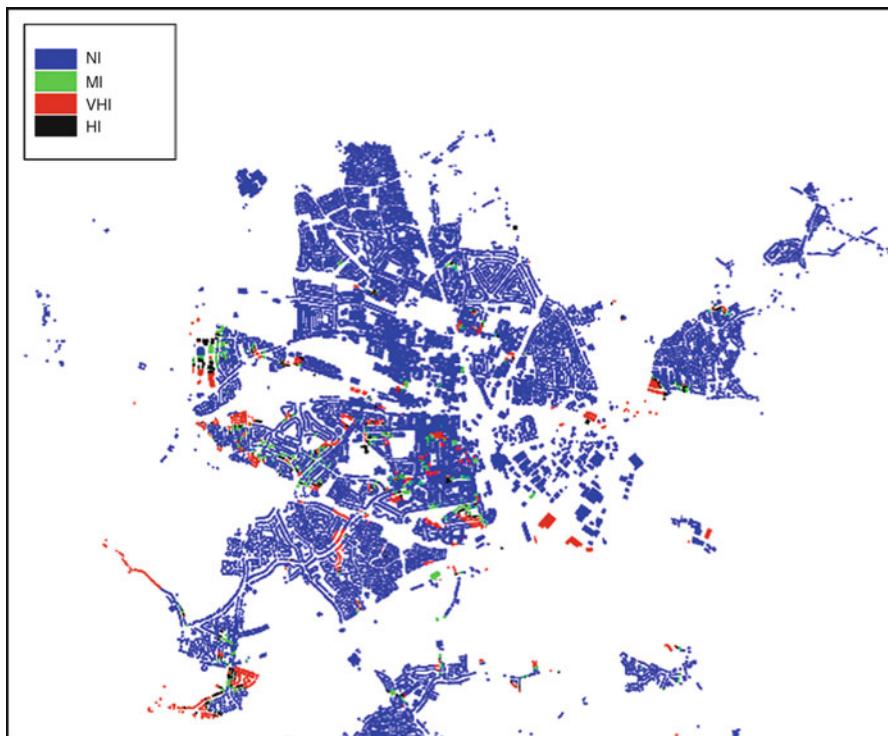
Figure 12.2 shows visual representation and geographical distribution of increase in flooding volumes of manholes in winter under the high scenario in 2080s compared with base period. Manholes with a spilling volume of more than 25 m^3 are considered to be significant in causing surface flooding. Some of flood volumes shown in Fig. 12.2 will re-enter the sewer system (when there is space) which considered store type, whereas some flood volumes leave the system from manholes whose flood type is classified as lost. The flood volume in this case would run the ground surface causing overland flow flooding.

Moreover, Fig. 12.3 shows properties in the catchment and the Flood Risk, due to sewer surcharge, they are posed at future climate. It can be seen that the very high flood risk impact (VHI) is concentrated in the middle of the network where the combined system is located. However, flood risk in areas served by a foul system only is also considered as DWF would also increase with increase in ground infiltration due to rainfall.

Fig. 12.2 Flooding manholes in winter of scenario A1FI of 60 min duration (top) as worst condition in 2080s which increase by 35 % of design storm compared by base period (bottom)
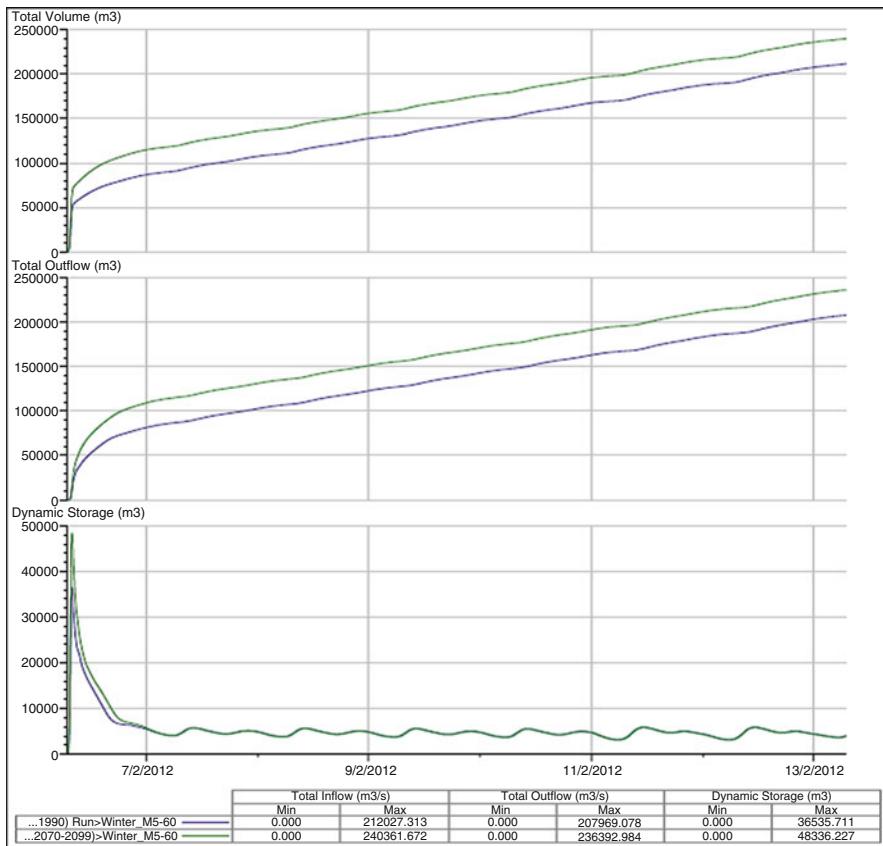
As mentioned earlier, the hydraulic capacity of the system is limited to or generally designed to convey a combined foul and storm flow of 1 in 5 year return period without significant surface flooding and CSOs spilling. Figure 12.4 is a comparison between the present and future inflow, outflow and storage in the

Fig. 12.3 Properties at risk of flooding during winter of 2080s under A1FI of 60 min duration in Crewe catchment. NI: no impact, MI: medium impact, VHI: very high impact, HI: High impact

system. It is clear that a system of future 1 in 5 years storm in the 2080s under scenario A1FI receives more water (inflow) and requires more storage capacity, which is increased by 32 % of the present capacity. The maximum storage was reached at the first day of simulation and became nearly constant until the end of the 7-day simulation. The increased inflow in the future ($240{,}361.672 \text{ m}^3/\text{s}$) would lead to an increase in the amount of required storage, but the system would not be able to maintain the extra water and hence would result in more flooding than the base period conditions.
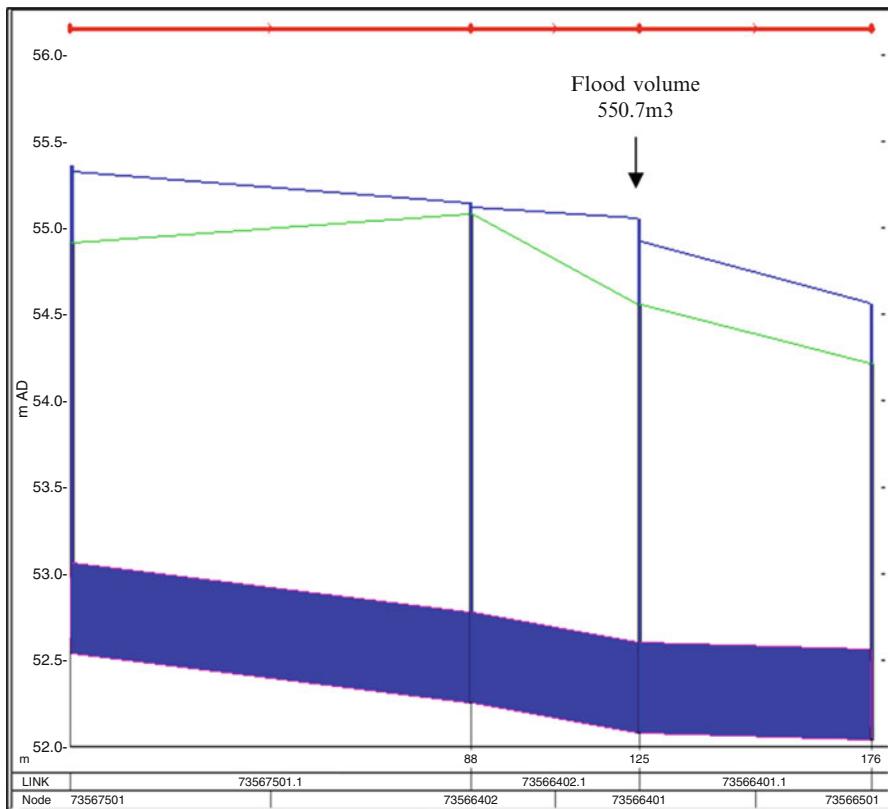
Figure 12.5 shows a longitudinal section of sewers and manholes, where the water level (blue line) is above the ground level (the green line). It indicates that there is surcharge in the pipes as well as manhole surface flooding in winter under scenario A1FI. The node indicated by the arrow in the long section, (Fig. 12.5) which is located in a significant area surrounding with buildings, is the worst flooding manhole in the catchment. The surface flooding volume in this manhole is about 550.7 m^3 which is more than 70 % of that of the base period (1961–1990) as result from 60 min storm duration. Other manholes in the section are less significant to be considered for surface flooding as they are located outside the building area as well as having small flood volumes.

Fig. 12.4 Total inflow, outflow and storage required during future of A1FI scenario in winter 2080s in Crewe network compared with base period (1961–1990)

From the results and analysis presented above, it is seen that climate change (driven by current global warming) is projected to have significant consequences and impacts in the Crewe sewers network. The severity of the impact is reduced with the increase in storm duration due to reduction in its intensity. The impact becomes considerably more significant in surface flooding than in sewer surcharge, depending on manhole location and the flood volume.

There are inherent uncertainties associated with the impact assessment presented here. These uncertainties are associated with the transformation of design storm to runoff using simulation models. These models consider effects of antecedent soil moisture conditions in the catchment before the start of the storm, therefore the uncertainties come from the way these models estimate such antecedent conditions.

Fig. 12.5 Longitudinal sectional view for part of network in built area for 1 in 5 years future 2080s design storm of 60 min under scenario A1FI

12.7 Conclusions

In this chapter, assessment of the future situation in the Crewe urban drainage system under two emission scenarios for climate change is addressed. The simulation is carried on the network for the base period (1961–1990) and future period (2080s). The design storm used in the simulation is a 1 in 5 year return period storm with different durations for winter and summer seasons.

In winter, when applying rainfall uplift of (35–42)% and (16–33)% under scenarios AIFI and B1, respectively, for all considered durations, the maximum water flooding volume from manholes associated with A1FI scenario is to be 144 % more than the base period during the 60 min storm. The corresponding increase in number of surcharged sewers and buildings at risk are increased by 22 % and 36 %, respectively, for this worst condition.

For summer design storms, which are reduced by (6–28)% and (27–39)% under scenarios A1FI and B1, respectively, the least surface flooding volume is 15 % less than that during the base period and occurred in the design storm of duration 1,440 min (24 h) under scenario A1FI. The number of surcharged sewers and properties at risk of flooding are both predicted to decrease during this period.

According to the simulation results presented here, the severity of the climate change impacts are more significant with increase in surface flooding, and that impacts are event-sensitive, as a small increase in rainfall can result in a significant impact.

References

1. Butler D, Davies J (2004) Urban drainage. Spon press, New York, NY
2. Read GF (ed) (2004) Sewers: replacement and new construction. Elsevier, Oxford
3. Glynn S (2005) Climate change in the Northwest and its impacts: a summary document. The Northwest Climate Group, Sustainability Northwest
4. CEA (2007) Reducing the social and economic impact of climate change and natural catastrophes. Insurance Solutions and public-Private Participations, Brussels. Available at: http://www.cea.eu/uploads/DocumentsLibrary/documents/Climate%20Change%20report%20final.pdf.   Accessed Aug 15 2011
5. Ashley R, Newman R, Molyneux-Hodgosn S, Blanksby J (2008) Active learning: building the capacity to adapt urban drainage to climate change. 11th International conference on urban drainage. Edinburgh, Scotland, UK
6. Bradford A, Gharabaghi B (2004) Evolution of Ontario's storm water management planning and design guidance. Water Qual Res Canada J 39(4):343–355
7. IPCC (2000) Special report on emission scenarios summary for policy makers. IPCC, working group III, UK
8. Arisz H, Burrell B (2006) Urban drainage Infrastructure planning and design considering climate change, IEEE, Ottawa, ON, USA, May 10–12 2006
9. Semadeni-Davies A, Hernebring C, Svensson G, Gustafsson L (2005) Development of climate and urban drainage scenarios for impact assessment for Helsingborg, southern Sweden.10th international Conference on Urban Drainage. Copenhagen, Denmark
10. Tait SJ, Ashley RM, Cashman A, Blanksby J, Saul AJ (2008) Sewer system operation into the 21st century, study of selected responses from a UK perspective. Urban Water J 5(1):79–88
11. Evans E, Ashley R, Hall J, Pennining-Rowsell P, Thorne C, Watkinson A (2004) Foresight future flooding. Office of Science and Technology, London
12. Nie L, Lindholm O, Lindholm G, Syversen E (2009) Impacts of climate change on urban drainage systems – a case study in Fredrikstad, Norway. Urban Water J 6(4):323–332
13. Abdellatif M, Atherton W, Alkhaddar R (2012) A Hybrid generalised linear & levenberg-marquardt ANN Approach for downscaling future rainfall. Hydrology Research J. Paper in press doi:10.2166/nh.2013.045
14. United Utilities (2004) Crewe UID Study, Need assessment reports. Report No RT – NW – 2370

15. Baguis P, Boukhris O, Ntegeka V, Roulin E, Willems P, Demarée G (2008) Climate change impact on hydrological extremes along rivers and urban drainage systems. I. Literature review, Belgian Science Policy – SSD research programme, Technical report CCI-HYDR project by KU Leuven – Hydraulics & Royal Meteorological Institute of Belgium
16. Chandler RE, Wheater HS (2002) Analysis of rainfall variability using generalized linear models – a case study from the West of Ireland. Water Resour Res 38(10):1192. doi:10.1029/2001WR000906
17. Pickands J (1975) Statistical inference using extreme order statistics. Ann Stat 3:119–131
18. Titerrington J (2008) Advanced wastewater modeling Course. Unpublished course notes for MWH modelers training, Warrington, UK
19. United Utilities, MWH (2011) Flood risk methodology, AMP5 model maintenance. Users guide notes for MWH engineers, Warrington, UK. Unpublished

Chapter 13
Preliminary Analysis on Phenological Data of Plants in an Urban Environment

Luciano Massetti

Abstract Phenology is the study of the influence of climate on periodic life cycle events of plants and animals, a discipline that has important applications in several research fields like Agrometeorology, Aerobiology, and climate change impact on the environment. Many studies have investigated the relationship between plant phenology and rising temperatures, however, even if the most evident effect of global warming is the increasing of heat island effect in urban areas, a few studies have focused on the impact of climate change on urban plants. In this type of research, monitoring and data collection activities are the most challenging and resource demanding. In 2004, the Institute of Biometeorology started a project aiming to test if the use of an Internet software application could improve phenological data collection by volunteers' participation. A prototype was developed and used to collect observations on the timing of the main phenological phases of plant species commonly widespread in the city of Florence. In this chapter the architecture of the system and the experience of the project is presented. Data on the timing of spring flowering of two species (early spring flowering *Prunus pissardii* and late spring flowering *Tilia x europaea*) are presented. Finally, preliminary results on the analysis of the relationship between the timing of flowering of the two species and the average monthly temperature are discussed.

Keywords Phenology • Flowering • *Prunus pissardii* • *Tilia x europaea* • Citizen Science • Data management • Urban environment • Air temperature • Agrometeorology • Aerobiology • Florence

L. Massetti (✉)
Institute of Biometeorology of the National Research Council, Florence, Italy
e-mail: l.massetti@ibimet.cnr.it

Acronyms

BBCH   Biologische Bundesantalt, Bundessortenamt und Chemische Industrie
BF   Begin of flowering
DOY   Day of the year
EF   End of flowering
EUPOL   Assessment of production, release, distribution and health impact of
         allergenic pollen in Europe
IPCC   Intergovernmental Panel on Climate Change
NDVI   Normalized Difference Vegetation Index
UHI   Urban heat island

13.1 Introduction

One of the major concerns of our society is the impact of Climate Change on ecosystems. Phenology, the study of the influence of climate on periodic life cycle events of plants and animals, is a discipline that has given an important contribution in the evaluation of climate change impacts, so much that an entire section of the IV IPCC Report [1] is based on the results of several phenological studies.

According to "Web of Science," the online academic scientific index provided by Thomson Reuters, since 2007 more than 1,000 papers containing the keyword "phenology" have been published. Some studies focus on the analysis of the relationship between rising temperatures and timing shift of phenological events at either European [2] or worldwide [3] level. The assessment of the phenological shifts of 677 species published in literature reports a significant spring phenophase advancement for 62 % of the cases [3]. Moreover, the analysis of more than 250 European phenological time series of plants and animals undoubtedly confirms that phenology is influenced by temperature regimes during the preceding months [2].

Indeed, air temperature is well recognized as the most important environmental factor regulating the timing of plant phenophases like vegetative bud burst and flowering [4–6]. For this reason, several phenological models based on temperature are used to predict these events. Phenological records are used to develop and validate such models [7, 8]. For similar reasons, phenological data are also used to test and validate Decision Support Systems for agriculture purposes: based on simulation models, they are able to predict and prevent plant disease outbreaks that might negatively affect both production quantity and quality [9].

In Aerobiology, phenological data were used to integrate pollen data. The prevalence of allergic pollen diseases is one of the major causes of a growing rate of morbidity and demand for healthcare (COST action ES0603 EUPOL http://www.unifi.it/COSTEupol/index.html). The presence of allergic pollen in the air is usually estimated with sample trapping methods. However, this methodology only allows a general identification of the parent provenience (at level of genre or family), while phenological data, associated to sampling, can be a useful tool to

define/detail airborne pollen sources such as the plant species. This information can be used to improve pollen forecast [10]. Several studies investigated the correlation between phenological data and aerobiological data of allergenic species [10–12].

Recently, many studies have investigated the effects of climate change and urbanization on plant phenology [13–15]. As urbanization is associated with increasing temperatures and CO_2 concentration, urban climate conditions might be useful to predict the impacts of global warming and evaluating the plant behavior in urban context might provide a low-cost alternative to the current experimental methods about the plant responses to climate change [15, 16].

Nevertheless, air temperature within the urban area may vary significantly due the complexity of the environment morphology [17, 18]. So the impact of urbanization on plant phenology at intra-urban scale is considered an important and challenging research topic by several authors [15, 19].

All these studies are based on the availability of regular observations (at least once a week during the growing season), but a regular data collection is still strongly limited by the personnel costs and the need of a wide distribution of data over large area. Since 1980s satellite data have been used to study regional and global vegetation dynamics [20]. These new technology allowed the implementation of land surface phenology based on indices, like the Normalized Difference Vegetation Index (NDVI, derived by satellite image [20, 21]) or the so-called near remote sensing (based on processing of digital camera images [22]). This discipline tries to address the limitation of field campaign for monitoring although ground observations are still a valuable information to validate the performance of these methods.

Recently, the so-called Citizen Science approach has been considered suitable to address this limitation. Citizen Science is an approach that invites the public to participate in both scientific thinking and data collection, aiding the researchers in the data collection process [23]. This approach is very popular because many WEB 2.0 tools, that provide an easy method to produce and publish information through the Internet, are now available.

In 2004 the Institute of Biometeorology started the project Gilia which aims to collect phenological data on plants and animals following the Citizen Science approach. In this project (http://www.gilia.ibimet.cnr.it), an Internet application that promotes this approach has been developed. In this chapter we present some results of this activity. Firstly the architecture of the system, its evolution and the lesson learnt during this work are presented. Secondly spring flowering data of *Prunus pissardii* and *Tilia x europaea* and the analysis of the relationship with average monthly temperature of the city of Florence are presented.

13.2 Background

The quality of a phenological study is strongly affected by the data collection process and particularly by the availability of reliable data at a suitable spatial and temporal scale. So, the observation protocol, the data collection system and the network of observers should be properly taken into account during a study design.

13.2.1   Observation Protocols

Plant phenophases (leaf budburst, flowering, leaf unfolding . . .) are determined by assessing visually the development stage of the various organs (buds, flowers, leaves). Usually the aim is to identify the calendar date when a phenophase starts (first flowers opened) or when it ends (all flowers fallen or dry) or to assess the degree of development of a certain phase. In both cases, an appropriate protocol should provide an exact definition of each phase to allow a quantitative evaluation of the phenophase as objective as possible. For this purpose many reference scales, depending on the species, have been used [11]. Among them, the extended BBCH-scale [24] is one of the most used. The extended BBCH-scale proposes a system for coding similar growth stages of all plant species. This system is based on a code of two digits. The first digit identifies the phenophase while the second identifies the development stage. For example the code 65 assigned to a tree means that it is in the flowering phase (6) and almost 50 % of the flowers are opened (5). Observations are collected and averaged on a sample of plants to limit the influence of intraspecific variations.

The characteristics of the observation site (geographical location, elevation. . .) and the frequency of the observations should be also considered carefully.

13.2.2   Observation Network and Data Management

Assessing the impact of climate change on plant development requires the availability of a large amount of data that allows to describe properly the spatial and temporal variability of this phenomenon. Therefore, the observation process should be designed to ensure a degree of continuity in time and cover many geographical locations.

However since this activity is very expensive approaches that foster citizen participation, network cooperation and data sharing are spreading. Citizen Science is an effective way to promote people participation. The USA National Phenology Network (http://www.usanpn.org/) and the Nature's Calendar Survey (http://www.naturescalendar.org.uk/) are two of the major organizations that bring together volunteers and provide them with powerful, easy to use and attractive Internet tools to collect and view data. The main features are: data input made pointing and clicking on a map, online data visualization, and access to a huge quantity of training and education material.

This networking approach is also spreading among researchers that work in collaboration and share data to reach a suitable spatial representation of a phenological event: The Italian Phenological Network—http://www.cra-cma.it/iphen/ and the Pan European Phenological Network—http://www.pep725.eu/ are two examples. Indeed software tools and interfaces used by these projects are less mature and developed than those used in Citizen Science. The development of

Internet application and databases could play an important role in enhancing the collection and management of large amount of data. Many phenological archives are still stored in text or spreadsheet files that are not accessible and cannot be easily integrated. Internet application and mobile application can improve data management and dissemination and databases can facilitate the integration of data collected by different networks.
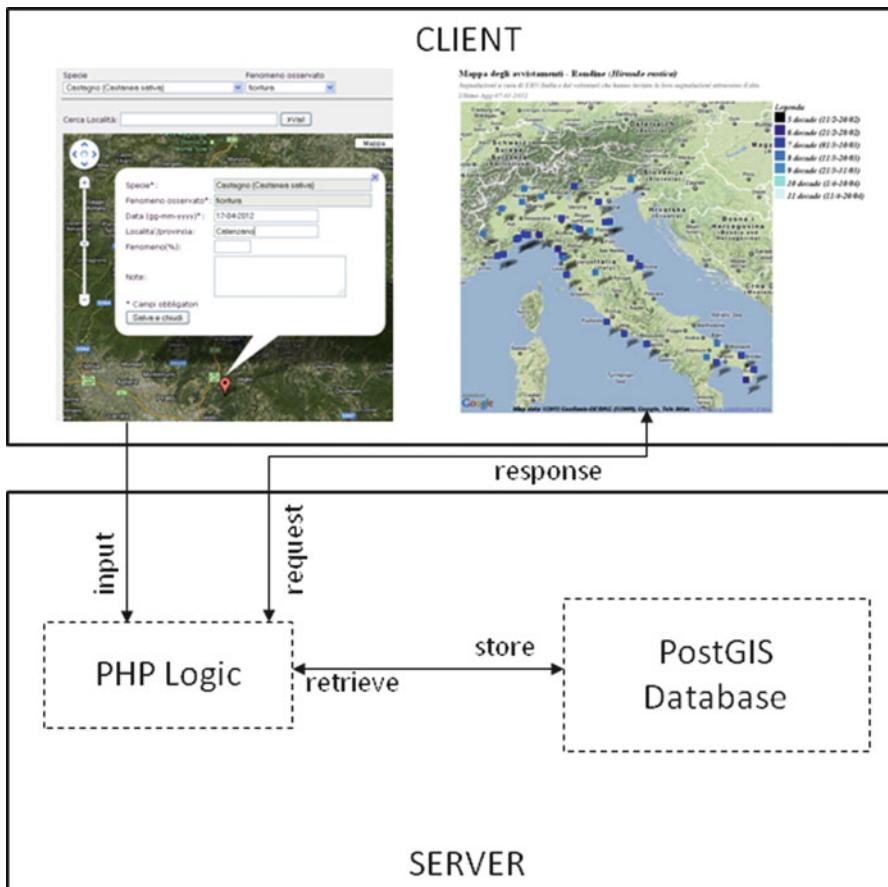
13.2.3   Type of Investigation

Phenological studies can be divided into two broad categories: those studying the relationship between the phenological stage appearance and climatic indices to identify future trend due to climate change and those aiming to develop simulation models to predict the development stage of a plant during the vegetative season.

The first type of studies focuses on the assessment of the start or the end of a phenological stage of a species and the relationship with monthly and seasonal temperature that could explain the inter-annual variability of these phenomena [2, 25]. The second type of studies investigates if plant phenology could be predicted effectively by simulation models based on air temperature. Some of these models only take into account the action of temperature forcing and assume that plants release dormancy when a critical state of forcing is reached These models, called thermal time models, assume that the growth stage of plants is proportional to the temperature forcing calculated as the sum of temperature exceeding a fixed threshold [4, 5, 26–28]. More complex models take into account the prevailing theory, that plants need to be exposed to a certain period with cold temperatures to avoid being induced into early flowering by mild temperatures in winter. These models assume that rest is broken when the accumulation of cold, calculated from the end of the previous growing season, reaches a critical chilling value state [5, 26].

13.3   The Internet Application

In 2004 the Institute of Biometeorology with a network of volunteers started to record the first sighting of Barn swallow (*Hirundo rustica*) during Spring migration from Africa to Italy. Data were collected by email and published regularly into the Web site of the project. In 2005, an Internet software application is designed and developed after the decision to increase the number of monitored species. This application includes an input form that is used both by volunteers and researchers to record their data into a database. These data are processed and presented on maps that are automatically made available into the Web site [29]. In 2008 the application has been further improved and a new prototype has been developed (Fig. 13.1).

Fig. 13.1 System architecture
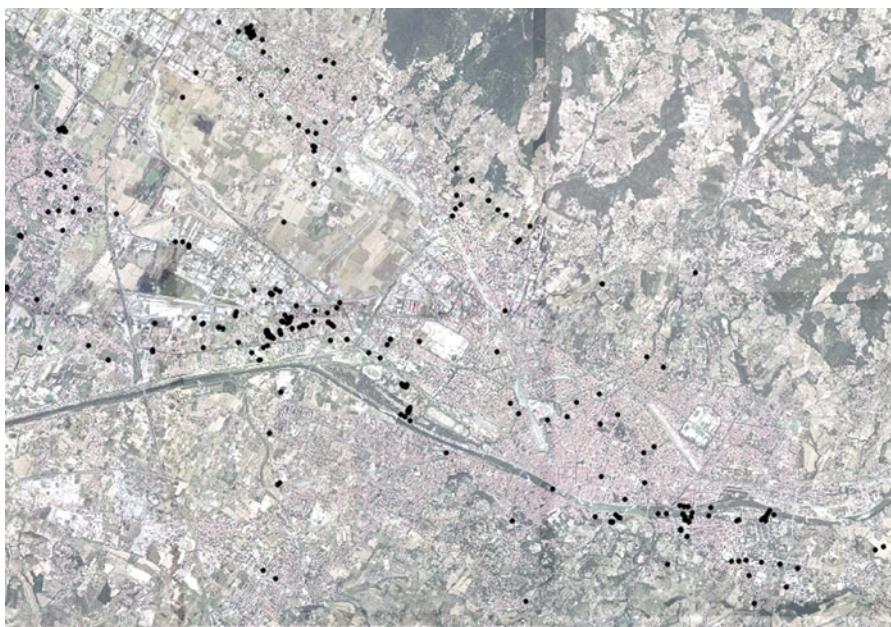
In this prototype the user interface is greatly improved. Data input is performed using Google Maps® interactive maps embedded in our Web pages. Since this version is still not mature enough to be publicly available, the access is limited to users that are registered (the registration is free of charge). The application is developed using open source software (PHP, JavaScript, Google Maps API, and PostGIS for database management). Input layout is designed to minimize the work of the operator and reduce the number of errors. Firstly the user browses the interactive map and points and clicks on the location of the observation. Then he fills in the form with the observation data and sends them to the server. Predefined lists of the species and phenological events are provided to reduce user input. Data is automatically checked for consistency and completeness and then stored into a database. After this process, data can be queried and displayed on thematic maps.

13.4 Data Collection and Methodology

This application is currently used to store data collected by some researchers and a network of birdwatchers which have been collaborating with our Institute since the beginning of the project. The system is used to collect data on phenophases of more than 20 tree species in the urban area of Florence (Fig. 13.2).

Prunus pissardii and *Tilia x europaea* data are selected for this study because these species are of particular interest since they are among the most diffused in public and private green areas of Florence. *Prunus pissardii* is an ornamental tree that flowers in March and is characterized by a purple foliage that it is widely used in public and private gardens for its attractiveness. *Tilia x europaea*, generally known as common lime, is a species used both in gardens and along the main avenues of the city. This tree has a great traditional, historical and cultural importance in many countries in Europe, where it is widely distributed [30]. In Florence *Tilia x europaea* is commonly used for urban vegetation in public parks and along the main streets of the city, in fact, more than 10 % of trees managed by the municipality belongs to this species. As regard the *Tilia x europaea* phenology, in Europe leaf buds start to swell in April and trees generally flower in June [30].

The Date of begin of flowering (BF) and end of flowering (EF) of several individuals located in different parts of the city were observed and recorded since 2006. BF and EF are assessed on each tree following the extended BBCH scale

Fig. 13.2 Distribution of observed trees in the city of Florence

[24]. BF is defined as 10 % flowers opened (code 61 of BBCH) and EF as all flowers fallen or dry and fruit set visible (code 69 of BBCH). Annual BF and EF were calculated as the average BF and EF of the observations for each species. All dates are represented as day of the year (doy). Monthly average temperatures were calculated on daily data collected by the meteorological station of the National Meteorological Service located outside the city center. Data are made publicly available in the framework of the Global Surface Summary of Day Product (http://www.ncdc.noaa.gov/cgi-bin/res40.pl?page=gsod.html). Data collected from 2006 to 2012 are presented and relationship with monthly average temperature is investigated by means of Pearson product–moment correlation.
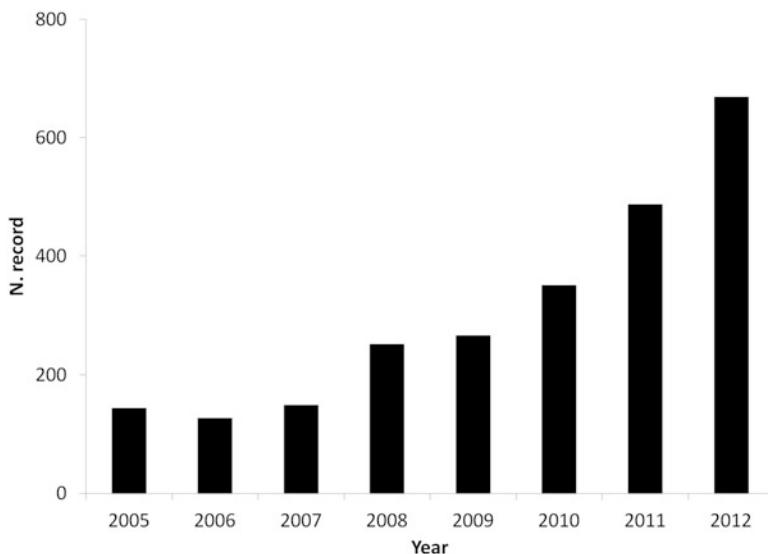
13.5   Results

Since the start of the project, 521 sightseeing dates concerning the Barn swallow first arrival have been provided by volunteers. In the same period 653 individuals of 20 tree species have been monitored by researchers (Table 13.1).

The collection of such a huge amount of data has been facilitated by the improvement of the application. Indeed the sharp increase of stored observations started from 2008 (Fig. 13.3), just when the Google Maps API was embedded in our application.

Table 13.1 Number of individual trees and phenophase observations collected from 2004 to present
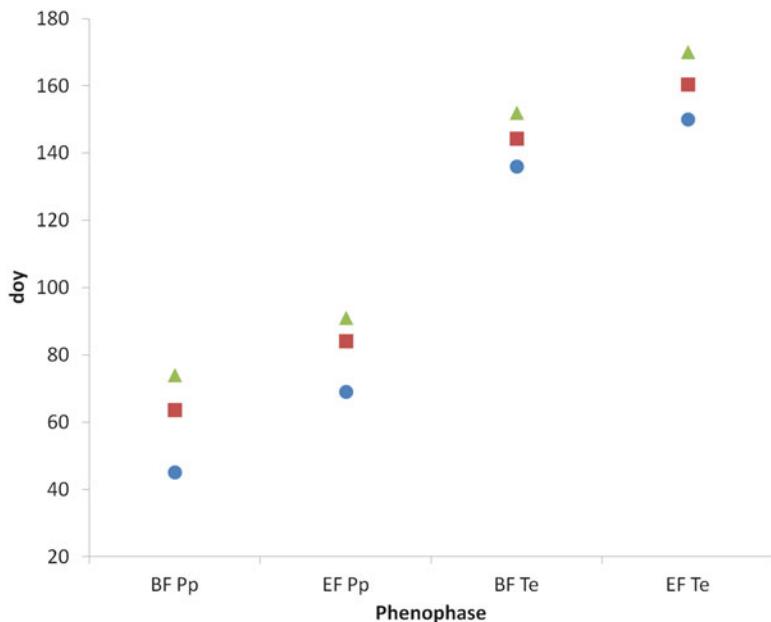
Species	Individuals	Observations
Acacia dealbata	155	375
Celtis australis L.	6	10
Cercis siliquastrum L.	31	91
Cupressus sempervirens L.	9	37
Forsythia spp.	18	29
Malus domestica B.	8	27
Platanus acerifolia	12	46
Populus alba	15	23
Populus nigra	7	28
Prunus armeniaca	35	150
Prunus avium	43	164
Prunus pissardii	51	237
Prunus domestica	19	52
Prunus dulcis	45	66
Prunus persica	15	33
Pyrus communis	8	15
Robinia hispida L.	4	11
Robinia pseudoacacia L:	61	136
Sambucus nigra	50	147
Tilia x europea	61	262
Total	653	1,939

Fig. 13.3 Number of recorded observations per year

Minimum mean and maximum BF and EF dates, expressed as doy, are presented in Fig. 13.4. In the studied period, the earliest date for *Prunus Pissardii* BF (BF: 64 ± 10 doy) was 14th February 2007 (doy 45), while the latest one was 15th March 2012 (doy 74). The earliest and latest dates for EF (EF: 84 ± 8 doy) were respectively 10th March 2007 (doy 69) and 1st April 2006 (doy 91). The duration of flowering varied between 13 days in 2007 and 24 days in 2012. The earliest *Tilia x europaea* BF (BF: 144 ± 5 doy) was 16th May 2007 (doy 136), while the latest one was in 1st June 2010 (doy 152). The earliest and latest dates for End Flowering (EF: 160 ± 6 doy) were respectively 30th May 2007 (doy 150) and 19th June 2010 (doy 170). The duration of flowering varied between 14 days in 2006 and 2007 and 18 days in 2010 and 2011.

Both begin and end of flowering resulted significantly anticipated by higher average temperature recorded during the previous months (Table 13.2). In *Prunus pissardii* BF was significantly correlated to January and February average temperature. EF correlation was only significant with January mean temperature, while the correlation was not significant with February mean temperature although high ($R = 0.69$, $p = 0.08$). *Tilia x europaea* BF and EF were negatively correlated both with March and April mean temperatures. When the thermal regime of the entire season preceding the flowering period was considered (Winter for *Prunus pissardii* and Spring for *Tilia x europaea*), correlation significance was higher than considering the effect of the single months.

Fig. 13.4 Minimum (*circle dot*) mean (*square dot*) and maximum (*triangle dot*) doy for each phenophase in 2006–2012 (*BF* begin flowering, *EF* end flowering, *Pp Prunus pissardii*, *Te Tilia x europaea*)

Table 13.2 Pearson correlation between each phenophase (*BF* begin flowering, *EF* end flowering, *Pp Prunus pissardii*, *Te Tilia x europaea*) and monthly average temperature in Florence (N = 7)

	N	Dec	Jan	Feb	Win	Mar	Apr	May	Spr
BF Pp	7	−0.50	−0.94**	−0.88**	−0.98**	−0.16	–	–	–
EF Pp	7	−0.68	−0.94**	−0.69	−0.96**	−0.45	–	–	–
BF Te	6	–	–	−0.58	–	−0.93**	−0.92**	−0.69	−0.97**
EF Te	6	–	–	−0.73	–	−0.95**	−0.82*	−0.54	−0.86*

*$p < 0.05$, **$p < 0.01$ significance level

13.6 Discussion

One of the main achievements of our project is that a properly designed Internet application system can be an effective tool to manage huge amount of data collected at different locations. For the development of our Web site we have taken into account the following design principles:

- Easy to use interface, since the application can be used by people with no specific skills on database.

- Facilitated data entry, because users are required to enter only the information to provide a complete description of the observed phenomenon and, if possible, the insertion is made by selecting a value from a predefined list (such as the name of the species and phenophase) to reduce the amount of inconsistencies.
- Automatic georeferentiation, provided by Google Maps API.
- No additional software cost: since the system is developed using open source software and the user needs only to have a browser.

In our experience all these features increase greatly the effectiveness of data input as the results show (Fig. 13.3). Furthermore the use of a shared database facilitates the integration of data produced by different sources (scientific organizations, network of volunteers ...) and the georeferentiation allows GIS cross analysis among these data and other GIS data layers (meteorological and climatic data, land use ...). Nevertheless, to reach these goals, some key points should be addressed in the future. First of all, the prototype should be improved to become a complete application (providing full functionality for data input, query, management and visualization). The Web site should also be made more attractive and provide more information and education material about the phenology of the observed species, guidelines and work-sheets to do observations and access to scientific results and publications. The improvement of these features could help to promote Citizen Science and encourage people to join the network and actively participating to monitoring. But this is not enough, even researchers are not always aware of the benefit that can be derived by the use of such a system. Therefore, proper actions should be taken to convince them about the effectiveness of these systems in getting a large and spatially distributed dataset in an easy way. The availability of this application as a mobile application for smartphones and tablets for instance is already giving a big boost to this kind of approach. These issues could be addressed if specific resources are available in the future. Unfortunately they are not available yet, but we believe it is worthwhile investing our time in system improvement and data collection, since the increase of our phenological data series could be useful for investigating future trends.

The analysis of seasonal temperatures and flowering phenology shows strong correlations between both *Prunus pissardii* and *Tilia x europaea* flowering phenophases and monthly and seasonal mean temperatures. Higher significant correlations are found when BF and EF are related to seasonal temperatures preceding the event, suggesting that plant development models should take into account temperature regimes since dormancy as many published phenological models already did [3, 8, 28]. EF correlation was slightly weaker than BF and this could be caused by the presence of wind or rain that might speed up petals fallen and by a larger uncertainty in estimating EF phase by the observers.

However this analysis has some limitations that should be pointed out. The estimate of BF and EF can be strongly influenced both by within species variability and local environmental conditions like urban geometry that can cause strong thermal variation within a city like Florence [18]. To limit the effect of this drawback, we have monitored BF and EF of several individuals at different sites and we have used the

respective average value to represent BF and EF in each year. The length of the data series is also another limitation. 10 years of data is considered the minimum length for this kind of study [2] even though at least 30 years is considered a more suitable length [24]. Seven years of data are very few to draw any conclusion even if both the correlation coefficient and the significance level are very high.

Recently, many studies focus on phenology variability between rural and urban areas due to UHI [31] or the relationship with the level of urbanization [13, 15]. A previous study conducted in Florence shows that average spring difference can be up to 1.7 °C between the coolest and the hottest site [18]. This difference can cause a significant phenological variability within the city if we consider that a previous study shows that a 1.0 °C temperature increase could cause a phenological shift of almost 4 days in several species [25]. In the future our purpose is to continue this activity, focusing on the investigation of the relationship between plant phenology and urban geometry.

13.7   Conclusion

A well-designed Internet application that exploits all the most advanced technological features can have beneficial effects on both quality and quantity of data collection by a monitoring organization and can promote citizen participation to research activities. Furthermore the use of a database for storing data and data georeferentiation facilitate integration of different data sources and cross-analysis with other spatial data layers. Since 2004 we have collected more than 1,900 phenological records and the preliminary analysis of BF and EF data series of *Prunus pissardii* and *Tilia x europaea* shows that both species are significantly influenced by air temperature in the preceding months.

References

1. Parry ML, Canziani OF, Palutikof JP, van der Linden PJ, Hanson CE (2007) Climate change 2007: impacts, adaptation and vulnerability. Cambridge University Press, Cambridge
2. Menzel A, Sparks TH, Estrella N, Koch E, Aasa A, Ahas R, Alm-Kübler K, Bissolli P, Braslavská O, Briede A, Chmielewski FM, Crepinsek Z, Curnel Y, Dahl Å, Defila C, Donnelly A, Filella Y, Jatczak K, Måge F, Mestre A, Nordli Ø, Peñuelas J, Pirinen P, Remišová V, Scheifinger H, Striz M, Susnik A, Van Vliet AJH, Wielgolaski FE, Zach S, Zust A (2006) European phenological response to climate change matches the warming pattern. Global Change Biol 12(10):1969–1976
3. Parmesan C, Yohe G (2002) A globally coherent fingerprint of climate change impacts across natural systems. Nature 421:37–42
4. Cannell MGR, Smith RI (1983) Thermal time, chill days and prediction of budburst in Picea sitchensis. J Appl Ecol 20:951–963
5. Sarvas R (1974) Investigations on the annual cycle of development of forest trees. II. Autumn dormancy and winter dormancy. Commun Inst For Fenn 84:1–101

6. Schleip C, Sparks TH, Estrella N, Menzel A (2009) Spatial variation in onset dates and trends in phenology across Europe. Clim Res 39(3):249–260

7. Cesaraccio C, Spano D, Snyder RL, Duce P (2004) Chilling and forcing model to predict bud-burst of crop and forest species. Agr Forest Meteorol 126:1–13

8. Chuine I, Cour P, Rousseau DD (1999) Selecting models to predict the timing of flowering of temperate trees: implications for tree phenology modelling. Plant Cell Environ 22:1–13

9. Orlandini S, Massetti L, dalla Marta A (2008) An agrometeorological approach for the simulation of plasmopara viticola. Comput Electron Agr 64(2):149

10. Tormo R, Silva I, Gonzalo A, Moreno A, Pérez R, Fernández S (2011) Phenological records as a complement to aerobiological data. Int J Biometeorol 55:51–65

11. Hidalgo PJ, Galán C, Domínguez E (2003) Male phenology of three species of Cupressus: correlation with airborne pollen. Trees 17:336–344

12. Torrigiani Malaspina T, Cecchi L, Morabito M, Onorari M, Domeneghetti MP, Orlandini S (2007) Influence of meteorological conditions on male flower phenology of Cupressus sempervirens and correlation with pollen production in Florence. Trees Struct Func 21:507–514

13. Jochner S, Sparks TH, Estrella N, Menzel A (2012) The influence of altitude and urbanisation on trends and mean dates in phenology (1980-2009). Int J Biometeorol 56:387–394

14. Luo ZK, Sun OJ, Ge QS, Zheng JY, Xu WT (2007) Phenological responses of plants to climate change in an urban environment. Ecol Res 22:507–514

15. Mimet A, Pellissier V, Quénol H, Aguejdad R, Dubreuil V, Rozé F (2009) Urbanisation is associated with early flowering: evidence from Platanus acerifolia and Prunus cerasus. Int J Biometeorol 53:287–298. doi:10.1007/s00484-009-0214-7

16. Ziska LH, Gebhard DE, Frenz DA, Faulkner S, Singer BD, Straka JG (2003) Cities as harbingers of climate change: common ragweed, urbanization, and public health. J Allerg Clin Immun 111:290–295

17. Oke TR (1987) Boundary layer climates. Methuen & Co. Ltd. British Library Cataloguing in Publication Data, Great Britain

18. Petralli M, Massetti L, Orlandini S (2011) Five years of thermal intra-urban monitoring in Florence (Italy) and application of climatological indices. Theor Appl Climatol 104 (3/4):349–356

19. Shochat E, Warren PS, Faeth SH (2006) Future directions in urban ecology. Trends Ecol Evol 21(12):661–662. doi:10.1016/j.tree.2006.09.006

20. Zhang XY, Friedl MA, Schaaf CB, Strahler AH, Hodges JCF, Gao F, Reed BC, Huete A (2003) Monitoring vegetation phenology using MODIS. Remote Sens Environ 84(3):471–475

21. Liang L, Schwartz MD, Fei S (2011) Validating satellite phenology through intensive ground observation and landscape scaling in a mixed seasonal forest. Remote Sens Enviro 115:143–157

22. Richardson AD, Jenkins JP, Braswell BH, Hollinger DY, Ollinger SV, Smith ML (2007) Use of digital webcam images to track spring green-up in a deciduous broadleaf forest. Oecologia 152:323–334

23. Cooper CB, Dickinson J, Phillips T, Bonney R (2007) Citizen science as a tool for conservation in residential ecosystems. Ecol Soc 12:11, http://www.ecologyandsociety.org/vol12/iss2/art11/

24. Estrella N, Sparks TH, Menzel A (2007) Trends and temperature response in the phenology of crops in Germany. Global Change Biol 13(8):1737–1747. doi:10.1111/j.1365-2486.2007.01374.x

25. Hack H, Bleiholder H, Buhr L, Meier U, Schenock-Fricke U, Stauss R, Weber E, Witzenberger A (1992) Einheitliche Codierung der phänologischen Entwicklungsstadien mono- und dikotyler Pflanzen. – Erweiterte BBCH-Skala, Allgemein –.Nachrichtenbl. Deut. Pflanzenschutzd 44(12):265–270

26. Hänninen H (1990) Modelling bud dormancy release in trees from cool and temperate regions. Acta Forest Fenn 213:1–47

27. Hunter AF, Lechowicz MJ (1992) Predicting the timing of budburst in temperate trees. J Appl Ecol 29:597–604
28. Linkosalo T (2000) Mutual regularity of spring phenology of some boreal tree species: predicting with other species and phenological models. Can J Forest Res 30:667–673
29. Massetti L, Brandani G (2007) An internet system for collecting spring phenological observations by a network of users. Ital J Agrometeorol 3:19–23
30. Pigott CD (1991) Biological Flora of the British Isles. No. 174. Tilia cordata Miller. J Ecol 79:1147–1207
31. Neil KL, Landrum L, Wu J (2010) Effects of urbanization on flowering phenology in the metropolitan phoenix region of USA: findings from herbarium records. J Arid Environ 74:440–444. doi:10.1016/j.jaridenv.2009.10.010

Chapter 14
Impacts of Climate Change on Cereal Production in the Setif High Plains (North-East of Algeria)

Mohamed Fenni

Abstract In Setif high plains (north-east of Algeria), the fallow-winter cereals rotation occupies every year more than 80 % of cultivated land. The grain yield average is less than 1,300 kg/ha^{-1}. The study of changes in precipitation in this region shows a tendency to drought, and directly influences the fluctuations of the cereal yields. Dryness in the Setifian high plains is already a reality. The number of dry years during the last 31 years, where precipitations are lower than the average, is 13 years. Variability of precipitation patterns reduces groundwater recharge ability. Cereal crops suffer from winter cold and drought stresses. Available water appeared as the most important factor limiting crop production under the semiarid highland of eastern Algeria. Climate change, as well as increases in climate variability, will alter precipitation, temperature, and evaporation regimes, and will increase the vulnerability of Setif high plains to changes in hydrological cycles. The impacts of climate change on crop production and food security could therefore be drastic. Biotechnological advances in improving crop yields and tolerances to aridity, coupled with climate and weather forecasting, is likely to bring significant payoffs for strategy of adaptation in the field of agricultural water management.

Keywords Climate change • Rainfall variability • Cereals • Drought • Setif • Algeria • Grain • Precipitation • Groundwater recharge ability • Semiarid • Evaporation • Vulnerability • Weather forecasting • Water management • Adaptation

M. Fenni (✉)
Laboratory of Valorisation of Biological and Natural Resources, Faculty of Natural and Life Sciences, University Ferhat Abbas, Sétif 19000, Algeria
e-mail: fennimodz@yahoo.fr

Nomenclature

q/ha	Quintals per hectare
m	Minimum temperature
Tmn	Mean temperature of month
W	Winter
S	Spring
Sm	Summer
A	Autumn

Acronyms

EEA	European Environment Agency
GDP	Gross Domestic Product
IISD	International Institute for Sustainable Development
MAGICC	Model for the Assessment of Greenhouse-gas Induced Climate Change

14.1 Introduction

Agriculture is extremely sensitive to climate change. Heat stress reduces yields significantly, especially in areas where crops are already near their maximum heat tolerance. Climate models show that rainfall patterns and the hydrological cycle will be affected. The drought-prone regions may experience longer dry periods and more stringent which will increase the probability of crop failure in the short term and a decline in long-term production. This models also show consistently that the extreme precipitation events will become more frequent in many areas and that the risk of drought becoming greater over continental areas in summer. In parts of Africa and Asia, the frequency and intensity of droughts seem to have increased [1].

An increase in temperature of 2 °C can cause a reduction in global cereal production by 5 % [2]. In North Africa, losses due to increased temperatures of 2.5 °C will be close to 7 % of GDP per capita by 2100 [3]. Climatic data recorded in this region indicate that the Mediterranean region will be among the areas most affected by the adverse effects of climate change in the world [4].

In Algeria, winter cereals (wheat, barley and oat) are the main crops. The rotation of cereal—fallow occupies each year nearly 80 % of the agricultural area. The average annual yield varies between 5 and 10 q/ha. The situation of cereal cultivation is very difficult, its production has increased only slightly in recent 50 years and today it responds only one third of needs. Natural conditions, especially climate, give the Algerian agriculture its particular character, and largely determine the rural landscape and crop production. The MAGICC model estimates for Algeria a warming of about 1 °C between 2000 and 2020 accompanied by a

fluctuation in rainfall with a downward trend, the order of 5–10 % in the short term [5]. Increased temperatures and fluctuating rainfall patterns will have a direct and negative impact on agriculture of the country.

The main objective of this chapter is to analyze the effect of variations of precipitation and temperature on yields of winter cereals in the Setif High Plains, north east of Algeria.

14.2   Materials and Methods

The Setif high plains climate is semiarid with rainy cold winters and dry and hot summers. The average altitude varies between 900 and 1,000 m. In general, soils are yellowish white to reddish trained exclusively on limestone rocks. They have low organic matter content, and a high concentration of $CaCO_3$ (20–30 %).

The dominant farming system in the high plains of Setif is the association of cereal–sheep. The cattle are mainly fed on stubble and fallow land. The rainfed grain speculation is by far the most practiced. The average area of cereals (wheat, barley, and oats) for the period 1996–2011 was 170,000 ha; the average area of fallow was 137,000 ha, representing successively 47 and 38 % of the area used for agriculture.
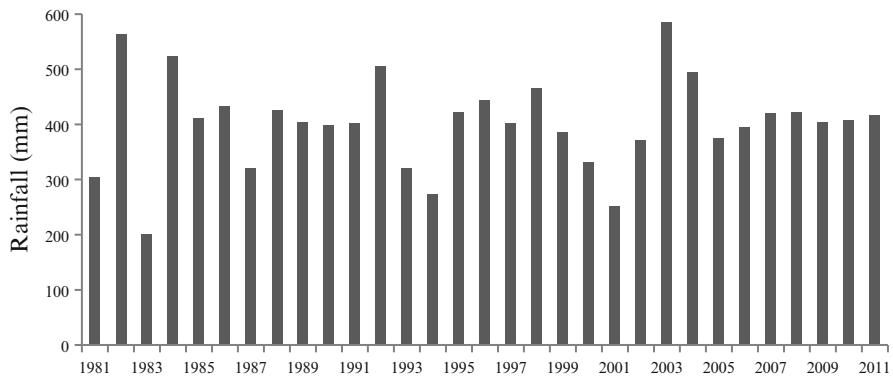
Climate data used in this study are monthly and annual precipitation and temperatures for the period 1981–2011 recorded at the meteorological station of Setif (altitude 1,000 m, $36°9'$ N and $5°21'$ E). We also used data of Selzer [6] for the period 1913–1938. The data of cereals yields (wheat, barley, and oats) are collected from Agricultural Services of Setif for the period 1996–2011. In this chapter, we analyze the variations in rainfall and temperatures, and their effects on yield variations of cereals.

14.3   Results and Discussion

Although the concept of average rainfall gives a general overview of the real climate, particularly in the Mediterranean region, his knowledge is still needed. The analysis of rainfall data shows for the Setif region an annual average of 469 mm for the period 1913–1938 and 402 mm for the period 1981–2011. The difference between these two periods, which represent the beginning and almost the end of the twentieth century, is 67 mm, a decrease of 15 % (Table 14.1). For both climatic series, July and August, are in order, the driest months of the year. Furthermore, November, December, and January are the wettest months. Nearly 90 % of precipitation occurs from October to May. According to forecasts by the European Environment Agency (EEA), published in his report of May 3, 2012; precipitation will fall by nearly 15 % in southern Europe between 2021 and 2050, and 30 % in North Africa [1].

Table 14.1 Monthly and annual rainfall means (mm) at Setif station

	Jan	Feb	Mar	Apr	May	Jun	Jul	Aug	Sep	Oct	Nov	Dec
P1[a]	60.0	45.0	43.0	36.0	51.0	28.0	11.0	14.0	37.0	39.0	53.0	52.0
P2[b]	39.7	35.7	35.2	42	45.4	21.3	12.1	14.3	41.2	33.4	35.4	46.2
P3[c]	30.8	27.9	23.1	24.7	37.6	14.6	13.5	14.8	36.7	28.7	37.4	42.7

[a]P1: 25 years (1913–1938)
[b]P2: 31 years (1981–2011)
[c]P3: 13 dry years

Fig. 14.1 Variation of annual rainfall (mm) at Setif station for the period 1981–2011

The analysis of rainfall distribution for the period 1981–2011 shows a double variation: seasonal and especially interannual. The highest rainfall (585 mm) are recorded in 2003, and the lowest (200 mm) in 1983 (Fig. 14.1). The number of years, during this period when rainfall was below average, is 13 years. The average rainfall for these 13 years of drought is 332 mm, representing a difference of 70 mm compared to the average of the period 1981–2011.

The annual rainfall regime was SWASm for the period 1981–2011 and AWSSm for the period of 13 years of drought (Table 14.2), during which the spring and winter, which are very important for crops, were relative to those for the period 1981–2011 very dry. Climate data recorded in the Maghreb region during the twentieth century indicate an increase in number of dry years. So we went from a drought every 10 years earlier in the century to 5–6 years of drought currently [7, 8].

The temperatures act throughout the development cycle of crops. Unlike the rainy seasons, the thermal seasons are clearly trenches in both periods. The annual averages of mean temperatures for the period 1981–2011 and the 13 dry years are respectively 15.1 °C and 15.3 °C. The hot season extends from May to October, months when average monthly temperatures are above annual average (Table 14.3, Table 14.4). The maximum temperature is reached in July and August around 33 °C and the minimum is in January, it is between 1 and 2 °C. Minimum temperature (m) indicates the frequency of frosts and the severity of winter. The period of frost begins in late October and

Table 14.2 Rainfall regimes

	Precipitation (mm)				
Periods	Winter (W)	Spring (S)	Summer (Sm)	Autumn (A)	Year
31 years (1981–2011)	121.6	122.9	47.7	110	402
13 dry years	101.4	85.4	42.9	102.8	332
Difference between the two periods	20.2	37.5	4.8	7.2	70

Table 14.3 Temperature means (°C) at Setif station for the period 1981–2011 (31 years)

	Jan	Feb	Mar	Apr	May	Jun	Jul	Aug	Sep	Oct	Nov	Dec
Tmin	1.7	2.2	4.5	6.8	11.2	16	19.6	19.5	15.4	11.4	6.3	2.8
Tmx	9.6	11.1	14.2	17.4	23.0	29.3	33.5	32.8	27.1	21.3	14.8	10.5
Tmn	5.6	6.6	9.3	12.1	17.1	22.6	26.5	26.1	21.2	16.3	10.5	6.6

Tmin minimum temperature, *Tmx* maximum temperature, *Tmn* mean temperature

Table 14.4 Temperature means (°C) at Setif station for 13 dry years

	Jan	Feb	Mar	Apr	May	Jun	Jul	Aug	Sep	Oct	Nov	Dec
Tmin	1.1	1.7	5.2	7.0	11.8	16.7	19.4	19.5	15.8	12.1	6.0	2.7
Tmx	9.3	10.7	15.3	18.0	24.0	30.1	33.3	32.7	27.6	22.3	14.4	10.5
Tmn	5.2	6.2	10.2	12.5	17.9	23.4	26.3	26.1	21.7	17.2	10.2	6.6

Tmin minimum temperature, *Tmx* maximum temperature, *Tmn* mean temperature

continues until April, the maximum is observed in winter, the growing cycle of crops experiencing interruptions of short duration during this cold and wet season. The frosts occur on average 60 days/year.

The combination of the two major climatic factors, temperature and precipitation, is interesting because it determines the really dry months, which correspond according to the definition of Bagnouls and Gaussen [9] to months where monthly rainfall is less than or equal to double mean temperature of same month, P mm $\leq$ 2Tmn °C. During the period 1981–2011, dry months were June, July, August, and September, while during the 13 years of drought, the dry season was longer, and it lasts from April to October, nearly 7 months.

The grain yield average on 15 years (1997–2011) is about 12 quintals per hectare (q/ha), with very large variations: near 21 q/ha in 2003 and 2011, but only about 4 q/ha in 1997, 1999, and 2002. The cereal that has proved most suitable for the climate of this period is barley, which recorded an average yield of 13.8 q/ha (Table 14.5). In general, these yields are very low compared to those recorded in most Mediterranean countries [10].

Eight years of the period 1997–2011 have recorded lower yields than the overall average. The yields obtained during these drought years have fallen compared to the average of 15 years of 40 % for wheat, 45 % for barley, and 43 % for oats (Table 14.5). In terms of timing, there is a clear correlation between the years when

Table 14.5 Average yield of winter cereals (q/ha)

Periods	Wheat	Barley	Oat	Average
15 years (1997–2011)	12	13.8	11.2	12.3
8 dry years	7.2	7.5	6.4	7
Reduction in yield %	40	45	43	43

winter cereals have recorded low yields and climatically dry years, especially during the months of April and May which correspond to the development and grain filling of cereal. The vulnerability of Southern countries of the Mediterranean to climate change depends on the part of their climate-sensitive economy. Thus, costs may be greater in agricultural countries [11].

14.4   Conclusions

The main factor limiting yields of winter cereals in the Setif high plains is variability of precipitation patterns. In dry years, the rainfall decreases of more than 15 %, the received rain is inadequately distributed and does not match the water needs of cereals, then the yields fall by over 40 % compared to the average. The improved farming techniques and the use of fertilizers and pesticides are not valued in those years. These variations in rainfall and crop yields, in the sense of decreasing, represent a transition to a climate less favorable to the cultivation of cereals in the Setif high plains under the current agricultural conditions. Reducing global emissions of greenhouse gases may limit the magnitude of climate change in the long term, but in short term, the development of adaptation strategies is essential to reduce the expected damage. To adapting the current agricultural system to climate change and cope with less water or with water at other periods of the year, we have to find a more suitable plant material and agricultural techniques that can cope with future climatic conditions. On the other hand we have to encourage and develop all processes that contribute in some way directly or indirectly to limit climate change.

References

1. http://www.eea.europa.eu. Accessed May 4, 2012
2. Stern N (2006) The economics of climate change. The stern review. Cambridge University Press, Cambridge
3. Lafi M (2009) Vulnérabilité de la céréaliculture tunisienne face aux changements climatiques. Energy, Climate Change, and Sustainable Development Conference, Tunisia
4. Agoumi A (2003) Vulnérabilité des pays du Maghreb face aux changements climatiques. Climate Change Knowledge Network. http://www.cckn.net.
5. Lakhdari H (2009) Les conséquences du changement climatique sur le Développement de l'agriculture en Algérie: Quelles stratégies d'adaptation face à la rareté de l'eau ? Énergie, Changements Climatiques et Développement Durable Conférence, Tunisie

6. Seltzer P (1946) Le climat de l'Algérie. Institut Météorologique Physique du Globe-Carbonnel, Alger, 219
7. Giannakopoulos CP, LeSager M, Bindi M, Moriondo M, Kostopoulou E, Goodess CM (2009) Climatic changes and associated impacts in the Mediterranean resulting from a 2°C global warming. Global Planet Change 68:209–224
8. http://www.iisd.org. Accessed May 5, 2012
9. Bagnouls F, Gaussen H (1953) Saison sèche et indice xérothermique. Bull Soc Hist Nat de Toulouse 88:193–240
10. http://faostat.fao.org. Accessed Apr 28, 2012
11. Fischer G, Shah M, Velthuizen H (2002) Climate change and agricultural vulnerability. International Institute for Applied Systems, Analysis, Laxenburg

Chapter 15
Environmental Impact of Soil Microorganisms on Global Change

Mohammadali Khalvati and Ibrahim Dincer

Abstract The following review introduces a novel environmental factor—Biomonitoring as a tool for the detoxification of soil contaminants by soil microorganisms. They contribute plant to increase pollutants resistance and caused by global warming. They function by detoxifying heavy hydrocarbon compounds and converting them to a soil protein called glomalin (glomalin-related soil protein—GRSP) whose content has been determined recently. It is proposed to be correlated by the abundance and activity of the soil beneficial microorganisms such as arbuscular mycorrhizal fungi (AMF) in some natural contaminated sites around the world. Recently our finding indicated that the combination of environmental stresses (e.g., pharmaceuticals compounds in the waste water, herbicide compounds, and drought) may enhance the symbiotic efficiencies and the synergistic beneficial interactions of the dominant plant species. The aim of this review is to highlight some recent advances in soil microorganism impacts on the contaminants detoxification as global changing main factor to enhance environmental quality against the global warming. Another approach in this review is to improve the understanding of the processes behind the global change, which will contribute to better maintenance of optimum environmental quality, an important component of soil fertility, and therefore is of increasing interest in the sustainable management of marginal and sensitive low-input soils. Our objectives are to discuss possible functioning of detoxification, allocation and partitioning of soil pollutants by AMF and their possible conjugation to glomalin soil protein.

M. Khalvati (✉)
Department of Biology, Queens University, BioSciences Complex,
116 Barrie st. Kingston, Ontario, Canada K7L3N6
e-mail: mk140@queensu.ca

I. Dincer
Faculty of Engineering and Applied Science, University of Ontario Institute of Technology,
2000 Simcoe Street North, Oshawa, ON, Canada L1H 7K4
e-mail: Ibrahim.Dincer@uoit.ca

Keywords Global change • Glomalin-related soil protein (GRSP) • Soil microorganism • Environmental pollution • Biomonitoring • Soil contaminants • Arbuscular mycorrhizal fungi • Pharmaceuticals compounds • Detoxification • Soil fertility • Soil pollutants

Nomenclature

AMF	Arbuscular mycorrhizal fungi
CDNB	1-chloro, 2,4-dinitrobenzene
DCNB	1,2-Dichloro-4-nitrobenzene
DNA	Deoxyribonucleic acid
GRSP	Glomalin-related soil protein
GST	Glutathione S-transferases
HEAR	High Erucic Acid Rapeseed
HM	Heavy metals
ITS	Internal transcribed spacer
KCS	b-Ketoacyl-CoA synthase
MCB	Monochlorobimane
PCR	Polymerase chain reaction
PGPR	Plant-growth-promoting
p-NBoC	1,2-Dichloro-4-nitrobenzoyl-chloride
rDNA	Recombinant DNA
RNA	Ribonucleic acid
rRNA	Ribosomal ribonucleic acid
SOM	Soil organic maters
TAGs	Triacylglycerols
USDA	United States Department of Agriculture

15.1 Introduction

The Earth's lower atmosphere, the troposphere (up to ~15 km thick) [1], consists of a blanket-like layer of gases the keeps the earth warm. As a political and societal point of view following to the 2006 climate summit, the European Union formally set the goal of limiting global warming to 2 °C. But even today, climate change is already affecting people and ecosystems. Examples are melting glaciers and polar ice, reports about thawing permafrost areas, dying coral reefs, rising sea levels, changing ecosystems and fatal heat periods. The Stern review provides a concise overview of the global climate change and addresses the issue of increasing atmospheric CO_2 concentrations caused by human activities. Within the last 150 years, CO_2 levels have risen from 280 ppm to currently over 400 ppm [2].

The review notes that if we continue on our present course, the CO_2 equivalent levels could approach 600 ppm by 2035. However, if CO_2 levels were not stabilized

at the 450–550 ppm level, the consequences could be quite severe. Hence, if we do not act now, the opportunity to stabilize at even 550 ppm is likely to slip away. Long-term stabilization will require that CO_2 emissions ultimately be reduced to more than 80 % below the current levels. Such a reduction will require major changes in how we operate. Carbon dioxide concentrations will not start falling unless a stronger agreement than the Kyoto Protocol materializes. Reducing greenhouse gases from burning fossil fuels seems to be the most promising approach to counterbalance the dramatic climate changes we would face in the near future. It is clear since the Kyoto protocol that the availability of fossil carbon resources will not match our future requirements. Furthermore, the distribution of fossil carbon sources around the globe makes them an even less reliable source in the future. Together with the economic fact that energy and raw material prices have drastically increased over the last decade they necessitate the development and the establishment of alternative concepts.

15.2 Background Soil Microorganisms and Global Change

Soil structure is a component of environmental ecosystem which may be influenced by the following factors:

- Vegetation cover and plant community structure are easily damaged and difficult to recover.
- Soils are often deficient in humus and/or nutrients especially P.
- Soil nutrients and organic matter are often low and easily lost.
- There are seasonal and/or diurnal extremes of temperature.
- Precipitation falls in short periods, commonly intense and erosive.
- Strong winds and bush fires are a risk, etc.

Scientist conducted two long-term experiments in a Mediterranean ecosystem, which demonstrated that inoculation with indigenous soil microorganism not only enhanced establishment of key plant species but also increased soil fertility and environmental quality [3]. Such symbiosis have increased soil nitrogen (N) content, organic matter and hydrostable soil aggregates, and enhanced nutrient-transfer among plant-species associated with the natural succession. It was concluded that the introduction of target indigenous species of plants associated with a managed community of microbial systems was a successful tool to aid the recovery of low vegetative ecosystems. In this chapter, the diversity of soil microorganism species relevant to the context of the present project is first presented, and then the postulated mechanisms of soil structure-development are reviewed. The fact that colonized plants are better able to obtain their nourishments in the resist environmental stresses gives microbial symbioses a biofertilizing and environmental stability role. In ecosystem, the increased uptake of soil minerals by colonized plants means that it is possible to consider substantially reducing applications of fertilizers and at the same time obtain equivalent or even higher crop yields.

Through appropriate management of microorganism in ecosystems, it is also possible to maintain environmental quality and increasing organic matters and sustainability which protecting the environment over the long term and reducing costs of production.

To reach an ecophysiological understanding of species coexistence is a most important challenge in modern ecology. Soil microorganisms, in particular, can modify the process of soil biological aspects—a key factor on the concept of "environmental quality"—through their effects on the physiology of host plants, their own activity, and their association with microbial N_2 fixing organisms. Indeed, it has been suggested that soil content of glomalin may be an indicator of "environmental health". However, the mechanisms controlling glomalin production by soil microorganism are still little understood. Furthermore, although ample functioning is suspected, little evidence is available on extent of their role in the glomalin production in soil. Recent publications dealing with responses to soil instability (erosion) and contaminated soil by high concentrations of hydrocarbon compounds and global warming are analyzed as to whether the results fit the concept. In general, an initial stress response was related to change in the soil organic maters (SOM) and appear as glomalin in mycorrhizosphere whereas acclimation was marked by increasing glomalin concentrations, increased related enzymes activities, and/or a more reduced redox state of glomalin.

Another approach in this proposal is to improve understanding of the processes behind the global change which will contribute to better maintenance of optimum soil quality, an important component of soil fertility, and therefore is of increasing interest in the sustainable management of marginal soils. Soil microorganism, in particular, can modify the process of soil biological aspects—a key factor on the concept of "environmental quality"—by mitigating soil organic compounds to soil proteins such as glomalin. The pathway is supposed to be applied by the operation of entire detoxification pathway through glomalin-conjugate in the mycorrhizosphere.

A further goal of this chapter is to introduce data on the well-developed plant metabolisms and proteomics analysis of some soil–plant ecosystems, which is common at each ecosystem. Regarding this point sampling methods have been carefully discussed in our recently published phytoremediation book [4], where such complex data on the physical–chemical–biological soil-characterization is not frequent. Among the soil biological tools the involvement of the PCR-based genetically investigations is increasing nowadays.

Recently, predominant plant and soil microorganism species have been tested for the general hypothesis that quality and quantity of glomalin depends strongly on the combination of particular soil microorganism genotypes and the presence or absence of N_2 fixing bacteria. In this chapter we highlight the benefit from the high complementarily of the participants—with ample experience in conducting field studies in environmental biology, with novel and proprietary molecular tools aimed at identifying AMF, and with expertise in the analysis of glomalin. The review is able to contribute to the topics global change and management as: Use of natural resources or matching with sustainable energy: To enhance the fertility and stability

of environment by implement of microbial resources, increase in biological diversity and the health of soil ecosystem and create sustainable energy supplement. Furthermore, improvement in our understanding of the global change and impact of soil microorganism to improve environmental tensions like soil pollutions.

Regarding the above points, research and development seem to be required to improve existing measures of the environmental quality at several environment–plant ecosystems. The following research gaps are to be considered:

1. Process underlying environmental functions
2. Spatial and temporal changes in environmental processes
3. Ecological, economic and social drivers of environment threats
4. Operational procedures and technologies for environmental protection and/or restoration

15.3 Soil Microorganisms' Symbioses Phenomena

It is a well-established fact that the majority of terrestrial plant roots (at about 80 %) live in a symbiosis with soil fungi and form structures called mycorrhiza. Today, arbuscular mycorrhizal fungi (AMF) are found in all ecosystems, regardless of the type of soil, vegetation or growing conditions. AMF are microscopic soil fungi which simultaneously colonize the plant and environment spread out up to several centimetres into the soil proper in the form of ramified filaments. Given that the majority of cultivated plants used for human and animal food purposes are colonized by soil microbes like AMF, one could consider utilizing this symbiosis for the benefit of agriculture and environment by selecting the best plant–fungus combinations [5]. This could promote production of healthier cropping systems and reduce the use of chemical inputs (fertilizers and pesticides), while ensuring crop profitability and environmental quality. It has been shown that the diversity of AMF is an important determinant of plant diversity and productivity [6, 7]. Majority of current research deals with outcomes of hypothetical situations of reduced or eliminated soil microorganism activity versus when it occurs. Some microorganism like AMF fungi can adapt to physical and chemical changes of soil, the amount and possible type, of external hyphae of some species of AMF fungi is affected by other microorganisms, root exudates, pests, clay content, pH, organic matter, nutrient content of soil and possible changes of the surface of the hyphae and the soil bulk density and other physical status as much as environmental stress like as drought and salinity [8–10]. However, beyond its conceptual merit, changes in AMF population might actually occur in ecosystems subjected to severe and prolonged soil mismanagement, disturbance or at any stress-conditions.

There is, however, another important dimension to soil microorganism research, namely that the fungal isolates and species. It has been known that the composition of the fungal community could change in the less disturbed (ploughed) soils as is the

case in the so-called no-till cultivation. It is thus conceivable that in soils subjected to mismanagement also a shift in the composition of fungal communities may take place the outcome of which is not known. There are, however, indications that different isolates of AMF may differ in their effects on the stability of soil aggregate in water [11–13]. This ability should be in relation with the adaptation to the conditions of the certain ecosystems, including its multifactorial manner. Adaptation therefore can be the result of a stress-pressure and a stress-selection procedure, where both the macrosymbiont and microsymbiont partners can change their ecophysiological character finally. Several previous experiments from different European laboratories have shown that indigenous well-adapted strains can confer their tolerance to the host-plants [14–17]. We confirm therefore that strains originating from a particular stress-condition are more appropriate for the stress-alleviation during the symbiosis with its hosts. This finding can develop a new stage and a new area for the microbial inoculations in the agriculture and the environment nowadays.

15.4 Methodological Approaches

Quantification of soil microorganism biomass and presence in field soils is hindered by tedious techniques. Recently, researchers have documented large differences in soil microbiota communities associated with the different AMF strains. Currently glomalin is operationally defined, meaning that the identification of this protein rests on the methods used to extract it (citric acid buffer, autoclaving at pH of either 7.0 or 8.0) and the assays (Bradford method/enzyme-linked immunosorbent assay) used for quantification [18]. Among the biochemical markers the glomalin-related soil protein (GRSP) assay can show a particular promise, due to the fact, that glomalin identification resting solely on the methods used to extract it from the soil. According to the current assumption technologies the most non-heat stable soil proteins are destroyed during the harsh extraction procedure. This critical assumption of glomalin is a safe and trustable measurement; however it has not been tested yet, according to our knowledge, especially as influencing the role of these symbionts in soil quality [19].

15.4.1 Complex Soil and Plant Sampling Methods and Metabolic Profiling of Plant Proteomics

Analyses of xenobiotics and complex biological/environmental sample mixtures require state-of-the-art instruments that can resolve different components of a mixture, provide individual molecular identities, yield relative abundance or concentration information, and unravel potential interactions among the various

constituents of the sample at a high level of confidence. Performance characteristics of modern instruments are continuously improved to address analytical requirements in emerging areas of science, including "x-omics". Ideally, for comprehensive characterization of a complex ensemble and in system biology studies, three general questions regarding: (a) types, (b) concentrations, and (c) nature of the interactions of all individual components of the mixture under investigation, must be addressed (as a function of time).

Numerous organic xenobiotics and xenobiotic organic pollutants are detoxified in plants to glutathione conjugates. Following these enzyme catalyzed reactions, xenobiotic GS-conjugates are thought to be compartmentalized in the vacuole of plant cells. These xenobiotics may interact deleteriously with an organism, causing toxic and in animal sometimes carcinogenic effects. Nevertheless, plants are able to detoxify organic pollutants by conjugation reactions, e.g. mediated by glutathione S-transferases (GST). Some GSTs are constitutively expressed in certain tissues, but GST regulation can be modified by agrochemicals, including herbicide safeners (antidotes) and synergists. It is hypothesized that plant GST gene promotes have multiple regulatory elements that respond differently to specific or more general stress-related singles [20]. The role of GSTs and GSH (glutathione) in plants may encompass several major functions. The first is the metabolism of secondary products, including cinnamic acid [21] and anthocyanins [22]. A second function may be the regulation and transport of both endogenous and exogenous compounds which are often GS-X tagged for compartmentalization in the vacuole or cell wall [23]. This is a particularly important aspect for herbicides [24], anthocyanins [22] and indole-3-acetic acid [25]. Protection against oxidative stress from herbicides, air pollutants [26], pathogen attack [27], and heavy metal exposure [28, 29] may be their third and most important function.

It is generally accepted that xenobiotic glutathione conjugates are sequestered in the vacuole of leaves. However, recent literature documents that vacuolar storage might be either an alternative or temporary stage in the fate of xenobiotic, as evidence accumulates for plasmalemma transporters for xenobiotic and extracellular degradation enzymes. Recently, we have been able to present evidence for long range transport of conjugates in barley plants. From these data, it becomes clear, that a significant fraction of the resulting metabolites reaches the plant growth environment, where they may impact other plants' roots and microorganisms in the root zone. In this proposal specific enzymes and processes including glutathione and other conjugation mechanisms will be investigated in microbial symbiosis plants and bacterial cultures. The proposal also highlights concepts of degradation in myco-bacteriosphere, organic xenobiotics metabolisms and in vitro methods for studying organic xenobiotics biotransformation. It is expected that this study will enlarge current knowledge of the metabolic action on organic xenobiotic in the manner that will be useful to further research on soil microorganisms.

Our recent study on detoxification of organic xenobiotics by symbiosis plants showed detoxifying phenomena in association with microorganisms [30]. The beneficial symbiosis obtains a capability to use conjugation reactions, e.g. mediated by glutathione S-transferases (GST). A significant fraction of the resulting
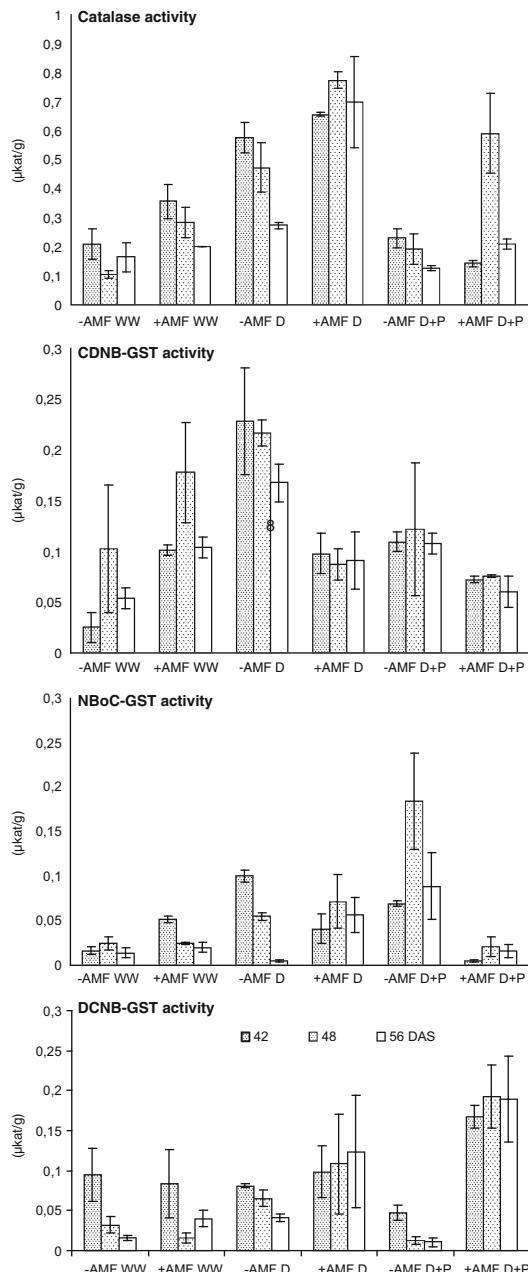
metabolites reaches the plant growth environment, where they may impact other plants' roots and microorganisms in the root zone. In this work we investigated the influence of a xenobiotic conjugate, dinitrobenzene–glutathione, on non-mycorrhizal hairy root of barley (*Hordeum vulgar* L.) and roots colonized with *Glomus hoi*. When hairy roots were incubated with glutathione conjugates, we found that GST-CDNB activity and dichloromethane detoxification were transiently induced during the first 18 hrs of treatment (Fig. 15.1) [30]. The roots colonized with fungi reacted faster than non-mycorrhizal roots. The roots were able to reduce conjugation of DCNB with glutathione at the cost of p-NBoC activity [30]. These observations are the first report on synergistic impacts of a soil fungus and a xenobiotic conjugate on plant roots since crucial studies on soil microorganisms' role in plant growth environment region has not yet been reported earlier. This symbiosis enables plants to change the detoxification capacity of plant roots significantly.

Averagely, 55 % of barley roots have the microorganism *Glomus hoi* at the end of 4 weeks of plant growth. For study in a fluorescence microscope, roots of barley seedlings were cut under water, and the end at which the conjugate was applied was fixed in an aperture with a thin latex foil and transferred into a drop of water on a cover slide. Monochlorobimane (MCB), a model xenobiotic, is conjugated rapidly at the tip of mycorrhizal root. In the present study, evidence is presented from experiments with mycorrhizal roots of barley that a part of these conjugates will undertake long range transport in extraradical hyphae and spores of mycorrhizal fungi and follow individual metabolisms.

15.4.2 Production of Glomalin and Parallel Measures of Soil Microorganisms' Occurrence

As a consequence, biochemical markers such as ergosterol, chitin and also the glomalin have been considered for the study of AMF. Because several organisms produce ergosterol and chitin, their usage as microorganism indicators is somewhat limited [31]. Furthermore, other researchers found that AMF may not contain ergosterol [32]. The C allocated to AMF and thus their contribution to soil C could particularly high in the semi-arid because of the low nutrient levels in highly weathered tropical soils [32]. One of the compounds produced by soil microorganisms is a recalcitrant glycoprotein, glomalin [33]. Concentrations of glomalin range from 2 to 15 mg g^{-1} of soil in temperate climates [33, 34] and over 60 mg cm^{-3} was found in a chronosequence of Hawaiian soils [18]. In addition to containing substantial carbon (and up to 5 % iron; Nichols, Wright and Dzantor, unpublished data), glomalin enhances soil aggregation [19, 34, 35]. AMF hyphal growth has been related to GRSP production in sand cores from tropical forest soils [36] and horticultural mesh traps from field soils [37]. The gene for the AMF

Fig. 15.1 GST activities in the roots of soil microorganism (AMF) plants and plants without microorganism symbiosis (non-AMF or Control) under conditions of well-watered (WW), drought (D) and a combination of drought and pharmaceutical stress (D + P). Plants were harvested 42 (*grey bars*), 48 (*dotted bars*) and 56 days after sowing (*empty bars*) after sowing (*Error bars* represent standard deviation) [30]

protein glomalin has recently been sequenced in our laboratory; yet it remains difficult to assess the relationship between GRSP obtained from soil and glomalin. Hence a new nomenclature has been introduced [16], clearly separating glomalin from soil derived protein pools (GRSP).
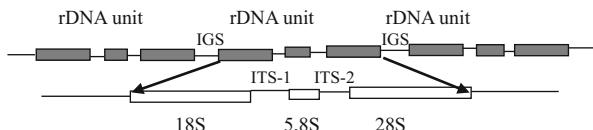
15.5 Which Techniques Can Be Used to Study the AMF in the Soil–Plant Ecosystems? (Morphology vs Molecular Identification)

AMF hyphae are coenocytic, and asexual spores form on the termini of hyphae. These spores may contain hundreds to thousands of nuclei per spore [38]. The spores are the only form by which individual species can be identified on the basis of morphological characteristics [39]. Several studies have shown that genetic diversity of the internal transcribed spacer (ITS) exists among and within single spores [40, 41]. The current project focuses on the use of molecular methods as a key tool for the identification of AMF the various species, originating from a certain ecosystem. The biosystematics, cultivability and field performance evaluation of this group of fungi are still some areas lagging behind of suitable techniques, which have become hurdles for further progress of research. rDNA region of the genome, with its variable and conserved regions, has been found to be an ideal location to offer solution to the issue. PCR-based techniques have become mandatory to obtain sufficient quantities of DNA, as these organisms are nonculturable and thus only a small quantity of DNA could be isolated from spores and infected roots. Employing DNA-based molecular markers, some advancements and success have already been achieved in areas like phylogeny, taxonomy and functional symbiosis.

Establishment of phylogenetic relations, identifications and classifications are based on morphological features of the asexually produced propagules. In the absence of spores, the intraradical structures at best allow identification up to family level. These criteria besides being insufficient also added confusion to the existing state of AMF classification and identification especially since more than one AM fungus may colonize a given root segment simultaneously. Problems associated with identification of different taxa based on spore morphology are brought froth elegantly [42]. Molecular identification approaches based on DNA analysis have the potential to revolutionize our understanding of AMF. The knowledge of mycorrhizal functioning at molecular level could be used for the sustainable improvement of crop plants. Few studies have also been made on taxonomic aspects of this group of fungi. Though several methodologies have been followed in understanding the biology of these organisms, molecular marker-based studies are almost missing. A welcome feature in this respect is the recent advances in new AM fungal species which have been described in molecular detail [43]. Other similar studies have shown by using the molecular tool that during the adaptation to the strong and long-term environmental stress the adapted AM fungi can survive and function in saline soils.

Molecular methods have been particularly successful for studying rDNA sequences from AMF [44]. Several investigators have reported that individual spores of AMF which are multinucleate show a high level of genetic diversity in the internal transcribed spacer (ITS) region of the nuclear rRNA genes [45, 46]. Ribosomal-based DNA sequence analysis has revealed genetic variation both within and between AMF species [41, 47]. ITS sequences in eukaryotic rRNA genes are located between the 18S and 5.8S rRNA coding regions (ITSI) and between the 5.8S and 28S rRNA

Fig. 15.2 Location and details of rDNA genes. *IGS* Intragenic space, *ITS* Internal transcribed spacer

coding regions (ITS2; Fig. 15.2). Studies on restriction site variation in the ribosomal DNA (rDNA) in population have shown that while coding regions are conserved, spacer regions are variable. These spacer sequences have high evaluation rate and are present in all known nuclear rRNA genes of eukaryotes [48].

Molecular markers: Molecular research involving identification of genetic diversity demands sufficient quantities of genomic DNA. However, the biggest constraint in case of AMF is their non-culturability due to their obligate symbiotic nature. This roadblock to obtain sufficient quantities of DNA for DNA-based molecular identification technique was removed by introduction of polymerase chain reaction (PCR). PCR amplification of the desired part of the DNA has become a mandatory step in any molecular techniques. With PCR, it is possible to amplify the genome or part of it from a single spore, colonized root or soil sample, directly. There are three main categories of molecular research on AMF, namely genes and their expression, genomics and genetic variation. Although gene cloning from AMF species has proved successful, genome size and structure could not be elucidated.

Our recent study using Nested PCR of the ITS-rDNA region of AMF with the primer pair LSU-Glom1/SSU-Glom` as specific primer for AMF and ITS4/ITS5 as general primers, RFLP patterns, cloning and sequencing of the PCR products, dominant species 153 were identified dominant AMF species including *Glomus mosseae* (G2), *G. intraradices* (G1) and *G. versiforme* (G3) from soils with high and moderate levels of HMs were isolated and propagated by trap and monospecies culture. Along to the transect from mine to margin regions, root colonization rate in the dominant native plants increased from 35 to 85 % and the spore numbers from 80 to 1,306 per 200 g dry soil along the transect. A total of ten AMF taxon were morphologically identified, which nine of them belonged to *Glomus* (*Glomus mosseae*, *G. intraradices*, *G. versiforme*, *G. ambisporum*, *G. fasciculatum*, *G. geosporum*, *G. sinosum* and *Glomus sp.*) and one to *Acaulospora*. In this research, the diversity and activity of different dominant arbuscular mycorrhizal fungi (AMF) in the Anguran (Zanjan State, Iran) Zn and Pb mining region were studied. For this purpose, 35 plots in the Anguran Zn and Pb mining region were selected along a transect from the mine to 4,500 m away. Within each plot, a composite sample of root and rhizospheric soil from a dominant indigenous plant was collected. After that, colonization, arbuscular and vesicular abundance, mycorrhizal frequency and intensity, spore density and relative abundance of AMF species were calculated for the soils with high, moderate and low levels of Zn and Pb as well as for non-polluted soils (*Acaulospora* sp.). *Glomus* was the dominant genus in all plots. Isolation frequency, spore density and relative abundance of AMF species were different in HMs polluted and non-polluted sites. *G. mosseae* was the "taxon" most commonly observed in different plots, with

higher spore density and relative abundance at high level of HMs pollution. *G. mosseae*, *G. intraradices* and *G. versiforme* were more abundant than other AMF species in the soils with moderate and low levels of Zn and Pb contents [49].

15.6 Impact of Global Changing on Environmental Characters of Ecosystems

Understanding changes in the environmental characteristics of ecosystems is relevant at a global scale. On the one hand, a more accurate knowledge would contribute to a better environmental management and protection of environmental structure thus reduce damages like soil contamination or erosion in ecosystem subjected to pollution, drought—or other environmental-stressed conditions. On the other hand, process of glomalin is particularly sensitive to the status of soil water content, which makes an alteration of the biochemical mechanisms between mycorrhizas and the beneficial N_2-fixing bacteria [50]. It is prudent to study these processes under conditions of periodic periods of drought which occurs in the sites proposed in this study.

More locally, a sustainable use of the various environmental species is a prerequisite to an economically and ecologically balanced development of major area, especially of we consider the global change conditions. In recent years funds for research have been drastically reduced in both various ecosystems which exasperated the problems dealing with the issues of sustainable ecosystems— i.e. providing incentives to preserve environmental quality and ensure functional microbial behaviour. The strong influence that environmental structure and physical-, chemical-, biological status makes it imperative to pursue a better understanding of the mechanisms, so as to appropriately control it. In particular, the impact of environmental management on soil microorganisms is essential for the progress in the knowledge applicable to keep the quality of such ecosystems. Recently, researches have evidenced an interesting finding which indicates the selection of the AM fungi during the various environmental stress conditions. Such adapted indigenous AMF species (i.e. *Glomus geosporum*, in 80 % of the population) were shown to cope better with the abiotic environmental stress, and their colonization values, therefore, are increasing during this process. Those results demonstrated that the use of natural resources enable researchers to manage individual sustainable ecosystems.

15.7 What Is the Relationship Between Glomalin and the Environmental Quality?

Glomalin is a fungal protein (or protein class) that is operationally quantified from soil as glomalin (glomalin-related soil protein-GRSP). Glomalin, the actual gene product, and glomalin need to be separated in this discussion, as it is not clear whether the soil-extraction and quantification tools only captures material of AMF

origin; in fact, recent evidence suggests that this is not the case [51]. Glomalin has received attention in the context of soil aggregation owing to the frequently observed correlation between glomalin and water stability of soil aggregates [52]. However, evidence linking glomalin to soil aggregation remains correlative, and the mechanisms involved are still unclear. Glomalin is hypothesized to act as a "glue" with hydrophobic properties, but direct biochemical evidence for this is lacking. Contrary to original expectations, glomalin (in a sterile hyphal culture system) has recently been showed to be mostly tightly bound in the fungal myce-lium, rather than being secreted into the medium. Given that it appears to not be secreted primarily, this implicates glomalin to have a role in the living fungus; functionality in the soil would then be only secondarily arising, perhaps by virtue of its relatively slow turnover rate in the environment [53]. Gadkar and Rillig recently sequenced the putative gene for glomalin, showing homology to a class of stress-induced proteins (broadly found amongst fungi) with a known cellular function (V. Gadkar & M.C. Rillig, unpublished); this provides additional evidence for effects observed in soil arising secondarily, and may provide clues about its mode of action in the soil. Research on glomalin provides an exciting possibility, espe-cially with the molecular biology data available, to specifically link fungal physiol-ogy with soil aggregation.

15.8   Soil Microbes and Sustainable Energy Strategy

The depletion of fossil fuel reserves and the necessity to reduce CO_2 emissions to limit Global Warming, in particular after the Kyoto agreements, are imposing the need to research on renewable sources of energy. Among other alternatives, the substitution of fossil diesel by biodiesel is a tempting alternative, as there is no need to modify existing engine technologies. In recent years, biofuel research has aimed to explore the elaboration of plant-based fuels. The use of plant-biodiesels is as old as the engine itself, as Rudolf Diesel operated his engine with peanut oil, but its use has been limited by the availability of cheaper petrol diesel. Biodiesels are elaborated mostly from renewable vegetable oils composed of triacylglycerols (TAGs), which contain different fatty acid classes bound to the glycerol backbone. Acyl chains have lengths ranging from 16 to 24 carbons and may contain several degrees of unsaturation (from one to three double bonds), the composition that varies greatly between plant species. Most of the biodiesel produced in Europe is obtained from Brassica species, which have been bred to accumulate TAGs suitable for food and industrial applications. In addition, this variety also contains low level of glucosinolate, a toxic metabolite that accumulates in most mustard species. On the other hand, erucic acid has a relevant value in industrial applications (plastics, lubricants), so for these uses it is desirable to increase its concentration above the original 45 % level, varieties that are known as High Erucic Acid Rapeseed (HEAR). Through conventional breeding approaches and using natural and artificially induced mutations different Brassica varieties have been developed.

For example, C22:1 accumulation in HEAR varieties is controlled by two loci with additive interaction which encoded b-ketoacyl-CoA synthase (KCS), components of an enzymatic complex elongase that catalyzes the elongation of fatty acid chains. On the other hand, through conventional or transgenic breeding some soil microorganism symbioses with energy crops like Brassica varieties contain for example modifications in the activity of desaturases or thioesterases that accumulated less polyunsaturated oils, which are more prone to oxidation and degradation.

Crop micro-biotechnology is one of the most effective and innovative tools to improve the vegetable oil yield, with a second task of reducing the environmental impacts with more sustainable energy strategy. So far, most research has been focused on already available high oil yield crops used generally for food production. In Europe and North America soil microbe symbioses with energy crops like sorghum (Sorghum bicolor L.) has been the model plant of study, as commented above. Despite this research effort, more research is needed to identify new feedstock capable to reduce production cost and increase sustainability in comparison with petrol diesel, with a minimal input of irrigation, fertilization and other labour practices. These new non-crop plants, grown on non-arable soils, could also help to increase the social acceptance of biodiesel, as no deviation from food supplies or valuable agricultural areas would occur. Research has been focused in last few years to analyze the production of plants that are able to grow in hazardous environments with high oil seed yield. Interactions of soil microbes and plants like Jatropha curcas, Calophyllum inophyllum (Polanga oil) or Pongamia pinnata (Karanja seed oil) produce high quality oils but are native from tropical or subtropical areas and are extremely sensitive to frost, i.e. unsuitable as feedstock producers in countries with cold winters. On the contrary, pennycress (Thlaspi arvense) is a non-edible plant that has been recently been identified as a good alternative. The symbioses between soil microbes and some energy crops like Brassicaceae weed that grows well occurs degradation of marginal soils in the Northern Hemisphere, and some accessions are available at the National Plant Germplasm System (USDA), isolated from Canada, The Balkans, France, Germany, Poland and the USA. This plant is able to accumulate a large proportion of erucic (32 %; C22:1), linoleic (22 %; C18:2) and oleic (11 %; C18:1) acids, with other unsaturated fatty acids for the remaining fatty acid profile.

Transesterification rendered a biodiesel with reasonable good quality for combustion in engines. The lowest scores were obtained for kinematic viscosity and oxidative stability, parameters that could be improved by using blends with other oils or by addition of antioxidants. Therefore, research has to be directed to characterize the composition of oils extracted from different accessions or ecotypes, to identify those meeting the most stringent quality specifications. Another problem to reach the high demands of biodiesel production relies on available arable soils, which is needed for edible crops. This could be solved by growing high seed oil yield plants in waste land and on polluted soils, such as those areas contaminated diffusely with toxic metals and metalloids. These inorganic substances accumulated in many areas after extensive human activities such as agriculture, melting and mining. Plants can be used to mitigate soil pollution based

on their natural capability to take up mineral elements by their roots, decontamination techniques known as phytoremediation. One alternative that could be exploited in conjunction with the cultivation of energetic crops is the phytostabilization of metal (oid)s to prevent mobilization of pollutants to other soil horizons and ground water. The main goal is the valorisation of high value plant products obtained from polluted soils caused by the global changing.

15.9 Conclusion

The potential beneficial effects of soil microorganisms and plant–microbe interactions impact on environmental quality and global change are well documented by a variety of studies. Some soil microorganisms named mycorrhiza, as well as plant associated bacteria (rhizospheric or endophytic), can contribute to the nutrient supply of their plant hosts, which is important for optimal plant growth in normal conditions, but also for improving plant survival in hostile environments. Mechanisms by which endophytic bacteria can promote plant growth include for example biological nitrogen fixation, tolerance or the presence of contaminant degradation pathways. The obtained biomass from those plants and soil microbes association can be a high valued resource for producing bio-energy as alternative fuels like biodiesel, bioethanol or biogas which are believed to reduce global changing speeds. In consequence, this could have happened as part of the compatible reaction during mycorrhization. Mycorrhiza may be beneficial to overcome xenobiotic or environmental stress during global changing.

References

1. Schesinger WH (1997) Biogeochemistry: an analysis of global change, 2nd edn. Academic, San Diego, CA
2. http://files.eesi.org/stern_111306.pdf
3. Requena N, Perez Solis E, Azcon Aguilar C, Jeffries P, Barea JM (2001) Management of indigenous plant-microbe symbioses aids restoration of desertified ecosystems. Appl Environ Microb 67:495–498
4. Schroeder P (2011) Organic xenobiotics and plants: from mode of action to ecophysiology. Springer, Berlin, p 312
5. Abbott LK, Robson AD (1991) Factors of affecting the occurrence of vesicular-arbuscular mycorrhizas. Agric Ecosyst Environ 35:39–64
6. Streitwolf-Engel R, van der Heijden MAG, Wiemken A, Sanders IR (2001) The ecological significance of arbuscular mycorrhizal fungal effects on clonal reproduction in plants. Ecology 82(10):2846–2859
7. van der Heijden MAG, Boller T, Wiemken A, Sanders IR (1998) Different Arbuscular mycorrhizal fungal species are potential determinants of plant community structure. Ecology 79(6):2082–2091
8. Gianinazzi-Pearson V, Branzanti B, Gianinazzi S (1989) In vitro enhancement of spore germination and early hyphal growth of a vesicular arbuscular mycorrhizal fungus by host root exudates and plant flavonoids. Symbiosis 7:243–255

9. Tisdall JM, Oades JM (1982) Organic matter and water-stable aggregates in soils. J Soil Sci 33:141–163
10. Ruth B, Khalvati MA, Schmidhalter U (2011) Quantification of water flow through hyphae of mycorrhizal plants measured by capacitance sensors for soil water content, plant and soil. Plant and Soil 342(1–2):459–468
11. Schreiner RP, Bethlenfalvay GJ (1997) Mycorrhizae, biocides, and biocontrol 3. Effects of three different fungicides on developmental stages of three AM fungi. Biol Fertil Soils 24:18–26
12. Piotrowski JS, Denich T, Klironomos JN, Graham JM, Rillig MC (2004) The effects of arbuscular mycorrhizae on soil aggregation depend on the interaction between plant and fungal species. New Phytol 164:365–373
13. Enkhtuya B, Vosatka M (2005) Interaction between grass and trees mediated by extraradical mycelium of symbiotic arbuscular mycorrhizal fungi. Symbiosis 38:261–277
14. Landwehr M, Hildebrandt U, Wilde P, Nawrath K, Toth T, Biro B, Bothe H (2002) The arbuscular mycorrhizal fungus Glomus geosporum in European saline, sodic and gypsum soils. Mycorrhiza 12:199–211
15. Vivas A, Vörös I, Biró B, Campos E, Barea JM, Azcón R (2003) Symbiotic efficiency of autochthonous arbuscular mycorrhizal fungus (G. Mossae) and Brevibacillus sp. isolated from cadmium polluted soil under increasing cadmium levels. Environ Pollut 126:179–189
16. Vivas A, Vörös I, Biró B, Barea JM, Ruiz-Lozano JM, Azcón R (2003) Beneficial effects of indigenous Cd-tolerant and Cd-sensitive Glomus mossae associated with Cd-adapted strain of Brevibacillus sp. in improving plant tolerance to Cd contamination. Appl Soil Ecol 24:177–186
17. Vivas A, Biró B, Ruíz-Lozano JM, Barea JM, Azcón R (2006) Two bacterial strains isolated from a Zn-polluted soil enhance plant growth and mycorrhizal efficiency under Zn-toxicity. Chemosphere 62:1523–1533
18. Rillig MC (2004) Arbuscular mycorrhizae, glomalin and soil quality. Can J Soil Sci 84:355–363
19. Rillig MC, Hoye AT, Carren A (2006) Minimal direct contribution of arbuscular mycorrhizal fungi to DOC leaching in grassland through losses of glomalin-related soil protein. Soil Biol Biochem 38:2967–2970
20. Droog F (1997) Plant glutathione S-transferases, a tale of theta and tau. J Plant Growth Regul 16:95–107
21. Edwards R, Dixon RA (1991) Glutathione 5-cirmamoyl transferases in plants. Phytochemistry 30:79–84
22. Marrs KA, Alfenito MR, Lloyd AM, Walbot V (1995) A glutathione S-transferase involved in vacuolar transfer encoded by the maize gene Bronze-2. Nature 375:397–400
23. Hatzios KK (2001) Functions and regulation of plant glutathione-S-transferases. In: Hall JC, Hoagland RE, Zablotowicz RM (eds) Pesticide biotransformation in plants and microorganisms: similarities and divergences. American Chemical Society, Washington, DC, pp 218–239
24. Marrs KA (1996) The functions and regulation of glutathione Stransferases in plants. Annu Rev Plant Physiol Plant Mol Biol 47:127–157
25. Bilang J, Sturm A (1995) Cloning and characterization of a glutathione S-transferase that can be photolabeled with 5-azido-indole-3-acetic acid. Plant Physiol 109(1):253–260
26. Davis KR, Sharma YK (1994) Ozone-induced expression of stress-related genes in Arabidopsis thaliana. Plant Physiol 105:1089–1096
27. Dudler R et al (1991) A pathogen induced wheat gene encodes a protein homologous to glutathione S transferases. Mol Plant Microbe Interact 4:14–18
28. Hagen G, Uhrhammer N, Guilfoyle TJ (1998) Regulation of expression of an auxin-induced soybean sequence by cadmium. J Biol Chem 263:6442–6446
29. Kusaba M, Takahashi Y, Nagata T (1996) A multiple-stimuli-responsive as-1-related element of parA gene confers responsiveness to cadmium but not to copper. Plant Physiol 111:1161–1167

30. Khalvati M, Bartha B, Dupigny A, Schroder P (2010) Arbuscular mycorrhizal association is beneficial for growth and detoxification of xenobiotics of barley under drought stress. J Soil Sediment 10:54–64
31. Foyer CH, Lelandais M, Kunert KJ (1994) Photooxidative stress in plants. Physiol Plant 92:696–717
32. Olsson PA, Larsson L, Bago B, Wallander H, van Aarle IM (2003) Ergosterol and fatty acids for biomass estimates of mycorrhizal fungi. New Phytol 159:7–10
33. Wright SF, Franke-Snyder M, Morton JB, Upadhyaya A (1996) Time-course study and partial characterization of a protein on hyphae of arbuscular mycorrhizal fungi during active colonization of roots. Plant and Soil 181:193–203
34. Wright SF, Upadhyaya A (1998) A survey of soils for aggregate stability and glomalin, a glycoprotein produced by hyphae of arbuscular mycorrhizal mycorrhizal fungi. Plant and Soil 198:97–107
35. Wright SF, Starr JL, Paltineanu IC (1999) Changes in aggregate stability and concentration of glomalin during tillage management transition. Soil Sci Soc Am J 63:1825–1829
36. Lovelock CE, Wright SF, Nichols KA (2004) Using glomalin as an indicator for arbuscular mycorrhizal hyphal growth: an example from a tropical rain forest soil. Soil Biol Biochem 36:1009–1012
37. Wright SF, Upadhyaya A (1999) Quantification of arbuscular mycorrhizal activity by the glomalin concentration on hyphae. Mycorrhiza 8:283–285
38. Hosny M, GianinazziPearson V, Dulieu H (1998) Nuclear DNA contents of 11 fungal species in Glomales. Genome 41:422–429
39. Hijri M, Hosny M, van Tuinen D, Dulieu H (1999) Intraspecific ITS polymorphism in Scutellospora casta-nea (Glomales, Zygomycota) is structured within multinucleate spores. Fung Genet Biol 26:141–151
40. Walker RG, Plint AG (1992) Wave- and storm-dominated shallow marine systems. In: Walker RG, James NP (eds) Facies models: response to sea-level change. Geological Association of Canada, St Johns, pp 219–238
41. Lanfranco L, Delpero M, Bonfante P (1999) Intrasporal variability of ribosomal sequences in the endomycorrhizal fungus Gigaspora margarita. Mol Ecol 8:37–45
42. Redecker D, Hijri I, Wiemken A (2003) Molecular identification of arbuscular mycorrhizal fungi in roots: perspectives and problems. Folia Geobotanica 38:113–124
43. Rani SS, Kunwar IK, Prasad GS, Manohara C (2004) Glomus hyderabadensis, a new species: its taxonomy and phy- logenetic comparison with related species. Mycotaxon 89:245–253
44. Simon S (1996) Physiology of the Glomus: deciphering the past to understand the present. New Phytol 133(95):101
45. Lloyd-MacGilp SA, Chambers SM, Dodd JC, Fitter AH, Walker C, Young JPW (1996) Diversity of the internal transcribed spacers within and among isolates of Glomus mosseae and related arbuscular mycorrhizal fungi. New Phytol 133:103–111
46. Antoniolli ZI, Schachtman DP, Ophel-Keller K, Smith SE (2000) Variation in rDNA ITS sequences in Glomus mosseae and Gigaspora margarita spores from a permanent pasture. Mycol Res 104:708–715
47. Clapp JP, van der Stoel I, van der Putten WH (2000) Identification of cyst nematodes (Heterodera, Globodera) and root-knot nematodes (Meloidogyne) on the basis of ITS2 sequence variation detected by PCR-SSCP (PCR-single-strand conformational polymorphism). Mol Ecol 9:1223–1232
48. White TJ, Bruns T, Lee S, Taylor J (1990) Amplification and direct sequencing of fungal ribosomal RNA genes for phytogenetics. In: PCR protocols: a guide to methods and applications. Academic, London, pp 315–322
49. Zarei Mehdi, Nahid Saleh Rastin, Gholamreza Savaghebi, Mojtaba Khayam Nekouie, Gholamreza Salehi Jouzani, Mohammad Ali Khalvati, 2006, Analysis of changes in spore numbers of Arbuscular Mycorrhiza and colonization percent of native plants roots in Angooran, Zanjan region, Proceeding book of The first congress on soil, Environment and Stable Development, Tehran University, p. 13–14

50. Rillig MC, Mummey DL (2006) Mycorrhizas and soil structure. New Phytol 171:41–53
51. Wright SF, Upadhyaya A (1996) Extraction of an abundant and unusual protein from soil and comparison with hyphal protein of arbuscular mycorrhizal fungi. Soil Sci 161:575–586
52. Rillig MC (2004) Arbuscular mycorrhizae and terrestrial ecosystem processes. Ecol Lett 7:740–754
53. Steinberg PD, Rillig MC (2003) Differential decomposition of arbuscular mycorrhizal fungal hyphae and glomalin. Soil Biol Biochem 35:191–194

Chapter 16
Environmental Consciousness of Local People of Yakutia Under Global Climate Change

Yury I. Zhegusov, Stanislav M. Ksenofontov, Trofim Ch. Maximov, Atsuko Sugimoto, and Go Iwahana

Abstract This charter analyzes the results of social research on environmental consciousness of Yakut people. Environmental consciousness regulates people's behavior in ecologically significant situations. Results of the sociological survey show that local people of Yakutia observe some changes in environment, caused by intensive industrial development and global changes in the nature. Changes in the nature such as the climate warming in the winter, flooding because of a high water during spring, and watering of meadows and forests are something that the local people stress special attention to. Climate warming also affects the daily life of northerners. Local people notice some changes in the state of health, conditions of traditional housekeeping, etc. Social studies show that global changes in nature gradually begin to affect daily life of the inhabitants of extreme north and influence their environmental consciousness.

Keywords Environmental consciousness • Types of environmental consciousness • Changes in nature • Global warming • Local people of Yakutia

Y.I. Zhegusov (✉)
The Institute of Humanities and the Indigenous Peoples of North of the Siberian Branch of the Russian Academy of Science, 1 Petrovsky st., Yakutsk 677027, Russia
e-mail: polar@rambler.ru

S.M. Ksenofontov • T.C. Maximov
The Institute for Biological Problems of Cryolithozone, the Siberian Branch of the Russian Academy of Science, 41 Lenin avenue, Yakutsk 677980, Russia
e-mail: edu_center@ibpc.ysn.ru

A. Sugimoto
The Global Centre of Excellence (IFES-GCOE), Hokkaido University, Kita 10 Nishi 5, Kita-ku, Sapporo 060-0810, Japan
e-mail: atsukos@ees.hokudai.ac.jp

G. Iwahana
The University of Alaska, 930 Koyukuk Drive, Fairbanks, AK 99775-7340, USA
e-mail: giwahana@alaska.edu

16.1 Introduction

The Republic of Sakha (Yakutia) is situated in the North-Eastern part of Russian Federation. The territory is 3.102 million km^2 that is equal to 2/3 of the Western Europe area. Yakutia is one of the coldest places in the world. The climate is extremely continental, the main characteristics of which are dryness and large fluctuations of both day and seasonal temperatures. Yakutia is the only place in the world with a seasonal temperature range that is more than 100 °C.

Nowadays Yakutia is one of the environmentally successful regions in Russian Federation, excluding ecologically challenging areas in urbanized and industrial zones. The territory of the Republic fits 10 % of the world intact landscape, 1/3 of it is reserved under specially protected natural areas, that don't have legal confirmation. Meanwhile, there are local problems in providing inhabitants with drinking water, in solving problems of domestic wastes. The atmosphere air is getting worse in Yakutsk, Neryungri, Mirny cities, where almost half of the Republic's population lives. These problems affect the inhabitants' health directly. New environmental threats occur with the beginning of new industrial development of Yakutia.

Due to global warming, there are changes in the natural environment of Yakutia that arouse concern among the population and the academic community. In this regard, over the past years, scientists in Yakutia have conducted research in environmental science—in ecology, biology, climatology, geology, hydrology, geocryology, etc. There are international research stations on studying environmental condition and global climate; foreign scientists visit the Republic regularly to conduct their investigations.

Lately social aspects of global warming have become the subject of scientific interest, and in particular, scientists are interested how environmental changes affect the life and the consciousness of people. In this respect, conducting social researches on environmental consciousness is highly important.

Investigations on global change impact on local people's daily life and traditional husbandry have been carried out by some Russian [1] and foreign scientists in Yakutia [2].

Social surveys on environmental consciousness have been conducted in some other countries. Most of these focused on single topics, i.e., not connected with global change, for example the impact of local environmental conflict on environmental consciousness in Finland [3], the attitude of Jordanian consumers to Green marketing [4], public estimation of environmental quality in China [5], and attitude of Turkish farmers to pesticide use in greenhouses [6].

The Global Center of Excellence (Hokkaido University, Japan) and Green Grants Fund (USA) supported the investigation on environmental consciousness of the local people of the Republic of Sakha (Yakutia).

The objective of the survey was to determine ecological knowledge, estimation of environmental condition, observation of the environmental change, thoughts and opinions regarding global climate change. This information will serve as a basis and advice for local people's adaptation under global climate change.

16.1.1 Methods of Survey

The research project was carried out in the different climatic and landscape zones: Saskylakh village of the Anabarsky region (North Yakutia, tundra zone); Yakutsk (the capital, Central Yakutia, bottomland of the Lena River); Ust-Maya (East Yakutia, mountain and taiga zone); Aldan and Neryungry (South Yakutia, forest-mountain zone).

The data of this research is based on three different methods: (1) questionnaire research of 1,600 city and village dwellers, (2) focus-group research with local people, and (3) face-to-face in-depth interviews with old residents, hunters, fishers, farmers, and reindeer breeders. In the first method, questionnaires were given to surveyed people by researchers and the respondents filled in the questionnaires themselves. The second was used to collect qualitative information using group interview and discussion with specially selected survey participants. The third method was mainly used for people who have experience of observing nature changes.

16.2 Environmental Consciousness of Yakutia Peoples and Climate Change

16.2.1 Structure and Types of Environmental Consciousness

Environmental consciousness has three main functions (cognitive, estimative, and regulative) that forms social and psychological components, the results of functioning and empirical parameters (Table 16.1). Firstly, ecological knowledge appears in human consciousness because of ecological socialization. Then, according to awareness, people estimate the environmental situation. Finally, based on knowledge and estimation, people regulate their own environmental behavior.

In the context of ecological problems' aggravation in the world, three types of environmental consciousness have been formed. We made the following typology of environmental consciousness based on the concern of ecological problems: indifferent, local, regional, and global. Let's discuss each of them.

Indifferent/passive ecological consciousness—the owner of this type of ecological consciousness is characterized by the extremely indifferent relation to the environment, he is not interested in environmental problems, does not participate in any ecological actions.

Local ecological consciousness—the owner of this type of ecological consciousness is interested in and excited by only the state of the environment of a district, in which he lives. He is not excited about the ecological condition of other cities, regions, and countries.

Table 16.1 Functional structure of environmental consciousness

Main function	Social and psychological components	The results of functioning	Empirical parameters
Cognitive	Intellectual	Ecological knowledge	Ecological/environmental awareness
Estimative	Intellectual and emotional	Individual and public opinion about environmental problems	Estimation of the ecological/environmental situation
Regulative	Intellectual–emotional–conative	Social and ecological attitude and orientations	Behavioral positions regarding environmental problems

Regional ecological consciousness is characterized by the interest and anxiety in the condition of, not only the local nature, but also the region and the country's environmental problems. For example, the villagers of Yakutia are disturbed by the industrial pollution in the cities of Yakutia or forest fires in Central Russia.

Global ecological consciousness means that the owner of ecological consciousness is well informed of global changes in the environment and equally seriously concerned about the local, regional, and the environmental problems.

16.2.2 Concern of Environmental Problems and Sources of Ecological Information

The regional type of environmental consciousness is dominant (46.7 %) among the citizens of Yakutia. First of all, the reason for this is probably the display of patriotism, the idea that Republic and country must have a favorable environment for a productive life and, secondly, fear of the negative impact of possible ecological accidents and disasters near their home. Global type of environmental consciousness is detected among 39.6 % of respondents, i.e., consciousness of interconnection and interdependence of natural processes, the idea that nature is integrated in the global system all this unites this group of respondents. Global environmental consciousness is mostly distributed among people with higher education (48.9 %), when index rates among the people with general secondary and vocational secondary education are 29.1 % and 35.8 % respectively. 9.3 % of respondents have a local type of environmental consciousness. Indifferent environmental consciousness is discovered among few respondents, only 4.4 %. It is worth mentioning, that people with incomplete secondary education predominate among this type of consciousness (26.8 %). Thus, the social survey found out that the type of environmental consciousness strongly depends on the person's education, i.e., the higher the education, the deeper the consciousness of importance of global environmental changes and impact on the mankind.

Information sources about the environment are an important aspect of the environmental consciousness cognitive element. Yakut people, first of all, get

environmental information via TV (83.5 %) and print media (55.8 %). In spite of geographical farness of Yakutia, Internet is getting much more popular, 33.6 % of respondents use it to get information. Interpersonal communication, i.e., communication with people is also an important source in exchanging environmental information (32.0 %). 17.9 % of respondents chose the version of "daily nature observation." The results show that mass media have great influence on knowledge formation about the environment and ecological problems, i.e., environmental worldview of the people is formed by indirect information, not comprehended on their own, that affects objectivity of opinions and views.

The respondents' answers to the question that reveals the interest level of the environmental condition and ecological problems prove the great influence of mass media on environmental consciousness. The majority of people (81.6 %) are interested in this problem, "sometimes when it is written and shown by mass media." There is a small number of people, who are always interested in the environment and purposely collect information (9.2 %). 6.5 % of respondents do not care about the ecological problems at all, 2.8 % of people gave another answer.

16.2.3 People's Observations of Climate and Nature Change

Some ecologists and climatologists believe that global changes in nature are greater in the northern regions of the planet. What environmental changes are observed in Yakutia? After considering the results of the questionnaire survey, the respondents' answers were grouped, according to the period, when they were mentioned.

1. group of answers (60 % and more from the total amount of respondents), this group includes answers such as "people often get sick with such infective diseases, as ARVI and influenza" (78.7 %); "air temperature changes abruptly" (75.6 %); "people often get sick with oncologic diseases" (73.2 %); "winter roads are opened later" (39.8 %); "people often get sick with allergic diseases" (70.5 %); "winters get warmer" (63.3 %)
2. group of answers (40 %–59 % of respondents' answers): "the number of wild animals decreases" (53.8 %); "there are more floods" (51.6 %); "the seasonal changes are late" (48.5 %); wind power and direction changes" (43.4 %)
3. group of answers (20–39 % of mentions): "summer gets rainy" (39.9 %); "summer gets colder" (36 %); "new bird species arrived" (25.5 %); much snow in winter" (32.7 %); "forests and fields watering due to permafrost thawing" (28.4 %); "found new insects species" (28.4 %); "animals' migration period changes" (23.1 %)

Qualitative methods were also used in this research, they are, face–face in-depth interviews and focus groups. Respondents noted some changes in nature that can be seen in daily life.

First of all, the citizens of Yakutia notice climate change. Very interesting information was given by people living in the Arctic, in Saskylakh village of

Anabarsky region. Respondent number 1 (male, 65 years old): "In winter, it gets much warmer, if it used to be cold for a month or more, now the cold lasts only for a few days. In general, the weather became unstable and unpredictable, there are abrupt changes in temperature." Respondent number 5 (female, 27 years old): ". . . last year in November the temperature was −40° C, but the next day there was a drastic warming, almost to plus degrees. I wanted to cook stroganina (raw frozen fish), brought a fish into the house, and it was melted, the tail was hanging" Respondent number 2 (Male, 50 years old): "The weather has changed, there have been no strong winds in winter over the past 15–20 years. In the past, there was a period of strong winter blizzards and storms, when a person was literally knocked off his feet, but now this has changed." Respondent number 3 (female, 72 years old): "In the summer it gets warmer, even hotter, especially last year we had the heat. How do we feel? Earlier in the summer you can swim only 3 days and then not always, but now the summer swimming season can last up to 10–12 days. I've been watching from a window in the summer, how young people organized a beach, swimming, sunbathing, and were drinking a beer in the river. Maybe it's fashion . . . ." The respondent number 8 (male, 57 years old): "I noticed the rain had changed. Previously, there was small rain, with the mist and it lasted for a long time. Recently, thunderstorms occur often. In our area, on the shores of the Arctic Ocean, it is a particularly unprecedented phenomenon. Rain is intermittent, but very strong almost like a tropical downpour."

For several years, the citizens of Yakutia have noticed changes in flora and fauna, which is reasonably connected with global warming. Respondent number 1 (male, 65 years old): "The tundra was overgrown with bushes and shrubbery is gradually moving to the north, toward the Arctic Ocean. Crows appeared in large numbers, some of them even spent winter in the tundra." Respondent number 7 (male, 47 years old): "There are a lot of hares now, there were very few of them before, then perhaps migration of animals occurred, now the tundra is full of hares. Even gluttons came to the tundra, one could not see them before." Respondent number 3 (female, 72 years old): "I live in the village outskirts, hares run even near my house. Every morning I see fresh tracks. There are a lot of Arctic foxes, but it is due to the fact that the price of its fur has increased and people stopped hunting. Arctic foxes sometimes come to the village, but those who are sick with rabies, and it is dangerous! Fish gets worse, with ulcers and sores, as well as parasites. Water quality has deteriorated, it were the diamond-miners, who poured out poisoned water into the river." Respondent number 6: (female, 55 years old): "I can see flies that sting. Our local flies are not stingy." Respondent number 4: "There are a lot of berries and that is good. We can gather a lot of cloudberries now, it grows well. Also, we collect red bilberries, it did not grow color till first snow before, but now we gather buckets of colored bilberries."

Research participants also noted changes in the period of seasons incoming. Respondent number 1 (male, 65 years old): "The winter is late, that is why, winter roads are opened late. Spring comes earlier, but it lasts very long. The interval between winter and summer was short before, but now snow has melted, and then summer comes in just 2 weeks. Now spring lasts for a long time and summer does

not come at all. I also noticed that the ice drift has changed. In the past, ice was the first to crack and then the ice drift began, but now the water comes over the ice, and ice drift occurs only after that."

During the interview, residents of the Anabarsky region noted changes in the duration of light and dark time of a day. In particular, they observe the actual disappearance of the polar night. If the polar night was very dark before and lasted for a long time, now the Arctic circle' residents note that the polar night is light and short. Some respondents expressed an opinion that it happened due to the displacement of the Earth's axis.

The vast majority of respondents are sufficiently aware of the global climate change: 35.3 %—"know well," 57.7 %—"heard something," and 7.1 %—"do not know." 40 % of respondents consider the reason of global climate change to be the anthropogenic impact on the environment (industrial development, transport), 14.0 % believe that climate is affected by "the natural cyclic changes, independent of human influence" and 31.4 % of respondents believe that global warming is equally affected by people and natural changes. This shows that, despite of the geographical farness, thanks to the development of information technology in Yakutia, residents are well informed about the problem of global warming and have an opinion on this matter.

According to subjective sensations, Yakut people notice climate change, and the respondents' answers vary depending on the survey sites. In northern Yakutia respondents often note the warming weather in summer, and the residents of South Yakutia, on the contrary, note steady cold summer. According to respondents' answers, we can see that the people living in the Northern and Central Yakutia feel the climate warming, both in winter and summer (Table 16.2).

The comparison of the survey results with meteorological data [7] at the survey sites shows the following tendency: the higher the observed average annual temperature, the higher the percent of people who choose the answer "the weather got warmer in summer, than before" and "the weather got warmer in winter, than before." The Anabarsky region is an exception, where an inconsiderable increase of the average annual temperature is observed and large number of people notice weather warming, especially in summer. Apparently, abnormal hot summer weather for these places in 2010, that was perceived as global warming has influenced the respondents' answers (Table 16.3).

How long have the people in the Arctic been observing changes in nature? The answers to this question show a specific character and principles of environmental consciousness of the research participants. Nearly half of respondents observed natural changes over the past 2–5 years, and only 1/3 noted a period of 10 years and more (Table 16.3). Such conflicting data indicate that the respondents have a different degree of observation. Research participants noted that environmental changes occur gradually and only a person with good memory will notice these changes. These events can attract the people's attention only with the growth of changes in nature year by year. Older people often notice environmental changes for "10 or more years" longer, than the younger generation, because they begin observing these changes in a more conscious age. But among the older respondents,

Table 16.2 Answers to the question: "Do you feel a change in climate?" (in %[a])

	Regions				
Responses:	Yakutsk	Saskylakh (Anabarsky region)	Ust-Maya	Aldan	Neryungry
No, I don't feel it at all	13.8	13.0	18.4	26.3	14.2
Yes, the weather in summer got warmer, than before	43.6	60.5	32.6	11.1	14.2
Yes, the weather in summer got colder, than before	6.3	9.8	17.1	39.1	29.1
Yes, the weather in winter got warmer, than before	57.9	32.6	40.6	33.0	56.7
Yes, the weather in winter got colder, than before	6.8	17.0	10.6	25.9	8.3
Yes, other	6.0	0.4	7.4	2.4	5.2

[a]Respondents chose a few options, and therefore the sum of answers exceeds 100 %

Table 16.3 Influence of average annual temperature increase to respondents' subjective sensations

	Regions				
Meterological data and responses:	Yakutsk	Saskylakh (Anabarsky region)	Ust-Maya	Aldan	Neryungry
Average annual temperature increase in 1966–2009, °C[a]	3.0	0.7	2.5	1.1	1.4
Total percentage of respondents who answered that "the weather got warmer in winter, than before" and "the weather got warmer in summer than before," %[b]	101.5	93.1	73.2	44.1	60.9

[a]*Data source:* Skachkov YB. 2010. Climatic parameters. In a Review of Recent Climatic and Environmental Changes in the Republic of Sakha (Yakutia). Yakutsk; 1–3 (in Russian)
[b]Respondents chose a few options, and therefore the sum of answers exceeds 100 %

the number of people correlated with the young people, who have noticed natural changes 2–5 years ago. Perhaps it traces the properties of the human psyche, which is more inclined to remember the events of the recent past, or more than a decade ago (Table 16.4).

16.2.4   Public Opinion and Estimation of the Global Warming Affects

In order to identify and estimate the attitude of the people living in Yakutia to environmental changes we asked the following question: "What effect will the global warming have in your life and traditional husbandry?" More than half of the

Table 16.4 Answers to the question: "How long (last years) have you been observing the changes in nature?" (in %) (analysis by age)

Responses	Age of respondents				
	18–29	30–44	45–54	55 and more	Total
Over the last year	5.5	1.2	1.8	0.4	2.5
Over the last 2–3 years	18.5	8.6	10.3	8.4	11.9
Over the last 4–5 years	19.3	18.7	14.7	12.5	17.0
Over the last 6–7 years	1.1	13.7	12.3	9.2	13.1
Over the last 8–9 years	4.2	6.0	5.6	7.6	5.6
Over the past 10 years and more	15.7	37.1	43.4	49.4	34.1
Do not feel changes in the nature	4.0	1.8	0.9	1.9	2.3
Do not know	17.0	11.8	10.0	13.6	12.6
Other	0.6	1.2	1.2	2.3	1.0

Table 16.5 Answers to the question: "How drastic will the effect of global warming of climate be?" (in %)

Responses	To the best	To the worse	Don't know
On your life	13.5	66.6	19.9
On the traditional farming (herding, hunting, fishing)	11.5	65.5	22.9

respondents believe that global warming will adversely affect the quality of life, as well as agriculture, which is the main job of local residents (Table 16.5). They are sure that global warming will, first of all, lead to permafrost thawing, it will increase the Arctic Ocean level, that will cause floods in the local peoples' land, and secondly, permafrost thawing will lead to swamping and watering of meadows and pastures, and thirdly, research participants consider that warm winters and hot summers have caused infectious diseases spreading among people and animals.

Research participants shared their own observations of global warming effects. Respondent No. 9 (male, 60 years old): "A further climate warming may lead to fatal effects for inhabitants of the North in the future. Thawing of the Arctic ice will cause an accident, in which the Anabarsky region will sink." The Respondent №12 (male, 52): "... permafrost thawing effects can already be seen now. There was a lake near the Anabar River, but because of underground ice thawing it had completely flown into the river. I can't believe—such a large lake, but there's no lake now." Respondent No. 10 (male, 54): "I often travel to the Arctic Ocean coast. During the past years it is extremely stormy in the summer, there are high waves. One could not see this before. The ocean is boiling, powerful waves washed away the melting permafrost ashore. The shore is falling from time to time. The Ocean is under incursion, every year 30–100 m of land disappears into the depths of the sea. There were buildings, 200 m far from the ocean before, remaining from the scientific expedition of the USSR. Everything has gone under the water."

16.3   Conclusions

The investigation shows that the people living in Yakutia have superficial knowledge about the global climate changes, and at the same time, they express concern for this problem. The respondents are mainly concerned about the regional and global environment. Mass media has a leading role in the formation of environmental consciousness. Most people get environmental information via TV, print media, and Internet. People living in Yakutia observe considerable changes in climate, flora, and fauna of the region. Comparison of the survey results with meteorological data at four survey sites shows the following tendency: the higher the observed average annual temperature, the higher the percent of people, who consider that the weather got warmer than before in summer and winter. Respondents consider that climate changes have impacts on the Yakut people's daily life, reflecting on human health and traditional husbandry. This problem requires further interdisciplinary investigation for developing recommendations in the field of the Far North inhabitants' adaptation under global warming.

References

1. Ksenofontov S, Maximov T, Sugimoto A, Yamashita T, Iwahana G (2012) Climate change awareness of rural population in a permafrost region. In: Proceedings 5th inernational workshop on C/H$_2$O/Energy balance and climate over boreal and arctic regions with special emphasis on eastern Eurasia, Wageningen, Netherlands, pp 19–20, 11–13 Nov 2010
2. Crate S (2008) Gone the bull of winter? Curr Anthropol 49(4):569–595
3. Ranikko P (1996) Local environmental conflicts and the change in environmental consciousness. Acta Sociol 39:57–72
4. Asmadi S (2007) Green marketing and the concern over environment: measuring environmental consciousness of Jordanian consumers. J Promot Manage 13(3–4):339–361
5. Li P, Stagnitti F, Gong Z, Xiong X, Li X, Hu Z, Sun Y, Wang Z, Gao K, Kong C, Li P (2009) Environmental quality: issues and causes of deterioration—a survey on environmental awareness among the public in Liaoning province, China. Int J Sust Dev World Ecol 16(3):143–150
6. Gun S, Ran M (2008) Pesticide Use in Turkish greenhouses: health and environmental consciousness. Polish J Environ Stud 18(4):607–6
7. Skachkov YB (2010) Climatic parameters. In: A review of recent climatic and environmental changes in the Republic of Sakha (Yakutia). Yakutsk; 1–3 (in Russian)

Chapter 17
Environmental Impact Assessment of Explosive Volcanoes: A Case Study

Faruk Aydın, Adnan Midilli, and Ibrahim Dincer

Abstract Although there are some parameters identified in the literature to quantify environmental impact of volcanic eruptions, e.g., Dust Veil Index (DVI), Volcanic Explosivity Index (VEI), and Volcanic Aerosol Index (VAI), no parametric studies have been undertaken to assess the environmental impact of explosive volcanoes. In this regard, this study deals with a parametric investigation of the environmental impact of the explosive volcanoes through some key parameters, such as (1) lateral blast effect, (2) debris avalanche effect, (3) lahars effect, (4) pyroclastic flow effect, (5) earthquake effect, (6) pyroclastic surge effect, (7) health effect, (8) tsunami effect, and (9) atmospheric effect. Considering these and their impact levels, a new parameter for explosive volcanic eruptions, so-called the "Environmental Impact Factor (EIF)," ranging from 0 to 1, is proposed as a function of the VEI which ranges between 1 and 8. We also conduct a quantitative evaluation of the environmental effects of the Mount St. Helens volcano (erupted on May 18, 1980) in USA. For this purpose, a case study for the St Helens eruption is conducted by taking into account the Volcanic Explosivity Index as 5, Environmental Correction Factor as 1.6, and the actual influence distances of the products and earthquake effect from the St Helens eruption. Of the above parameters, the first five parameter and also ash effect that can be commonly observed after the St. Helens eruption is considered. As a result of the analysis, the EIF will provide a

F. Aydın (✉)
Faculty of Engineering, Department of Geological Engineering, Karadeniz Technical University, 61080 Trabzon, Turkey
e-mail: faydin@ktu.edu.tr

A. Midilli
Faculty of Engineering, Recep Tayyip Erdoğan University, 53100 Rize, Turkey
e-mail: adnan.midilli@erdogan.edu.tr

I. Dincer
Faculty of Engineering and Applied Science, University of Ontario Institute of Technology (UOIT), 2000 Simcoe Street North, Oshawa, ON, Canada L1H 7K4
e-mail: ibrahim.dincer@uoit.ca

quantitative record of environmental impact of the explosive volcanic products in terms of the influence distance and the VEI. Moreover, it is estimated that, in the case study, the environmental impact factors corresponding to the actual influence distances of the explosive products and earthquake effect become 0.568 in 12.8 km for lateral blast, 0.635 in 14 km for debris avalanche, 0.525 in 100 km for lahar, 0.875 in 8 km for pyroclastic flow, 0.978 in 16 km for ash (with an ash depth of 25 cm), and 0.921 in 1.6 km for earthquake effects.

17.1   Introduction

Environmental pollution, which affects human health and welfare, causes the shortage of the water resources and serious natural disasters and so on, has been one of the most significant problems in the world during the past three decades. If so, the key question is: is it possible to combat and prevent from the environmental pollution? It has two dimensions: man-made and natural cycles. It is of course quite difficult to determine how much naturally happens and how much is caused by man-made activities. Man-made activities are directly related to the following important parameters: Pollution, population growth, energy and food demand, energy shortage, transportation, energy production and consumption, methane resources, etc. As a result of these, it can be said that environmental destruction will increase all over the world. As known, environmental destruction is an important result of the processes and systems affecting the livings and destroying their livable environment. On the other hand, in terms of the natural cycles, the volcanic eruptions can be considered one of the most important natural causes to create and increase the environmental destruction. Volcanic eruptions are of many different types. Some are termed effusive; they are dominated by the relatively slow and well behaved flow of lavas at the Earth's surface. However, others eruptions, such as the eruption of the Mount St. Helens, are explosive, often involving huge amounts of pyroclastic material (ash, lapilli, bombs, etc.). As a comparison between the effusive and explosive eruptions, it can be said that the explosive eruptions have primary effects on the environment, while the effusive types have secondary or tertiary effects.

Considering these important facts, there is an urgent need to study the environmental impacts of the products from an explosive volcanic eruption. In this regard, a new environmental impact factor (EIF) is developed as a function of the Volcanic Explosivity Index (VEI) and the influence distance of the explosive volcanic products. Particularly, the VEI is taken as one of the most important parameters and has greatest effect on this parameter, describing the magnitude of explosive volcanic eruption and including some key volcanic parameters, e.g., volume of ash production, height of eruption cloud above the vent, and duration of eruption [1]. As it is noticed, various aspects of the active volcanoes have been studied to date by many researchers (e.g., [2–14]). However, no any parametric investigation is found on the assessment of environmental impact of explosive

volcanoes. Lack of such work in the literature makes the paper original and becomes the main motivation behind this research. It is thus aimed to develop a new parameter to identify and quantify the environmental damage caused by such volcanic activities and provide an impact assessment methodology for practice. On the other hand, in order to test and verify this new factor, the products from the Mount St. Helens eruption (May 18, 1980) are taken into consideration for a case study. Accordingly, it is expected that this study provides a quantitative record of environmental impact of the explosive volcanic products in terms of the influence distance and the VEI.

17.2 Model Development
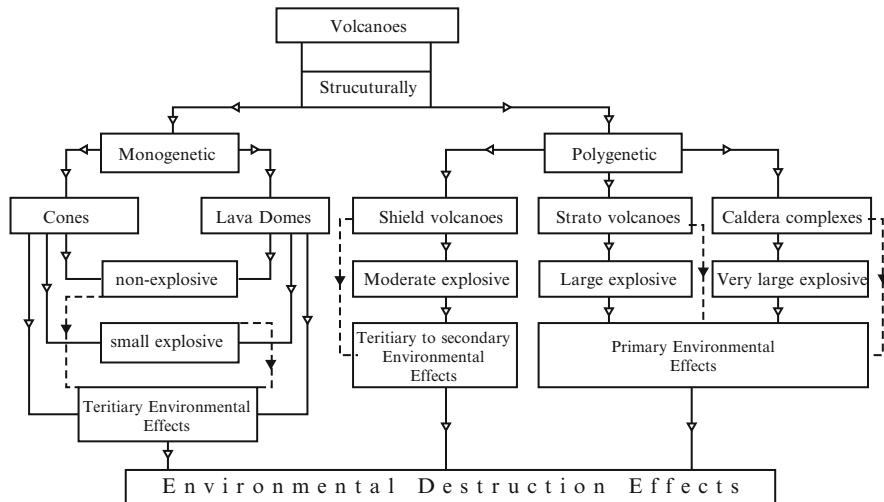
17.2.1 Environmental Impact Assessment

Before parametrically studying and assessing the environmental impact of the explosive volcanoes, and develop the EIF, the following key topics are discussed:
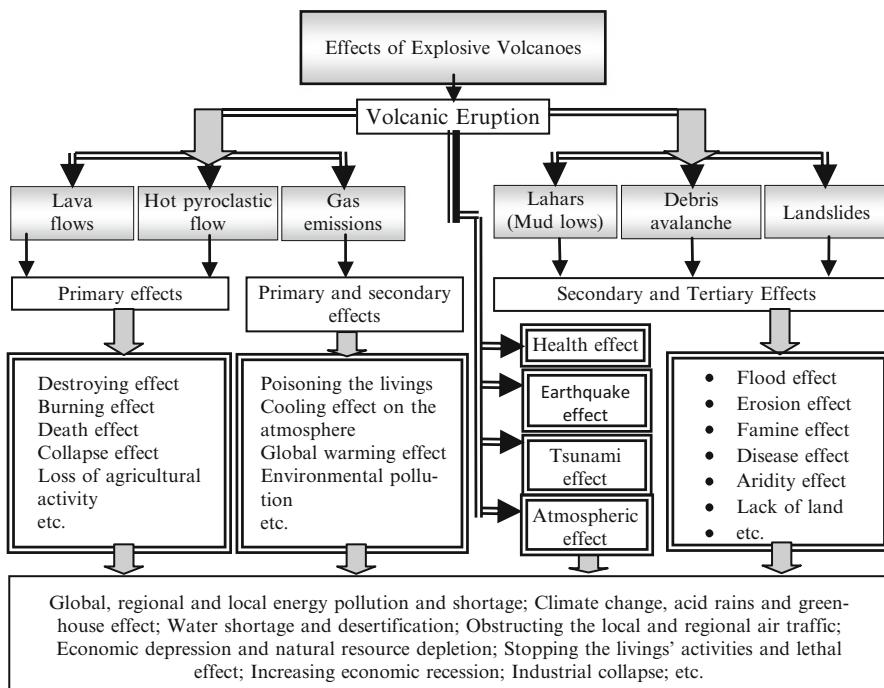
General Classification and Environmental Aspects of Volcanoes

According to some literature works [15, 16], in terms of structural characteristics, volcanoes can generally be classified in two main types (Fig. 17.1): monogenetic (nonexplosive or the least explosive) and polygenetic (moderate to very large explosive). Monogenetic volcanoes have a simple magma conduit system and are built up by the products of one eruption phase, while polygenetic volcanoes largely have complex plumbing system and comprise the products of many eruption phases [16]. Monogenetic volcanoes can be subdivided into several types. These are scoria cones, tuff rings, maars and lava domes which have the least effect on the environmental damage. On the other hand, polygenetic volcanoes are generally known as shield volcanoes, stratovolcanoes, and caldera complexes. Of these volcanoes, the shield volcanoes have secondary or tertiary effects on the environmental damage, while the last two types have primary effect, and so on, as shown in Fig. 17.1. Furthermore, Figure 17.2 illustrates the general environmental effects of explosive volcanoes. These effects can be classified as primary, secondary, and tertiary effects.

Of the general effects of an explosive volcanic eruption, atmospheric effect has been discussed in this part. Volcanic gases (water vapor, carbon dioxide, and sulfur compounds like sulfur dioxide) and particles (dust and ash) resulting from the eruptions may be assumed to be some of the reasons changing the earth's climate in terms of the global warming and global cooling. Water vapor is typically the most abundant volcanic gas, followed by carbon dioxide and sulfur dioxide. Other principal volcanic gases include hydrogen sulfide, hydrogen chloride, and hydrogen

Fig. 17.1 A brief classification of volcanoes and their environmental effects (compiled from the literature [15–17])
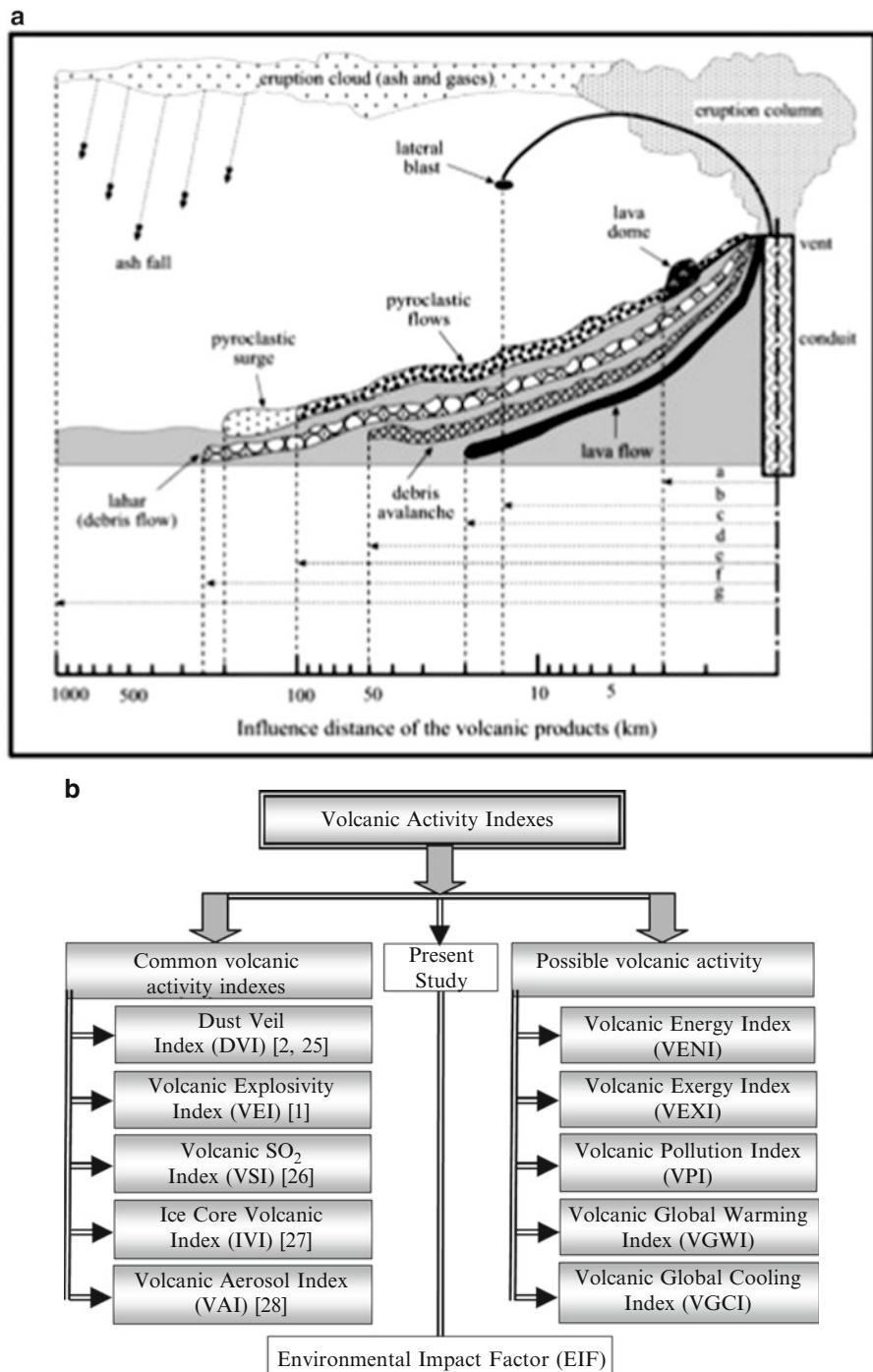
Fig. 17.2 Schematic illustration of general environmental effects of explosive volcanoes

fluoride. A large number of minor and trace gases are also found in volcanic emissions, for example hydrogen, carbon monoxide, halocarbons, organic compounds, and volatile metal chlorides. If so, it may be said that volcanic gases and particles can cause the real problems as a result of their blocking the sunlight. Actually, the volcanic gases affect the earth, people, and animals in different ways. The volcanic gases that pose the greatest potential hazard to people, animals, agriculture, and property are sulfur dioxide, carbon dioxide, and hydrogen fluoride [18]. Of these gases, for example, H_2O and SO_2 can cause the air pollution, global cooling, and ozone depletion, while CO_2 can cause the global warming, and be lethal to the living beings.

Explosive Volcanoes and Their Emissions

Generally, explosive volcanoes are stratovolcanoes or composite volcanoes, which have characteristic volcanic landform and are found at subducting plate margins, and are the most abundant type of large volcano on the Earth's surface. They have medium to high volatiles, volume and viscosity, which are the most important features of explosive volcanoes, as well as caldera complexes of rift zones. The moderate to high explosive stratovolcanoes produce generally the following emissions [17]: pyroclastic flows, lahars (mud flows), debris avalanches, pyroclastic falls (lateral blast, lapilli, ash), pyroclastic surge (especially ash), partly lava flows, and gases such as H_2O, HCl, H_2S, HF, CO_2, SO_2, N_2O, etc.

Regarding volcanic gas emissions, the explosive stratovolcanoes primarily release water vapor, CO_2, and SO_2 as the most common volcanic gases emitted by explosive volcanoes in different tectonic setting (convergent-plate, rift zone, etc.). In lesser amounts, the explosive volcanoes release CO, H_2S, carbonyl sulfide (COS), carbon disulfide (CS_2), HCl, H_2, CH_4, HF, boron, HBr, Hg vapor [3, 19]. Of these gases produced by explosive volcanoes, water vapor is also a strong absorber of infrared radiation more than carbon dioxide but this gas is usually not considered to a greenhouse gas [20]. However, it is considered that water vapor greatly affects the Earth's heat balance [21]. Regarding SO_2, stratospheric injection of SO_2 is the principal atmospheric and global impact of volcanic eruptions [4]. In fact, SO_2 converts to sulfuric acid aerosols that block incoming solar radiation and contribute to the stratospheric ozone depletion, and thus, the blocked solar radiation can cause global cooling [12]. Regarding the carbon dioxide that has the highest global warming potential, the CO_2 produced by the volcanoes causes the global warming as well as atmospheric pollution. Moreover, chlorine gas emitted from volcanoes in the form of hydrochloric acid (HCl) can damage the environment [5]. In addition, fluorine gas can condense in rain or on ash particles and coats grass and pollutes streams and lakes with excess fluorine [9, 22]. Under these considerations, a schematic illustration of maximum theoretical distance of the explosive products for a stratovolcano has been presented in Fig. 17.3a, b.

a

b

Fig. 17.3 (**a**) A generalized schematic illustration of the explosive products for a stratovolcano (their maximum theoretical influence distances have been taken from the literature [23, 24]). (**b**) A flowchart of volcanic activity indexes (Index data from [1, 2 and 25–28])

Volcanic Activity Indexes

Volcanic activity indexes are commonly known in the literature, and some possible indexes are presented in Fig. 17.3. In addition to these indexes, it can be recommended that, for the future investigations, the following volcanic activity indexes should be studied in order to find out the various aspects of an explosive volcano. (1) Volcanic Energy Index (VENI) indicating the thermodynamic aspects of an active volcano. (2) Volcanic Exergy Index (VEXI) indicating the useful energy gain from an active volcano. (3) Volcanic Pollution Index (VPI) indicating the global, regional and local pollution impacts of an explosive volcano. (4) Volcanic Global Warming Index (VGWI) indicating the global warming aspects of an explosive volcano as a result of CO_2, HF, etc. (5) Volcanic Global Cooling Index (VGCI) indicating the global cooling aspects of an explosive volcano as a result of H_2O, H_2S and S_2O emissions. Meanwhile, it is emphasized that the indexes recommended here require multidisciplinary efforts.

17.3 Development of the EIF

In the present study, a new parameter describing the environmental impact of the explosive volcanic products, called Environmental Impact Factor (EIF) is developed. In order to develop such a parameter, some important assumptions are necessary to make. In this regard, the main assumptions are listed below.

17.3.1 Assumptions

- The present parameter is a function of the influence distances of the volcanic products and their effects as a result of the explosive eruptions, and of the VEI taking into account the magnitude (erupted volume) and intensity (eruption column height) of an eruption (e.g., [1]).
- The VEI is scale from 1 to 8 and not used to describe eruptions of lava which are nonexplosive [1].
- The environmental damage potentials (from moderate to high explosive volcanic products) are considered as the main parameters in developing the EIF. They are lateral blast effect, debris avalanche effect, pyroclastic flow effect, pyroclastic surge effect, lahar effect.
- As the important environmental effects (for moderate to high explosive volcanoes), the earthquake effect, health effect, and tsunami effect resulting from the explosive volcanic eruption are also considered.
- Theoretical influence distances of the explosive volcanic products and their environmental effects are taken in accordance with the literature (e.g., [23, 24]).

Table 17.1 Parameters considered for EIF

Parameter	Symbol	Unit	Maximum influence distance for products	References
Lateral blast	$L_{\max}^{lb}$	km	35	[29]
Debris avalanche	$L_{\max}^{da}$	km	50	[23, 24]
Pyroclastic flow	$L_{\max}^{pf}$	km	100	[23, 24]
Pyroclastic surge	$L_{\max}^{ps}$	km	200	[23, 24]
Lahar	$L_{\max}^{l}$	km	250	[23, 24]
Ash and/or gases	$L_{\max}^{ag}$	km	1,000	Assumed from [23, 24]
General environmental effects of the moderate to high explosive volcanic eruption				
Earthquake effect	$L_{\max}^{ee}$	km	30	[23, 24]
Health effect	$L_{\max}^{he}$	km	60	[23, 24]
Tsunami effect	$L_{\max}^{te}$	km	250	[23, 24]
Atmospheric effect	$L_{\max}^{ae}$	km	1,000	Assumed from [23, 24]
Intensity and magnitude of a volcanic eruption				
Volcanic Explosivity Index	VEI	–	Scale 1–8	[1]

Meanwhile, it should be emphasized that the theoretical influence distances of ashes and gases indicating the atmospheric effect and tsunami effect are assumed as 1,000 km.

- Theoretical influence distance is considered as a function of flow velocity, temperature, viscosity, density, melt composition, friction, etc. of the explosive volcanic products because these parameters affected practically the maximum influence distance of the explosive volcanic products.
- The analytical form of the present parameter is considered in exponential form due to the natural behavior of the environmental impact as a result of the time-dependent volcanic eruption.

17.3.2 Parameters

In order to develop the EIF, the following parameters and their theoretical influence distances considered in the study are listed in Table 17.1.

Of these parameters in Table 17.1, the VEI ranges from 1 to 8, as a function of the volume of products, eruption cloud height, and duration of eruption. It provides the most comprehensive geological record of past volcanism [1]. Considering the above assumptions and parameters listed in Table 17.1, the following analytical form of the EIF is developed:

$$EIF = \exp(-\beta \times \alpha) \, (\text{ranging from 0 to 1}) \qquad (17.1)$$

Table 17.2 Some calculated values for EIF correction factor (α)

α	VEI
1.00	8
~1.14	7
~1.34	6
1.60	5
2.00	4
~2.67	3
4.00	2
8.00	1

Increasing environmental damage effect →

where β describes dimensionless influence distance, and α is the EIF correction factor.

When Eq. (17.1) is analyzed in terms of the physical basis, it is understood that, if α is equal to 1, the EIF has a maximum value of "1," meaning that the explosive volcanism causes the maximum environmental damage. However, if β is "1," the EIF will have a minimum value, suggesting a minimum environmental damage. Additionally, using Eq. (17.1), the reference value of EIF is determined by depending on the theoretical influence distance of any product (or the types of environmental effects of the explosive volcano) of the explosive volcano that has the maximum value of VEI ($=8$), and the minimum of α ($=1$). Moreover, Eq. (17.1) makes us determine the critical influence distance of any product (or the types of environmental effects of the explosive volcano) of the explosive volcano that has the lower VEI values than 8, and higher α values than 1 (see Table 17.2). Consequently, as a scientific importance of Eq. (17.1), the EIF provides a reasonable environmental damage record of the explosive volcanic products in terms of the influence distance and the VEI.

Furthermore, β and α in Eq. (17.1) can be described as

$$\beta = \frac{L}{L_{\max}} \, (0 \leq L \leq L_{\max}) \tag{17.2}$$

where L symbolizes the theoretical influence distance and $L_{\max}$, the maximum theoretical influence distance.

Considering Eq. (17.2), for the explosive volcanic products and their environmental effects, the dimensionless influence distance for explosive volcanic products may be respectively written as

$$\beta^P = \frac{L^P}{L^P_{\max}} \tag{17.3}$$

where β^P indicates dimensionless influence distance of a explosive volcanic product; L^P, the theoretical influence distance of a product; $L^P_{\max}$, the maximum

theoretical influence distance of a product; $L_{\max}^{P}$ is selected from Table 17.1 in accordance with the product type.

For the environmental effects of volcanic eruptions, it becomes

$$\beta^{E} = \frac{L^{e}}{L_{\max}^{e}} \tag{17.4}$$

where β^{E} symbolizes dimensionless influence distance of the environmental effect (earthquake, health, tsunami, etc.) of the volcanic eruption, L^{e}, influence distance of the environmental effect of the volcanic eruption; $L_{\max}^{e}$, the maximum theoretical influence distance of the environmental effect of the volcanic eruption; $L_{\max}^{e}$ is selected from Table 17.1 in accordance with the effect type.

In Eq. (17.1), the EIF correction factor is assumed to be a function of VEI and $VEI_{\max}$ in order to determine the reference value of EIF and estimate the critical influence distance of the explosive volcanic products and their environmental effects corresponding to this reference value. Thus, we propose α as

$$\alpha = \frac{VEI_{\max}}{VEI} \tag{17.5}$$

where $VEI_{\max}$ explains the maximum volcanic explosivity index (is equals to 8). Based upon Eq. (17.5), the values of α are presented in Table 17.2, corresponding to the VEI values.

17.4 Case Study

In the present study, in order to estimate the environmental impact factors (EIFs) [30] of the explosive volcanic products from the Mount St. Helens eruption, a case study has been accomplished by taking into consideration the following assumptions: (1) the Volcanic explosivity index is 5 [1], (2) the effects of the explosive volcanic products from the Mount St. Helens eruption, having the most environmental destruction potential, are taken into consideration, which are lateral blast effect, debris avalanche effect, lahar effect, pyroclastic flow effect, ash fall effect, and earthquake effect, (3) the actual influence distances of the explosive volcanic products and their environmental effects caused by the Mount St. Helens eruption are taken in accordance with the literature [29, 31, 32] (4) the actual distance is considered as a function of flow velocity, temperature, viscosity, density, melt composition, friction, etc. of the explosive volcanic products because these parameters affected practically the maximum influence distance of the explosive volcanic products, and (5) some of these hazards (e.g., lava flows) only affect areas very near the volcano [31]. Therefore, lava flow and lava dome have not been considered for the case study.
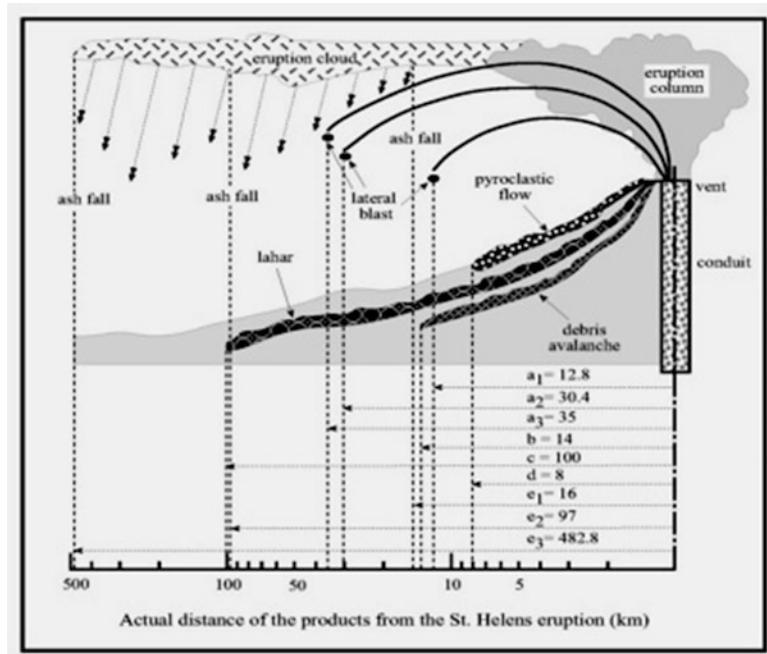
17.4.1   Details of the St. Helens Explosive Volcano

Volcanic eruptions often involve several distinct types of hazards to people and property, as well evidenced by the Mount St. Helens eruption. Major volcanic hazards include: lateral blast, debris avalanche, lahar, pyroclastic flow, the ash fall, and earthquake effect. Lateral blast, which occurs with violent eruptions, may have excessive lethal effect on the lives near the vent of the volcano. Debris avalanche triggered by eruptions or by earthquakes or simply by heavy rainfall, are the rapid downslope movement of rocky material, snow and/or ice. Lahars that are a major hazard because highly populated areas are built on lahar flows from previous eruptions are common during eruptions of volcanoes with heavy loading of ice and snow. Pyroclastic flows are high-speed avalanches of hot ash, rock fragments and gases. Ash fall results when explosive eruptions blast rock fragments into the air. Such blasts may include tephra. In very large eruptions, the depth of ash falls may be much more near the vent [31, 32].

Under these considerations, the general specifications of the St. Helens explosive volcano can be presented as below [33]. The volcano's elevation was 2,950 m before eruption, 2,549 m after eruption. Time of initial blast was 8:32 a.m. Pacific Daylight Time (UTC-7). Eruption triggered a magnitude 5.1 earthquake about 1.6 km beneath the volcano. As a result of the eruption, the following products and effect were observed: Landslide/debris avalanche, which had 2.8 km^3 volume and the velocity ranging from 113 km/h to 241 km/h, covered 60 km^2 areas. Lateral blast, which had 0.19 km^3 volume and 483 km/h velocity, and 349 °C covered 596 km^2 area and released 24 megatons thermal energy, and caused 57 of human fatalities. Lahars, which had the velocity ranging from 16 km/h to 80 km/h, damaged 27 bridges, nearly 200 homes. Blast and lahars destroyed more than 298 km of highways and roads and 24 km of railways. Its eruption column and clouds reached about 24,400 m in less than 15 min. Its ash volume was almost 1 km^3, and the ash erupted from the volcano covered 57,000 km^2, and its ash fall depth was 25 cm at 16 km, 2.5 cm at 97 km, and 1.3 cm at 482.8 km. Pyroclastic flows, which had the velocity ranging from almost 80 km/h to 130 km/h, and 700 °C of temperature, covered 16 km^2, and reached 8 km. A schematic illustration of the explosive products for the St. Helens eruption has been presented in Fig. 17.4.

17.4.2   Key Parameters

In order to perform a case study to test the EIF in terms of the explosive products from the Mount St. Helens Volcanic eruption (May 18, 1980), the following products and influence distances which are available in the literature are taken into consideration [29, 31, 32]. In the case study, (1) the actual influence distances of lateral blast in direct blast zone (also called innermost zone), the channelized blast zone (also called an intermediate zone), the seared zone (also called the "standing dead" zone) have been respectively taken as 12.8 km, 30.4 km [34] and 35 km [29], (2) the actual influence distance of debris avalanche is 14 km, (3) the

Fig. 17.4 A generalized schematic illustration of the main explosive products for the St. Helens volcano (their actual influence distances taken from [29, 31, 32])

actual influence distance of lahar is ~100 km, (4) the actual influence distance of pyroclastic flow is 8 km, (5) the actual influence distances of ash are 16 km (ash depth = 2.5 cm), 97 km (ash depth = 2.5 cm), 482.8 km (ash depth = 1.3 cm), (6) the actual influence distance of earthquake effect is 1.6 km.

For the case study, the following parameters in Table 17.3 have been taken into consideration.
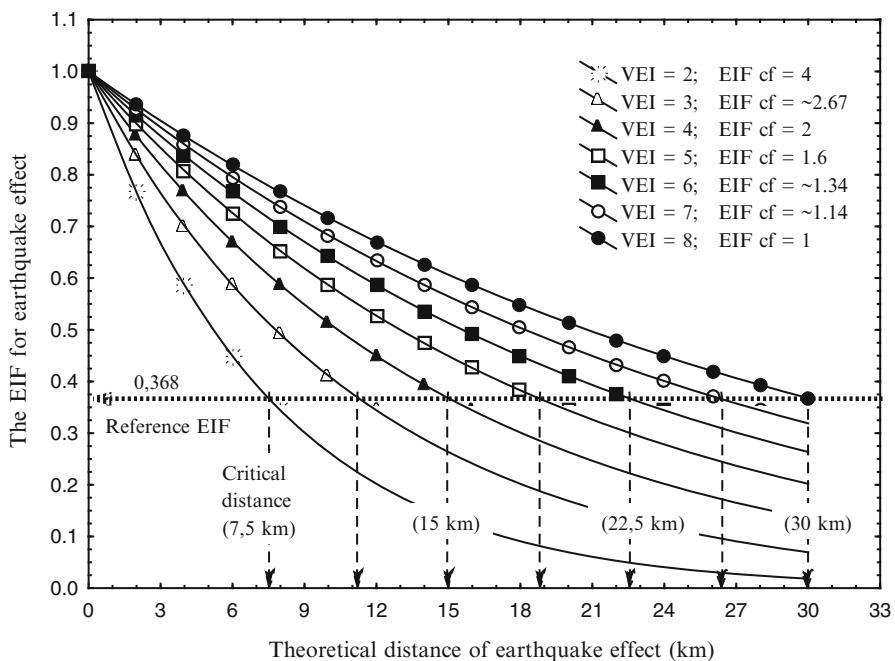
17.5 Results and Discussion
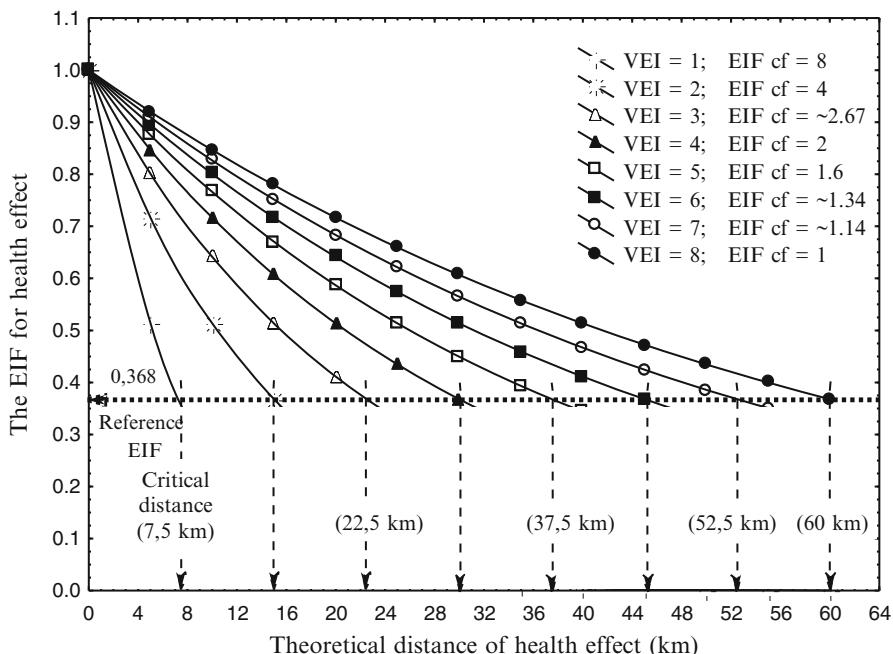
17.5.1 Theoretical Results

In this paper, environmental impact factor (EIF), providing a quantitative record of environmental impact of the explosive volcanic products in terms of the influence distance and the VEI, has been developed. In its development of such a parameter, we have then considered the significant aspects. Moreover, an EIF correction factor has been derived as a function of the VEI. The critical influence distances of the effects resulting from the explosive volcanic eruption are illustrated in (Figs. 17.5, 17.6, 17.7, and 17.8). Also, the variations of EIF with theoretical distances of the explosive volcanic products are presented in Fig. 17.9a–f.
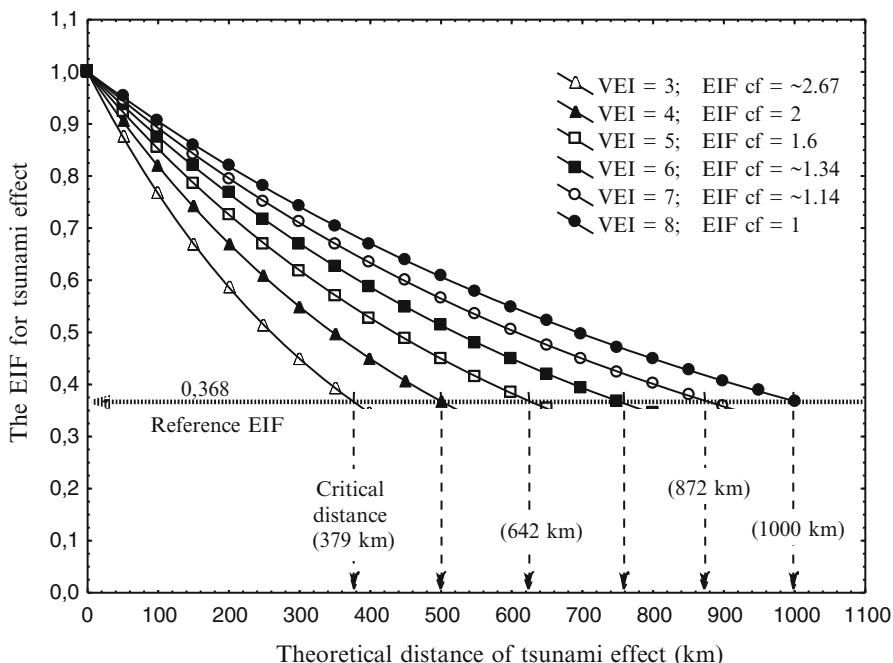
Table 17.3 The required parameters used in Eq. (17.1) for the case study

Parameter	Symbol	Unit	Actual distance for the products	References
Lateral blast	L_{a1}^{lb}	km	12.8	[29, 31, 32]
	L_{a2}^{lb}		30.4	
	L_{a3}^{lb}		35	
Debris avalanche	L_b^{da}	km	14	[29, 31, 32]
Lahar	L_c^{l}	km	100	[29, 31, 32]
Pyroclastic flow	L_d^{pf}	km	8	[29, 31, 32]
Ash fall	L_{e1}^{ag}	km	16	[29, 31, 32]
	L_{e2}^{ag}		97	
	L_{e3}^{ag}		482.8	
General environmental effects of the moderate to high explosive volcanic eruption				
Earthquake effect	L_{max}^{ee}	km	1.6	[29, 31, 32]
Intensity and magnitude of a volcanic eruption				
Volcanic Explosivity Index	VEI	–	Scale 1–8	[1]
EIF correction factor	α	–	1.6	Table 17.2
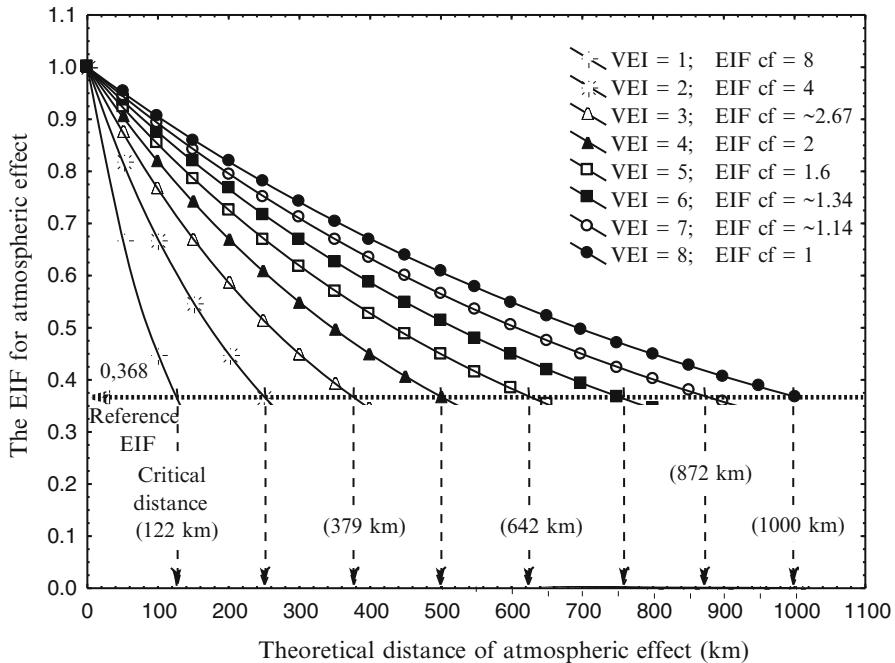
Fig. 17.5 Variation of the EIF as a function of the theoretical distance of earth quake effect based on the VEI [1] and EIF cf (VEI: Volcanic Explosivity Index; EIF: Environmental Impact Factor; cf: correction factor)

Fig. 17.6 Variation of the EIF as a function of the theoretical distance of health effect based on the VEI [1] and EIF cf (VEI: Volcanic Explosivity Index; EIF: Environmental Impact Factor; cf: correction factor)
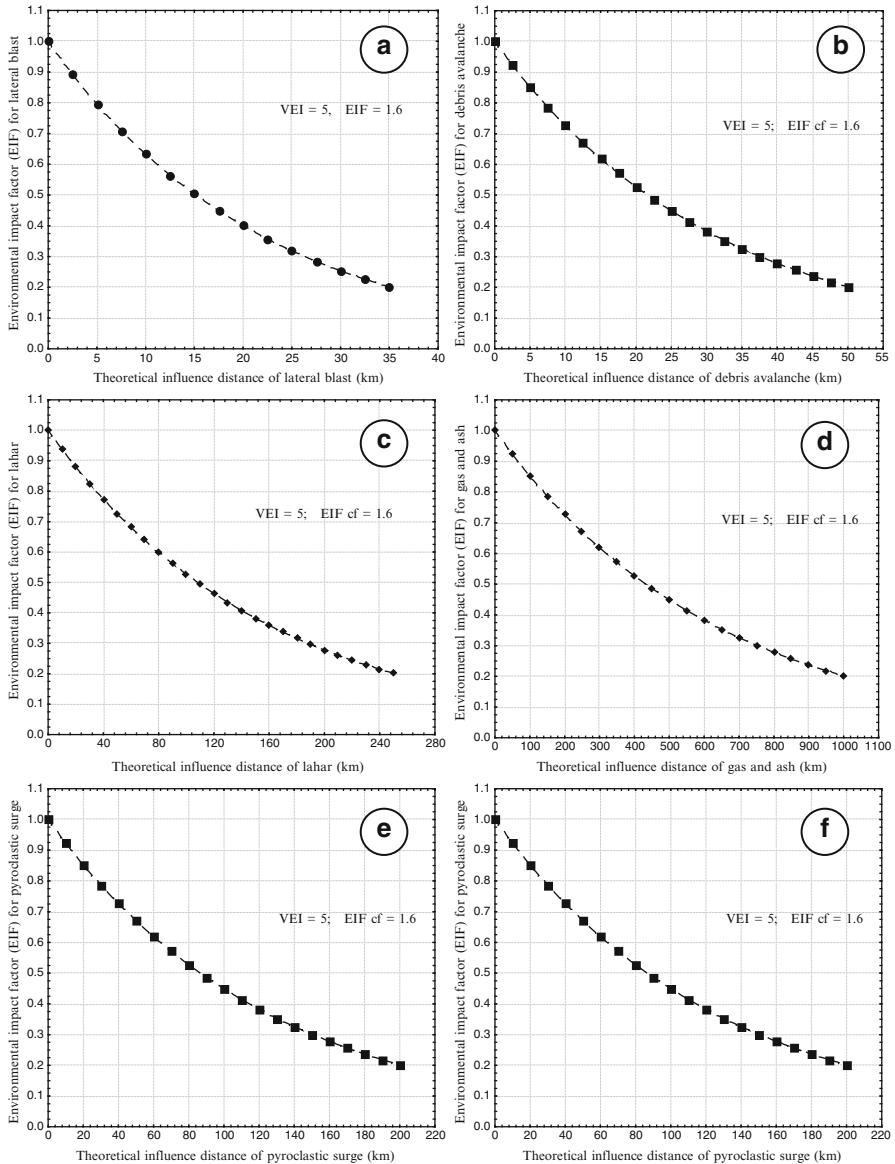
Fig. 17.7 Variation of the EIF as a function of the theoretical distance of the Tsunami effect based on the VEI [1] and EIF cf (VEI: Volcanic Explosivity Index; EIF: Environmental Impact Factor; cf: correction factor)

Fig. 17.8 Variation of the EIF as a function of the theoretical distance of atmospheric effect based on the VEI [1] and EIF cf (VEI: Volcanic Explosivity Index; EIF: Environmental Impact Factor; cf: correction factor)

Earthquake Effects

The general effects of an explosive volcanic eruption are considered as earthquake effect, health effect, tsunami effect, and atmospheric effect. Figure 17.5 shows the variation of the EIF as a function of the theoretical distance of earthquake effect based on the VEI and the EIF correction factor. According to the literature [23, 24], the maximum theoretical distance of the earthquake effect is 30 km for a very large explosive volcanoes (VEI = 8, and EIF correction factor = 1). As shown in Fig. 17.4, for VEI = 8, and $\alpha = 1$, the minimum value of EIF corresponding the maximum theoretical distance of earthquake effect is calculated as 0.368, which indicates the reference EIF value meaning that the primary effect (lethal and destructive effects, etc.) comes to an end, and also referring to the maximum distance of the primary effects. Taking into consideration this reference EIF value, the critical distances of the primary effects of the earthquake have been determined for decreasing VEI (from 8 to 2) and increasing EIF correction factor (from 1 to 4). The critical distances corresponding the reference EIF value in case of VEI = 8 or EIF correction factor = 1 give us those of the primary effects of the earthquake in case VEI ranges from 2 to 7. For example, if VEI ranges from 2 to 7 and EIF correction factor ranges from 4 to ~1.14, the critical distances of the

Fig. 17.9 Variations of the EIF as a function of the theoretical influence distance of the explosive volcanic products (**a–f**) based on the VEI = 5 and EIF correction factor = 1.6 (VEI: Volcanic Explosivity Index; EIF: Environmental Impact Factor; cf: correction factor)

primary effect of earthquake are respectively estimated as 7.5 km, 11.2 km, 15 km, 18.8 km, 22.5 km, and 26.4 km by using Eq. (17.1) or as shown in Fig. 17.5. Thus, it can be said that, considering the above discussions and the theoretical distance of earthquake effect, the primary effect zone is between 0.368 and 1 of EIF.

The values, which are lower than the EIF reference value (<0.368), indicate the secondary or tertiary effects of the earthquake (Fig. 17.5). For example, if VEI = 2 and EIF correction factor = 4, the primary effect of earthquake can be observed until maximum distance of 7.5 km from the vent of the explosive volcano. However, the secondary and/or tertiary effects of earthquake can be experienced after critical distance of 7.5 km.

Consequently, for practical applications in determining the effects of earthquake, it is expected that this figure will help estimate the primary and the secondary and/or tertiary effect zones and the EIF values of earthquake caused by the active explosive volcano by depending on the actual influence distance of earthquake, and to develop the required strategies concerning with determination of the safe settling areas around the active explosive volcanoes, particularly, in subduction zone or active continental margin.

Health Effect

Of the general effects of an explosive volcanic eruption, the possible health effect is discussed here. Fig. 17.6 shows the variation of the EIF as a function of the theoretical distance of health effect based on the VEI ranging from 1 to 8 and the EIF correction factor from 1 to 8. According to the literature [23, 24], the maximum theoretical distance of health effect is 60 km for a very large explosive volcanoes (VEI = 8, and α = 1). As shown in Fig. 17.6, for VEI = 8, and α = 1, the minimum value of EIF, corresponding to the maximum theoretical distance of the active explosive volcano based-health problems, is also estimated as 0.368, which indicates the reference EIF value meaning that the primary health problems (death, etc.) stops partly, and also referring to the maximum distance of the active explosive volcano based-primary health problems. Taking into consideration this reference value, the critical distances of the active explosive volcano based-primary health effect are determined for decreasing VEI (from 8 to 1) and increasing EIF correction factor (from 1 to 8). The critical distances corresponding the reference EIF value in case of VEI = 8 or α = 1 give us those of the active explosive volcano based-primary health effect in case VEI ranges from 1 to 7. For example, if VEI ranges from 1 to 7 and EIF correction factor ranges from 8 to ~1.14, the critical distances of the active explosive volcano based-primary health effect are respectively estimated as 7.5 km, 15 km, 22.5 km, 30 km, 37.5 km, 45 km, and 52.5 km by using Eq. (17.1). Thus, it can be said that, considering the theoretical distance of the active explosive volcano based-primary health effect, the primary effect zone is between 0.368 and 1 of EIF. The values, which are lower than the reference EIF value (<0.368), indicate the secondary and/or tertiary health problems of the active explosive volcano such as respiratory problems, ocular problems, skin irritation, accident risks, etc. For example, if VEI = 1 and α = 8, the primary health effect of the active explosive volcano can be observed until maximum distance of 7.5 km from the vent of the explosive volcano. However, the secondary and/or tertiary health problems can be mostly experienced after the critical distance of 7.5 km.

Accordingly, for practical applications in determining the active explosive volcano based-health problems, it is expected that this figure will be used to designate the primary and the secondary and/or tertiary health effects and the EIF values corresponding the influence distance indicating the active explosive volcano based-health problems by using the actual influence distance getting from an active explosive volcano, and to develop the required strategies concerning with minimizing, stopping and remedying the health problems caused by the active explosive volcanoes.

Tsunami Effect

Of the general effects of an explosive volcanic eruption, the tsunami effects discussed here. The volcanic eruptions can cause the destructive tsunami effects under the sea, and at the sea surface, and at the sea coasts (e.g., lethal effect on the marine life and the livings, damaging the terrestrial plants, destructive effect on the coasts, etc.). The lethal effect of tsunami created by the explosive volcanic eruption can be assumed as the primary effects while the others are the secondary and/or tertiary effects. Figure 17.7 presents the variation of the EIF as a function of the theoretical distance of tsunami effect based on the VEI and EIF correction factor. According to the literature [23, 24], the maximum theoretical distance of tsunami effect is assumed to be 1,000 km of 10,000 km for a very large explosive volcanoes (VEI = 8, and α = 1). As shown in Fig. 17.7, for VEI = 8 and α = 1, the minimum value of EIF corresponding to the maximum theoretical distance of the Tsunami effect is estimated to be 0.368, which indicates the reference EIF value meaning that the primary effect (lethal and destructive effects, etc.) comes to an end, and also referring to the maximum distance of the primary effects. Taking into consideration this reference EIF value, the critical distances of the primary effects of the Tsunami are determined for decreasing VEI (from 8 to 3) and increasing EIF correction factor (from 1 to ~2.67). The critical distances corresponding the reference EIF value in case of VEI = 8 or α = 1 give us those of the primary effects of the tsunami in case VEI ranges from 3 to 7. For example, if VEI ranges from 3 to 7 and EIF correction factor ranges from ~2.67 to ~1.14, the critical distances of the primary effect of tsunami are respectively estimated as ~379 km, ~500 km, ~642 km, ~748 km, and ~872 km by using Eq. (17.1) or as shown in Fig. 17.7. Thus, it can be said that, considering the above discussions and the theoretical distance of tsunami effect, the primary effect zone is between 0.368 and 1 of EIF. The values, which are lower than the EIF reference value (<0.368), indicate the secondary or tertiary effects of tsunami (Fig. 17.7). For example, if VEI = 3 and EIF correction factor = ~2.67, the primary effect of the tsunami can be observed until maximum distance of ~379 km from the vent of the explosive volcano. However, the secondary and/or tertiary effects of earthquake can be experienced after critical distance of ~379 km.

Consequently, for practical applications in determining the effects of the tsunami, it is expected that this figure will be used to estimate the primary and the

secondary and/or tertiary effect zones and the EIF values of the tsunami caused by the active explosive volcano by depending on the actual influence distance of the Tsunami, and to develop some strategies to minimize the problems created by the Tsunami as a result of the explosive volcanic eruption under sea and sea surface and/or near the coasts.
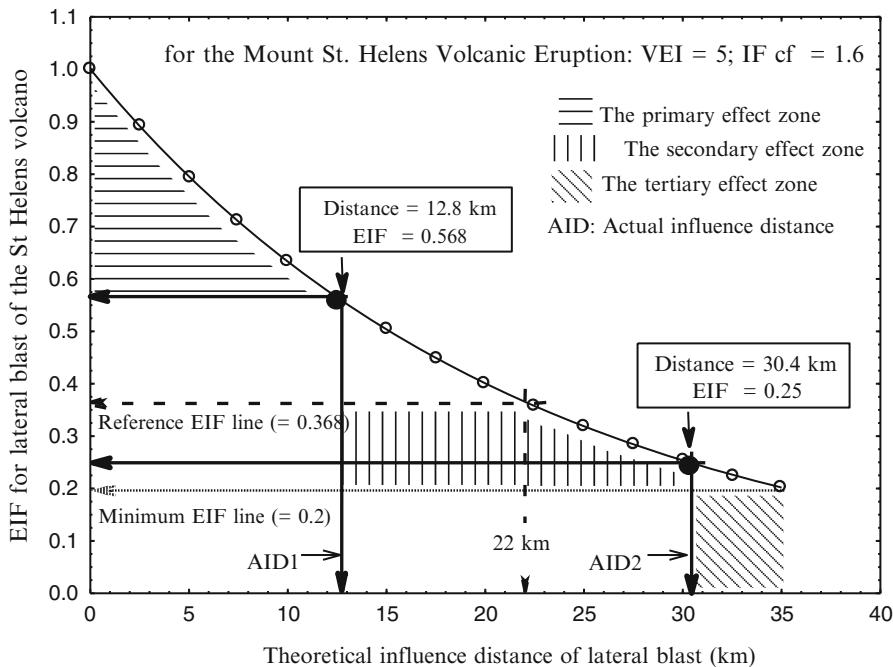
Atmospheric Effect

Of the general effects of an explosive volcanic eruption, atmospheric effect has been discussed in this part. Volcanic gases (water vapor, CO_2, and sulfur compounds like SO_2) and particles (dust and ash) resulting from the eruptions may be assumed to be some of the reasons changing the earth's climate in terms of the global warming effects. The water vapor is typically the most abundant volcanic gas, followed by carbon dioxide and sulfur dioxide. Other principal volcanic gases include hydrogen sulfide, hydrogen chloride, and hydrogen fluoride. A large number of minor and trace gases are also found in volcanic emissions, for example hydrogen, carbon monoxide, halocarbons, organic compounds, and volatile metal chlorides. If so, it may be said that volcanic gases and particles can cause the real problems as a result of their blocking the sunlight. Actually, the volcanic gases affect the earth, people and animals in different ways. The volcanic gases that pose the greatest potential hazard to people, animals, agriculture, and property are sulfur dioxide, carbon dioxide, and hydrogen fluoride. Of these gases, for example, H_2O and SO_2 can cause the air pollution, global cooling and ozone depletion while CO_2 can cause the global warming, and be lethal to the livings. Under these considerations, the intensive air pollution, instantaneous regional warming, cooling and climate change, acid rains, hot ash falls resulting from the explosive volcanic eruption may be assumed as the primary atmospheric effect. They can cause the livings' death near the vent of the explosive volcano. Less environmental pollution, long period-global warming, cooling and climate change, light effect-acid rains, and low temperature-ash falls may be assumed as the secondary and/or tertiary atmospheric effects. The primary atmospheric effects can be felt in a short time after eruption while the secondary and/or tertiary atmospheric effects require long time. In this regard, Fig. 17.8 indicates the variation of the EIF as a function of the theoretical distance of atmospheric effect based on the VEI and α. According to the literature (e.g., McGuire [23], Chester et al. [24]), the maximum theoretical distance of atmospheric effect is assumed to be 1,000 km of 10,000 km for a very large explosive volcanoes (VEI = 8, and α = 1). As shown in Fig. 17.8, for VEI = 8 and α = 1, the minimum value of EIF corresponding to the maximum theoretical distance of atmospheric effect is calculated to be 0.368. This shows the reference EIF value meaning that the primary atmospheric effects are rarely felt or come to an end, and also referring to the maximum distance of the primary atmospheric effects. Considering this reference EIF value, the critical distances of the primary atmospheric effect are determined for decreasing VEI (from 8 to 1) and increasing α (from 1 to 8). The critical distances corresponding to the reference EIF value in the

case of VEI = 8 or α = 1 give us such results of the primary atmospheric effects
for VEI ranging from 1 to 7. For example, if VEI ranges from 1 to 7 and α ranges
from 8 to ~1.14, the critical distances of the primary atmospheric effect are
respectively estimated as ~122 km, ~250 km, ~379 km, ~500 km, ~642 km,
~760 km, and ~872 km by using Eq. (17.1). Thus, it can be said that, considering
the theoretical distance of atmospheric effect, the primary effect zone is between
0.368 and 1 of EIF. The values, which are lower than the EIF reference value
(<0.368), indicate the secondary or tertiary atmospheric effects (Fig. 17.8). For
example, if VEI = 1 and α = 8, the primary atmospheric effect can be observed
until maximum distance of ~122 km from the vent of the explosive volcano.
However, the secondary and/or tertiary atmospheric effects can be experienced
after critical distance of ~122 km. Thus, for practical applications, it is expected
that this figure will contribute to estimate the zones and EIF values of the primary
and the secondary and/or tertiary atmospheric effects by depending on the actual
influence distance of atmospheric effect.

Explosive Volcanic Products (VEI = 5 and α = 1.6)

Figure 17.9a–f illustrate the variations of the EIF as a function of the theoretical
influence distance from the vent of an explosive volcanic product based on the
VEI = 5 and α = 1.6. Meanwhile, it should be emphasized that the VEI is selected
to be 5 because the actual influence distances of the products from the Mount
St. Helens volcanic eruption in May 18, 1980 is considered for the case study. The
environmental impact factors are estimated as a function of the VEI and α as in
Eq. (17.1) for the common products from a large explosive volcano. As shown in
Fig. 17.9a–f respectively, considering the maximum theoretical influence distances
of the large explosive volcanic products such as lateral blast, debris avalanche,
lahar, pyroclastic flow, pyroclastic surge, and gases and ashes, the theoretical
profiles of the EIF are illustrated, and it is therefore noticed that the EIF values
range from 0 to 1. These theoretical profiles help determine the values of the EIF
corresponding to the maximum distance from the vent of a product erupted from a
large explosive volcano. This value of EIF indicates the environmental damage
effect (e.g., primary, secondary, or tertiary) of that product. Considering each
product as shown in Fig. 17.9a–f, the primary, secondary and tertiary effect zones
are considerably determined as follows: the minimum EIF values corresponding to
the theoretical influence distance of each product, resulting from a large explosive
volcano with a VEI of 5, is estimated to be 0.2. We understand from the graphs as
given in (Fig. 17.5, 17.6, 17.7, and 17.8), the reference value of EIF is 0.368. Thus,
in case of VEI = 5 and α = 1.6, the primary effect zone for each product ranges
from 0.368 to 1 while the secondary effect zone from 0.2 to 0.368, and the tertiary
effect zone or safe area from 0 to 0.2 in terms of environmental impact factor. These
zone values can change as a function of theoretical influence distance of the
explosive volcanic product and the VEI.

Fig. 17.10 The EIF distribution for lateral blast of the St. Helens volcanic eruption taken place on May 18, 1980
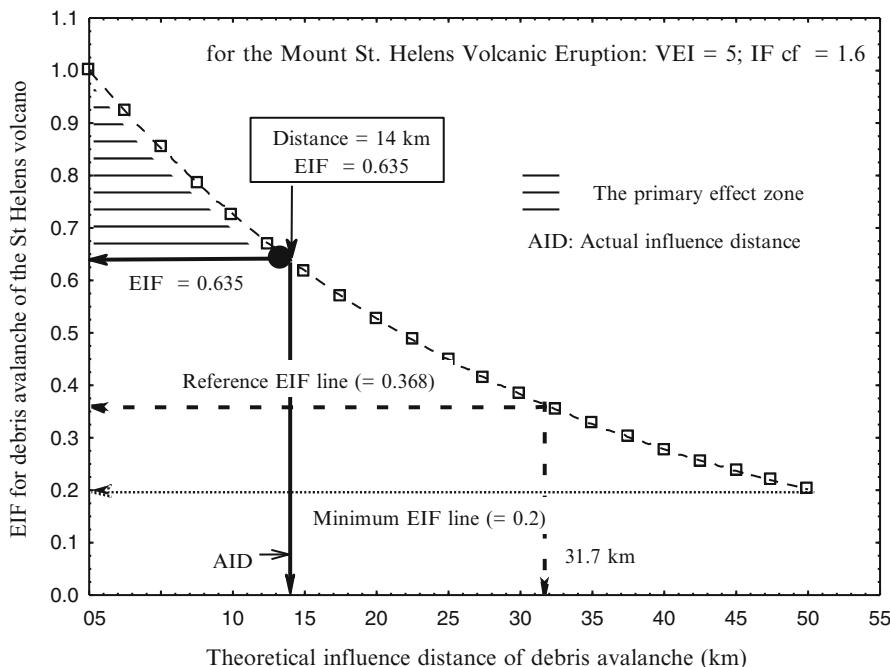
17.5.2 Results for Case Study

In order to determine the EIF values corresponding the actual influence distances of the explosive products from the Mount St. Helens volcanic eruption (May 18, 1980), the required values presented in Table 17.3 have been taken into account. Moreover, the EIF value for the earthquake effect has been designated. For the case study, the theoretical profiles of the products and earthquake effect have been considered. The points that represent the actual influence distances of the products and the earthquake effect on x-axis have been marked on the theoretical profiles representing each product, and the corresponding EIF values on the y-axis have been determined. Based on the actual influence distances and the EIF values, the primary, secondary, and tertiary effect zones have been subdivided. This procedure has been applied to determine the EIF values corresponding the actual influence distances of each products and the earthquake effect, and subdivide the effect zones.

Figure 17.10 presents the EIF value for lateral blast of the St. Helens volcanic eruption (May 18, 1980). The harmful effects of lateral blast in the primary effect zone (Direct blast zone, so-called the innermost zone that is 12.8 km far from the vent) can be assumed as excessive lethal and destructive effects on the living beings

and environment that are closer to the vent of the volcano. Moreover, in the secondary effect zone (Channelized blast zone, so-called an intermediate zone that is 30.4 km far from the vent), the secondary effects of lateral blast can be assumed as rarely lethal and less destructive effects on the living beings and environment in this zone. If lateral blast reaches approximately 35 km, then, it can be assumed that, in tertiary effect zone, lethal and destructive effects will minimize and/or come to an end. Under these considerations, in order to determine the EIF values, corresponding the actual influence distance of lateral blast from the St. Helens volcanic eruption, theoretical lateral blast curve or profile derived by means of Eq. (17.1) has been considered. As shown in Fig. 17.10, the actual primary influence distance of lateral blast in direct zone has been assumed to be 12.8 km. Moreover, the actual secondary influence distance has been assumed to be 30.4 km [33], the actual tertiary influence distance has been assumed to be 35 km [29]. Considering the theoretical primary effect zone ranging from 0.368 to 1 of the EIF and from 0 to 22 km of the theoretical influence distance in Fig. 17.10, it is noticed that the actual primary effect zone of the lateral blast has been found between these values. Thus, it is found that the primary EIF value corresponding the actual influence distance of the lateral blast range from 0.568 to 1 of the EIF and from 0 to 12.8 km of the influence distance, which can be assumed to refer to the excessive lethal and destructive effects on the living beings and environment that are closer to the vent of the volcano. These vital effects of the lateral blast can be observed up to 12.8 km of the influence distance. However, it is determined that the secondary EIF values corresponding the actual influence distance of the lateral blast range from 0.25 to 0.368 of the EIF and from 12.8 to 30.4 km of the influence distance, which can be assumed to refer to rarely lethal and less destructive effects on the livings and environment. These negative effects of the lateral blast can be observed up to 30.4 km of the influence distance. On the other hand, it is found that the tertiary EIF values, corresponding the actual influence distance of the lateral blast, range from 0 to 0.2 of the EIF and from 30.4 to 35 km of the influence distance, which can be assumed to refer to less destructive effects on the living beings and environment. These minimum effects of the lateral blast can be observed after 30.4 km of the influence distance. Accordingly, it can be said that the increasing EIF values indicates the severely lethal and destructive effects.

Figure 17.11 shows the EIF values for debris avalanche of the St. Helens volcanic eruption (May 18, 1980). The harmful effects of debris avalanche in the primary effect zone that is 14 km far from the vent can be assumed to cause lethal, severely injuring the living beings and destructive effects on the environment that are closer to the vent of the volcano. Moreover, after 14 km, the secondary and/or tertiary effects of debris avalanche can cause injury to the living beings and less damaging the environment. Under these considerations, in order to determine the EIF values, corresponding the actual influence distance of debris avalanche from the St. Helens volcanic eruption, theoretical debris avalanche curve or profile derived by means of Eq. (17.1) has been considered. As shown in Fig. 17.11, the actual primary influence distance of debris avalanche is given to be 14 km in the literature (see Table 17.3). Considering the theoretical primary effect zone ranging
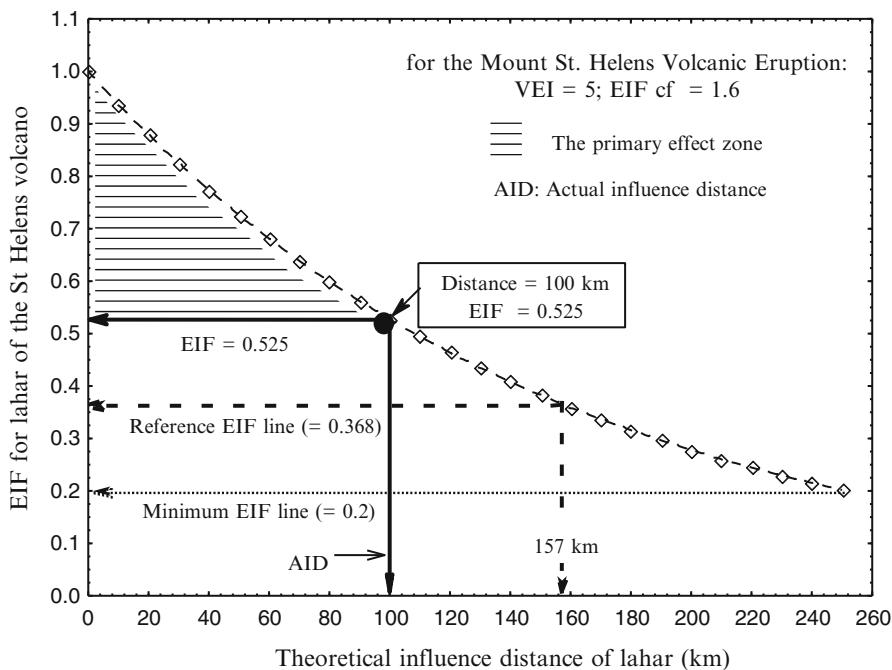
Fig. 17.11 The EIF distribution for debris avalanche of The St. Helens volcanic eruption taken place on May 18, 1980

from 0.368 to 1 of the EIF and from 0 to 31.7 km of the theoretical influence distance in Fig. 17.11, it is noticed that the actual primary effect zone of debris avalanche has been found between these values. Thus, it is found that the primary EIF value corresponding to the actual influence distance of debris avalanche ranges from 0.635 to 1 of the EIF and from 0 to 14 km of the influence distance, which can be assumed to refer to the primary effects stated above. These vital effects of debris avalanche can be observed up to 14 km of the influence distance. However, the secondary and tertiary effects of debris avalanche can be seen up to 31.7 km that is the critical distance of debris avalanche.

Figure 17.12 illustrates the EIF variation for lahar of the St. Helens volcanic eruption (on May 18, 1980). The harmful effects of lahar in the primary effect zone that is 100 km far from the vent can be assumed to cause lethal damage severely injuring the living beings and destructive effects on the environment that are closer to the vent of the volcano. Moreover, after 100 km, the secondary and/or tertiary effects of lahar can cause injury to the living beings and less damaging the environment.
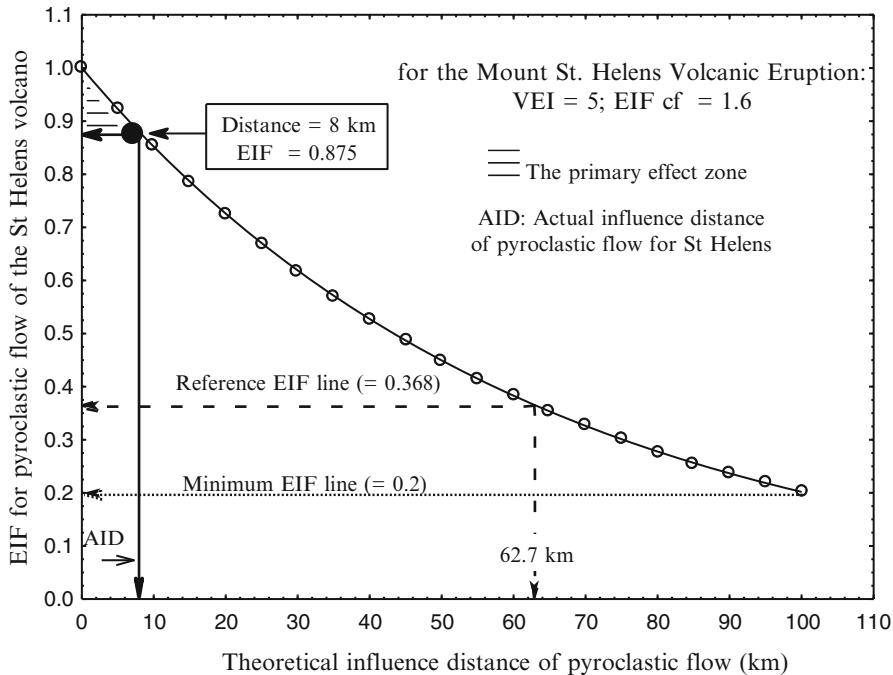
Under these considerations, in order to determine the EIF values, corresponding the actual influence distance of lahar from the St. Helens volcanic eruption, the theoretical lahar curve or profile derived by means of Eq. (17.1) has been considered. As shown in Fig. 17.12, the actual primary influence distance of lahar is given

Fig. 17.12 The EIF variation for lahar of The St. Helens volcanic eruption (on May 18, 1980)

to be 100 km in the literature (see Table 17.3). Considering the theoretical primary effect zone ranging from 0.368 to 1 of the EIF and from 0 to 157 km of the theoretical influence distance that is the critical distance for the lahar in Fig. 17.12, it is noticed that the actual primary effect zone of lahar has been found between these values. Thus, it is found that the primary EIF value corresponding the actual influence distance of lahar ranges from 0.525 to 1 of the EIF and from 0 to 100 km of the influence distance, which can be assumed to refer to the primary effects stated above (e.g., 27 bridges, nearly 200 homes destructed). Moreover, lahars destroyed more than 298 km of highways and roads and 24 km of railways (Web site 4). These vital effects of lahar can be observed up to 100 km of the influence distance. However, the secondary and tertiary effects of lahar can be observed up to 157 km that is the critical distance of lahar.
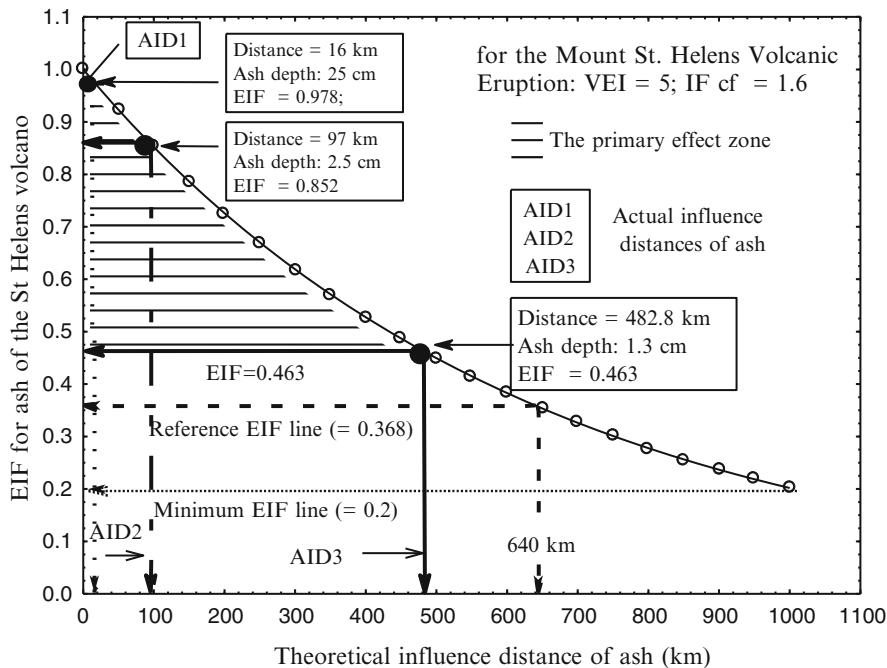
Figure 17.13 shows EIF value for pyroclastic flow of the St. Helens volcanic eruption (on May 18, 1980). The harmful effects of pyroclastic flow in the primary effect zone that is 8 km far from the vent can be assumed as the lethal effect on the living beings and severely destructive effect on the environment that are closer to the vent of the volcano. Moreover, after 8 km, the secondary and/or tertiary effects of pyroclastic flow can cause injury to the living beings and less damaging the environment. Under these considerations, in order to determine the EIF values, corresponding the actual influence distance of pyroclastic flow from the St. Helens volcanic eruption, theoretical pyroclastic flow profile derived by means of

Fig. 17.13 The EIF variation for pyroclastic flow of the St. Helens volcanic eruption (on May 18, 1980)

Eq. (17.1) has been considered. As shown in Fig. 17.13, the actual primary influence distance of pyroclastic flow is given to be 8 km in the literature (see Table 17.3). Considering the theoretical primary effect zone ranging from 0.368 to 1 of the EIF and from 0 to 62.7 km of the theoretical influence distance that is the critical distance for the pyroclastic flow in Fig. 17.13, it is noticed that the actual primary effect zone of pyroclastic flow has been found between these values. Thus, it is found that the primary EIF value corresponding the actual influence distance of pyroclastic flow ranges from 0.875 to 1 of the EIF and from 0 to 8 km of the influence distance, which can be assumed to refer to the primary effects stated above (e.g., About 600 km^2 of forest were knocked down within an 13 km inner-fan area, and extreme heat killed trees miles beyond the blow-down zone [35]). These effects of pyroclastic flow can be observed up to 8 km of the influence distance. However, the secondary and tertiary effects of pyroclastic flow can be observed up to 62.7 km that is the critical distance of pyroclastic flow.
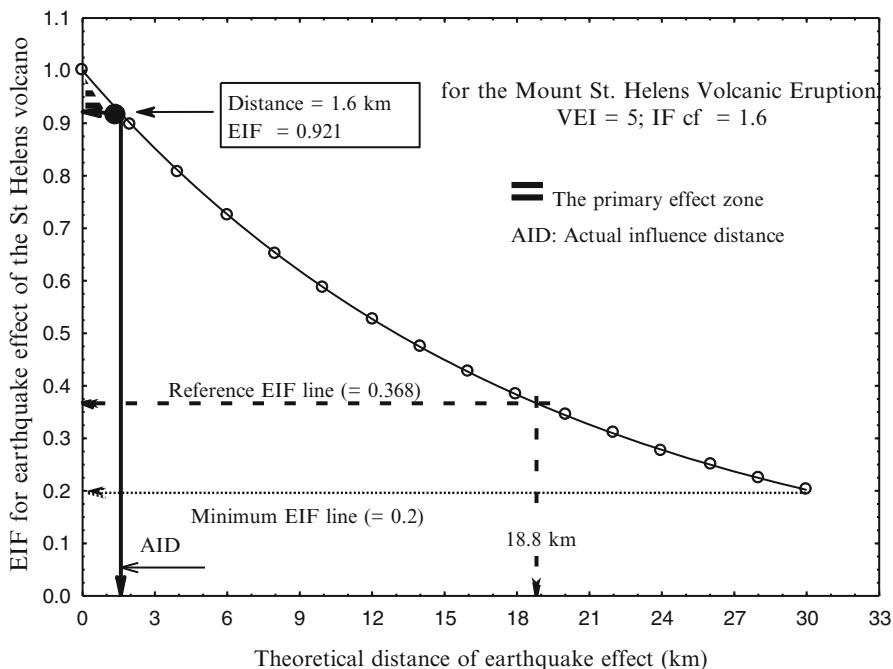
Figure 17.14 describes the EIF values for ash falls of the St. Helens volcanic eruption (on May 18, 1980). The harmful effects of ash fall in the primary effect zone can be assumed to be the intensive air pollution, instantaneous regional warming, cooling and climate change, acid rains. They can cause death in the places closer to the vent of the explosive volcano. Less environmental pollution,

Fig. 17.14 The EIF distribution for ash falls of The St. Helens volcanic eruption (on May 18, 1980)

long period-global warming, cooling and climate change, light effect-acid rains, and low temperature-ash falls may be assumed as the secondary and/or tertiary atmospheric effects. Under these considerations, in order to determine the EIF values, corresponding the actual influence distance of ash from the St. Helens volcanic eruption, theoretical ash profile derived by Eq. (17.1) has been considered. As shown in Fig. 17.14, Considering the theoretical primary effect zone ranging from 0.368 to 1 of the EIF and from 0 to 640 km of the critical influence distance in Fig. 17.14, it is noticed that the actual primary effect zone of the ash has been found between these values. Thus, it is found out that the primary EIF values corresponding the actual influence distance of the ashes range from 0.978 to 1 of the EIF and from 0 to 16 km of the influence distance for 25 cm of ash depth, from 0.852 to 0.978 of the EIF and from 16 to 97 km of the influence distance for 2.5 cm of ash depth, and from 0.463 to 0.852 of EIF and from 97 km to 482.8 km of the influence distance for 1.3 cm of ash depth, respectively, which can be assumed to refer to the primary effects stated above. After 482.8 km, the secondary and tertiary effects can be observed up to 640 km.

Figure 17.15 presents the EIF value for earthquake effect of the St. Helens volcanic eruption (May 18, 1980). The harmful effects of earthquake in the primary effect zone that is 1.6 km far from the vent can be assumed as the lethal effect on the

Fig. 17.15 The EIF variation for earthquake effect of The St. Helens volcanic eruption (on May 18, 1980)

living beings and severely destructive effect on the environment that are closer to the vent of the volcano. Moreover, after 1.6 km, the secondary and/or tertiary effects of earthquake can be observed, which are injuring the living beings and damaging the environment. Under these considerations, in order to determine the EIF value, corresponding the actual influence distance of earthquake caused by the St. Helens volcanic eruption, the theoretical earthquake profile derived by means of Eq. (17.1) has been considered. As shown in Fig. 17.15, the actual primary influence distance of earthquake is given as 1.6 km in the literature (see Table 17.3). Considering the theoretical primary effect zone ranging from 0.368 to 1 of the EIF and from 0 to 18.8 km of the theoretical influence distance that is the critical distance for the earthquake in Fig. 17.15, it is noticed that the actual primary effect zone of earthquake has been found between these values. Thus, it is found that the primary EIF value corresponding the actual influence distance of earthquake ranges from 0.921 to 1 of the EIF and from 0 to 1.6 km of the influence distance, which can be assumed to refer to the primary effects stated above. The vital effects of earthquake can be observed up to 1.6 km of the influence distance. However, the secondary and tertiary effects of earthquake can be observed up to 18.8 km that is the critical distance of earthquake.

17.6 Conclusions

In this study we propose a new parameter as the "Environmental Impact Factor (EIF)" to quantify the environmental impact of explosive volcanoes as a function of the VEI, α, and the theoretical influence distances of the products and their effects. Moreover, in order to test and verify the EIF by using the actual influence distances of the explosive products from the Mount St. Helens volcanic eruption (on May 18, 1980), a case study has been performed. Based on the main findings, the following concluding remarks can be drawn:

- The EIF correction factor (α) developed in this study is one of the most important parameters that should be taken into account to estimate the critical influence distances of the explosive products and their effects.
- The EIF values which are higher than the reference EIF value (0.368) and correspond to the lower values of the theoretical influence distances indicate the primary effect zone of explosive volcanic eruptions.
- The EIF values that are lower than 0.368 and correspond to the higher values of the theoretical influence distances indicate the secondary and/or tertiary effect zone of the explosive volcanic eruption.
- The EIF is a key parameter to estimate the environmental effects of the explosive products and their effects and compare and rank them based upon their environmental damage.
- The critical maximum influence distances indicate the primary effect zones ranging from 0.368 to 1 of the EIF values.
- The critical maximum influence distances of the environmental effects caused by the explosive volcanoes indicate the beginning of the safety zone of the explosive volcanic eruption with the difference EIF correction factors and VEI values.
- The actual primary effect-zone of lateral blast ranges from 0.568 to 1 of the EIF corresponding from 0 to 12.8 km of the influence distance. In this zone, the excessive lethal and destructive effects on the living beings and environment that are closer to the vent of the volcano can be observed. However, its secondary effect-zone ranges from 0.25 to 0.368 of the EIF corresponding from 12.8 to 30.4 km, indicating rarely lethal and less destructive effects on the living beings and environment while the tertiary effect-zone from 0 to 0.2 of the EIF corresponding from 30.4 to 35 km of the influence distance, referring less destructive effects on the living beings and environment.
- The actual primary effect-zone of debris avalanche ranges from 0.635 to 1 of the EIF corresponding from 0 to 14 km of the influence distance, causing lethal damage, severely injuring the living beings and destructive effects on the environment that are closer to the vent of the volcano.
- The actual primary effect zone of lahar ranges from 0.525 to 1 of the EIF corresponding from 0 to 100 km of the influence distance, causing lethal damage, severely injuring the living beings and destructive effects on the environment that are closer to the vent of the volcano.

- The actual primary effect zone of pyroclastic flow ranges from 0.875 to 1 of the EIF corresponding from 0 to 8 km of the influence distance, referring to lethal effect on the living beings and severely destructive effect on the environment that are closer to the vent of the volcano.
- The actual primary effect-zone of ash fall ranges from 0.978 to 1 of the EIF corresponding from 0 to 16 km of the influence distance for 25 cm of ash depth while the EIF from 0.852 to 0.978 corresponding from 16 to 97 km of the influence distance for 2.5 cm of ash depth, and from 0.463 to 0.852 corresponding from 97 km to 482.8 km of the influence distance for 1.3 cm of ash depth, suggesting the primary effects such as intensive air pollution, instantaneous regional warming, cooling and climate change, acid rains.
- The actual primary effect-zone of earthquake ranges from 0.921 to 1 of the EIF corresponding from 0 to 1.6 km of the influence distance, indicating the lethal effect on the living beings and severely destructive effect on the environment that are closer to the vent of the volcano.

Thus, it is expected that this study will provide a quantitative record to compare the environmental effects of the active explosive volcanoes all over the world.

References

1. Newhall CH, Self S (1982) The volcanic explosivity index (VEI): an estimate of explosive magnitude for historical volcanism. J Geophys Res 87:1231–1238
2. Lamb HH (1970) Volcanic dust in the atmosphere; with a chronology and assessment of its meteorological significance. Phil Trans R Soc Lond Series A-Math Phys Sci 266:425–533
3. Thorarinsson S (1979) On the damage caused by volcanic eruptions with special references to tephra and gases. In: Sheets PA, Grayson DK (eds) Volcanic activity and human ecology. Academic Press, New York, NY, pp 125–159
4. Berresheim H, Jaeschke W (1983) The contribution of volcanoes to the global atmospheric sulfur budget. J Geol Res 88:3732–3740
5. Devine JD, Sigurdsson H, Davis AN (1984) Estimates of sulfur and chlorine yield to the atmosphere from volcanic eruptions and potential climatic effects. J Geophys Res 89:6309–6325
6. Carey S, Sparks RSJ (1986) Quantitative models of the fallout and dispersal of tephra from volcanic eruption columns. Bull Volcanol 48:109–125
7. Woods AW (1988) The dynamics and thermodynamics of eruption columns. Bull Volcanol 50 (3):169–193
8. Palais JM, Sigurdsson H (1989) Petrologic evidence of volatile emissions from major historic and pre-historic volcanic eruptions. In: Berger AR, Dickinson E, Kidson JW (eds) Understanding climate change. Am Geophys Union Geophys Monogr 52:31–53
9. Sigurdsson H (1990) Assessment of the atmospheric impact of volcanic eruptions. In: Sharpton VL, Ward PD (eds) Global catastrophes in earth history; and interdisciplinary conference on impacts, volcanism, and mass mortality. Geol Soc Am Special Paper. 247:99–110
10. Rampino MR (1991) Volcanism, climatic change, and the geological record. Sedimentation in volcanic settings. Soc Sediment Geol Spec Publ 45:9–18

11. Bekki S, Pyle JA (1994) A two-dimensional modeling study of the volcanic eruption of Mt Pinatubo. J Geophys Res 99:18861–18869
12. Pyle DM, Beattie PD, Bluth GJS (1996) Sulphur emissions to the stratosphere from explosive volcanic eruptions. Bull Volcanol 57:663–671
13. Textor C, Graf HF, Timmreck C, Robock A (2003) Emissions from volcanoes. In: Granier C, Reeves C, Artaxo P (eds) Emissions of chemical compounds and aerosols in the atmosphere. Kluwer, Dordrecht, 269–303
14. Textor C, Graf HF, Longo A, Neri A, Ongaro TE, Papale P, Timmreck C, Ernst GGJ (2005) Numerical simulation of explosive volcanic eruption from the conduit flow to global atmospheric scales. Ann Geophys 48(4/5):817–841
15. Williams H, McBirney A (1979) Volcanology. Freeman Cooper Co, San Francisco, CA, pp 1–391
16. Cas RAF, Wright JV (1988) Volcanic successions - modern and ancient. Unwin Hyman, London
17. Schmincke HU (2004) Volcanism. ISBN: 3-540-43650-2. Springer-Verlag, Berlin.
18. Web site 1: http://en.wikipedia.org/wiki/Volcano. Accessed 2 June, 2009
19. Giggenbach WF (1996) Chemical composition of volcanic gases. In: Tilling RI, Scarpa R (eds) Monitoring and mitigation of volcano hazards. Springer, Berlin, pp 221–256
20. Eby GN (2004) Principles of environmental geochemistry. ISBN-ISSN 0122290615, Brooks/Cole Publishers: Australia
21. Manahan SE (1993) Fundamentals of environmental chemistry. ISBN: 0-87371-587-X. Lewis Publishers: USA
22. Symonds RB, Rose WI, Bluth G, Gerlach TM (1994) Volcanic gas studies: methods, results, and applications. In: Carroll, M. R. and J. R. Holloway (eds) Volatiles in Magmas. Mineral Soc Am Rev Mineral. 30:1–66
23. Mcguire WJ (1998) Volcanic hazards and their mitigation. In: Maund JG, Eddleston M (eds) Geohazards in engineering geology, vol 15. Geological Society Engineering Geology Special Publication, London, pp 79–95
24. Chester DK, Degg M, Duncan AM, Guest JE (2001) The increasing exposure of cities to the effects of volcanic eruptions: a global survey. Environ Hazards 2:89–103
25. Lamb HH (1983) Update of the chronology of assessment of the volcanic dust veil index. Clim Monitoring 12:79–90
26. Schnetzler CC, Bluth GJS, Krueger AJ, Walter LS (1997) A proposed volcanic sulfur dioxide index (VSI). J Geophys Res 102(B9):20087–20091
27. Robock A, Free MP (1995) Ice cores as an index of global volcanism from 1850 to the present. J Geophys Res 100:11549–11567
28. Robertson A, Overpeck J, Rind D, Mosley-Thompson E, Zielinski G, Lean J, Koch D, Penner J, Tegen I, Healy R (2001) Hypothesized climate forcing time series for the last 500 years. J Volcanol Geol Res 106:14783–14803
29. Crandell DR, Hoblitt RP (1986) Lateral blast at Mount St. Helens and hazard zonation. Bull Volcanol 48:27–37
30. Aydın F, Midilli A, Dincer I (2009) A parametric study on environmental impact assesment of explosive volcanoes. In: Dincer I, Coplan CO, Midilli A (eds) Proceedings of the Global Conference on Global Warming (GCGW-2009), July 5–9, 2009, Istanbul, Turkey. ISBN: 978-605-89885-1-4. 1180-1191, 2009
31. Wolfe EW, Pierson TC (1995) Volcanic-Hazard Zonation for Mount St. Helens, Washington. U.S. Geol Survey. Open-File Report 95–497
32. Brantley SR, Myers B (1997) Mount St. Helens—from the 1980 Eruption to 1996. U.S. Geol Survey Fact Sheet: 070–97
33. Web site 2: http://vulcan.wr.usgs.gov/Volcanoes/MSH/May18/summary_may18_eruption.html. Accessed 2 June 2009
34. Web site 3: http://pubs.usgs.gov/gip/msh//lateral.html. Accessed 2 June 2009
35. Web site 4: http://en.wikipedia.org. Accessed 2 June 2009

Chapter 18
Probabilistic Health Risk Assessment of PCDD/Fs in Vegetable Foods at Highly Polluted Area in Turkey

Seda Aslan Kilavuz, Ertan Durmusoglu, and Aykan Karademir

Abstract Polychlorinated dibenzo-*p*-dioxins and polychlorinated dibenzofurans (PCDD/Fs) are highly toxic and persistent organic pollutants that are ubiquitous in the environment. The main pathway of these compounds for human exposure is animal food consumption. On the other hand, plant-derived foods should be also considered for especially vegetarians in an exposure assessment. In this study, dietary intake and health risks of PCDD/Fs have been assessed for adult population living in Kocaeli, Turkey. Exposure levels have been calculated based on a combination of concentration data of locally and non-locally grown vegetable foods and a matrix of environmental exposure factors. The Monte Carlo technique has been applied to calculate dietary exposure and carcinogenic risk distributions. The results have showed that the mean PCDD/F intake via the consumption of vegetable foods are 0.652, 0.672, and 0.661 pg WHO-TEQ kg^{-1} body weight (bw) day^{-1} for urban, semi-urban, and rural receptors, respectively. These results are within the range of 1–4 pg WHO-TEQ kg^{-1} bw day^{-1} adopted by WHO as the tolerable daily intake. On the other hand, estimated carcinogenic risks related to the PCDD/Fs doses are above the acceptable carcinogenic risk level of 1 in 1,000,000, as proposed by the US EPA. Sensitivity analyses indicate that the cereal consumption has significance effect on the PCDD/F intake for all receptor groups.

Keywords PCDD/Fs • Kocaeli • Turkey • Exposure level • Environmental exposure factors • The Monte Carlo technique • Dietary exposure • Carcinogenic risk distribution • Carcinogenic risk level • Dioxins • Exposure assessment • Health risk assessment • Dioxins in foodstuff

S.A. Kilavuz (✉) • E. Durmusoglu • A. Karademir
Department of Environmental Engineering, Faculty of Engineering,
University of Kocaeli, Umuttepe Campus, 41380 Kocaeli, Turkey
e-mail: sedaaslan@kocaeli.edu.tr; ertan@kocaeli.edu.tr; aykan@kocaeli.edu.tr

Acronyms

ADI	Average daily intake
AhR	Aryl hydrocarbon receptor
AT	Averaging time (day)
BW	Body weight of receptors (kg)
C	PCDD/F concentration in food (pgTEQ/g fresh weight)
ED	Exposure duration (year)
EF	Exposure frequency (day year^{-1})
F	Site-specific fraction of food (non-)locally produced
HQ	Hazard quotient
HRGC/HRMS	High-resolution gas chromatography coupled with a high-resolution mass spectrometry
HRGC/LRMS-NCI	High-resolution gas chromatography coupled with a low-resolution mass spectrometry
IARC	International Agency for Cancer Research
IR	Ingestion rate of foods
Q	Food consumption rate (kg day^{-1})
PCDD/Fs	Polychlorinated dibenzo-*p*-dioxins and polychlorinated dibenzofurans
POPs	Persistent organic pollutants
TCDD	Tetrachlorodibenzo-*p*-dioxin
TDIs	Tolerable daily intakes
TEF	Toxic equivalency factor
TEQ	Toxic equivalents
US EPA	United States Environmental Protection Agency
WHO	World Health Organization

18.1 Introduction

Polychlorinated dibenzo-*p*-dioxins and polychlorinated dibenzofurans (PCDD/Fs), commonly known as dioxins, are member of the persistent organic pollutants (POPs) that are ubiquitous in the environment.

Although several studies have been conducted on the levels of PCDD/Fs in plant food groups and their risks related to the consumption of these foods in the world, there are only two studies reported for Kocaeli, Turkey, providing data on PCDD/F levels in food and related health risks [1, 2]. In the study related to PCDD/F exposure from plant food, PCDD/F intake from plant food groups consumed by the population living in Kocaeli has been estimated between 3.195 and 12.14 pg I-TEQ kg^{-1} bw day^{-1} for adult receptors, based on the limited data on the PCDD/F levels in local food groups [2]. Plant food consumption has been also identified as the main contributor to the intake of dioxins.

The main objective of this chapter is to estimate the dietary intake of PCDD/Fs via different plant foodstuffs for adult population living in Kocaeli, Turkey. Another objective of the study is to assess the noncarcinogenic and carcinogenic health risks, and to determine the parameters of significant effects on the PCDD/F exposure. In order to evaluate the PCDD/F intake of individuals with different consumption behavior and lifestyles, adult population living in Kocaeli have been divided into several groups according to their specific traits. The PCDD/F doses and related risks have been determined as distribution using Monte Carlo analysis.

18.2   Background

18.2.1   Properties and Environmental Fate of Dioxins

PCDD/Fs classified as halogenated aromatic hydrocarbons include 75 individual polychlorinated dibenzo-*p*-dioxin (PCDDs) and 135 polychlorinated dibenzofuran (PCDFs) compounds that are referred to as congeners. Only 17 of the 210 congeners of PCDD/Fs, those with chlorine substitution in the 2,3,7,8 positions are toxicologically important. Among these congeners, 2,3,7,8-tetrachlorodibenzo-*p*-dioxin (TCDD) is the most toxic compound of dioxins [3–6].

PCDD/Fs have widely different physicochemical properties between congeners. In general, they are highly lipophilic and have high octanol–water partition coefficients and low vapor pressure and consequently they tend to bioaccumulate in fatty tissues.

PCDD/Fs have never been deliberately produced; they are by-products of various combustion and chemical processes (waste incineration and other industrial thermal processes, production of chemicals, traffic, etc.). Once PCDDs and PCDFs are released to the atmosphere, they are dispersed in air and deposited at varying rates on different environmental media such as land, surface water, or vegetation. Due to their high lipophilicity and low water solubility, PCDD/Fs are primarily associated with particulate and organic matter [3–6]. The compounds are generally stable under most environmental conditions. In air, they are partitioned as gaseous phase and particle-bound products based on their vapor pressure and ambient air temperature. Photodegradation is thought to be a significant transformation process for especially lower chlorinated PCDD/PCDF congeners in vapor phase. PCDD/Fs bounded to particulate matter are extremely stable compounds and resistant to degradation [5, 7]. Removal of atmospheric PCDD/Fs and their inputs to terrestrial and aquatic ecosystem are via wet and dry deposition processes. Although small amount of PCDD/Fs sorbed to soil can be returned to atmosphere through re-suspension and some volatilization, most of them remain in undisturbed soil surface. A portion of the contaminated soil can move to soil with erosion of soil and then they undergo sedimentation. The ultimate environmental sink of these PCDD/Fs is thought to be aquatic sediments [7].

It has been recognized that all 2,3,7,8-substituted PCDD/Fs are highly toxic. Human and animal studies have shown their adverse health effects. Toxicological effects of these compounds include dermal toxicity, immunotoxicity,

carcinogenicity, and reproductive and developmental toxicity and chloracne. The toxicity of PCDD/Fs is mediated through the binding of PCDD/F congener to the intracellular aryl hydrocarbon (AhR) receptor present in animal and human tissues [8]. As the most toxic congener of all dioxins, 2,3,7,8-TCDD has been classified as human carcinogen (class I) by International Agency for Research on cancer (IARC) [5].

In almost all environmental and biological samples, dioxins are found as complex mixtures and they have different toxicity. In order to assess the risks of a mixture and to express analytical results, toxic equivalency factor (TEF) to most toxic ones (17 congener) has been developed by World Health Organization (WHO). TEF values indicate the degree of toxicity of different congeners compared to 2,3,7,8-TCDD. TEF value of this compound equals 1. Analytical results are converted into toxic equivalents (TEQ) by multiplying the concentrations of each congener by their corresponding TEF and total TEQ concentrations of the mixture obtained by summing the individual TEQs [9–11].

Peoples may be exposed to dioxins via several routes including inhalation, ingestion of contaminated soils, dermal adsorption, and food consumption. However, major exposure of human to PCDD/Fs occurs mainly through the food consumption (more than 90 %). Due to the lipophilic properties of these compounds, they tend to accumulate in fatty contents of foods [12]. Therefore, the main pathway for human exposure is animal food consumption. On the other hand, plant-derived foods should be also considered especially for people having different eating habits, e.g., vegetarians. For example, in a study conducted in Turkey [2], consumption of locally grown plant was indicated to be dominant pathway in PCDD/F intake.

18.2.2 Health Risks of Dioxins

PCDD/Fs cause both carcinogenic and noncarcinogenic effects in humans. Several international institutions carried out numerous comprehensive epidemiological and animal studies in order to identify the threshold levels of noncarcinogenic end points (i.e., tolerable daily intakes (TDIs)). The TDIs recommended in these studies generally range from 1 to 10 pg WHO-TEQ kg^{-1} body weight (bw). Recently, there is a general tendency to accept TDIs between 1 and 4 pg WHO-TEQ kg^{-1} bw, as proposed by WHO [13].

Human health risks of PCDD/F are divided into two parts:

- Noncarcinogenic risk: Total exposure (sum of all exposures) is compared with TDI in ng kg^{-1} day^{-1}, and the risk for noncarcinogenic pollutants is expressed as the hazard quotient (HQ).
- Carcinogenic risk: Risk for carcinogenic pollutants expressed as the probability of contracting cancer through exposure to related chemicals assessed by multiplying total exposure (mg kg^{-1} day^{-1}) by the carcinogenic slope factor (kg day mg^{-1}).

Parameters in health risk assessment are not deterministic but variable and uncertain. Data variability refers to true heterogeneity or diversity due to the

distinctions in response or exposure. On the other hand, uncertainty due to the lack of total knowledge should be reduced by more data. Probability density function can be used to characterize uncertainty and variability of each parameter in risk estimates instead of being explained by one point value [14].

18.3 Materials and Methods

18.3.1 The Study Area and Sampling

As a metropolitan city, Kocaeli is located on the South and North side of Izmit Bay. Almost all types of environmental pollution in the region exist as the city has undergone a dense industrialization and rapid urbanization since 1970s. Despite some attempts to reduce the environmental pollution in the area since mid-1990s, pollution levels in the area are still high and posing significant health hazards. Two very busy traffic arteries, three major tire factories, an automotive industry, a pulp and paper industry, several petrochemical and iron and steel industries, a hazardous waste incinerator, and the largest petroleum refinery of Turkey are the major source of environmental pollutants [2, 15].

Commercial plant food products have been purchased from supermarkets and open market by checking the origin of samples. Sampling points of locally grown food samples have been described in detail elsewhere [1]. Sampling points have been selected according to the location of the pollutant sources, meteorological conditions (i.e., dominant wind sectors), plant food-growing regions, and food consumption habits of the people living in the area. Plant food groups have been selected considering consumption behavior of dwellers in the area. These products have been classified as fruits, flour, and vegetables (leafy, fruiting, and rooty). Daily diet characteristics for the different receptor groups in Kocaeli have been provided in previous study [15].

18.3.2 PCDD/F Concentrations in Plant Foods

In this study, the PCDD/F concentrations used in exposure calculations have been taken from previous study [1], in which 131 plant and animal food samples have been analyzed for 2,3,7,8-substituted PCDD/Fs. In the study [1], while majority of the samples have been analyzed by a high-resolution gas chromatography coupled with a low-resolution mass spectrometry (HRGC/LRMS-NCI), some of them have been analyzed by a high-resolution gas chromatography coupled with a high-resolution mass spectrometry (HRGC/HRMS). In that study, the PCDD/F concentrations in local and commercial plant foods have been eliminated except for local leafy vegetables since the majority of PCDD/F congeners in other plants measured especially by HRGC/LRMS-NCI have been lower than the detection limits. Hence, in this study, the PCDD/F concentrations obtained from HRGC/HRMS for exposure

Table 18.1 Mean TEQ concentrations of PCDD/Fs in local and commercial plant foods collected from Kocaeli

Foods	PCDD/F-TEQ local (pg/g fw)	Sampling number	PCDD/F-TEQ commercial (pg/g fw)	Sampling number
pg/g fresh weight				
Rooted vegetables	0.031	1	0.046	1
Leafy vegetables	0.061 ± 0.07	12	0.03 (0.028–0.031)[a]	2
Leafless vegetables	0.03 (0.0305–0.0308)	3	0.047 (0.046–0.049)	3
Fruit	0.028 ± 0.003	4	0.031 (0.0316–0.0317)	2
Cereal	0.079	1	0.077 (0.076–0.078)	2

[a]Concentrations in the parenthesis indicate min. and max. levels for sampling number ≤ 3

calculations have been used. Since most of congeners in local leafy vegetables have been detectable by HRGC/LRMS-NCI, the PCDD/F concentrations given by previous study [1] have been used in the exposure evaluation for these groups of foods. The PCDD/F congener concentrations and their mean TEQ values calculated using TEFs proposed by WHO [10] are summarized in Table 18.1.

18.3.3 Estimation of Exposure of PCDD/Fs

General exposure estimation has been given elsewhere [14, 16]. In this study, adult receptors living in Kocaeli have been divided into three groups, i.e., rural, semi-urban, and urban, on the basis of their lifestyles and behavior patterns. While the residents living in the central area of the city have been considered in the urban receptors, the farmers living in the rural area have been considered in the rural setting. An additional group of people has been represented by the semi-urban setting, a transition from rural to urban as a result of the irregular industrialization and urbanization in Kocaeli. The individual exposure expressed as the average daily intake (ADI) in pg TEQ kg^{-1} bw d^{-1} has been calculated as follows [17]:

$$ADI = C \times \frac{IR \times EF \times ED}{BW \times AT} \tag{18.1}$$

For food ingestion, C is the concentration in food in terms of TEQ; IR is the ingestion rate of foods calculated by multiplying site-specific fraction of food (non-)locally produced (F) by food consumption rate (Q in kg d^{-1}); EF is the exposure frequency (day $year^{-1}$); ED is the exposure duration (year); AT is the averaging time to define noncarcinogenic exposure (d); and BW is the body weight of receptors (kg).

Total exposure to PCDD/Fs from plant food has been determined by the summation of the exposures through consumption of local and nonlocal plant products for each setting. The site-specific food consumption data and their local fractions related to receptor groups have been provided by previous studies [2, 15]. The exposure parameters used in this study have been given in Table 18.2.

Table 18.2 Distribution functions for input parameters

Parameter	Distribution type	Explanation
PCDD/F Conc.	*(pg WHO-TEQ. g^{-1})*	
Local rooted vegetables	Not distributed[a]	Unpublished data
Commercial rooted vegetables	Uniform[b] (0-det. Lim.)	Unpublished data
Local leafy vegetables	Log normal (Geo mean; SD)	Taken from pre. stud. [1]
Commercial leafy vegetables	Triangular (min; mean; max)	Unpublished data
Local leafless vegetables	Triangular (min; mean; max)	Unpublished data
Commercial leafless vegetables	Triangular (min; mean; max)	Unpublished data
Local fruits	Triangular (min; mean; max)	Unpublished data
Commercial fruits	Triangular (min; mean; max)	Unpublished data
Local cereal	Uniform[b] (0-det. lim.)	Unpublished data
Commercial cereal	Triangular (min; mean; max)	Unpublished data
Congeners below det. lim.	Uniform (0-det. lim.)[c]	Unpublished data
Exposure parameters		
Body weight (kg)	Lognormal (mean, SD)	Taken from pre. stud. [2]
		SD was taken as 20 % of the mean
Food ingestion rates (g d^{-1})	Lognormal (mean, SD)	Taken from pre. stud. [2]
		SD was taken as 50 % of the mean
Local fractions of foods	For urban and semi-urban receptors: triangular (low, most likely, high)	Taken from pre. stud. [2]
		Low value is zero, the most likely value is the mean value for corresponding setting, and high value is the mean value for a farmer
	For rural receptors	
	Restricted lognormal (mean, SD, minimum, maximum)	SD was taken as 50 % of the mean, minimum is 0 and maximum is 1
Exposure frequency (d)	Triangular (low, most likely, high)	(335, 350, 365)
Exposure duration (year)	Not distributed	30 years for urban adults, and 50 years for semi-urban and rural adults

[a]A single value was used for calculation as only one sample could be analyzed
[b]All PCDD/F congeners in the food were measured below the detection limit, so distribution was chosen as uniform between zero and detection limit value
[c]Distribution functions were chosen for each congener separately and congeners measured below the detection limits were distributed uniform between zero and detection limit value

18.3.4   Risk Characterization

In this study human health risks of PCDD/F have been assessed in two parts:

- Noncarcinogenic risk: In order to evaluate the noncarcinogenic risks in this study, daily intake data have been compared with the TDIs between 1 and 4 pg WHO-TEQ kg^{-1} bw, as proposed by WHO [13].
- Carcinogenic risk: In this study, carcinogenic slope factor of 156,000 kg day mg^{-1} recommended by the US EPA has been adopted [18]. According to the US EPA [19], carcinogenic risks below 10^{-6} (i.e., one occurrence over one million people) would be acceptable.

In this study, the Monte Carlo analysis has been applied to calculate the intake levels and to determinate sensitivity and uncertainty. Each modelling parameter has been expressed as a probability distribution function to characterize the variation of the parameter within a given range of values. Here, the Monte Carlo approach has been carried out using @Risk software (*Palisade Inc.*). This program calculates risks on the basis of propagation of variability and uncertainty given by each parameter probability function throughout the whole risk assessment model, resulting in a final probability distribution function. An iteration size of 2,000 has been used to produce the relative frequencies of the intake and the risk estimates through consumption of plant foods for each receptor groups. Sensitivity analysis has been performed to calculate the contribution of model inputs to model output variability and uncertainty. Regression coefficients between the input parameters and the risk outputs have been calculated and assessed in the sensitivity analysis [12]. Table 18.2 provides the Monte Carlo input parameter distributions along with the other details for the calculation of human health risks.

18.4   Results and Discussion

Dietary PCDD/F exposure estimated by the exposure model for each receptor group is provided in Table 18.3. Intakes for each group of receptors have been expressed as distribution percentiles (5th, 50th (median), and 95th) and mean, since input parameters such as PCDD/F levels in foods have been considered as a distribution function in the risk analysis.
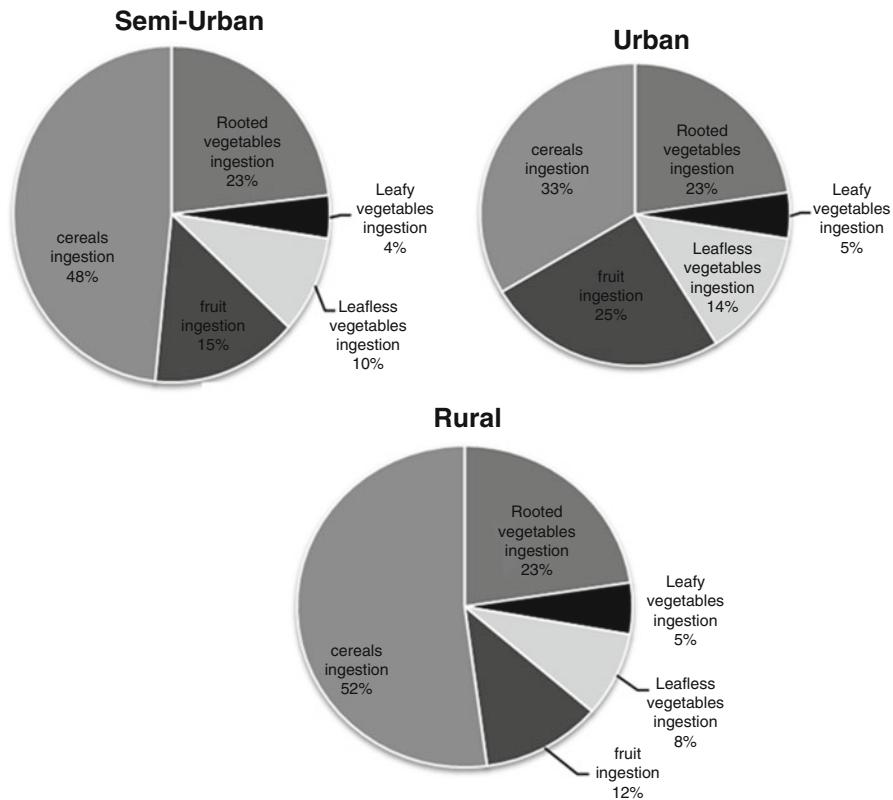
Mean PCDD/F total exposure levels from the consumption of animal foods for urban, semi-urban, and rural receptors are 0.652, 0.672, and 0.661 pg WHO-TEQ kg^{-1} bw day^{-1}, respectively. The results are fairly lower than the total PCDD/F doses estimated in a previous study (between 3.7 and 13.1 pg I-TEQ kg^{-1} bw day^{-1} for adult receptors) conducted for Kocaeli [2]. Furthermore, in contrast to that study, in which rural adult receptors had the highest PCDD/F intakes, no difference has been observed among the receptor groups. One reason for this would be the lack of data in the PCDD/F concentrations used for exposure

Table 18.3 Estimated PCDD/F exposure levels for receptor groups in Kocaeli

Receptor/exposure way	5th percentile	50th percentile	95th percentile	Mean
Urban				
Rooted vegetable ingestion	0.054	0.127	0.310	0.148
Leafy vegetable ingestion	0.012	0.025	0.070	0.032
Leafless vegetable ingestion	0.037	0.075	0.180	0.089
Fruit ingestion	0.074	0.141	0.336	0.165
Cereal ingestion	0.091	0.188	0.459	0.218
Total vegetable doses	0.380	0.610	1.040	0.652
Semi-urban				
Rooted vegetable ingestion	0.060	0.133	0.320	0.156
Leafy vegetable ingestion	0.012	0.023	0.056	0.028
Leafless vegetable ingestion	0.027	0.053	0.133	0.063
Fruit ingestion	0.045	0.086	0.204	0.100
Cereal ingestion	0.142	0.285	0.643	0.325
Total vegetable doses	0.386	0.636	1.070	0.672
Rural				
Rooted vegetable ingestion	0.062	0.127	0.301	0.150
Leafy vegetable ingestion	0.013	0.027	0.077	0.034
Leafless vegetable ingestion	0.026	0.048	0.111	0.056
Fruit ingestion	0.036	0.066	0.140	0.076
Cereal ingestion	0.154	0.300	0.660	0.345
Total vegetable doses	0.368	0.612	1.060	0.661

calculations in the earlier study in which the PCDD/F concentrations in plant products have been assumed to be equal to those measured in grass samples. Another reason would be that commercial food data considered in this study have not been taken into account in the earlier study. The PCDD/F intakes for rural receptors can be expected to be higher than those for the other receptors depending on the higher local plant food consumption rate of people living in the rural area. However, in this study, the PCDD/F concentrations both in local and commercial plant foods are fairly low and very close to each other. Hence, the PCDD/F intakes for each receptor groups show similarity. In general, the 5th percentiles of the estimated PCDD/F intakes are approximately 55 % of the mean value, while the 95th percentiles are almost two times higher than the mean value in all settings. It can be concluded that neither mean values nor worst-case values of PCDD/F intakes (95th percentiles) exceed the threshold value of 1–4 pg WHO-TEQ kg^{-1} bw day^{-1} adopted by WHO as the TDI of the PCDD/Fs for noncarcinogenic toxicological effects.

Contributions of each exposure pathway to total intake are presented in Fig. 18.1. Although receptor groups have different consumption behaviors based on their lifestyles and socio-economical situations, the contribution of food groups to the total PCDD/F intake generally shows some similarities among the receptor groups. Ingestion of cereals has the highest contribution in all settings and it is in an agreement with a recent study conducted in another Mediterranean country [20]. The contribution of ingestion of leafy vegetable pathways has been estimated

Fig. 18.1 Contributions of each plant products to the total PCDD/F intake

to be lower than 10 % for all receptor groups. Moreover, consumption of fruits is important for especially urban receptors in the PCDD/F intake.

Results of sensitivity analysis for the exposure levels are provided in Table 18.4. The results show the similarities with the contribution percentages of the consumption of different food groups given in Fig. 18.1. According to the regression coefficients between the inputs and outputs for rural, semi-urban, and urban settings, consumption rates of cereals are by far the most significant parameter affecting the total intake. Fruit consumption has also considerable effects on the total intake for especially urban and semi-urban receptors. On the other hand, the PCDD/F concentrations in both local and commercial foods such as cereals, leafy vegetables, and rooty vegetables are found as the most significant parameters in the PCDD/F exposures in all settings.
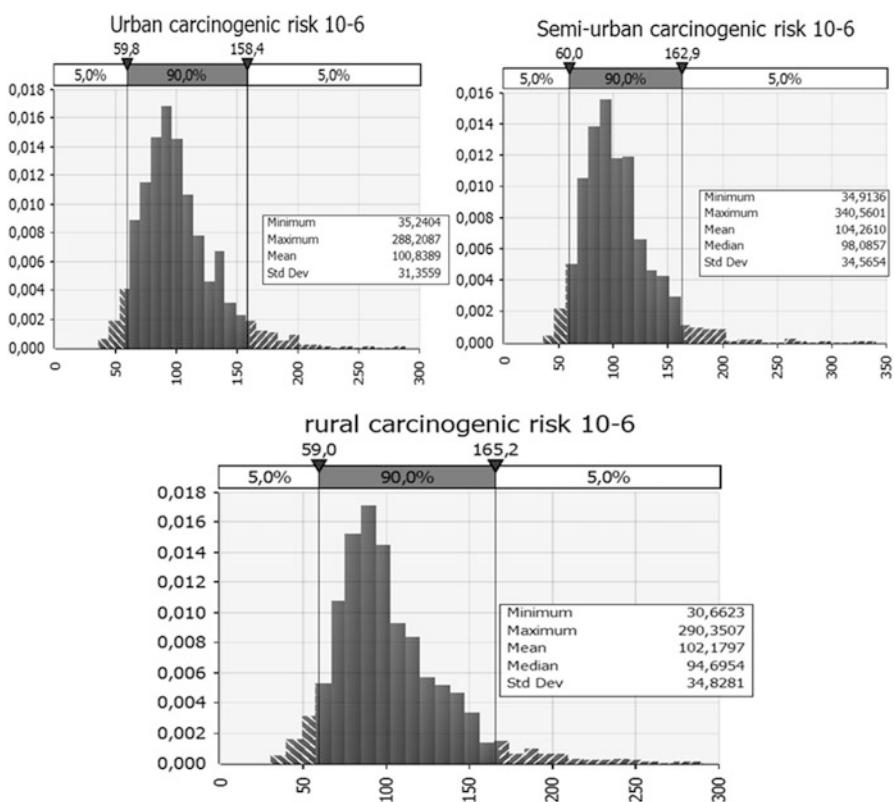
For the assessment of carcinogenic risks, distribution of cancer risks for all receptor groups is given in Fig. 18.2. The mean carcinogenic risks due to the total PCDD/F exposure for urban, semi-urban, and rural receptors are 100.8×10^{-6}, 104.2×10^{-6}, and 102.17×10^{-6}, respectively. The carcinogenic risks estimated related to the PCDD/F doses are found to be above the acceptable carcinogenic risk level of 1 in 1,000,000, as proposed by the US EPA [21, 22].

Table 18.4 Regression sensitivity for all receptor groups

Setting parameter	Urban[a]	Semi-urban[a]	Rural[a]
PCDD/F Concentrations in			
Local cereal			0.309
Com[b]. cereal	0.307	0.412	0.126
Local leafy veg.			0.137
Com root veg.	0.192	0.183	0.137
Com. fruit	0.232		
Food consumption rate			
Cereal	0.45	0.68	0.69
Root vegetables	0.376	0.347	0.312
Leafless vegetables	0.204	0.148	0.124
Fruit	0.409	0.202	
Exposure frequency (day/year)	0.116		
Body weight	−0.462	−0.397	−0.399

[a]The coefficients higher than 0.100 were shown
[b]Com. is commercial, i.e., nonlocal

Fig. 18.2 Distribution of carcinogenic risks

18.5 Conclusion

The exposure methodology has showed that the PCDD/F exposure levels from plant foods in Kocaeli are fairly lower than the recommended TDIs in all receptors. In spite of the low PCDD/F intake levels, it should be noted that the levels determined in this study would be higher if the animal data is included. Therefore, in order to evaluate the health risks from PCDD/F intake, exposure from animal food and other pathways should be considered. On the other hand, carcinogenic risks for all receptors are found in considerable levels in terms of the US EPA carcinogenic risk assessment.

References

1. Aslan S, Korucu MK, Karademir A, Durmusoglu E (2010) Levels of PCDD/Fs in local and non-local food samples collected from a highly polluted area in Turkey. Chemosphere 80 (10):1213–1219
2. Karademir A, Durmusoglu E, Bakoglu M (2007) Health risk assessment of background PCDD/F exposure levels in Kocaeli, Turkey. J Environ Sci Health A 42:729–739
3. Roots O, Henkelmann B, Schramm KW (2004) Concentration of polychlorinated dibenzo-p-dioxins and polychlorinated dibenzofurans in soil in the vicinity of a landfill. Chemosphere 57:337–342
4. Steenland K, Bertazzi P, Bacarelli A, Kogevinas M (2004) Dioxin revisited: developments since the 1997 IARC classification of dioxin as a human carcinogen. Environ Health Perspect 112–113:1265–1268
5. Fiedler H (2003) Dioxins and furans (PCDD/PCDF). In: Fiedler H (ed) The handbook of environmental chemistry, persistent organic pollutants, vol 3. Springer, Berlin, Part O
6. Fries GF (1995) A review of the significance of animal food products as potential pathways of human exposures to dioxins. J Anim Sci 73:1639–1650
7. US EPA (1992b) Estimating exposure to dioxin-like compounds. Office of Research and Development, EPA/600/6-88/005B
8. Larsen JC (2006) Review Risk assessments of polychlorinated dibenzo*p*-dioxins, polychlorinated dibenzofurans, and dioxin-like polychlorinated biphenyls in food. Mol Nutr Food Res 50:885–896
9. Bergkvist C, Öberg M, Appelgren M, Becker W, Aune M, Ankarberg EH, Berglund M, Hakansson H (2008) Exposure to dioxin-like pollutants via different food commodities in Swedish children and young adults. Food Chem Toxicol 46:3360–3367
10. Van den Berg M, Birnbaum LS, Denison M et al (2006) The 2005 World Health Organization reevaluation of human and mammalian toxic equivalency factors for dioxins and dioxin-like compounds. Toxicol Sci 93:223–241
11. Scientific Committee on Food (SCF) (2000) Opinion of the Scientific Committee on Food, on the risk assessment of dioxins and dioxins-like PCBs in food. European Commission, Health and Consumer Protection Directorate-General, SCF/CS/CNTM/DIOXIN/20 Final

12. Schuhmacher M, Granero S, Rivera J, Müller L, Llobet JM, Domingo JL (2000) Atmospheric deposition of PCDD/Fs near an old municipal solid waste incinerator: levels in soil and vegetation. Chemosphere 40:593–600
13. Llobet JM, Domingo JL, Bocio A, Casas A, Teixido A, Muller L (2003) Human exposure to dioxins through the diet in Catalonia, Spain: carcinogenic and non-carcinogenic risks. Chemosphere 50:1193–1200
14. Nadal M, Schuhmacher M, Domingo JL (2004) Probabilistic human health risk of PCDD/F exposure: a socioeconomic assessment. J Environ Monit 6:926–931
15. Karademir A (2004) Health risk assessment of PCDD/F emissions from a hazardous and medical waste incinerator in Turkey. Environ Int 30:1027–1038
16. US EPA (1992a) Guidelines for exposure assessment. US EPA Risk Assessment Forum, EPA/600/Z-92/001
17. US EPA (2001) Process for conducting probabilistic risk assessment, risk assessment guidance for superfund: Volume III - Part A. Office of Emergency and Remedial Response U.S. Environmental Protection Agency Washington, DC 20460. EPA 540-R-02-002
18. Paustenbach DJ, Fehling K, Scott P, Harris M, Kerger B (2006) Identifying soil cleanup criteria for dioxins in urban residential soils: how have 20 years of research and risk assessment experience affected the analysis? J Toxicol Environ Health B 9:87–145
19. LaGrega MD, Buckingham PL, Evans JC (1994) Hazardous waste management. McGraw-Hill, New York
20. Loutfy N, Fuerhacker M, Tundo P, Raccanelli S, El Dien AG, Ahmed MT (2006) Dietary intake of dioxins and dioxin-like PCBs, due to the consumption of dairy products, fish/seafood and meat from Ismailia city. Egypt Sci Total Environ 370:1–8
21. US EPA (1990) Clean Air Act, 42, USC 7412
22. Valberg PA, Drivas PJ, Mccarthy S, Watson AY (1996) Evaluating the health impacts of incinerator emissions. J Hazard Mater 47:205–227

Chapter 19
Selenium Adsorption on Activated Carbon by Using Radiotracer Technique

A. Beril Tugrul, Sevilay Haciyakupoglu, Sema Akyıl Erenturk, Nilgun Karatepe, A. Filiz Baytas, Nesrin Altinsoy, Nilgun Baydogan, Bulent Buyuk, and Ertugrul Demir

Abstract Selenium (Se) is an essential trace element for human beings and plays important roles in human health but it is also toxic at concentrations above 1 mg of selenium per kg of body weight. Therefore, elimination of selenium ions from aqueous solutions is important. Se can be eliminated by using activated carbon as an adsorbent. Radiotracer concept is applicable for observation of elimination mechanism. For this reason, selenium radioisotope can be used as tracer. Selenium dioxide is irradiated in the central thimble of ITU TRIGA Mark II Training and Research Reactor for radiotracer production. Radioactivity measurements are carried out by the gamma-ray spectroscopy system to determine the effect of different experimental parameters. The relative importance of test parameters like concentration of adsorbate, pH of the solution, and contact time on adsorption performance of activated carbon for selenium ion is examined. Typical adsorption isotherms (Langmuir, Freundlich, Dubinin–Radushkevich, and Temkin) are determined for the mechanism of sorption process. Evaluation of experiments for different parameters shows possibility of elimination of selenium from aqueous media by using activated carbon.

Keywords Selenium adsorption • Radiotracer technique • Human health • Aqueous solutions • Radioactivity measurement • Gamma-ray spectroscopy • Adsorbate • Adsorption isotherms • Langmuir • Freundlich • Dubinin–Radushkevich • Temkin • Selenium elimination • Activated carbon • Radiotracer • Adsorption • Aqueous media • TRIGA

A.B. Tugrul (✉) • S. Haciyakupoglu • S.A. Erenturk • N. Karatepe
A.F. Baytas • N. Altinsoy • N. Baydogan • B. Buyuk • E. Demir
Istanbul Technical University, Istanbul, Turkey
e-mail: beril@itu.edu.tr

Nomenclature

A	Adsorption capacity (mg Se/g AC)
C_i	Se concentration of the initial solution (mg/L)
C_e	Se concentration of the solution in equilibrium (mg/L)
m_{AC}	Mass of activated carbon (g)
q_e	Amount of selenium ions sorbed onto activated carbon adsorbent (mg/g)
Q_m	Langmuir constant related to sorption capacity and sorption energy (µg/g)
b	Langmuir constant related to sorption capacity and sorption energy (g/L)
K_f	Freundlich constants related to the sorption capacity and sorption intensity (µg/g)
X_m	Maximum sorption capacity (µg/g)
R	Gas constant (kJ/mol)
T	Temperature (K)
b_t	Constant related to the heat of adsorption
K_t	Equilibrium binding constant (µg/L)
B_1	Temkin constant related to heat of adsorption
C_{ads}	Adsorbed selenium onto activated carbon mol
S_{BET}	BET surface area
V_{mi}	Micropore volume
V_T	Total pore volume
$V_{CO2(D-R)}$	Narrow micropore volume
V_{super}	Super micropore volume

Greek Symbols

β	The activity coefficient related to mean sorption energy (mmol^2/J^2)
ε	Polanyi potential (kJ/mol)

Acronyms
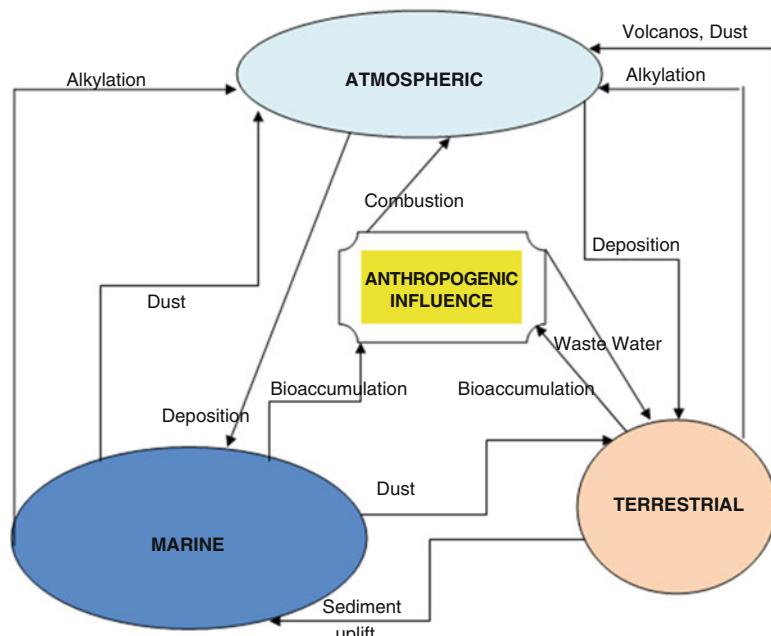
AC	Activated carbon
BET	Brunauer, Emmett, and Teller
D–R	Dubinin–Radushkevich
FTIR	Fourier transform infrared
TRIGA	Training Research Isotopes General Atomics

19.1 Introduction

An essential trace element for human beings is selenium (Se) and it plays important roles in human health. But, selenium is toxic at concentrations above 1 mg per kg of body weight. Selenium is introduced in the environment from different sources, both natural and anthropogenic [1, 2]. Naturally, Se is present in earth's crust in low amounts (0.05 μg/g). Selenium is an element in coal and mining can result in leaching of Se into surface waters. Selenium mobility in the environment, availability for biota, and toxicity depend on its oxidation state and so its speciation is necessary [3]. Anthropogenic activities interfere with the global selenium cycle influencing it crucially as seen in Fig. 19.1.

It has been estimated that between 37.5 and 40.6 % of the total selenium emissions to the atmosphere are due to anthropogenic activities [4]. In the atmosphere, selenium is transported associated to particulate matter and subsequently dry and wet deposited. Agricultural drainage waters, oil-refining wastewaters, and coal combustion residues contaminate the lotic, lentic, and marine environment [3].

Once in the aquatic environment, waterborne selenium can enter the food chain and reach levels that are toxic to fish and wildlife like some other radioisotopes [5]. Impacts may be rapid and severe, eliminating entire communities of fish and causing reproductive failure in aquatic birds [6]. Few environmental contaminants

Fig. 19.1 Global selenium cycle with the interference of anthropogenic activities

have the potential to detrimentally impact aquatic resources on such a broad scale, and even fewer exhibit the complex aquatic cycling pathways and range of toxic effects that are characteristic of selenium. This places added importance on identifying potential selenium sources and taking steps to effectively control discharges before aquatic habitats become contaminated.

Selenium can exist in different oxidation states, elemental selenium (Se), selenite (SeO_3^{2}), selenide (Se^{2-}), selenate (SeO_4^{2-}), and organic selenium in the environment. Selenate is the predominant form under ordinary alkaline and oxidized conditions. In the most aqueous media selenite and selenate are found to be thermodynamically stable under the pH and redox conditions that are found and are the predominant chemical forms. Selenite is present in mildly oxidizing, neutral pH environments and typical humid regions. In the view of biological effects of selenium, it may be explained from its chemical form, which shows different toxicities being exhibited for organic and inorganic compounds. Inorganic Se (IV) has been found to be 500 times more toxic than common organo-Se compounds and is considered more dangerous to aquatic organisms than Se(VI) due to its higher solubility and bioavailability. As a result, inorganic Se speciation in the environmental water is extremely desirable [7–9].

The most important principle to understand when evaluating the hazard of selenium from mountaintop removal coal mining is its ability to bioaccumulate [6]. This means that selenium is an element which is concentrated with carbon cycle in the ecosystem. On the other hand, carbon is affected by global warming and climate change, so selenium would be also affected by the environment when the coal mining increases.

There are a variety of treatment technologies that have been reported for selenium removal from contaminated waters [10–14]. The most widely used methods for removing heavy metals from wastewaters include ion-exchange, chemical precipitation, reverse osmosis, evaporation, membrane filtration, adsorption, and biosorption [10, 15, 16].

Adsorption onto activated carbon is one of the most effective and reliable technologies for wastewater treatment. Generally, activated carbons are broadly applied effective adsorbents for wastewater treatment. Many review articles have appeared on activated carbon adsorption of heavy and toxic metals from water/wastewater [17–26]. High efficiency for removal of contaminants over a wide range of concentration and ease in operation can be counted as advantages of the method. But, the usage of activated carbon has been limited by its high cost because the carbon is derived from high-cost sources.

This chapter reviews selenium adsorption from aqueous media onto activated carbon relating to the initial selenium concentration, pH, and contact time. Understanding of adsorption characteristic of selenium and adsorption isotherms such as Langmuir, Freundlich, Dubinin–Radushkevich (D–R), and Temkin are described for sorption data.

19.2 Radiotracer Applications

For the selenium elimination in media, radiotracer technique can be used successfully. Therefore, tracer method is a technique for obtaining information about a system or some part of a system by observing the behavior of a specific substance, the tracer that has been added to the system [27]. The tracer method is clearly one of the most powerful tools in scientific research. Radiotracing technique can be used for physical, chemical, or biological properties of substance. System elements or compounds can be selected as the tracer materials and used for radiotracer after the irradiation. That is an advantage for radiotracer applications due to no chemical impurity in the system. So, the radiotracers would be appropriate to studying chemical reaction kinetics, solubility, vapor pressure, processes dominated by atomic and molecular diffusion, and others.

Radioactive isotopes of the traced elements and labeled molecules are used as intrinsic tracers. Therefore, the method provides for the identification, observation, and study of the behavior of various physical, chemical, or biological processes [28].

Radioisotopes and their special properties have been widely used in industrial, medical, and agricultural research with different types of flows and diffusion events [29–31]. There are two requirements for a tracer. First, it must behave exactly like the traced material. Second, it must have one property that distinguishes it from the traced material so that it can be easily detected in the presence of another material. The radioisotope, or radiotracer, however, is the most universal and practical tracer. Radiotracer applications are appropriate for observing the related dynamic events in the aqueous media [30]. So, Se radioisotope can be used for the investigation of elimination mechanism in the substance.

The main particularity of radiotracers is their radiation emission. Generally, gamma-emitted radioisotopes are preferred for the soil application. They offer possibility of online and in situ measurements, providing information in the shortest possible time. They have high detection sensitivity for extremely small concentrations [28]. Se-75 is a radioisotope of selenium which emits gamma rays, so it is appropriate for using as radiotracer with also high intensity and measurable half-life.

19.3 Preparation of Radioactive Selenium Solution

Determination of selenium using as radioactive tracer differs from other methods of chemical analysis because of its detection limit. Selenium can be determined in a very low concentration (0.43 μg) using this method [32]. To produce radioactive selenium isotope (^{75}Se) with the (n, γ) reaction, the original selenium dioxide compound in polyethylene tube is irradiated in a nuclear research reactor [33, 34].

An example for typical experimental conditions which is applied in the TRIGA Mark II Training and Research Reactor at Istanbul Technical University is given in

Table 19.1 Irradiation properties

Original isotope	Produced radioisotope	Irradiation time (h)	Irradiation power (kW)	Half-life (days)
Se-74	Se-75	1	250	119.769

Table 19.1 to explain the irradiation properties of the samples. It is possible to obtain high-level neutron irradiation in the vertical port located at the point of maximum neutron fluence of ITU TRIGA Mark II nuclear reactor. Thermal neutron fluence rate can be obtained at ~1.13 × 10^{12} cm^{-2} s^{-1} in the central thimble of the nuclear reactor. The samples are installed in the core region to provide high-level neutron absorbed dose at the irradiated specimens [35, 36]. The mixed gamma/neutron dose is determined at approximately 55 kGy using an equivalent gamma dose approach for high-level neutron irradiation at that place of the reactor for 5-min irradiation [37, 38].

Gamma-ray energies, absolute decay intensities, and half-lives of radioactive selenium isotopes are well known [39]. The stock solution of radioactive selenium is prepared by dissolving appropriate amounts of irradiated selenium dioxide compound.

19.4 Gamma Measurements for Selenium

GAMMA-X HPGe coaxial n-type germanium detector can be used to determine ^{75}Se radioisotope activities of the samples. In the measurements, adjusting the statistical confidence level to 1σ raises the accuracy of results [40, 41]. Counting time can be applied as 30 min related to the expected activity. The area of the peak in a gamma spectrum is a measure of the interested isotope resulting from interaction of gamma radiation of corresponding energy in the radiation detector. Peak areas of ^{75}Se at 136 keV gamma rays in the spectrums are determined by using nuclear analysis software programs [42]. Calibration of gamma detection system is based on the rightly determination of net peak areas in the gamma-ray spectrum to the amounts of the elements present in the sample under studied experimental conditions. A standard point source such as ^{152}Eu is used in energy calibrations of the spectra [43].

19.5 Production of Activated Carbon

Activated carbon is one of the most widely used adsorbents due to their extensive surface area, favorable pore size distribution, and high degree of surface reactivity. Over the last few decades, adsorption systems involving activated carbon have gained importance in purification and separation processes on an industrial scale.

Table 19.2 Proximate analysis and BET surface value of Tuncbilek lignite

Sample	Moisture (%)	Volatile matter (%)	Fixed carbon (%)	Ash (%)
Tunçbilek lignite	15.42	34.11	35.61	14.86

Table 19.3 Porous textural properties of the activated carbon sample

Sample	S_{BET} (m^2/g)	V_{mi} (cm^3/g)	V_T (cm^3/g)	$V_{CO2(D-R)}$ (cm^3/g)	V_{super} (cm^3/g)
AC	505	0.070	0.473	0.138	0.088

The characteristics of activated carbon depend on the physical and chemical properties of the precursor as well as on the activation method [44, 45]. Activated carbon can be prepared from a large number of materials. Coals and lignocellulosic materials are commonly used as the starting material for preparing activated carbon. The production of an active carbon must balance economic viability with performance. Cheap precursor materials must be readily available and convertible to an active carbon using a minimum of resources.

There are basically two methods for preparing activated carbon: physical and chemical activation. Physical activation consists of two steps: the carbonization of the starting material and the activation of the char by using carbon dioxide or steam. In physical activation both the carbonization and the activation step proceed simultaneously. The other method, chemical activation, consists of carbonization at a relatively low temperature (e.g., 673–973 K) with the addition of a dehydrating agent (e.g., $ZnCl_2$, KOH, and H_3PO_4). These chemical reagents may promote the formation of a rigid matrix, less prone to volatile loss and volume construction upon heating to high temperatures [46].

An example study of activated carbon production can be given as follows: Tuncbilek lignite is selected as raw material and grinded to the granule size of $-1,700 + 700$ μm. The characteristics of lignite sample are reported in Table 19.2.

Activated carbon is prepared by applying physical activation using CO_2 as the activation agent for the experiment. Original lignite sample is first carbonized at 1,073 K for 1 h under N_2 atmosphere and then activated with CO_2 at 1,223 K for 3 h [47].

Characterization of the porous texture of activated carbon is of relevance since many of their properties are determined or strongly influenced by this characteristic. Information on the carbon pore structure is derived from N_2 adsorption isotherms obtained at 77 K and from CO_2 adsorption isotherms obtained at 273 K on a NOVA 1200 apparatus (Quantachrome, USA). Samples are degassed under vacuum at 473 K for 2 h prior to all adsorption measurements. The BET surface area of the activated carbon sample is calculated from the N_2 adsorption isotherms using the BET equation and is given in Table 19.3.

Micropore volume of the activated carbon sample is calculated by applying t-plot equation to the experimental N_2 isotherms measured at 77 K. The amount of N_2 adsorbed at pressures near unity corresponds to the total amount adsorbed at overall pores. Total pore volume is assessed from the amount of N_2 adsorbed

Table 19.4 Surface functional properties of the activated carbon sample

	BOEHM				Chemical characteristics
Sample	Basic (meq/g)	Carboxylic (meq/g)	Lactone + Lactol (meq/g)	Phenolic (meq/g)	The FTIR band (cm^{-1})
AC	0.2289	1.2188	0.0164	0.7073	798, 1,091, 1,562, 2,055, 2,885, 2,961

at $p/p_0 = 0.95$. The Dubinin–Radushkevich equation is also applied to both N_2 and CO_2 adsorption data to determine micropore volumes, such as narrow micropore, and super micropore volumes. The D–R equation to the CO_2 adsorption data is applied to give the narrow micropore volume.

The surface functional groups on the activated carbon sample are also studied by a FTIR spectroscopy. The spectra are recorded from 650 to 4,000 cm^{-1}. By comparison to the standard frequency patterns, various characteristic chemical bonds or stretching are determined, from which certain surface functional groups could be derived. Boehm titration method is also applied to the activated carbon sample to obtain some functional groups quantitatively. The results are given in Table 19.4.
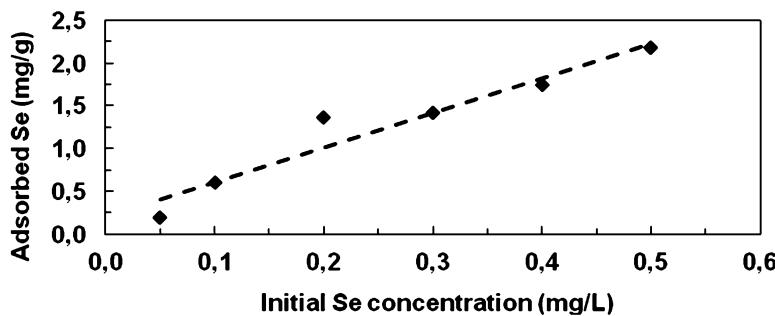
19.6 Selenium Adsorption onto Activated Carbon

Batch and column techniques are used for the selenium adsorption studies to obtain the equilibrium data [1, 10, 11, 16, 21]. Experimental data of the study applied by batch technique is given as follows [48].

The experiments are performed in a thermostated shaker bath with agitating in small volumes (2 mL) because of the high activity of selenium solution. Solid phase is separated from liquid by centrifuging. After that, 1 mL of each initial adsorption solution and separated solution are transferred into polyethylene tubes for activity measurements at gamma spectrometry system. The amount of adsorbed selenium is estimated from the difference between the initial and final relative activities of selenium. The experiments are performed at ambient temperature and in duplicate. The adsorption amount of selenium from aqueous solution is computed as follows:

$$A = \frac{(C_i - C_e)}{m_{AC}} \tag{19.1}$$

where A: adsorption capacity (mg Se/g AC), C_i: Se concentration of the initial solution (mg/L), C_e: Se concentration of the solution in equilibrium (mg/L), and m_{AC}: mass of activated carbon.

Fig. 19.2 The effect of initial concentration on the uptake of Se by activated carbon

The adsorption behavior of selenium on activated carbon is investigated and discussed as follows with respect to the effects of the initial selenium concentration, pH, and contact time.
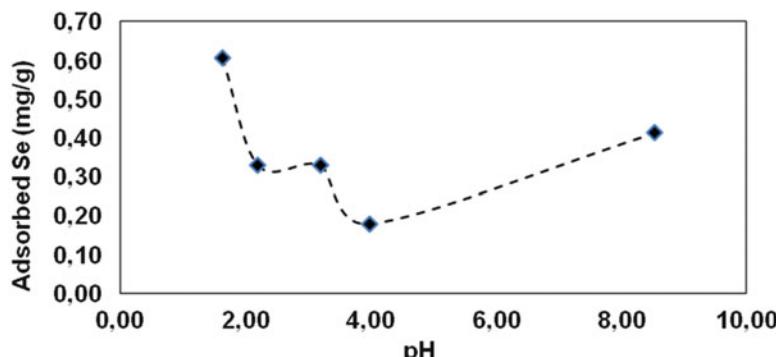
Effect of the initial concentration of the selected ion in the solution is one of the most important parameters on the sorption process, which can influence the sorption behavior of the ion. To investigate the influence of the initial selenium concentration on selenium removal from the aqueous solution, tests are made under the conditions: a selected initial pH, concentration range, and contact time at ambient temperature.

The effect of the initial selenium concentration (0.05–0.5 mgSe/mL) on the adsorption for 2 h at pH 3.0 by activated carbon is shown in Fig. 19.2. It is clearly seen that the amount of adsorbed Se ($HSeO_3^-$, SeO_3^{2-}) increases with increasing initial selenium concentration in the aqueous solution: from 0.19 mg Se/g AC to 2.18 mg Se/g AC. According to the experimental data, the activated carbon removes the low Se(IV) concentration from aqueous solution.
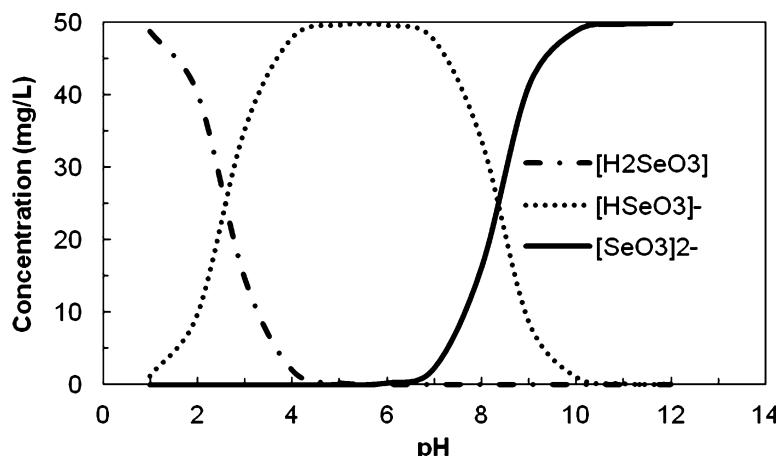
pH of the solution is another important parameter affecting selenium ion sorption onto adsorbent. Hydrogen and hydroxyl ions in the solution have an enormous impact on the surface charge of the activated carbon. Furthermore, H^+ and OH^- ions would strongly compete with selenium ions during adsorption process. Influence of pH values on the adsorption is given in Fig. 19.3 by keeping the conditions of 40 mg activated carbon: 20 °C, 2 mL of 50 mg/L Se(IV).

Part of activated carbon might be dissolved in the solution at low pH value. Therefore, a number of H^+ ions will occupy many adsorption sites which should belong to Se(IV); consequently, amount of activated carbon is not ideal. While a strange phenomenon can be seen at the left of Fig. 19.3, the removal of Se (IV) enhances when pH value is higher than 4.0. A similar study for selenium by El-Shafey [12, 13] combines with this result. This author showed that the highest selenium adsorption would be obtained at pH 1.5 because of proton sufficiency relating to more reduction of Se(IV) to elemental selenium to take place on the sorbent surface.

Impact of pH can be described with the different species of selenium in the solution as a function of pH. As it is seen from Fig. 19.4, the formation of various
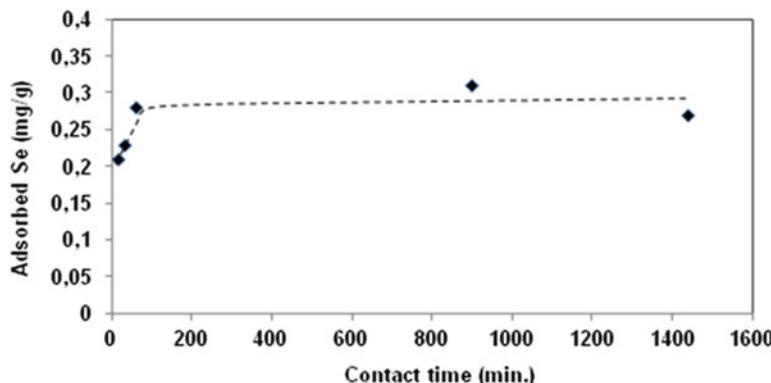
Fig. 19.3 The effect of pH values on the uptake of Se by activated carbon

Fig. 19.4 The occurred selenium complexes depending on pH for 50 mg/L Se concentration

selenium complexes is important in the adsorption of Se(IV). H_2SeO_3, $HSeO_3^-$, and SeO_3^{2-} complexes basically exist as a function of pH depending on selenium concentrations. $HSeO_3^-$ complex is the dominant species in the wide pH range from 1 to 10 for 50 mg/L Se concentration. The dominant species in the range of pH lower than 4 is the H_2SeO_3 complex.

Adsorption capability depends on the adsorption surface charge of the adsorbents. Low removal amount at close to weak acidic region may be due to the type of anionic selenium complexes present in solution. Charge repulsion may occur between selenium ions and activated carbon, which would lead to the decrease of removal efficiency. Consequently, as shown in Fig. 19.3, the extent of sorption increases with the increase of pH from 1.0 to 4.0. Adsorption surface charge increases in higher pH values and adsorption capacity increases after pH 4.

Fig. 19.5 The effect of contact time on the uptake of selenium by activated carbon

Dobrowolski and Otto [49] have reported that selenium adsorption process using Fe-loaded activated carbon depends strongly on its chemical form in the solution and surface properties of adsorbent. They have obtained the highest selenium adsorption capacity at equilibrium pH 4.8 onto adsorbent surface by positive charge up.

The effect of contact time on sorption can be studied for different contact times with fixed amounts of adsorbent at ambient temperature while keeping all other parameters constant. The results are presented in Fig. 19.5.

Seen from Fig. 19.5, removal of selenium by activated carbon is increased with increasing time and reaches equilibrium within 60 min. The selenium adsorption by the adsorbent reaches a plateau after these contact intervals. For this reason, the optimum contact time is chosen as 60 min for activated carbon. As noted by El-Shafey [11, 12] Se(IV) can reach equilibrium in longer contact times such as 260 and 330 h for another adsorbent and system.

19.7 Adsorption Isotherms

Sorption equilibrium isotherm is important for describing how the adsorbate molecules distribute between the liquid and the solid phases when the sorption process reaches an equilibrium state [50]. The isotherm models are widely used parameters to examine the relationship between sorption capacity and sorbate concentration at equilibrium. Langmuir, Freundlich, Dubinin–Radushkevich, and Temkin models are widely used for fitting the data, among the various sorption isotherm models.

Recently, adsorption isotherms are studied by mixing a known amount of activated carbon with various initial selenium solution concentrations (between 0.05 and 0.5 mg/mL) at ambient temperature and at pH 3. The adsorption isotherms are obtained by analyzing solutions in contact with activated carbon before and

after equilibrium and plotted in terms of the equivalent fraction of selenium in the activated carbon phase against the equivalent fraction in the solution phase. Experimental data obtained is tested with the Langmuir, Freundlich, Dubinin–Radushkevich, and Temkin isotherm equations. Linear regression is frequently used to determine the best-fitting isotherm, and the applicability of isotherm equations is compared by judging the correlation coefficients.

The Langmuir model represents one of the first theoretical treatments of nonlinear sorption and suggests that sorption is monolayer and the strength of the intermolecular attractive forces is believed to fall off rapidly with distance. The Langmuir adsorption isotherm is tested in the following linearized form:

$$\frac{C_e}{q_e} = \frac{1}{bQ_m} + \frac{C_e}{Q_m} \tag{19.2}$$
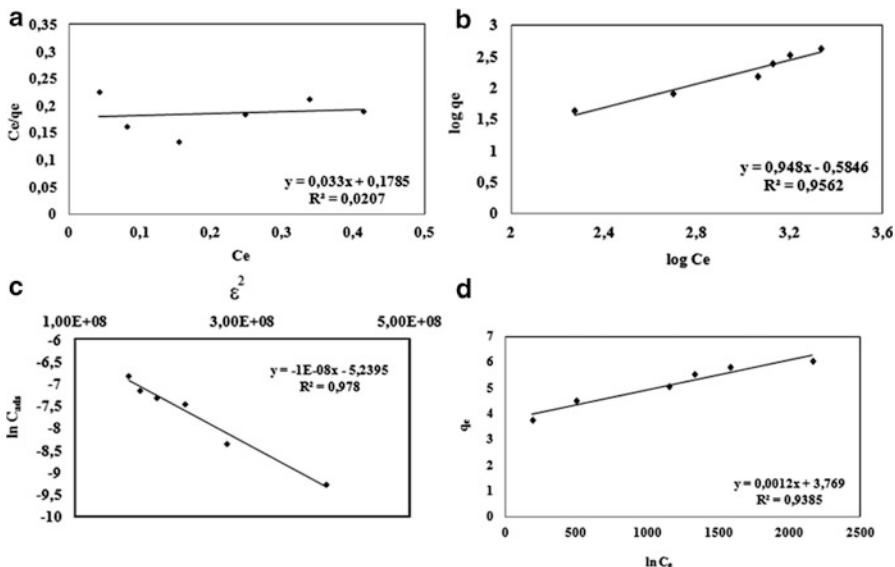
where C_e is the equilibrium concentration of selenium in solution (mg/L), q_e is the amount of selenium ions sorbed onto activated carbon adsorbent (mg/g), and Q_m and b are Langmuir constant related to sorption capacity and sorption energy, respectively. Linear plot is obtained when C_e/q_e was plotted against C_e over the entire concentration range of selenium ions investigated. From the slope and intercept of this plot the values of Q_m and b are evaluated as shown in Fig. 19.6a. The Langmuir model is developed to represent chemisorption on a set of well-defined localized adsorption sites having same sorption energies independent of surface coverage and no interaction between adsorbed molecules. Maximum sorption capacity (Q_m) represents monolayer coverage of sorbent with sorbate and b represents enthalpy of sorption and should vary with temperature [51].

The Freundlich equation is an empirical expression based on sorption on a heterogeneous surface and the exponential distribution of active sites and their energies [52]. Therefore, the sorption data obtained are then fitted to the Freundlich sorption isotherm, which is the earliest relationship known describing the sorption equilibrium and is expressed by the following equation:

$$\log q_e = \log K_f + \frac{1}{n} \log C_e \tag{19.3}$$

C_e here denotes the equilibrium concentration (µg/L) of the adsorbate and q_e, the amount sorbed (µg/g) and K_f and n are the Freundlich constants related to the sorption capacity and sorption intensity, respectively [53]. Freundlich isotherm for selenium is shown in Fig. 19.6b. The constants K_f and n are calculated from Eq. (19.3) using Freundlich plots.

The values for Freundlich constants and correlation coefficients (R^2) for the sorption process are also presented in Table 19.5. The numerical value of $1/n < 1$ indicates that sorption capacity is only slightly suppressed at lower equilibrium concentration. This isotherm does not predict any saturation of the sorbent by the sorbate; thus infinite surface coverage is predicted mathematically, indicating a

Fig. 19.6 Adsorption isotherms ((**a**) Langmuir isotherm, (**b**) Freundlich isotherm, (**c**) D–R isotherm, (**d**) Temkin isotherm)

multilayer sorption of the surface. The values of n between 1 and 10 (i.e., 1/n less than 1) represent a favorable sorption. The values of n, which reflects the intensity of sorption, also reflected the same trend. The n values obtained for the sorption process represented a beneficial sorption [54]. The Freundlich isotherm model best fitted with the equilibrium data since it presents higher R^2 value.

D–R model has been applied to the sorption data. It is postulated within an adsorption space close to sorbent surface. If the surface is heterogeneous and an approximation to a Langmuir isotherm is chosen as a local isotherm for all sites that are energetically equivalent then the quantity $\beta^{1/2}$ can be related to the mean sorption energy, E, which is the free energy of the transfer of 1 mol of selenium ions from infinity to the surface and sorbent. According to Polanyi and later developed by Dubinin and his co-workers, the difference in the free energy between the adsorbed phase and saturated liquid sorbate is referred as adsorption potential. The D–R equation is examined in the following linearized form:

$$\ln C_{ads} = \ln X_m - \beta \varepsilon^2 \tag{19.4}$$

where X_m is the maximum sorption capacity, β is the activity coefficient related to mean sorption energy, and ε is the Polanyi potential which is equal to

$$\varepsilon = RT \ln\left(1 + \frac{1}{C_e}\right) \tag{19.5}$$

Table 19.5 Adsorption isotherm constants for the adsorption of selenium onto activated carbon

Isotherm model	Constants
Langmuir	$Q_m = 0.0303$ µg/g
	$b = 5.4091$ g/L
	$R^2 = 0.0207$
Freundlich	$n = 1.0549$
	$K_F = 3.8424$ µg/g
	$R^2 = 0.9562$
Dubinin–Radushkevich	$X_m = 67.20$ µg/g
	$E = 0.2236$ kJ/mol
	$R^2 = 0.9780$
Temkin	$B_1 = 1.1613$
	$K_t = 1.10$ µg/L
	$R^2 = 0.9385$

where R is the gas constant in kJ/mol K and T is the temperature in K. The quantity of ε between 8 and 16 kJ/mol corresponds to a chemical sorption process while the value of $\varepsilon < 8$ kJ/mol represents a physical process. If the surface is heterogeneous and roughly near to the Langmuir isotherm is chosen as a local isotherm for all sites that are energetically equivalent, then the quantity of $\beta^{1/2}$ can be referred to the mean sorption energy, E, the free energy of the transfer of one mol of selenium ions from infinity to the surface of the sorbent. The numerical value of the mean free energy of sorption is calculated from the experimental data as 0.028 kJ/mol, indicating that the sorption mechanism may be followed as physical sorption process type. The saturation limit (X_m) may represent the total specific micropore volume of the sorbent. The sorption energy can also be worked out using the following relationship [55, 56]:

$$E = \left(\frac{1}{\sqrt{-2\beta}} \right) \qquad (19.6)$$

Figure 19.6c indicates D–R isotherm. From the slope and intercept of the plot of ln C_{ads} versus ε^2 the values of $\beta = -1 \times 10^{-5}$ mmol^2/J^2 and $X_m = 0.0672$ mg/g have been estimated. Here, the value of E is estimated to be 0.2236 kJ/mol.

Temkin and Pyzhev [57] developed a new isotherm firstly and it is based on the assumption that the heat of adsorption would decrease linearly with the increase of coverage of adsorbent [58]. They considered the effects of some indirect adsorbate/adsorbate interactions on adsorption isotherms. They suggested that, because of these interactions and ignoring very low and very large values of concentration, the heat of adsorption of all molecules in the layer would decrease linearly with coverage [59]:

$$q_e = \frac{RT}{b_t \ln (K_T C_e)} \qquad (19.7)$$

Equation (19.7) can be linearized as

$$q_e = B_1 \ln K_t + B_1 \ln C_e \qquad (19.8)$$

where $B_1 = RT/b$, in which R is the gas constant, T the absolute temperature in Kelvin, b_t the constant related to the heat of adsorption, and K_t the equilibrium binding constant (mg/L).

The Temkin isotherm equation has been applied to describe adsorption on heterogeneous surface [60, 61]. The Temkin isotherm equation assumes that the heat of adsorption of all the molecules in layer decreases linearly with coverage due to adsorbent–adsorbate interactions, and that the adsorption is characterized by a uniform distribution of the bonding energies, up to some maximum binding energy. The Temkin isotherm equation is given in Eq. 19.8 above. B_1 is the Temkin constant related to heat of adsorption (kJ/mol). K_t is the equilibrium binding constant (L/mol) corresponding to the maximum binding energy (Fig. 19.6d).

19.8 Conclusion

Adsorption of selenium from aqueous media has been performed successfully with batch technique by using activated carbon via radiotracer applications. Characterization results of the adsorbent activated carbon produced from the Turkish Tunçbilek lignite by applying physical activation method show that properties are appropriate. The adsorbate selenium obtained by irradiation of selenium dioxide compound has supplied the investigation of adsorption.

The adsorption characteristics have been quantified with the variations in the parameters of initial concentration of Se(IV), pH value, and contact time. It is shown that activated carbon is effective for the removal of the Se(IV) ions from aqueous solutions. The amount of adsorbed selenium ($HSeO^{3-}$, SeO_3^{2-}) increases with increasing initial selenium concentration in the aqueous solution. Removal of selenium by activated carbon enhances with increasing time and reaches equilibrium within 60 min. The adsorption efficiency of selenium anions at low pH values is high; because of the formation of various selenium complexes and solubility of adsorbent atoms the usage of pH values higher than 4.0 could be more reasonable for practical applications.

Langmuir, Freundlich, Dubinin–Radushkevich, and Temkin equations are used for analyzing the experimental results. The Freundlich model appears to be the best-fitting model for Se(IV) sorption on the adsorbent due to its high correlation coefficient and indicates a multilayer sorption of the surface. Dubinin–Radushkevich model points out the sorption mechanism as physical sorption. The Temkin isotherm specifies the uniform distribution of the bonding energies, up to some maximum binding energy. Consequently, the results provide information for

the elimination of Se(IV) and its species in natural surface and groundwater. In this frame, it can be also said that activated carbon can be used to remove toxic Se (IV) ions from aqueous solutions or wastewater under optimized conditions to impede their environmental impact. Therefore, it can be said that the increasing carbon inventory due to coal mining that is affected on global warming and climate change, and also the rising selenium amounts in the environment, the remedition of Se is being important increasingly.

References

1. Hasan SH, Ranjan D, Talat M (2010) Agro-industrial waste 'wheat bran' for the biosorptive remediation of selenium through continuous up-flow fixed-bed column. J Hazard Mater 181:1134–1142
2. Wang YD, Wang X, Wong YS (2012) Proteomics analysis reveals multiple regulatory mechanisms in response to selenium in rice. J Proteomics 75:1849–1866
3. Lenz M, Lens PLM (2009) The essential toxin: the changing perception of selenium in environmental sciences. Sci Total Environ 407:3620–3633
4. Wen H, Carignan J (2007) Reviews on atmospheric selenium: emissions, speciation and fate. Atmos Environ 41:7151–7165
5. Gungor N, Tugrul AB, Topçuoglu S, Gungor E (2001) Experimental studies on the biokinetics of ^{134}Cs and ^{241}Am in the mussel (*Mytilus gall*oprovicialis). Environ Int 27:259–264
6. Lemly AD (1985) Toxicology of selenium in a freshwater reservoir: implications for environmental hazard evaluation and safety. Ecotoxicol Environ Saf 10:314–338
7. Bidari A, Jahromi EZ, Assadi Y, Milani Hosseini MR (2007) Monitoring of selenium in water samples using dispersive liquid–liquid microextraction followed by iridium-modified tube graphite furnace atomic absorption spectrometry. Microchem J 87:6–12
8. Zhang L, Liu N, Yang L, Lin Q (2009) Sorption behavior of nano-TiO_2 for the removal of selenium ions from aqueous solution. J Hazard Mater 170:1197–1203
9. Chand V, Prasad S (2009) Trace determination and chemical speciation of selenium in environmental water samples using catalytic kinetic spectrophotometric method. J Hazard Mater 165:780–788
10. Tuzen M, Sarı A (2010) Biosorption of selenium from aqueous solution by green algae (*Cladophora hutchinsiae*) biomass: Equilibrium, thermodynamic and kinetic studies. Chem Eng J 158:200–206
11. Zhang N, Lin LS, Gang D (2008) Adsorptive selenite removal from water using iron-coated GAC adsorbents. Water Res 42:3809–3816
12. El-Shafey EI (2007) Removal of Se(IV) from aqueous solution using sulphuric acid-treated peanut shell. J Environ Manage 84:620–627
13. El-Shafey EI (2007) Sorption of Cd(II) and Se(IV) from aqueous solution using modified rice husk. J Hazard Mater 147:546–555
14. Wake BD, Bowie AR, Butler ECV, Haddad PR (2004) Modern preconcentration methods for the determination of selenium species in environmental water samples. Trends Anal Chem 23(7):491–500
15. Najafi NM, Seidi S, Alizadeh R, Tavakoli H (2010) Inorganic selenium speciation in environmental samples using selective electrodeposition coupled with electrothermal atomic absorption spectrometry. Spectrochim Acta B 65:334–339
16. Bleiman N, Mishael YG (2010) Selenium removal from drinking water by adsorption to chitosan–clay composites and oxides: batch and columns tests. J Hazard Mater 183:590–595

17. Mohana D, Charles U, Jr P (2006) Activated carbons and low cost adsorbents for remediation of tri- and hexavalent chromium from water. J Hazard Mater B 137:762–811

18. Sathishkumar P, Arulkumar M, Palvannan T (2012) Utilization of agro-industrial waste Jatropha curcas pods as an activated carbon for the adsorption of reactive dye Remazol Brilliant Blue R (RBBR). J Cleaner Prod 22:67–75

19. Ghaedia M, Biyareh MN, Kokhdan SN, Shamsaldini S, Sahraei R, Daneshfar A, Shahriyar S (2012) Comparison of the efficiency of palladium and silver nanoparticles loaded on activated carbon and zinc oxide nanorods loaded on activated carbon as new adsorbents for removal of Congo red from aqueous solution: Kinetic and isotherm study. Mater Sci Eng C 32:725–734

20. López-Antón MA, Díaz-Somoano M, Fierro JLG, Martínez-Tarazona MR (2007) Retention of arsenic and selenium compounds present in coal combustion and gasification flue gases using activated carbons. Fuel Process Technol 88:799–805

21. Sandoval R, Cooper AM, Aymar K, Jain A, Hristovski K (2011) Removal of arsenic and methylene blue from water by granular activated carbon media impregnated with zirconium dioxide nanoparticles. J Hazard Mater 193:296–303

22. Muniza G, Fierroa V, Celzard A, Furdin G, Gonzalez-Sánchez G, Ballinas ML (2009) Synthesis, characterization and performance in arsenic removal of iron-doped activated carbons prepared by impregnation with Fe(III) and Fe(II). J Hazard Mater 165:893–902

23. Leyva RR, Bernal Jacome LA, Mendoza BJ, Fuentes RL, Guerrero Coronado RM (2002) Adsorption of zinc(II) from an aqueous solution onto activated carbon. J Hazard Mater B 90:27–38

24. Zhang QL, Lin YC, Chenc X, Gao NY (2007) A method for preparing ferric activated carbon composites adsorbents to remove arsenic from drinking water. J Hazard Mater 148:671–678

25. Ren L, Zhang J, Li Y, Zhang C (2011) Preparation and evaluation of cattail fiber-based activated carbon for 2,4-dichlorophenol and 2,4,6-trichlorophenol removal. Chem Eng J 168:553–561

26. Tsoi YK, Leung K (2011) Toward the use of surface modified activated carbon in speciation: selective preconcentration of selenite and selenate in environmental waters. J Chromatogr A 1218:2160–2164

27. Foldiak G (1986) Industrial application of radioisotopes. Elsevier, Amsterdam

28. IAEA (2011) Radiotracer applications in wastewater treatment plants. Training Course Series No. 49, Vienna.

29. Altınsoy N, Tugrul AB (2002) A new proposal for Lagrangian correlation coefficient. Int J Heat Fluid Flow 23:766–768

30. Altınsoy N, Tugrul AB (1999) A radiotracer application for the turbulent dispersion of fluids. Appl Radiat Isot 51:367–375

31. Tugrul AB, Altınsoy N (2002) A new modification of the radiotracer balance method for open channel flow measurement. Flow Meas Instrum 12:341–344

32. Orucoglu E, Haciyakupoglu S (2011) Investigation of ^{75}Se adsorption by gamma-ray spectroscopy. Particulate Systems Analysis 2011 Conference, Conference USB Paper 72, 5–7 September 2011, Edinburgh

33. Erdtmann G, Petri H (1986) Nuclear activation analysis fundamentals and techniques. In: Elving PJ (ed.) Treatise of analytical chemistry, part I, vol. 14, 2nd ed. Wiley, New York, 414 p

34. Alfassi ZB (1990) Activation analysis, vol. II. CRC, Boca Raton, FL

35. Dogan N, Tugrul AB (1999) Comparative evaluation of soda glasses that are exposed by the different radiation sources. 15th European Trıga Conference, VTT Symposia, Vol. 197. pp 81–102

36. Dogan N, Tugrul AB (1998) An investigation of the radiation effect on lead glass by different radiation. Annual Meeting on Nuclear Technology'99, Proceedings. Jahrestagung Kerntechnik. pp. 681–686

37. Baydogan N, Tugrul AB (2012) Solid State Sci 14:1692–1697

38. Baydogan N, Tugrul AB (2013) The effect of neutron and mixed gamma/neutron irradiation on the solar parameters of borosilicate glass. Res Chem Intermed. Springer, DOI 10.1007/s11164-012-0964-4

39. Firestone RB (1998) Table of isotopes [electronic resource]. Chu F, CD-ROM (eds.), 8th ed., update, Wiley, New York
40. Varier KM (2009) Nuclear radiation detection, measurements and analysis. Alpha Science Intl. Ltd., Amsterdam
41. Tsoulfanidis N, Landsberger S (2010) Measurement and detection of radiation, 3rd edn. Taylor and Francis, New York
42. ORTEC (2003) Gamma Vision-32 A66-B32 Software Users Manual
43. DKD-K-36901-000386 (2006) Calibration certificate. Isotope Products Laboratory, Valencia, CA
44. Bansal RC, Donnet JB, Stoeckli F (1988) Active carbon. Marcel Dekker, New York
45. Yavuz R, Akyıldız H, Karatepe N, Çetinkaya E (2010) Influence of preparation conditions on porous structures of olive stone activated by H_3PO. Fuel Process Technol 91:80–87
46. Illán-Gómez MJ, García-García C, Salinas-Martínez de Lece C, Linares-Solano A (1996) Activated carbons from spanish coal: 2. Chemical activation. Energy Fuel 10:1108–1114
47. Karatepe N, Orbak I, Yavuz R, Ozyuguran A (2008) Sulfur dioxide adsorption by activated carbons having different textural and chemical properties. Fuel 87:3207–3215
48. Haciyakupoglu S, Erenturk (Akyıl) S, Karatepe N, Tugrul AB, Baytas AF, Altinsoy N, Baydogan N, Buyuk B, Demir E (2012) Remediation ınvestigation of selenium in aqueous environment with using activated carbon. Global conference on global warming-2012 (GCGW-12), July 8–12, 2012, Istanbul, Proceedings ISBN 978-605-89885-1-5. pp. 940–949
49. Dobrowolski R, Otto M (2013) Preparation and evaluation of Fe-loaded activated carbon for enrichment of selenium for analytical and environmental purposes. Chemosphere 90:683–690
50. Almeida CAP, Debacher NA, Downs AJ, Cottet L, Mello CAD (2009) Removal of methylene blue from colored effluents by adsorption on montmorillonite clay. J Colloid Interface Sci 46–53
51. Songkasiri W, Reed DT, Rittmann BE (2002) Biosorption of neptunium(V) by *Pseudomonas fluorescens*. Radiochim Acta 90:785
52. Akar T, Kaynak Z, Ulusoy S, Yuvaci D, Ozsari G, Tunali Akar S (2009) Enhanced biosorption of nickel (II) ions by silica-gel-immobilized waste biomass biosorption characteristics in batch and dynamic flow mode. J Hazard Mater 163:1134–1141
53. Mittal A, Kaur D, Mittal J (2009) Batch and bulk removal of a triarylmethane dye, Fast Green FCF, from wastewater by adsorption over waste materials. J Hazard Mater 163:568–577
54. Kumar NT, Kumar BA, Mandal S, Kumar DS (2009) The sorption of lead (II) ions on rice husk ash. J Hazard Mater 163:1254–1264
55. Helferrich F (1962) Ion exchange, vol 138. McGraw-Hill, New York, p. 133
56. Sari A, Mendil D, Tuzen M, Soylak M (2009) Biosorption ofpalladium(II) from aqueous solution by moss (racomitrium lanuginosum)biomass: equilibrium, kinetic and thermodynamic studies. J Hazard Mater 162:874–879
57. Temkin MJ, Pyzhev V (1940) Kinetics of ammonia synthesis on promoted iron catalysts. Acta Physiochim URSS 12:217–222
58. Aharoni C, Ungarish M (1977) Kinetics of activated chemisorption. Part 2. Theoretical models. J Chem Soc Faraday Trans 73:456–464
59. Gimbert F, Morin-Crini N, Renault F, Badot P, Crini G (2008) Adsorption isotherm models for dye removal by cationized starch-based material in a single component system: error analysis. J Hazard Mater 157:34–46
60. Liu Y, Liu Y (2008) Biosorption isotherms, kinetics and thermodynamics. Sep Purif Technol 61:229–242
61. Amin NK (2009) Removal of direct blue-106 dye from aqueous solution using new activated carbons developed from pomegranate peel adsorption equilibrium and kinetics. J Hazard Mater 52–62

Chapter 20
Teaching the Carbon Cycle Using IBL in the Secondary Schools

Francesca Ugolini and Luciano Massetti

Abstract *Inquiry-based learning* (IBL) is a didactic approach that stimulates pupils to experiment, observe, and investigate, to answer the questions on phenomena and find problem solutions. In certain countries the approach is widely and ordinarily used in science teaching while in other contexts the use of textbooks is still rooted as traditional teaching method. IBL can be applied even through a variety of learning models which include knowledge-building, learning by design, and computer simulation. In this chapter the application of the 5E Instructional Model developed by the Biological Sciences Curriculum Study in the context of 30 secondary schools of Tuscany region, Italy, is described.

The model was applied as a learning tool for the production of didactic modules on environmental issues and thematics, among which the carbon cycle.

The model is structured in five steps characterized by different activities in order to stimulate the active participation of the pupils. Pupils involved in the module on carbon cycle were engaged with games, practical experiences during which they analyzed and interpreted real data. The module was highly appreciated by both target groups of teachers and pupils although it was out of the ordinary work and in some classes it was limited by the time restriction.

Keywords Inquiry-based learning • Education • Science • Climate change • Science teaching

F. Ugolini (✉) • L. Massetti
Institute of Biometeorology-National Reseach Council,
G. Caproni 8, 50145 Florence, Italy
e-mail: f.ugolini@ibimet.cnr.it; l.massetti@ibimet.cnr.it

20.1 Introduction

One of the greatest challenges for human communities is the reduction of CO_2 emissions and the increase of actions aiming at a sustainable development. Environmental scenarios are recording extra CO_2 in the atmosphere which increases the natural greenhouse effect and changes the climate. It becomes very important that future generations get the awareness about the causes of these phenomena and their effects on the ecosystems.

Education should give people the means and the knowledge to understand these issues and form own opinions and choices of lifestyle. Education plays an important role on the awareness of the responsibility of human activities in the climate crisis [1].

On the base of this educational objective, "Acariss" (Italian Acronym for Increasing the knowledge on environment and risks of pollution involving schools through experimental activities) was ideated and then funded by the Tuscany Region Government (PAR-FAS Action Line 1.1.a.3.). The project was a collaboration between scientific partners (Institute of Biometeorology—Italian National Research Council and Polo Valdera of the Scuola Superiore Sant'Anna) and psychologists (Department of Education and Psychology—University of Florence) for offering didactic modules and innovative communication abilities to teachers.

A group of scientists developed activities on such thematics targeted to secondary schools. These activities were implemented in didactic modules, arranged in a way to engage and stimulate pupils' interest on science and scientific issues. Pupils were involved for several weeks in a learning process during which they could interact and debate with scientists and teachers, reproduce and study natural phenomena, and therefore learn by doing.

School science is often perceived as boring, theoretical, and disconnected from social issues and real life [1]. For this reason, it was also important to introduce a new way of teaching scientific topics. In the Italian context, many science teachers (depending on the school typology) have only a few hours of science lessons a week and more extra work at home and moreover, many school laboratories are scarcely equipped. These conditions very often discourage any willingness to make science lesson more attractive for pupils and more related to actual environmental issues.

Acariss project aimed to sustain teachers by giving them didactic material (disciplinary contents, exercises, experiments, etc.) on thematics related to pollution and environmental risks in a new didactic methodology.

From educators and bibliography nowadays it is confirmed that an effective research-based instructional model can help students to learn concepts and preferably it should be supported by relevant research [1]. Inquiry-based learning (IBL) can be applied even through a variety of learning models which include knowledge-building, learning by design, and computer simulation.

Among them, the 5E Instructional Model, developed by the Biological Sciences Curriculum Study [2], was the pillar of Acariss project since it was considered appropriate for the Italian context, not much used to inquiry.

The project, at regional scale, involved about 70 teachers and more than 2,000 pupils.

In this chapter the module about the "carbon cycle" is described according to the structure of the 5E Model.

20.2   Background

In recent years, several studies have highlighted at international level an alarming decline of the interest of young generations for science and mathematics and in addition the imbalance of genders sees males more interested to science than females [3].

For these reasons, schools and teachers have a great responsibility concerning science education while being policy makers concerning the cultural model of the society. It is proved that scientific thematics are fascinating for young people but the teaching methodology may affect this interest through the "top-down" transmission of concepts and the use of textbooks instead of experimentations and investigations. Moreover, teachers have to face difficulties such as the limitation of time and scarcely equipped laboratories. Some teachers also demonstrate a sort of shyness to learn and apply new methods of teaching.

On the other hand, scientists have rare opportunities to communicate their research to the public and only a few scientists are sensitive to science dissemination so as to give specific seminars or open the doors of their laboratories in special events.

Science at schools has also the key role to attract pupils to a scientific career. Thus the way of transferring contents becomes very important and particularly the introduction of a method which attempts to stimulate students' hypothesis and experimentation.

IBL mainly involves the learner and leads him or her to understand by making questions and finding answers or solutions while gaining new information. The 5E Instructional Model is a structured model of IBL based on five steps: engagement, exploration, explanation, elaboration, and evaluation.

First, the model *e*ngages pupils using activities which stimulate pupils' curiosity. In this step, teachers' ability to communicate with pupils has core role, because it is expected that students propose activities and experiments on the subject of study.

The next step deals with *e*xploration. Pupils are involved in experiments and hands-on activities as scientists. Results and observations from their experiments are *e*xplained through the data elaboration and the clarification of doubts with teachers and scientists. The acquired knowledge is extended to other contexts or new situations through the *e*laboration of concepts. Teachers and scientists support pupils with useful information and provide further knowledge from scientific research. Eventually, pupils produce outcomes which are *e*valuated by teachers and scientists.

The carbon cycle has great interest by scientists because it implies the relationships between different terrestrial systems and it is also linked to current environmental issues (e.g., rising of atmospheric CO_2, climate change).

It is also one of the main research areas of the Institute of Biometeorology which has been working on carbon fluxes in different natural ecosystems. The carbon cycle is also part of the science curriculum and connected to photosynthesis which is studied in all grades of schools.

The module on "carbon cycle" engages pupils using a game in which pupils play as carbon atoms and move between Earth systems (atmosphere, hydrosphere, lithosphere, biosphere). In this step, pupils are expected to formulate ideas to reproduce one or more processes explaining the carbon movements.

Pupils of seven classes have focused on carbon exchange between atmosphere and biosphere through two experiments. The first one was the demonstration of photosynthesis by terrestrial plants, and the second one was the demonstration of carbon dioxide efflux from soil (soil respiration).

It is worthy to notice that experiments and hands-on activities are rather challenging for the students. More than learning the scientific issue, they identify the responsibility of own actions especially in group work. Moreover, they have the opportunity to test their ability to present results to general public.

20.3   Methodology: The 5E Instructional Model

The methodology applied in this project was based on the 5E Instructional Model [1] for *IBL* which aims to stimulate pupils on scientific issues. The model suggests the application of five phases defined with five actions beginning with "E":

- Engagement begins the learning process and exposes students' current conceptions.
- Exploration: In this phase students gain experience with phenomena reproduction or descriptions of events.
- Explanation: The teacher may give an explanation to guide students toward a deeper understanding.
- Elaboration: Students apply their understanding in a new situation or context.
- Evaluation: Student understanding is assessed.

The module of carbon cycle was developed according to the previous steps with diverse activities which are described in the next paragraph.

The module was tested in seven classes of secondary schools (three middle schools and four high schools). Critical observations by scientists and teachers raised during the application of the module allowed a partial modifications to the module itself in order to make it simple enough to be autonomously run by the teacher. Apart from the use of expensive technical devices (which are lent by the research institute), the teachers should be able to conduct the module on their own.

Nevertheless, the scientist has also the role of major supervisor, and he or she also plays an important role for the students: he or she brings new knowledge and new tools and makes easier their understanding.

20.4   The Carbon Cycle Structured on the 5E Model

Carbon cycle is a scientific thematic of great interest since carbon is the most present element on Earth, being part of abiotic and biotic compounds. Carbon can make links with other carbon atoms but also with other elements; for this reason it is found in carbonates, shells, living organisms, organic matter, sugars, atmospheric gases, etc.

Carbon is present in atmosphere such as in trace gas, carbon dioxide and methane, and organic volatile compounds but it can move also from the atmosphere to other spheres. For instance it can move to biosphere through the photosynthesis of plants and turn back to the atmosphere through the respiration of living organisms and the combustion of organic material. Beyond this, volcanism and decomposition processes move carbon from the lithosphere and soils into the atmosphere. In terrestrial environments, carbon is also stored in lithosphere as fossil compounds and fossil fuels. In water bodies it is present as ion and CO_2 can move toward the deep or it is exchanged between air and water surface. But also in the waters, carbon can be absorbed by plants or deposited as carbonate in the lithosphere.

So, many processes are involved in the carbon cycle and many of them can be proved and experimented in the classroom. Some of these passages have been explored within the module according to the Instructional 5E Model.

Phase 1: Engagement
The first part of the module *engages* the pupils using the game with dice "the incredible journey through the carbon cycle" [4].

The game involves the whole class: pupils play as carbon atoms. They are grouped in four groups, each representing one Earth system (atmosphere, hydrosphere, lithosphere, biosphere). Each Earth system is physically identified with one of the room corners. Each Earth system has also its own dice (Fig. 20.1, left). The dice faces represent the probability of one carbon atom to move to another Earth system or to sink in the same system like it happens in real. They also bring a brief description of the reason of the command "stay" or "move."

The game has a duration of about 5 min (Fig. 20.1, right) during which pupils roll their dice and move (or stay) to the other systems.

The game is followed by discussions. This part aims to fix on the blackboard the movements done by the carbon atoms (pupils) during the game. The impressions and the movements are gathered and written. This is useful to resume in a theoretical way the processes involved in the carbon cycle. The debate should bring to the next phase. Rarely pupils are promptly willing to invent experiments or deepening activities on their own; thus the teacher has the important role to stimulate their curiosity. A way is to ask pupils in which way they would like to focus on a certain process or represent that process.

Once they start to think how to do that, doubts and questions begin to rise. They list the materials and propose the methodology to carry out the experimental part.

Fig. 20.1 *Left*: Example of dices of the game "the incredible journey through the carbon cycle." *Right*: Pupils plays the game in the classroom

Fig. 20.2 Pupils observe the carbon dioxide concentrations inside the greenhouse, detected by the gas analyzer

Phase 2: Exploration

In this phase students reproduce one or more phenomena. In the best case, they develop the practical activity on their own. However, teachers and scientists support students. In most of the classes, the experiments concerned the exchange of carbon between atmosphere and biosphere through the observation of photosynthesizing plants.

A small plant of *Hedera helix* L. was put under a small greenhouse. The system was connected to the gas analyzer which measures atmospheric CO_2 concentration instantaneously. The behavior of the plant exposed to sunlight or artificial light was detected through the observation of carbon dioxide values recorded by the device.

In 15 min it is possible to observe what the plant does when exposed to the light. After that, the system was placed in the dark (Fig. 20.2). Pupils recorded the CO_2 changes during 15 min.

All recorded data were used in the next phase of the module.

The second activity concerned soil respiration (or carbon dioxide emission from soil). This activity was proposed by the scientist and encouraged by the teachers.

Fig. 20.3 Pupils measure the carbon dioxide emission from the soil of their school garden

This is a hands-on activity which presumes field work in which pupils make real scientific research (Fig. 20.3). The carbon dioxide in the soil is produced by the respiration of plant roots and living organisms. Then, it diffuses in the atmosphere through soil porosity. Therefore, soil physical characteristics and biological mass are the main factors which control the process.

In this activity, pupils used the gas analyzer for atmospheric CO_2 connected to the gas accumulation chamber. Pupils were assisted by the scientist: they learnt the functioning of the device and made measurements in the field (school garden).

Pupils were directly responsible for the data recording and had to take care of the work sheets. Measurements were taken over a long period in order to compare measurements taken in different seasons or in different soil covers.

In this kind of activity, pupils make experience of the scientist's field work.

Other kinds of activities concerning the carbon cycle can be run, such as experiments on the water acidification by carbonic acid, carbonate degradation by acidic rains, and carbon dioxide produced by combustion.

Phase 3: Explanation

In this phase pupils elaborate the data collected during the exploration (Fig. 20.4). They interpret the results and find the relationships between the observed variables. Teachers and scientists give support guiding them during the discussion of results and providing scientific knowledge and sources like web sites and papers.

In the first experiment, students identified the variables connected to the exchanges of carbon dioxide between ivy and atmosphere. They learnt that ivy, like many other species, under a light source absorbs CO_2 from the air and in the dark it produces CO_2, by respiration.

Students sometimes face with unexpected results and they have to make assumptions about the causes.

In the second experiment pupils observed that soil covered by grass recorded the highest CO_2 emissions in comparison to bared soil. They identified also the environmental variables like soil temperature and soil moisture to explain the changes of soil respiration over the weeks.

Fig. 20.4 Pupils elaborate
the data taken from
field work

Phase 4: Elaboration

In this phase students should fix the concepts and extend the acquired knowledge to other contexts.

In this module, they were encouraged to discuss about the results and, guided by the teacher or the scientist, extended their knowledge to a wider scale.

The discussion, indeed, brought to the definition of ecosystems in terms of their carbon storage capacity. They learnt that ecosystems can be *sink* and/or *source* of carbon and that human activities play an important role on the alteration of carbon exchanges between ecosystems and atmosphere. The discussion was the moment in which pupils made questions and articulated opinions and believes.

Phase 5: Evaluation

This final phase aims to summarize the students' activities in a final outcome.

The evaluation is done by the teachers who should take into consideration what has been learnt by the students as well as skills and attitudes (field work, responsibility in carrying on the activities, data elaboration, ability to synthesize and present the work).

20.5   Discussion

A first challenge concerned the application of IBL in the Italian context which is still anchored to the teaching through textbooks and frontal lessons even because there is an ordinary scarcity of equipped laboratories.

The teachers involved in this project (coming from a variety of school typologies like technical high schools or middle schools) were highly motivated and formerly, they expressed willingness to learn a new methodology. They were also keen to attend the courses on communication techniques (organized by the University of Florence) in order to enhance competences on the relationship of student–teacher and to learn tools of empowering and self-monitoring. The module on the carbon cycle was applied by a subsample of teachers.

The scientist played an important role. He or she was precious in supporting the teachers and the pupils during the exploration and elaboration phases bringing his or her experiences and latest results from scientific research. The scientist, together with the teacher, planned the field work and gave tips and instructions for tools and protocols.

The challenge of IBL in teaching science at schools is represented by the limitation of time. Pupils might act and research on their own on a certain subject but this usually needs teacher's time to guide their work.

A structured model perhaps limits the pure investigative spirit of pupils because in a certain way teachers have to decide which activities are feasible and how much time to spend for them.

On the other hand, pupils seemed to be interested and active during the implementation of the project. They could make experience of a variety of works and discover their skills and favorite abilities. Moreover this approach enabled pupils to interact in work groups and live innovative experiences like real scientific research.

So far, the quality of learning was not evaluated by the researchers, but teachers were satisfied by the application of the 5E Model. Many studies have evidenced the positive impact of some level of inquiry in science education especially if the activities engage pupils in hands-on projects. An improvement of content learning has been demonstrated thanks to the stimulation of active thinking and more participation in the investigation [5]. Benefits of hands-on activities include not only science concept learning but also the improvement of inquiry skills, accuracy in data acquisition, group work responsibility, communication skills, and student responsibility for learning.

20.6   Conclusions

This chapter refers to the implementation of the didactic module on the "carbon cycle" developed within the frame of the project Acariss, which offered to teachers and pupils didactic modules based on the 5E Instructional Model of IBL. Hands-on activities are generally very much appreciated by the students, as documented also from the European project Carboschools, thanks to the stimulation of active thinking and more participation in the investigation.

Finally, we may conclude that *IBL* structured according the 5E Model can be highly worthy and useful for teachers regardless of the school context.

References

1. Carboschools consortium (2010) Third carboschools educational booklet: Global change: from research to the classroom: http://www.carboschools.org
2. Bybee RW, Taylor JA, Gardner A, Van Scotter P, Carlson Powell J, Westbrook A, Landes N (2006) The BSCS 5E Instructional Model: Origins and Effectiveness. BSCS Colorado Springs
3. Rocard M, Csermely P, Jorde D, Lenzen D, Walberg-Henriksson H, Hemmo V (2007) Science education now: a renewed pedagogy for the future of Europe. European Commission, Directorate-General for Research, Directorate L—Science, Economy and Society, Unit L4—Scientific Culture and Gender. Website accessed 17th April 2012 : http://ec.europa.eu/research/science-society/
4. Burnes R (2010) The incredible journey: a trip through the carbon cycle. NAAEE's 39th Annual Conference. 7th Annual research symposium. September 29–October 2, Buffalo-Niagara, New York
5. Minner DD, Levy AJ, Century J (2010) Inquiry-Based Science Instruction—What is it and does it matter? Results from a research synthesis years 1984 to 2002. J Res Sci Teach 47(4):474–496

Chapter 21
BTEX in the Exhaust Emissions of Motor Vehicles

Dragan Adamović, Jovan Dorić, and Mirjana Vojinović-Miloradov

Abstract Transportation involves the combustion of fossil fuels to produce energy translated into motion. Pollution is created from incomplete carbon reactions, unburned hydrocarbons, or other elements present in the fuel or the air during combustion. These processes produce pollutants of various species, including carbon monoxide, soot, various gaseous and liquid vapour hydrocarbons, oxides of sulphur and nitrogen, sulphate and nitrate particulates, and ash and lead. These primary pollutants can, in turn, react in the atmosphere to form ozone, secondary particulates, and other damaging secondary pollutants. Benzene, toluene ethylbenzene, and xylenes, known collectively as the BTEX group, are an important fraction of non-methane hydrocarbons and have been found to be ubiquitous in the urban air. BTEX are known to be toxic and genotoxic and they also actively participate in the photochemical reactions. This chapter presents the results of research in the field of BTEX concentration in the exhaust gases of spark ignition engines under different operating conditions. The aim of this chapter is to obtain a clearer insight into the impact of different engine working parameters on the concentration of BTEX gases. Exhausts have been sampled directly at the tail pipe. Detection and quantification of BTEX concentration levels have been performed by using mobile GC Voyager Photovac equipped with capillary column Supelcowax 10 and photoionisation detector. The results indicate high concentration levels of target compounds, especially in conditions of incomplete combustion simulated by creating hydrocarbon–air-rich mixtures, low engine load, and low revolutions per minute of the experimental motor.

Keywords Exhaust emissions • Global warming • BTEX • Fossil fuels • Motor vehicles • Transportation • Pollution • Carbon reactions • Unburned hydrocarbons

D. Adamović (✉) • J. Dorić • M. Vojinović-Miloradov
Faculty of Technical Sciences, University of Novi Sad,
Trg Dositeja Obradovica 6, 21000 Novi Sad, Serbia
e-mail: draganadamovic@uns.ac.rs; jovan_d@uns.ac.rs; miloradov@uns.ac.rs

• Carbon monoxide • Soot • Oxides of sulphur • Nitrogen • Sulphate • Nitrate particulates • Ash • Lead

Nomenclature

SOx   Oxides of sulphur
NOx   Oxides of nitrogen

Greek Symbols

λ   Air–fuel ratio

Acronyms

BTEX   Benzene, toluene, ethylbenzene, and xylenes
ECU   Engine control unit
GC   Gas chromatograph
HC   Hydrocarbons
LOD   Limit of detection
MTBE   Methyl tertiary butyl ether
NMHC   Non-methane hydrocarbons
PID   Photoionisation detector
RPM   Revolutions per minute
SI   Spark ignition
VOC   Volatile organic compound

21.1   Introduction

Increasing air pollution is one of the most important problems of developed countries today. Exhaust emissions from motor vehicles occupy a main role in this pollution [1]. Almost all motorised means of transportation today involve the combustion of fossil fuels, which produces energy to be transformed into motion. This combustion is the reaction of the hydrogen and carbon present in the fuels with oxygen in the air to produce—in the ideal world—water vapour (H_2O) and carbon dioxide (CO_2). Neither of these products is damaging to human health. However, CO_2 is the principal gas responsible for the "greenhouse" effect, an increase in the average temperature of the planet resulting from the trapping of solar energy, with which the increased presence of this gas in the atmosphere is associated. The more energy consumed for transportation, the more CO_2 emitted. Increase in the average temperature of the planet is believed to lead to unpredictable changes in the global

climate, potentially creating, exacerbating, or increasing the frequency of natural disasters. The combustion of hydrocarbons produces a number of other by-products more directly damaging to human health than water vapour and CO_2. These other pollutants have three possible origins: (1) the carbon present in the fuel does not adequately react with the oxygen during combustion, for a variety of complex reasons, either producing carbon monoxide (CO) or condensing to form solid carbonaceous particles (soot), a basic component of particulate matter; (2) the hydrocarbons do not combust completely (or evaporate prior to combustion), and are released as gaseous hydrocarbons called volatile organic compounds (VOCs) or adsorbed onto carbonaceous particles, thereby increasing the particulate mass; and (3) other elements present in the fuel and air (including sulphur, lead, nitrogen, zinc, and magnesium) also become involved in the combustion process, producing various oxides of sulphur (SO_x), oxides of nitrogen (NO_x), sulphate (SO_3) aerosols, and ash—also important components of particulate matter—and lead aerosols. These by-products directly cause damage to human health, but they can also react in the atmosphere, producing "secondary" transport pollutants such as sulphuric acid, sulphates, and ozone, all of which are also damaging for human health. The type and extent of secondary-pollutant production are heavily dependent on local atmospheric and climate conditions. Atmosphere and climate, together with urban form, population densities, and street densities, also influence the extent to which populations are exposed to primary and secondary pollutants [2].

The degree to which people may be exposed to these primary or secondary pollutants depends on what kinds of activities they engage in, and where, because the highest concentrations of pollutants tend to be in urban areas. The relative dose of the pollutants individuals receive depends on their own physiological conditions during exposure, and responses to doses can vary from one person to another. The principal pollutants from the transport sector responsible for adverse health effects include lead, various types of particulate matter, ozone (formed from atmospheric reactions of oxides of nitrogen [NOx] and VOCs), various toxic VOCs (for example BTEX), nitrogen dioxide, carbon monoxide, ammonia, and sulphur dioxide. However, the proportion of these various pollutants attributable to the transport sector varies significantly across different cities. Transportation accounts for about 21 % of greenhouse gas emissions worldwide; it is projected that this proportion will rise significantly in certain regions such as Europe and Latin America. In conditions of limited industrial production in Serbia, the traffic is certainly the dominant source of greenhouse gases and BTEX emissions.

The term VOC refers to a range of non-methane hydrocarbons (NMHCs) which evaporate at normal surface temperatures. NMHCs are released during combustion because of the incomplete burning of the fuel, usually because the flame temperature is too low or the residence time in the combustion chamber is too short. Changes in engine calibration that increase temperatures and residence times will therefore decrease hydrocarbon emissions. VOCs are usually regulated as a class because of their contribution to ozone formation. Ozone seems to impair respiratory function as a short-run response to exposure, but the long-term effects are less clear; some pieces of evidence suggest "reason for concern" [3]. The production of ozone

in the atmosphere occurs through complex reactions in sunlight of VOCs and oxides of nitrogen (also produced in combustion). Some VOCs also contribute to particulate formation, by coagulating onto soot and other particles, increasing their size and mass. In addition, some VOCs are in and of themselves toxic and hazardous to human health; they include BTEX, polycyclic aromatic hydrocarbons, 1,3-butadiene, aldehydes, and, through groundwater seepage, methyl tertiary butyl ether (MTBE).

Hazardous BTEX are the simplest alkylbenzenes. They are all liquids at room temperature and are characterised by high vapour pressures and moderate solubility in water. BTEX come mainly from anthropogenic sources, and vehicle exhaust has been recognised as the dominant source in the atmosphere, followed by gasoline evaporation, emissions from the use of solvents and paintings, leakage from natural gas and liquefied petroleum gas, etc. [4–6]. BTEX have become the most abundant component of VOCs in the atmosphere of most urban areas, and their negative impacts on environmental and public health have already triggered general concern [7–9]. The components of BTEX are known to cause serious health-damaging effects in humans. Benzene exposure can cause damage to bone marrow, decrease in red blood cells, excessive bleeding, and damage to the immune system [10]. Benzene is also a known carcinogen that can lead to leukaemia [11]. Toluene is known to cause liver and kidney damage as well as disruption of the function of the nervous system [12]. Ethylbenzene exposure has been found to cause damage to the inner ear and hearing [13]. The IARC also lists it as being a possible human carcinogen [14]. Xylene can have effects on the nervous system, and is believed to cause damage to the kidneys [15]. This chapter presents the results of research in the field of BTEX concentration in the exhaust gases of spark ignition engines under different operating conditions. The aim of this chapter is to obtain a clearer insight into the impact of different engine working parameters on the concentration of BTEX gases.

21.2   Background: Combustion of Fuel

In a conventional spark ignition (SI) engine, the fuel is, as a rule, added to the air outside the combustion chamber, via carburetors in older engines and via injection into the intake manifold before the intake valve in newer engines. Load regulation of the engine occurs quantitatively, i.e. air and fuel always exist globally in the same (stoichiometric) ratio; the load is adjusted by adjusting the amount of mixture via the throttle. In direct fuel injection, the fuel is injected directly into the combustion chamber. Load regulation occurs in this case both quantitatively and qualitatively, i.e. via the mixture ratio between air and fuel. Engine performance is regulated, contingent on the load, through both fuel quantity as well as air mass. The mixture formation process has the task of creating a mixture distribution optimal for the combustion process in question, e.g. a mixture which is as homogeneous as possible for the normal combustion process and the so-called stratified

charge for the lean combustion process. The majority of petrol or spark ignition engines operate on a four-stroke cycle of suck (draw in petrol and air mixture), squeeze (compress the mixture), bang (ignite the mixture with a spark), and blow (exhaust the waste gases). For both petrol and diesel engines, complete and incomplete combustion of the fuel generates a complex mixture of gaseous and particulate pollutants, many of which are detrimental to human health [16].

21.2.1 The Importance of Air–Fuel Ratio

All of the gaseous emissions vary systematically in air–fuel ratio. This variation is central to the understanding of recent developments in engine management and emission reduction.

The chemically optimal air–fuel ratio, regardless of air pollution production, is called stoichiometric (just the right weight of oxygen to be (exactly) combined with the available fuel on a molecule-for-molecule basis). This ratio is typically about 14.7 kg of air per kg of fuel, although it varies with fuel composition. At this ratio, NO production is close to a peak, while CO and HC are both low. With richer mixtures (lower air–fuel ratio, $\lambda < 1$), there is not enough oxygen to fully combust the available fuel, so CO and HC increase. Less energy is released, so less NO is created in the cooler conditions. When the air–fuel ratio is increased above 16 (leaner combustion, $\lambda > 1$), there is excess oxygen so that CO and HC stay low.

21.3 Materials and Methods

21.3.1 Engine

Engine tests have been performed on a fiat 1.2 SI engine. Table 21.1 lists the engine specifications and operating conditions used in this study.

21.3.2 SI Engine ECU
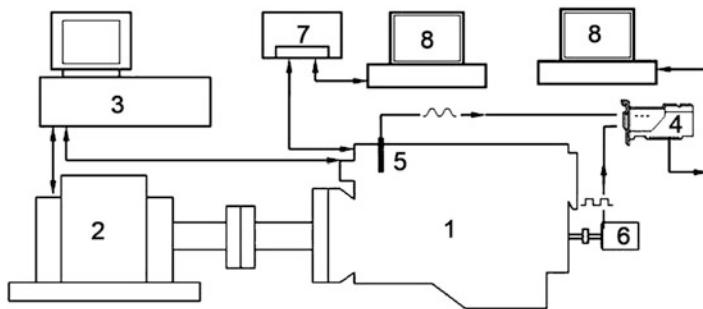
For this experimental investigation a special category of engine control unit (ECU), which is programmable, has been used, in order to achieve different working parameters. This ECU unit does not have a fixed behaviour, but can be reprogrammed by the user. The examples include adding or changing of the turbocharger, adding or changing of the intercooler, changing of the exhaust system, and conversion to run on alternative fuel. As a consequence of these changes, the ordinary ECU may not provide appropriate control for the new

Table 21.1 Main engine data

Engine parameter	Description
Engine model	Fiat 1.2
Engine type	In-line, 4-stroke
Total engine displacement	1.1 L
Firing order	1-3-4-2
Valves per cylinder in tale/exhaust	1/1
Aspiration	Atmospheric
Injection system	Multipoint
Peak power at 6,000 RPM	40 kW
Peak torque at 3,500 RPM	60 Nm
Engine speed	1,000–6,000 RPM
Testing load range	10–50 %
Fuel	Euro premium

configuration. In these situations, a programmable ECU can be wired in. These can be programmed or mapped with a laptop connected using a serial or a USB cable while the engine is running. The programmable ECU may control the amount of fuel that is injected into each cylinder. This varies depending on the engine's RPM and the position of the accelerator pedal (or the manifold air pressure). The engine tuner can adjust this by bringing up a spreadsheet-like page on the laptop where each cell represents an intersection between a specific RPM value and an accelerator pedal position (or the throttle position, as it is called). In this cell, a number corresponding to the amount of fuel to be injected is entered. This spreadsheet is often referred to as a fuel table or a fuel map. By modifying these values while monitoring the exhausts using a wide-band lambda probe to see if the engine runs rich or lean, the tuner can find the optimal amount of fuel to inject into the engine at every different combination of RPM and throttle position. Figure 21.1 provides a schematic view of the equipment used in the experimental studies.

Target VOC compounds (benzene, toluene, ethylbenzene, and xylenes) have been sampled directly at tailpipe and analysed in exhaust air samples by Perkin Elmer Photovac Voyager-mobile GC. The Voyager uses the principles of gas chromatography (GC) to separate and identify VOCs. The Voyager mobile GC employs a unique set of analytical columns and preprogrammed temperatures and flow rates to optimise the separation of complex VOC mixtures found in exhaust gases. The sample components become separated from one another as they are carried through the column due to the differences in their rates of interaction with the sorptive material. For the separation of sample components Supelcowax 10-Polyethylene glycol (PEG) column has been used. The target VOCs have been identified by GC retention times in comparison with authentic Messer standards. Ideally, each compound will be retained in the column for a different length of time, having a unique retention time (benzene 284.3 s, toluene 482.0 s, ethylbenzene 825.1 s, p,m-xylene 854.4 s, and o-xylene 1,105.0 s). Photoionisation detector has been used for detection of target compounds. The limit of detection (LOD) of the applied method is 0.01 ppm.

Fig. 21.1 Schematic layout of the experimental setup: *1* engine, *2* dynamometer, *3* dynamometer controller, *4* high-speed data acquisition board, *5* pressure transducer, *6* optical encoder, *7* ECU, *8* computer
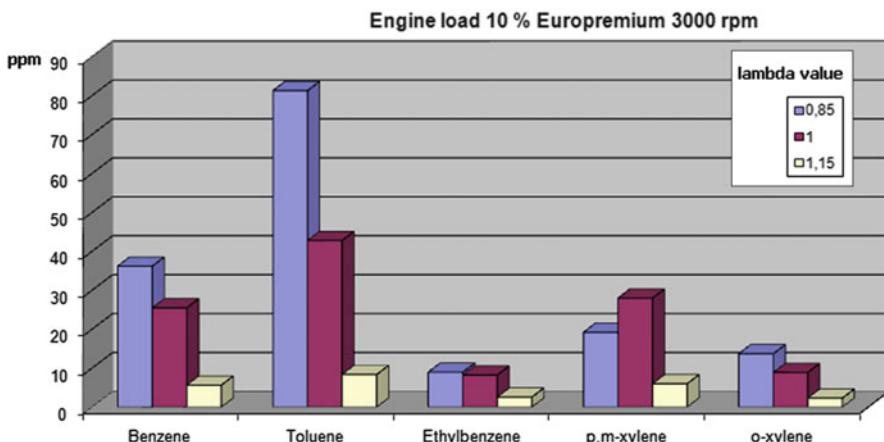
21.4   Results and Discussion

The first series of measurements has been conducted at engine load of 10 % and a speed of 3,000 RPM. During the implementation of measurements lambda value was varied in order to determine the correlation between the concentration levels of BTEX compounds and different combustion conditions. The results of the first series of measurements are shown in Fig. 21.2.
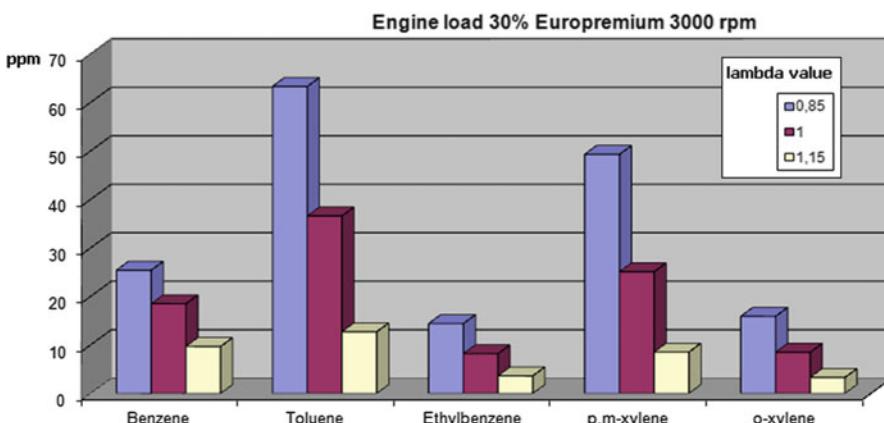
Obtained results indicate high concentration levels of all pollutants from the group BTEX, especially benzene and toluene. With the increase of air–fuel ratio, decrease in concentration levels of BTEX has been observed as a result of a more powerful combustion in the presence of air excess. It has also been observed that at a given engine load and RPM, concentration levels of toluene have been twice higher in comparison to the benzene concentrations. During the implementation of measurements lambda value has been changed and controlled by ECU. Concentration levels of BTEX compounds have been in range from 2.305 to 81.300 ppm.

A second series of measurements has been carried out under conditions of considerable increase in engine load and the same speed as in the previous series of measurements. These results point to the high concentrations of BTEX compounds in exhaust gases. Motor load increase has resulted in reduction of the concentration levels of BTEX compounds in comparison with the previous series of measurements. The results of second series of BTEX measurements are shown in Fig. 21.3.

Concentration levels of BTEX compounds have been in range from 3.292 ppm for o-xylene to 63.300 ppm for toluene. The increase of the engine load has resulted in the reduction of BTEX concentrations.

Fig. 21.2 The results of BTEX measurements at the engine load of 10 % and 3,000 RPM

Fig. 21.3 The results of BTEX measurements at the engine load of 30 % and 3,000 RPM

Next series of measurements has been carried out under conditions of slightly higher RPM (3,500) with the unchanged value of engine load (10 %). The results are shown in Fig. 21.4.

The results indicate that the increase of speed by 500 RPM, at the same load, does not significantly effect the change in concentration levels of BTEX compounds. Concentrations of target compounds have been in range from 3.125 to 102.000 ppm.
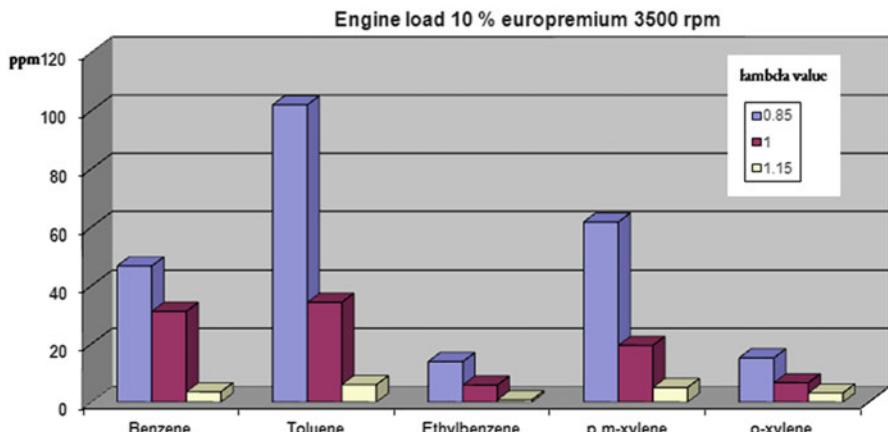
Fig. 21.4 The results of BTEX measurements at the engine load of 10 % and 3,500 RPM

21.5 Conclusions

Transport emissions include greenhouse gases, most notably CO_2, as well as particulate matter, lead, nitrogen oxides, sulphur oxides, and VOCs, all of which have negative impacts on local and often on regional levels as well. We cannot ignore the presence of aromatic organic compounds in exhaust emissions due to the proven harmful effects to human health and the environment. In interpretation of the experimental results it is important to note the following facts:

- The unambiguous conclusion is that the increase of lambda value reduces the concentration levels of BTEX components.
- Concentration levels of toluene have been twice higher than the concentration levels of benzene at $\lambda = 0.85$. With the increase of lambda value this ratio decreases.
- Increasing the engine load, at the same RPM, reduces the concentration levels of BTEX.
- The speed increased by 500 RPM on the same load does not significantly effect the change in concentration levels of BTEX.

The data obtained as a result of experimental research in this chapter finds its application as a basis for the development and improvement of detection and propagation models of ubiquitous BTEX by GC/PID as a completely new method.

References

1. Mustafa Koç, Yakup Sekmen, Tolga Topgül, Huseyin Serdar Yucesu, 2009, The effects of ethanol–unleaded gasoline blends on engine performance and exhaust emissions in a spark-ignition engine, Renewable Energy 34: 2101–2106

2. Gorham R (2002) Air pollution from ground transportation an assessment of causes, strategies and tactics, and proposed actions for the international community. Division for Sustainable Development, Department of Economic and Social Affairs United Nations, New York, NY

3. Romieu I (1999) Epidemiological studies of health effects arising from motor vehicle air pollution. In: Schwela D, Zali O (eds) Urban traffic pollution. World Health Organization, London

4. Liu Y, Shao M, Zhang J, Fu LL, Lu SH (2005) Distributions and source apportionment of ambient volatile organic compounds in Beijing City, China. J Environ Sci Health A Tox Hazard Subst Environ Eng 40:1843–1860

5. Lu SH, Liu Y, Shao M, Huang S (2007) Chemical speciation and anthropogenic sources of ambient volatile organic compounds (VOCs) during summer in Beijing, 2004. Front Environ Sci Eng China 1:147–152

6. Song Y, Shao M, Liu Y, Lu SH, Kuster W, Goldan P et al (2007) Source apportionment of ambient volatile organic compounds in Beijing. Environ Sci Technol 41:4348–4353

7. Mehlman MA (1990) Dangerous properties of petroleum-refining products: carcinogenicity of motor fuels (gasoline). Teratog Carcinog Mutagen 10:399–408

8. Lee SC, Chiu MY, Ho KF, Zou SC, Wang XM (2002) Volatile organic compounds (VOCs) in urban atmosphere of Hong Kong. Chemosphere 48:375–382

9. Ras-Mallorquí MR, Marcé-Recasens RM, Borrull-Ballarín F (2007) Determination of volatile organic compounds in urban and industrial air from Tarragona by thermal desorption and gas chromatography-mass spectrometry. Talanta 72:941–950

10. Agency for Toxic Substances and Disease Registry (ATSDR) (2007) Toxicological profile for benzene (Update). U.S. Public Health Service, Department of Health and Human Services, Atlanta, GA

11. U.S. Environmental Protection Agency (2002) Integrated risk information system (IRIS) on benzene. National Center for Environmental Assessment, Office of Research and Development, Washington, DC

12. Agency for Toxic Substances and Disease Registry (ATSDR) (2000) Toxicological profile for toluene (Update). U.S. Public Health Service, U.S. Department of Health and Human Services, Atlanta, GA

13. Agency for Toxic Substances and Disease Registry (ATSDR) (2007) Toxicological profile for ethylbenzene (Draft for Public Comment). Public Health Service, U.S. Department of Health and Human Services, Atlanta, GA

14. Agency for Toxic Substances and Disease Registry (ATSDR) (2007) Toxicological profile for xylenes (Update). Public Health Service, U.S. Department of Health and Human Services, Altanta, GA

15. International Agency for Research on Cancer (2000) Ethylbenzene. IARC Monogr Eval Carcinog Risks Hum 77:227–259

16. Colls J (2002) Air pollution, 2nd edn. Spon Press, London

Chapter 22
Construction Criteria for the Sustainable Ecosystem

Necat Ozgur

Abstract During the present global warming process it is taken for granted that human activities whereby ecological balance or the integrity of ecosystem is not considered cannot be sustained after a while. Various new economic structures, namely, eco-agriculture and ecotourism which claims integration with the ecological balance, are increasing in time. Eco-building or eco-construction is now under consideration in the construction sector to contribute to the life quality in the planet. It is observed in every part of the world that several big investments that have destroyed the ecosystems are no more allowed to be used and that the resources exploited for their realization have been wasted. Many wrong investments could have been prevented if it were possible to price the environmental losses incurred in the feasibilities that dwell on simple cost/benefit ratio, disregarding the environmental constraints of the economy. However, engineering should also challenge the nature in search for the solutions to meet the basic requirements of the mankind. This chapter tries to give some approaches towards the ecological balance concept to be followed up in different implementations of the construction sector for an acceptable "environmental impact assessment."

Keywords Ecosystem • Landscape • Investment • Construction • Engineering • Istanbul • Emissions • Ecological balance • Eco-agriculture • Ecotourism • Environmental impact assessment

N. Ozgur (✉)
General Directorate of the Protection of Natural Assets, Ankara, Turkey
e-mail: necatozgur@yahoo.com

22.1 Introduction

Organisms are systems operating together with their physical environment by the transfer of material and energy. Such a functional structure that has attained internal dynamic equilibrium is called "the ecosystem." The number of individuals who are satisfied by the natural resources *to survive a qualified living* is called the "carrying capacity" of the region for the certain species.

The chain of "technological progress-population increase-diversified economic life" has given way to *new* implementation types to support the overlapped urban carrying capacity, by artificial ways. Urban life which is characterized by intensive human settling necessarily brought in the concept of "physical planning" as the first issue to tackle the overcapacity problems. Planning is still not necessary in the rural area.

In the beginning of the twentieth century when world population has reached two billions, wastewater treatment starts as a remedy to increasing overcapacity. Then (in the middle of the century with the world population of three billion) sanitary landfill and towards the end—with six billion to take care of—desalination for drinking water are under way. Natural ecosystems, defined as the functional structures with internal dynamic equilibrium, have been replaced by new ones designed by very fine calculations.

Let us recall: *Before urbanization*, *the carrying capacity of the world was not under threat*. *Like all creatures mankind also did not follow up special precautions for the provision of the needs*, *nor for the disposal of the wastes*. *When it became necessary to look for solutions to the problems of overlapped carrying capacity*, *engineering underestimated the ecology*.

Ecology, the science investigating the interaction of organisms with each other and with nonliving things, warns that chain reactions follow, once an ecosystem has been disturbed. The sustainability of the relation of settlement places with natural ecosystems necessitates serious scientific investigation.

It is not a must to go to extreme ecological examples like the so-called eco-town or Cittaslow in order to be happy in the urban life. It is sufficient if we can follow an investment planning to apply the principles of ecological balance in our ecosystem.

The balance must also include services for other species that we share our geography with. In this respect it is worth mentioning that living area access for various wild species is achieved by "ecological corridors." Human access might as well be limited to rare regions of biodiversity announced as "sensitive zones."

The high probability of threats to the life quality encountered in the engineering techniques has become the subject of the "environmental impact assessment" (EIA) studies since 1970s. EIA is aimed to find out the dimension of the risk that is created by an investment to the sustainability of the ecosystem and to prevent the environmental hazards of investments during the construction and operation phases.

Construction is an inevitable human activity that is also not friendly with nature and environment. However, the level of human knowledge and sensitivity achieved as the result of bad experiences must overcome this contradiction that had an

antagonistic character by now in disturbing the landscape, air, and water and land sources. Basic principles should be set forward to diminish the hazards to tolerable levels.

Several systems and models proposed in the following sections are oriented towards sustaining the ecological balance—disturbance of which is a main factor of global warming—during the construction process.

22.2 Engineering and Ecology

22.2.1 Background

The main ecological balance issue is to search for the means of consuming the CO_2 emission incurred in all human activities. This emission is highly remarkable in the construction sector due to the intensive use of the heavy equipment.

Protection of landscape and wetlands, maintaining occurrence of natural processes, planning proper commissioning phases, waste reduction, reuse, recycle, not making concession in the quality criteria, risk assessment, and realistic and bankable feasibilities are the other tools in the sector that help hinder climate change.

Systems and models to approach these tools and avoid environmental destruction are discussed herewith.

22.2.2 Eco-Design

The vital importance encountered in the relation of the building and the ecosystem has lately been the prerequisite of the civil engineering designs. The fuel and waste management during the construction–operation phases must guaranty the conformity with the nature (by definition, nature is the medium where human activity should not result in any impact) and with the environment (defined as the nature exploited by the mankind). Below is a simple example to explain the impact of the disturbance of ecological balance in civil engineering, in the small ecosystem of a construction site:

> Kralkizi Dam construction in southeast Turkey started in 1985. Site buildings were assembled; construction machinery began to work. To the surprise of the site people, mice covered the entire site in a short time. People were not able to sleep on their beds. Then it was understood: The operation of heavy excavation equipment scared the snakes, forcing them to leave the territory. The mice free from their predators were overpopulated and had to look for food in the places where site people lived. Then, a new ecosystem had to be developed in order to survive in the construction site, by bringing cats from neighboring settlements into the site.

It is observed in all parts of the world that various big investments that disturb the ecosystems cannot be used after a while, which means that resources have been wasted. It is known that many heavy industry and mining investments in the developed countries have been stopped for this reason, shifting this sector to other countries where environmental sensitivity is still not the governing factor. The way to have sustainable investments is to integrate the feasibilities with *nature- and environment-oriented* site selection and proper technology and precise management methods, beyond the cost of only "digging the land." Economy is in the ecology!
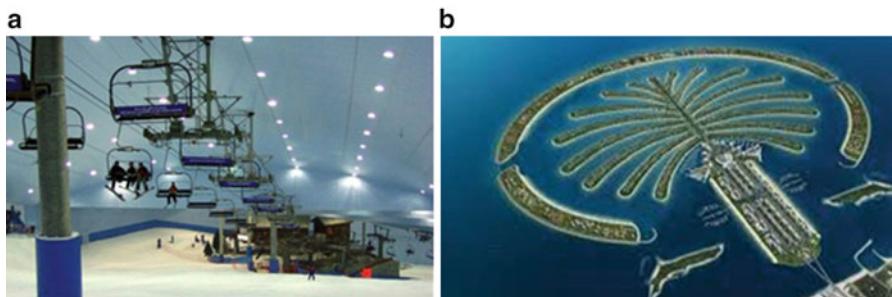
Presently, each engineering branch—apart from environmental—is learning and implementing protection and pollution prevention techniques in its area. "Mine area rehabilitation" has become the main course in mining engineering. "Evaluating saline aquifers for CO_2 disposal purposes" in petroleum engineering is researched. The need for solution to land and groundwater contamination by means of rehabilitation design has created a new civil engineering branch, geo-environment. If realistic material equivalents of environmental losses were assigned in the feasibilities, many wrong investments would have been prohibited before start. The idea of pricing environmental losses through EIA approach can now be applied by several methods, namely, "minimum discharge," "willingness to pay," and "contingent evaluation" [1].

We are in a medium where a variety of international widely echoing environmental agreements are being signed [2]. A period marked with nature and environment destruction has possibly come to an end at least in certain geographies. The period that hopefully is over was no doubt connected to production types motivating wild earnings, beyond only ignorance.

22.2.3 The Ecological Balance to Be Considered in the Constructions

To secure the condition of sustainability of the interaction between the ecological balance and the engineering structures, detailed studies interpreting the opportunities rendered by the hi-tech period we benefit have to be done within the framework of resource economy and ecosystem consideration.

However, it is a fact that investment is not composed of just the technology and the ecology dimensions. The public is to be sufficiently trained on environmental values, to put the public pressure when necessary. Modern projects of excessive CO_2 emission and awful resource wastes without any ecological concern like the indoor ski hall or man-made islands—now under threat of sinking—in a rich hot country (Fig. 22.1a, b) where latest technologies are tested indicate how environmental exploitation is shifted to parts of the world with low level of public awareness.

Fig. 22.1 (**a**) Dubai Indoor Ski center, (**b**) Dubai Palm Islands [4]

The concept of ecological balance in civil engineering is installed into the student's mind with the (transverse and longitudinal) "cut-and-fill" equilibrium requirement which may be the main issue to decide on the alignment in the highway design. This awareness must prevail in every area covered by the engineer. There will be some radical change in the look of our profession to the concept of balance, in case various branches of science mainly biology take place in engineering education.

The most important ecological balance in the global sense can be attained by the landscape design favoring sufficient photosynthesis to utilize CO_2 emitted during construction–operation phases. This is especially crucial in inlands which lack the microorganisms of oceans that contribute to the atmospheric balance with their high O_2 production rate. It is also to be mentioned that the CO_2 to come out from the respiration of the plants at night is negligible in increasing the atmospheric pollution, whereas the O_2 produced by the plants during photosynthesis can really help reset the balance.

The processes in the world, the largest ecosystem, necessitate that the investments in the regions without sufficient plant cover must be buffered by constructed forests and/or vegetation that will emit O_2 during their photosynthesis, using the CO_2 produced by the construction equipment and later by the operations of the power plants, factories, and houses. That is, O_2 "from the emission of photosynthesis" must at least be equal to CO_2 "from the construction and operation activities."

Besides this general equilibrium formula, the engineering projects may tackle with various balance problems in their small-scale ecosystems. There is certainly something to be said especially for the concrete mix, from the viewpoint of ecological balance. Easy but threatening way of producing construction materials in civil engineering whereby basic balance issues are neglected is schematized to indicate the negative consequence in the arrow direction:

"Sand-aggregate excavation" → "Coastal loss"

Millions of tons of sand-aggregate used each year to produce concrete are obtained somehow by preventing the natural process. Extraction of this material from riverbeds increases valley erosion and coastal loss as a result of the decrease in

Fig. 22.2 Spurs of the Black Sea Motorway (*upper right*: place in Turkey) [4]

the alluvial feeding in the deltas where rivers meet with the sea. This is a direct impact on the agricultural activity of the delta.

The environmentalist alternative for concrete production is to use crushed stone from the stone pit as concrete aggregate as shown by the below consequence chain:

Rock excavates (open/tunnel) → Protected landscape + Provision of aggregate

It is to be added that ecological quarry administration must also take into account *preserving the sight during the operation period and landscaping at the end of the operation period*. This is something written in the regulations but still many highways have such disturbed quarry sites within their horizons.

It will be a milestone in environmentalist construction engineering if a design approach prevails whereby an interior balance of "rock excavation-crushed stone-concrete aggregate and stone fills" is attained in big construction projects. This simply means a kind of closed system where all excavated rock is used in concrete and in designed stone fills, not taken to dump areas.

Had we realized the Black Sea Motorway by this approach in Turkey, how different our observations would have been now? Our beautiful valleys would not be sand–gravel quarries; the farmers of the valleys would not sit in the coffee houses spending their expropriation income; the coasts would not be banned to pedestrians by the road embankments under the protection of easy-solution sight-polluting products, the so-called the spurs (Fig. 22.2). We would have owned a monumental engineering work of art oriented behind the settlements passing through tunnels and viaducts. The excavated rock of the tunnels would be transformed to concrete aggregates. The loss of environment and landscape has never been reflected in the feasibility of this motorway.

The Drammen Harbor in Norway is a brilliant example that goes back to 1961, for the material balance in construction. A 7 km long spiral tunnel had been excavated from the sea level to the summit to use the excavated rock as harbor embankment and crushed stone for the concrete.

The tunnel later has become a highway with six spirals to reach a nice-view park area attracting visitors. The landscape of the hillside previously planned for the open pit has been protected. Thanks to public awareness, an integrated project is realized whereby transportation and recreation have been solved together, without any impact to the nature (Fig. 22.3).

Fig. 22.3 Harbor and undisturbed general view at Drammen–Norway [4]

Fig. 22.4 Reconstructed Temelli Lake–Ankara (*upper right*: place in Turkey) [4]

22.2.4   The Wetland Balance

A wetland in an ecosystem has a vital function. The main issue of balance is the enormous capacity of the microorganisms in a wetland to contribute to the O_2 content of the medium. The reeds of the wetland provide the natural treatment of the agricultural and household pollution of the region. The birds, natural visitors of the wetland, keep the insect population in balance. The balance is also valid for the hydrologic cycle in water collecting capacity.

   In Ankara a project supported by international funds to reconstruct the Temelli Lake (Fig. 22.4) was realized in 2007, upon the insect problem that could not be handled when birds left the region after draining the lake for land development purposes in 2004. (There are engineers—underrating the ecology and landscape dimensions—who think that shortening the distance by aligning the road in the middle of the lake is economic.)

Fig. 22.5 Flood in Hatay airport (*bottom left*: place in Turkey) [4]

The Amik Lake in Hatay—Turkey was dried in 1950s to obtain land for agriculture and for building airport. The airport was out of service for months in early 2012 after a flood inundating the region (Fig. 22.5).

22.3 Environmentalist Approach in Various Constructions

22.3.1 Network Projects

The importance of planning the construction stages of network projects such as rail systems, roads, sewerage, and water distribution from the ecological and economic viewpoints, once the main design has been decided on, must not be underestimated.

In rail systems, "synchronous start and completion of several lines together" is a spendthrift logic. The financial, managerial power and urban operational comfort are so arranged that a line will be opened, and with its income the other line will start without hindering the urban life in all directions. In the Moscow subway which is said to be the most developed underground network, new lines in the development areas are still and continuously constructed and added to the main system with only minor disturbance to the public.

Urban water distribution must follow the logical link below:

"Source (treatment) → collector → distribution"

On the other hand, sewage disposal system must start from the end point:

"Wastewater treatment plant → collector → distribution"

To emphasize the importance of the construction stages, a case frequently met in small settlements is to be revealed: Local administrators, who like to appear hardworking, allocate the limited finance opportunities to sewerage networks before the treatment and the collector construction so that they may commission

the system in a short time. However, wastewater is collected without being treated and sent to the receiving medium with concentrated contamination, to result in an unforeseen environmental disaster, in opposition with the purpose of the investment.

22.3.2 Energy Investments

It is not foreseen that sufficient quantity of renewable energy (the inconvenience regarding the noise and the landscape contamination should not be underestimated while evaluating the clean energy sources like the wind) will be produced to meet all the human requirements in near future. Therefore we will survive together with unclean energies. Appropriate precautions for ecological balance have to be taken against the hazards of such energies.

Let us start with nuclear plants that produce energy by the steam coming from the boiler to rotate turbines with the principle just as the same as the other types of thermal plants. The heat necessary for this process is the result of exothermic nuclear reaction that does not emit CO_2 opposite to the other thermal power plants burning fossil fuel.

We have assigned the most beautiful and untouched coasts of Turkey for nuclear plant building: Sinop and Silifke (Fig. 22.6). There is a coastal obligation in site selection due to the cooling water need. The negative impacts of this issue to the marine ecology including various professions, mainly the fishery, are inevitable.

Let us assume that the feasibility of the nuclear power plant is positive in spite of the price and safety factors. Do we not have coasts already broken down? Why not the abandoned open coal mines on the Black Sea coast of the European part of Istanbul (Fig. 22.6), if a technology comprising high safety is going to be used! This region is close both to the industrial and consumer centers. Moreover, its environment destroyed as a result of previous activities will possibly be rehabilitated through new investment. However, this does not solve the problem; the disposal plans of the nuclear waste should also satisfy the public.

The extraction and combustion of fossils that stay in bottom layers of the Earth harmlessly is a direct threat for the CO_2 balance in the atmosphere. This source which previously has given way to welfare increase by the production blowup as of the industrial revolution now makes the world uninhabitable, by global warming.

Interesting chats are heard regarding oil production, like for instance "oil price is increasing, so to extract deeper oil will be economic." Petroleum and its products have certain calorific values. The basis of evaluation must be the calorie value rather than the monetary value of the efforts to bring these materials ready for use. If you spend two calories from a cheaper source in order to attain oil of one-calorie value, you waste the resources and contribute to the global warming.

Imported coal with high calorific value has been added to the fuels of our thermal power plants besides the imported natural gas and oil. There is a strong objection to the usage of low-calorie lignite abundant in our country because of the sulfur and

Fig. 22.6 Nuclear sites planned on Turkey coasts (*bottom left*: picture from proposed site) [4]
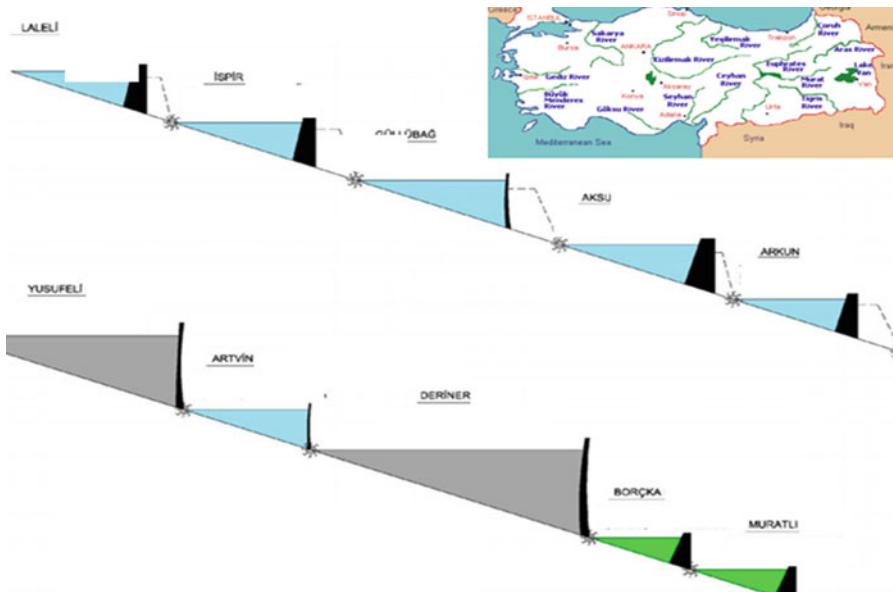
exhaust gas pollution related to this fuel. Such issues must be well investigated by experts not influenced by lobbies. In essence, the "fluidized bed" technology replacing the "flue gas desulfurization" has brought the waste levels to sustainable ratios.

More than half of our electricity production is realized by the natural gas plants. The agreements of natural gas purchasing have to be made on daily fixed quantity. However, the consumption is mostly in the winter period. Adopting the natural gas as the main item of our electricity production is a political conformism and weakness. Instead, the quantity necessary for heating must be the basis for import, the excess to be used in electricity production during the warm months.

How clean are the renewable sources? The destruction of nature caused by the plants built for exploiting the potential and/or kinetic energy of water may end the "green" characteristic of this energy, as in the Coruh Basin in Turkey.

The reality that there will be no place for rafting and for scarce local products of this microclimate such as tomato and olive that will no more be grown upon the completion of the projects in the Coruh Basin which is going to be a continuous lake system instead of the high-discharge 376 km long Coruh River (Fig. 22.7) is not a phenomenon to pass over lightly, saying "energy benefit is higher than the loss of tourism and agriculture incomes." The river will not flow any more. Who knows what we are going to face with after years, upon a vanishing ecosystem and a living style? The main idea in such basin planning should be the integrated regulation of flood prevention, energy and landscape issues, and protecting the human activities of the region in a certain ratio, instead of 100 % regulation of flowing water.

It is an ecological must to clear off vegetation in the reservoir area of the dams before filling the reservoir, both for recycling and for prevention of CO_2 emitting for years. In dam body design, the criterion for the material selection must be "minimum intervention to nature" instead of "easiest access." The logical

Fig. 22.7 Coruh Basin dams (*upper right*: Basin's place in NE Turkey) [4]

conclusion of this proposal is to use rock derivatives like cement instead of erosion products like clay, sand, and gravel to attain the stability with less quantity.

In river-type power plants the minimum water needed for natural life in the bed between intake and tail water, called the ecological water, should be reliably calculated. Energy production must be planned with respect to the net flow.

22.3.3 Industrial Investments

"Integrated Pollution Prevention and Control," IPPC, principles [3] have been formed as a directive, to state the main rules of permission to be applied to the industrial plants in the EU. All environmental performances such as the emissions of the plant to air, water and land, waste formation, raw material use, energy efficiency, noise, accident prevention, and risk management are taken into consideration by this method in advance, before the operation phase.

The concept of industrial ecology that covers environment, economy, and technology together now presents the principles of transferring the resources to production without damaging natural ecosystems. The main approach is to transform the production process from the "open system producing waste" to the "close system using wastes as input," instead. The construction sector should adopt this principle in all aspects. Engineers can easily follow these in the sites: Tire wastes can be additives in asphalt material. Demolished concrete can be used as aggregate in low-strength concrete.

Fig. 22.8 Amuderya River–Karakum Channel (*upper left*: Aral Lake after diversion) [4]

22.3.4 Irrigation Schemes

The underestimation of the balance of incoming-discharge water in the irrigation sources results in environmental disasters in many implementations. The Aral Lake in Central Asia, once fourth big inland sea of the world, is almost completely drying up. The resource of the lake, Amuderya River, has been diverted to Karakum Channel for irrigation of the Karakum Desert to grow cotton, leaving almost no water neither in the lake nor in the channel, in time (Fig. 22.8).

Several lakes have also been dried in Turkey with similar reasons. Streams flowing to the Apolyont Lake in the Marmara Region have been diverted to channels ending Lake's crayfish economy, just to favor the irrigation of some thousands of hectares.

Basin diversion may have more significant impact if underestimated: Now water is going to be transmitted by the Mavi Tunnel from the Goksu Basin to support the Konya Plain in Central Turkey where the groundwater level excessively dropped down as the result of wrong agricultural policies. No one deals with how to compensate the inevitable water and alluvium loss of the Goksu Delta (Fig. 22.9) following this operation.

22.3.5 Transportation

Build–operate–transfer (b.o.t.) method is highly relied upon in the transportation sector. This may make the investment more costly for a country in the absence of positive feasibility and competition. The efforts to increase bankable feasibility will

Fig. 22.9 Goksu Basin and Delta on Mediterranean (*upper right*: Delta's place in Turkey) [4]

Fig. 22.10 Sketch of Istanbul projects (*upper right*: Istanbul–Izmir Motorway) [4]

not necessarily be compatible with the total benefit of the society. Let us investigate the near-future Istanbul projects (Fig. 22.10). The third bridge—deriving only 4 % of the drivers—which is too far north from the center of gravity of the city transport has not attracted the investors. The Black Sea–Marmara canal does not include any incentive for tankers to shift their routes. The third airport (it is not known if it will be a b.o.t. project) is planned at a remote place that passengers will not prefer. Is it not a market failure?

Fig. 22.11 (**a**) Fikirtepe–Istanbul, (**b**) Mamak–Ankara [4]

It is declared by officials that 2 one-million-population cities (one in Europe and the other in Asia) are planned in the vicinity of the third bridge piers to make it feasible for the investor. Moreover, profit guaranty will also be secured. The bridge will be joined to the canal by a highway. Two sides of the canal will also be populated to use the land rant in the canal investment. The third airport's location will be justified when the canal project is accomplished together with the settlements. Three very big projects without solving Istanbul's transportation problems will have increased the population by at least three million, thus multiplying the problems as well. Their ecological impacts have never been discussed by now: the loss of forests, loss of water basins, loss of fish life, and unresolved marine movement. It is not decided where to dump the 200 million m^3 excavated canal soil. Let us propose to dump them into the sea to form two new islands (one in the Black Sea, the other in Marmara).

On the contrary, the Istanbul–Izmir Motorway attracted interest of investors (Fig. 22.10). It will start once the EIA problem has been resolved. However, it is for sure that the b.o.t. solution is more expensive compared with public tender process. Investors do not care about high interest rates of banks on credits because of the presumed very high user prices due to the Izmit Bay Bridge at Gebze that decreases the travel time by 1 h. Another type of market failure!

22.3.6 Services

The settlement planning in the towns must reflect lines to make people feel that they are part of the nature. Settlement is to take place on the slopes, not on the summits or in the valley bottoms. Thus, the infrastructure is secured and the individual perceives the surrounding topography while looking around. Even such simple settlement rules may also control global warming.

The unplanned housing that we underrate in our country is generally composed of houses respecting each other and well adjusted to the topography. Look at those built as "urban transformation" (Fig. 22.11a, b) where parcel settlement rights are excessively increased! Ask yourself where you would prefer to live in, the high rise or the unplanned. If urban transformation has been made protecting

the human character of the old tissues, all society would have benefited instead of the speculators.

We are surrounded by buildings which do not reflect the quality criteria in the construction sector, namely, the performance, reliability, durability, accessibility, and aesthetics. Quality assurance and control are still not applied in the regular sense. Consequently, insurance will be either too expensive or a losing sector.

The missing items regarding safety tolerated in buildings are calls for disasters. The media is full of news about buildings collapsed due to after-interventions to the main frame, burnt buildings due to fake electrical ware, and many more. Cinema halls converted from underground parking places which will be graves of hundreds in panic operate in front of the municipality officials. This is the "reliability" side. The "accessibility" factor must remind us how the N.Y. World Trade Center, a sample for perfection in the building technology, *failed* during the 9/11 attack when 3,000 people died.

Many things can be said on anomalies regarding the environmental health of our buildings. Incentives for ecological design approaches such as solar energy-supported house heating systems and rain water collecting for garden or cleaning needs do not take place in the specifications of our municipalities.

It is a fact that the expenses made by the building residents for repairing all kinds of insulation like water, heat, and noise which is the first principle of ecological approach will pay back after the first season. In our ten-house building we have made 15 % economy in fuel, just by changing the leaking valves of the heating system.

22.4 Results and Discussion

The negative impact of the construction activities on ecosystems triggers global warming. The basic factor causing the ecological imbalance is the CO_2 emission of the heavy machinery.

Investments must be buffered by constructed forests and/or plants that will emit O_2 during their photosynthesis with the CO_2 they receive from the surrounding produced by the construction equipment and following operations of the power plants, factories, and other buildings commissioned. The *landscape design* of the construction projects of all type and scale must secure this balance on a computational basis as a basic EIA requirement. However, nuclear sources which do not emit CO_2 are still far from being reliable in that their fuel and waste management have not been fully resolved yet.

Generally speaking, proper site selection, correct technology, and precise management techniques must govern investment strategies to secure the ecological balance whereby global warming components can be controlled.

Production sector must shift from the "open system producing waste" to the "close system using wastes as input." In the construction sector there are also other special methods and models to follow, shown as the results of below discussions.

The environmentalist alternative for concrete production is to use the crushed stone from the stone pit or tunneling as the aggregate of the concrete, as indicated by the chain "Rock excavation → Protected landscape + Provision of concrete aggregates," to overcome "Riverbed sand-aggregate excavation → Coastal loss" consequence. Significant physical balance issues have to be followed up, in order to secure the sustainability of the resources. Millions of tons of sand-aggregate used each year to produce concrete are obtained in a way hindering the natural process. Extraction of this material from riverbeds increases valley erosion and coastal loss, resulting in decrease in the alluvial feeding of the deltas. This is a direct impact on the agricultural activity of the lands in the deltas.

Wetland in ecosystems also has a vital function. Moreover, the wetland balance is another significant factor for the favorable hydrologic cycle in flood protection with its high water storage capacity.

The role of "planning the construction stages" of network projects such as rail systems, roads, sewage, and water distribution must not be underestimated in feasible commissioning. In urban rail systems, only when a certain line is completed, the construction of another line is to start so as to be financed by the income of the commissioned line. Similar logic is true for other networks: Urban water distribution must be implemented in the order "source–collector–distribution" and sewage disposal must follow the order "treatment–collector–distribution." Otherwise, economic and ecologic wasting of public resources is inevitable.

Appropriate precautions for ecological balance have to be taken, knowing the hazards of unclean energies with which we will have to survive together for years. Destruction of nature caused by the improper hydropower plants built for exploiting the potential and/or kinetic energy of water may also end the "green" characteristic of this energy.

Balance of incoming-discharging water is to be secured for the sustainability of resources in the irrigation schemes. River basin diversion will certainly have even more significant impacts on the environment if downstream conditions are underestimated.

B.o.t. method is highly relied upon in the transportation sector. This may make the investment more costly and environmentally unfriendly for a country in the absence of positive feasibility and competition.

"Urban transformation" aimed to modernize buildings, where parcel settlement rights are excessively increased compared to the present *unplanned* low-intensity dwellings, will, on the contrary, result in a crowded unhappy society in increased global warming.

The quality criteria in the construction sector which still misses the proper quality assurance and control techniques in implementation should take the ecological balance into consideration, as well. In this respect, incentives for ecological design approaches must take place in the technical specifications of our municipalities, to include the contributions of renewable energy sources, rainwater usage, and recycling in the urban parcel settlement.

22.5   Conclusions

A period marked with nature and environment destruction has possibly come to an end at least in certain geographies. The period that hopefully is over was—beyond ignorance—no doubt connected to production types motivating wild earnings. Many wrong investments would have been prohibited before start, in case realistic material equivalents of environmental losses were assigned in the feasibilities. The historical weakness of the mankind is repeated in environmental issues too: we started to think of the resolution, only when we were actually faced with the trouble.

The main issue in "construction factor in global warming" is that the "investor's feasibility" is not necessarily the feasibility of the whole society which we can name as the "total feasibility." Cost–benefit evaluation of the investor has no meaning for the whole community and in struggle with "global warming" if the costs do not include the loss of natural and environmental values as a cost item in the feasibility studies. Engineering must include the "ecological approach" in solving the problems of the mankind with its "struggle with the natural forces." This appears to be the basic contradiction.

A radical change in the look of civil engineering to the concept of ecological approach or rather ecological balance may occur if—as the first prerequisite—in the education phase, biology as a basic course—like chemistry and physics—is included in the schedule. The engineer, above all, should gain the ecological awareness.

It is strange that the mankind with an unpleasant experience in environmental protection shifts hazardous investments to some parts of the world with low level of awareness. However, nature has no borders. The single atmosphere we live under is a source of threat to all mankind and nature, not only to those who are responsible for the global warming. One final word to those who underestimate world ecology: Now, science works on measuring and preventing possible impacts of total activities in the world to the space system, by the methods of "galactic ecology."

References

1. Markandya A (2000), Best practice methods for valuing energy benefits. In: Final report dams and development. World Commission on Dams
2. United Nations Framework Convention on Climate Change (1997) The Kyoto Protocol
3. European Parliament (2008) Directive 2008/1/EC
4. Modified from Google Images. (2011–2012)

Part II
Potential Solutions

Chapter 23
An Approach to Assessment of Sustainability of Energy Systems

Kevork Hacatoglu, Marc A. Rosen, and Ibrahim Dincer

Abstract Measuring progress towards sustainability is an important step in achieving sustainable development, but a standard and universally accepted approach for measuring sustainability does not yet exist. Here, a sustainability assessment methodology for energy systems is developed based on a systems approach. A set of 22 indicators is identified that link a community energy system to technology, economy, society, environment, and institutional subsystems. The new approach is illustrated on a gas-turbine power plant and a single-flash geothermal steam power plant. The results of the sustainability analyses demonstrate that the gas-turbine power plant is more technologically sustainable but its renewability and environmental impacts are serious concerns, while the single-flash geothermal steam power plant rates well with the society and environment subsystems although reliability of energy supply is identified as an area where improvement is necessary. The new sustainability assessment methodology is expected to prove useful as a tool for understanding and fostering sustainable energy systems, alone or in concert with other approaches.

Nomenclature

CRF	Capital recovery factor
ex	Specific exergy (kJ kg^{-1})
$\dot{Ex}$	Exergy rate (kW)

K. Hacatoglu (✉) • M.A. Rosen • I. Dincer
Faculty of Engineering and Applied Science, University of Ontario Institute of Technology,
2000 Simcoe Street North, Oshawa, ON, Canada L1H 7K4
e-mail: Kevork.Hacatoglu@uoit.ca

h	Specific enthalpy (kJ kg^{-1})
HHV	Higher heating value (kJ kg^{-1})
i	Interest rate
$\dot{m}$	Mass flow rate (kg s^{-1})
N	Plant lifetime (year)
P	Pressure (kPa)
$\dot{Q}$	Heat rate (kW)
s	Specific entropy (kJ kg^{-1} K^{-1})
$\dot{S}$	Entropy rate (kW K^{-1})
T	Temperature (K)
$\dot{W}$	Work rate (kW)

Greek Letters

η	Energy efficiency
ϵ	Exergy efficiency

Subscripts

0	Reference environment
C	Compressor
T	Turbine
D	Destruction
Gen	Generation

Acronyms

ARI	Advanced Resources International
CFC	Chlorofluorocarbon
EROI	Energy return on investment
ESI	Environmental Sustainability Index
ExROI	Exergy return on investment
GHG	Greenhouse gas
IAEA	International Atomic Energy Agency
IPCC	Intergovernmental Panel on Climate Change
UOIT	University of Ontario Institute of Technology
WCED	World Commission on Environment and Development

Chemical Compounds

CH_4	Methane
CO_2	Carbon dioxide
CO_2e	Carbon dioxide equivalent
NO	Nitric oxide
NO_2	Nitrogen dioxide
NO_x	Nitrogen oxides
SO_2	Sulfur dioxide
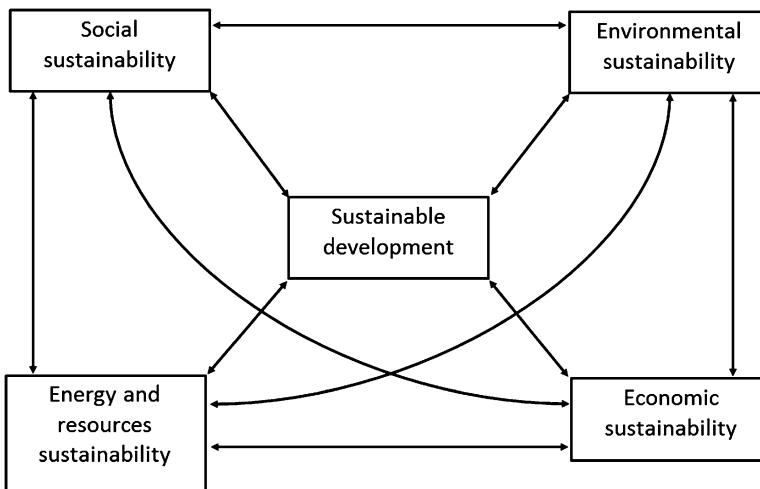
23.1   Introduction

The struggle to achieve a sustainable society is not unique to the modern age. Sustainability has been a goal since the earliest human civilizations. Ever since the Neolithic Revolution approximately 10,000 years ago, when human beings transitioned from mobile hunter-gatherers to agriculture and settlements, the sustainability of the local lifestyle has been essential to avoid societal collapse.

A classic example of how an unsustainable lifestyle can lead to societal collapse is that of the Polynesians on Easter Island. The inhabitants of Easter Island exhausted the resources of their remote habitat at an unsustainable rate to the point where they could no longer feed themselves or even build canoes to escape. The ecological destruction of Easter Island led to a catastrophic societal collapse that decimated its population [1].

Another notable illustration of societal collapse is the decline of the Western Roman Empire which, unlike the circumstances of Easter Island, occurred without complete environmental destruction. Although diminishing returns from natural resource production played a role in the decline, there were also contributing social factors, highlighting the multidimensional nature of sustainability [2].

The concept of sustainable development was popularized by the World Commission on Environment and Development (WCED) of the United Nations and its report "Our Common Future," published in 1987. The report defines sustainable development as "meeting the needs of the present without compromising the ability of future generations to meet their own needs." The subsequent United Nations Conference on Environment and Development in 1992 produced an international environmental treaty known as the United Nations Framework Convention on Climate Change based on the first assessment report of the Intergovernmental Panel on Climate Change (IPCC). This eventually led to the adoption of the legally binding Kyoto Protocol in 1997. The purpose of the treaty and the protocol is to stabilize greenhouse gas (GHG) concentrations in the atmosphere at a level that avoids dangerous anthropogenic climate change.

Fig. 23.1 A model illustrating the link between sustainable development and social, environmental, economic, and energy and resource dimensions (modified from [6])

The long-term goal of achieving a sustainable society requires sustainable development—an ambiguously defined multidimensional concept. Sustain means to continue without lessening and develop means to improve, but not necessarily grow bigger [3]. The aforementioned WCED report defines sustainable development as "meeting the needs of the present without compromising the ability of future generations to meet their own needs" [4]. The Committee on Earth Resources [5] defines sustainability based on physical resources and human living standards but acknowledges that measuring the socioeconomic component is a challenge.

According to Dincer and Rosen [6], the sustainability of a path of development can be assessed based on its impact on social, environmental, economic, and resource dimensions (Fig. 23.1). This model of sustainable development extends the concept of sustainability beyond carrying capacity to include economic and social factors.

There is an ongoing debate between advocates of weak sustainability (usually economists) and those who favor strong sustainability (usually natural scientists). The debate is centered on the substitutability of human-made versus natural capital. Adherents of weak sustainability argue that sustainability is equivalent to non-decreasing total capital stock, which is the sum of manufactured and natural capital [1]. Advocates of strong sustainability hold that natural capital provides essential ecosystem services that human-made capital cannot substitute. Adherence to the precautionary principle favors the strong sustainability perspective due to our limited knowledge of the complexity and functioning of ecosystems and the unknown services they provide.

Although sustainable development is generally regarded as a positive evolutionary course, making sustainability operational is a challenge. Before a system can be declared sustainable, a method for measuring sustainability has to be in place. Otherwise, the practical value of sustainability and sustainable development diminishes. Although there are numerous methods of assessing sustainability, a standard and universally accepted approach does not exist.

The dominant energy paradigm in modern capitalist economies is centralized generation using hydrocarbon fuels. However, there are growing concerns related to access to adequate and affordable energy supplies as well as accelerated rates of climate change. The combination of reliable energy supplies and climate change undermines sustainability. The purpose of this chapter is to develop a methodology for assessing the sustainability of energy systems.

23.2   Background

23.2.1   Sustainability Assessment Methodologies

In one of the earliest studies on sustainability assessment methodologies, Daly [7] develops operational principles of sustainable development for renewable resources and quasi-sustainable use of nonrenewable resources. Daly's assessment approach follows the strong sustainability paradigm, where the substitutability between capital and natural resources is limited.

Another early treatment analyzes indicators based on both weak and strong sustainability. Rennings and Wiggering [8] propose indicators measuring sustainable development that link ecological (physical) and economic (monetary) approaches. They argue that economic approaches can be used to develop strong sustainability indicators as long as they are supplemented by physical indicators that consider threshold values of critical ecological functions.

Ness et al. [9] review an umbrella of sustainability assessment tools discussed in the literature. The first umbrella is comprised of sustainability indicators and indices. Indicators are defined as simple quantitative proxies that measure economic, social, and environmental factors. An aggregate of indicators forms an index. Non-integrated indicators measure a single aspect of sustainability, while integrated indicators combine different nature–society dimensions. Although it follows a reductionist approach, integrated indicators offer a more holistic perspective on complex human–environmental systems. The second umbrella consists of product-related assessment tools built on evaluating flows in connection with production and consumption of a good or service. Well-known tools such as life cycle assessment focus on resource use and environmental impact while others may integrate the economic and environmental dimensions (e.g., life cycle costing).

The third umbrella includes integrated assessment tools used as decision-support methods for managing complex issues. Tools based on systems analysis approaches such as multi-criteria analysis, vulnerability analysis, and cost–benefit analysis can be extended across disciplinary boundaries and used in sustainability assessment.

A comprehensive review of sustainability assessment methodologies is conducted by Singh et al. [10]. They discover that only a few of the methodologies have an integral approach that considers economic, social, and environmental aspects of sustainability. Furthermore, they find that the construction of composite indicators involves subjective decisions in data normalization, weighting, and aggregation methods.

Parris and Kates [11] identify over 500 attempts at developing quantitative indicators of sustainable development in the literature. However, although the conflicting objectives to be both sustained and developed are often acknowledged, the indicators developed are mostly one-dimensional. Their review of twelve popular assessment methodologies concludes that there are no indicator sets that are universally accepted. One of the 12 methodologies analyzed was the Environmental Sustainability Index (ESI), which ranks nations according to an aggregation of several indicators. An analysis by Morse and Fraser [12] concludes that the ESI is misleading and biased towards Western countries, resulting in overly simplistic ideas correlating economic growth to environmental sustainability.

There are numerous indices that aggregate sustainability indicators to provide a one-dimensional metric of valuation. According to Böhringer and Jochem [13], policy makers demand an aggregate sustainability index that can be easily interpreted and communicated to the general public. Their analysis of eleven prominent sustainability indices reveals that scientific rules for normalization, weighting, and aggregation towards composite indices are not taken into account. Since the indices also fail to adequately represent the different dimensions of sustainability, Böhringer and Jochem conclude that sustainability indices currently employed in policy making are ineffective and misleading.

Gasparatos et al. [14] review reductionist methodologies in measuring progress towards sustainability. Although the reductionist paradigm simplifies the task of assessment, those authors are critical of some of its other characteristics such as single-variable measurements of dimensions of sustainability. Another criticism is the loss of useful information that occurs when aggregating indicators from different dimensions into a single composite index. They also consider monetary- and biophysical-based approaches to sustainability assessment. Financial approaches attach monetary values to social and environmental capital. However, the valuation of non-market goods and services is controversial and not well developed. Biophysical approaches such as exergy and ecological footprint analysis [6] apply a natural science perspective to sustainability assessment. Although biophysical models do a good job of quantifying resource use and environmental impact, they are inadequate in addressing social issues and some economic aspects of sustainability.

Bossel [15] applies a systems approach to develop comprehensive indicators of sustainable development, identifying seven basic orientors essential for system viability and sustainability: existence, effectiveness, freedom of action, security, adaptability, coexistence, and psychological needs. Reed et al. [16] extend the work of Bossel [15] by integrating reductionist and participatory approaches to measure progress towards sustainability. They identify reductionist and participatory approaches as the primary methodological paradigms in the literature on developing sustainability indicators. They argue that participatory approaches are essential to engage communities in sustainability assessment.

23.2.2 Sustainability Assessment of Energy Systems

Afgan et al. [17] develop a set of sustainability indicators related to resource, economic, social, and environment criteria. Resource indicators measure the fuel, carbon steel, copper, and aluminum intensity of energy services. Economic indicators measure the efficiency, capital investment, and local economic impact. Social indicators measure impacts on job creation, standard of living, and energy diversification. Environment indicators assess carbon dioxide (CO_2), nitrogen oxide (NO and NO_2), and sulfur dioxide (SO_2) emissions as well as waste generation. Subsequent works by Afgan and Carvalho [18] and Afgan [19] employ a multi-criteria evaluation to create a general index of sustainability based on aggregation of a selected number of energy indicators.

Vera and Langlois [20] summarize the efforts of an international partnership initiative led by the International Atomic Energy Agency (IAEA) to identify indicators for sustainable energy development [21]. The project identifies 30 energy indicators within the economic, social, and environmental spheres. Economic indicators are related to patterns of energy use, supply efficiency, diversification of supply, price, and security. Social indicators include concerns over equity and accessibility, affordability and disparities, and health and safety. Environmental indicators are mostly concerned with air and water emissions, deforestation, and waste production. Due to an uneven distribution across the various spheres, an index for sustainable energy development is not generated by aggregating indicators.

Evans et al. [22] assess renewable electricity generation technologies against a range of indicators and rank their relative sustainability. The indicators used in their study are price of electricity generation, GHG emissions, availability of technology, conversion efficiency, land use requirements, water consumption, and social impacts. Each indicator is then ranked on a scale of 1–4 for photovoltaic, wind, hydro, and geothermal energy, where lower numbers indicate better performance.

Genoud and Lesourd [23] develop a decision-support method for selecting power generation technologies based on sustainable development criteria.

The criteria for assessing technologies are based on economic, social, and environmental considerations. Economic criteria are exergy efficiency, renewability, storability, flexibility, growth potential, and production cost. Social criteria include non-rivalry in the consumption of a primary energy source (i.e., similar to a public good), land area requirements, energy payback ratio, job creation, supply risk, and local energy resources. Environmental criteria include life cycle emissions of several pollutants such as CO_2, SO_2, nitrogen oxides, particulate matter, biochemical oxygen demand, cadmium, methane (CH_4), and radioactivity as well as noise.

Gnanapragasam et al. [24] derive an energy system assessment methodology by considering indicators within the technological, sociological, and ecological dimensions of sustainability. Dimensions contain ten indicators each, which are assigned performance values between 0 and 1. The usefulness of this methodology is to compare alternative energy systems based on their final numerical score. Measuring the approach of an energy system to sustainability is only possible by comparing system performance to actual reference values.

Neves and Leal [25] develop local energy sustainability indicators for municipalities based on a review of existing sets of sustainability indicators. They build a core set of 8 local energy sustainability indicators and a complementary set of 18 indicators. Case studies of municipalities employing sustainability indicators reveal that very few local authorities are using indicators as decision criteria.

Brent and Rogers [26] perform a sustainability assessment of a stand-alone renewable energy system in a rural village in Africa. Their sustainability assessment model is based on the principles of sustainability science: transdisciplinarity, resilience, complexity, adaptive management, and adaptive capacity. A systems approach to sustainability assessment decomposes the overall system into technological, economic, ecological, institutional, and social subsystems. The integrated renewable energy system is not viable for a number of reasons such as the high-cost of electricity and lack of resilience of the technological subsystem.

Some of the studies in the literature relate sustainability to entropy generation and the second law of thermodynamics. Dewulf et al. [27] and Ferrari et al. [28] quantify the sustainability of a technological process by its degree of irreversibility. Both studies develop an exergy-based sustainability coefficient, and each concludes that a process can only be sustainable if driven exclusively by renewable resources. Dewulf and Van Langenhove [29] use second-law approaches integrated with industrial ecology principles to evaluate environmental sustainability. Production pathways are assessed according to five exergy-based indicators: renewability of resources, toxicity of emissions, input of used materials, recoverability of products, and process efficiency. Zvolinschi et al. [30] calculate exergy-based sustainability indicators to compare gas- and hydrogen-fired combined-cycle power plants. The indicators are exergy renewability, environmental compatibility, and exergy efficiency. The analysis reveals that there is often a trade-off between exergy renewability and exergy efficiency. Frangopoulos and Keramioti [31]

implement a multi-criteria approach to determine a composite sustainability index of energy systems. The index aggregates technical, economic, social, and environmental sustainability indicators. Exergy efficiency indicators consist of half of the technical indicators.

23.2.3   Discussion and Comparison

Based on reports in the literature on sustainability assessment, a number of shortcomings with existing methodologies exist. As shown by Singh et al. [10], very few of the methodologies follow an integral approach and the construction of composite indicators is often done incorrectly. Even when aggregation of indicators is done correctly, there is an inevitable loss of information since the resulting composite index does not identify where the system under investigation needs improvement.

Another difficulty with some of the existing approaches is when indicators are ranked on a numbered scale to estimate the approach to sustainability. This method is only useful when comparing different systems and does not indicate sustainability. To measure sustainability, there need to be sustainability reference values for indicators and systems have to be compared to those targets.

Assessment methodologies that take a weak sustainability approach tend to concentrate on economic considerations and neglect the biophysical aspects of sustainability. However, biophysical approaches are mostly concerned with environmental sustainability while neglecting the socioeconomic dimension. A comprehensive sustainability assessment methodology needs to consider all aspects of sustainability without any disciplinary bias that favors one area over another.

The primary shortcoming of existing techniques of measuring sustainability is the lack of a systems perspective, and addressing this concern forms the focus of this article. Even those methodologies that incorporate economic, social, and environmental sustainability indicators tend to neglect interaction effects and how well an energy system is integrated with other subsystems. For example, a common criterion of many assessment methodologies is the renewable energy content of an energy system, yet the ability of the system to deliver adequate and reliable energy services is ignored. Moreover, the production cost of generating local heat and power is often considered. However, affordability strongly depends on the incomes and living expenses of the members of the community. The sustainability of an energy system integrated within a community cannot be measured solely based on a few indicators.

The novelty of this research is an integral approach to sustainability assessment that views system behavior as a whole. Previous works have not considered whether the whole system is sustainable based on criteria essential for the sustainability of an energy system.

23.3 Systems Approach to Sustainability Assessment
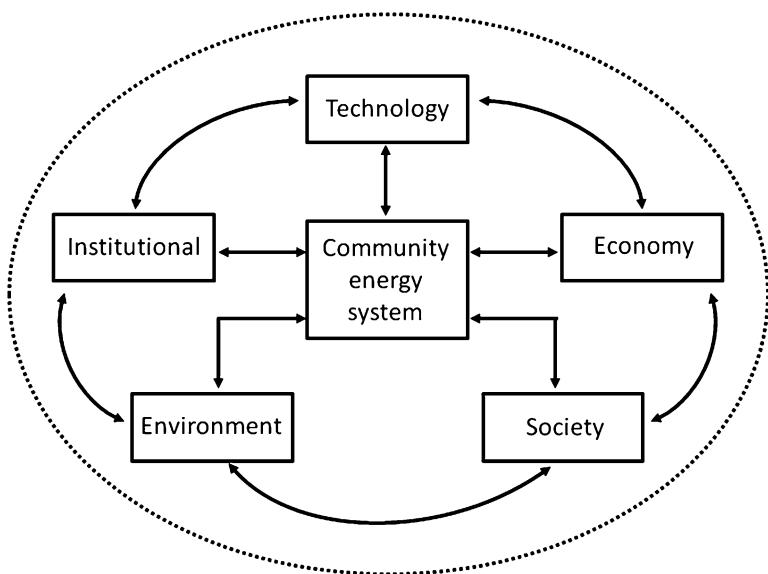
A system can be defined as a set of components that work together for the overall objective of the whole [32]. Interconnections between the elements of a system result in feedback loops and internal restructuring. Self-organization of open systems is driven by incoming flows of high-quality energy (high exergy) that move the system away from equilibrium. Systems respond by reorganizing their structure to enhance exergy dissipating capacity [33]. These nonlinear phenomena lead to emergent properties of real systems not explainable by the sum of their parts.

The reductionist approach is a dominant modern scientific paradigm. Reductionist thinking follows the premise that the behavior of the whole can be explained by aggregating its individual elements [34]. However, this type of thinking has difficulties with situations where synergy and emergence are important factors and the whole is more than the sum of its parts. Systems behave in unpredictable ways and are not understandable in terms of traditional linear causality [34]. Understanding how the parts of a system effectively work together is frequently overlooked [35].

Assessing the sustainability of a community energy system needs to consider how the system interacts with other human–environmental systems. Reductionist methods of measuring sustainability are inadequate for assessing integrated systems and should be replaced by a systems perspective. A systems viewpoint captures the various connections between subsystems that may have otherwise been overlooked. For example, human activities (e.g., filling in a wetland) can affect the organization of ecological systems (reduced absorption capacity), which cascades through to affect societal systems (increased flooding) [33]. Another example of the consequences of not adopting a systems perspective is the disruption of the annual flooding of the Nile due to the construction of the Aswan dam. The Nile provided nutrients for downstream agriculture, which now has to be supplied by synthetic fertilizers. The energy required to replace the nutrients once provided by the Nile exceeds the energy generated by the dam [34]. A systems approach to sustainability assessment allows the researcher to have a more complete mental map of the system in question.

A life cycle approach is a key element of systems thinking. It is important to understand the upstream processes and transformations a material or energy input underwent before entering a system. Similarly, researchers have to track the fate of outputs downstream of the system to assess any economic, social, or environmental impact. Considering the full life cycle of products such as leaded gasoline and chlorofluorocarbon (CFC) refrigerants could have revealed their adverse health and environmental impacts and delayed their introduction to the market.

An adapted version of the systems approach to assessing sustainability as described by Brent and Rogers [26] is shown in Fig. 23.2. In the proposed model, a community energy system is nested within a larger whole that encompasses technology, economy, society, environment, and institutional subsystems. Exchanges of mass, energy, and information connect the community energy system

Fig. 23.2 Systems model of sustainability that illustrates the interactions of a community energy system with technology, economy, society, environment, and institutional subsystems

to each of the other subsystems. Similarly, the technology, economy, society, environment, and institutional subsystems are also interdependent. Measuring the sustainability of the community energy system is not complete without assessing the sustainability of the whole, which includes all the other subsystems.

The general conditions of a sustainable community energy system need to be defined before indicators are developed. There are a number of objectives the overall system has to achieve to ensure sustainability:

1. Production from renewable energy sources.
2. Minimal GHG and pollutant emissions.
3. Continuous and reliable energy supply.
4. Affordable energy services.
5. Public acceptance.

There is no universal consensus as to the criteria of sustainable energy systems. However, an argument could be made that each of the above five criteria are essential components of sustainability. The indicators developed in the following sections are intended to measure the ability of the community energy system to meet the above sustainability objectives. Many of the selected indicators can be found elsewhere in the literature although precise definitions and evaluation techniques could differ.

23.3.1   Technology

The technical performance of a community energy system is a significant factor when measuring sustainability. Two of the most critical criteria related to the sustainability of an energy system are adequate and reliable energy supply. The design of a sustainable energy system needs to consider the availability of local resources and how they can be integrated to meet community energy needs.

Successful implementation of a community energy system requires integration with the local energy supply infrastructure. Potential designs need to consider the compatibility of the proposed system with the existing infrastructure.

A systems approach to assessing the sustainability of the technology subsystem requires a number of critical indicators:

- *Adequacy*: The extent to which an energy system can meet the energy needs of a community. Target value is 100 % of local energy demand.
- *Compatibility*: The degree to which the energy system is compatible with the existing technological infrastructure. Target value is 100 % compatible.
- *Energy return on investment (EROI)*: The ratio of net energy generated by the system to life cycle fossil energy inputs. This includes energy consumed during the construction phase of the system. The EROI of an energy system has to be at least greater than 1.
- *Exergy return on investment (ExROI)*: The ratio of net exergy generated by the system to life cycle fossil exergy inputs. This includes exergy consumed during the construction phase of the system. The ExROI of an energy system has to be at least greater than 1.
- *Reliability*: The ability of an energy system to continuously deliver an uninterruptible supply of energy. Target value is 100 % reliability.
- *Renewability*: The amount of incoming energy that comes from renewable sources. Target value is 100 % renewable.

The traditional first- and second-law efficiencies of an energy system are useful measures but not the most appropriate indicators of sustainability. For example, an energy system driven by a nonrenewable energy source may have a higher efficiency than a system powered by a renewable energy source. It is obvious that in this case the more efficient system is not necessarily more sustainable. The EROI and ExROI are better indicators of sustainability.

Another common metric used to assess the technical performance of an energy technology is capacity factor, which is the ratio of actual output to theoretical maximum output. In general, energy conversion devices that have high capacity factors are more economical. However, capacity factor is omitted as an indicator because a systems approach reveals that the sustainability of the whole is more dependent on an adequate and reliable energy supply.

23.3.2   Economy

Members of a community are primary stakeholders in the relationship between an energy system and the economy. Consequently, unsatisfactory economic indicators can fuel local opposition and derail an energy project. There are two major economic criteria that a proposed community energy system has to address: affordability and local job creation.

A systems approach to assessing the sustainability of the economy subsystem yields a number of critical indicators:

- *Affordability*: The production cost of energy generated by the system relative to the median income of the community. As a guideline, total energy costs of a household should not exceed 10–15 % of after-tax income [36].
- *Job creation*: The total number of local jobs created and local jobs created per unit of energy production. Target value is 100 % local.

Renewable energy systems can be more expensive and less affordable than fossil-based systems. However, renewable energy provides several social and environmental benefits that are treated as externalities in traditional economic cost accounting. A flow of subsidies from the institutional to the economy subsystem could be justified to offset affordability concerns and encourage the development of local renewable energy systems.

23.3.3   Society

The development and implementation of a community energy system needs to be a participatory process involving local stakeholders. Encouraging local participation accelerates public acceptance and mitigates the risk of opposition. Moreover, both top-down and bottom-up approaches are useful when developing appropriate sustainability indicators.

There are several criteria that need to be met to ensure the social sustainability of a community energy system. The energy system should rely upon local natural resources and talent to build upon existing social capital. A community energy system should be a source of civic pride, which is only possible if there are minimal adverse health effects and security concerns. Most of all, public acceptance is required.

A systems approach to assessing the sustainability of the society subsystem leads to a number of critical indicators:

- *Health*: The number of illnesses as a result of the energy system and illnesses per unit of energy production. Target value is 0 illnesses.
- *Local resources*: The amount of energy inputs to the system derived from local resources. Target value is 100 % local resources.

- *Public acceptance*: The fraction of the community that supports the construction and operation of the energy system. Target value is 100 % public acceptance.

There are parallels between indicators for technology, economy, and society subsystems such as reliability and local job creation, all of which could be considered social metrics as well. A good sustainability indicator is a multidimensional measure that connects criteria from different subsystems.

23.3.4 Environment

Material and energy by-products emitted from a community energy system ultimately end up in the environment subsystem. Identifying the impact of emissions is crucial for assessing the environmental sustainability of an energy project. Waste products can end up in any of the three compartments of the biosphere—land, water, or air. All waste emissions should be assessed on a life cycle basis (i.e., not just the waste generated during operation).

A fundamental aspect of environmental sustainability is carrying capacity. As discussed earlier, societies that overshoot the carrying capacity of the land are susceptible to collapse. Although a full discussion of carrying capacity is beyond the scope of our study (e.g., agricultural land requirements of a community) an estimate of the land area occupied by the energy system can be a meaningful indicator.

A systems approach to assessing the sustainability of the ecology subsystem identifies a number of critical indicators:

- *Air pollution*: Air pollutant emissions per unit energy production. Potential emissions include sulfur oxides, nitrogen oxides, particulate matter, and mercury. Target value is zero air pollution.
- *Biodiversity*: The effects on biodiversity over the life cycle of an energy system. Target value is zero impact on biodiversity.
- *Embodied water*: Life cycle water use of the energy system. No set target value.
- *GHG intensity*: GHG emissions per unit energy production. Target value is zero GHG emissions.
- *Land area*: The area of land required to meet the energy needs of a community. No set target value.
- *Ozone depletion*: The release of ozone depleting substances per unit energy production. Target value is zero emissions of ozone depleting substances.
- *Solid waste*: Solid waste generated per unit energy production. Target value is zero solid waste production.
- *Water pollution*: Wastewater production per unit energy production. Target value is zero wastewater production.

It is possible to transfer pollution from one medium to another through end-of-pipe treatment options such as filters and scrubbers. However, the objective should

be to minimize overall pollution production from the whole. Moreover, it is unrealistic to expect zero generation of wastes and GHG emissions over the life cycle of an energy system. Waste production should be minimized but specific targets to ensure sustainability do not exist.

23.3.5 Institutional

Moving from centralized heat and power delivery to small-scale distributed networks is a transformational shift in energy systems thinking. The institutional subsystem can play a significant role to either help or hinder an energy transition based on its laws and policies. As previously mentioned, subsidies that offset higher costs of renewable community energy systems can improve affordability. Subsidies are justified in recognition of the environmental and local economic development benefits associated with community energy systems.

The energy industry is heavily regulated and a community with limited resources could encounter bureaucratic barriers when trying to develop its own energy system. Support and guidance by the institutional subsystem is essential to overcoming regulatory barriers that delay energy projects from moving forward. Local political support as a result of widespread public acceptance could be instrumental in removing institutional barriers.

A systems approach to assessing the sustainability of the institutional subsystem points out a number of critical indicators:

- *Regulatory*: Laws that support the construction and operation of a community energy system and accelerate their implementation.
- *Policy*: Subsidies or other benefits available to community energy systems. Target value is at least one policy in support of community energy systems.
- *Political*: Support of local politicians in developing a community energy system. Target value is all local elected officials.

The institutional subsystem can encourage the development of community energy systems by other means as well such as funding related research or mandating a certain capacity of distributed generation in each jurisdiction.

23.3.6 Discussion

The proposed systems approach to sustainability assessment of a community energy system identifies 22 indicators in the technology, economy, society, environment, and institutional subsystems. Each of the proposed indicators in some way measures one of the five sustainability criteria identified earlier. Evaluating the various indicators and comparing to target values provides a measure of the proximity of a community energy system to sustainability. Benchmarking the

system also identifies indicators that need improvement. The progress of a community energy system towards sustainability can be monitored over time by continually reevaluating indicators.

It is important to recognize the limitations of the proposed sustainability assessment methodology. It is not possible to devise a standard sustainability assessment approach that applies to all communities and the unique contexts in which they exist. Thus, a systematic and participatory approach that involves local stakeholders is essential to develop comprehensive and effective sustainability indicators for a community energy system.

23.4 Case Studies

The systems-based sustainability assessment methodology is applied to two case studies involving community power plants. The first case study applies the sustainability assessment approach to a gas-turbine power plant driven by natural gas. The second assesses the sustainability of a single-flash geothermal steam power plant. Each system is designed to meet the annual electrical energy needs of a community of 50 households with a peak demand of 2 kW per household.
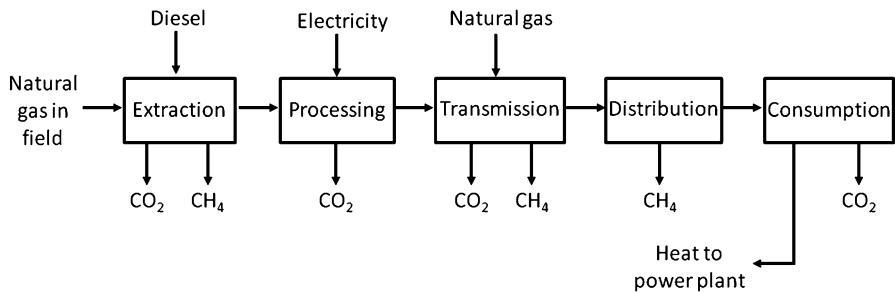
23.4.1 *Gas-Turbine Power Plant*

The first case study is a local thermal power plant driven by natural gas. The power plant operates on a standard Brayton cycle with air/combustion products as the working fluids.

A systems approach to sustainability assessment needs to consider the entire life cycle of natural gas from extraction to consumption. The supply chain can be separated into five stages: extraction, processing, transmission, distribution, and consumption by the end user [37]. Each stage of the life cycle has energy inputs and waste outputs (Fig. 23.3).

Natural gas is extracted from the ground by drilling wells using equipment powered by diesel engines. Combustion of diesel fuel generates CO_2 while fugitive emissions of CH_4 also occur. Natural gas venting and flaring can reduce CH_4 emissions, which has a 100-year global warming potential of 25 [38]. Gas processing facilities then upgrade natural gas to meet pipeline specifications. The carbon footprint of the gas processing stage is largely determined by the gas composition, which determines energy requirements and the amount of CO_2 vented to the atmosphere.

Transmission and distribution through an extensive network of gas pipelines delivers natural gas to end users. There are compressor stations at various points along the transmission grid that maintain the high pressure in the pipeline. The exhaust from gas-powered compressors and fugitive CH_4 emissions are the

Fig. 23.3 Life cycle processes of natural gas production
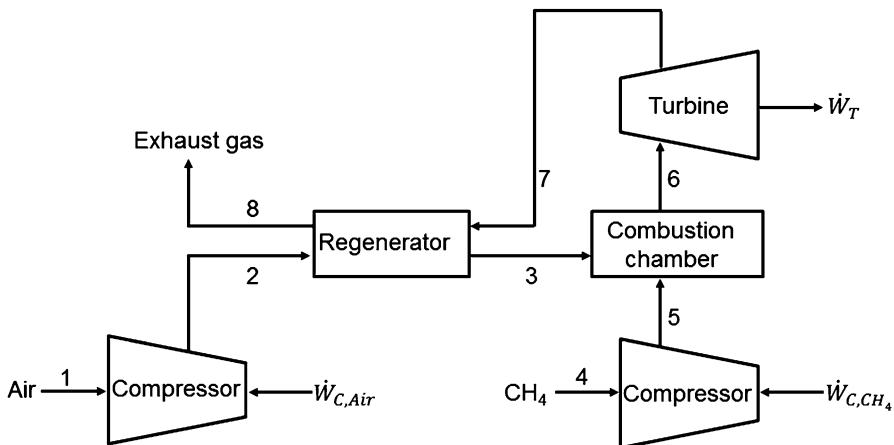
Table 23.1 Efficiency and GHG intensity of natural gas extraction and delivery to the end user

Stage	Efficiency (%)	Life cycle GHG emissions (kgCO$_2$e GJ^{-1})
Extraction	97	5.6
Processing	98	2.9
Transmission	97	2.4
Distribution	–	1.3
Consumption	–	50.3
Total	92	62.5

principal sources of GHG emissions in transmission. High-pressure gas from the transmission system flows through the low-pressure distribution grid without additional energy inputs although fugitive emissions are still a source of GHG emissions. Complete combustion of natural gas by the end user releases a stoichiometric amount of CO_2 emissions and heat.

The overall delivery efficiency [39] and life cycle emission factor of natural gas [37] derived from the supply chain analysis is presented in Table 23.1. It is seen that for every unit of natural gas extracted from the ground, 0.92 units of gas are delivered to the end user. Moreover, although the stoichiometric amount of CO_2 emissions from one GJ of natural gas is 50.3 kg, the amount of GHG emissions over its life cycle is approximately 25 % higher (62.5 kgCO$_2$e GJ^{-1}).

The exothermic thermal energy generated by complete combustion of natural gas can potentially meet the electricity needs of a community. The general layout of a gas-turbine power plant is shown in Fig. 23.4. The temperature and pressure of air is increased from environmental conditions at state 1 to state 2 in an electrically driven compressor. The temperature of air is then increased to state 3 through contact with hot exhaust gases in a regenerator. After compression of CH_4, an air–CH_4 mixture is ignited in the combustion chamber generating hot combustion products at state 6. The high-temperature gas then expands in a gas turbine producing mechanical work, which is then converted to electricity in a generator.

Fig. 23.4 General layout of a gas-turbine power plant

Table 23.2 Modeling results of a gas-turbine power plant (negative sign denotes heat or work flowing out of the system)

State	P (kPa)	T (°C)	h (kJ kg^{-1})	s (kJ kg^{-1} K^{-1})	ex (kJ kg^{-1})	$\dot{S}_{Gen}$ (kW K^{-1})	$\dot{Ex}_D$ (kW)	$\dot{Q}$ (kW)	$\dot{W}$ (kW)
1	100	25	0	6.9	−44				
						0.04	11.7	0	110
2	810	320	300	7.0	230				
						0.02	5.3	110	0
3	810	590	600	7.4	400				
						–	–	–	–
4	100	25	−4,650	11.6	0				
						0.00	0.4	0	4
5	810	220	−4,140	11.8	440				
						0.58	171.4	−92	0
6	810	1,140	260	8.2	910				
						0.04	12.5	0	−210
7	100	670	−320	8.3	300				
						–	–	−110	0
8	100	430	−610	8.0	120				

The combustion products then pass through a regenerator to preheat air before finally being exhausted to the environment.

The technical performance of the gas-turbine power plant is assessed by constructing a thermodynamic model of the system. The results of the model for a 100 kW facility are presented in Table 23.2. The pressure and temperature of the working fluid as well as its specific enthalpy, entropy, and exergy at each state are shown in the table. The rate of entropy generation, exergy destruction, heat flow,

and work flow resulting from the transition from one state to another is illustrated in the row between two points.

The first-law (energy) efficiency for this system is defined as the net work generated divided by the higher heating value (HHV) of the fuel:

$$\eta = \frac{\dot{W}_T - \dot{W}_{C,Air} - \dot{W}_{C,CH_4}}{(\dot{m}HHV)_{CH_4}} \tag{23.1}$$

where the HHV of CH_4 is 55,510 kJ kg^{-1}. Similarly, the second-law (exergy) efficiency is defined as the net work generated divided by the chemical exergy of the fuel:

$$\varepsilon = \frac{\dot{W}_T - \dot{W}_{C,Air} - \dot{W}_{C,CH_4}}{(\dot{m}ex)_{CH_4}} \tag{23.2}$$

where the chemical exergy of CH_4 is 51,840 kJ kg^{-1} [40]. Since the only distinction between Eqs. (23.1) and (23.2) is the different HHV and chemical exergy values, the exergy efficiency of this system will always be higher than its energy efficiency.

Based on the results of Table 23.2, the first- and second-law efficiency of the system is 26 % and 27 %, respectively. When the delivery efficiency of natural gas (Table 23.1) is taken into account, the energy and exergy efficiency decrease to 23 % and 25 %, respectively.
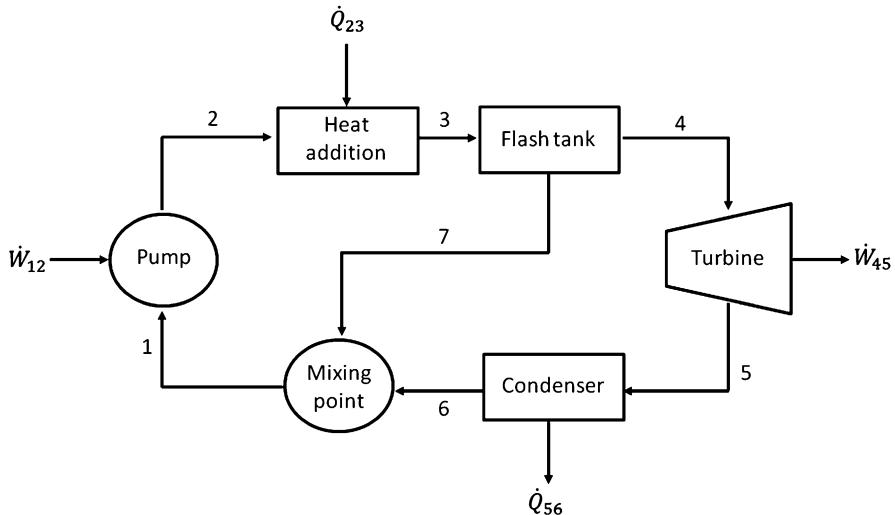
An economic analysis can estimate the levelized cost of electricity. The capital cost of a gas-turbine power plant was estimated to be $1,000 kW^{-1} on a peak power basis. For a 210 kW facility (Table 23.2), the initial investment is approximately $210,000. The lifetime of the plant is assumed to be 20 years and a 5 % interest rate amortizes the initial investment. The capital recovery factor (CRF) is then calculated as:

$$CRF = \frac{i(1+i)^N}{(1+i)^N - 1} \tag{23.3}$$

Annual investment costs are calculated as $17,000 per year at a CRF of 8 %. Annual operating and maintenance costs are estimated to be 4 % of the initial investment cost. Consequently, annual operating and maintenance costs are $8,400 per year.

Total annual consumption is required to find natural gas costs. Although peak demand of a household is assumed to be 2 kW, average demand over the course of a year is estimated to be 0.7 kW. At a price of $3 GJ^{-1}, the annual cost of gas is $13,000. The total annual cost of the system is therefore $38,700.

The levelized cost of electricity is determined by dividing the total annual cost of the system by the amount of electricity generated. If average demand is 0.7 kW, then average annual generation is approximately 307,000 kWh. The production cost of electricity is therefore $0.13 kWh^{-1}.

Fig. 23.5 General layout of a single-flash geothermal steam power plant

Median household income in Ontario was \$69,790 in 2009 with an overall tax rate of 25 % [41]. The after-tax median income is therefore \$52,343. The total annual cost of the community energy system is \$770 per household or 1.5 % of after-tax income. A gas-turbine power plant should be affordable for most Ontario communities.

The GHG intensity of the gas-turbine power plant is estimated based on the life cycle emission factor of natural gas (Table 23.1). The product of annual consumption (4,330 GJ) and its life cycle emission factor (62.5 $kgCO_2e$ GJ^{-1}) yields the annual amount of GHG emissions (270,000 $kgCO_2e$). Since the system generates 307,000 kWh per year, the GHG intensity of the gas-turbine power plant is 880 gCO_2e kWh^{-1}.

23.4.2 Single-Flash Geothermal Steam Power Plant

The second case study considers a geothermal-based system. A community can utilize local geothermal resources to generate electricity. Geothermal energy can be harnessed by pumping water down an injection well and extracting it at a higher temperature through the production well. In general, accessing higher geothermal temperatures requires digging deeper wells, as is the case with enhanced geothermal systems [42]. The depth of a well depends on the nature of local geothermal resources and the desired temperature of the working fluid.

A common type of geothermal facility is a flash steam power plant (Fig. 23.5). Water is pumped down into an injection well, where it gains heat from its surroundings. The high-pressure saturated water exits the geothermal system and enters

Table 23.3 Modeling results of a single-flash geothermal steam power plant (negative sign denotes heat or work flowing out of the system)

State	P (kPa)	T (°C)	h (kJ kg^{-1})	s (kJ kg^{-1} K^{-1})	ex (kJ kg^{-1})	$\dot{S}_{Gen}$ (kW K^{-1})	$\dot{Ex}_D$ (kW)	$\dot{Q}$ (kW)	$\dot{W}$ (kW)
1	380	142	597	1.76	77				
						0.002	0.5	0	4
2	1,554	142	599	1.76	79				
						0.081	24.3	581	0
3	1,554	200	852	2.33	162				
						0.067	19.9	0	0
4	500	152	2,749	6.82	719				
						0.080	23.9	0	−104
5	12	50	2,299	7.17	166				
						0.125	37.2	−481	0
6	12	50	209	0.70	4				
						–	–	0	0
7	500	152	640	1.86	90				
						0.031	9.2	0	0
1	380	142	597	1.76	77				

a flash tank at reduced pressure. An isenthalpic flash evaporation process results in a vapor–liquid mixture of liquid water and steam. Steam from the flash tank is expanded in a steam turbine, generating mechanical work $(\dot{W}_{45})$. The exhaust from the steam turbine is then condensed and combined with the liquid condensate from the flash tank for reinjection into the well.

The technical performance of the single-flash geothermal steam power plant is assessed by constructing a thermodynamic model of the system. The results of the model for a 100 kW facility are presented in Table 23.3. The energy and exergy efficiencies of the cycle are calculated as in Eqs. (23.1) and (23.2). Based on the results of Table 23.3, the energy and exergy efficiency of the system is 17 % and 47 %, respectively.

An economic analysis of the geothermal flash steam power plant is performed to determine the production cost of electricity. The capital cost of a single-flash geothermal steam power plant is estimated to be $3,000 kW^{-1} on a peak power basis [43]. For a facility that generates 104 kW of power (Table 23.3), the initial investment is approximately $310,900. The lifetime of the plant, interest rate, and annual operating and maintenance costs are estimated to be the same as the gas-turbine power plant. Consequently, annual capital and operating and maintenance costs are $24,900 and $12,400, respectively.

Unlike the gas-turbine power plant, there are no fuel costs for geothermal power plants. The total annual cost of the system is therefore $37,400 while the production cost of electricity is $0.12 kWh^{-1}. The annual cost per household is $748 or 1.4 % of after-tax median income. A single-flash geothermal steam power plant should be affordable for most Ontario communities.

Table 23.4 Sustainability assessment results of the gas-turbine and geothermal flash steam power plant systems

Indicator	Target	Gas-turbine system	Geothermal system
Technology			
Adequacy	100 %	100 %	50 %
Compatibility	100 %	100 %	100 %
Energy return on investment	>1	N/A	N/A
Exergy return on investment	>1	N/A	N/A
Reliability	100 %	99 %	50 %
Renewability	100 %	0 %	100 %
Economy			
Affordability	<5 % income	1.5 %	1.4 %
Job creation	100 %	Medium	High
Society			
Health	Minimal	Minimal	Minimal
Local resources	100 %	0 %	100 %
Public acceptance	100 %	N/A	N/A
Environment			
Air pollution	0	Low	0
Biodiversity	No effect	N/A	N/A
Embodied water	0	N/A	N/A
Greenhouse gas intensity	0	880 $gCO_2e\ kWh^{-1}$	30 $kgCO_2e\ kWh^{-1}$
Land area	Minimal	N/A	N/A
Ozone depletion	0	0	0
Solid waste	0	Low	Low
Water pollution	0	0	Low
Institutional			
Regulatory		N/A	N/A
Policy	>1	N/A	N/A
Political	100 %	N/A	N/A

There are a range of estimates of the GHG intensity of geothermal systems in the literature. Bloomfield et al. [44] calculate a GHG intensity of approximately 10 $gCO_2e\ kWh^{-1}$ based on a weighted average of US geothermal plants. Hondo [45] applies a life cycle analysis of GHG emissions from a geothermal double flash power plant (15 $gCO_2e\ kWh^{-1}$). Sullivan et al. [46] analyzes a range of geothermal technologies, with GHG intensity varying from 5 to 30 $gCO_2e\ kWh^{-1}$. Based on these studies, the carbon footprint of a geothermal flash steam power plant can be approximated as 30 $gCO_2e\ kWh^{-1}$.

23.4.3 Sustainability Assessment

A sustainability assessment of the gas-turbine and the geothermal flash steam power plants is performed by estimating the value of the various indicators. The results of the assessment are presented in Table 23.4, and reveal the weaknesses associated

with each community energy system. The gas-turbine power plant performs well according to technology criteria such as adequacy and reliability. Unfortunately the system is entirely dependent on a nonrenewable fuel that generates significant GHG emissions. The non-GHG environmental impacts of a gas-turbine power plant are not as substantial although this strongly depends on the natural gas life cycle. For example, extracting gas from shale deposits (unconventional natural gas) by hydraulic fracturing requires the injection of water along with a combination of chemicals that have adverse health and environmental impacts [47].

The single-flash geothermal steam power plant exhibits better society and environment ratings but poorer grades from a technology perspective. The system makes more use of local resources, creates more local jobs, and generates fewer environmental impacts. Moreover, the geothermal-based system is predicted to be just as affordable as the gas-fired plant. The system may be capable of generating an adequate supply of electricity but there are concerns with respect to its year-round reliability. A back-up generator or thermal energy storage system would most likely be required to improve reliability to 100 %.

23.5   Conclusions

The primary shortcoming of existing sustainability assessment methodologies are discovered to be a reductionist approach that is inadequate for accounting for the various dimensions of sustainability and interconnections of real systems. A systems approach to sustainability assessment is proposed that involves a number of indicators in the technology, economy, society, environment, and institutional subsystems. A gas-turbine power plant powered by a nonrenewable fuel produces GHG emissions and other potential harmful environmental impacts, while a geothermal power plant raises reliability concerns. Neither system can therefore be considered sustainable until its respective challenges can be ameliorated. The new sustainability assessment methodology is expected to prove useful as a tool for understanding and fostering sustainable energy systems, alone or in concert with other approaches.

References

1. Graedel TE, Allenby BR (2010) Industrial ecology and sustainable engineering. Prentice Hall, New Jersey
2. Tainter JA (1988) The collapse of complex societies. Cambridge University Press, Cambridge
3. Hart M (1999) Guide to sustainable community indicators. Hart Environmental Data, West Hartford

4. World Commission on Environment and Development (WCED) (1987) Our common future. Oxford University Press, New York

5. Committee on Earth Resources (1996) Mineral resources and sustainability: challenges for earth scientists. National Academy, Washington, DC

6. Dincer I, Rosen MA (2007) Exergy: energy, environment, and sustainable development. Elsevier, Oxford

7. Daly HE (1990) Toward some operational principles of sustainable development. Ecol Econ 2:1–6

8. Rennings K, Wiggering H (1997) Steps towards indicators of sustainable development: linking economic and ecological concepts. Ecol Econ 20:25–36

9. Ness B, Urbel-Piirsalu E, Anderberg S, Olsson L (2007) Categorising tools for sustainability assessment. Ecol Econ 60:498–508

10. Singh RK, Murty HR, Gupta SK, Dikshit AK (2009) An overview of sustainability assessment methodologies. Ecol Indic 9:189–212

11. Parris TM, Kates RW (2003) Characterizing and measuring sustainable development. Annu Rev Env Resour 28:559–586

12. Morse S, Fraser EDG (2005) Making 'dirty' nations look clean? The nation state and the problem of selecting and weighting indices as tools for measuring progress towards sustainability. Geoforum 36:625–640

13. Böhringer C, Jochem PEP (2007) Measuring the immeasurable—a survey of sustainability indices. Ecol Econ 63:1–8

14. Gasparatos A, El-Haram M, Horner M (2008) A critical review of reductionist approaches for assessing the progress towards sustainability. Environ Impact Asses 28:286–311

15. Bossel H (2001) Assessing viability and sustainability: a systems-based approach for deriving comprehensive indicator sets. Conserv Ecol 5:12

16. Reed MS, Fraser EDG, Morse S, Dougill AJ (2005) Integrating methods for developing sustainability indicators to facilitate learning and action. Ecol Soc 10:6

17. Afgan NH, Carvalho MG, Hovanov NV (2000) Energy system assessment with sustainability indicators. Energy Policy 28:603–612

18. Afgan NH, Carvalho MG (2002) Multi-criteria assessment of new and renewable energy power plants. Energy 27:739–755

19. Afgan NH (2010) Sustainability paradigm: intelligent energy system. Sustainability 2:3812–3830

20. Vera I, Langlois L (2007) Energy indicators for sustainable development. Energy 32:875–882

21. International Atomic Energy Agency, United Nations Department of Economic and Social Affairs, International Energy Agency, Eurostat, European Environment Agency (2005) Energy indicators for sustainable development: guidelines and methodologies. International Atomic Energy Agency, Vienna, Austria

22. Evans A, Strezov V, Evans TJ (2009) Assessment of sustainability indicators for renewable energy technologies. Renew Sustain Energy Rev 13:1082–1088

23. Genoud S, Lesourd J (2009) Characterization of sustainable development indicators for various power generation technologies. Int J Green Energy 6:257–267

24. Gnanapragasam NV, Reddy BV, Rosen MA (2010) A methodology for assessing the sustainability of hydrogen production from solid fuels. Sustainability 2:1472–1491

25. Neves AR, Leal V (2010) Energy sustainability indicators for local energy planning: review of current practices and derivation of a new framework. Renew Sustain Energy Rev 14:2723–2735

26. Brent AC, Rogers DE (2010) Renewable rural electrification: sustainability assessment of mini-hybrid off-grid technological systems in the African context. Renew Energy 35:257–265

27. Dewulf H, Van Langenhove H, Mulder J, van den Berg MMD, van der Kooi HJ, de Swaan AJ (2000) Illustrations towards quantifying the sustainability of technology. Green Chem 2:108–114

28. Ferrari S, Genoud S, Lesourd J (2001) Thermodynamics and economics: towards exergy-based indicators of sustainable development. Swiss J Econ Stat 137:319–336
29. Dewulf H, Van Langenhove H (2005) Integrating industrial ecology principles into a set of environmental sustainability indicators for technology assessment. Resour Conserv Recycl 43:419–432
30. Zvolinschi A, Kjelstrup S, Bolland O, van der Kooi HJ (2007) Exergy sustainability indicators as a tool in industrial ecology. J Ind Ecol 11:85–98
31. Frangopoulos CA, Keramioti DE (2010) Multi-criteria evaluation of energy systems with sustainability considerations. Entropy 12:1006–1020
32. Haines SG (2000) The complete guide to systems learning and thinking. HRD, Amherst
33. Kay JJ, Boyle M (2008) Self-organizing, holarchic, open systems (SOHOs). In: Waltner-Toews D, Kay JJ, Lister NE (eds) The ecosystem approach. Columbia University Press, New York
34. Kay JJ (2008) An introduction to systems thinking. In: Waltner-Toews D, Kay JJ, Lister NE (eds) The ecosystem approach. Columbia University Press, New York
35. Blanchard BS, Fabrycky WJ (2011) Systems engineering and analysis: fifth edition. Prentice Hall, New Jersey
36. Fankhauser S, Tepic S (2007) Can poor consumers pay for energy and water? An affordability analysis for transition countries. Energy Policy 35:1038–1049
37. Advanced Resources International (ARI) and ICF International (2008) Greenhouse gas life-cycle emissions study: fuel life-cycle of US natural gas supplies and international LNG. Sempra LNG, San Diego
38. Forster P, Ramaswamy V, Artaxo P, Bernsten T, Betts R et al (2007) Changes in atmospheric constituents and in radiative forcing. In: Climate change 2007: the physical science basis. Contribution of Working Group I to the Fourth Assessment Report of the Intergovernmental Panel on Climate Change. Cambridge University Press, Cambridge York
39. Hekkert MP, Hendriks FHJF, Faaij APC, Neelis ML (2005) Natural gas as an alternative to crude oil in automotive fuel chains well-to-wheel analysis and transition strategy development. Energy Policy 33:579–594
40. Morris DR, Szargut J (1986) Standard chemical exergy of some elements and compounds on the planet earth. Energy 11:733–755
41. Statistics Canada (2011) Median total income, by family type, by province and territory. CANSIM Tables, Ottawa
42. Kreith F, Kreider JF (2011) Principles of sustainable energy. CRC, Boca Raton, FL
43. Kitz K (2007) Geothermal power generation. In: Kreith F, Goswami DY (eds) Handbook of energy efficiency and renewable energy. CRC, Boca Raton, FL
44. Bloomfield KK, Moore JN, Neilson RM Jr (2003) Geothermal energy reduces greenhouse gases. Stud Environ Sci March/April:77–79
45. Hondo H (2005) Life cycle GHG emission analysis of power generation systems: Japanese case. Energy 30:2042–2056
46. Sullivan JL, Clark CE, Han J, Wang M (2010) Life-cycle analysis results of geothermal systems in comparison to other power systems. Center for Transportation Research, Energy Systems Division, Argonne National Laboratory, Argonne
47. Bramley M (2011) Is natural gas a climate change solution for Canada? David Suzuki Foundation, Vancouver

Chapter 24
Comparative Environmental Impact and Sustainability Assessments of Hydrogen and Cooling Production Systems

Tahir A.H. Ratlamwala, Ibrahim Dincer, and Mohamed A. Gadalla

Abstract In this chapter, we study two integrated systems for hydrogen and cooling productions. The first system is a combination of solar PV/T, quadruple effect absorption cooling system, and an electrolyzer, while the other is a combination of solar PV/T, quadruple effect absorption cooling system, and a steam methane reformer. Detailed exergetic, environmental impact and sustainability assessments are conducted to investigate which one of these integrated systems is more environmentally benign. It is noted that the month of July in the United Arab Emirates (UAE) is most beneficial from both exergetic and environmental impact point of views for both systems. For the month of July, the environmental impact factor, environmental impact coefficient, environmental impact index, environmental impact improvement, exergetic stability factor, and exergetic sustainability factor for the first system are obtained to be 0.78, 4.65, 3.65, 0.27, 0.21, and 0.058, respectively. However for the second system for the month of July environmental impact factor, environmental impact coefficient, environmental impact index, environmental impact improvement, exergetic stability factor, and exergetic sustainability factor are found to be 0.93, 14.96, 13.96, 0.07, 0.06, and 0.004, respectively. The results show that the first system performs much better than the second one from both exergetic and environmental impact perspectives.

T.A.H. Ratlamwala (✉) • I. Dincer
Faculty of Engineering and Applied Science, University of Ontario Institute of Technology, 2000 Simcoe Street North, Oshawa, ON, Canada L1H 7K4
e-mail: tahir.ratlamwala@uoit.ca; ibrahim.dincer@uoit.ca

M.A. Gadalla
College of Engineering, American University of Sharjah, Sharjah, UAE
e-mail: mgadalla@aus.edu

Nomenclature

A	Area of PV module (m^2)
b	Breadth of PV module (m)
$\dot{E}$	Energy rate (kW)
$\dot{E}x$	Exergy rate (kW)
h	Specific enthalpy (kJ/kg)
h_{ba}	Heat transfer coefficient from black surface to air (W/m^2 K)
h_t	Heat transfer coefficient from back surface to air through glass (W/m^2 K)
h_{p1G}	Penalty factor due to presence of solar cell material, glass and EVA for glass to glass PV/T system (W/m^2 K)
h_{p2G}	Penalty factor due to presence of interface between glass and working fluid through absorber plate for glass to glass PV/T system (W/m^2 K)
$\dot{I}$	Incident solar intensity (W/m^2)
L	Length of the PV module (m)
LHV	Lower heating value
$\dot{m}$	Mass flow rate (kg/s)
MW	Molecular weight (kg/kmol)
P	Power produced by PV/T
$\dot{Q}$	Heat transfer rate (kW)
T	Temperature (K)
U_b	Overall heat transfer coefficient from bottom to ambient (W/m^2 K)
U_L	Overall heat transfer coefficient from solar cell to ambient through top and back surface of insulation (W/m^2 K)
U_t	Overall heat transfer coefficient from solar cell to ambient through glass cover (W/m^2 K)
U_{tb}	Overall heat transfer coefficient from glass to black surface through solar cell (W/m^2 K)
$\dot{W}$	Work rate (kW)
x	Concentration of ammonia–water

Greek Letters

α_c	Absorptivity of solar cell
α_b	Absorptivity of black surface
β_c	Packing factor of solar cell
η	Efficiency
τ_g	Transitivity of glass
θ	Index

Subscripts

a	Air
ai	Air inlet
abs	Absorber
bs	Back surface of PV/T
c	Solar cell
C	coefficient
ch	Chemical
CHX	Condenser heat exchanger
con	Condenser
f	Factor
elec	Electrolyzer
ei	Exergetic impact
eii	Exergetic impact improvement
en	Energy
es	Exergetic stability
est	Exergetic sustainability
ex	Exergy
eva	Evaporator
G	Subscript for glass to glass PV/T system
geo	Geothermal
HTG	High temperature generator
HHX	High temperature heat exchanger
H_2	Hydrogen
LHX	Low temperature heat exchanger
LTG	Low temperature generator
MTG	Medium temperature generator
MHX	Medium temperature heat exchanger
ph	Physical
sys	System
V.HTG	Very high temperature generator
V.HHX	Very high temperature heat exchanger
1. . .33	State numbers
0	Ambient or reference condition

Acronyms

QEAS	Quadruple effect absorption system
SMR	Steam methane reforming

24.1 Introduction

Since the industrial revolution, humankind's demand for better lifestyle and comfort has considerably increased. In order to meet such demands more and more energy consuming devices have been introduced. In order to cope up with such an increase in energy demand, a large numbers of power plants running on fossil fuels are commissioned every week throughout the world. This huge energy consumption of fossil fuels is blamed for changes in climate patterns and the depletion of stratospheric ozone layer. In addition, systems running on fossil fuel release harmful gasses such as CO_2, NOx, etc., which are not only harmful to living things but also to the environment. Recently environmental friendly fuels are introduced to cater the need of future energy demands. One such very attractive and completely environmental neutral fuel which is looked at is hydrogen.

Due to the harmful effects of using fossil fuels, renewable energy resources are becoming essential options for replacing fossil fuels due to their clean and renewable nature [1]. Photo Voltaic/Thermal (PV/T) systems have received greater attention due to their capability of producing both power and heat which makes them more effective as compared to the stand alone photo voltaic or thermal system. A major benefit of using solar PV/T system is that they have no operating cost a part from rarely occurring cleaning of panels and duct costs because they use solar intensity as an energy source. Erdil et al. [2] stated that solar PV/T systems have become very popular due to their capability of producing both heat and power. Ibrahim et al. [3] mentioned that sustainable energy sources such as solar energy in a form of solar radiation has been identified as one of the promising resources of energy to replace the dependency on other energy carriers such as fossil fuels. Solar PV/T hybrid collectors producing electricity and thermal energy simultaneously have been reported earlier as cost effective collectors [4]. Apart from cost effectiveness, the other major benefit of using solar PV/T system is that it has no by-products and therefore, has zero emission of greenhouse gasses.

Combined power and heat production capabilities of solar PV/T system make them a great contender for multi-generation purposes and have received attention from many researchers such as Ratlamwala et al. and Beccali et al. [5, 6]. The heat produced by concentrated solar PV/T system can be used to produce cooling using an environmental benign system such as absorption system. The absorption cooling technology is one of the best alternatives to the compression cooling in the aspects of energy diversification and environmental protection. The major benefit of absorption system is that it omits the use of compressors which are the major energy consuming source in conventional air-conditioning systems. Also, it is very easy to integrate absorption systems with the renewable/alternative energy sources because of their low energy demand and capability of utilizing low grade energy such as heat produced by solar PV/T system. The performance of a cooling cycle is represented by the coefficient of performance (COP) which is the ratio of cooling capacity to energy input. In recent times absorption systems have attracted many researchers due to its capability of having high COP at low operating cost.
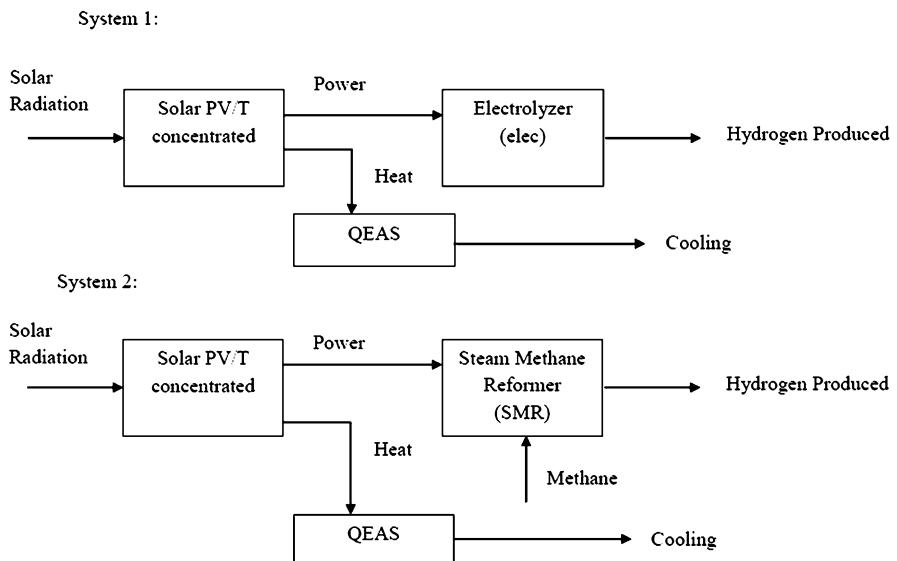
The energy need especially for food refrigeration applications is huge and requires potential solutions through renewable/alternative sources such as solar. Absorption refrigeration systems appear to be a key solution to meet the cooling demand in a renewable manner [7]. Two types of absorption systems are available such as lithium bromide–water and ammonia–water system. Lithium bromide–water chillers are suited for space cooling applications while ammonia–water systems provide industrial cooling to as low as $-50\ ^{\circ}C$ [8]. Gomri and Hakim [9] stated that the use of lithium bromide-based working fluid has been greatly hindered by the corrosion problem caused by the high generator temperature above 473.15 K and the crystallization problem. Most amount of work is being done on single and double effect absorption systems by researchers [10, 11]. Some researchers such as Ratlamwala et al., Gadalla et al., and Gomri [5, 12, 13] have investigated triple effect absorption systems (TEAS). A study conducted by Gomri [13] concluded that by increasing number of effects from double effect to triple effect absorption systems, the COP is found to be increasing by 30 %. The research conducted by Ratlamwala et al. [14, 15] showed that the quadruple effect absorption systems (QEAS) have higher coefficient of performance as compared to TEAS. Kanoglu et al. [16] stated that the cogeneration option which uses absorption cooling system appeared to provide significant savings in energy requirements.

The common method of producing hydrogen using power is the water electrolysis or steam methane reforming (SMR). Dufour et al. [17] stated that at present 96 % of hydrogen is produced using the SMR. The SMR has a disadvantage of releasing CO_2, while electrolysers consume high electrical power in order to produce hydrogen through dissociation of water molecules. Burman [18] mentioned in the report that to produce an amount of hydrogen which is capable of yielding 1,000 J of energy, it requires an input of 1,600 J of energy. These technologies are well developed and have reached a mature level for dissociation of water molecules into hydrogen and oxygen molecules. Hydrogen offers capabilities as an alternative fuel which is environmental friendly and sustainable at the same time. As suggested by many researchers [19–21] hydrogen is expected to play a key role in the near future as an energy carrier for sustainable development.
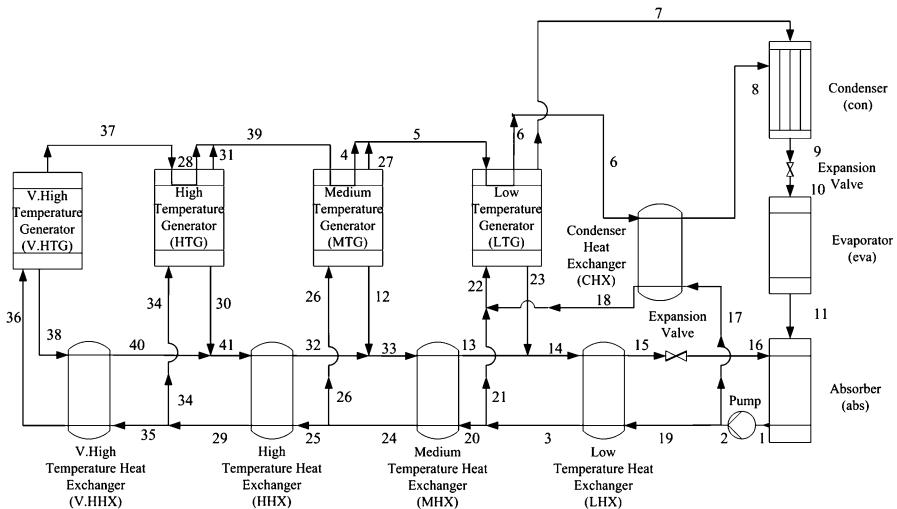
In this chapter, we study concentrated solar PV/T system integrated with QEAS and electrolyzer or SMR for cooling and hydrogen production. A comparative study is conducted to compare the amount of hydrogen produced, energy and exergy efficiencies, and impact of these systems on the environment and to see how sustainable these systems are from exergy perspective. The effect of monthly weather data of United Arab Emirates (UAE) on the performance of the system from energy, exergy, environment, and sustainability perspective is studied.

24.2 System Description
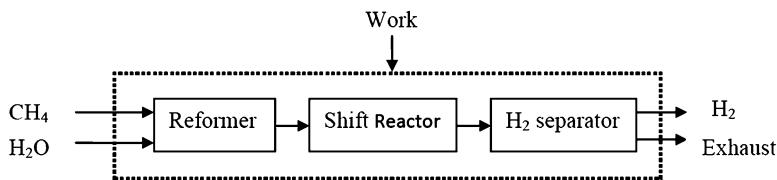
In this chapter two integrated systems, namely, concentrated solar PV/T integrated with quadruple effect cooling system and electrolyzer and concentrated solar PV/T integrated with quadruple effect cooling system and SMR are studied. The systems studied in this chapter are shown schematically in Fig. 24.1. The process starts when solar radiation falls on top of concentrated PV/T system which is made of PV modules and a duct. Solar radiations falling on PV modules make the molecules inside the module vibrate, hence producing power. The air passing through the duct placed underneath the PV/T system gets heated up and leaves the duct at relatively higher temperature to enter the QEAS. In the absorption system heat is supplied to the generator where strong ammonia–water solution is converted to concentrated ammonia vapor and weak solution of ammonia–water as shown in Fig. 24.2. The weak solution of ammonia–water passes through heat exchanger network where it releases heat to the strong solution going to the generator. The concentrated ammonia vapor passes through several generators, a heat exchanger, and a condenser where it releases heat to the incoming fluid in order to drop its temperature. This comparably lowers the temperature of ammonia vapor and then enters the evaporator where it provides cooling to the incoming fluid before entering the absorber. In the absorber heat is released by the concentrated ammonia coming from the evaporator and weak ammonia–water solution coming from the generator to leave as strong ammonia–water solution in order to enter a pump. Detailed description of QEAS can be found in [14]. The power produced by the solar PV/T system is

Fig. 24.1 Schematic of the two systems

Fig. 24.2 Schematic of QEAS

Fig. 24.3 Schematic of SMR

supplied to the electrolyzer and SMR for hydrogen production. In the electrolyzer, power is used to break the bond of water molecule in order to produce hydrogen. In the SMR, methane is compressed to increase the pressure and water is pumped to match the pressure of the methane. Methane and steam are then passed through the reformer, shift reactor, and hydrogen separation system as showing in Fig. 24.3. The hydrogen produced in these systems can later be used to produce heat and power using a Proton Exchange Membrane Fuel Cell (PEMFC). The exhaust gasses produced by SMR are released to the environment.

24.3 Energy and Exergy Analyses

In the analysis, the evaporator is divided into two-phase and superheated regions.

24.3.1 Solar PV/T System

The equations which are used to solve the mathematical model of solar PV/T system are derived from Joshi et al. [22, 23]. The equation used to calculate power produced by PV module is

$$\dot{W}_{solar} = \eta_c \times \dot{I} \times \beta_c \times \tau_g \times A \tag{24.1}$$

The rate of heat produced by solar PV/T system is calculated using following equation:

$$\dot{Q}_{solar} = \frac{\dot{m}_a \times cp_a}{U_L} \times \left(\left(h_{p2G} \times z \times \dot{I} \right) - U_L \times (T_{ai} - T_0) \right)$$
$$\times \left[1 - \exp \left(\frac{-b \times U_L \times L}{\dot{m}_a \times cp_a} \right) \right] \tag{24.2}$$

where $z = \alpha_b + \tau_g^2 \times (1 - \beta_c) + h_{p1G} \times \tau_g \times \beta_c \times (\alpha_b - \eta_c)$.

The rate of exergy of solar energy is calculated by

$$\dot{E}_{X_{solar}} = \left[1 - \left(\frac{T_0 + 273.15}{T_{sun}} \right) \right] \times \dot{I} \times A \tag{24.3}$$

The electrical and thermal efficiencies are defined as

$$\eta_{el} = \eta_c \times (1 - 0.0045 \times (T_c - 25)) \times 100 \tag{24.4}$$

$$\eta_{th} = \frac{\dot{Q}_{solar}}{I \times A} \times 100 \tag{24.5}$$

where

$$T_c = \frac{\tau_g \times \beta_c \times \dot{I} \times (\alpha_c - \eta_c) + U_t \times T_0 + h_t \times T_{bs}}{U_t + h_t},$$

$$T_{bs} = \frac{z \times \dot{I} + (U_t + U_{tb}) \times T_0 + h_{ba} \times T_{air}}{U_b + h_{ba} + U_{tb}} \quad \text{and}$$

$$T_{air} = \left[T_0 + \frac{h_{p2G} \times z \times \dot{I}}{U_L} \right] \times \left[1 - \frac{1 - \exp\left(\frac{-b \times U_L \times L}{\dot{m}_a \times cp_a} \right)}{\frac{b \times U_L \times L}{\dot{m}_a \times cp_a}} \right] + T_{ai}$$
$$\times \left[\frac{1 - \exp\left(\frac{-b \times U_L \times L}{\dot{m}_a \times cp_a} \right)}{\frac{b \times U_L \times L}{\dot{m}_a \times cp_a}} \right].$$

24.3.2   QEAS Unit

The rate of heat to the V.HTG of an absorption system is provided using solar PV/T system. The rate of heat transfer obtained from geothermal water source is calculated using

$$\dot{Q}_{VHTG} = \dot{Q}_{solar} \qquad (24.6)$$

The mass balance equations of VHTG are given as follows

$$\dot{m}_{36}x_{36} = \dot{m}_{37}x_{37} + \dot{m}_{38}x_{38} \qquad (24.7)$$

$$\dot{m}_{36} = \dot{m}_{37} + \dot{m}_{38} \qquad (24.8)$$

In order to obtain the outlet conditions of the VHTG, the following equation is used

$$\dot{m}_{36}h_{36} + \dot{Q}_{V.HTG} = \dot{m}_{37}h_{37} + \dot{m}_{38}h_{38} \qquad (24.9)$$

The exergy destruction in V.HTG becomes

$$\dot{Ex}_{VHTG} = \dot{Ex}_{37} - \dot{Ex}_{38} - \dot{Ex}_{36} \qquad (24.10)$$

where $\dot{Ex}_{37} = \dot{m}_{37}((h_{37} - h_0) - T_0(s_{37} - s_0))$ and the same relationship is employed for other states.

The energy balance equations for VHHX are given below:

$$\dot{m}_{35}h_{35} + \dot{Q}_{VHHX} = \dot{m}_{36}h_{36} \qquad (24.11)$$

$$\dot{m}_{38}h_{38} = \dot{Q}_{VHHX} + \dot{m}_{40}h_{40} \qquad (24.12)$$

The mass and energy balance equations for the condenser are given below

$$\dot{m}_9 = \dot{m}_7 + \dot{m}_8 \qquad (24.13)$$

$$\dot{m}_9h_9 = \dot{m}_7h_7 + \dot{m}_8h_8 + \dot{Q}_{con} \qquad (24.14)$$

The equations for mass and energy balances of the evaporator are

$$\dot{m}_{10} = \dot{m}_{11} \qquad (24.15)$$

$$\dot{m}_{10}h_{10} + \dot{Q}_{eva} = \dot{m}_{11}h_{11} \qquad (24.16)$$

The following energy balance equation is used to calculate the heat rejected from the absorber

$$\dot{m}_{11}h_{11} + \dot{m}_{16}h_{16} = \dot{m}_1 h_1 + \dot{Q}_{abs} \qquad (24.17)$$

The work done by the pump is calculated using the equation given below

$$\dot{W}_p = \dot{m}_1(h_2 - h_1) \qquad (24.18)$$

24.3.3 Electrolyzer

The rate of hydrogen produced by electrolyzer is calculated using

$$\eta_{electrolyzer} = \frac{\dot{m}_{H_2 elec} \times LHV_{H_2}}{\dot{W}_{electrolyzer}} \qquad (24.19)$$

where $\eta_{electrolyzer} = 56\ \%$ and $\dot{W}_{electrolyzer} = \dot{W}_{solar}$.

24.3.4 Steam Methane Reforming

The rate of hydrogen produced by SMR is calculated using

$$\eta_{SMR} = \frac{\dot{m}_{H_2 SMR} \times LHV_{H_2}}{\dot{W}_{SMR} + \dot{m}_{CH_4} \times LHV_{CH_4}} \qquad (24.20)$$

where $\eta_{SMR} = 56\ \%$ and $\dot{W}_{SMR} = \dot{W}_{solar}$.

The exergetic content of hydrogen is obtained using

$$\dot{Ex}_{H_2} = \dot{m}_{H_2}\left[ex_{H_2, ch} + ex_{H_2, ph}\right] \qquad (24.21)$$

where

$ex_{H_2, ch} = \frac{235.153 \times 1,000}{MW_{H_2}}$ and $ex_{H_2, ph} = [(h_{H_2} - h_0) - T_0(s_{H_2} - s_0)]$.

The exergetic content of supplied methane is obtained using

$$\dot{Ex}_{CH_4} = \dot{m}_{CH_4}\left[ex_{CH_4, ch} + ex_{CH_4, ph}\right] \qquad (24.22)$$

where

$ex_{CH_4, ch} = \frac{830.212 \times 1,000}{MW_{CH_4}}$ and $ex_{CH_4, ch} = [(h_{H_2} - h_0) - T_0(s_{H_2} - s_0)]$.

The overall energy and exergy efficiency of system 1 is found using

$$\eta_{en, sys, elec} = \frac{\dot{m}_{H_2 elec} \times LHV_{H_2} \times \dot{Q}_{eva}}{I \times A} \times 100 \qquad (24.23)$$

$$\eta_{ex, sys, elec} = \frac{\dot{E}x_{H_2 elec} + \dot{E}x_{eva}}{\dot{E}x_{solar}} \times 100 \qquad (24.24)$$

The overall energy and exergy efficiency of system 2 is found using

$$\eta_{en, sys, SMR} = \frac{\dot{m}_{H_2 SMR} \times LHV_{H_2} + \dot{Q}_{eva}}{(I \times A) + \dot{m}_{CH_4} \times LHV_{CH_4}} \times 100 \qquad (24.25)$$

$$\eta_{ex, sys, SMR} = \frac{\dot{E}x_{H_2 SMR} + \dot{E}x_{eva}}{\dot{E}_{x_{solar}} \times \dot{E}x_{CH_4}} \times 100 \qquad (24.26)$$

The environmental impact factor is the positive effect of the system on exergy-based sustainability. By positive effect we mean to supply more desired exergy output and decrease the irreversibilities and minimize the waste exergy outputs during the systems operation. The reference value for this factor should be "zero" for better exergy based sustainability and is defined as

$$f_{ei, elec} = \frac{\dot{E}x_{des, tot, elec}}{\dot{E}_{x_{solar}}} \qquad (24.27)$$

$$f_{ei, SMR} = \frac{\dot{E}x_{des, tot, SMR}}{\dot{E}_{x_{solar}} + \dot{E}x_{CH_4}} \qquad (24.28)$$

The environmental impact coefficient is related to the exergetic efficiency of the system. In ideal case its value should be one indicating that the system is working under ideal condition with no exergy destruction. This coefficient is defined as

$$C_{ei, elec} = \frac{1}{\eta_{ex, sys, elec}/100} \qquad (24.29)$$

$$C_{eiSMR} = \frac{1}{\eta_{ex, sys, SMR}/100} \qquad (24.30)$$

The environmental impact index is an important parameter to indicate whether or not the system damages the environment due to its unusable waste exergy output and exergy destruction. The smaller the value the better the system performance is. It is defined as

$$\theta_{ei, elec} = f_{ei, elec} \times C_{ei, elec} \qquad (24.31)$$

$$\theta_{ei, SMR} = f_{ei, SMR} \times C_{ei, SMR} \qquad (24.32)$$

Environmental impact improvement indicates the environmental appropriateness of the system. In order to improve the environmental appropriateness of the system, its environmental impact index should be minimized to be closer to the best

reference value. The higher value of environmental impact improvement means system is more useful for the environment and it is defined as

$$\theta_{eii,\,elec} = \frac{1}{\theta_{ei,\,elec}} \tag{24.33}$$

$$\theta_{eii,\,SMR} = \frac{1}{\theta_{ei,\,SMR}} \tag{24.34}$$

The exergetic stability factor is a function of the desired output, exergy destruction, and exergies by unused fuel. In this study it is assumed that all the fuel is utilized in the system. The best value of this factor should be close to "one." This factor is defined as

$$f_{es,\,elec} = \frac{\dot{E}x_{tot,\,out,\,elec}}{\dot{E}x_{tot,\,out,\,elec}\dot{E}x_{des,\,tot,\,elec}} \tag{24.35}$$

$$f_{es,\,SMR} = \frac{\dot{E}x_{tot,\,out,\,SMR}}{\dot{E}x_{tot,\,out,\,SMR}\dot{E}x_{des,\,tot,\,SMR}} \tag{24.36}$$

The exergetic sustainability index is defined as multiplication of environmental benign index and exergetic stability factor of the system. The higher the value of this index means better is the performance of the system from exergetic sustainability perspective. This index is defined as

$$\theta_{est,\,elec} = f_{es,\,elec} \times \theta_{eii,\,elec} \tag{24.37}$$

$$\theta_{est,\,SMR} = f_{es,\,SMR} \times \theta_{eii,\,SMR} \tag{24.38}$$

24.4   Results and Discussion

In this chapter, a comparative study of concentrated solar PV/T integrated with QEAS and electrolyzer or SMR is carried out. Effect of monthly solar data on the performance of the system from energy, exergy, environmental, and sustainability perspective is studied. Results obtained are compared to see which of the two systems are beneficial from environment and sustainability point of view.

Figures 24.4 and 24.5 show the monthly average amount of solar radiation and outside air temperature for the Abu Dhabi in order to analyze the integrated system under different operating conditions. These average values are calculated based on the data available in ASHRAE [24].

Figure 24.6 illustrates how much hydrogen is produced by system 1 and system 2. Results show that the maximum amount of hydrogen produced by system 1 and system 2 is 364 kL/day and 17,037 kL/day, respectively. The highest hydrogen production rate by both systems is obtained in the month of June. This is observed because in June solar radiation is on the higher side as well as the time for which it is
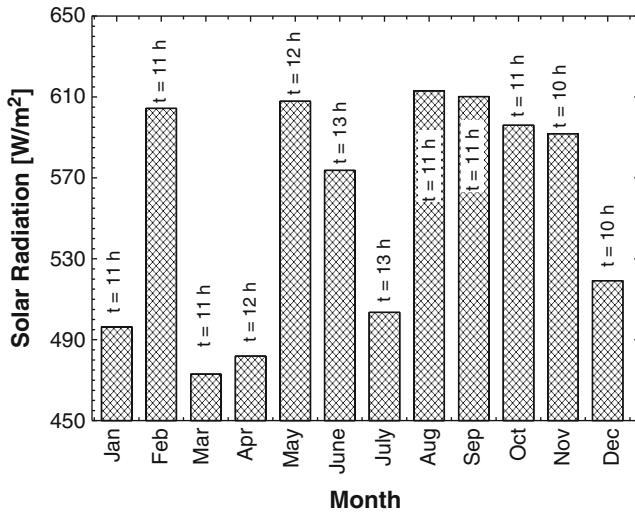
Fig. 24.4 Average solar radiation per month
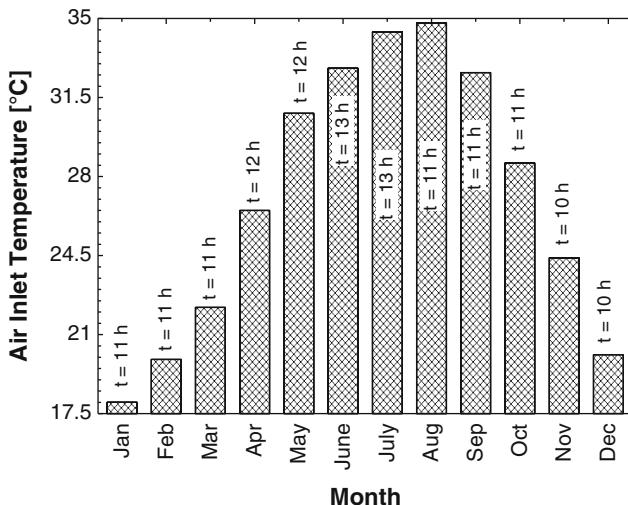
Fig. 24.5 Average air inlet temperature per month

available is highest. The high solar radiation and the time for which it is available result in considerably higher amount of power production and that also for a longer time frame as compared to other months. The higher power production rate and longer time result in longer operation of the electrolyzer or SMR. It is also noticed that SMR produces a lot more hydrogen as compared to electrolyzer and this is the reason that SMR technology is vastly used for large scale hydrogen production. Figure 24.7 helps us see the cooling production rate of the QEAS for each month. It is observed that
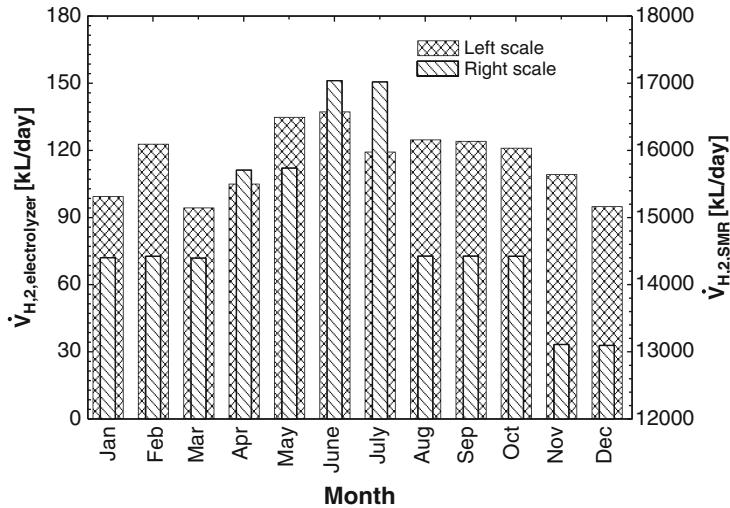
Fig. 24.6 Variation in amount of hydrogen produced per month
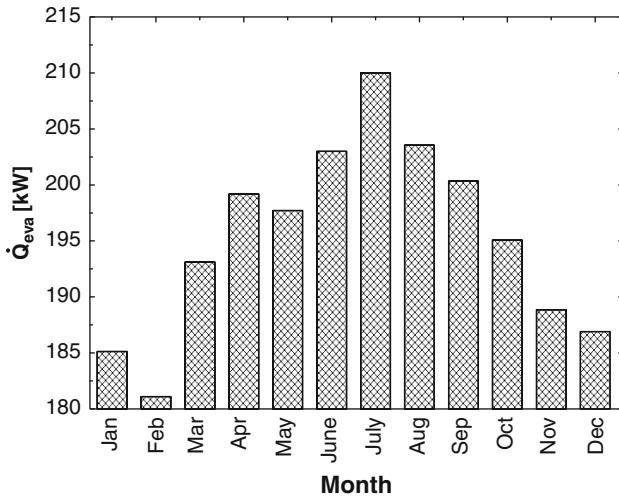
Fig. 24.7 Variation in amount of cooling produced per month

highest amount of cooling is produced in the month of July and its value is 210 kW. This is observed because in the month of July the outside air temperature is high and is not capable of carrying huge amount of heat rejected by the back surface of the PV/T system and as a result the rate of heat supplied to the QEAS is considerably lower than other months. As the rate of heat supplied to the QEAS for same condenser load decreases its cooling capacity increases because of lower temperature of the concentrated ammonia vapor entering the evaporator. Contradictory to the hydrogen
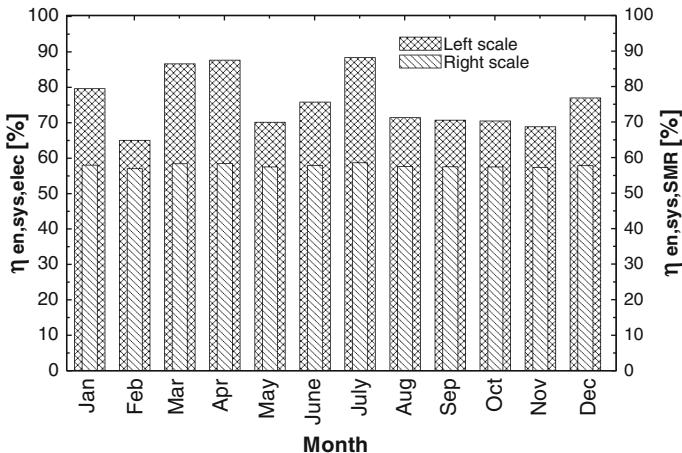
Fig. 24.8 Variation in energy efficiency per month
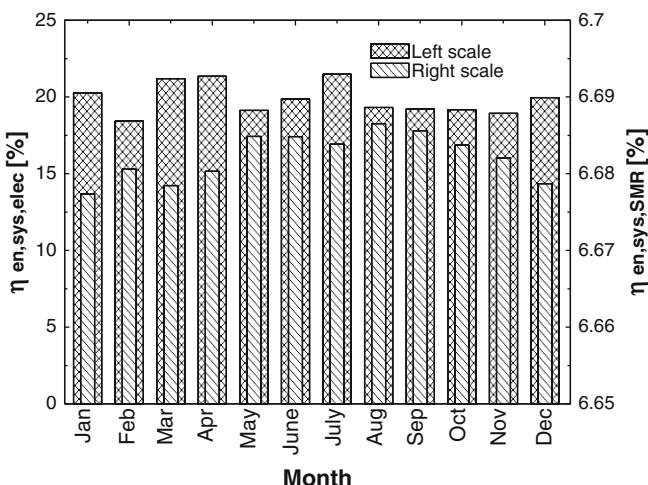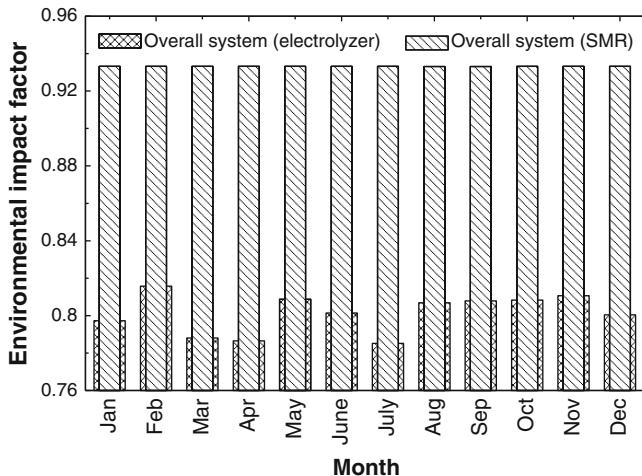
Fig. 24.9 Variation in exergy efficiency per month
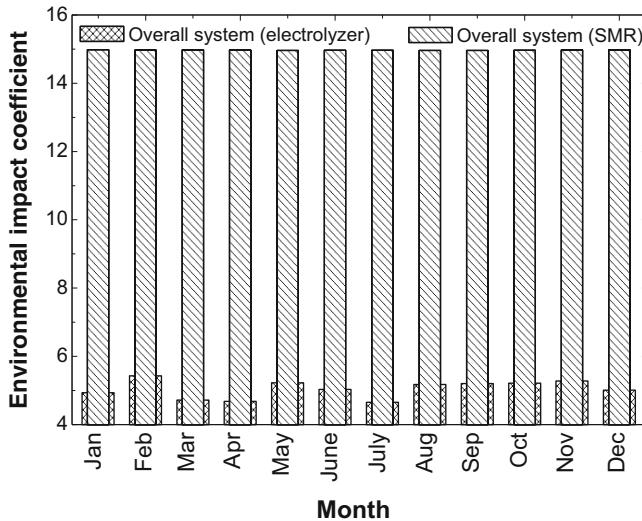
production rate the energy and exergy efficiencies of the electrolyzer system are higher than that of SMR as seen in Figs. 24.8 and 24.9. The results show that maximum energy and exergy efficiencies of both electrolyzer and SMR are obtained in the month of July and there values are 88.3 % and 21.5 % and 58.4 % and 6.7 %, respectively. This shows that although the integrated SMR system produces greater amount of hydrogen but the process is not as effective as integrated electrolyzer system. It is also seen that energy efficiency value is greater than exergy efficiency value indicating that system has losses which are not considered in energy efficiency. The study helps reflecting the importance of exergy analysis.
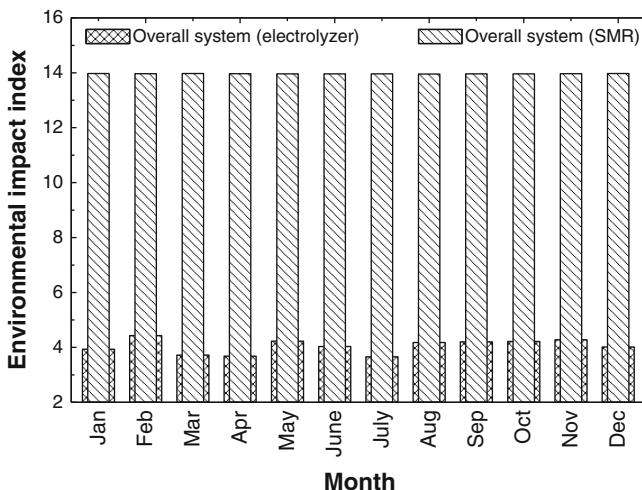
Fig. 24.10 Variation in environmental impact factor per month

Figure 24.10 shows how both the systems perform from environmental impact factor perspective. The objective of this factor is to show how much of the total exergy is destructed by the system. The results show that minimum environmental impact factor for both electrolyzer system and SMR system is obtained in the month of July and its value is 0.7852 and 0.9332, respectively. For SMR system the environmental impact factor hardly changes but for electrolyzer system this factor is seen to be varying. The results show that month of July is best for the environment as in this month most amount of exergy supplied to the system is utilized as compared to other months. The environmental impact coefficient shows how much environmentally benign the system is by taking the inverse of its exergy efficiency. The results show that minimum environmental impact coefficient for both electrolyzer system and SMR system is obtained in the month of July and its value is 4.655 and 14.96, respectively as shown in Fig. 24.11. This shows that the electrolyzer system is closer to the ideal value of 1 of environmental impact coefficient as compared to SMR system hence indicating that SMR system performs worst from environment point of view.

The third environmental parameter studied is environmental impact index as shown in Fig. 24.12. This index helps us visualize weather any of the system damages the environment due to their waste exergy output and exergy destruction and in ideal case this index should approach 0. The results show that minimum environmental impact index for electrolyzer system and SMR system is obtained for the month of July and its value is 3.655 and 13.96, respectively. This shows that electrolyzer system has lower amount of waster exergy output and exergy destruction as compared to SMR system. This makes sense because SMR system releases harmful by-products such as carbon monoxide and carbon dioxide as compared to zero by-products released by the electrolyzer system. The comparison of both the systems from the environmental impact improvement perspective is shown in
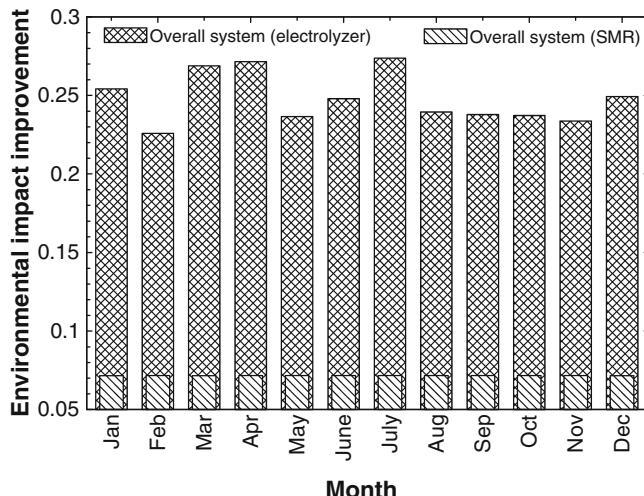
Fig. 24.11 Variation in environmental impact coefficient per month
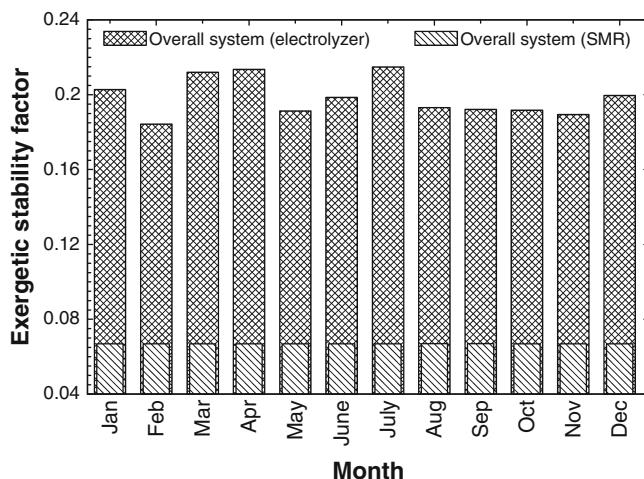
Fig. 24.12 Variation in environmental impact index per month

Fig. 24.13. The environmental impact improvement indicates the environmental appropriateness of the system and it is desirable to get this factor as high as possible. The study reveals that maximum environmental impact improvement for electrolyzer system and SMR system is obtained in the month of July and its value is 0.2736 and 0.07163, respectively. The environmental impact improvement values show that electrolyzer system is more beneficial to the environment as compared to SMR system. The exergetic stability factor helps us realize how
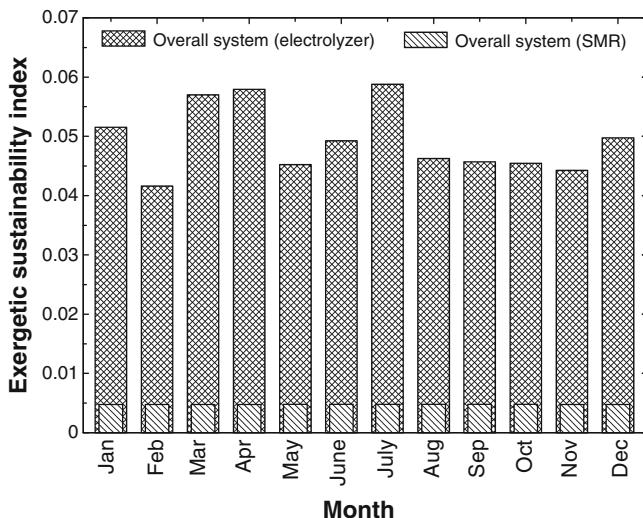
Fig. 24.13 Variation in environmental impact improvement per month

Fig. 24.14 Variation in exergetic stability factor per month

much stable the system is from exergy perspective. The comparison done on monthly basis as shown in Fig. 24.14 reveals that the highest value of exergy stability factor for electrolyzer system and SMR system is obtained in the month of July and it value is 0.2148 and 0.06684, respectively. The desired value of exergetic stability factor is 1 which indicates that system is 100 % stable from exergy perspective. The results show that electrolyzer system is far more stable from exergy perspective than SMR system because of lower overall exergy destruction and better utilization of input exergy. The last parameter studied is exergetic

Fig. 24.15 Variation in exergetic sustainability index per month

sustainability index as shown in Fig. 24.15. The purpose of this index is to show how much sustainable the system is from exergy perspective and it is desired to have high value of this index. Analysis conducted show that maximum value of exergetic sustainability index for electrolyzer system and SMR system is obtained in the month of July and its value is 0.05878 and 0.004787, respectively. This index reveals that electrolyzer system is far more sustainable than SMR system.

24.5 Conclusions

In this chapter, a comparative study of concentrated solar PV/T, QEAS, and electrolyzer system and concentrated solar PV/T, QEAS, and SMR system is presented. The comparison between these two systems is performed, based on energy, exergy, environment, and sustainability performance criteria. The results show that although the SMR system produces greater amount of hydrogen as compared to electrolyzer system but electrolyzer system has higher energy and exergy efficiencies. The environmental impact assessment shows that the electrolyzer system is more environmentally benign than SMR system and it perform best in the month of July. The sustainability study also shows that electrolyzer system is more sustainable than SMR system from exergy perspective and its best value is obtained in the month of July. The study concludes that although SMR system produces far more hydrogen than electrolyzer system but it fails to perform better than electrolyzer system from efficiency, environmental, and sustainability perspective.

References

1. Sarhaddi F, Farahat S, Ajam H, Behzadmehr A (2010) Exergetic performance assessment of a solar photovoltaic thermal (PV/T) air collector. Energy Buildings 42:2184–2199
2. Erdil E, Ilkan M, Egelioglu F (2008) An experimental study on energy generation with a photovoltaic (PV)–solar thermal hybrid system. Energy 33:1241–1245
3. Ibrahim A, Othman MY, Ruslan MH, Mat S, Sopian K (2011) Recent advances in flat plate photovoltaic/thermal (PV/T) solar collectors. Renew Sustain Energy Rev 15:352–365
4. Davidsson H, Perers B, Karlsson B (2010) Performance of a multifunctional PV/T hybrid solar window. Solar Energy 84:365–372
5. Ratlamwala TAH, Gadalla MA, Dincer I (2011) Performance assessment of an integrated PV/T and triple effect cooling system for hydrogen and cooling production. Int J Hydrogen Energ 36:1282–1291
6. Beccali M, Finocchiaro P, Nocke B (2009) Energy and economic assessment of desiccant cooling systems coupled with single glazed air and hybrid PV/thermal solar collectors for applications in hot and humid climate. Solar Energy 83:1828–1846
7. Dincer I, Dost S (1996) Energy analysis of an ammonia-water absorption refrigeration system. Energy Sources 18:727–733
8. Zhai XQ, Qu M, Li Y, Wang RZ (2011) A review for research and new design options of solar absorption cooling systems. Renew Sustain Energy Rev 15:4416–4423
9. Gomri R, Hakimi R (2008) Second law analysis of double effect vapour absorption cooler system. Energy Conv Manage 49:3343–3348
10. Tozer R, Syed A, Maidment G (2005) Extended temperature–entropy (T–s) diagrams for aqueous lithium bromide absorption refrigeration cycles. Int J Refrig 28:689–697
11. Mathews T, Oliviera AC (2009) Energy and economic analysis of an integrated solar absorption cooling and heating system in different building types and climates. Appl Energy 86:949–957
12. Gadalla MA, Ratlamwala TAH, Dincer I (2010) Energy and exergy analysis of an integrated fuel cell and absorption cooling system. Int J Exergy 7:731–754
13. Gomri R (2008) Thermodynamics evaluation of triple effect absorption chiller. Proc. of the thermal issues in emerging technologies ThETA'12, Cairo, Egypt, Dec. 17-20th 245–250
14. Ratlamwala TAH, Dincer I, Gadalla MA (2012) Thermodynamic analysis of a novel integrated geothermal based power generation-quadruple effect absorption cooling-hydrogen liquefaction system. Int J Hydrogen Energ 37:5840–5849
15. Ratlamwala TAH, Dincer I, Gadalla MA (2012) Performance analysis of a novel integrated geothermal-based system for multi-generation applications. Appl Thermal Eng 40:71–79
16. Kanoglu M, Bolatturk A, Yilmaz C (2010) Thermodynamic analysis of models used in hydrogen production by geothermal energy. Int J Hydrogen Energ 35:8783–8791
17. Dufour J, Serrano DP, Galvez JL, Moreno J, Garcia C (2009) Life cycle assessment of processes for hydrogen production: environmental feasibility and reduction of greenhouse gases emissions. Int J Hydrogen Energ 34:1370–1376
18. Burman G (2003) hydrogen isn't yet the miracle fuel of the future. Fresno Bee
19. Barelli L, Bidini G, Gallorini F, Ottaviano A (2010) Analysis of the operating conditions influence on PEM fuel cell performances by means of a novel semi-empirical model. Int J Hydrogen Energ 36:10434–10442
20. Saeed A, Ali M, Mahrokh S (2010) Study of PEM fuel cell performance by electrochemical impedance spectroscopy. Int J Hydrogen Energ 35:9283–9290
21. Midilli A, Dincer I (2009) Development of some exergetic parameters for PEM fuel cells for measuring environmental impact and sustainability. Int J Hydrogen Energ 34:3858–3872
22. Joshi AS, Dincer I, Reddy BV (2009) Thermodynamic assessment of photovoltaic systems. Solar Energy 83:1139–1149
23. Joshi AS, Tiwari A, Tiwari GN, Dincer I, Reddy BV (2009) Performance evaluation of a hybrid photovoltaic thermal (PV/T) (glass-to-glass) system. Int J Thermal Sci 48:154–164
24. ASHRAE (2006) ASHRAE handbook of refrigeration. American Society of Heating, Refrigerating and Air-Conditioning Engineers, Inc., Atlanta, GA

Chapter 25
Integration of Cu–Cl Cycle of Hydrogen Production with Nuclear and Renewable Energy Systems for Better Environment

Seyedali Aghahosseini, Ibrahim Dincer, and Greg F. Naterer

Abstract Process integration opportunities for the Cu–Cl cycle of hydrogen production with nuclear and renewable energy sources are investigated. The advantages and disadvantages of each system are studied, and the cost of hydrogen production is analyzed and compared for various cases. In order to evaluate the environmental performance of the integrated hydrogen production systems, an environmental impact assessment of the proposed systems with a focus on the amount of CO_2 emission is conducted and compared.

Keywords Hydrogen production • Cu–Cl cycle • Renewable energy systems • Nuclear energy • Process integration • Cost analysis • CO_2 emission • Environment

Nomenclature

$\dot{e}x$	Exergy content (kJ/kg)
LHV	Lower heating value (kJ kg^{-1})
$\dot{m}$	Mass flow rate (kg s^{-1})
$\dot{Q}$	Heat rate (kW)
T	Temperature (K)

S. Aghahosseini (✉) • I. Dincer
Faculty of Engineering and Applied Science, University of Ontario Institute of Technology, 2000 Simcoe Street North, Oshawa, ON, Canada L1H 7K4
e-mail: Seyedali.Aghahosseini@uoit.ca; Ibrahim.Dincer@uoit.ca

G.F. Naterer
Faculty of Engineering and Applied Science, Memorial University, 240 Prince Phillip Drive, St. John's, NL, Canada A1B 3X5
e-mail: Gnaterer@mun.ca

T_0 Reference temperature (K)
$\dot{W}e$ Electric power (kW)
η Energy efficiency
ψ Exergy efficiency

25.1   Introduction

The increase in the average temperatures over the globe since the mid-20th century is mainly attributed to the recorded increase in the anthropogenic greenhouse gas concentration. Carbon dioxide (CO_2), water vapor, and methane known as greenhouse gases (GHGs) absorb solar radiation and create a natural greenhouse cover effect around the Earth. It is estimated that the earth average temperatures could be 30 °C lower without this effect [1]. CO_2 can remain in the atmosphere for hundreds of years [2]. Human activities have been the significant contributor to GHGs emission which has been increased significantly since pre-industrial times. For example, carbon dioxide concentrations have escalated by over one third from 280 parts per million (ppm) in 1750, to 379 ppm in 2005 [2]. It has been also stated that CO_2 level could reach 550 ppm by 2050, leading to warming of at least 2 °C [1]. Some effects of the global warming on earth are the rise of sea level, glacial retreat, species extinction, and increased possibility of extreme weather condition. For example, a temperature rise of just 2.7 °C could lead to the melting of the Greenland ice cap [2]. Therefore, it is crucial to start taking actions to restrain global warming and its effects.

The world energy demand is increasing at a very quick rate and the concentration of conventional fossil fuel reserves in the world represents a challenge to reliability and security of energy supplies [3]. Furthermore, there is an essential need for a significant reduction of GHG emissions and decarbonize global energy systems to mitigate the risks associated with global warming [4, 5]. Energy is the major interface between nature and humans, and is one of the important factors in sustainable development. Energy resources are necessary to fulfil human needs and enhance life quality which could harm the environment [6]. United Nations obligated the energy sector to follow effective atmosphere-protection strategies to boost efficiency and transition to environmentally friendly energy systems [7]. Improving energy efficiency and transition to alternative energy resources in industry result in cutbacks in the use of fossil fuels which can directly decreases CO_2 emissions [6]. Fossil fuels are used commonly for generating heat and power and are an enormous danger to environment and global sustainability.

Quantitative sustainability factors need to be established to make any activity sustainable. In the energy sector, these factors go well beyond the conventional energy, exergy, or economic indicators such as production, consumption, conversion efficiencies, and costs [2]. Moreover, they must include both short term and long term social, political, be ecological considerations. However, they are typically very difficult to be quantified and change by country, and even by community, in which they are studied. Design and implementing of sustainable

energy systems are much more complex than conventional planning and design that does not include the rigorous investigation of sustainable factors [8]. Energy industries have two major challenges of mitigating GHGs emission and replacing traditional fossil fuel based energy systems. These require substantial changes in our energy systems and utilization. Nuclear and renewable energy sources can make marketable energy by transforming natural phenomena into practical energy. These energy sources are potentially considered as the most efficient and effective solutions [9]. This suggests strong bond between nuclear and renewable energy systems toward sustainable development [10]. Renewable energy is subcategorized to geothermal, solar, wind, hydro, and biomass.

Hydrogen is a promising clean energy carrier of the future, and potentially best solution to climate change which is widely used in numerous industry applications [11, 12]. In view of its vast usage in industry, the production of hydrogen at lower cost, more efficient and environmentally benign methods is vital for GHG reductions [13]. The climate and energy challenges necessitate shifting from fossil fuels to renewables. Moreover, efficient production of hydrogen may require tight integration of different energy sources such as nuclear and renewables. Hydrogen could potentially being used as a transportation fuel or being utilized to match electricity production to electricity demand, or alternatively meet other energy demands. One of the promising emerging technologies for hydrogen production is thermochemical water splitting with the copper–chlorine (Cu–Cl) cycle. The Cu–Cl thermochemical cycle consists of a closed loop of thermally driven chemical reactions, where water is decomposed into hydrogen and oxygen, and all other intermediate compounds are recycled internally, with no emissions to the environment [14–17].

The Cu–Cl cycle has numerous advantages over other existing methods of hydrogen production, particularly lower environmental impact than carbon-based technologies and the adaptability of integration with renewable energy systems. In comparison to conventional electrolysis, it has a significant margin of higher overall conversion efficiency, with more than one-third improvement over electrolysis. It has much lower operating temperatures than other thermochemical cycles, thereby potentially reducing material and maintenance costs [16]. Also, it can effectively utilize waste heat from nuclear reactors or renewable based heat such as solar radiation, thereby improving cycle environmental and performance efficiencies [13]. The University of Ontario Institute of Technology (UOIT), Atomic Energy of Canada Limited (AECL), Argonne National Laboratory (ANL), and other partner institutions are currently collaborating on the development of enabling technologies for the Cu–Cl cycle, through the Generation IV International Forum (GIF) [18].
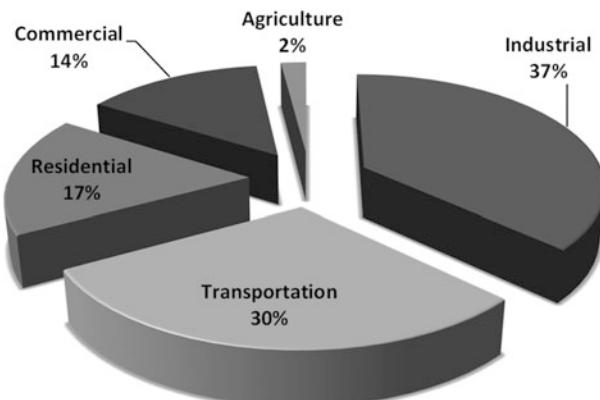
The main objective of this study is investigation on the integration of the Cu–Cl cycle of hydrogen production with nuclear and renewable energy sources and comparison between different possible alternatives. The advantageous and disadvantageous of each system are analyzed and the cost of hydrogen production is compared. Moreover, environmental impact assessment of the proposed systems with a focus on the amount of CO_2 emission are conducted and compared.

25.2 Energy Utilization and Sectors in Canada
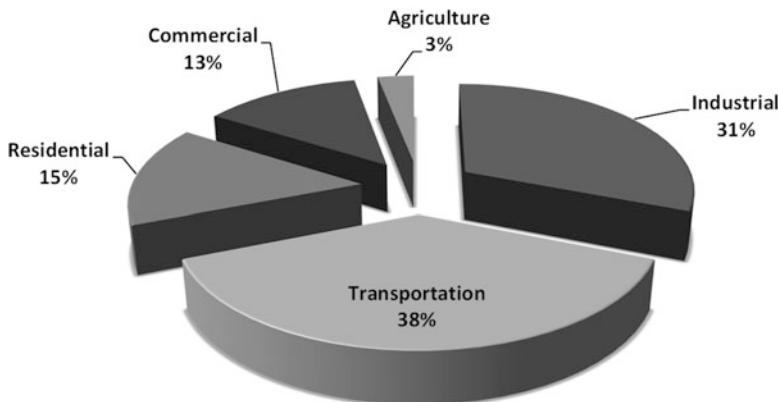
Canada is a country rich in resources and in its variety of energy resources. According to Statistics Canada, Canada is a gigantic energy consumer, almost equal to the USA and number one in the G-8 nations [19]. Long travel distance, long, bitterly cold winters, and the fact that Canada's economy is based on energy intensive industries like mining, pulp and paper, aluminum smelters, refining and steel manufacturing are the reasons that have put Canada in the list of high energy consumer countries. Three main resources of energy in Canada are electricity, natural gas, and motor gasoline. All these resources are high in producing GHG emissions. In other words, Canada contributes largely to GHG emissions. According to the Kyoto Protocol, Canada must reduce energy consumption based on fossil fuel resources in order to control related environmental damages [19].

The industrial sector accounts for the largest share of energy use and is second in terms of GHG emissions in Canada [20]. Energy is used in five sectors of residential, commercial/institutional, industrial, transportation and agriculture for a total of 8,541.6 PJ of energy [20]. One petajoule (PJ), or 10^{15} J, is equivalent to the energy required by more than 9,000 households (excluding transportation requirements) over 1 year. The industrial sector accounted for the largest share of energy, followed by transportation, residential, commercial/institutional, and agriculture. Total GHG emissions associated with the energy use of the mentioned five sectors was about 463.9 Mt in 2009 [20]. Figure 25.1 depicts Canada energy use by consuming sectors in 2009.
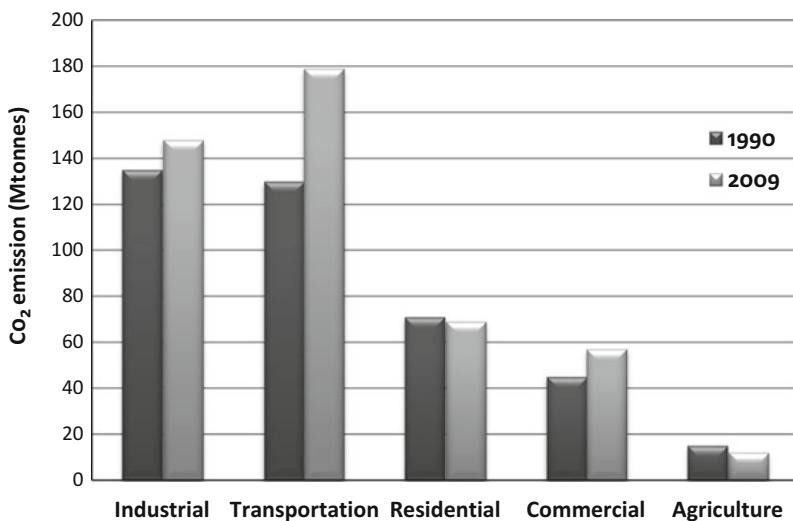
Electricity use does not give out any GHG emissions at the point of consumption in contrast of other end-use energy sources. GHG emissions related to electricity are emitted at the point of generation. These are sometimes referred to as indirect emissions. Therefore, it is a common practice in energy end-use analysis to allocate GHG emissions associated with electricity production to the sector that uses that electricity. This allocation is done by multiplying the amount of electricity used by a national average emission factor that indicates the average mix of fuels used to electricity generation in Canada [20]. Figure 25.2 shows the GHG emissions by

Fig. 25.1 Canada energy use by consuming sectors in 2009

Fig. 25.2 Canada GHG emission by energy consuming sectors in 2009

Fig. 25.3 Sectoral GHG emissions in Canada

energy consuming sectors. Energy consumed by the transportation sectors is considerably more GHG-intensive than the other sectors.

It could be clearly concluded that growth in energy use is reflected in growth of GHG emissions. In 2009, Canada's GHG emissions excluding electricity-related emissions declined 1 % compared to 2008, while emissions including those from electricity generation dropped 4 % [21]. Decrease in electricity generated from coal particularly contributed to 52 % of the total decline in electricity generated between 2008 and 2009 [21]. The CO_2 emissions mitigated from the reduction of coal use contributed 83.6 % to the total CO_2 decrease. The total GHG emissions by energy consuming sectors in Canada are depicted and compared for 1990 and 2009 [20] (Fig. 25.3).

25.3 Renewable and Nuclear Energy Technologies
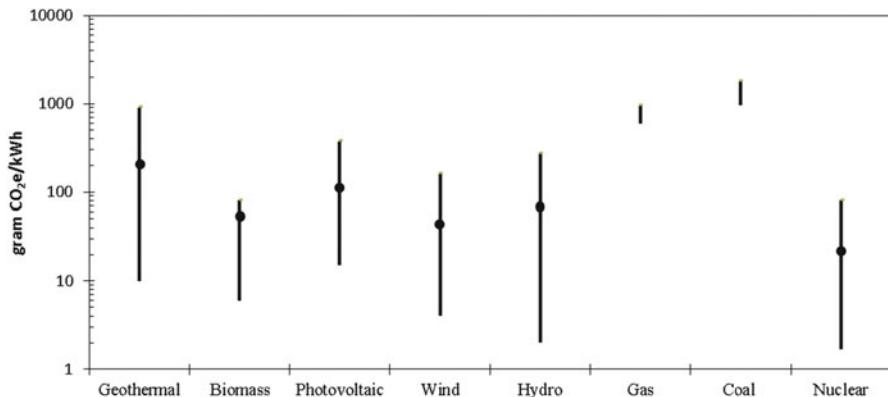
Renewable energy sources are perhaps the best candidate for satisfying most of the criteria for sustainable energy development. However, it is still more expensive in comparison to the present low prices of fossil and nuclear power. The renewable energy sources are known to be diffuse, fluctuating, intermittent, and partially unpredictable. Therefore, the collection and conversion of renewable energy flows require significant investment which need feed-forward control, storage facilities, and makeup [2]. Moreover, the inevitable back-up power supplies, in case of interruption, is another challenging issue. As it was mentioned before, most of renewable options in power sector struggle with the high total system cost. The extra prices of construction, and both installation and operational costs are the main reasons to be phased-out by cheaply priced fossil fuels. In addition, when renewable sources address the ancillary services in a continuous supply of power, the price of the average kWh delivered by a full renewable system will also remain at the higher end [2].

In contrast to fossil fuels, the efficiency of renewable technologies is usually site specific. For example, it would be expected that photovoltaic solar panel in the higher latitudes would require a higher cost per unit energy than a place located at lower latitudes. In contrast, fossil fuels are internationally traded and thus have a similar cost throughout the world. Therefore, cost comparison between energy sources should be made on the basis of the optimal conditions that include the cost of every aspect. For example, photovoltaic solar panels are generally calculated as distributed electricity sources and the associated costs should be compared with the electricity cost of other sources that includes transmission and distribution costs [22]. Cost range of delivered electricity and efficiency range of different power generation technologies are given in Table 25.1. Although the cost of generating electricity is still in favor of the fossil fuel technologies in many developing countries, but this difference would be much smaller when delivery cost is not included.

Table 25.1 Cost of delivery and efficiency range for power generation technologies

Power generation technology		Cost of delivery (US-cents/kWh)	Efficiency range (%)
Geothermal		3–14	10–20
Biomass		6–19	16–43
Photovoltaic	1,000 kWh/m^2	63–104	4–22
	2,000 kWh/m^2	31–60	
	3,000 kWh/m^2	22–49	
Wind	Offshore	7–14	23–45
	Onshore	4–6	
Hydro		3–13	>90
Gas		2.5–6	45–53
Coal		3.5–6	32–45
Nuclear		5–9	30–36

Source: [23–33]

Fig. 25.4 CO_2 equivalent emission range for power generation technologies

The conversion efficiency of fuel source into electricity is an important parameter which needs to be considered when comparing electricity production technologies. Efficiency strongly influence the cost of production and considered as an important criteria in sustainability analysis, since the high levels of waste associated with an inefficient process are considerably unsustainable [22]. Hydropower has the highest efficiency, from double to five times more the highest achieved in all other technologies. When located at a high quality wind resource, wind power is the second most efficient renewable energy technology, followed closely by high efficiency biomass. Natural gas is the second highest efficient and is the best among thermal technologies. It should be considered that gas, coal and nuclear, have small ranges of efficiency, varying by up to 13 %. Biomass has a large data range, varying by up to 27 %. At its highest efficiency, biomass is comparable with coal and higher than nuclear. At its lowest efficiency the electricity produced from biomass is one of the least efficient choices. The lowest presented efficiencies are mostly for outdated technologies and methods. The large efficiency range for photovoltaics is due to differing cell types, with amorphous silica cells showing the lowest efficiencies and crystalline silica cells the highest. Geothermal efficiencies vary due to the temperature of the geothermal source and off course hotter geothermal sources give greater efficiencies.

Renewable energy technologies are mainly considered as methods for reducing global GHG emissions; however each renewable energy technology is not entirely GHG neutral. For instance, although wind turbines and photovoltaic cells do not emit CO_2 during operation, but there are CO_2 emissions associated with construction, installation and disposal/recycling of each system. Hydro dams have GHG emissions during construction, but also during operation as a result of the decay of organic material such as methane forming decay within the dam [22]. GHG emissions for each power generation technology are illustrated in Fig. 25.4, as carbon dioxide equivalent, or "CO_2e." It is shown that the range of emissions for nuclear has the lowest average of 15 g CO_2e/kWh and the lowest amount of 1.9 g CO_2e/kWh [34–47].

25.4   Cu–Cl Cycle of Hydrogen Production

The Cu–Cl cycle is a sequence of processes for hydrogen production by thermo-chemical water splitting. This cycle has been identified by Atomic Energy of Canada Ltd. (AECL) [48, 49] at its Chalk River Laboratories (CRL) as a highly promising cycle for thermochemical hydrogen production. The Cu–Cl cycle involves four chemical reactions in which net reaction decomposes water into hydrogen and oxygen. All other chemicals are internally recycled. The Cu–Cl cycle can be linked to nuclear power plants and/or other heat sources such as solar and industrial process/waste heat (i.e., incinerators, chemical plants, or lost energy from furnaces) to potentially achieve higher efficiencies, lower environmental impact and lower costs of hydrogen production in comparison to other conventional technologies [50].
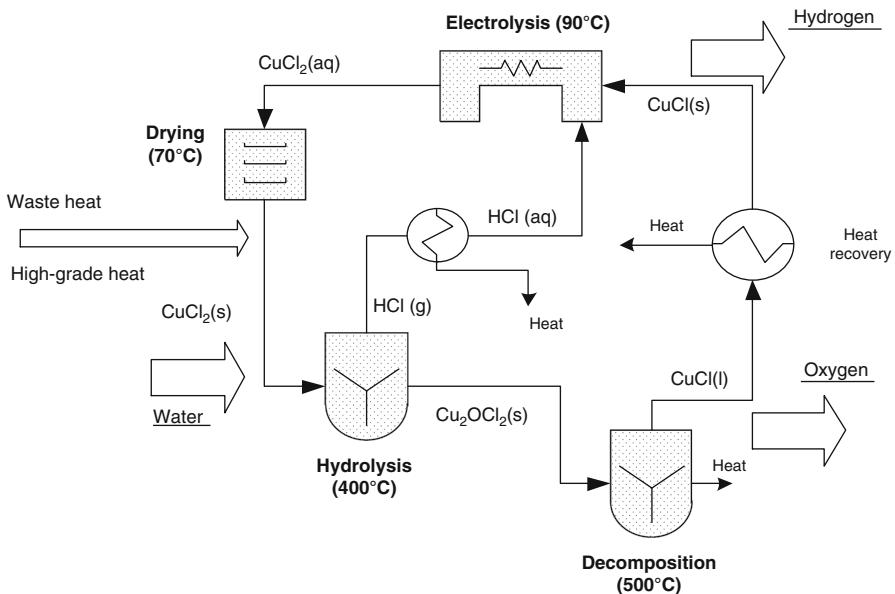
The Cu–Cl thermochemical cycle uses a series of reactions to achieve the overall splitting of water into hydrogen and oxygen. There are three key variations of the Cu–Cl cycle: 5-step, 4-step, and 3-step cycles [18]. In the 5-step cycle, copper is produced electrolytically, moved to an exothermic thermochemical hydrogen reactor and then reacted with HCl gas to produce hydrogen gas and molten CuCl. The 4-step cycle combines the hydrogen and electrochemical reactions together to eliminate the intermediate production and handling of copper solids. AECL has successfully demonstrated this combined process through a CuCl/HCl electrolyzer which produces hydrogen and aqueous Cu(II) chloride [51]. The 3-step cycle further combines steps by supplying aqueous Cu(II) chloride directly into the hydrolysis chamber. In this research, the main focus is the 4-step cycle since separation of hydrolysis and drying processes provides the advantages of higher thermal efficiency and more viable practical adaptation. Table 25.2 shows the reactions in the 4-step Cu–Cl cycle.

The advantages of the Cu–Cl cycle over other thermochemical cycles include lower operating temperatures, ability to utilize low-grade waste heat to improve energy efficiency, and potentially lower cost of construction materials. In comparison to other thermochemical cycles, the Cu–Cl process requires lower maximum temperatures of 530 °C [8].

Table 25.2   Reactions in the Cu–Cl cycle of hydrogen production

Step (Temp. range (°C))	Reaction	Feed-output[a]
1 (Electrolysis), (<80)	$2CuCl(aq) + 2HCl(aq)$ $\rightarrow H_2(g) + CuCl_2(aq)$	Aqueous CuCl and HCl + V + Q $H_2 + CuCl_2(aq)$
2 (Drying), (<70)	$CuCl_2(aq) \rightarrow CuCl_2(s)$	Slurry containing HCl and $CuCl_2$ + Q Granular $CuCl_2$ + H_2O/HCl vapors
3 (Hydrolysis), (400)	$2CuCl_2(s) + H_2O(g) \rightarrow$ $Cu_2OCl_2(s) + 2HCl(g)$	Powder/granular $CuCl_2$ + $H_2O(g)$ + Q Powder/granular Cu_2OCl_2 + HCl(g)
4 (Decomposition), (500)	$Cu_2OCl_2(s) \rightarrow 2CuCl(l)$ $+ 1/2O_2(g)$	Powder/granular $Cu_2OCl_2(s)$ + Q Molten CuCl salt + Oxygen

[a]Q = thermal energy, V = electrical energy

Fig. 25.5 Process flow diagram of the Cu–Cl cycle of hydrogen production

The overall efficiency of the Cu–Cl cycle has been estimated to be about 43 % [16], excluding the additional potential gains of utilizing waste heat in the cycle. Figure 25.5 shows process flow diagram of the Cu–Cl cycle.
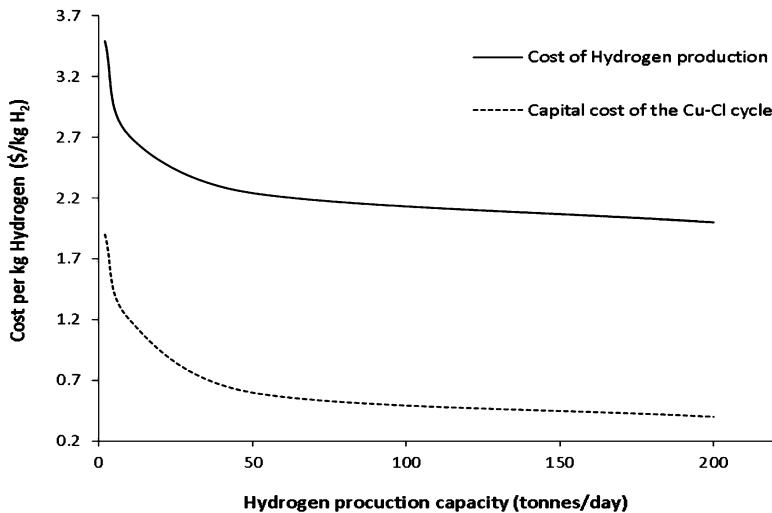
In order to analyze the Cu–Cl cycle performance, the cycle energy efficiency is defined as below,

$$\eta_{CuCl} = \frac{\dot{m}_{H_2} \times LHV_{H_2}}{\dot{W}e_{in} + \dot{Q}_{in}} \qquad (25.1)$$

where $\dot{m}_{H_2}$ is the amount of produced hydrogen in kg/s, LHV_{H_2} is the lower heating value of the hydrogen in kJ/kg, $\dot{W}e_{in}$ is the sum of required electric power to run the electrolysis process and auxiliary work for pumps in and is the net input heat rate that both are in kW. The exergy efficiency for the Cu–Cl cycle can be expressed in the following manner,

$$\psi_{CuCl} = \frac{\dot{m}\dot{e}x_{H_2}}{\dot{W}e_{in} + \left(1 - \frac{T_0}{T_i}\right)\dot{Q}_{in}} \qquad (25.2)$$
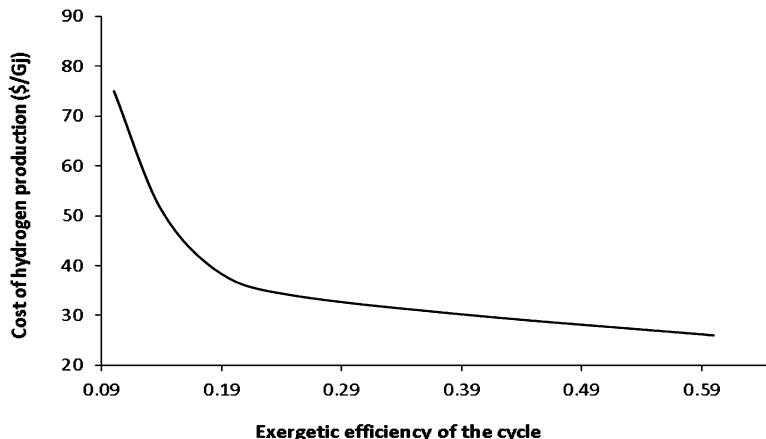
where $\dot{e}x_{H_2}$ is the exergy content of produced hydrogen in kJ/kg, T_0 and T_i are the reference and heat source temperature respectively.

Fig. 25.6 Variation of the cost of produced hydrogen and capital investment of the Cu–Cl cycle with the production capacity

The capital cost associated with the Cu–Cl cycle of hydrogen production as shown in Fig. 25.6 is very sensitive to the production capacity [52]. It is observed that the larger the capacity of the cycle, the more economical hydrogen production system. The main portions of the cost are the capital cost of the Cu–Cl cycle and the cost of storage and distribution of hydrogen. For small scale productions rate, less than 50 tons H_2/day, capital cost of the cycle accounts for the main share of the overall cost in comparison to the other associated costs such as storage and distribution costs. In contrast, for the large scale production, mainly more than 50 tons/day, storage would keep the major cost portion. Storage and distribution costs are constant with capacity, and about 0.7 \$/kg H_2 and 0.1 \$/kg H_2, respectively [52]. It is important to know that the cost of required energy to run the cycle is not included here and will be presented later based on different energy sources. Moreover, oxygen as the cycle by-product can be used in various chemical processes. In this case, the revenue from selling of oxygen should be reduced from the cost of produced hydrogen.

Improvement in the cycle efficiency could substantially decreases energy or exergy losses from the cycle and exergy destruction within the system. It means, the cycle efficiency determine the external energy requirement for the specific amount of production rate. This often results in decrease in cost creation for a unit production of hydrogen. Consequently, the better the cycle efficiency, the cheaper the unit cost of hydrogen production. Figure 25.7 depicts variation of the unit cost of hydrogen production with the Cu–Cl cycle for different production capacity [2].

Fig. 25.7 Variation of the cost of produced hydrogen with the Cu–Cl cycle exergetic efficiency

25.5   Nuclear and Renewable Integrated Cu–Cl Cycle

Power generation worldwide is heavily dominated by the use of fossil fuels. The combustion of these fuels releases large amounts of carbon dioxide and pollutants to the atmosphere. While coal reserves are still abundant, the excessive consumption of coal by the electricity sector is responsible for the greatest share of CO_2 emissions globally, as well as emitting large amounts of pollutants, such as NOx, SO_2, CO, particulate matter, and air toxics to the environment [53].

In order to satisfy the increasing energy demand with a minimal environmental impact, shifting to renewable energy systems are essential. Renewable energy sources provide freedom from the price fluctuations, trade, and transportation issues associated with uranium, gas, and coal, and can potentially help the world energy security. Power generation from flexible sources could significantly reduce the grid demand and associated environmental impacts. Therefore, nuclear and renewable integrated hydrogen production systems are potential solutions to the challenge of producing power at the peak energy demand. Without hydrogen, the contributions of renewable energy will be limited since there is not yet any cost-effective way to store electricity. A more practical approach is the construction of nuclear power plants in series, operating permanently at full load, and directing extra capacity that the grid cannot absorb to hydrogen generation. Conventional electrolysis methods are not practical for the hydrogen mass production due to high cost of construction and low efficiencies. Moreover, producing hydrogen with the current commercial thermochemical cycles requires high-temperature heat.

It could be concluded that low temperature thermochemical cycle, such as Cu–Cl cycle, can be one of the great hydrogen production options to couple with renewable and nuclear energy sources [13]. The Cu–Cl cycle can be integrated with nuclear plants and/or other heat sources such as solar and industrial process/waste heat
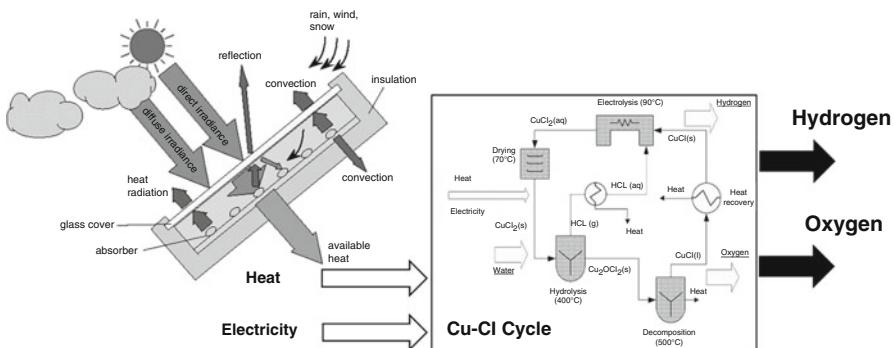
processes (i.e., incinerators, chemical plants, or waste heat from furnaces) to potentially achieve higher efficiencies, lower environmental impact, and lower costs of hydrogen production than other conventional technologies [50]. The Cu–Cl cycle is a hybrid process that employs both thermochemical and electrolysis steps with an estimated overall efficiency of 43 % [54], excluding the additional potential gains of utilizing waste heat in the cycle. Figure 25.2 shows a schematic representation of the Cu–Cl cycle. About 71 % of the net heat required for the Cu–Cl cycle occurs in the form of external heat input, while the remainder can be obtained by internally recycled heat from exothermic processes [55]. Before starting to analyze different integration possibility of the Cu–Cl cycle with nuclear and renewable energy sources, it is necessary to briefly talk about process integration technology.

25.5.1 Process Integration Technology

There are two main considerations in reviewing the impact of technology on industrial demand. The first is the consistent trend of improving energy efficiency. The second is the potential impact of several innovative new technologies or processes. Improvements in industrial sector energy efficiency should continue at least as well as previous trends due to generally increasing energy costs and GHG emissions. Technologies which represent examples of innovative change in the energy sector include fuel switching to renewable energy, gasification, combined heat and power, known as cogeneration, and material substitution including recycling processes. All of these are capable of considerably reduce established energy consumption trends.

In response to the environmental and energy problems associated with the fossil fuel based power generation systems, the energy industry has recently dedicated much attention and resources to mitigating its detrimental impact on the environment, conserving resources, and reducing the intensity of energy usage. These efforts have significantly shifted from a single-based approach to a systems-level solution. It means that the various process objectives such as technical, economic, environmental, and safety must be integrated and reconciled. These challenges call for the application of a systematic approach that target the specific circumstances of the process and views the environmental, energy, and resource conservation problems from an integrated perspective.

Process Integration (PI) is an integrated approach to process design and operation which emphasizes the unity of the process [56]. The primary applications of the process integration have focused on resource conservation, pollution prevention and energy optimization. The initial efforts in the field of process integration were focused on the energy dimension of a chemical process. The primary efforts occurred during the late 1970s and 1980s and resulted in the development of several novel design methodologies such as heat exchanger network analysis that collectively involve heat integration technology [57–61].
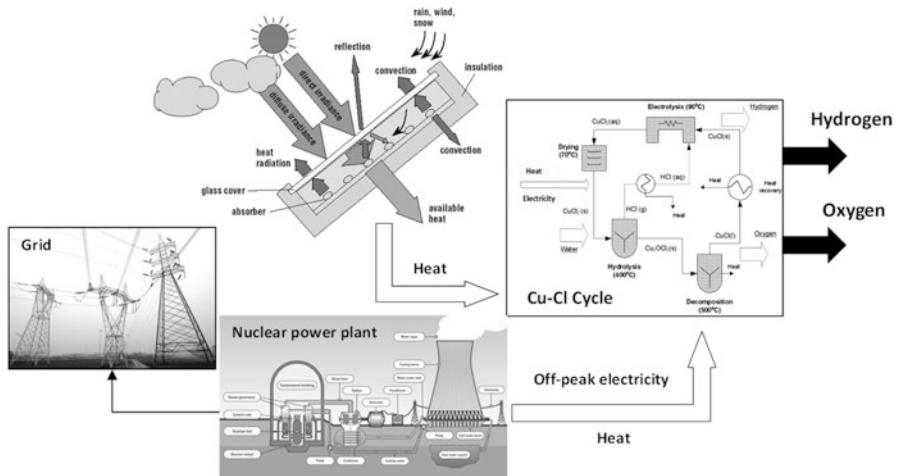
Fig. 25.8 Solar based Cu–Cl cycle of hydrogen production

Process integration has recently been developed to simultaneously address both the mass and energy aspects of the process [62–65]. The development of this integrated methodology has been advanced to address waste reduction processes by the announcement of more stringent environmental regulations coupled with the desire to improve industrial competitiveness. Process integration combined with process simulation, is a powerful approach that allows engineers to systematically analyze an industrial process and the interactions between its various parts. It may be applied to address the most important industrial issues such as energy saving and GHG emissions reduction, minimization of water/steam use and wastewater production, multi-generation system design and waste minimization, and optimization of hydrogen use in an integrated hydrogen production systems.

25.5.2 Solar Based Cu–Cl Cycle

Solar photovoltaic (PV) technology converts sunlight directly into electrical energy. Direct current electricity is produced, which can be used in that form, converted to alternating current or stored for later use. Solar PV systems operate in an environmentally benign manner, have no moving components, and have no parts that wear out if the device is correctly protected from the environment [66]. By operating on sunlight, PV devices are a practical way to harvest solar energy in any place on earth. PV systems can be sized over a wide range, so their electrical power output can be customized for any application, from low-power consumer uses like battery chargers to significantly energy-intensive applications such as generating power at industrial facility.

Instead of nuclear reactor, solar plant could be linked to the Cu–Cl cycle to provide heat and electricity to run the cycle, as shown in Fig. 25.8. This system has drawbacks of no backup energy-source connection and generating of the imbalance charges [2]. Direct coupling of the Cu–Cl cycle to the solar plant

Fig. 25.9 Nuclear-solar based Cu–Cl cycle of hydrogen production
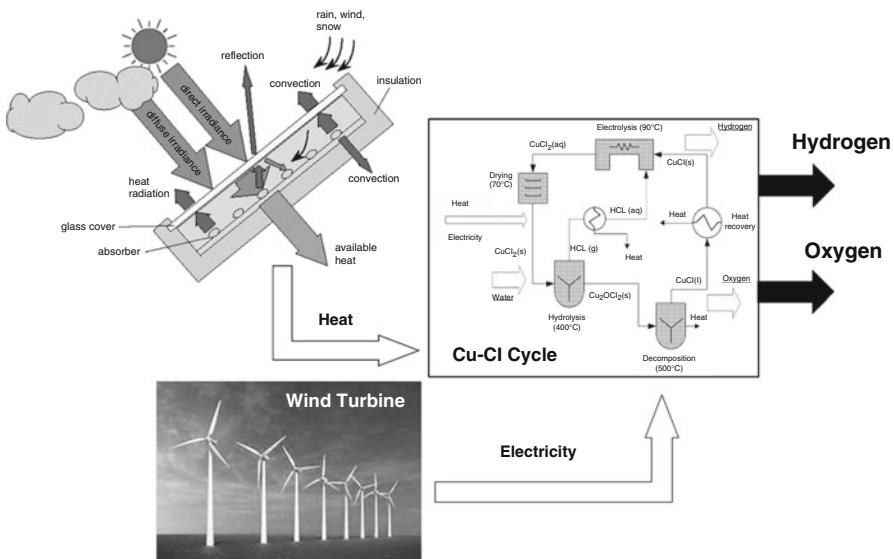
implies irregular operation with highly variable power output. So, the cycle gets exposed to the variable power supply that makes the operation of the integrated system challenging. Economics of the solar based Cu–Cl cycle significantly related to the configuration of the system and its control system, beside the available solar insolation [2].

In some cases, the energy conversion factor of a solar PV system is described as the system efficiency which is completely wrong. The efficiency of a solar PV cell can be considered as the ratio of the electricity generated to the total, or global, solar irradiation. In this definition, which is correctly defined, still the electricity generated by a solar PV cell is only considered. Other properties of PV systems, which may affect efficiency, such as ambient temperature, cell temperature, and chemical components of the solar cell, are not directly taken into account.

For solar PV cells, efficiency measures the ability to convert solar radiation energy to electrical energy. The electrical power output is the product of the output voltage and the current out of the PV device, taken from the current–voltage curve. The conversion efficiency does not have a constant value, even under constant solar irradiation [66].

25.5.3   Nuclear-Solar Based Cu–Cl Cycle

In the proposed integrated system, the problems with intermittent energy supply is eliminated by assuming the combined solar radiation and nuclear power plant as the source of heat and electricity for the Cu–Cl cycle. This configuration will secure constant energy input to the Cu–Cl cycle as depicted in Fig. 25.9.

Fig. 25.10 Wind-solar based Cu–Cl cycle of hydrogen production

25.5.4 *Wind-Solar Based Cu–Cl Cycle*

With the growing significance of environmental problems, clean energy generation has become increasingly important. Wind energy is clean, but it usually does not persist continually for long periods of time at a given location. Other source of energy often must supplement wind energy systems.

Wind power is a form of renewable energy in that it is formed daily by the sun. Warm air rises as portions of the earth which are heated up by the sun, and other air is pushed in to fill the low-pressure areas, creating wind power [66]. The characteristics of wind affect the design of systems to exploit its power. Wind is slowed considerably by friction as it flows over the ground, often causing it not to be very windy at ground level. When wind power is converted to electricity, it can be transported over long distances and thus can serve the needs of urban centers whit a large population.

The simplest integration opportunity is to couple wind turbine with an electrolyzer to produce hydrogen. Since the Cu–Cl cycle needs heat to operate, it cannot work with only electrical power that produced by the wind turbine. Moreover, one of the natural drawbacks of wind power is that the wind velocity is highly intermittent. It is also experienced that power from the wind turbine or wind-farm fluctuates significantly with time. It means that wind power generation system could be incorporated with the solar plant to be coupled with the Cu–Cl cycle, as shown in Fig. 25.10, and ensure security and versatility of power supply. Combined wind and solar systems are in operation at the Desert Research Institute (Reno, Nevada), and in the Hydrogen Research Institute (HRI) at the Universite du

Quebec, Trois Rivieres [2]. These independently operational systems use solar radiation and wind energy together to generate hydrogen effectively. They generate hydrogen at relatively small capacity, with a compressed hydrogen storage system.
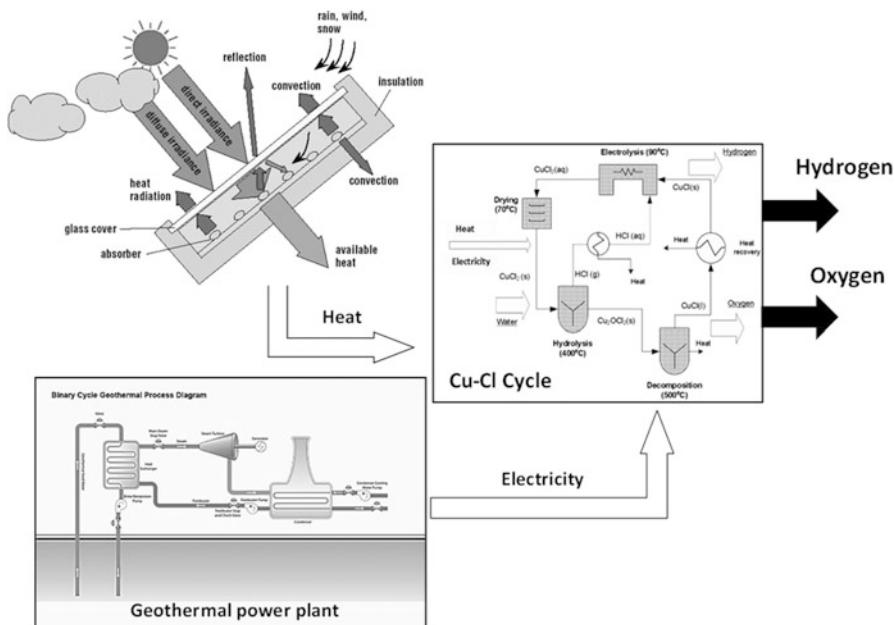
Although turbine technology for wind energy is in good progress, some of the thermodynamic characteristics of wind energy are not yet clearly understood and also prediction of accurate wind condition is not completely predictable. The capacity factor of a wind turbine sometimes is described as the efficiency of a wind energy turbine. But there are difficulties associated with this definition. The efficiency of a wind turbine can be considered as the ratio of the electricity generated to the wind potential within the area swept by the wind turbine. In this definition only the kinetic energy component of wind is considered. Other components and properties of wind, such as temperature differences and pressure effects, are neglected.

25.5.5 Solar-Geothermal Based Cu–Cl Cycle

Geothermal energy is clean and sustainable. Geothermal energy resources are located over a wide range of depths, from shallow ground to hot water and hot rock found several kilometers beneath the Earth's surface, and down even deeper to the extremely high temperatures of molten rock called magma. Geothermal energy is to some extent renewable since a geothermal resource usually has a life of 30–50 years [66]. Geothermal energy has been used commercially for over 80 years and for four decades on the scale of hundreds of megawatts for electricity generation and direct use.

There are three general types of geothermal fields: hot water, wet steam, and dry steam. Hot water fields contain reservoirs of water with temperatures between 60 and 100 °C, and are most suitable for space heating applications. For hot water fields to be commercially viable, they must contain a large amount of water with a temperature of at least 60 °C and lie within 2,000 m of the surface. Wet steam fields contain water under pressure and are at 100 °C [67, 68]. When the water is brought to the surface, some of it flashes into steam, and the steam may drive turbines that produce electrical power. Dry steam fields are similar to wet steam fields, except that superheated steam is extracted from the ground. Dry steam fields are relatively rare. Because superheated water explosively transforms to steam when exposed to the atmosphere, it is safer and generally more economical to use geothermal energy to generate electricity, which is more easily transported. Because of the relatively low temperature of the steam/water, geothermal energy is usually converted to electricity with an energy efficiency of 10–15 %, in contrast to the 20–40 % values typical of fossil fueled electricity generation [66].

Another renewable-based Cu–Cl cycle of hydrogen production option is a combined geothermal electricity generation and solar heating system getting integrated to the Cu–Cl cycle. The main disadvantage of the geothermal energy sources is generally low temperature operating condition that could not satisfy
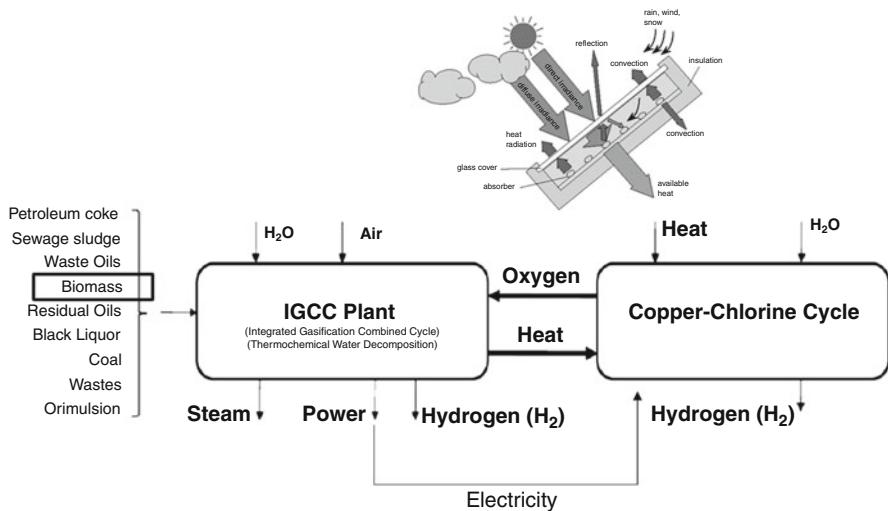
Fig. 25.11 Solar-geothermal based Cu–Cl cycle of hydrogen production

the Cu–Cl cycle heat demand temperature. But it could efficiently generate electricity that is consumed by Cu–Cl cycle. Figure 25.11 is a simple demonstration of this system.

25.5.6 Integrated Gasification and Cu–Cl Cycle

Gasification is the thermochemical conversion of either a solid (coal, coke, biomass, solid waste) or liquid (oil, tar, pitch) fuel into a synthesis gas, or syngas, composed primarily of H_2 and carbon monoxide (CO) [69]. Unlike combustion processes that only produce carbon dioxide and water, gasification is a partial oxidation process that occurs in an oxygen-limited environment. The resulting syngas is more useful than combustion flue gas and it has the potential to generate electricity more efficiently. During the last century, gasification has been used to convert coal into fuel gas for domestic heating and lighting. More recently, gasification has been used in the petrochemical industry for the production of chemical products [70].

Modern gasification technologies can be integrated with power generation cycles, acting as a link between coal or heavy fuel oils and gas turbines. Syngas from gasification can be cleaned to very low levels of contaminants, involving sulfur compounds and particulates [53]. After cleaning, syngas can be utilized in
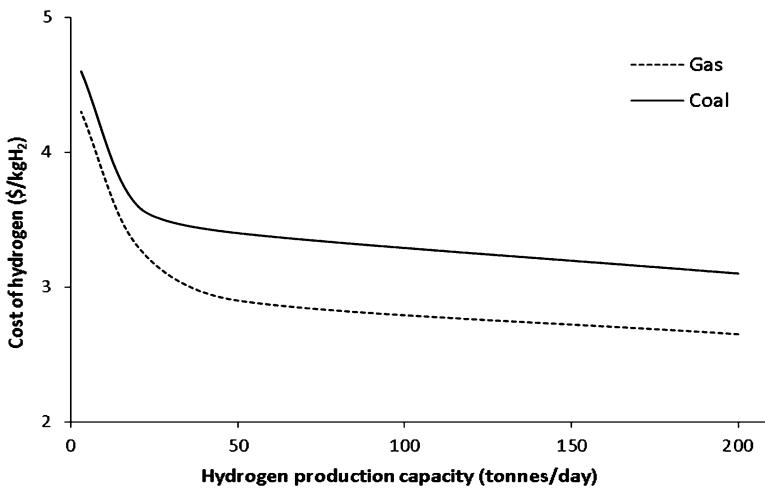
Fig. 25.12 Integrated gasification and Cu–Cl cycle

gas-steam turbine combined cycle power plants, namely, Integrated Gasification Combined Cycle (IGCC), which generates electricity more efficiently than traditional combustion-based plants [53]. The resulting process configuration of IGCC is the only power generation technology, including burning coal, high sulfur residues, or biomass that can approach the technical and environmental performance of natural gas-fired systems. The environmental impact of IGCC systems can be minimized even further when coupled with carbon capture and storage techniques.
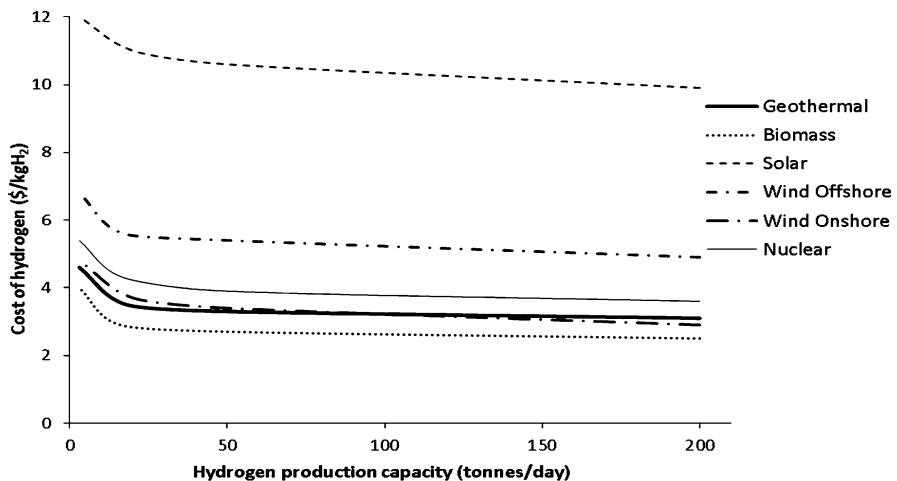
The proposed system is the linkage of the biomass gasification and Cu–Cl cycle processes. In this system, heat provided by the syngas cooling section of an Integrated Gasification Combined Cycle (IGCC) plant, previously used for low-pressure steam generation, is used as the major input of external heat required for the Cu–Cl cycle. At the same time, the produced oxygen in the Cu–Cl cycle can be used instead of input air in the gasification process to improve the combustion efficiency, increase the hydrogen content of produced syngas, and reduce the NOx and CO_2 emissions [13]. Figure 25.12 shows a schematic diagram of this integrated process. It should be mentioned that the electricity requirement to run the Cu–Cl cycle is also provided by the IGCC. The remaining higher temperature heat needed for the Cu–Cl cycle could be provided by solar heating system.

25.6   Results and Discussion

Based on the costs of different energy sources presented earlier in Table 25.1 and the capital cost and the cost of hydrogen production for the Cu–Cl cycle which is presented in Fig. 25.6, the overall cost rate balance of the hydrogen production for the Cu–Cl cycle using different energy sources can be estimated and compared
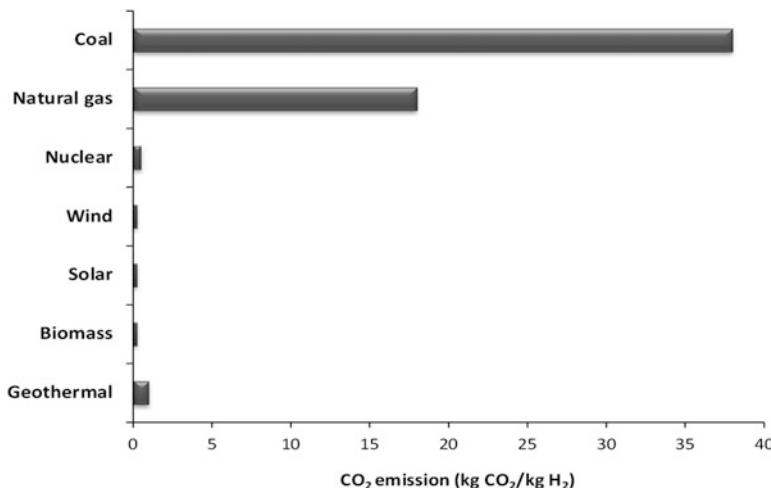
Fig. 25.13 Cost of hydrogen production for the Cu–Cl cycle using coal and natural gas

Fig. 25.14 Cost of hydrogen production for the Cu–Cl cycle using nuclear and renewable energy sources

[2]. Costs of the input energy, including heat and electricity, combined with the capital and processing cost of the Cu–Cl cycle, result in a total cost of hydrogen production. Figure 25.13 shows the cost of hydrogen production in the fossil-fuel-based Cu–Cl cycle using coal or natural gas. Figure 25.14 depicts and compares the cost of hydrogen production in the Cu–Cl cycle using nuclear and renewable energy sources like solar, wind, geothermal, and biomass, in terms of production capacity. It is shown that natural gas and coal are the most inexpensive energy sources for the Cu–Cl cycle of hydrogen production comparing to the nuclear and renewables.

Fig. 25.15 CO_2 emission of hydrogen production for the Cu–Cl cycle using different energy sources

The production cost for nuclear-based Cu–Cl cycle is varied between 3.6 $/kgH$_2$ and 5.4 $/kgH$_2$ while capacity approaches to 200 tons/day. It is again confirmed that the price of hydrogen production is less for the larger production capacities. Solar energy is the most expensive energy source for hydrogen production which could be up to 12 $/kgH$_2$, but it is expected to drop sharply in the future as new and cheaper solar technology become available. Wind energy has the second highest cost of hydrogen production, after solar. As illustrated, there is a large cost difference between the onshore and offshore wind energy sources. The cost of hydrogen for offshore-based Cu–Cl cycle currently varies between 4.9 $/kgH$_2$ and 6.8 $/kgH$_2$, while for the onshore-based Cu–Cl cycle changes between 2.9 $/kgH$_2$ and 4.8 $/kgH$_2$. Similar to the solar energy, these ranges are expected to drop with the progress in the wing power technology. The cost of hydrogen production for geothermal-based Cu–Cl cycle is estimated to vary from 3.1 $/kgH$_2$ to about 4.6 $/kgH$_2$ which is cheaper than the solar and offshore energy sources. The cost of biomass powered Cu–Cl cycle changes between 2.5 $/kgH$_2$ and 4 $/kgH$_2$ and is inversely proportional to the cycle production capacity. Since the gasification process is a well-established technology, the cost of gasification-based Cu–Cl cycle is predicted to remain constant in future.

As mentioned before, despite coal and natural gas are the most inexpensive energy sources for hydrogen production, they are mostly contributing to the GHG emissions and climate changes. The CO_2 emission in terms of unit rate of hydrogen production in the Cu–Cl cycle using different energy sources are depicted in Fig. 25.15. It is shown that using coal energy to produce hydrogen releases 38 kg of CO_2 per kg of produced hydrogen. It is 18 kg CO_2/kg H_2 for natural gas, while it is negligible for renewable and nuclear sources compared to the fossil fuels [2].

25.7 Conclusions

Cu–Cl cycle of hydrogen production is one of the promising emerging technologies for sustainable hydrogen production. The Cu–Cl cycle has numerous advantages over other existing methods of hydrogen production, particularly lower environmental impact than carbon-based technologies and potential higher overall efficiency for its adaptability of integration with nuclear an renewable energy systems. Process integration analysis of the Cu–Cl cycle of hydrogen production with the nuclear and renewable energy sources such as solar, wind, geothermal, and biomass provides valuable insight into further development of this cycle. This study analyzes the advantages and disadvantages of various integrated system options and compares associated cost of hydrogen production. Moreover, environmental impact assessment of the proposed systems with a focus on the amount of CO_2 emission are conducted and compared.

References

1. Elder R, Allen R (2009) Nuclear heat for hydrogen production: coupling a very high/high temperature reactor to a hydrogen production plant. Progr Nucl Energy 51:500–525
2. Orhan MF (2011) Conceptual design, analysis and optimization of nuclear-based hydrogen production via copper-chlorine thermochemical cycles. PhD thesis, FEAS, UOIT, Canada
3. Hirsch RL, Bezdek R, Wendling R (2005) Peaking of world oil production: impacts, mitigation, and risk management. In Proceedings of the IV International Workshop on Oil and Gas Depletion, pp 19–20
4. Intergovernmental Panel on Climate Change (2007) Fourth assessment report. United Nations Framework Convention on Climate Change
5. Schiermeier Q, Tollefson J, Scully T, Witze A, Morton O (2008) Electricity without carbon. Nature 454(7206):816–823
6. Dincer I, Kanoglu M, Rosen MA (2008) Role of exergy in increasing efficiency and sustainability and reducing environmental impact. Energy Policy 36:128–137
7. Strong MF (1992) Energy, environment and development. Energy Policy 20:490–494
8. Lior N (2008) Energy resources and use: the present situation and possible paths to the future. Energy 33:842–857
9. Hartly DL (1990) Perspectives on renewable energy and the environment. In: Tester JW, Wood DO, Ferrari NA (eds) Energy and the environment in the 21st century. MIT, Massachusetts
10. Dincer I (2000) Renewable energy and sustainable development: a crucial review. Renew Sustain Energy Rev 4:157–175
11. International Energy Agency (2009) World energy outlook. Organization of Economic Cooperation and Development
12. International Energy Agency (2009) Energy technology perspectives. Organization of Economic Cooperation and Development
13. Aghahosseini S, Dincer I, Naterer GF (2011) Integrated gasification and Cu-Cl cycle for trigeneration of hydrogen, steam and electricity. Int J Hydrogen Energ 36:2845–2854
14. Lewis Michele A, Masin Joseph G, O'Hare PA (2009) Evaluation of alternative thermochemical cycles, Part I: the methodology. Int J Hydrogen Energ 34(9):4115–4124

15. Lewis MA, Ferrandon MS, Tatterson DF, Mathias P (2009) Evaluation of alternative thermo-chemical cycles e Part III further development of the Cu-Cl cycle. Int J Hydrogen Energ 34(9):4136–4145
16. Naterer G, Suppiah S, Lewis M, Gabriel K, Dincer I, Rosen MA et al (2009) Recent Canadian advances in nuclear-based hydrogen production and the thermochemical Cu-Cl cycle. Int J Hydrogen Energ 34(7):2901–2917
17. Stolberg L, Boniface H, Suppiah S, York S., Naterer G, Dincer I (2009) (eds.) In: Proceedings of the International conference on hydrogen production. pp. 167, Oshawa, Canada
18. Sadhankar RR, Li J, Li H, Ryland D, Suppiah S (2005) Hydrogen generation using high-temperature nuclear reactors. In: 55th Canadian chemical engineering conference, Toronto, Ontario, October
19. Rezaie B, Esmailzadeh E, Dincer I (2011) Renewable energy options for buildings: case studies. Energy Build 43:56–65
20. Natural resource Canada (2011) Energy efficiency trends in Canada 1990 to 2009, Cat. No. M141-1/2009E-PDF, Canada
21. Environment Canada (2010) Overview of the reported greenhouse gas emissions 2009, Cat. No. En81-6/1-2009E-PDF, Canada
22. Evans A, Evans T (2010) Comparing the sustainability parameters of renewable, nuclear and fossil fuel electricity generation technologies. In: World Energy Council for Sustainable Energy, Congress Papers, Montréal, vol. 27. p. 2011
23. Owen AD (2006) Renewable energy: externality costs as market barriers. Energy Policy 34:632–642
24. Ansolabehere S, Deutch, J et al (2003) The future of nuclear power, Massachusetts Institute of Technology
25. International Energy Agency (2006) Geothermal energy annual report 2005
26. Ito M, Kato K et al (2003) A preliminary study on potential for very large-scale photovoltaic power generation (VLS-PV) system in the Gobi desert from economic and environmental viewpoints. Solar Energy Mater Solar Cells 75(3–4):507–517
27. Mock JE, Tester JW et al (1997) Geothermal energy from the earth: its potential impact as an environmentally sustainable resource. Annu Rev Energy Environ 22:305–356
28. Sims REH, Rogner HH et al (2003) Carbon emission and mitigation cost comparisons between fossil fuel, nuclear and renewable energy resources for electricity generation. Energy Policy 31(13):1315–1326
29. Andersson BA, Jacobsson S (2000) Monitoring and assessing technology choice: the case of solar cells. Energy Policy 28(14):1037–1049
30. Jungbluth N, Bauer C et al (2005) Life cycle assessment for emerging technologies: case studies for photovoltaic and wind power. Int J Life Cycle Assess 10(1):24–34
31. Fthenakis V, Alsema E (2006) Photovoltaics energy payback times, greenhouse gas emissions and external costs: 2004-early 2005 status. Progr Photovolt Res Appl 14(3):275–280
32. Energy Information Agency, E. I. A. (2007) International Energy Outlook 2007, Energy Information Administration
33. Tripanagnostopoulos Y, Souliotis M et al (2005) Energy, cost and LCA results of PV and hybrid PV/T solar systems. Progr Photovolt Res Appl 13(3):235–250
34. Dudhani S, Sinha AK et al (2006) Renewable energy sources for peak load demand management in India. Int J Electr Power Energy Syst 28(6):396–400
35. El-Kordy MN, Badr MA et al (2002) Economical evaluation of electricity generation considering externalities. Renew Energy 25(2):317–328
36. Pacca S, Horvath A (2002) Greenhouse gas emissions from building and operating electric power plants in the upper Colorado River Basin. Environ Sci Technol 36(14):3194–3200
37. United Nations Development Program, U. N. D. P. (2000) World energy assessment energy and the challenge of sustainability
38. Armannsson H, Fridriksson T et al (2005) CO2 emissions from geothermal power plants and natural geothermal activity in Iceland. Geothermics 34(3):286–296

39. Brown MT, Ulgiati S (2002) Emergy evaluations and environmental loading of electricity production systems. J Cleaner Prod 10(4):321–334
40. Denholm P, Kulcinski GL et al (2005) Emissions and energy efficiency assessment of baseload wind energy systems. Environ Sci Technol 39(6):1903–1911
41. Fthenakis VM, Kim HC (2007) Greenhouse-gas emissions from solar electric- and nuclear power: a life-cycle study. Energy Policy 35(4):2549–2557
42. Kato K, Murata A et al (1997) An evaluation on the life cycle of photovoltaic energy system considering production energy of off-grade silicon. Solar Energy Mater Solar Cells 47(1–4):95–100
43. Meier P (2002) Life-cycle assessment of electricity generation systems and applications for climate change policy analysis. PhD dissertation, College of Engineering. University of Wisconsin, Madison. p. 161.
44. Proops JLR, Gay PW et al (1996) The lifetime pollution implications of various types of electricity generation—an input-output analysis. Energy Policy 24(3):229–237
45. Spadaro J, Langlois L et al (2000) Assessing the difference: greenhouse gas emissions of different electricity generating chains. IAEA Bull 42(2):19–24
46. Uchiyama Y (2007) Life cycle assessment of renewable energy generation technologies. IEEJ Trans Electr Electron Eng 2(1):44–48
47. Vattenfall (2004) Summary of Vattenfall AB's certified environmental product declaration of electricity from the nuclear power plant at Ringhals. Environmental product declaration
48. Sadhankar RR, Li J, Li H, Ryland DK, Suppiah S (2006) Future hydrogen production using nuclear reactors. Ottawa: Engineering Institute of Canada - Climate Change Technology Conference, May, Canada
49. Sadhankar RR (2006) Leveraging nuclear research to support hydrogen economy. In: 2nd green energy conference, Oshawa, June, Canada.
50. Rosen MA, Naterer GF, Sadhankar R, Suppiah S (2006) Nuclear-based hydrogen production with a thermochemical copper-chlorine cycle and supercritical water reactor. Quebec: Canadian Hydrogen Association Workshop, October 19–20
51. Naterer GF et al (2011) Clean hydrogen production with the Cu-Cl cycle - Progress of international consortium. I: Experimental unit operations. Int J Hydrogen Energ. doi:10.1016/ j.ijhydene.2011.08.012
52. Orhan MF, Dincer I, Naterer GF (2008) Cost analysis of a thermochemical Cu-Cl pilot plant for nuclear-based hydrogen production‖. Int J Hydrogen Energ 33:6006–6020
53. Aghahosseini S, Dincer I, Naterer GF (2011) Environmental impact assessment of sustainable hydrogen, steam and electricity trigeneration through integrated gasification and Cu-Cl cycle. Proceedings of the global conference on global warming, Lisbon, Portugal
54. Chukwu C, Naterer GF, Rosen M (2008) Process simulation of nuclear-produced hydrogen with a Cu-Cl cycle. 29th conference of the Canadian Nuclear Society, Toronto, Ontario, Canada, June 1–4.
55. Naterer GF, Gabriel K, Wang Z, Daggupati V, Gravelsins R (2008) Thermochemical hydrogen production with a copper-chlorine cycle. I: oxygen release from copper oxychloride decomposition. Int J Hydrogen Energ 33(20):5439–5450
56. El-Halwagi MM (1997) Pollution prevention through process integration: systematic design tools. Academic, San Diego
57. Linnhoff B, Hindmarsh E (1983) The pinch design method for heat exchanger networks. Chem Eng Sci 38:745–763
58. Papoulias SA, Grossmann IE (1983) A structural optimization approach in process synthesis II. Heat recovery networks. Comp Chem Eng 7:707–721
59. Cerda J, Westerberg D, Mason D, Linhoff B (1983) Minimum utility usage in heat-exchanger network synthesis: a transportation problem. Chem Eng Sci 38:373–383
60. Gundersen T, Naess L (1988) The synthesis of cost optimal heat exchanger networks: an industrial review of the state of the art. Comp Chem Eng 12(6):503–530

61. Shenoy UV (1995) Heat exchange network synthesis: process optimization by energy and resource analysis. Gulf Publishing Company, Houston
62. Dunn RF, El-Halwagi MM (1994) Selection of optimal VOC-condensation systems. Waste Manage 14:103–113
63. Dunn RF, El-Halwagi MM (1994) Optimal design of multi-component VOC-condensation systems. J Hazard Mater 38:187–206
64. El-Halwagi MM, Srinivas BK, Dunn RF (1995) Synthesis of heatinduced separation networks. Chem Eng Sci 50:81–97
65. Dunn RF, Zhu M, Srinivas BK, El-Halwagi MM (1995) Optimal design of energy-induced separation systems for VOC recovery. AIChE Symp Ser 90:74–85
66. Dincer I, Rosen MA (2007) Exergy: energy, environment and sustainable development. Elsevier, Oxford, UK
67. Kanoglu M (2002) Exergy analysis of a dual-level binary geothermal power plant. Geothermics 31(6):709–724
68. DiPippo R (2007) Ideal thermal efficiency for geothermal binary plants. Geothermics 36(3):276–285
69. Zwart RWR, Boerrigter H (2005) High efficiency co-production of synthetic natural gas (SNG) and Fischer-Tropsch (FT) transportation fuels from biomass. Energy Fuel 19(2):591–597
70. Dickenson R, Biasca F, Schulman B, Johnson H (1997) Refiner options for converting and utilizing heavy fuel oil. Hydrocarbon Process 76(2)

Chapter 26
Comparative Environmental Impact Assessment of Nuclear-Based Hydrogen Production via Mg–Cl and Cu–Cl Thermochemical Water Splitting Cycles

Ahmet Ozbilen, Ibrahim Dincer, and Marc A. Rosen

Abstract The environmental impacts of nuclear-based hydrogen production processes are evaluated and compared, considering magnesium–chlorine (Mg–Cl) and copper–chlorine (Cu–Cl) thermochemical water decomposition cycles and using life cycle analysis. Variations of environmental impacts (acidification potential and global warming potential) with hydrogen production plant lifetime are reported. An artificial neural network model is used to develop the results. Relations between environmental impacts and economic factors are also presented using the social cost of carbon concept. The results show that the Cu–Cl thermochemical cycle has lower acidification and global warming potentials per unit mass of hydrogen produced compared to the Mg–Cl thermochemical cycle due to its lower electrical work requirement.

A. Ozbilen (✉) • I. Dincer • M.A. Rosen
Faculty of Engineering and Applied Science, University of Ontario Institute of Technology, 2000 Simcoe Street North, Oshawa, ON, Canada L1H 7K4
e-mail: Ahmet.Ozbilen@uoit.ca; Ibrahim.Dincer@uoit.ca; Marc.Rosen@uoit.ca

Nomenclature

W_n Weights of ANN
x_n Inputs of ANN
y_n Outputs of ANN

Greek Symbols

α   Activation function
Σ   Summation function

Acronyms

ANN   Artificial neural network
AP   Acidification potential
AECL   Atomic Energy of Canada Limited
CML   The Center of Environmental Science of Leiden University
DC   Direct current
GHG   Greenhouse gas
GWP   Global warming potential
HTE   High temperature electrolysis
ISO   International Organization for Standardization
LCA   Life cycle assessment
LCI   Life cycle inventory
LCIA   Life cycle impact assessment
PEM   Proton exchange membrane
SCC   Social cost of carbon
SCWR   Super-critical water cooled reactor
SOEP   Solid oxide electrolysis cell
TC   Thermochemical cycle

26.1   Introduction

Many environmental issues such as global warming and acidification are related to the production, transformation, and utilization of fossil fuels [1]. The risk of global climate change is of great concern to policy makers and the public. The relation between the energy generation sector and environmental impact is being carefully considered in industrialized and non-industrialized countries [2]. Environmentally benign technologies are being developed to help ensure that future generations have cleaner energy systems, and a more sustainable economy. The energy carrier hydrogen can facilitate improved environmental performance and sustainability of energy systems [3, 4]. Although addressing future energy challenges requires

numerous measures and approaches, hydrogen is expected by many to play a major role, in part due to it not emitting greenhouse gases (GHGs) during oxidation.

Many substances found in nature contain hydrogen, for example water, fossil fuels, biomass, hydrogen sulfide. Close to half of the global hydrogen demand is supplied by steam reforming of natural gas, about 30 % from oil/naphtha reforming from refinery/chemical industrial off-gases, 18 % from coal gasification, 3.9 % from water electrolysis, and 0.1 % from other sources [5]. However, current hydrogen production methods cannot be considered as sustainable and environmentally benign since these processes use either nonrenewable energy sources or electricity which is mostly generated by fossil fuels.

Hydrogen production using thermochemical water splitting cycles has the potential to be cleaner and more cost-effective than other production methods. With thermochemical water decomposition, hydrogen and oxygen are obtained by decomposing water using a series of thermally driven chemical reactions. Water can be directly split in one step, but the required process temperature is too high to be practical. However, a series of selected chemical reactions can be utilized to achieve the same hydrogen output at much lower temperatures. Many thermochemical water decomposition cycles have been identified in the literature [6]. The copper–chlorine (Cu–Cl) thermochemical water decomposition cycle is a promising hydrogen production process due to its relatively low-temperature requirements (not exceeding 530 °C). Numerous investigations have been carried out on hydrogen production using thermochemical Cu–Cl cycles [3, 7–12]. The magnesium–chlorine (Mg–Cl) thermochemical water splitting cycle is another promising low temperature alternative for hydrogen production. However, few performance assessments have been conducted on this cycle [13].

Fossil fuels, nuclear energy, and renewable energy resources can be utilized as energy sources to produce hydrogen. Nuclear power has significant potential for future hydrogen production because nuclear reactors do not emit GHGs during operation, and nuclear energy is capable of large-scale energy production [4, 14, 15]. Generation IV nuclear reactors, particularly the supercritical water-cooled reactor (SCWR), have been proposed by Atomic Energy of Canada Limited (AECL) and others as an energy source for low temperature thermochemical cycles.

Environmental impacts associated with hydrogen production need to be investigated to ascertain the extent to which hydrogen is an environmentally benign energy carrier. Such an investigation is the focus of the present undertaking. An environmental impact analysis method, life cycle assessment (LCA), is used which provides an understanding of the potential harm of a product or a process and improvement opportunities. LCA is essentially a cradle-to-grave analysis to investigate environmental impacts of a system or process or product.

An artificial neural network (ANN) approach is used together with LCA in the present analysis. A previously developed ANN based on a LCA of the Cu–Cl cycle is applied to the Mg–Cl cycle. The advantage of incorporating an ANN approach is that it makes it easier to forecast accurately system performance using small data sets, avoiding the need for many experiments and the need to use LCA software separately.

The objective of this study is to investigate the environmental impacts of nuclear-based hydrogen production via thermochemical water splitting using the

Mg–Cl and Cu–Cl cycles by performing a neural network-based life cycle assessment. The specific objectives are given as follows:

- To conduct an LCA of nuclear-based hydrogen production using the Mg–Cl and Cu–Cl cycles using ANNs.
- To perform a parametric study for various plant lifetimes.
- To present the relation between environmental impacts with economic aspects using the social cost of carbon concept.
- To compare the environmental impact results of the Mg–Cl and Cu–Cl cycles with other hydrogen production methods.

26.2 Background: Hydrogen Production Methods
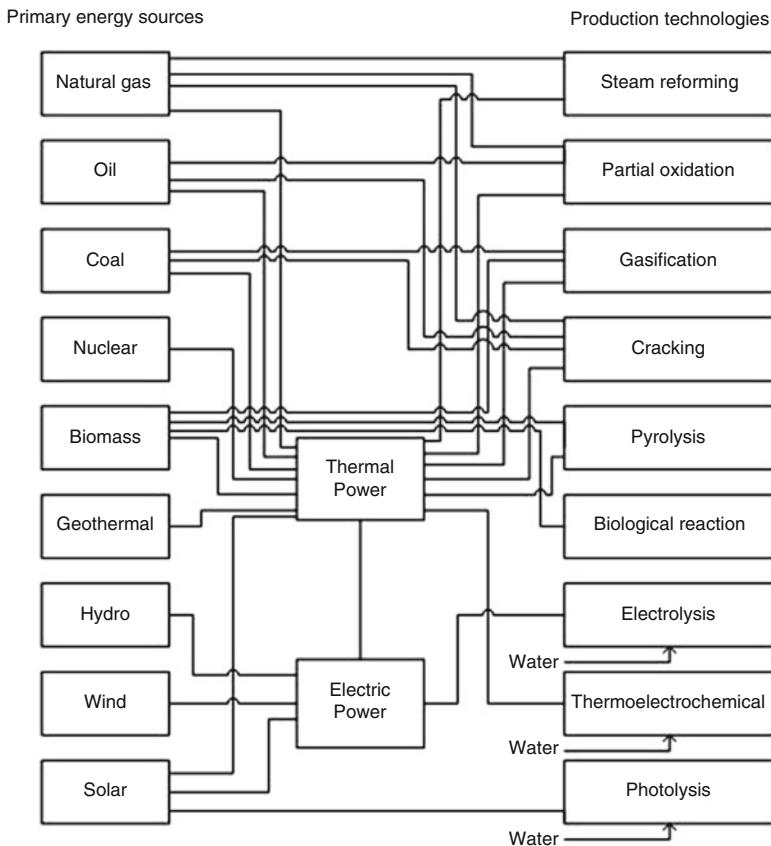
The energy carrier hydrogen is expected by many to become an important fuel that will help in solving several energy challenges we face today since its oxidation does not emit GHGs and does not contribute to climate change, provided it is derived from clean energy sources. Numerous researchers anticipate that hydrogen will replace petroleum products for fuelling of transportation vehicles, in turn decreasing the dependence on petroleum. Industrial sectors, such as petrochemical, agricultural, food processing, plastics, manufacturing, use hydrogen heavily as a commodity [3]. Hydrogen complements the energy carrier electricity, which can be generated from a variety of primary energy sources and is widely used in a broad range of applications. These two energy carriers are expected to have complementary roles in the future, in part since hydrogen adds the capability of storage [16]. Renewable energy-based hydrogen production, with a corresponding storage system, is considered to be useful for energy management since renewable energy systems have intermittent characteristics [17].

Many substances found in nature contain hydrogen. Among them water—naturally found as brine (sea water), river or water, rain or well water—is the most abundant. Hydrogen can also be extracted from hydrocarbons, biomass, hydrogen sulfide, or other substances. When hydrogen is extracted from fossil fuels, all carbon dioxide must be processed (separated, sequestered, etc.) and no GHGs or other pollutants can emitted to the atmosphere for the hydrogen extraction process to be considered "green" [4].

26.2.1 Current Practices for Hydrogen Production

Currently, 96 % of world hydrogen production is from fossil fuels. Natural gas is the main raw material and steam methane reforming (SMR) is the most commonly used method [18]. The main methods for hydrogen production using various energy sources are shown in Fig. 26.1.

Figure 26.2, on the other hand, proposes various paths along which four types of energy to drive hydrogen production can be obtained from "green" energy sources.
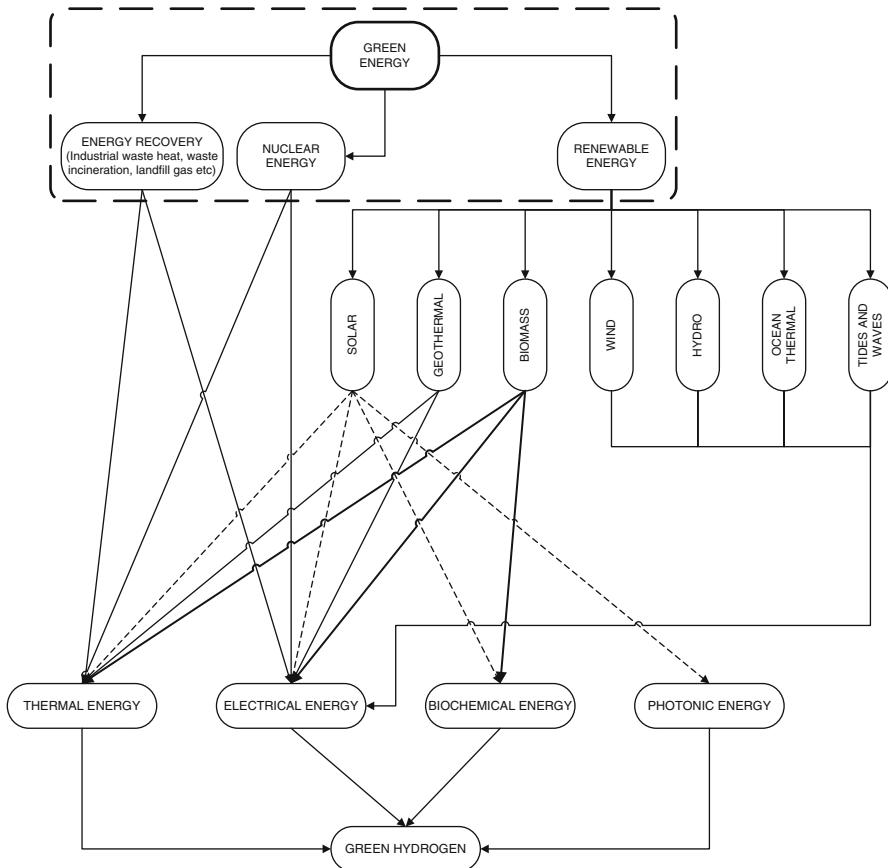
Fig. 26.1 The main methods for hydrogen production, considering various energy sources (modified from [19])

The electrical and thermal energy can be derived from renewable energies (like solar, wind, geothermal, tidal, wave, ocean thermal, hydro, biomass), or from nuclear energy, or from recovered energy. The photonic energy is comprised of solar radiation only. The biochemical energy is that stored in organic matter (in form of carbohydrates, glucose and sugars, etc.) and can be manipulated by certain microorganisms that can extract hydrogen from various substrates or can be chemically converted to thermal energy. Biochemical energy can be assisted by solar radiation to generate energy, depending on the case (viz. bio-photolysis or dark fermentation) [4].

26.2.2 Review of Nuclear Hydrogen Production Methods
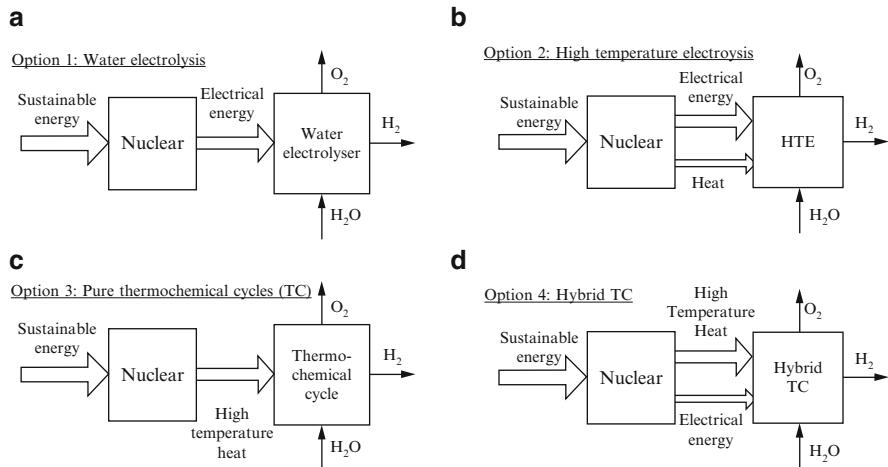
Using nuclear energy as the primary energy source for hydrogen production is attractive because: (1) the GHG emissions associated with nuclear energy

Fig. 26.2 Paths of hydrogen production using forms of energy derived from primary green energy sources [4]

production are more significantly reduced than with conventional fossil fuel combustion; and (2) nuclear energy is adaptable to large-scale hydrogen production. Significant progress in nuclear-based hydrogen production has been reported in recent years in the open literature. Nuclear-based hydrogen production methods, such as water electrolysis, high temperature electrolysis, thermochemical water splitting and hybrid thermochemical cycles for water splitting, are promising (Fig. 26.3).

The simplest method to obtain hydrogen from nuclear power is by coupling an electrolyzer to a nuclear power plant. The advantage of such system is the possibility to operate at design load without direct interference with the grid. Another important advantage of nuclear/water electrolysis is that there is no need to modify the reactor. Such systems were applied on nuclear submarines to generate oxygen (for maintaining life) and hydrogen. It is possible to adapt the system to existent nuclear power plants to generate off-peak electricity.
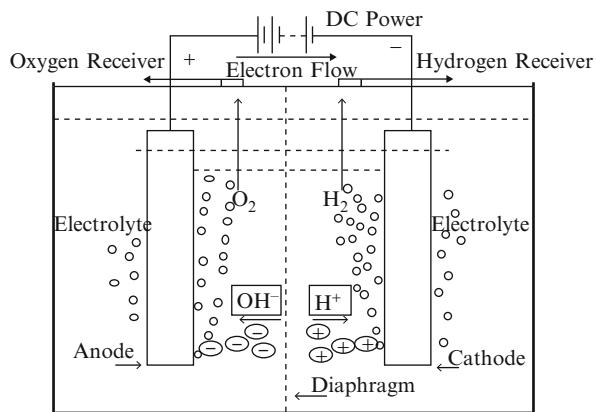
Fig. 26.3 Nuclear-based hydrogen production methods: (**a**) water electrolysis, (**b**) high temperature electrolysis, (**c**) thermochemical cycles, and (**d**) hybrid thermochemical cycles (modified from [21])

The various nuclear reactor technologies that can be combined with thermally driven hydrogen production processes, that are adaptable to nuclear reactors, will likely complement, not compete, in shaping nuclear-based hydrogen generation capability in the future. Hydrogen production using thermochemical water splitting cycles has the potential to be cleaner and more cost-effective than other production methods. Although hydrogen production systems using thermochemical cycles have not yet been commercialized, studies have shown that such systems can be expected to compete with conventional H_2 production methods, including steam methane reforming [11, 20]. Although water can be directly split in one step, a series of selected chemical reactions can be utilized to achieve the same result at reasonable temperatures [6].

Water Electrolysis

Water electrolysis is a common method to produce hydrogen by water splitting which is achieved by passing an electric current through water. An anode, a cathode, a power supply, and an electrolyte are main components of a basic water electrolysis unit, as shown in Fig. 26.4. A direct current (DC) is applied and electrons flow from the negative terminal of the DC source to the cathode at which the electrons react with hydrogen ions (protons) to form hydrogen. In keeping the electrical charge in balance, hydroxide ions (anions) transfer through the electrolyte solution to the anode, at which the hydroxide ions release electrons and these electrons return to the positive terminal of the DC source [22]. Water electrolysis can be conducted with proton exchange membrane (PEM) electrolyzers or alkaline electrolyzers [4, 21].

Fig. 26.4 Schematic of a
basic water electrolysis
system [22]

High-Temperature Electrolysis
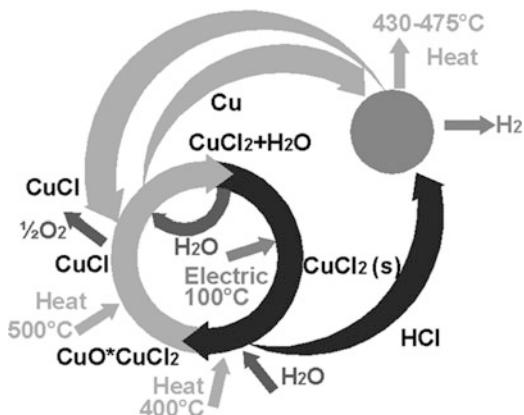
In electrolysis a portion of the required energy can be provided in form of heat. Thus the total energy needed to drive the reaction can be partially electricity and practically transmitted heat. High temperature electrolysis is conducted in solid oxide electrolysis cells (SOEC) at temperatures of 1,100–1,250 K. In these systems water is converted to steam using thermal energy. Also, the electrochemical stack is heated directly (by the supplied steam) or indirectly (through heat transfer). The cell voltage and current density in a typical high temperature electrolyzer are 0.95–1.3 V and 0.3–1.0 A/cm^2, respectively. The high temperature electrolysis process has both thermodynamic and kinetic advantages over conventional methods [21, 23]. Potentially, high temperature steam electrolysis coupled to advanced nuclear reactors can generate hydrogen at 45–55 % energy efficiency [24].

Thermochemical Water Splitting

Thermochemical cycles do not normally require catalysis to drive the chemical reactions. All chemicals involved in the process can be recycled except water which is the material source from which hydrogen is derived. Water-splitting thermochemical cycles are attractive for the following reasons: (a) oxygen separation membranes are not needed; (b) the temperature of the required thermal energy source is at a reasonable range (600–1,200 K); and (c) little or no electrical energy is required to drive the process [4].

Several review articles on the topic have been published in the open literature, as summarized by [25]. The sulfur–iodine (S–I) cycle operates at maximum temperature of 825–900 °C, which is needed to drive the oxygen-evolving reaction. The S–I cycle has been demonstrated in both Japan and the US and has been shown to be technically viable. However, the commercial viability of any of these cycles has yet to be demonstrated.

Fig. 26.5 The Cu–Cl thermochemical water splitting cycle (modified from [25])
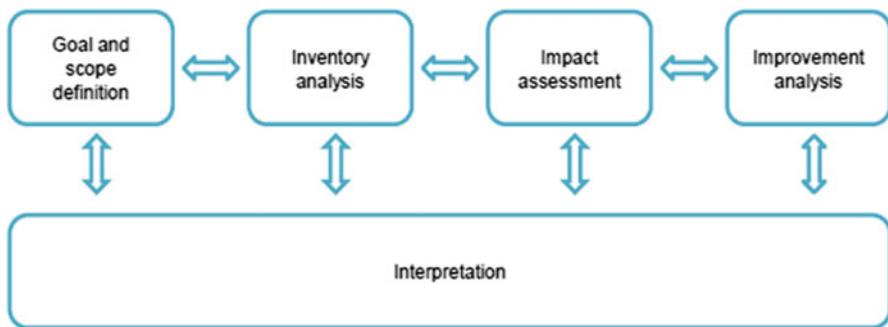
Hybrid Thermochemical Cycles for Water Splitting

Apart from the thermally driven thermochemical water splitting cycles mentioned above, three other thermochemical water splitting cycles—called hybrid cycles— are of interest because they operate at lower temperatures. Hybrid cycles use thermal and electrical energies to drive endothermic chemical and electrochemical reactions. As a consequence of their lower operating temperature, other sustainable thermal sources—apart from solar, high temperature nuclear and biomass combustion—can be used to drive the relevant processes. The additional heat sources are present nuclear reactors operating at 250–650 °C, as well as geothermal and waste heat [4].

The Cu–Cl thermochemical water splitting cycle has several potential advantages. The maximum temperature level required from the heat source is about 550 °C, to drive the oxygen generation reaction. There are several variants of the Cu–Cl cycle, of which the most commonly examined is the "five-step" version. Three- and four-step cycles are also reported in the literature. The five-step Cu–Cl cycle comprises three thermally driven chemical reactions, one electro-chemical reaction and one physical step of drying. The processes involved in the five-step cycle are shown in Fig. 26.5.

26.3 Life Cycle Assessment

LCA is a useful method for investigating the environmental impacts of a product or process [26]. It is a cradle-to-grave analysis in which not only the usage stage but also other stages in the life of a product are taken into consideration, such as production, transportation, and disposal. LCA is used to determine and assess overall environmental impacts and to define the most environmentally critical phase in order to decrease the negative environmental effects of a product or a

Fig. 26.6 Life cycle assessment framework, showing the main steps in LCA and the relations between them

process. LCA is also conducted to compare competing products or processes and to identify the more environmentally benign options.

The International Standards of Organization (ISO) developed its 14,000 series for life cycle assessment, including several parts:

- ISO-14040, Life Cycle Assessment—Principles and Framework [27]
- ISO-14041, Life Cycle Assessment—Goal and Scope Definition and Inventory Analysis [28]
- ISO-14042, Life Cycle Assessment—Life Cycle Impact Assessment [29]
- ISO-14043, Life Cycle Assessment—Life Cycle Interpretation [30]
- ISO-14044, Life Cycle Assessment—Requirements and Guidelines [31]

A life cycle assessment consists of four main phases (Fig. 26.6), which are explained further in the following sections. Arrows in Fig. 26.6 indicate that all phases of the LCA are linked to each other. The life cycle interpretation is also linked to all phases, since the phases of the LCA should be reviewed and necessary modifications made depending on the results of a LCA.

26.3.1 Goal and Scope Definition

Goal and scope definition is the first phase of LCA, and identifies the system and the audience considered as well as the objectives and insights of interest from the LCA. In defining the scope of the LCA, the system boundary is indicated, which indicates the region to be analyzed. A definition of scope also considers the function of the system. It is often necessary to define a functional unit (e.g., 1 kg of product), to provide a reference for relating the inputs and outputs. Further details on goal and scope definition are presented elsewhere [28].

26.3.2   Life Cycle Inventory Analysis

Life cycle inventory (LCI) analysis is the second LCA phase. The first step in LCI analysis is to identify, for all processes, energy and material inputs and outputs associated with all flows across and within the system boundary. LCI analysis includes data collection and calculation procedures that quantify relevant inputs and outputs of the system. Data acquisition often involves measuring data, collecting data from literature, and calculating data by modelling the process. Due to logistical as well as other barriers, such as a reluctance by industry to share data considered confidential, obtaining data to be used in LCI is often difficult [32]. An inventory analysis is often an iterative procedure in which, to achieve the goals of LCA, as data are collected and more is learned about the system, new data requirements or limitations are identified that necessitate a change in the data collection procedures. Further details on LCI analysis are presented elsewhere [27].

26.3.3   Life Cycle Impact Assessment

The third phase of LCA is life cycle impact assessment (LCIA), for which the aim is to evaluate environmental impacts of the material and energy flows identified in the inventory analysis. ISO 14042 [29] divides LCIA into the following steps:

- Classification: This step involves determination of impact categories, which must be consistent with the goal and scope of the study. Then, inventory data are assigned to the impact categories, such as potentials for global warming and ozone depletion.
- Characterization: Inventory data within impact categories are characterized, first by matching to impact categories and then by quantifying their contributions to the impact categories. Hence, the impacts of different environmental flows are assessed using a common indicator unit for each impact category. This calculation can be done with previously developed factors or using LCA software.
- Normalization and weighting: Normalization and weighting combine all environmental impacts and reduce them to a single measure. Although optional, this LCIA step is but often helpful for comparing alternatives.

Examples of impact assessment methods include CML 2001 [33], Eco-indicator 95 [34], EPS 2000 [35], IMPACT 2002+ [36], and IPCC 2007 [37]. The CML 2001 method is used in the illustrative example at the end of this chapter.

The Center of Environmental Science of Leiden University (CML) published an "operational guide to the ISO standards" in 2001, which has a set of impact categories and characterization methods and factors for a list of substances (accounting for resources from and emissions to the natural environment) to use in the impact assessment phase of LCA. Guinee et al. [33] explain these environmental impact categories, important examples of which follow:

- Acidification Potential (AP): AP is the deposition of acidifying pollutants on soil, groundwater, surface waters, biological organisms, ecosystems and materials, and is measured in units of kg SO_2-eq. Major contributors to this category are SO_2, NOx, and NHx. The natural environment, the anthropogenic environment, human health and natural resources are protection areas where AP has notable effects.
- Global Warming Potential (GWP): GWP is the impact of human emissions on the radiative forcing (i.e., thermal radiation absorption) of the atmosphere, and is measured in units of kg CO_2-eq. Global warming, which leads to climate change, may affect ecosystem and human health. Most GHG emissions increase radiative forcing, which increases the earth's surface temperature (the "greenhouse effect").

26.3.4   Life Cycle Interpretation (Improvement Analysis)

Life cycle interpretation is the final LCA phase, and integrates the LCI and LCIA results to develop conclusions and recommendations that relate to the goal and scope of the study. Life cycle interpretation can help decision makers make improvements by identifying and choosing the most environmental benign alternative, bearing in mind that the decision process is also affected by technical, economic, social, and other factors.

26.4   Literature Review: LCA of Hydrogen Production Methods

Life cycle analyses of several H_2 production methods have been reported. Spath and Mann presented two reports for the National Renewable Energy Laboratory (NREL) related to life cycle assessments of hydrogen production via natural gas steam reforming [38] and via wind/electrolysis [39]. The first report [38] presents the environmental impacts of hydrogen production via natural gas steam reforming for a hydrogen plant capacity of 1.5 million Nm^3/day. The results are given in term of air, GHG and water emissions. The global warming potential (GWP) of the system is found to be 11,888 g CO_2-eq/kg hydrogen produced. The second report [39] investigates the environmental impacts of hydrogen production based on wind power. Three wind turbines, each of 50 kW capacity, are incorporated into the system which has a hydrogen production capacity of 100 kg/week. The LCA results indicate that the GWP of hydrogen production is 970 g CO_2-eq and system energy consumption is 9.1 MJ/kg hydrogen produced. Sensitivity analyses are presented in both studies.

Marquevich et al. [40] conducted a life cycle inventory analysis to assess the environmental load, specifically GWP, associated with H_2 production by steam reforming of feedstocks (methane and naphtha) and vegetable oils (rapeseed oil, soybean oil, and palm oil). While the GWP of H_2 produced from rapeseed oil, palm oil and soybean oil are found to be 6.42 kg CO_2-eq/kg H_2, 4.32 kg CO_2-eq/kg H_2, and 3.30 kg CO_2-eq/kg H_2, respectively, the GWPs associated with the production of H_2 by steam reforming are 9.72 kg CO_2-eq/kg H_2 and 9.46 kg CO_2-eq/kg H_2 for methane and naphtha, respectively. Thus, the GWP may be reduced by up to 60 % if natural gas and naphtha are replaced by vegetable oils.

Koroneos et al. [41] used a comparative LCA to investigate the environmental impacts of natural gas steam reforming and hydrogen production based on renewable energy sources. The fuel systems considered in the analysis follow:

- Fuels produced from conventional sources:

    - Hydrogen produced from steam reforming of natural gas

- Hydrogen produced from renewable energy sources:

    - From solar energy using photovoltaics for direct conversion
    - From solar thermal energy
    - From wind power
    - From hydro power
    - From biomass

Life cycle impact assessment (LCIA) is conducted using CML 2001 impact categories and Eco-indicator 95 methods. The total impact scores show that the use of wind, hydropower, and solar thermal energy are the most environmentally benign methods. In terms of GWP, hydrogen production using wind power has the lowest environmental impact while hydrogen from steam reforming of natural gas has the highest CO_2-eq emissions.

Utgikar and Thiesen [23] performed a life cycle assessment of high temperature electrolysis for H_2 production via nuclear energy. High temperature electrolysis is advantageous to low-temperature alkaline electrolysis because of its higher efficiency, which is due to reduced cell potential and consequent electrical energy requirements. The high temperature electrolysis system has a GWP of 2000 g CO_2-eq and acidification potential (AP) of 0.15 g H_2 ion equivalent per kg of H_2 produced. A comparison of the environmental impact of the system with natural gas steam reforming and wind, solar photovoltaic, solar thermal, hydroelectric, and biomass based electrolysis indicates that emissions of the high temperature water vapor electrolysis process are much lower than those for conventional natural gas steam reforming and comparable with the emissions for H_2 production using renewable based electrolysis.

Utgikar and Ward [42] presented a LCA of a nuclear-assisted ISPRA Mark 9 thermochemical water splitting cycle, a three-step thermochemical cycle involving iron chlorides (Fe-Cl). GWP and AP of the nuclear-based hydrogen production system, per kg hydrogen produced, are found to be 2,515 g CO_2-eq and 11.25 g SO_2-eq, respectively.

Solli et al. [43] presented a comparative hybrid life cycle assessment to evaluate and compare environmental impacts of two H_2 production methods: nuclear assisted thermochemical water splitting using the S-I cycle and natural gas steam reforming with CO_2 sequestration. An overall advantageous option could not be determined since a weighting method was not applied. The results show that thermochemical water splitting has lower environmental impacts in terms of GWP, AP and eutrophication potential (EP), and much higher impacts in terms of radiation (RAD) and human toxicity potential (HTP). While the GWP of natural gas steam reforming is 1.3×10^4 kg CO_2-eq, the GWP of thermochemical water splitting via the S–I cycle is 2.9×10^3 kg CO_2-eq for the production of 1 TJ (on the basis of higher heating value (HHV)) of H_2.

Koroneos et al. [44] compared two biomass-to-hydrogen systems: biomass gasification by reforming of the syngas, and gasification followed by electricity generation and electrolysis. Environmental impacts in terms of GWP, AP, and EP are determined, and a weighting using the Eco-indicator 95 method is applied to compare the overall environmental impacts. While the gasification to electrolysis system has a greater eutrophication effect, biomass gasification by reforming of syngas has higher environmental impacts in terms of GWP and AP. In addition, the weighting results demonstrate that the biomass-gasification-electricity-electrolysis route has better environmental performance than the process involving reforming of the syngas.

Djomo et al. [45] proposed potato steam peels as a feedstock for producing H_2 through fermentation and conducted an LCA for this process. The authors utilized the IMPACT 2002+ method in the LCIA phase. The results show that the two-stage bioreactor, which is used for H_2 production, emits 1,000–1,500 g of CO_2 per kg of H_2 produced. There are two main sources of CO_2 emissions. First, photoheterotrophic bacteria convert all organic acids to H_2 and CO_2. There is also an electricity requirement for both pretreatment and fermentation processes in H_2 production, and this is another source of GHG emissions. The study also demonstrates that hydrogen production using potato steam peels offers advantages compared to direct use of peels to feed animals, including reductions in GHGs emissions, nonrenewable resource utilization, and human health impacts.

Dufour et al. [18] investigated from an environmental point of view four H_2 production systems: steam reforming of natural gas (the reference system), a coupling of the reference system with CO_2 capture, thermal cracking, and autocatalytic decomposition of natural gas. The results show that autocatalytic decomposition with a total conversion is the most environmentally benign process. Steam reforming of natural gas with CO_2 capture and storage options lead to a lower GWP but a higher general environmental impact, as calculated with the Eco-indicator method, than conventional steam methane reforming without CO_2 capture.

Lubis et al. [46] presented a preliminary LCA for hydrogen production using nuclear energy, based on the Cu–Cl thermochemical cycle. Results are presented in terms of CML 2001 impact categories and show that the GWP of the system over its lifetime is 0.0025 g CO_2-eq, and that major contributors to the GWP are construction of nuclear and hydrogen plants.

Variations of environmental impacts with lifetime and production capacity were reported for nuclear based hydrogen production plants using the three-, four-, and five-step Cu–CI thermochemical water decomposition cycles by Ozbilen et al. [9]. The LCA is performed using GaBi 4 environmental impact assessment software. The parametric studies show that increasing plant hydrogen production capacity and lifetime does not significantly affect the values of the impact categories per kg hydrogen production, if the capacities and lifetimes are sufficiently great. The parametric studies also indicate that APs and GWPs for the four-step Cu–Cl can be reduced from 0.0031 to 0.0028 kg SO_2-eq and from 0.63 to 0.55 kg CO_2-eq, if the lifetime increases from 10 years to 100 years.
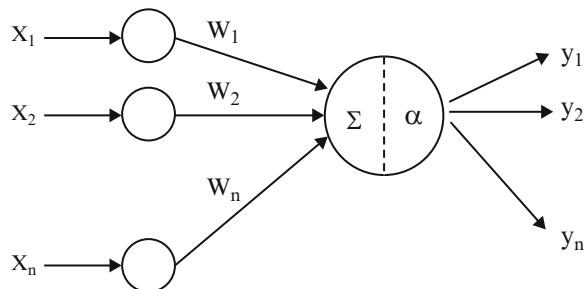
The environmental impacts of nuclear based hydrogen production via thermochemical water splitting using the Cu–Cl cycle have been quantified and described using life cycle analysis by Ozbilen et al. [10]. The LCAs for the three-, four-, and five-step Cu–Cl cycles consider four scenarios, which relate to electrical power distribution. Multiple scenarios are considered to account for possible future Cu–Cl cycle designs using GaBi 4 LCA software. Results are presented in seven impact categories defined by CML, including global warming potential, and show that negative impacts can be associated with hydrogen production, depending on its source, even though hydrogen is a clean energy carrier. The four-step Cu–Cl cycle linked with a Generation IV SCWR, which supplies all electricity requirements for the production processes, is seen to have the lowest environmental impact due to its lower thermal energy requirement. If electrical energy output of the nuclear plant is used for all processes in nuclear-based hydrogen production, the GWP can be decreased from an initial value 15.8 kg to 0.56 kg CO_2-eq. The four-step Cu–Cl thermochemical water splitting cycle exhibits lower environmental impacts compared to the three- and five-step cycles. The primary contributors to environmental impact categories are observed to be fuel processing, especially mining and conversion due to the fossil fuel use in these processes, and nuclear plant utilization.

26.5   Artificial Neural Networks

Artificial neural networks (ANNs) consist of large numbers of computational units connected in a large parallel structure and work similar to a human brain [47]. Because of their simple and unlimited structure, they have a wide operating area in artificial intelligence applications such as mathematics, engineering, energy systems, medicine, economics, etc. Today neural networks can be trained to solve problems that are difficult for conventional computers or human beings. Throughout the artificial neural network toolbox (e.g., MATLAB nftool, and nntool) emphasis is placed on neural network paradigms that apply to or are themselves used in engineering, financial and other practical applications.

Neural networks are composed of simple elements operating in parallel. These elements are inspired by biological nervous systems. As in nature, the network function is determined largely by the connections between elements. A neural

Fig. 26.7 Architecture of a neural network unit
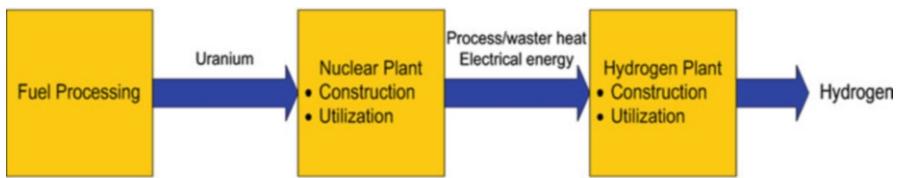
network can be trained to perform a particular function by adjusting the values of the connections (weights) between elements.

Commonly neural networks are adjusted, or trained, so that a particular input leads to a specific target output. Then, the network is adjusted, based on a comparison of the output and the target, until the network output matches the target. Typically many such input/target pairs are used, in this supervised learning, to train a network.

There are several learning algorithms that can be applied to train a neural network. It is difficult to know which training algorithm will be the fastest for a given problem, and the best one is usually chosen by trial and error. The most popular is the backpropagation algorithm, which has several variants. The backpropagation algorithm was created by generalizing the Widrow–Hoff learning rule to multiple-layer networks and nonlinear differentiable transfer functions. Standard backpropagation is a gradient descent algorithm, in which the network weights are moved along the negative of the gradient of the performance function. The term backpropagation refers to the manner in which the gradient is computed for nonlinear multilayer networks [48].

The architecture of a neural network unit is shown in Fig. 26.7. Each artificial neural unit consists of inputs (x_n), weights (W_n), a summation function (Σ), an activation function (α), and outputs (y_n). Figure 26.7 illustrates how the information is processed through a single node. The node receives weighted activations of other nodes through its incoming connections. These weighted activations are summed, and the result is passed through an activation function, the outcome being the activation of the node. For each of the outgoing connections, this activation value is multiplied by the specific weight and transferred to the next node.

The input layer feeds data to the network; therefore it is not a computing layer since it has no weights or activation function. The output layer represents the output response to a given input. Here, x is input vector which can be expressed $xT = [x1, x2, \ldots, xn]$. W is the vector including the weights and is represented as $WT = [W1, W2, \ldots, Wn]$.

Fig. 26.8 Simplified overview of nuclear-based hydrogen production system for LCA

26.6   System Description

Fuel (uranium) processing, the nuclear plant, and the hydrogen plant are three main subsystems of nuclear-based hydrogen production via thermochemical water splitting. Figure 26.8 shows simplified overview of the nuclear-based hydrogen production. Mining, milling, conversion, enrichment, and fuel fabrication are the main steps of fuel (uranium) processing. The output of fuel processing, which is fabricated uranium (UO_2), is then transported to the nuclear plant. The thermal and electrical energy output of the nuclear plant is required for the hydrogen plant, in order to produce the final output, hydrogen. In this assessment, only the construction and operation stages of the nuclear-based hydrogen production system are included, to be consistent with other LCA studies in the literature.

26.6.1   Mg–Cl Cycle

The Mg–Cl thermochemical water decomposition cycle is a hybrid process using heat and electricity to split water into produce hydrogen at a maximum temperature of 550 °C. The Mg–Cl cycle consists of three main steps (two thermochemical and one electrochemical). A conceptual layout of the cycle with primary reactions is presented in Fig. 26.9. In the hydrolysis step, a solid gas reaction takes place, in which hydrogen chloride (HCl) and magnesia (MgO) are produced during the hydrolysis of magnesium chloride ($MgCl_2$). This reaction is endothermic and has a temperature range of 450–550 °C, which is the highest temperature requirement of the Mg–Cl cycle. The reactants of the hydrolysis step are H_2O and $MgCl_2$ [13].

In the chlorination step of Mg–Cl cycle, MgO (s) and Cl_2 (g) enter as reactants to form $MgCl_2$ (s) and oxygen at a reaction temperature of about 400–500 °C. $MgCl_2$ is then fed back to the hydrolysis step to form a closed internal loop that recycles all of the Mg compounds on a continuous basis. Hydrogen can be produced by a thermochemical or an electrochemical reaction in the third step of Mg–Cl cycle. Thermochemical dissociation of HCl is an energy-intensive process and the reaction occurs at high temperatures. The electrochemical process is a low temperature operation compared to thermochemical dissociation [13]. Anhydrous HCl electrolysis is considered in the Mg–Cl cycle, which can be achieved with a voltage of about 1.6 V at 8 kA/m^2 [49, 50]. Further details on the Mg–Cl cycle are presented elsewhere [13, 49, 51].

Step	Chemical reaction	T (ºC)
1. Hydrolysis	$MgCl_2$ (s) + H_2O (g) → MgO (s) + 2HCl (g)	450 – 550
2. Chlorination	MgO (s) + Cl_2(g) → $MgCl_2$ (s) + ½ O_2 (g)	400 – 500
3. Hydrogen production	2HCl (g) → H_2 (g) + Cl_2 (g)	70 – 90

Fig. 26.9 Principal chemical reactions in the Mg–Cl cycle for thermochemical water decomposition and conceptual layout (modified from [13])

26.6.2 Cu–Cl Cycle

Cu–Cl thermochemical cycles involve a series of chemical reactions, and are characterized by the number of major chemical steps they incorporate. Two-, three-, four-, and five-step Cu–Cl cycles for thermochemical water decomposition have been identified previously. The chemical reactions used in the Cu–Cl cycle, which utilizes a series of copper and chlorine compounds, form a closed loop, and all chemicals are recycled. The participating chemicals are relatively safe, inexpensive and abundant. All chemical reactions in the Cu–Cl cycle are also proven in the laboratory with no significant side reactions [3]. Inputs to the Cu–Cl thermochemical water decomposition cycle are water, thermal energy, and electricity, while oxygen and hydrogen are the outputs. The principal chemical reactions in five-, four-, and three-step Cu–Cl cycles for thermochemical water decomposition and a conceptual layout of the five-step cycle are presented in Fig. 26.10. The five main chemical reaction steps in the cycle are (1) HCl (g) production (hydrolysis) using such equipment as a fluidized bed, (2) oxygen production (copper oxychloride decomposition), (3) copper (Cu) production, (4) drying of cupric chloride, and (5) hydrogen production. The four-step cycle combines the third

Cu-Cl Cycle	Step	Chemical reaction	T (°C)
5-step	1. HCl production	$2CuCl_2(s) + H_2O(g) \rightarrow Cu_2OCl_2(s) + 2HCl(g)$	450
	2. O_2 production	$Cu_2OCl_2(s) \rightarrow 2CuCl(l) + 1/2O_2(g)$	500
	3. Cu production	$4CuCl(aq) \rightarrow 2CuCl_2(aq) + 2Cu(s)$	25
	4. Drying	$2CuCl_2(aq) \rightarrow 2CuCl_2(s)$	90
	5. H_2 production	$2Cu(s) + 2HCl(g) \rightarrow 2CuCl(l) + H_2(g)$	450
4-step	1. H_2 production	$2Cu(s) + 2HCl(g) \rightarrow 2CuCl(l) + H_2(g)$	450
	2. Combined step	$4CuCl(aq) \rightarrow 2CuCl_2(s) + 2Cu(s)$	25-90
	3. HCl production	$2CuCl_2(s) + H_2O(g) \rightarrow CuO \cdot CuCl_2(s) + 2HCl(g)$	450
	4. O_2 production	$CuO \cdot CuCl_2(s) \rightarrow 2CuCl(l) + 1/2O_2(g)$	500
3-step	1. Combined Step	$2CuCl(l) + 2HCl(g) \rightarrow 2CuCl_2(s) + H_2(g)$	100
	2. HCl production	$2CuCl_2(s) + H_2O(g) \rightarrow CuO \cdot CuCl_2(s) + 2HCl(g)$	430
	3. O_2 production	$CuO \cdot CuCl_2(s) \rightarrow 2CuCl(l) + 1/2O_2(g)$	550

Fig. 26.10 Principal chemical reactions in five-, four-, and three-step Cu–Cl cycles for thermo-chemical water decomposition and conceptual layout of the five-step cycle

and fourth steps in the five-step cycle, whereas the three-step Cu–Cl cycle integrates the H_2 production step and the combined step in the four-step cycle to reduce the complexity and equipment requirements. Some of the reactions are exothermic while others are endothermic, and the reaction temperatures differ for the steps. Heat exchangers are utilized to ensure appropriate temperatures are maintained and to allow for effective thermal management and waste heat recovery.
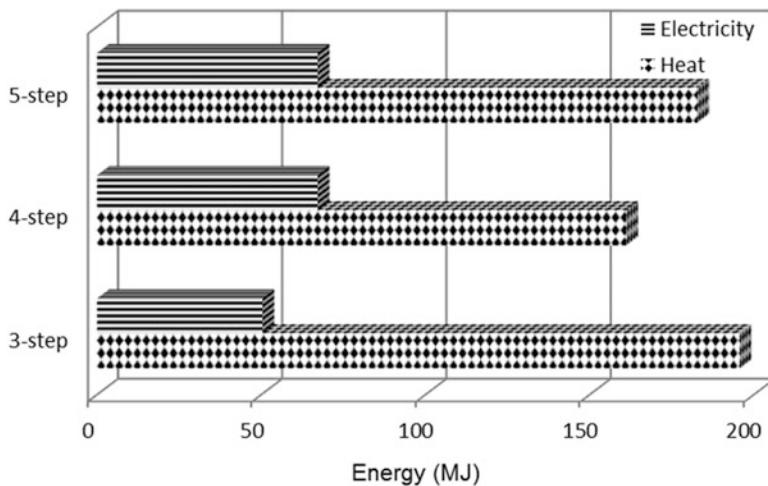
The first step of the five-step cycle is the hydrogen production step in which solid copper particles coming from step 2 (Cu production) react with HCl which comes from step 4 (HCl production). The hydrogen production step is exothermic and occurs at a temperature of 450 °C. The products are hydrogen gas which is the desired output, and CuCl. The second step is the copper production step in which copper is produced from molten CuCl. The reaction temperature for this step is as low as 25 °C. This reaction also requires electrical energy. While product copper moves to hydrogen production step, the other product $CuCl_2$ is transferred to third step (drying). In the drying step, the molten $CuCl_2$ is dried to solid $CuCl_2$ which is used in step 4 (HCl production). $CuCl_2$ reacts with water in this step to produce HCl and $CuOCuCl_2$ at a temperature around 450 °C in a fluidized bed. In the O_2 production step, oxygen and CuCl are produced by splitting of $CuOCuCl_2$. Since the reaction temperatures are not the same for each step, heat exchangers are utilized prior to each reaction to obtain the required temperature.

The total energy requirements of the five-step Cu–Cl thermochemical water decomposition cycle are calculated using the study of Wang et al. [7], in which heat requirements for each step of the cycle are evaluated. The total required heat input is 554.7 kJ/mol H_2 and the total heat output is 232 kJ/mol H_2. The external thermal energy requirement of the five-step Cu–Cl cycle is 391.4 kJ/mol H_2, i.e., 195.7 MJ/kg H_2 assuming 70 % heat recovery, i.e., only low-grade heat is recovered. The electrical energy required for the Cu production step is 62.6 kJ/mol H_2.

Also, 38 kJ/mol H_2 of work is estimated to be required for auxiliary equipment [8]. Energy requirements of the three- and four-step Cu–Cl thermochemical cycles are calculated using the approach followed by Rosen et al. [8]. Energy inputs to the three Cu–Cl cycles are presented in Fig. 26.11.

The thermal energy requirements for the Cu–Cl cycles are the basis of the present analysis of the integrated system. The electrical energy needed by the hydrogen plant and other processes (e.g., heavy water production, uranium milling) is met using power output of the nuclear plant. In addition, ratios of electrical energy produced to thermal energy (process heat and waste heat) are found using the study of Pioro and Duffey [52].

Uranium to be used in the Generation IV SCWR is processed through the following steps: mining, milling, conversion, enrichment, and fuel fabrication. First, uranium ore is extracted from the environment via mining, and concentrated in the form of U_3O_8 during milling. In the conversion process, the U_3O_8 is then converted to UF_6 to be ready for enrichment, which increases the concentration of the fissile isotope U-235 to a desired level (4 % for a SCWR). The chemical composition is then altered to UO_2 in the fuel production step for use in the SCWR. Further details on the systems considered here are presented elsewhere [9, 10].

Fig. 26.11 Energy requirements for three-, four-, and five-step Cu–Cl cycle for 1 kg H_2 production

26.7   Analysis

A previously developed ANN model, created using neural network toolbox of the MATLAB software, is used to perform the environmental impact assessment of the Mg–Cl cycle. There are four inputs and two outputs for the system (Fig. 26.12). The inputs are hydrogen production plant capacity, plant lifetime, and heat and electrical work input to hydrogen plant. The output parameters are GWP and AP. The number of neurons in the hidden layer is selected to be in the range of 10–20, with the best results obtained using ten neurons in the hidden layer.

The training function selected is the Levenberg–Marquardt algorithm and sigmoid transfer function. The number of datasets used to develop the ANN is 150, and these are obtained using the GaBi 4 software. 80 % of these data patterns are used for training, while 5 % and 15 % are used for validation and testing, respectively.

The training of the network is accomplished by adjusting the weights and is carried out through training sets and training cycles (epochs). The goal of the learning procedure is to find the optimal set of weights, which in an ideal case produce the proper output for any input. The output of the network is compared with a desired response to produce an error. The performance of the network is measured in terms of a desired signal and the criterion for convergence. For one sample, the absolute fraction of variance (R^2) is determined as follows [53]:

$$R^2 = 1 - \frac{\sum_i (t_i - o_i)^2}{\sum_i (o_i)^2} \tag{26.1}$$

Fig. 26.12 ANN model for nuclear-based hydrogen production
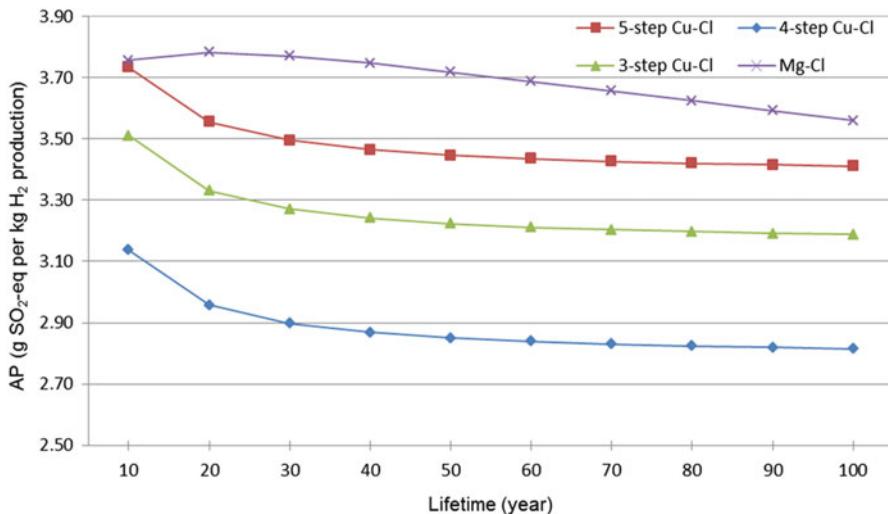
26.8   Results and Discussion

ANN results for the Mg–Cl cycle are presented and compared with the LCA results of the Cu–Cl thermochemical cycle [9, 10]. Variations of environmental impact measures (acidification potential and global warming potential) with hydrogen production plant lifetime are reported. The relation between environmental impacts and economic aspects is also presented using the social cost of carbon concept.
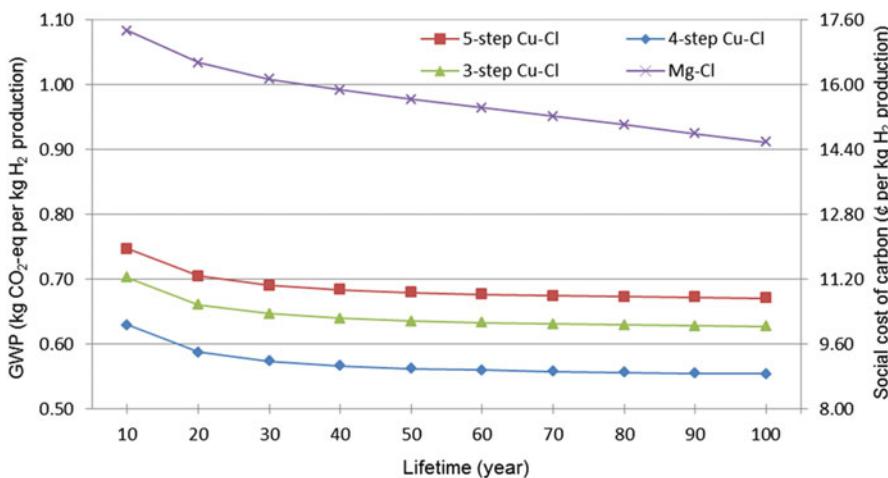
Figure 26.13 shows the change in AP for various plant lifetimes. Acidification potential values decreases with increasing lifetime of the plant. The lowest AP for the thermochemical hydrogen production methods considered here is for the four-step Cu–Cl cycle (2.8 g SO_2-eq/kg H_2 production), while the highest AP is approximately 3.8 g SO_2-eq/kg H_2 production for the Mg–Cl cycle.

The variation of global warming potential and the social cost of carbon with plant lifetime are presented in Fig. 26.14. The primary axis shows GWP values for each thermochemical cycle, and the secondary axis shows the social cost of the carbon. The social cost of carbon (SCC) is the value of the climate change impacts from 1 tonne of carbon emitted today as CO_2, aggregated over time and discounted back to the present day [54]. The average social cost of carbon is $160 per tonne of CO_2 emissions [37]. 2007 US dollars are used in this paper. The difference in the GWP values between the reference lifetime (60 years) and a lifetime of 100 years is relatively small, which indicates that lifetime is not a significant factor specifically for the Cu–Cl cycle after 60 years. The highest environmental impact in terms of GWP is 1.08 kg CO_2-eq/kg H_2 production and the corresponding social cost of carbon value is 17.3 ¢/kg H_2 production for the Mg–Cl cycle. The lowest GWP value is for the four-step Cu–Cl cycle (0.55 kg CO_2-eq/kg H_2 production) and the corresponding SCC value is 8.8 ¢/kg H_2 production.

Figure 26.15 compares several hydrogen production methods with the Mg–Cl and the Cu–Cl thermochemical cycles in terms of (a) GWP and (b) SCC. The results are for a 60-year hydrogen plant lifetime and a daily production of 125,000 kg. GWP data of other hydrogen production methods are reported in the literature [23, 38, 39]. The GWP is higher for the Mg–Cl cycle than other thermochemical cycles
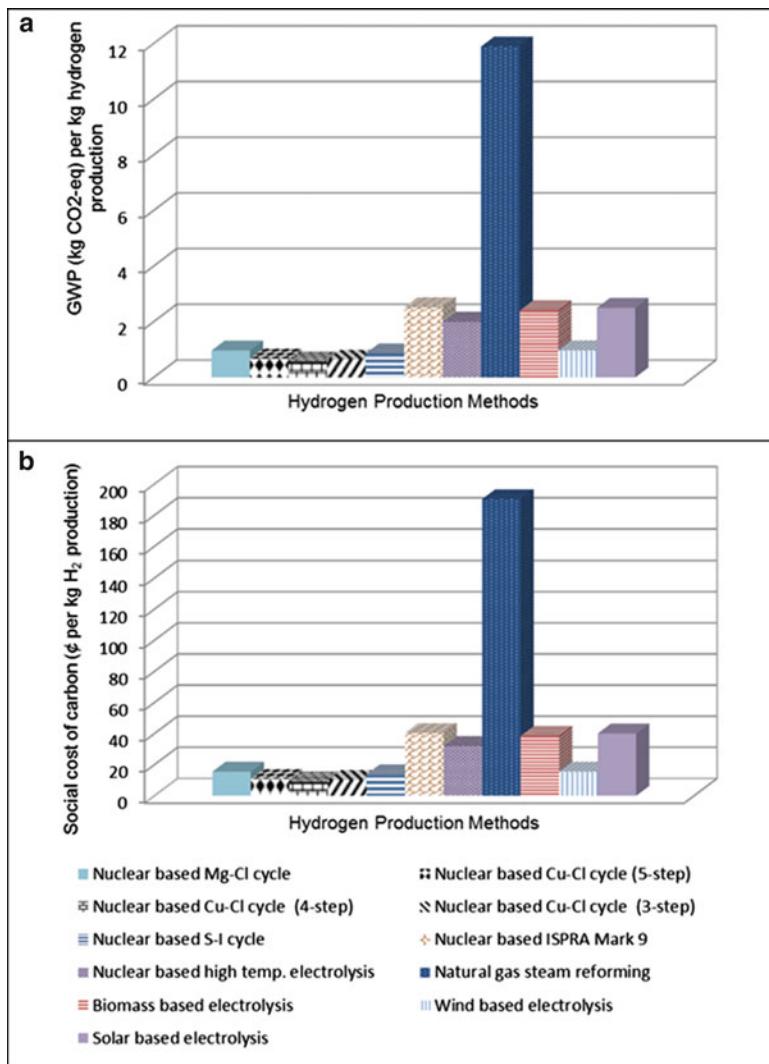
Fig. 26.13 Variation of acidification potential (g SO_2-eq/kg H_2 production) with plant lifetime

Fig. 26.14 Variation of global warming potential (kg CO_2-eq/kg H_2 production) and social cost of carbon with plant lifetime

(Cu–Cl and S–I cycles), mainly due to its higher electrical energy requirements in the hydrolysis step. The Mg–Cl cycle has a similar environmental impact as wind-based electrolysis, and lower impacts than other hydrogen production methods such as natural gas steam reforming and solar-based electrolysis. The four-step Cu–Cl exhibits the lowest GWP and SCC values, while natural gas steam reforming has the highest, primarily because it is a fossil fuel based method.

Fig. 26.15 GWP and SCC for several hydrogen production methods: nuclear-based thermochemical cycles, natural gas steam reforming and renewable based electrolysis

26.9   Conclusions

The environmental impacts of nuclear based hydrogen production via thermochemical water splitting using the Mg–Cl cycle have been quantified using an artificial neural network model. The results are compared with the three-, four-, and five-step Cu–Cl cycles performing a parametric study for various plant lifetimes. Results are presented in terms of global warming potential and acidification potential. The social cost of

carbon concept is also introduced to show the relation between economics and the environment. Environmental impact results of the Mg–Cl cycle are compared with those for many hydrogen production methods. The results show that the higher the CO_2 emissions the higher the cost of carbon to society. GWP and AP values for the Mg–Cl cycle are found to be higher than for Cu–Cl cycle, which is another low temperature water splitting cycle, mainly because of the higher electrical work requirement of the hydrolysis step of the Cu–Cl cycle. The highest environmental impact in terms of GWP is evaluated to be 1.08 kg CO_2-eq/kg H_2 production and the corresponding social cost of carbon value is 17.3 ¢/kg H_2 production for Mg–Cl cycle. The lowest GWP value is for the four-step Cu–Cl cycle (0.55 kg CO_2-eq/kg H_2 production) and the corresponding SCC value is 8.8 ¢/kg H_2 production. The Cu–Cl cycles have the lowest GWP values compared to other hydrogen production methods, while steam methane reforming has the highest values. The nuclear-based Mg–Cl cycle has relatively lower environmental impacts compared to conventional hydrogen production methods.

References

1. Dincer I (2007) Environmental and sustainability aspects of hydrogen and fuel cell systems. Int J Energy Res 31:29–55
2. Dincer I, Balta MT (2011) Potential thermochemical and hybrid cycles for nuclear-based hydrogen production. Int J Energy Res 35:123–127
3. Naterer GF, Suppiah S, Stolberg L, Lewis M, Ferrandon M, Wang Z, Dincer I, Gabriel K, Rosen MA, Secnik E, Easton EB, Trevani L, Pioro I, Tremaine P, Lvov S, Jiang J, Rizvi G, Ikeda BM, Lu L, Kaye M, Smith WR, Mostaghimi J, Spekkens P, Fowler M, Avsec J (2011) Clean hydrogen production with the Cu-Cl cycle—progress of international consortium, II: simulations, thermochemical data and materials. Int J Hydrogen Energ 36:15486–15501
4. Dincer I (2012) Green methods for hydrogen production. Int J Hydrogen Energ 37:1954–1971
5. Muradov NZ, Veziroglu TN (2005) From hydrocarbon to hydrogen-carbon to hydrogen economy. Int J Hydrogen Energ 30:225–237
6. Funk JE (2001) Thermochemical hydrogen production: past and present. Int J Hydrogen Energ 26:185–190
7. Wang ZL, Naterer GF, Gabriel K (2008) Multiphase reactor scale-up for Cu-Cl thermochemical hydrogen production cycle. Int J Hydrogen Energ 33:6934–6946
8. Rosen MA, Naterer GF, Chukwu CC, Sadhankar R, Suppiah S (2012) Nuclear-based hydrogen production with a thermochemical copper-chlorine cycle and supercritical water reactor: equipment scale-up and process simulation. Int J Energy Res 36:456–465
9. Ozbilen A, Dincer I, Rosen MA (2011) Environmental evaluation of hydrogen production via thermochemical water splitting using the Cu-Cl cycle: a parametric study. Int J Hydrogen Energ 36:9514–9528
10. Ozbilen A, Dincer I, Rosen MA (2012) Life cycle assessment of hydrogen production via thermochemical water splitting using multi-step Cu-Cl cycles. J Clean Prod 33:202–216
11. Lewis MA, Masin JG, O'Hare PA (2009) Evaluation of alternative thermochemical cycles-Part I. The methodology. Int J Hydrogen Energ 34:4115–4124
12. Orhan MF, Dincer I, Rosen MA (2011) Design of systems for hydrogen production based on the Cu-Cl thermochemical water decomposition cycle: configurations and performance. Int J Hydrogen Energ 36:11309–11320

13. Balta MT, Dincer I, Hepbasli A (2012) Energy and exergy analyses of magnesium-chlorine (Mg-Cl) thermochemical cycle. Int J Hydrogen Energ 37:4855–4862

14. Elder R, Allen R (2009) Nuclear heat for hydrogen production: coupling a very high/high temperature reactor to a hydrogen production plant. Prog Nucl Energy 51:500–525

15. Ball M, Wietschel M (2009) The future of hydrogen—opportunities and challenges. Int J Hydrogen Energ 34:615–627

16. Urbaniec K, Ahrer W (2010) Conference report: 18th World Hydrogen Energy Conference. J Clean Prod 18:S123–S125

17. Ozbilen A, Dincer I, Naterer GF, Aydin M (2012) Role of hydrogen storage in renewable energy management for Ontario. Int J Hydrogen Energ 37:7343–7354

18. Dufour J, Serrano DP, Galvez JL, Moreno J, Garcia C (2009) Life cycle assessment of processes for hydrogen production: environmental feasibility and reduction of greenhouse gases emissions. Int J Hydrogen Energ 34:1370–1376

19. Boehm R, Chen Y, Earl B, Hsieh S, Moujaes S (2003) H2 Technology Survey. UNLV Program, University of Nevada Las Vegas, Center for Energy Research, November 25. Available from www.unlv.edu

20. Pilavachi PA, Chatzinapagi AI, Spyropoulou AI (2009) Evaluation of hydrogen production methods using the analytic hierarchy process. Int J Hydrogen Energ 34:5294–5303

21. Dincer I, Zamfirescu C (2012) Sustainable hydrogen production options and the role of IAHE. Int J Hydrogen Energ. doi:http://dx.doi.org/10.1016/j.ijhydene.2012.02.133

22. Zeng K, Zhang D (2010) Recent progress in alkaline water electrolysis for hydrogen production and applications. Prog Energy Combust Sci 36:307–326

23. Utgikar V, Thiesen T (2006) Life cycle assessment of high temperature electrolysis for hydrogen production via nuclear energy. Int J Hydrogen Energ 31:939–944

24. Herring S, Gougar H (2011) High-temperature electrolysis for hydrogen production from nuclear energy, INL, Idaho National Laboratory, Publication: 05-GA50193-19

25. Balta MT, Dincer I, Hepbasli A (2009) Thermodynamic assessment of geothermal energy use in hydrogen production. Int J Hydrogen Energ 34:2925–2939

26. Curran MA (ed) (2012) Life cycle assessment handbook: a guide for environmentally sustainable products. Wiley, Hoboken, NJ

27. International Organization for Standardization (ISO) (1997) ISO 14040, Environmental management - life cycle assessment – principles and framework

28. International Organization for Standardization (ISO) (1998) ISO 14041, Environmental management - life cycle assessment – goal and scope definition and inventory analysis

29. International Organization for Standardization (ISO) (2000a) ISO 14042, Environmental management - life cycle assessment – life cycle impact assessment

30. International Organization for Standardization (ISO) (2000b) ISO 14043, Environmental management - life cycle assessment – life cycle interpretation

31. International Organization for Standardization (ISO) (2006) ISO 14044, Environmental management - life cycle assessment – requirements and guidelines

32. Curran MA (2000) Life cycle assessment: an international experience. Environ Progress 19:65–71

33. Guinée JB, Gorrée M, Heijungs R, Huppes G, Kleijn R, Koning A de, Oers L van, Wegener Sleeswijk A, Suh S, Udo de Haes HA, Bruijn H de, Duin R van, Huijbregts MAJ (2002) Handbook on life cycle assessment. Operational guide to the ISO standards. I: LCA in perspective. IIa: Guide. IIb: Operational annex. III: Scientific background. Kluwer Academic Publishers, Dordrecht.

34. Goedkoop M, Demmers M, Collignon M (1996) The eco-indicator 95 manual for designers, national reuse of waste research programme, Netherlands

35. Steen B (1999) A systematic approach to environmental priority strategies in product development (EPS). Version 2000 – general system characteristics. CPM report 1999:4, Center for Environmental Assessment, Chalmers University of Technology, Gothenburg, Sweden

36. Jolliet O, Margni M, Charles R, Humbert S, Payet J, Rebitzer G, Rosenbaum R (2003) IMPACT 2002+: a new life cycle impact assessment methodology. Int J Life Cycle Assess 8:324–330
37. Parry ML, Canziani OF, Palutikof JP, van der Linden PJ, Hanson CE (2007) Contribution of Working Group II to the Fourth Assessment Report of the Intergovernmental Panel on Climate Change, 2007. Cambridge University Press, Cambridge, UK
38. Spath PL, Mann MK (2001) Life cycle assessment of hydrogen production via natural gas steam reforming. National Renewable Energy Laboratory (NREL), Golden, CO, TP-570-27637
39. Spath PL, Mann MK (2004) Life cycle assessment of hydrogen production via wind/electrolysis. Technical report. NREL, National Renewable Energy Laboratory, Golden, CO, MP-560-3504
40. Marquevich M, Sonnemann GW, Castells F, Montane D (2002) Life cycle inventory analysis of hydrogen production by the steam-reforming process: comparison between vegetable oils and fossil fuels as feedstock. Green Chem 4:414–423
41. Koroneos C, Dompros A, Roumbas G, Moussipoulos N (2004) Life cycle assessment of hydrogen fuel production processes. Int J Hydrogen Energ 29:1443–1450
42. Utgikar V, Ward B (2006) Life cycle assessment of ISPRA Mark 9 thermochemical cycle for nuclear hydrogen production. J Chem Technol Biotechnol 81:1753–1759
43. Solli C, Stromman AH, Herrtwich EG (2006) Fission or fossil: life cycle assessment of hydrogen production. Proc IEEE 94:1785–1794
44. Koroneos C, Dompros A, Roumbas G (2008) Hydrogen production via biomass gasification: a life cycle assessment approach. Chem Eng Process 47:1267–1274
45. Djomo SN, Humbert S, Blumberga D (2008) Life cycle assessment of hydrogen produced potato steam peels. Int J Hydrogen Energ 33:3067–3072
46. Lubis LL, Dincer I, Rosen MA (2010) Life cycle assessment of hydrogen production using nuclear energy: an application based on thermochemical water splitting. J Energy Resour Technol 132:210041–210046
47. Chouai A, Laugier S, Richon D (2002) Modeling of thermodynamic properties using neural networks application to refrigerants. Fluid Phase Equilibr 199:53–62
48. Kizilkan O (2011) Thermodynamic analysis of variable speed refrigeration system using artificial neural networks. Expert Sys Appl 38:11686–11692
49. Simpson MF, Herrmann SD, Boyle BD (2006) A hybrid thermochemical electrolytic process for hydrogen production based on the reverse Deacon reaction. Int J Hydrogen Energ 31:1241–1246
50. Motupally D, Mah DT, Freire FJ, Weidner JW (1998) Recycling chlorine from hydrogen chloride. Electrochem Soc Interf 7:32–36
51. Petri MC, Yildiz B, Klickman AE (2006) US Work on technical and economic aspects of electrolytic, thermochemical, and hybrid processes for hydrogen production at temperatures below 550 °C. Int J Nuclear Hydrog Prod Appl 1:79–91
52. Pioro IL, Duffey RB (2007) Heat transfer and hydraulic resistance at supercritical pressures in power engineering applications. ASME, New York
53. Akdag U, Komur MA, Ozguc AF (2009) Estimation of heat transfer in oscillating annular flow using artificial neural Networks. Adv Eng Softw 40:864–870
54. Hope CW (2006) The social cost of carbon: what does it actually depend on? Clim Policy 6:565–572

Chapter 27
Large Scale Photo-reactors for Environmentally Benign Solar Hydrogen Production

Ehsan Baniasadi, Ibrahim Dincer, and Greg F. Naterer

Abstract In this entry, photo-reactors for catalytic solar hydrogen production are introduced and explained. To be an economical environmentally benign and sustainable pathway, hydrogen should be produced from a renewable energy source, i.e., solar energy. Solar driven water splitting combines several attractive features for sustainable energy utilization. The conversion of solar energy to a type of storable energy has crucial importance. In the first part of the entry, background information is presented regarding different photo-reactor configurations for water dissociation with light energy to generate hydrogen. The photo-electrochemistry of water splitting is discussed, as well as photo-catalytic reaction mechanisms. The design and scale-up of photo-reactors for photo-catalytic water splitting are explained by classification of light-based hydrogen production systems. At the end, a new photo-catalytic energy conversion system is analyzed for continuous production of hydrogen at a pilot-plant scale. Two methods of photo-catalytic water splitting and solar methanol steam reforming are investigated as two potential solar-based methods of catalytic hydrogen production. The exergy efficiency, exergy destruction, environmental impact, and sustainability index are investigated for these systems. The light intensity is found to be one of the key parameters in design and optimization of the photo-reactors, in conjunction with light absorptivity of the catalyst.

Keywords Photo-reactor • Environmentally benign • Solar hydrogen production • Catalytic solar hydrogen production • Sustainable energy utilization

E. Baniasadi (✉) • I. Dincer
Faculty of Engineering and Applied Science, University of Ontario Institute of Technology (UOIT), 2000 Simcoe Street North, Oshawa, ON, Canada L1H 7K4
e-mail: ehsan.baniasadi@uoit.ca; ibrahim.dincer@uoit.ca

G.F. Naterer
Faculty of Engineering and Applied Science, Memorial University of Newfoundland, St. John's, NL, Canada A1C 5S7
e-mail: gnaterer@mun.ca

• Photo-electrochemistry • Water splitting • Photo-catalytic reaction mechanisms
• Solar methanol steam reforming • Exergy efficiency • Exergy destruction • Environmental impact • Sustainability index • Absorptivity • Catalyst

Nomenclature

A	Surface area (m^2)
D_P	Depletion number
$\overline{ex}$	Molar specific exergy (kJ $kmol^{-1}$)
ex	Specific exergy (kJ kg^{-1})
Ex	Exergy (kJ)
$\dot{Ex}_S$	Exergy rate of solar radiation per unit area (W m^{-2})
F	Faraday constant (C mol^{-1})
G	Gibbs free function (kJ)
h	Convective heat transfer coefficient (kW m^{-2} K^{-1})
$\overline{h}$	Molar specific enthalpy (kJ $kmol^{-1}$)
j	Radiosity (kW m^{-2})
K	Monochromatic intensity of radiation, depending on λ (kWm^{-3} srd^{-1})
$\dot{n}$	Hydrogen production rate (mol s^{-1})
P	Pressure (Pa)
Q	Heat flow (kJ kg^{-1})
R	Gas constant (J mol^{-1} K^{-1})
s	Specific entropy (kJ kg^{-1} K^{-1})
S	Entropy of the monochromatic intensity of radiation (kW m^{-3} K^{-1} srd^{-1})
$\overline{s}$	Molar specific entropy (kJ $kmol^{-1}K^{-1}$)
T	Temperature (K)
U	Voltage (V)
V	Velocity (m s^{-1})

Acronyms

CPC	Compound parabolic concentrator
Emi	Emission (kg kWh^{-1})
HER	Hydrogen evolving reaction
HHV	Higher heating value
OER	Oxygen evolving reaction
SI	Sustainability index
NHE	Standard hydrogen electrode
VIS	Visible wavelength, 400–700 nm
UV	Ultraviolet

Greek Symbols

α Absorptivity
γ Radiation weakening factor
λ Wavelength (m)

Subscripts

0   Environment
r   Reaction
nV   Non-visible wavelength range
s   Surface
S   Sun
V   Visible wavelengths range

Superscripts

ch   Chemical
ph   Physical

27.1 Introduction

Conventional fossil fuel energy resources, which are used to meet most of the world's energy requirements, have been depleted to a great extent. Almost all resources of green energy involve variation, regional, or seasonal limitations. Following the quick rise in the world energy demand the consumption of chemicals, materials, and fuels is an increasing necessity of each society. It is therefore necessary to produce an alternative fuel that should be pollution-free, storable, and economical. Recent global climate changes have raised many concerns and led to extensive R&D on alternative, clean energy sources. Hydrogen is envisioned being an attractive candidate for a clean, sustainable fuel and underpins the intense interest in creating artificial systems that use catalysts based on abundant elements in the Earth to achieve efficient hydrogen production from water [1–3].

With respect to hydrogen economy, hydrogen has emerged as the ideal energy carrier to store and distribute renewable energy resources. One of the most reliable ways of utilizing solar energy is to convert and store it in the form of an energy carrier such as hydrogen. This valuable chemical compound can be utilized in fuel cell or combustion engine facilities to generate power or heat with zero carbon emission, providing water as a reusable by-product.

Today, electricity is the principal energy carrier and will be still considered as remarkable commodity in long term future. However, the promising role of the

Table 27.1 A DOE roadmap for hydrogen economy transition (modified from [5])

| | Hydrogen industry segments | | | | |
	Public policy framework	Production process	Delivery	Storage technologies	Conversion technologies
2000	• Security • Climate • Hydrogen safety ↓	Natural gas reforming/ biomass	• Pipeline • Trucks, rail, garages	Pressurized tanks	Combustion
2010	Outreach and acceptance	Gasification of coal			
2020		Electrolysis using renewables and nuclear	Onsite distributed facilities	Solid state (hydrides)	• Fuel cells • Advanced combustion
2030	Public confidence in hydrogen	Thermochemical water splitting		Mature technologies for mass production	Mature technologies for mass production
2040	gas as an energy carrier	Photo-catalytic water splitting	Integrated central distributed network	Solid state	

hydrogen as a complementary career in large scale storage and long distance distribution should not be ignored. The US Department of Energy (DOE) has proposed a roadmap for the transition to a hydrogen economy, as illustrated in Table 27.1.

Nowadays, the industry market demand for hydrogen is more than 5,000,000 kg consumption per year [4]. The low density, high thermal conductivity, and strong chemical reducing properties make hydrogen the major applicant for industries including the chemical production, semiconductor processing, generator cooling, etc. The current application of hydrogen to upgrade conventional petroleum products, large-scale ammonia and methanol production, and production of pharmaceuticals is quickly rising. As the global population continues to increase, the demand for hydrogen will significantly increase.

To meet the uprising demands, current H_2 production technologies based on fossil fuel conversions are mainly in use. Steam reforming of natural gas supplies almost 50 % of the global demand for hydrogen, oil/naphtha reforming in refinery industries provides about 30 %, and the rest is mainly produced by coal gasification, and water electrolysis. Steam reaction with methane at high temperature as a high efficiency method, called steam methane reforming (SMR), is highly invested in North America [6].

The common ways of hydrogen production impose many concerns regarding the fossil fuel sources declination, CO_2 emission, and ecological impacts. Subsequently, all the downstream industries that consume hydrogen involve the aforementioned drawbacks and risks. Therefore, H_2 production technologies with almost

zero greenhouse gas emissions are the ideal candidates to address the hydrogen supply issue. In one approach, biomass gasification can be utilized to release hydrogen and carbon monoxide. Considering the CO_2 adsorption characteristics during photosynthesis process, this method is basically carbon neutral. Alternatively, water electrolysis using renewable power sources such as geothermal, wind, and solar cells can be utilized.
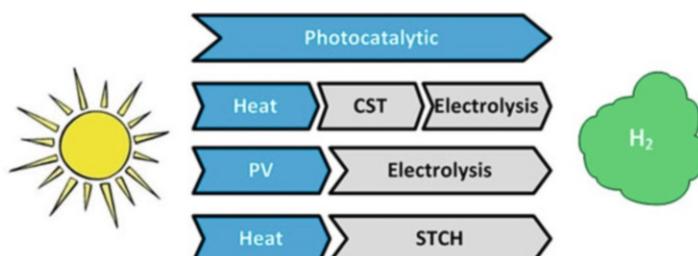
27.2   Background

Water as the most available source on the earth is the major resource of hydrogen. Various procedures may be utilized to extract hydrogen including electrolysis, photolysis, water purification, etc. Hydrogen production from water splitting requires two molecules of water to donate four-valence electrons to the oxygen nucleus and protons in a general reaction according to: $2H_2O \rightarrow 2H_2 + O_2$. This process consumes at least 4.92 eV of energy to generate one molecule of oxygen and two molecules of hydrogen. Additionally, a hydrogen separation method should be utilized to distinct a pure hydrogen and oxygen stream [7, 8].
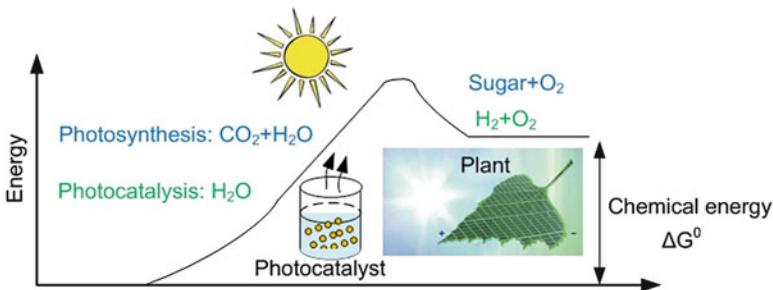
Among various water splitting technologies, water electrolysis is more maturely developed. Water splitting via sunlight to produce hydrogen can be achieved through several conversion routes, as shown in Fig. 27.1. However, more progress with regard to efficiency improvement and water impurities is required. The energy required for water splitting can be supplied through thermal, electrical, photonic, and biological sources plus hybridization of these possibilities [9, 10].

High-temperature direct thermo-electrolysis of water (>2,500 K) [11], and lower-grade thermal energy thermochemical methods (below 1,000 K) are mainly developed to split the water molecule and separate the products by conducting a series of chemical reactions through intermediate compounds [12]. Photonic radiation can be used in several routes to split the water molecule, either through photolysis or in hybrid manner such as photo-electrochemical processes.

As shown in Fig. 27.1, the so-called solar thermochemical (STCH) approach triggers by a photon-to-thermal conversion step followed by a thermal-to-chemical

Fig. 27.1 Technical routes for solar-to-hydrogen conversion

Fig. 27.2 Analogy of the photo-catalytic water splitting (artificial photosynthesis) with photosynthesis of the green plants

process. In another two-step route, photon-to-electric process initiates the process and an electric-to-chemical conversion step accomplishes afterward. The concentrating solar thermal (CST) electrolysis pathway comprises three steps of photon-to-heat, heat-to-electricity, and electric-to-chemical conversions. The direct process of photon-to-chemical conversion, so-called photo-electrochemical, is another alternative pathway.
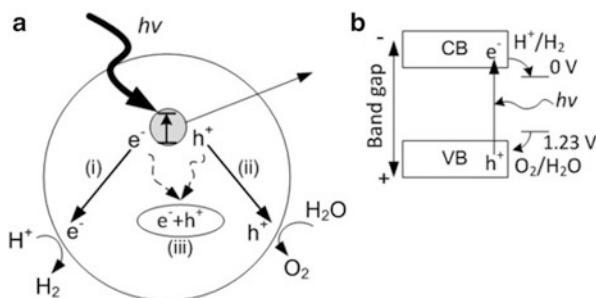
Hydrogen and electricity play a key role as effective energy carriers in the future of energy economics. Therefore, the hydrogen production routes like PV-electrolysis and CST-electrolysis that implement both could be more beneficial. Recent progresses in science indicate the viability of producing inexpensive electricity and hydrogen using semiconductors in near future. The high energy losses associated with the multistep conversion pathways of the aforementioned techniques has to be treated in a way. From this perspective, the single-stage techniques like photo-catalysis could be beneficial in terms of minimum process irreversibilities (Fig. 27.2). The direct conversion processes for hydrogen production, as one of the most promising alternatives, mimics photosynthesis to absorb light and convert water into H_2 and O_2 using inorganic semiconductors through water-splitting reaction [13].

The pioneering efforts by Fujishima and Honda [14] in 1972 on the semiconductors ,that are capable of absorbing light energy, introduced this type of materials as effective means of water splitting reaction for hydrogen generation. Since then, numerous studies are inspired to develop various types of semiconductors for photo-catalytic water dissociation and to enhance their performance under visible light by more efficient utilization of the solar spectrum [15, 16].

27.3 Photo-electrochemical Water Splitting

The possibility to transmit energy to every point of a volume using photonic radiation is applicable to water cleavage process. Since pure water does not absorb radiation in the visible and near-ultraviolet ranges, the dissociation of water is

Fig. 27.3 Basics of photo-catalytic water splitting: (**a**) Photo-excitation and subsequent processes on catalyst surface. (**b**) Photo-excitation and electron–hole generation
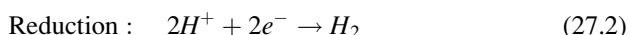
technically possible by either electromagnetic rays, e.g., exposing water to higher-frequency radiation such as extreme UV, X, and gamma rays, or using molecular photosensitizers dissolved/suspended in water, to capture the solar radiation in the visible and UV ranges. The latter approach constitutes important paths for solar driven water splitting. In this regard, the interaction of photonic radiation with photo-catalyst and water molecules is important for technology development.

The theoretical potential for water splitting process is 1.23 eV per molecule. This energy corresponds to the wavelength of 1,010 nm that makes about 70 % of the solar irradiated photons eligible for deriving water cleavage reaction. However, the amount of the energy per photon should be higher than the minimum value of 1.23 eV in order to compensate the intrinsic energy losses associated with the redox reactions on the surface of the photo-catalyst [17].

The photo-catalytic water splitting is initiated with the absorption of light photons with energies higher than the band-gap energy (Eg) of a semiconductor. As depicted in Fig. 27.3, following the absorption process excited photoelectrons are generated in the conduction band (CB) and holes in the valence band (VB) of the semiconductor. Once the photo-excited electron–hole pairs are created in the material bulk, they migrate to the surface separately (represented by routes i and ii).

This process is in continuous competition with the electron–hole recombination process (route iii in Fig. 27.3) that leads to heat generation. Eventually, the water molecules in vicinity of catalytic active sites are reduced and oxidized by photo-induced electrons and holes to produce gaseous hydrogen and oxygen, respectively. The decomposition of water into H_2 and O_2 requires a large positive change in the Gibbs free energy ($\Delta G_0 = 237$ kJ mol^{-1}, 2.46 eV per molecule). The following reactions are performed in an acidic medium:

$$\text{Oxidation}: \quad H_2O + 2h^+ \rightarrow 2H^+ + 1/2O_2 \qquad (27.1)$$

$$\text{Reduction}: \quad 2H^+ + 2e^- \rightarrow H_2 \qquad (27.2)$$

The water dissociation process refers to either half-processes such as water reduction to hydrogen and hydroxyl ions or water oxidation to oxygen and protons, or to the complete conversion of water to hydrogen and oxygen. The photochemical process of water splitting does not necessarily involve a complete water splitting process.

Fig. 27.4 General configu-
rations for photo-catalytic
water splitting;
(**a**) electrode-based, and
(**b**) particle-based
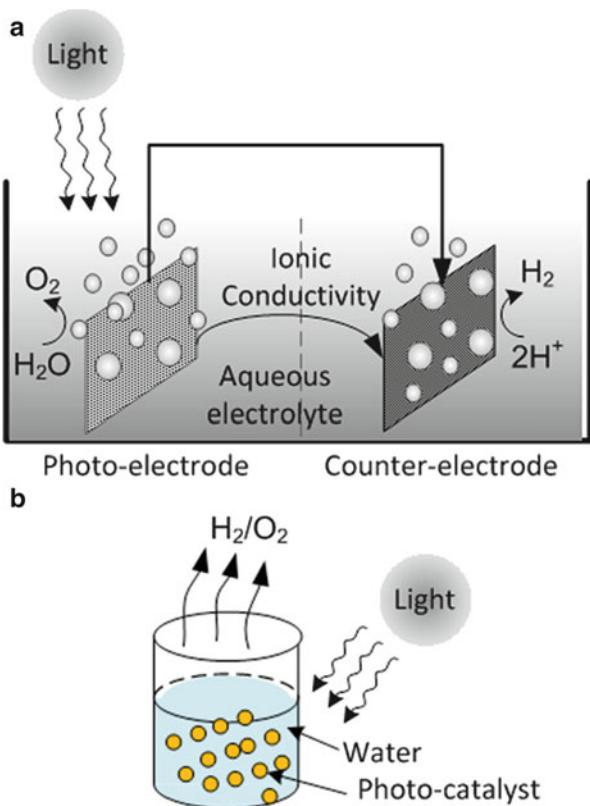
Photo induced half-reactions to generate hydrogen mainly occur according to $\left[2H_2O + 2e^- \xrightarrow{h\nu} H_2(g) + 2OH^-\right]$ in alkaline medium. The hydroxide ion by-product can be further processed through electro-catalytic oxidation to generate oxygen.

Two major configurations of photo-catalytic technique for water cleavage are electrode-based, and particle-based. The first method implements two electrodes immersed in an aqueous electrolyte, one is the semiconductor photo-catalyst exposed to light and the other is a counter-electrode to facilitate the electron flow circuit (Fig. 27.4). The second system is based on photo-catalysts in the form of suspended particles in an electrolyte (Fig. 27.4).

In this system, each particle acts as a micro-photo-electrode to conduct redox active sites for splitting water. In comparison, particle based configuration has some disadvantages with respect to electron–hole separation efficiency and reverse reaction of the products on the surface of the photo-catalyst, that leads to conversion rates. However, photo-catalysts in particle form have the advantage of much simpler and less expensive synthesize. Aside from these two configurations that undergo heterogeneous catalysis, another approach of homogenous catalysis based on interaction of complex molecular structures in a solution is also feasible.

27.3.1 Heterogeneous Photo-catalysis

The photo-catalysts in solid phase implemented in reaction of water dissociation in liquid phase, is denoted as heterogeneous. These catalysts are applied in powder and electrode form. Photo-electrodes are widely being developed to enhance the efficiency of water catalysis. The photo-electrode structure consists of a conductive material like noble metals doped with photo-catalysts. The conductivity of electrode material facilitates the migration of electrons from its conduction band to valence band and eventually to the active catalytic sites where water electrolysis is performed. The photo-electrodes in a photo-reactor configuration are exposed to solar radiation through transparent windows. Direct incident light together with electrical potential bias, supplied by an external electrical power supply, is utilized to activate active sites.

The small band gap between the valence and conduction bands of semiconductors make them suitable to develop heterogeneous photo-catalysis. Some semiconductors such as titanium dioxide have both photosensitization and photo-catalytic attributions. So when semiconductor is exposed to light, it absorbs photons and dislocates electrons from the valence band to the conduction band. It eventually facilitates redox reactions at the photo-catalyst surface. The performance of photo-catalysts is usually enhanced to overcome the redox potentials through two possible routes:
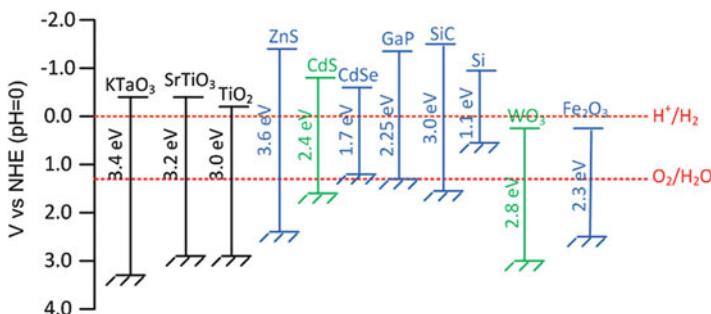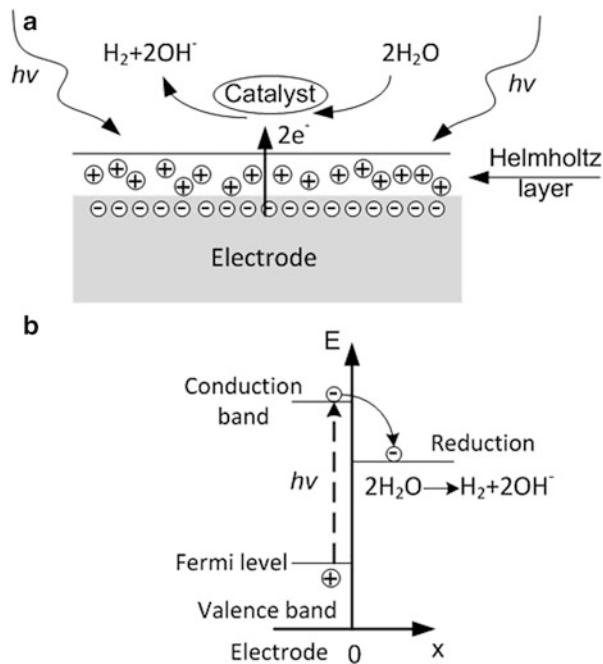
(i) Applying a bias voltage to the electrode via an external power supply
(ii) Electrode coating or doping with photo-synthesizer materials

The heterogeneous photo-catalysis process is illustrated in Fig. 27.5. The reaction mechanism is introduced in Fig. 27.5a, and the reduction pathway is shown in Fig. 27.5b, respectively. Following the light absorption and activation of catalytic sites heterogeneous catalysis occurs at the solid surface. The catalyst reduces the activation energy without being consumed. In order to quantify its ability of photo-catalyst to interact with reactant molecules the turnover number (TON) is defined as the number of reactants that are treated with catalyst before degradation. The turnover frequency (TOF) is also an indicative parameter that represents the number of converted reactants by photo-catalyst per unit of time.

A layer of ionized solvent molecules called Helmholtz layer hosts the electron transfer from the active site to the reactant molecules. This layer is adjacent to the solid–liquid interface with a thickness of 1 Å. The electrons migrate to the reacting molecules through the Helmholtz layer. The semiconductor has the same Fermi energy levels of Helmholtz layer, and therefore the process of electron transfer is iso-energetic. The dislocated electron in the conduction band then falls into a lower energetic level to accomplish the reduction reaction (Fig. 27.5a).
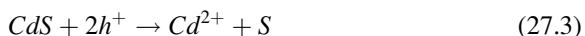
Figure 27.6 shows the band levels of various semiconductor materials. The pH of the solution usually changes the band levels by -0.059 V/pH for oxide materials. According to the information in Fig. 27.6, ZrO_2, $KTaO_3$, $SrTiO_3$, and TiO_2 have suitable band structures for water splitting. These materials are usually modified with co-catalysts to be active for water splitting.

Fig. 27.5 (**a**)
Heterogeneous photo-
catalysis mechanism,
(**b**) reduction reaction
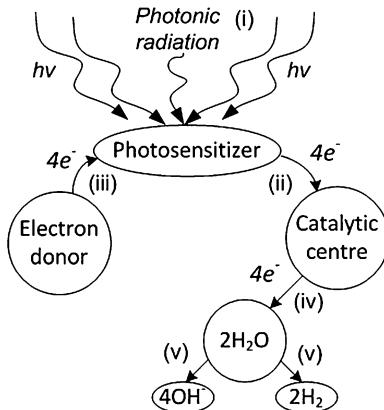
Fig. 27.6 Relationship between band structure of semiconductor and redox potentials of water splitting (modified from [19])

The n-type semiconductors such as cadmium sulfide or zinc sulfide are recognized as potential photo-catalyst for large scale hydrogen production. However, they involve anodic photo-corrosion in aqueous solutions that leads to the formation of sulfur and/or sulfate ions according to:

$$CdS + 2h^+ \rightarrow Cd^{2+} + S \tag{27.3}$$

However, they are promising photo-catalysts for H_2 evolution under visible and ultra-violate light irradiation if reducing agents acting as hole scavengers, like S^{2-},

Fig. 27.7 Homogeneous
photo-catalysis process with
complex molecular
structure

SO_3^{2-}, or $S_2O_3^{2-}$ exist in the aqueous solution to stabilize cadmium sulfide and
zinc sulfide efficiently [18].

27.3.2   Homogeneous Photo-catalysis

Homogeneous photo-catalysts consist of complex molecular structures that perform
photo-catalytic water splitting starting from photosensitization. Subsequently,
charge separation, charge transfer, and catalysis processes are conducted by the
molecular structure. Figure 27.7 shows the process of homogeneous photo-catalysis
for hydrogen-evolution.

The series of events initiates with photon absorption of the photo-sensitizers that
turns to its excited state. The excited state form of photo-sensitizer interacts with
the catalyst and it translocates an electron to the active catalytic center. The photo-
sensitizers returns to reactive state by absorbing an electron from the electron donor
dissolved in the solution. The electron donor remains stable in the solution. Water
reduction reaction is then accomplished by electron transfer through catalytic active
centers. Four catalytic cycles are performed following four times photon absorption
to complete a water dissociation reaction.

27.4   Design and Scale-up of Photo-reactors
     for Photo-catalytic Water Splitting

Among industrial applications photo-catalytic water splitting is limited due to
process efficiency and the lack of knowledge on engineering scale-up. Comparing
with conventional reactors, the design and scale-up of photo-reactors involve more

complexity due to intervention of radiation transfer along with mass, momentum, and heat transfers. The catalysts in liquid-phase photo-catalytic systems are either suspended or immobilized in reactors.

In general, the efficiency of suspended systems is higher than immobilized systems. However, the attenuation of light intensity through absorption and scattering by suspended particles creates a challenge from design stand point. This also makes difficulties to simulate the kinetic model and subsequently in the scale-up of reactors. The kinetic model of suspended systems cannot be extrapolated to another reactor size and configurations unless it accompanies an explicit light irradiation model. Dealing with radiation transfer in immobilized systems is quite simpler than suspended systems since absorption and scattering effects are not involved. Hence, the kinetic modeling and scale-up analysis of immobilized surface area of catalysts under illumination are simpler. Due to the uncertainties of the light and mass transfer effect, photo-reactor scale-up methodologies based on the illuminated surface area of catalysts in liquid-phase photo-catalysis are still immature.
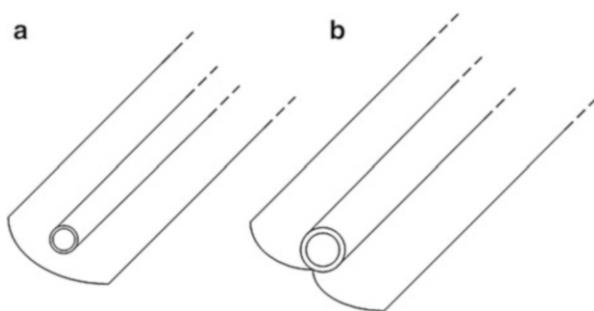
In order to develop industrial photo-reactors, a device with high capability of capturing photons and bringing the reactants into contact with the photo-catalyst, as well collecting the reaction product should be designed. The critical importance of reactor geometry to ensure the effective collection of photons makes a significant difference between photo-reactors and traditional chemical reactors. Various aspects of photo-catalytic systems have been investigated, however, photo-reactor design has not been standardized and each research team in obeying individual designs. In fact, any performance difference is attributed to specific number of variables which differ between studies. The solar photo-reactors for hydrogen production are mainly distinguished in either form of parabolic trough system, inclined plate collectors, optical fiber photo-reactors, and fluidized bed photo-reactors.

27.4.1 Parabolic Trough Reactors

Despite the significant difference between operational requirements of solar photo-reactors and solar thermal collectors, the well-established parabolic reflectors in solar thermal engineering can be implemented for efficient collection and absorption of photons on a specific area or volume of a solar photo-reactor. Adopting the solar thermal collector design, parabolic trough reactor is developed that consists of a long, reflective, parabolic surface to concentrate solar radiation on a transparent tube. This tube conveys reactant fluid flows along the parabolic focal line. Since the surface area of the reflecting surface is essentially larger than absorber tube, the light intensity on the photo-catalyst increases through concentration of the photons.

The direct concentration of sunlight onto the photo-catalyst creates both an advantage and disadvantage for parabolic trough reactors. The greatest benefit

attributes to the increase of light intensity, which reduces the photo-catalyst consumption comparing to non-concentrating photo-reactors with the same light collecting area [20]. Consequently, it provides the capability of utilizing absorber tube with smaller diameters, greater operating pressures and higher quality materials without high increase of the capital investment.

Industrial-scale plants incorporate several absorber tubes and associated components with significant pressure losses. Therefore, the advantage of operating at higher pressures is accounted as a significant benefit. A reduction in the quantity of required photo-catalyst is in favor of reducing operating costs. It reduces particle agglomeration and simplifies the separation process and recycling of the suspended photo-catalyst as well as material handling requirements.
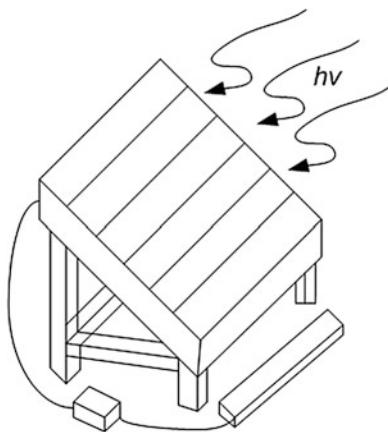
Utilization of compound parabolic collector overcomes some of the problems associated with parabolic trough reactors. The reflector geometry of these components has the advantage of reflecting the indirect light onto the absorber tube surface. There is a concentration factor associated with each compound parabolic collector according to:

$$CF = \frac{1}{\sin \theta_a} = \frac{w}{2\pi r} \tag{27.4}$$

where CF is the concentration factor, θ_a is the acceptance half angle, w is the width of the reflector aperture, and r is the radius of the absorber tube. Therefore, an acceptance half angle of 90° makes a concentration factor of 1 sun that means all direct and diffuse light entering the aperture is reflected onto the absorber tube. Figure 27.8 shows the reflector profile of parabolic trough reactor and compound parabolic collector.

This aperture increases the total quantity of photons comparing to a parabolic trough reactor and also provide the capability of working on cloudy days when direct light is unavailable. A parabolic trough reactor concentrates the light on the bottom hemisphere of the absorber tube, whereas compound parabolic collector distributes the incident light over the entire surface of the absorber tube homogenously.

Fig. 27.9 A reactor layout for an inclined plate collector (modified from [23])

27.4.2 Inclined Plate Collectors

The main design considerations of the concentrating parabolic and non-concentrating compound-parabolic reactors have roots in commercial solar thermal technologies. The photo-catalytic processes based on these systems seems to be viable, but it doesn't necessarily offer the optimal design. If a solar photo-catalytic reactor is designed specifically for convenient accommodation of the photo-catalyst and maximizing the mass transfer between the photo-catalyst and the reactant fluid through effective illumination of the photo-catalyst, higher efficiency than conventional parabolic reflecting reactors can be achieved.

An inclined plate collector is basically an assembly of a flat, inclined surface for thin film reactant fluid flows. This design in particular matches the supported photo-catalyst on the surface of the inclined plate. The photons essentially migrate through the reactant fluid and eventually reach the photo-catalyst. Different types of material can be used to fabricate the backing plate [21].

This design is extensively used in research facilities because of the relative simplicity, low cost materials, and suitability for supported photo-catalyst. It has the advantage of eliminating efficiency losses due to reflective surface in parabolic trough reactor and compound parabolic collector, although the lack of concentration of the incoming photons does not allow capturing diffuse light. To further increase the efficiency the reactor may be fabricated with open face to the atmosphere to eliminate light adsorption by the reactor covering and prevent forming an opaque film by suspended photo-catalyst. The maximum diffusion thickness is essentially limited to the thickness of the film, and thin-fluid film enable the maximum mass-transfer rates between the different phases of the reactor [22]. Figure 27.9 illustrates a typical layout of an inclined plate reactor.

The effectiveness of inclined plate collectors at commercial scale is limited due to some practical drawbacks regarding the thin fluid film. The thin fluid film for this

type of photo-reactors are typically in the range of 100–200 μm, that requires maintaining flow rates of about 0.15–1 L min^{-1} m^{-2} collection plate area. In contrast to parabolic trough reactor and compound parabolic collector, the reactant fluid is not enclosed over the surface, and adjusting the flow rate or pressurizing through an open surface plate cannot be easily handled. Increase of the flow rate causes decrease of the residence time of the reactant fluid on the collector plate which leads to increase of the fluid film thickness [24]. The mass-transfer constraint is then ignored and the efficiency of the reactor decreases. The use of a transparent covering may help in a way but it adsorbs some photons and reduces the efficiency of the photo-reactor. There is also a potential for suspended solids to form an opaque solid film on the interior surface of the covering and enhance the photonic absorption.

The simplicity of inclined plate collector in fabrication, and design and their compatibility with a supported photo-catalyst makes them ideally suitable for small scale productions with low fluid volumes.

27.4.3 Optical Fiber Photo-reactors

The solar photo-reactors are basically designed to utilize an external light source. This introduces a drawback regarding effective access of photo-catalyst to light. In fact, light scattering and adsorption phenomenon by photo-catalyst suspensions makes it difficult to provide homogeneous external illumination, and also supported photo-catalysts with compacted surface areas require an un-obscured path for arriving light.

These issues can be addressed by accommodating artificial light sources within the reactor volume. This can be done either by direct immersion of lamp in the reactant fluid or install it within an inner annulus. In an alternative approach, an optical fiber can be implemented to conduct the light from an external light source into the fluid bulk of reactants. In these types of reactors, supporting the photo-catalyst on either the internal lamps or waveguides is superior to a suspended photo-catalyst because the surface area to volume ratios will be significantly enhanced. The implementation of optical fibers with artificial light has been well addressed [25].

Peill et al. has extensively investigated an optical fiber photo-reactor using a bundle of 537 quartz optical fibers at concentration point of a 24 in. parabolic dish with 3.5 in. convex secondary reflector. The fiber is coated with a photo-catalyst and immersed in the reactant fluid. This configuration provided almost 300 suns concentration factor at the entrance of the fiber bundle and lead to a two order-of magnitude reduction in 4 L of a 13 mg L^{-1} solution of 4-chlorophenol during 13 h solar radiation [26].

The advantage of optical fiber photo-reactor over other photo-reactor designs is related to isolation of light gathering process from photo-catalytic components of the reactor. This allows remote collecting the light and transmitting over a long distance through the optical fibers to the photo-reactor that contains solution of reactants and photo-catalyst. Therefore, this design is suitable for indoor facilities, providing appropriate light gathering device and connecting fiber optics. The mechanical

complexity and low efficiency of these reactors compared to other photo-reactor designs limited wider application of this technology.

27.4.4   Fluidized and Fixed Bed Photo-reactors
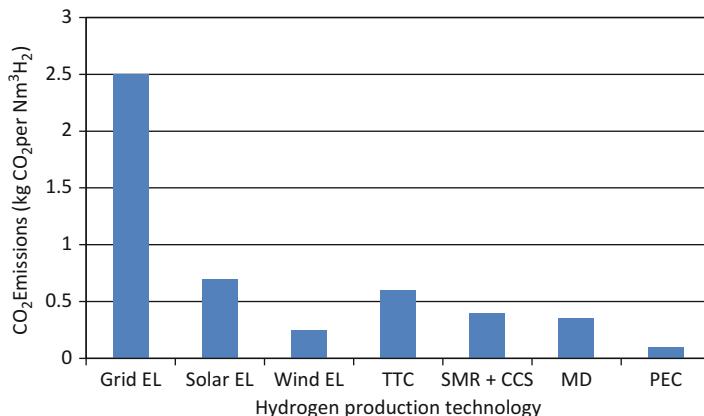
A hybrid approach in photo-catalyst handling is to support photo-catalyst particles on larger particles such as glass beads, to have both advantages of suspended and supported photo-catalysts. Supporting the photo-catalyst on packing materials provides high photo-catalyst surface areas and consequently high mass-transfer rates. Also, the separation process as in supported systems is not necessary anymore. Therefore, Fluidized and fixed bed photo-reactors can effectively serve the gas-phase photoreactions due to the intensive interaction between the reactant and photo-catalyst particles.

The supporting particles or packing has a strong interaction with the incoming light, and leads to a heterogeneous radiation field within the reactor. The major portion of light is absorbed by the particles at around the edge of the photo-reactor within a relatively thin region, and results in poor illumination of the majority of the reaction volume. This effect varies depending on the void fraction and expansion of the bed.

Solar packed/fixed bed photo-reactors are relatively very common in use. Fluidized/fixed bed photo-reactors may introduce an optimal method of photo-catalyst handling as very high quantum efficiency is achievable using this technology [27]. However, the current status of fluidized/fixed bed reactors with solar radiation is limited. In fact, homogeneous illumination of particles throughout the fluidized bed volume is a significant challenge. This issue can be addressed by use of a compound parabolic collector at the exterior of the bed and use of internal reflectors or waveguides to provide homogeneous illumination. However, this configuration has not been investigated so far. The fluidized bed photo-reactors may be introduced as an effective option in water photo-catalysis if the challenges with regard to optimum particle size and photo-catalyst attachment methods are addressed.

27.5   Environmental Impacts of Hydrogen Production and Solutions

Hydrogen with a significant heating value and clean combustion and storage advantages has been recognized as a great fuel alternative. Since hydrogen is regarded as a long-term solution for transport, the environmentally friendly production processes, safe storage and transport methods should be developed. Different methods of hydrogen production either at commercial or laboratory level consist of natural gas and propane gas steam reforming (or partial oxidation, auto-thermal reforming, plasma reforming), coal gasification, petroleum fractions dehydrocyclization and

Fig. 27.10 CO_2 emissions of different H_2 production methodes (*EL* electrolysis, *SMR* steam methane reforming, *CCS* carbon capture and storage, *TTC* two-step thermochemical cycle, *MD* methane decomposition, *PEC* photo-electrochemical water splitting). Modified from [28]

aromatization (or oxidative steam reforming, pyrolytic decomposition), biomass gasification (or steam reforming, biological conversion), water electrolysis, and water photo-catalytic decomposition. The major hydrogen production method in large scale is steam reforming of methane gas. This production technology consumes an important portion of non-renewable resources and incorporates greenhouse gas emissions.

The environmentally friendly hydrogen production methods should be assessed from life cycle perspective. This would assure an effective investigation of real environmental issues and avoid the underestimation of environmental impacts. Therefore, life cycle assessment tools with a focus on the greenhouse gas emissions, consumption of nonrenewable resources, and exergy efficiency should be implemented. Dofour et al. [28] performed a life cycle assessment on different hydrogen production methods. Figure 27.10 shows the highest amount of CO_2 emissions due to hydrogen production from electrolysis process when electricity is assumed to be supplied by a power grid (Grid-EL). In comparison, the solar electrolysis (Solar-EL) and the two-step thermochemical decomposition of water (TTC) has negligible contribution among production processes.

Photo-electrochemical water reduction (PEC) appears to have the lowest environmental impact. However, the simple process of this method comparing with the other multistage processes, durability of the cell and the sacrificial agents should be adjusted for real-scale processes, since the mass balance is considered for lab scale performance. Among the commercial processes, the electrolysis coupled with wind turbines (Wind EL) shows the best performance, while the steam reforming of methane, even with a carbon capture and storage (SMR + CCS) is still emitting considerable amounts of greenhouse gases. Thermal decomposition of methane (MD) performs hydrogen production more environmentally than natural gas reforming.
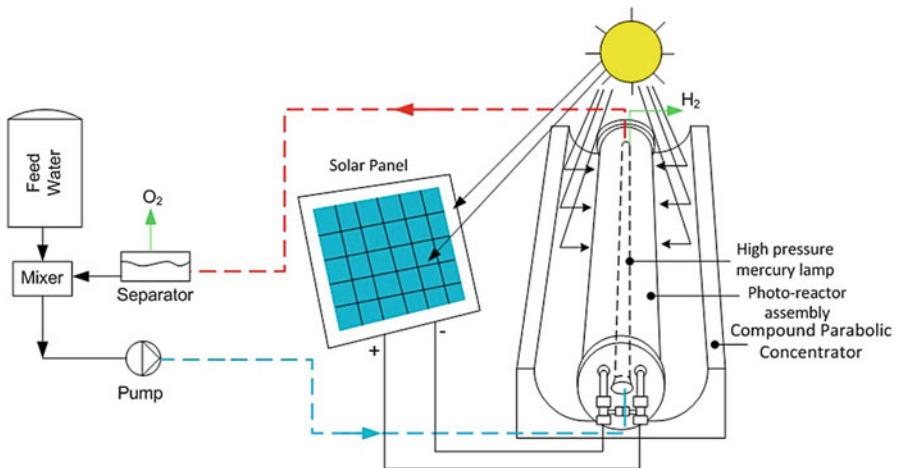
Exergy is one of the most significant tools to assess the impact of energy resource utilization on the environment. The exergy establishes the basis for an effective measure of the potential of a substance or energy form to impact the environment. Dincer et al. [29, 30] enhanced the understanding of the linkages between exergy and energy, and environmental impact in energy systems. The utilization of energy-resources incorporates environmental impact that prevents sustainable development of a society. However, increased efficiency can somewhat compensate the negative impacts of environmental emissions. In order to achieve sustainable development in a society, various hydrogen energy-related solutions can be established as follows:

- Increase of public awareness about the benefits of sustainable energy systems and their environmental advantages through education and training.
- Extensive research and development of environmentally benign hydrogen production technologies.
- Utilization of renewable energy resources to develop sustainable hydrogen infrastructures.
- Implementation of reasonable financing and incentives for cleaner hydrogen related technologies in production, transportation, distribution, and storage.
- Cost-effective utilization of sustainable energy resources such as solar, wind, hydro and biomass for sustainable development of hydrogen economy.
- Sustainability assessment of the processes and systems through exergy–environmental analysis.
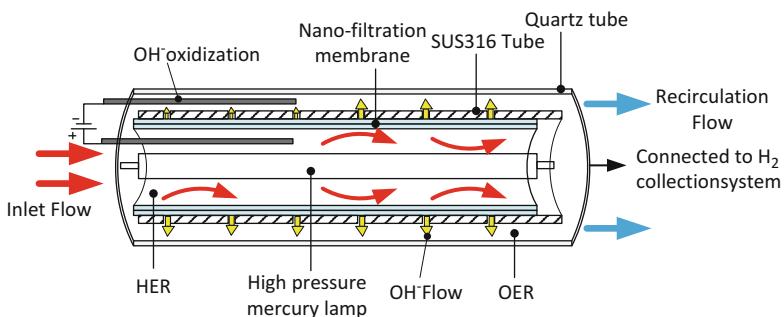
27.6 Case study: Exergy and Environmental Impact Assessment of Solar Photo-reactors

A photo-catalytic reactor activated by sunlight and UV-visible lamps capable of continuous operation under real process conditions is considered here for scale-up purposes. Figure 27.11 shows a schematic of a hybridized photo-catalysis reactor that utilizes light energy from both the sun and a lamp, in conjunction with electrodes to substitute sacrificial electron donors that consume photo-generated holes and transfer charges to a metallic active center of a catalyst that leads to hydrogen production from water. Solar panels are utilized to generate electricity and deliver electrons through the electrode-solution interface. Utilization of UV-visible lamps inside a sunlight concentrator provides the capability of performing photoreactions during night-time or cloudy periods. More details are shown in Fig. 27.12.

This design addresses one of the challenges regarding oxidation and reduction mechanisms in photo-catalysis that involves replenishment of electron acceptors and donors. The analysis will apply an external power source and two electrodes immersed in the catalyst solution to supply and transfer electrons inside two reactors to avoid replenishment of the electron donors. An anion exchange membrane is utilized to separate hydrogen and oxygen in the reactor. This membrane retains the catalyst while allowing passage of the negative ions such as hydroxide

Fig. 27.11 Pilot plant scale hybrid photo-catalytic system for continuous operation, under sunlight and artificial illumination

Fig. 27.12 Schematic of hybrid photo-reactor

ion by-products into a second reactor. The water photo-reduction reaction occurs as follows:

$$2H_2O(l) + 4e^- \xrightarrow{h} H_2(g) + 4OH^-; \quad U_{red} = -0.82\,V, NHE. \tag{27.5}$$

Hydrogen is separated from water in the hydrogen evolution chamber and used for measurement and storage. The transfer of hydroxide ions from the hydrogen evolving reactor to the oxygen evolving reactor and decomposition of these ions to constituent molecules are necessary processes to avoid any rate limiting effects. Subsequently, the pH of the aqueous solution is balanced and the excess charge is

neutralized. The hydroxide ion decomposition at the anode occurs based on the following reaction:

$$4OH^- \rightarrow 2O_2 + 2H_2O(l) + 2e^-; \quad U_{ox} = -0.41\,V, NHE. \qquad (27.6)$$

The neutralized solution recirculates to the inlet flow in order to maintain the species concentration constant. Oxygen is then separated from water in a gas–liquid separation unit after the reactor bed. In conjunction with a solar light source, a 500 W high pressure mercury lamp is utilized to enhance the light intensity and operation at night. Prior to the photo-catalytic reaction, a 10 kW constant-flow pump is used. After the system has reached a steady state, the mercury lamp can be turned on and the photo-catalytic reaction for water splitting is boosted due to a higher light intensity.
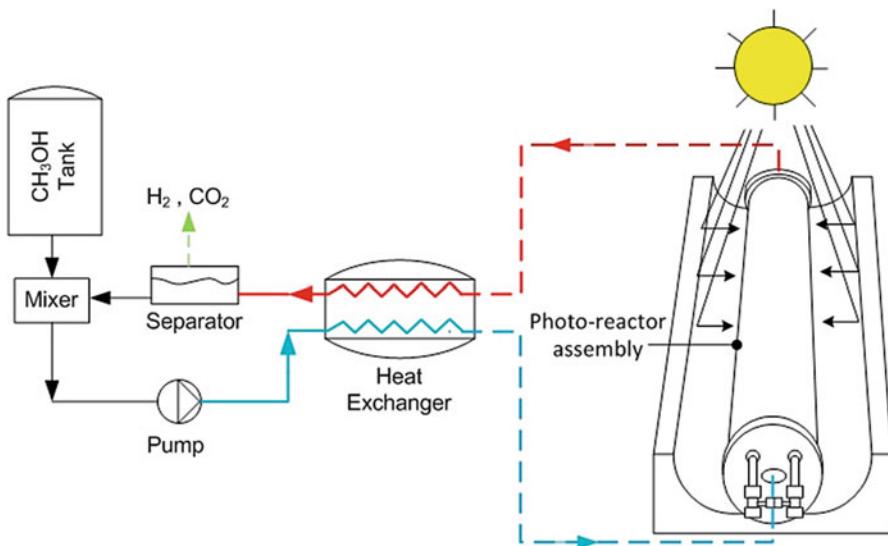
As reported by Malato et al. [31], a Reynolds number between about 10,000–50,000 is selected to ensure fully turbulent flow and avoid the sedimentation and settlement of TiO_2 particles in the tubes. It is also necessary to keep a uniform flow in the reactor to prevent nonuniform residence times that would lower the efficiency compared to ideal conditions. Furthermore, every photo-reactor design must ensure that the useful incoming photons are mostly used and do not escape without having intercepted a particle in the reactor. For the maximum absorbance of solar radiation, the aperture of the CPC should be perpendicular to the incident light as far as possible.

For photo-catalytic hydrogen production, the total volume of recirculating water in the hydraulic loop is 10 L. In this analysis, the catalyst concentration effect on hydrogen production is investigated in the range of 0.3–2 g L^{-1} and the flow rate from 1 to 8 L min^{-1}. The concentration of Na_2S as a sacrificial agent is kept at 0.05 mol L^{-1} during the operation. Photo-catalytic hydrogen production is considered under visible-light irradiation ($\lambda \geq 430$ nm). The reaction temperature is 60 °C. The reactor temperature is controlled to avoid water boiling.

Figure 27.13 shows a general schematic of a system for solar thermal hydrogen production using methanol steam reforming (MSR), which consists of a heat exchanger, solar receiver/reactor, separator, and solar parabolic trough concentrator. During this process, the fresh methanol liquid fuel and the feeding water were initially mixed and fed to the evaporator. The mole ratio of water to liquid methanol was investigated in the range of 1–2.5. The solar flux is also varied from 350 to 850 W m^{-2} and it affects the conversion rate from 20 % to 100 %, respectively [32]. The superheated vapor of methanol and steam generated in an evaporator heat exchanger, as shown in Fig. 27.11, were made to flow into the middle-temperature solar receiver/reactor. The following reaction takes places at relatively low reforming temperatures (150–300 °C):

$$CH_3OH + H_2O \rightarrow CO_2 + 3H_2, \quad \Delta_r H_{298\,K} = 50.7\,kJ\,mol^{-1} \qquad (27.7)$$

In the solar receiver/reactor, methanol steam reforming was driven by solar thermal energy at 150–300 °C. The gas products included H_2, CO_2, non-reacted

Fig. 27.13 Schematic of solar thermal hydrogen production by methanol steam reforming

CH_3OH, and H_2O, which left the reactor and were cooled in a plate-fin condenser by a water-cooling system, where the non-reacted methanol fuel and water were separated from one another. The non-reacted mixture can enter the next loop using a 10 kW constant-flow pump. Production of CO gas is neglected in this analysis.

For both photo-catalytic water splitting and solar-thermal methanol reforming systems, a solar receiver/reactor is considered that consists of a parabolic trough concentrator and a tubular bed receiver/reactor. The parabolic trough concentrator is composed of glass mirrors with 4 m length. The aperture area is 10 m^2 and it delivers up to 6-kW at a peak solar flux. The solar reactor dimensions are designed as 30 mm in outer diameter and 4.5 m in length. A transparent glass with an outer diameter of 50 mm and 0.9 transmissivity level is considered as the receiver/reactor insulation. The catalyst for methanol steam reforming is immobilized in a packed tubular bed, whereas the photo-catalyst for water splitting is suspended in aqueous solution and flows though the hydraulic loop.

27.6.1   Analysis

The analysis of exergy and greenhouse gas emission/reduction of the proposed systems is presented in this section. Exergy analysis is a useful tool to develop strategies and guidelines to enhance the use of energy quality, and recently the method has been successfully applied to hydrogen production systems.

The exergy balance for a process involving chemical reactions can be written as [33]:

$$\sum Ex_{in} - \sum Ex_{out} - Ex_{destruction} = \Delta Ex_{system} \tag{27.8}$$

For a steady-state system, ΔEx_{system} is zero. The exergy associated with a process at a specified state involves physical and chemical contributions. Thus, the specific exergy of a stream associated with the process is:

$$\overline{ex} = \overline{ex}^{ph} + \overline{ex}^{ch} = \left(\overline{h} - \overline{h}_0\right) - T_0(\overline{s} - \overline{s}_0) + \frac{V^2}{2} + gz + \overline{ex}^{ch} \tag{27.9}$$

Combining (27.3) and (27.4) yields:

$$\overline{ex}_{destruction} = \sum \left[\left(\overline{h} - \overline{h}_0\right) - T_0(\overline{s} - \overline{s}_0) + \frac{V^2}{2} + gz + \overline{ex}^{ch}\right]_{in}$$
$$- \sum \left[\left(\overline{h} - \overline{h}_0\right) - T_0(\overline{s} - \overline{s}_0) + \frac{V^2}{2} + gz + \overline{ex}^{ch}\right]_{out} + \left(1 - \frac{T_0}{T_{reaction}}\right)Q \tag{27.10}$$

where Q is the heat flow that interacts with the system (negative for exothermic reactions).

The standard chemical exergy is defined as the chemical exergy of any exergy reference environment with standard values of the environmental temperature T_0 and pressure P_0, such as 298.15 K and 1 atm. In order to determine the standard chemical exergy of any substance, the reaction of the substance with other substances with known standard chemical exergies can be utilized as follows [34]:

$$\overline{ex}^{ch} = -\Delta g + \sum_P n\overline{ex}^{ch} - \sum_R n\overline{ex}^{ch} \tag{27.11}$$

where Δg is the change in the Gibbs function for the reaction, for each separate substance at the temperature T_0 and pressure P_0. The other two terms on the right side of (27.11) are calculated together with n values, which represent the moles of these reactants and products per mole of the substance with a known chemical exergy value. Therefore, the chemical exergy content of methanol can be obtained from the following equation:

$$\overline{ex}^{ch}_{CH3OH} = -\Delta g_{reforming} + 3\overline{ex}^{ch}_{H_2} + \overline{ex}^{ch}_{CO_2} \tag{27.12}$$

Exergy of Solar Radiation Exchange

The following equation for uniform and direct solar radiation exergy, $\dot{Ex}_S$, arriving at the Earth's atmosphere can be written as follows [35]:

$$\dot{Ex}_S = 4.329 \times 10^{-5} \pi \left(\frac{9.445 \times 10^{-12}}{\pi} T_0^4 + \sum_n (K_\lambda \Delta \lambda)_n - T_0 \sum_n (S_\lambda \Delta \lambda)_n \right) \quad (27.13)$$

By substituting $T_0 = 293$ K, and related values for entropy and intensity of each wavelength interval in equation (27.13), the exergy of total solar radiation, $\dot{Ex}_S = 1.2835\,\text{kW}\,\text{m}^{-2}$ and the exergy of visible portion, $\dot{Ex}_V = 0.5155\,\text{kW}\,\text{m}^{-2}$, are calculated.

Exergy of Radiation Exchange at a Surface

The exergy of radiative emission from any surface at the temperature of the local environment, T_0, is zero. Therefore, the exergy of environmental radiation arriving at the reactor surface is zero. The exergy $\dot{Ex}_S$ of emissions from the surface at temperature T_s can be determined by the following equation of Petela [35]:

$$\dot{Ex}_S = \alpha_s \frac{\varepsilon_b}{3} \left(3T_s^4 + T_0^4 - 4T_0 T_s^3 \right) \quad (27.14)$$

Exergy Efficiency

In order to evaluate the irreversibility of photo-catalysis processes, the exergy balance of a system can be evaluated, comprising the entropy changes occurring as a consequence of the process. As the sun or source of light emits radiation, regardless of the presence of a catalyst, the space is filled with radiation exchange and its respective entropy transfer.

When the reactor is illuminated by source of light, a portion of the incident solar radiation is absorbed by the catalyst. Other effects are the convective and radiation heat transfer from the reactor surface to the environment of a temperature T_0. The following exergy balance equation can be written for the water splitting photo-reactor system:

$$\gamma \left[\alpha_V \dot{Ex}_V + \alpha_{nV} \left(\dot{Ex}_S - \dot{Ex}_V \right) \right] + \dot{n}_{H2O,\,in} \overline{ex}_{H2O,\,in}$$
$$= \dot{n}_{H2} \overline{ex}_{H2} + \dot{n}_{O2} \overline{ex}_{O2} + \dot{n}_{H2O,\,out} \overline{ex}_{H2O,\,out} + \dot{Ex}_{conv} + \dot{Ex}_{em} + \delta \dot{Ex} \quad (27.15)$$

The exergy equation for solar thermal conversion of methanol is given as follows:

$$\gamma A \dot{Ex}_S + \dot{n}_{CH3OH} ex_{CH3OH} + \dot{n}_{H2O,\,in} ex_{H2O,\,in}$$
$$= \dot{n}_{CO2} ex_{CO2} + \dot{n}_{H2} ex_{H2} + \dot{n}_{H2O,\,out} ex_{H2O,\,out} + \dot{Ex}_{conv} + \dot{Ex}_{em} + \delta \dot{Ex} \quad (27.16)$$

where $\delta\dot{E}x$ is the total exergy loss due to all irreversible processes occurring within the system. The following input values have been used in the computations for the model associated with the water splitting photo-reactor [35]:

– The environment temperature is $T_0 = 293$ K
– The environment pressure p_0 equals the standard pressure 101.325 kPa
– The weakening radiation factor is $\gamma = 0.8$
– The catalyst absorptivity within visible wavelength range is $\alpha_V = 0.31$
– The catalyst absorptivity beyond the visible range is $\alpha_{nV} = 1.8$

The exergy efficiency reflects the degree of thermodynamic losses in the photo-catalytic hydrogen production process. All terms of the exergy balance equations are categorized either as useful products, process inputs, or losses. The denominator of the efficiencies represents the input terms, whereas the numerator expresses the useful products. Exergy efficiencies for water splitting processes can be defined as

$$\eta_{ex} = \frac{\dot{n}_{H2}\Delta G_{H2O \to H2 + 1/2O2}}{\gamma\left[\alpha_V\dot{E}x_V + \alpha_{nV}\left(\dot{E}x_S - \dot{E}x_V\right)\right] + \dot{n}_{H2O}\left(\overline{ex}_{H2O} + \frac{V_{H2O,in}^2}{2}\right)} \tag{27.17}$$

Using the same approach, the exergy efficiency of solar thermal methanol steam reforming is

$$\eta_{ex} = \frac{n_{H2}\Delta G_{CH3OH \to 3H2 + CO2}}{\gamma\dot{E}x_S + \dot{n}_{CH3OH}\overline{ex}_{CH3OH} + \dot{n}_{H2O}\left(\overline{ex}_{H2O} + \frac{V_{H2O,in}^2}{2}\right)} \tag{27.18}$$
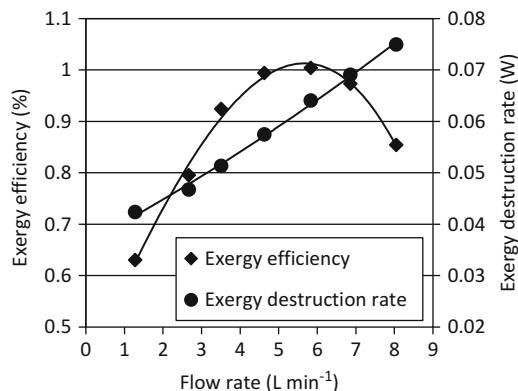
The losses of component processes should be taken into account. Although hydrogen and oxygen are produced in a complete photo-catalytic process, only hydrogen exergy is considered as a useful output. In the present approach, the total exergy loss consists of four components including the chemical reaction, physical changes in water flow, radiation, and convective heat transfer from the reactor surface.

To improve environmental sustainability, it is important to minimize the environmental damage while using sustainable or renewable sources of energy. This leads to a reduction in the use of limited resources and extended lifetimes. Accordingly, a sustainability index SI is used to connect exergy and environmental impact [36]:

$$SI = \frac{1}{D_P} \tag{27.19}$$

where D_P is a depletion number, which is defined as the exergy destruction/input exergy [37]. This relation characterizes the ability to reduce a system's environmental impact by decreasing its exergy destruction.

Fig. 27.14 Exergy efficiency and CO_2 emissions reduction of water splitting photo-reactor

The emissions of CO_2 are defined in kg kWh^{-1}. The mitigation of CO_2 emissions from photo-catalytic water splitting and CO_2 emissions from solar thermal methanol reforming are normalized based on the incident irradiation as follows:

$$\text{Emi,}_{CO2} = \frac{\dot{m}_{CO2}}{j_S \times A} \times 3,600 \tag{27.20}$$
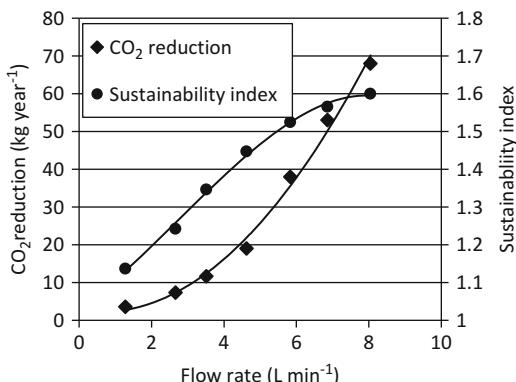
In order to calculate the amount of reduced CO_2 by the photo-catalytic water splitting method, the electricity consumed by the lamp and pump is assumed to be provided by methane gas combustion in a gas turbine.

Exergo-environmental Assessment Results of the Photo-reactor

This analysis evaluates different output parameters that include exergy efficiency and exergy destruction rates of photo-catalytic hydrogen production, as well as the carbon dioxide emissions. These parameters are examined under the variation of the catalyst concentration, flow velocity, light intensity, and ambient temperature. The exergy efficiency and carbon dioxide emissions are examined for two photo-catalytic hydrogen production systems, namely, water splitting and methanol steam reforming. Exergy efficiency analysis is an effective method to establish the optimal system design that provides the necessary insight to move from small scale to larger scale systems and longer term operation.

The effect of water flow rate on continuous operation of the reactor is investigated in terms of exergy efficiency and exergy destruction rate, as shown in Fig. 27.14. An increase of water flow rate can enhance the hydrogen production within a certain range. In this design, an increase of flow rate is provided by an increase of velocity and the reactor radius is fixed. Higher kinetic energy of the solution increases the photochemical interactions between active sites of the catalyst and water molecules

Fig. 27.15 Exergy
destruction rate and
sustainability index of water
splitting photo-reactor
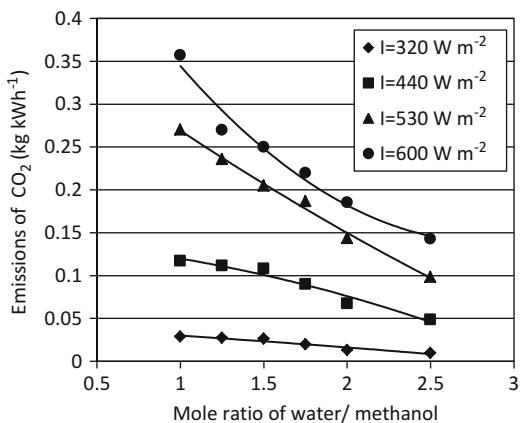
to exchange electrons and hydroxyl ions. The optimum flow rate inside the reactor is found to be 6 L min^{-1}, since exergy efficiency starts decreasing afterwards. This is due to an increase of physical exergy loss compared with the hydrogen production rate at high flow rates. The total exergy destruction rate increases with a higher flow rate as the physical and chemical losses increase accordingly.

Figure 27.15 shows the CO_2 reduction rate and sustainability index variation at various flow rates. The CO_2 emissions that are reduced by this process increase at higher flow rates. CO_2 emissions reduction is calculated based on the assumption that the energy to derive the photo-catalytic water splitting system is substituted by fossil fuel combustion. Since the rate of hydrogen production increases at higher water flow rates, the system performance will be better environmentally. The sustainability index increases up to same point, which is associated with the optimum flow rate of the system. Exergy depletion of the water splitting system is optimized at an inlet flow rate of about 6 L min^{-1} corresponding to 2 L h^{-1} of hydrogen production capacity.
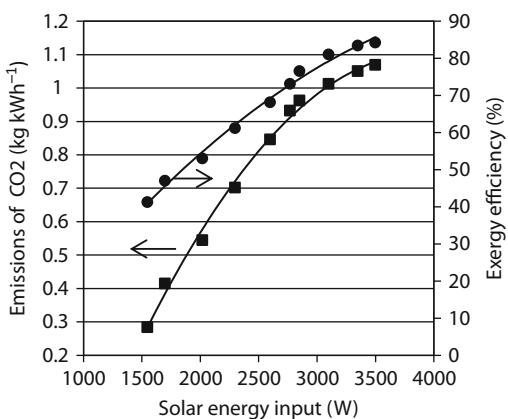
The rest of the results pertain to solar thermal hydrogen production via methanol steam reforming. The greenhouse gas emissions of this process can be compared with CO_2 reduction of which presented for photo-catalytic water splitting process in the previous section. The CO_2 emissions of solar thermal methanol steam reforming are shown in Fig. 27.16. The results are calculated for different light intensities. The light intensity is one of the key parameters in optimization of photo-reactor design, which should be considered in conjunction with light absorptivity of the catalyst over irradiated wavelengths of the light source to determine the hydrogen production of the system. At higher light intensities, an increase of feed flow rate causes rapid degradation of the inlet exergy utilization. Similarly, the emissions of greenhouse gases are more affected at higher light intensities. A trade-off exists in terms of exergy efficiency improvement and CO_2 emissions of the solar thermal hydrogen production system. The light intensity range of 530 W m^{-2} < J < 600 W m^{-2} and water–methanol mole ratio of 1.5–2 are found to be optimal criteria from exergy–environmental point of view.

The irreversibilities due to heat transfer, chemical reactions, and physical variations in the system are affected by the solar irradiation into the system.

Fig. 27.16 CO_2 emissions variations versus mole ratio of water and methanol
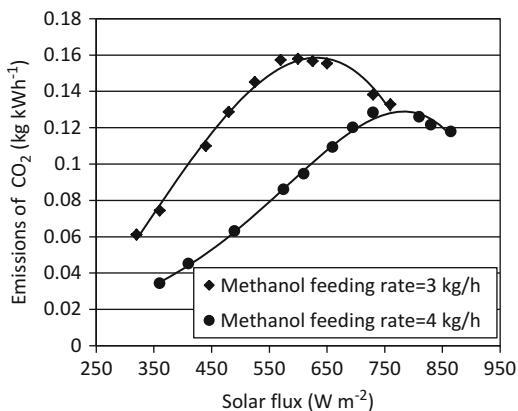
Fig. 27.17 Exergy efficiency and CO_2 emissions of photo-catalytic methanol steam reforming

As shown in Fig. 27.17, both exergy efficiency and emissions of greenhouse gases increase with higher irradiated solar energy. The rates of exergy efficiency and CO_2 emissions decrease at higher solar energy inputs. Solar input of more than 3,000 W involves high environmental pollution while it does not improve the exergy efficiency significantly. The effect of solar flux on CO_2 emissions at two different feed flow rates is shown in Fig. 27.18.

It should be mentioned that a reactor temperature corresponds to a fixed methanol conversion rate for the two feed rates of the reactants. It occurs because methanol conversion is usually a monotone function of reactor temperature, $X_{CH3OH} = f(T_{reactor})$. Therefore, an increase of feed rate causes lower reactor temperatures by improving the potential energy of the flow stream and subsequently lower conversion of methanol which decreases the CO_2 emissions of the system. It is also found that CO_2 emissions are maximized at an optimum feed rate, which indicates the amount of solar flux that drives the conversion of methanol to hydrogen.

Fig. 27.18 CO_2 emissions of photo-catalytic methanol steam reforming at different feeding rates

Fig. 27.19 Exergy destruction ratios of solar reactor at different ambient temperatures
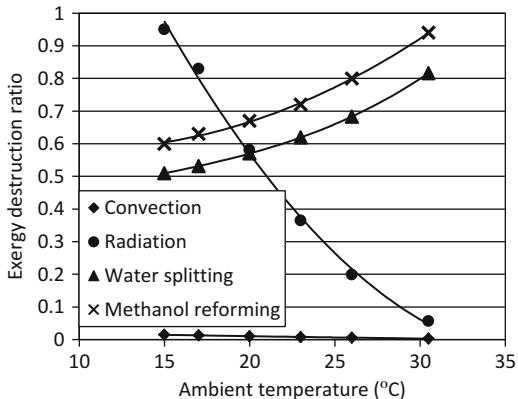
Figure 27.19 shows the effects of ambient temperature on exergy losses of the system in terms of the exergy destruction ratio due to heat transfer, chemical and physical reactions. The exergy destruction ratio is the ratio of irreversibility to input exergy. The chemical and physical exergy destruction ratios for photo-catalytic water splitting and solar thermal methanol steam reforming are differentiated. It can be concluded that a higher ambient temperature reduces the exergy destruction due to heat transfer from the reactor surface area, whereas chemical and physical exergy losses are increased by almost 35 % over a 15° temperature increase. These results confirm the advantage of lower ambient temperature conditions for photo-catalytic hydrogen production systems. The exergy destruction ratios for the methanol reforming process are higher than water splitting system due to higher working temperatures and higher chemical exergy content of the methanol–water mixture.

27.7   Conclusions

In this chapter, the photo-reactors for light-based hydrogen production are explored. In photo-catalytic hydrogen production processes, the photonic energy directly conducts chemical reactions to produce hydrogen. The implementation of these processes at an industrial scale requires the use of a device which facilitates the interactions between photons, a photo-catalyst, and reactants, as well as collecting the reaction products. In this work, the state-of-the-art solar photo-reactor designs are presented and those systems which are most applicable for industrial scale implementation are investigated. In the first part of the chapter, a background is given with regard to the photo-electrochemistry of photo-catalytic hydrogen production. Two main possible routes to conduct photo-catalysis including heterogeneous and homogeneous catalysis are also explained. In heterogeneous process the organized structure of a solid phase catalyst conducts electron transport. The homogeneous process facilitates chemical reactions using chemical species mobility in a solution.

Among the photo-reactor designs that are surveyed in this chapter, those based on CPC technology are currently most utilized for operation at pilot scale and beyond. The inclined plate collector as an effective photo-reactor design has been demonstrated to be suitable for smaller scale operations. Although the relatively low flow rates in this design limits its suitability for large-scale applications, the low capital cost and simplicity of design makes it ideal for small, dispersed operations. Fluidized/fixed bed photo-reactors are known as an optimal configuration of photo-catalyst handling, with very high quantum efficiencies. However, the significant challenge regarding an effective illumination of catalyst particles limits their use with solar radiation.

The case study at the end of the chapter introduces a scaled up photo-catalytic reactor for continuous operation under large-scale process conditions for two light initiated methods of hydrogen production, namely photo-catalytic water splitting and solar methanol steam reforming. An exergy–environmental analysis of a complete system is performed to quantify, compare, and evaluate the performance of these two systems based on the operational parameters. The results indicate that higher kinetic energy of the solution increases the photochemical interactions in the vicinity of active sites and enhances the hydrogen production rate within a certain range. The optimum flow rate inside the reactor is found to be 6 L min^{-1}, since the exergy efficiency starts decreasing afterwards. The amount of CO_2 emissions reduced by this process increases at higher flow rates. There is an optimum for each feed rate where CO_2 emissions are maximized. This point is associated with the amount of solar flux that drives the conversion of methanol to hydrogen.

References

1. Lewis NS, Nocera DG (2007) Powering the planet: chemical challenges in solar energy utilization. Proc Natl Acad Sci U S A 103:15729–15735
2. Turner JA (2004) Sustainable hydrogen production. Science 305:972–974
3. Dincer I, Zamfirescu C (2011) Sustainable energy and applications. Springer, New York
4. Rajeshwar K, McConnell RD, Licht S (2008) Solar hydrogen generation: toward a renewable energy future. Springer, New York
5. U.S. Department of Energy, A National Vision of America's Transition to A Hydrogen Economy – to 2030 and Beyond. p. iii. http://www1.eere.energy.gov/hydrogenandfuelcells/pdfs/vision_doc.pdf. Accessed February 2002
6. Plunkett JR (2011) Energy information administration, international energy outlook and projections. Nova Science Publishers, New York
7. Crabtree RH (2010) Energy production and storage: inorganic chemical strategies for a warming world. Wiley, United Kingdom
8. Vayssieres L (2010) Solar hydrogen and nanotechnology. Wiley, New York
9. Navarro RM, Valle F, Villoria de la Mano JA (2009) Photocatalytic water splitting under visible light: concept and catalysts development. Adv Chem Eng Photocatal Technol 36:111–143
10. Akkerman I, Janssen M, Rocha J, Wijffels RH (2002) Photobiological hydrogen production: photochemical efficiency and bioreactor design. Int J Hydrogen Energ 27(11–12):1195–1208
11. Funk JE, Reinstrom RM (1967) Energy requirements in production of hydrogen from water. Ind Eng Chem Process Des Dev 5:336–342
12. Naterer GF, Suppiah S, Stolberg L, Lewis M, Wang Z, Daguppati V, Gabriel K, Dincer I, Rosen MA, Spekkens P, Lvov SN, Fowler F, Tremaine P, Mostagimi J, Easton EB, Trevani L, Rizvi G, Ikeda BM, Kaye MH, Lu L, Pioro I, Smith WR, Seknik E, Jiang J, Avsec J (2010) Canada's program on nuclear hydrogen production and the thermochemical Cu-Cl cycle. Int J Hydrogen Energ 35:10905–10926
13. Kudo A, Miseki Y (2009) Heterogeneous photocatalyst materials for water splitting. Chem Soc Rev 38:253–278
14. Fujishima A, Honda K (1972) Electrochemical photolysis of water at a semiconductor electrode. Nature 238:37–38
15. Ni M, Leung MKH, Leung DYC, Sumathy K (2007) A review and recent developments in photocatalytic water-splitting using TiO_2 for hydrogen production. Renew Sustain Energy Rev 11:401–425
16. Matsuoka M, Kitano M, Takeuchi M, Tsujimaru K, Anpo M, Thomas JM (2007) Photocatalysis for new energy production: recent advances in photocatalytic water splitting reactions for hydrogen production. Catal Today 122:51–61
17. Archer MD, Bolton JR (1990) Requirements for ideal performance of photochemical and photovoltaic solar-energy converters. J Phys Chem 94:8028–8036
18. Inoue T, Watanabe T, Fujishima A, Honda K, Kohayakawa K (1977) Suppression of surface dissolution of CDS photoanode by reducing agents. J Electrochem Soc 124(5):719–722
19. Serpone N, Pelizzetti E (1989) Photocatalysis. Wiley, New York
20. Goswami D (1997) A review of engineering developments of aqueous phase solar photocatalytic detoxification and disinfection processes. J Solar Energy Eng 119:101–107
21. Roselin LS, Rajarajeswari GR, Selvin R, Sadasivam V, Sivasankar B, Rengaraj K (2002) Sunlight/ZnO-mediated photocatalytic degradation of reactive red 22 using thin film flat bed flow photoreactor. Solar Energy 73:281–285
22. Turchi C, Ollis D (1990) Photocatalytic degradation of organic water contaminants mechanisms involving hydroxyl radical attack. J Catal 122:178–192
23. Braham RJ, Harris AT (2009) Review of major design and scale-up considerations for solar photocatalytic reactors. Ind Eng Chem Res 48:8890–8905

24. Freudenhammer H, Bahnemann D, Bousselmi L, Geissen SU, Ghrabi A, Saleh F, Si-Salah A, Siemon U, Vogelpohl A (1997) Detoxification and recycling of wastewater by solar-catalytic treatment. Water Sci Technol 35:149–156
25. Sun RD, Nakajima A (2000) TiO_2-coated optical fiber bundles used as a photocatalytic filter for decomposition of gaseous organic compounds. J Photochem Photobiol A Chem 136:111–116
26. Peill N, Hoffman M (1997) Solar-powered photocatalytic fiber-optic cable reactor for waste stream remediation. J Solar Energy Eng 119:229–236
27. Pozzo RL, Brandi RJ, Giombi JL, Cassano AE, Baltans MA (2007) Fluidized bed photoreactors using composites of titania CVD-coated onto quartz sand as photocatalyst: Assessment of photochemical efficiency. Chem Eng J 118(3):153–159
28. DufourJ SDP, Galvez JL, Morenoa J, Garcia C (2009) Life cycle assessment of processes for hydrogen production; environmental feasibility and reduction of greenhouse gases emissions. Int J Hydrogen Energ 34:1370–1376
29. Dincer I, Rosen MA (1999) The intimate connection between exergy and the environment. In: Bejan A, Mamut E (eds) Thermodynamic optimization of complex energy systems. Kluwer Academic, The Netherlands
30. Dincer I (2007) Environmental and sustainability aspects of hydrogen and fuel cell systems. Int J Energy Res 31:29–55
31. Malato S, Blanco J, Campos A, Caceres J, Guillard C, Herrmann JM et al (2003) Effect of operating parameters on the testing of new industrial titania catalysts at solar pilot plant scale. Appl Catal B 42(4):349–357
32. Dincer I, Rosen MA (2007) Energy, environment, and sustainable development. Elsevier, Oxford
33. Liu Q, Hong H, Yuan J, Jin H, Cai R (2009) Experimental investigation of hydrogen production integrated methanol steam reforming with middle-temperature solar thermal energy. Appl Energy 86:155–162
34. Bejan A (1997) Advanced engineering thermodynamics. Wiley, New York
35. Petela R (1964) Exergy of heat radiation. Trans ASME J Heat Transf 2:187–192
36. Rosen MA, Dincer I, Kanoglu M (2008) Role of exergy in increasing efficiency and sustainability and reducing environmental impact. Energy Policy 36:128–137
37. Dincer I, Naterer GF (2010) Assessment of exergy efficiency and Sustainability Index of an air water heat pump. Int J Exergy 7:37–50

Chapter 28
Comparative Environmental Impact Evaluation of Hydrogen Production Methods from Renewable and Nonrenewable Sources

Canan Acar and Ibrahim Dincer

Abstract In this chapter, a comparative environmental impact study of possible hydrogen production methods from renewable and nonrenewable sources is undertaken with a special emphasis on Turkey. The goal is to make useful and practical recommendations to the authorities in terms of research and development, demonstration projects and applications. Environmental impacts (global warming potential, GWP and acidification potential, AP), production costs, energy and exergy efficiencies of eight different methods are compared. These methods are natural gas steam reforming, coal gasification, water electrolysis via wind and solar electrolysis, thermochemical water splitting with a Cu–Cl and S–I cycles, and high temperature electrolysis. The relations between environmental impacts and economic factors are also presented using the social cost of carbon (SCC) concept. The global warming and acidification potentials of the selected production methods show that thermochemical water splitting with the Cu–Cl and S–I cycles are advantageous over the other methods, followed by wind, solar, and high temperature electrolysis. In terms of hydrogen production costs, electrolysis methods are found to be least attractive. Energy and exergy efficiency comparisons show that biomass gasification becomes advantageous over the other methods.

Keywords Hydrogen production • Global warming potential • Emissions • Energy • Exergy • Efficiency • Environmental impact evaluation • Renewable sources • Nonrenewable sources • Turkey • Acidification potential • Energy • Exergy efficiency • Natural gas steam reforming • Coal gasification • Water electrolysis • Wind • Solar electrolysis • Thermochemical water splitting • S–I cycle • High temperature electrolysis
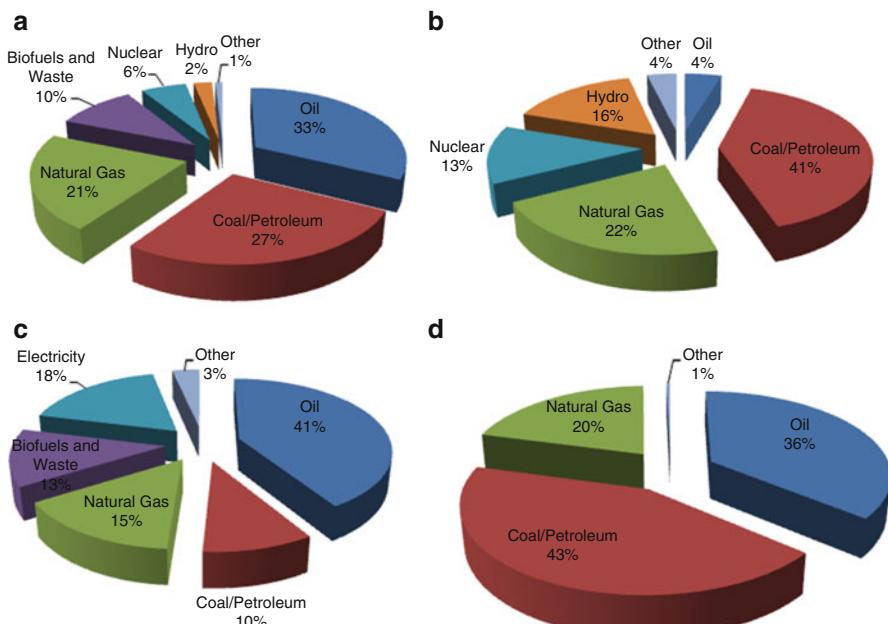
C. Acar (✉) • I. Dincer
Faculty of Engineering and Applied Science, University of Ontario Institute of Technology, 2000 Simcoe Street North, Oshawa, ON, Canada L1H 7K4
e-mail: Canan.Acar@uoit.ca; Ibrahim.Dincer@uoit.ca

28.1   Introduction

As a result of growing worldwide population and the rising standards of living globally, the world's energy consumption has increased steadily during the twentieth and the beginning of twenty-first century. World's primary energy supply, electricity generation, energy consumption, and the resulting CO_2 emission shares by energy source are presented in Fig. 28.1.

In 2010, the total primary energy supply was 12,717 MTOE [1]. Figure 28.1a shows that about 80 % of this amount came from fossil fuels. The amount of worldwide electricity generation was 21,431 TWh in 2010 [1]. And from Fig. 28.1b it can be seen that about 70 % of the electricity was generated by using fossil fuels. Figure 28.1c shows fuel shares of total final consumption in the world. The dominance of fossil fuels can be seen here. Figure 28.1d shows the CO_2 emissions of various fuels. In 2010, the worldwide CO_2 emissions were 30,326 Mt [1]. This amount was mainly the result of using fossil fuels as can be seen from Fig. 28.1d. Switching to a CO_2-neutral energy carrier could greatly reduce the emissions.

World's energy need is expected to increase in the future. The increased demand for more energy will require a growth in energy generation capacity, more secure and diversified energy sources, and a successful strategy to reduce and eliminate greenhouse gas emissions [2].

Fig. 28.1   2010 fuel shares: (**a**) total primary energy supplies (TPES), (**b**) electricity generation, (**c**) total final consumption, and (**d**) CO_2 emissions (data from [1])

If one compares various alternative energy strategies, hydrogen offers a large number of benefits and provides better environment and sustainable development. Obviously, this helps drastically reduce the dependence on imported oil and greenhouse gas emissions.

Hydrogen is the simplest and lightest of all chemical elements and the most spread in the universe. It is not a primary source of energy as it occurs only in nature in combination with other elements, primarily with oxygen in water and with carbon, nitrogen and oxygen in living materials and fossil fuels. However, when split from these other elements to form molecular hydrogen, a process requiring another source of energy, it becomes an environmentally attractive fuel. It can be burned or combined with oxygen in a fuel cell without generating CO_2, producing only water. Like electricity it is a very clean energy at the point of use, but like natural gas it can form explosive mixtures with air [3].
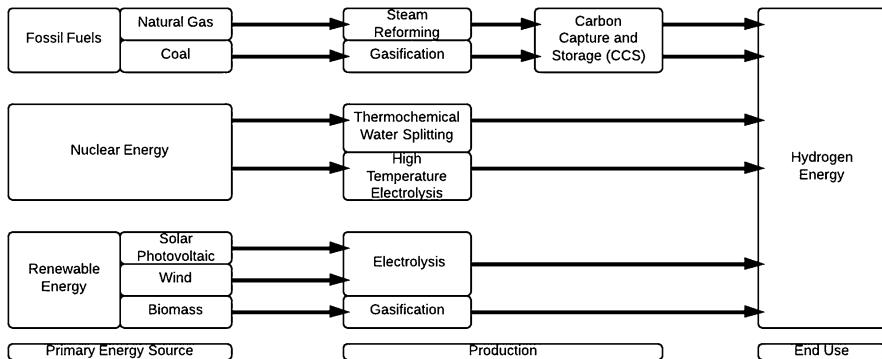
Some of the advantages of the hydrogen economy can be summarized as:

- Energy security: H_2-powered vehicles could significantly reduce imports of foreign oil.
- Sustainability: H_2 production technologies can potentially take advantage of abundant renewable energy resources.
- Climate change: Vehicles produce near-zero carbon emissions when operating on H_2.
- Urban air quality: H_2 can reduce or eliminate regulated tailpipe emissions (e.g., hydrocarbons, GHG, NOx).
- Economic vitality: Leading the development and commercialization of H_2 and fuel cell technology can shape the future global energy markets.

While the hydrogen economy represents a visionary strategy for future energy security, significant scientific and technical challenges must be overcome to achieve its implementation. The hydrogen economy spans three functional areas: production, storage, and use; each area has its special set of grand technical challenges. Recent advances in materials science, chemistry, physics, biology, computation, and nanoscience provide considerable promise for breaking through many of these current barriers.

28.2   Background: Hydrogen Production Methods

The selected hydrogen production methods investigated in this study is presented in Fig. 28.2.

Fig. 28.2 Selected hydrogen production methods (modified from [4])

28.2.1 Hydrogen Production from Fossil Fuels

Steam Reforming

Steam reforming of natural gas is currently the least expensive method and is responsible for more than 90 % of hydrogen production worldwide. Natural gas is first cleared from sulfur compounds. It is then mixed with steam and send over a nickel–alumina catalyst inside a tubular reactor heated externally, where carbon monoxide (CO) and hydrogen (H_2) are generated. This step is followed by a catalytic water-gas shift reaction which converts the CO and water to hydrogen and carbon dioxide (CO_2). The hydrogen gas is then purified [3].

The endothermic reforming reaction is: $CH_4 + H_2O + 206 \text{ kJ/kg} \rightarrow CO + 3H_2$
It is usually followed by: $CO + H_2O \rightarrow CO_2 + H_2 + 41 \text{ kJ/kg}$
The overall reaction is: $CH_4 + 2H_2O + 165 \text{ kJ/kg} \rightarrow CO_2 + 4H_2$
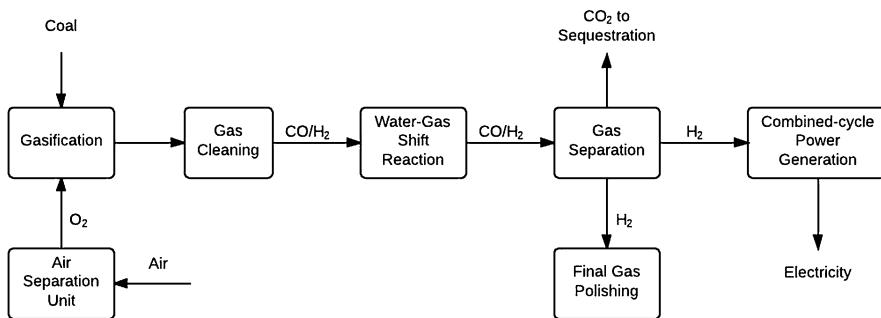
The technology is suitable for large reformers (e.g., 100,000 tons per year), where yields higher than 80 % can be achieved. Smaller-scale reformers especially designed for feeding small fuel cells, show lower efficiencies [3].

Gasification

Coal is a practical option for making hydrogen in large plants. Worldwide coal reserves are very important indeed and technologies for converting coal to hydrogen are commercially available. The major concern is that, due to the high carbon content of coal, the corresponding carbon dioxide emissions are larger than those from any other feedstock. Large-scale use of coal gasification implies that carbon capture and storage technologies can be developed [3].

Coal can also be used to produce electricity and then hydrogen through the electrolysis process. The gasification technology however is better for making

Fig. 28.3 Schematic representation of an integrated coal gasification process (modified from [4])

hydrogen from coal. Coal gasification involves partial oxidation of the coal with oxygen and steam in a high-temperature and high-pressure reactor. The reaction proceeds in a highly reducing mixture that creates mainly CO and H_2, mixed with steam and CO_2. This "syngas" undergoes the shift reaction, increasing the H_2 yield. The gas can then be cleaned in conventional ways to recover elemental sulfur (or make sulphuric acid). Part of the syngas goes to a gas turbine, which makes electricity for the air distillation, and process steam [3].

Schematic representation of an integrated coal gasification process is presented in Fig. 28.3.
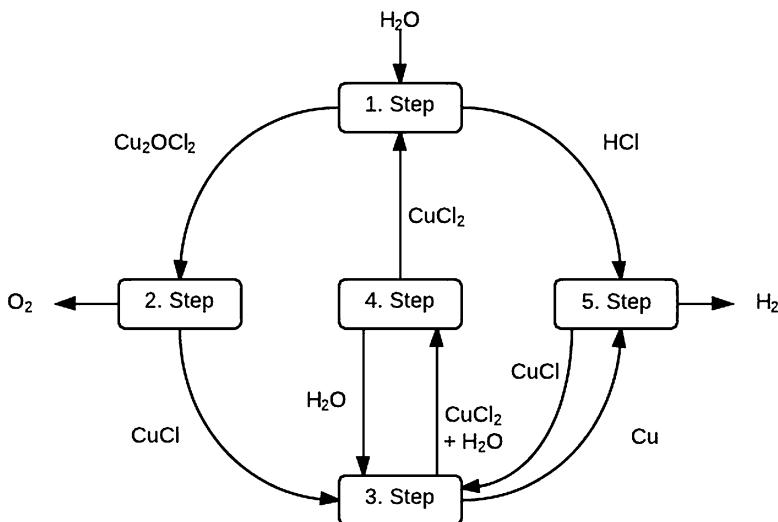
The cost of producing hydrogen in a large coal gasification plant is today slightly higher than that made from natural gas. Coal gasification techniques are however less mature than the steam reforming of natural gas. The economics of making hydrogen from coal differ somewhat from other fossil fuels: the unit capital costs are larger for the coal plants, while the unit raw material costs are lower [3].

28.2.2   *Hydrogen Production from Nuclear Energy*

Thermochemical Water Splitting

Hydrogen can be produced by using nuclear reactors to drive thermochemical water-splitting cycles, the overall output of which is water splitting to hydrogen and oxygen without intervening electricity generation. These cycles need temperatures of 500 °C or more, higher than the temperatures can be achieved by today's light-water reactors. However, these temperatures are within the range of present-day, gas-cooled reactors and designs for future nuclear power plants [5]. The reactor operating temperature is a key factor because higher temperatures enable faster chemical reactions and higher efficiencies, at the expense of a harsh thermal and chemical materials environment. High-temperature thermochemical water splitting cycles have been demonstrated and could potentially drive very efficient cycles [2].

More than 100 different thermochemical cycles have been proposed for performing the overall water splitting reaction in high-temperature reactors

Fig. 28.4 The five-step Cu–Cl thermochemical cycle for hydrogen production (modified from [7])
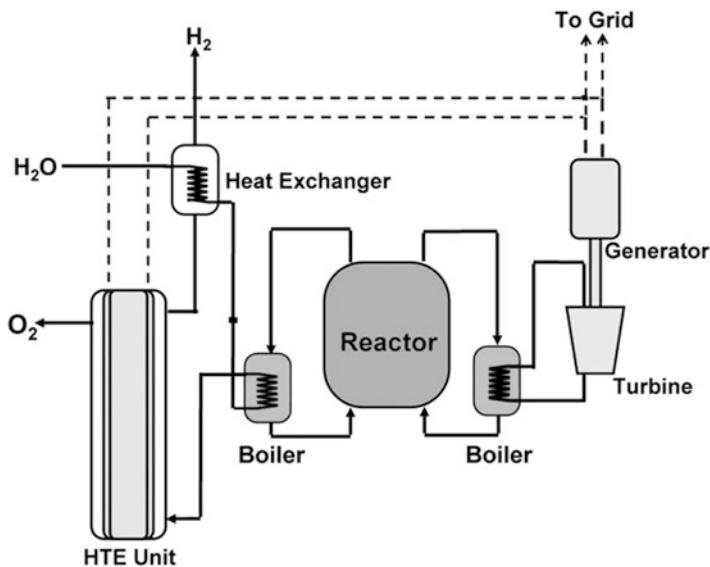
[6]. At present, the most promising high-temperature cycles appear to be the calcium bromide–iron oxide cycle, the sulfuric acid–hydrogen iodide (sulfur-iodine or S–I) cycle, and the Westinghouse cycle. Also, an important lower-temperature cycle, (copper-chlorine [Cu–Cl]), can produce hydrogen using heat from current and near-future reactors [2]. Figure 28.4 illustrates a 5-step Cu–Cl thermochemical cycle for hydrogen production.

The Cu–Cl cycle, originally proposed in the 1970s, has recently been proven in the laboratory, and several commercially appealing variants are being evaluated. This cycle has an estimated efficiency of ~40 % at its envisioned operating temperature of 550 °C, not including cogeneration of electricity. A key challenge for the Cu–Cl cycle is effective catalysis of the low-temperature reactions [2].

In the S–I cycle, which uses all fluid reagents, a higher temperature (825–900 °C) is used for the oxygen-evolving reaction, and higher efficiencies (~50 % and ideally 60 % with cogeneration of electricity) are possible. The individual reactions in the S–I cycle have been demonstrated, although not in a continuous process, nor at the temperatures envisioned for implementation of the technology. Among the key challenges with this approach is the verification of durable high-temperature, chemically inert materials for fabrication of the chemical reactors needed to withstand the thermochemical cycle over economically useful lifetimes [8].

High Temperature Electrolysis

Hydrogen can be produced from nuclear electricity by electrolysis. Despite the rather high efficiency of converting electricity into hydrogen (up to 80 % under

Fig. 28.5 Conceptual design of a high temperature electrolysis plant [10]

pressure), the global efficiency is much reduced by the rather weak efficiency of the nuclear power plant (around 33 % for current reactors) [3]. Conceptual design of a high temperature electrolysis plant is illustrated in Fig. 28.5. A more efficient hydrogen production would be obtained from high temperature water electrolysis coupled to new reactors operating at much higher outlet temperatures. The efficiency of the high temperature electrolysis of steam increases from about 20 % at 350 °C to about 50 % at 950 °C, respectively [9].

28.2.3   Hydrogen Production from Renewable Energies

Electrolysis

Electrolysis is a process for breaking water (H_2O) into its constituent elements (hydrogen and oxygen) by supplying electrical energy. The advantage of this process is that it supplies a very clean hydrogen fuel that is free from carbon and sulfur impurities. The disadvantage is that the process is expensive, relative to steam reforming of natural gas, because of the cost of the electrical energy needed to drive the process [2]. Making electrolytic hydrogen uses considerably more energy than the hydrocarbon processes. Nevertheless, electrolysis is of interest for several reasons. First it is seen as a potentially cost-effective way of producing hydrogen locally. Electrolyzers are compact and can realistically be located at existing fuelling stations. Secondly, electrolysis offers a way to produce hydrogen with electrical power generated from renewable sources [3].

Solar Photovoltaic

The most efficient and also the most costly sources of solar electricity for water electrolysis are solid-state photovoltaic (PV) devices. At the present time the cost of hydrogen from photovoltaic electricity through electrolysis is 25 times higher than that of hydrogen produced from coal or natural gas plants. The expected decrease in the cost of photovoltaic cells and of electrolyzers would bring this down to a factor of 6 [3]. The potential capacity for solar hydrogen is quite large [2].

Wind

Of all renewable sources, wind shows possibly the highest potential for producing pollution-free hydrogen, using the electricity generated by the wind turbines for electrolysis. This is particularly true for distributed systems. In order to succeed the cost of the wind turbines and electrolyzers has to decrease, and the turbine–electrolyzer–storage system has to be further optimized. Today the cost of hydrogen produced from wind amounts to six to ten times that of large-scale units using natural gas. This gap could be halved in the near future [3].

Biomass Gasification

Using biomass instead of fossil fuels to produce hydrogen reduces the average amount of carbon dioxide in the atmosphere, since the carbon dioxide released when the biomass is oxidized was previously absorbed from the atmosphere and fixed by photosynthesis in the growing biomass [3].

Hydrogen can be produced from biomass resources such as forestry, wood processing, and agricultural residues, animal and consumer (municipal) waste or crop specifically grown for energy uses. Current technologies for converting biomass into molecular hydrogen include gasification/pyrolysis of biomass coupled to subsequent steam reforming. The main conversion processes are indirect-heat gasification, oxygen-blown gasification, and anaerobic fermentation [3].

Biomass-to-hydrogen conversion is presently unable to produce hydrogen on a large scale at a competitive price, even when compared with hydrogen generated from distributed natural gas. It could however contribute to recover energy from domestic and agricultural waste in a very clean way. The environmental impact of growing significant quantities of biomass as energy crops, including genetically engineered, high-yield crops, will most likely place significant strains on natural resources and land availability [3].

The cost for collecting and transporting biomass is inherently high. It would result in building many small biomass gasification plants without the economy of scale. The route to biofuels might prove more attractive.

Table 28.1 Key benefits and critical challenges of hydrogen production methods (modified from [3])

Natural gas steam reforming	Coal and biomass gasification	Thermochemical	Water electrolysis
Key benefits			
Most viable approach in the near term	Low-cost synthetic fuel in addition to H_2	Clean and sustainable	No pollution with renewable sources
Lowest current cost	Abundant and affordable		
Existing infrastructure			
Critical challenges			
Capital, operation and maintenance costs	Reactor costs		Low efficiency
	System efficiency	Effective and durable materials of construction	Capital costs
	Feedstock impurities		Integration with renewable energy sources
	Carbon capture and storage		

28.2.4 Summary of Hydrogen Production Methods
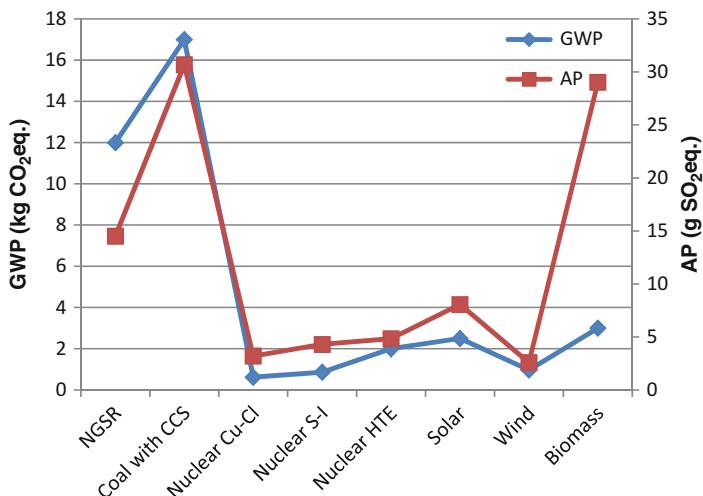
The key benefits of various hydrogen production methods are outlined in Table 28.1. The initial review shows that the cheapest method is to use excess hydrogen from large industrial gas plants and natural gas as feedstocks. This method can therefore be used for cost comparison and cost-optimization. Secured supply is an important criterion in energy services that need to be addressed. Mature gas technology and direct applications as well as the small environmental gain from reforming gas to hydrogen discourages that pathway for long term hydrogen production but can give rise to further studies on cost development.

According to Table 28.1, high capital, operation and maintenance, and design are the main critical challenges for almost all of the selected hydrogen production methods. Addressing these challenges and identifying the research and development needs could be a good step towards hydrogen economy.

28.3 Comparative Assessment of Hydrogen Production Methods

28.3.1 Environmental Impact Comparison

The primary greenhouse gas emitted through fuel combustion is CO_2. CO_2 emissions are of great concern in view of its impact on global warming [11]. Therefore, they should be managed, either as a waste, or as a commodity for another purpose [12].

Fig. 28.6 GWP and AP of selected hydrogen production methods (data from [13])
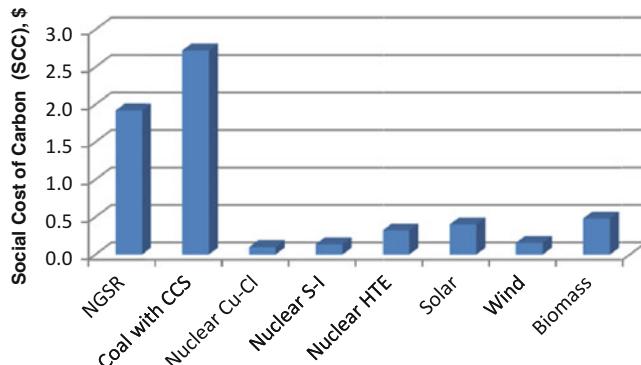
Either in coal gasification or natural gas steam reforming, the CO_2 emissions may avoid the full application of Carbon Capture and Sequestration (CCS), which is considered an adaption technology, as the risk of gas release may imply a final emission to the atmosphere.

The environmental impact categories can be summarized based on the "operational guide to the ISO standards" published by The Center of Environmental Science of Leiden University (CML) in 2001. The operational guide describes the LCA procedures according to ISO standards. A set of impact categories and the characterization methods and factors for an extensive list of substances (resources from/ emissions to nature) are recommended for the impact assessment phase of LCA. GWP (Global Warming Potential, g CO_2 eq.) relates to the increasing concentration of CO_2 in Earth's atmosphere and AP (Acidification Potential, g SO_2 eq.) relates to acid deposition on soil and into water, which may change the degree of acidity [13].

Figure 28.6 shows the environmental impact results, in terms of global warming potential (GWP) and acidification potential (AP), for selected hydrogen production methods. It can be seen that hydrogen production using thermochemical cycles are the most environmentally benign of the selected methods, in terms of CO_2 emissions and acidification potential. Natural gas steam reforming and coal gasification are seen to be the most harmful. The acidification potential results show that gasification has the highest impact on environment and the Cu–Cl cycle has the lowest [13].

28.3.2   Social Cost of Carbon Comparison

The social cost of carbon (SCC) is the marginal external cost of a unit emission of CO_2, denominated in terms of forgone consumption and based upon the damages inflicted by that emission upon global society through additional climate change.

Fig. 28.7 Social cost of carbon (SCC) of selected hydrogen production methods (per kg of hydrogen)

The value of the SCC is generally estimated in an integrated assessment modeling (IAM) framework that couples a baseline socioeconomic scenario, a climate–carbon cycle model that transforms emissions into temperature, and a function for transforming temperature change (implicitly or explicitly by way of climate change impacts) into economic damages [18].
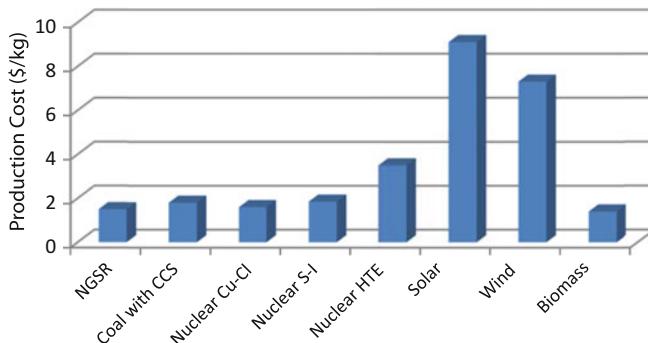
In this study, the work of Parry et al. (2007) [19] is taken as a basis to calculate the SCC of selected hydrogen production methods. The average SCC is $160 per tonne of CO_2 emissions [19]. The SCC per kg of hydrogen produced using selected methods is presented in Fig. 28.7.

It can be seen from Fig. 28.7 that hydrogen production using thermochemical cycles are the most advantageous processes considered for hydrogen production, in terms of SCC. Natural gas steam reforming and coal gasification are seen to be the most harmful.

28.3.3 Financial Comparison

Hydrogen cost in the future has some uncertainties that will depend on the technological development in the case of hydrogen from renewable sources, and the price in the case of fossil fuels. On the other hand, there are a lot of components in the cost for hydrogen delivery that will make a difference. Hydrogen cost depends on the cost of the production technology (which is comprised of capital investment, operation and maintenance and feedstock cost), and the cost of hydrogen transportation.

Figure 28.8 shows the average production cost of some hydrogen production methods. The most competitive means for hydrogen production are based on coal gasification and steam methane reforming [14]. Wang et al. [15] gives a range of 2.35–4.80 for the cost ($/kg) of HTE (High Temperature Electrolysis). In this study, an average of $3.5/kg H_2 is taken as basis of the comparison. The highest production cost per kg of hydrogen is observed to be the wind and solar electrolysis

Fig. 28.8 Cost comparisons of selected hydrogen production methods

methods [14, 16]. Given the fact that one of the major advantages of electrolysis is its local applications, the cost of distributed electrolysis is used in Fig. 28.8 [14]. Electrolysis cost calculations are based on distributed, small scale production assumption, while other alternatives refer to central production. Small stations have significantly higher hydrogen cost because of scale economies. The electrolysis costs are predicted to come down as technology advances. High temperature electrolysis, Cu–Cl and S–I thermochemical cycle production costs seem to compete with fossil fuel based prices [15].

28.3.4 Energy and Exergy Efficiency Comparisons
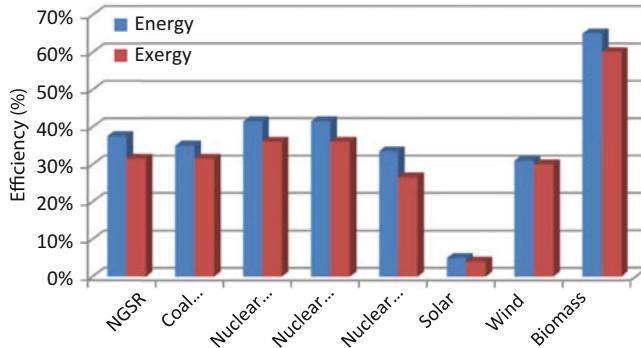
The energy and exergy efficiencies of the selected hydrogen production methods are based on the literature screening provided by Dincer and Zamfirescu [17]. In their work, two kinds of efficiencies are studied, namely exergy and exergy efficiency. They define efficiency as useful output by consumed input. In energy efficiency both the output and inputs are expressed in terms of energy, while for exergy efficiency they are expressed in terms of exergy. Energy efficiency of a hydrogen generation facility is defined by the following equation:

$$\eta = \frac{\dot{m} \times LHV}{\dot{E}_{in}}$$

where $\dot{m}$ is the mass flow rate of hydrogen produced, LHV is the lower heating value of hydrogen (121 MJ/kg) and $\dot{E}_{in}$ is the rate of energy input to drive the process. And exergy efficiency of a hydrogen generation facility is defined by the following equation:

$$\Psi = \frac{\dot{m} \times ex^{ch}}{\dot{E}x_{in}}$$

Here, ex^{ch} is the chemical exergy of hydrogen and $\dot{E}x_{in}$ is the rate of exergy input into the system.

Fig. 28.9 Energy and exergy efficiencies of selected hydrogen production methods (data from [17])

Table 28.2 Overall comparisons of selected hydrogen production methods (normalized)

Hydrogen production method		GWP	AP	SCC	Cost	Energy efficiency	Exergy efficiency
Fossil Fuel	Natural gas steam reforming	2.94	5.27	2.94	8.35	3.75	3.15
	Coal gasification with CCS	0	0	0	8.02	3.50	3.15
Nuclear Energy	Cu–Cl cycle	9.64	8.96	9.64	8.24	4.15	3.6
	S–I cycle	9.49	8.60	9.49	7.97	4.15	3.6
	High temperature electrolysis	8.82	8.42	8.82	6.15	3.35	2.65
Renewable Energy	Solar based electrolysis	8.53	7.37	8.53	0	0.50	0.4
	Wind based electrolysis	9.43	9.16	9.43	1.98	3.10	3.00
	Biomass gasification	8.24	0.54	8.24	8.46	6.50	6.00
Ideal (0 emissions and cost, 100 % efficiency)		10	10	10	10	10	10
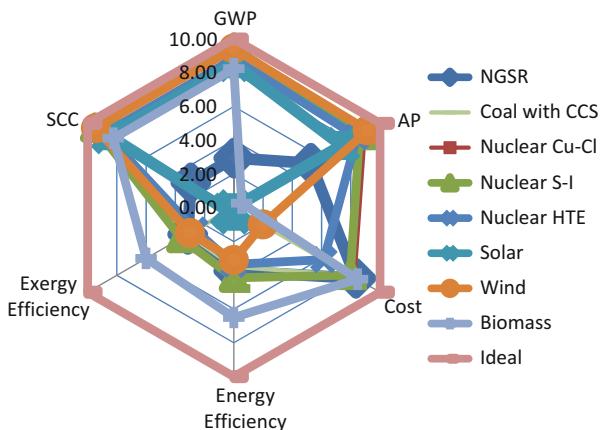
The energy and exergy efficiency data of selected hydrogen production methods are presented in Fig. 28.9 which shows that in terms of energy and exergy efficiencies, biomass gasification has an advantage compared to other methods. Solar based electrolysis, on the other hand, shows a poor performance compared to the selected production methods.

28.3.5 Overall Comparison

In order to be able to compare each production method, the GWP, AP, SCC, production cost, energy and exergy efficiency data of the selected methods are normalized and the results are presented in Table 28.2. GWP, AP, SCC and production costs are normalized based on:

$$Rank(method\ i) = \frac{Maximum - Method\ i}{Maximum} \times 10$$

Fig. 28.10 Overall comparison of selected hydrogen production processes (normalized)

It should be noted that the ranking range is between 0 and 10, where 0 means poor performance and 10 indicates the ideal case. The higher ranking means fewer emissions and lower costs. In all cases, 0 is given to the highest emissions and costs of that category. For instance, in terms of GWP, coal gasification is presented to have the highest emissions; therefore, 0 is assigned to the corresponding production method. Other ranking data is calculated based on the equation provided above. Efficiencies are normalized based on:
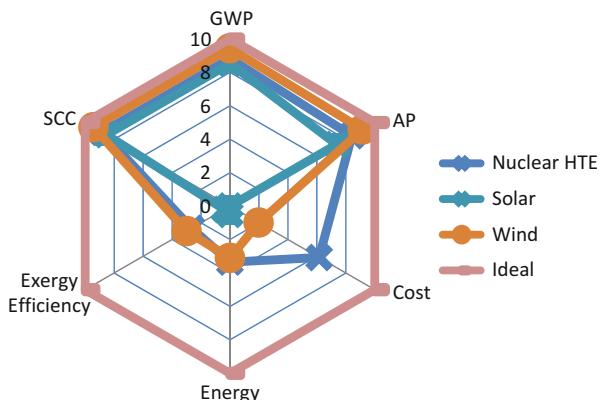
$$Efficiency\ Rank(method\ i) = Efficiency(method\ i) \times 10$$

The efficiency range is also between 0 and 10, where 0 means poor performance and 10 indicates the ideal case. The higher ranking means higher efficiency. 10 of assigned to 100 % efficiency.
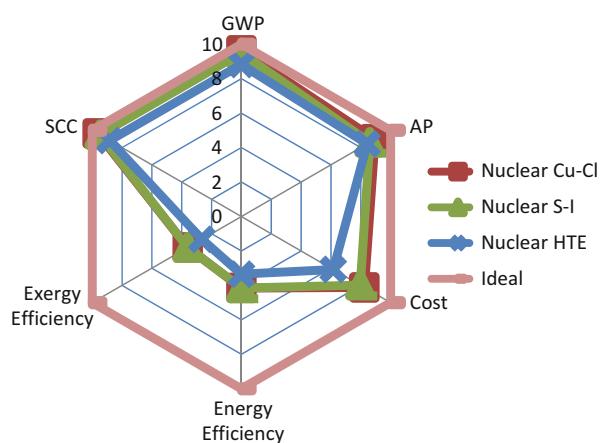
The normalized emissions, cost, and efficiency rankings are presented in Table 28.2. Figure 28.10 graphically represent the findings mentioned in Table 28.2. The ideal case is a hypothetical (and desired) production method where there are zero emissions, therefore zero SCC, maximum energy and exergy efficiency (100 %), and zero production cost. It can be seen from the figure that in terms of energy and exergy efficiency, biomass gasification shows closest performance to the ideal case. However, the AP ranking of biomass gasification is very low compared to other methods. Also, GWP and SCC performance of biomass gasification is lower than thermochemical cycles (S–I and Cu–Cl) and solar, wind, and high temperature (HTE) electrolysis.

In order to compare the electrolysis alternatives, the solar and wind based electrolysis, and HTE (high temperature electrolysis) data presented in Table 28.2 is used to construct Fig. 28.11. According to Fig. 28.11, in terms of environmental and social criteria (SCC, GWP, and AP) all of the selected electrolysis options have a high performance (low emissions, low emission related costs). It should be noted that the scale is based on the highest emission and emission related cost (the highest emission and emission cost presented in these tables are assigned the rank "0").

Fig. 28.11 Overall comparisons of selected electrolysis options (normalized)

Fig. 28.12 Overall comparisons of nuclear options: HTE, S–I, and Cu–Cl cycles (normalized)

On the other hand, the electrolysis options show a poor performance in terms of energy and exergy efficiency, and cost. Among the options presented here, solar electrolysis gives the poorest cost and efficiency performance (highest cost among the selected methods, therefore assigned a rank of "0"). Compared to wind and solar electrolysis, HTE gives closest results to the ideal case. But it should be noted that high temperature requirements still negatively affect the efficiency and cost of the production, and as mentioned in the early sections, future research should focus on improving the efficiency, and lowering the cost of the available electrolysis systems.

Figure 28.12 compares the overall performance of the nuclear options: HTE to thermochemical S–I and Cu–Cl cycles. From Fig. 28.12, it can be seen that in terms of GWP, SCC, and AP the Cu–Cl and S–I cycles give closer results to the ideal case than the HTE (the normalization procedure is explained in the beginning of Sect. 28.3.5). Cu–Cl and S–I cycles show a very close performance in terms of the selected criterion. As explained in the previous paragraph, due to the temperature requirements, the efficiency and cost performance of HTE, S–I, and Cu–Cl should be improved to get closer to the ideal case.
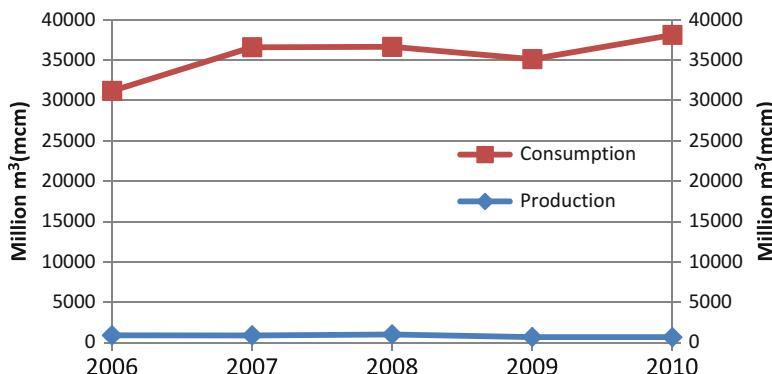
28.4   Regional Analysis: Turkey

28.4.1   Natural Gas in Turkey

Turkey holds a limited amount of natural gas reserves, estimated by IEA for the end of 2010 to around six billion m^3. The R/P ratio is calculated based on the reserves remaining at the end of any year divided by the net consumption (consumption – production) in that year. The R/P ratio result is the length of time that those remaining reserves would last if production were to continue at that rate. R/P ratio of Turkey is 8.9 years [20]. The increasing gap between Turkey's natural gas production and consumption is presented in Fig. 28.13. Although the cost and efficiency advantages of natural gas steam reforming are mentioned in Sect. 28.3, this option might not be viable to produce hydrogen in Turkey due to the limited production and increasing dependency on foreign natural gas.

28.4.2   Coal in Turkey

Until the beginning of 1990s, the amount of production and consumption of coal were about the same in Turkey. After 1990's, the consumption rate started exceeding the production rate and the gap between the production and consumption kept increasing. This trend is shown in Fig. 28.14. Similar to natural gas, although coal has advantages in terms of cost and efficiency, it might not be a viable option to produce hydrogen from coal in Turkey due to the increasing gap between the production and consumption rates.

Fig. 28.13 Natural gas production and consumption in Turkey (data from [20])
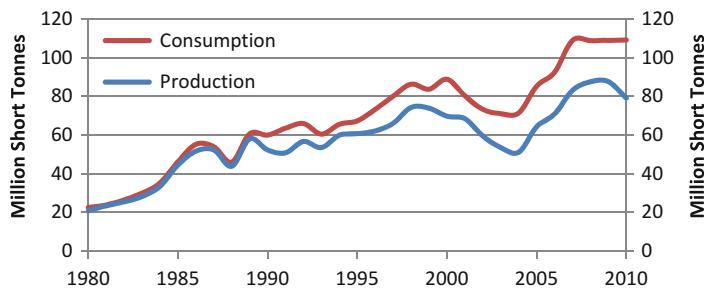
Fig. 28.14 Coal production and consumption in Turkey (data from [21])
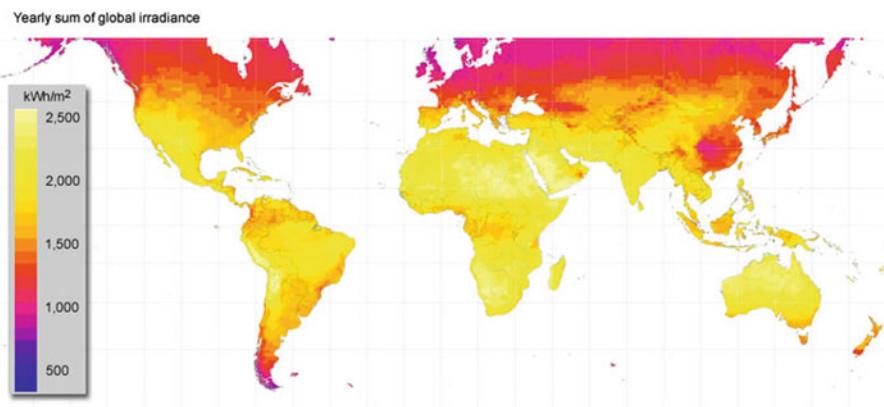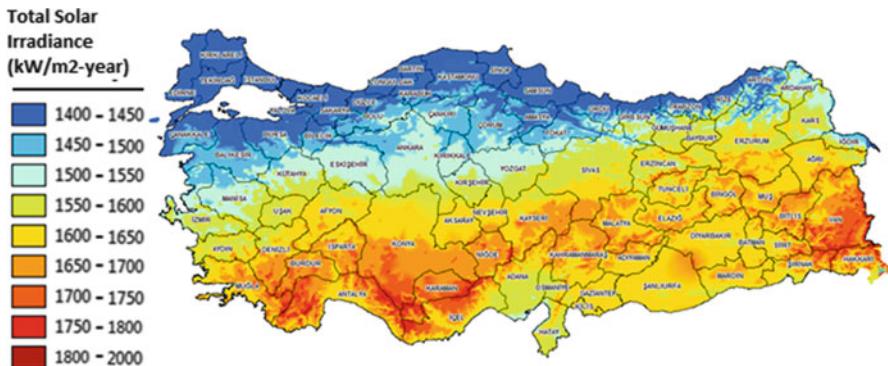
Fig. 28.15 Global mean solar irradiance map [22]

28.4.3 Solar Energy in Turkey

Due to its geographical location, Turkey can be considered to have a good potential in terms of solar energy. Figure 28.15 shows the global mean solar irradiance map. Turkey is located in the Mediterranean sun-belt; it has similar irradiance levels as Spain and Portugal.

Between April and September, Turkey has an average solar potential greater than 100 kW/m^2-month. Between these months, the average sunshine duration is above 200 h/month. On average, the daily average of solar energy is 3.6 kW/m^2-day and sunshine duration is 7.2 h/day. Figure 28.16 shows Turkey's solar energy potential atlas.

Figure 28.16 shows that southeastern part of Turkey has the highest solar energy potential. The sunshine duration of Mediterranean region is almost about the same as the southeastern region; however, the total solar radiation is lower in this region compared to southeastern Turkey. East and central Turkey follow the southeastern and Mediterranean regions. Aegean region has higher sunshine duration compared

Fig. 28.16 Turkey's solar energy potential atlas [23]
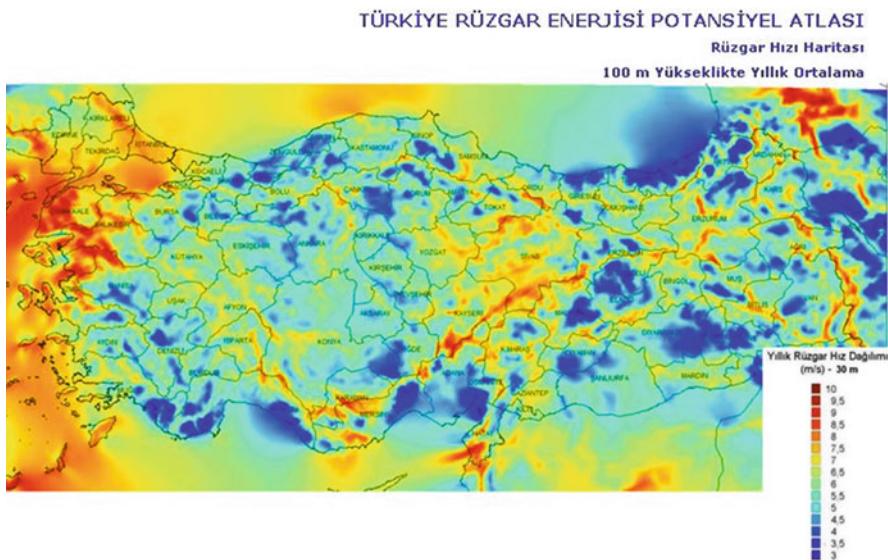
Table 28.3 Wind energy potential of Turkey compared to selected European OECD countries (data from [24])

European OECD countries	Territory (1,000 km^2)	Specific wind potential (class>3) (1,000 km^2)	Side potential (km^2)	Technical potential	
				MW	TWh/year
Turkey	781	418	9,960	83,000	166
UK	244	171	6,840	57,000	114
Spain	505	200	5,120	43,000	86
France	547	216	5,080	42,000	85
Norway	324	217	4,560	38,000	76
Italy	301	194	4,160	35,000	69
Greece	132	73	2,640	22,000	44
Ireland	70	67	2,680	22,000	44
Sweden	450	119	2,440	20,000	41
Iceland	103	103	2,080	17,000	34

to east and central Turkey but the total solar radiation in these three regions are about the same. Compared to the other regions, Marmara and Black Sea have lower total solar radiation and sunshine duration.

28.4.4 Wind Energy in Turkey

Turkey is a country with wind-rich regions. Table 28.3 shows the wind energy potential of Turkey compared to selected European OECD countries. According to the same table, Turkey's technical wind energy potential, which represents the achievable energy generation based on topographic limitations, environmental and land-use constraints, is 83,000 MW and higher than the selected OECD countries [24].

Fig. 28.17 Turkey's wind energy potential atlas (REPA) [25]

According to TÜREP, Turkey has a wind-based electricity production capacity of 48,000 MW, 803.55 MW of this amount is in operation, and 1,000 MW of it is in built-in progress, according to ETBK. In order to determine the characteristics and distribution of the wind resources, EIE developed Turkey Wind Energy Potential Atlas (REPA) in 2006. Figure 28.17 shows Turkey's wind atlas (REPA) [25]. This figure shows that some regions in Turkey have relatively high wind speeds. These have been classified into 6 wind regions with a low of about 3.5 m/s and a high of 5 m/s at 10 m altitude, which corresponds to a theoretical power production of between 1,000 and 3,000 kWh/(m^2/year). The most attractive sites are the Marmara Sea region, Southeast, the Mediterranean and the Aegean Sea Coast.

28.4.5   Biomass in Turkey

Annual biomass potential of Turkey is approximately 32 MTOE (million tonnes of oil equivalent). Total available bioenergy potential is estimated to be approximately 17.2 MTOE. In 2008, Turkey's total biomass consumption was 4.8 MTOE [26]. Turkey's planned biomass energy production is shown in Table 28.4.

According to the Republic of Turkey Ministry of Energy and Natural Resources "Biomass" report, Aegean, Black Sea, Central and Eastern Anatolia have good biomass potentials [26]. However, the 2006 Corine land cover data show that land in Turkey consists of 42.35 % agricultural areas and 54.04 % forestry and semi-natural vegetation where almost 96 % of the country's land can be defined as natural environment. The increases in population, urbanization and industrialization have

Table 28.4 Planned biomass-energy productions in Turkey (data from [26])

Year	Total biomass production (MTOE)
2015	7.320
2020	7.520
2025	7.810
2030	8.250

Table 28.5 Land cover classes in Turkey in 2000 and 2006 (data from [27])

Land class	Land size (%)		Change (m^2)
	2000	2006	
Artificial areas	1.56	1.61	+377,290,004.06
Agricultural areas	42.36	42.35	−134,513,788.38
Forests and semi-natural areas	54.08	54.04	−259,525,930.4
Wetlands	0.36	0.36	−15,159,025.99
Water bodies	1.64	1.64	+41,415,305.55
Total	100	100	

raised the use of non-intentional agricultural fields [27]. Table 28.5 summarizes the land use change in Turkey. From Table 28.5, it can be seen that as the size of artificial areas increase, the sizes of agricultural, forest, and semi-natural areas decrease. This trend could be a disadvantage in terms of hydrogen production via biomass gasification process.

28.4.6 Results and Discussion

In this section, the fossil fuel and renewable energy potentials in Turkey is discussed. The potential effect of land area on biomass gasification is briefly explained. The comparison and evaluation results are used to propose hydrogen production methods that are appropriate for Turkey.

Although Table 28.5 suggests that the land cover class change might have a negative impact on biomass potential of Turkey, Turkish government is planning to increase the biomass production in Turkey (Table 28.4), which could make the biomass a promising hydrogen feedstock. In addition to the feedstock availability; technical, financial, environmental and social impact comparison show that although it has very low AP rankings, biomass gasification can be a very promising hydrogen production method for Turkey [28]. When geographical data presented in the earlier subsections is combined, the following "suggested pathway for hydrogen production" could be made for different regions of Turkey. Table 28.6 summarizes the findings of this section by suggesting possible renewable hydrogen pathways for different regions of Turkey.

Table 28.6 Region-specific suggested renewable hydrogen production methods for Turkey

Region	Suggested H_2 production method
Marmara	Wind
Southeast	Solar
Aegean	Solar/wind/biomass
Mediterranean	Solar/wind
Black Sea	Wind/biomass
Central Anatolia	Solar/biomass
East Anatolia	Biomass

28.5 Conclusions

The literature survey and environmental, economic, social and technical performance comparisons of selected hydrogen production methods suggests that optimal hydrogen supply strategies may differ between geographic regions since hydrogen will be produced from a variety of feedstock. It is important to compare and analyze energy, environment, economic and social impacts of each stock as well as their availability in a given region. In this study, natural gas steam reforming, coal and biomass gasification, solar, wind, and high temperature electrolysis, Cu–Cl and S–I thermochemical cycles are compared based on their GWP, AP, production cost, energy and exergy efficiency, and SCC. Hydrogen production options and availability of the required feedstocks in Turkey are investigated as a case study. And it is concluded that different regions have a different potential promising method for hydrogen production. This potential should also be taken into account when comparing the advantages and disadvantages of different hydrogen production methods.

References

1. Key World Energy Statistics (2012) International Energy Agency (IEA)
2. Argonne National Laboratory (2004) Basic research needs for the hydrogen economy. Basic energy sciences workshop on hydrogen production, storage, and use
3. Hydrogen as an Energy Carrier (2006) Royal Belgian Academy Council of Applied Science
4. Rand DAJ (2009) Fuels—hydrogen production: coal gasification. Encyclopedia of electrochemical power sources. pp. 276–292
5. Marcus GH, Levin AE (2002) New designs for the nuclear renaissance. Phys Today 55(4):54–64.
6. Brown LC et al (2002) High efficiency generation of hydrogen fuels using thermochemical cycles and nuclear power. AIChE spring meeting
7. Naterer GF et al (2011) Clean hydrogen production with the cu-cl cycle - progress of international consortium, I: Experimental unit operations. Int J Hydrogen Energ 36:15472–15485

8. Trester PW, Staley HG (1981) Assessment and investigation of containment materials for thesulfur-iodine thermochemical water-splitting process for hydrogen production: final report. July 1979 to December 1980, Gas Research Institute

9. Yildiz, B.; Kazimi, M. S. "Nuclear Energy Options for Hydrogen and Hydrogen-Based Liquid Fuels Production." *DSpace@MIT* (**2003**)

10. Fujiwara S et al (2008) Hydrogen production by high temperature electrolysis with nuclear reactor. Progr Nucl Energy 50:422–426

11. Kone AC, Buke T (2010) Forecasting of CO_2 emissions from fuel combustion using trend analysis. Renew Sustain Energy Rev 14:2906–2915

12. Abánades A (2012) The challenge of hydrogen production for the transition to a CO_2-free economy. Agron Res Biosyst Eng Special 1:11–16

13. Ozbilen A, Dincer I, Rosen MA (2011) A Comparative life cycle analysis of hydrogen production via thermochemical water splitting using a Cu-Cl cycle. Int J Hydrogen Energ 36:11321–11327

14. Guerrero-Lemus R, Martínez-Durant JM (2010) Updated hydrogen production cost and parities' for conventional and renewable technologies. Int J Hydrogen Energ 35:3929–3936

15. Wang ZL et al (2010) Comparison of sulfur–iodine and copper–chlorine thermochemical hydrogen production cycles. Int J Hydrogen Energ 35:4820–4830

16. Pregger T et al (2009) Prospects of solar thermal hydrogen production processes. Int J Hydrogen Energ 34:4256–4267

17. Dincer I, Zamfirescu C (2012) Sustainable hydrogen production options and the role of IAHE. Int J Hydrogen Energ 37:16266–16286

18. Kopp RE, Mignone BK (2012) The U.S. government's social cost of carbon estimates after their first two years: pathways for improvement. Economics 6:1–43

19. Parry ML, Canziani OF, Palutikof JP, van der Linden PJ, Hanson CE (2007) Contribution of working group II to the fourth assessment report of the intergovernmental panel on climate change, Cambridge University Press

20. Country Gas Profiles – Turkey. Energy Delta Institute Website http://www.energydelta.org/mainmenu/energy-knowledge/country-gas-profiles/country-gas-profile-turkey

21. Turkey Coal Production and Consumption by Year. Index Mundi Website http://www.indexmundi.com/energy.aspx?country=tr&product=coal&graph=production+consumption

22. Green Rhino Energy Website http://www.greenrhinoenergy.com/solar/radiation/empiricalevidence.php

23. Gunes Enerjisi (Solar Energy) in Turkish T.C. Enerji ve Tabii Kaynaklar Bakanligi, Yenilenebilir Enerji Genel Mudurlugu (Republic of Turkey Ministry of Energy and Natural Resources, General Directorate of Renewable Energy) Website http://www.eie.gov.tr/yenilenebilir/gunes.aspx

24. Büyükkara G (2012) The potential of the Netherlands and Turkey in the renewables arena. Afr J Bus Manage 6(9):3413–3427

25. Ruzgar Enerjisi (Wind Energy) in Turkish T.C. Enerji ve Tabii Kaynaklar Bakanligi, Yenilenebilir Enerji Genel Mudurlugu (Republic of Turkey Ministry of Energy and Natural Resources, General Directorate of Renewable Energy) Website http://www.eie.gov.tr/yenilenebilir/ruzgar.aspx

26. Biyokutle (Biomass) in Turkish T.C. Enerji ve Tabii Kaynaklar Bakanligi, Yenilenebilir Enerji Genel Mudurlugu (Republic of Turkey Ministry of Energy and Natural Resources, General Directorate of Renewable Energy) Website http://www.eie.gov.tr/yenilenebilir/biyokutle.aspx

27. Land Use (Turkey) - The European Environment State and Outlook (2010) European Environment Agency

28. Schindler J et al (2006) Where will the energy for hydrogen production come from? Status and alternatives. European Hydrogen Association Website http://www.lbst.de/ressources/docs2007/EHA_WhereWillH2ComeFrom_2007.pdf

Chapter 29
Current Status of Fabrication of Solid Oxide Fuel Cells for Emission-Free Energy Conversion

Ayhan Sarikaya, Aligul Buyukaksoy, and Fatih Dogan

Abstract Solid oxide fuel cells (SOFCs) are promising energy conversion devices due to their environment friendly operation with relatively high efficiencies (>60 %). High power densities and stability upon interruption of fuel supply are required to realize the applications of the SOFC technology. The two main approaches for SOFC fabrication, namely; co-sintering of powders and infiltration of catalytically active components into porous scaffolds are described. It is stressed that the fabrication technique determines the performance of the SOFCs. Co-sintering of powders allow achieving high power densities while infiltration technique yields SOFC that show no performance degradation upon fuel interruption.

Keywords Energy conversion • Solid oxide fuel cells • Fabrication techniques • Electrochemical performance • Fabrication • Co-sintering of powders • Infiltration • Catalytically active components • Porous scaffolds • Power density • Degradation • Fuel interruption

29.1 Introduction

Solid oxide fuel cells (SOFCs) are devices which convert chemical energy to electrical energy with near-zero pollutant emissions [1]. Their high efficiency and fuel flexibility due to relatively high operating temperatures (600–1,000 °C) make SOFCs quite promising for power generation [2]. However, the multi-component
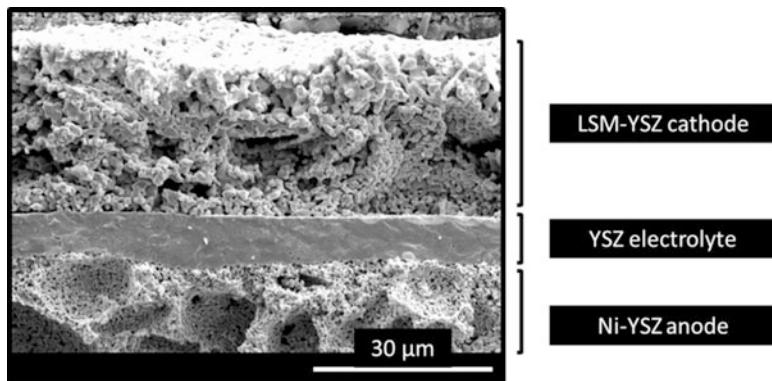
A. Sarikaya (✉)
Saint-Gobain Research and Development Center, Northborough, MA 01532, USA
e-mail: Ayhan.Sarikaya@saint-gobain.com

A. Buyukaksoy • F. Dogan
Department of Materials Science and Engineering, Missouri University of Science and Technology, Rolla, MO 65409, USA
e-mail: abd7d@mst.edu; doganf@mst.edu

Fig. 29.1 Scanning electron microscopy image of the cross section of a solid oxide fuel cell

configuration of SOFCs along with the required elevated temperatures for its operation forms a relatively complex system. As each SOFC component consists of different materials with distinct chemistries, melting temperatures and thermal expansion, significant material challenges arise also during their fabrication.

Conventional SOFCs consist of a porous Ni–YSZ cermet anode, a dense YSZ electrolyte, and a porous LSM–YSZ composite cathode. The electrochemical reactions in both electrodes occur at the interface where the catalytically active phase, the ionically conductive phase, and the gas phase meet (i.e., triple phase boundaries, TPBs). Therefore, it is essential that the electrodes are fabricated in such a way that the TPB lengths in both electrodes are maximized for enhanced electrode performance. It is also important to note that all of the three phases must be contiguous for efficient SOFC operation. On the other hand, the YSZ electrolyte is required to be well-sintered and gas-tight for high ionic conductivity and efficient separation of fuel and oxidizer (e.g., air) from anode and cathode sides, respectively. It is also critical that the YSZ electrolyte is as thin as possible to minimize the resistance associated with the ionic conduction through this layer. Scanning electron micrograph of the fractural cross section of an SOFC is shown in Fig. 29.1.

The commonly employed conventional SOFC electrode fabrication route is the co-sintering of the powders of the electrode components at elevated temperatures. This method is widely used and significantly high performances are achieved [3–5]. Infiltration of the catalytically active components into porous YSZ scaffolds is utilized as an alternative technique to form the electrodes. Substantial electrode performances and other novel properties such as time and redox stability are obtained [6–8]. This chapter describes these two main processing routes and their advantages to fabricate sustainable SOFCs. The discussion is limited to the SOFCs using the conventional materials (i.e., Ni–YSZ composite anode, YSZ electrolyte, and LSM–YSZ cathode) for the sake of eliminating the material dependent effects while comparing the processing approaches.
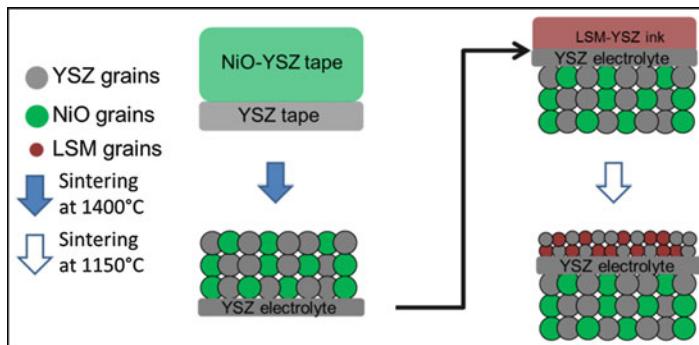
29.2   Processing Routes

Co-sintering of the component powders and infiltration of the catalytically active components into porous YSZ scaffolds are two distinct routes to fabricate SOFC electrodes and they both offer different properties and advantages in the final SOFC configurations. Co-sintering technique allows reduction of the electrolyte thickness to ~10 μm which allows achieving impressive power densities over 1 W/cm^2 at 800 °C. On the other hand, infiltration technique allows fabrication of efficient Ni–YSZ composite anodes which maintain their structural integrity during the expansion of the Ni phase when the fuel flow from the anode side is interrupted.

29.2.1   Powder Based Processing Techniques

Tape casting is the most widely employed consolidation method for the preparation of the component layers used for the co-sintering technique. A slurry mixture is formed by mixing solvent, binder, plasticizer, dispersant and the desired ceramic powders. The slurry of the homogeneously dispersed components is cast on a carrier film and leveled using a special blade to obtain a flexible tape with a controllable thickness after removal of the solvent. Two types of tapes consisting of YSZ powders for the electrolyte and NiO–YSZ powders for the anode layers are prepared with desired thicknesses and laminated together to obtain anode-electrolyte bilayers. The laminated anode–electrolyte tapes are sintered together at elevated temperatures (~1,400 °C to achieve dense YSZ electrolyte layer). It allows realizing an SOFC design with a relatively thick Ni–YSZ anode layer as a mechanical support (0.35–1.00 mm) and a relatively thin YSZ electrolyte (~10 μm). LSM–YSZ is deposited on the YSZ electrolyte after obtaining the sintered electrolyte-anode bilayer. The deposition is carried out by forcing an ink of the cathode powder, a binder, and a solvent, through the holes of a screen mesh using a rubber squeegee. This technique, referred to as "screen-printing," allows the deposition of a relatively thin LSM–YSZ cathode layer (10–60 μm). Deposited cathode layers are sintered at elevated temperatures (i.e., 1,100–1,250 °C) following their deposition. The processing route to obtain the NiO–YSZ/YSZ/LSM–YSZ based SOFC structure is illustrated in the schematic shown in Fig. 29.2.

Although the NiO phase inhibits the densification of the YSZ phase at the sintering temperatures (~1,400 °C), it is not sufficient to form the required contiguous pore structure. Therefore, pyrolyzable pore forming agents are introduced into the NiO–YSZ slurry to generate additional porosity for facile penetration of fuel through the supporting anode layer. The utilization of materials such as graphite, sucrose, polymethylmethacrylate (PMMA), polystyrene, and starch as pyrolyzable pore forming agents was widely investigated [3, 9, 10]. It was shown that the properties of pore forming agents (e.g., shape, size, and decomposition temperature) have a significant impact on the size, shape, and connectivity of the pores.

Fig. 29.2 Schematic representation of the processing steps of the co-sintering based SOFC fabrication

Thus, it has a strong effect on the electrical conductivity of the cermet and the length of TPBs, which in turn determine the performance of the SOFCs [3, 11].

Since the LSM–YSZ cathode is deposited on the YSZ electrolyte after sintering the electrolyte-anode bilayer, it allows processing the cathode layer at any desired temperature. However, LSM and YSZ have different densification behaviors. Hence, optimizing the microstructure for high performance requires well-controlled modifications on the processing parameters. For instance, YSZ particles form an ionically conductive network when they are sintered at least at 1,150 °C. It yields ~50 % of the theoretical density of YSZ [12]. On the other hand, LSM reaches a density of ~90 % of its theoretical density upon sintering at this temperature range [13]. As a result, YSZ particles do not form a connected network at low co-sintering temperatures (<1,100 °C) while co-sintering temperatures higher than the optimum temperature cause over-densification of the LSM and result in reduced TPB lengths. Highly resistive phases (i.e., $La_2Zr_2O_7$) may also form at the YSZ–LSM interface at high co-sintering temperatures (<1,100 °C) [14–16]. Therefore, detailed optimization of the processing parameters and comprehensive selection of the starting materials are required to achieve efficient LSM–YSZ cathodes. LSM–YSZ cathodes with high efficiencies are reported as a result of such an optimization effort [17].
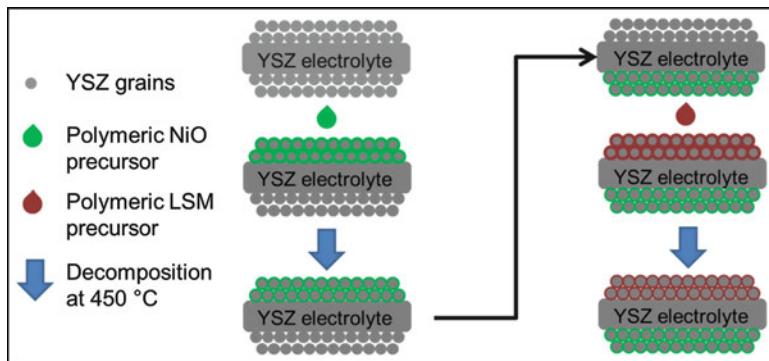
29.2.2 Infiltration Techniques

Infiltration of the precursors of the desired components into previously sintered porous YSZ scaffolds is an attractive alternative to the co-sintering technique. It allows low temperature fabrication of the SOFC electrodes and has the potential to achieve relatively high TPB length, hence performance. These techniques offer important advantages such as formation of composites of materials with distinct sintering temperatures without forming any undesired phases. It has recently been

reported that another important problem in SOFCs could be solved by fabrication of the Ni–YSZ anode by the infiltration technique. Stable SOFCs are required to operate for >40,000 h and it is expected that there would be an interruption in the fuel supply from the anode side (reduction-oxidation, redox cycle). In the case of such an interruption, Ni readily transforms to NiO which is accompanied by a 67 % expansion in volume. SOFCs with co-sintered Ni–YSZ composite anodes show severe degradation in performance due to the cracks formed in the anode layer as a result of the change in its volume [18, 19]. However, it is shown that the relatively low Ni/YSZ ratio required for the percolated and the mechanically weaker Ni phase obtained by the low temperature processing allows the performance of the SOFCs with Ni–YSZ anodes prepared by infiltration to remain stable upon redox cycles [6, 8].

The infiltration approach strictly requires YSZ scaffolds with sufficient amount of porosity and connected pores. It has been previously mentioned that it is possible to obtain porous microstructures by incorporating pyrolyzable pore formers into the ceramic matrix [9]. It allows processing porous YSZ (0.35–1 mm)/dense YSZ (10 μm)/porous YSZ (0.35–1 mm) structures by sintering at 1,400 °C (to achieve dense YSZ electrolyte). Precursor solutions of NiO and LSM can be infiltrated to the anode and the cathode sides of the sintered scaffold, respectively. However, the YSZ grain size increases to 1–2 μm at this sintering temperature range and large YSZ grains are undesirable due to the low surface area-to-volume ratio they yield [9]. It is crucial that the YSZ grains of the porous skeleton are maintained at their initial size to a maximized surface area-to-volume ratio which allows achieving high TPB lengths upon infiltration. The straight forward way to achieve such porous layers is partial sintering at relatively low temperatures (i.e., 1,150 °C). Obviously, it is not possible to achieve a dense YSZ electrolyte at these temperatures. Therefore, the fabrication of porous YSZ layers by partial sintering dictates that the porous YSZ layers are deposited on a dense YSZ electrolyte layer processed in advance. An important drawback is that the dense YSZ electrolyte layer has to be at a thickness of >100 μm for adequate mechanical support which increases cell resistance, hence decreases power density.

The fabrication of the SOFCs with thick electrolytes by the infiltration route requires the deposition of the porous YSZ layers (5–20 μm) on both sides of the electrolyte by spin coating or screen printing of YSZ (Tosoh, Japan) ink followed by sintering at 1,150 °C. In order to achieve a continuous thin coating of the infiltrated components on the YSZ grains, suitable polymeric precursors should be prepared. The polymeric NiO precursor solution infiltration into porous YSZ layer and subsequent heating to 450 °C allows forming NiO–YSZ composite anode. Several infiltration–decomposition cycles (depending on the precursor solution concentration) are required to obtain adequate NiO content. The cathode is processed following a similar approach. Polymeric LSM precursor is infiltrated into the porous YSZ scaffold followed by its decomposition at 450 °C and these steps are repeated for several times. The infiltration-based processing route of the SOFCs is illustrated in the schematic shown in Fig. 29.3.
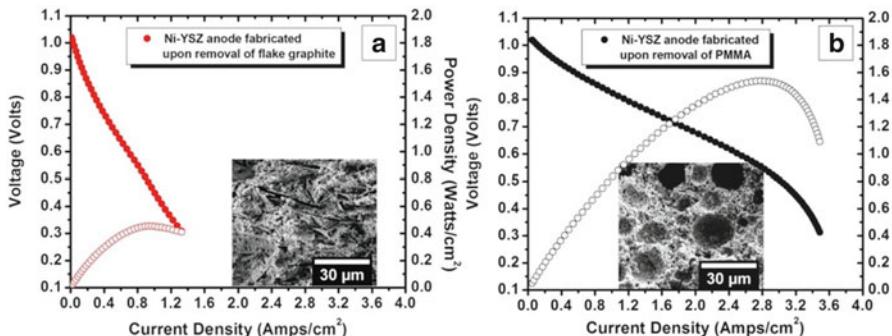
Fig. 29.3 Schematic representation of the processing steps of the infiltration based SOFC fabrication

29.3 Impact of Processing Techniques on the Performance

Testing and characterization of SOFCs is an important part of their research and development. The most commonly used methods to characterize SOFCs are impedance spectroscopy and voltammetric (e.g., current density–voltage) measurements. Impedance spectroscopy is a very useful method which allows identifying different processes contributing to the total cell resistance. It is widely used to extract the ohmic resistance and the electrode polarization resistances from the total resistance of the cells. While the ohmic resistance is induced by the electrolyte resistance and contact resistances, electrode polarizations represent the performance of anode and cathode layers. The performance of the cathode layers can be also evaluated by symmetrical cell (cathode/electrolyte/cathode) measurements in air. Although detailed information can be obtained by using the appropriate kinetic equations, current density–voltage measurements are commonly employed to evaluate the power generation characteristics of the SOFCs.

As mentioned earlier, co-sintering route is suitable for the fabrication of SOFCs with significantly thin YSZ electrolytes (10 μm) which results in reduced ohmic losses. Since YSZ exhibits and ionic conductivity of 0.02 S/cm at 800 °C, an ohmic resistance of 0.05 Ω cm^2 can be expected from YSZ electrolytes with such thicknesses. The effect of the Ni–YSZ anode microstructure formed upon the removal of different type of pore formers on the SOFC performance is reported. It was shown that the cell with the anode formed upon removal of flake graphite showed 0.4 W/cm^2 at 800 °C and it was possible to reach a power density of 1.53 W/cm^2 at 800 °C by changing the pore structure by using another pore former with distinct properties (i.e., PMMA) (Fig. 29.4) [3]. Even higher power densities (e.g., 1.75 W/cm^2) were achieved at the same temperature (800 °C) with similar SOFCs using polystyrene to form the anode pore structure [17]. As the anode thickness was reduced to ~300 μm, the transport of fuel and product gases is improved and allowed achieving improved power densities. Significantly low anode polarizations
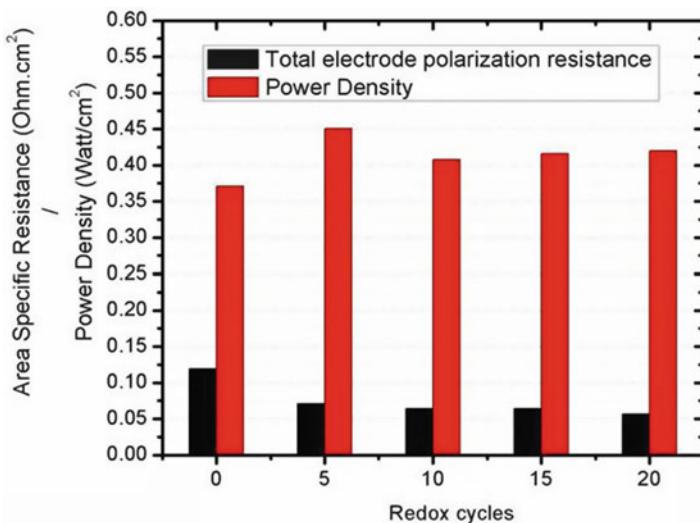
Fig. 29.4 Current density–voltage curve of the SOFCs prepared by the co-sintering approach. Anode pore structures are formed upon removal of flake graphite (**a**) and PMMA (**b**) pore formers (Modified from [3])

($\sim$0.065 Ω cm^2) were revealed by the impedance spectroscopy analyses of the optimized SOFCs. Several other researchers worked on the optimization of SOFC microstructures and obtained significantly high performances [5, 10].

Since the infiltration route requires low temperature sintering of the porous YSZ scaffolds, a previously sintered and relatively thick YSZ electrolyte is required. It was reported that the SOFCs prepared by infiltration of porous layers by Ni from anode side and LSM from the cathode side shows an electrode polarization resistance of 0.2 Ω cm^2 at 800 °C. These findings are comparable to the performances achieved with SOFCs prepared by co-sintering [6]. However, the thicker electrolyte in the infiltration based cell (180 μm) resulted in lower power densities of 0.31 W/cm^2 at 800 °C whereas the co-sintered cell with a similar electrode polarization resistance resulted in a power density of 1.53 W/cm^2 at 800 °C due to its thinner electrolyte (10 μm) [3]. On the other hand, it was possible to obtain redox stable SOFCs due to the mechanically weaker Ni phase and its sufficient electrical conductivity achieved at much lower Ni content by infiltration technique. It was shown that the power density as well as the electrode polarization resistance does not change after 15 redox cycles [6]. Further optimizations allowed achieving a total electrode polarization resistance of $\sim$0.070 Ω cm^2 at 800 °C and a power density of 0.41 W/cm^2 at 800 °C which remains stable after 20 redox cycles [8]. The changes in power density and electrode polarization resistance upon redox cycling at 800 °C are shown in Fig. 29.5.

29.4   Conclusions and Future Remarks

The processing route selected for the SOFC fabrication is critical in the design and consequently the performance of the SOFCs. Co-sintering of the constituent powders and infiltration of the catalytically active components into porous scaffolds are two distinct approaches for the fabrication of SOFCs. Co-sintering of powders

Fig. 29.5 Change in the power density and electrode polarization resistance of the SOFCs fabricated by the infiltration route upon redox cycling at 800 °C (Modified from [8])

allows fabrication of the SOFC configurations with relatively thin electrolytes and efficient electrodes which yield substantial power densities. On the other hand, they exhibit a severe degradation in performance and mechanical integrity upon the interruption of the fuel supply on the anode side. It is possible to obtain SOFCs with efficient electrodes which are stable during the changes that occur upon the interruption of the fuel flow. However, the low temperature processing of porous YSZ scaffolds necessary to achieve high surface area requires the use of electrolytes much thicker than those used in SOFCs prepared by co-sintering route. It results in relatively low power densities. Decreasing the electrolyte thickness by modifying the design of processing routes will allow combining the desired properties of the SOFCs fabricated by two different routes.

References

1. Stambouli AB, Traversa E (2002) Solid oxide fuel cells (SOFCs): a review of an environmentally clean and efficient source of energy. Renew Sustain Energ Rev 6:433–455
2. Minh NQ (1993) Ceramic fuel cells. J Am Ceram Soc 76:563–588
3. Sarikaya A, Petrovsky V, Dogan F (2012) Effect of anode microstructure on the enhanced performance of solid oxide fuel cells. Int J Hydrogen Energ 37:11370–11377
4. Jiang Y, Virkar AV (2001) A high performance, anode-supported solid oxide fuel cell operating on direct alcohol. J Electrochem Soc 148:A706–A709
5. Zhao F, Virkar AV (2005) Dependence of polarization in anode-supported solid oxide fuel cells on various cell parameters. J Power Sources 141:79–95

6. Buyukaksoy A, Petrovsky V, Dogan F (2012) Redox stable solid oxide fuel cells with Ni-YSZ cermet anodes prepared by polymeric precursor infiltration. J Electrochem Soc 159: B232–B234
7. Buyukaksoy A, Petrovsky V, Dogan F (2012) Stability and performance of solid oxide fuel cells with nanocomposite electrodes. J Electrochem Soc 159:B666–B669
8. Buyukaksoy A, Petrovsky V, Dogan F (2012) Optimization of redox stable Ni-YSZ anodes for SOFCs by two-step infiltration. J Electrochem Soc 159:F841–F848
9. Sarikaya A, Dogan F (2012) Effect of various pore formers on the microstructural development of tape-cast porous ceramics. Ceram Int 39:403–413
10. Wilson JR, Barnett SA (2008) Solid oxide fuel cell Ni–YSZ anodes: effect of composition on microstructure and performance. J Electrochem Soc 11:B181–B185
11. Suzuki T, Hasan Z, Funahashi Y et al (2009) Impact of anode microstructure on solid oxide fuel cells. Science 325:852–855
12. Petrovsky V, Jasinski P, Anderson HU et al (2005) Influence of the grain boundaries on conductivity of yttrium stabilized zirconia. MRS Proc 835:187–192
13. Tangtrakarn N, Swanson M, Moran P et al (2007) Sintering behavior and phase characterization of composite perovskite/fluorite ceramics for intermediate temperature SOFCs and oxygen separation membranes. MRS Proc 972:187–192
14. Jiang SP (2008) Development of lanthanum strontium manganite perovskite cathode materials of solid oxide fuel cells: a review. J Mater Sci 43:6799–6833
15. Choi JH, Jang JH, Oh SM (2001) Microstructure and cathodic performance of $La_{0.9}Sr_{0.1}MnO_3$/yttria-stabilized zirconia composite electrodes. Electrochim Acta 46:867–874
16. Chervin C, Glass RS, Kauzlarich SM (2005) Chemical degradation of $La_{1-x}Sr_xMnO_3$/Y_2O_3-stabilized ZrO_2 composite cathodes in the presence of current collector pastes. Solid State Ion 176:17–23
17. Sarikaya A, Petrovsky V, Dogan F (2012) Effect of microstructural evolution on the electrochemical properties of high performance SOFCs. ECS Trans 45:25–32
18. Sarantaridis D, Atkinson A (2007) Redox cycling of Ni-based solid oxide fuel cell anodes: a review. Fuel Cell 7:246–258
19. Klemensø T, Mogensen M (2007) Ni-YSZ solid oxide fuel cell anode behavior upon redox cycling based on electrical characterization. J Am Ceram Soc 90:3582–3588

Chapter 30
Algae, Biofuels, and Modeling

Ilhami Yildiz, Tri Nguyen-Quang, Thomas Mehlitz, and Bryan Brooker

Abstract This chapter first presents and discusses a dynamic mathematical model which is developed to simulate a tubular photobioreactor (PBR) and microalgae growth within at any desired location. The model has options to evaluate the effects of location, time of the year, orientation, shading and night curtains, heating and cooling systems, and indoor and outdoor operating conditions. Then the chapter focuses on the algal growth kinetics of microalgae cultivated with coal-fired flue gas, and presents two algal strains, *Chlorella vulgaris* and *Tetraselmis* sp. cultivated in lab-scale PBRs to assess the feasibility of using flue gas as a carbon source. And then, the chapter presents an economic feasibility analysis for manufacturing biodiesel from algae using a PBR. The chapter then introduces a mathematical model to investigate the thermal effects on algae population in growth in both fluid and porous media. The study reveals the potential feedback between hydrodynamic and local demographic processes in microorganism populations in the context of the influence of climate change on natural ecological systems. Finally, the chapter discusses the relationship dynamics between algae and nutrient or herbivore and algae using the predator–prey approach based on classical Lotka–Volterra system.

Keywords Microalgae growth kinetics • Photobioreactors • Carbon sequestration and storage • Economic feasibility analysis • Thermal effects on microalgae population • Microalgae and nutrient relationship dynamics • Modeling • Taxis behavior • Classical Lotka–Volterra system

I. Yildiz (✉) • T. Nguyen-Quang
Department of Engineering, Faculty of Agriculture, Dalhousie University,
Truro-Bible Hill, NS, Canada B6L 3H9
e-mail: iyildiz@dal.ca

T. Mehlitz
Solar Millennium AG (Flagsol GmbH), Agrippinawerft 30, 50678 Köln, Germany

B. Brooker
Amgen Inc., Longmont, CO 80503, USA

Nomenclature

a	Dimensionless prey capture rate, $a = \alpha_{NP}rL^2/\alpha_{PN}D_P$
A	Area, m^2; algae water; initial filter, and crucible weight, g
AEH	Air exchange per hour, 1/h
b	Distance between ground and the first PBR tube, m; dimensionless conversion rate of prey into predators $b = \alpha_{PN}rL^2/D_P$
B	Dry weight of residue, filter, and crucible, g
c	Dimensionless predator starvation rate, $c = \beta L^2/D_P$
C	Ash weight of residue, filter, and crucible, g; cell carrying capacity, cell/m^3
Cp	Specific heat, Wh/kg K
Cpv	Specific volumetric heat capacity, J/m^3 C
d	Tube diameter, m; dimensionless growth rate of prey, $d = rL^2/D_p$
D	Floor thickness; vial diameter, m; ratio of diffusion coefficients prey/predator D_N/D_P
D_N	Specific diffusion coefficient of prey or algal diffusivity, m^2/s
D_P	Specific diffusion coefficient of predator, m^2/s
dt	Distance between PBR tube centers, m
dT	Temperature change, K
dtt	Distance between PBR twin tube centers, m
E	Calculation parameter
EF	Extinction factor (also known as K)
f	Flow rate photobioreactor
F	Shape factor of the medium ($F = L/H$)
$\vec{g}$	Gravitational acceleration, m^2/s
GHG	Greenhouse gable height, m
GHL	Greenhouse length, m
GHN	Number of greenhouse bays
GHW	Greenhouse width, m
GHWH	Greenhouse wall height, m
h	Heat transfer coefficient, W/m^2 K
H	Height of column, m; height of the medium, m; hypothesis
HS	Heat storage
I	Total solar radiation, W/m^2
IR	Index of refraction n
JD	Julian Day
k	Wave number based on the length scale H
K	Thermal conductivity, W/m K; permeability, m^2
k_c	Critical wave number
L	Length of the porous or fluid medium, m
Le	Diffusion fraction or Lewis number, α/D
lt	PBR tube length, m
$\overline{n}$	Mean cell concentration, cell/m^3
N(x,t)	Dimensionless prey or algae population density

$N^*(x^*,t^*)$	Dimensional prey or algae population density, cell/m^3
na, nc	Number of PBR columns axial and parallel, respectively
Nu	Nusselt number
p	Dynamic pressure, Pa
P	Percent shading of tubes, %
P	Dimensionless pressure
$P(x,t)$	Dimensionless predator population density
$P^*(x^*,t^*)$	Dimensional predator population density, cell/m^3
PL	Actual pathlength in the algae medium, m
Pr	Prandtl number
Q	Heat transfer, radiation, kW
r	Population intrinsic growth rate of prey or algal communities, 1/s
R	Reflectivity, %
Ra_b	Algal Rayleigh number
Ra_T	Thermal Rayleigh number
Re	Reynolds number
S	Percent shading, %
Sc	Schmidt number v/D
SF	Shade factor
STIM	Solar time on a specific day of the year
t	Number of tubes per PBR column time
t	Dimensionless time
t^*	Dimensional time, s
T	Temperature, °C or K
T^*	Temperature, °C
T	Dimensionless temperature
TC	Critical sun angle
TIME	Time on a specific day
TSS	Total suspended solids, mg/L
U	Heat transfer coefficient, KW/m^2 K
V	Volume, m^3; volume of aqueous sample, mL
$\vec{V}_N^*$	Dimensional moving speed of prey or algae, m/s
$\vec{V}_P^*$	Dimensional moving speed of predator, m/s
$\vec{V}_N$	Dimensionless moving speed of prey or algae
$\vec{V}_P$	Dimensionless moving speed of predator
$\vec{V}^*$	Fluid velocity (fluid medium) or Darcy velocity (porous medium), m/s
$\vec{V}$	Dimensionless fluid velocity or dimensionless Darcy velocity
$\vec{V}_c^*$	Cell gravitactic swimming speed, m/s
$\vec{V}_c$	Cell dimensionless swimming speed $\vec{V}_c = H\vec{V}_c^*/D$ or Peclet number
VSS	Volatile suspended solids, mg/L
WS	Wind speed, m/s
x	Distance between PBR columns (parallel), m

X	Variable, e.g., cell concentration
xa	Distance between PBR columns (axial), m
(x^*, y^*, t^*)	Cartesian coordinates, m, and time, s
(x, y, t)	Dimensionless coordinates $x=X/H$; $y=Y/H$, $t=D_N t^*/H^2$

Greek Symbols

α	Absorptivity; rate for predator consuming prey or predator converting prey into predator new generation, cell/m^3/s
α_T	Thermal diffusivity, m^2/s
β	Slope of virtual surface for beam incidence; per capita mortality rate of predator in the absence of the prey, 1/s
β_c	Density variation coefficient of cell suspension
β_T	Thermal expansion coefficient
δ	Declination, the angular position of the sun at solar noon
ΔT	Difference of the top and bottom temperature, $\Delta T = T_b - T_t$
ΔN	Difference of the top and bottom concentration, $\Delta N = N_t - N_b$
ε	Emissivity of the glass/plexiglass tubes
Φ	Latitude, degrees
γ	Surface azimuth angle
ϑ	Algal cell volume, m^3/cell
λ	Dimensionless growth rate of algal communities
μ	Growth rate, maximum specific growth rate; dynamic viscosity of fluid, kg/m s
ν	Kinematic viscosity of the suspension, m^2/s
θ	Angle of incidence, refraction angle
ρ	Density, kg/m^3; specific mass of suspension "fluid-cell", kg/m^3
ρ_c	Algal cell specific mass, kg/m^3
ρ_w	Water specific mass density, kg/m^3
$\Delta\rho$	Specific mass difference of algal cell/water, $\Delta\rho = \rho_c - \rho_w$
σ	Stefan–Boltzmann constant, $5.67 * 10^{-8}$ W/m^2 K^4
τ	Transmissivity, %
ψ^*	Stream function, m^2/s
ψ	Dimensionless stream function $\psi = \psi^*/D$
Ω	Hour angle, the angular displacement of the sun

Subscripts

a	Alternative
A	Air
ALG	Algae or PBR
AP	Algae probe
CO2	Pure carbon dioxide
EFT	The PBR tube

F, FL	Floor, floor layer; poured concrete (152 mm)
FLUE	Flue gas
FR	First PBR column
FBOT, FMID, FTOP	Bottom, middle, and top floor layers, respectively
G, GR	Ground, deep ground, single layer glass
GH	Greenhouse, greenhouse cover
GHC	Free convection
GHI	Heat transfer due to infiltration
GHHG	Heat gains due to solar radiation
GHLC	Heat transfer due to conduction
GHLR	Radiation exchange with the ground and sky
GSRA	Solar radiation absorbed by the PBR
GSUR	Greenhouse floor
inf	Lower end
ILL1	Illuminated
MAX	Maximum
N	Denoting for prey
NP	Indicating predator converts prey into new generation of predator
o	Null
OS	Outside; with the sky and the ground
opt	Optimal
OSC	Outside convective heat transfer
P	Denoting for predator
PN	Indicating predator consumes prey
PBR	Photobioreactor
PARA	Parallel
PERP	Perpendicular
RLF	Between the sky and floor
S	Outside
SKY	Sky
SRAF	Solar radiation absorbed by the floor
sup	Upper end
T	Total, PBR tube
tt	Twin tube PBR
tt1	One twin tube column
TPS	Total projected surface
TSRA	Total solar radiation absorbed
TSUR	Total outside surface
W	Water

Superscripts

*   Denoting for dimensional quantity

30.1   Modeling Microalgae Growth and Photobioreactor

Microalgae have received substantial research interest for the purpose of producing biofuels and bioproducts in recent years. Strictly in comparison to other feedstocks for biodiesel, microalgae have been speculated as having the greatest yield in liters of fuel per hectare. This high yield is essential to the economic feasibility of biodiesel to compete with the cost of petrodiesel. Microalgae is the only major feedstock in consideration that does not require or compete with agricultural land, thereby dedicating land for cultivating microalgae does not adversely affect the supply or the price of food. In addition, among the potential bioproducts yielded are nutritional supplements, proteins, secondary metabolites, antioxidants, and neuroprotective agents. An essential consideration for the realization of microalgae based biofuels and bioproducts is the cost effective cultivation of biomass on a large scale. This concept drove mass microalgae cultivation from outdoor ponds to enclosed bioreactors. These enclosed bioreactors are widely accepted as the only viable means for cultivating large amounts of microalgae biomass for production of biofuels and bioproducts because of the substantially enhanced biomass production and the vastly improved control that are most probable for economically viable commercial applications. An advantage for microalgae as a biodiesel prospect is the integration of waste streams as valuable inputs to the growth process. High concentrations of ammonium and nitrate in some wastewater sources provide extremely favorable growth conditions for many microalgae strains. Also, CO_2 is required by microalgae to conduct photosynthesis and to control pH in the bioreactor, and can easily be provided from waste sources such as power plants and others. Microalgae are most efficiently grown in photobioreactors (PBRs) [1]. However, further research and improvements are needed to optimize and enhance the existing systems for commercial applications [2–5]. The major technical challenges are how to sustain highest photosynthesis and biomass productivity levels, reduce cell damage by hydrodynamic stress, reduce costs in fabrication and installation maintenance, and how to increase the capability of the system to expand to an industrial scale [6]. The objective of this section is to introduce a dynamic simulation model developed for being able to determine the best PBR configuration and operating conditions for a specific microalgae strain, and evaluate different geographic locations for microalgae production. The model has options to evaluate the effects of location, time of the year, orientation, greenhouse glazing, shading and the use of night curtains, heating and cooling systems, and both indoor and outdoor operating conditions. The coupled model developed in this study is useful for ecologists, biologists, and engineers for evaluating individual or combined effects of various forcing functions on the PBR environment and microalgae responses; and for developing control strategies for different environmental variables.

Table 30.1 PBR and greenhouse characteristics

Description	Value
Index of refraction n for the air	1[a]
Index of refraction n for the glass tube	1.526 [8]
Latitude for location (San Luis Obispo)	35.23°
Surface azimuth angle	0° [10]
Slope of virtual surface for beam incidence	45° (assumed)
Reflectivity of the ground	20 % (assumed)
Reflectivity of the algae	5 % (assumed)
Transmissivity of the greenhouse cover	60 % [9]
Emissivity of the glass/plexiglass tubes	94 % [10, 11]
Infiltration rate	1.5 (air exchanges/h) [9]
Heat transfer coefficient—single layer glass	0.00628 kW/m^2 K [9]
Heat transfer coefficient—poured concrete 152 mm	0.000872 kW/m^2 K [9]
Temperature at maximum algae growth rate	29 °C
Maximum algae growth rate	1.44/day
Temperature at 10 % of max growth rate—lower and upper	11 and 35 °C
Number of PBR parallel columns and axial columns	19 and 10
PBR tube diameter and length	0.03 and 10 m
Distance between PBR tube centers	0.18 m
Distance between PBR twin tube centers	0.06 m
Distance between ground and first PBR tube	0.3 m
Distance between PBR columns (parallel) and (axial)	1.5 and 1.5 m
Number of tubes per PBR column	32
Greenhouse width and length	7.2 and 57.6 m
Greenhouse wall height and gable height	2.4 and 1. 8 m
Number of greenhouse bays	12

30.1.1   Resources and Procedures

An experimental study is performed using a lab-scale PBR, and *Chlorella vulgaris* as the algal strain. The PBRs are operated at different growth temperatures, and *Chlorella* growth dynamics are monitored under controlled environments. A coupled dynamic mathematical model employing ordinary differential equations for algae growth and a horizontal tubular PBR is developed and executed to provide an accurate prediction of a horizontal tubular PBR's performance as a function of dynamic environmental factors such as solar energy, outside air temperature, and wind speed. This dynamic prediction model is developed in Microsoft Excel environment using VBA (Visual Basic for Application) from basic energy conservation and heat transfer principles for a single glass-glazing greenhouse. The PBR and greenhouse characteristics used in the simulation model are presented in Table 30.1. Hourly weather data (temperature, solar radiation, wind speed, relative humidity) are obtained from the California Irrigation Management Information System for San Luis Obispo (35°17′N; 120°39′W), California, USA for the month of April 2007 [7]. However, the simulation model is flexible enough to

simulate any other location, any other month, or even any other year. Simulations are performed starting at the beginning of the fifth day and ended at the end of 30th day of the month providing 26-day simulations. First 5 days of simulations are ignored in order to generate more reliable estimates, and productivity (not yield) is evaluated in sensitivity analyses. Sensitivity analyses are performed on the indoor PBR system, which has a glass greenhouse glazing. The shading system is not operational during these analyses. Each parameter (outside temperature, solar radiation, ground reflectivity, PBR column distance, etc.) is varied individually while all other parameters are held constant at their standard values. In addition to the sensitivity analyses, responses of some key parameters to step inputs in outside air temperature and outside solar radiation are also determined.

Microalgae Culturing Equipment

In this study, for determining temperature responses of microalgae under controlled environments, a vertical column Plankton Reactor (Aqua Medic GmbH, Plankton Reactor, Bissendorf, Germany) is used. This lab-scale PBR is basically a transparent plastic cylinder with a holding volume of 2.25 L. A fluorescent light (8 W, 6,700 K, 1,300 lm; Aqua Medic GmbH, Plankton Light Reactor, Bissendorf, Germany) provides the necessary light for photosynthesis to occur. A timer providing 16 h of light and 8 h of dark periods, respectively, controls the lighting. All bulbs that are above 5,600 K are considered daylight bulbs, offering a clean, bright light condition. These bulbs are used to simulate outdoor conditions providing 65 W/m^2. As microalgae grow, the pH of the algal slurry increases due to the consumption of the carbonic species. A pH meter (Milwaukee, SMS 122, Romania) continuously monitors the pH of the algal solution. The pH meter is coupled with CO_2 control valves (Red Sea, CO_2 Magnetventil, Israel), which acts as the gas dosing solenoid, in essence maintaining a constant pH level by supplying the proper amount of carbon. An optimal pH of approximately 7.2 is maintained by supplying the right amount of CO_2. As soon as the pH rise over 7.25, the valve opens and CO_2 dosing is provided, which decreases the pH below 7.15. An ambient air pump (Fusion Quiet Power, 400, Taiwan) is used to continuously agitate the culture and keep the algal solution homogeneous. Digital thermometers (Coralife, ESU Reptile) monitor the aqueous solution temperature. The temperature is varied from 9 to 39 °C by an off-the-shelf aquarium chiller and an aquarium heater. A submersible heater (Marine Land, Stealth Pro, China) is used for monitoring Chlorella at temperatures higher than the ambient and is set at the specific experimental temperature. An optical microscope is used to ensure that the purity of algae cultures, and total magnification was "1,000×." Keeping the light, pH, and nutrient levels constant enables the variable in question, the effect of temperature on algae growth to be investigated. A Bausch & Lomb Spectronic 21 spectrophotometer is used to monitor algal growth kinetics. Samples from each PBR are taken twice a day. The optical density of each sample is determined by measuring the transmittance at 560 nm. Since the density is a limiting growth factor (too high of a density can limit
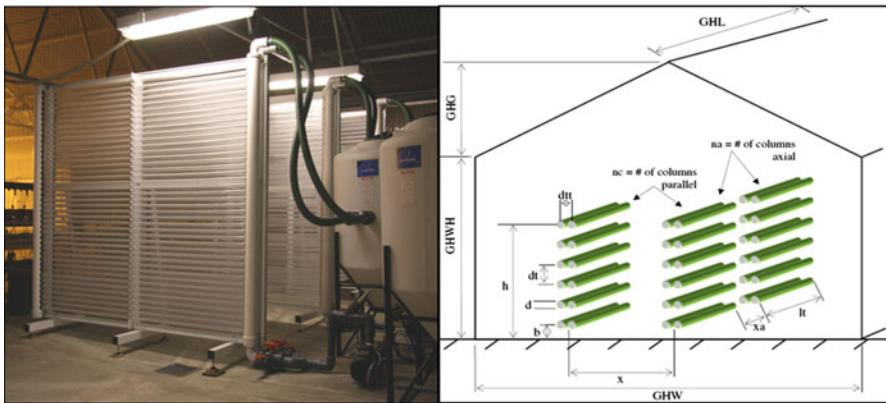
growth), the growth medium is diluted as soon as the transmittance reached 10 %. A Hanna Instruments® multimeter is used to measure phosphate and nitrate concentration at each start of a new batch (approximately every fourth day).

Quantifying Growth Kinetics

The algal strains are expected to follow a typical noncontinuous batch culture growth curve. Batch growth is characterized by four distinct phases: lag, exponential, stationary and death [12]. Usually nutrient depletion or toxic product accumulation causes the microorganism population to decline. *Chlorella* inoculum is grown in two 2-L Erlenmeyer flasks. The idea in maintaining the culture inoculum is to keep the strain in a subdued yet healthy condition. The photoperiod is 1:1, at 12 h of light and 12 h of dark. Ambient air is constantly diffused into the media to provide agitation and minimal CO_2. In this way microalgae strain grows slowly and after a week of inhibited growth the culture is ready for inoculation. All PBRs are taken apart and sanitized before inoculation. All other equipment in contact with the algal solution is also cleaned including the submersible heaters, pH probes, thermometers, and algal sampling ports. A phosphoric acid solution (Star San, Five-Star, Commerce City, CO) is used for all equipment sanitation. Maintaining aseptic culturing techniques is essential to avoid contamination and culture crashes. Each PBR has a holding volume of 2.25 L; however, the displacement causes by the submersible heater, pH probe and thermometer yields an operating volume of 2.0 L. In addition, 2 in. of headspace is required to accommodate the algal uproar upon gas dosing. Beginning inoculation, 200 mL of algal solution at a transmittance of 40 % is used. The remaining 1,800 mL is filled with distilled water. Schultz Plant Food Plus provides the necessary nutrients and the nutrient breakdown was10% total nitrogen (ammonium N, 1.6 %; nitrate N, 0.2 %; urea N, 8.2 %), 15 % available phosphate (P_2O_5), 10 % soluble potash (K_2O), 0.1 % iron (Fe), 0.05 % manganese (Mn), and 0.05 % zinc (Zn). The nutrient concentration is kept above 10 mg/L for Phosphorous and above 50 mg/L for Nitrogen. The photoperiod is set at 2:1 resulting to 16 h of light and 8 h of dark. Once all PBRs are inoculated, the growth period begins and the first samples are collected for analysis. Samples for analysis are collected twice daily throughout the growth period. Twice daily monitoring of temperature and pH are performed to ensure no adverse effects on microalgae growth from these two variables, as well as preserving consistency among sample replicates.

Physical Model and Photobioreactor Architecture

The dynamic simulation tool developed in this study is based on a PBR system also known as "BioFence." The BioFence system is developed by Varicon Aqua Solutions Ltd., UK (Fig. 30.1, left). Horizontal plastic tubes are stacked in a rack to allow a high surface-to-volume ratio. The expandability of the system allows a scale-up to basically all desired sizes. According to Varicon Aqua Solutions Ltd.,

Fig. 30.1 The actual BioFence system (*left*) installed at Cal Poly, and the schematic view and basic dimensions of photobioreactor (PBR) used in the simulation model (*right*)

the BioFence can produce an equivalent of 2,000 L of bag grown algae per day in an array of tubes of 10 m × 1.8 m. Each meter of transparent tube has an internal volume of 0.66 L and an internal surface area of 0.1 m^2. It is expandable in blocks of 16 m × 5 m tubes. A light-to-dark ratio of at least 50 % is recommended. The tank size required is therefore equal or greater than the internal tube volume [13]. A description of the PBR as a series of parallel rows is extended to an overall greenhouse model for indoor operation, whereas the same parallel rows are modeled without a greenhouse for the outside operation, as schematically shown in Fig. 30.1. In dealing with the energy exchanges, the outside weather conditions and the deep ground temperature served as boundary conditions. The bulk air is analyzed by adopting the assumption of "perfect mixing." All dimensions of the PBR are kept as variables in the model. This feature allows optimization and flexibility for different PBR configurations.

Energy Balances

The simulation model is able to determine the heating requirements for an outdoor operation as well as for an indoor (greenhouse) operation. Different heat transfer modes occur under the two different conditions. In the case of an outdoor operation, heat losses due to convection and radiation (ground and sky), and gains due to solar radiation are present. Considering the heat storage term, the energy balances for the outdoor PBR (Eq. 30.1), greenhouse air (Eq. 30.2), and PBR (Eq. 30.3) in the greenhouse are expressed as:

$$\rho_W * V_{PBR} * Cp_W * dT_{PBR}/dt = Q_{TSRA} - Q_{OS} - Q_{OSC} \tag{30.1}$$

$$\rho_A * V_{GH} * Cp_A * dT_{GH}/dt = Q_{GHHG} - Q_{GHI} - Q_{GHC} \qquad (30.2)$$

$$\rho_W * V_{PBR} * Cp_W * dT_{PBR}/dt = Q_{GSRA} - Q_{GHLR} + Q_{GHCL} \qquad (30.3)$$

An one-dimensional heat conduction equation is used in dealing with the floor for inside and outside conditions, by dividing the floor into three layers with the assumption of homogeneous thermal and hydraulic properties within each layer [14, 15]. The ground layer thicknesses are 0.05, 0.10, and 0.50 m for the top, middle, and bottom layers, respectively. It is assumed that the deep ground temperature is constant at 15 °C [16]. Then, the energy balance for the three floor layers are expressed as:

Top layer $\quad : V_{F1} * Cv_F * dT_{F1}/dt = Q_{SRAF} - Q_{RLF} - Q_{FTOP} \qquad (30.4)$

Middle layer $\quad : V_{F2} * Cv_F * dT_{F2}/dt = Q_{FTOP} - Q_{FMID} \qquad (30.5)$

Bottom layer $\quad : V_{F3} * Cv_F * dT_{F3}/dt = Q_{FMID} - Q_{FBOT} \qquad (30.6)$

General Equations

For both inside and outside operations, general equations used in developing the model are presented here. For all the following equations, the Julian Day for a specific date of the year has to be determined. The solar time is calculated using the following equations [10]:

$$STIM = TIME + 2.4 + E \qquad (30.7)$$

$$
\begin{aligned}
E = 229.2 * \big(& 0.000075 + 0.001868 * Cos\,(b * \pi/180) \\
& - 0.032077 * Sin\,(b * \pi/180) - 0.014615 * Cos\,(2 * b * \pi/180)\big) \\
& - 0.04089 * Sin\,(2 * b * \pi/180)
\end{aligned} \qquad (30.8)
$$

$$b = (JD - 1) * 360/365 \qquad (30.9)$$

One major parameter of the model is the direction of the sunlight, and consequently the sun angle with respect to the PBR. Main angles of solar radiation are the zenith angle, slope, surface azimuth angle, and solar azimuth angle for a tilted surface [8]. In this study, approximate equations are used to determine the declination, hour angle, and angle of incidence [17]. Shading of the PBR has a major impact on the performance of the system since the tubes shade each other differently throughout the day. An equation construct is developed, covering all possible shading options within every PBR column, and also through multiple columns standing next to each other. A shade factor as a function of the Julian Day and the time of the day are derived and later multiplied by the incoming solar radiation. A critical sun angle (TC) exists, where the tubes shade each other and is estimated as in Eq. (30.10). For the angle of incidence (θ) greater than the critical angle (TC),

no shading occurs. For an angle of incidence less than the critical angle, however, Eq. (30.11) is used to determine the percentage of shading. For the second to the nth column, the illuminated height is calculated using Eq. (30.12).

$$TC = A\tan(dt/d) \tag{30.10}$$

$$S_{FR} = (TC - \theta) * 100/TC \tag{30.11}$$

$$H_{ILL1} = x/\mathrm{Tan}\,(\theta * \pi/180) \tag{30.12}$$

The illuminated height should not be greater than the total height of tubes stacked over each other (i.e., total height (h) minus the distance of the tube next to the ground (b)). Turning this height into a percentage value of illuminated tubes, delivered Eq. (30.13). The remainder of tubes in column n is not illuminated fully, however, receives solar rays through the gaps of tubes of the previous column as expressed in Eq. (30.14), where $P_{ERCNSHADE1}$ is the shading percentage of tubes in a column n receiving solar rays through the gaps of the previous columns, expressed by the diameter to distance ratio, ddr = d/dt. Related to the critical sun angle, the total percentage of shading is expressed as in Eq. (30.15). Putting all columns together, and considering that the top tube of each column receives solar radiation without shading all day long, the final equation for total shading is developed:

$$P_{ERCNILL} = H_{ILL1} * 100/(h - b) \tag{30.13}$$

$$P_{ERCNSHADE1} = ddr * (100 - P_{ERCNILL}) \tag{30.14}$$

$$P_{ERCNSHADE} = P_{ERCNILL} * P_{ERCNILL}/100 + P_{ERCNSHADE1} \tag{30.15}$$

$$SF = ((((S_{FR} + (nc - 1) * P_{ERCNSHADE})/nc) * (t - 1) + 1/t)/t)/100 \tag{30.16}$$

Shading for the second half of the day (i.e., after solar noon) is treated the same as the first half of the day. Since the simulation model has an option to handle twin tubes within one column (i.e., two tube rows are hold by one frame), the shading factor has to be adjusted to this case. Equations (30.14–30.20) are used to calculate the shading factor for one twin tube column (SF_{tt1}). The distance between two different columns (x) is therefore substituted with the distance between the twin tubes (dtt). Then, the usual shading factor (SF) for the entire PBR setting is determined as described above. The shading factor for one twin tube column is then multiplied by the remaining illumination height (1—SF). Adding this percentage to the usual shading factor results in an overall shading factor for twin tubes (SF_{tt}). In general, the twin tubes increase the total shading factor. Further steps have to be considered to handle the air and PBR interface. The total incoming solar radiation are partly reflected or transmitted through the PBR tubes. Absorption of the glass or plexiglass tubes is neglected. The transmitted portion is partly absorbed by the growth media (algae water). The reflected portion is exposed to the other tubes consequently. The relationship between total incoming beams and refraction

at a surface of a different media is described by Duffiie and Beckman [8]. The refraction angle (θ_2) is calculated by using Snell's Law [18]:

$$\theta_2 = \text{Asin}((IR_A/IR_T) * \text{Sin}(\theta * \pi/180))/\pi * 180 \tag{30.17}$$

In order to determine how much radiation is transmitted through the tube and algae water, the transmittance of the tube and water is multiplied (Eq. 30.18). The transmittance of the tube is a function of the parallel and perpendicular reflection of the tube in accordance with Fresnel's equation (Eqs. 30.19–30.21) [8]. The total reflection of the tube is calculated assuming that the mean angle the beams hit the tubes were $45°$ (Eq. 30.22).

$$\tau = \tau_T * \tau_A \tag{30.18}$$

$$\tau_T = 0.5 * ((1 - R_{PARA})/(1 + R_{PARA}) + (1 - R_{PERP})/(1 + R_{PERP})) \tag{30.19}$$

$$R_{PARA} = (\text{Tan}(\theta2 - \theta) * \pi/180)^2 / \left((\text{Tan}(\theta + \theta2) * \pi/180)^2\right) \tag{30.20}$$

$$R_{PERP} = \left((\text{Sin}((\theta2 - \theta) * \pi/180))^2\right) / \left((\text{Sin}((\theta + \theta2) * \pi/180))^2\right) \tag{30.21}$$

$$R_{EFT} = 0.5 * (R_{PERP} + R_{PARA}) \tag{30.22}$$

The transmittance of the algae water is calculated using Bouguer's Law [8], which is based on the assumption that the absorbed radiation is proportional to the local intensity in the medium and the distance the radiation has traveled in the medium (Eq. 30.23). Integrating along the actual pathlength (PL) in the medium (i.e., from zero to PL/Cos $\theta2$) yields Eq. (30.24). The pathlength is assumed to be approximately 60 % of the tube diameter (d in m). The extinction factor (Eq. 30.25) is calculated from experimental data; and a mean transmittance (optimal density for algae) of 0.3 as well as a vial with a diameter of 0.00127 m was used.

$$dI = -I * K \ dx \tag{30.23}$$

$$\tau_A = \text{Exp}(-EF * PL/\text{Cos}(\theta2 * \pi/180)) \tag{30.24}$$

$$EF = -\text{Ln}(\tau_{AP})/D_{AP} \tag{30.25}$$

Outdoor Photobioreactor

The total solar radiation absorbed is calculated using Eqs. (30.26 and 30.27). The reflectivity of the ground, R_{GR}, is assumed to be 0.2, and the absorptivity of the algae water which is also assumed to be 1 minus the total transmittance (τ) minus the reflection of single algae cells (R_{ALG} assumed to be 0.05). According to Newton's law of cooling, the PBR convective heat transfer is developed as in Eq. (30.28).

$$I_T = I_S * \{(1 - SF) + R_{GR} + R_{EFT} + \tau \} \tag{30.26}$$

$$Q_{TSRA} = I_T * A_{TPS} * (1 - \tau - R_{ALG})/1,000 \tag{30.27}$$

$$Q_{OSC} = h_{HTC} * A_{TSUR} * (T_{ALG} - T_{OS})/1,000 \tag{30.28}$$

The heat transfer coefficient, h_{HTC}, is calculated using $h_{HTC} = Nu * k/d$ [11], where Nu is the Nusselt number, k is an air constant (0.0263 W/m K) [19]. The value of the Reynolds number (Re) provides the information about the flow conditions (i.e., laminar or turbulent flow over a tubular surface), and it is calculated using $Re = WS * d/v$ [11]. With a maximum wind speed of 5.2 m/s obtained from the weather file, a tube diameter of 0.003 m, and v being 0.00001589 m^2/s at room temperature [19], the Reynolds number results in 9,820, which is smaller than 10^7, hence a laminar flow condition is assumed [11]. For laminar flow, $Nu = c * Re^m * Pr^{(1/3)}$ is used [11], where c and m are constants; for the range of Reynolds numbers for the given conditions, their numerical values are 0.193 and 0.618, respectively [11]. The Prandtl number (Pr) for air at 300 K is 0.707 [19]. The Reynolds number is calculated each time as a function of the wind speed. The radiative heat transfers with the sky and ground are determined using the simplified radiation equations for an object in a large enclosure [11]. For the outside PBR:

$$Q_{SKY} = \varepsilon * A_{GH} * \sigma * \left(T_{ALG}{}^4 - T_{SKY}{}^4\right)/1,000 \tag{30.29}$$

$$Q_{FL} = \varepsilon * A_{GH} * \sigma * \left(T_{ALG}{}^4 - T_{FL}{}^4\right)/1,000 \tag{30.30}$$

$$Q_{OS} = 0.5 * Q_{SKY} + 0.5 * Q_{FL} \tag{30.31}$$

$$Q_{SRAF} = A_{GSUR} * I_S * \alpha_{FL}/1,000 \tag{30.32}$$

$$Q_{FTOP} = K_{FL} * A_{GSUR} * (T_{FL} - T_{FMID})/D_{FL1} \tag{30.33}$$

$$Q_{FMID} = K_{FL} * A_{GSUR} * (T_{FMID} - T_{FBOT})/D_{FL2} \tag{30.34}$$

$$Q_{FBOT} = K_{FL} * A_{GSUR} * (T_{FBOT} - T_G)/D_{FL3} \tag{30.35}$$

It is assumed that the total outside radiative heat exchange (Q_{OS}) is 50 % with the sky (Q_{SKY}) and 50 % with the ground (Q_{FL}). ε is the emissivity of the glass (or plexiglass) tubes, which is 0.9 [19]; and T_{SKY} is the sky temperature (K), which is determined as a function of the ambient air temperature as defined by Swinbank [20], $T_{SKY} = 0.0552 * T_{OS}{}^{1.5}$. The heat exchange done by the floor layers are calculated using the following equations, where K_{FL} is the thermal conductivity of floor layers (1.75 W/m K) [21].

Solving Differential Equations

The ordinary differential equations (Eqs. 30.1–30.6, 30.26, and 30.36) with an initial value, are solved using Euler's method, which is used to advance in time

and to obtain a new solution at the next time step. In this study, a time interval of 1 h is used. Because of the fairly large time constants of the heat storage elements, no stability problems are observed. The system is calculated as follows, taking the heat storage term into account (Eqs. 30.36–30.38). For the PBR, the equation is modified to Eq. (30.39), where Cpv_{FL} is the volumetric heat capacity of the floor $(2.93 * 10^6$ $J/m^3.°C)$ [16], Cp_W is the specific heat of water $(4,186$ $J/kg.°C)$. Reorganizing Eq. (30.39), the new PBR temperature is determined (Eq. 30.40).

$$Q = \rho * V * Cp * dT/dt \tag{30.36}$$

$$HS_{FTOP} = A_{GSUR} * D_{FL1} * Cpv_{FL} * (T_{FLNEW} - T_{FL}) \tag{30.37}$$

$$T_{FLNEW} = HS_{FTOP}/(A_{GSUR} * D_{FL1} * Cpv_{FL}) + T_{FL} \tag{30.38}$$

$$Q_{TOSHR} = \rho_W * V_{PBR} * Cp_W * (T_{ALGNEW} - T_{ALG}) \tag{30.39}$$

$$T_{ALGNEW} = Q_{TOSHR} * (\rho_W * V_{PBR} * Cp_W) + T_{ALG} \tag{30.40}$$

Indoor Photobioreactor

The gained heat due to solar radiation, conductive heat losses and the infiltration losses are estimated by using Eqs. (30.41–30.43) [9], where the transmissivity of the greenhouse walls is 94 %, the heat transfer coefficients for the greenhouse cover and floor are 0.00628 kW/m^2 K and 0.000872 kW/m^2 K, respectively [9]; and the air exchange per hour is assumed to be 1.5 per hour. 0.0002928 is a conversion factor used to convert Btu/h into kW. The temperature response of the greenhouse air is calculated taking the heat storage term into account (Eq. 30.44).

$$Q_{GHHG} = \tau_{GH} * I_S * (A_{GH} + A_{TPS} * (1 - SF))/1,000 \tag{30.41}$$

$$Q_{GHLC} = A_{GHGSUR} * U_G * (T_{GH} - T_{OS}) + A_{GH} * U_{FL} * (T_{GH} - T_O) \tag{30.42}$$

$$Q_{GHI} = 0.02 * AEH * V_{GH} * (T_{GH} - T_{OS}) * 0.0002928 \tag{30.43}$$

$$T_{GHNEW} = Q_{GHHG}/(\rho_A * V_{GH} * Cp_{AIR}) + T_{GH} \tag{30.44}$$

As previously described, three heat transfer modes are considered for the inside PBR: heat gain due to absorbed solar radiation, convective heat exchange, and radiative heat exchange with the sky and the ground. The total solar radiation absorbed, I_T, is calculated using Eqs. (30.45–30.47), where the transmissivity of the greenhouse cover of 94 % [9]. Heat fluxes due to convection are calculated using equations for free convection, since no wind and hardly any air movement occurred around the tubes. Newton's law of cooling is modified to calculate the convective heat transfer for the indoor PBR (Eq. 30.48) [11].

$$Q_{GSRA} = \tau_{GH} * Q_{TSRA} \tag{30.45}$$

$$Q_{TSRA} = I_T * A_{TPS} * (1 - \tau - R_{ALGAE})/1,000 \tag{30.46}$$

$$I_T = I_S * \{(1 - SF) + R_G + R_{EFT} + \tau\} \tag{30.47}$$

$$Q_{GHC} = h_{HTC} * A_{TSUR} * (T_{ALG} - T_{GH})/1,000 \tag{30.48}$$

$$h_{HTC} = 1.32 * ((T_{ALG} - T_{GH})/d)^{0.25} \tag{30.49}$$

The radiative heat exchange with the sky and ground are calculated using the simplified radiation equations (Eqs. 30.50–30.52), where it is assumed that the total radiative heat exchange is 50 % with the sky and 50 % with the ground. The emissivity of the glass (or plexiglass) tubes is 0.9 [9]. The floor temperatures are calculated using the same approach as in outdoor conditions; however, here the long and shortwave transmittance of the greenhouse roof is considered as well. The temperature response of the PBR is calculated, taking the heat storage term into account (Eqs. 30.53 and 30.54).

$$Q_{SKY} = \tau_{GH} * \varepsilon * A_{TSUR} * \sigma * (T_{ALG}^4 - T_{SKY}^4)/1,000 \tag{30.50}$$

$$Q_{FL} = \varepsilon * A_{TSUR} * \sigma * (T_{ALG}^4 - T_{FL}^4)/1,000 \tag{30.51}$$

$$Q_{GHLR} = 0.5 * Q_{SKY} + 0.5 * Q_{FL} \tag{30.52}$$

$$Q_{TGHR} = \rho_W * V_{PBR} * Cp_W * (T_{ALGNEW} - T_{ALG}) \tag{30.53}$$

$$T_{ALGNEW} = Q_{TGHR}/(\rho_W * V_{PBR} * Cp_W) + T_{ALG} \tag{30.54}$$

Temperature Effect on Microalgae Growth

Temperature is a widely measured environmental variable, and an important factor that affects the performance of algal growth [12, 22]. Keeping all other variables constant can identify the effect of temperature on algal growth rate. The growth rate reaches a maximum at a specific temperature. For microalgae, the growth rate, and therefore the yield, will follow a skewed normal distribution [23, 24], where μ_{max} is the peak. Every single algae strain has a different specific growth rate, which needs to be determined. The skewed normal distribution can be described through Eqs. (30.55 and 30.56), one for the specific growth rate below the maximum and one for the specific growth above the maximum. The temperature dependent growth rate (μ_{maxT}) reaches a maximum at the optimal temperature (T_{opt}). The growth rate declines therefore, when the temperature rises or falls. Temperature limits are reached when $\mu_{maxT} = 10$ % of the maximum growth rate μ_{max} under optimal conditions. The lower temperature limit is expressed as T_{inf}, whereas the upper limit is shown as T_{sup} [24]. The temperature coefficient (Q_{10}) represents the factor by which the rate (R) of a reaction increases for every $10°$ rise in the temperature (T) (Eq. 30.57).

The rate (R) may represent any measure of the progress along the process. If the rate of the reaction is temperature independent, the resulting Q_{10} will be equal to 1.0. If the reaction rate increases with increasing temperature, Q_{10} will equal greater than 1.0. Thus, the more temperature dependent a process is, the higher the Q_{10} value will be [25]:

$$\mu_{maxT} = \mu_{max} * EXP\left\{-2.3 * \left[(T - T_{opt})/(T_{sup} - T_{opt})\right]^2\right\} \text{ for } T > T_{opt} \quad (30.55)$$

$$\mu_{maxT} = \mu_{max} * EXP\left\{-2.3 * \left[(T - T_{opt})/(T_{inf} - T_{opt})\right]^2\right\} \text{ for } T < T_{opt} \quad (30.56)$$
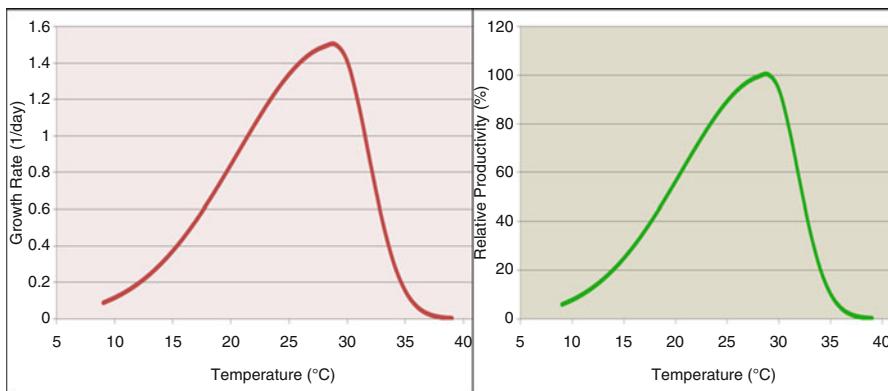
$$Q_{10} = (R_2/R_1)^{\left(10/(T_2 - T_1)\right)} \quad (30.57)$$

The Q_{10} value for microalgae grown in batch cultures is 1.88 at the maximum growth rate, μ_{max}. For continuous cultivation in large-scale PBRs, the Q_{10} value is between 2.08 and 2.19 at μ_{max}. A number of researchers reported that the Q_{10} value becomes greater below the optimal growth rate [22, 26, 27]. In this study, the temperatures are rounded to full degrees Celsius (e.g., 15.3–15 °C). In accordance with Eqs. (30.55 and 30.56), only the temperature for the maximum growth (anticipated to be between 23 and 31 °C), the temperature at 10 % of the maximum growth rate at the lower end (anticipated to be between 9 and 14 °C), and the temperature at 10 % of the maximum growth rate at the upper end (anticipated to be between 34 and 40 °C) are to be determined. This study therefore mainly focuses on these regions. For the evaluation, the time interval (Δt in hours) from the previous reading to the current and the corresponding change in transmittance ($\Delta \tau$) are calculated. The growth rate per day (24 h) is interpolated from these two parameters and reported with the corresponding temperature. Then, a mean growth rate for each temperature experiment is determined.

30.1.2 Results and Discussions

The total growth rate distribution with respect to temperature is as expected in the form of a skewed normal distribution (Fig. 30.2 left). The maximum growth rate, μ_{max} (MGR) (1.44/day) is observed at a medium temperature (at μ_{max}, T_{opt}) of 29 °C.

The observed maximum growth rate is in agreement with the previous studies, i.e., 1.44 doublings per day versus 1.0–2.0 doublings per day in the literature [22, 24, 28]. For our study, the goal is not to reach the maximum growth rate, rather to monitor the growth distribution and develop a growth function as a function of temperature. The important outcome is the percent losses and gains with respect to the maximum growth rate. Beside the maximum growth rate, the upper and lower 10 % maximum growth rates has to be determined. Ten percent of
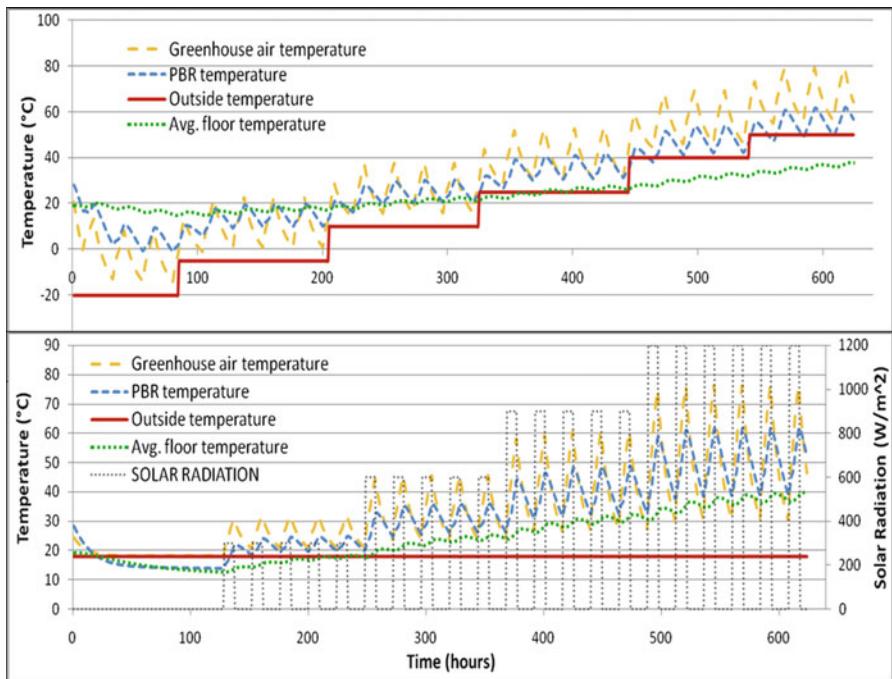
Fig. 30.2 *Chlorella* growth curve (*left*) and relative productivity (*right*) with respect to growth medium temperature

1.44 doublings per day is 0.144 doublings per day. For the lower value, a growth medium temperature (at 10 % μ_{max} lower, T_{inf}) of 11 °C is determined. The upper value is determined at the temperature (at 10 % μ_{max} upper, T_{sup}) of 35 °C. And then, all these parameters are incorporated into the model.

This study shows that *Chlorella* is very sensitive to high temperatures. This indicates that special considerations with respect to the temperature management of large-scale systems have to be taken into account. Using the data collected, a growth function described above is generated and plotted accordingly (Fig. 30.2 left). The differences in the mean growth rates at specific temperatures can also be expressed as percent losses with respect to the maximum growth rate. This is especially important for the productivity considerations. Considering that the temperature at the maximum growth rate has 100 % productivity, the temperatures below and above the maximum will be a fraction thereof and can be presented as in Fig. 30.2 (right).

Sensitivity Analyses
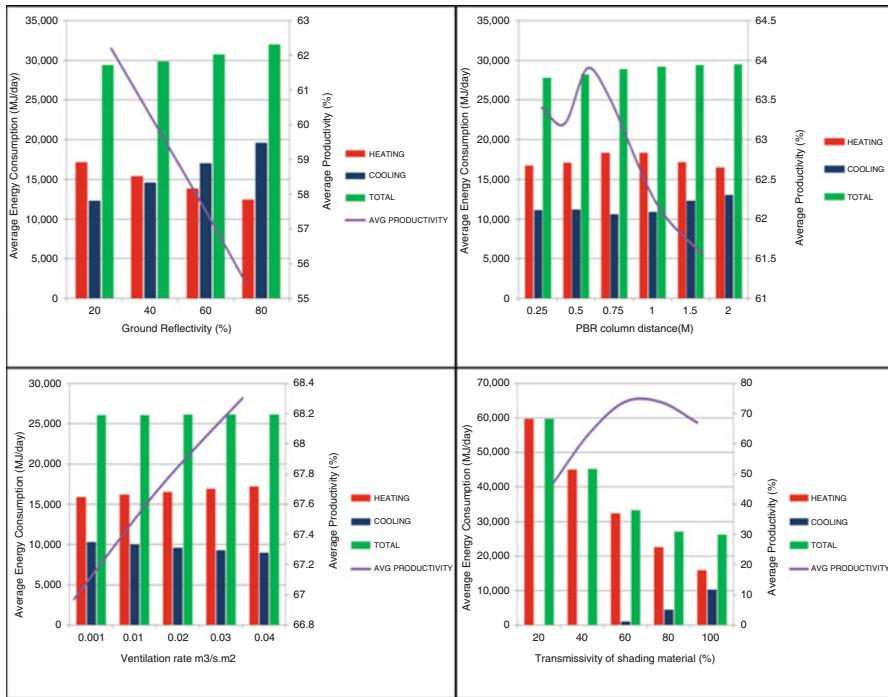
For the temperature sensitivity analysis (Fig. 30.3 top), the solar radiation is kept constant at 600 W/m^2 for 9 h each day. The outside temperature is kept the same for 5 consecutive days at each temperature starting at -20 °C and ending at 40 °C. It takes roughly 2 days for the responding temperatures to adjust to the new climatic condition. The maximum temperatures for the greenhouse and the PBR have a phase lag of about 2–3 h due to the difference in their thermal masses. Due to shading effects within the PBR columns, the temperature rises rapidly until the critical sun angle (TC) and slower afterwards due to less direct sunlight reaching the PBR tubes. The temperature differences at the maximums are between 8 and 10 °C. For the solar radiation sensitivity analysis, the outside air temperature is kept constant at 18 °C for day and night (Fig. 30.3 bottom). The solar radiation is varied

Fig. 30.3 Sensitivity analyses on outside air temperature (*top*) and solar radiation (*bottom*)

in 300 W/m^2 step increments between 0 and 1,200 W/m^2 for 5-day durations. Due to the difference in thermal masses, the PBR reaches the maximum temperature about 1–2 h after the greenhouse air temperature reaches its maximum. Also, the temperature variability of the PBR is due to higher thermal mass less than that of the greenhouse air. The shape of the temperature distribution looks similar to the previous sensitivity analysis, and is again a result of the shading function, and therefore, of the sun angle. However, the magnitudes are different.

The temperature differences at the maximums are between 5 and 18 °C, depending on the level of incoming solar radiation. The simulations are also performed for ground reflectivities of 20, 40, 60, and 80 % (Fig. 30.4). The results show that the higher the reflectivity is, the lower the average productivity is (a function of the PBR temperature). The higher the reflectivity, the less heating and the more cooling are required. The total energy needs for heating and cooling increases with rising ground reflectivity. The simulations are performed for PBR column distances of 0.25, 0.5, 0.75, 1.0, 1.5, and 2.0 m (Fig. 30.4). In each simulation, the greenhouse size is kept the same, which means that there is same number of PBRs in the greenhouse, but they are closer or wider apart. The distance between the PBR columns has a major impact on the energy requirements and the average productivity. The most heating (18,331 MJ per day) is required at a distance of 0.75 m, the least (16,474 MJ per day) at 2 m.

Fig. 30.4 Energy requirements and average productivity for different ground reflectivities (*top left*), PBR column distances (*top right*), ventilation rates (*bottom left*), and shading material transmissivities (*bottom right*)

The most cooling (12,974 MJ per day) is required for a distance of 2 m, the least (10,531 MJ per day) at 0.75 m. The total energy needs increased with larger distances and peaked at the 2 m with 29,448 MJ per day. The distance between the PBRs influences the shading factor as previously described. Apparently, an optimal distance between columns exists, where heat gains due to solar radiation and the shading at midday (avoids overheating) are in a most advantageous ratio. For this particular PBR, the best distance seemed to be about 0.75 m. However, the total productivity (biomass output and price per area) is also a function of the cost of greenhouse space. A smaller distance would eventually save space. Whether space savings outweigh the higher productivity rate or not is still to be investigated. The simulations are performed for ventilation rates of 0.01, 0.02, 0.03, and 0.04 m^3/s m^2 as well as for the default value (0.001 m^3/s m^2) that reflected the natural ventilation only (no mechanical ventilation) (Fig. 30.4).
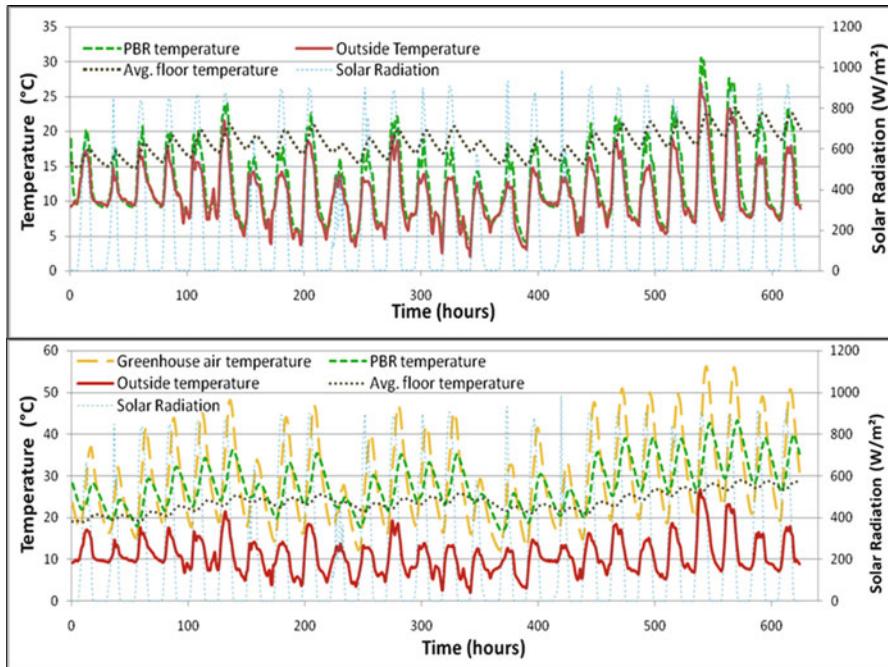
Ventilation is only supplied when the PBR temperature is over its optimum of 29 °C. The ventilation rate has an impact on the energy requirements and the average productivity. The most heating (17,207 MJ per day) is required for the highest ventilation rate (0.04 m^3/s m^2), the least (15,830 MJ per day) for no ventilation. The most cooling (10,243 MJ per day) is required for no ventilation, the

least (8,942 MJ per day) for the highest ventilation rate, as expected. The total energy needs rose with higher ventilation rates and is the most at the highest ventilation rate with 26,149 MJ per day. The algal productivity as a function of the PBR temperature and its distribution during the day is directly correlated to the energy consumption. The higher the ventilation rate is, the higher the average productivity. However, the magnitudes are very small. The highest productivity (68.3 %) is determined for a ventilation rate of 0.04 m^3/s m^2, whereas the lowest productivity (66.97 %) is determined for no ventilation. The simulations are performed for greenhouse shading material transmissivities of 20, 40, 60, and 80 % as well as for a greenhouse without shading (100 % transmissivity) (Fig. 30.4). The transmissivity of the shading material has a major impact on the energy requirements and the average productivity. The most heating (59,678 MJ per day) is required for a transmissivity of 20 %, the least (15,830 MJ per day) for 100 % (without shading material). The most cooling (10,243 MJ per day) is required for no shading material (100 % transmissivity), the least (0 MJ per day) for a transmissivity of 20 %. The total energy needs rose with lesser transmissivity and is the least for 100 % transmissivity with 26,073 MJ per day. However, the algal productivity as a function of the PBR temperature and its distribution during the day cannot be correlated to the energy consumption. The highest productivity (73.9 %) is determined at 60 % transmissivity, whereas the lowest productivity (47.1 %) is determined for a transmissivity of 20 %. Important for further considerations is the productivity rate of 66.9 % for a transmissivity of 100 % (no shading). Apparently, an optimal shading transmissivity exists, where heat gains due to solar radiation and the shading at midday (avoid overheating) are in a most advantageous ratio. The productivity increases by 7 % by using a shading material with 60 % transmissivity. The next question is whether more energy input (using a shading material with less transmissivity) would outweigh the higher algal productivity or not.

Simulations

The first scenario studied is how the PBR system would perform in local weather without heating or cooling. And then, an outdoor operation is compared to an indoor (greenhouse) operation to be able to draw a conclusion about feasibility in a future study.
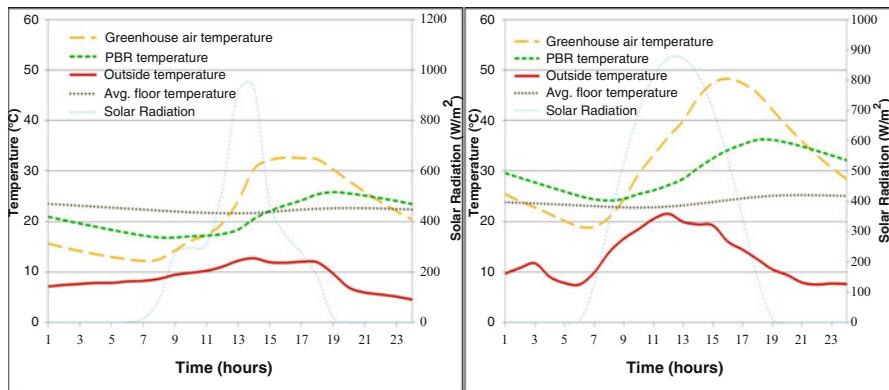
Figure 30.5 shows the temperature variations for outdoor and indoor PBR operations. In the case of outdoor operation, the PBR temperature follows the outside temperature closely. The PBR itself functions as a thermal storage device due to its thermal mass, and responds to the outside temperature change with a phase lag. The PBR temperature is higher during the day due to solar radiation gains, and as a result, the PBR temperature does not fall below the outside temperature. The same is true for the floor temperature with a longer time lag due to a bigger thermal mass. The temperature peaks are skewed by about 1–3 h. The maximum PBR temperature occurs about 2 h after the greenhouse air temperature reaches its peak. The floor temperature peaks about 1–2 h after the PBR does due to

Fig. 30.5 Temperature variations for outdoor (*top*) and indoor (*bottom*) PBR operations

the same reasons discussed above. For indoor operation, the outside air, greenhouse air, floor, and PBR temperatures are compared over the entire period (Fig. 30.5 bottom). The greenhouse air functions as a buffer; therefore, the PBR temperature is approximately 10–15 °C higher than the outside temperature. The PBR temperature responds to the greenhouse air temperature with a time lag of approximately 1–3 h. The greenhouse air temperature responds to the outside air temperature with a time lag of 1–4 h. Due to a long time interval between simulation steps (1 h) in the model, it takes about 2–4 days to adjust the PBR and floor temperature to the outside conditions. The first 5-day simulations (120 h) are not used in evaluations.

Figure 30.6 shows the temperature distribution for an indoor operation on a clear day and an overcast day. The main eye catchers are the much higher greenhouse, floor and PBR temperatures, compared to the outdoor conditions, where the temperature follows the outside air temperature closely. Here, the greenhouse air is used as a buffer and keeps the surrounding air of the PBR at relatively higher temperatures (what also can turn into a disadvantage on hot days if proper ventilation is not provided, due to a rise in PBR temperature). As typical for greenhouses, the inside air temperature is mainly a function of the incoming solar radiation rather than that of the outside air temperature, which also explains the temperature differences between the outdoor and indoor operations. The outdoor PBR is exposed to the outside air and the indoor PBR is exposed to the greenhouse air. The inside air temperature fluctuates more than the inside PBR temperature, and the

Fig. 30.6 Temperature distribution on a clear day (*left*, April 10, 2007), and overcast day (*right*, April 20, 2007)

inside PBR temperature more than the floor temperature, due to relatively smaller heat storage capacities. The PBR temperature responds to the greenhouse temperature with a lag phase of 1–3 h due to the greater thermal mass. The floor temperature follows the PBR temperature by another 1–3 h. The maximum air temperatures in the greenhouse reach up to 50 °C and above, especially at the end of the month when the solar radiation is much higher (980 W/m^2 rather than 820 W/m^2). Even the PBR temperature rises to the upper 40 °C, and the floor temperature to almost 30 °C. This phenomenon is experienced during trial runs of a lab-scale PBR in a greenhouse with no cooling, shading or ventilation on Cal Poly campus in Spring 2008. Greenhouse temperatures of up to 50 °C and PBR temperatures of far more than 40 °C are recorded. As a consequence, the algae die. Not only too high temperatures, but also too low temperatures harm algae growth. The theoretical yield losses due to not maintaining the temperature at optimal level can be determined with the data obtained from the experiments.

30.1.3   Concluding Remarks

Experimental data is needed to develop a mathematical model for temperature management purposes. For the *Chlorella* strain, the developed method results in a similar maximum growth rate as previously presented in the literature, i.e., 1.44 doublings per day versus 1.0–2.0 doublings per day. In this study, it is not required to reach the maximum growth rate, rather to monitor the growth distribution as a function of temperature. The important outcome is the percent losses and gains with respect to the observed maximum growth rate. This goal is fulfilled, and the data is successfully incorporated into the simulation model. The nutrient availability is critical and maintained at high nutrient levels. The nutrients (fertilizer) in this study are chosen only based on the N–P–K ratio. For further experiments, micronutrients,

vitamins, and silicon additions should be considered at proper concentrations. The developed coupled model delivers good results comparable to the observations made for the same location at the same time of the year in the Cal Poly campus greenhouse. From the temperature data, the heat management requirements for any specific location can be estimated. Using the model one can in advance (at the planning stage) precisely estimate its production levels, future heating or cooling loads, or estimate the productivity with different environmental control strategies. The developed model is a fundamental tool for economic decision making processes related to algae growth in PBRs. Changing parameters (e.g., diameter, distance, reflectivity, number of PBRs) in the model has direct impact on the algae productivity rate and can be compared easily to the base case. With the knowledge of the actual energy requirements, PBR operators would be able to estimate their operational costs in advance and see what changes to their system would decrease their costs optimizing the system efficiency. In addition to the analyses presented here, many other parameters could be examined. Since all greenhouse and PBR dimensions are kept as variables, heat requirements for different greenhouse types and sizes or PBRs could be compared easily. The model can now easily be extended to a comprehensive model, and all operational costs could be estimated and optimized accordingly. An all-in-one application for the planning, design, and operation of PBRs is the future target.

30.2 Microalgae Growth Kinetics Using Coal-Fired Flue Gas

In 2009, the United States' anthropogenic greenhouse gas (GHG) emissions totaled to 6,600 million metric tons of carbon dioxide equivalent [29]. Energy related CO_2 emissions make up the majority of total GHG emissions at approximately 82 % of the total emissions. Within the energy sector, coal utilization contributes 35 % of CO_2 emissions. Electricity production from coal fired power plants make up 93 % of the total coal derived emissions, resulting to approximately 1,750 million metric tons of CO_2 emitted in 2009 from the combustion of coal [29]. Global GHG emissions from human activities are the driving force for climate change and the evidence of global climate change is indisputable [30]. Carbon dioxide is the dominant GHG, and CO_2 emissions have steadily risen since the industrial revolution, and are projected to increase globally by 1.3 % per year [31]. Therefore, emission mitigation strategies must be implemented to reduce CO_2 emissions and slow the effects of global climate change.

For instance, coal currently provides about one half of all electricity generated in the USA [32]. To sustain the United States' electric energy demand, fossil fuel will continue to be used as an energy resource. One quarter of the global coal reserves are located in the USA ensuring the prolonged usage of coal as an energy resource. The combustion of coal releases an assortment of toxic gases into the atmosphere.

Such gases are commonly known as flue gases, and include carbon dioxide (CO_2), nitrogen oxides (NO_x), sulfur dioxide (SO_2), and particulate matter [32]. The typical constituents of coal fired flue gas are 80 % nitrogen, 10–15 % carbon dioxide, 5–10 % oxygen, 100–150 ppm nitrogen oxides, 300–500 ppm sulfur dioxide, and approximately 50 mg/m^3 particulate matter [33]. The precise flue gas composition depends on the type of coal being burned and the combustion characteristics.

Carbon dioxide is the primary GHG responsible for global warming. CO_2 has become the basis for determining the global warming potential of other greenhouse gases. The sheer quantity of CO_2 emissions has made CO_2 the most important GHG in need of a sequestration mechanism. Nitric oxide (NO) and nitrogen dioxide (NO_2) are known as NO_x because the two gases cycle between each other in the atmosphere. NO can oxidize in the presence of ozone (O_3) forming NO_2. NO_2 in turn can be reduced back to NO by photolysis [34]. Due to the constant transformations between NO and NO_2, a steady state concentration is reached with NO as the dominant species. At high temperature conditions, those similar to coal combustion, the thermodynamics favor the formation of NO. Therefore, typical combustion exhaust streams contain 90 % NO [35]. NO_x has been linked to the formation of acid rain and photochemical smog [32]. The consequences of emitting GHGs include global climate change, acid rain, smog and ozone depletion. Seeing that coal will continue to be used for electricity generation and GHG emissions must be alleviated to reduce the effects of global climate change, methods need to be developed and implemented for GHG abatement. Carbon trading has been proposed, and would place a "cap" or upper limit on the amount of pollutants emitted [36]. The cap is set lower than the historical emissions in an effort to decrease GHG emissions. Carbon trading would encourage emission abatement strategies because emissions exceeding the pollutant allowance would be fined. With carbon trading likely to become a reality, industries will be forced to buy additional allowances for their GHG emissions or invest in mitigation mechanisms. In 2010, the United Nations Framework Convention on Climate Change announced their global atmospheric CO_2 concentration cap at 450 parts per million (ppm), although this goal is a non-legally binding agreement [37]. To achieve a stable atmospheric CO_2 concentration of 450 ppm, GHG emissions must be reduced by 80 % [38]. Recalling that energy-related emissions accounted for 82 % of total emissions in 2009 such a reduction would require energy sector emissions to be eliminated [37].

Currently, the method of carbon capture and storage (CCS) is to inject CO_2 into geologic formations. CCS entails three distinct steps: carbon isolation, transportation and storage [32]. Carbon isolation is achieved through various separation techniques isolating the CO_2 from flue gas. Then the CO_2 is compressed and transported to the storage site. Long-term carbon storage sites include geologic formations such as oil and gas reservoirs, methane coal beds, and saline formations [37]. The main goals in pumping CO_2 into geologic formations are to (1) store CO_2 while maintaining the environmental integrity of the geologic formation and (2) enhance the recovery of hydrocarbons yielding value-added by-products. Pumping CO_2 into oil and gas reservoirs can improve oil and gas recovery and is

known as enhanced oil recovery [37]. Methane coal beds are used in a similar fashion to oil and gas reservoirs, and by pressurizing a coal bed with CO_2 the methane is displaced for more efficient methane recovery. Saline formations are believed to have large carbon loading capacities making them a viable long-term solution for carbon sequestration. However, saline formations lack the aspect of value-added by-products found in enhanced oil recovery (EOR) and enhanced methane recovery. The biggest hurdle remaining for saline formation sequestration is proving that this method is environmentally acceptable. Containing the carbon dioxide within the saline formation is of highest priority to guarantee that it does not permeate through the earth's subsurface and ultimately contaminate groundwater. To fully illustrate the early stages of development for CCS, there are 234 globally recognized CCS projects, and 77 provide both capture and storage while only 8 of the 77 are in operation [37]. A viable alternative emission sequestration methodology is the cultivation of microalgae. CO_2 fixation by microalgae grown outdoors is considered the best way to sequester CO_2 because the solar energy utilization is much higher than that of terrestrial plants [39]. As microalgae require CO_2 to undergo photosynthesis, cultivating microalgae provides a living carbon sink that continually produces algal biomass. The biomass can be used for the production of biofuels, pharmaceuticals, nutraceuticals, pigments, and cosmetics [33]. Algal biomass can even be used as a fuel source to generate electricity. Microalgae cultivation has a large potential for successful GHG mitigation due to their rapid reproduction, versatile living conditions, and variety of applications to utilize the biomass. Similar to EOR, algal biomass provides the ingredients to produce value added by-products. With the multitude of uses for biomass, potentially profitable markets exist to help offset the capital cost of implementing microalgae cultivation as a CCS method.

Algae are a diverse group of aquatic organisms. In the past blue-green algae and cyanobacteria were included in the classification of "algae." However cyanobacteria are prokaryotic organisms and lack a defined nucleus. Therefore, cyanobacteria/blue-green algae are now classified within the Bacteria Kingdom. Algae are in the Eukarya domain due to a membrane-enclosed nucleus, making them eukaryotic organisms. Algae exist as autotrophic and heterotrophic organisms. Autotrophs require CO_2 as their exclusive carbon supply, while heterotrophs utilize organic carbon for energy, metabolism, and growth [40]. Algae are subdivided into two classes—macroalgae and microalgae. The largest and most complex forms of macroalgae are commonly known as kelp. Microalgae can exist as individual cells, in cell colonies, or as long filamentous chains [41]. Microalgae cells range in size from a couple micrometers (μm) to a few hundred micrometers. Microalgae lack features of higher order plants such as roots, stems, and leaves [42]. Able to perform photosynthesis, microalgae produce oxygen while consuming atmospheric CO_2. Photoautotrophic microalgae obtain sunlight for energy and CO_2 provides the carbon supply, both of which are necessary for reproduction. Due to the abundant microalgae population, there is a large domain of environmental conditions acceptable for cultivation. Microalgae growth is governed by light and nutrient supply, as well as the environmental parameters influencing growth for the specified algal strain.

Microalgae have a specific set of requirements for growth, similar to that of other photosynthetic plants. Basic inputs for microalgae growth include water, sunlight, nutrients, and an acceptable range of environmental conditions specific to the algal species. Environmental conditions like temperature, pH, salinity, and dissolved gases all affect the growth characteristics of microalgae. Growth inputs have an optimum range of supply, and providing the optimum growth conditions yields the largest algal population. Generally speaking, larger algal populations result to greater quantities of algal biomass. Managing the algal growth variables to remain within an optimum range of tolerance produces the greatest amount of biomass, yielding the largest carbon consumption. Microalgae require a light period as well as a dark period to grow, known as a photoperiod [43]. The light period allows photosynthesis to occur while the dark phase allows the algae to respire. Chloroplasts absorb light energy, and in the presence of CO_2 and water, convert the captured energy into potential chemical energy [41]. In this way photosynthesis transforms light energy along with CO_2 and water into chemical energy in the form of carbohydrates and releases oxygen in the process. During the dark phase, respiration follows the same equation proceeding in the opposite direction. Carbon is an indispensable nutrient for the growth of microalgae. CO_2 is a key ingredient driving photosynthesis and is the primary GHG to be sequestered. When CO_2 is injected into water it becomes carbonic acid (H_2CO_3), thus lowering the water pH [34]. Besides carbon, the next most important nutrients are nitrogen (N), phosphorous (P), and potassium (K). N, P, and K are the fundamental macronutrients required by all plants, and usually plant fertilizers are categorized by their N–P–K ratios. Various micronutrients such as calcium, iron, magnesium, sulfur, zinc, and various trace elements are also necessary to fully satisfy the nutrient requirements of microalgae. Because microalgae are suspended in water, the nutrient availability is great, and therefore maintaining sufficient nutrient levels is essential for optimum algal growth. Environmental parameters such as temperature, pH, salinity, and dissolved oxygen content ultimately affect the success of algal cultivation. The microalgae population is composed of around 100,000 identified species, and currently 2,800 different strains are available for purchase [2, 44]. Therefore, the optimum environmental conditions are specific to the individual algal strain.

In summary, GHG emissions are beginning to be regulated and therefore methods for reducing emissions will be implemented. As said by the Intergovernmental Panel on Climate Change (IPCC), all energy related emissions must be eliminated to effectively stabilize the atmospheric CO_2 concentration at 450 ppm. Further, utilizing microalgae as a CCS method gives rise to a biofuel feedstock that could help nations become independent of foreign oil. Overall, the importance of sustainability and environmental consciousness is greater than ever, and seeing that energy related emissions will not cease, the need to mitigate GHGs is unprecedented. Cultivating microalgae provides a biological mechanism for sequestering CO_2 and provides a renewable feedstock for biofuels. This is of utmost value, the fact that one process, *cultivating microalgae* satisfies two prevalent global needs; the need to reduce CO_2 emissions while producing a renewable feedstock for biofuels. Here the old saying, to *kill two birds with one stone* has never been

more appropriate. The overall purpose of this section is to investigate and evaluate the use of coal fired flue gas as a carbon source for microalgae cultivation. Lab scale PBRs are used to grow microalgae and demonstrate that microalgae cultivation provides a viable CCS method. Analytical methods are used to model the algal growth kinetics. Using the biomass produced and the maximum specific growth rate a comparison is drawn between flue gas and pure CO_2 dosing for each algal strain. The purpose of this study is divided into four specific project outcomes: (1) confirm the feasibility of cultivating microalgae with flue gas as a carbon source, (2) maximize algal biomass production, (3) quantify microalgae growth kinetics, and (4) analyze the growth kinetics among gas dosing treatments.
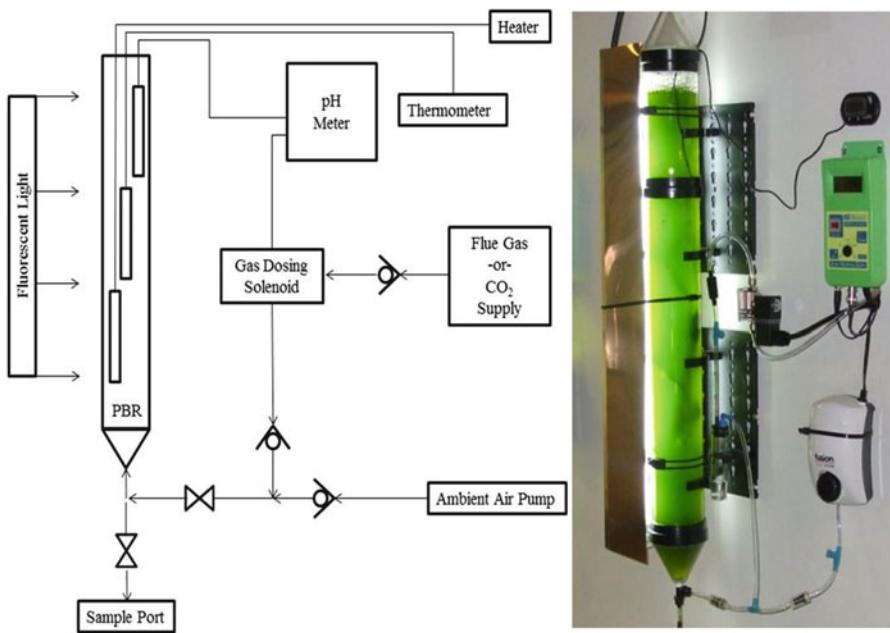
30.2.1 Materials and Methods

This section covers the culturing equipment, cultivation method, and quantifying microalgae growth kinetics, as well as the statistical analyses employed.

Microalgae Culturing Equipment

PBRs serve as the holding tank allowing algal growth and carbon fixation. Twelve vertical column Plankton Reactors (Aqua Medic GmbH, Plankton Reactor, Bissendorf, Germany) are used and for the remainder of this article will be called PBRs. Each PBR is a transparent plastic cylinder with a holding volume of 2.25 L. A fluorescent light (8 W, 6,700 K, 1,300 lm; Aqua Medic GmbH, Plankton Light Reactor, Bissendorf, Germany) provides the necessary light for photosynthesis to occur.

As microalgae grow the pH of the algal slurry increases due to the consumption of the carbonic species present. By setting a pH target point, CO_2 or flue gas is injected into the aqueous solution upon reaching the upper target value. The upper pH limit is set at 7.5 and 8.0 for *Chlorella* and *Tetraselmis* respectively. Injecting CO_2 into the aqueous solution forms carbonic acid, thus lowering the pH. Therefore, the pH is in constant balance between algal carbon fixation and gas injection. Twelve pH meters (Milwaukee, SMS 122, Romania) continuously monitor the pH of the algal solution. They are coupled with CO_2 control valves (Red Sea, CO_2 Magnetventil, Israel), which acts as the gas dosing solenoid, in essence maintaining a constant pH level by supplying the proper amount of carbon. Ambient air pumps (Fusion Quiet Power, 400, Taiwan) are used to continuously agitate the culture and keep the algal solution homogeneous. Digital thermometers (Coralife, ESU Reptile) monitor the aqueous solution temperature. Submersible heaters (Marine Land, Stealth Pro, China) are used for cultivating *Chlorella* and are set at 30 °C. Ambient temperature conditions in the lab are sufficient for *Tetraselmis* as its optimum temperature is around 22 °C. Combining this set of cultivation equipment allow the major growth variables to be controlled and

Fig. 30.7 Laboratory PBR schematic (*left*) and PBR in use (*right*)

maintained at constant levels. Keeping the temperature, pH, and nutrient levels constant enables the variable in question, *the effect of direct flue gas injection* to be investigated. Each PBR is accompanied by the same additional components to make 12 complete PBR sets as seen in Fig. 30.7.

Cultivation Method

Each growth trial is limited to 5 days of growth. Upon inoculation algal samples would be taken for analysis. For the remainder of the growth period samples are taken at approximately the same time of day. The algal strains are expected to follow a typical noncontinuous batch culture growth curve. Batch growth is characterized by four distinct phases: lag, exponential, stationary and death. The four phases adopted from Shuler and Kargi [12] is briefly explained here: (1) *Lag*: Immediately after inoculation the culture experiences a lag phase as it acclimates to the new environmental conditions; (2) *Exponential*: After the culture has fully adapted to the batch conditions the culture begins reproducing exponentially. This is the optimum growth seen throughout the growth cycle, and the cell population doubles at regular time intervals, known as the doubling time (t_d). (3) *Stationary phase*: The stationary phase begins after exponential growth decelerates and the microorganism population is maintained. At this point the culture has reached its maximum population. At stationary phase the growth rate is equal to the death rate,

Table 30.2 Liquid macronutrients and micronutrients (10-15-10) and flue gas composition

Nutrient constituents	Percent	Flue gas constituents	Concentration
Total nitrogen		Carbon dioxide (CO_2)	14 %
Ammoniac nitrogen, 1.6 %	10		
Nitrate nitrogen, 0.2 %			
Urea nitrogen, 8.2 %			
Available phosphate (P_2O_5)	15	Nitric oxide (NO)	100 ppm
Soluble potash (K_2O)	10	Sulfur dioxide (SO_2)	300 ppm
Iron (Fe)	0.10	Nitrogen (N_2)	Balance
Manganese (Mn)	0.05		
Zinc (Zn)	0.05		
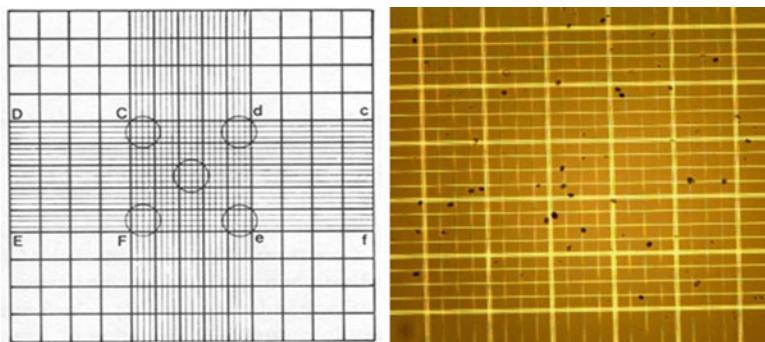
and the population is held constant. (4) *Death phase*: The death phase occurs once the maximum population has been supported for a period of time and the culture begins to die faster than it can reproduce. Usually nutrient depletion or toxic product accumulation causes the microorganism population to decline [12]. In order to begin batch growth for each trial, algal inoculum is maintained throughout the study. *Chlorella* and *Tetraselmis* inoculum are grown in two 2-L Erlenmeyer flasks. The idea in maintaining the culture inoculum is to keep each strain in a subdued yet healthy condition. The photoperiod is 1:1, at 12 h of light and 12 h of dark. Ambient air is constantly diffused into the media to provide agitation and minimal CO_2. In this way each strain grows slowly and after a week of inhibited growth the culture is ready for inoculation. The goal is to have each strain at a transmittance of 40 % for inoculation. All 12 PBRs are taken apart and sanitized before inoculation. All other equipment in contact with the algal solution is also cleaned including the submersible heaters, the pH probes, the thermometers, and the algal sampling ports. A phosphoric acid solution (Star San, Five-Star, Commerce City, CO) is used for all equipment sanitation. Maintaining aseptic culturing techniques is essential to avoid contamination and culture crashes. Each PBR has a holding volume of 2.25 L, however the displacement caused by the submersible heater, pH probe and thermometer yields an operating volume of 2.0 L. In addition, 2 in. of headspace is required to accommodate the algal uproar upon gas dosing. Beginning inoculation, 200 mL of algal solution at a transmittance of 40 % is used. The remaining 1,800 mL is filled with distilled water. Distilled water is used for *Chlorella*, while *Tetraselmis* requires a salt-water additive. Salt water is made with distilled water and *Instant Ocean* to an achieved specific gravity between 1.020 and 1.024 at 25 °C. The necessary nutrients are provided by *Schultz Plant Food Plus*, and the nutrient breakdown is seen in Table 30.2.

Liquid plant food is administered in doses of 1.5 mL per PBR. This is the only nutrient supply provided for the duration of the growth period besides the gas dosing. The photoperiod is set at 2:1 resulting to 16 h of light and 8 h of dark. Once all 12 PBRs are inoculated, the growth period begins and the first samples are collected for analysis. Samples for analysis are collected daily throughout the 5-day growth period. Upon analyzing the samples on the fifth and final day, the PBRs are taken apart, sanitized and put back together for the proceeding growth trial. Daily

monitoring of temperature and pH are performed to ensure no adverse effects on microalgae growth from these two variables, as well as preserving consistency among sample replicates. Pure CO_2 is used as the control for cultivating both algal strains. Flue gas is purchased from a local supplier (Praxair) and the composition is meant to imitate coal-fired flue gas. The flue gas composition can also be seen in Table 30.2.

Quantifying Growth Kinetics

There are multiple ways to quantify microorganism growth and each method has its advantages and disadvantages. Three methods are used to model the growth kinetics including cell counting, mass determination by volatile suspended solids (VSS) and optical density. Cell counting and optical density are performed daily throughout the growth cycle, while VSS is carried out at the beginning and end of each growth cycle. Microscopic inspection of microalgae is essential for cultivating monocultures. Quantifying the number of cells per unit volume is difficult, however necessary to verify culture purity. The difficulty arises in counting the microalgae cells because it is subject to human error and is labor intensive. A microscope (Motic, BA310) is used for sample inspection and cell counting. Duplicate cell counts for each sample are performed to obtain an average cell count per sample per day. A hemocytometer is used to count the number of cells. A hemocytometer has a counting chamber defined by a known depth and a grid with known surface area. The depth is the space between the grid surface and the underside of the coverslip and the standard depth is 0.1 mm. Using the specified hemocytometer coverslip is important to maintain the intended chamber volume because the aqueous sample relies on capillary action to stay within the grid surface and therefore preserve a constant volume. The counting method is taken from *Standard Methods for the Examination of Water and Wastewater*, *Method 10200E and 10200F* [45] and called for counting the four corner squares and the center square seen in Fig. 30.8 with circles. This method is used to quantify *Chlorella*. *Tetraselmis* is larger in diameter than *Chlorell*a and very motile, therefore the method for counting *Tetraselmis* is slightly modified. A digital picture is taken of *Tetraselmis* (Fig. 30.8) to provide a snapshot and enable cell counting. The entire grid surface area (all 25 squares composed of 16 smaller squares are counted) is used for counting because it is more representative taking into account the larger cell size and motility of *Tetraselmis*. Before each sample is loaded for counting the hemocytometer and the coverslip are rinsed with distilled water and dried via *Lense Paper*. It is important to note that using *Kim Wipes* can scratch the glass due to its abrasiveness and is never used. Ensuring the hemocytometer and the coverslip are clean the sample is ready to be loaded. After mixing the sample well, a sterile *Pasteur pipet* is used to dispense the sample into the counting chamber. Caution is taken upon injecting the sample into the counting chamber because if the sample spills over the grid surface the chamber volume becomes compromised and the process must be repeated.

Fig. 30.8 Standard hemocytometer grid (*left*) and counting *Tetraselmis* at 200× (*right*)

Measuring volatile suspend solids (VSS) provides a mass based method for determining organic content within an aqueous solution. As biomass is organic, VSS is an estimate for the quantity of biomass in an aqueous solution. These methods are commonly used for wastewater examination and the method is adapted from *Standard Methods for the Examination of Water and Wastewater*, *Method 2540* [45]. Total suspended solids (TSS) must be found first in order to determine VSS. TSS is the total amount of solids within an aqueous sample after the sample has been filtered through a glass fiber filter. The increase in weight from the residue retained on the filter represents TSS. VSS is the difference between the weight of dried residue and the weight of residue after ignition (also known as ash weight). The result yields an estimated biomass concentration in units of mg/L. The detailed procedure is as follows:

Filter preparation:

1. Prepare G4 glass fiber filters by rinsing with distilled water under vacuum until all water is pulled through the filter.
2. Place filter in crucible and bake in furnace (550 °C) for approximately 15 min.
3. Remove filter and crucible from furnace and place in bell jar desiccator until sample reaches room temperature.
4. Weigh filter and crucible and record A.

TSS:

5. Filter uniform aqueous sample of known volume (V) through filter under vacuum.
6. Return filter to corresponding crucible.
7. Bake in oven at 103–105 °C for 1 h.
8. After baking remove from oven and allow cooling in desiccator.
9. Reweigh dry residue, filter, and crucible and record B.
10. TSS is then calculated using Eq. (30.58) below:

$$TSS = (B - A)/V \tag{30.58}$$

VSS:

11. Place filter with dry residue and crucible in furnace at 550 °C for 5 min.
12. After ignition remove from furnace and allow cooling in desiccator.
13. Reweigh ash residue, filter, and crucible and record C.
14. VSS can be calculated using Eq. (30.59) below:

$$VSS = (B - C)/V \qquad (30.59)$$

15. Units of TSS and VSS are (mg/L) and below is the description of each recorded weight:

    A: Initial filter and crucible weight, g
    B: Dry weight of residue, filter, and crucible, g
    C: Ash weight of residue, filter, and crucible, g
    V: Volume of aqueous sample, mL

16. Conversions used: 1 g = 1,000 mg; and 1 L = 1,000 mL.

VSS is performed at the beginning and end of each treatment. In this way the biomass produced over the duration of the treatment is found. There are no duplicates executed for this method due to the lack of resources, large number of samples and the extensive time required to obtain VSS data.

A spectrophotometer (Hach, DR3800) is used to measure the absorbance and transmittance of algal samples. The spectrophotometer passes a light of known wavelength through an aqueous sample and measures the light entering and exiting the sample. From the measured incident and exiting light the absorbance and percent transmittance are determined. The wavelength is set at 665 nm because this value is the best estimate of chlorophyll content. Chlorophyll is not a direct measure of algal density; however, it provides an estimated value. The advantages of such a method are the ease of use. It is quick, reliable and easy to replicate. The disadvantages include not being able to distinguish between dead and alive cells, and cellular conglomerates can give faulty readings. Similar to cell counting, optical density is measured daily in sample duplicates.

Cell count data is used to model the growth kinetics of both algal species. Optical density is not used to model growth kinetics because absorbance and percent transmittance are arbitrary measures of analysis. Rather, cell count and optical density are correlated, so the cell count could be estimated by percent transmittance. The number of cells per milliliter yields an easy to understand growth curve, in which the maximum specific growth rate is calculated. The growth rates are then compared in a *t*-test to determine if there is a statistically significant difference in growth rates between gas treatments. The biomass produced over the growth period is also statistically compared by a *t*-test to conclude whether a significant difference exists among gas dosing treatments. Optical density and cell counting are correlated to estimate the cell concentration from optical density. This correlation yields an easy analytical method using a spectrophotometer to estimate the number of microalgae cells per milliliter. As spectrophotometry is widely used throughout

the biotechnology industry, optical density is usually the most used method for determining cellular concentrations. The correlation between optical density (% transmittance) and cells per milliliter yield a quick way to determine a sample cell density. The average transmittance and average cell count for all three trials are used for the correlation. Correlating cell density with absorbance yields a much more intuitive graph with a positive slope. However, using absorbance the slopes are identical per algal strain making the y-intercept the only differing aspect betweeen flue gas dosing and CO_2 dosing. Therefore, percent transmittance is used to correlate cell density and Eq. (30.60) shows the governing relationship.

$$Cells/mL = (-Slope \times Transmittance) + y_{intercept} \qquad (30.60)$$

Due to the strong correlation between cell counting and optical density, there is no need to include growth curves modeled from optical density. Cell counting is used to graphically illustrate the microalgae growth kinetics. By using cell counting to model the growth kinetics, the maximum specific growth rate (μ_{max}) is deteremined. The growth rates are then analyzed to determine if there is a signficant difference in growth between the gas dosing treatments per algal species. Algal biomass determination by VSS is used to quantify the amount of biomass produced over the 5-day growth period. The difference between final and initial biomass concentration yields the dry weight of ash-free biomass produced in mg/L. Similarly to the analysis of growth rates, the biomass produced is statistically analyzed to conclude whether there is a statistically signficant difference in biomass produced between flue gas and CO_2 dosing per algal strain. The maximun specific growth rate is calculated by taking the natural log of the cell concentration and plotting it over time. Equation (30.61) shows the relationship between cell concentration (x), maximum specific growth rate (μ_{max}), and time (t). Integrating Eq. (30.61) yields a linear relationship where the maximum specific growth rate is represented by the slope of the linear portion in the plot of the natural log of cell concentration verse time.

$$dX/dt = \mu_{max} * X \qquad (30.61)$$

$$ln(x) = (\mu_{max} * t) + ln(x_0) \qquad (30.62)$$

$$t_d = ln\,(2)/\mu_{max} \qquad (30.63)$$

The resulting relationship after integration can be seen in classic $y = mx + b$ form. The linear portion for determining the growth rate is comprised of cell count data from day 0 to day 3. These data points are chosen to maximum the specific growth rate. The data for day 4 and day 5 exhibits a deceleration in growth and would decrease the growth rate if they have been included. The doubling time (t_d) is also determined to give a conceptual idea of the speed at which the algal strains were growing. The doubling time is calculated by rearranging Eq. (30.62) into the form seen in Eq. (30.63), and represents the time required for the number of cells in the population to double during exponential growth.

Statistical Analyses
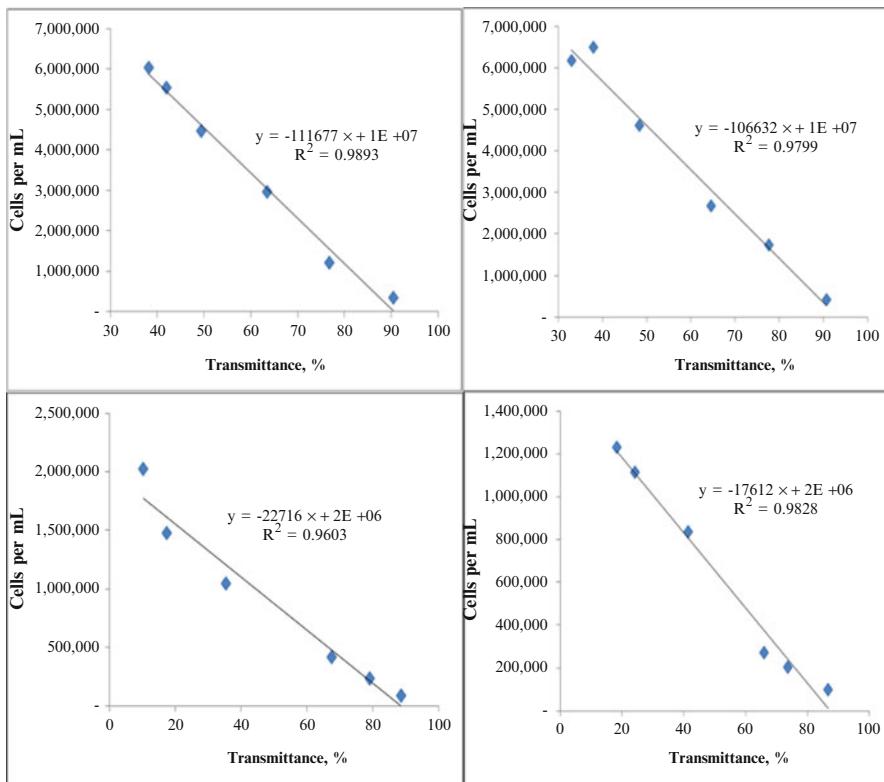
One freshwater and one saltwater strain are selected for growth for the reason that power plants are located near bodies of water for cooling, whether it is fresh or salt water. *Chlorella vulgaris* is the chosen freshwater strain, and *Tetraselmis* sp. is the saltwater strain used. Both algal strains are tested in three trials with a growth period of 5 days each. Using 12 lab-scale PBRs, a spilt plot design is implemented to maintain consistency among gas treatments and growth trials. Therefore, both algal strains and both gas-dosing techniques are applied for every growth trial. Pure CO_2 dosing is the control variable for algal growth, while flue gas dosing is the variable of interest. The algal growth characteristics under flue gas dosing are compared to the algal growth characteristics exhibits by the control variable per algal species. Executing three growth trials with this experimental design totally yields nine replicates per algal strain for each gas treatment. Each PBR configuration aims to maintain optimum environmental conditions such as light influx, temperature and pH. Setting these variables at the optimum level per algal species promotes the fastest reproductive rates and resulted in the largest carbon sequestering capacities. The photoperiod is the same for each algal strain. The temperature is controlled for *Chlorella* only due to its optimum temperature at 29 °C [5]. *Tetraselmis* being the saltwater strain prefers cooler water and therefore it is subject to ambient temperature conditions. The pH is monitored and maintained at relatively constant levels by gas injection. Equal nutrient supplements are provided upon inoculation. Through these methods the variables affecting microalgae growth are isolated, effectively eliminating the influence on algal growth from such variables. Maintaining consistent environmental conditions allows the variable of interest, *flue gas dosing,* to be compared against the control variable, *CO_2 dosing.* The experimental design intends to maximize algal biomass production and confirm flue gas as a carbon substitute for algal cultivation. The hypothesis is to determine whether or not a statistically significant difference exists between microalgae grown with two different carbon sources, flue gas verses pure CO_2. Modeling the microalgae growth kinetics enables a comparison between CO_2 and flue gas treatments per algal strain. The degree of difference between cultivation methods is tested to determine if flue gas inhibits algal growth. Using *Minitab 15*, an unpaired *t*-test is used to conclude whether there is a statistically significant difference in the growth characteristics between the gas treatments for each algal strain. The *t*-test assumes that the sample data is Gaussian and follows a normal distribution. Biological data can never be precisely Gaussian because the normal distribution extends infinitely in the positive and negative directions. However, many times biological data follow a near bell-shaped curve and can be approximated as Gaussian. An Anderson–Darling normality test is used to ensure that the data approximate a normal distribution. Due to the small sample size of this study, the sample data cannot be determined to be decisively Gaussian, rather the sample data are concluded to not be inconsistent with a normal distribution.

30.2.2   Results and Discussions

The temperature and pH are maintained at optimum levels to promote the largest algal population. Keeping the temperature and pH constant is important in limiting growth influences from these two variables. Persevering optimum temperature and pH levels, took away any influence on algal growth from such variables. The use of heaters for *Chlorella* keep the temperature distribution very close to 30 °C. The error bars are plus and minus 1 standard deviation. The standard deviation for *Chlorella* (1.1 °C) is small compared to that of *Tetraselmis* (2.5 °C). This is due to the temperature control provided by the submersible heaters. *Tetraselmis* is subject to ambient temperature conditions and therefore the standard deviation is much larger due to temperature fluctuations throughout the three growth trials. The pH is also kept constant. As previously mentioned, algal growth increases the pH by consuming carbonic species, which in turn activates the gas dosing solenoid and administers CO_2/flue gas into the sample. The entering CO_2 forms carbonic acid and causes the pH to decrease. This cultivation method provides the algal species with an appropriate supply of carbon, never too much and never too little. Because the flue gas contains 14 % (mole percent) CO_2 the flue gas is consumed far quicker compared to pure CO_2 in order to fulfill the necessary carbon demand. The error bars are plus and minus 1 standard deviation. The standard deviation for *Chlorella* is 0.3 and 0.4 for *Tetraselmis*. Overall, the pH remains relatively constant. The pH values for both algal strains exceed the pH optimums rarely. *Tetraselmis* is subject to the temperature swings within the room. *Chlorella* is cultivated with heaters, which enables constant temperature. Cultivating microalgae in this way provides optimum growth conditions per algal species. This is an essential element to quarantine growth variables, provide optimum environmental conditions to produce the greatest amount of biomass and enable the variable in question, *gas-dosing treatments* to be examined.

As mentioned earlier, the growth rates are compared in a *t*-test to determine if there is a statistically significant difference in growth rates between gas treatments. The biomass produced over the growth period is also statistically compared by a *t*-test to conclude whether a significant difference exists among gas dosing treatments. Optical density and cell counting are correlated to estimate the cell concentration from optical density. This correlation yields an easy method using a spectrophotometer to estimate the number of microalgae cells per milliliter. The correlations for *Chlorella* and *Tetraselmis* under both gas treatments are seen in Fig. 30.9.

The correlation between optical density (% transmittance) and cells per milliliter yields a quick way to determine a sample cell density. The average transmittance and average cell count for all three trials are used for the correlation. The results are summarized in Table 30.3. The correlations are strongly tied with the coefficent of determination (R^2) all greater than 0.96. Correlating cell density with absorbance yields a much more intuitive graph with a positive slope. However, using absorbance the slopes are identical per algal strain making the y-intercept the only
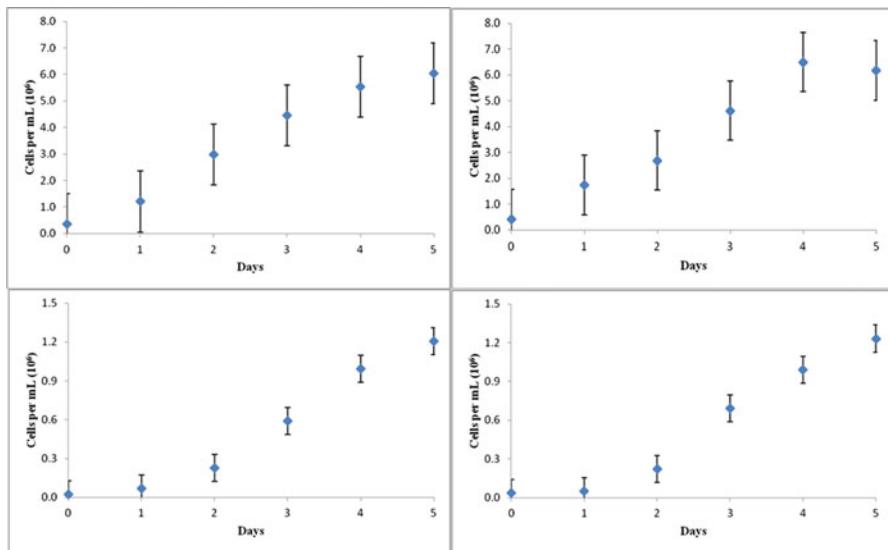
Fig. 30.9 Correlation between analytical methods for *Chlorella* (*top*) and *Tetraselmis* (*bottom*) grown with CO_2 (*left*) and flue gas (*right*), respectively

Table 30.3 Relationship between cells/mL and percent transmittance, and growth rates

Strain	Factor	Slope ($-$)	Y-intercept	R^2	Growth rate (per day)	R^2	Doubling time (days)
Chlorella	CO_2	111,677	1.0E+07	0.9893	0.8488	0.9609	0.82
	Flue gas	106,632	1.0E+07	0.9799	0.7714	0.9175	0.90
Tetraselmis	CO_2	22,716	2.0E+06	0.9603	1.1022	0.9956	0.63
	Flue gas	17,612	2.0E+06	0.9828	1.1034	0.9319	0.63

differing aspect betweeen flue gas dosing and CO_2 dosing. Therefore, percent transmittance is used to correlate cell density and the governing relationship is given in Eq. (30.60) earlier.
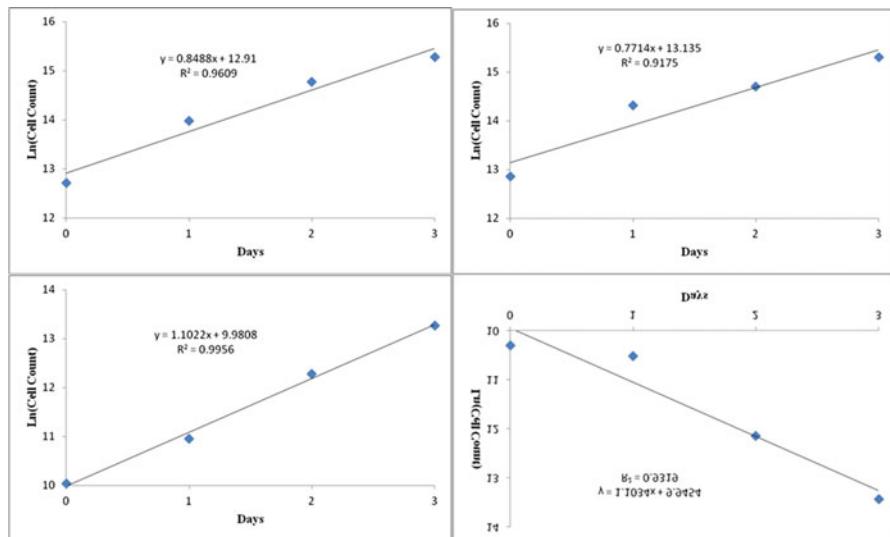
As microalgae cultures grow, the cell density increases, causing a reduction in light transmitted through the sample. Therefore, the negative slope infers algal growth and increasing cell density. The gas treatment slopes for *Chlorella* and *Tetraselmis* does not differ greatly from each other, suggesting that growth between

Fig. 30.10 Growth curve for *Chlorella* (*top*) and *Tetraselmis* (*bottom*) grown with CO_2 (*left*) and flue gas (*right*), respectively

flue gas and CO_2 per algal strain is not signifcantly different. In the upcoming sections, a hypothesis test will conclude if the differences in growth kinetics are significant.

The growth kinetics of *Chorella* and *Tetraselmis* resembles the expected microbial growth kinetics characterized by a lag phase, exponential growth, and stationary phase. In some cases the stationary phase is never reached due to the shortened growth period of 5 days. Seeing that the stationary phase is rarely reached the death phase is never reached. The *Chlorella* and *Tetraselmis* growth curves looks strikingly similar between the two gas dosing regimens. The average maximum cell concentration for *Chlorella* is greater for flue gas at about 6.5 million cells per milliliter compared to 6.0 million cells per milliliter. However, the standard deviation for counting *Chlorella* is approximately one million cells per milliliter, making a difference of 500,000 cells irrevelent. The error bars for *Chlorella* and *Tetraselmis* are plus and minus 1 standard deviation. The standard deviation is strain specific due to the different methods executed to quantify cell density. Such a large standard deviation for *Chlorella* is a result to the inaccuracies in cell counting. Inaccuracies such as cellular conglomerates and not being able to distinguish between living and dead cells makes enumeration difficult. The maximum cell concentration for *Tetraselmis* between the gas factors are nearly identical reaching approximately 1.2 million cells per milliliter. The standard deviation for *Tetraselmis* is about 100,000 cells per milliliter. The lower standard deviation for *Tetraselmis* is attributed to the larger cell size and the modified technique used for counting. The growth curves are depicted in Fig. 30.10 for each algal strain and gas dosing treatment. The maximun specific growth rate is calculated by taking the natural log of the cell concentration

Fig. 30.11 Maximum specific growth rates for *Chlorella* (*top*) and *Tetraselmis* (*bottom*) grown with CO_2 (*left*) and flue gas (*right*), respectively

and plotting it over time. Figure 30.11 is used to determine the maximum specific growth rates and the results are summarized in Table 30.3.

The growth rate of *Chlorella* grown with CO_2 is larger than that of flue gas. The growth rates for *Tetraselmis* are nearly identical for flue gas and CO_2 dosing. The doubling time (t_d) is also determined to give a conceptual idea of the speed at which the algal strains are growing.

Biomass Production

Based upon VSS measurements the total algal biomass produced is determined. Biomass production is defined as the difference between final and initial biomass quantities. *Chlorella* produces more biomass being grown with flue gas while *Tetraselmis* behaves in an opposite fashion and produces more biomass being grown with CO_2. The overall biomass produced for each sample is shown in Table 30.4. Certain sample values are discarded due to negative biomass production values or extreme outliers.

Inferences Based on Two-Sample Populations

An analysis on two sample populations is performed for *Chlorella* and *Tetraselmis*. A two sample *t*-test is carried out to determine if the average growth rates and biomass production between CO_2 and flue gas treatments differed for each algal

Table 30.4 Mean volatile suspended solids (VSS) measurements
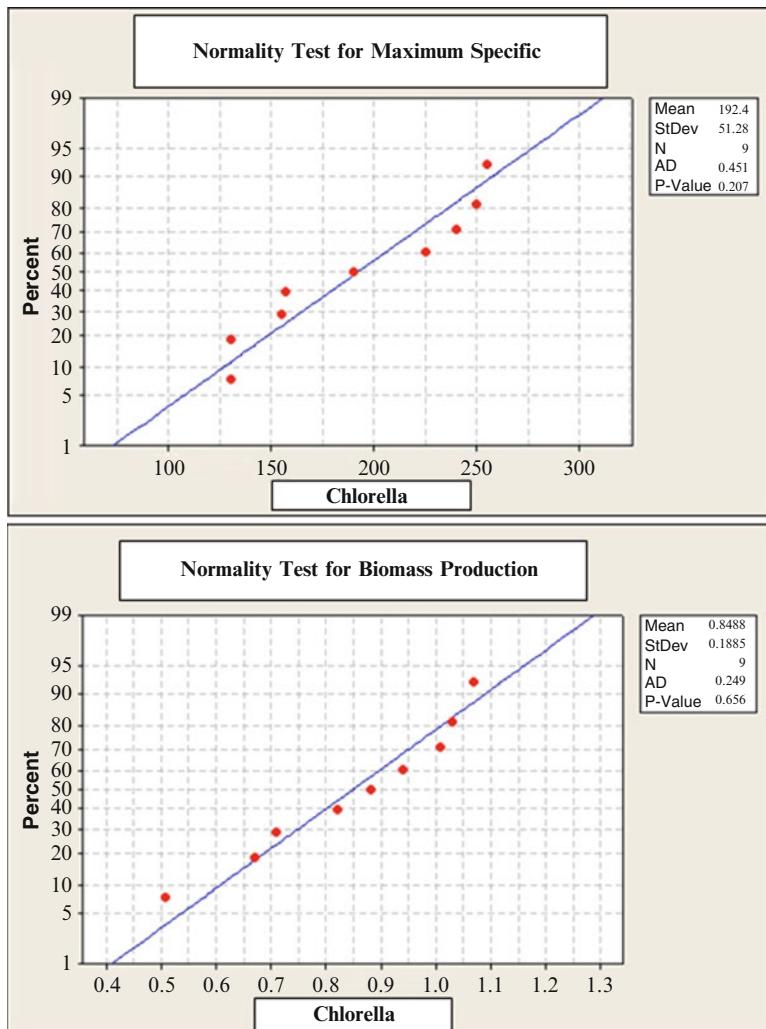
Strain	Factor			Estimated biomass (dry weight and ash free)	
				Final (mg/L)	Biomass produced (mg/L)
Chlorella	CO_2	9	35.4	227.8	192.4
	Flue gas	8	39.0	276.9	237.9
Tetraselmis	CO_2	7	95.0	789.3	694.3
	Flue gas	6	110.8	670.0	559.2

strain. Using a confidence interval of 95 % and a corresponding alpha (α) value of 0.05, a hypothesis test evaluates the difference in maximum specific growth rates and biomass production among the gas treatments. To ensure the validity of this test, the sample populations are first tested for normal distrubutions, a prerequiste to the *t*-test.

For the cell count analysis, using an Anderson–Darling normality test the sample populations are tested to determine if the data follows a normal distribution. For each algal strain and gas dosing treatment, the sample population data is subjected to the Anderson–Darling Normality Test (*Null Hypothesis*: H_o: μ is normally distributed; *Alternative Hypothesis*: H_a: μ is not normally distrubuted). Seen in Fig. 30.12, *Chlorella* grown with CO_2 dosing yields a p-value of 0.656 which is greater than alpha of 0.05. Therefore, fail to reject the null hypothesis and conclude that the sample population of *Chlorella* grown with CO_2 is not inconsistent with a normal distribution. The Anderson–Darling normality test is performed for all sample populations and the summarized results are provided in Table 30.5.

All the sample populations have a p-value greater than 0.05 providing that the maximum specific growth rate data per algal strain for both gas treatments could be approximated as a Gaussian distribution. Confident that the small sample sizes are not inconsistent with a Gaussian distribution, a two sample *t*-test is performed to determine if the mean growth rates differed between the gas dosing treatments per algal strain. The two sample *t*-test is governed by the following hypotheses: *Chlorella vulgaris* (*Null Hypothesis*: H_o: $\mu_{CO2} = \mu_{FLUE}$; *Alternative Hypothesis*: H_a: $\mu_{CO2} \neq \mu_{FLUE}$) and *Tetraselmis* sp. (*Null Hypothesis*: H_o: $\mu_{CO2} = \mu_{FLUE}$; *Alternative Hypothesis*: H_a: $\mu_{CO2} \neq \mu_{FLUE}$). The resulting p-value for *Chorella* flue gas dosing compared to CO_2 dosing is 0.357. Again the p-value is greater than alpha (0.357 > 0.05), so the null hypothesis cannot be rejected. The maximum specific growth rates for *Chlorella* grown with flue gas and CO_2 are not signifcantly different from one another. The p-value for *Tetraselmis* is even larger at 0.991. Such a large p-value concludes that there is little doubt that maintaining the null hypothesis is false. Table 30.5 summarizes the *t*-test results for *Chlorella* and *Tetraselmis*. Overall, there is no statistically significant difference between maximum specific growth rates for the two gas dosing treatments.

For the algal biomass analysis, the same procedure is carried out to determine if there is a significant difference in the average algal biomass produced between gas treatments. First, the sample populations are tested for normality using the Anderson–Darling normality test (*Null Hypothesis*: H_o: μ is normally distributed

Fig. 30.12 Normality tests for maximum specific growth rate data (*top*) and biomass produced data (*bottom*) for *Chlorella* grown with CO_2

Alternative Hypothesis: H$_a$: μ is not normally distrubuted), followed by a two-sample *t*-test. For all sample populations the p-value is greater than 0.05, concluding that despite the small sample sizes the algal biomass data can be approximated as a normal distribution. Table 30.6 summarizes the results from the individual normality tests. Figure 30.12 illustrates the normality test on *Chlorella* grown with CO_2. The two sample *t*-test is performed to determine if there is a significant difference in biomass produced among the gas treatments for each algal strain. The *t*-test is governed by the following hypotheses: *Chlorella vulgaris* (*Null Hypothesis*: H$_o$: μ$_{CO2}$ = μ$_{FLUE}$; *Alternative Hypothesis*: H$_a$: μ$_{CO2}$ ≠ μ$_{FLUE}$) and

Table 30.5 Anderson–Darling normality test for maximum specific growth rate data, and testing the difference of growth rates (two sample t-test) between gas dosing treatments

				Anderson–Darling normality test		Two sample t-Test	
Strain	Factor	N	Mean	St. dev.	P-value	SE mean	P-value
Chlorella	CO_2	9	0.849	0.188	0.656	0.063	0.357
	Flue gas	9	0.771	0.156	0.428	0.052	
Tetraselmis	CO_2	6	1.102	0.163	0.183	0.067	0.991
	Flue gas	6	1.103	0.205	0.507	0.083	

Table 30.6 Anderson–Darling normality test for biomass produced from VSS measurements, and testing the difference in algal biomass production between gas dosing treatments

	Anderson–Darling normality test					Two sample t-test	
Strain	Factor	N	Mean	St. dev.	P-value	SE mean	P-value
Chlorella	CO_2	9	192.4	51.3	0.207	17	0.060
	Flue gas	8	237.9	40.1	0.577	14	
Tetraselmis	CO_2	7	694.3	84.2	0.181	32	0.008
	Flue gas	6	559.2	62.1	0.939	25	

Tetraselmis sp. (*Null Hypothesis*: H_o: $\mu_{CO2} = \mu_{FLUE}$; *Alternative Hypothesis*: H_a: $\mu_{CO2} \neq \mu_{FLUE}$) *Chlorella* has no significant difference in the production of biomass from CO_2 and flue gas treatments. A p-value of 0.06 concludes that the null hypothesis cannot be rejected. The gas treatments for *Tetraselmis* yields a different result with a p-value of 0.008. Since the p-value is less than 0.05, the null hypothesis is rejected and concluded that there is a significant difference in the biomass produced between CO_2 and flue gas treatments. *Tetraselmis* produces more algal biomass under CO_2 dosing producing an average of aproximately 700 mg/L over the 5-day growth period compared to 560 mg/L produced under flue gas dosing. The difference between gas treatments for *Tetraselmis* biomass production ranges from 44.5 to 225.8 mg/L using a 95 % confidence interval.

The maximum specific growth rates across gas treatments are not significantly different, and the the difference in algal biomass production is only statistically significant for *Tetraselmis*. The similarities in growth characteristics using flue gas and CO_2 strongly support the feasibility of using algal cultivation as a CCS methodology. The effects of flue gas exhibits no growth inhibition for cultivating *Chlorella*. Minimal growth inhibition is seen for *Tetraselmis* and only in the form of reducing algal biomass.

30.2.3   Concluding Remarks

The robust characteristics of microalgae are shown in this experiment, illustrating the ability of microalgae to adapt and survive under different carbon source treatments. Integrating microalgae cultivation alongside coal fired power plants to

sequester flue gas emissions is a viable carbon capture (CCS) and storage method. The additional benefit of producing biomass and providing a renewable and sustainable feedstock for biofuels further supports this CCS methodology. The differences in growth characteristics for *Chlorella* are not statistically significant between the gas dosing treatments. Maximum cell counts for both gas treatments reaches about six million cells per milliliter with a standard deviation of one million cells per milliliter. The maximum specific growth rates are not significantly different at 0.849 and 0.771 per day for CO_2 and flue gas treatments, respectively. Biomass determination by VSS further concludes no significant difference between gas treatments; producing approximately 195 mg/L of biomass for CO_2 and 240 mg/L of biomass for flue gas dosing. The insignificant difference in growth characteristics between flue gas and CO_2 dosing for the cultivation of *Chlorella vulgaris* supports the existing literature, and proves that *Chlorella* is a viable microalgae strain to be implemented for the abatement of CO_2 emissions from coal-fired flue gas. Flue gas exhibits minimal signs of growth inhibition and the cultivation of *Chlorella vulgaris* from coal-fired flue gas is deemed successful. The quantification of growth kinetics for *Tetraselmis* sp. gives statistically significant and insignificant differences in growth, depending on the analytical method used. Generating growth curves using cell counts yields the same maximum cell concentration of 1.2 million cells per milliliter for both gas treatments. The maximum specific growth rates are indistinguishable at 1.1 per day for both CO_2 and flue gas. Biomass production by VSS proved there is a statistically significant difference in the biomass produced under CO_2 and flue gas treatments. CO_2 dosing produces approximately 700 mg/L of algal biomass while flue gas only produces 560 mg/L. With a confidence interval of 95 %, the difference in biomass production between the two gas treatments ranges from 45 to 225 mg/L. Although the conclusions drawn from cell counting and VSS contradict each other, *Tetraselmis* is able to grow under flue gas dosing. The lack of biomass production under flue gas treatments suggests NO and SO_2 inhibit the cell development seen in the absence of biomass. The overall result supports the fact that *Tetraselmis* sp. can be successfully cultivated with flue gas fulfilling the carbon supply.

30.3   Economics of Algae to Biodiesel Production

With increasing prices of fossil fuel the development of biofuels from alternative sources is gaining prominence. Existing research is the fields like bioethanol, biodiesel production from crops, hydrogen fuel cell and biogas upgrades for use in gas-fired vehicles is faced with various disadvantages. These methods have proved to be nonproductive, are in contrast with public interests and require abundance of resources like water and land. Biomass produced from algae can be supplied without impacting the cost of agricultural land, competing with food production or harming the environment. However, whether we have sufficient land to devote to these activities or not is a question that still needs to be addressed.

Fig. 30.13 Actual view of the tubular PBR in outdoor environment

Growing algae as a biofuel feedstock can be one solution to the growing problems due to fossil use. Algae have emerged as a viable resource for biodiesel and bioethanol production. Algae can be grown in two different systems, in PBRs (Fig. 30.13) or in raceway ponds. Raceway ponds are less productive than PBR's and also require extensive land area. Hence PBRs will be the favorable application for the future [1]. The technology (PBR) itself is quite new; therefore, much more research and improvements need to be done to optimize and enhance the existing systems for commercial applications [2–4, 46, 47]. Some of the technical challenges include sustaining the highest photosynthesis and biomass productivity levels reduce cell damage due to hydrodynamic stress, fabrication costs, installation and maintenance, and increasing the capability of the system to expand to an industrial scale [6, 48].

Unlike other crops that are currently being used for oil production such as soybean oil, palm oil, corn, and jatropha, some strains of algae contain as much as 70 % oil. They are capable of producing more than 30-times the amount of oil (per year per unit area of land) when compared to oil seed crops [4]. A major advantage of algae is its use of CO_2 to grow. Algae can extract the carbon dioxide from sources such as power plant exhausts or other CO_2 emitting processes when the PBR is integrated with it. Hence growing algae using a PBR is ideal for an energy self-sufficient community. A yield of 200–400 t of oil/ha/year can be considered reachable with a standard PBR system [33, 47]. Biodiesel produced from algae appears to be a theoretically feasible solution for replacing petrodiesel since no other feedstock has an oil yield high enough. It has been found that approximately ten million acres of land would be needed for biodiesel production in order to produce enough biodiesel to replace all the petrodiesel currently used in the USA [33]. This is just 1–3 % of the total land used today for both farming and grazing in the USA (about one billion acres). Algae cake, which is a by-product of

the biofuels production from algae, is a protein-rich algae cake that can be used as an animal feed. Thus PBRs make it possible to supply biomass without impacting the cost of agricultural land or competing with food production.

This section of the chapter focuses on the economic side of producing biodiesel from Algae. It is based on analyzing the feasibility of a PBR production plant with an output of 100 t of dry biomass per day located in a region with geographic conditions similar to Central California or Arizona which has extensive unused land. An investment in a large scale manufacturing facility is attractive if the consequences lead to a favorable economic outcome for the senior management or the owner as highlighted by the choice of the minimum acceptable rate of return (MARR). The investments fall under one of the categories: initial capital investment, operating costs and taxes. The benefits include: revenue, grants and subsidies. The net difference between the two categories is the periodic cash flow from the investment. The data on investment, productivity rate and raw material input (CO_2, nutrients) are provided by the manufacturer of PBR (AlgaeLink, the Netherlands). The study can be extended by comparing the results of PBRs produced by other manufactureres. In the sections that follow a general description of the investment and operational costs and the rationale behind evaluating the outcomes under a specific choice of MARR are provided. Additionally, the results of sensitivity analyses deliver deeper insights into optimization opportunities and further improvements.

30.3.1   Specifications and Resource Utilization

The desired amount of dry biomass produced per day for this study is approximately 100 t (100,000 kg or 220,400 lb). The oil yield of 20–70 t of vegetable oil equivalent (raw material for biodiesel) can be produced with this algae biomass. The size of the production plant can be chosen based on the values stated above. A complete turnkey industrial PBR, which includes harvesting and drying equipment and has a volume of 97 m^3 costs 194,000 Euros. Their estimated productivity rate is 3.5 kg/day/m^3 for fast growing algae strains in optimal climates. Purchasing 320 of those bioreactors would result in a theoretical daily production of 108 t, which results in yearly production of 39,653 t. With an exchange rate of 1.27 US/Euro, the total investment for the bioreactors was $79.3 million US. The total area needed for the set-up is approximately 38.4 ha (96 acres). Foundations (mainly leveling) for the fields also have to be provided. Since bioreactors could be placed in the desert or largely marginal land, the price is estimated to be $100/acre. The cost for foundation is another $10, summing up to $19.2 million US. The cost for additional plumbing and electricity hook-up is estimated to be $800,000 US.

Dividing oil from algae cake requires the use of specific presses. A complete press-container with a capacity between 5,000 and 15,000 t per year is available from the manufacturer of the PBR. Two 15,000-t containers and one 10,000-t container for Euro 412,000 and 312,000, respectively, are considered for this study. With the same

exchange rate as previously used the total investment for the presses sum up to $1.44 million. The total initial investment of $81.51 million is needed. A salvage value of 15 % of the initial investment is estimated for the end of the 20 years useful life. An overhaul is estimated to take place every fifth year and costs about 10 % of the initial investment.

The bioreactor and presses are depreciated using a 10-year property MACRS depreciation. The operation would result in three revenue streams: The sale of biodiesel, algae cake and carbon credits earned (or sold) for the consumption of CO_2. The selling price for biodiesel is similar to the petrodiesel price. A price of $1.00 per liter or $3.79 per gallon is assumed. Algae cake can be sold at a price of about $170 per ton (depending on the exact composition and location). The revenues from carbon credits are estimated at $8 per ton CO_2 sequestrated. However, different scenarios estimate a CO_2 price of $15–95 per ton [49] in the coming years. The main operational cost factors are the nutrients and the water consumption. About 0.13 kg of fertilizer is needed for every kilogram of dry algal biomass. A combined price (for a fertilizer mix) of $0.2 per kg is assumed. A water use of 500 L (132 gal) per produced ton and water price of $0.058 per liter are assumed [50]. Furthermore, labor with different qualifications is required to run the plant (one person at $100,000 US, three at $60,000 US, and four at $40,000 US). Electricity is assumed to be $0.15 per kWh. The electricity consumption would be approximately 39.24 million kWh per year for the PBR and another 22.4 million kWh for the presses. Optimal algae productivity rate requires maintaining an optimal temperature. The amount of heat required can be estimated using a mathematical model [51] and is approximately 154 million kWh. The price per kWh heat is assumed to be $0.01 US. Frequent maintenance is required and is estimated to be 1 % of the PBR's initial price per year and 10 % for the presses initial price per year. $100,000 US for miscellaneous maintenance issues is considered. The total maintenance costs sum up to $1.037 million per year. Costs for insurance are anticipated to be 0.1 % of the initial investment per year ($503,400 US). Finally, it is assumed that the conversion of algae oil to biodiesel is done externally. The price of the conversion per liter is expected to be $0.14 [4].

Table 30.7 lists the variables used in the analysis. Deviation from assumptions can have a variable impact on the final result based on the sensitivity of each input. The prices for nutrients, water, heat and CO_2 are widely variable and depend on the location and the market development. The long life of 20 years combined with a significantly new technology increases the risk. A drop in the productivity rate or longer downtimes would also have major impact on the profit. In the absence of standardized production data and work standards, there is uncertainty associated at every step in the production process. Simulation techniques in combination with this basic economic data can prove to be useful in decision making related to mass production. This initial analysis provides a background for ongoing experimentation with a system, which can be entirely PBRs or a combination of raceway ponds with PBR, whichever proves most efficient and profitable.

Table 30.7 Unit prices and quantity of inputs and outputs used in the model study

Revenue streams	Unit price	Quantity
Algae cake (ton)	$170.00	11,896.08
Biodiesel (gallon)	$3.80	4,263,157.89
CO_2 (ton)	$8.00	60,117.57
Expenses		
Labor 1 ($)	$40,000.00	4.00
Labor 2 ($)	$60,000.00	3.00
Labor 3 ($)	$100,000.00	1.00
Water (L)	$0.06	19,826,800.00
Nutrients (kg)	$0.20	39,653,600.00
Electricity PBR kWh (pumps, centrifuge, dryer)	$0.15	39,244,800.00
Electricity presses (kWh)	$0.15	22,425,600.00
Heat (kWh)	$0.01	154,176,000.00
Maintenance PBR 1 % of investment ($)	$792,480.00	1.00
Maintenance of presses 10 % of investment ($)	$144,272.00	1.00
Maintenance misc ($)	$100,000.00	1.00
External biodiesel production (L)	$0.15	27,757,520.00
Insurance	$503,453.60	1.00
Depreciation (MARCS 10 year class)		
Overhaul	10 % of price	Every 5 years
Income tax rate	40 %	

30.3.2 Economics, Justification and Sensitivity Analyses

A positive present worth value at the acceptable MARR for a project is attractive to investors. Data for the analysis are collected through personal communication with the manufacturer of the equipment.

From the basic analysis economic justification cannot be proven. A negative net present worth value of the after tax cash flow occurs. Hence sensitivity analyses are performed on various input factors in order to determine the most influential parameters towards the profitability. The Project has a payback period of 11 years (Table 30.8). The annual revenues (mainly from biodiesel and algae cake) are the determining factors for a positive net present worth (NPW) and an acceptable internal rate of return (IRR). The price of these factors in an open market scenario is largely determined by the market supply and demand. Hence they are subject to a deviation. The results of sensitivity analysis of the NPW are based on the price variables, which are summarized in Table 30.9. The investment is not profitable for a reasonable market-selling price in the range of $3.00–4.50/gal for biodiesel and algae cake price between $150 and $180/t. A trend and ratio analysis of the investments, particularly profitability analysis ratios (profit margin on sales, return on total assets and return on common equity) provide a more reliable background for decision making.

Table 30.8 Payback period

Year	Cash flow ($ millions)	Cumulative cash flow
0	(90.59)	(90.59)
1	10.33	(80.26)
2	9.23	(71.03)
3	8.36	(62.67)
4	12.95	(49.72)
5	7.17	(42.55)
6	11.83	(30.72)
7	7.08	(23.65)
8	7.18	(16.47)
9	7.29	(9.18)
10	6.35	(2.83)
11	16.08	13.25
12	11.72	24.98
13	9.46	34.44
14	14.16	48.60
15	8.49	57.09
16	13.29	70.38
17	8.68	79.06
18	8.95	88.01
19	9.23	97.24
20	1.36	98.60
MARR	10.00 %	
NPW	($8.99)	
IRR	8.46 %	
Payback	11 Years	
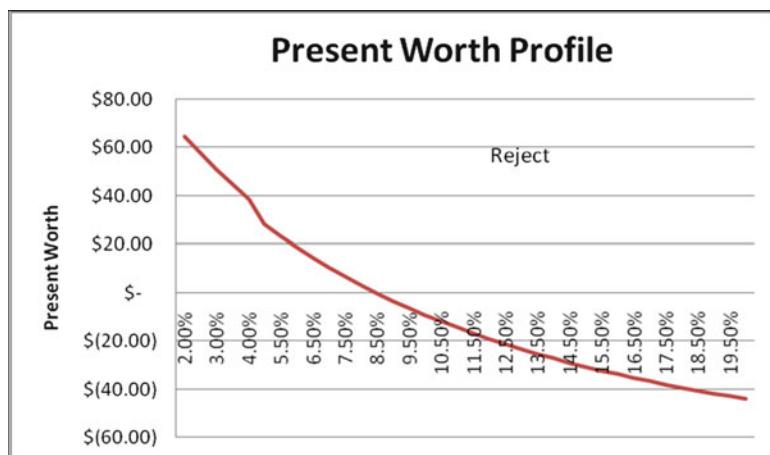
The cost of borrowing also determines the profitability of an investment. Figure 30.14 presents the effect of changes in the market interest rate on the net present worth of the project. It is evident that as the cost of borrowing increases the net present worth reduces further. Under the current market conditions, the existing trend towards raising interest rates will have a considerable impact on the project's net present worth.
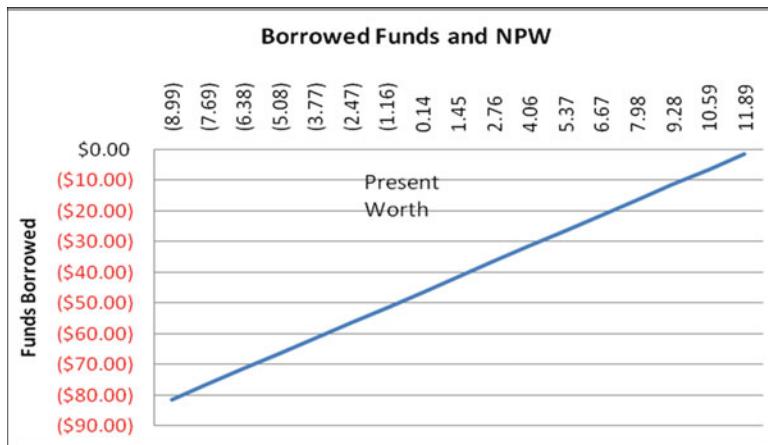
The changes in the initial investment are shown in Fig. 30.14. The initial investment costs do not play a significant role in this model. The initial capital required could be borrowed or raised with a combination of several financial instruments.

From Fig. 30.15, it is evident that as amount of borrowed funds increase, the internal rate of return (IRR) and NPW for the project change significantly. For the project to be successful in terms of the return it provides, due consideration need to be given to the cost of capital. The cost of capital will determine how this business can raise money: either through issuing of stock, borrowing or a mix of two. From Table 30.10 it is evident that the Present Worth for the project tends to be positive for borrowed capital in the range of $2–46 million, indicating that the remaining requirement can be raised by equity. Since the technology is still in its evolutionary stage, the cost of capital will be associated with a high risk premium. Therefore the

Table 30.9 Summary of financial statements (income and cash flow) analyzed for the investment period of 20 years

Year	Total revenue	Expenses	Depreciation	Taxable income	Net income	Cash flow
0	0.00	0.00	0.00	0	0	(90.59)
1	23.03	32.39	14.52	(9.36)	(5.62)	10.33
2	23.03	29.63	11.62	(6.60)	(3.96)	9.23
3	23.03	27.46	9.30	(4.43)	(2.66)	8.36
4	23.03	38.95	20.61	(15.91)	(9.55)	12.95
5	23.03	24.47	5.95	(1.44)	(0.86)	7.17
6	23.03	15.95	5.29	7.08	4.25	11.83
7	23.03	24.25	5.29	(1.22)	(0.73)	7.08
8	23.03	24.51	5.29	(1.48)	(0.89)	7.18
9	23.03	24.78	5.29	(1.75)	(1.05)	7.29
10	23.03	22.45	2.65	0.59	0.35	6.35
11	23.03	26.59	14.52	(3.56)	(2.13)	16.08
12	23.03	29.63	11.62	(6.60)	(3.96)	11.72
13	23.03	30.20	9.30	(7.17)	(4.30)	9.46
14	23.03	41.96	20.61	(18.93)	(11.36)	14.16
15	23.03	27.79	5.95	(4.76)	(2.86)	8.49
16	23.03	19.60	5.29	3.43	2.06	13.29
17	23.03	28.27	5.29	(5.24)	(3.14)	8.68
18	23.03	28.93	5.29	(5.90)	(3.54)	8.95
19	23.03	29.64	5.29	(6.61)	(3.97)	9.23
20	23.03	19.72	2.65	3.31	1.98	1.36
Net present worth (NPW)						($8.99)
Internal rate of return (IRR)						8 %

Fig. 30.14 Net present worth profile (simple investment)

Fig. 30.15 Sensitivity of borrowed funds and present worth of the project

Table 30.10 Borrowed funds and present worth

Borrowed funds	IRR (%)	Present worth
($81.51)	8.50	(8.99)
($76.51)	8.64	(7.69)
($71.51)	8.80	(6.38)
($66.51)	8.98	(5.08)
($61.51)	9.19	(3.77)
($56.51)	9.43	(2.47)
($51.51)	9.71	(1.16)
($46.51)	10.04	0.14
($41.51)	10.45	1.45
($36.51)	10.94	2.76
($31.51)	11.58	4.06
($26.51)	12.40	5.37
($21.51)	13.51	6.67
($16.51)	15.08	7.98
($11.51)	17.48	9.28
($6.51)	21.53	10.59
($1.51)	29.71	11.89

MARR for this project will also be much higher during the initial period. The corporate tax rate varies significantly based on state, province or country where the business is located. Table 30.11 provides a deeper insight into the relationship of tax rate changes, borrowed funds and the IRR for this project. For the investment to be acceptable, the IRR under the existing tax rates should closely match the MARR selected. The choice of MARR is usually a policy decision and is subject to revision with the changing market conditions. The tax credits and subsidies given by many countries towards renewable energy resources vary considerably and do not stay constant through the life of the project. They are not included in this analysis and hence the estimated NPW and IRR values are more conservative.

Table 30.11 Internal rate of return as a function of borrowed funds and tax rate

IRR (%)		Borrowed funds ($ millions)												
		50.0	55.0	60.0	65.0	70.0	75.0	80.0	85.0	90.0	100.0	105.0	110.0
Tax rate (%)	25	8.21	8.17	8.13	8.10	8.07	8.05	8.03	8.01	7.99	7.97	7.96	7.95
	27	7.39	7.41	7.42	7.43	7.44	7.44	7.45	7.46	7.46	7.47	7.47	7.48
	29	6.58	6.65	6.71	6.76	6.81	6.84	6.88	6.90	6.93	6.97	6.99	7.01
	31	5.77	5.90	6.01	6.10	6.18	6.24	6.30	6.35	6.40	6.48	6.51	6.54
	33	4.97	5.15	5.31	5.44	5.55	5.65	5.73	5.81	5.87	5.98	6.03	6.07
	35	4.17	4.42	4.62	4.79	4.93	5.06	5.16	5.26	5.35	5.49	5.55	5.61
	37	3.39	3.68	3.93	4.13	4.31	4.46	4.60	4.72	4.82	5.00	5.07	5.14
	39	2.61	2.95	3.24	3.49	3.69	3.88	4.03	4.17	4.30	4.51	4.60	4.68
	41	1.84	2.23	2.56	2.84	3.08	3.29	3.47	3.63	3.77	4.02	4.12	4.21
	43	1.08	1.52	1.89	2.20	2.47	2.70	2.91	3.09	3.25	3.53	3.64	3.75
	45	0.32	0.81	1.21	1.56	1.86	2.12	2.35	2.55	2.73	3.04	3.17	3.29
	47	0.43	0.10	0.55	0.93	1.26	1.54	1.79	2.02	2.2	2.55	2.70	2.83

Table 30.12 Sensitivity analysis of the net present worth as a function of price of outputs

NPW		Price of algae cake per ton						
		$150	$155	$160	$165	$170	$175	$180
Price of biodiesel	$3.00	(48.25)	(48.03)	(47.81)	(47.59)	(47.37)	(47.15)	(46.93)
per gallon	$3.10	(46.68)	(46.46)	(46.24)	(46.02)	(45.80)	(45.58)	(45.36)
	$3.20	(45.10)	(44.88)	(44.67)	(44.45)	(44.23)	(44.01)	(43.79)
	$3.30	(43.53)	(43.31)	(43.09)	(42.87)	(42.65)	(42.44)	(42.22)
	$3.40	(41.96)	(41.74)	(41.52)	(41.30)	(41.08)	(40.86)	(40.64)
	$3.50	(40.39)	(40.17)	(39.95)	(39.73)	(39.51)	(39.29)	(39.07)
	$3.60	(38.82)	(38.60)	(38.38)	(38.16)	(37.94)	(37.72)	(37.50)
	$3.70	(37.25)	(37.03)	(36.81)	(36.59)	(36.37)	(36.15)	(35.93)
	$3.80	(35.67)	(35.45)	(35.23)	(35.02)	(34.80)	(34.58)	(34.36)
	$3.90	(34.10)	(33.88)	(33.66)	(33.44)	(33.22)	(33.01)	(32.79)
	$4.00	(32.53)	(32.31)	(32.09)	(31.87)	(31.65)	(31.43)	(31.21)
	$4.10	(30.96)	(30.74)	(30.52)	(30.30)	(30.08)	(29.86)	(29.64)
	$4.20	(29.39)	(29.17)	(28.95)	(28.73)	(28.51)	(28.29)	(28.07)
	$4.30	(27.81)	(27.60)	(27.38)	(27.16)	(26.94)	(26.72)	(26.50)
	$4.40	(26.24)	(26.02)	(25.80)	(25.59)	(25.37)	(25.15)	(24.93)
	$4.50	(24.67)	(24.45)	(24.23)	(24.01)	(23.79)	(23.57)	(23.36)

From the above discussion it is clear that for this investment to be profitable the factors internal to the project such as production costs need to be reduced. The market prices of the output although have a major impact on the profitability, cannot be controlled directly (Table 30.12).

There is very little information available on the microalgae nutrient feed and hence the values provided by the manufacturer. The nutrients and water are the inputs, which can be controlled directly by the process. The cost of water is more stable and hence less likely to change with the region indicating that the price of nutrients is one of the determining factors. The prices of nutrients are stochastic and

Table 30.13 Price of nutrients and water
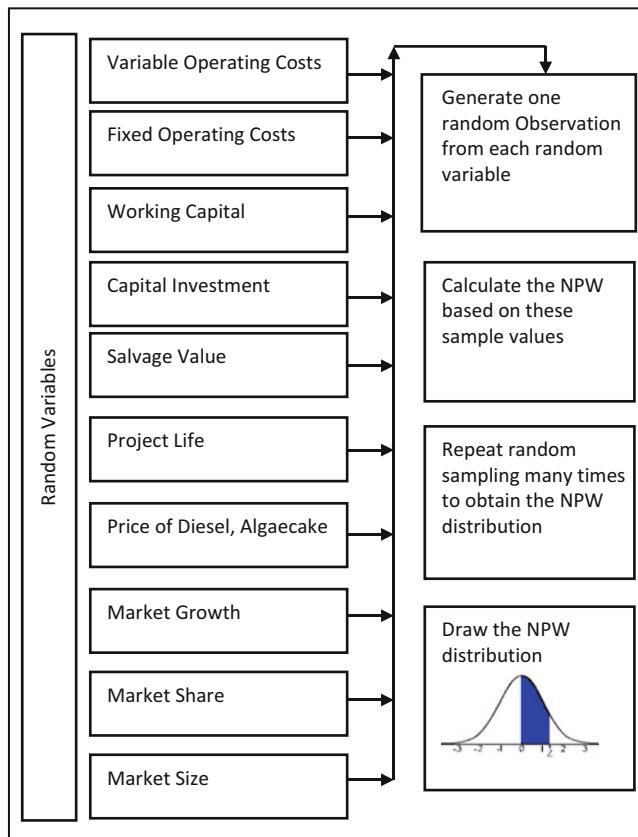
NPW		Price of water per liter					
		$0.05	$0.06	$0.07	$0.08	$0.09	$0.10
Price of nutrients per kg	$0.10	(19.59)	(20.32)	(21.05)	(21.79)	(22.52)	(23.25)
	$0.15	(26.90)	(27.63)	(28.36)	(29.09)	(29.83)	(30.56)
	$0.20	(34.21)	(34.94)	(35.67)	(36.40)	(37.14)	(37.87)
	$0.25	(41.52)	(42.25)	(42.98)	(43.71)	(44.44)	(45.18)
	$0.30	(48.83)	(49.56)	(50.29)	(51.02)	(51.75)	(52.49)
	$0.35	(56.14)	(56.87)	(57.60)	(58.33)	(59.06)	(59.80)
	$0.40	(63.45)	(64.18)	(64.91)	(65.64)	(66.37)	(67.10)
	$0.45	(70.76)	(71.49)	(72.22)	(72.95)	(73.68)	(74.41)
	$0.50	(78.07)	(78.80)	(79.53)	(80.26)	(80.99)	(81.72)
	$0.55	(85.38)	(86.11)	(86.84)	(87.57)	(88.30)	(89.03)
	$0.60	(92.69)	(93.42)	(94.15)	(94.88)	(95.61)	(96.34)
	$0.65	(100.00)	(100.73)	(101.46)	(102.19)	(102.92)	(103.65)
	$0.70	(107.31)	(108.04)	(108.77)	(109.50)	(110.23)	(110.96)

Table 30.14 Impact of water and nutrient use reduction on net present worth

NPW			Reduction nutrient use					
			60 %	50 %	40 %	30 %	20 %	10 %
			$15 (M)	$20 (M)	$25 (M)	$30 (M)	$35 (M)	$40 (M)
Reduction in water use	60 %	$8 (M)	$19.70	$14.59	$9.48	$4.37	($0.73)	($5.84)
	50 %	$10 (M)	$19.11	$14.00	$8.89	$3.78	($1.33)	($6.43)
	40 %	$12 (M)	$18.51	$13.41	$8.30	$3.19	($1.92)	($7.03)
	30 %	$14 (M)	$17.92	$12.81	$7.70	$2.60	($2.51)	($7.62)
	20 %	$16 (M)	$17.33	$12.22	$7.11	$2.00	($3.10)	($8.21)
	10 %	$18 (M)	$16.74	$11.63	$6.52	$1.41	($3.70)	($8.80)

based on the historical variability. Table 30.13 provides the results of sensitivity analysis for changes in NPW with the change in price of water and nutrients. Assuming all other factors constant, the net present worth was not positive for any price within the range of $0.10—0.70/kg. It is evident from the Table 30.13 that the NPW of the project reduces at a higher rate with increasing price of nutrients than increase in the price of water.

Through a sophisticated nutrient management, the fraction of lipids in the algae can be raised by 20 % consequently reducing the productivity rate. Filtered municipal water is high is nitrogen and phosphorus content and provides an alternative to purchasing nutrients. This can help reduce costs and when efficiently managed eliminate the cost of water and nutrients. Reducing the water use by 10 % and nutrient use by 30 % provides a positive NPW of $1.41 million. A detailed sensitivity analysis of amount of nutrient and water use and its relation to the NPW was provided in Table 30.14.

Fig. 30.16 Steps for simulating the project NPW

Although both sensitivity and breakeven analyses are useful, they have limitations. Often, it is difficult to specify precisely the relationship between a particular variable and the NPW. The relationship is further complicated by interdependencies among variables. Scenario analysis considering the sensitivity of the NPW both to changes in key variables and to the range of likely values of those variables adds greater certainty to the predicted values. Using the range of values, the worst-case, best case and the most likely scenarios can be analyzed.

These estimates can generate a probability distribution to predict the changes in the NPW with key input variables. A thorough risk analysis and simulation modeling will provide greater confidence related to the behavior of NPW with changes in key input variables. Figure 30.16 provides the logical steps that will be involved in simulating this risky investment.
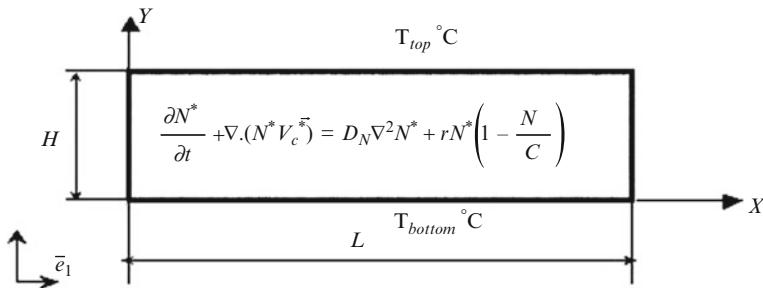
30.3.3   Concluding Remarks

In the absence of a low cost source of nutrients and water, the feasibility of a large scale manufacturing plant that is producing biodiesel from microalgae cannot be proven. However, municipal wastewater can be used as a source of the required nutrients. Additionally most countries provide certain amount of tax credit or subsidies towards green energy projects. With the above-mentioned incentives, the project can prove to be a feasible investment. The price of biodiesel is a critical component of this investment analysis since it is the most significant revenue generating output. The market for biodiesel has not stabilized yet resulting in a large scope for uncertainty in market speculation. Government policies like mandatory blending petrodiesel with biodiesel, which is prevalent in certain parts of Europe, can increase the demand for biodiesel and further push the need towards up-scaling manufacturing facilities for biodiesel. A rough estimate of the price of biodiesel made from algae oil is $2.35 per gallon, which is slightly higher than the petrodiesel prices in the USA, but far below the price of biodiesel a few years ago [52]. The technology is still not at a competitive stage resulting in high risk. Future endeavors in this field should look at standardizing the production process through use of simulation tools and identifying the key factors of deviation from the established process. With an increasing awareness about energy self-sufficiency, the day is not far when biodiesel will be the most viable option for our increasing energy demands.

30.4   Modeling the Effect of Thermal Stratification on the Algal Population in Growth

In the following part, we deal with the abundance and diversity of algal communities in aquatic open systems under the temperature condition. The temperature can influence many biological processes and may be an important factor involving population and community responses to climate change. The existence and implications of feedbacks between such biological and physical processes in ecosystems are still unknown. Algal abundance and diversity generally address to the questions of algal communities experiencing thermal stratification: can they adapt to the range of temperatures in which they are found? What is their distribution under the stratification effects? A more general approach is to integrate the potential for such thermal stratification to generate significant feedbacks between biological and physical mechanisms of the environment.

Directional motion (movement per se) is an essential physiological process in some algal species seeking out new environments to colonize for continued growth and reproduction. Complex sensing and signaling mechanisms that allow algae to move in response to external and internal stimuli have been described under the broad term "taxis." Once a signal (e.g., light, gravity, temperature, chemical) is

Fig. 30.17 Physical description of algal community with logistic growth in fluid or porous medium

received and decoded, movement may occur via mechanical processes such as flagellar or ciliar propulsion or gliding motility [53–56]. Biological convection, or bioconvection, is the spontaneous formation of patterns by microorganisms through their collective mobility. Algae are typically denser than water and move randomly, but on average upwardly against environmental gradients such as gravity. The upswimming causes individual cells to accumulate in a thin layer near the upper surface, resulting in an unstable density distribution and in the formation of bioconvective cells or fingering patterns at the scale of the population.

   In this part, a model is developed for spatial dynamics of a population of mobile algae under the thermal stratification within an open system, using a continuum model of coupled equations: momentum conservation equation for fluid dynamic motion (Navier–Stokes' equation for fluid medium and Darcy's equation for porous medium), equation for algal cell conservation with gravitactic behavior, energy/ mass conservation equation for the heated fluid or porous medium, and the Boussinesq's approximation for the mass density dependence of algae. This coupled biological–hydrodynamic model under the convection mechanism generated by the *taxis* and double-diffusion allows predicting interactions between biological and physical drivers of heterogeneity in aquatic systems characterized by temperature gradients. The equation for cell conservation of algal population is modified in adding a logistic term for the algal growth (Fisher's equation form), and the possibility of coupling effects of *gravitaxis* motion and logistic growth will be discussed. The model, based on a molecular diffusion approach, predicts possible impacts of thermal stratification on the coupled algal-fluid dynamic process, e.g., fluid flow regimes where the algal population persists, and vice-versa.

30.4.1 Mathematical Formulation

A 2D layer of height H and length L is considered, containing an initial uniform concentration $\overline{n}$ of suspended cells of algae as shown in Fig. 30.17.

This layer can be porous or fluid medium depending on the considered context hereafter. The algal communities swim with a mean velocity $\vec{V}_c^{*}$ vertically upward to the top of the water surface (i.e., $\vec{V}_c^{*} = \vec{V}_c^{*}(0, V_c)$). The upper and lower boundaries of the considered domain are subjected to constant temperatures *(Dirichlet conditions)*. It is assumed that all physical properties of the fluid are constant except the specific density in the buoyancy term. It is further assumed that there is no change in algae metabolism. In all equations, N stands for the concentration (density) of algal population and T for the temperature at one considered point at the considered time. Regarding the porous medium, it is assumed that (1) the medium is isotropic with a permeability K; (2) the porous matrix does not absorb microorganisms; (3) the pores sizes are significantly larger than the algal cell sizes; (4) algal cells do not alter the temperature of the fluid; (5) the temperature does not affect the endogenous behavior of algae. The other parameters and signs are detailed in the "Nomenclature."

30.4.1.1   Dimensionless Governing Equations

Equation of mass conservation:

$$\nabla \vec{V}^{*} = 0 \tag{30.64}$$

Momentum conservation equation for fluid medium or Navier–Stokes equation:

$$\rho_w \frac{\partial \vec{V}^{*}}{\partial t^{*}} + \rho_w \nabla \left(\vec{V}^{*} \vec{V}^{*} \right) = -\nabla p + \mu \nabla^2 \vec{V}^{*} + \rho \, \vec{g} \tag{30.65}$$

Momentum conservation equation for porous medium or Darcy's equation:

$$-\nabla p - \frac{\mu}{K} \vec{V}^{*} + \rho \, \vec{g} = 0 \tag{30.66}$$

It should be noted that the velocity term in Eqs. (30.65 and 30.66) are not the same for the fluid flow velocity. $\vec{V}^{*}$ in the Navier–Stokes equation (30.65) is the exact fluid flow velocity while $\vec{V}^{*}$ in Eq. (30.66) is Darcy's velocity (average velocity of the fluid flow in porous medium).

Equation of algal population in growth:

$$\frac{\partial N^{*}}{\partial t} + \nabla \cdot \left(N^{*} \vec{V}^{*} \right) + \nabla \cdot \left(N^{*} \vec{V}_c^{*} \right) = D_N \nabla N^{*} + r N^{*} \left(1 - \frac{N^{*}}{C} \right) \tag{30.67}$$

The net algal cell production described by logistic growth is represented by the term $rN^*(1 - N^*/C)$

Equation of conservation of energy:

$$\frac{\partial T^*}{\partial t} + \nabla \cdot \left(\vec{V}^* T^* \right) = \alpha \nabla T^* \tag{30.68}$$

Boussinesq approximation:

$$\rho = \rho_w [1 + \beta_c \Delta N - \beta_T \Delta T] \tag{30.69}$$

With

$$\beta_c = \frac{\Delta \rho_c \vartheta}{\rho_w} \qquad \text{specific mass variation coefficient of the algal suspension} \tag{30.70}$$

$$\beta_T = -\frac{1}{\rho} \left(\frac{\partial \rho}{\partial T} \right)_p \quad \text{thermal expansion coefficient} \tag{30.71}$$

Boundary and Initial Conditions

At the impermeable boundaries, the conditions of rigid no-slip and zero flux are applied, which leads to:

$$y^* = 0, H: \quad \vec{V}^* = 0; \quad \vec{j}^* \cdot \vec{e} = 0 \tag{30.72}$$

The thermal conditions at bottom and top walls are *Dirichlet conditions*

$$y^* = 0: \quad T^* = T_b \tag{30.73}$$

$$y^* = H: \quad T^* = T_t \tag{30.74}$$

The initial conditions are as follows

$$\text{at } t^* = 0: \quad N^* = N_0 \text{ and } T^* = T_0 \tag{30.75}$$

Dimensionless Governing Equations Under the Stream Function Form and Corresponding Boundary Conditions

In introducing the definition of stream function,

$$\psi^*: \quad \vec{V}^* = \frac{\partial \psi^*}{\partial y^*}, \quad -\frac{\partial \psi^*}{\partial x^*} \tag{30.76}$$

and using the scaling technique with more specifically setting scaled variables as follows:

$$F = \frac{L}{H}; \quad x = \frac{x^*}{H}; \quad y = \frac{y^*}{H}; \quad t = \frac{t^*D}{H^2}; \quad \psi = \frac{\psi^*}{D}; \quad \overrightarrow{V} = \frac{\overrightarrow{V^*}L}{D}; \quad T$$

$$= \frac{T^*}{\Delta T}; \quad N = \frac{N^*}{\Delta N} \tag{30.77}$$

The number of variables that could intervene within the system will be significantly reduced. Substituting these scaled variables into the governing equations (Eqs. 30.65–30.68) in using the Boussinesq's approximation (Eq. 30.69), the systems of governing equations under the stream function form are obtained as follows.

For the fluid medium:

$$\frac{\partial (\nabla^2 \psi)}{\partial t} + \nabla \left(\overrightarrow{V} \nabla^2 \psi \right) = Sc \nabla^4 \psi + Sc \left(Ra_b Le \frac{\partial N}{\partial x} - Ra_T \frac{\partial T}{\partial x} \right) \tag{30.78}$$

$$\frac{\partial N}{\partial t} + \nabla \left(\overrightarrow{V} N \right) + \nabla \left(\overrightarrow{V}_c N \right) = \nabla^2 N + \lambda N \left(1 - \frac{N}{\xi} \right) \tag{30.79}$$

$$\frac{\partial T}{\partial t} + \nabla \left(\overrightarrow{V} T \right) = Le \nabla^2 T \tag{30.80}$$

For the porous medium:

$$\nabla^2 \psi = Ra_b \frac{\partial N}{\partial x} - Ra_T Le \frac{\partial T}{\partial x} \tag{30.81}$$

$$\frac{\partial N}{\partial t} + \nabla \left(\overrightarrow{V} N \right) + \nabla \left(\overrightarrow{V}_c N \right) = \nabla^2 N + \lambda N \left(1 - \frac{N}{\xi} \right) \tag{30.82}$$

$$\frac{\partial T}{\partial t} + \nabla \left(\overrightarrow{V} T \right) = Le \nabla^2 T \tag{30.83}$$

Therefore, Eqs. (30.78–30.80) and Eqs. (30.81–30.83) are the governing equations of the fluid and porous systems, respectively. Scaling method also releases the following governing parameters.

Dimensionless growth rate

$$\lambda = rH^2/D \tag{30.84}$$

The Lewis number, $Le = \alpha/D$ and the Schmidt number

$$Sc = \nu/D \tag{30.85}$$

The Peclet number, dimensionless velocity of the motile algae, is defined by

$$\vec{V}_c = H \vec{V}_c * / D \qquad (30.86)$$

Bio-Rayleigh number, Ra_b is a combination of algal characteristics ($\vartheta,\Delta\rho,V_c,D$) and environmental qualities (geometrical and physical effects: $H,K,g,\rho_w,\nu,\overline{n}$) while thermal Rayleigh number, Ra_T represents the temperature capacity in the environment. In other words, Ra_T stands for the intensity of thermal effects on the whole system. These governing parameters are obtained for two distinguished cases of fluid and porous medium as:

For the fluid medium:

$$\text{Bio-Rayleigh number } Ra_b = g\vartheta\Delta\rho\overline{n}V_cH^3/\rho\nu D \qquad (30.87)$$

$$\text{Thermal Rayleigh number } Ra_T = g\beta_T\Delta TH^3/\nu\alpha \qquad (30.88)$$

For the porous medium:

$$\text{Bio-Rayleigh number } Ra_b = gKH\beta_b\Delta N/\nu D_c \qquad (30.89)$$

$$\text{Thermal Rayleigh number } Ra_T = gKH\beta_T\Delta T/\nu\alpha \qquad (30.90)$$

The term $1/\xi = \Delta n/C = \overline{n}V_c/C$ is coined the name *normalized carrying capacity of mobility algae*. It is assumed that this parameter equals 1 throughout this study. Therefore, there are six governing dimensionless parameters for the whole system: Sc, Ra_b, Ra_T, V_c, Le, and λ (*for the case of fluid medium*) and five parameters Ra_b, Ra_T, V_c, Le, and λ (*for the porous medium*). These parameters represent biological and physical interactions.

The corresponding boundary conditions are $\vec{V} = 0$ (rigid no-slip) and the zero cell flux at walls $\vec{j} \cdot \vec{e} = 0$ that lead to:

$$\vec{j} \cdot \vec{e} = \vec{V}N + \vec{V}_cN - \nabla N = 0 \quad \text{or} \quad \vec{V}_cN = \nabla N$$

Since $\vec{V}_c = \vec{V}_c(0, V_c)$, then finally

$$V_cN = \partial N/\partial y \qquad (30.91)$$

The dimensionless *Dirichlet* boundary conditions of temperature at the bottom and top walls are

$$\text{at } y = 0 : T = T_b \text{ and at } y = 1 : T = T_t \qquad (30.92)$$

Two main convection mechanisms govern our system: convection generated by temperature, which is strongest when the thermal gradient is against the gravity, and convection created by mobile algae (bioconvection). The amplitude of bioconvection is enhanced when algal speed V_c increases, and converges with

thermal convection under flux constant conditions when V_c approaches zero [57, 58]. Hence, algal Rayleigh number, Ra_b denotes the capacity of the cell to generate bioconvection, while thermal Rayleigh number, Ra_T represents the intensity of thermal factor on the whole system. The model simplifies to pure thermal double-diffusion model if the algae is assumed immobile ($V_c = 0$), that means just inter-action of "solute" cells of algae and temperature diffusivities. When growth rate neglected ($\lambda = 0$), the system becomes bioconvection with double-diffusion. In choosing the *gravitaxis* cue for algal population, i.e., $\vec{V}_c = \vec{V}_c(0, V_c)$' the model is simplified for the algae behavior.

30.4.2 Numerical Approach
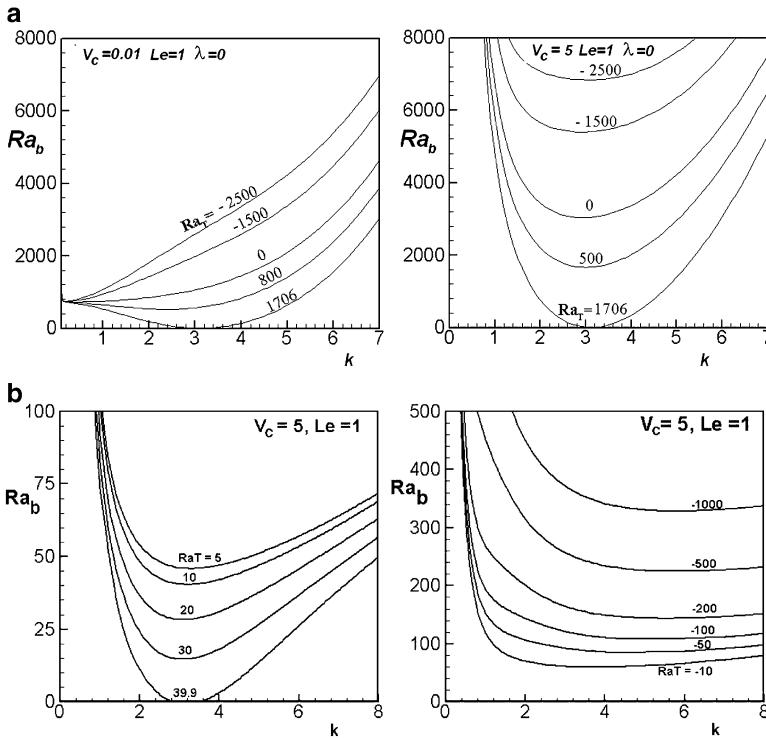
The control volume method [59] is employed to solve the governing equations (systems 30.78–30.80 and 30.81–30.83) with staggered grids. A numerical code was built based on this approach. The stream function is calculated on one set of nodes while the concentration and temperature are calculated on another set of nodes. The discretized equations are derived using central differences *for spatial derivatives and backward differences for* time derivatives. The method PDMA (Penta-Diagonal Matrix Algorithms) are used to solve the system of algebraic equations. And it is considered that convergence is reached when

$$\frac{\left| f_{i,j}^{m+1} - f_{i,j}^m \right|}{\max \left| f_{i,j}^m \right|} \leq \varepsilon \tag{30.93}$$

where f corresponds to the variables *(ψ,N,T)*, ε stands for the tolerance, m is the iteration number, and i, j denote the grid points. To check the grid independence of the solutions, the grid was varied from *21x21* to *81x 81* nodes *(for F = 1)* and from *21x41* to *41x81* nodes (*for F = 1 and 4*). We adopt the grid for which the variations in the solution were less than 10^{-4}. The results presented in following sections are obtained with grids of 61×61 nodes for square enclosures ($F = 1$), and with *41x61* nodes for rectangular enclosures ($F = 4$), in conjunction with a time step, $\Delta t = 0.0001$ and a convergence tolerance, $\varepsilon = 10^{-6}$. For the algebraic nonlinear growth rate term, the linearization scheme of Patankar [59] is used.

30.4.3 Results and Discussions

The solutions are distinguished into two cases as follows.

Fig. 30.18 (**a**) Stability diagrams for $V_c = 0.01$ (*left*) and $V_c = 5$ (*right*), fluid layer heated from above and below. (**b**) Stability diagrams for $V_c = 5$, porous layer heated from below (*left*) and from above (*right*)

In Case of Algal Growth Rate Negligible, $\lambda = 0$

The system is under the mechanism of the gravitactic bioconvection with double-diffusion. The onset of the pattern can be determined by the linear stability analysis [58, 60].

Stability Diagrams and Critical Regimes

The onset of double diffusion convection caused by gravitactic algal cells and thermal effects is obtained by the linear stability analysis. The diagrams showing the critical Rayleigh number, Ra_b versus wave number, k, and as a function of thermal critical Rayleigh number, Ra_T. From an analysis for an infinite layer, the relationships between governing parameters Ra_T, Ra_b and V_c are presented in Fig. 30.18a, b. It should be noted that the critical Rayleigh number, Ra_b for the

onset of stationary convection does not depend on the Lewis number Le. Therefore, only the results obtained with $Le = 1$ are shown here. Two cases of thermal gradients are considered: heated from below (with positive Ra_T) and heated from above (with negative Ra_T). Figure 30.18a shows the critical Rayleigh number, Ra_b and Ra_T versus wave number, k in the fluid medium for two values of $V_c = 0.01$ and 5, respectively. It can be observed that when the critical bio Rayleigh number, Ra_b as a function of the wave number, k with minima occurred at a critical wave number, k_{cr}. When the system is heated from below (positive Ra_T), there exists a destabilization of the convection motion created by algae swimming, i.e., the thermal effect decreases the critical value of Ra_b. Figure 30.18b shows the stability diagrams for $V_c = 5$, porous layer heated from below (left) and from above (right). The mechanism in the whole system, fluid or porous, is convectively additive by thermal effect and algae mobility effect. It can be seen that when Ra_T reaches the critical value of pure thermal convection system (Benard convection) with $Ra_T = 1,706$ (*fluid layer*) and 39.9 (*porous layer*), the value of Ra_b becomes zero. The system is then purely governed by thermal convection. In the case of heating from above, the critical Rayleigh number, Ra_b increases with Ra_T, meaning that thermal effects now tend to stabilize the system.
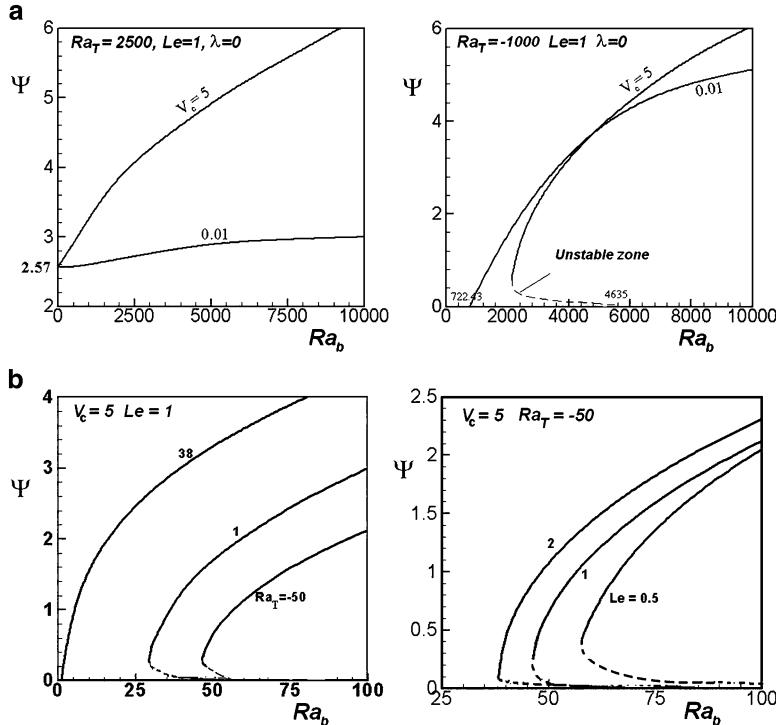
Supercritical States

Our analysis are conducted via the Hoft bifurcation curves of flow regimes by simulation experiments to verify critical Rayleigh numbers for the onset of spatio-temporal pattern predicted by linear stability, and to exploit steady supercritical regimes (regimes above the critical one), both focusing on the predicted impacts of thermal stratification on algae-hydrodynamic processes. Hydrodynamic processes, or flow regimes, are represented by the streamlines traced from the stream function, ψ. This dimensionless function denotes the path of a fluid particle. In our analysis, streamlines reveal the path of algae and/or temperature trajectories in a flow field where temperature and algae interact. The intensity of stream function reflects the importance of hydrodynamic processes (the stronger value of ψ, the higher hydrodynamic effect). All our analyses rely on a number assumptions related to all six parameters governing the fluid system: Sc, Ra_b, Ra_T, V_c, Le, and λ, and five parameters for the porous one: Ra_b, Ra_T, V_c, Le, and λ. The Schmidt number, Sc is set to 7 as a constant because the ratio between viscosity and thermal diffusivity has no particular effect on the pattern in the laminar regime if the water is the considered medium.

The choice of some representative values of dimensionless algae velocity herein *for the stability analysis* in all simulations can be explained by the fact that a universal stability curve (not shown here) was obtained by a normalization based on length scale D_c/V_c^* for the velocity greater than 1 instead of the length scale, H for $V_c < 1$, for both porous and fluid medium [58, 60]. Biological and physical interactions of the system are then governed by the remaining parameters: Ra_b, Ra_T, Le (and λ, *if treated the coupling effect of growth rate*). Interrelationships

between these four parameters at fixed values of V_c and Sc can then be understood from their effects on the spatial temporal variables ψ, N, T. For development of convection state beyond the critical threshold, a 2D fluid media is studied under thermal stratification with dimensionless length $L = 4$, corresponding to an "infinite" space for the qualitative description of fingering patterns [61]. An assumption of "infinite" space for $L \geq 4$ was used for the sake of simplicity, but it can be violated in natural systems with the modification of multiple biological and physical factors with increasing length [62, 63].

- *Temperature of the bottom is greater than temperature of the top ($T_b > T_t$; $Ra_T > 0$):* The medium is heated from below, the vector of temperature gradient is opposite to the gravity vector and the thermal Rayleigh number Ra_T is positive. In natural systems, this situation can be observed in certain geothermal areas [64]. Physical implications of $Ra_T > 0$ can be understood under one of three scenarios: *(i) $Ra_T < Ra_{Tcritical}$, (ii) Ra_T very near $Ra_{Tcritical}$, and (iii) $Ra_T > Ra_{Tcritical}$.* The critical Rayleigh number, $Ra_{Tcritical}$ caused by temperature is around 1,706 for fluid medium and 39.9 for porous layer for this geometrical configuration with *Dirichlet* conditions. For the sub-case *(i)*, there is no thermal convection and flow regime in the system is only governed by bioconvection. For the sub-case *(ii)*, thermal convection starts contributing to the overall convection mechanism. In the sub-case *(iii)*, when Ra_T is sufficiently superior to $Ra_{Tcritical}$ (supercritical state), the flow regime becomes more convective (ψ *stronger*) due to the two additive convective operating at the same time: bioconvection and thermoconvection (additive convection pattern). Fig. 30.19a on the left shows the bifurcation curves ψ *vs* Ra_b under the effect of $Ra_T = 2,500$ with two swimming speeds $V_c = 0.01$ and 5 in the fluid layer. The value of $\psi = 2.57$ in Fig. 30.19a on the left is actually the thermal convection value obtained by the heated from below condition $Ra_T = 2,500$ when $Ra_b = 0$ ($V_c = 0$ or $\overline{n} = 0$). If Ra_b is increased (or if $Ra_T > 2,500$), the convective motion is more solicited, and the value of ψ in this case becomes certainly greater than 2.57 as illustrated in the bifurcation curves. *In the porous layer*, Fig. 30.19b on the left side shows the bifurcation curves ψ vs Ra_b under the effect of *different* Ra_T with swimming speeds $V_c = 5$. From Fig. 30.19b, it is shown that there exists a subcritical regime.

- *Temperature of the top is greater than temperature of the bottom ($T_b < T_t$; $Ra_T < 0$):* Most natural systems with thermoclines correspond to this case where the fluid is heated from above. The vector of temperature gradient is in the same direction as the gravity vector and the thermal Rayleigh number Ra_T is negative. In this case, because of heating from above, the Rayleigh Benard convection theory predicted no thermal convection, and algae motion convection (bioconvection) is then the only mechanism that governs the system [60]. However, temperature can have an important stabilizing effect on the convection generated by algae motion via Ra_b. Fig. 30.19a on the right shows the bifurcation curves ψ vs Ra_b under the effect of $Ra_T = -1,000$ with two swimming speeds $V_c = 0.01$ and 5. In the curve of $V_c = 5$, one can observe the *subcritical flow*
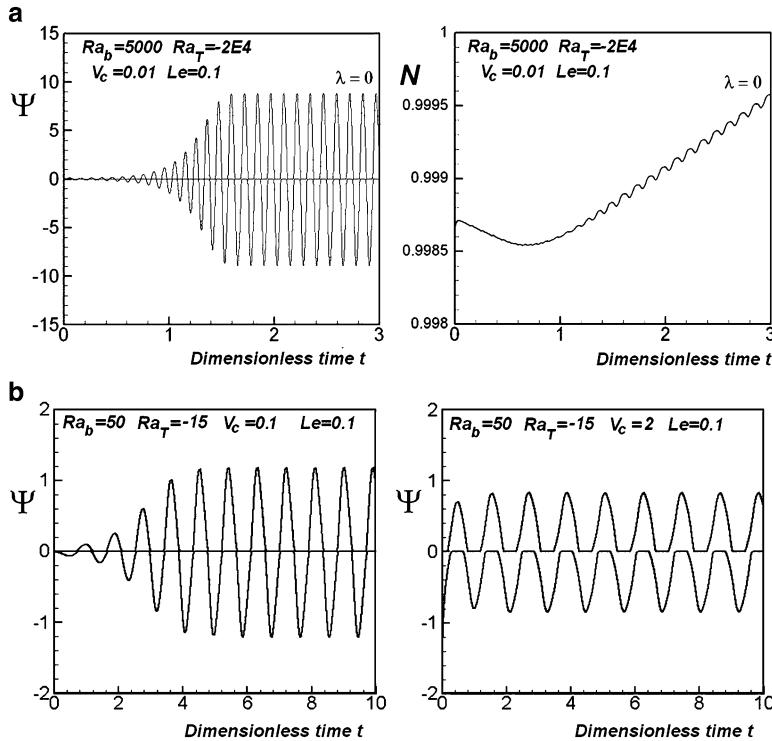
Fig. 30.19 (**a**) Bifurcation curves (supercritical states) for the fluid layer, heated from below (*left*) and from above (*right*). (**b**) Bifurcation curves (supercritical states) for porous cavity $F = \pi/k_c$, $V_c = 5$. *Left*: $Le = 1$ and various Ra_T; *Right*: $Ra_T = -50$, various Lewis numbers

regime at Rayleigh numbers below the supercritical threshold, meaning that the bifurcation curve in the case of high swimming speed, for example $V_c = 5$ is not reversible. That defines the unstable zone near the threshold. The same observation is made for the porous medium in Fig. 30.19b.

Oscillatory State

One particular aspect of algal pattern formation one can expect to observe in the model and natural systems is the spatiotemporal oscillation regime. This oscillatory state may be established within a system with negative thermal Rayleigh due to the double molecular diffusion mechanisms in which the diffusivity of heat is less than the diffusivity of algae (Lewis number, $Le \ll 1$). This oscillatory state is characterized by the intensity of the motion (represented by the ψ amplitude) and the period of oscillation with corresponding oscillation curves of algal density N for porous and fluid media (Fig. 30.20a, b). Oscillations of ψ and N are sustained because of the physical interference between two molecular diffusivities (thermal
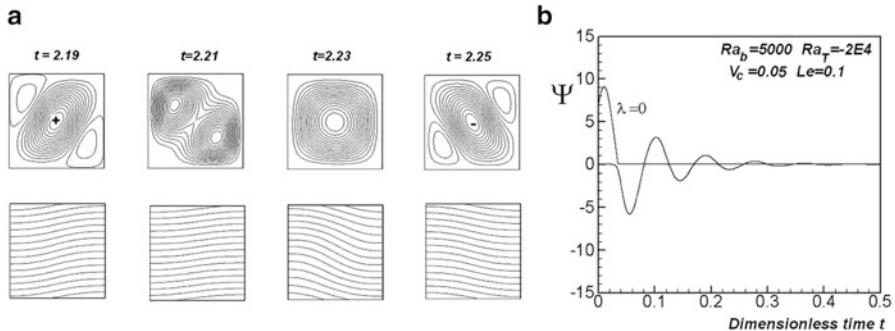
Fig. 30.20 (**a**) Oscillation state for *fluid square space*, heated from above, $Le = 0.1$, $Ra_b = 5,000$, $Ra_T = -20,000$, $\lambda = 0$, $V_c = 0.01$. (**b**) Oscillation state for *porous square space*, heated from above, $Le = 0.1$, $Ra_b = 50$, $Ra_T = -15$, $\lambda = 0$, $V_c = 0.1$ (*left*) and $V_c = 2$ (*right*)

and algal). These results predict conditions in experimental or natural algal populations under which the path of fluid particles and of algal organisms could be oscillating (Fig. 30.21a). Under the same conditions of Ra_T and Ra_b, the oscillations become weaker and even disappear as V_c increases (Fig. 30.21b).

In Case of Algal Growth Rate $\lambda \neq 0$

When the time scale is much larger, the biological convective pattern generated by algal motion can disappear or be transformed under nonlinear different pattern forms. In fact, in a time scale of minutes to hours, the gravitactic mechanism of some species can create the bioconvection pattern. The time scale for the birth and death processes accounted in the logistic term is generally understood much larger than that of bioconvection process. However, in some species, there is an interfacial status where the growth and death could happen in the same time with the gravitactic process. Some laboratory experiences have shown that for the protozoan *Tetrahymena pyriformis*, there are two processes, which could happen, in the same
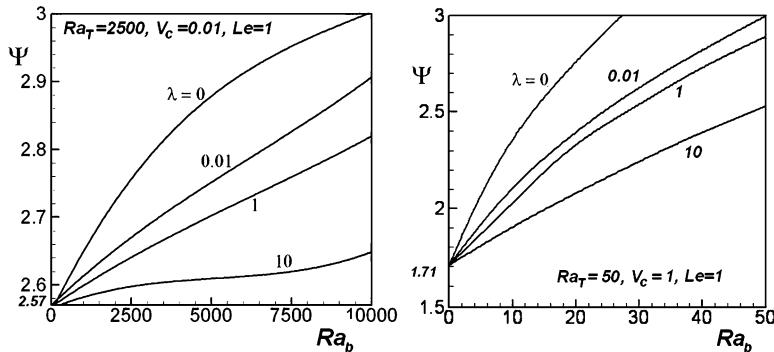
Fig. 30.21 (**a**) *Left*: Oscillation case at different time in one cycle in the square fluid space. The signs "+" and "−"stand for the rotation direction of steady state convection. Above: streamlines. Below: algal iso-density. (**b**) *Right*: Oscillation state (ψ versus t) in the heated from above case *in a fluid square space* with $Le = 0.1$, $Ra_N = 5,000$, $Ra_T = -20,000$ and $\lambda = 0$, $V_c = 0.05$

scale of time [63, 65]. It is assumed that bioconvection affects culture growth and vice-versa. That leads to two following reflections:

1. In general cases, the bioconvection time scale is in minutes, much shorter than time scale of growth in the algal cultures. The first approach is then growth in number density could be incorporated as a slow parametric change in the bioconvection equations, and similarly the bioconvective pattern would allow a modeling of the effect on nutrient uptake and hence growth.
2. However, by experiments with the protozoan species *Tetrahymena pyriformis*, it is recognized that there exists an intermediate period where the cells divide themselves and continue in the same time to move up gravitacticly. More precisely, the life cycle of *Tetrahymena pyriformis* is around 2 h for a new generation [66], and the bioconvection pattern observed is in the rank of 0.5–3 h [63]. The second approach is to couple the growth rate in population and taxis effects, i.e., which may create bioconvection in a short scale of time (0.5–3 h). The coupling according to our opinion is possible and makes sense because there exists anyway in the nature different intermediate periods where the time scale for mobility overlaps the time scale of growth and death processes.
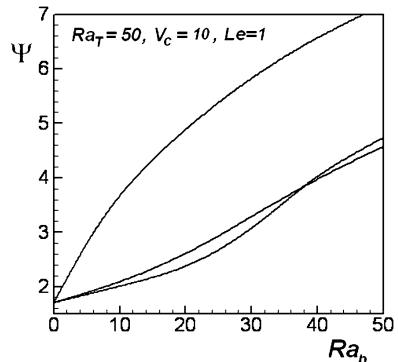
The coupling possibility of the growth rate in population and *gravitaxis* effects, which may create bioconvection, may exist in the nature at intermediate periods where the time scale for mobility overlaps the time scale of growth and death processes. Under the additive convection scenario, increasing growth rate of algae can damp their hydrodynamic process. The bifurcation curves (Fig. 30.22) show that when Ra_b increases (i.e., algal swimming speed or density increases according to Eqs. (30.87 and 30.89), the hydrodynamic process may also increase.

Regarding the influence of the thermal diffusivity/algal diffusivity ratio (Le) for this scenario $Ra_T > 0$, it is shown that in algal population with a fixed density and swimming speed, if algae diffuse faster than the temperature (algal diffusivity greater than thermal diffusivity), they may generate a strong hydrodynamic process

Fig. 30.22 Bifurcation curves ψ versus Ra_b for the case heated from below with $Ra_T = 2{,}500$, $V_c = 0.01$, $Le = 1$ (*Left, fluid layer*) and for $Ra_T = 50$, $V_c = 1$, $Le = 1$ (*Right, porous layer*)

Fig. 30.23 Bifurcation curves ψ versus Ra_b for the case *porous layer* heated from below with $Ra_T = 50$, $V_c = 1$, $Le = 1$

in the medium. The flow regime is hence more convected. For more details of the effects of this ratio, readers are referred to Nguyen-Quang et al. [60]. The increasing swimming speed of algal cells can reinforce generated hydrodynamic consequences (stronger ψ amplitude as shown in Fig. 30.23) while the increasing growth rate could diminish this convective tendency. The interactive effects between V_c and λ are actually very complex and need further studies in the future.

30.4.4 Concluding Remarks

In porous or fluid systems where temperature and algal motility can both result in hydrodynamic patterns, strong interactions were found between thermal and population processes on hydrodynamic processes and on the spatial distribution of algae.

In the case of upper layer temperature less than the lower layer one ($Ra_T > 0$): when Ra_T was smaller than the critical value $Ra_{Tcr} \approx 1,706$ for fluid medium and $Ra_{Tcr} \approx 39.9$ for porous medium, there was no significant effect of temperature on the algal hydrodynamic processes because the thermal convection state was prevented (temperature was at diffusion state). In contrast, when $Ra_T > Ra_{Tcr}$ (supercritical state), thermal convection appeared and the effects of temperature on algal population were stronger. Temperature gradient then played a destabilizing role on hydrodynamic processes. The convection state in the system is additive because there were two concurrent mechanisms, one from suspended motile algal and the other from temperature. Spatial distribution of algae was driven by this additive convection. When the upper layer temperature higher than the bottom layer ($Ra_T < 0$), then bioconvection emerging from algal motion was the only operating convection mechanism (no thermal convection). The temperature gradient in this case played a stabilizing role on bioconvection intensity, which also depended on algal velocity and diffusivity ratio. It is underlined that thermal effects can create a subcritical regime for emerging bioconvection with the high swimming speed.

A particular feature of hydrodynamic process observed in the heating from above case ($Ra_T < 0$) was the oscillation state caused the molecular double-diffusion under well-defined physico-biological conditions: when the suspended cells (disturbing factor) diffused faster than temperature (stabilizing factor, i.e., $Le \ll 1$). While the oscillation regime and the formation of spatiotemporal algal patterns can be sustained under some combinations of governing parameters of Ra_T and Ra_b, it can also be damped by increasing growth rate and at higher swimming speeds of algae. This study provides a first attempt to explicitly couple biological and physical processes at the scale of algal organisms to predict larger scale algal and fluid dynamics. Our results revealed the interaction between algae demography and motion through their effect on bioconvection, with important implications for natural algal populations. In both cases of thermal stratification studied here, increasing algal growth rate weakened the convection state and played a stabilizing role. Although the pertinent observation in the nature is not realized yet, laboratory experiments with protozoan species *Tetrahymena pyriformis* clearly show that they never stop moving gravitacticly even when they are growing and dividing. It was also observed that bioconvection pattern of *T. pyriformis* occurs during their death and birth time scale [63].

30.5 The Relationships Between Nutrient Input, Algal and Herbivore Densities in Motion

The dynamics of the relationship between nutrient supply and algal density cannot be adequately explored by a simple model when nonlinear relationships exist, especially, when the system of algae–nutrient or herbivore–algae possess a *taxis* behavior (movement per se) as mentioned above. This section deals with the

relationship between algae–nutrient or herbivore–algae using the predator–prey modeling approach. The model suggested in this study is based on classical Lotka–Volterra system in which the predator and prey diffusions and their taxis behaviors are considered.

30.5.1 Background and Fundamental Aspects

The Lotka–Volterra model [67, 68], hereafter denoted by LV, describes the interaction between preys and predators in ecosystems and assumes that interaction parameters involved between different species in a fixed habitat are constant. This classical model is mathematically conservative and exhibits neutrally stable dynamics [69]. This shows that both species of predator and prey can coexist with the population densities regularly oscillating in time. The model also predicts that in the absence of the predator, the prey density will grow without limit, contrary to what has been observed in realistic predator–prey ecosystems. The actual existence of cyclic variation between predator and prey organisms is first shown by Gause [70], and it is shown that in reality, the interacting parameters are not constant like in the original assumption. This investigator also observed that at low prey densities, some prey could escape when their predators cannot find them. To make the original model more realistic clearly necessitated integration of behavioral details with population dynamics [71] and then Bazykin [72] added the predator saturation and predator competition terms to improve the classical LV model. Some other assumptions in which random variability is considered, with or without the prey self-competition term are also made [73, 75, 87]. Singular point analysis and linear approximation methods are applied by Curds [76] to a similar culture system and predicted that they are (1) a stable limit cycle variation (2) a damped oscillatory variation, and (3) non-oscillation variation *which asymptotically approached constant or steady state values*. These methods of prediction are tested and confirmed by a computer-simulation study [77] that developed a mathematical and numerical model describing the growth of two microorganisms, one preying upon the other, in a completely mixed single-stage continuous-culture reactor. His numerical results are validated by an experimental study on the living system of the predator–prey couple: ciliate *Tetrahymena pyriformis* and bacterium *Klebsiella aerogenes* [77].

The diffusion effects in the LV model are introduced by McLaughlin and Roughgarden [78]. Dispersal of predators and prey is well taken into account in their study, both as a potentially stabilizing mechanism and as a means to generate or maintain spatial heterogeneity in species distributions [78]. Introducing a hierarchy of scales to the spatially heterogeneous LV diffusion model, they have concluded that different scales of predator and prey dispersal do not stabilize the interaction [78]. Their model predicts that, for prey populations that are limited by widely ranging predators, species with low dispersal ability should be restricted to discrete high-density patches. However, species with greater mobility should be

more uniformly distributed at lower density [78]. In fact, a particular characteristic feature of such living system of predator–prey is the ability to respond to changes in the environment. Because of various undesirable factors, which arise due to ecological and environmental gradients in natural habitats, the tendency of the species is to migrate from unfavorable to favorable regions for their survival. As migration of the species plays an important role in the evolution of the species, its effects should be taken into account in prey–predator models. In general, migration of the species can be studied by identifying it with convective and dispersive processes. The migration could happen by external flows (*forced advection*) by winds, flows and streams, etc., or by themselves. *Taxis* is actually one of the simplest responses of movement of individuals towards (or away from) the stimuli.

From a laboratory experimental approach, *taxis* appearing in predator–prey interactions is also observed. These are cyclic population data for a case where *Paramecium aurelia* served as a host organism for *Woodruffia metabolica* [80]; bacterium *Klebsiella aerogenes* and its predator protozoa *Tetrahymena pyriformis* [77]; bacterium *Pseudomonas fluorescens* with predator *Tetrahymena pyriformis* [81], or the classical predator–prey pair *Paramecium aurelia* and *Didinium nasutum*, etc. In terms of the modeling approach, a model for population system is described by the "reaction-taxis-diffusion" [82], and they have shown that the intensity of *taxis* is significantly dependent on population density. According to them, the *taxis* behavior can have *a stabilizing effect on the dynamics of a spatially distributed population* and create appropriate conditions for the potential existence of populations in the regime of bounded spatial oscillations. Using the example of the *copepod–microalgae* community, a minimal conceptual model of the predator–prey system dynamics with taxis behavior is developed by Comins and Blatt [83]. According to these researchers, this model in which the *taxis* term is determined by predator satiety proves the most suitable for describing the *harpacticoid–diatom* dynamics.

The introduction of the taxis term makes the system of equations become physically equivalent to a "convective migration system." The effects of convective and dispersive migration due to environmental and ecological gradients have been discussed on the two species systems with mutualistic interactions [55, 84, 85]. In particular, Nallaswamy and Shukla [84] discusses the dynamics of prey–predator association on a spatially nonuniform habitat by means of a biased dispersal and observed that the effect of asymmetry in dispersal is to stabilize the otherwise stable LV model. They have concluded that the stabilizing effect is not only produced by dispersal, but may also be caused by ecological variation. Under the restriction that the ratio of convective velocity to dispersal coefficient is the same for both species, McMurtrie [85] has shown that convective migration has a stabilizing effect on the equilibrium state of the system in a finite habitat and the degree of stability increases with convective velocities. It should be noted that no attempt has been made to study such effects on the stability of systems of interacting species without any restriction on convective velocities.

In this part, the effects of a *taxis* behavior on the predator–prey population distribution is numerically investigated. The reasons for using classical LV model

are: (1) this is the simplest predator–prey model available; (2) it contains no complex regulatory mechanisms that might obscure the effects of environmental variation; (3) the behavior of LV model is well known, so any change due to *taxis term* might be apparent. The taxis behavior appears under the simplest form: the velocity term has one non-zero component, while other components being zero. That means in the 1D model, $\overrightarrow{V}_N* = V_N$ (dimensional moving speed of prey) or $\overrightarrow{V}_P* = V_P$ (dimensional moving speed of predator), *taxis* is just one directional motion. This kind of taxis could be found, for example, in the *Tetrahymena* populations and named *gravitaxis* [63]. The model suggested here is the classical LV system in a constant environment, and besides the passive diffusion (*random mobility*) of the prey and predators in the model, the "taxis term" is added in the model to present the "active dispersal" of species. That means, it is assumed that individuals move actively, but not only randomly in space, unaffected by currents, crosswinds or each other, but also by their collective behavior towards a *stimuli source*. Our suggested model is actually under the *reaction-taxis-diffusion* type and will treat space as an explicit and continuous variable (*spatiotemporal*). Many kinds of dispersal and passive diffusion have been analyzed by using this type of continuous space models [78, 79, 86]. Through the numerical simulation results, we will discuss the other important feature: effects of boundary conditions on prey–predator persistence/stability.

30.5.2 Mathematical Formulation

Assuming that prey and predator dimensional population densities $N*$, $P*$ respectively; $\overrightarrow{V}_N^*$, $\overrightarrow{V}_P^*$ are the taxis behavior of prey and of predator. In the following section, the "asterisked" variables are the dimensional quantities while "non asterisked" variables are the dimensionless ones. Others parameters can be found in the "Nomenclature."

Dimensional Governing Equations

The classical LV model is described as follows:

$$\frac{dN^*}{dt^*} = rN^* - \alpha_{NP}N^*P^* \quad \textit{prey equation} \tag{30.94}$$

$$\frac{dP^*}{dt^*} = \alpha_{PN}N^*P^* - \beta P^* \quad \textit{predator equation} \tag{30.95}$$

By integrating the diffusion and taxis behavior into the above system, the general form of the predator–prey system was obtained as follows:

$$\frac{\partial N^*}{\partial t^*} + \nabla\left(\overrightarrow{V}_N^* N^*\right) = D_N \nabla^2 N^* + rN^* - \alpha_{NP} N^* P^* \quad \textit{prey equation} \qquad (30.96a)$$

$$\frac{\partial P^*}{\partial t^*} + \nabla\left(\overrightarrow{V}_P^* P^*\right) = D_P \nabla^2 P^* + \alpha_{PN} N^* P^* - \beta P^* \quad \textit{predator equation} \quad (30.96b)$$

By introducing the following dimensionless parameters into Eqs. (30.96a) and (30.96b):

$$x = \frac{x^*}{L}; \quad y = \frac{y^*}{L}; \quad t = \frac{D_P}{L^2} t^*; \quad D = \frac{D_N}{D_P} \qquad (30.97)$$

$$N = \frac{\alpha_{NP}}{r} N^*; \quad P = \frac{\alpha_{PN}}{r} P^*; \quad \overrightarrow{V}_N = \frac{\overrightarrow{V}_N^* L}{D_P}; \quad \overrightarrow{V}_P = \frac{\overrightarrow{V}_P^* L}{D_P} \qquad (30.98)$$

The dimensionless governing equations are then obtained as follows:

$$\frac{\partial N}{\partial t} + \nabla\left(\overrightarrow{V}_N N\right) = D\nabla^2 N + dN - aNP \qquad (30.99)$$

$$\frac{\partial P}{\partial t} + \nabla\left(\overrightarrow{V}_P P\right) = \nabla^2 P + bNP - cP \qquad (30.100)$$

where there are the presence of governing parameters of the system:

$$a = \frac{\alpha_{NP} r L^2}{\alpha_{PN} D_P} \quad b = \frac{\alpha_{PN} r L^2}{D_P} \quad c = \frac{\beta L^2}{D_P} \quad d = \frac{r L^2}{D_P} \qquad (30.101)$$

Boundary Conditions
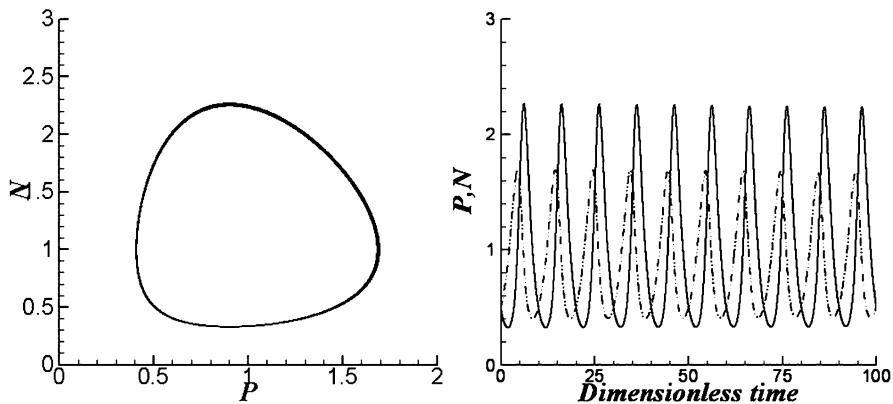
The *zero density flux conditions* are applied at the boundaries for both models. *At $x = 0.1$ (i.e., $x^* = 0, L$):*

$$\overrightarrow{j}_N = -\left(D\nabla N - \overrightarrow{V}_N N\right) = 0 \qquad (30.102)$$

$$\overrightarrow{j}_P = -\left(\nabla P - \overrightarrow{V}_P P\right) = 0 \qquad (30.103)$$

30.5.3   Results and Discussions

The same numerical approach as in the previous part is used to solve the coupling equations above (Eqs. 30.99–30.103). The calculating field is 1D medium.
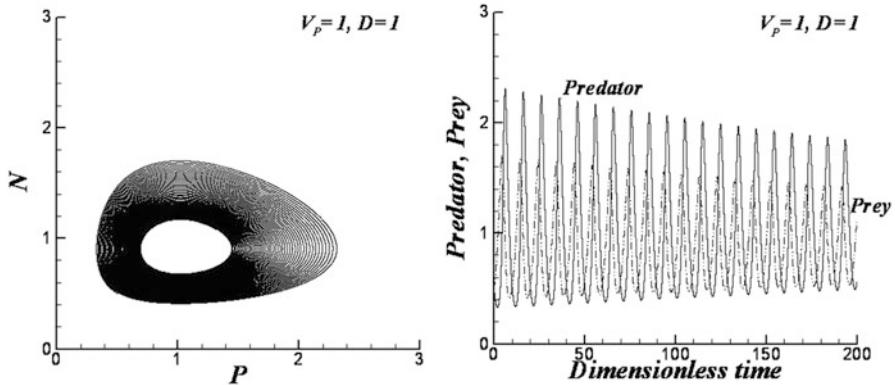
Fig. 30.24 Limit cycle (*right*) and temporal evolution (*left*) of predator and prey density in the classical LV model, positive nondimensional constants $a = 1$, $b = 0.5$, $c = 0.5$, $d = 0.9$, initial conditions of $(N-P) = (0.5; 0.5)$ [75, 88]

To check the grid independence of the solutions, the grid is varied from 21 to 61. The results presented herein are obtained with grids of 41 nodes, in conjunction with a time step, $\Delta t = 0.001$ and a convergence tolerance, $\varepsilon = 10^{-6}$.
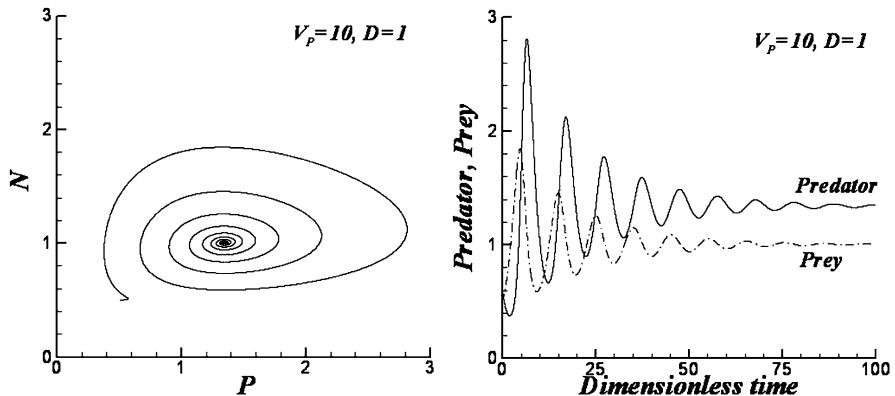
The starting point (initial conditions) for predator and prey for both models is $(P, N) = (0.5; 05)$. Fig. 30.24 shows the equilibrium point corresponding to $(0.5; 0.5)$ and limit cycle of the classical system LV without $\vec{V}_N$ and $\vec{V}_P$, and with positive nondimensional constants $a = 1$, $b = 0.5$, $c = 0.5$, and $d = 0.9$. Canale [75] and Cai and Lin [88] have actually used these dimensionless parameters at which the prey and predator populations vary periodically in time, along a path in the phase plane (N–P plane), depending only on the initial states of N and P.

Taxis Behavior Effect via Predator or Prey Motion on System

When the prey or predator is in motion $\left(\vec{V}_P \neq 0 \text{ or } \vec{V}_N \neq 0\right)$, the system is affected by a taxis behavior. Figs. 30.25 and 30.26 show the results for predator moving case $\left(\vec{V}_P \neq 0\right)$ with various values of $\vec{V}_P = 1$ and 10. With the same value of the constant parameters for classical model, Fig. 30.25 depicts a trajectory of a system predator–prey with taxis behavior $\vec{V}_P = 1$ while Fig. 30.26 for $\vec{V}_P = 10$. The motions of the considered system began all from the point (0.5; 0.5). We can observe that the system moves around the stable equilibrium state with decreasing amplitude, and finally "reaches" the equilibrium state. The degree of decreasing amplitude depends clearly on the value of $\vec{V}_P$: the stronger $\vec{V}_P$, the stronger

Fig. 30.25 Limit cycles (*right*) and temporal evolution (*left*) of predator/prey density in the system, predator in motion $V_P = 1$ and ratio of dispersion $D = 1$
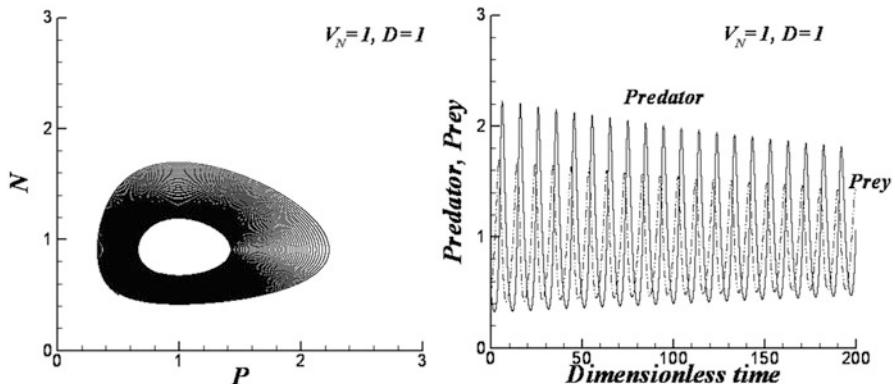
Fig. 30.26 Limit cycles (*right*) and temporal evolution (*left*) of predator and prey density, $a = 1$, $b = 0.5$, $c = 0.5$, and $d = 0.9$; predator in motion $V_P = 10$ and $D = 1$
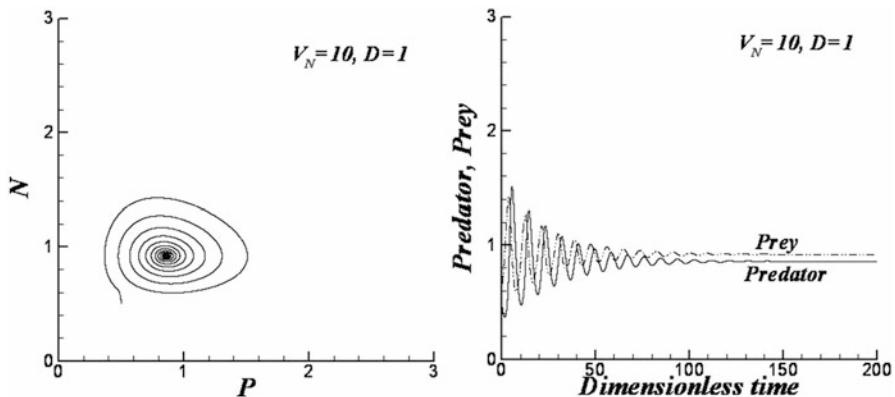
decreasing amplitude, i.e., the faster stability reaching. By comparing the system with taxis behavior and the classical LV system (i.e., comparing Figs. 30.25 and 30.26 to Fig. 30.24), we can see that *the taxis plays a dissipation role,* term used by Cai and Lin [88] *to the original system, and it changes a periodic trajectory of prey and predator populations into the final state of a single stable point.* This dissipating role depends strongly on the value of $\vec{V}_P$: the higher value of $\vec{V}_P$, the more significant dissipating effect, and the system goes then to and moves around the stability point clearer. With the presence of *taxis* term, oscillations are damped (Figs. 30.25 and 30.26, *right*). These oscillations become more damped when the speed of motion is higher.

The same characteristic of dissipating role and damped oscillations is exactly reproduced for the prey in motion $\vec{V}_N = 1$ and 10 (Figs. 30.27 and 30.28).

Fig. 30.27 Limit cycles (*right*) and temporal evolution (*left*) of predator and prey density, prey in motion $V_N = 1$ and $D = 1$
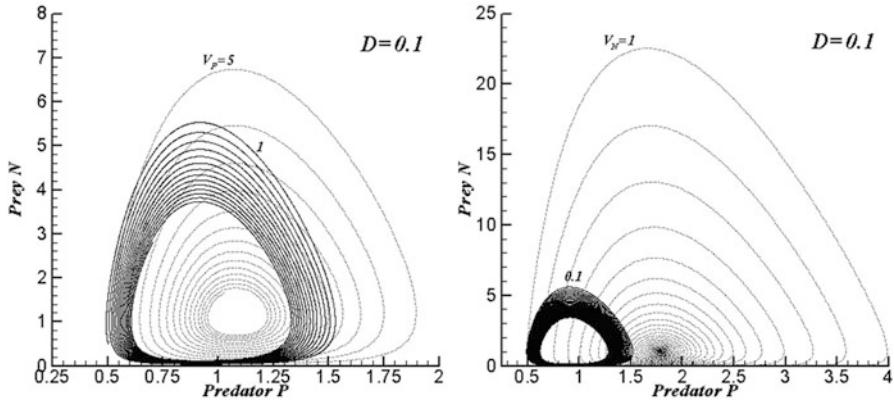
Fig. 30.28 Limit cycles (*right*) and temporal evolution (*left*) of predator and prey density, prey in motion $V_N = 10$ and $D = 1$

However, it should be noted that the amplitudes created by prey movement are quantitatively smaller than the one created by predator movement with the same value of motion speed (Figs. 30.26 and 30.28).

Threshold and Stability Points

When $\vec{V}_P$ and $\vec{V}_N$ get a non-zero value, even very small, the system has a tendency to be stabilized, oscillations are slightly damped. Since the governing system of equations is highly nonlinear (coupled system of differential and algebraic
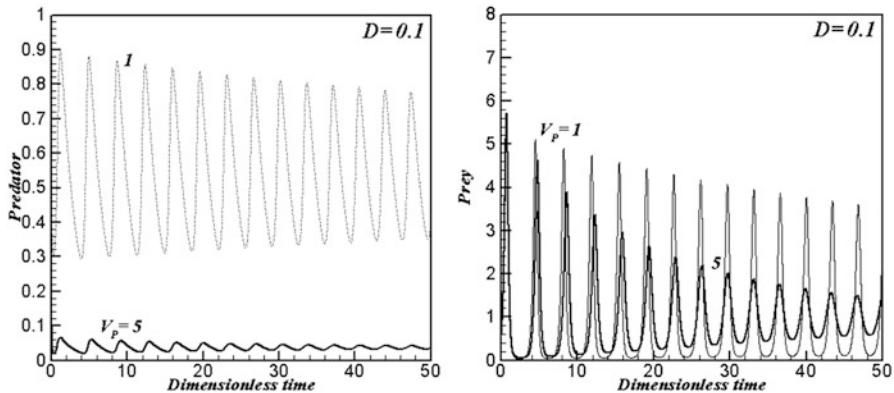
Fig. 30.29 Effects of the taxis behavior on the limit cycles with dispersion ratio $D = 0.1$, predator in motion $V_P = 1$ and 5 (*left*) prey in motion $V_N = 0.1$ and 1 (*right*)
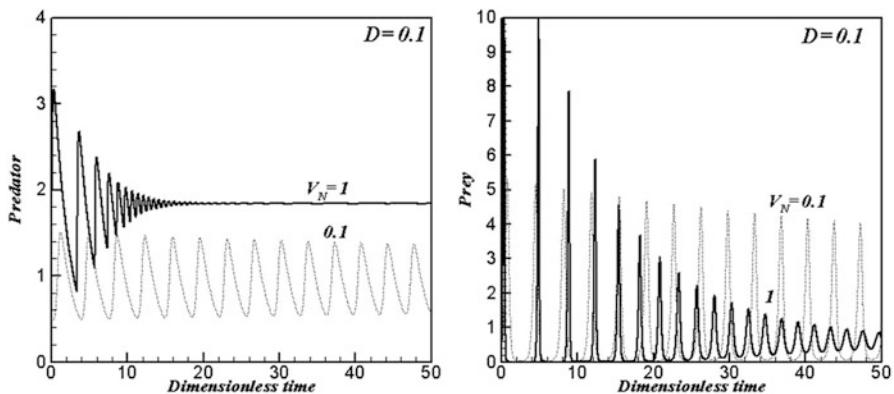
equations), analytical solutions for stability are impossible. There are some authors tried to solve analytically the stability analysis in some specific cases. However, their conclusions are still very controversial, depending on the boundary condition situations (see discussion next about boundary conditions). Simulations may be providing us more general results numerically, which satisfy both the governing system of equations and the implied boundary conditions. For example, in realizing many numerical simulations, we can show that even with very small motion of prey or predator, the system gets immediately the tendency to go to a stable situation. However, time to reach a stability point is dependent on different factors: *prey speed*, *predator speed*, *dispersion coefficient D*, etc. The system for the case in Fig. 30.26 $\left(\vec{V}_P = 10, \ D = 1 \right)$ tends to a stability point *(P; N)* = (1.282; 1.241) when the simulation time reaches the value of 12 (dimensionless time) or higher. With the same simulation process for the case in Fig. 30.28, a stability point is obtained around *(P; N)* = (0.822; 1.037). For the case of $\left(\vec{V}_N = 10, D = 0.1 \right)$ (Fig. 30.32, right, and Fig. 30.34), the stability point was *(P; N)* = (1.789; 1.02).

Coupling Effects of Diffusion and Taxis Behavior

The findings proves that, with the presence of the ratio D when the taxis speed is zero (no taxis behavior, $\vec{V}_P = \vec{V}_N = 0$), there is no particular phenomenon occurred in the system. The same conclusion is made by McLaughlin and Roughgarden [78] saying that diffusion has no influence on the classical LV model. However, when taxis are present, the diffusion will make more sense. Figure 30.29 shows the relationships of predator–prey in the case of $D = 0.1$ ($D_P = 10D_N$, i.e., predators
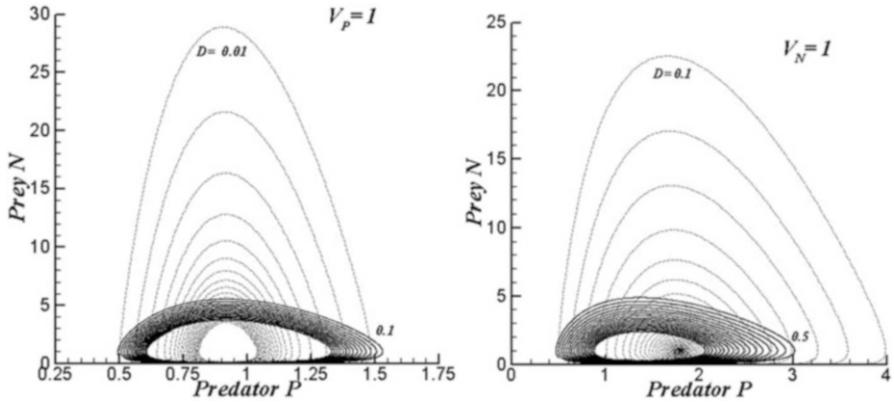
Fig. 30.30 Temporal evolution of the predator (*right*) and prey densities (*left*), predator in motion $V_P = 1$ and 5 with $D = 0.1$
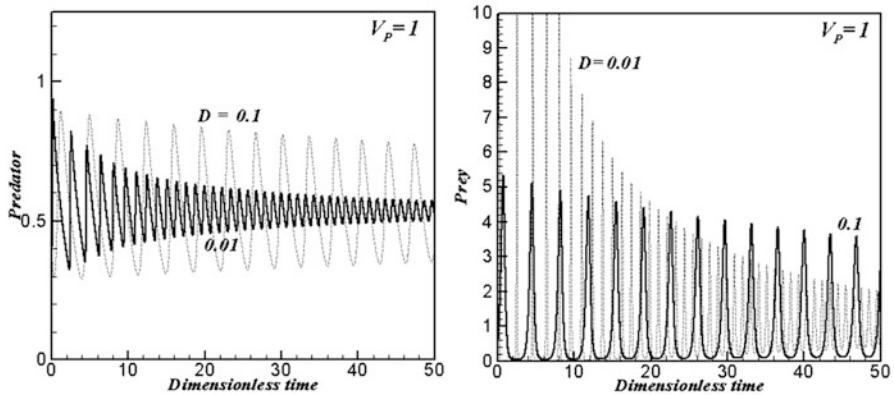
Fig. 30.31 Temporal evolution of the predator (*right*) and prey densities (*left*), prey in motion $V_N = 1$ and 5 with $D = 0.1$

diffuse ten times faster than prey) under two different speeds of predator $\vec{V}_P = 1, 5$ and of prey $\vec{V}_N = 0.1, 1$.

Figure 30.29 shows that the dissipating effect of taxis on the limit cycle form depends on the amplitude of movement velocity. The faster predator or prey moves, the quicker system goes to the equilibrium point and moves around this point with a decreasing amplitude. Damped oscillations from Figs. 30.30 and 30.31 for these cases prove that the dependence on taxis velocity is very significant. Figures 30.30 and 30.31 show that the system stability is more sensible with prey movement than predator one: i.e., for the same dispersion $D = 0.1$, the steady state of the system is already well established when the prey speed $\vec{V}_N = 1$, versus the case of predator
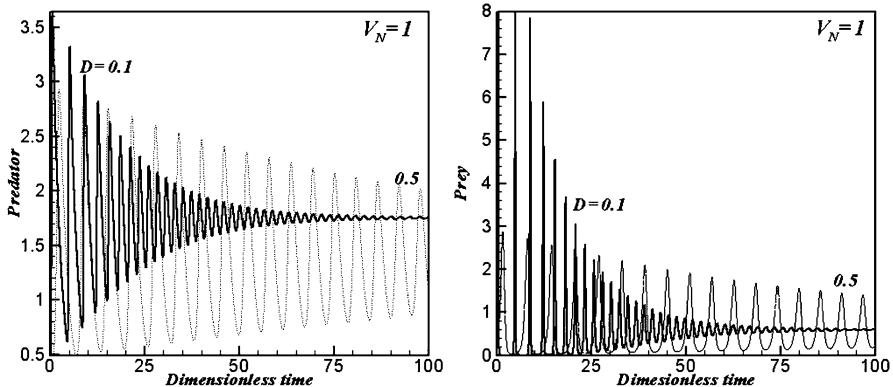
Fig. 30.32 Effects of dispersion ratio D on the limit cycles, predator in motion $V_P = 1$ (*left*) and prey in motion $V_N = 1$ (*right*)

Fig. 30.33 Temporal evolution of the predator (*right*) and prey densities (*left*), predator in motion $V_P = 1$; $D = 0.01$ and 0.1

speed $\vec{V}_P = 5$. Coupling effects of taxis and dispersion are more highlighted in Figs. 30.32, 30.33, and 30.34. When the movement of predator or prey took a value of 1 (Fig. 30.32), any variation of dispersion coefficient $D < 1$ lead to significant changes of the stability. More precisely, the smaller D (predator diffuses faster than prey), the stronger dissipating system and the more damped oscillation status for both cases of predator or prey movement. However, again, it is found that the system of prey movement is more sensitive than the system of predator movement (Figs. 30.32–30.34).

Fig. 30.34 Temporal evolution of the predator (*right*) and prey densities (*left*), *prey in motion* $V_N = 1; D = 0.5$ and 0.1

Boundary Conditions

In this study, the zero flux boundary conditions (BC), that is, the naturalized conditions for species in the enclosure are adopted. The solution given by numerical procedure satisfies evidently governing system of equations and the BC. By analytical linear analysis stability in 1D problem, McMurtrie [85] also showed that in finite and semi-finite habitats under flux and reservoir boundary conditions, the effects of dispersive and convective were significant. Precisely, according to these researchers, in the case of no convective migration, the stable equilibrium state always remains stable with dispersal under flux and reservoir boundary conditions. In the case of finite habitat, they pointed out analytically that the degree of stability increases with dispersal coefficients of the species in absence of convective migration. The effect of convective term herein (i.e., taxis term) of the species is to stabilize the equilibrium state and the degree of stability increases as taxis behavior increases: this conclusion fits well with the analytical findings of McMurtrie [85] for convective migration term (whatever boundary conditions). Another type of BC: periodic boundary conditions could also be suggested for the system, especially when the species in infinite habitat. However, this kind of conditions is out of the objective of study. We hope to address this problem in another future study. Side-conditions in the system of species interactions with diffusion is introduced by Hadeler [55] and it is concluded that a side condition, e.g., a population reservoir or a barrier, leads to standing spatial population waves. It is concluded by McMurtrie [85] and Shukla et al. [89] that convective migration stabilizes the unstable equilibrium state of the system in cases of finite and infinite habitat boundary conditions. Nevertheless, using Liapunov's direct method [90], shows contrarily that stability or instability of the equilibrium state of a two interacting species system is not affected by convective migration under reservoir, finite and infinite habitats conditions.

Our numerical results presented in this chapter have confirmed that the convective term stabilize the system with the zero flux BC. An arising question is hence: what would happen to the system with convective migration (*or advective term of taxis*) with heterogeneous BC, e.g., if we introduce the side-conditions for boundaries? This question will be mentioned and explored further in our near future studies.

30.5.4 Concluding Remarks

The model suggested in this article is a classical Lotka–Volterra system in a constant environment with the presence of diffusion (passive dispersion) and taxis behavior (active dispersion, prey or predator directed movement). In a constant environment for both models, the diffusion itself has no particular role in the prey or predator density distribution, and the homogeneous distributions were normally generated. Nevertheless, this characteristic is strongly modified with the presence of prey or predator directed movement together with diffusion. Our suggested model contains a potential damping structure, which depends strongly to the level of this active, and passive dispersion coupling. The taxis behavior coupling with dispersal can radically modify the dynamics of migration in the system of predator–prey. The models present herein two important features: (1) *taxis* is considered as a simple mechanism to stabilize the prey–predator system; (2) the coupling effect *(dispersion + taxis)* generates heterogeneous distributions of both species of prey or of predator even in the homogenous environment. These distributions might either oscillate with time and space or not. One consequence of this heterogeneity is increased viability of the predator (or prey) population, compared to the equivalent homogeneous model without taxis, and hence increased consumption. Although the similarity of our models with the model of two species interaction in convective media is well underlined, there are some subtle features due to taxis term to be kept in mind, for example boundary conditions applied on the system.

References

1. Chen F (1996) High cell density culture of microalgae in heterotrophic growth. Trends Biotechnol 14(11):421–426
2. Sheehan J, Dunahay T, Benemann J, Roessler P (1998) A look back at the U.S. Department of Energy's Aquatic Species Program: biodiesel from algae. U.S. Department of Energy's Office of Fuels Development, National Renewable Energy Laboratory, Golden, CO
3. Pulz O (2001) Photobioreactors: production systems for phototrophic microorganisms. Appl Microbiol Biotechnol 57:287–293
4. Chisti Y (2007) Biodiesel from microalgae. Biotechnol Adv 25:294–306
5. Mehlitz T, Yildiz I (2011) Dynamic simulation of microalgae growth and microclimate in large-scale closed photobioreactors. Acta Hort (ISHS) 893:413–420

6. Barbosa MJ (2003) Microalgal photobioreactors: scale-up and optimisation. Dissertation, Wageningen University
7. CIMIS (2007) http://www.cimis.water.ca.gov. Accessed 14 Aug 2008
8. Duffiie JA, Beckman WA (2006) Solar engineering of thermal processes. Wiley, Hoboken, NJ
9. Aldrich R, Bartok JW (1992) Greenhouse engineering. Northeast Regional Agricultural Engineering Service, Ithaca, NY
10. Iqbal M (1983) An introduction to solar radiation. Academic, Toronto, ON
11. Incropera F, Dewitt D, Bergman T, Lavine A (2007) Introduction to heat transfer. Wiley, Hoboken, NJ
12. Shuler M, Kargi F (2002) Bioprocess engineering: basic concepts, 2nd edn. Prentice-Hall, Upper Saddle River, NJ
13. Varicon Aqua Solutions Ltd (2004) http://www.variconaqua.com. Accessed 1 Nov 2008
14. Kindelan M (1980) A dynamic modeling of greenhouse environment. Trans ASAE 23(5):1232–1239
15. Yildiz I (1993) Simulation of greenhouse microclimates and environmental control strategies using a Rankine cycle heat pump. Dissertation, The Ohio State University, Columbus, OH
16. Takakura TK, Jordan A, Boyd LL (1971) Dynamic simulation of plant growth and environment in the greenhouse. Trans ASAE 14(5):964–971
17. Cooper PI (1969) The absoption of solar radiation in solar stills. Solar Energy 12(3)
18. Dietz AG (1963) Introduction to the utilization of solar energy. McGraw-Hill, New York
19. Vargaftik N (1975) Tables of thermophysical properties of liquids and gases. Hemisphere Publishing, New York
20. Swinbank WC (1963) Long-wave radiation from clear skies. J Roy Meteorol Soc 89:339–348
21. Arinze EA, Schoenau GJ, Besant RW (1984) A dynamic thermal performance simulation model of an energy conserving greenhouse with thermal storage. Trans ASAE 27:508–519
22. Raven J, Geider R (1988) Temperature and algal growth. New Phytol 110:441–461
23. Lehman J, Botkin D, Likens G (1975) The assumptions and rationales of a computer model of phytoplankton population dynamics. Limnol Oceanogr 20:343–364
24. Dauta A, Devaux FP (1990) Growth rate of four freshwater algae in relation to light and temperature. Hydrobiologia 207:221–226
25. Eskandari S (2008) http://www.csupomona.edu/~seskandari/physiology/physiological_calculators/Q10. Accessed 10 Oct 2008
26. Eppley R (1972) Temperature and phytoplankton growth in the sea. Fish Bull 70:1063–1085
27. Goldman J, Carpenter E (1974) A kinetic approach to the effect of temperature on algal growth. Limnol Oceanogr 19(5):756–766
28. Reynolds C (1984) The ecology of freshwater phytoplankton. Cambridge University Press, Cambridge
29. U.S. Energy Information Administration (2011) Emissions of greenhouse gases in the United States 2009. U.S. Department of Energy, Washington, DC
30. Intergovernmental Panel on Climate Change (2007) Climate change 2007: synthesis report. http://www.ipcc.ch/publications_and_data/publications_ipcc_fourth_assessment_report_synthesis_report.htm. Accessed 2 Apr 2011
31. International Energy Outlook (2010) http://www.eia.gov/oiaf/ieo/pdf/0484(2010).pdf. Accessed 2 Apr 2011
32. US Department of Energy (2011) http://www.fossil.energy.gov/programs/sequestration/index.html. Accessed 12 Mar 2011
33. Oilgae (2011) http://www.oilgae.com/algae/cult/cos/flu/flu.html. Accessed 2 Mar 2011
34. Sawyer C, McCarty P, Parkin G (2003) Chemistry for environmental engineering and science, 5th edn. McGraw Hill, New York
35. Ozkan U, Agarwal S, Marcelin G (1995) Reduction of nitrogen oxide emissions. Division of Petroleum Chemistry, Inc., American Chemical Society, Washington, DC
36. U.S. Environmental Protection Agency (2009) Clean air markets. http://www.epa.gov/airmarkets/trading/basics.html. Accessed 12 Mar 2011

37. Global Carbon Capture and Storage Institute (2010) http://www.globalccsinstitute.com/resources/publications/global-status-ccs-2010. Accessed 12 Mar 2011
38. Stern N (2007) The economics of climate change: the stern review. Cambridge University Press, Cambridge
39. Tapie P, Bernard A (1988) Microalgae production: technical and economic evaluations. Biotechnol Bioeng 32:873–885
40. Sigee D (2005) Freshwater microbiology, biodiversity and dynamic interactions of microorganisms in the aquatic environment. Wiley, Chichester
41. Sheeler P, Bianchi D (1987) Cell and molecular biology, 3rd edn. Wiley, Hoboken, NJ
42. Lee RE (1999) Phycology, 3rd edn. Cambridge University Press, Cambridge
43. South GR, Whittick A (1987) Introduction to phycology. Blackwell Scientific Publications, Oxford
44. UTEX (2011) http://web.biosci.utexas.edu/utex/default.aspx. Accessed 25 Jan 2011
45. American Public Health Association (APHA) (1998) Standard methods for the examination of water and wastewater, 20th edn. American Water Works Association, Water Environment Federation, Washington, DC
46. Richmond A (2000) Microalgal biotechnology at the turn of the millennium: a personal view. Appl Phycol 441–451
47. Huntley ME, Redalje DG (2007) CO_2 mitigation and renewable oil from photosynthetic microbes: a new appraisal. Mitig Adapt Strat Global Change 12:573–608
48. AlgaeLink (2007) http://www.algaelink.com. Accessed 2 Sept 2007
49. Spicher D (2008) Auswirkungen von Retrofit im deutschen Kraftwerkspark: implementierung im GEMS-Modell des Energiewirtschaftlichen Instituts Köln. University of Cologne, Cologne
50. Hamer WG (2007) The cost of water and water markets in Southern California, USA. In: Brebbia C and Kungolos, AG (eds) Water Resources Management IV. WIT Trans Ecol Environ 103:489–498
51. Mehlitz TH (2008) Temperature influence and heat management requirements for microalgae production in hotobioreactors. Thesis, California Polytechnic State University, San Luis Obispo, CA
52. Richardson JW, Outlaw JL, Allison M (2011) The economics of micro algae oil. AgBioForum 13(2):119–130
53. Kessler JO (1985) Hydrodynamic focusing of motile algal cells. Nature 313:218–220
54. Charlson RJ, Lovelock JE, Andreae MO, Warren SG (1987) Oceanic phytoalgal, atmospheric sulphur, cloud albedo and climate. Nature 326:655–661
55. Hadeler KP, Van der Heiden U, Rothe F (1974) Nonhomogeneous spatial distributions of population. J Math Biol 1:165–176
56. Pedley TJ, Kessler JO (1992) Hydrodynamic phenomena in suspensions of swimming micro-organisms. Annu Rev Fluid Mech 24:313–358
57. Nguyen-Quang T, Bahloul A, Nguyen TH (2005) Stability of gravitactic micro-organisms in a fluid-saturated porous medium. Int Comm J Heat Mass Transfer 32(1–2):54–63
58. Bahloul A, Nguyen-Quang T, Nguyen TH (2005) Bioconvection of gravitactic micro-organisms in a fluid layer. Int Comm J Heat Mass Transfer 32(1–2):64–71
59. Patankar SV (1980) Numerical heat transfer and fluid flow. McGrawHill, New York
60. Nguyen-Quang T, Nguyen TH, LePalec G (2008) Gravitactic bioconvection in a fluid-saturated porous medium with double diffusion. J Porous Media 11(8):751–764
61. Mamou M, Vasseur P, Hasnaoui M (2001) On numerical stability analysis of double-diffusive convection in confined enclosures. J Fluid Mech 433:209–250
62. Nguyen-Quang T (2006) Gravitactic bioconvection analysis in porous media – etude de la bioconvection gravitactique en milieux poreux. Dissertation, Ecole Polytechnique de Montréal – University of Montreal
63. Nguyen-Quang T, Nguyen TH et al (2009) Two dimensional gravitactic bioconvection in a protozoan (*Tetrahymena pyriformis*) culture. Zoolog Sci 26:54–65

64. Reading HG (1996) Sedimentary environments: processes, facies, and stratigraphy. Blackwell Publishing, Oxford
65. Winet H, Jahn TL (1971) Two-step growth curve from undisturbed cultures of *Tetrahymena pyriformis*. J Cell Physiol 78(2):277–280
66. Sauvant MP, Papin D, Piccini E (1999) Tetrahymena pyriformis, a tool for toxicological studies. A review. Chemosphere 38:1631–1669
67. Lotka AJ (1925) Elements of physical biology. Williams and Wilkins, Baltimore, NJ
68. Volterra V (1926) Variazioni e fluttuazioni del numero d'individui in specie d'animani conviventi. MemAcadLincei Roma 2:31–113
69. May RM (1981) Models for two interacting populations. Sianauer, Sunderland, MA
70. Gause G (1934) The struggle for existence. Williams and Wilkins, Baltimore, MD
71. Rosenzweig ML, MacArthur RH (1963) Graphical representation and stability conditions of predator-prey interactions. Am Nat 97:205–223
72. Bazykin AD (1998) Nonlinear dynamics of *interacting populations. World Scientific, Singapore
73. Arnold L, Horsthemke W, Stucki JW (1979) The influence of external real and white noise on the Lotka-Volterra model. Biomed J 21:451–471
74. Dimentberg MF (2002) Lotka-Volterra system in a random environment. Phys Rev E 65:036204
75. Canale RP (1969) Predator–prey relationships in a model for the activated process. Biotechnol Bioeng 11:887–907
76. Curds CR (1971) A computer-simulation study of predator-prey relationships in a single stage continuous culture system. Water Res 5:793–812
77. McLaughlin JF, Roughgarden J (1991) Pattern and stability in predator-prey communities: how diffusion in spatially variable environments affects the Lotka-Volterra model. Theor Popul Biol 40:148–172
78. McLaughlin JF, Roughgarden J (1992) Predation across spatial scales in heterogeneous environments. Theor Popul Biol 41:277–299
79. Van den Ende P (1973) Predator–prey interactions in continuous culture. Science 181:562–564
80. Ratsak CH, Kooi BW, Kooijman B (1995) Modeling the individual growth of *Tetrahymena* sp. and its population consequences. J Euk Microbiol 42:268–276
81. Berezovskaya FS, Karev GP (1999) Bifurcations of traveling waves in population taxis models. Physics – Uspekhi. Russ Acad Sci 42:917–929
82. Tyutyunov Y, Zagrebneva AD et al (2009) Microscale patchiness of the distribution of copepods (*Harpacticoida*) as a result of trophotaxis. Biophysics 54:508–514
83. Comins HN, Blatt DWE (1974) Prey–predator models in spatially heterogeneous environments. J Theor Biol 48:75–83
84. Nallaswamy R, Shukla JB (1982) Effects of convective and dispersive migration on the linear stability of a two species system with mutualistic interactions and functional response. Bull Math Biol 44:271–282
85. McMurtrie R (1978) Persistence and stability of single-species and prey–predator systems in spatially heterogeneous environments. Math Biosci 39:11–51
86. Okubo A, Levin S (2002) Diffusion and ecological problems: modern perspectives, 2nd edn. Springer, New York
87. Cai GQ, Lin YK (2004) Stochastic analysis of the Lotka-Volterra model for ecosystems. Phys Rev E 70:041910
88. Cai GQ, Lin YK (2007) Stochastic analysis of predator–prey ecosystems. Ecol Complex 4:242–249
89. Shukla VP, Shukla JB, Das PC (1981) Environmental effects on the linear stability of a three species food chain model. Math Biosci 57:35–58
90. Nallaswamy R (1983) Global stability of a system of two interacting species with convective and dispersive migration. Math Biosci 67:101–111

Chapter 31
Assessment of Sewage Sludge Potential from Municipal Wastewater Treatment Plants for Sustainable Biogas and Hydrogen Productions in Turkey

Aysegul Abusoglu, Sinan Demir, and Mehmet Kanoglu

Abstract Being utilized to produce biogas in anaerobic sludge digestion reactors in wastewater treatment facilities, sludge can also be defined as a carbon neutral biomass and is an effective resource that can be used in preventing global warming. On the other hand, hydrogen production from sludge is a highly noteworthy topic due to hydrogen's quality of being the clean energy carrier of tomorrow and its production can be achieved through the fermentation of sludge. In this chapter, biogas and hydrogen production potentials of the municipal wastewater treatment facilities in Turkey are evaluated on the basis of sludge generation, and the impact of the developed hydrogen production models on global warming is set forth.

Keywords Hydrogen production • Sewage sludge • Municipal wastewater treatment • Biohydrogen • Electrolysis process • Dark fermentation • Global warming • Municipal wastewater treatment plant • Sewage sludge potential • Biogas • Turkey • Anaerobic sludge digestion • Biomass • Hydrogen • Energy carrier • Fermentation

Nomenclature

$Cost_{H_2}$	Cost of hydrogen, \$
$C_{electricity}$	Unit cost of electricity, \$/kW h
$E_{\Delta H}$	Equilibrium voltage, V
E_{cell}	Cell voltage, V
ΔG	Gibbs free energy, kJ/kmol
$\Delta G_{elect, H_2O}$	Gibbs free energy of the water, kJ/kmol

A. Abusoglu (✉) • S. Demir • M. Kanoglu
Department of Mechanical Engineering, University of Gaziantep, 27310 Gaziantep, Turkey
e-mail: ayabusoglu@gantep.edu.tr; sinandemir@gantep.edu.tr; kanoglu@gantep.edu.tr

$\Delta G_{elect,H_2S}$	Gibbs free energy of the hydrogen sulfide, kJ/kmol
ΔH	Enthalpy change, kJ/kg
M_{H_2}	Molar mass of hydrogen, kg/kmol
w_{act}	Actual electricity work, kJ/kg
w_{min}	Minimum electricity work, kJ/kg
$\dot{W}$	Work rate, kW h

Greek Symbols

η	Thermal efficiency
Δ	Change of variables

Acronyms

WWTP	Wastewater treatment plant
COD	Chemical oxygen demand

31.1 Introduction

Sewage sludge can be obtained after the treatment of municipal sewage by wastewater treatment plants (WWTPs). Like other urban wastes, sewage sludge may contain different kinds of pathogens that are infectious for different species of animals and plants as well as for humans. The origin and nature of organic wastes, such as different types of sludge, always causes a hygienic risk in storage, collection, processing, handling, and utilization. Beside this, sludge can be seen as alternative renewable energy source because of its energy production potential. There are many sludge management options in terms of production of energy (heat, electricity, or biofuel) and these options seem to be some of the key treatment steps. The most important options are anaerobic digestion, co-digestion, incineration in combination with energy recovery, co-incineration in coal-fired power plants, co-incineration in combination with organic waste focused on energy recovery, use as an energy source in the production of cement or building materials, pyrolysis, gasification, supercritical (wet) oxidation, hydrolysis at high temperature, production of hydrogen, acetone, butanol, or ethanol, and direct generation of electrical energy by means of specific microorganisms [1].

Many researchers have focused on the anaerobic digestion process due to its importance and utility in WWTPs [2–8]. Anaerobic digestion of sewage sludge is an established technology for environmental protection through the wastewater treatment, and it takes place with the absence of oxygen. The end product is biogas, a mixture of methane, carbon dioxide, and hydrogen sulfur; a useful renewable energy source [9]. This biogas can be used as a fuel for power production in WWTPs.
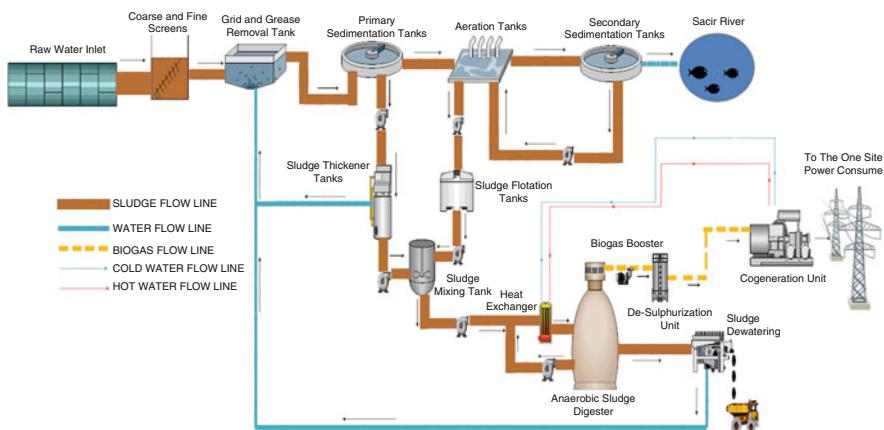
Hydrogen is considered as a clean and high-quality energy carrier, since its combustion only produces water as a by-product. Electricity produced from the WWTP's cogeneration facilities can be used as energy input for the installed water electrolysis unit, which then produces hydrogen. This hydrogen production method in which biogas is used as a renewable energy source is a completely eco-friendly and green process. The importance of electricity obtained from renewable energy sources increases in the production of hydrogen [10]. In the literature some scientists have focused on fermentative hydrogen production from sewage sludge in WWTPs [11–14]. In part, this is because fermentative hydrogen production is more cost-effective, since sludge is a free by-product. Also, the electricity demand for hydrogen production via fermentation is much lower than other typical electrolysis processes.

This chapter presents a comprehensive study on the sludge, biogas, electricity, and hydrogen production capacities of the municipal WWTPs for the seven regions of Turkey. First, an existing municipal WWTP located in the city of Gaziantep, Turkey, is defined. Then, three hydrogen production models, which consist of high temperature steam, hydrogen sulfur electrolysis, and dark fermentation process, are improved. Energy analysis is performed through these models, using the actual operational data of the plant. The environmental impact of the developed hydrogen production models on global warming is assessed using three life cycle impact categories: Global warming, acidification, and eutrophication. Last, by considering the case study given, the sludge, biogas, and hydrogen production potentials of Turkey are estimated.

31.2   System Description

Sewage treatment, or domestic wastewater treatment, is the process of removing contaminants, both effluents and domestic, from wastewater and household sewage. It includes physical, chemical, and biological processes to remove all hazardous contaminants. The flow schematic of an existing WWTP is given in Fig. 31.1.

A WWTP is composed of a combination of unit operations and unit processes designed to reduce certain constituents of wastewater to an acceptable level. Municipal WWTPs are often divided into primary, secondary, and tertiary subsystems. The purpose of *primary treatment* is to remove solid materials from the incoming wastewater. *Secondary treatment* usually consists of biological conversion of dissolved and colloidal organics into a biomass that can be subsequently removed by sedimentation. Secondary sludges are usually combined with primary sludge for further treatment by anaerobic biological processes. Sometimes, primary and secondary treatment can be accomplished together. In most cases, secondary treatment of municipal wastewater is sufficient to meet effluent standards. In some instances, however, additional treatment may be required. *Tertiary treatment* most often involves further removal of suspended solids and/or the removal of nutrients [15].

Fig. 31.1 Schematic of an existing municipal WWTP

The most important process in a WWTP in terms of energy recovery is the sludge stabilization process, which includes a variety of processes, some biological, some chemical, and some physical, which may be applied to favorably alter the physical and chemical characteristics of sludge to improve its dewaterability. Anaerobic digestion of sludge involves the biological breakdown of a portion of the solids. The dewaterability of sludge is primarily related to the particle size distribution, with poor dewatering being associated with a high percentage of small particles. The destruction of these particles occurs in a two-staged process, in which the complex organics in waste solids are first broken down to simpler compounds, notably the short-chain volatile fatty acids [16]. These intermediates are then further broken down, by a separate group of bacteria, to methane, carbon dioxide (biogas), and some trace gases of which hydrogen sulfide is the most evident. The hydrogen sulfide (H_2S) is a real subject of concern because of its odors, corrosiveness, and hazardous properties. Methane (CH_4) is a fuel, and when burned produces very low emissions of pollutants. Its flue gases contain 2 mol of H_2O for each mol of CO_2. This is the best ratio among the industrial fuels from the global warming standpoint. This tradeoff is much better than discharging methane directly into the atmosphere. Biogas which is produced in WWTPs consists of 50–60 % of CH_4, 35–40 % of CO_2, 1–3 % H_2S, and trace amounts of other gases.

GASKI WWTP treats nearly 215,000 m^3 per day of domestic wastewater. The sludge in the reactors are mechanically mixed to ensure better contact between the organics and the microorganisms. The units are also heated to increase the metabolic rate of the microorganisms, thus speeding up the digestion process. The optimum heating temperature in reactors is approximately 35 °C. The activated sludge loading rate to the reactors is 800–1,200 ton per day with a density of 35–55 g/l. The total volume of reactors is 32,000 m^3. At the end of the anaerobic-activated sludge digestion process, 10,000–18,000 m^3 biogas is generated daily which means approximately 60 % of the organic fraction is converted to gaseous

Table 31.1 The produced biogas composition in GASKI WWTP

Content	Volumetric values (%)
CH_4	60
CO_2	37
N_2	1.5
H_2	0.4
O_2	0.6
H_2S (2,500–3,000 ppm)	2.5–3.0

Table 31.2 Exhaust gas composition of biogas engine for 1 Nm^3 biogas combustion

Content	Values
CO_2	207 g
NO_x	400 mg
CO	500 mg
VOC	400 mg
SO_2	9.4 mg

end products after a 30 days period. Biogas produced through anaerobic sludge digestion process is first transferred to desulphurization ($DeSO_x$) unit for lowering sulfur content to the acceptable legal values. It is then sent to a gas engine for electricity production. Content of the obtained biogas is presented in Table 31.1. In the cogeneration unit of GASKI WWTP, two Deutz brand biogas-fed engines are used. Total electricity and heat generation of the cogeneration unit are 1,000 kW_e and 456.1 kW_{th}, respectively. Components of the exhaust gas as a consequence of the combustion of biogas in engine are presented in Table 31.2.

31.3   Hydrogen Production Models

Three hydrogen production models are developed for the GASKI WWTP. In the Model-1 (see Fig. 31.2), a high temperature steam electrolysis process is considered for hydrogen. In this model, the work demand for the electrolysis system is provided by the biogas engine powered cogeneration system of GASKI WWTP. The biogas used as fuel in this cogeneration system is produced by a totally renewable process which takes place in the anaerobic digestion reactors of the WWTP. The biogas consumed for 1,000 kW h electricity generation in the existing cogeneration system is nearly 61 % (0.129 kg/s) of the total biogas produced in the anaerobic digesters, which is 0.212 kg/s. A small amount of the remaining part (0.083 kg/s) of the biogas can be used to obtain high temperature steam production in the boiler, which is 0.025 kg/s. Before the boiling and electrolysis processes, the water must be purified through a clean water treatment system. The mass flow rate of the water entering the electrolysis process is taken as 0.09 kg/s. The temperature and pressure of the steam produced in the boiler are 800 °C and 5 bar, respectively.

In the Model-2 (see Fig. 31.3), a hydrogen sulfide (H_2S) electrolysis process is developed for hydrogen production. Biogas produced by the anaerobic digestion
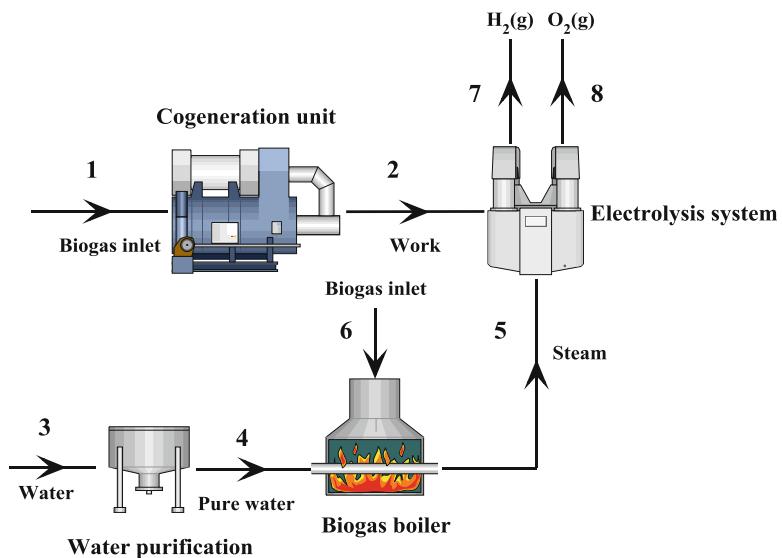
Fig. 31.2 Hydrogen production Model-1
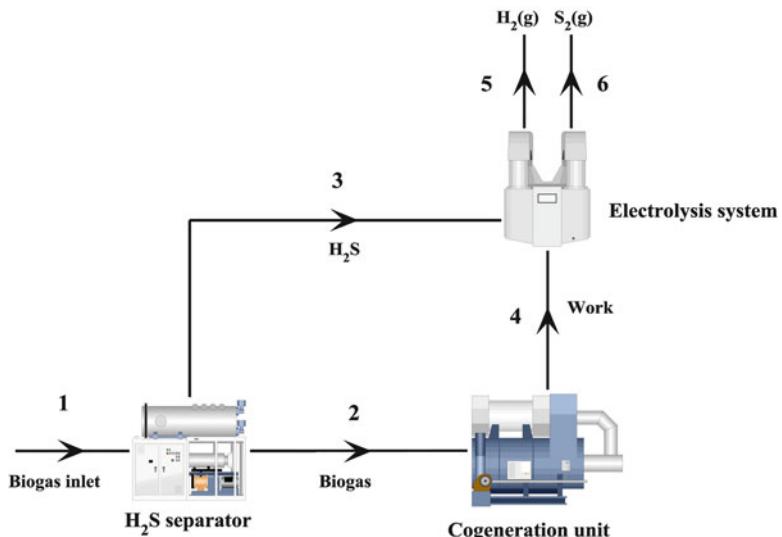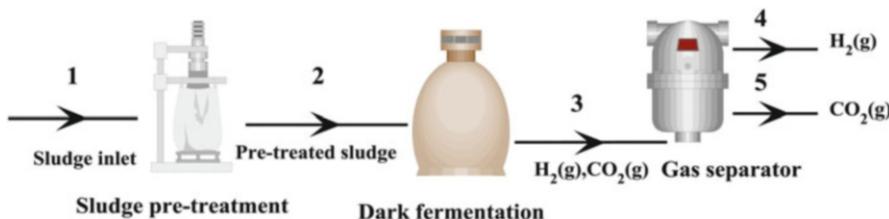
Fig. 31.3 Hydrogen production Model-2

of sludge is mostly methane (up to 60 %). The remaining part is mainly acid gases, primarily carbon dioxide, with hydrogen sulfide causing the most problems. When biogas is directly burned as a fuel, engines tend to wear out quickly. To prevent this, H_2S in the biogas is eliminated in a desulfurization unit ($DeSO_x$)

Fig. 31.4 Hydrogen production Model-3

before the combustion process. Although its presence in the biogas may cause lots of environmental problems, the energy demand for the electrolysis process of H_2S is lower about 3.25 times than that of the water. In the Model-2, biogas produced by the anaerobic digestion of sludge in the WWTP is first passed through a hydrogen sulfide separator and H_2S content of it is collected. Biogas with H_2S free enters the cogeneration unit with the same mass flow rate as in the case of Model-1 and 1,000 kWh electricity is produced. The mass flow rate of H_2S entering the electrolysis process is 0.0021 kg/s, which can be found theoretically by taking the H_2S content of the biogas produced. In this model, due to the small amount of H_2S collected, the work demand of the electrolysis process is in small quantities (5.83 kW h for GASKI WWTP case).

In the Model-3 (see Fig. 31.4), a fermentative hydrogen production (biohydrogen) model is considered. In this process, digested sewage sludge can be used directly for hydrogen production in the fermentative conditions. In contrast to anaerobic methane digestion in which the intermediate product hydrogen is converted to methane, the final product of the dark fermentation process is hydrogen. An important distinction with anaerobic methane digestion is that in hydrogen fermentations only hydrogen producing microorganisms are active. Another essential difference is that complex organic compounds in the feedstock are converted to simple molecules, not during the digestion process, but rather in a separate process preceding the fermentation [13]. This pretreatment process is performed by means of physical or chemical methods. The resulting organic compounds are converted into hydrogen, acetic acid, and carbon dioxide. In the Model-3, pretreatment process is applied to the activated sludge to increase hydrogen production. The mass flow rate of the sludge before the digestion and fermentation processes in the WWTP is 12.06 kg/s. Since hydrogen produced through dark fermentation is only 60 % by volume, it must be purified by using a gas separator.

31.4 Energy and Economic Analyses of Hydrogen Production Models

The minimum work needed for 1 kg hydrogen production by the water and hydrogen sulfide electrolysis processes can be calculated by following equations:

$$w_{\min,\,elect} = \frac{\Delta G_{elect,H_2O}}{M_{H_2}} \; (kJ/kg) \tag{31.1}$$

$$w_{\min,\,elect} = \frac{\Delta G_{elect,H_2S}}{M_{H_2}} \; (kJ/kg) \tag{31.2}$$

where $\Delta G_{elect,H_2O}$ and $\Delta G_{elect,H_2S}$ are the Gibbs free energy (kJ/kmol) of the water and hydrogen sulfide, respectively and M_{H_2} is the molar mass of hydrogen (kg/kmol). Thus, the actual work demand can be calculated as

$$w_{act,\,elect} = \frac{w_{\min,\,elect}}{\eta_{th}} \; (kJ/kg) \tag{31.3}$$

Thermal efficiency of the electrolysis unit can be calculated as [17]

$$\eta_{th} = \frac{\Delta H}{\Delta G + Losses} = \frac{E_{\Delta H}}{E_{cell}} \tag{31.4}$$

where ΔH is the enthalpy change of water decomposition reaction as energy input. $E_{\Delta H}$ is the equilibrium voltage and E_{cell} is the cell voltage which is always between 1.8 and 2.0 V at the current density of 1,000–300 A m^{-2} in an alkaline water electrolysis [18]. For the alkaline electrolysis Eq. (31.3) can be rewritten in a simple form as,

$$\eta_{th} = \frac{1.48}{E_{cell}} \tag{31.5}$$

The cost of hydrogen can be calculated with the following equation:

$$Cos\,t_{H_2} = C_{electricity} \times \dot{W}_{demand} \tag{31.6}$$

where $C_{electricity}$ is the unit cost of electricity produced by cogeneration unit in WWTP and it is taken as 0.0893 \$/kW h, and $\dot{W}_{demand}$ is the electricity needed for the hydrogen production in the developed models as kW h/kg H_2.

31.5 Results and Discussion

For the Model-1, the value of Gibbs free energy of steam is 18,519 kJ/kmol at 800 °C. The heat requirement of the boiling process for steam production is calculated to be 363 kW. Hydrogen produced by Model-1 is calculated as 868.6 kg/day and the actual electricity cost of hydrogen production is found to be 2.47 \$/kg H_2. By using Eq. (31.3), the thermal efficiency of electrolysis process for Model-1 is found as 94 %. The thermodynamic data and the results of the energy

Table 31.3 Thermodynamic data and results of the energy and economic analyses of Model-1 with respect to the state points in Fig. 31.2.

State no.	Property	Value
1	Biogas inlet	0.129 (kg/s)
2	Work	1,000 kW h
3	Water	0.09 (kg/s) @25 °C and 1 bar
4	Pure water	0.09 (kg/s) @25 °C and 1 bar
5	Steam	0.09 (kg/s) @800 °C and 5 bar
6	Biogas	0.025 (kg/s)
7	Hydrogen gas	868.6 kg/day
8	Oxygen gas	6,948.8 kg/day

Type of electrolysis: High temperature electrolysis
Efficiency of electrolysis: 94 %
Minimum power consumption of electrolysis: 93,511.4 kJ/kg (25.98 kW h/kg H_2)
Actual power consumption of electrolysis: 99,480.2 kJ/kg (27.63 kW h/kg H_2)
Cost of electricity: 0.0893 \$/kW h
Minimum electricity cost of hydrogen: 2.32 \$/kg H_2
Actual electricity cost of hydrogen: 2.47 \$/kg H_2

and economic analyses for the Model-1 according to the nomenclature shown in Fig. 31.2 is given in Table 31.3.

For the Model-2, the value of Gibbs free energy of the hydrogen sulfide is 73,289 kJ/kmol at 25 °C, while Gibbs free energy of water is 237,180 kJ/kmol at the same temperature for the comparison. As stated previously, the energy demand for the electrolysis process of H_2S is about 3.25 times lower than that of the water at the present temperature. Biogas produced in WWTP includes nearly 1 % of H_2S and assuming that all of the hydrogen sulfide is collected through by separator, the mass flow rate of H_2S for the electrolysis process is found to be 7.63 kg/day. Hydrogen produced by Model-2 is calculated as 10.8 kg/day and the actual electricity cost of hydrogen production is found to be 1.16 \$/kg H_2. By using Eq. (31.4), the thermal efficiency of alkaline electrolysis process for Model-2 is found as 78 %. If hydrogen sulfide presence in the biogas was higher than that of the present case, it would be possible to produce 79.23 kg of hydrogen in terms of 1,000 kW h work input to the electrolysis system. The thermodynamic data and the results of the energy and economic analyses for the Model-2 according to the nomenclature shown in Fig. 31.3 is given in Table 31.4.

The mass flow rate of the sludge on a dry mass basis for GASKI WWTP is 2,170.8 kg/h. Following Wang et al. [13], the hydrogen yield of sewage sludge with a dark fermentation process can be up to 0.9 mmol-H_2/g on the dry mass basis. Then, the hydrogen production in GASKI WWTP will be 3.94 kg/h. Applying a pretreatment process such like acidification before the dark fermentation process, may increase hydrogen production up to 1.5–2.1 mmol-H_2/g on the chemical oxygen demand (COD) basis. Since the COD value of the sludge for GASKI WWTP is 65.28 g-COD/l, hydrogen production will be increased to 11.9 kg/h by incorporating a pretreatment to the dark fermentation processes. Hydrogen produced by Model-3 is calculated to be 171.4 kg/day with 100 % of H_2 by volume and

Table 31.4 Thermodynamic data and results of the energy and economic analyses of Model-2 with respect to the state points in Fig. 31.3.

State no.	Property	Value
1	Biogas inlet	0.212 (kg/s)
2	Biogas	0.129 (kg/s)
3	H_2S	0.0021 (kg/s)
4	Work	5.83 kW h
5	Hydrogen gas	10.8 kg/day
6	Sulfur gas	170.6 kg/day

Type of electrolysis: Alkaline
Efficiency of electrolysis: 78 %
Minimum power consumption of electrolysis: 36,353.7 kJ/kg (10.1 kW h/kg H_2)
Actual power consumption of electrolysis: 46,607.3 kJ/kg (12.95 kW h/kg H_2)
Cost of electricity: 0.0893 $/kW h
Minimum electricity cost of hydrogen: 0.90 $/kg H_2
Actual electricity cost of hydrogen: 1.16 $/kg H_2

Table 31.5 Thermodynamic data and results of the energy and economic analyses of Model-3 with respect to the state points in Fig. 31.4.

State no.	Property	Value
1	Sludge	12.06 (kg/s) @25 °C
2	Pre-treated sludge	12.06 (kg/s)
3	Hydrogen gas	285.6 kg/day with 60 % of H_2 by volume
4	Hydrogen gas	171.4 kg/day with 100 % of H_2 by volume
5	Carbon dioxide gas	114.2 kg/day

Type of hydrogen production: Dark fermentation + pretreatment
Power consumption of system: 176.4 kW h (24.8 kW h/kg H_2)
Cost of electricity: 0.0893 $/kW h
Electricity cost of hydrogen: 2.2 $/kg H_2
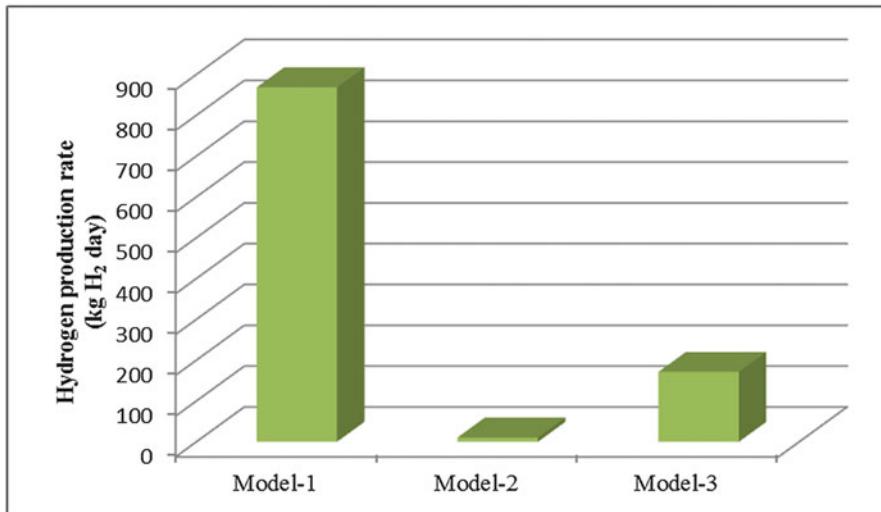
the actual electricity cost of hydrogen production is found to be 2.2 $/kg H_2. The thermodynamic data, and the results of the energy and economic analyses for the Model-3 according to the nomenclature shown in Fig. 31.4 is given in Table 31.5.

In Fig. 31.5 the hydrogen production rates of the models developed for an existing municipal WWTP are compared to each other. As shown, Model-1 has the highest maximum hydrogen production rate. Among the three models developed, Model-2 has the lowest hydrogen production rate. In Model-1, all electricity produced by biogas powered cogeneration system of WWTP is consumed in the electrolysis process for hydrogen production. For Model-2, only a small amount of electricity produced by the cogeneration system is consumed. This is due to the inadequate amount of H_2S present in the biogas produced by the anaerobic digestion system. Although its biggest disadvantage is the low hydrogen production rate from sewage sludge, the performance of a dark fermentation process can be improved by a pretreatment unit. Thus, Model-3 is clearly the most appropriate option for a municipal WWTP for two important reasons.
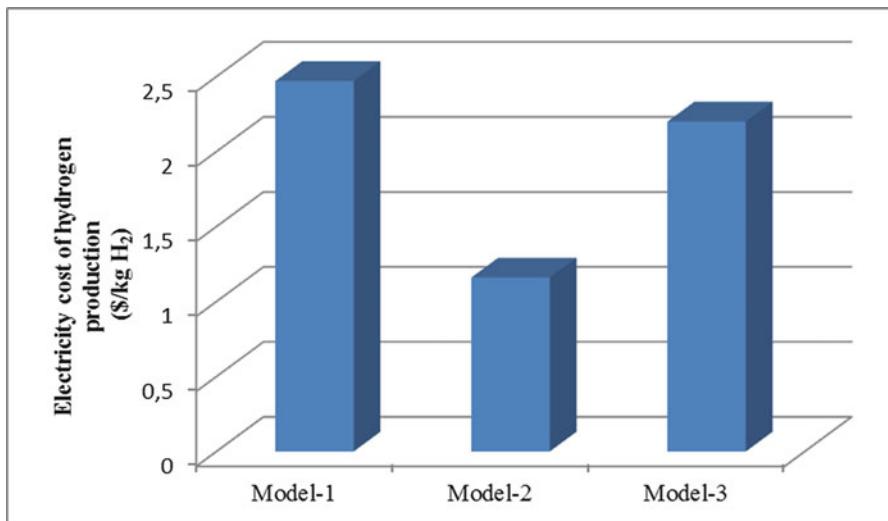
Fig. 31.5 Comparison of hydrogen production rates of the models developed for a municipal WWTP

Firstly, the sludge utilized through Model-3 is digested sludge and is the by-product of wastewater treatment application. This sludge, before the dark fermentation process for hydrogen production, is first used to produce biogas in the anaerobic digestion process. Thus, the biogas output is used for the power production, which provides the energy demand of Model-3. Note that the power demand of Model-3 is only one-fourth of the total power produced by the cogeneration system (176.4 kW h).

Secondly, after biogas production in the anaerobic digestion system, sludge is considered as a waste of the treatment facility which must be eliminated. In Model-3, this elimination process is replaced by a dark fermentation process with pretreatment for hydrogen production. The benefit of this is the digested sludge can be used for the production of hydrogen. Thus, Model-3 is the most sustainable model in terms of material resource, and power demand through processes.

According to the economic analysis on the electricity cost for the models developed, Model-2 has the lowest hydrogen production cost (see Table 31.4). This is due to the low hydrogen production rate which is caused by the low amounts of hydrogen sulfide present in the biogas. Model-3 presents the second costly process, due to the low energy demand of the dark fermentation process. However, considering the remarkable economical and environmental advantages of the direct usage of sludge in both for biogas and hydrogen production, Model-3 can be considered the most cost-effective model for the municipal WWTPs. Model-1 has the highest hydrogen production cost (see Table 31.3) due to the highest hydrogen-production rate and power demand among the models developed. In Fig. 31.6, the comparison of the hydrogen production costs for the models developed is presented.

Fig. 31.6 Comparison of hydrogen production costs of the models developed for a municipal WWTP

Table 31.6 Comparison of impact assessments for the models

Impact assessment	Model-1	Model-2	Model-3
Global warming (kg/s CO$_2$-eq)	0.324	0.00189	0.0585
Acidification (kg/s SO$_2$-eq)	0.000491	2.86×10^{-6}	8.66×10^{-5}
Eutrophication (kg/s NO$_x$-eq)	0.000124	7.23×10^{-7}	2.19×10^{-5}

In a life cycle assessment carried out by taking the exhaust emission of the gas engine cogeneration unit as basis, environmental impacts of the models developed for hydrogen production are calculated with the CMLCA [22] software by taking three different impact categories into consideration. Obtained results are presented in Table 31.6.

According to the impact assessments presented in Table 31.6, the environmental impact of Model-1 is higher than the other models in all three impact categories. The most important reason for this is the fact that the whole electricity generated by the biogas engine powered cogeneration system is used by the Model-1. Since the electricity requirements of Model- 2 and -3 are quite lower than that of Model-1, also the allocation of the exhaust emission due to the electricity drawn from the cogeneration system turns out to be low and therefore causes the environmental impacts of Model-1 and -2 to decrease. As it can be clearly seen from Table 31.6, environmental impacts of the developed models are directly proportional to the electricity required for hydrogen production.

31.6   Sludge, Biogas, and Hydrogen Production Potentials of WWTPs in Turkey

The first wastewater treatment plant in Turkey with a capacity of 751,000 m^3/year was constructed in 1982. By the end of 1994, the total number of WWTPs with a capacity of 602 Mm^3/year was 45. Most of them (41 WWTPs) were biological treatment plants, which have 37.35 % of total treated water amount. Between 1994 and 2010, the number of constructed plants drastically increased, reaching 326. The total capacity of the WWTPs was 5,293 Mm^3/year by the end of 2010, and the amount of wastewater treated by the treatment plants was about 2,719 Mm^3/year. The majority of them have primary and secondary treatment units (91 % of total capacity), while a few have advanced treatment units [19, 20]. In Turkey, 52 of its 81 provinces have urban WWTPs and approximately 73 % of the country's population is being served (see Table 31.7).

Sewage sludge is regarded as the residue produced by the WWTPs. Liquids are being discharged to aqueous environments, while solids are removed for further treatment and final disposal [21]. Currently, the annual sewage sludge production of Turkey is over 1 million ton. The produced municipal sludges are commonly stored in municipal solid waste landfill areas, and spread to the land for agricultural usage. Sludges produced in municipal or industrial WWTPs have been processed using some common treatment processes globally, including gravity or flotation thickening, anaerobic stabilization, and dewatering [19].

Figure 31.7 illustrates the amount of treated wastewater, sludge production, biogas, and electricity production potential of the 326 WWTPs currently in use in the seven geographic regions of Turkey. The total amount of wastewater treated by WWTPs in Turkey is given according to the 2010 data of TSI [20]. Sludge production of each WWTP can be calculated by taking their treated wastewater capacity into consideration, as well as biogas production, and the corresponding electricity production. For these calculations, the actual data of the existing WWTP presented is taken into account as a starting point. As can be seen from Fig. 31.7, the annual biogas production potential of all existing WWTPs of Turkey is slightly above 200 million m^3. Moreover, biogas production potential may be increased by using newly developed sludge stabilization techniques before the anaerobic digestion of sludge. If the estimated biogas production potential was totally used for power production, the annual electricity production from sewage sludge-based biogas in Turkey would be over 530 GWh, which can nearly meet 1 % of the total annual energy demand of the country. Considering the digested sludge output as a secondary valuable fuel source for incineration facilities for further power production, this percentage would be increased to 2 %. This reveals the fact that WWTPs are unmistakably remarkable renewable energy sources. Besides, energy recovery from a sustainable waste source is not influenced by international prices or political fluctuations, which is important when considering Turkey's dependency on foreign sources of energy.

Table 31.7 The main wastewater indicators of municipalities in Turkey between 2001 and 2010 [20]

		2001	2002	2003	2004	2006	2008	2010
Number of municipalities served by sewerage system		2,003	2,115	2,195	2,226	2,321	2,421	2,235
Rate of population served by sewerage system in total population (%)		63	65	67	68	72	73	73
Amount of wastewater discharged from municipal sewerage to receiving bodies (million m³/year)		2,301	2,498	2,861	2,923	3,367	3,261	3,582
Number of wastewater treatment plants	Physical	25	28	31	35	26	29	39
	Biological	98	114	121	133	135	158	199
	Advanced	3	3	4	4	23	32	53
	Natural	–	–	–	–	–	17	35
	Total	126	145	156	172	184	236	326
Total capacity of wastewater treatment plants (million m³/year)	Physical	770	771	1,046	1,385	1,329	1,538	1,839
	Biological	1,250	1,320	1,484	1,751	1,511	1,595	1,733
	Advanced	267	267	275	275	808	1,001	1,709
	Natural	–	–	–	–	–	10	12
	Total	2,288	2,359	2,805	3,410	3,648	4,143	5,293
Amount of wastewater treated by wastewater treatment plants (million m³/year)	Physical	325	345	482	599	714	736	751
	Biological	663	746	877	1,071	927	861	931
	Advanced	206	222	227	231	500	649	1,032
	Natural	–	–	–	–	–	6	5
	Total	1,194	1,312	1,587	1,901	2,140	2,252	2,719
Number of municipalities served by wastewater treatment plants in total population (%)		27	28	30	36	42	46	52
Amount of wastewater discharged per capita in municipalities (liters/capita-day)		147	154	173	174	181	173	182

Hydrogen does not have any significance as an energy carrier in today's energy systems. However, hydrogen is an indisputable clean energy source for the future, and definitely merits to be taken into consideration. Renewable energy sources are the most desired sources for hydrogen production due to their diversity, abundance, and potential for sustainability. In this chapter, three models are presented for the hydrogen production assessment of an existing WWTP. Each model developed uses the electricity produced by a biogas engine powered cogeneration plant.

Assuming that the actual data provided by GASKI WWTP and the theoretical calculations for hydrogen production, the models are more or less similar to the rest of the municipal WWTPs in Turkey. Hydrogen production potentials of WWTPs in the seven regions of Turkey are calculated, and results are presented in Table 31.8. Marmara region having the biggest capacity in terms of sludge

Fig. 31.7 Sludge, biogas, and electricity production potential of WWTPs in Turkey

output, biogas, and power productions. According to the three models considered, it also has the highest potential for hydrogen production. Since the hydrogen production rate, by the high temperature electrolysis process of water developed for Model-1 is the highest, it seems to be the most promising method for future assessments. Eastern Anatolia region has the lowest potential for hydrogen production rate, due to its smallest wastewater treatment plant capacity. From the assessment of seven regions of Turkey, Model-1 shows the highest potential to be evaluated for hydrogen production in municipal WWTPs. Also Model-3 has the most renewable and sustainable characteristics. Considering the three models developed, daily hydrogen production potential of all municipal WWTPs in Turkey would be 52,487 kg for Model-1, 464 kg for Model-2, and 1,231 kg for Model-3.

Table 31.8 Hydrogen production potential of WWTPs in the seven regions of Turkey

Regions	Model-1		Model-2		Model-3	
	Actual hydrogen production rate (kg/day)	Actual electricity consumption (kW h)	Actual hydrogen production rate (kg/day)	Actual electricity consumption (kW h)	Actual hydrogen production rate (kg/day)	Actual electricity consumption (kW h)
Black Sea Region	1,881.7	2,166.3	28.52	15.39	930.34	961.04
Central Anatolia Region	8,168.5	9,404.02	123.79	66.80	4,038.67	4,171.95
Marmara Region	23,475.3	27,025.93	355.76	191.96	11,606.62	11,989.64
Aegean Region	8,153.6	9,386.84	123.57	66.68	4,031.30	4,164.33
Mediterranean Region	6,386.6	7,352.55	96.79	52.23	3,157.65	3,261.85
Southeastern Anatolia Region	2,777.7	3,197.79	42.10	22.72	1,373.34	1,418.66
Eastern Anatolia Region	1,643.6	1,892.25	24.91	13.44	812.65	839.47

31.7 Conclusion

In this chapter, we present the assessment of sewage sludge potential from municipal WWTPs for sustainable biogas and hydrogen productions in Turkey. Based on the actual operational data of an existing municipal WWTP in the city of Gaziantep, a general assessment is performed on the potential of biogas and electricity production and also the impact of the developed hydrogen production models on global warming. Annual biogas production potential of all the existing WWTPs of Turkey is slightly above 200 million m^3. If this estimate of biogas production potential was totally used for power production, the annual electricity production from sewage sludge, based on biogas in Turkey, would be over 530 GWh. This can meet nearly 1 % of the total annual energy demand of the country. Considering the digested sludge output as a secondary valuable fuel source for incineration facilities for further power production, this percentage would increase by 2 %, which indicates that WWTPs are obviously remarkable renewable energy sources. From the assessment of seven regions of Turkey, Model-1 shows the highest potential for hydrogen production in municipal WWTPs. Also Model-3 has the most renewable and sustainable characteristics. Considering three models developed, the daily hydrogen production potential of all municipal WWTPs in Turkey would be 52,487 kg for model-1, 795 kg for model-2, and 25,951 kg for model-3. According to the impact assessments of the developed hydrogen production models, the environmental impact of Model-1 is found to be higher than the other models in all three impact categories, namely global warming, acidification, and eutrophication.

References

1. Rulkens W (2008) Sewage sludge as a biomass resource for the production of energy: overview and assessment of the various options. Energ Fuel 22:9–15
2. Dalis D, Anagnostidis K, Lopez A, Letsiou I, Hartmann L (1996) Anaerobic digestion of total raw olive-oil wastewater in a two-stage pilot-plant (up-flow and fixed-bed bioreactors). Bioresour Technol 57:237–243
3. Appels L, Baeyensc J, Degrevea J, Dewil R (2008) Principles and potential of the anaerobic digestion of waste-activated sludge. Progr Energ Combust Sci 34:755–781
4. Chen Y, Cheng JJ, Creamer KS (2008) Inhibition of anaerobic digestion process: a review. Bioresour Technol 99:4044–4064
5. Osorio F, Torres JC (2009) Biogas purification from anaerobic digestion in a wastewater treatment plant for biofuel production. Renew Energ 34:2164–2171
6. Hyaric RL, Canler JP, Barillon B, Naquin P, Gourdon R (2010) Pilot-scale anaerobic digestion of screenings from wastewater treatment plants. Bioresour Technol 101:9006–9011
7. Kalloum S, Bouabdessalem H, Touzi A, Iddou A, Ouali MS (2011) Biogas production from the sludge of the municipal wastewater treatment plant of Adrar city (southwest of Algeria). Biomass Bioenerg 35:2554–2560
8. Sun L, Wan S, Yu Z, Wang Y, Wang S (2012) Anaerobic biological treatment of high strength cassava starch wastewater in a new type up-flow multistage anaerobic reactor. Bioresour Technol 104:280–288

9. de Mes TZD, Stams AJM, Reith JH, Zeeman G (2003) Methane production by anaerobic digestion of wastewater and solid wastes. In: Reith JH, Wijffels RH, Barten H (eds) Bio-methane & bio-hydrogen: status and perspectives of biological methane and hydrogen production. Dutch Biological Hydrogen Foundation - NOVEM, The Hague, The Netherlands, pp 58–94

10. Coskun C, Akyuz E, Oktay Z, Dincer I (2011) Energy analysis of hydrogen production using biogas-based electricity. Int J Hydrogen Energ 36:11418–11424

11. Huang CH, Lin HY, Tsai YY, Hsie YK (2000) The preliminary studies of hydrogen production from anaerobic digestion with different substrates and cultivations. The Twenty-fifth Wastewater Technology Conference, Yunlin, Taiwan (in Chinese)

12. Lin HY, Tsai YY, Wu RH (2001) Study of hydrogen production from the anaerobic digestion of hydrolyzed biological sludge. The Twenty-sixth Wastewater Technology Conference, Kaohsiung, Taiwan (in Chinese)

13. Wang CC, Chang CW, Chu CP, Lee DJ, Chang BV, Liao CS (2003) Producing hydrogen from wastewater sludge by Clostridium bifermentans. J Biotechnol 102:83–92

14. Zhu H, Beland M (2006) Evaluation of alternative methods of preparing hydrogen producing seeds from digested wastewater sludge. Int J Hydrogen Energ 31:1980–1988

15. Tchobanoglous G, Burton FL, Stensel HD (2003) Wastewater engineering: treatment and reuse. Hemisphere-McGraw-Hill, New York, NY

16. McGhee T (1991) Water supply and sewerage. McGraw-Hill, New York, NY

17. Zeng K, Zhang D (2010) Recent progress in alkaline water electrolysis for hydrogen production and applications. Progr Energ Combust Sci 36:307–326

18. Kinoshita K (1992) Electrochemical oxygen technology. Wiley, New York, NY

19. International Water Association (IWA) (2011) Global atlas of excreta, wastewater sludge, and biosolid management: Turkey overview, http://www.iwawaterwiki.org. Accessed Mar 2012

20. Turkish Statistical Institute (TSI) http://www.turkstat.gov.tr. Accessed Apr 2011

21. Fytili D, Zabaniotou A (2008) Utilization of sewage sludge in EU application of old and new methods - a review. Renew Sustain Energ Rev 12:116–140

22. CMLCA (2012) http://www.cmlca.eu/. Accessed Nov 2012

Chapter 32
Possibilities of Improving the Bioethanol Production from Cornmeal by Yeast *Saccharomyces cerevisiae* var. *ellipsoideus*

Svetlana Nikolić, Ljiljana Mojović, and Aleksandra Djukić-Vuković

Abstract Bioethanol has become one of the most promising biofuels today. In Serbia, the most suitable and available raw materials are conventional starch-based energy crops such as corn and triticale. Bioethanol production by simultaneous saccharification and fermentation (SSF) process of cornmeal using free and immobilized cells of *Saccharomyces cerevisiae* var. *ellipsoideus* yeast, with and without media supplementation (mineral salts $ZnSO_4 \cdot 7H_2O$ and $MgSO_4 \cdot 7H_2O$), in a batch system is studied. The ethanol concentration after 48 h of SSF is increased for 6.68 % by yeast immobilization compared to the free cell system, and a percentage of the theoretical ethanol yield of 86.66 % is achieved. Further improvement is accomplished with the addition of mineral salts which contributed to the highest increase in ethanol concentration by 15.86 % compared to the SSF process with free yeast and without yeast activators. In this case, ethanol concentration of 10.23 % (w/w), percentage of the theoretical ethanol yield of 94.11 %, and glucose consumption of 98.32 % are achieved after 48 h of the SSF process.

Keywords Bioethanol • Biofuel • Yeast • *Saccharomyces cerevisiae* var. *ellipsoideus* • Immobilization • Media supplementation

32.1 Introduction

The increased world population and energy consumption, and inability to replenish such increased energy needs from the limited energy sources, boost the interest in producing energy from renewable feedstock, alternative to fossil resources. Conventional energy resources (such as fossil fuels) cannot meet the increasing

S. Nikolić (✉) • L. Mojović • A. Djukić-Vuković
Faculty of Technology and Metallurgy, University of Belgrade,
Karnegijeva 4, Belgrade, Serbia
e-mail: snikolic@tmf.bg.ac.rs; lmojovic@tmf.bg.ac.rs; adjukic@tmf.bg.ac.rs

energy demand and they have considerable negative environmental impact [1, 2]. Key drivers for renewable energy have been the concern over global climate change associated with greenhouse gas (GHG) emissions, as well as the energy security threatened by increased nonrenewable oil production. The International Energy Agency (IEA) forecasted a 450 Scenario in their 2008 World Energy Outlook (WEO) in which atmospheric GHG would be stabilized at a volume fraction of 450 ppm CO_2 equivalents, and estimated that by 2030 the world demand for transport biofuels will be 11.64 EJ and supply 9.2 % of total global transport fuels [3]. Biofuels with bioethanol as the most promising representative are both renewable and environmentally friendly energy resources.

32.2 Background

Biofuels, as liquid transportation fuels produced from biomass, now represent major contributors to the bioenergy portfolios in many countries [4]. Biofuels are easily available from common biomass sources, are biodegradable, and contribute to the sustainability [1]. Biofuels are used as a means to reduce GHG emissions, promote energy security, and support local economic development [5]. Other advantages are lower dependency on the import of oil for non-oil-producing countries, new employment opportunities, and development of rural communities [6]. To achieve those goals, many countries set mandate for the amount of biofuels to be used and give tax credits to biofuel producers. The United States mandates 36 billion gallons of biofuels by 2022 under the Energy Independence and Security Act of 2007. A number of directives cover biofuel use in the European Union (EU) including the Renewable Energy Directive 2009/28/EC, the Fuel Quality Directive, and the Biofuels Directive 2003. The EU mandates that biofuels must make up 10 % of the liquid fuels in the transport sector by 2020, according to the EU Directive 2009/28/EC [7]. According to the IEO2011 Reference case, biofuel production in the Reference case increases from 1.5 million barrels per day in 2008 to 4.7 million barrels per day in 2035, at an average annual growth rate of 4.3 % [5].

Bioethanol—fermentation-derived fuel alcohol—is the world's leading transportation biofuel and one of the most promising biofuels from renewable resources. Bioethanol currently accounts for more than 94 % of global biofuel production [8]. In 2011 world bioethanol production reached 84.6 billion liters, which is nearly five times higher than the production in 2000. The United States as the top producer with 52.6 billion liters (produced from corn), accounting for 62.2 % of global production, has been followed by Brazil with the production of 21.1 billion liters. Brazil is the world's largest exporter of bioethanol besides being a second largest producer after the United States. All of Brazil's bioethanol is produced from sugarcane; most is used domestically, thus substituting 40 % of Brazilian petrol consumption, and approximately 20 % is exported to the United States, EU, and other markets [1]. The third large bioethanol producers are the countries of EU (France, Germany, Spain, Sweden) with production of 4.54 billion liters in 2011 [9]. With all of the new

government programs in America, Asia, and Europe, total bioethanol demand could grow to exceed 125 billion liters by 2020 [1].

Bioethanol can be blended with gasoline in various proportions or used as neat alcohol in dedicated engines, taking advantage of the higher octane number, low cetane number, and higher heat of vaporization. In addition, it is also an excellent fuel for future advanced flexi-fuel hybrid vehicles [10, 11]. Bioethanol is most commonly blended with gasoline in concentrations of 10 % of bioethanol to 90 % of gasoline, known as E10. In Brazil, bioethanol is used pure or blended with gasoline in a mixture called gasohol (24 % bioethanol and 76 % gasoline). Bioethanol can be used also as a 5 % blend with petrol under the EU quality standard EN 228, which requires no engine modification. With engine modification, bioethanol can be used at higher level of 85 %, known as E85 [12, 13]. The bioethanol is an oxygenated fuel containing 35 % oxygen, which reduces particulate and nitrate oxide (NOx) emissions from combustion [1]. The calculation of exactly how much carbon dioxide is produced in the production of bioethanol is a complex and inexact process, and is highly dependent on the production process and the assumptions made in the calculation. Farrel et al. [14] reported that corn ethanol reduces GHG emissions only moderately, by about 13 %. Given adequate policy incentives for GHG emission control, the performance of corn ethanol in terms of GHG emissions can likely be improved. They concluded that only cellulosic ethanol offers large reductions in GHG emissions.

Fermentation-derived ethanol can be produced from sugar, starch, or lignocellulosic biomass. Sugar- and starch-based feedstocks are currently predominant at the industrial level and they are so far economically favorable. However, the future lies with more sustainable fermentation substrates, including biowastes from agriculture and lignocellulosic biomass. In Serbia, starch-based raw materials, corn and triticale (hybrid of wheat and rye), are the most suitable and available agricultural raw material which can be used for industrial bioethanol production. In the last few years, the average annual corn yield in Serbia has been approximately 40 % higher than the calculated domestic needs [15]. That means that from the usual annual corn production remains 2–2.5 million tons, which can be used as raw material for bioethanol production instead of exporting, and it would also decrease the quantities of imported oil. Therefore, significant amounts of this raw material can be used for bioethanol production since there is enough corn for other purposes besides the food.

The current bioethanol research is driven by the need to reduce the cost of production. The development of cost-effective technologies for bioethanol production is a priority for many research centers, universities, private firms, and even different governments. Whichever system for bioethanol production is chosen, the attention must be paid to the overall economics and energy consumption. One of the methods enhancing the ethanol productivity and reducing production costs is to use simultaneous enzymatic saccharification and fermentation (SSF) process [2, 16]. SSF process has been found to be economically favorable compared to the traditional separate hydrolysis and fermentation (SHF) process in terms of higher ethanol yield, lower energy consumption, and shorter processing time.

In SSF process the end-product inhibition of the enzymes is avoided because the fermenting organism immediately consumes the released sugars. Capital investments are lower in SSF process since this process mode can be performed in one reactor instead of two reactors in the case of SHF [17]. On the other hand, the critical problem with SSF is different optimum temperatures of hydrolyzing enzymes and fermenting organisms. *Saccharomyces* strains are most widely used ethanol-producing microorganisms but they require operating temperature of about 30–35 °C, which differs from the optimal temperature for the saccharification step, i.e., 55–60 °C in the case of using glucoamylase in starch conversion to glucose [18, 19]. Some researchers managed to avoid this problem by applying thermotolerant microorganisms such as *Kluyveromyces marxianus*, *Candida lusitaniae*, and *Zymomonas mobilis* or mixed culture of some microorganisms like *Brettanomyces claussenii* and *Saccharomyces cerevisiae* [20].

Saccharomyces strains are well-known ethanol-producing microorganisms. One of the most critical components of management of the yeast fermentation is to make sure that the yeasts have all the requisite nutrients to maintain favorable fermentation rates and optimal ethanol and temperature tolerance. The doses of the mineral compounds and vitamins, as micronutrients, depend on the raw material used, which can be sometimes characterized by too poor chemical composition as a substrate for yeasts. The addition of mineral salts and vitamins has a stimulatory effect on yeasts and contributes to an increase in efficiency of ethanol fermentation. These compounds have a protective effect on growth, fermentation, or viability, which overall stimulates the rate of ethanol production [21].

Many strategies have been explored to overcome the substrate and product inhibition and to improve the ethanol tolerance of yeasts. Among them, the most explored is immobilization of yeasts. Immobilization techniques can be divided into four main categories based on the physical mechanism employed: (1) attachment or adsorption on solid carrier surfaces; (2) entrapment within a porous matrix; (3) self-aggregation by flocculation (natural) or with cross-linking agents (artificially induced); and (4) cell containment behind barriers [22]. Various immobilization substrates have been used, including Ca-alginate beads [22], diatomaceous earth, DEAE-cellulose [23], k-carrageenan gel, polyacrylamide, γ-alumina [24], wooden chips [25, 26], PVA gel [27], orange peel [28], chitosan [29], cellulose [30], agar agar [31], sorghum bagasse [32], wheat starch granules [33], silicon carbide [34], and spent grains [35]. Immobilizing cells in alginate is simple, cheap, and nontoxic. Calcium alginate is the most widely used gel matrix in laboratory, pilot-plant, and industrial-scale fermentation projects [36]. The use of immobilized cells offers a number of advantages, such as prolonged cellular stability, increased ethanol yield, greater volumetric productivity as a result of higher cell density, increased tolerance to high substrate concentration, reduced end-product inhibition, decreased energy demands and process expenses due to easier product recovery, regeneration and reuse of cells for extended periods in batch system, feasibility of continuous processing, and reduction of risk of microbial contamination due to high cell densities [37–39]. However, Prasad [39] also reported that in some cases, the effectiveness of immobilized cells will be lower

than for a system with free cells. The main reason is because the cells deep inside a bioparticle can become inactive due to either considerable substrate and product mass transfer limitation or accumulation of product to inhibiting concentrations. Another drawback for application of polymer beads as cell carrier is a problem of gel degradation, low physical strength, and gel particle disruption due to intensive CO_2 evolution [40].

In this chapter, the possibilities of improving productivity of bioethanol production from cornmeal by applying yeast immobilization in Ca-alginate and media supplementation with mineral salts in SSF by *Saccharomyces cerevisiae* var. *ellipsoideus* in a batch system are presented. The kinetics of SSF process was assessed and determined and the improvement of the ethanol production by adding yeast activators, mineral salts—$ZnSO_4 \cdot 7H_2O$ and $MgSO_4 \cdot 7H_2O$, was investigated.

32.3 Materials and Methods

32.3.1 Starch

Cornmeal obtained by dry milling process is a product of corn processing factory "RJ Corn Product," Sremska Mitrovica, Serbia. The cornmeal consists of particles with diameter 0.2–1.7 mm (95 % or more particles pass through a 1.70 mm sieve). The content of the main components in the cornmeal is the following: starch 76.75 % (w/w), proteins 6.35 % (w/w), lipids 4.50 % (w/w), fibers 1.36 %, ash 0.70 % (w/w), and water 10.34 % (w/w), as determined by chemical analysis in our previous study [41].

32.3.2 Enzymes and Microorganism

Termamyl SC, a heat-stable α-amylase from *Bacillus licheniformis*, is used for cornmeal liquefaction. The enzyme activity is 133 KNU/g (kilo novo units, KNU α-amylases—the amount of enzyme which breaks down 5.26 g of starch per hour according to Novozyme's standard method for the determination of α-amylase). SAN Extra L, *Aspergillus niger* glucoamylase, activity 437 AGU/g (AGU is the amount of enzyme which hydrolyzes 1 µmol of maltose per minute under specified conditions) is used for cornmeal saccharification. The enzymes are gift from Novozymes, Denmark.

Saccharomyces cerevisiae var. *ellipsoideus* is used for the fermentation of hydrolyzed cornmeal. The culture originates from the collection of Department of Biochemical Engineering and Biotechnology, Faculty of Technology and Metallurgy, University of Belgrade (BIB-TMFB), and was maintained on a malt agar slant. The agar slant consists of malt extract (3 g/l), yeast extract (3 g/l), peptone (5 g/l), agar (20 g/l), and distilled water (up to 1 l). Before use as an inoculum for the fermentation, the culture was aerobically propagated in 500 ml flasks in a shaking bath at 30 °C for 48 h and then separated by centrifugation. The liquid media

consisted of yeast extract (3 g/l), peptone (3.5 g/l), KH$_2$PO$_4$ (2.0 g/l), MgSO$_4$·7H$_2$O (1.0 g/l), (NH$_4$)$_2$SO$_4$ (1.0 g/l), glucose (10 g/l), and distilled water.

32.3.3   Immobilization and Cultivation Procedure

The yeast cells are immobilized in Ca-alginate using an electrostatic droplet generation method. The 2 % (w/w) Na-alginate solution is prepared by dissolving 4.8 g of Na-alginate powder (Sigma medium viscosity) into 240 ml of distilled water. Polymer/cell suspension is formed by mixing of 240 ml of Na-alginate solution with 60 ml of thick yeast suspension at room temperature. Spherical microbeads are formed by extrusion of Na-alginate/yeast cell suspension through a blunt stainless steel needle using a syringe pump (Harvard Apparatus, Pump 11) with a 20 ml plastic syringe and an electrostatic droplet generator (Nisco Encapsulator, Switzerland). The cell suspension is forced out of the tip of the needle at constant flow rate (0.25 ml/min), and droplets are formed by the action of electrostatic and gravitational forces. Electrostatic potential is formed by connecting the positive electrode of a high-voltage dc unit to the gelling bath which is 2.65 % (w/v) CaCl$_2$ solution while the needle is grounded. In this way, the yeast cells are entrapped in the gel matrix of Ca-alginate. After gelling the microbeads are placed in double-distilled water to remove unreacted material. Microbeads with cells are stored in physiological solution at 8 °C.

32.3.4   Liquefaction and SSF Experiments

A 100 g of cornmeal is mixed with water at the weight ratio (hidromodul) 1:3, and 60 ppm of Ca^{2+} (as CaCl$_2$) ions are added. The liquefaction is carried out at 85 °C and pH of 6.0 for 1 h by adding 0.026 % (v/w of starch) enzyme Termamyl SC. The liquefaction and SSF process are performed in flasks in thermostated water bath with shaking (100 rpm), as described by Mojović et al. [42].

The liquefied mash is cooled, pH is adjusted to 5.0 using 2 M HCl, and KH$_2$PO$_4$ (4.0 g/l), MgSO$_4$·7H$_2$O (0.4 g/l), and (NH$_4$)$_2$SO$_4$ (2.0 g/l) are added. The SSF process is performed by adding 0.156 % (v/w of starch) enzyme SAN Extra L and 2 % (w/v) of free or immobilized yeast cells to the liquefied mash, and carried out for up to 48 h at 30 °C. Initial viable cell number is ~10^7 CFU/ml when the free yeast is used. In case of immobilized yeast, 2 % (w/v) of Ca-alginate beads with entrapped cells corresponded well to 5.0 × 10^7 CFU/g of beads. Improvement of the ethanol production is investigated by adding additional mineral salts as yeast activators: ZnSO$_4$·7H$_2$O (0.3 g/l) and MgSO$_4$·7H$_2$O (2.0 g/l). It is considered that the pasteurization of the substrate achieved during the enzymatic liquefaction (85 °C for 1 h) is sufficient thermal treatment, and thus no additional sterilization prior to SSF process is performed.

32.3.5   Analytical Methods

During the SSF process, the content of reducing sugars, calculated as glucose, is determined by 3,5-dinitrosalicylic acid [43]. A standard curve is drawn by measuring the absorbance of known concentrations of glucose solutions at 570 nm. The ethanol concentration is determined based on the density of the alcohol distillate at 20 °C and expressed in % (w/w) [44]. Indirect counting method, i.e., pour plate technique, is used to determine the number of viable cells. Serial dilutions of the samples are performed, and after the incubation time at 30 °C, colonies grown in Petri dishes are used to count the number of viable cells. In case of immobilized yeast cells, the first dilution is performed in 2 % (w/v) sodium citrate solution (instead of physiological solution) in order to dissolve alginate gel. At least three measurements are made for each condition and the data given represents the average values of the measurements.

32.4   Results and Discussion
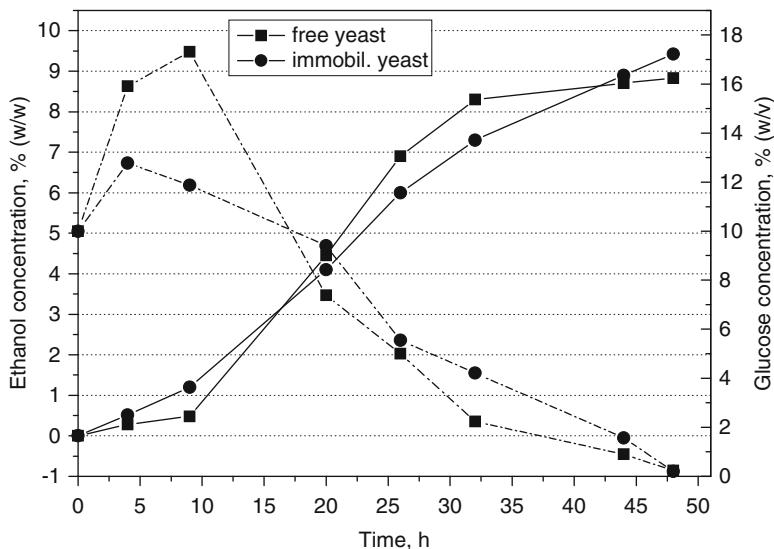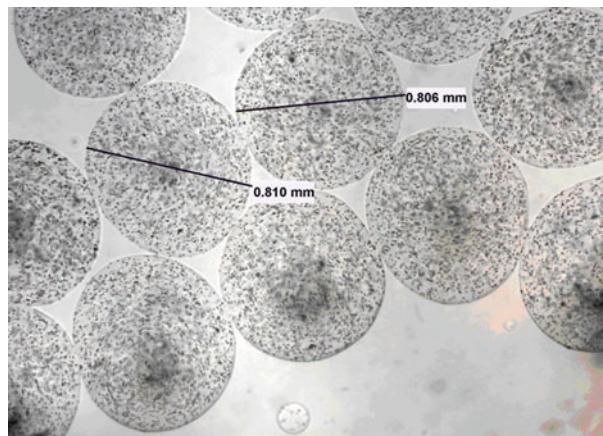
32.4.1   Effect of the Yeast Immobilization

In the experiments with immobilized yeast the Ca-alginate microbeads have an average diameter of 0.8 mm, and are presented in Fig. 32.1. Small-diameter beads are generally preferred because of the more favorable mass transfer. The significance of this immobilization method is that the matrix is porous enough for substrate and products to traverse where a level of cell retention is maintained within the immobilization matrix [45]. Alginate as a suitable cell entrapment matrix is nontoxic, less expensive, and reversible and has good mechanical properties [46]. According to our results, the yeast *S. cerevisiae* var. *ellipsoideus* cells entrapped in Ca-alginate showed good physical and chemical stability and no substrate and product diffusion restrictions were noticed.

In order to reduce the time of the complete process and make beneficial energy savings, a simultaneous process of the second hydrolysis step (saccharification) and fermentation (SSF) of cornmeal at 30 °C is performed. The first set of experiments is conducted in order to investigate the influence of yeast immobilization on ethanol production. Figure 32.2 presents the time course of ethanol production and glucose consumption in the SSF process by free and immobilized yeast.

As shown in Fig. 32.2, the ethanol concentration gradually increases without any declining phase during the SSF with immobilized yeast, probably due to the fact that the immobilization increases the ethanol tolerance of the yeast cells, as reported earlier [47]. This behavior suggests protective effect of immobilization against substrate and product inhibition. Also, these results show that applied immobilization method by electrostatic droplet generation is appropriate and thus no substrate diffusion restrictions are noticed. On the contrary, in the sample with

Fig. 32.1 Yeast
S. cerevisiae var.
ellipsoideus cells entrapped
in the gel matrix of
Ca-alginate (modified
from [47])

Fig. 32.2 Time course of glucose consumption and ethanol production in SSF process by free and immobilized cells of *S. cerevisiae* var. *ellipsoideus*. Process conditions: pH 5.0, 30 °C, 100 rpm, enzyme SAN Extra L was added at concentration of 0.156 % (v/w of starch), inoculum concentration 2 % (w/v). *Solid lines*—ethanol concentration, *dashed lines*—glucose concentration

free yeast, ethanol concentration asymptotically approaches to a value around 9 % (w/w), most probably because the product inhibition took place due to yeast inhibition by ethanol accumulation. Therefore, at the end of the SSF process the maximum ethanol concentration of 9.42 % (w/w) is achieved in immobilized system (Fig. 32.2 and Table 32.1).

Table 32.1 The effect of immobilization and media supplementation on values of the significant process parameters obtained after 48 h of the SSF process by *Saccharomyces cerevisiae* var. *ellipsoideus*

Process parameter	SSF process with free yeast	SSF process with immobilized yeast	SSF process with immobilized yeast and media supplementation
Ethanol concentration (% w/w)	8.83 ± 0.09	9.42 ± 0.11	10.23 ± 0.10
Ethanol yield $Y_{P/S}$ (g ethanol/g starch)	0.460 ± 0.005	0.490 ± 0.006	0.530 ± 0.005
Percentage of the theoretical ethanol yield (%)	81.23 ± 0.83	86.66 ± 1.01	94.11 ± 0.92
Volumetric productivity P (g/l h)	1.83 ± 0.03	1.96 ± 0.03	2.13 ± 0.03
Utilized glucose[a] (%)	97.70 ± 0.44	98.00 ± 0.56	98.40 ± 0.48

Presented data are expressed as the mean value and standard deviation from three independent experiments

Process conditions are the same as in Fig. 32.2

[a]Utilized glucose (%) is calculated as the ratio of the consumed mass of glucose to initial mass of glucose
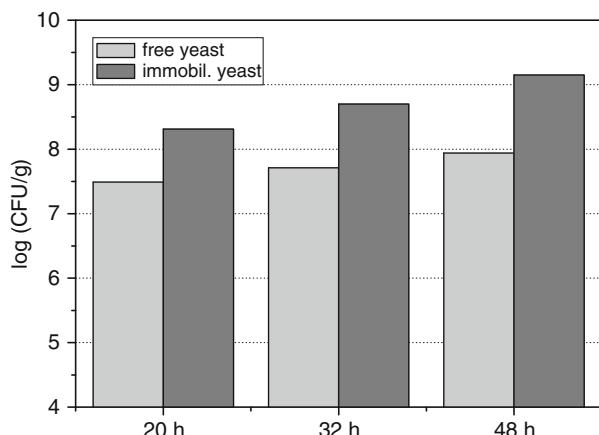
As shown in Fig. 32.2, the glucose consumption is in accordance with the results of ethanol concentration since glucose is consumed as a carbon source by the yeast and fermented to ethanol. An increase in glucose concentration is observed in both free and immobilized systems at the beginning of the SSF. This indicates that the saccharification is much faster than the ethanol fermentation, since the yeast cells are still in the adaptation phase and during this time there is not a significant ethanol production. This phenomenon was also observed by other authors [48, 49]. At the end of SSF process, in samples with free and immobilized yeast cells glucose concentrations are 0.23 and 0.20 g/l, respectively, indicating the end of fermentation. Thus, in sample with immobilized yeast cells a total amount of utilized glucose of 98.00 % is higher than in sample with free yeast cells (Table 32.1). This is in accordance with the obtained ethanol concentrations.

The values of number of cells achieved after 20, 32, and 48 h of the SSF process using free and immobilized yeast are presented in Fig. 32.3.

The number of viable yeast cells in both free and immobilized system increases with time in all flasks. During the SSF, higher values of number of cells are obtained in immobilized system indicating protective effect of immobilization, as mentioned above. After 48 h the maximum number of cells of 1.41×10^9 CFU/g is achieved in immobilized system.

Previous studies showed that the yeast viability significantly decreased in free cell system due to the great accumulation of intracellular ethanol which altered the structure of the membrane decreasing its functionality [50, 51]. On the other hand, it is reported that immobilized cells have increased ethanol tolerance because the matrix provides protective environment against ethanol toxicity [36, 52]. This is in agreement with presented results, since higher values of number of cells during the SSF process are achieved in immobilized than in free system.

Fig. 32.3 Number of cells obtained after 20, 32, and 48 h of the SSF process using free and immobilized *S. cerevisiae* var. *ellipsoideus* yeast. Process conditions are the same as in Fig. 32.2

32.4.2 Effect of the Yeast Activators (Mineral Salts)
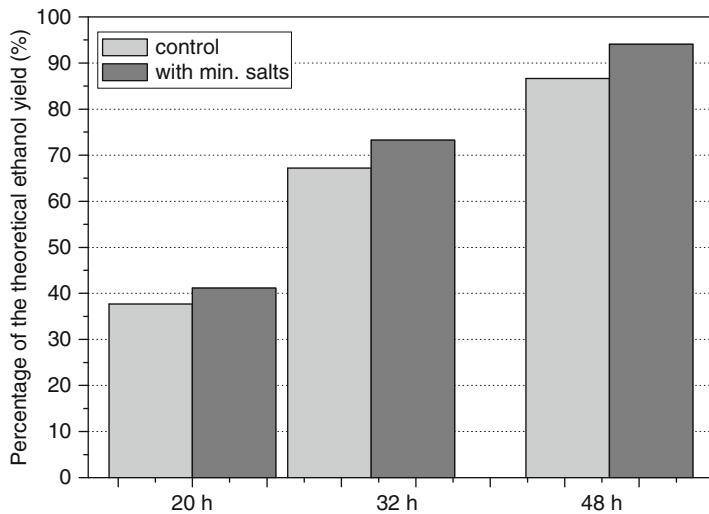
Vitamins and minerals, as yeast micronutrients, are needed to facilitate the biochemical reactions. The mineral compounds take part in metabolism of yeasts as the activators of enzymes or elements of cell components [53]. Metal ions (such as K^+, Mg^{2+}, Ca^{2+}, and Zn^{2+}) can change the rate of glycolysis and the conversion of pyruvate to ethanol and therefore significantly impact on the progress and efficiency of the fermentation. Magnesium is involved in many physiological functions—yeast growth, cell division, and enzyme activity, and it has an important role in the cellular protection of toxic levels of ethanol. If the media is magnesium limited the conversion of sugar to ethanol may lead to slow or incomplete fermentation process [54]. Zinc is a trace element that is necessary for several enzyme activities such as alcohol dehydrogenase, aldolase, alkaline phosphatase, and DNA and RNA polymerase [55].

Further experiments are conducted in order to investigate the improvement of the ethanol production by addition of yeast activators: mineral salts—$ZnSO_4 \cdot 7H_2O$ (0.3 g/l corresponding to 1 mM Zn^{2+}) and $MgSO_4 \cdot 7H_2O$ (2.0 g/l corresponding to 10 mM Mg^{2+}). The concentration of Mg^{2+} before the mineral salt addition is 1.5 mM. The values of percentage of theoretical ethanol yield achieved after 20, 32, and 48 h of the SSF process with addition of mineral salts are compared with a control (samples without any activators), and presented in Fig. 32.4.
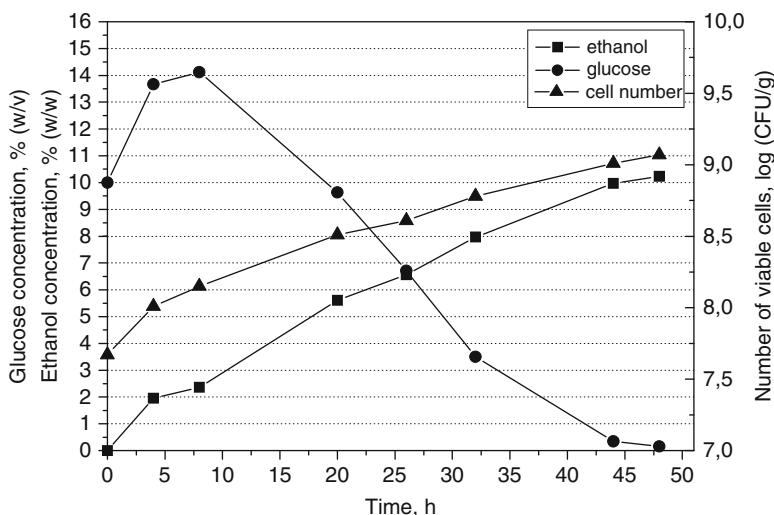
According to the results presented in Fig. 32.4, the addition of mineral salts contributes to the increase in ethanol production in all samples. A maximum increase in the percentage of theoretical ethanol yield (8.60 % compared to the control sample) is achieved when mineral salts are added after 48 h of the SSF process.

Figure 32.5 presents the time course of ethanol production, glucose consumption, and the number of cells in the SSF process by immobilized yeast and with addition of mineral salts.

As shown in Figs. 32.2 and 32.5, the kinetic profiles for ethanol production, glucose consumption, and yeast growth show similar trend in the presence and

Fig. 32.4 Effect of mineral salts on percentage of theoretical ethanol yield after 20, 32, and 48 h of SSF process by immobilized cells of *S. cerevisiae* var. *ellipsoideus*. Process conditions are the same as in Fig. 32.2. Concentration of mineral salts (activators): $ZnSO_4 \cdot 7H_2O$ 0.3 g/l and Mg $SO_4 \cdot 7H_2O$ 2.0 g/l

Fig. 32.5 Time course of glucose consumption, number of viable cells, and ethanol production in SSF process by immobilized cells of *S. cerevisiae* var. *ellipsoideus* with the addition of mineral salts. Process conditions are the same as in Fig. 32.2. Concentration of mineral salts (activators): $ZnSO_4 \cdot 7H_2O$ 0.3 g/l and Mg $SO_4 \cdot 7H_2O$ 2.0 g/l

absence of mineral salts. But, much higher value of ethanol concentration (10.23 % w/w) and other significant fermentation parameters are achieved in SSF process with addition of mineral salts (Fig. 32.5 and Table 32.1).

Metal ions in fermentation media are important factors that have an effect on yeast cell physiology and alcohol production. Magnesium ions directly influence the rate of yeast growth, sugar consumption, and ethanol production [56]. It is generally required by the yeast in millimolar concentration range. In this chapter it is shown that the addition of 10 mM of Mg^{2+} successfully contributes to the increase in ethanol production. Dombek and Ingram [57] have shown that supplementing the ethanol fermentation with magnesium at a level of 0.5 mM prolonged the exponential growth, increased the yeast cell mass accumulation, and reduced the decrease in fermentation rate during the completion of batch fermentation. Birch and Walker [54] reported that elevated concentrations of magnesium in medium (up to 50 mM) resulted in the improvement in survival of the cells under conditions with high ethanol concentrations. Zinc as a trace element is very important in yeast fermentative metabolism not only because it is essential for alcohol dehydrogenase (terminal alcohologenic Zn-metalloenzyme), but also because it can stimulate the uptake of maltose and maltotriose into yeast cells, thereby increasing fermentation rates [58]. However, zinc and other necessary trace elements for yeast growth (such as calcium, manganese, iron, copper) can be toxic to yeast even at lower concentrations. The toxicity could be diminished due to interactions with other trace elements or nutrients of the substrate as well as due to protection by immobilization [59, 60]. In this chapter, applied concentrations of zinc are not found to be toxic to the yeast. Additionally, Ca-alginate gel could express instability in the presence of certain concentrations of substances which have a high affinity for Ca^{2+} ions such as phosphate, citrate, and lactate, and ions such as K^+ and Mg^{2+}. On the other hand, avoidance of magnesium, phosphate, and other necessary nutrients in the medium is not possible as they are essential for the yeast metabolism, maintenance of cell viability, and cell wall integrity. In this investigation we manage to attain a high productivity of batch SSF process of cornmeal and to preserve physical and chemical stability of gel beads by addition of mineral salts in appropriate amounts.

The comparison of the significant process parameters achieved in SSF process with immobilized and free cells of *S. cerevisiae* var. *ellipsoideus* with or without media supplementation is presented in Table 32.1. Comparing the values of all process parameters obtained in these three systems, the SSF process with immobilized yeast and media supplementation has been found to be the most superior system.

32.5 Conclusions

Taking into consideration parameters such as ethanol concentration, ethanol yield, percentage of the theoretical ethanol yield, volumetric productivity, and utilized glucose, the SSF process with immobilized yeast and addition of mineral salts as

activators has been found to be superior system in terms of all process parameters compared to the SSF process with free yeast and without media supplementation. In this case, the maximum ethanol concentration of 10.23 % (w/w) and percentage of the theoretical ethanol yield of 94.11 % are achieved after 48 h of the SSF process. By immobilization of the yeast into Ca-alginate using a method of electrostatic droplet generation, the system exhibits high tolerance to ethanol since there is no declining phase in ethanol production during the SSF process. The yeast *S. cerevisiae* var. *ellipsoideus* entrapped in Ca-alginate is appropriate for SSF of cornmeal since no substrate and product diffusion restrictions are noticed.

Mineral salts $ZnSO_4 \cdot 7H_2O$ and $MgSO_4 \cdot 7H_2O$ as yeast activators (10 mM of Mg^{2+} and 1 mM of Zn^{2+}) cause an increase in ethanol concentration by 15.86 % compared to the SSF process with free yeast and without yeast activators. Addition of the applied amounts of magnesium and zinc contributes to the achievement of high productivity of the batch SSF of cornmeal while still preserving a physical and chemical stability of Ca-alginate gel beads.

References

1. Balat M, Balat H (2009) Recent trends in global production and utilization of bio-ethanol fuel. Appl Energy 86:2273–2282
2. Mojović L, Pejin D, Grujić O, Markov S, Pejin J, Rakin M, Vukašinović M, Nikolić S, Savić D (2009) Progress in the production of bioethanol on starch-based feedstocks, Review paper. Chem Ind Chem Eng Q (CI&CEQ) 15:211–226
3. International Energy Agency (2009) World energy outlook. OECD Publishing, Paris
4. Pejin DJ, Mojović LV, Pejin JD, Olgica S, Grujić OS, Markov SL, Nikolić SB, Marković MN (2012) Increase in bioethanol production yield from triticale by simultaneous saccharification and fermentation with application of ultrasound. J Chem Technol Biotechnol 87:170–176
5. International Energy Outlook IEO2011 (2011) U.S. Energy Information Administration EIA, Washington DC www.eia.gov/ieo/pdf/0484(2011).pdf
6. Nigam PA, Singh A (2011) Production of liquid biofuels from renewable resources. Prog Energy Combust Sci 37:52–68
7. European Biofuels Technology Platform, Biofuels Policy and Legislation. http://www.biofuelstp.eu/legislation.html#RenEnDir. Accessed 05 Nov 2012
8. Nitin V (2010) Bioethanol from biomass: a review. J Biofuels 1:245–225
9. Renewable Fuels Association (2012) Acelerating industry innovation—2012 ethanol industry outlook. http://ethanolrfa.3cdn.net/d4ad995ffb7ae8fbfe_1vm62ypzd.pdf. Accessed 6 Nov 2012
10. Chum HL, Overend RP (2001) Biomass and renewable fuels. Fuel Process Technol 71:187–195
11. Kim S, Dale BE (2005) Environmental aspects of ethanol derived from no-tilled corn grain: nonrenewable energy consumption and greenhouse gas emissions. Biomass Bioenergy 28:475–489
12. Demirbas A (2008) The importance of bioethanol and biodiesel from biomass. Energy Sources Part B 3:177–185

13. Oliveria MED, Vaughan BE, Rykiel EJ Jr (2005) Ethanol as fuel: energy, carbon dioxide balances, and ecological footprint. Bioscience 55:593–602
14. Farrell AE, Plevin RJ, Turner BT, Jones AD, O'Hare M, Kammen DM (2006) Ethanol can contribute to energy and environmental goals. Science 311:506–508
15. Nikolić S, Mojović L, Rakin M, Pejin D, Pejin J (2011) Utilization of microwave and ultrasound pretreatments in the production of bioethanol from corn. Clean Technol Environ Policy 13:587–594
16. Mielenz J (2001) Ethanol production from biomass: technology and commercialization status. Curr Opin Microbiol 4:324–329
17. Zhang L, Zhao H, Gan M, Jin Y, Gao X, Chen Q, Guan J, Wang Z (2011) Application of simultaneous saccharification and fermentation (SSF) from viscosity reducing of raw sweet potato for bioethanol production at laboratory, pilot and industrial scales. Bioresource Technol 102:4573–4579
18. Karimi K, Emtiazi G, Taherzadeh MJ (2006) Ethanol production from diluteacid pretreated rice straw by simultaneous saccharification and fermentation with *Mucor indicus*, *Rhizopus oryzae*, and *Saccharomyces cerevisiae*. Enzyme Microb Technol 40:138–144
19. Öhgren K, Bura R, Lesnicki G, Saddler J, Zacchi G (2007) A comparison between simultaneous saccharification and fermentation and separate hydrolysis and fermentation using steam-pretreatment corn stover. Process Biochem 42:834–839
20. Binod P, Sindhu R, Singhania RR, Vikram S, Devi L, Nagalakshmi S, Kurien N, Sukumaran RK, Pandey A (2010) Bioethanol production from rice straw: an overview. Bioresour Technol 101:4767–4774
21. Alfenore S, Molina-Jouve C, Guillouet SE, Uribelarrea JL, Goma G, Benbadis L (2002) Improving ethanol production and viability of *Saccharomyces cerevisiae* by a vitamin feeding strategy during fed-batch process. Appl Microbiol Biotechnol 60:67–72
22. Lee KH, Choi IS, Kim YG, Yang DJ, Bae HJ (2011) Enhanced production of bioethanol and ultrastructural characteristics of reused *Saccharomyces cerevisiae* immobilized calcium alginate beads. Bioresour Technol 102:8191–8198
23. Virkajarvi I, Pohjala N (2000) Primary fermentation with immobilized yeast: some effects of carrier materials on the flavour of the beer. J Inst Brew 106:311–318
24. Öztop HN, Yasemin Öztop A, Karadağ E, Işikver Y, Saraydin D (2003) Immobilization of *Saccharomyces cerevisiae* on to acrylamide–sodium acrylate hydrogels for production of ethyl alcohol. Enzyme Microb Technol 32:114–119
25. Razmovski R, Pejin D (1996) Immobilization of *Saccharomyces diastaticus* on wood chips for ethanol production. Folia Microbiol 41:201–207
26. Vidgren V, Virkajarvi I, Ruohonen L, Salusjarvi L, Londensborough J (2003) The free and carrier-bound yeast population from a two-stage immobilized yeast reactor are in different physiological conditions. Proc Eur Brew Conv 29:609–617
27. Bezbradica D, Obradovic B, Leskosek-Cukalovic I, Bugarski B, Nedovic V (2007) Immobilization of yeast cells in PVA particles for beer fermentation. Process Biochem 42:1338–1351
28. Plessas S, Bekatorou A, Koutinas AA, Soupioni M, Banat IM, Marchant R (2007) Use of *Saccharomyces cerevisiae* cells immobilized on orange peel as biocatalyst for alcoholic fermentation. Bioresource Technol 98:860–865
29. Shinonaga M, Kawamura Y, Yamane T (1992) Immobilization of yeast cells with cross-linked chitosan beads. J Ferment Bioeng 74:90–94
30. Sakurai A, Nishid Y, Saito H, Sakakibara M (2000) Ethanol production by repeated batch culture using yeast cells immobilized within porous cellulose carriers. J Biosci Bioeng 90:526–529
31. Behera S, Kar S, Mohanty RC, Ray RC (2010) Comparative study of bio-ethanol production from mahula (*Madhuca latifolia* L.) flowers by *Saccharomyces cerevisiae* cells immobilized in agar agar and Ca-alginate matrices. Appl Energy 87:96–100
32. Yu J, Zhang X, Tan T (2007) Novel immobilization method of *Saccharomyces cerevisiae* to sorghum bagasse for ethanol production. J Biotechnol 129:415–420

33. Farmakis L, Kapolos J, Koliadima A, Karaiskakis G (2007) Study of the growth rate of *Saccharomyces cerevisiae* strains using wheat starch granules as support for yeast immobilization monitoring by sedimentation/steric field-flow fractionation. Food Res Int 40:717–724

34. Tata M, Bower P, Bromberg S, Duncombe D, Fehring J, Lau V, Ryder D, Stassi P (1999) Immobilized yeast bioreactor systems for continuous beer fermentation. Biotechnol Prog 15:105–113

35. Branyik T, Vicente AA, Machado Cruz JM, Teixeira JA (2001) Spent grains—a new support for brewing yeast immobilization. Biotechnol Lett 23:1073–1078

36. Ciesarová Z, Dömény Z, Šmogrovičová D, Pátková J, Šturdík E (1998) Comparison of ethanol tolerance of free and immobilized Saccharomyces uvarum yeasts. Folia Microbiol 43:55–58

37. Groboillot A, Boadi DK, Poncelet D, Neufeld RJ (1994) Immobilization of cells for application in the food industry. Crit Rev Biotechnol 14:75–107

38. Kourkoutas Y, Bekatorou A, Banat IM, Marchant R, Koutinas AA (2004) Immobilization technologies and support materials suitable in alcohol beverages production: a review. Food Microbiol 21:377–397

39. Prasad B (1995) On the kinetics and effectiveness of immobilized whole-cell batch cultures. Bioresource Technol 53:269–275

40. Razmovski R, Vučurović V (2012) Bioethanol production from sugar beet molasses and thick juice using *Saccharomyces cerevisiae* immobilized on maize stem ground tissue. Fuel 92:1–8

41. Nikolić S, Mojović L, Rakin M, Pejin D, Savić D (2008) A microwave-assisted liquefaction as a pretreatment for the bioethanol production by the simultaneous saccharification and fermentation of corn meal. Chem Ind Chem Eng Q (CI&CEQ) 14:231–234

42. Mojović L, Nikolić S, Rakin M, Vukašinović M (2006) Production of bioethanol from corn meal hydrolyzates. Fuel 85:1750–1755

43. Miller GL (1959) Use of dinitrosalycilic acid for determining reducing sugars. Anal Chem 31:426–428

44. Official Method 942.06 (2000) Official methods of analysis of AOAC International, 17th edn. AOAC International, Gaithersburg

45. Margaritis A, Kilonzo PM (2005) Production of ethanol using immobilised cell bioreactor systems. In: Nedović V, Willaert R (eds) Applications of cell immobilisation in biotechnology. Springer, Netherlands

46. Vogelsang C, Wijffels RH, Østgaard K (2000) Rheological properties and mechanical stability of new gel-entrapment system applied in bioreactors. Biotechnol Bioeng 70:247–253

47. Nikolić S, Mojović L, Rakin M, Pejin D, Nedović V (2009) Effect of different fermentation parameters on bioethanol production from corn meal hydrolyzates by free and immobilized cells of *Saccharomyces cerevisiae* var. e*llipsoideus*. J Chem Technol Biotechnol 84:497–503

48. Choi GW, Moon SK, Kang HW, Min J, Chung BW (2008) Simultaneous saccharification and fermentation of sludge-containing cassava mash for batch and repeated batch production of bioethanol by *Saccharomyces cerevisiae* CHFY0321. J Chem Technol Biotechnol 84:547–553

49. Zhu S, Wu Y, Yu Z, Zhang X, Wang C, Yu F, Jin S, Zhao Y, Tu S, Xue Y (2005) Simultaneous saccharification and fermentation of microwave/alkali pre-treated rice straw to ethanol. Biosyst Eng 92:229–235

50. Torija MJ, Rozes N, Poblet M, Guillamon JM, Mas A (2003) Effects of fermentation temperature on the strain population of Saccharomyces cerevisiae. Int J Food Microbiol 80:47–53

51. Lucero P, Peňalver E, Moreno E, Lagunas R (2000) Internal trehalose protects endocytosis from inhibition by ethanol in *Saccharomyces cerevisiae*. Appl Environ Microbiol 66:4456–4461

52. Verbelen PJ, De Schutter DP, Delvaux F, Verstrepen KJ, Delvaux FR (2006) Immobilized yeast cell systems for continuous fermentation applications. Biotechnol Lett 28:1515–1525

53. Kotarska K, Czupryński B, Kłosowski G (2006) Effect of various activators on the course of alcoholic fermentation. J Food Eng 77:965–971

54. Birch RM, Walker GM (2000) Influence of magnesium ions on heat shock and ethanol stress responses of *Saccharomyces cerevisiae*. Enzyme Microb Technol 26:678–687
55. Mayalagu S, Patturajan M, Chatterji D (1997) The presence of two tightly bound Zn^{2+} ions is essential for the structural and functional integrity of yeast RNA polymerase II. Gene 190:77–85
56. Rees EMR, Stewart GG (1999) The effects of increased magnesium and calcium concentrations on yeast fermentation performance in high gravity worts. J Inst Brew 103:287–291
57. Dombek KM, Ingram LO (1986) Magnesium limitation and its role in apparent toxicity of ethanol during yeast fermentation. Appl Eviron Microbiol 52:975–981
58. Magonet E, Hayen P, Delforge D, Delaive E, Remacle J (1992) Importance of the structural zinc atom for the stability of yeast alcohol dehydrogenase. J Biochem 287:361–365
59. Filipović-Kovačević Ž, Mikšaj M, Berčuk N, Jukić M (2002) Amperometric biosensor for monitoring respiration activity of *Saccharomyces cerevisiae* in the presence of cobalt and zinc. Food Technol Biotechnol 40:111–117
60. Stehlik-Thomas V, Grba S, Runjic-Peric V (1997) Zinc uptake by *Saccharomyces cerevisiae* and its impact on alcoholic fermentation. Chem Biochem Eng Q 11:147–151

Chapter 33
Utilizing Bamboo Biochar for Carbon Sequestration and Local Economic Development

Michael Hall

Abstract This chapter explains the diverse benefits, the long-term stability, and the economic efficiency of using bamboo biochar as a means to sequester carbon while improving the local environment and economy. It involves Master's students from the Department of Design Strategy at Kyushu University, Undergraduate and Graduate students from the Department of Agriculture at Kyushu University, local volunteer *Satoyama* members, and support from the Japan Biochar Association. In this initial stage of the project, the students conducted a survey of people living in Fukuoka, Japan, to determine their general knowledge about the environment and the carbon credit scheme, and their interest in buying pesticide-free vegetables in order to determine if environmental education and promotion are necessary for the success of the project's goal of using biochar as a means for carbon sequestration and marketing strategy for vegetables. Results showed that there is no knowledge about the carbon credit scheme, only some general environmental awareness, and modest interest in buying pesticide-free biochar grown vegetables if more expensive than the ones grown under normal conditions. Therefore, the next step will be to develop effective materials, carry out events to educate and promote the positive impacts of the system, and develop production methods that maintain a competitive price to widely used pesticides.

Keywords Bamboo biochar • Carbon sequestration • Project-based learning

M. Hall (✉)
Kyushu University, 4-9-1 Shiobaru, Minami-ku, Fukuoka, Japan
e-mail: mwhall@design.kyushu-u.ac.jp

Acronyms

CCS   Carbon capture and storage
CEC   Cation exchange capacity
EC   Electric current (in soil)
MLITT   Ministry of land, infrastructure, transport, and tourism
NGO   Nongovernment organization
NPO   Nonprofit organization
PETM   Paleocene-Eocene thermal maximum
PDCA   Plan, do, check, act
SWOT   Strengths, weaknesses, opportunities, threats

33.1 Introduction

The effects of climate change are complex and comprehensive. The mechanisms triggering the change have sparked debate as to whether they are due to a natural cyclical event or human activities. Whichever side of the argument one takes is less relevant to the fact that the earth is responding in extreme ways to an increase in carbon dioxide (CO_2), nitrogen dioxide (NOx), and methane (CH_4) levels. The impact affects our health, safety, and human sustainability. The WHO estimates that 166,000 deaths and 5.5 million disability-adjusted life years were attributable to climate change in just one year [1]. A study that compared Paleocene-Eocene thermal maximum (PETM), 55.9 million years ago, provides an accurate baseline to determine a greenhouse gas profile. The results indicate that the rate of carbon released into the atmosphere is occurring ten times faster than in our ancient past [2]. Research on how our safety is at risk when extreme climate conditions exist was conducted to determine the correlation between climate change and population decline through war and disease [3]. Data from China and Europe covering AD 1,400–1,900 uncovered a significant correlation between climate change and the outbreak of armed conflicts in part due to the decrease of agricultural output during extreme long-term cold periods. The study found two major peaks in population decline: one in the seventeenth century and the other in the nineteenth century. In addition to wars, famine and epidemics during these cold periods also contributed to the high mortality rate. The future question is how global warming will affect agricultural production. Historically warmer periods have brought about better crop yields, but as recent research indicates, extreme and prolonged heat waves are having more negative impacts than in the past [4]. One example is the record-breaking temperatures and drought in Texas. According to government estimates, crop and livestock damages were estimated at nearly $8 billion in 2011. Yields for corn, cotton, and wheat decreased by approximately 50 %, and the drought continues adding more economic damage [5].

According to the International Energy Agency, if the current trend of dependence on coal and oil is not addressed more aggressively and replaced by

renewables then the goal to limit global warming to 2 °C range will be impossible. The 2012 Executive Report highlights the need to increase carbon capture and storage (CCS) techniques and facilities in order to reach this goal at the current increasing CO_2 levels [6]. There are various methods to capture carbon and inject it back into the ground, but they are all very costly, and as yet, there are no commercially viable CCS plants. One method is to burn coal or gas and capture the CO_2 in specially equipped plants, which then convert it into liquid. This liquid is then injected into a deep saline aquifer, which has been drilled to around 1,000–2,500 m deep. The cost of constructing these high-tech power plants, the conversion from a gas state to a liquid one, and the extensive long-term monitoring to ensure that there is no release into the drinking supply have so far proved unsustainable without large government subsidies. The United Kingdom, the United States, and China have test plants in operation, but commercialization to become an effective carbon sequestration method cannot be considered a viable solution for the present.

33.2 Background

The project in this chapter introduces biochar, which is a carbon sequestration method that has been proven to be stable for centuries, cost effective, and environmentally sustainable and safe. What is biochar? It is not a replacement for organic or inorganic fertilizers; however, it is an effective soil amendment that is thermally modified by either slow or fast pyrolysis in a no/low oxygen state using a wide variety of biomass feedstocks and municipal wastes. The carbonization of biomass at temperatures above 300 °C fixes carbon that would decay under normal conditions and release CO_2 and CH_4 back into the atmosphere.

Biochar as a soil amendment dates back to thousands of years. In Japan, the mention of rice hull charcoal can be found in the *Nogyo Zensho* (Encyclopedia of Agriculture) written by Yasusada Miyazaki. He wrote that mixing charcoal rice husks with manure and allowing it to mature improve crop yields [7]. Longevity is an essential criterion for any method to effectively sequester carbon. Proof of its durability lies in the discovery of a carbon-rich black soil called *Terra Preta* in Portuguese, discovered in 1870 by an American geologist in the Amazon basin. This and other tropical areas usually only have nutrient-poor ferralsol, so his discovery surprised not only him but also other researchers. Further research uncovered that natives as far back as 8,000 BC produced this high-carbon and nutrient-fortified soil. This remnant anthrosol from pre-Columbian settlements is still highly productive because of its high cation exchange capacity (CEC), suitable ph level, and high concentration of phosphorous, all of which are necessary for healthy plant growth [8]. Even with this long history, its agricultural benefits were pretty much forgotten, and it was not until 1966 when Wim Sombroek, the father of biochar, wrote a book titled *Amazon Soils* about how biochar could be used to restore nutrient-poor soil in poverty-stricken nations to improve their crop yields

and help alleviate starvation. In1992 his work drew further attention to biochar as an effective carbon sequestration method [9]. Recent data on the rising CO_2 and methane (CH_4) gas levels has helped increase recent interest in biochar as a sequestration alternative.

Its unique properties provide soil-enhancing qualities that separate it from the charcoal used for cooking and improving agricultural production. Its graphitic domains create a porous structure, which provides a high surface area that harbors beneficial nutrients, bacteria, and fungi and gives it a unique water retention capability [10]. In a small way, it also reduces secondary CO_2 releases by reducing the production and transportation of fertilizers. In addition, it acts as a water purifier and water retainer that binds the nutrients to the soil preventing leaching into the groundwater and polluting aquifers and tributaries. One example is its ability to retain nitrogen, which supports healthy plant growth, and prevents it from leaching into rivers from farmland. This phenomenon has been responsible for creating dead zones in ocean areas near large river tributaries like the Mississippi in the United States [11]. Another example is its ability to retain CH_4, which is one of the major contributors to global warming [12]. According to recent studies, biochar acts as a long-term CCS [13]. One study estimates that 10 % of anthropogenic carbon emissions can be mitigated by redirecting as little as 1 % of net yearly plant uptake into biochar [14]. The International Biochar Initiative (IBI) has produced four scenarios using biomass from agriculture and forestry that would otherwise be waste and turn it into biochar using the slow pyrolysis method, which carbonizes biomass at 40 % efficiency. According to even the most conservative scenario, if biochar production using waste biomass materials is carried out on a worldwide scale, one "wedge" [15], which is equal to 1 Gton per year, can be accomplished by 2054 [16]. Considering these facts about biochar it should be considered by governments as an effective carbon sequestration method and be included in the carbon credit scheme, but unfortunately, it is only under review.

The feedstock can be any non-contaminated waste organic material, but the most common are animal manure, wood, and, in Asia, rice husk and bamboo. The molecular structure is influenced by the feedstock and method of pyrolysis. Fast pyrolysis occurs at temperatures from 700 °C and above and in a much shorter time than slow pyrolysis. The main purpose is to derive syngas and biofuels from the biomass, whereas the slow method is carried out to produce biochar. Even at the lower temperatures from 300 to 550 °C, gas is released, and depending on the type of pyrolysis vessel used, it can provide further energy to complete the burn to create a closed loop process that prevents any release of CO_2. Wood vinegar can also be collected in the more advanced kilns, and it is used to improve the soil and protect plants from invasive insects [17]. Biochar production in the United States and Australia has been increasing recently using large-scale pyrolysis machines, some of which can be transported to the field by large flatbed trucks. Contrarily, in Asia, a majority of pyrolysis kilns are of small scale because fields are small and the demand is much less than in the United States and Australia.

This project has three major goals: one is to promote the use of biochar to improve the local economy and environment through sequestering carbon; next is to promote environmentally friendly biochar grown vegetables by home gardeners and farmers; and the last is to utilize local and university tacit knowledge to provide university students with a project-based learning environment that adds social value. It is hoped that the benefits biochar can bring will attract young family members to continue the family farming business as was the norm in past generations, reduce the overgrowth of bamboo to restore forest to a healthy state, which can support more wildlife and native foliage, and attract young city people to move to a healthy country lifestyle, thereby supplying more local income and tax revenue.

As mentioned earlier, carbon credits are not available for bamboo biochar as yet, but a similar project in Kameoka City in Kyoto Prefecture has built a strong network of participants including prefectural and city government staffs, local volunteers, the local Coop, corporations, and Ritsumeikan University students [18]. The scheme is gaining more support and interest each year, so public awareness about reducing CO_2 emissions is improving. The major difference between the two projects is the donations by corporations. The Itoshima project prefers not to engage with corporate donations, and instead, rely on students and local volunteers to drive the project forward. Being dependent on donations poses the risk that during an economic recession donations will cease, thereby endangering the project. Japan is currently in a recession and the government's huge debt presents serious challenges in the years to come. However, even in a difficult economic situation, projects like these provide essential environmental education and civic action at a low cost.

33.3 Materials and Methods

Japanese Timber Bamboo (*Phyllostachys bambusoides*), which is a prevalent species throughout Japan and China, is used for construction scaffolding and furniture because of its straight thick-walled culm, and provides a sustainable source of material for this project because of its resistance to disease and tenacious growth. Its rhizomes spread out in a wide radius and reach a maximum height of 23 m and 15 cm diameter. Bamboo shoots appear in early spring, and can grow 100 cm a day [19]. The *Satoyama* volunteer members cut the new growth in August because when it is cut at this time, it kills off new rhizome growth, which is important for forest maintenance. The hillsides in Itoshima are overgrown with bamboo, so this method will not create a problem for a sustainable supply.

The cut bamboo is dried from 6 to 12 months to ensure a smoother and quicker burn during pyrolysis. Then, it was cut and split into roughly 1.5 m sections put in the Smokeless Moki Carbonizing Kiln exhibited in Fig. 33.1 in a crisscross layered manner to ensure an efficient burn. During the pyrolysis, extra bamboo planks are

Fig. 33.1 Biochar production using a Moki Smokeless Carbonizing Kiln (Moki Manufacturing Co. Ltd.)

added to increase the total volume. After reaching the proper state of carbonization (about 20 min), the fire is extinguished. It is doused with about 40 l of rainwater to terminate the carbonization and prevent it from turning to ash. Ample water also needs to be applied after the fire is extinguished because it has the potential for spontaneous ignition. There are many kinds of pyrolysis machines: kilns, retorts, colliers, and small-scale stoves that can produce biochar while used for cooking. The Moki Smokeless Carbonizing Kiln uses the slow pyrolysis method. During any of those processes it is important to keep the oxygen in the vessel to a bare minimum and the temperature between 400 and 550 °C to assure high-quality biochar [20]. The Moki Kiln with its simple, but effective, shape is used because of its mobility, efficient production capability, and low cost compared to high-tech kilns. Mobility is essential because bamboo in Japan is usually found on steep hillsides, so it is difficult to transport off site. Conducting onsite pyrolysis vastly reduces the labor needed to transfer the heavy bamboo to the burning site, thereby improving cost-effectiveness and reducing the carbon footprint. The photo appears to be an open bonfire, which would include lots of oxygen that fuels the large flame; however, the cone shape and stainless steel reflect the heat off the wall to the center, and that forces conductive heat downward creating a low oxygen condition. The bottom of the kiln is buried in the soil to prevent any oxygen supply coming from the bottom (Figs. 33.2 and 33.3).

Fig 33.2 Map of Itoshima
(Itoshima Government)
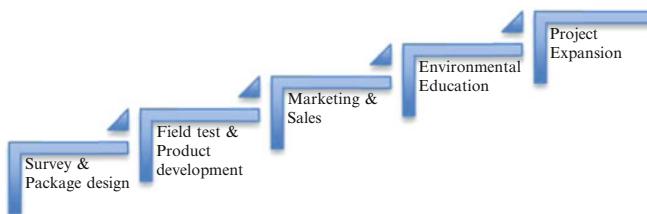
Fig 33.3 Map of Japan
(MLITT)

33.3.1   Location

Itoshima City (33°35′23.95″ N; 130°11′34.24″ E) was chosen for two main reasons: First, Kyushu University built its new campus in the northeastern part of the city and is eager to develop programs that benefit the local community; second, the author has lived in the city for many years and wants to support community development. It has a population of a little over 100,000 [21], and is located on a peninsula with a beautiful ocean, hills, and rice paddies. The main employment sector is divided into fishing and farming followed by an increasing number of service-related companies. It provides a good case study because it represents a typical rural area in Japan facing an increasing elderly population unable to continue farming operations, an inability to maintain hillside forests, and a local government with limited financial resources to invest in economic development projects. Twenty-one percent of the city's population is 65 years or older, which is roughly the same as the national average. If this system proves successful in Itoshima City, it has potential for a wider nationwide application.

Fig. 33.4 Itoshima carbon minus bamboo biochar project scaffold scheme

Table 33.1 SWOT analysis carried out in 2011

Strengths	*Weaknesses*
• Sustainable supply	• Free market access
• Low-cost material	• Low consumer demand
• Multi-faceted applications	• Labor intensive
• Improves hills and fields ecosystems	• No standardization
Opportunities	*Threats*
• Local carbon credits	• Improper application
• Few competitors in the agriculture and home garden sector	• Misinformation leading to loss of brand trust
• Biofuel production	• Restrictive laws
• Improved local economy	
• Expanded university-local networking	

33.3.2 Project-Based Learning

The project is divided into semesters, but the members remain the same for each one, and each of the Master's students from the Department of Design Strategy receives four credits for each semester. Each class meets for 90 min at the university, but it also involves extracurricular fieldwork producing biochar, conducting surveys, and meeting the local *Satoyama* volunteers. Each stage depicted in Fig. 33.4 goes through a continuous process of planning, do, check, and act (PDCA) cycle to stimulate creative student input and project improvements. Only three students participated for each of the 2 years, but this project in the Department of Design Strategy usually has a low teacher-to-student ratio.

In the first year (2010–2011) the content focused on marketing approach through a SWOT analysis (Table 33.1), and sales and distribution research even though there are few current competitors and the ones that exist have poor packaging and promotion strategies, which seemed to provide some business potential; however, the SWOT analysis also showed that biochar production and sales are at risk because competitors have free market access due to the lack of patent protection; therefore, it seems too risky to invest large amounts of capital for high-tech machinery and staff. However, from a university-community standpoint, the opportunities to improve relations and the local economy are great. The university

Fig. 33.5 One pot portion
disposable container

staff and students are not allowed to profit from any project, and so any gains
acquired through the sale of biochar can be funneled into the Satoyama group,
which then is more able to help local elementary and junior high school students
learn about agriculture and nature. Another advantage is that the bamboo used to
produce biochar in this project is currently free of charge because the local
Satoyama volunteers cut and transport it to the site as a part of their hillside
protection efforts, but for a large constant supply, which is needed for commercial
production, labor, transportation, and packaging costs must be considered in future
cost calculations. Cutting, transporting, and producing biochar are labor intensive
because the bamboo is located on fairly steep hills in Japan, and grows to heights of
23 m, with many branches, making it difficult to handle after cutting. Even though
pyrolysis is fairly quick (20 min per batch), the splitting of bamboo is very labor
intensive, so an easy and efficient method using a specially designed mobile
machine is another area the author is going to include in the next phase.

During the second school year (2011–2012), students focused on package design
and conducted a market survey to determine citizens' awareness of the issues and
attitudes toward the environment and food purchasing. The students conducted a
survey of Fukuoka City citizens about their vegetable-buying habits and knowledge
about the carbon credit scheme, CO_2, and other significant environmental issues
related to climate change. They also presented a proposal for two types of packaged
biochar: one for pure bamboo biochar, and the other containing a mix of organic
material and biochar. Both target home gardeners. Results from two specific studies
that analyzed the viability of a biochar business as an agricultural supplement
suggest that a business model focusing on the home gardener market has better
potential than the one focusing on large-scale farms [22, 23].

Figure 33.5 illustrates the single pot portion design for pure power bamboo
charcoal. The package is designed to break in the middle to allow for easy applica-
tion without consumers having to touch the biochar. Research shows that the
maximum percent of biochar for effective soil amendment is in the range of
3–5 % and should never exceed 10 %, so the students calculated the amount of
soil needed for the most commonly purchased flowerpot size, which is 18 cm wide

Fig. 33.6 Design strategy
student's original logo
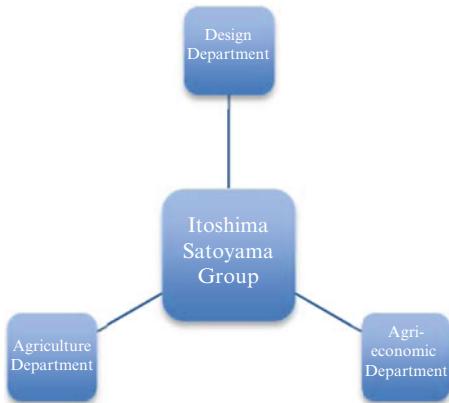
and 14 cm high, and holds roughly 400 g of soil (dry weight) when creating a package that holds 20 g of bamboo biochar. Students felt that this compact size was not only easy to handle, but the breakaway middle design provides a convenient, non-spill delivery. It also maintains a safe level of 5 % biochar-to-soil ratio for the popular sized pot. Instructions, benefits, and a pot size diagram for other sizes were not included on the design, but need to be included to make sure that the purchaser maintains the proper percentage of biochar-to-soil ratio for optimal growth, and inform them about the benefits of biochar soil amendment.

The generic name "biochar" in Fig. 33.6 will be part of the next phase's assignment. The new project members will propose three different brand names and three new logo designs and then conduct a survey in Fukuoka Prefecture to determine a strong brand name and image. In addition, attitudes toward home gardening activities, purchasing habits for potting soil and fertilizer for their gardening needs, and the size of pot usually purchased or size of the home garden will be surveyed.

33.4   Results and Discussion

As mentioned in the Project-based Learning section, students conducted a survey of people living in Fukuoka, Japan, to determine the general knowledge about the environment: for example, the level of understanding about the carbon minus and the carbon credit scheme in Japan, and their daily activities to protect the environment. In addition, questions about their buying habits for vegetables were surveyed. The results indicate that environmental awareness activities and new promotion strategies are necessary elements for the success of the project's goal of using biochar as a means for carbon sequestration and the proposed marketing strategy for biochar grown vegetables. For the questions on carbon credits and carbon minus scheme, only 5 out of the 68 respondents knew about either of them. However, there was strong interest in buying vegetables that could reduce CO_2. Forty-eight percent said that they would buy those vegetables even if they were more expensive than normally grown ones. From a marketing and sales viewpoint, 80 % said that they

buy vegetables at a supermarket. Initially, it was hoped that Japan Agriculture Coops and small shops could be the major distribution chain, but this strategy will have to be modified. On the positive side, AEON, the major supermarket chain, is looking for methods to reduce its CO_2 footprint, which should allow for selling future products from this project, and wider promotional opportunities.

As of May 2012, the project has added additional graduate and undergraduate students and faculty from the Department of Agriculture at Kyushu University. One group is from agro-environmental science and the other from the agriculture and resource economics division. Technical knowledge from agriculture specialists, a thorough economic and business model, and an attractive design and branding strategy are essential for this project to succeed, Fig. 33.7. The addition of the Department of Agricultural members has produced a strong collaborative triangle of knowledge, and fulfills the author's efforts to promote interdisciplinary research within the university.

The project has moved up a step by making a test field. All the students from project along with Satoyama members recently made enough bamboo biochar to make a 60 cm wide, 80 cm high, and 20 m long test row planted with sweet potatoes. A photo of the design and agriculture students planting sweet potato seedlings in test field is shown in Fig. 33.8. Three other rows were planted with no biochar as a control group. The pH of the soil from various locations both surface and at a depth of 15 cm was tested prior to planting and it was found to be overly acidic (4.6); therefore, the addition of the alkaline bamboo biochar with a pH of 9.7 will help improve the soil pH to reach the ideal range of 5.6–6.5 [24]. However, the electrical current (EC) reading was significantly higher than normal, which could indicate that an excess of substances in the soil may affect the flavor or impair healthy growth. After harvesting in October, samples from the biochar and control group will be analyzed by the Agriculture Department for sweetness and vitamin content. This planting and testing cycle will continue for 3 years, monitoring the changes to the soil and effects on the sweet potatoes before attempting a full-scale marketing and sales effort.

After the initial field tests are completed, and the results are recorded, educational materials for elementary, junior high, and high school students will be

Fig. 33.8 Design and agriculture students planting sweet potato seedlings in test field

produced and distributed to schools throughout Fukuoka Prefecture. Events that involve using biochar in fields and home gardens will be held for those students to increase their knowledge and awareness to the importance of carbon sequestration and how individuals can reduce CO_2 emissions. In order for the project to expand to its full potential, a management organization as an NPO or an NGO should be considered. The current volunteer-university cooperation style cannot provide the full-time participation needed to operate a successful larger scale production.

The response to this project by the students and Satoyama members has been very positive about the mission, goals, and actions because they have become more aware of the importance of bamboo as a sustainable resource, carbon sequestration, and collaborative teamwork in the field in order to improve the local environment.

33.5 Conclusions

The biochar produced in this project provides a safe low-tech approach that effectively sequesters carbon. The project-based learning approach has provided new experiences for students to learn about the environment, local citizens' attitudes about organic food-buying attitudes, and acquired tacit knowledge from

Satoyama members. The SWOT analysis provided students with vital hints into the current situation for the biochar market, and possible directions for package design and marketing strategies in the future.

References

1. Campbell-Lendrum D, Woodruff R (2007) Climate change: quantifying the health impact at national and local levels. In: Prüss-Üstün A, Corvalán C (eds) World Health Organization, Geneva. WHO Environmental Burden of Disease Series No. 14. Annex, p 59
2. Cui Y, Kump L, Ridgewell A, Charles A, Junium C, Diefendorf A, Freeman K, Urban N, Harding I (2011) Slow release of fossil carbon during the palaeocene-eocene thermal maximum. Nat Geosci. 4(7):481–485
3. Zhang DZ, Brecke P, Lee H, He Y, Zhang J (2007) Global climate change, war, and population decline in recent human history. PNAS 104(49):19214–19219
4. Furuya J, Kobayashi S, Meyer S (2011) Economic impacts of climate change on global food supply and demand. In: Lal R et al (eds) Climate change and food security in South Asia, Springer, Netherlands, p 377–394
5. Anderson D, Welch M, Robinson J (2012) Texas's driest year on record. Choices and the agriculture and applied economics association, 3rd Quarter 27(3):1–3
6. International Energy Agency (2012) In: World Energy Outlook, p 3
7. Miyazaki Y (1697) Nogyozensho (Encyclopedia of Agriculture) Vol. 1 in Nihon Nousho Zenshu, vol 12. Nousangyoson Bunka Kyokai, Tokyo, pp 91–104
8. Lehmann J, Pereira J, Steiner C, Nehls T, Zech W, Glaser B (2003) Nutrient availability and leaching in an archaeological anthrosol and ferralsol of the Central Amazon basin: fertilizer, manure and charcoal amendments. Plant Soil 249:343–357
9. Wayne E (2012) Conquistadors, cannibals and climate change: a brief history of biochar. Pro-Natura International. http://www.pronatura.org/wp-content/uploads/2012/07/History-of-biochar.pdf
10. McLauglin H (2010) What is biochar? In: Taylor P (ed) The Biochar Revolution. Global Publishing Group, Australia, p 67
11. Laird D, Fleming P, Davis D, Horton R, Wang B, Karlen D (2010) Impact of biochar amendments on the quality of a typical Midwestern agriculture soil. Geoderma 158:443–449
12. Baranick M, McElwee D, Zazycki M (2011) Biochar feasibility study: exploring the environmental, social, and economic value of a biochar business in the Methow Valley. Seattle University, Seattle, p 7
13. Bell MJ, Worrall F (2011) Charcoal addition to soils in NE England: a carbon sink with environmental co-benefits. Sci Total Environ 409:1704–1714
14. Lehmann J, Joseph S (2009) Biochar for environmental management: an Introduction. Biochar for environmental management. Science and technology. Earthscan Publishers Ltd., London, pp 1–12
15. Pacala S, Socolow R (2004) Stabilization wedges: solving the climate problem for the next 50 years with current technologies. Science 305:968–972
16. International Biochar Initiative (2011) How much carbon can biochar systems offset—and when? http://www.biochar-international.org
17. Hayashi R (1990) Effects of purified wood vinegar as soil amendment and leaf surface spray. In: Sugiura G et al (eds) The research report on the new uses of wood charcoal and wood vinegar, Technical Research Association for Multiuse of Carbonized Materials, Tokyo p 331–341
18. McGreevy S, Shibata A (2010) A Rural Revitalization Scheme in Japan utilizing biochar and eco-branding: the carbon minus project, Kameoka City. Ann Environ Sci 4:11–22

19. Japanese Timber Bamboo—Phyllostachys bambusoides. Complete Bamboo http://www.completebamboo.com
20. Gaskin JW, Steiner C, Harris K, Das KC, Bibens B (2008) Effect of low-temperature pyrolysis conditions on biochar for agricultural use. Trans ASABE 51:2061–2069
21. Itoshima City web site http://www.city.itoshima.lg.jp/site/prof/jinkou20110727.html. Accessed 20 Mar 2012
22. Brown T, Wright M, Brown R (2011) Estimating the profitability of two biochar production scenarios: slow pyrolysis vs. fast pyrolysis. Biofuels Bioproducts Biorefining 5:54–68
23. Baranick M, McElwee D, Zazycki M (2011) Biochar feasibility study: exploring the environmental, social and economic value of a biochar business in the Methow Valley. Seattle University, Seattle, pp 1–30
24. Lemer R (2011) The sweet potato. Department of Horticulture. Purdue University Extension Service, West Lafayette, Indiana

Chapter 34
The Integrated Solid Waste Management System: Its Implementation and Impacts Towards the Environment

O. Norazli, A.B. Noor Ezlin, M.Y. Muhd Noor, C. Shreeshivadasan, and O. Nor'azizi

Abstract In Malaysia, the present practice of solid waste management has affected the valuable resource wastage, the economy, the environment and the society's health. Past decisions on waste management strategy and the structure of waste management system have relied on the waste management hierarchy. The hierarchy gives the following order of preference, i.e. waste reduction, reuse, material recycling, composting, incineration with energy recovery, incineration without energy recovery and landfilling. However, such use of a priority list for the various management options has serious limitations. Technically, the hierarchical concept is far from scientific for the reason that none of the management technology resulted in an optimal result. Due to this reason, there is a need to radically improve solid waste management practices. Recently, the Malaysian Government Policy has outlined an emphasis on the policy and the management of solid wastes in which it has to be implemented in holistic and well-planned manners. In order to implement the strategy, the concept of integrated solid waste management (ISWM) is considered in this study. The integrated waste management system starts from the point of accumulation, i.e. residential areas, commercial buildings and industrial premises, until the point of disposal, i.e. waste disposal sites. The mediatory components between the two points according to their order are the pre-sorting technology, collection, central sorting, recycling, biological treatment, thermal treatment and,

O. Norazli (✉) • C. Shreeshivadasan • O. Nor'azizi
Universiti Teknologi Malaysia, Kuala Lumpor, Malaysia
e-mail: norazli@ic.utm.my; shreeshivadasan@ic.utm.my; azizi@ic.utm.my

A.B. Noor Ezlin
Universiti Kebangsaan Malaysia, Bangi, Malaysia
e-mail: ezlin@vlsi.eng.ukm.my

M.Y. Muhd Noor
Malaysian Nuclear Agency, Bangi, Malaysia
e-mail: muhdnoor@nuclearmalaysia.gov.my

finally, landfilling. The advantages of ISWM techniques are that it can reduce the effect of pollution on the environment and is able to increase country economy. The less pollutants such as CO_2, CH_4, CO, NH_3, SO_2, HCI and others escape to the environment, and the less environmental impact such as global warming, acid rain, depletion of ozone layer and climate change is created. This chapter discusses the practices of ISWM towards the environment quality enhancement. From the reviews, it reveals that the environmental impacts can be reduced if an integrated, systematic, technologically enhanced and innovative solid waste management system is created.

Keywords Solid waste management • Malaysia • Economy • Environment • Society • Health • Waste management hierarchy • Waste reduction • Reuse • Material recycling • Composting • Incineration • Energy recovery • Landfilling • Thermal treatment • Acid rain • Depletion of ozone layer • Climate change

34.1 Introduction

Solid waste generated is linked with the rapid growth of population, industry, urbanisation and population standards in the area. Solid waste generated must be handled with the best technology that is focused on environmental sustainability. To achieve the objectives of environmental sustainability, technology management should expect more than just a safe disposal as well, trying to get back the source of the waste generated. The objective of management should examine the root problem, while the technology will have to be adapted in line with the goal of achieving environmentally friendly forms of management. In Malaysia, the waste management strategy in the past was more focused on waste management system based on the concept of hierarchy. In summary, the proposed hierarchical system according to the priority starts with the waste reduction technology, reuse, recycling, composting, incineration with energy production, incineration without energy production and finally landfill technology. However, solid waste management based on the concept of hierarchy has several disadvantages. This is because there is no single technology capable of producing optimum management effect to the environment [30]. Given this, strategies and policies on solid waste management practices need to be changed in Malaysia on an urgent basis.

In general, an effective solid waste management system should have the following characteristics: environment-friendly, economy-friendly, integrated, strategic marketing and scale (need for a uniform quality of recycled materials and energy) including variable [30]. Environment-friendly management features mean it can minimise the impact of the management system of energy use and pollution on land, sea and air. To achieve the design of environmentally friendly waste management, integrated solid waste management (ISWM) should be implemented. The concept of an integrated system includes the system of waste collection and segregation, followed by one or more management options such as recycling, thermal treatment technology or landfill technology [30].

An integrated management system combines waste flow, system of collection, treatment and disposal with the objectives to achieve benefits for the environment to be accepted by the society. An important aspect of the system is the method to minimise the amount of accumulated solid wastes. Therefore, the manufacturing technology has to be upgraded in which each component created and designed is stronger and lighter and able to reduce the usage of raw materials. Another way to manage solid wastes is through producing energy from the incineration method. The solid wastes will be incinerated in a special furnace chamber and the energy generated is used to produce steam and electricity. This process is able to reduce 90 % of solid wastes. Inert compounds from the chamber will be sent to sanitation disposal sites. This integrated approach will reduce disposal sites' burden and open an opportunity to a new technology in managing solid wastes. The objective of this chapter is to elaborate the concept of ISWM and discuss the impact of the system towards the environment.

34.2   The Solid Waste Management Concept

The solid waste management system can be implemented either as in gradual implementation of technological parts of the system or as in the whole system in totality. However, if only one particular technology is considered at one time, there is a probability of that particular technology to negatively affect other options in the system. Hence, to implement the whole system at once it is necessary to obtain an effective management system [8]. The implementation of the whole system is known as the ISWM system [6, 14, 30].

The integrated system concept includes collection and waste sorting systems followed by one or more of these management technologies:

(a) Regaining secondary materials (recycling) in which the technology requires effective and suitable waste sorting system facilities.
(b) Biological treatment for organic materials in which this technology will produce composite compounds that can be marketed and reduce the waste volumes at the disposal sites including producing energy from methane gas.
(c) Thermal treatment in which this technology will reduce volumes and produce energy.
(d) Landfilling in which this technology is able to increase the amount of land reclamation and reduce the effects of pollution [30].

The concept of the system has to be integrated towards the management of waste materials, waste sources and methods of collection including methods of treatment. However, in order to achieve an optimum effectiveness of the management, the main highlighted technique is the method of waste reduction followed by the integrated management strategy approach. The waste reduction method, among others, is the re-evaluation of manufacturing concepts of a product by manufacturers such as the manufacturing process, plants' apparatus or products' formula [23] including purchasing necessities of a product or re-using products by

users [3]. As for the integrated management strategy, it can be made better by combining all the present management options [4].

Fundamentally, the integrated management concept combines a holistic and an environment-friendly approach. An environment-friendly approach means it needs to be friendly towards the environment, the economy and the users, whereas holistic is in the sense that it illustrates the whole management system from the point of accumulation until the point of disposal. According to McDougall et al. [14], the advantages of being holistic are the following:

(a) The concept is able to give a holistic picture of the overall waste management process. The overall picture of the system is important in planning for effective management strategies as compared to describing one particular part at one particular point of time.
(b) Basically, the overall parts of the system originate from the same ecosystem. Thus, rationally, the environmental impacts have to be described in a holistic manner. If only one particular part is considered in reducing the environmental burden, there is a possibility that the other parts in the system may experience an increment in the environmental burden.
(c) The holistic picture of the whole system ensures an effective and economical system of operation. For each part of the system, the value-added debit and credit cost can be evaluated.

34.3 The Integrated Management System Components

The integrated management system starts from the initial point of waste accumulation by accumulators from residential areas, commercial buildings and industry premises until the point of disposal at the waste disposal sites. The in-between components between the two points, according to their list of order, are the pre-sorting technology, waste collection, central sorting, recycling, biological treatment, thermal treatment and finally landfilling. The following subtitle of this chapter further elaborates on each of the management system component.

34.3.1 Pre-sorting

Pre-sorting involves sorting wastes according to their categories after they have been accumulated. Pre-sorting is the most important component in the waste management system because it can reduce waste volumes and separate toxic and dangerous wastes from the others [22]. The effectiveness of pre-sorting process depends on the awareness and the sorting techniques of the accumulators. Accumulators have to be exposed and educated with the correct waste sorting techniques. For example, in Japan, every accumulator is provided with brochures that contain information on the initial stage of waste sorting [10].

Pre-sorting process can also be carried out by garbage collectors. In brief, wastes can be categorised into four, i.e. dry recyclable materials, bio waste and garden wastes, hazardous materials and bulky wastes. If the waste-collecting vehicles are divided into several parts, these wastes can be sorted at an early stage. Therefore, if both methods are applied in our country, the effectiveness of pre-sorting process can be further improved.

34.3.2   Waste Collection

The waste collection method is divided into two. The first is the "bring method" and the second is the "kerbsite collection method". In the first, accumulators will bring their wastes to the central sorting and in the latter garbage collectors will collect wastes from the curb-sides. In Malaysia, both methods are practiced mandatorily in which waste collection is carried out based on the nature of the areas and the facilities provided. Some of the applied collection techniques are waste collection from home to home for residential areas; waste collection from barrel centre for apartments, condominiums and public areas; and waste collection from waste chambers for squatter and traditional village areas. However, there are by back centre for any accumulators who want to practice the first method.

The collection and transporting of solid wastes cover almost 60 % of the total allocated fund spent for managing solid wastes in Malaysia [21]. The types of vehicles commonly used are lorries that have open trunks and those that have compacting facilities [21]. However, there are various problems related to the waste collection system in Malaysia such as the increase of population that gives rise to the increase of the amount and types of wastes, the source of revenue that affects the technical facilities and the amount of workers, the unexecuted pre-sorting techniques and the lack of professional garbage collector contractors [9]. These problems are setbacks to the efficiency of waste collection system in Malaysia.

In order to execute an efficient collection system, an integrated waste collection technique has to be highlighted in which the "bring" and the "kerbsite" collection methods are to be practiced in togetherness in order to achieve the objectives of minimising the collection costs and reducing the environmental impacts [30]. Other factors like the usage of technologically enhanced transporters, the additional constructions of transfer stations and the usage of geographical information system (GIS) and global positioning system (GPS) technologies are some that can increase the effectiveness of the waste collection system in Malaysia [17].

34.3.3   Central Sorting

Basically, central sorting will receive wastes collected by the transporters including those brought by the accumulators. Techniques used at the centre depend on two

facilities, namely, the facilities to produce recycled materials or known as MRF sorting facilities and the facilities to produce fuel resources or known as RDF sorting facilities. The latter will sort wastes that can be burnt and those that cannot.

Recycle Energy Sdn. Bhd. (RESB) located in the district of Semenyih in Selangor is one of the companies that have both the above-mentioned facilities in Malaysia. This company acts as the waste sorting centre for the district of Hulu Langat. This centre sorts recycled materials such as plastics, metal and woods including RDF pellets, composites and bulky wastes. The sorted recycled materials will be sold to recycling centre whereas the composites will be sold to factories that will further compose the materials to become land conditioner and others. The RDF pellets will be used to generate energy.

Normally, there are two sorting methods performed at the central sorting, i.e. manual or automatic. The manual will be carried out by workers and the automatic will be carried out by sorting machines such as magnetic sorting machines that are able to sort between ferrous metal and non-ferrous metal or Eddy current separators that are able to sort between non-ferrous metal such as aluminium or cuprum from other wastes [11]. According to studies conducted by Newell Engineering Ltd. [15], the automatic sorting is more effective than the manual. This is due to the rate of sorting output in which manually, 5 tonnes per worker in a day will be generated as compared to 5 tonnes per hour if automatic sorting is applied. Manual sorting activities will also bring negative effects towards health and safety. However, in order to implement sorting centre facilities in an integrated and effective way, the automatic sorting will need to be supported by the manual.

34.3.4   Recycling

One of the effective techniques of management is by organising the management components within proximity. As an example, a recycling centre and a sorting centre that are nearby each other may reduce the cost of transporting recycled materials to be processed from the sorting centre to the recycling centre. This will indirectly reduce the environmental pollution produced by the transporters.

Recycled materials that can be processed are papers, glasses, ferrous metal, non-ferrous metal, plastics and textiles. Usually, the process of recycling papers will be done according to the quality of used papers in which those with high quality will be recycled into writing papers, printer papers, tissues and wrappers. On the other hand, those of low quality will be recycled into packing papers and cardboards. The process of recycling glasses will start with manual and automatic sorting in order to eliminate pollutants, metal, labels, etc. Then, the glasses will be crushed and sifted and later mixed with natural raw materials. This mixture is smelted and formed to produce new products. The recycling process for ferrous and non-ferrous metal basically has the same techniques as glasses [30]. Processed plastics that can be recycled are from the thermoplastic types. In its initial process,

plastics are sorted according to its resins and then they are mechanically or chemically recycled. In mechanical recycling process, the sorted plastics are crushed into pieces which then are mixed with natural raw materials to produce new products. As in chemical recycling process, the polymers will be reduced into monomers and then re-processed into polymer materials. For textiles, the recycling method is divided into two, i.e. to reuse the textiles as spent clothes, wiper cloth or filling materials and to recycle the textiles into secondary fibrous materials [30].

In Malaysia, a recycling programme was launched on January 1993 which involved 23 local authorities across the country [21]. The recycling programme strategies aim to save the cost of managing solid wastes by recycling them, to reduce the usage of natural raw materials and to protect the quality of the environment. However, the programme which initially received warm responses from the locals has now become dormant. Since the recycling technology is one of the components of the integrated management system, the authorities in this country have to reconstruct their strategies in encouraging the public to be actively involved in this activity.

34.3.5 Thermal Treatment

Incineration options, refused-derived fuel (RDF) burning and catalytic de-polymerisation process (CDP) technology are some of the ISWM technologies that use the thermal treatment concept. In short, incineration concept means to incinerate the whole mass of a solid waste in a burner and RDF burning concept means to burn only those selected materials in solid wastes that can be burnt [14]. The CDP concept is to transform mixture of plastics or other materials that contain hydrocarbon into diesel [5]. The thermal treatment concept for these three options is further elaborated in the following subsections.

Incineration (Thermal Treatment)

The incineration technology facilities are divided into three types, namely, fluidised-bed incinerator, grate incinerator and rotary combustor. These facilities will accept the whole sent wastes and then these are burnt in an incinerator chamber. The incineration process will produce residues in the form of bottom ashes and fly ashes. This process may also convert wastes into energy if the produced hot air is channelled to a boiler that can further change it into steam. The produced steam has to be reheated in order to generate energy. The higher the temperature and the pressure of the steam, the larger volume of energy generated [14].

The incineration method is able to reduce the volume of solid wastes and produce energy from the incinerated wastes. However, this activity can increase

the density of pollutants released into the environment as compared to the usage of RDF burning. This is because in incineration method the whole mass is burnt whereas in RDF burning it is done only on materials that can be burnt in the wastes. This incineration method also has another drawback, that is, the volume of energy produced from incinerated wastes is far lower than the volume of energy produced through RDF burning.

RDF Burning (Thermal Treatment)

RDF materials are produced from the mechanical sorting of wastes that can be burnt and those that cannot. RDF consists of papers and plastics sorted from the municipal solid waste in which later they are crushed, sifted, dried and then processed into fuel in the forms of RDF pellets or loose RDF. The mechanism for RDF material burning in producing energy is the same as the incineration method. However, the advantages of RDF burning as compared to incineration are the following:

1. RDF materials have higher calorific values (3,000–4,000 kcal/kg) than the municipal solid waste's raw materials (1,000–3,000 kcal/kg) which also possess uniformed burning characteristics.
2. The content of heavy metal in RDF materials is also lower than the municipal solid waste's raw materials. Thus, the needs for tools in eliminating resultant pollutants during the burning process can be reduced.
3. RDF materials have fewer wastes that cannot be burnt as compared to the municipal solid waste's. Therefore, the resulting disposed ashes can be reduced.
4. The efficiency of the whole RDF burning method is higher than the incineration method because the characteristics of RDF materials are almost the same as the characteristics of fuel [29].

Catalytic De-polymerisation Process Technology (Thermal Treatment)

CDP is one of the waste management options that use the thermal treatment approach. CDP technology is a type of biomass-to-liquid fuel technology in which this technology can produce energy in the form of synthetic diesel from solid wastes [16]. The synthetic diesel production process is similar to the natural geological process in producing fossilised fuel. The types of solid wastes that can be converted into diesel are all types of plastics including PVC and PET, leather and rubber materials including vehicle tyres; oil waste, varnish and all types of grease including transformer oil, hydraulic fluid, butemin, and tar; sterilised and dried hospital disposals, organic residues and woods; and electronic waste [24]. The benefit of using CDP technology as compared to other technologies under the thermal treatment concept is that it is able to produce high-quality diesel from solid waste sources while pollutants such as chlorine, dioxin, furan and other toxic

substances are not accumulated during the process of converting such wastes into energy [24]. However, there are by-products resulting from the CDP process, i.e. inorganic materials such as metal and glasses, that need to be modified or disposed using suitable methods.

Shajeran Resources (M) Sdn. Bhd. is one of the companies that are in the process of introducing the above technology to the Malaysian Government agencies ([16], 10 December, 2007). This German technology is under the surveillance of a company called Alphakat Engineering GmbH. According to the News Straits Times' report, this technology has the capability to produce 3,500 tonnes of synthetic diesel within a year with an investment of RM20 million. The report also stated that although the initial amount of investment was high-priced, this technology is very environment friendly and able to bring equilibrium to recent intense issues related to fuel and solid waste management in our country.

34.3.6   Biological Treatment

According to a study by Tchobanoglous et al. [27], 40–85 % of municipal solid wastes is organic wastes. The organic wastes resulting from the remaining of food and twigs can be managed using biological treatment technology. The concept is performed by digesting organic wastes using microorganisms with the presence of oxygen (aerobic) or the absence of oxygen (anaerobic) to produce stable compost materials. The by-products of the digestion are energy release, methane and carbon dioxide. The composition has a potential to reduce the total volume of wastes to be disposed. However, there are constraints in the potentials of composition method as an option to manage wastes. The constraints are the resulting pollutants due to the composition activities, the high cost to compose wastes (due to the expensive cost in producing nutrient fertilisers) and the difference in the nutrient content for every composition activity including the difficulty to market compost materials to consumers [3]. In sum, this biological treatment technology is able to produce three types of products, namely, biogas that can be converted into electrical energy, compost materials and energy.

34.3.7   Landfilling

Landfill technology is the final option in the ISWM system. This technology can be divided into two methods, namely, filling of land method and sea filling method. In Japan, both methods are practiced to dispose wastes in an absolute manner [10].

Waste central sorting, recycling centre, thermal treatment plants and composting plants each of them needs a landfill technology in order to dispose residuals

Table 34.1 Contamination of Sg. Kundang caused by pollutants in leachate that comes from Kundang disposal site at Selangor, Malaysia [2]
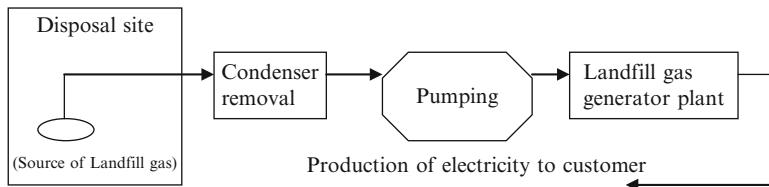
Perimeter	Level of contamination (g/day)	Level of contamination (tonne/year)
	1237.5	BOD5
COD	280440.0	102.4
TSS	2.7	9.855×10^{-4}
Hardness (CaCO$_3$)	19319.9	7.52
Cd	–	–
Cr	8.7	3.176×10^{-3}
Cu	0.135	4.928×10^{-5}
Pb	1.215	4.43×10^{-4}
Zn	2.7	9.855×10^{-4}
Mg	191.0	0.0697

resulting from every processing activities performed. Landfilling is a technique that returns formed residuals back to nature. The by-products resulting from this process are leachate and landfill gas. Leachate is resulted from the process of leaching rainwater at disposal sites and landfill gas is produced from the reactions of solid wastes at such sites. These by-products can pollute the environment if measures to monitor them from time to time are not taken. There are three types of disposal sites for the landfill method, namely:

1. Open dumping—This type of disposal site is specified for non-hazardous solid wastes in which the by-products such as landfill gas and leachate are not monitored and modified (e.g. Sungai Kembong, Semenyih disposal site in Malaysia).
2. Sanitary landfill—This type of disposal site is specified for non-hazardous solid wastes in which the by-products such as landfill gas and leachate are monitored and modified before being released to the environment (e.g. Air Hitam, Puchong disposal site in Malaysia).
3. Secure landfill—This type of disposal site is specified for hazardous solid wastes that have gone through treatment process and later these wastes will be buried at concretised disposal sites (e.g. Kualiti Alam, Bukit Nanas disposal site in Malaysia).

In Malaysia, the total amount of disposal sites until April 2007 was 261 sites in which 111 of them have been closed and the remaining 150 are still operating. 140 from 150 operating disposal sites are non-sanitary and some of them have been identified as located near to the surface water resources such as rivers, water basins and others [31]. Table 34.1 shows one of the examples of water pollution caused by pollutants from disposal sites in our country.

The main weakness of landfill technology is the presence of pollutants that are released to the environment and if this technology is considered in managing solid wastes, this means wastes as a whole are just mere wastes and they are not solid wastes that can be converted into valuable resources [7]. Nevertheless, with the

Fig. 34.1 Flow chart of energy that can be generated from landfill gas [20]
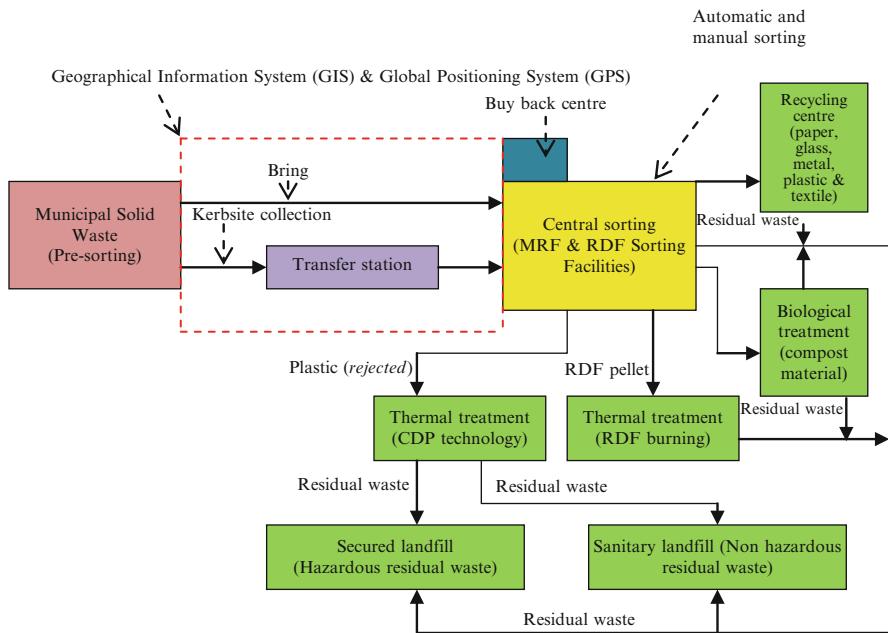
rapid development of knowledge and technology, landfill gas has been identified as able to generate electrical energy. Figure 34.1 illustrates the flow chart of energy that can be generated from landfill gas.

34.4 The Integrated Solid Waste Management Concept

Basically, an integrated management system incorporating a holistic and sustainable approach, Integrated management system starts from the point of generation by generators until the point of disposal (landfill). Intermediate components between the two points following a sequence are pre-sorting technology, collection, central sorting, recycling, biological treatment, thermal treatment and finally landfilling. To produce an efficient management system, systematic and innovative technology is necessary to consolidate all existing management technologies, and each one is better diversified technology and engineering approaches to ensure that each component is functioning effectively. Figure 34.2 shows a flow chart of the various technologies and management techniques that can be adapted to manage solid waste.

34.5 The Emission Controls

In general, the impact of the overall management system is towards human's health and the environment in which the resulting pollutants from the waste management activities will be channelled through the medium of air and water to the environment. The sources of pollutants in the integrated management system are divided into two parts, i.e. sources as the result from the usage of energy such as electricity, gas, diesel or petrol and sources as the result from the waste processing activities by each management component in the system. This presence of pollutants is known as emission. The emission resulting from the usage of energy is divided into two types which are air emission and water emission while the emission resulting from waste processing activities is categorised into three types which are air emission, water

Fig. 34.2 Flow chart for various management technologies and techniques that can be adapted in managing solid waste

Table 34.2 Water and air emission categories [30]

Air emission	Particulates, CO, CO_2, CH_4, NO_x, N_2O, SO_x, HCl, HF, H_2S, HC, chlorinated hydrocarbons, dioxins/furans, ammonia, arsenic, cadmium, copper, lead, mercury, nickel, zinc
Water emission	BOD, COD, suspended solids, total organic compounds, "adsorbable organic halides", "chlorinated HCs", dioxins/furan, phenol, ammonium, total metals, arsenic, cadmium, chromium, copper, zinc, mercury, zinc, chloride, fluoride, nitrate, sulphide

emission and residual waste emission. Table 34.2 lists the categories of emission through the medium of air and water.

The emission originating from the usage of energy such as diesel and petrol is the result of the transporting activities such as the delivery and collection of wastes from the accumulation areas to central sorting, from the central sorting to thermal treatment plants, composting plants and disposal sites including the transportation of residuals from the thermal treatment and composition plants to disposal sites. Some activities at thermal treatment plants and disposal sites may also contribute to emissions resulting from the usage of diesel. The emission originating from the usage of electrical energy is the result of the activities at central sorting, recycling centres, thermal treatment plants and disposal sites. These activities include

activities from the waste-sorting machines, sifting machines, drying machines, crushing machines, furnacing machines, etc.

As for the emission originating from the waste processing activities, it is the result of waste sorting, recycling and conversion into energy including landfill activities. Activities at the central sorting such as the process of drying, crushing and washing and the presence of leachate from collected wastes will produce emissions such as dusts, leachate, washing wastewater and residuals. The waste recycling activities such as the process of crushing, furnacing and washing will produce emissions such as dusts, volatile organic compounds, washing wastewater and residuals while activities at thermal treatment plants such as burning and producing of energy will produce emissions such as bottom ashes, fly ashes and air pollutants. For landfill activities, leachate and landfill gas are the produced emissions.

The pollution control resulting from the waste management activities can be divided into three, namely, air pollution control, water pollution control and residual disposal control. The air pollution control system acts as pollutant eliminators in gasses before they are released into air. This system is usually used at processing plants and it consists of filter bags, hydrated lime, active carbon and SNCR De-Nox system. The filter bags function as eliminators for solid particles while the hydrated lime is to eliminate acidic gasses such as hydrochloric acid or sulphur dioxide. The active carbon eliminates dioxin and heavy metals such as arsenic, cadmium, plumbum, mercury and others while SNCR De-Nox functions to eliminate NOx [18].

A wastewater treatment plant acts as a water pollution control system for wastewater resulting from waste managing activities such as leachate and washing wastewater. The treatment plant basically consists of sediment tanks, biological treatment tanks and germ disinfectants. The plant will usually eliminate parameters such as the biochemical oxygen demand (BOD), suspended solids, heavy metal and others that are in the wastewater before the water is released into waters [13]. As for the control of residual disposals at disposal sites, it is done by disposing the residuals at sanitary disposal sites for non-hazardous residuals while the hazardous residuals will have to be initially modified before disposing them at secured landfill sites.

The air pollution control caused by the waste transporting activities can be carried out by creating waste exchange stations located between the accumulation premises and the other technologies in the system, if the route between the two places is at a great distance. The transfer stations function as compressors for the collected solid wastes in order to add space on the transporters. This method can reduce the amount of the transporters' diesel usage and reduce the release of emissions into the environment.

34.6   The Impacts of the ISWM Towards the Environment

The present practices of the solid waste management have given depressing impacts on the valuable resources, the country's economy, the environment and the health of the Malaysian society. The management that only emphasises on the collection and disposal of wastes has affected the environment such as the decline of the environment's aesthetic values due to solid waste, air, water, smell and sound contaminations [12]. In order to mend and upgrade the present management practices, the ISWM is the solution for the country's solid waste management problems.

The ISWM method can contribute to the increase of a country's economy and it can reduce the impacts of pollutants to the environment if properly implemented. The reduction of an amount of energy can be made if a technologically enhanced, systematic and integrated waste collection system is practiced. This reduction can also be made if the manufacturing of a product uses secondary raw materials in addition to the natural raw materials. Secondary raw materials are the products of re-processed solid wastes. Table 34.3 shows the percentage of energy reduction, water pollution reduction and air pollution reduction when processing secondary raw materials in addition to natural raw materials as implemented in the manufacturing of a product.

Generation of energy from wastes using technologies such as RDF burning and CDP including the production of energy from methane as a result from landfill activities and biological treatment enables wastes that raise crisis to the societal livelihood to be converted into fuel that eventually becomes a basic societal need (waste to wealth). In the early 1980s, the Malaysian Government had launched the fifth fuel policy in which the re-generation of energy would become the fifth source of fuel apart from petroleum, natural gas, coals and hydro. The policy stated that in the near year of 2005, 5 % of the generated electrical energy has to have its origin from the re-generation of energy [26]. Studies widely conducted by various researchers found a biomass of an identified solid waste as one of the potential materials to achieve the above-mentioned purpose.

Briefly, an implementation of central sorting that has MRF and RDF facilities is important to reduce dependency on the country's waste disposal sites. The implementation of such can reduce 80 % of waste from being disposed at the disposal sites. This phenomenon may also reduce the accumulation of leachate and landfill gas due to the lessening volumes of wastes at the disposal sites. As a result, the environmental pollution is able to be reduced [1]. The summation from all the elaborated factors is that the environmental impacts can be reduced if an integrated, systematic, technologically enhanced and innovative solid waste management system is created.

Table 34.3 The environmental benefits from the usage of secondary raw materials [19]

Benefits to the environment	Aluminium (%)	Steel (%)	Paper (%)	Glass (%)
Reduction of energy	90–97	47–74	23–74	4–32
Reduction of air pollution	95	85	74	20
Reduction of water pollution	97	76	35	–

34.7 The Integrated Waste Management Practice in Malaysia

An amount of 30,000 tonne/day of solid waste is expected to be accumulated in our country in the year 2020 in which 45 % of them are organic wastes, 24 % plastics, 7 % papers, 6 % metal, 3 % glasses and the remaining is the other wastes [32]. In managing the increasing amount of solid waste, the waste management technologies have to be further integrated between one and another. At present, the solid waste management patterns in Malaysia are focusing more on landfill method in which it contributes 95 % of the management option and the other remaining 5 % is for the recycling technology [1].

The Tenth Malaysian Plan (from the year 2010 to 2015) has outlined an emphasis on the solid waste policy and management in which it has to be carried out in its totality and in an organised manner. In order to enhance the management effectiveness, focus must be given in upgrading the existing non-sanitary landfill sites and in building more technologically enhanced management facilities such as disposal sites, transfer stations, central sorting, recycling centres and others. In answering to the government's call, some companies in Malaysia have taken measures in creating an integrated management system. The companies are RESB located in the district of Hulu Langat, Trinekers Sdn. Bhd. located in Kuching and SPM Holdings Sdn. Bhd. located in Kota Kinabalu.

RESB Company has taken an integrated approach in managing wastes from the point of accumulation and it continues with the following list of order: technological option for waste collection, central sorting (MRF and RDF sorting facilities), thermal treatment and landfilling [18]. Trinekens (Sarawak) Sdn. Bhd. has taken these approaches: waste collection technology, recycling centres, thermal treatment using incinerators and landfilling [25]. The solid waste management approaches carried out in Kota Kinabalu include the options of waste collection, central sorting (MRF recovery facilities), recycling centres, composition centres and landfilling [7]. According to Tsiung [28], Trinekens (Sarawak) Company has been planning to further upgrade the effectiveness of its ISWM by suggesting the concept of energy production from the wastes of landfill gas and RDF burning.

In the year of 2007 and 2010, there was a convention in Malaysia called WASTE TO WEALTH in which issues related to ISWM practices were highlighted with the purpose to convert solid wastes into beneficial resources for the society. The emphasis on solid wastes as valuable resources and not as problems is achievable through the society's awareness that is channelled through learning, the usage of innovative technologies, the financial resources and the government's policy and supports including the practices of the locals [33].

34.8 Conclusion

In essence, it can be summarised that the integrated management system combines both holistic and sustainable environment-friendly approaches. The advantages of managing solid wastes in an integrated manner are that it can give rise to job opportunities for the society; reduce the usage of energy and natural raw materials; produce energy and secondary raw materials from wastes; eliminate hazardous pollutants emitted to the environment; reduce environmental pollution impact such as global warming, acid rain, depletion of ozone layer and climate change; prolong the lifespan of waste disposal sites; and reduce the needs to treat leachate and landfill gas from disposal sites including reducing the waste management cost. The drawback of hierarchical system is that the waste management system cannot depend only on one particular technology at one time. The waste management technologies have to be interdependent in order to produce an efficient and effective system. Thus, the full implementation of the ISWM system should be emphasised in Malaysia.

References

1. Agamuthu P (2007) Material recovery from Malaysia MSW: a practical approach. Proceedings of waste to wealth international conference & exhibition (W2W)
2. Agamuthu P, Fauziah SH, Nis H (2006). Degradation of surface Water quality—is solid waste a culpit. Proceedings of waste management international conference & exhibition
3. Ali H, Ahmad AR, Tajuddin M, Mohd NH (2001) Strategies minimization of municipal solid waste. In: Policies to improve municipal solid waste management, Lestari, pp 41–51
4. Basri H (2001) Solid waste in Malaysia: technical perspectives. In: Policies to improve municipal solid waste management, Lestari, pp 73–83
5. Dennis BH (2007) Assessment of the catalytic depolymerization process for fuel production from biomass. Department of Mechanical & Aerospace Engineering, The University of Texas at Arlington
6. Fishbern B, Gelb C (1992) Making less gabage. A planning guide for communities. INFORM Inc., New York
7. Hing CK (2007) Material recovery facilities; converting waste to wealth—the kota kinabalu experience. Proceedings of waste to wealth international conference & exhibition
8. Hossain MA, Siwar C (2001) The impact of household income on waste minimization: a case study of Kuching City, Sarawak. In: Policies to improve municipal solid waste management, Lestari, pp 167–173
9. Jahi JM (2001) Issues and problems in management of solid waste by local authorities. In: Policies to improve municipal solid waste management, Lestari, pp 7–11
10. Japan International Cooperation Agency (2005) Industrial Pollution Control Management course, lecture note. Kitakyushu, Japan
11. Kang HY, Schoenung JM (2005) Electronic waste recycling; a review of U.S. infrastructure and technology options. Resour Conserv Recycling 45:368–400
12. Ministry of Housing and Local Government (2006) Strategy to develop sustainable solid waste management in Malaysia. Conference & exhibition
13. Metcalf and Eddy (1991) Waste water engineering treatment disposal, reuse. McGraw-Hill, Singapore

14. McDougall F, White P, Franke M, Hindle P (2001) Integrated solid waste management: a life cycle inventory. Published by Blackwell Science, Oxford. ISBN 0-632-05889-7
15. Newell Engineering (1993) Black Magic non-ferrous separator. Literature from Newell Engineering Ltd., Burnt Meadows Rd., North Moons Moat. Redditch, Wores, UK
16. News Straits Times (2007) Shajeran in synthetic diesel test plant talks. 10 Dec 2007
17. Ramly NH (2006) Sustainable integrated solid waste management: the way forward for Malaysia. Conference & exhibition
18. Recycle Energy Sdn. Bhd. (2004). Detailed environmental impact assessment of the proposed resource recovery centre (waste to energy) plant in Mukim Semenyih, Daerah Hulu Langat, Selangor Darul Ehsan, Malaysia
19. Rhyner CR, Schwartz LJ, Wenger RB, Kohrell MG (1995) Waste management and resource recovery. Lewis Pub, Boca Raton
20. Sairan S (2007) Waste to energy landfill gas for power generation. Asia Solid & Hazardous Waste Management. Proceeding of waste to wealth international conference exhibition
21. Salleh MN (2001) Solid waste management at Malaysian Local Authority in Malaysia. In: Method to improve municipal solid waste, Lestari, pp 1–6
22. Sangaralingam M (2001) Policies to improve municipal solid waste management: community participation issues. In: Policies to improve municipal solid waste management, Lestari, pp 129–137
23. Seong CY (1990) Waste minimization through reduction, recycling and reuse. Hazardous Wastes regulation & management. Ensearch, pp 41–45
24. Shajeran Resource Sdn. Bhd., Alphakat Engineering GmBH (2007) Proposal on catalytic de-polymerization process (CDP) plant (500 litre/hour plant). Kuala Lumpur
25. Siphon M (2007) The Integrated Solid Waste Management (ISWMS) in Sarawak. Breaking the barrier in wastes management delivery models. Proceedings of waste to wealth international conference & exhibition
26. Sopian K (2004) Opportunities and challenges in renewable energy technology development. Proceedings of the 2nd Bangi world conference on environmental management
27. Tchobanoglous G, Theisen H, Vigil S (1993) Integrated solid waste management: engineering principles and management issues. McGraw-hill, Inc, New York
28. Tsiung CT (2006) Waste management framework planning in Sarawak. Waste management conference & exhibition 2006
29. Warmer (1993) Refuse derived fuel. Warmer Information Sheet
30. White P, Franke M, Hindle P (1995) Integrated solid waste management: a life cycle inventory. Blackwell Science, Oxford
31. Yahaya N (2007) Solid waste management in Malaysia. Proceedings of waste to wealth international conference & exhibition (W2W), PWTC, Kuala Lumpur, 26–30 Nov
32. Yassin SM (2006). Key note address towards a better environment. Proceedings of waste management conference & exhibition. Kuala Lumpur, 2006
33. Yunus MNM, Muhamad D (2007) Towards the realization of Malaysian waste to wealth. Proceedings of waste to wealth international conference & exhibition (W2W)

Chapter 35
Modelling Anaerobic Digestion Process for Grass Silage After Beating Treatment Using Design of Experiment

Fatma Alfarjani, Ayad K.M. Aboderheeba, Khaled Benyounis, and Abdul-Ghani Olabi

Abstract Anaerobic digestion (AD) is one of the most biomass conversion technologies currently deployed for power and heat. Beating treatment is a mechanical treatment whose technique has recently been introduced. The main goal of beating treatment is to improve degradability of the material which will enhance biogas production and anaerobic digester performance. In this work the effect of beating time (0–10 min) and temperature (35–39 °C) as input factors on the production of biogas as a response were investigated using design of experiment. Face-central composed design and response surface methodology were employed to create design matrix. Mathematical models were developed to determine the effect of temperature and beating time on the response as well as to predict the process performance. The results indicate that the two factors have a positive effect on the response and also show that any increase in the beating time will result in an increase in the biogas production up to beating time of about 3 min. The mathematical models developed are used for any further optimisation analysis.

Keywords Anaerobic digestion • Beating treatment • Optimisation • DOE

Nomenclature

AD	Anaerobic digestion
°C	Temperature
DOE	Design of experiment
FCCD	Face-central composed design
RSM	Response surface methodology
UCD	University College Dublin
TS	Total solids

F. Alfarjani (✉) • A.K.M. Aboderheeba • K. Benyounis • A.-G. Olabi
Dublin City University, Dublin, Ireland

VS   Volatile solids
COD   Chemical oxygen demand
VFA   Volatile fatty acids

35.1   Introduction

With the increasing demand for energy and the limited resource of fossil fuels amid growing concerns for the environment, the development of an alternative energy source has become the forefront of research. In recent years biogas has been receiving increasing attention as an alternative to fossil fuels in solving the problems of rising energy prices, waste treatment/management and creating a sustainable development [1, 2]. Biogas is a product of anaerobic digestion processes in biomass by certain bacteria. This consists mainly of methane and carbon dioxide, with trace amounts of other gases. Its technology plays an important role in producing energy from renewable and clean resources, in addition to its application to treat animal manure and organic waste from the industry and household sectors [3]. Furthermore, it is a flexible form of renewable energy that can produce heat and electricity, is commonly used for cooking and lighting and also serves as a vehicle fuel [4]. Biogas can be produced through various types of energy crops. The most commonly used crops are maize, sunflower, grass and Sudan grass [5]. These materials are known as lignocellulosic materials [6, 7]; they consist of three main types of polymers, namely, cellulose, hemicellulose and lignin, which are associated with each other, and smaller amounts of pectin, protein, extractives and ash. Cellulose, hemicelluloses and lignin are present in varying amounts in different parts of the plant and they are intimately associated to form the structural framework of the plant cell wall. The composition of lignocellulose depends on plant species, age and growth conditions. Distribution of cellulose, hemicelluloses and lignin varies significantly between different plants [8, 9]. Cellulose is the major polymer in lignocellulosic biomass with 35–48 % [10], and consists of D-glucose subunits, linked by B-1,4 glycosidic bonds [11, 12]. Cellulose in biomass is present in both crystalline and amorphous forms. Crystalline cellulose comprises the major proportion of cellulose, whereas a small percentage of unorganised cellulose chains form amorphous cellulose. Cellulose is more susceptible to enzymatic degradation in its amorphous form [13]. Hemicellulose is the second major constituent of lignocellulosic biomass with 22–30 % [10]. Hemicelluloses are heterogeneous polymers of pentoses (xylose, arabinose), hexoses (mannose, glucose, galactose) and sugar acids. Unlike cellulose, hemicelluloses are not chemically homogeneous and easily hydrolysed to its constituent [14]. Though hemicellulose is known as the weakest compound in lignocellulose, it plays a fundamental role in strengthening the structure: hemicellulose is linked to other polysaccharides, to lignin and to proteins, forming a network [7]. The third largest polymer composition of lignocellulosic biomass is lignin (15–27 %) [10]. It is present in the cell wall, conferring structural support, impermeability and resistance against microbial attack and

oxidative stress. Structurally, lignin is an amorphous heteropolymer, non-water soluble and optically inactive; this consists of phenylpropane units joined together by different types of linkages [15].

Several researchers have shown that the barrier to the production and recovery of lignocellulosic material is the structure of lignocelluloses. Lin and Tanaka [16] and Xiao et al. [17] indicate that the structure of lignocelluloses resists degradation due to cross-linking between the polysaccharides (cellulose and hemicellulose) and the lignin via ester and ether linkages. Hendriks and Zeeman [18] in their review conclude that the crystallinity of cellulose is just one of the factors that make hydrolysis of lignocellulose limited, and as well support other factors reported in [19–21, 22] (1) degree of polymerisation (DP), (2) moisture content, (3) available surface area and (4) lignin content. Therefore pretreatments are necessary to improve degradation of cellulosic materials and enhance methane yield; these treatments can be mechanical, biological or physico-chemical [23, 24]. Mechanical pretreatment methods such as chipping, grinding and milling (often referred to as physical methods) reduce crystallinity but more importantly give reduction of particle size, make material handling easier and increase surface/volume ratio [25]. Significant research effort has been dedicated focusing on mechanical treatment to improve the performance of digesters treating different biomass resources. Carrère et al. [24] and Alfarjani et al. [26] in their review papers classified the mechanical treatment as ultrasonic treatment, lysis-centrifuge, liquid shear and grinding.

The energy crop selected for this experiment was grass silage. Grass silage is the second most frequent crop used as feedstock (50 %) after maize silage (80 %); this is shown in the assessment of recent biogas plants in Germany and Austria [27, 28]; these types of crops can generate large amounts of energy through anaerobic digestion (AD) processes.

In this work, beating treatment as new mechanical treatment is applied via Hollander Beater to treat grass silage as lignocellulosic material [29]. Beating lignocellulosic materials will result in decreased particle size of the substrate, increased surface area, disruption of the crystalline structure of the cellulose cells and assistance in the breakdown of the lignin component, thus improving hydrolysis and overall methane yield. Treated and untreated grass with digester sludge is involved in anaerobic co-digestion process.

AD processes in stage 1 (pretreatment) and stage 2 (digestion) are very much related in terms of efficiency. In order to obtain high production levels of biogas from any AD process, pretreatment processes must take place. There are a range of factors that affect the AD process, the most important being temperature and pH. Additionally, the degree of beating (in terms of beating time) associated to the first stage of the process is also imperative. Several researchers have identified that the optimum value of pH varies within the ranges of ± 7 [30, 31]. For the optimisation of the other two factors, design of experiment (DOE) as a statistical technique is used in this work, instead of the traditional methods which are criticised because they depend on trial and error, are time consuming and increase the overall cost of the process. The objective of this study is to investigate the effect

of beating treatment on the grass silage, and develop mathematical models using response surface methodology (RSM), to predict the productivity of biogas from grass silage after beating treatment aerobically co-digested with digester sludge in different periods of retention time of process.

35.2 Background: Biomass Energy and Environment

The extraction, conversion and utilisation of various forms of energy is recognised as one of the major contributors to environmental degradation at a global and local level, be it greenhouse gas emissions or local air pollution due to combustion of fossil fuels, coal, nuclear energy and deforestation [32]. Burning fossil fuels increases the effect of greenhouse gases in the atmosphere; this is also known as global warming. Global warming threatens animal extinction, extending pollution, human migration and sudden climate changes [33]. There appears to be an agreement among the world's leading environmental scientists that there is a discernable level of activity attributed to human influence on the climate where a direct link between the concentration of greenhouse gases and the increase in global temperatures is prominent. Gases such as carbon dioxide, nitrous oxide, ozone, chlorofluorocarbon (CFC) and methane allow the Sun's energy to penetrate the Earth's atmosphere and at the same time act as a blanket, trapping the heat radiated from the Earth's surface. Therefore, the issue of global climate change is gaining greater interest in the scientific community. To address this phenomenon, the Kyoto Protocol was introduced in 1997. The purpose of the Kyoto Protocol was to reduce the total greenhouse gas emissions of developed countries (and countries with economies in transition) to 5 % below the level they were in 1990 (United Nations, 1998). The protocol set targets for greenhouse gas emissions of developed countries for the period 2008 to 2012. EU has specifically set a target to tackle climate change by reducing greenhouse gases emissions by 8 % between 2008 and 2012 and target further reduction of CO_2 by 20 % in 2020 [34]. In order to achieve such an ambitious target, motivation for renewable energy has become a principle for sustaining energy in the future. Therefore the need for renewable energy technologies has emerged significantly in recent years.

Biomass is a simple term for all organic material that has been derived from plants or animals such as trees, crops (including algae) and agricultural and industrial residues along with forestry processes and human or animal wastes. In nature, all biomass ultimately decomposes to its elementary molecules with the release of heat. Therefore, the release of energy from the conversion of biomass into useful energy imitates natural processes (but at a faster rate), and this energy can be considered renewable energy. Converting biomass to fuel can be as simple as cutting trees into small pieces so that they can be burned to produce heat or electricity, or as complicated as converting it into a liquid or a gaseous fuel (e.g. sugar cane or cereal crops to liquid fuels such as ethanol). Unlike any other energy resource, using biomass to produce energy is often a way of disposing of

biomass waste materials that otherwise would create environmental risks [35, 36]. The main biomass utilisation technologies that produce energy from biomass that are useful are direct combustion, gasification, anaerobic digestion and pyrolysis.

35.2.1 The Anaerobic Digestion

AD is defined as the biological breakdown of organic material by the microorganisms in an airtight environment with no oxygen present [37]. The AD process can be used to turn residues from livestock farming, food processing industries, waste water treatment sludge and water treatment plant sludge among other organic wastes into biogas and digestate. The biogas can be used to generate heat and/or electricity and fibre. The biogas produced in AD plants comprises largely methane (60–80 %) and carbon dioxide (20–40 %) but also usually contains a small amount of hydrogen sulphide (H_2S) and ammonia (NH_3), as well as traces of other gases [38].

35.2.2 Anaerobic Digestion: Biochemical Reaction

The full process can be considered to occur in four stages.

Hydrolysis stage: where complex organic materials are broken down into their constituent parts in a process known as hydrolysis. The result is soluble monomers: Proteins are converted to amino acids; complex carbohydrates are converted to simple sugars [39].

Acidogenesis: which is acid-forming phase of acidogenesis. In this process, acidogenic bacteria turn the solubilised monomers produced of hydrolysis into simple organic compounds, mostly short-chain volatile fatty acids (VFA) [40].

Acetagenesis: The next stage of acetagenesis is often considered with acidogenesis to be part of a single acid-forming stage. The long-chain VFA formed during acidogenesis are oxidised to acetate or propionate and hydrogen gas by the acetogenic bacteria [40].

Methanogenesis: Final step involves in converting acetate and hydrogen to form methane by the methanogenic microorganisms. Biomethanisation is primarily originated from the derivation of acetate acid. Hydrogen is also converted along with carbon dioxide during methanogenesis to produce methane [41].

35.2.3 Improvement of the Biogas Process

Biogas process optimisation through better monitoring and control is one way of improving process efficiency [42]. Other ways can be through pretreatment of the substrate to release more biodegradable compounds, or co-digestion with different wastes and/or with animal manure. This will limit the inhibition from the substrate and enhance the biogas production.

Pretreatment of Substrate

Pretreatment is used extensively to improve degradability and rate of hydrolysis material being fed into digesters to increase the methane yield in the anaerobic digestion process [43]. Some biomass wastes which are composed of cellulose, hemicelluloses and lignin have evolved to resist degradation. Pretreatment therefore is needed to alter or remove structural and compositional impediments to the hydrolysis process and subsequent degradation processes in order to enhance digestibility, improve the rate of enzyme hydrolysis and increase yields of intended products [44]. Pretreatment could be done in any of the following ways [24]:

- Biological treatment
- Chemical treatment
- Thermal treatment
- Mechanical treatment

Co-digestion Strategy

In general, co-digestion refers to the AD of multiple biodegradable substrates (feedstocks) in an AD system. The idea of co-digestion offers several possible ecological, technological and economical advantages, so it can improve organic waste treatment through anaerobic digestion [45]. Co-digestion with other wastes, whether industrial (glycerin), agricultural (fruit and vegetable wastes) or domestic (municipal solid waste), has been a successful option for improving biogas production [46, 47].

Combined Pretreatment and Co-digestion

Besides adding co-substrates, pre-treating substrates using various pretreatment methods prior to anaerobic digestion is also reported as a potential approach in the improvement of biogas production efficiency [48]. Neves et al. found out that when the waste is subjected to alkaline hydrolysis pretreatment before co-digestion with activated sludge, the methane production increased by 67 %, while if co-digested

with kitchen waste, the methane production increased by 61 % [49]. In this chapter the new mechanical pretreatment (beating treatment) is used to treat the main substrate (grass silage) which is then co-digested with digested sludge.

35.2.4 Response Surface Methodology

RSM is a set of mathematical and statistical techniques that are useful for modelling and predicting the response of interest, affected by several input variables with the aim of optimising the response [50]. RSM also specifies the relationships among one or more measured responses and the essential controllable input factors [51]. If all independent variables are measurable and repeated with negligible of error, the response surface can therefore be expressed as

$$y = f(x_1, x_2, \ldots x_k) \qquad (35.1)$$

where k is the number of independent variables.

To optimise the response "y", it is necessary to find an appropriate approximation for the true functional relationship between the independent variables and the response surface. Usually a second-order polynomial (35.2) is used in RSM:

$$y = b_o + \sum b_i \chi_i + \sum b_{ij} \chi_i \chi_j + \sum b_{ii} \chi_{ii}^2 + \varepsilon \qquad (35.2)$$

In this chapter, the RSM design central composite design (CCD) is used to develop mathematical models to predict the production of biogas from grass silage anaerobically digested with activated sludge after beating treatment. Design-Expert V7 software is used to code the data, develop the design matrix and analyse the case. The limits for each factor are coded via this relationship $X_I = 2(2X - (X_{max} + X_{min}))/(X_{max} - X_{min})$, where X_i is the required coded value, X is any value of the factor that requires coding and X_{max} and X_{min} are the upper and lower limit of the factor being coded, respectively [49]. Once the design matrix is developed and experiment carried out, RSM will apply to the collected experiment data in order to build and validate the mathematical models of the process, using the same software (Design-Expert V7). An analysis of variance (ANOVA) is used to test the adequacy of the models developed. The statistical significance of the models developed and each term in the regression equation were examined using the sequential F-test, lack-of-fit test and other adequacy measures (i.e. R^2, Adj- R^2, Pred. R^2 and Adeq. Precision ratios). Stepwise regression method will be used to eliminate model terms that have a p-value greater than the level of significance α. At this stage, the final reduced mathematical model contains only the significant terms and the terms that are necessary to maintain hierarchically can be built. Furthermore, a reduced quadratic ANOVA table can also be produced.

In addition, plots such as 3D graphs, contours and perturbation plots represent the factors that affect the response. Moreover, there is a possibility of employing the developed model for finding the optimal condition for optimised anaerobic co-digestion processes.

35.3 Experimental Set-Up

35.3.1 Substrate

In this work anaerobic co-digestion of fresh grass and fresh digester sludge is used in order to duplicate the improvement of the efficiency of the process.

Grass silage was obtained from UCD Lyons Research Farm. The farm consists of approximately 580 acres of land. It is used for teaching and research field activities by the School of Agriculture, Food Science and Veterinary Medicine in University College Dublin (UCD) (www.ucd.ie). Characteristics of the grass silage are reported in [52].
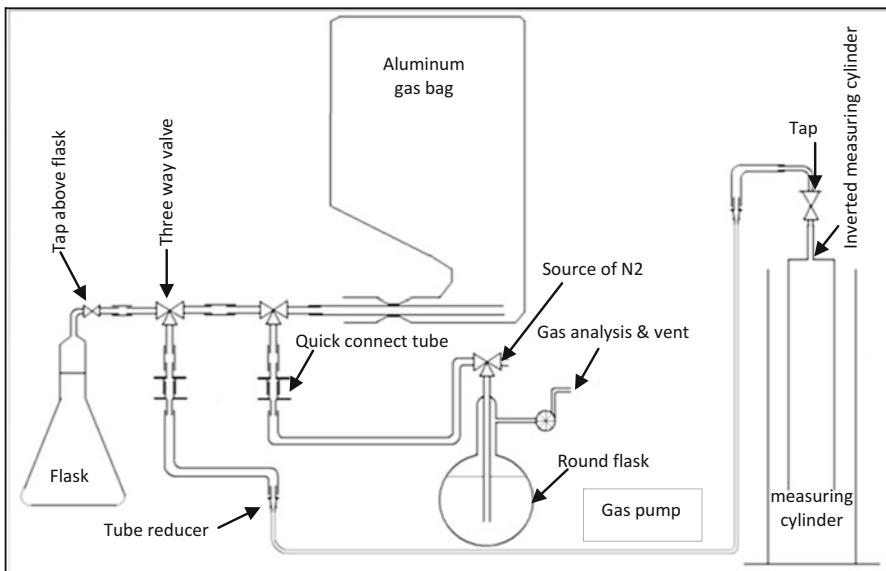
Digester sludge with its characteristics was obtained from Celtic Anglian Water Ltd in Dublin; the sludge characteristic are listed in Table 35.1.

35.3.2 Beating Pretreatment

Beating treatment method which is based on employing Hollander beater device [30] has been employed in this work. The beating process was conducted in accordance with the design matrix developed by using RSM. 30 L of water and 1 kg of grass silage were taken and added to the beater; this was operated for 5 min according to the design matrix. The first sample was taken after 5 min of beating and was achieved by (1) switching off the beater following a beating experiment, and (2) the mixed silage was mixed with water and then emptied into the drum. It was swirled around continuously to mix and then a sample was taken to the bucket of approximately 10 L; after that the 10 L bucket filled with mixed grass silage and water was separated into two fractions: liquid and suspension. This was performed

Table 35.1 Characteristics of sludge

Parameters	Value
TS	5.6 %
VS	72 %
COD	65.500 mg/l
Ammonia	2.770 mg/l
Alkalinity	12.135 mg/l
VFA	42 mg/l

Fig. 35.1 Anaerobic digestion equipment set-up

to enable the prepared solution to be of equal composition of designed matrices accordingly. The same processes were repeated with a 10-min beating time.

35.3.3 Bioreactor Set-Up

Figure 35.1 above illustrates the anaerobic reactor which has been built and used. It consists of flask 500 ml, two-way valve, three-way valve and quick-release tubing connectors as well as plastic tube and plastic bags. Water baths also have been used to control the temperature according to the design matrix. A measuring procedure was set to collect the biogas every 3 days. The measuring process will be stopped when the amount of the biogas produced is less than 2 % of the total amount of biogas produced.

35.3.4 Experimental Procedure

As mentioned earlier, RSM is used in designing the experiment, based on face-centred composite design (FCCD). Temperature (with range of 35 °C–39 °C) and beating time (with range of 0.0–10 min) were used as two main factors of grass silage anaerobic digestion process (see Table 35.2).

Table 35.2 Process parameters and experimental design levels

Factor	Name	Units	Type	Low actual	High actual	Low coded	High coded	Mean	Std. Dev.
A	Beating time	Min.	Numeric	0.00	10.00	−1.00	1.00	5.00	3.54
B	Temp.	°C	Numeric	35.00	39.00	−1.00	1.00	37.00	1.41

Table 35.3 Design matrix for grass silage AD

		Factor 1	Factor 2
Std	Run	A: beating time (Min).	B: temperature (°C)
1	9	0	35
2	6	10	35
3	5	0	39
4	7	10	39
5	12	0	37
6	2	10	37
7	11	5	35
8	10	5	39
9	4	5	37
10	8	5	37
11	3	5	37
12	1	5	37

35.3.5 Experimental Procedure

As mentioned earlier, RSM is used in designing the experiment, based on FCCD. Temperature (with range of 35 °C–39 °C) and beating time (with range of 0.0–10 min) were used as two main factors of grass silage anaerobic digestion process (see Table 35.2).

RSM was applied to the experimental data using a statistical software package, Design-expert V7. Table 35.3 shows the design matrix that was developed using the software. Linear and second-order polynomials were fitted to the experimental data to obtain the regression equations. The sequential F-test, lack-of-fit test and other adequacy measures were used in selecting the best models. A stepwise method was used to fit the second-order polynomial equation (2) to the experimental data and to identify the relevant model terms.

35.3.6 Determine the Dry Solid in Each Sample Before and After Beating Treatment

Dry solid or dry matter was determined for each sample by calculating the percentage of moisture in the sample. Oven has been used to dry samples to determine the dry matter of each sample. Tables 35.4, 35.5 and 35.6 illustrate the total dry solid of

Table 35.4 Total dry solid content for each sample without treatment

Sample No.	Empty dish plate weight (g)	Total wet sample weight (g)	Net wet sample weight (g)	Total dry sample weight (g)	Net dry sample weight (g)
1	173.1	188.4	15.3	175.5	2.4
2	137.4	152.7	15.3	139.7	2.3
3	148.5	163.8	15.3	150.9	2.4
					2.37

Table 35.5 Total dry solid content for each sample after 5-min treatment

Sample No.	Empty beaker weight (g)	Total wet sample weight (g)	Net wet sample weight (g)	Total dry sample weight (g)	Net dry sample weight (g)
4	172.5	380	207.5	174.5	2
5	230.9	437.3	206.4	232.9	2
6	231.4	439.8	208.4	233.5	2.1
			207.43		2.03

Table 35.6 Total dry solid content for each sample after 10-min treatment

Sample No.	Empty beaker weight (g)	Total wet sample weight (g)	Net wet sample weight (g)	Total dry sample weight (g)	Net dry sample weight (g)
7	233.1	443.9	210.8	236	2.9
8	233.1	443.6	210.5	236.2	3.1
9	231.7	442.3	210.6	234.3	2.6
			210.63		2.87

samples without treatment (0.0-min beating time), 5-min treatment and 10-min treatment, respectively. The net dry matter of untreated samples was 2.37 g, and 5- and 10-min beating was 2.03 and 2.87 g, respectively.

35.4 Results and Discussion

The experiment is carried out according to the design matrix shown in Table 35.3 in a random order to avoid any systematic error. For this material, seven mathematical models were developed successfully to predict the biogas yield every 3 days for 21 days, in a total seven responses. The averages of three measurements for each response are presented in Table 35.7.

Table 35.7 Experimentally measured responses

Exp. no.	First collection (cc)	Second collection (cc)	Third collection (cc)	Fourth collection (cc)	Fifth collection (cc)	Sixth collection (cc)	Seventh collection (cc)
1	1,021	1,769	2,052	2,225	2,425	2,560	2,673
2	1,049	1,538	1,807	2,061	2,272	2,386	2,477
3	1,570	2,128	2,471	2,694	2,858	2,950	3,027
4	1,409	1,877	2,252	2,464	2,576	2,664	2,728
5	1,490	2,079	2,425	2,674	2,798	2,926	3,023
6	1,252	1,762	2,149	2,422	2,521	2,606	2,675
7	1,111	1,651	1,939	2,160	2,370	2,497	2,592
8	1,418	1,983	2,400	2,629	2,788	2,887	2,973
9	1,394	1,918	2,306	2,551	2,669	2,768	2,868
10	1,491	1,998	2,368	2,609	2,707	2,807	2,901
11	1,526	2,072	2,486	2,723	2,859	2,969	3,063
12	1,582	2,106	2,518	2,754	2,887	2,991	3,088

35.4.1 Development of Biogas Models

Analysis of Variance

The resulting ANOVA (Tables 35.8 and 35.9) for the reduced quadratic models outline the analysis of variance of each response and show the significant model terms. The same tables also show any other adequacy measurements of R^2, adjusted R^2 and predicted R^2. The entire adequacy measures are close to 1, which is in reasonable agreement and indicates adequate models [53]. The adequate precision compares the range of the predicted value at the design points to the average prediction error. In all cases the value of adequate precision is dramatically greater than 4. An adequate precision ratio above 4 indicates adequate model discrimination [49]. For the seven collection models, the analysis of variance indicates that the main effects are beating time (A), temperature (B), the second-order effect of beating time (A^2) and the quadratic effect of temperature (B^2) which are also significant model terms.

Actual Mathematical Models

The final mathematical models developed using experimental data and regression analysis in terms of actual factor are shown below (35.3, 35.4, 35.5, 35.6, 35.7, 35.8 and 35.9):

Table 35.8 ANOVA table for first collection reduced quadratic model

Source	Sum of squares	DF	Mean square	F value	Prob > F	
Model	462,449	4	115,612	21	0.0005	Significant
A-beating time	22,918	1	22,918	4	0.0808	
B-temp.	327,844	1	327,844	60	0.0001	
A^2	33,147	1	33,147	6	0.0439	
B^2	41,427	1	41,427	8	0.0288	
Residual	38,567	7	5,510			
Lack of fit	19,821	4	4,955	1	0.6001	Not significant
Pure error	18,746	3	6,249			
Cor total	501,016	11				
$R^2 = 0.9230$			Pred $R^2 = 0.7637$			
Adj $R^2 = 0.8790$			Adeq precision $= 13.374$			

Table 35.9 ANOVA table for seventh collection reduced quadratic model
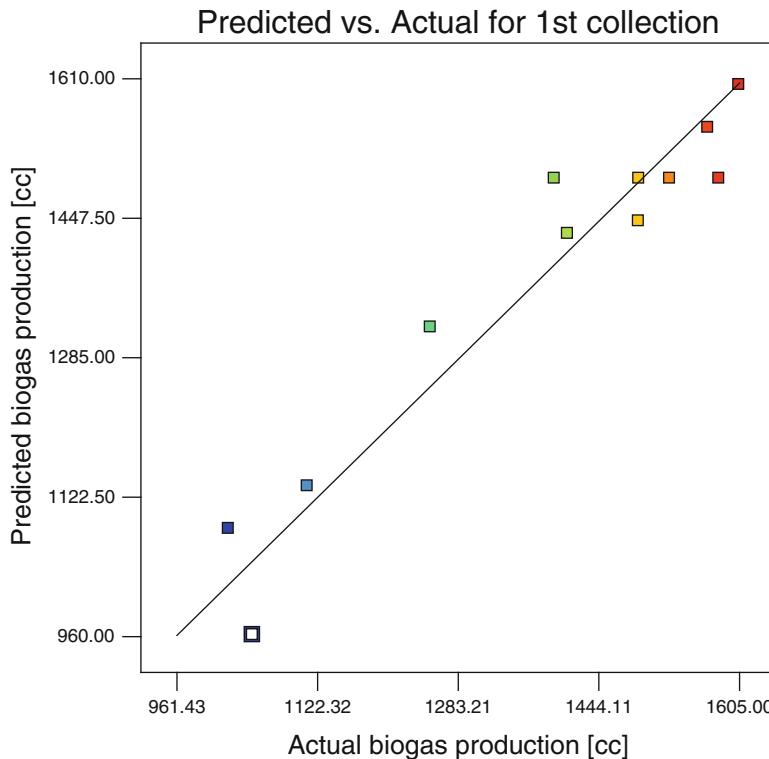
Source	Sum of squares	DF	Mean square	F value	Prob > F	
Model	476,709	4	119,177	12	0.0027	Significant
A-beating time	118,194	1	118,194	12	0.0098	
B-temp.	229,290	1	229,290	24	0.0018	
A^2	52,549	1	52,549	5	0.0517	
B^2	34,097	1	34,097	4	0.1012	
Residual	67,049	7	9,578			
Lack of fit	29,833	4	7,458	1	0.6895	Not significant
Pure error	37,216	3	12,405			
Cor total	543,757	11				
$R^2 = 0.8,767$			Pred $R^2 = 0.6,552$			
Adj $R^2 = 0.8,062$			Adeq precision $= 10.633$			

$$\text{First collection} = -45539 + 32.235^* \text{ beating time} + 2422.71667^* \text{ temp.} \\ -4.459^* \text{ beating time}^2 - 31.16^* \text{temp.}^2 \tag{35.3}$$

$$\text{Second collection} = -36773.79 + 10.507^* \text{ beating time} + 1997.71458^* \text{ temp} \\ -.712^* \text{ beating time}^2 - 25.62563^* \text{ temp.}^2 \tag{35.4}$$

$$\text{Third collection} = -53190.5 + 25.545^* \text{ beating time} + 2879.61667^* \text{ temp} \\ -5.0176^* \text{ beating time}^2 - 37.2^* \text{ temp.}^2 \tag{35.5}$$

$$\text{Fourth collection} = -63385.306 + 26.085^* \text{ beating time} + 3442.020^* \text{ temp} \\ -.758 * \text{ beating time}^2 - 44.79125 * \text{ temp.}^2 \tag{35.6}$$

Fig. 35.2 Scatter diagram for the first collection model
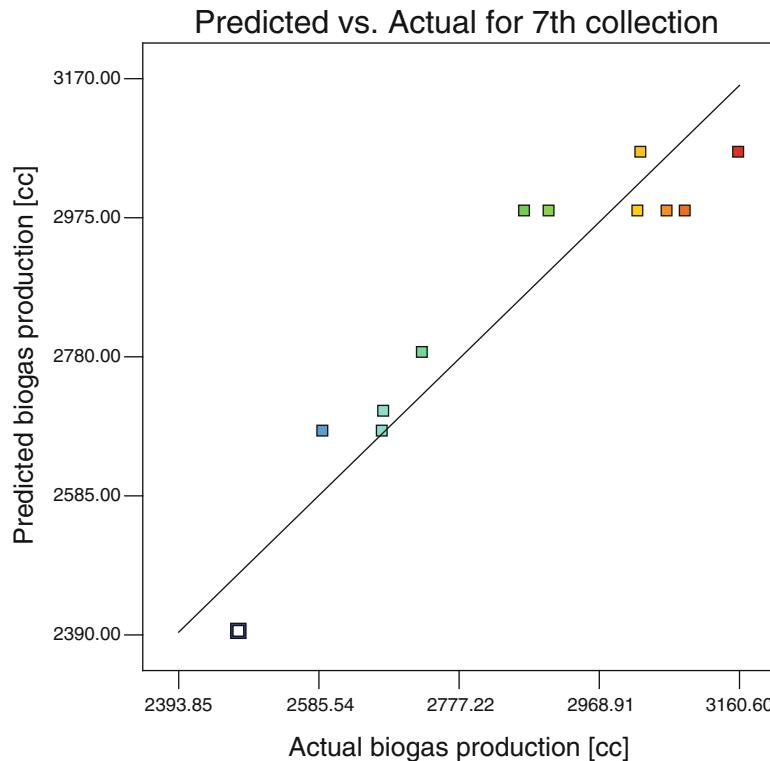
$$\text{Fifth collection} = -41608.634 + 28.307^* \text{ beating time} + 2287.077^* \text{ temp}$$
$$-5.207 * \text{beating time}^2 - 29.39438 * \text{temp.}^2$$

(35.7)

$$\text{Sixth collection} = -39412.414 + 26.668^* \text{ beating time} + 2182.595^* \text{ temp}$$
$$-5.262 * \text{beating time}^2 - 28.0912 * \text{temp.}^2$$

(35.8)

$$\text{Seventh collection} = -39334.15938 + 28.08033^* \text{ beating time} + 2189.67708^*$$
$$\text{temp.} - 5.61510 * \text{beating time}^2 - 28.26938 \text{ temp.}^2$$

(35.9)

Validation of the Models

The analysis indicates that the developed models are adequate owing to the residuals in prediction of each response being small, as the residuals tend to be close to the diagonal line (Figs. 35.2 and 35.3 are two examples depicting the relationship between the actual and predicted values of first collection and seventh

Fig. 35.3 Scatter diagram for the second collection model

Table 35.10 Confirmation experiments

Beating time (min)	Temperature (°C)	Responses	Prediction [cc]	Actual [cc]	% of error
0	38	First collection	1,529	1380.8	−10.7
		Second collection	2,136	2,044	−4.5
		Third collection	2503.7	2372.8	−5.5
		Fourth collection	2732.9	2564.8	−6.6
		Fifth collection	2854.8	2,712	−5.3
		Sixth collection	2962.5	2824.8	−4.9
		Seventh collection	3052.59	2926.44	−4.31

collection of biogas). To verify the adequacy of the developed models a further three confirmation experiments were carried out using new randomly selected test conditions, each within the experiment range defined previously. Using the point prediction option in the software, the seven responses of the validation experiment were predicted using the previous developed models and compared with the actual measured responses of this confirmation experiment. Tables 35.10, 35.11 and 35.12

Table 35.11 Confirmation experiments

Beating time (min)	Temperature (°C)	Responses	Prediction [cc]	Actual [cc]	% of error
1.6	37.3	First collection	1518.1	1439.2	−5.5
		Second collection	2097.3	2145.6	2.2
		Third collection	2479.6	2509.6	1.2
		Fourth collection	2716.2	2752.0	1.3
		Fifth collection	2835.0	2910.4	2.6
		Sixth collection	2946.4	3011.2	2.1
		Seventh collection	3042.26	3097.16	1.77

Table 35.12 Confirmation experiments
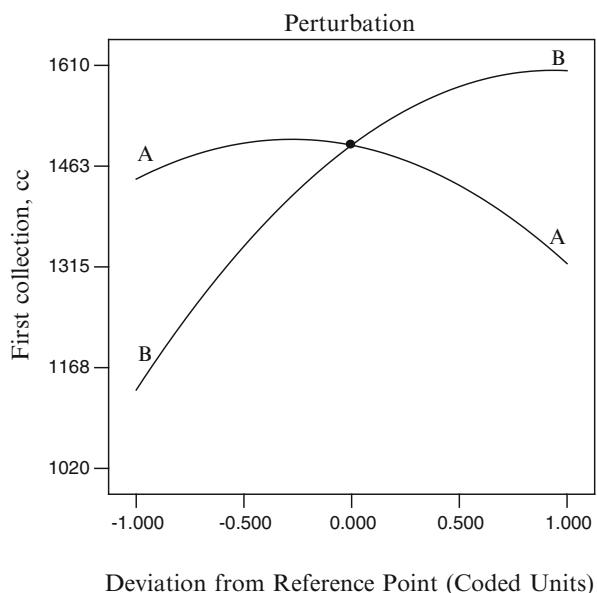
Beating time (min)	Temperature (°C)	Responses	Prediction [cc]	Actual [cc]	% of error
2.7	37.3	First collection	1530.5	1569	2.3
		Second collection	2089.3	2352.6	11.1
		Third collection	2481.6	2744.2	9.5
		Fourth collection	2720.2	3036.85	10.3
		Fifth collection	2841.7	3199.65	11.1
		Sixth collection	2948.9	3314.75	11.0
		Seventh collection	3044.77	3410.25	10.71

summarise the experiments, conditions, actual experimental values, predicted values and percentage error in prediction. It is evident that the models can adequately describe the responses within the ranges considered as the error % in prediction ranged between 1.2 and 11.1 %, which is in agreement with the results reported in [52].
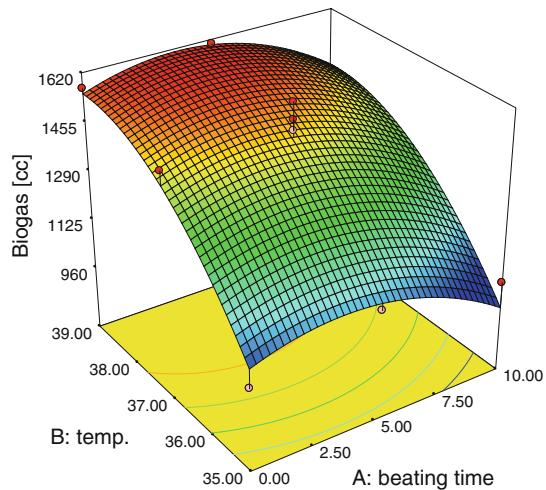
35.4.2 Effect of Anaerobic Digestion Factors on the Production of Biogas

It is necessary to indicate that all responses (collections of biogas) are related to biogas production and determined in a cumulative way. The analysis demonstrates that the effect of the beating time and the temperature on all responses all have the same trend. Figure 35.4 (perturbation plot) and Fig. 35.5 (3D surface) plot show the effect of the beating time (A) and temperature (B) on the first collection of biogas, while Fig. 35.6 (3D surface) and Fig. 35.7 (perturbation plot) show the effect of the same factors on the seventh collection of biogas. Temperature is the most significant factor associated with the collection models; further analysis can verify that temperature has the highest influence on the process; this is in agreement with the findings reported in [54 and 55].
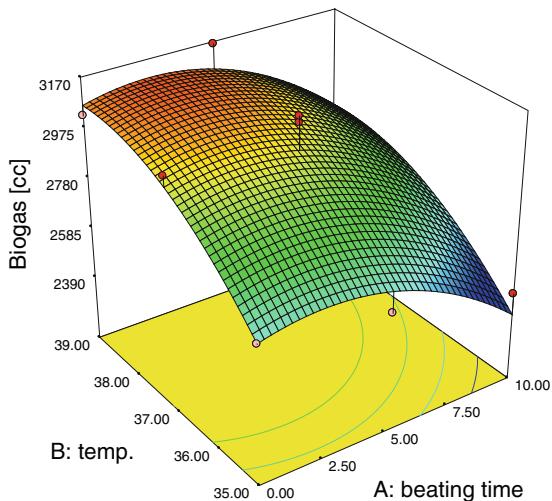
Fig. 35.4 The effect of the beating time (**a**) and temperature (**b**) on the first collection of biogas
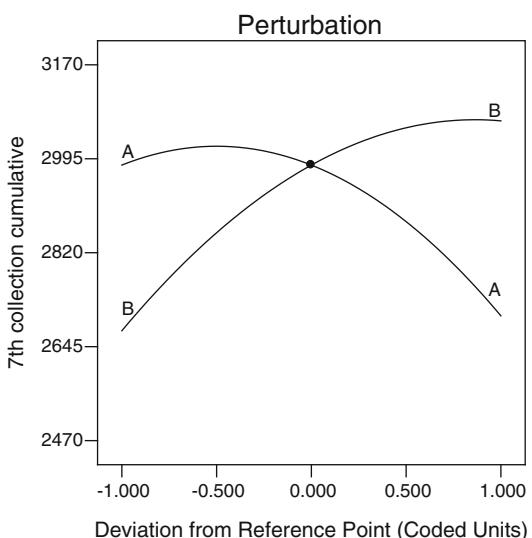
Fig. 35.5 The effect of the beating time (**a**) and temperature (**b**) on the first collection of biogas

Fig. 35.6 The effect of the beating time (**a**) and temperature (**b**) on the first collection of biogas

Fig. 35.7 The effect of the beating time (**a**) and temperature (**b**) on the first collection of biogas

35.5 Conclusion

From this work we can conclude the following:

- Beating treatment as mechanical pretreatment method is effective and accelerates the degradability for grass silage.
- RSM is an effective tool to optimise anaerobic digestion of grass silage combined with beating treatment.

- Both factors (temperature and beating time) have a significant effect on the overall AD process.
- Seven adequate mathematical models have been developed for this process. These models can be used successfully for prediction of optimisation analysis.

References

1. Mshandete AM, Parawira W (2009) Biogas technology research in selected sub-Saharan African countries—A review. Afr J Biotechnol 8(2):116–125
2. Matsui T, Koike Y (2010) Methane fermentation of a mixture of seaweed and milk at a pilot-scale plant. J Biosci Bioeng 110(5):558–563
3. Sannaa MN (2004) The development of biogas technology in Denmark: achievements & obstacles. Department of environment, technology and social studies Roskilde University, Denmark
4. Marchaim U (1992) Biogas processes for sustainable development, MIGAL Galilee Technological Centre Kiryat. Shmona, Israel
5. Amon T, Amon B, Kryvoruchko V, Machmu A, Hopfner-Sixt K, Bodiroza V et al (2007) Methane production through anaerobic digestion of various energy crops grown in sustainable crop rotations, , vol 98. Bioresource Technology, Austria, pp 3204–3212
6. Qi BC, Aldrich C, Lorenzen L, Wolfaardt GW (2005) Acidogenic fermentation of lignocellulosic substrate with activated sludge. Chem Eng Commun 192:1221–1242
7. Bruni E (2010) Improved anaerobic digestion of energy crops and agricultural residues, PhD thesis, Department of Environmental Engineering, Technical University of Denmark
8. Fengel D, Wegener G (1984) Wood: chemistry, ultrastructure. Reactions, De Gruyter, Berlin
9. Jørgensen H, Kristensen JB, Felby C (2007) Enzymatic conversion of lignocellulose into fermentable sugars: challenges and opportunities. Biofuels Bioprod Bioref 1(2):119–134
10. Blaschek HP, Ezeji TC (2007) Science of alternative feedstocks. In: Report from the Department of Agricultural and Consumer Economics, Corn-Based Ethanol in Illinois and the U.S., University of Illinois, Urbana-Champaign, 2007, pp. 112–128
11. Fengel D, Wegener G (1989) Wood: chemistry, ultrastructure, reactions. Walter De Gruyter Inc., Berlin
12. Kumar P, Barrett D, Delwiche M, Stroeve P (2009) Methods for pretreatment of lignocellulosic biomass for efficient hydrolysis and biofuel production. Ind Eng Chem Res 48 (8):3713–3729
13. Béguin P, Aubert J-P (1994) The biological degradation of cellulose. FEMS Microbiol Rev 13 (1):25–58
14. Saha BC (2003) Hemicellulose bioconversion. J Ind Microbiol Biotechnol 30:279–291
15. Perez J, Dorado JM, Rubia TD, Martinez J (2002) Biodegradation and biological treatment of cellulose, hemicellulose and lignin: An overview. Int Microbiol 5:53–63
16. Lin Y, Tanaka S (2006) Ethanol fermentation from biomass resources: current state and prospects. Appl Microbiol Biotechnol 69:627–642
17. Xiao C, Bolton R, Pan WL (2007) Lignin from rice straw Kraft pulping: effects on soil aggregation and chemical properties, Bioresour Technol 98:1482–1488
18. Hendriks ATWM, Zeeman G (2009) Pretreatments to enhance the digestibility of lignocellulosic biomass. Bioresour Technol 100:10–18

19. Chamg VS, Holtzapple MT (2000) Fundamental factors affecting enzymatic reactivity. Appl Biochem Biotechnol 84–86:5–37
20. Koullas DP, Christakopoulos P, Kekos D, Macris BJ, Koukios EG (1992) Correlating the effect of pretreatment on the enzymatic hydrolysis of straw, Biotechnol Bioeng 39:113–116
21. Laureano-Perez L, Teymouri F, Alizadeh H, Dale BE (2005) Understanding factors that limit enzymatic hydrolysis of biomass. Appl Biochem Biotechnol 124:1081–1099
22. Puri VP (1984) Effect of crystallinity and degree of polymerization of cellulose on enzymatic saccharification. Biotechnol Bioeng 26:1219–1222
23. Zheng Y, Lin H-M, Tsao GT (1998) Pretreatment for cellulose hydrolysis by carbon dioxide explosion. Biotechnol Prog 14(6):890–896
24. Carrère H, Dumas C, Battimelli A, Batstone DJ, Delgenès JP, Steyer JP et al (2010) Pretreatment methods to improve sludge anaerobic degradability: a review. J Hazard Mater 183:1–15
25. Harmsen P, Huijgen W, Bermúdez L, Bakker R (2010) Literature review of physical and chemical pretreatment processes for lignocellulosic biomass. Energy Research Centre of the Netherlands (ECN). http://www.ecn.nl/docs/library/report/2010/e10013.pdf
26. Alfarjani FA, Mohamed AK, Benyounis KY, Olabi AG (2011) Mechanical Pre-treatment to enhance anaerobic digestion process: overview, proceedings of ECOS 2011. Novi Sad, Serbia, pp 3573–3582
27. Hopfner-Sixt K, Amon T (2007) Monitoring of agricultural biogas plants in Austria –Mixing technology and specific values of essential process parameters. In: Proceedings of the 15th European Biomass Conference and Exhibition, Berlin, pp. 1718–1728
28. Weiland P (2006) Biomass digestion in agriculture: a successful pathway for the energy production and waste treatment in Germany. Eng in Life Sci 6:302–309
29. Mohamed AK, Alfarjani F, Benyounis KY, Prescott T, Olabi AG (2011) Application of Mechanical Pre-treatment to Produce Methane from Maize, ECOS 2011 conference, Nova Sad Serbia
30. Liu C, Yuan X, Zeng G, Li W, Li J (2008) Prediction of methane yield at optimum Ph for anaerobic digestion of organic fraction of municipal solid waste. Bioresour Technol 99:882–888
31. Ward AJ, Hobbs PJ, Holliman PJ, Jones DL (2008) Optimisation of the anaerobic digestion of agricultural resources. Bioresour Technol 99:7928–7940
32. Ravindranath NH, Hall DO (1995) Biomass energy and environment: a developing country perspective from India. Oxford University, Press, Technology & Engineering. http://books.google.ie/books?id=ARms6L3xklEC&source=gbs_navlinks_s
33. Gore A (2007) An inconvenient truth the crisis of global warming. Published by (Viking)
34. http://unfccc.int/kyoto_protocol/items/2830.php. Accessed August 2010
35. Stavroulia, H, Umit Bititci PR (2003) Socio-economic impacts of biomass deployment for the production of heat and electricity thesis, University of Strathclyde. http://www.esru.strath.ac.uk/Documents/MSc_2002/stavroulia.pdf
36. Siddharth S (2006) Green energy-anaerobic digestion, 2006, heat transfer, thermal engineering and environment, conference, Elounda, Greece pp 276–280
37. http://www.esru.strath.ac.uk/Documents/MSc_2002/stavroulia.pdf. Accessed Nov 2010
38. Epa, Strategic Policy Unit (2005) Anaerobic digestion: benefits for waste management, agriculture energy and the environment. Discussion Paper, http://www.epa.ie/downloads/consultation/epa_discussion_paper_anaerobic_digestion.pdf
39. Ostrem KM, Millrath K, Themelis NJ (2007) Combining anaerobic digestion and waste-to-energy, 12th North American waste to energy conference. Columbia University. http://www.seas.columbia.edu/earth/wtert/sofos/ostrem-millrath-themelis_nawtec12_2004.pdf
40. Lens P (2007) Biofuels for fuel cells renewable energy from biomass fermentation. IWA, London
41. Monnet F (2003) An introduction to anaerobic digestion of organic wastes. http://www.biogasmax.co.uk/media/introanaerobicdigestion

42. Boe K (2006) Online monitoring and control of the biogas process. Institute of environment and resources, Technical University of Denmark (DTU). Ph.D. Thesis
43. Ge H, Jensen PD, Batstone DJ (2010) Pre-treatment mechanisms during thermophilic–mesophilic temperature phased anaerobic digestion of primary sludge. Water Res 44:123–130
44. Mosier N, Wyman C, Dale B, Elander R, Lee YY, Holtzapple M, Ladisch M (2005) Features of promising technologies for pretreatment of lignocellulosic biomass, 2004. Bioresour Technol 96:673–686. doi:10.1016/j.biortech.06.025
45. Álvarez JA, Otero L, Lema JM (2010) A methodology for optimising feed composition for anaerobic co-digestion of agro-industrial wastes. Bioresour Technol 101:1153–1158
46. Amon Th, Amon B, Kryvoruchko V, Bodiroza V, Pötsch E, Zollitsch W (2006) Optimising methane yield from anaerobic digestion of manure: effects of dairy systems and of glycerin supplementation. International Congress Series, 1293, pp. 217–220
47. Macias-Corral M, Samani Z, Hanson A, Smith G, Funk P, Yu H, Longworth J (2008) Anaerobic digestion of municipal solid waste and agricultural waste and the effect of co-digestion with dairy cow manure. Bioresour Technol 99(17):8288–8293
48. Dohányos MZ, Kutil J, Jeníček P (2004) Improvement of anaerobic digestion of sludge. Water Sci Technol 49(10):89–96
49. Neves L, Ribeiro R, Oliveira R, Alves MM (2006) Enhancement of methane production from barley waste. Biomass Bioenergy 30:599–603
50. Montgomery DC (1984) Design and analysis of experiments, 2nd edn. John Wiley & Sons, New York
51. Khuri AI, Cornell JA (1996) Response surfaces design and analysis, 2nd edn. Marcel Dekker, New York
52. Nizami AS, Orozco A, Groom E, Dieterich B, Murphy JD (2012) How much gas can we get from grass? Appl Energy 92:783–790
53. Benyounis KY, Olabi AG, Hashmi MSJ (2008) Multi-response optimization of CO_2 laser-welding process of austenitic stainless steel. J Optics Laser Technol 40(1):76–87
54. Vindis P, Mursec B, Janzekovic M, Cus F (2009) The impact of mesophilic and thermophilic anaerobic digestion on biogas production. J Achiev Mat Manuf Eng 36(2):192–198
55. Yadvika S, Sreekrishnan TR, Kohli S, Rana V (2004) Enhancement of biogas production from solid substrates using different techniques—a review. Bioresour Technol 95(1):1–10

Chapter 36
Biogas Potential of Animal Wastes for Electricity Generation in Ardahan City of Turkey

Betül Özer

Abstract Turkey has to adopt long-term energy policies depending on the mitigation of the greenhouse gases and other environmental effects. Thus indigenous renewable energy potential should be utilized especially in the electricity production, which has a big share in the energy sector. Biogas is a significant renewable energy source that can be produced from wood, plant, animal, and all other organic wastes, and can be utilized for producing electricity, heat, and organic fertilizer. Local evaluation of biogas is important for energy production mainly due to the transportation issues. In this context this chapter conducts the evaluation of the potential of biogas from animal wastes for Ardahan city of Turkey. Since Ardahan's socioeconomic structure is mainly based on the livestock farming the city has significant biogas potential from animal wastes. Calculations in this chapter are made according to the available statistical data and literature review. The biogas energy potential of Ardahan for electricity generation is estimated from the animal quantities of 2010. As a result, the biogas potential is calculated to be approximately 18.4 million m^3/year, which has energy equivalence of 107 GWh/year, originated from 95 % cattle, 1.1 % small ruminant, 1.4 % equines, and 2.5 % poultry.

Keywords Animal waste • Biogas potential • Electricity generation • Mitigation of greenhouse gases (GHGs) • Energy policy • Renewable energy • Sustainability • Ardahan

B. Özer (✉)
Ardahan University, Ardahan, Turkey
e-mail: betlozer@hotmail.com
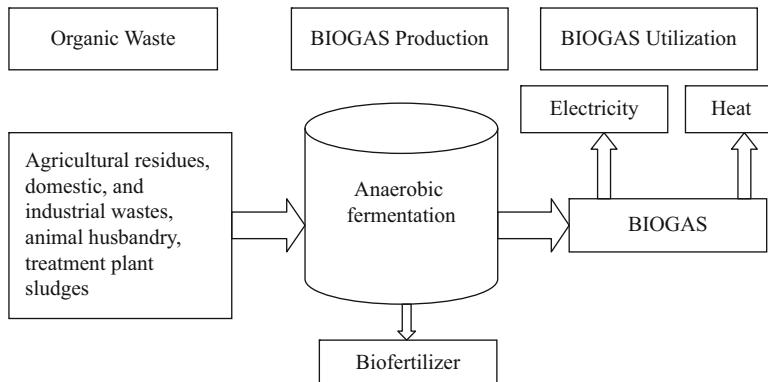
Nomenclature

CH_4	Methane
CO_2	Carbon dioxide
ETKB	Republic of Turkey Ministry of Energy and Natural Resources
GHG	Greenhouse gas
GWh	Giga watt-hour
HFC	Hydrofluorocarbons
LPG	Liquefied petroleum gas
m^3	Cubic meter
MJ	Megajoule
Mtoe	Million tons of oil equivalent
N_2O	Nitrous oxide
Nm^3	Normal cubic meters
PFC	Perfluorocarbons
SF_6	Sulfur hexafluoride
UNFCCC	United Nations Framework Convention on Climate Change

36.1 Introduction

The worldwide energy consumption has risen inexorably since the beginning of industrialization in the nineteenth century [1]. Since then fossil fuels have had the largest share in energy supply all over the world and they are responsible for the current environmental problems. Thus energy is intended to be supplied from new, clean, and renewable resources and countries are establishing environment-oriented energy policies due to sustainable development and climate change concerns and to comply with all environmental regulations. Against the background of limited fossil energy resources and global warming, the development of pathways to low-carbon-energy systems is one of the most challenging tasks of the twenty-first century [1]. Renewable energy sources such as solar, wind, hydropower, and biomass are potential candidates to meet global energy requirements in a sustainable way [2, 3].

The term "biomass" refers to forestry, purposely grown agricultural crops, trees, plants, and organic wastes such as agricultural, agro-industrial, domestic (municipal and solid), animal, and certain types of industrial wastes. Unlike fossil fuel deposits, biomass is renewable in the sense that only a short period of time is needed to replace what is used as an energy resource [4]. The importance of solar-based renewable energy sources for the reduction of greenhouse gas (GHG) emissions has been widely recognized. Since the signing of the United Nations Framework Convention on Climate Change (UNFCCC) in Rio de Janeiro in 1992, there has been an intensification of interest. Among these solar-based renewable sources, energy from biomass is considered to be one of the most promising to replace some of the fossil fuels whose combustion is by far the main source of anthropogenic

Fig. 36.1 The mainstreams of biogas production

GHGs, notably carbon dioxide (CO_2) [5]. Biomass in the form of biofuels is the only renewable energy source that can directly replace fossil fuels, either fully or in blends of various percentages [6].

Biogas can be produced through anaerobic fermentation of organic fraction in biomass and it consists of between 40 and 70 % methane, with the remainder being carbon dioxide, hydrogen sulfide, and other trace gases [7, 8]. It has several unique characteristics that distinguish it from the other renewable energy sources, such as it can be stored over long periods of time, it is not freely available, and producing it requires a chain of activities [6]. Its importance is in controlling and collecting organic waste material and at the same time producing energy as electricity and heat, high-quality fermented fertilizer, and water for use in agricultural irrigation, which are also essential for sustainable energy supply. Figure 36.1 shows the mainstream of biogas production process. Unlike other forms of renewable energy, biogas neither has any geographical limitations and required technology for producing energy nor is it complex or monopolistic [3, 9].

Biogas technology offers a very attractive route to utilize certain categories of biomass for meeting partial energy needs. In fact, proper functioning of biogas systems can provide multiple benefits to the users and the community resulting in resource conservation and environmental protection [10]. The benefits of biogas can be summarized as below:

- Supplying sustainable energy as both electricity and heat
- Mitigation of GHGs and solution to the other environmental problems
- Incentive effects for livestock farming and agriculture
- Increased use of high-quality organic fertilizer
- Also supplying sustainability via mitigating the usage of chemical fertilizer
- Decreasing the need to import energy sources

There are several technologies available in the market for the conversion of biogas into power, e.g., direct combustion of biomass, advanced direct combustion, gasification, and pyrolysis technologies, which are almost ready for commercial

scale use. The major research and developments of the biomass power industry are focusing on gasifier scale-up, system analysis, and site-specific commercial feasibility studies. Biomass power plants use technology that is very similar to that used in coal-fired power plants. For example, biomass plants use similar steam-turbine generators and fuel delivery systems. Biomass is burned to produce steam; the steam turns a turbine and drives a generator, producing electricity. Gasifiers are used to convert biomass into a combustible gas (biogas). The biogas is then used to drive a high-efficiency, combined-cycle gas turbine. Heat is used to convert biomass thermochemically into a pyrolysis oil. The oil, which is easier to store and transport than solid biomass material, is then burned like petroleum to generate electricity. Biomass can be used as a primary or a secondary energy source to power gas turbines. As a secondary energy source, biomass is used to make a fuel, which can be used to fire a gas turbine [11].

Biomass offers important advantages as a combustion feedstock due to the high volatility of the fuel and the high reactivity of both the fuel and the resulting char. Biomass has a significantly lower heating value than most coal. This is in part due to the generally higher moisture content and in part due to the high oxygen and much less carbon content. Biomass firing, in comparison with coal firing, helps reduce the total emissions per unit energy produced. A renewable fuel such as waste product or energy crop-derived biomass fuel is a lowest cost option for reducing GHG emissions [12].

Biomass supplies are more spatially dispersed than fossil fuel supplies. Whereas dispersion tends to increase harvest and transport costs, modern biomass options offer the potential for generating employment and thus additional income in rural areas. Moreover, the local availability of biomass for energy has the potential of reducing energy imports, and hence, increasing a country's self-sufficiency [5].

In Turkey approximately 65 million tons of residues from field crops (wheat, barley, tobacco, cotton, rice, etc.) and 160 million tons of wet animal manure from animal production occur annually. Agricultural wastes which are not used for animal feeding are burned in the field or abandoned to degrade naturally and animal manure is usually either applied to the field directly without implementing any process and accumulated in a pile outside in rural areas or used only for heating by direct combustion. As a result, the quality of the manure decreases, and its total energy is not utilized. Thus environmental problems, such as odor, visual problems, soil and water pollution, and related health problems, occur. Uncontrolled storage of the animal wastes causes 75 million tons of methane (CH_4) release to the atmosphere annually, where it is 40 million tons of CH_4 from organic solid waste dumpsites [13].

Animal manure is a good source of biogas and the best way for utilizing this kind of waste is to produce biogas. Evaluation of existing biogas production potential from animal wastes of Turkey and promote the use of these wastes must be brought under control in terms of environmental health, energy supply, and climate change issues.

The local evaluation of biogas for energy production is important mainly due to the transportation issues. In this chapter, the biogas energy potential of animal wastes which is the major biogas resource of Ardahan city of Turkey is determined.

Calculations are made from the number of cattle, small ruminants, equine, and poultry taking into consideration various criteria such as the availability factors and solid ratio of the manure.

36.2   Background: Turkey's Energy Structure

Turkey, with a young and growing population, low per capita electricity consumption, rapid urbanization, and strong economic growth, has been one of the fastest growing power markets in the world for nearly two decades. Besides having large lignite reserves and renewable energy resources, Turkey is an energy importer country which imports 70 % levels of her energy requirement. In 2011 the largest share belonged to natural gas with 32 % in the total energy supply and it was followed by oil (26.6 %) and imported coal (13.4 %). Figure 36.2 indicates the distribution of energy supply in 2011, and others including geothermal, wind, electricity, heat, and solar. As seen with Fig. 36.2 biomass has only 3 % share in total energy supply with 3.5 Mtoe (million tons of oil equivalent) where about 2.5 Mtoe comes from wood [14].
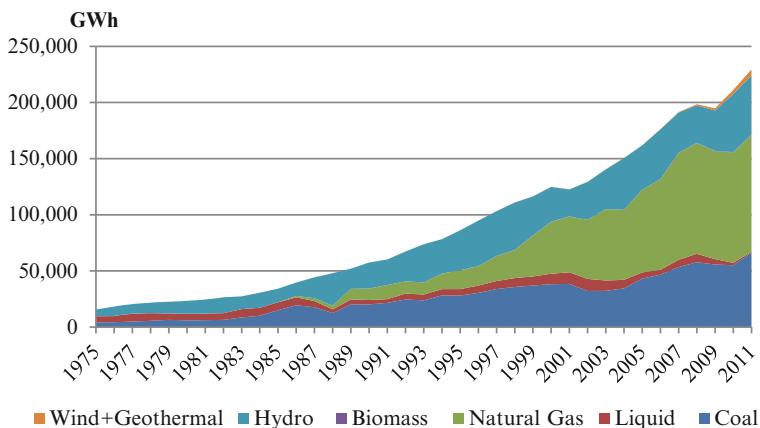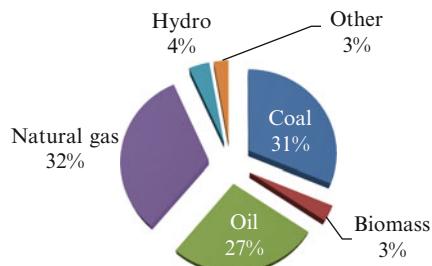
According to the latest report of the Ministry of Energy and Natural Resources (ETKB), as of 2011 Turkey had recoverable reserves of 11.75 billion tons of lignite, 1.3 billion tons of hard coal, and 8.6 Mtoe of biomass, whereas relatively little oil and natural gas production: 43 million tons of crude oil and 6.2 billion cubic meters of natural gas [15]. Furthermore, there is a technically recoverable shale gas volume of 420 billion cubic meters [16]. And Turkey's biogas potential only from animal waste is estimated about 1.5–2 Mtoe [17].

Electricity generation in Turkey is heavily dependent on thermal power plants consuming fossil fuels with the share of above 70 % in total electricity generation. Figure 36.3 indicates the generated electricity based on fuel type [18]. Liquid includes oil derivates as fuel oil, diesel, LPG, and naphtha. As seen with Fig. 36.3 coal, natural gas, and hydro are the primary energy sources used in the electricity generation. The amounts of non-hydro renewable and oil derivatives are negligible.

As a party to UNFCCC and Kyoto Protocol, like other ratified countries, Turkey also has established energy policies for reducing GHG emissions. Both decreasing the dependency on energy imports for supply security and climate change concern energy policies are based on increasing usage of domestic and renewable energy sources, such as wind, geothermal, hydro, and biomass, for power generation, e.g., the share of renewable energy sources in electricity supply is aimed to be at least 30 % in the year 2023 [19].

According to the national GHG emission inventory of Turkey, GHG (CO_2, CH_4, N_2O, HFC, PFC, and SF_6) emissions have increased 115 % from 187 to 402 million tons CO_2 equivalent between 1990 and 2010. The CO_2 emissions for the same period increased from 141 to 327 million tons. In addition, the CO_2 emissions from electricity generation increased 252 % from 30.3 to 106.8 million tons for the same period, covering on average approximately 30 % of the total CO_2 emissions in

Fig. 36.2 Distribution of Turkey's energy supply in 2011 (modified from [14])
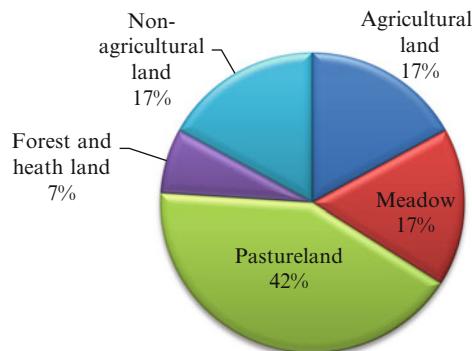
Fig. 36.3 Turkey's electricity generation by fuel type (modified from [18])

Turkey [20]. Consequently, the electricity generation between 1990 and 2011 in Turkey increased approximately 300 % from 57,543 to 229,395 GWh [18]. A reduction in electricity generation-associated CO_2 emissions can be achieved by increasing the usage of renewable energy sources, such as wind, geothermal, hydro, and biomass, for power generation. Thus utilization of biogas especially for electricity generation is getting more importance in Turkey, and its regional potentials should be determined in order to set the capacity for meeting the electricity demand of rural areas.

36.3 Materials and Methods

Ardahan is located in the north-eastern part of Turkey, frontier with Erzurum, Kars, and Artvin cities and also with the countries of Georgia and Armenia. The population of Ardahan is 112,721 people and 68 % of the population lives in the rural areas. The socioeconomic structure of the city is mainly based on the agriculture and livestock farming. There are 23,000 agricultural enterprises; 95 % of them are

Fig. 36.4 Land use of Ardahan in 2010 (modified from [21])

polycultural which have both agricultural and livestock production. Land use of Ardahan is given with Fig. 36.4 [21]. The largest share belongs to pasture land with 42 % convenient with livestock farming. Meadow, agricultural, and nonagricultural areas have the same share with 17 %, where the forest has the least with 7 %. Animal numbers of Ardahan according to the types and the shares of them in Turkey's total value in 2010 are given in Table 36.1 [21, 22]. Poultry has the largest share with 50.5 % in total animal numbers of 593,481 in the city. It is followed by 42 % cattle, 6 % small ruminants, and 1.6 % equines. In poultry the largest share belongs to goose with almost 50 %, broiler has 2 %, laying hens have 43 %, turkeys have 3 %, and ducks have 2 % for a total of 299,783 pieces. 71 % in 248,388 of cattle group is crossbred, whereas 7 % is culture and 22 % is domestic. Only 4 % of all small ruminants are goats, where the sheep have the remaining largest share and they are all domestic.

The amounts of waste are obtained by taking the number of population of each kind of animal. There are many factors affecting the amount of waste and biogas obtainable from animal husbandry. These are type of animal, body weight, ratio of total solids in the manure, volatile solids ratio, availability of the waste, and biogas yields. Factors taken into consideration in this chapter for the calculation of biogas are given in Table 36.2 from the literature [23, 24, 25].

In the equine group, daily manure per animal was considered as 10 kg for Ardahan. According to Sabuncu [25] 0.21 % of the manure is organic solid matter and the biogas production potential is 250 liter per kilogram of organic solid matter.

Theoretical energy potential of biomass is defined as the total energy released in a combustion process from a certain material (organic or inorganic). The theoretical energy describes the maximal energy content of the combusted material. Besides, technical energy potential describes the actual useful energy part from theoretical energy potential of the combustible material, under consideration of given converted technique (e.g., CHP, biogas turbine generator, and incinerator process) [26]. Due to the different converting techniques available in the market it is not possible to use all the theoretical energy potential but part of it [26, 27]. For determination of the available technical energy potential of waste, availability factors and solid matter ratios of the manure are taken into consideration in this chapter.

Table 36.1 Number of animals in Ardahan and their shares in Turkey for 2010 (modified from [21, 22])

Animal type	Number of animals	Share in the total of Turkey, %
Cattle	248,388	2.17
Small ruminants	35,969	0.12
Poultry	299,783	0.13
Equine	9,341	2.25
Total	593,481	0.21

Table 36.2 Waste amounts and biogas yields by type of animal (modified from [23, 24])

	Ton wet manure/year-animal	m^3 biogas/ton wet manure
Cattle	3.6	33
Small ruminants	0.7	58
Equine [25]	3.65	52.5
Poultry	0.022	78

The values used for the calculations are given in Table 36.3 [28, 29]. The availability factor which means the usable amount of the manure is an important issue to utilize the potential. The values according to the type of the wastes are selected as 65 % for cattle, 13 % for small ruminants and equine, and 99 % for poultry, where solid ratios are 15 % for cattle, 30 % for small ruminants and equine, and 35 % for poultry. Biogas yield is accepted as 200 m^3 per ton of solid animal waste [28]. Electricity generation efficiency was accepted as 38.5 % [30]. The biogas is assumed to be consisting of 55.5 % CH_4 and 44.5 % CO_2 whereas the heating value of CH_4 was 37.78 MJ/Nm^3 [25].

36.4 Results and Discussion

The theoretical annual biogas potential of Ardahan was calculated as 33.3 million m^3 for the year 2010 from the values given in Tables 36.1 and 36.2, whereas the technical annual biogas potential was calculated as 18.4 million m^3 according to the values given in Table 36.3. The results are summarized in Table 36.4. Technical annual biogas potential is capable of producing electrical energy of 107 GWh annually, which indicates 41 GWh annual electricity supply by taking into consideration 38.5 % electricity generation efficiency.

Looking at the distribution of 18.4 million m^3 of biogas which has energy equivalence of 107 GWh/year it consists of 95 % from cattle, 1.1 % from small ruminants, 1.4 % equine, and 2.5 % from poultry; those are given in Fig. 36.5.

Ardahan has annual net electricity consumption of approximately 82.3 GWh [31] that seems that approximately 50 % of it can be obtained from animal waste-originated biogas.

Table 36.3 Availability factors and solid ratios of animal manure (modified from [28, 29])
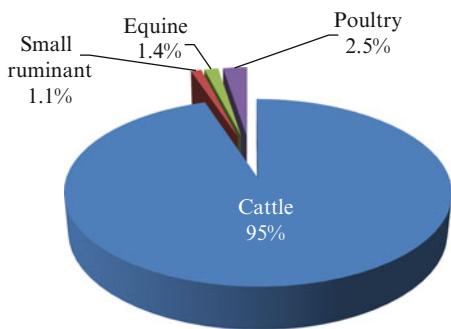
	Availability factor, %	Solid ratio, %
Cattle	65	15
Small ruminants	13	30
Equine	13[a]	30[a]
Poultry	99	35

[a]Accepted as same value with small ruminants

Table 36.4 Available animal waste biogas potential and energy equivalence

	Biogas potential, m^3/year	Energy equivalence, MJ/year
Cattle	17,436,838	365,613,867
Small ruminants	196,391	4,117,901
Equine	265,938	5,576,167
Poultry	457,049	9,583,361
Total	18,356,216	384,891,297

Fig. 36.5 Distribution of biogas from animal manure in Ardahan (2010)

As per one of the recent studies on Turkish biogas energy potential from animal wastes [28] Turkey's biogas potential was 2.18 billion m^3/year for the year 2009, and Ardahan had 18.4 million m^3/year biogas potential which indicates the share of 0.84 % in Turkey.

36.5 Conclusions

In this chapter the animal waste potential of Ardahan is investigated and the related biogas amount is calculated with 2010 data, taking into consideration the solid components and the availability factors of the manure. The situation of Ardahan's biogas potential in Turkey is tried to be determined. Results indicate that Ardahan has a significant biogas potential from animal wastes which is able to supply up to 50 % of its own electricity demand. Cattle have the largest share with 95 % in all biogas potential where poultry has the second with 2.5 %. The usage of this potential will contribute to the sustainable development of Ardahan and will also

pioneer for other cities of Turkey. The results of this chapter are important as the determination of the potential is the first step of building up biogas systems.

References

1. Scholz L, Aurich Meyer A, Kirschke D (2011) Greenhouse gas mitigation potential and mitigation costs of biogas production in Brandenburg, Germany. AgBioForum 14(3):133–141
2. Muneer T, Maubleu S, Asif M (2006) Prospects of solar water heating for textile industry in Pakistan. Renew Sustain Energy Rev 10:1–23
3. Balat M, Balat H (2009) Biogas as a renewable energy source—A review. Energy Sources, Part A 31:1280–1293, Taylor&Francis
4. Klass DL (2004) Biomass for renewable energy and fuels. In: Cleveland CJ (ed) Encyclopedia of energy, vol 1. Elsevier, New York, NY, pp 193–212
5. Bilgen S, Keles S, Kaygusuz K (2007) The role of biomass in greenhouse gas mitigation. Energy Sources, Part A 29:1243–1252, Taylor and Francis
6. Kaygusuz K (2009) Bioenergy as a clean and sustainable fuel. Energy Sources, Part A 31:1069–1080, Taylor&Francis
7. Singh KJ, Sooch S (2004) Comparative study of economics of different models of family size biogas plants, for state of Punjab, India. Energy Convers Manag 45:1329–1341
8. Surroop D, Mohee R (2012) Technical and economic assessment of power generation from biogas, International Conference on Environmental Science and Technology IPCBEE vol.30 IACSIT Press, Singapore
9. Taleghani G, Kia AS (2005) Technical-economical analysis of the Saveh biogas power plant. Renew Energy 30:441–446
10. Santosh Y, Sreekrishnan TR, Kohli S, Rana V (2004) Enhancement of biogas production from solid substrates using different techniques—A review. Bioresour Technol 95:1–10
11. Demirbaş A (2002) Production potential of electricity from biomass in Turkey. Energy Sources 24:921–929, Taylor &Francis
12. Demirbaş A, Pehlivan E, Altun T (2006) Potential evolution of Turkish agricultural residues as bio-gas, bio-char and bio-oil sources. Int J Hydrogen Energy 31:613–620
13. Kaya D, Tırıs M, Yaldız O, Saraç Hİ, Ekinci K, Koçar G, Karaman N, Ayan E, Saraç M (2009) The production of biogas from agricultural and animal wastes and its utilization in the integrated energy system (Biogas) Project. Engineers and Machinery, in Turkish 50(593):2–14
14. Republic of Turkey Ministry of Energy and Natural Resources (ETKB in Turkish) (2011) General Energy Balance Table of 2011, http://www.enerji.gov.tr/EKLENTI_VIEW/index. php/raporlar/raporVeriGir/71073/2. Accessed on 30 Oct 2012
15. Republic of Turkey Ministry of Energy and Natural Resources (ETKB in Turkish) (2012) Blue Book in Turkish, The Aims and the Activities of The Ministry of Energy and Natural Resources with Affiliated and Related Institutions, Ankara
16. EIA (US Energy Information Administration) (2011) World shale gas resources: an initial assessment of 14 regions outside the United States
17. Republic of Turkey Ministry of Energy and Natural Resources (ETKB in Turkish) web page http://www.enerji.gov.tr/index.php?dil= tr&sf= webpages &b= biyoyakit&bn=235&hn=& nm=384&id=40698. Accessed on 10 Dec 2012
18. Turkish Electricity Transmission Company (TEIAS in Turkish) (2012) Turkish electricity generation-transmission statistics 2011. http://www.teias.gov.tr/TürkiyeElektrikİstatistikleri/ istatistik2011/istatistik% 202011. htm. Accessed on 30 Oct 2012
19. Republic of Turkey Ministry of Energy and Natural Resources (ETKB in Turkish) (2009) Electricity energy market and supply security strategy paper, Ankara

20. TURKSTAT (Turkish Statistical Institute TUİK in Turkish) (2012) Turkey GHG Emission Inventory 1990–2010, National Inventory Report, Ankara
21. Republic of Turkey Ardahan Governorship Agriculture City Directorate (2011), Brifing
22. TURKSTAT (Turkish Statistical Institute TUİK in Turkish) (2010) Livestock Production Statistics
23. http://www.eie.gov.tr/turkce/YEK/biyoenerji/01-biyogaz/bg_haykay.html. Accessed on 20 Jan 2012
24. Akbulut A, Dikici A (2004) Biogas potential and cost analysis of Elazığ City, in Turkish, Researches of East Anatolia Region, 36–41
25. Sabuncu ÖC (2010) Technical, economical and environmental analysis of biogas production, in Turkish MSc. Thesis, Hacettepe University, Ankara, Turkey
26. Karaj S, Rehl T, Leis H, Müller J (2010) Analysis of biomass residues potential for electrical energy generation in Albania. Renew Sustain Energy Rev 14:493–499
27. Torsten R (2006) Investigation to the energy production potential of biomass in proportion to energy demand of the Administrative District of Güstrow. Stralsund, Germany
28. Avcıoğlu OA, Türker U (2012) Status and potential of biogas energy from animal wastes in Turkey. Renew Sustain Energy Rev 16:1557–1561
29. Kaya D, Eyidoğan M, Çoban V, Çağman S, Aydoner C, Tırıs M (2009) Animal originated biogas potential and economy of Turkey, in Turkish. ICCI 2009 Proceedings, 59–62
30. Tolay M, Yamankaradeniz H, Yardımcı S, Reiter R (2008) Biogas production from animal wastes in Turkish, VIIth National Clean Energy Symposium, UTES 2008, s:259–264, December 17–19, İstanbul
31. Turkish Electricity Distribution Company, TEDAS in Turkish (2012) 2010-Turkey Electricity Distribution and Consumption Statistics

Chapter 37
Clean Technology for Volatile Organic Compound Removal from Wastewater

Filiz Ugur Nigiz and Nilufer Durmaz Hilmioglu

Abstract Volatile organic compounds (VOCs) are the main contaminants in industrial wastewater. It is well known that the presence of these compounds in water—even if they are at low concentration—causes a carcinogenic effect. At industrial scale, removal of these compounds is possible commercially. Membrane-based pervaporation (PV) promises to be clean energy system when it is accompanied with the membrane which has high affinity to VOCs. Compared to the other methods, PV offers some advantages. It is energy intensive, cost effective, clean, and modular technology. In this work, pristine and 20 wt.% and 30 % of ZSM-5-filled zeolite-loaded composite polydimethylsiloxane membranes are prepared and they are employed in pervaporation process to separate toluene from toluene–water mixtures. PV performance is evaluated as a function of flux and enrichment factor. ZSM-5 zeolite is selected as inorganic particle due to the highly hydrophobic characteristic. Pervaporation experiments are carried out at room temperature.

Keywords Pervaporation • VOC removal • Toluene removal • ZSM-5 zeolite • Polydimethylsiloxane

Nomenclature

A	Effective area of the membrane
J	Flux
S_d	Degree of swelling
t	Time
W_d	Weights of dry membrane

F.U. Nigiz (✉) • N.D. Hilmioglu
Chemical Engineering Department, Kocaeli University, Kocaeli 41380, Turkey
e-mail: filiz.ugur@kocaeli.edu.tr; niluferh@kocaeli.edu.tr

W_p	Total permeate weights of mixtures
W_s	Weights of swollen membrane
X_a	Concentration of the toluene in the feed mixture
Y_a	Concentration of the toluene in the permeate mixture

Greek Symbols

β	Enrichment factor

Acronyms

PV	Pervaporation
DCP	Dicumylperoxide
EPDM	Ethylene propylene diene monomer
PDMS	Polydimethylsiloxane
PEBA	Polyether-block-polyamide
PEG	Polyethyleneglycol
PI	Polyimide
PTFE	Polytetrafluoroethylene
PTMSP	Polytrimethylsilylpropyne
PVC	Polyvinylchloride
UV	Ultraviolet–visible
VOC	Volatile organic compound

37.1   Introduction

Volatile organic compounds (VOCs) such as benzene, toluene, ethyl benzene, xylene, and chlorinated solvents are hazardous materials for environment and human health. VOCs are emitted from several man-made (aerosol, traffic), industrial, agricultural, and groundwater sources. Water is important for human life and environment; therefore the main issue is removing the VOC from ground, drinking, and industrial wastewater. But these compounds have low solubility in water (ppm level) at low temperature (20–30 °C); hence the purification processes become complex and costly. Biological treatment, adsorption with active carbons, and air stripping are the conventional processes to remove VOCs from aqueous solutions [1, 2]. Active carbon adsorption method is effective at low VOC concentration; however carbon must be regenerated in the following steps. Biological treatment method has limited activity on the microorganism; therefore, this technique is only available at restricted VOC concentration and temperature. Using of air stripping method is also limited by the Henry's constant compounds [3].

Pervaporation is a new environment-friendly and cost-effective membrane process which separates close boiling point, azeotropic, thermal sensitive mixtures with low energy consumption and more efficiency. Recently it has become an attractive method for wastewater treatment. PV does not emit pollution; it does not need an entrainer solvent or regeneration steps compared to other VOC removal methods. PV is modular, so it is possible to use it as hybrid with industrial process [4–6]. PV is commercially used in the following three main areas: separation of organic–organic mixtures, removal of organic compounds from dilute solution, and dehydration of aqueous mixtures [7–10].

Pervaporation is the most widely used and commercialized in alcohol purification processes. Particularly, it has been used as a commercial process in fuel ethanol production facilities. It is environmentally and economically important to break the ethanol–water azeotrope by pervaporation process. This process is carried out by using hydrophilic membranes to separate water from broth or hydrophobic membrane to separate ethanol from product.

37.2 Background: Pervaporation Process

There are two kinds of PV system: vacuum PV and purge gas PV [7]. The vacuum PV system is mostly used commercially and it simply consists of a feed tank, circulation and vacuum pump, membrane cell, and cold traps (permeate vessels).

The feed mixture, which is kept at the desired temperature, is pumped to the membrane cell with a specific flow rates. According to the affinity of membrane, one of the components dissolves on the membrane surface. Due to the difference in concentration on either side of the membrane, the selected component diffuses through the membrane. This stream is called as "permeate." The rejected stream is called as "retentate." At the downstream side, vacuum pressure is applied in order to create a pressure difference so that permeate leaves the membrane as vapor phase. Vapor permeate is condensed into cold traps by liquid nitrogen. Flux and selectivity are calculated by determination of concentration and weight of that permeate.

The purge gas PV system does not require a vacuum application but different costs arise because the gas should be sent to the system. This method is useful in many cases which is required diluted product [8].

Separation via pervaporation depends on the concentration gradient which is maintained by pressure difference in two sides of the membrane. In this system, nonporous membranes are used and the transport through the membrane is described by the solution-diffusion model which simply consists of three steps: solution of selected compound onto the membrane, diffusion through the membrane, and desorption into downstream side [11]. Thereby selective sorption and selective diffusion play an important role on PV performance which is characterized by the flux and enrichment factor values.

The advantages of this technique which can be used as a hybrid with conventional methods are listed as follows:

- The method is quite simple and easy to operate.
- Additional chemicals to separate azeotropic and close-boiling-point components are not needed.
- It is modular and it can easily be added to other systems.
- It is not a temperature-based separation system, so it can be used to separate thermal sensitivity organic solutions.
- Energy consumption is in minimum level.
- Product separation range is quite large (acids, esters, oils, alcohols, and ketones can be separated from each other or water).
- Membrane-based material manufacturing and recycling are easy.
- Because of all advantages, it is an environment-friendly and a cost-effective process [8–10].

37.2.1 Membrane Selection

Membrane is "the heart" of this system, so PV investigation depends on not only the operation condition but also the membrane material selection and production. The membrane which will be used in PV should be chemically and thermally stable and mechanically durable.

Due to the cheapness and modification ability of polymeric membrane materials, they are mostly used in PV. However polymers which have organic chain structure are thermally and chemically unstable, so it is hard to operate them at high process temperature [12].

Transition through polymer molecules depends on the free volume of polymer, active polymer chains, and structural movements. The other factors which affect the transition rates are listed as follows:

- The glass transition temperature of the polymer
- The degree of unsaturation of the polymer
- The number of branched methyl groups
- Average polymer molecular weight
- Plasticizers and fillers which are added to the polymer [13]

Besides polymeric ones, inorganic membranes (ceramic or zeolite membranes) are commercially used in PV unit. Inorganic membranes are used in high-temperature processes. They can be used in desired feed concentration because they do not tend to swell. Although they are more durable at long-term operation time, they are expensive and brittle [14]. Also it is hard to form them as a uniform membrane.

Recently inorganic particles (such as clay, zeolite) are incorporated to the polymer matrix in order to make polymeric membrane more stable and durable over the long-term operations [15]. Inorganic particle-filled membrane is called as mixed matrix or composite membrane. These membranes show good performance

in long-term PV operation at high temperature. Compared to the inorganic ones, mixed matrix membranes are cheap and it is easy to form them as membrane.

The most preferred inorganic additives are zeolites. They are known as inorganic and regular crystalline structures with different molecular pores. They are commercially used as catalysts, adsorbents, or ion-exchanger. Zeolites are composed of tetrahedral structures, and these structures consist of aluminum silicate atoms. The rates of Si/Al determine the degree of hydrophobicity or hydrophilicity of zeolites. The smaller Si/Al ratio increases the hydrophilicity of the zeolite [16–18].

37.2.2   Literature Research on Membrane Selection

In literature different types of membrane such as poly(dimethylsiloxane) (PDMS), polyimide (PI), polyether-block-polyamide (PEBA), ethylene propylene diene monomer (EPDM), poly(trimethylsilylpropyne) (PTMSP), poly(vinylchloride) (PVC), and poly(ethyleneglycol) (PEG) have been used to separate VOCs from model wastewater [1, 4, 19–23]. PDMS is mostly used in PV to separate organic compounds from water due to the hydrophobic and rubbery nature. It has chain flexibility and huge free volume; thereby organic components are able to pass through the membrane easily. It is compatible with inorganic materials due to the rubbery nature, so it is one of the rare hydrophobic membranes used commercially. Polymer chains of PDMS are in motion even at low temperatures.

There are many pervaporation studies in which the composite PDMS membranes are used. However, a small part of them is in the separation of VOCs [5, 24–28].

37.3   Experimental

In this study pristine- and ZSM-5-filled PDMS composite membranes have been prepared by the solution-casting and pressing method. Pristine and 20 wt.% and 30 % of ZSM-5-filled composite membranes have been used in PV system to separate toluene from water. Effect of feed composition on flux and enrichment factor has been evaluated.

37.3.1   Materials

PDMS and ZSM-5 have been purchased from Aldrich Chemicals. Toluene of 99.5 % purity has been purchased from Merck Chemical from Turkey.

Deionized water has been supplied from laboratory.

37.3.2 Membrane Preparation

PDMS is dissolved in toluene. Solution is stirred overnight. Desired amount of ZSM-5 (with respect to the pure polymer mass) is added to the polymer–water solution for composite membranes and total solution is stirred for 10 h. Then 2 wt.% of dicumylperoxide (DCP) is added to solution and stirring is continued for 5 h. Solution is poured onto glass petri dishes and it is dried at room temperature. Bulk polymer mixture is taken to a hot press for cross-linking reaction for 2 min. After membrane forms as a flat sheet, it is taken to a vacuum oven to remove the remaining acid.

37.3.3 Swelling Experiments

The membrane samples are cut into small pieces of about 2 cm^2. The samples are immersed in toluene–water mixtures which contain 5 wt.% of toluene. Swollen membrane's weight is measured and the swelling degree is calculated as

$$S_d = (W_s - W_d)/W_d * 100 \tag{37.1}$$

S_d represents the swelling degree of the membrane, and W_s and W_d are the weight of the swollen and dry membranes, respectively.

37.3.4 Pervaporation Procedure
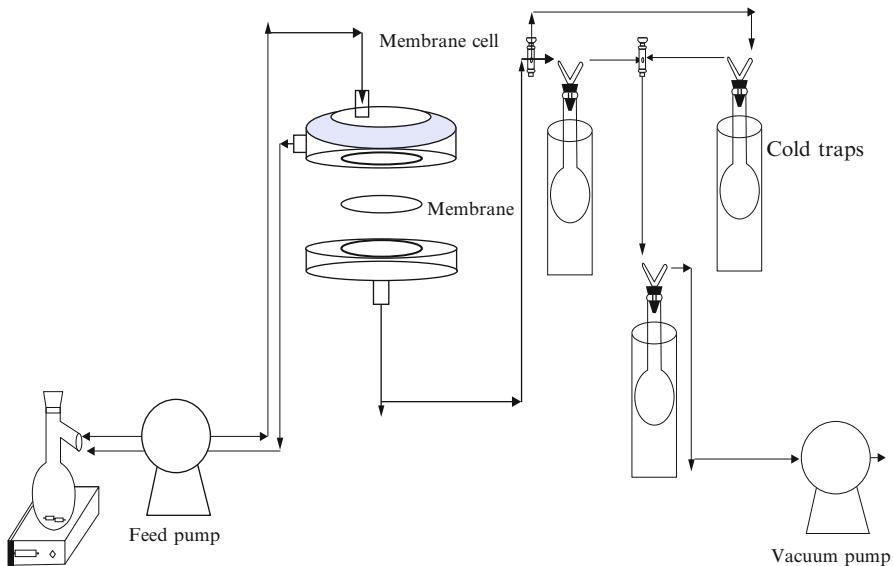
Experimental PV setup has been shown in Fig. 37.1.

Experiments are carried out at room temperature. At downstream side vacuum is applied and the pressure is measured as 20 mbar. Membrane cell is made from PTFE (Teflon) that has 28 cm^2 effective areas and the volume capacity of the cell is 500 ml. The toluene–water mixture is fed to cell continuously. The permeated mixture is condensed in liquid nitrogen traps. Two traps are operated; one of them is replaced with another after an hour and sample is taken from operated ones.

Every hour the feed and the permeate mixture are measured and the concentration of toluene is determined by UV analysis to calculate flux and enrichment factor of the membranes [4]. The flux is calculated from the weight of permeate. Flux (J) and enrichment factor (β) are calculated as

$$J = W_p/A.t \tag{37.2}$$

$$\beta = (Y_a/X_a) \tag{37.3}$$

Fig. 37.1 Schematic diagram of experimental pervaporation unit

W_p represents the total permeate mass of mixtures, A is the effective area of membrane, and t is the time. X_a is the concentration of the toluene in the feed mixture and Y_a is the concentration of the toluene in the permeate mixture [4].
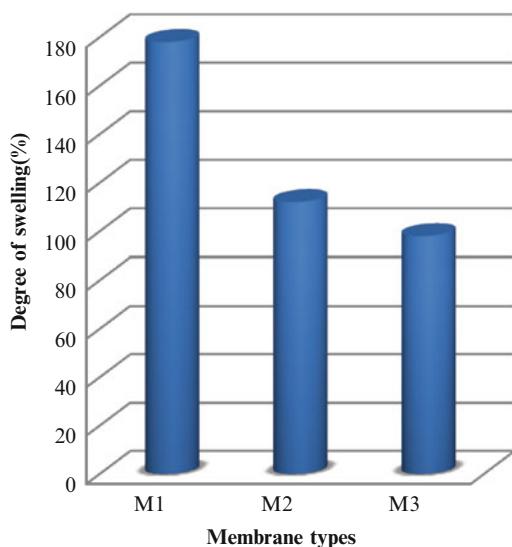
37.4   Results and Discussion

Before the pervaporation experiments, membranes are immersed in toluene–water solution for about 4 h for determining the swelling degree. Because the solubility of toluene is quite low in water, the free volumes of membranes are increased by swelling experiments for selective removal of the organic molecules even if their concentration is quite low. In this respect, the swelling character of the membrane gives an idea about membrane flux and enrichment factor.

37.4.1   Effect of Zeolite Loading on Pervaporation Performance

As shown in Fig. 37.2, swelling degrees of the pristine and loaded membranes decrease when the ZSM-5 zeolite loading increases.

Fig. 37.2 Effect of zeolite
loading on swelling degree
(M1: pristine, M2: 20 wt.%
ZSM-5, M3: 30 wt.%
ZSM-5)

Adding of inorganic particles into polymeric matrix improves the mechanical
and chemical stability of the membrane. Also free volume increasing of the
polymer is restricted by the inorganic filler, so it causes a reduction in swelling
degree of the membrane.
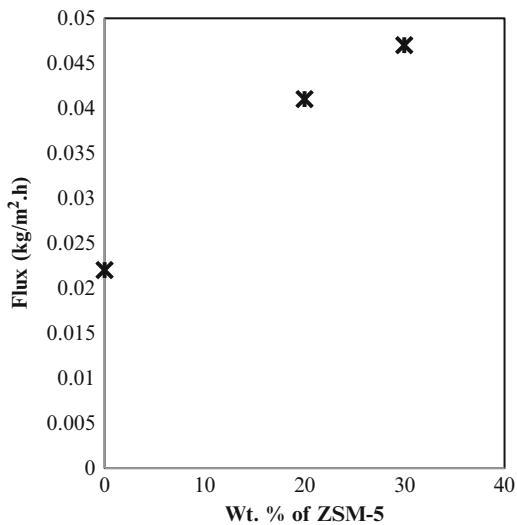
Degree of swelling is desired up to a certain point because permeability of the
membrane increases with swelling degree. However, the selective characteristics of
membranes are often lost with swelling due to the drifting of unselected
components. Hence it reduces the enrichment factor. One of the ways to limit the
degree of swelling of the polymer is cross-linking procedure. Cross-linking process
restricts the chain flexibility of polymer and increases the mechanical strength of
membrane [29]. In this way, the solubility and diffusivity of components are
reduced. Thus, permeability decreases and enrichment factor increases. In this
study PDMS has been cross-linked by DCP.

Figures 37.3 and 37.4 show the flux and enrichment factor of all membranes.
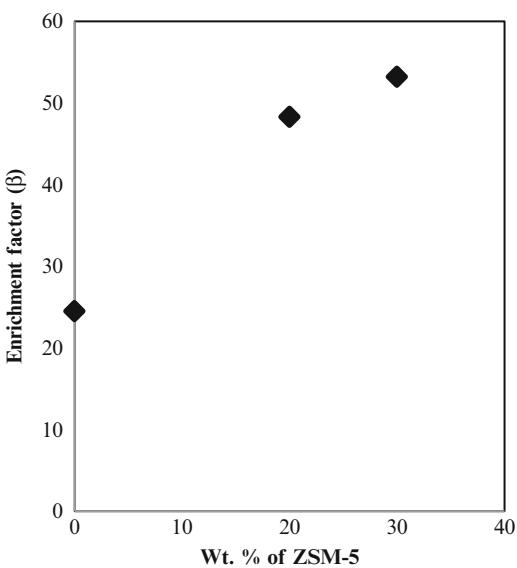
As seen in Fig. 37.3, with the incorporation of ZSM-5 particles into the PDMS
matrix, flux values enhance. Despite the decrease in the free volume of the
membrane, flux values increase by the addition of zeolite because of the hydropho-
bic nature of ZSM-5. This zeolite shows high affinity to organic molecules. These
selective properties of composite membranes cause an increase in enrichment factor
as shown in Fig. 37.4.

In previous studies, it was observed that the addition of ZSM-5 was effective to
enhance pervaporation performance but this effect was lost after a certain loading
point. After an optimum point, zeolites begin to cluster. This effect reduces the
effectiveness of the polymer to make the selective sorption and diffusion. Therefore
it becomes an important subject to find out an optimum zeolite loading. In previous

Fig. 37.3 Effect of zeolite loading on flux

Fig. 37.4 Effect of zeolite loading on enrichment factor

pervaporation experiments [30], flux and enrichment factor values have been decreased slowly in 40 wt.% of ZSM-5 ratio; therefore, the optimum zeolite loading has been determined as 30 %.

37.5 Conclusions

In this study the membrane character—which is responsible for the system performance—has been investigated as a function of swelling degree, flux, and selectivity. According to this study the following results are obtained:

- The degree of swelling of the membrane has been restricted by adding zeolite into the polymer matrix. Also cross-linking by DCP has prevented the excessive swelling of the membrane.
- Incorporation of zeolite particles into the polymer matrix enhances flux values because of the hydrophobic nature of ZSM-5.
- Enrichment factors increase with zeolite addition due to the selective nature of zeolite.
- It is seen that the PDMS is an appropriate membrane material if it will be desired to remove the organic components.

References

1. Peng M, Vane LM, Liu SX (2003) Recent advances in VOCs removal from water by pervaporation. J Hazard Mater B98:69–90
2. Vane LM, Alvarez FR (2002) Full-scale vibrating pervaporation membrane unit:VOC removal from water and surfactant solutions. J Membr Sci 202:177–193
3. Ghoreyshi AA, Jahanshahi M, Peyvandi K (2008) Modelling of volatile compounds removal from water by pervaporation process. Desalination 222:410–418
4. Panek D, Konieczny K (2007) Preparation and applying the membranes with carbon black to pervaporation of toluene from the diluted aqueous solutions. Sep Purif Technol 57:507–512
5. Ohshima T, Kogami Y, Miyata T, Uragami T (2005) Pervaporation characteristics of cross-linked poly (dimethylsiloxane) membranes for removal of various volatile organic compounds from water. J Membr Sci 260:156–163
6. Wang BG, Miyazaki Y, Yamaguchi T, Nakao S (2000) Design of a vapor permeation membrane for VOC removal by the filling membrane concept. J Membr Sci 164:25–35
7. Vallieres C, Favre E (2004) Vacuum versus sweeping gas operation for binary mixtures separation by dense membrane processes. J Membr Sci 244:17–23
8. Brazinha C, Alves VD, Viegas RMC, Crespo JG (2009) Aroma recovery by integration of sweeping gas pervaporation and liquid absorption in membrane contactors. Sep Purif Technol 70:103–111
9. Lipnizki F, Field RW, Ten PK (1999) Pervaporation-based hybrid process: a review of process design, applications and economics. J Membr Sci 153:183–193
10. Hoof VV, Abeele LV, Buekenhoudt A, Dotremont C, Leysen R (2004) Economic comparison between azeotropic distillation and different hybrid systems combining distillation with pervaporation for the dehydration of isopropanol. Sep Purif Technol 37:33–49
11. Feng X, Huang RYM (1997) Liquid separation by membrane pervaporation: a review. Ind Eng Chem Res 36:1048–1066
12. Wee SL, Tye CT, Bhatia S (2008) Membrane separation process—Pervaporation through zeolite membrane. Sep Purif Technol 63:500–516
13. George SC, Thomas S (2001) Transport phenomena through polymeric systems. Prog Polym Sci 26:985–117

14. Chapman PD, Oliveira T, Livingston AG, Li K (2008) Membranes for the dehydration of solvents by pervaporation. J Membr Sci 318:5–37
15. Chung TS, Jiang LY, Li Y, Kulprathipanja S (2007) Mixed matrix membranes (MMMs) comprising organic polymers with dispersed inorganic fillers for gas separation. Prog Polym Sci 32:483–507
16. Shah D, Kissick K, Ghorpade A, Hannah R, Bhattacharyya D (2000) Pervaporation of alcohol–water and dimethylformamide–water mixtures using hydrophilic zeolite NaA membranes: mechanisms and experimental results. J Membr Sci 179:185–205
17. Caro J, Noack M (2008) Zeolite membranes–Recent developments and progress. Microporous Mesoporous Mater 115:215–233
18. Bowen TC, Noble RD, Falconer JL (2004) Fundamentals and applications of pervaporation through zeolite membranes. J Membr Sci 245:1–33
19. Panek D, Konieczny K (2008) Applying filled and unfilled polyether-block-amide membranes to separation of toluene from wastewaters by pervaporation. Desalination 222:280–285
20. Roizard D, Teplyakov V, Favre E, Fefilatiev L, Lagunstsov N, Khotimsky V (2004) VOC's removal from water with a hybrid system coupling a PTMSP membrane module with a stripper. Desalination 162:41–46
21. Konieczny K, Bodzek M, Panek D (2008) Removal of volatile compounds from the wastewaters by use of pervaporation. Desalination 223:344–348
22. Ray S, Singha NR, Ray SK (2009) Removal of tetrahydrofuran (THF) from water by pervaporation using homo and blend polymeric membranes. Chem Eng J 149:153–161
23. Kim HJ, Nah SS, Min BR (2002) A new technique for preparation of PDMS pervaporation membrane for VOC removal. Adv Environ Res 6:255–264
24. Lu SY, Chiu CP, Huang HY (2000) Pervaporation of acetic acid/water mixtures through silicalite filled polydimethylsiloxane membranes. J Membr Sci 176:159–167
25. Nasiri H, Aroujalian A (2010) A novel model based on cluster formation for pervaporation separation of polar components from aqueous solutions. Sep Purif Technol 72:13–21
26. Liu G, Xiangli F, Wei W, Liu S, Jin W (2011) Improved performance of PDMS/ceramic composite pervaporation membranes by ZSM-5 homogeneously dispersed in PDMS via a surface graft/coating approach. Chem Eng J 174:495–503
27. Wu H, Liu L, Pan F, Hu C, Jiang Z (2006) Pervaporative removal of benzene from aqueous solution through supramolecule calixarene filled PDMS composite membranes. Sep Purif Technol 51:352–358
28. Lei L, Xiao Z, Tan S, Pu L, Zhang Z (2004) Composite PDMS membrane with high flux for the separation of organics from water by pervaporation. J Membr Sci 243:177–187
29. Semenova S, Ohya H, Soontarapa K (1997) Hydrophilic membranes for pervaporation: An analytical review. Desalination 110:251–286
30. Nigiz FU, Hilmioglu ND (2012) Seperation with zeolite filled poly(dimethylsiloxane) Membranes, I. National Rubber Congress, İstanbul

Chapter 38
Comparison of Thermal Properties and Kinetics of Selected Waste Wood Samples in Two Different Atmospheres

Sema Yurdakul and Aysel Atımtay

Abstract Knowledge of the kinetics and thermal decomposition properties of woods are of great importance. Successful design and control of technologies for the pyrolysis and combustion of lignocellulosic raw materials require a good understanding of the kinetics of the thermochemical processes. In this chapter, thermal properties and kinetic constants of selected waste wood samples (pine, medium-density fiberboard, and plywood) are examined in two different atmospheres, nitrogen and air, by thermogravimetric analysis. Samples were sieved to 3 mm and a heating rate of 10 °C/min was used. In nitrogen atmosphere, two peaks were observed for all samples due to moisture and volatile content of the samples. However, in air atmosphere three peaks were observed owing to removal of moisture, active oxidation of volatile matter, and char combustion. Activation energies of the samples in air atmosphere were higher than in the nitrogen atmosphere. Consequently, it can be said that all samples were more thermally stable in an air atmosphere than in a nitrogen atmosphere. Furthermore, a diffusion-controlled reaction starting on the exterior of spherical particles was found to be the main mechanism for all waste wood samples.

Keywords Waste wood • TGA • Thermal decomposition • Thermal kinetics • Solid-state mechanisms

Nomenclature

A   Thermal constant (1/min)
DTG   Derivative thermogravimetry
E   Activation energy (kJ/mole)

S. Yurdakul (✉) • A. Atımtay
Environmental Engineering Department, Middle East Technical University,
Ankara 06800, Turkey
e-mail: ysema@metu.edu.tr; aatimtay@metu.edu.tr

MDF   Medium-density fiberboard
P   Pine
Pl   Plywood
TG   Thermogravimetry
TGA   Thermogravimetric analysis

38.1 Introduction

There is a great need for research into renewable energies due to worldwide decrease of fossil fuel resources and the negative environmental effects of fossil fuel combustion pollution. There is also a pressure to decrease carbon dioxide (CO_2) emissions to prevent the greenhouse effect in the world according to Kyoto Protocol. Therefore, biomass has gained a great amount of interest as one of the potential renewable energy sources (RES) [1].

Biomass-based fuels are considered environmentally friendly for several reasons. CO_2 generated during the combustion of biomass was originally absorbed from the atmosphere during the growth of the plants. Therefore, net CO_2 production during combustion of biofuels is considered to be zero due to the fact that they originated as biomass [2]. However, burning of fossil fuels uses old biomass and it is converted into new CO_2; this contributes to the greenhouse effect and decreases reserves of nonrenewable sources. Burning new biomass contributes no new CO_2 to the atmosphere because replanted biomass ensures that CO_2 is absorbed and returned to a cycle of new growth. When biomass is used for the production of 1 GJ of energy, 0 kg of CO_2 is produced; however, when fossil fuels are used for the production of the same amount of energy, 60–110 kg of CO_2 will be released to the atmosphere [3].

Greenhouse gases, especially carbon dioxide and methane, have considerable effects on the climate. Greenhouse gases are mainly produced from the combustion of the fossil fuels and they can cause significant changes in the world climate patterns. Increase of the concentration of greenhouse gases in the atmosphere can cause warmer temperatures on the earth [4]. A temperature increase of 1.5–4 K in this century would have very important and complex effects on the world climate. There would be water shortage in some areas of the world, and humans, plants, and animals will be adversely affected by this situation. In order to prevent global warming and keep the temperature increase at about or beneath a couple of degrees, scientists suggest that the current level of emissions must be reduced by about 60 %. In order to reduce the potential warming effect of greenhouse gases, the use of fossil fuel sources should be decreased and the use of renewable energy sources such as biomass, wind, and solar energy should be increased. Increasing the efficiency of energy production is also very important for decreasing the production of greenhouse gases [5]. In this chapter, waste wood is considered as a biomass resource because it can be used for heating, steam production, and energy production due to its considerable energy content. Moreover, wood has a strategic role in prevention

of global warming because trees absorb CO_2 during photosynthesis and stores it until natural, biological, or thermal degradation. Replacing fossil fuel with wood fuel would be predicted to decrease net CO_2 production by over 90 % [4].

Main sources of waste wood are waste materials from board production (plywood, chip, and fiberboard—MDF), log and timber production, old electricity transmittance poles, old telephone and mining poles, and waste materials from railway constructions, furniture production, and demolished buildings.

In order to produce energy from waste wood, suitable combustion systems should be designed. Otherwise, very harmful pollutants can be generated during combustion because of the chemical contents of waste wood. Determination of the kinetics of the thermal behavior of waste wood is important because designing systems based on the pyrolysis and combustion of renewable lignocellulosic raw materials requires good knowledge of the kinetics of these processes [6].

This chapter aims to determine the kinetic parameters of three different types of waste wood samples (plywood, pine, and fiberboard—MDF) both in air and nitrogen atmospheres. For this purpose, thermal behavior and thermal decomposition results of these samples are investigated using thermogravimetric analysis (TGA). The results obtained in both atmospheres were compared with one another.

38.2   Theoretical Background

For the combustion of wood, shrinking core model can be used. Despite certain problems, the "shrinking core" model is the best simple representation for the majority of reacting gas–solid systems on the basis of studies of numerous systems. According to the model, when no ash is formed, such as in the burning of pure carbon, the reacting particle shrinks during the reaction and then finally disappears [7].

When wood is exposed to elevated temperatures, changes in the structure of the wood occur. At a temperature below 100 °C, permanent reductions in strength can occur. There is no carbohydrate degradation below 100 °C. At temperature above 100 °C, chemical bonds begin to break. The number of broken bonds increases as temperature increases. Between 100 and 200 °C, noncombustible products such as carbon dioxide, trace organic compounds, and water vapor are produced. Above 200 °C, celluloses are destroyed and flammable volatiles are produced. If volatile compounds are mixed with air and heated to the ignition temperature, combustion reactions occur. Above 450 °C, all volatile material is consumed, and only char residue remains. This char can be oxidized to carbon dioxide, carbon monoxide, and water vapor; oxidation of this char is called afterglow. Thermal reactions of the wood can vary depending on the individual components and chemical content of the wood. Cellulose is mainly responsible for the production of flammable volatiles. Hemicellulose is less thermally stable than cellulose and it evolves more noncombustible gases. Lignin produces more residual char than cellulose [8].

Thermal decomposition of a solid is a very complex process which occurs in a hetero-phase system in several stages. These stages can be related to heat transport as well as discharge of vapor–gas products of decomposition or development of a new solid phase [9].

Three factors control the design of a gas–solid reactor: the reaction kinetics for single particles, the size distribution of solids being treated, and the flow patterns of solids and gas in the reactor. Where the kinetics are complex and not well known, analysis of the problem will be difficult. Therefore, the responsible mechanisms and characteristics of the particles must be determined in advance in order to achieve correct design. The temperatures at which decomposition reactions of wood start and the changes in sample weight as the reactions progress can be characterized by TGA. Quantitative methods can be applied to TGA curves to obtain kinetic parameters. The kinetic parameters usually include the activation energy, the pre-exponential factor, and the order of the reaction [8].

38.3   Materials and Methods

Pine (P), MDF, and plywood (PL) samples were obtained from a manufacturing center of these products. The pine (P) sample did not contain any added chemicals; on the other hand, chemically treated MDF and PL samples contained different types of chemicals.

Thermal analyses of the waste wood samples were carried out by using a Perkin Elmer-Pyris-1, Thermal Gravimetric Analyzer. Approximately 17–25 mg sample was used for each experiment and average particle size of the samples was 3 mm. Each experiment was repeated three times and the average of the results was reported. During the experiments, reproducible results were obtained by using these sample sizes. Experiments were performed at 20 mL/min airflow rate in a temperature range of 30–900 °C. Heating rate was 10 °C/min. A temperature increase program was used. Thermal kinetic constants for the samples were calculated by using Coats–Redfern method [10] which is given in Eqs. (38.1a) and (38.1b):

$$\ln \frac{g(\alpha)}{T^2} = \ln \frac{AR}{\beta E} - \frac{E}{RT} \qquad (38.1a)$$

$$\alpha = (m_0 - m_t)/(m_0 - m_\infty) \qquad (38.1b)$$

where, m_0—initial weight of the reactant, m_t—weight at time t, and m_∞—weight at equilibrium. A is the pre-exponential constant, E is the activation energy, T is the absolute temperature, R is the gas constant, and β is the heating rate. According to Eq. (38.1a), a plot of $\ln[g(\alpha)/T^2]$ against the reciprocal of temperature should give a straight line with a slope equal to $-E/R$ and the intercept of the line will give the

Table 38.1 Selected Coats and Redfern mechanisms used in this chapter (adapted from ref. 12)

Mechanism	$g(\alpha)$	Symbol
Diffusion mechanism		
One-way transport	α^2	D1
Two-way transport	$\alpha + (1+\alpha)\ln(1-\alpha)$	D2
Three-way transport	$((1-\alpha)^{1/3})^2$	D3
Ginstling–Brounshtein equation	$1 - 2\alpha/3 - (1-\alpha)^{2/3}$	D4
Limiting surface reactions, both phases		
Three dimensions	$1 - (1-\alpha)^{1/3}$	R3
Chemical reaction		
First order	$-\ln(1-\alpha)$	F1

pre-exponential constant, A. $g(\alpha)$ is the integral function of conversion [11]. Therefore, if the correct $g(\alpha)$ is used for a mechanism, a straight line is obtained with a high correlation coefficient. Table 38.1 demonstrates the $g(\alpha)$ functions which are used in the chapter for the selected six different solid-state mechanisms. Detailed information about the six solid-state mechanisms can be found in previous work [6].

38.4 Results and Discussions

In this regions were identified based on the thermogram curves of the samples carried out in air atmosphere. The first peak in the temperature interval of 30–130 °C appears due to moisture in the sample. It is not included in the calculations. The second peak appears in a temperature interval of 250–380 °C for pine samples, 250–350 °C for MDF samples, and 270–370 °C for plywood samples. The third peak appears in a temperature interval of 400–550 °C for pine samples, 400–550 °C for MDF samples, and 400–510 °C for plywood samples. TG and DTG curves of the samples obtained in air atmosphere are given in Fig. 38.1.
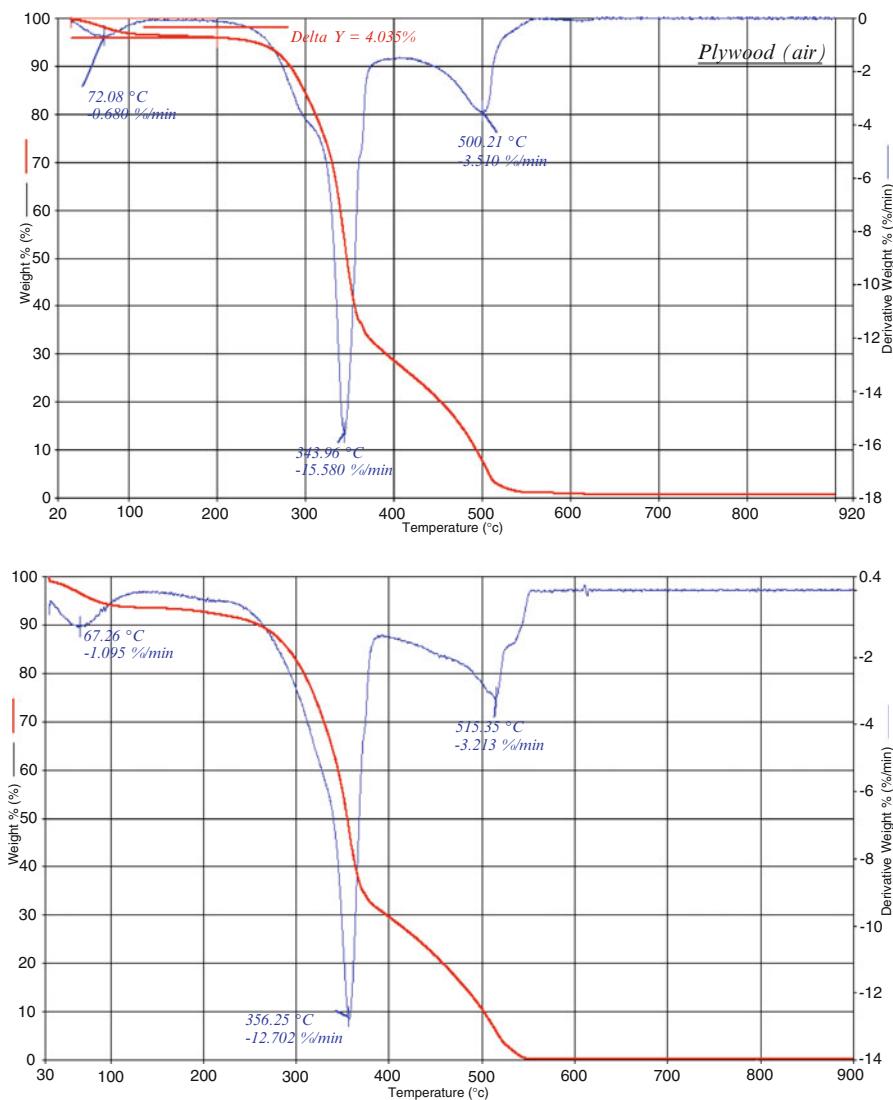
Peak and burnout temperatures are important parameters that affect the combustibility of the samples. Peak and burnout temperatures are the temperatures where the rate of the weight loss is maximal and sample oxidation is complete, respectively [6]. Peak and burnout temperatures of the samples are given in Table 38.2.

Two peaks were observed in nitrogen atmosphere. The first peak in the temp interval of 30–150 °C appears because moisture is not included in the calculations. The second peak appears in a temperature interval of 280–380 °C for MDF samples, 280–380 °C for pine samples, and 275–400 °C for plywood samples. TG and DTG curves of the samples obtained in air atmosphere are given in Fig. 38.2.
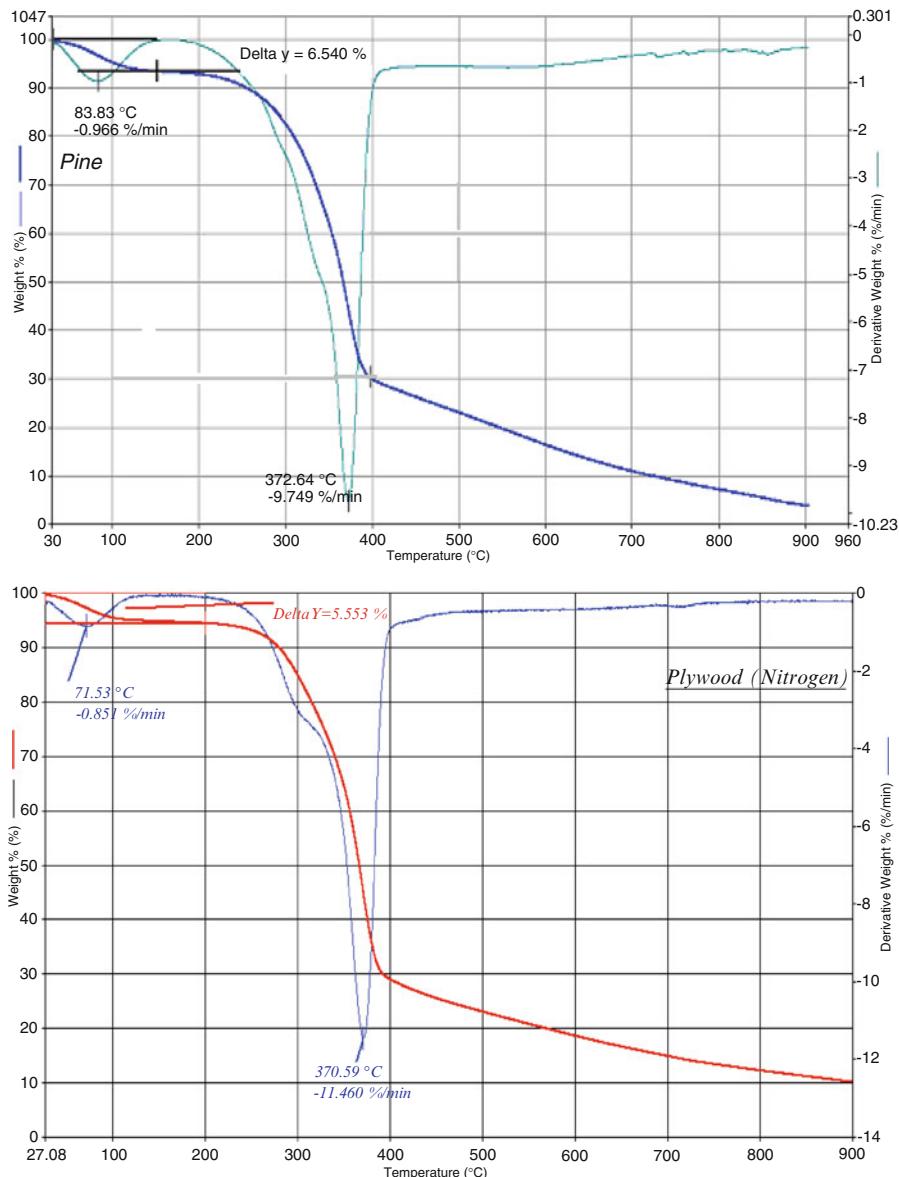
Thermogravimetric parameters of pine, MDF, and plywood samples in nitrogen atmosphere are given in Table 38.3.

Comparison of the data shown in Tables 38.2 and 38.3 reveals that peak and burnout temperatures of the samples are different from each other in different atmospheres. Moreover, volatile matter content of the untreated pine samples was

Sema Yurdakul, Aysel Atimtay

Fig. 38.1 TG and DTG curves of pine and plywood samples in air atmosphere

Table 38.2 Thermogravimetric parameters for pine, MDF, and plywood samples in air atmosphere

Parameters	Samples						
	Pine		MDF			Plywood	
Peak temperature (°C)	356	515	331	502	549	344	500
Burnout temperature (°C)	550		560			550	
Approximate moisture content (%)	8		7			5	

Fig. 38.2 TG and DTG curves of pine and plywood samples in nitrogen atmosphere

lower than in the treated samples, likely due to the chemical treatment involved in the production of MDF and plywood.

In this chapter, thermal kinetic constants of the samples were also calculated for reactions proceeding under both atmospheres (i.e., air and nitrogen) for each six solid-state mechanism. The results are given in Tables 38.4 and 38.5 for air and

Table 38.3 Thermogravimetric parameters for pine, MDF, and plywood samples in nitrogen atmosphere

	Samples		
Parameters	Pine	MDF	Plywood
Peak temperature (°C)	372	366	371
Approximate moisture content (%)	8	7	5
Volatile matter content (%)	81	79	65

Table 38.4 Kinetic parameters for the non-isothermal decomposition of selected samples in air atmosphere (E in kj/mol, A in 1/min)

Sample/air	Region	Mech	E	A	R^2
P	Second	D4	121.8	1.45E+08	0.98
	Third	D1	17.3	4.31E+01	0.98
MDF	Second	D4	123.4	6.19E+08	0.99
	Third	D1	16.5	3.51	0.98
PL	Second	D4	183.0	3.29E+13	0.95
	Third	D1	16.97	4.28	0.95

Table 38.5 Kinetic parameters for the non-isothermal decomposition of selected samples in nitrogen atmosphere (E in kj/mol, A in 1/min)

Sample/N_2	Region	Mech	E	A	R^2
P	Second	D4	106.46	2.2E+06	0.99
MDF	Second	D4	102.72	7.43E+06	0.99
PL	Second	D4	134.40	1.57E+09	0.99

nitrogen atmospheres, respectively. In these tables, only effective mechanisms which give the highest correlation coefficients are displayed.

As can be seen from Tables 38.4 and 38.5, activation energies of the samples in air atmosphere were found to be higher than in nitrogen atmosphere. Therefore, samples were more thermally stable in air atmosphere than in the nitrogen atmosphere.

Although thermal properties of the samples show some differences, effective solid-state mechanisms of the samples during the thermal decomposition processes were found to be similar for the tested waste wood samples. D4 mechanism, which is a function for a diffusion-controlled reaction starting on the exterior of a spherical particle, was found as the main mechanism during the thermal decomposition of all samples in both atmospheres in the main decomposition region.

38.5 Conclusions

In nitrogen atmosphere two peaks were observed for all samples. However, in the air atmosphere three peaks were observed for all samples from the DTG diagram.

Activation energies of the samples in air atmosphere were found to be higher than in the nitrogen atmosphere. Consequently, it can be said that all samples are thermally more stable in air atmosphere than in nitrogen atmosphere. Furthermore, diffusion-controlled reaction starting on the exterior of a spherical particle was found as the main mechanism for all waste wood samples at the main thermal decomposition region for both atmospheres.

References

1. Kajikawa Y, Takeda Y (2008) Structure of research on biomass and bio-fuels: a citation-based approach. Technol Forecast Soc 75:1349–1359
2. Escudero M, Jimenez Á, Rodriguez J (2012) Use of alternative fuels obtained from renewable sources in Brayton cycles. Global NEST J 14:157–165
3. IPCC (Intergovernmental Panel on Climate Change) (1996). Greenhouse gas inventory reference manual: revised 1996 IPCC guidelines for national greenhouse gas inventories, 3, 3–28, Paris
4. Scotland R (2003) The recycling of waste wood by thermal conversion: a report to identify the feasibility of utilizing waste wood as a feedstock for use in bioenergy technologies, Glasgow
5. Demirbaş A (2004) Bioenergy, global warming and environmental impacts. Energ Source 24:225–236
6. Yorulmaz S, Atimtay AT (2009) Investigation of combustion kinetics of treated and untreated waste wood samples with thermogravimetric analysis. Fuel Process Tech 90:939–946
7. Levenspiel O (1972) Chemical reaction engineering, Wiley international edition, 2nd edn. John Wiley and Sons, New York
8. Schniewind AP (1989) Concise encyclopedia of wood and wood based materials, 1st edn. Pergamon Press, Elmsford
9. Zakrzewski R (2003) Pyrolysis kinetics of wood comparison of iso and polythermal thermogravimetric methods. EJPAU 6:2
10. Barral L, Diez FJ, Gabal G, Lopez J, Montero B, Montes R, Ramirez C, Rico M (2005) Thermodegradation kinetics of a hybrid inorganic–organic epoxy system. Eur Polym J 41:1662–1666
11. Minying L, Lijun G, Qingxiang Z, Yudong W, Xiaojuan Y, Shaokui C (2003) Thermal degradation process and kinetics of poly (dodecamethyleneisophthalamide). CJI 5:43
12. Sun JT, Huang YD, Gong GF, Cao HL (2006) Thermal degradation kinetics of poly (methylphenylsiloxane) containing methacryloyl groups. Polym Degrad Stabil 91:339–346

Chapter 39
Reducing Global Warming by Process Integration

Abdulwahab Giwa and Suleyman Karacan

Abstract In an attempt to contribute to the reduction of global warming, the integration of both reaction and separation in a single unit to bring about an improvement in the energy efficiency of the overall process is studied in this chapter. The esterification reaction between acetic acid and ethanol for the production of ethyl acetate (desired product) and water (by-product) is used as the case study. In order to demonstrate the role of the integrated process in global warming reduction, both the conventional system and the integrated one are studied. The conventional system is made up of a reactor (in which the chemical reaction takes place) and a distillation column (in which the desired product is purified) whereas the integrated system consists of a single unit having a single main column divided into three sections (rectification section, reaction section, and stripping section). Comparing the two systems, the results that are obtained from the studies reveal that, for the integrated system, the heat released to the atmosphere from the condenser (that is, the condenser duty) and the one supplied to the reboiler (the reboiler duty) are less than those of the conventional system. These results have actually shown the importance of process integration in reducing global warming and increasing process efficiency. It is therefore suggested to the industrial engineers to always integrate their processes, where possible, in order to contribute their quotas in reducing global warming.

Keywords Global warming • Process integration • Esterification reaction • Reactive distillation column • Process efficiency • Condenser duty • Reboiler duty

A. Giwa (✉) • S. Karacan
Faculty of Engineering, Chemical Engineering Department,
Ankara University, Tandogan, 06100 Ankara, Turkey
e-mail: agiwa@ankara.edu.tr; karacan@eng.ankara.edu.tr

Nomenclatures

C_p	Specific heat capacity, J/(kmol K)
k_b	Backward reaction rate constant
k_f	Forward reaction rate constant
m	Total number of components
M'	Molar flow rate, kmol/h
mw	Molecular weight, kg/kmol
Q	Heat transfer rate, J/h
Q_{cond}	Heat transfer rate from the condenser, kJ/h
Q_{reb}	Heat transfer rate to the reboiler, kJ/h
$Q_{released}$	Total heat transfer rate to the surroundings, kJ/h
Q_{rxn}	Heat transfer rate from the reactor/reaction section, kJ/h
T	Temperature, °C
T_{top}	Product temperature, °C
V	Volumetric flow rate, cm^3/h
x	Liquid mole fraction

Greek Letters

ρ	Density, kg/m^3
α	Volatility

Subscripts

av	Average
i	Component number

39.1   Introduction

One of the major issues in the present century is global warming. Studies on global warming and its effect on climatic change are being pursued vigorously as a multidisciplinary problem [1] because climate change and global warming have been the growing concerns in the recent years [2]. By ignoring the hypothesis that the current warming is part of a natural cycle [3, 4], two causes of the warming have been suggested: (1) the accumulation of greenhouse gases in the earth's atmosphere [3], which is generally accepted by majority of researchers, and (2) heat emissions [5, 6]. Both these explanations imply that the current warming is anthropogenic and lead to the conclusion that more efficient use of energy and increased use of renewable energy are the best ways to counteract global warming [7] because the energy demand for heating and cooling largely depends on the ambient

temperature [8]. This is an indication that the industries have to develop novel methodologies for their processes to solve the problems occurring in the societies owing to global warming.

In response to these industrial and societal requirements, several novel methodologies have emerged since 1970. They include "process systems engineering" and "process integration" followed by a number of works from the University of Manchester Institute of Science and Technology (UMIST) Group. Both disciplines are involved in dedicated conferences such as European Symposium on Computer Aided Process Engineering (ESCAPE), which is facilitated by the European Federation of Chemical Engineering Working Party on Computer Aided Process Engineering (CAPE 2009), and PRES (Conference on Process Integration, Modelling and Optimisation for Energy Saving and Pollution Reduction, PRES 2009), which is supported on an annual basis by Chemical and Chemical Engineering Societies (e.g., Hungarian Chemical Society, Czech Society of Chemical Engineering, Italian Association of Chemical Engineering, Canadian Society for Chemical Engineering) [9].

Actually, it has become evident that resource inputs and effluents of industrial processes are often connected to each other. Examples of this connection include the following [9]:

1. Reducing external heating utility is usually accompanied by an equivalent reduction in the cooling utility demand; obviously, this also tends to reduce CO_2 emissions from the corresponding sites.
2. Reducing wastewater effluents usually leads to reduced freshwater intake.

Reducing the consumption of resources is typically achieved by increasing the internal recycling and reuse of energy and material streams instead of fresh resources and utilities. Projects for improving process resource efficiencies can offer economic benefits and also improve public perceptions of the company undertaking them [9]. This reuse of energy and material streams can be achieved by employing process integration.

Process integration (PI) is a family of methodologies for combining several processes together in order to reduce consumption of resources and/or to reduce harmful emissions [9]. Process integration has been an ideal method for reducing energy and raw material consumption of process industries [10]. It has started mainly as heat integration (HI), stimulated by the energy crisis of the 1970s. Heat integration has examined the potential for improving and optimizing the heat exchange between heat sources and heat sinks in order to reduce the amount of external heating and cooling required, thereby reducing costs and emissions [9]. However, motivating, launching, and carrying out process integration require proper studies that are based on adequate models of the process plants because not all processes can be integrated.

One of the processes that accommodate process integration is "esterification process" involving a reactor and a separation unit because the reaction can be accomplished inside the separation unit. The phenomenon in this case is more or less like integrating the reactor into the separation unit. If the separation unit involved is a distillation column, the process is called "reactive distillation (RD)."

Reactive distillation is a promising multifunctional reactor to improve an ordinary process, as chemical reaction and thermodynamic separation are combined in a single unit [11]. In the past two decades, reactive distillation has emerged as a promising technology for process intensification with significant economic benefits over conventional "reactor followed by separator" processes [12]. When chemical reactions and physical separations have some overlapping operating conditions, the combination of these tasks in a single process unit can offer significant benefits. These benefits include avoidance of reaction equilibrium restrictions, higher conversion, selectivity and yield, removal of side reactions and recycling streams, circumvention of nonreactive azeotropes, reduction of the number of units (investment cost), and reduction of energy demands (through heat integration) [13]. The last mentioned advantage of this process is very important to the society because the heat of an exothermic reaction, instead of being released to the atmosphere, can be used in the volatilization of the mixture to be separated in the column. If the heat released to the atmosphere is minimized, consequently, the occurrence of global warming is expected to be minimized.

According to the information gathered from the literature, some researches have been carried out on global warming. Among them is that of Alexiadis [14] that uses control theory to study the connection between human activities and global warming. Also, Nordell [5] demonstrates in his work that thermal pollution contributes to global warming. Zevenhoven and Beyene (2011) [15] discuss the relative contribution of waste heat from power plants to global warming. In their research, they evaluate the impact of waste heat rejection combined with CO_2 emissions using Finland and California as case studies and find that the immediate effects of waste heat released from power production and radiative forcing by CO_2 are similar. Some researches concerning process integration are also found in the literature. For instance, Dunn and Bush [16] study how to use process integration for combining lower emissions and networked energy recovery. Friedler [17] reviews some major presentations contributing to the development of process integration and optimization tools for energy saving and pollution reduction. Morar and Agachi [18] also review the development through the years 1975–2008 of heat integration and heat exchanger network synthesis (HENS) as a technique of process integration and conclude that the development of process integration techniques is conferring important advantages for the industrial processes in terms of process improvement, increased productivity, energy resource management and conservation, pollution prevention, and reductions in the capital and operating costs of chemical plants. Now, it is deemed necessary to look into how integration of chemical processes (such as reactive distillation) is related to global warming, for the benefits of mankind.

Therefore, in this chapter, the contribution of reactive distillation process to the reduction of global warming is carried out using the esterification reaction between acetic and ethanol for the production of ethyl acetate and water (by-product) that is implemented with the aid of HYSYS model as well as in a pilot plant setup as the case study process.

39.2   Theoretical Backgrounds

Chemical engineering is a branch of engineering that makes use of the principles of physical sciences and life sciences as well as mathematics and economics to the process of converting raw material(s) into (another) more valuable form(s) referred to as the product(s).
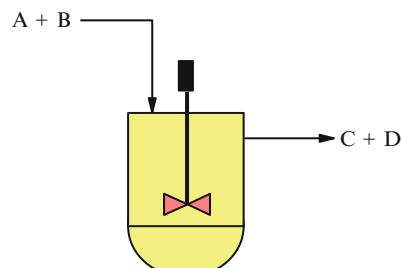
Generally, reactions are carried out inside what is known as the reactors (batch, continuous stirred tank, plug flow, etc.). After the accomplishment of the reactions, in a situation where there are more than one product, there comes the need for the purification of the products especially the desired one. The purification stage is normally achieved using unit operations like distillation, crystallization, extraction, and absorption.

For the esterification process, which is the one concerned with in this chapter, the normally employed reactor is the continuous stirred tank reactor (CSTR) shown in Fig. 39.1 below. Taking the inputs to the reactor as A and B and the outputs as C and D, the equilibrium reaction occurring in the CSTR can be given as

$$A + B \underset{k_b}{\overset{k_f}{\rightleftharpoons}} C + D \tag{39.1}$$
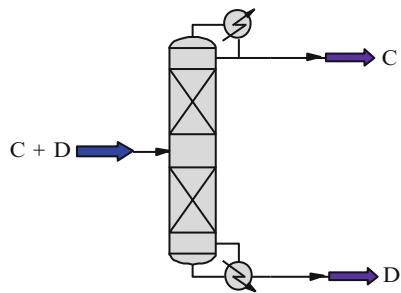
The purification stage involves passing the outputs of the reactor into a distillation column to separate the lighter components through the top section and the heavier ones through the bottom section of the column. If the distillation column type that is used contains packing, then the column is referred to as a packed distillation column (Fig. 39.2).

What is actually happening in a reactive distillation column can be viewed as inserting the reactor into the distillation column (see Fig. 39.3) and allowing the reaction to occur inside the column wherein the products of the reactions are automatically passed to the separation section of the column where the separations of the various components take place.
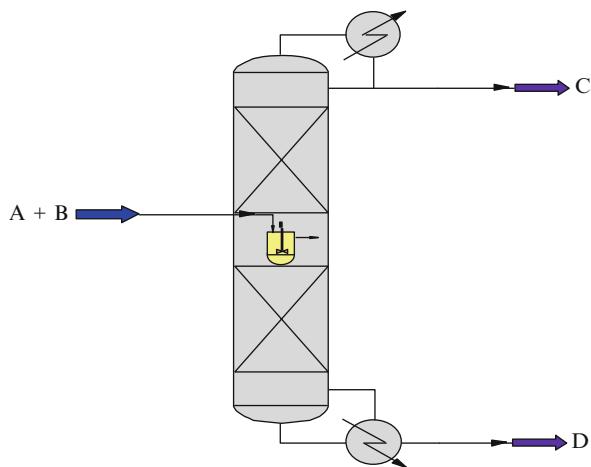
Fig. 39.1 A continuous stirred tank reactor

Fig. 39.2 A packed
distillation column

Fig. 39.3 A packed
distillation column with an
inserted CSTR
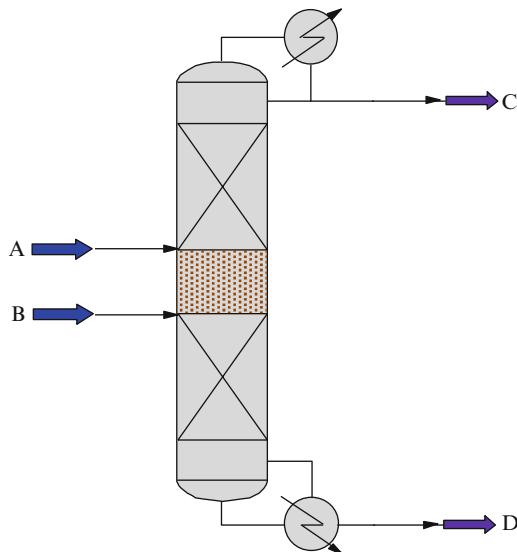
In the real sense, the phenomenon is not inserting the reactor into the distillation column but making a section of the column to be the reaction section as depicted in Fig. 39.4 below.

For the reactive distillation process given above to be feasible, the products (C and D) should be able to be removed from the reaction medium by distillation. That is, the products should be lighter and/or heavier than the reactants. In a special case, the desired product should be the lightest/heaviest of all the components involved in the process. In other words, in terms of the relative volatilities of the four components considered above, the products should have the lowest/highest volatility. Mathematically, for the feasibility of the above system,

$$\alpha_C > \alpha_B > \alpha_A > \alpha_D \tag{39.2}$$

Actually, the choice of the reaction section depends on the methods decided to be used. For example, a reactive distillation column can be operated in batch, semi-batch, or continuous mode. The method shown in Fig. 39.4 above as an illustration

Fig. 39.4 A reactive
packed distillation column

is a continuous one. In the continuous mode of a reactive packed distillation column, the middle section is usually the reaction section where the equilibrium reaction shown in Eq. (39.1) takes place; the section above the reaction section is the rectification section where the light product (in this case, the desired product) is expected to be separated from the heavy components while the section below the reaction section is referred to as the stripping section where the heavy product is separated from the light ones. The heavier reactant is fed just above the reaction section (upper feed section—between the reaction section and the rectifying section) while the lighter one is fed just below the reaction section (lower feed section—between the reaction section and the stripping section). For this illustration, reactant B, being the more volatile, is fed into the column through the lower feed section and as it moves upwards it comes in contact with the heavy reactant A flowing downward in the reaction section and the esterification reaction thereby occurs. After the reaction, the light product moves upwards while the heavy one finds its way to the bottom part of the column.

In reactive distillation, the temperatures in the column affect both the phase equilibrium and chemical kinetics. A low temperature that gives high relative volatilities may give small specific reaction rates that would require very large liquid holdups (or amount of catalyst) to achieve the required conversion. In contrast, a high temperature may give a very small chemical equilibrium constant (for exothermic reversible reactions), which makes it more difficult to drive the reaction to produce products. High temperatures may also promote undesirable side reactions.

39.3 Procedures

In this chapter, both theoretical simulation and experimental studies are carried out to demonstrate how global warming can be reduced by process integration. The theoretical simulation is carried out with the aid of HYSYS model developed while the experimental studies are carried out in the reactive packed distillation pilot plant that is set up.
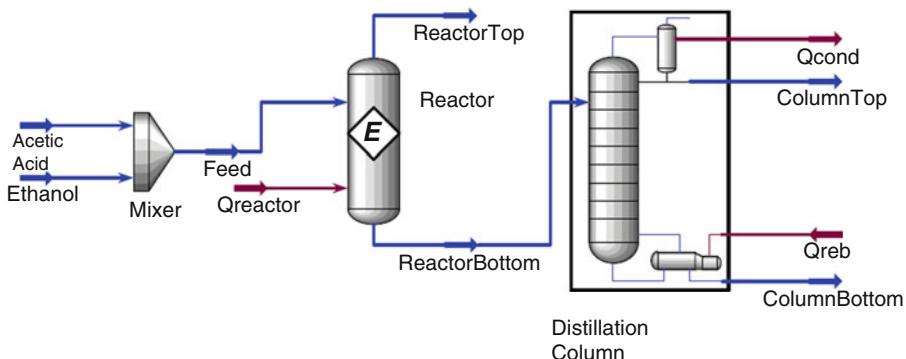
39.3.1 HYSYS Modeling Procedure

Table 39.1 below shows the specifications that are used to develop the HYSYS model for the conventional and integrated processes of this chapter for the production of ethyl acetate and water from the esterification reaction between acetic acid and ethanol.
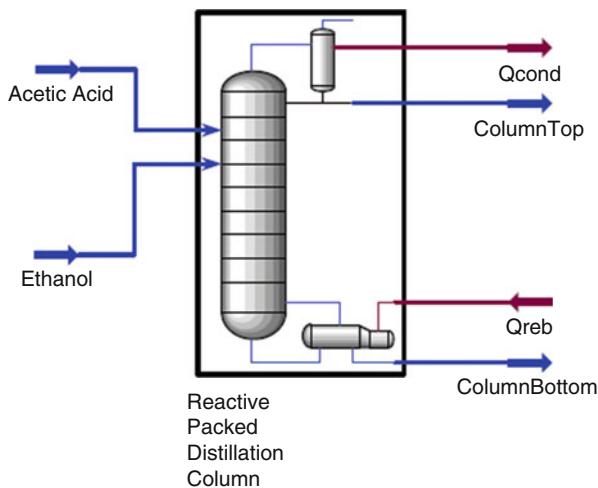
The HYSYS models of the systems (conventional and integrated systems shown in Figs. 39.5 and 39.6, respectively, below) are developed with the aid of HYSYS 3.2 [19] by first specifying the appropriate units according to the data shown in Table 39.1 using the "Tools" menu of the HYSYS software. Then, the fluid package

Table 39.1 HYSYS model specifications for conventional and integrated processes

	Conventional process	Integrated process
Acetic acid feed		
Flow rate (L/h)	0.75	0.75
Temperature (°C)	25	25
Pressure (atm)	1	1
Ethanol feed		
Flow rate (L/h)	0.75	0.75
Temperature (°C)	25	25
Pressure (atm)	1	1
Reactor/reaction section		
Reaction type	Equilibrium	Equilibrium
K_{eq} source	Fixed, 6.68 at 55 °C	Gibbs free energy
Volume (L)	3	
Level (%)	50	
Distillation column		
Type	Packed	Packed
Packing type	Raschig ring	Raschig ring
Number of stages	17	17
Feed stage	6	6
Reflux ratio	2	2
Distillate rate (L/h)	1.041	1.041
Condenser pressure (atm)	1	1
Reboiler pressure (atm)	1	1

Fig. 39.5   Conventional process flow sheet for the production of ethyl acetate

Fig. 39.6   Integrated (reactive distillation) process flow sheet for the production of ethyl acetate

and the components involved in the process are selected using the "Simulation Basis Manager" of the software before entering the "Simulation Environment" where the flow sheets are constructed by picking the appropriate equipment from the "Object Palette," placing them on the simulation page and joining them together appropriately with the aid of "Attach Mode" of the software. Afterwards, the specifications shown in Table 39.1 are entered into the models and each model is simulated separately by making the solver to be active. The fluid package that is used in this chapter is General Non-Random Two-Liquid (General NRTL) and the components involved are acetic acid, ethanol, ethyl acetate, and water.
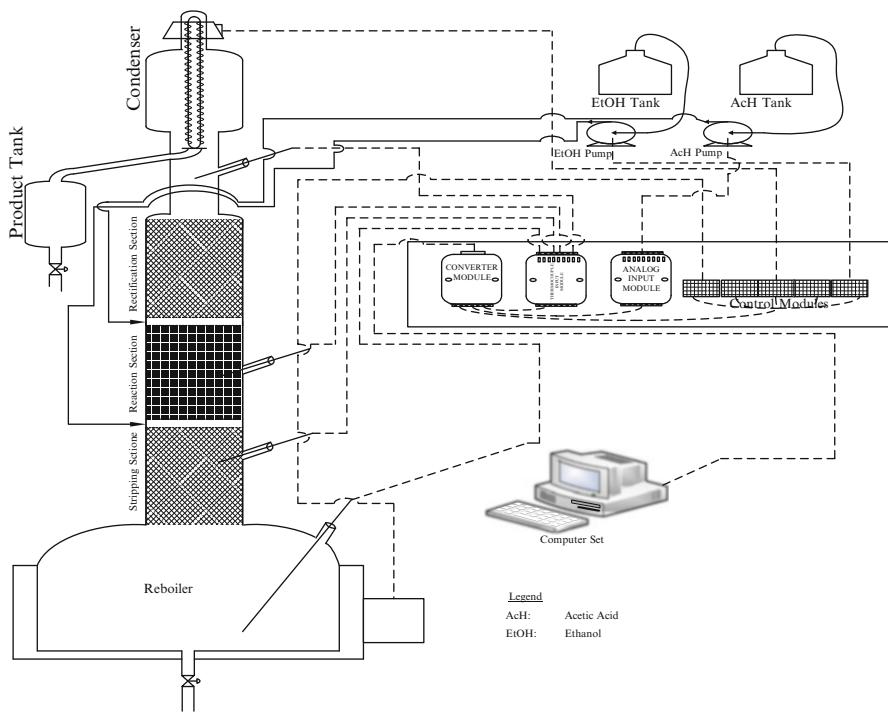
Fig. 39.7 Pictorial view of reactive packed distillation column setup

39.3.2 Experimental Procedures

The experimental pilot plant in which the experiments are carried out is a reactive packed distillation column setup as shown in Fig. 39.7 (pictorial view) and Fig. 39.8 (sketch view) below, described also in the researches of Giwa and Karacan [20–22]. The plant has, excluding the condenser and the reboiler, a height of 1.5 m and a diameter of 0.05 m. The plant consists of a cylindrical condenser of a diameter and a height of 5 and 22.5 cm, respectively. The column section of the plant is divided into three subsections of 0.5 m each. The upper, middle, and lower sections are the rectification, reaction, and stripping sections, respectively. The rectification and the stripping sections are packed with Raschig rings while the reaction section is filled with Amberlyst 15 solid catalyst that has a surface area of 5,300 m^2/kg, a total pore volume of 0.4 cc/g, and a density of 610 kg/m^3. The reboiler is spherical in shape with a volume of 3 L.
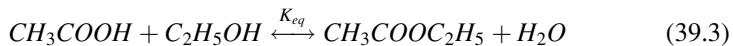
In carrying out the experiment for the conventional process, the reboiler is used as the reactor. The product obtained is thereafter distilled using the distillation column part of the pilot plant. However, while carrying out the reactive distillation process experiments, the reaction (that is, the middle) section of the column is used

Fig. 39.8 Sketch view of reactive packed distillation column setup

as the reactor. It is observed that reaction also occurs in the reboiler section of the plant in the reactive distillation process experiments.

All the signal inputs and the measured outputs to and from the column are sent and recorded, respectively, online with the aid of MATLAB/Simulink computer program and electronic input–output (I/O) modules that are connected to the equipment and the computer system. The esterification reaction (which is an equilibrium reaction) involved in this process is given as in Eq. (39.3) below:

$$CH_3COOH + C_2H_5OH \xrightarrow{K_{eq}} CH_3COOC_2H_5 + H_2O \tag{39.3}$$
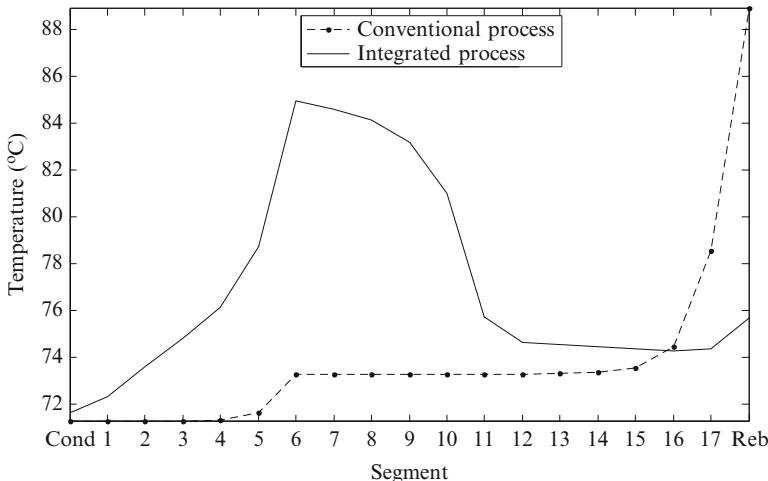
39.4 Results and Discussions

This chapter has been carried out to investigate how global warming can be reduced with the aid of process integration by considering conventional and integrated processes (systems) for the production of ethyl acetate. Actually, the important aspect of the chapter has much to do with the thermal behaviors of the processes; however, the qualities of the products obtained from the processes are also

Table 39.2 Mass fraction of the desired product obtained from HYSYS simulation

Description	Desired product mass fraction
Conventional process	0.8227
Integrated process	0.9351
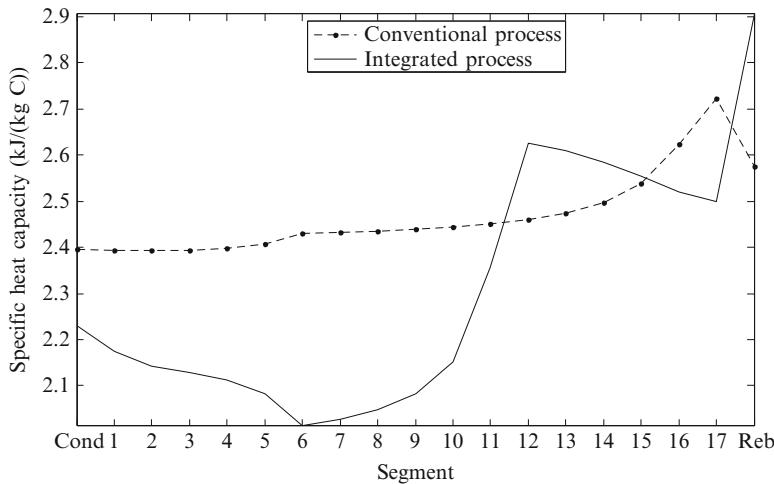
Fig. 39.9 Temperature profiles of the processes

considered. The results of the qualities of the products obtained from the HYSYS simulation of both conventional process and integrated one are as shown in Table 39.2. As can be seen from the table, the mass fraction of ethyl acetate (desired product) obtained from the integrated process is found to be higher than that of the conventional process because the value obtained from the conventional process is approximately 0.8227 while that of the integrated process is 0.9351.

The results of Table 39.2 above are pointing to higher economic advantage of the integrated process because it is able to give higher product purity than that obtainable from the conventional one. After ascertaining the performance of the integrated process over the conventional one in producing better product purity, it is necessary to consider the thermal behaviors of the processes so as to know their contributions (positive or negative) towards reducing global warming.

Figure 39.9 below shows the temperature profile of both conventional and integrated processes for the production of ethyl acetate that is used as the case study process of this chapter. As can be seen from the figure, although the temperatures of the desired product (top product) for the conventional process and the integrated one are found to be close to each other with the values of 71.24 and 71.62 °C, respectively, their profiles do not follow the same trend at all. For the integrated process, the temperatures of the segments within the reaction section are found to be very high when compared to those of the conventional one. The reason for this high temperature value at the reaction section is due to the fact that, at that section, for the integrated process, both reaction and separation occur
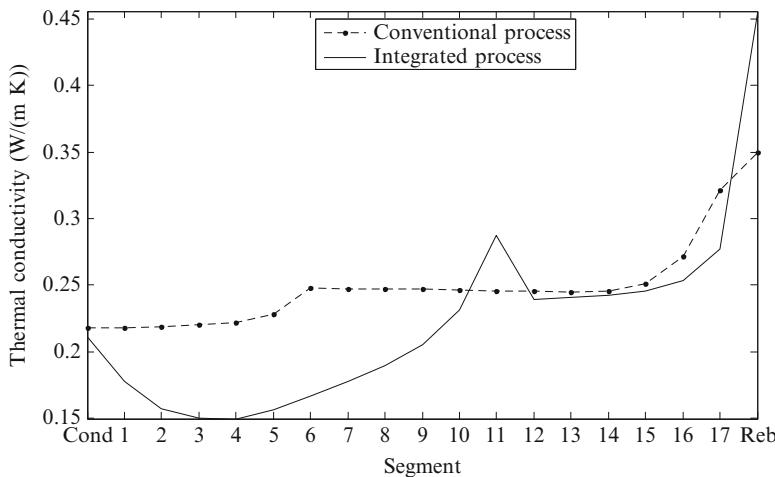
Fig. 39.10 Specific heat capacity profiles of the processes

simultaneously unlike in the case of the conventional process where only separation occurs in the column. The difference in the profiles of the two processes is noted very well in the reboiler section of the column because the difference in the profiles is very clear there.

Also estimated and shown as profile (Fig. 39.10) in this chapter is the amount of heat required to raise a unit mass of the mixture involved in the process by one degree of temperature for both the conventional and the integrated processes. This quantity is referred to as the "specific heat capacity." As can be seen from Fig. 39.10, the specific heat capacity profile for the conventional process is found to increase down the column (that is, from the condenser segment to the segment before the reboiler segment) and a sharp decrease is observed at the reboiler segment. The decrease in the specific heat capacity of the mixture in the reboiler is due to the nature of the liquid accumulated (holdup) in the reboiler. Considering the specific heat capacity of the mixture for the integrated process, it is noticed that the profile does not follow any particular trend because a zigzag profile is observed. This zigzag profile given by the integrated process is due to the complex nature of the process. As can be seen from the figure, the specific heat capacity of the mixture for the integrated process is found to be lower than that of the conventional process in the condenser while that of the conventional process is lower in the reboiler.
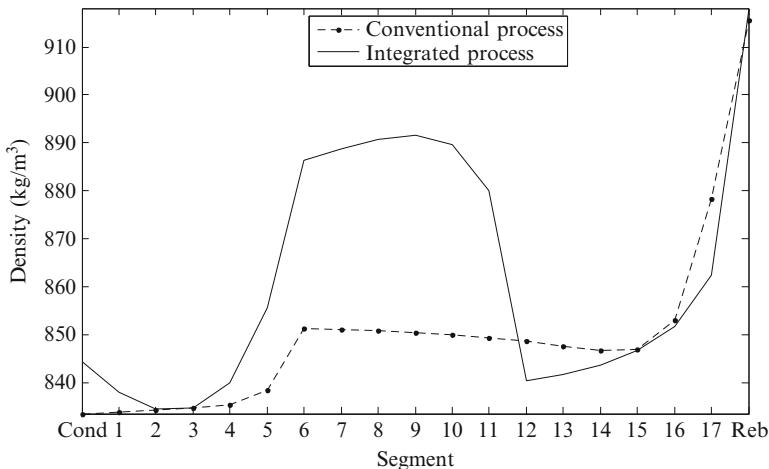
It can be noticed from this system that the liquid mixture is flowing downward while the vapor mixture is flowing upward and, as they are flowing, heat is being transferred from one segment of the column to another. The quantity of the heat that is carried by any mixture flowing to another segment is also being passed to the liquid holdup present in that segment. That is to say, heat is being conducted from one mixture to another within the column. This phenomenon necessitates the need for bringing out the nature at which the mixtures are conducting heat from one column segment to another in the form of a thermal conductivity profile for the conventional and integrated processes, as shown in Fig. 39.11.

Fig. 39.11 Thermal conductivity profiles of the processes

As can be seen in Fig. 39.11, the thermal conductivity of the mixture for the conventional process is observed to increase slightly from the condenser segment of the column down the column towards the reboiler segment while that of the mixture for the integrated process decreases and increases until it gets to the reboiler section. As it is pointed out in the case of the zigzag nature of the specific heat capacity profile of the integrated process, the increasing and decreasing nature of the thermal conductivity profile that is observed for the integrated process is also as a result of the complex nature of the reactive distillation process. The thermal conductivities of the mixtures in the condenser section for the two (conventional and integrated) processes are found to be very close to each other but they are found to be very different in the reboiler.

According to what is noticed in Fig. 39.9 above, the temperature profiles are observed not to be constant. As such, the properties of the process mixture that are functions of temperature, such as the density of the mixture, are not expected to be constant either. Therefore it is worthwhile saying that the density profiles of the processes should also be investigated. Based on this, shown in Fig. 39.12 are the density profiles of the conventional and the integrated processes. From the density profiles shown in the figure, it is observed that the mixture densities for the conventional and integrated processes are very close to each other in the reboiler. However, they are found to be different from each other in the condenser. In addition, the mixture densities in the condenser for the two processes are found to be lower than those of the reboiler. This observation is found to conform to what is being expected because light components are expected to be at the top of the column while the heavy ones are expected to be present in the reboiler which is the bottom section of the column. In other words, the low-density mixtures of the process are obtained as the top products while the high-density ones are collected as the bottom products.

Fig. 39.12 Density profiles of the processes

Table 39.3 Product temperature and heat involved in the processes

Description	HYSYS simulation		Experimental study	
	Conventional	Integrated	Conventional	Integrated
T_{top} (°C)	71.24	71.62	71.32	71.70
Q_{rxn} (kJ/h)	134.74	375.21	129.27	402.04
Q_{cond} (kJ/h)	1562.17	1386.63	1593.70	1402.90
Q_{reb} (kJ/h)	1638.29	1245.70	1764.00	1260.00
$Q_{released}$ (kJ/h)	1696.91	1386.63	1722.97	1402.90

Apart from the profiles shown for the two processes, the heat involved, especially those of the condenser and the reboiler, are also investigated because they are the ones actually involved in the reduction of global warming. The investigation of how process integration can be used to reduce global warming is carried out not only with HYSYS simulation but also experimentally using the conventional reactor plus packed distillation column and the reactive packed distillation pilot plant setup. The results obtained from the HYSYS simulation and the calculations (Appendix A) of the experimental studies are as shown in Table 39.3.

From the results shown in Table 39.3, the experimental product temperature is measured to be 71.32 and 71.70 °C for the conventional process and the integrated one, respectively. These temperature values are found to compare well with the HYSYS simulation results of 71.24 and 71.62 °C, respectively, for the conventional and integrated processes, also shown in the table. The good conformities between the simulated and the experimental temperatures are indications of the good representations of the real system by the developed HYSYS models.

As it is mentioned before, apart from comparing the top segment temperatures of the processes, the energy involved (the heat released from the reactor and the

reaction section of the column, the heat released from the condenser, the heat supplied to the reboiler, and consequently the total heat released to the surroundings) in the processes are also investigated and compared to those of the HYSYS simulation, as can be seen in Table 39.3.

It is also said earlier that the conventional process comprises a reactor from which heat is released to the surroundings. The heat released from the reactor to the surroundings is estimated from the HYSYS simulation to be 134.74 kJ/h while that of the experimental study is estimated to be 129.27 kJ/h. Apart from the heat released from the reactor, heat is also rejected from the condenser and it is estimated to be 1562.17 kJ/h for the HYSYS simulation and 1593.70 kJ/h for the experimental study. Based on the amount of heat released from the reactor and the condenser, the total amounts of heat released to the surrounding from the conventional process are found to be 1696.91 and 1722.97 kJ/h for the HYSYS simulation and experimental study, respectively.

Actually, heat is also released from the reaction section of the reactive distillation column but the heat released from there is not passed to the surroundings like that of the conventional process; it is rather used for the separation operation of the process mixture components. The heat released from the integrated process and passed to the environment is just the one coming from the condenser section of the system. Therefore, from the HYSYS simulation carried out for the integrated process, the heat released to the surrounding from the condenser is estimated to be 1386.63 kJ/h. This heat value is found to be lower than the amount of heat released from the condenser in the case of the conventional process and, consequently, the total amount of heat released from the integrated process to the surrounding is estimated to be less than that of the conventional process. This is one of the very good benefits of the integrated process in contributing to the reduction of global warming. This benefit is also investigated further using an experimental study where the heat released from the condenser is estimated to be 1402.90 kJ/h and also found to be lower than that of the conventional process. This means that the integrated process is found to be more environmentally friendly, and, hence, advantageous in reducing global warming because less amount of heat is released from it to the surroundings; the less the heat released to the surrounding from a particular process, the more environmentally friendly the process and the better the process is in reducing global warming.

In addition, it is discovered from this study, as shown in the results presented in Table 39.3, that the amounts of heat supplied to the reboiler when the conventional process is used are higher than those of the integrated process for both the HYSYS simulation and the experimental study. In the case of HYSYS simulation, the amounts of heat supplied to the reboiler are 1638.29 and 1245.70 kJ/h, respectively, for the conventional and the integrated processes. From the experimental studies, 1764.00 kJ/h of heat is supplied to the reboiler when the conventional process is implemented while 1260.00 kJ/h of heat is supplied when the integrated process is carried out. It can be noticed at this point that the integrated system requires less heat for its reboiler and this is one of the reasons why less heat is also released from its condenser to the surroundings. This is in accordance with the fact that reducing

external heating utility of a process is usually accompanied by an equivalent reduction in the cooling utility demand of that process. As can be observed, apart from the contribution towards reducing global warming, engaging in process integration has also resulted in energy saving of the process.

39.5 Conclusions

The results obtained from the investigations carried out in this chapter confirm that process integration can be used to reduce global warming because, using the integrated process, the heat released to the surroundings from the production of ethyl acetate that is used as the case study process of this chapter is found to be less than the one released when conventional process is used. This fact is proved both theoretically using HYSYS simulation and experimentally using the reactive packed distillation pilot plant setup. Therefore, integrated process should always be employed in all the processes in which it is possible so as to reduce the negative effects of global warming on our environments.

Appendix A

Calculation of Average Molecular Weight

The average molecular weight of the components is calculated using Eq. (39.A1) shown below:

$$mw_{av} = \sum_{i=1}^{m} (x_i mw_i) \qquad (39.A1)$$

Calculation of Average Density

The average density of the components is calculated with the expression shown in Eq. (39.A2) below:

Table 39.A1 Specific heat capacity coefficients of the components [23]

Component	Coefficients				
	a	b	c	d	e
Acetic acid	1.40E + 05	−3.21E + 02	8.9850E − 01	0.00E + 00	0.00E + 00
Ethanol	1.03E + 05	−1.40E + 02	−3.03E − 02	2.04E − 03	0.00E + 00
Ethyl acetate	2.26E + 05	−6.25E + 02	1.47E + 00	0.00E + 00	0.00E + 00
Water	2.76E + 05	−2.09E + 03	8.13E + 00	−1.41E−02	9.37E − 06

$$\rho_{av} = \sum_{i=1}^{m} \left(\frac{x_i mw_i \rho_i}{mw_{av}} \right) \tag{39.A2}$$

Calculation of Molar Flow Rate

The molar flow rate of the mixture is calculated using Eq. (39.A3) shown below:

$$M' = \frac{V\rho_{av}}{mw_{av}} \tag{39.A3}$$

Calculation of Heat Transfer Rate

The heat capacity contained in the heat transfer rate equation (Eq. 39.A5) is estimated with the expression given in Eq. (39.A4) while the heat flow rate itself is obtained using Eq. (39.A5):

$$C_p = a + bT + cT^2 + dT^3 + eT^4 \tag{39.A4}$$

$$Q = M' \int_{T_{initial}}^{T_{final}} C_p dT \tag{39.A5}$$

The coefficients used for calculating the specific heat capacities are as shown in Table 39.A1 below.

References

1. Goyal RK (2004) Sensitivity of evapotranspiration to global warming: a case study of arid zone of Rajasthan (India). Agric Water Manage 69:1–11
2. Radhi H (2009) Evaluating the potential impact of global warming on the UAE residential buildings—a contribution to reduce the CO_2 emissions. Build Environ 44:2451–2462
3. Deming D (1995) Climatic warming in North America: analysis of borehole temperatures. Science 268:1576–1577
4. Harris RN, Chapman DS (1997) Borehole temperatures and a baseline for 20th century global warming estimates. Science 275:1618–1621
5. Nordell B (2003) Thermal pollution causes global warming. Global Planet Change 38:305–312
6. Nordell B, Gervet B (2009) Global energy accumulation and net heat emission. Int J Global Warming 1:373–391
7. Kharseh M, Altorkmany L, Nordell B (2011) Global warming's impact on the performance of GSHP. Renew Energy 36:1485–1491
8. Durmayaz A, Kadioglu M, Sen Z (2000) An application of the degree-hours method to estimate the residential heating energy requirement and fuel consumption in Istanbul. Energy 25:1245–1256
9. Klemes J, Friedler F, Bulatov I, Varbanov P (2010) Sustainability in the process industry: integration and optimization (green manufacturing & systems engineering). McGraw-Hill, New York, NY
10. Patel J, Uygun K, Huang Y (2008) A path constrained method for integration of process design and control. Comp Chem Eng 32:1373–1384
11. Jantharasuk A, Gani R, Górakc A, Assabumrungrat S (2011) Methodology for design and analysis of reactive distillation involving multielement systems. Chem Eng Res Design 8:1295–1307
12. Singh BP, Singh R, Kumar MVP, Kaistha N (2005) Steady state analysis of reactive distillation using homotopy continuation. Chem Eng Res Design 83:959–968
13. Almeida-Rivera CP, Swinkels PLJ, Grievink J (2004) Designing reactive distillation processes: present and future. Comp Chem Eng 28:1997–2020
14. Alexiadis A (2007) Global warming and human activity: a model for studying the potential instability of the carbon dioxide/temperature feedback mechanism. Ecol Model 203:243–256
15. Zevenhoven R, Beyene A (2011) The relative contribution of waste heat from power plants to global warming. Energy 36:3754–3762
16. Dunn RF, Bush GE (2001) Using process integration technology for CLEANER production. J Cleaner Prod 9:1–23
17. Friedler F (2010) Process integration, modelling and optimisation for energy saving and pollution reduction. Appl Thermal Eng 30:2270–2280
18. Morar M, Agachi PS (2010) Review: Important contributions in development and improvement of the heat integration techniques. Comput Chem Eng 34:1171–1179
19. Aspen T (2003) HYSYS v3.2 (Build 5029). Aspen Technology, Inc. United States
20. Giwa A, Karacan S (2012) Modeling and simulation of a reactive packed distillation column using delayed neural networks. Chaotic Model Simul 1:101–108
21. Giwa A, Karacan S (2012) Simulation and optimization of ethyl acetate reactive packed distillation process using Aspen Hysys. J Sci Technol 2(2):57–63
22. Giwa A, Karacan S (2012) Black-Box modelling of ethyl acetate reactive packed distillation column. AU J Technol 15(3):172–178
23. Liley PE, Thomson GH, Friend DG, Daubert TE, Buck E (1999) Perry's chemical engineers' handbook, 7th edn. McGraw-Hill, New York, NY

Chapter 40
Environmental Impact Assessments of Integrated Multigeneration Energy Systems

Pouria Ahmadi, Ibrahim Dincer, and Marc A. Rosen

Abstract Multigeneration refers to an energy process which produces several useful outputs from one or more kinds of primary energy inputs. The main aims, when using multigeneration, are to increase efficiency and sustainability while reducing environmental impact and cost. In this chapter, thermodynamic modeling is performed of a multigeneration system consisting of a micro gas turbine, a double-pressure heat recovery steam generator, an absorption chiller, a domestic water heater that produces hot water at 60 °C, and a proton exchange membrane electrolyzer. In order to determine the irreversibilities in each component and the system performance, an exergy analysis is conducted. In addition, an environmental impact assessment of the multigeneration system is performed, and the potential reductions in CO_2 and CO emissions when the system shifts from power generation to multigeneration are investigated. To understand system performance more comprehensively, a parametric study is performed to study the effects of several important design parameters on the system energy and exergy efficiencies.

Keywords Energy • Efficiency • Exergy • Greenhouse gas emission • Multigeneration

Nomenclature

ex	Specific exergy, kJ/kg
$\dot{E}x_D$	Exergy destruction rate, kW
h	Specific enthalpy, kJ/kg
LHV	Lower heating value (kJ/kg)

P. Ahmadi (✉) • I. Dincer • M.A. Rosen
Faculty of Engineering and Applied Science, University of Ontario Institute of Technology, 2000 Simcoe Street North, Oshawa, ON, Canada L1H 7K4
e-mail: Pouria.Ahmadi@uoit.ca; Ibrahim.Dincer@uoit.ca; Marc.Rosen@uoit.ca

$\dot{m}$	Mass flow rate, kg/s
$\dot{Q}$	Heat transfer rate, kW
s	Specific entropy, kJ/kg K
T	Temperature (°C)
T_{PZ}	Adiabatic flame temperature (°C)
$\dot{W}$	Work rate (kW)

Greek Letters

ε	Normalized CO_2 emission
ζ	H/C atomic ratio
η	Energy efficiency
η_{GT}	Gas turbine isentropic efficiency
θ	Dimensionless temperature
π	Dimensionless pressure
Φ	Molar ratio
Ψ	Exergy efficiency

Subscripts

ABS	Absorber
AC	Air compressor
CC	Combustion chamber
ch	Chemical
CHP	Combined heat and power
$Comb$	Combustion chamber
$Cond$	Condenser
D	Destruction
DHW	Domestic water heater
EVP	Evaporator
EXV	Expansion valve
f	Fuel
Gen	Generator
GT	Gas turbine
HEX	Heat exchanger
$Multi$	Multigeneration
Mix	Mixture
ORC	Organic Rankine cycle
P	Pump
Ph	Physical
PRH	Preheater
ref	Reference
ST	Steam turbine

Acronyms

COP   Coefficient of performance
HRSG   Heat recovery steam generator
HRVG   Heat recovery vapor generator
PEM   Proton exchange membrane

40.1   Introduction

Global warming, which is one facet of global climate change, refers to an increase in the average temperature of the atmosphere and oceans, which appears to have occurred in recent decades and is projected to continue. The drivers of climate change are generally agreed to be changes in the atmospheric concentrations of greenhouse gases (GHGs) and aerosols. According to the Intergovernmental Panel on Climate Change (IPCC), most of the increase in global average temperatures since the mid-twentieth century is linked to the observed increase in the anthropogenic GHG concentrations. A GHG is a gas in an atmosphere that absorbs and emits radiation within the thermal infrared range [1]. This process is the fundamental cause of the greenhouse effect. The primary GHGs in the Earth's atmosphere are water vapor, carbon dioxide, methane, nitrous oxide, and ozone. The greenhouse effect is a process by which thermal radiation from a planetary surface is absorbed by atmospheric GHGs, and is re-radiated in all directions. Since part of this re-radiation is back towards the surface and the lower atmosphere, it results in an elevation of the average surface temperature above what it would be in the absence of the gases [1]. Global warming is agreed by many to be a direct effect of GHG emissions which have increased notably over the last century.

Human activity since the industrial revolution has increased the amount of GHGs in the atmosphere, leading to increased radioactive forcing from CO_2, methane, tropospheric ozone, chlorofluorocarbons (CFCs) and nitrous oxide. The effect of GHGs on global warming is assessed using an index called global warming potential (GWP), which is a measure of how much a given mass of GHG contributes to global warming relative to a reference gas (usually CO_2) for which the GWP is set to 1. For a 100-year time horizon, GWPs of CO_2, CH_4, and N_2O are reported to be 1, 25, and 298, respectively [2]. Using this index, one can calculate the equivalent CO_2 emission by multiplying the emission of a GHG by its GWP. Some main causes of global warming are listed as follows [2]:

- Carbon dioxide emissions from fossil fuel burning power plants.
- Carbon dioxide emissions from burning gasoline for transportation.
- Methane emissions from animals, agriculture such as rice paddies, and Arctic seabeds.
- Deforestation, especially tropical forests for wood, pulp and farmland.
- Use of chemical fertilizers on croplands.

CO_2 is widely believed to be a significant cause of global warming. Research shows that concentrations of CO_2 and methane have increased by 36 and 148 %, respectively, since 1750 [2]. Fossil fuel combustion is responsible for about three-quarters of the increase in CO_2 from human activity over the past 20 years. The rest of this increase is caused mostly by changes in land use, particularly deforestation. The main source of CO_2 emissions is fossil fuel-based electricity generation units, which account for about 32 % of the total CO_2 emissions. The next largest source of CO_2 emissions is heating and cooling purposes, which account for about 33 % of the total CO_2 emissions, followed by emissions from cars and trucks, which account for 23 % of the total global CO_2 emissions, and other major transportation, which accounts for 12 % of CO_2 emissions [3]. Hence, about 65 % of the total CO_2 emissions are attributable to electricity generation and heating and cooling, both of which are directly associated with energy needs of human beings.

Energy drives processes and is essential to life. Energy exists in several forms, e.g., light, heat, and electricity. Concerns exist regarding limitations on easily accessible supplies of energy resources and the contribution of energy processes to global warming as well as such other environmental concerns as air pollution, acid precipitation, ozone depletion, forest destruction, and radioactive emissions [4]. There are various alternative energy options to fossil fuels, including solar, geothermal, hydropower, wind, and nuclear energy. The use of many of the available natural energy resources is limited due to their reliability, quality, and energy density. Nuclear energy has the potential to contribute a significant share of large-scale energy supply without contributing to climate change. Advanced technologies to mitigate global warming are being proposed and tested in many countries. Among these technologies, multigeneration processes, including trigeneration, can make important contributions due to their potential for high efficiencies as well as low operating costs and pollution emissions per energy output. Issues like fossil fuel depletion and climate change amplify the advantages and significance of efficient multigeneration energy systems.

Cogeneration, or combined heat and power (CHP), represents a relatively simple, integrated multigeneration energy system involving the use of waste or other heat from electricity generation to produce heating. The overall energy efficiency of a cogeneration system, defined as the part of the fuel converted to both electricity and useful thermal energy, typically is 40–50 % [5]. Recently, researchers have extended CHP to trigeneration, a system for the simultaneous production of heating, cooling, and electricity from a common energy source. Trigeneration often utilizes the waste heat of a power plant to improve overall thermal performance [6], and is suitable for some energy markets.

Numerous energy and exergy analyses have been reported for both CHP and trigeneration. Athanasovici et al. [7] proposed a unified comparison method for the thermodynamic efficiency of CHP plants, and used the method to compare various separate and combined energy production processes. Havelsky [8] analyzed the problem of energy efficiency evaluation of trigeneration systems, and developed expressions for energy efficiency and primary energy savings. Sahoo [9] performed an exergoeconomic analysis and optimization of a cogeneration system using

evolutionary programming. Khaliqh et al. [10] carried out an exergy analysis of a combined electrical power and refrigeration cycle, as well as a parametric study of the effects of exhaust gas inlet temperature, pinch-point and gas composition on energy and exergy efficiencies, electricity-to-cold ratio, and exergy destruction for the cogeneration system and its components. Through an energy analysis of a trigeneration plant based on a solid oxide fuel cell and an organic Rankine cycle, Al-Sulaiman et al. [6] demonstrated an efficiency gain of more than 22 % using trigeneration relative to only generating power. They also showed a maximum efficiency of 74 % for trigeneration, 71 % for heating cogeneration, 57 % for cooling cogeneration, and 46 % for electricity generation, and concluded that exergy analysis is a significant tool for assessing and improving both CHP and trigeneration cycles.

Energy analysis, which is based on the first law of thermodynamics, does not provide a clear picture of thermodynamic efficiencies and losses. Exergy analysis overcomes these deficiencies and can help identify pathways to sustainable development. Exergy is a useful tool for determining the location, type, and true magnitude of exergy losses, which appear in the form of either exergy destruction or waste exergy emission [11]. Therefore, exergy can assist in developing strategies and guidelines for making the use of energy resources and technologies more effective. Furthermore, exergoeconomics, which combines exergy analysis with economic principles, can facilitate improved designs, partly by incorporating the associated costs of thermodynamic inefficiencies in the total product cost of an energy system [12, 13], as can exergoenvironmental analysis [5], which combines exergy and environmental analyses.

Recently, combinations of exergy, economic, and environmental assessment have received increasing attention around the world, motivated in part by global warming challenges. Ahmadi et al. [14] carried out an exergoenvironmental analysis of a trigeneration system based on a micro gas turbine and an organic Rankine cycle (ORC), and performed a parametric study involving the main design parameters of the trigeneration system. Al-Sulaiman et al. [15] conducted energy and exergy analyses of a biomass trigeneration system using an ORC. They also performed energy and exergy analyses of a novel trigeneration system using parabolic trough solar collectors for combined cooling, heating, and electricity generation [16]. Recently researchers have gone beyond trigeneration to produce more products like hot water, hydrogen, and potable water using a single resource. The focus here is on multigeneration energy systems that can produce more than three products. Often the efficiencies for multigeneration energy systems are higher than those for trigeneration or CHP.

Research on multigeneration has increased recently. Ahmadi et al. [17] carried out an exergy-based optimization of a multigeneration system consisting of a gas turbine as a prime mover to produce electricity, heating, cooling, and domestic hot water, and applied a multi-objective evolutionary-based optimization to find the best design parameters considering exergy efficiency and total cost of the system as two objective functions. Ratlamwala et al. [18] analyzed the performance of an integrated geothermal based system for multigeneration, consisting of a geothermal
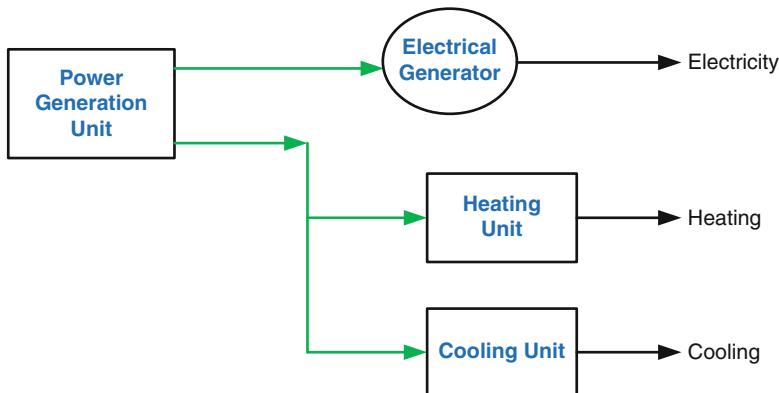
based double-flash power-generating unit, an ammonia–water quadruple effect absorption unit, and an electrolyzer system for cooling, heating, power, hot water, and hydrogen production. The authors note that increasing the geothermal source temperature, pressure, and mass flow rate increases the output power and hydrogen production rate. Also, Ratlamwala et al. [19] thermodynamically analyzed an integrated geothermal based quadruple effect absorption system for multi-generation. Dincer and Zamfirescu [20] performed energy and exergy analyses of renewable energy-based multigeneration, considering several options for producing such products as electricity, heat, hot water, cooling, hydrogen, and freshwater.

In this chapter, we describe integrated multigeneration. We then propose a system with a single useful output and then extend it to multigeneration. Energy, exergy, and environmental impact assessments are conducted in order to better understand the topic. In addition, environmental impacts of various systems are compared and the benefits of multigeneration investigated.

40.2 Multigeneration Energy Systems

The benefits of integrating energy system became pronounced with the application of cogeneration for heat and electricity. In this simple energy system, waste or other heat is used to produce either cooling or heating. In general, cogeneration is the production of heat and electricity in one process, often considerable reductions in input energy compared to separate processes. Cogeneration is often associated with the combustion of fossil fuels, but can also be carried out using some renewable energy sources, nuclear energy, and waste thermal energy (obtained directly or by burning waste materials). The trend recently has been to use cleaner fuels for cogeneration such as natural gas. The strong long-term prospects for cogeneration in global energy markets are related to its ability to provide significant operational, environmental, and financial benefits. The product thermal energy from cogeneration can be used for domestic hot water heating, space heating, pool heating, heating for laundry processes, and absorption cooling. The more the product heat from cogeneration can be used year round in existing systems, the more financially attractive it is. Cogeneration helps overcome a drawback of many conventional electrical and thermal systems: the significant heat losses which detract greatly from efficiency [6]. Heat losses are reduced and efficiency is increased when cogeneration is used to supply heat to various applications and facilities.

The overall energy efficiency of a cogeneration system is the percent of the fuel converted to both electricity and useful thermal energy. Typical cogeneration systems have overall efficiencies of 45–60 %. Recently, researchers have extended CHP to have more output purposes. In this regard, trigeneration energy systems have become more suitable for energy markets. Trigeneration is the simultaneous production of heating, cooling, and electricity from a common energy source. Trigeneration utilizes waste or other heat of a power plant to improve overall

Fig. 40.1 A typical trigeneration energy system
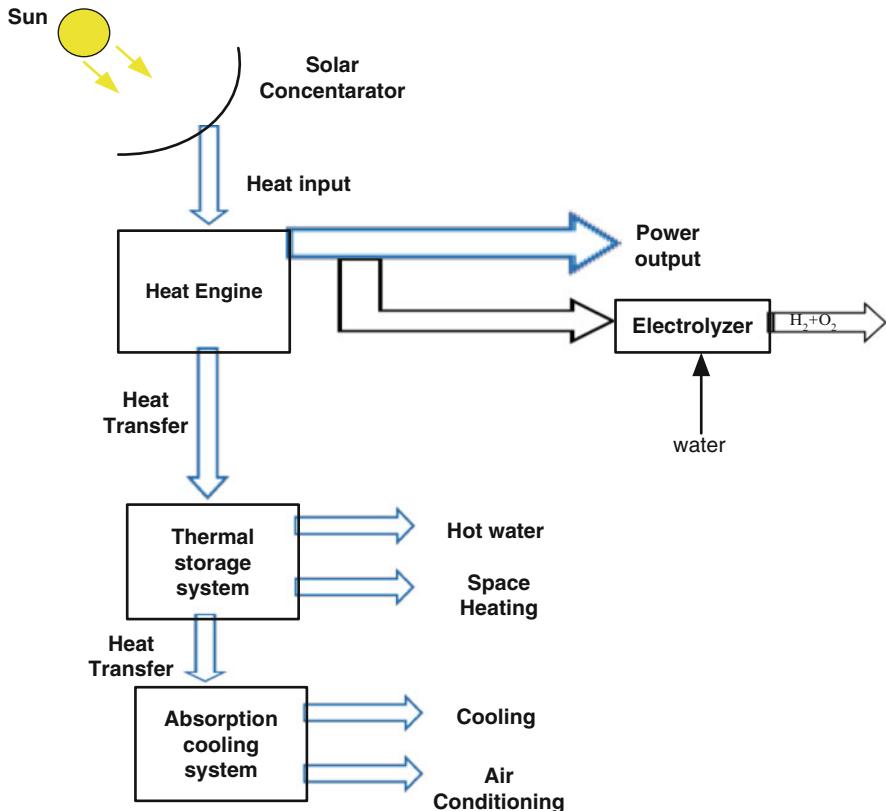
thermal performance, often utilizing the free energy available via waste energy. In a trigeneration system, waste heat from the plant's prime mover (e.g., gas turbine or diesel engine or Rankine cycle [13]), sometimes with temperature enhancement, drives heating and cooling devices. The heat can be used for space heating and domestic hot water production or to produce steam for process heating. The heat can also be used for cooling, by driving an absorption chiller. Much research on trigeneration has been conducted in the last few years, likely due to its benefits and plans for applications. Trigeneration can be applied widely, e.g., in the chemical and food industries, airports, shopping centers, hotels, hospitals, and houses. Figure 40.1 illustrates a trigeneration energy system, consisting of the following four major parts:

- A power generation unit, i.e., a prime mover, such as a gas turbine
- A cooling unit, such as a single-effect absorption chiller
- A heating unit, such as a boiler or a heat recovery steam generator (HRSG)

  The following processes occur in a trigeneration plant:
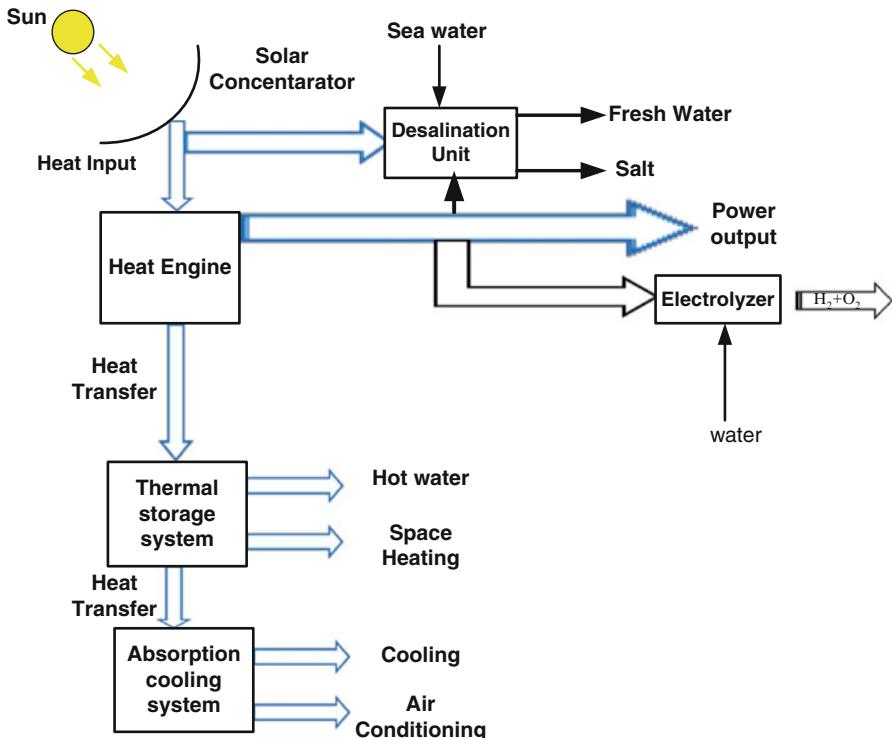
- Mechanical power is produced via a mechanical power generator unit, such as a gas turbine.
- The mechanical power is used to drive an electrical generator.
- Waste heat exits the mechanical generator unit directly or via heated materials like exhaust gases.

It can be seen from Fig. 40.1 that with a single prime mover we can produce heating, cooling, and electricity simultaneously. Recently researchers have extended trigeneration to produce more products like hot water, hydrogen, and potable water using a single prime mover. The efficiency for multigeneration energy systems often is higher than that for either trigeneration or CHP because of the additional products (hydrogen, potable and hot water, etc.). Figures 40.2 and 40.3 illustrate two multigeneration energy systems. The system in Fig. 40.2

Fig. 40.2 A multigeneration energy system for producing electricity, cooling, heating, hot water, and hydrogen [21]

produces electricity, cooling, heating, hot water, and hydrogen. To produce hydrogen, an electrolyzer is used which is driven by a part of electricity generated via a solar concentrating collector. Hot water enters the electrolyzer and is reacted electrochemically to hydrogen and oxygen. The heating system is composed of two parts, one for hot water production and another for space heating. Heat rejected from the storage system enters the absorption cooling system to produce cooling and air conditioning. If we extend this multigeneration system to produce potable water, a desalination system must be used and such a multigeneration energy system is shown in Fig. 40.3. In this case, part of the heat produced by the solar concentrator is used to run a desalination system, while part of electricity generated by the power unit drives the pumps. Other parts of the system are same as in Fig. 40.2. These two figures are representative of typical multigeneration energy systems that use only solar energy as energy input. Other configurations that combine renewable and conventional energy sources are also possible, and are discussed subsequently.

Fig. 40.3 A multigeneration energy system for producing electricity, cooling, heating, hot water, hydrogen, and freshwater [21]

40.2.1   Benefits of Multigeneration Energy Systems

There are many benefits of multigeneration energy systems, including higher plant efficiency, reduced thermal losses and wastes, reduced operating costs, reduced GHG emissions, better use of resources, shorter transmission lines, fewer distribution units, multiple generation options, increased reliability, and less grid failure [21]. These benefits are discussed below. Multigeneration improves the overall efficiency of the plant and reduces operating costs. The overall efficiency of conventional power plants that use fossil fuel with a single prime mover is usually less than 40 %. That is, more than 60 % of the heating value of the fuel entering a conventional power plant is lost. On the other hand, the overall efficiency of a conventional power plant that produces electricity and heat separately is around 60 % [17].

However, with the utilization of the waste heat from the prime mover, the efficiency of multigeneration plants could reach 80 % [9, 10]. In a multigeneration plant, the waste heat from electricity generation is used to operate the cooling and heating systems without the need for extra fuel, unlike a conventional power plant that requires extra energy resources. Thus, a multigeneration plant uses less energy

to produce the same output as a conventional plant, and has correspondingly lower operating costs.
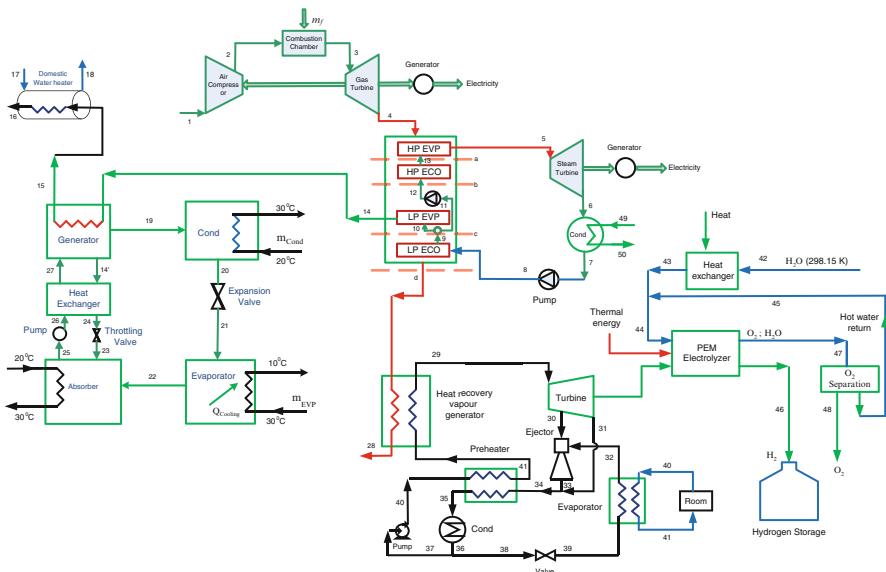
Multigeneration also reduces GHG emissions. Since a multigeneration energy system uses less fuel to produce the same output compared with a conventional power plant, a multigeneration plant emits less GHGs. Although the GHG emissions from multigeneration plants are less than conventional plants, there are some limitations to using multigeneration plants in a distributed manner because of their on-site gas emissions.

Another important benefit of using multigeneration energy systems is that they reduce costs and energy losses due to the fact that they need fewer electricity transmission lines and distribution units. The conventional production of electricity is usually from a centralized plant that is generally located far from the end user. The losses from transmission and distribution of electricity from a centralized system to the user can be about 9 % [17].

These benefits have encouraged researchers and designers to develop multigeneration energy systems. The improvement in efficiency is often the most significant factor in implementing a multigeneration energy system. Further assessments before selecting multigeneration plants, such as evaluations of initial capital and operating costs, are needed to ensure efficient and economic multigeneration plants [17].

40.3   System Description

Figure 40.4 illustrates an integrated multigeneration system containing a compressor, a combustion chamber (CC), a gas turbine, a double-pressure HRSG, a single-effect absorption chiller, a heat recovery vapor generator (HRVG) which is driven by heat from flue gases from the HRSG, an ORC ejector refrigeration system, and a PEM electrolyzer for hydrogen production. Air at ambient conditions enters the air compressor at point 1 and exits after compression (point 2). Then the hot air enters the combustion chamber. Fuel is injected into the combustion chamber and hot combustion gases exit (point 3) and pass through a gas turbine to produce shaft power. The hot gas expands in the gas turbine to point 4. Hot flue gases enter the double-pressure HRSG to provide high- and low-pressure vapor at points 5 and 14. High-pressure vapor enters the steam turbine to generate shaft power while the low-pressure steam enters the generator of the absorption system to provide the cooling load of the system. The low-pressure line leaving the generator has adequate energy for use in a domestic water heater that provides hot water at 50 °C. Furthermore, flue gases leaving the HRSG at point C enter a HRVG to provide electricity and cooling. Since the flue gases have a low temperature, around 160 °C, an ORC cycle is used, consisting of an ORC turbine to generate electricity and a steam ejector to provide the system cooling load. These flue gases enter the HRVG at point d to produce saturated vapor at point 29, which leaves the HRVG at point 28. Saturated vapor at point 29 enters the ORC turbine and work is produced.

Fig. 40.4 A multigeneration energy system based on a gas turbine and PEM electrolysis

The extraction turbine and ejector play important roles in this combined cycle. The high-pressure and -temperature vapor is expanded through the turbine to generate power, and the extracted vapor from the turbine enters the supersonic nozzle of the ejector as the primary vapor. The stream exiting the ejector (point 33) mixes with turbine exhaust (point 31), is cooled in the preheater, and enters the condenser where it becomes a liquid by rejecting heat to the surroundings. Some of the working fluid leaving the condenser enters the evaporator after passing through the throttle valve (point 39), and the remainder flows back to the pump (point 37). The ORC pump increases the pressure (point 40), and high-pressure working fluid is heated in the preheater (point 41) before entering the HRVG. The low-pressure and low-temperature working fluid after the valve (point 39) enters the evaporator, providing a cooling effect for space cooling. Some of the electricity is considered for residential applications while some directly drives a PEM electrolyzer to produce hydrogen. In this analysis, waste heat is used as a heat source to simulate the multigeneration system and R123 is selected as the working fluid because it is a nontoxic, nonflammable, and non-corrosive refrigerant with suitable thermophysical characteristics.

40.4 Modeling and Energy Analysis

For thermodynamic modeling, the multigeneration system considered here (Fig. 40.4) is divided into five main parts: gas turbine (Brayton) cycle, Rankine cycle with double-pressure HRSG, a single-effect absorption chiller, ORC, domestic water heater, and PEM electrolyzer. The fuel injected to the combustion

chamber is natural gas. We determine the temperature profile in the plant, input and output enthalpy and exergy flow rates, exergy destructions rates, and energy and exergy efficiencies. In order to model the system, energy balances are considered for each system component. The dead state is taken to be $P_0 = 1.01$ bar and $T_0 = 293.15$ K. Details on the modeling of the steady state and steady flow process occurring in the system are provided elsewhere [12–15].

40.4.1 Assumptions

Several simplifying assumptions are made here to render the analysis more tractable while retaining adequate accuracy and allowing the principal points of the chapter to be illustrated:

- All processes occur at steady state.
- Air and combustion products are ideal-gas mixtures.
- Heat loss from the combustion chamber is 2 % of the fuel lower heating value, and all other components are adiabatic.
- Both HP and LP pinch temperatures are constant at 10 °C.
- The flow across the throttle valve is isenthalpic.
- The ORC condenser outlet is a saturated liquid, and its temperature is approximately 5 °C higher than the reference environment temperature.
- The ORC working fluid at the evaporator outlet is a saturated vapor.
- Pressure drops in ORC cycle are negligible.
- Heat losses from piping and other auxiliary components are negligible.

40.4.2 Energy Efficiency

The energy, or first law, efficiency is defined as the ratio of useful energy produced by the system (cold, heat, electricity) to the input energy of the fuel supplied to the system. In this study, we consider three energy efficiencies for the system: the gas turbine cycle, the CHP portion of the system, and the overall multigeneration system, i.e.,

$$\eta_{Power} = \frac{\dot{W}_{net,GT}}{\dot{m}_f LHV_f} \tag{40.1}$$

$$\eta_{CHP} = \frac{\dot{W}_{net,GT} + \dot{Q}_{heating}}{\dot{m}_f LHV_f} \tag{40.2}$$

$$\eta_{multi}$$
$$= \frac{\dot{W}_{net,GT} + \dot{W}_{net,ST} + \dot{W}_{net,ORC} + \dot{Q}_{heating} + \dot{Q}_{cooling,chiller} + \dot{Q}_{cooling,ORC} + \dot{m}_{H_2} LHV_{H_2} + \dot{m}_{18} h_{18}}{\dot{m}_f LHV_f}$$

$$\tag{40.3}$$

where LHV_f denotes the lower heating value of the fuel (natural gas) and is assigned a value $LHV_f = 50{,}000$ kJ/kg, $\dot{m}_f$ is the mass flow rate of the fuel entering the combustion chamber, and $\dot{W}_{net,GT}$, $\dot{W}_{net,ST}$, and $\dot{W}_{net,ORC}$ denote the net power outputs of the gas turbine cycle, the steam cycle, and the ORC cycle. Also, $\dot{Q}_{heating}$ $\dot{Q}_{cooling,chiller}$ and $\dot{Q}_{cooling,ORC}$ denote the heating load of the multigeneration system, the absorption cooling load and ORC cooling load, while the last two terms in the numerator denote the energy values of the hydrogen and hot water products. It can be seen from these expressions that the energy efficiency of the multigeneration system must exceed that of the gas turbine (GT) cycle. Note that the multigeneration energy efficiency is often problematic, as the cooling terms in the numerator can cause the energy efficiency to exceed 100 %; this explains in part why exergy efficiencies are more advantageous.

40.5 Exergy Analysis

Exergy analysis can help develop strategies and guidelines for more effective use of energy, and has been applied to various thermal processes, especially power generation, CHP, trigeneration, and multigeneration. The exergy of a substance is often divided into four components. Two common ones are the physical and chemical exergy. The two others, kinetic and potential exergy, are assumed to be negligible here, as the elevation changes are small and speeds are relatively low [5, 6, 9, 12]. Physical exergy is defined as the maximum useful work obtainable as a system interacts with an equilibrium state [11]. Chemical exergy is associated with the departure of the chemical composition of a system from its chemical equilibrium. The chemical exergy is important in processes involving combustion and other chemical changes [11]. Applying the first and the second laws of thermodynamics, the following exergy balance is obtained:

$$\dot{Ex}_Q + \sum_i \dot{m}_i ex_i = \sum_e \dot{m}_e ex_e + \dot{Ex}_W + \dot{Ex}_D \qquad (40.4)$$

Note in Eq. (40.4) that subscripts i and e denote the control volume inlet and outlet flow, respectively, $\dot{Ex}_D$ is the exergy destruction, and other terms are as follows:

$$\dot{Ex}_Q = \left(1 - \frac{T_0}{T_i}\right)\dot{Q}_i \qquad (40.5)$$

$$\dot{Ex}_w = \dot{W} \qquad (40.6)$$

$$ex = ex_{ph} + ex_{ch} \qquad (40.7)$$

Here, $\dot{E}x_Q$ and $\dot{E}x_W$ are, respectively, the exergy of heat transfer and work which cross the boundaries of the control volume, T is the absolute temperature, and the subscript 0 refers to the reference environment conditions. The term ex_{ph} is defined as follows:

$$ex_{ph} = (h - h_0) - T_0(s - s_0) \tag{40.8}$$

The mixture chemical exergy is defined as follows [11]:

$$ex_{mix}^{ch} = \left[\sum_{i=1}^{n} x_i ex_i^{ch} + RT_0 \sum_{i=1}^{n} x_i \ln x_i\right] \tag{40.9}$$

In this exergy analysis, the exergy of each flow is calculated at all states and the changes in exergy are determined for each major component. The cause of exergy destruction (or irreversibility) in the combustion chamber is mainly combustion or chemical reaction and thermal losses in the flow path [13]. However, the exergy destruction in the system heat exchangers (i.e., condenser and HRSG) is due to the large temperature differences between the hot and cold fluids. The exergy destructions for all components in the multigeneration system are shown in Table 40.1.

40.5.1 Exergy Efficiency

The exergy efficiency, defined as the product exergy output divided by the exergy input, for the gas turbine, CHP, and overall multigeneration systems can be expressed as follows:

$$\Psi_{power} = \frac{\dot{W}_{net,GT}}{\dot{E}x_f} \tag{40.10}$$

$$\Psi_{CHP} = \frac{\dot{W}_{net,GT} + \dot{E}x_{heating}}{\dot{E}x_f} \tag{40.11}$$

$$\Psi_{multi}$$
$$= \frac{\dot{W}_{net,GT} + \dot{W}_{net,ST} + \dot{W}_{net,ORC} + \dot{E}x_{heating} + \dot{E}x_{cooling,chiller} + \dot{E}x_{cooling,ORC} + \dot{E}x_{H_2} + \dot{E}x_{18}}{\dot{E}x_f} \tag{40.12}$$

Here,

$$\dot{E}x_{heating} = \dot{Q}_{cond}\left(1 - \frac{T_0}{T_{cond}}\right) \tag{40.13}$$

Table 40.1 Expressions for exergy destruction rates for components of the system

Component	Exergy destruction rate expression
Air compressor	$\dot{Ex}_{D,AC} = \dot{Ex}_1 - \dot{Ex}_2 - \dot{W}_{AC}$
Combustion chamber (CC)	$\dot{Ex}_{D,CC} = \dot{Ex}_2 + \dot{Ex}_f - \dot{Ex}_3$
Gas turbine (GT)	$\dot{Ex}_{D,GT} = \dot{Ex}_3 - \dot{Ex}_4 - \dot{W}_{GT}$
HRSG	$\dot{Ex}_{D,HRSG} = \dot{Ex}_4 + \dot{Ex}_8 - \dot{Ex}_5 - \dot{Ex}_c$
Steam turbine (ST)	$\dot{Ex}_{D,ST} = \dot{Ex}_5 - \dot{Ex}_6 - \dot{W}_{ST}$
Steam condenser	$\dot{Ex}_{D,Cond} = \dot{Ex}_6 + \dot{Ex}_{49} - \dot{Ex}_7 - \dot{Ex}_{50}$
Pump	$\dot{Ex}_{D,P} = \dot{Ex}_7 - \dot{Ex}_8 + \dot{W}_P$
Heat recovery vapor generator	$\dot{Ex}_{D,HRVG} = \dot{Ex}_c + \dot{Ex}_{41} - \dot{Ex}_{28} - \dot{Ex}_{29}$
ORC turbine	$\dot{Ex}_{D,ORC\ T} = \dot{Ex}_{29} - \dot{W}_{ORC} - \dot{Ex}_{30} - \dot{Ex}_{31}$
Ejector	$\dot{Ex}_{D,Ejector} = \dot{Ex}_{30} + \dot{Ex}_{32} - \dot{Ex}_{33}$
Preheater	$\dot{Ex}_{D,PRH} = \dot{Ex}_{34} + \dot{Ex}_{40} - \dot{Ex}_{35} - \dot{Ex}_{41}$
ORC pump	$\dot{Ex}_{D,ORC\ Pump} = \dot{Ex}_{37} + \dot{W}_{ORC} - \dot{Ex}_{40}$
ORC condenser	$\dot{Ex}_{D,Cond} = \dot{Ex}_{35} - \dot{Ex}_{36} - \dot{Ex}_{Q,Cond}$
ORC evaporator	$\dot{Ex}_{D,EVP} = \dot{Ex}_{39} + \dot{Ex}_{40} - \dot{Ex}_{32} - \dot{Ex}_{41}$
ORC expansion valve	$\dot{Ex}_{D,EXV} = \dot{Ex}_{38} - \dot{Ex}_{39}$
Domestic water heater	$\dot{Ex}_{D,DWH} = \dot{Ex}_{15} + \dot{Ex}_{17} - \dot{Ex}_{16} - \dot{Ex}_{18}$
PEM electrolyzer	$\dot{Ex}_{D,PEM} = \dot{Ex}_{44} + \dot{W}_{PEM} - \dot{Ex}_{46} - \dot{Ex}_{47} + \dot{Ex}_Q$
Absorption condenser	$\dot{Ex}_{D,Cond} = \dot{Ex}_{19} - \dot{Ex}_{20} - \dot{Ex}_Q$
Absorption expansion valve	$\dot{Ex}_{D,EXV} = \dot{Ex}_{20} - \dot{Ex}_{21}$
Absorption evaporator	$\dot{Ex}_{D,EVP} = \dot{Ex}_{21} - \dot{Ex}_{22} + \dot{Ex}_Q$
Absorber	$\dot{Ex}_{D,Abs} = \dot{Ex}_{22} + \dot{Ex}_{23} - \dot{Ex}_{25} - \dot{Ex}_Q$
Absorption pump	$\dot{Ex}_{D,P} = \dot{Ex}_{25} + \dot{W}_P - \dot{Ex}_{26}$
Absorption heat exchanger	$\dot{Ex}_{D,HEX} = \dot{Ex}_{26} + \dot{Ex}_{14'} - \dot{Ex}_{24} - \dot{Ex}_{27}$
Absorption generator	$\dot{Ex}_{D,Gen} = \dot{Ex}_{14} + \dot{Ex}_{27} - \dot{Ex}_{15} - \dot{Ex}_{14'} - \dot{Ex}_{19}$

$$\dot{Ex}_{Cooling} = \dot{Q}_{cooling}\left(\frac{T_0 - T_{EVP}}{T_{EVP}}\right) \tag{40.14}$$

$$\dot{Ex}_{H_2} = \dot{m}_{H_2} ex_{H_2} \tag{40.15}$$

$$\dot{Ex}_{18} = (h_{18} - h_0) - T_0(s_{18} - s_0) \tag{40.16}$$

40.6 Environmental Impact Assessment

An important measure for reducing environmental impact, including emissions of carbon dioxide, a primary GHG, is increasing the efficiency and thereby decreasing fuel use. Although numerous exergy and exergoeconomic analyses have been reported for CHP and trigeneration, many do not address environmental impact. Addressing this deficiency is one objective of this chapter, in which emissions of

Table 40.2 Values for parameters in Eqs. (40.17–40.20)

| Constants | $0.3 \leq \varphi \leq 1.0$ | | $1.0 \leq \varphi \leq 1.6$ | |
	$0.92 \leq \theta \leq 2$	$2 \leq \theta \leq 3.2$	$0.92 \leq \theta \leq 2$	$2 \leq \theta \leq 3.2$
A	2361.764	2315.75	916.826	1246.177
α	0.115	−0.049	0.288	0.381
β	−0.948	−1.114	0.145	0.347
λ	−1.097	−1.180	−3.277	−2.036
a_1	0.014	0.010	0.031	0.036
b_1	−0.055	−0.045	−0.078	−0.085
c_1	0.052	0.048	0.049	0.051
a_2	0.395	0.568	0.025	0.009
b_2	−0.441	−0.550	0.260	0.502
c_2	0.141	0.131	−0.131	−0.247
a_3	0.005	0.010	0.004	0.017
b_3	−0.128	−0.129	−0.178	−0.189
c_3	0.082	0.084	0.098	0.103

CO, CO_2, and NO_x are considered. The amount of CO and NO_x produced in the combustion chamber due to the combustion reaction depends on various combustion characteristics including the adiabatic flame temperature [12, 13]. The adiabatic flame temperature in the primary zone of the combustion chamber can be expressed as follows:

$$T_{pz} = A\sigma^{\alpha}\exp\left(\beta(\sigma + \lambda)^2\right)\pi^{x^*}\theta^{y^*}\xi^{z^*} \tag{40.17}$$

Here, π denotes the dimensionless pressure (P/P_{ref}), θ the dimensionless temperature (T/T_{ref}), and ξ the H/C atomic ratio. Also, $\sigma = \phi$ for $\phi \leq 1$, where ϕ is the mass or the molar ratio and $\sigma = \phi - 0.7$ for $\phi \geq 1$. Further, x, y, and z are quadratic functions of σ based on the following equations:

$$x^* = a_1 + b_1\sigma + c_1\sigma^2 \tag{40.18}$$

$$y^* = a_2 + b_2\sigma + c_2\sigma^2 \tag{40.19}$$

$$z^* = a_3 + b_3\sigma + c_3\sigma^2 \tag{40.20}$$

The values for the parameters in Eqs. (40.17–40.20) are listed in Table 40.2. The amount of CO and NO_x produced in a combustion chamber depends on various combustion characteristics including the adiabatic flame temperature [12]. Here, the emissions for these species (in grams per kilogram of fuel) are determined as follows [14]:

$$m_{NO_x} = \frac{0.15 \times 10^{16}\tau^{0.5}\exp\left(\frac{-71100}{T_{PZ}}\right)}{P_3^{0.05}\left(\frac{\Delta P_3}{P_3}\right)^{0.5}} \tag{40.21}$$

$$\cdot m_{CO} = \frac{0.179 \times 10^9 \exp\left(\frac{7800}{T_{PZ}}\right)}{P_3^2 \tau \left(\frac{\Delta P_3}{P_3}\right)^{0.5}} \tag{40.22}$$

where τ is the residence time in the combustion zone (assumed constant here at 0.002 s [12]), T_{pz} is the primary zone combustion temperature given in Eq. (40.17), P_3 is the combustion inlet pressure, and $\Delta P_3/P_3$ is the non-dimensional pressure drop in the combustion chamber.

40.6.1   Cost of Environmental Impact

The desire of preserving the environment while converting energy resources into different forms can be assessed quantitatively using an environmental index of performance. The outputs of the energy conversion process are not only the desired products like electricity, heating, and cooling but also pollutant emissions (e.g., NO_x and CO), CO_2 emissions, thermal pollution (e.g., warming of process air and water), solid wastes, etc. Reduction or minimization of these undesired effects may be an objective from the energetic perspective. A single pollutant can be considered in such an environmental impact assessment objective according to its degree of harmfulness. If more than one pollution source is taken into account, their degrees of harmfulness can be introduced as relative weights of each pollutant measure. The weighting may also be considered from economic point of view when the unit damage cost of each pollutant is available. These criteria can also be combined to form a hybrid criterion which includes information from each.

In this analysis, we express the environmental impact as the total cost rate of pollution damage ($/s) due to CO, NO_x, and CO_2 emissions by multiplying their respective flow rates by their corresponding unit damage costs (C_{CO}, C_{NOx}, and C_{CO2}, which are taken to be equal to 0.02086 $/kg, 6.853 $/kg, and 0.024 $/kg, respectively) [14]. The cost of pollution damage is assumed here to be added directly to other system costs.

40.6.2   Sustainability Analysis

To improve environmental sustainability, it is necessary not only to use sustainable energy sources but also to utilize nonrenewable sources like natural gas fuel more efficiently, and to limit environmental damage. In this way, society can reduce its use of limited resources and extend their lifetimes. Here, a sustainability index SI is used to relate exergy with environmental impact [14]:

$$SI = 1/D_P \tag{40.23}$$

where D_P is the depletion number, defined as the ratio of exergy destruction to input exergy. This relation demonstrates how reducing a system's environmental impact can be achieved by reducing its exergy destruction. Also, the sustainability index is then determined as a measure of how the exergy efficiency affects sustainable development as follows:

$$SI = \frac{1}{1 - \psi} \tag{40.24}$$

40.6.3 Normalized CO_2 Emissions

To assess CO_2 emissions for the system, three cases are considered and the CO_2 emissions are calculated for each case. In the first case, the gas turbine cycle is used to produce electricity. In the second, electricity and heating systems are considered simultaneously and, in the last case, the entire system for multiple products is considered. The amount of CO_2 produced in each case can be expressed as

$$\varepsilon_{power} = \frac{\dot{m}_{CO_2}}{\dot{W}_{net}} \tag{40.25}$$

$$\varepsilon_{CHP} = \frac{\dot{m}_{CO_2}}{\dot{W}_{net} + \dot{Q}_{heating}} \tag{40.26}$$
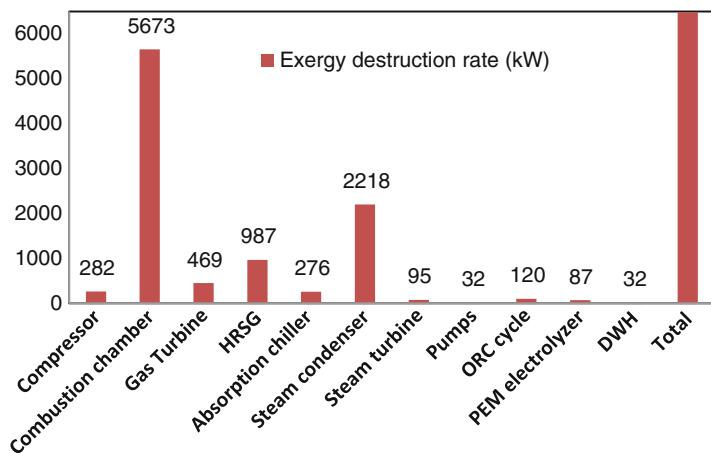
$$\varepsilon_{multi} = \frac{\dot{m}_{CO_2}}{\dot{W}_{net} + \sum \dot{Q}_{heating} + \sum \dot{Q}_{cooling} + \dot{E}_{HW} + \dot{E}_{H_2}} \tag{40.27}$$

40.7 Results and Discussion

The results of the thermodynamic modeling and exergy and environmental analysis are presented in this section, including assessments of the effects of varying several design parameters on cycle performance. In these examinations, it is assumed that the volumetric composition of the inlet air is 0.7567 N_2, 0.2035 O_2, 0.003 CO_2, and 0.036 H_2O [13]; the approach point temperatures in the dual-pressure HRSG are 10 °C; and the fuel injected to the combustion chamber is natural gas, modeled as pure methane with an *LHV* of 50,000 kJ/kg. Table 40.3 lists the thermodynamic specifications of the multigeneration system, including heating and cooling loads, electricity generated by the turbines, COP of the absorption chiller, combustion chamber mass flow rate, hydrogen production rate, hot water mass flow rate, and cost of environmental impact.

Table 40.3 Parameter values resulting from energy and exergy analyses of the system
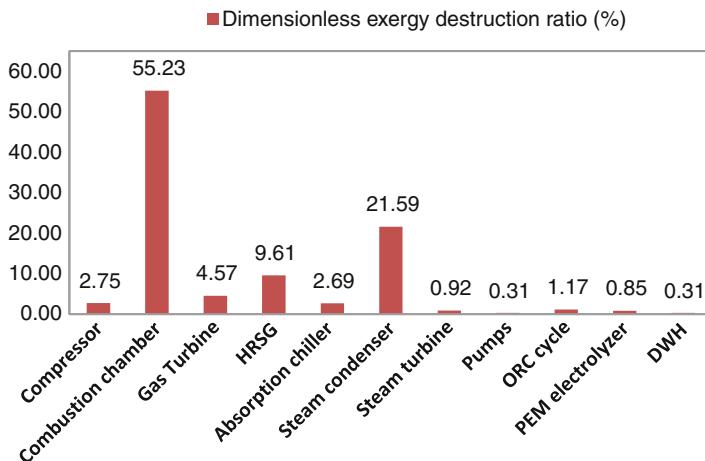
Parameter	Value
$\dot{m}_f$ (kg/s)	0.34
$\dot{Q}_{heating}$ (kW)	4,216
$\dot{Q}_{cooling,absorption}$ (kW)	668.14
$\dot{Q}_{cooling,ORC}$ (kW)	23.10
$\dot{W}_{GT}$ (kW)	5,000
$\dot{W}_{ST}$ (kW)	978.90
$\dot{W}_{ORC}$ (kW)	128.43
η_{multi} (%)	61
Ψ_{multi} (%)	57
$\dot{m}_{H_2}$ (kg/h)	0.67
$\dot{m}_{DWH}$ (kg/s)	0.2
Absorption chiller COP	0.44
CO_2 emissions (kg/MWh)	127.9
$\dot{C}_{env}$ ($/h)	36.17

Fig. 40.5 Exergy destruction rates for the multigeneration system and its components

40.7.1 Exergy and Environmental Impact Assessment Results

The exergy analysis results are summarized in Fig. 40.5, and show that the highest exergy destruction occurs in the CC, mainly due to the irreversibilities associated with combustion and the large temperature difference between the air entering the CC and the flame temperature. The condenser in the Rankine cycle exhibits the next largest exergy destruction, mainly due to the temperature difference between two fluid streams passing through it, but also due to the pressure drop across the device.

Fig. 40.6 Dimensionless exergy destruction ratio for the multigeneration system and its components
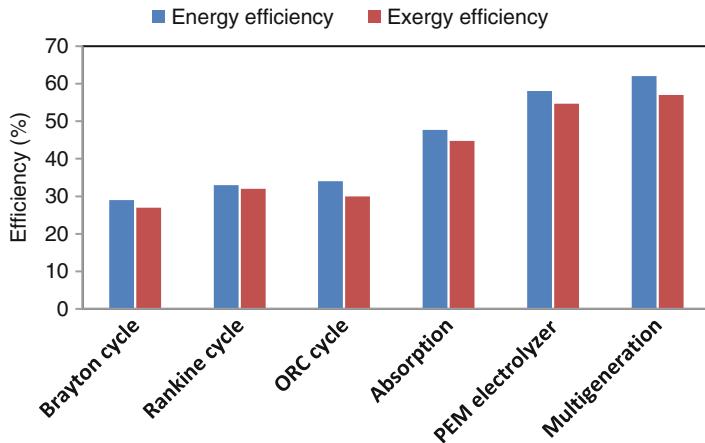
Figure 40.6 shows for each component the dimensionless exergy destruction ratio. This measure is useful for prioritizing exergy losses in an intuitive manner. Both exergy destruction and the dimensionless exergy destruction ratio are higher in the combustor than in other components, suggesting that it would likely be worthwhile to focus improvement efforts on this component. Moreover, the results show that the absorption cycle does not exhibit significant exergy destructions, in part because it does not directly utilize fuel energy but instead uses steam produced by the HRSG.

In order to better understand the system performance, energy and exergy efficiency of each subsystem are calculated (see Fig. 40.7). It is seen that energy and exergy efficiencies are higher for the multigeneration system compared to other cycles when it is not configured in an integrated manner. It is also seen that both energy and exergy efficiencies for the multigeneration system are almost double those of a power generation system, mainly due to an increase in the numerator of Eq. (40.12).
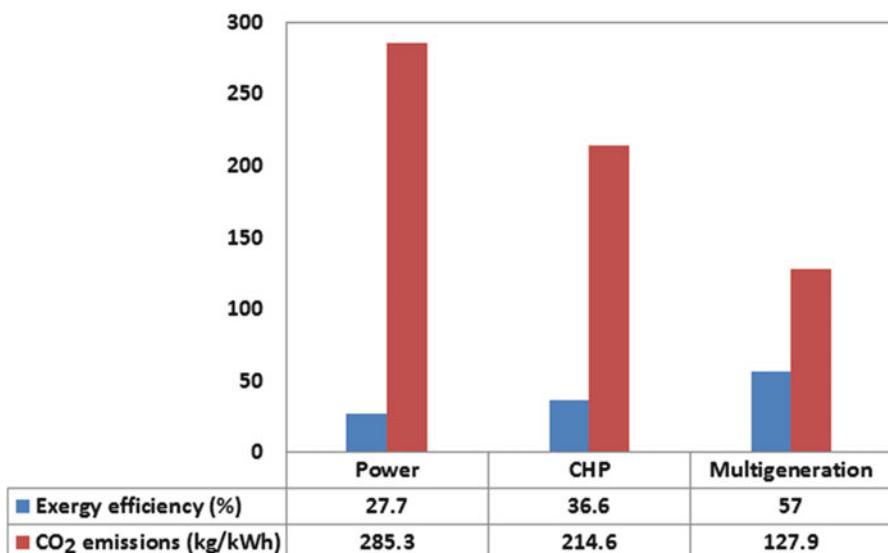
To provide environmental insights, the environmental impact of the gas turbine cycle is compared to that of the multigeneration system in Fig. 40.8. It is seen that the multigeneration cycle has less CO_2 emissions than the GT and CHP cycles, providing a significant motivation for the use of multigeneration cycles. It is also observed that the multigeneration system has a higher exergy efficiency than the other cycles.

Figure 40.9 also shows that the multigeneration cycle has less CO emissions than the GT and CHP cycles, providing another motivation for the use of multigeneration cycles. However, the amount of CO emission is significantly less than the amount of CO_2 emissions of the system.

Figure 40.10 shows the effect on compressor pressure ratio on the CO_2 emissions for various cases. It is seen that the multigeneration cycle has less CO_2 emissions
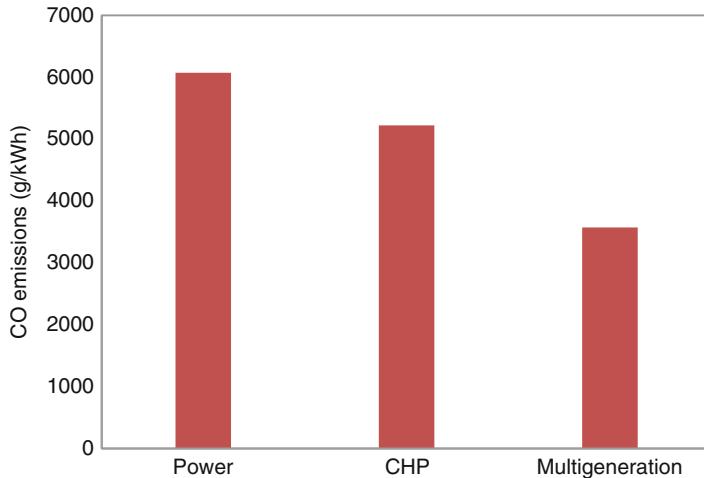
Fig. 40.7 Energy and exergy efficiency for the subsystems of the multigeneration system

	Power	CHP	Multigeneration
Exergy efficiency (%)	27.7	36.6	57
CO$_2$ emissions (kg/kWh)	285.3	214.6	127.9
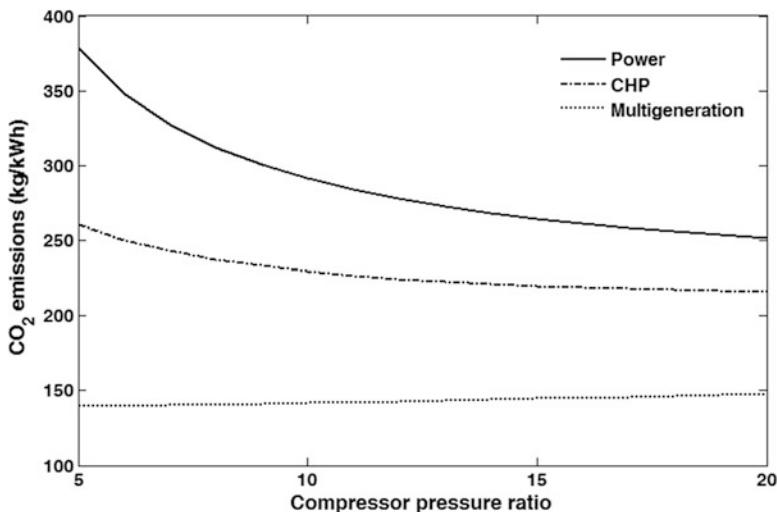
Fig. 40.8 Comparison of exergy efficiency and unit CO$_2$ emissions of selected types of plants

than the power and CHP cycles, another benefit of multigeneration. In addition, increasing the compressor pressure ratio is seen to decrease CO$_2$ emissions for the power cycle, but to increase the CO$_2$ emissions up to a certain ratio and then to decrease them for the CHP and multigeneration cycles. It can be seen in Fig. 40.10 that above $R_{AC} = 10$ the CO$_2$ emissions for the CHP and multigeneration cycles
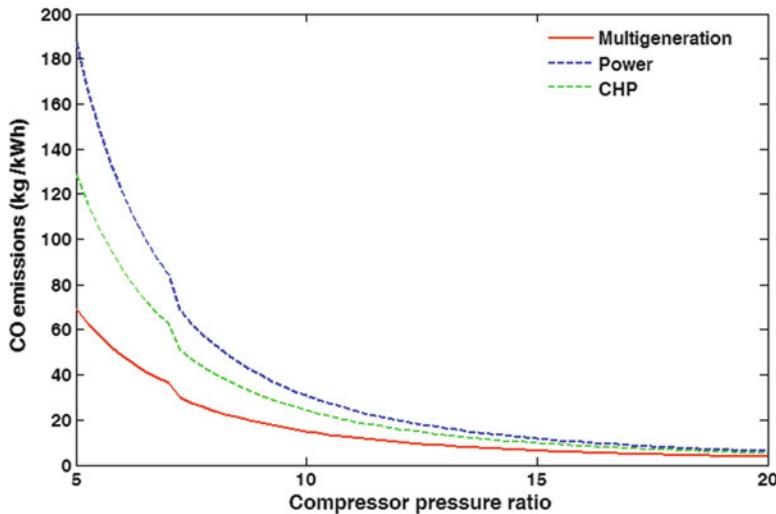
Fig. 40.9 Unit CO emissions of selected types of plants
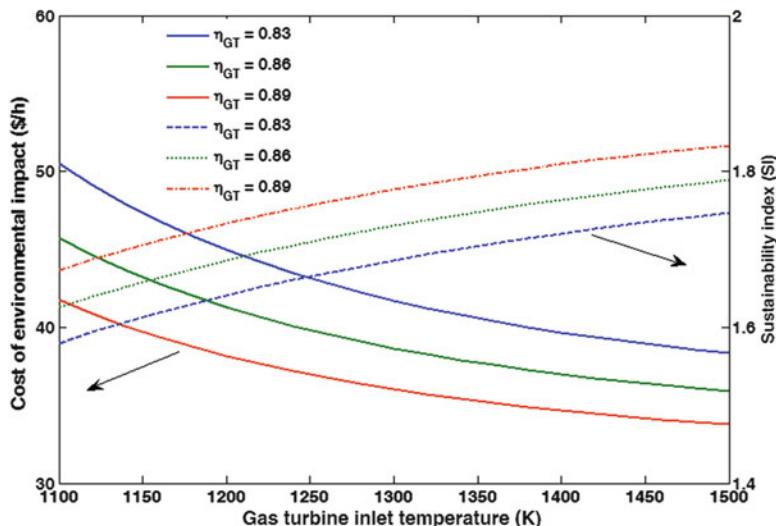
Fig. 40.10 Variation of unit CO_2 emissions with compressor pressure ratio for selected cases

increase, but only slightly. The reason is the reduction in procuring heating and cooling by increasing the compressor pressure ratio above $R_{AC} = 10$. When the compressor pressure ratio increases, the gas turbine outlet temperature decreases. Since this temperature has a significant effect in producing heating and cooling, the unit CO_2 emission of the cycle increases, where the CO_2 emission is in units of kg of CO_2 per MWh of electricity, cooling, and heating. Similar results are obtained for CO emissions of the system, as shown in Fig. 40.11.
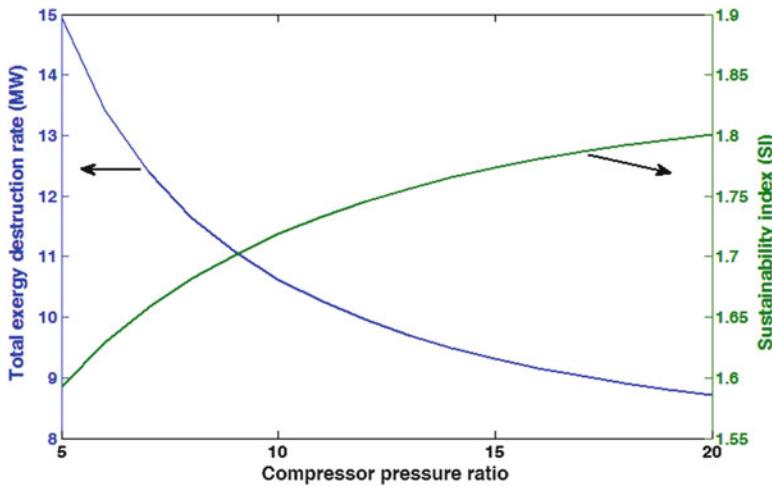
Fig. 40.11 Variation of unit CO emissions with compressor pressure ratio for selected cases

Fig. 40.12 Variation with compressor pressure ratio of sustainability index and cost rate of environmental impact

Expanding the results for CO_2 emissions, we investigate the effect of compressor pressure ratio on cost of environmental impact and sustainability index. Figure 40.12 shows that increasing the compressor pressure decreases the cost of environmental impact due to the reduction of mass flow rate injected into the

Fig. 40.13 Variation with compressor pressure ratio of total exergy destruction rate and sustainability index

combustion chamber. The sustainability index increases correspondingly for all three cycles considered (GT, CHP, and multigeneration).

Figure 40.13 shows the effect of compressor pressure ratio on total exergy destruction of the cycle and sustainability index, and similar results are obtained as in Fig. 40.12. That is, the overall exergy destruction of the cycle decreases and the sustainability index increases with increasing compressor pressure ratio. Exergy efficiency, exergy destruction, environmental impact, and sustainability are thus observed to be linked in such systems, supporting the utility of exergy and environmental impact assessment.

A significant design parameter is the gas turbine inlet temperature (GTIT). Raising this parameter can increase gas turbine output power. But an energy balance of the combustion chamber indicates that the fuel input rate also increases as the GTIT rises. The increased fuel input is also reflective of an increase in turbine exhaust temperature. The variations of CO_2 emissions for the cycles with GTIT are shown in Fig. 40.14. CO_2 emissions are seen to decrease with increasing GTIT. As the mass flow rate of gases through the combustion chamber increases with GTIT, so do the net output power and the heating and cooling loads. Multigeneration is observed to be the most advantageous option from an environmental point of view. The variations with GTIT of both cost of environmental impact and sustainability index are shown in Fig. 40.15, where the cost of environmental impact is seen to decrease with increasing GTIT.
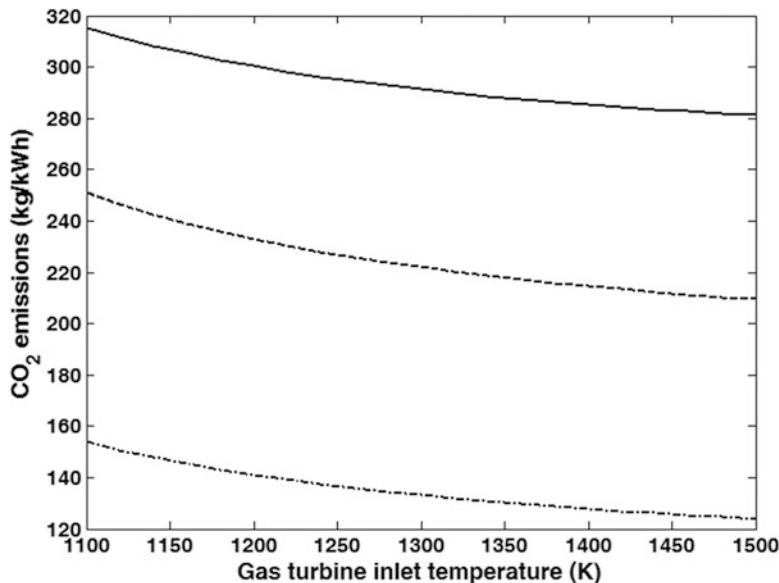
Fig. 40.14 Variation of gas turbine inlet temperature (GTIT) on normalized CO_2 emissions
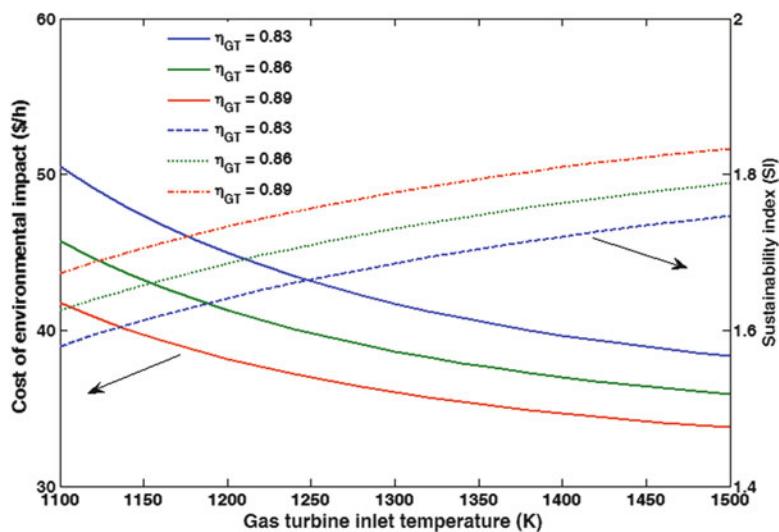
Fig. 40.15 Variation with gas turbine inlet temperature of sustainability index and cost rate of environmental impact

40.8   Conclusions

The comprehensive thermodynamic modeling and exergy and environmental impact assessment of a multigeneration system for heating, cooling, electricity, hot water, and hydrogen provide useful insights. The exergy results show that the combustion chamber, steam condenser, and HRSG are the main sources of irreversibility, with the high exergy destruction attributable to the high temperature difference for heat transfer in both devices and the combustion reaction in the combustion chamber. In addition, the multigeneration cycle exhibits less CO_2 and CO emissions than micro gas turbine and CHP cycles. Additional conclusions are as follows:

- The exergy efficiency of the multigeneration cycle increases with gas turbine isentropic efficiency.
- The overall exergy destruction of the cycle decreases and the sustainability index increases with increasing compressor pressure ratio.
- The exergy efficiency and sustainability index for the multigeneration, gas turbine, and CHP cycles increase with turbine inlet temperature, and the exergy efficiency of the system is slightly lower than the energy efficiency.
- The cost of environmental impact for the multigeneration system is significantly less than for the power and CHP cycles.
- Multigeneration energy systems are good options to mitigate global warming as they can reduce CO_2 and CO emissions and also help reduce the cost of environmental impacts by producing several useful outputs from an energy input.

References

1. Colpan CO, Dincer I, Hamdullahpur F (2009) Reduction of greenhouse gas emissions using various thermal systems in a landfill site. Int J Global Warming 1(1–3):89–105
2. Renato S (2005) Atmospheric methane and nitrous oxide of the late pleistocene from antarctic ice cores. Science 310(5752):1317–1321
3. Environmental Protect Agency (2012) http://www.epa.gov. Accessed Sept 2012
4. Dincer I (2000) Renewable energy and sustainable development: a crucial review. Renew Sustain Energy Rev 4(2):157–175
5. Ahmadi P, Dincer I (2010) Exergoenvironmental analysis and optimization of a cogeneration plant system using Multimodal Genetic Algorithm (MGA). Energy 35:5161–5172
6. Al-Sulaiman F, Dincer I, Hamdullahpur F (2010) Exergy analysis of an integrated solid oxide fuel cell and organic Rankine cycle for cooling, heating and power production. J Power Sources 195(8):2346–2354
7. Athanasovici V, Le Corre O, Brecq G, Tazerout M (2000) Thermo-economic analysis method for cogeneration plants. In: Proc. of international conference on efficiency, cost, optimization, simulation and environmental impact of energy systems, Netherlands., pp 157–164

8. Havelsky V (1999) Energetic efficiency of cogeneration systems for combined heat, cold and power production. Int J Refrig 22:479–485
9. Sahoo PK (2008) Exergoeconomic analysis and optimization of a cogeneration system using evolutionary programming. Appl Therm Eng 28(13):1580–1588
10. Khaliq A, Kumar R, Dincer I (2009) Performance analysis of an industrial waste heat-based trigeneration system. Int J Energ Res 33:737–744
11. Dincer I, Rosen MA (2013) Exergy: energy, environment and sustainable development, 2dth edn. Elsevier, UK
12. Ahmadi P, Barzegar Avval H, Ghaffarizadeh A, Saidi MH (2011) Thermo-economic-environmental multi-objective optimization of a gas turbine power plant with preheater using evolutionary algorithm. Int J Energ Res 35(5):389–403
13. Ahmadi P, Rosen MA, Dincer I (2011) Greenhouse gas emission and exergo-environmental analyses of a trigeneration energy system. Int J Greenhouse Gas Control 5(6):1540–1549
14. Ahmadi P, Dincer I, Rosen MA (2011) Exergo-environmental analysis of an integrated organic Rankine cycle for trigeneration. Energ Convers Manage 64:447–453
15. Al-Sulaiman FA, Dincer I, Hamdullahpur F (2012) Energy and exergy analyses of a biomass trigeneration system using an organic Rankine cycle. Energy 45:975–985
16. Al-Sulaiman FA, Hamdullahpur F, Dincer I (2012) Performance assessment of a novel system using parabolic trough solar collectors for combined cooling, heating, and power production. Renew Energy 48:161–172
17. Ahmadi P, Rosen MA, Dincer I (2012) Multi-objective exergy-based optimization of a polygeneration energy system using an evolutionary algorithm. Energy 46:21–31
18. Ratlamwala T, Dincer I, Gadalla MA (2012) Performance analysis of a novel integrated geothermal-based system for multi-generation applications. Appl Therm Eng 40:71–79
19. Ratlamwala T, Dincer I, Gadalla MA (2012) Thermodynamic analysis of an integrated geothermal based quadruple effect absorption system for multigenerational purposes. Thermochim Acta 535:27–35
20. Dincer I, Zamfirescu C (2012) Renewable-energy-based multigeneration systems. Int J Energ Res 36(15):1403–1415
21. Dincer I (2010) Development of solar-driven multi-generation system. Introduction to energy system course. University of Ontario Institute of Technology (UOIT), Oshawa, Canada

Chapter 41
Integrated Renewable Energy-Based Systems for Reduced Greenhouse Gas Emissions

Mehdi Hosseini, Ibrahim Dincer, and Marc A. Rosen

Abstract Efforts to develop systems to mitigate environmental pollution are increasing. Renewable energy resources, e.g., solar, wind, and hydro, provide clean energy with almost no greenhouse gas emissions. However, these forms of energy are intermittent, and the costs of systems utilizing renewable energy for power generation or heating/cooling are often not competitive with conventional systems. Using hybrid systems and recovering waste energy are two ways to enhance the utilization of renewable energy resources. In this chapter, numerous integrated renewable-based energy systems are reviewed, based on a number of previous studies by the present authors. The aims of these systems are to enhance energy management and reduce environmental pollution. The chapter starts with a brief introduction of integrated renewable energy systems and their role in mitigating environmental pollution. The description of some integrated systems for residential and community usage is presented. Moreover, the systems are compared with conventional power generation systems in terms of efficiency and carbon dioxide emission. The results show that although the energy efficiency of the residential photovoltaic-fuel cell system is considerably lower than the conventional power generation systems, they release zero amount of emission into the environment during their operation. Fuel cell-micro gas turbine system integrated with biomass gasification has energy efficiencies around 55 %. This renewable-based energy integrated system produces 741 gram of carbon dioxide per kWh, which is comparable with the emission of fossil power plants.

M. Hosseini (✉) • I. Dincer • M.A. Rosen
Faculty of Engineering and Applied Science, University of Ontario Institute of Technology,
2000 Simcoe Street North, Oshawa, ON, Canada L1H 7K4
e-mail: mehdi.hosseini@uoit.ca; ibrahim.dincer@uoit.ca; marc.rosen@uoit.ca

Nomenclature

ex	Specific exergy, kJ/kg
$\dot{Ex}$	Exergy flow rate, kW
i	Current density, A/cm^2
$\dot{I}$	Exergy destruction rate, kW
LHV	Lower heating value, kJ/kg
$\dot{m}$	Mass flow rate, kg/s
n	Reaction coefficient
$\dot{n}$	Molar flow rate, kmol/s
N	Number of cells in the SOFC
$\dot{Q}$	Heat flow rate, kW
SC	Steam-to-carbon ratio
T	Temperature, °C
$\dot{W}$	Electric power, kW

Greek Letters

η	Energy efficiency %
ψ	Exergy efficiency %
γ	Specific heat ratio

Subscripts

0	Ambient or standard condition
a	Air
$cell$	SOFC cell
ex	Exergy
g	Gas
i	Species
mb	Moist biomass
MGT	Micro gas turbine
DH	District heating heat demand
p	Product gas
Q	Heat
s	Surface or steam
TIT	Turbine inlet temperature
WB	Wet biomass

Superscripts

*	Reference condition

Acronyms

HRSG   Heat recovery steam generator
MGT   Micro gas turbine
SOFC   Solid oxide fuel cell
PV   Photovoltaic
PV-FC   Photovoltaic-fuel cell

41.1   Introduction

Many feel that present-day production and use of energy threaten the environment in terms of global warming, mainly as a consequence of greenhouse gas (GHG) emissions, and depletion of energy resources. According to the Carbon Dioxide Information Analysis Center (CDIAC), half of the GHG emissions during the period of 1751 to 2008 were released into the environment after 1971 [1]. Figure 41.1 shows the trend in carbon dioxide emissions due to the burning of fossil fuels since 1950. More than 70 % of the emissions reported in Fig. 41.1 are due to the use of solid and liquid fossil fuels [1]. The trend towards increasing energy consumption will likely exacerbate such environmental problems.

Attention towards developing systems to mitigate these environmental problems is increasing. Improving the efficiency of energy systems usually requires reducing irreversibilities and waste exergy losses, as well as the use of less environmentally impacting alternative energy resources. The use of renewable energy resources in power generation is receiving much focus. Renewable energy resources, e.g., solar,
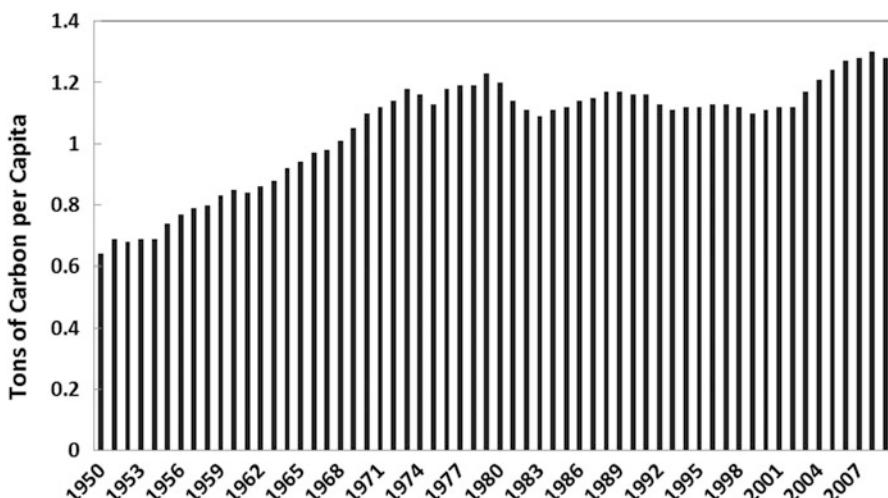
Fig. 41.1 Annual global fossil fuel carbon dioxide emissions per capita (modified from ref. 1)
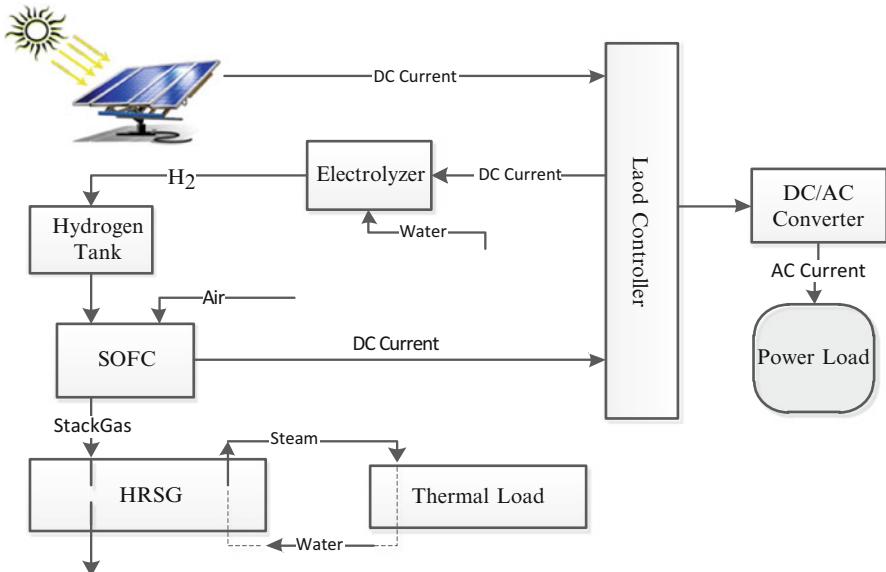
wind, and hydro, provide clean energy with almost no GHG emissions. However, these forms of energy are intermittent, and the cost of systems utilizing renewable energy for power generation or heating/cooling is often not competitive with that of conventional systems. Using hybrid systems and recovering waste energy are two ways to enhance the utilization of renewable energy resources. Solar energy can be used for space heating/cooling and for electricity generation with photovoltaic (PV) systems. Such systems normally require supplementary devices to meet peak demands or to harvest surplus generated electricity. Producing the energy carrier hydrogen is one method for storing electricity from solar PV systems. Surplus electricity can be converted to hydrogen via water electrolysis, and the hydrogen can be stored and used to generate electricity, when required, in a fuel cell. The fuel cell also can cogenerate heat for district heating or other purposes. Biomass, another renewable energy resource, can be used directly (direct burning) or indirectly (as a biofuel) to generate electricity. Biomass gasification has been demonstrated to be a feasible and promising technology and may play an important role in future energy markets. The syngas produced by gasification can be used in internal combustion engines (ICEs), gas turbines (GTs), and fuel cells (FCs). A power generation system utilizing biomass gasification can be integrated with bottoming cycles for heat recovery to increase efficiency. Integrated renewable energy-based systems (IRESs) combine power generation technologies with heat recovery and energy storage technologies to provide cooling, heating, and energy storage using thermal energy normally wasted in the production of electricity. Since the input energy is provided by renewable resources, IRESs exhibit almost no GHG emissions.

The configuration of the IRES components is important to optimize energy utilization. These systems consist of electricity generation technologies, process equipment, heat recovery units, and energy storage systems. Several configurations and technologies have been investigated. For instance, a market assessment for integrated energy systems (IESs) for buildings by LeMar [2] shows that the potential building market for IESs is expected to exceed 35 GW by the year 2020.

The current work is a review based mainly on previous research by the authors on the integration of renewable energy resources in supplying the electricity demand of a house or a community [3–7]. The presented IRESs are aimed in large part at decreasing the level of GHG emissions and enhancing energy management.

41.2 Hybrid Solar-Fuel Cell CHP Systems for Residential Applications

Numerous studies have been undertaken to improve the understanding of residential applications of solar-hydrogen combined heat and power (CHP). Here we consider such a hybrid system and describe its components and compare it with
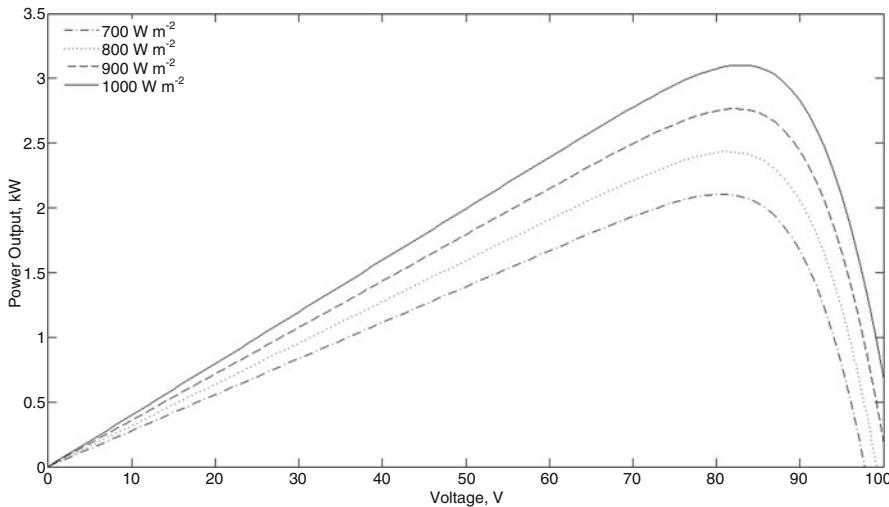
Fig. 41.2 Schematic of a photovoltaic-fuel cell CHP system for residential applications [4]

conventional CHP systems and solar-hydrogen CHP systems. The solar PV system is the main part of the electricity generation module. A proton exchange membrane (PEM) water electrolyzer is utilized for hydrogen production from surplus PV electricity. Hydrogen is stored during day when loads are below the peak and input into a solid oxide fuel cell (SOFC) to provide residential electricity at night. High-temperature gases leaving the fuel cell stack are directed to a heat recovery steam generator (HRSG), as shown in Fig. 41.2, for steam generation.

Gibson and Kelly [8] optimized a solar power hydrogen production system with water electrolysis. They showed that if all the components are selected and sized in an optimized way, so that the PV output voltage matches the electrolyzer input voltage, the overall solar-PV-hydrogen production system efficiency can reach 12.4 %. Lagorse et al. [9] investigated three PV-hydrogen production configurations for residential applications focusing on optimum size, cost, and operation. Pregger et al. [10] discussed four hydrogen production systems using solar thermal energy and performed cost evaluations.

The power output of the PV system depends strongly on the solar irradiance, as shown in Fig. 41.3 for a 210 W SunPower solar panel.

The intermittent and variable intensity solar irradiance affects the performance of the hybrid system. However, with appropriate design and using energy storage, the electricity demand of the house and a part of its thermal energy demand can be met. The surplus electricity generated by the PV modules is stored as hydrogen in a compressed hydrogen tank. Hydrogen can be stored as a liquid at cryogenic temperatures in relatively small volumes. The hydrogen liquefaction process

Fig. 41.3 Effect of solar irradiance on PV power-voltage characteristics

normally consumes more than 30 % of the hydrogen lower heating value (LHV) [7]. Hydrogen can also be stored as a compressed gas in pressure vessels, and via metal hydrides. In residential applications, especially when fuel cells are used in solar-fuel cell hybrid systems, large-scale hydrogen storage is not needed, so compressed gas hydrogen storage is usually preferred. During the storage of hydrogen as a compressed gas some physical exergy is lost due to pressure and temperature drops. The storage tank state of charge (SOC) and the pressure and temperature distribution depend on the tank filling rate, initial SOC, and pressure. The authors report the thermodynamic evaluation of filling a high-pressure storage tank [7]. At the tank initial temperature, the initial pressure has a positive effect on the exergy efficiency during filling. The exergy efficiency of the filling process rises from 86 to 89 % with an increase of initial tank pressure from 0.2 to 20 bar at the 20 °C initial temperature [7].

Fuel cells can be used for electricity generation, although technical and economic enhancements are still needed. They can also be used for CHP, and in hybrid configurations. Micro gas turbine-fuel cell (MGT-FC), MGT-steam turbine-FC, and MGT-FC district heating and cooling systems are operating in different regions of the world. For instance, Hosseini et al. [11] performed energy and exergy analyses for a residential hybrid MGT-FC system, and other works have been reported on residential fuel cell applications [12, 13]. Velumani et al. [14] proposed a hybrid SOFC/micro gas turbine/absorption chiller to provide electricity and cooling for a residential area, while Hartkopf et al. [15] investigated fuel cell use for a multipurpose building in the United States.

The exergy efficiency, which is an index of efficiency of the hybrid PV-fuel cell system relative to an ideal version of such a system, is presented based on the solar irradiance in Toronto and the electricity demand of a Canadian house. Figure 41.4
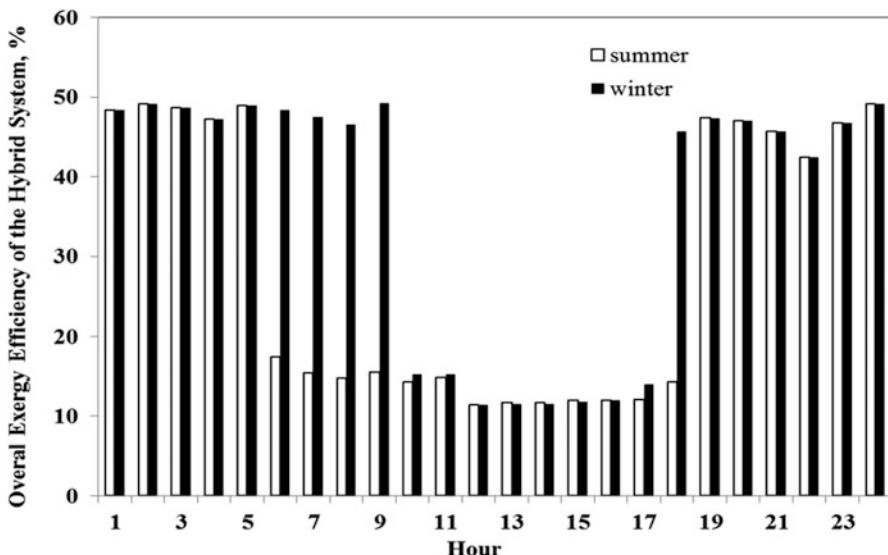
Fig. 41.4 Total exergy efficiency of a solar PV-FC CHP system broken down by hour of the day [4]

shows the exergy efficiency during two typical summer and winter days as a comparison. The efficiency graph shows that the time that the fuel cell is in operation is longer in winter. This is mostly due to less solar availability in winter. The minimum total efficiency is achieved when the surplus electricity generation is a maximum. In summer, the system exhibits a minimum total exergy efficiency between 6 am and 6 pm, because the surplus power generated by the PV system is consumed in the electrolyzer for hydrogen production. This minimum efficiency operation period for winter is from 10 am to 5 pm.

41.2.1   Comparison of Conventional and Solar-Hydrogen Residential CHP Systems

Fuel cells and solar PV systems are both undergoing extensive development, and their uses in industrial and residential applications are presently limited. Several CHP systems (e.g., micro gas turbines, internal combustion engines, and diesel generators) are being used to provide electricity and heating/cooling for houses. It is possible for these systems to operate independently of the power grid. These systems also allow heat recovery from the system flue gas. For both conventional and solar-fuel cell CHP systems, reliability, control, economics, and emissions are major concerns.

Table 41.1 Electrical and thermal power outputs and efficiencies for several CHP systems

CHP system	Product power output (kW)		Energy efficiency (%)	
	Electrical	Thermal	Electrical	Thermal
Gas engine	5.5	12.5	27	61
Internal combustion engine	2.0–9.5	8.0–26	24	72
Fuel cell	4.0	9.0	25	55
PV-fuel cell	3.6	0.50	–	14.5

Source: Ref. 4

Table 41.2 Energy efficiency and specific CO_2 emissions for several electricity generation plants

Electricity generation plant	Energy efficiency (%)	Specific CO_2 emission (g/kWh)	Reference
Combined cycle power plant	50	404	[16]
Fossil fuel power plant	42	617	[16]
Nuclear power plant and conventional steam power plant	37	272	[16]
Residential PV-fuel cell	14.5	0	[4]

The results of a comparative analysis based on selected micro-CHP technologies for residential applications are shown in Table 41.1. The nominal power and the energy efficiency during the maximum load are considered in the analysis, which are adapted from the work by Paepe et al. [16]. Table 41.1 shows the electrical and thermal power outputs and energy efficiencies of the selected CHP systems.

Every electricity and heat generation system has emissions, the magnitude of which depends on system type. Paepe et al. [16] predicted that, if the heat is generated by a gas boiler, the specific CO_2 emission is 404 g/kWh of natural gas combusted. The CO_2 produced through electricity generation is strongly dependent on the electricity generation technology and its efficiency. Table 41.2 shows the energy efficiency and CO_2 emissions for the three electricity generation methods operating in Belgium. Also, the results for a residential PV-FC CHP system are presented.

To compare the CHP systems with the power generation technologies in Table 41.2, the same procedure is used to determine the CO_2 emissions. Since the gas engine and the Stirling internal combustion engine use natural gas, the specific CO_2 emission is considered to be 56.1 g per 1 MJ natural gas consumption. For the fuel cells, it is assumed that no CO_2 is produced during operation. However, CO_2 is produced during the production of the H_2 for the fuel cells (from the methane-reforming reaction if natural gas is the fuel). The efficiency of the reforming reaction is taken into account in the efficiency of the fuel cell. Assuming that natural gas is used to produce the hydrogen in the fuel cell, one can consider 56.1 g/MJ as applicable to the fuel cell, too.

In the next step, Paepe et al. [16] simulated the electrical and thermal demands of a house in Belgium, and determined the annual electricity demand to be 3.61 MWh and the annual thermal load to be 34.19 MWh. The energy consumption for the

Table 41.3 Fraction of energy consumption for several CHP systems relative to several conventional power generation systems

CHP system	Type of power generation system		
	Combined cycle	Fossil fuel	Nuclear and conventional steam
Fuel cell	0.87	0.79	0.70
Gas engine	0.81	0.71	0.64
Internal combustion engine	0.73	0.65	0.59

three CHP systems and the cases in which electricity is supplied by a power grid are compared in Table 41.4, where values are relative to the reference cases: a gas-fired combined power plant, a fossil fuel power plant, and a nuclear power plant and conventional steam power plant. Table 41.3 demonstrates that the internal combustion engine has the greatest energy saving compared to the conventional power generation systems. Compared to the nuclear power plant, the internal combustion engine CHP systems reduce energy consumption the most. All three CHP systems have lower emissions than the fossil fuel power plant. Energy use and CO_2 emission reductions strongly depend on the power plant efficiency. Since the energy efficiency of the fuel cell CHP system is less than that of other CHP systems, its energy saving fraction is also less [16].

Although the PV-fuel cell system for the residential applications produces zero GHG emissions during operation, emissions occur during manufacturing of the system components. A detailed life cycle analysis is required to assess residential CHP systems in terms of resource consumption and environmental pollution during the manufacturing processes. Nonetheless, with improving manufacturing processes, implementing a renewable-based integrated system to power a residential area will likely help in sustaining the environment.

41.3   Integrating a Solid-Oxide Fuel Cell and Micro Gas Turbine with Biomass Gasification

Gasification is a chemical process that converts materials such as biomass into convenient gaseous fuels. In this process biomass is broken into simpler substances like CO, H_2, CH_4, and CO_2. The process occurs in the presence of a gasification medium [17–19]. Biomass gasification is a complicated process, which is affected by many parameters, including gasification medium, biomass composition and moisture content, gasification temperature and pressure, and process configuration. A good understanding of the effects of these parameters on the performance of a gasification system is required for effective design [5]. Thermodynamic analysis, based on exergy as well as energy, is one approach to develop such an understanding. Various studies have been performed on biomass gasification from the point of energy and exergy. For example, Cohce et al. [17] analyzed a hydrogen production

unit based on biomass gasification; a simplified model is presented for biomass gasification based on chemical equilibrium considerations, with the Gibbs free energy minimization approach, hydrogen production and exergy destruction rates in each component are found. Abuadala et al. [18] presented an exergy analysis of a hydrogen production system via biomass gasification in the range of 10–32 kg/s from sawdust. The study focuses on the influence of gasification temperature, biomass feed, and steam injection on the hydrogen yield and energy efficiencies. The results indicate that the performance of hydrogen production from steam-fed biomass gasification depends on the quantities of steam and biomass input to the gasifier.

The product gas mixture for biomass gasification contains several species, depending on the process type and operational conditions. Stoichiometric calculations can help determine the products of reaction [19]. Abudallah and Dincer [20] considered the use of biomass gasification product gas as the fuel feed to an SOFC, as a potential integrated application. The current authors consider a similar system in which the product gas is fed to the fuel cell stack after gas cleaning and CO_2 removal [6].
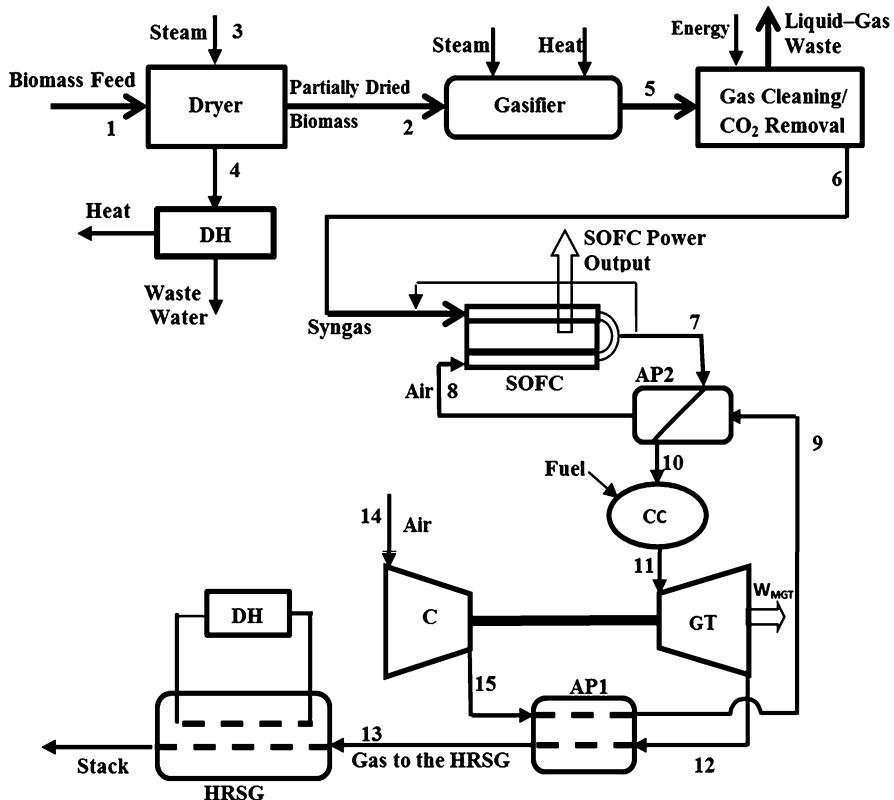
The integrated system includes a biomass gasification unit, an SOFC, a micro gas turbine, and a heat recovery unit (see Fig. 41.5). Sawdust is fed to the biomass dryer before entering the gasifier. In the analyses, a direct-steam drying process is considered to remove 50 % of the biomass moisture content. In the gasifier, biomass is converted to a mixture of gases in the presence of superheated steam. Biomass gasification is an endothermic process, and the gasification system is considered to be indirectly heated by an external heat source.

The product gas mixture leaving the gasifier contains CO, H_2, CH_4, CO_2, H_2O, N_2, and C. The LHV of the product gas is highly dependent on the mixture composition. Moreover, downstream components in the integrated system are affected by the gas properties. Therefore, gas cleaning and CO_2 removal are added to the system. With these post-gasification processes, the product syngas consists of CO, H_2, and CH_4 and is fed to the solid oxide fuel cell for power production.

The basic electrochemical reactions taking place in an SOFC stack are given by [21, 22]

$$CH_4 + H_2O \leftrightarrow 3H_2 + CO \tag{41.1}$$

$$CO + H_2O \leftrightarrow H_2 + CO_2 \tag{41.2}$$

$$2H_2 + O_2 \rightarrow 2H_2O \tag{41.3}$$

Characteristic curves of SOFCs are obtained based on the equilibrium constants and reaction rates of Eqs. 41.1–41.3. The oxygen ions are formed in the cathode side of the fuel cell and pass through the electrolyte to the anode. The electrochemical reaction of hydrogen and oxygen ions releases electrons, which pass through an external electric circuit providing the power output of the SOFC. To avoid cell
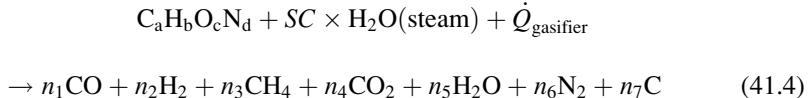
Fig. 41.5 Schematic of the integrated SOFC-micro gas turbine with biomass gasification

starvation, only a certain percent of the syngas reacts with oxygen ions in the anode. This is specified by a fuel utilization factor. The by-product gas of the electrochemical reactions leaves the fuel cell stack with a temperature between 800 and 1,000 °C. Also, the by-product contains some non-reacted syngas. In order to recover the energy from the SOFC exhaust gas, an afterburner is utilized to burn the remaining syngas and provide the micro gas turbine with the required input energy. Therefore, the by-product gas leaving the fuel cell anode side mixes with the air from the cathode side. The combustion process in the afterburner produces a high-enthalpy gas which can be used in the MGT for electric power generation. Before the combustion gas enters the micro gas turbine, it is utilized to preheat the air entering the fuel cell stack. The combustion chamber of the micro gas turbine is used to fix the turbine inlet temperature (TIT). The combustion gases enter the MGT, produce mechanical energy, and leave the MGT with a temperature between 550 and 750 °C, depending on the compressor pressure ratio. The mechanical energy of the MGT is converted to electricity in the generator. The MGT flue gas has a significant amount of energy, which is recovered in the heat recovery steam

generator. The flue gas enters the HRSG and transfers its energy to the water flowing inside the tubes of the HRSG. Unless applied for power generation purposes, most HRSGs produce saturated steam for steam-utilizing units.

Superheated steam is used as the gasification medium in the gasifier. Sawdust is gasified in the presence of steam according to the following overall chemical equation:

$$C_aH_bO_cN_d + SC \times H_2O(\text{steam}) + \dot{Q}_{\text{gasifier}}$$

$$\rightarrow n_1CO + n_2H_2 + n_3CH_4 + n_4CO_2 + n_5H_2O + n_6N_2 + n_7C \qquad (41.4)$$

Minimization of the Gibbs free energy or the equilibrium reaction rate approach is used to obtain the reaction coefficients (n_1 to n_7) [5, 19].

The biomass dryer and district heating unit are parts of the gasification system. The energy and exergy balances, which permit the calculation of the steam input to the dryer and heat flow rate of the district heating unit, are presented by the authors elsewhere [5]. Considering these two components, the total energy and exergy efficiencies, respectively, of the gasification system can be obtained:

$$\eta_{\text{gasification}} = \frac{\dot{m}_{\text{syngas}} \times LHV_{\text{syngas}} + \dot{Q}_{\text{DH}}}{\dot{m}_{\text{biomass}} \times LHV_{\text{biomass}} + \dot{En}_{\text{Steam}} + \dot{Q}_{\text{gasifier}} + \dot{En}_{\text{gas-cleaning}}} \qquad (41.5)$$

$$\psi_{\text{gasification}} = \frac{\dot{m}_{\text{syngas}} \times ex_{\text{syngas}} + \dot{Ex}_{\text{q,DH}}}{\dot{m}_{\text{biomass}} \times ex_{\text{biomass}} + \dot{Ex}_{\text{Steam}} + \dot{Ex}_{\text{Q}} + \dot{Ex}_{\text{gas-cleaning}}} \qquad (41.6)$$

Here, steam use is considered for both the dryer and the gasifier.

Colpan et al. [22] developed a model for the electrochemical reaction in an SOFC. Their model considers a mixture of H_2, CO, and CH_4 as the syngas fuel.

The electric power output of the fuel cell stack can be expressed as

$$\dot{W}_{\text{SOFC}} = V \times i \times A_{\text{cell}} \times N_{\text{SOFC}} \qquad (41.7)$$

where V denotes the output voltage, i the current density, A_{cell} the single cell active area, and N_{SOFC} the total number of cells in the stack.

The modeling of the afterburner and the combustion chamber is based on combustion reactions of the remaining syngas in the fuel cell exhaust and the gas TIT. The gas turbine and the compressor are modeled based on isentropic relations and isentropic efficiencies. The gases leaving the MGT are fed to the HRSG to produce steam for steam/hot water utilization purposes. Accounting for the heat recovered in the HRSG, the total efficiencies of the SOFC-MGT CHP system are

$$\eta_{\text{SOFC-MGT CHP}} = \frac{\dot{W}_{\text{SOFC}} + \dot{W}_{\text{MGT}} + \dot{Q}_{\text{HRSG}}}{\dot{m}_{\text{fuel,SOFC-MGT}} \cdot LHV_{\text{syngas}}} \qquad (41.8)$$

Table 41.4 Input parameters for the gasification system

Parameter	Value
Dryer	
Biomass feed rate (kg/s)	0.011
Superheated steam pressure (bar)	3
Superheated steam temperature (°C)	200
Moisture fraction of feed biomass ($kg_{moisture}/kg_{WB}$)	0.5
Gasifier	
Steam pressure (bar)	10
Steam temperature (°C)	400

Table 41.5 Input parameters for the SOFC system

Parameter	Value
Stack outlet temperature (°C)	1,000
Activation area (cm^2)	834
Cell current density (A/cm^2)	0.35
Fuel utilization factor	0.85
Compressor pressure ratio, r_c	9
AP1 outlet temperature (Point 9 in Fig. 41.1) (°C)	527

$$\psi_{\text{SOFC-MGT CHP}} = \frac{\dot{W}_{\text{SOFC}} + \dot{W}_{\text{MGT}} + \dot{Ex}_{\text{Q,HRSG}}}{\dot{m}_{\text{fuel,SOFC-MGT}} \cdot ex_{\text{syngas}}} \qquad (41.9)$$

The aim is to improve the understanding of integrated system performance, and this is accomplished by performing a parametric study of the effect of steam-to-carbon (SC) ratio on the performance of the SOFC-micro gas turbine (SOFC-MGT) cycle integrating biomass gasification. The variations in molar fraction and LHV of the syngas, and the gasification process exergy destruction and energy and exergy efficiencies, are reported, as SC changes.

The following assumptions are made in the analyses of the integrated SOFC-MGT system with biomass gasification [6]:
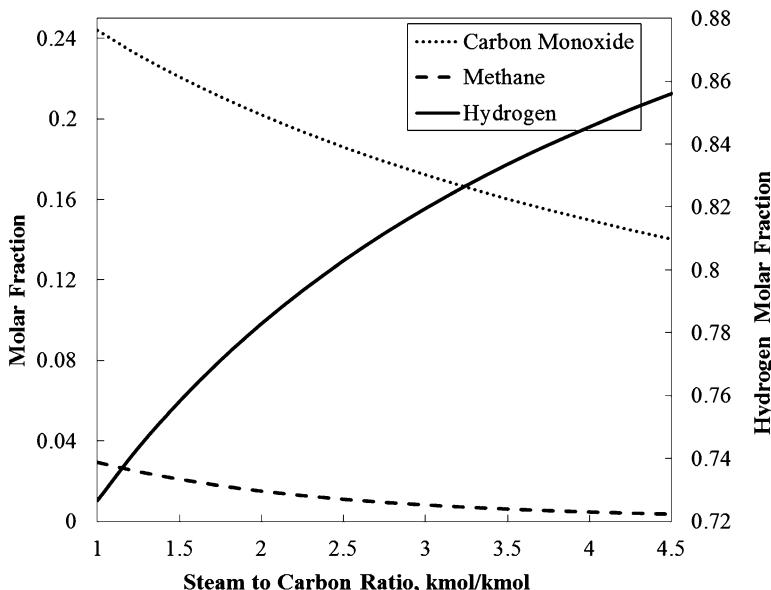
- The system operates at steady state.
- All gases are ideal.
- Heat losses to the environment from the system boundary are negligible.
- Pressure drops along the system are negligible.
- Gasification takes place in equilibrium.
- The sawdust biomass has a chemical formula $C_{4.643}H_{6.019}O_{2.368}N_{0.021}$.

Tables 41.4–41.6 list the input parameters for the analyses of the integrated system.

The effect of steam-to-carbon ratio on the syngas species molar fraction is shown in Fig. 41.6. When SC varies from 1 to 4.5, the hydrogen molar fraction increases 17.8 %, while the carbon monoxide and methane molar fractions decrease by 42.5 and 87.7 %, respectively. These significant changes in the molar fraction result in the variation of the total mass flow rate of the syngas with SC shown in Fig. 41.7. At SC = 2, the syngas mass flow rate reaches its maximum value, after

Table 41.6 Input parameters for the MGT-HRSG system

Parameter	Value
Micro gas turbine	
MGT isentropic efficiency	0.93
Turbine inlet temperature (K)	1,400
Heat recovery steam generator	
Pinch point temperature difference (°C)	10
Outlet steam pressure (bar)	10

Fig. 41.6 Variation of molar fractions of syngas species with steam-to-carbon ratio

which it reduces gradually. The LHV of the syngas is calculated based on the molar fraction of each species in the mixture. The trade-off between the variations of molar fractions with the SC results in the final variation of LHV and is illustrated in Fig. 41.7.

The gasification heat requirement and exergy destruction rate are affected by the steam-to-carbon ratio. Introducing more steam to the gasifier decreases the need for external heat for the gasification process. The steam acts as the gasification medium and its energy content is used by the gasification process. With more steam entering the gasifier, more energy is introduced and the required heat input decreases.

According to Fig. 41.8, increasing the gasification temperature results in an increase in the heat requirement of the gasifier. Although, the heat requirement of the gasifier varies significantly with the change in temperature, the gasification process exergy destruction rate does not seem to be affected noticeably. This is seen in Fig. 41.9, where the exergy destruction rate is observed to decrease with increasing steam-to-carbon ratio.
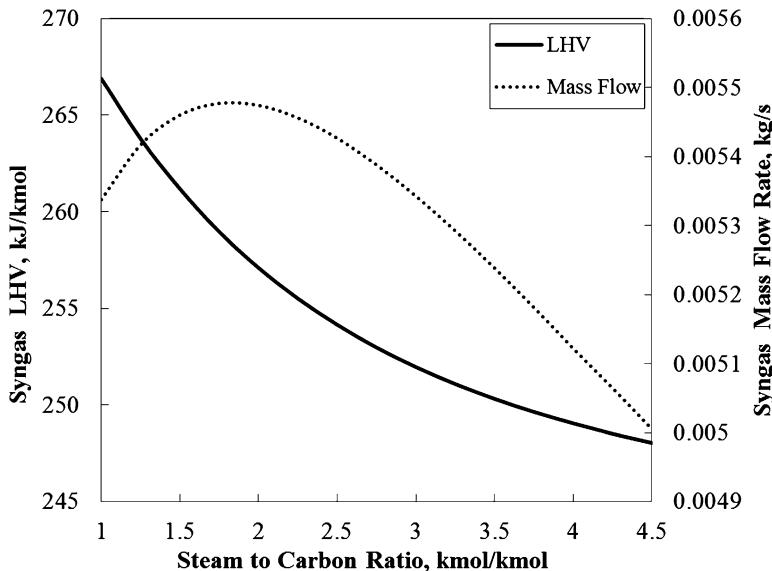
Fig. 41.7 Variation of syngas lower heating value and mass flow rate with steam-to-carbon ratio
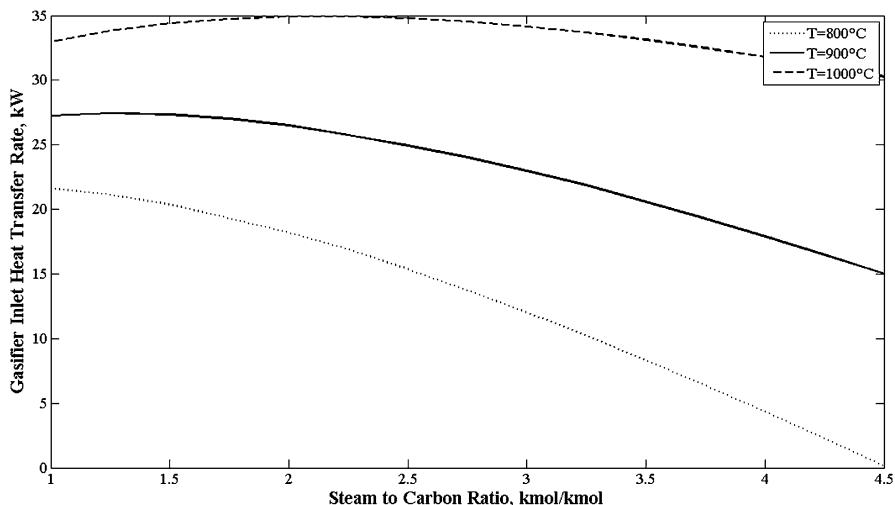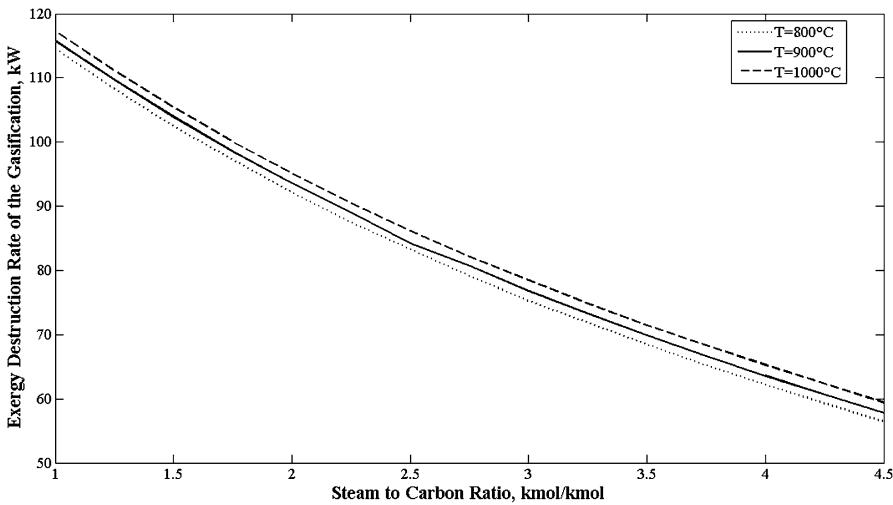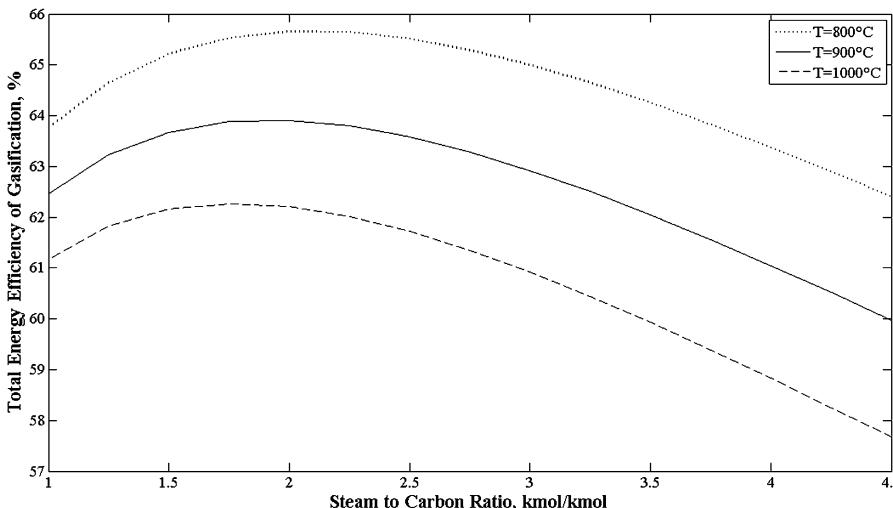
Fig. 41.8 Effect of steam-to-carbon ratio on gasifier heat requirement rate for various gasification temperatures

Energy and exergy efficiencies of biomass gasification are obtained using Eqs. 41.5 and 41.6. The variations of these efficiencies with SC and the gasifier temperature are illustrated in Figs. 41.10 and 41.11, respectively.
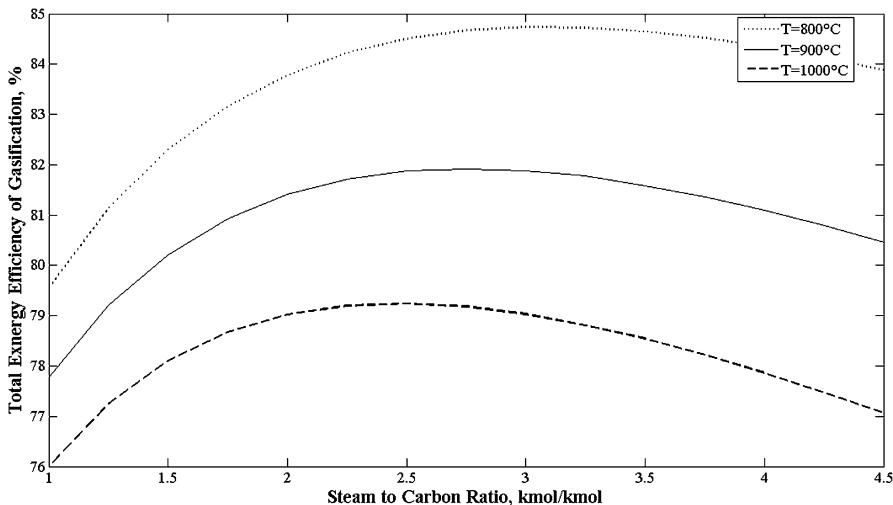
Fig. 41.9 Gasification exergy destruction rate vs. steam-to-carbon ratio for various gasifier temperatures

Fig. 41.10 Total energy efficiency of sawdust gasification vs. steam-to-carbon ratio, for various gasifier temperatures

Figure 41.6 shows that, for a gasifier temperature of 800 °C, the total energy efficiency of the gasification process reaches its maximum value of 65.6 % at SC = 2. With further increases in the temperature of the gasification medium into the gasifier, the energy efficiency drops, reaching 62.4 % for SC = 4.5. Increasing the gasification temperature reduces the total energy efficiency, as
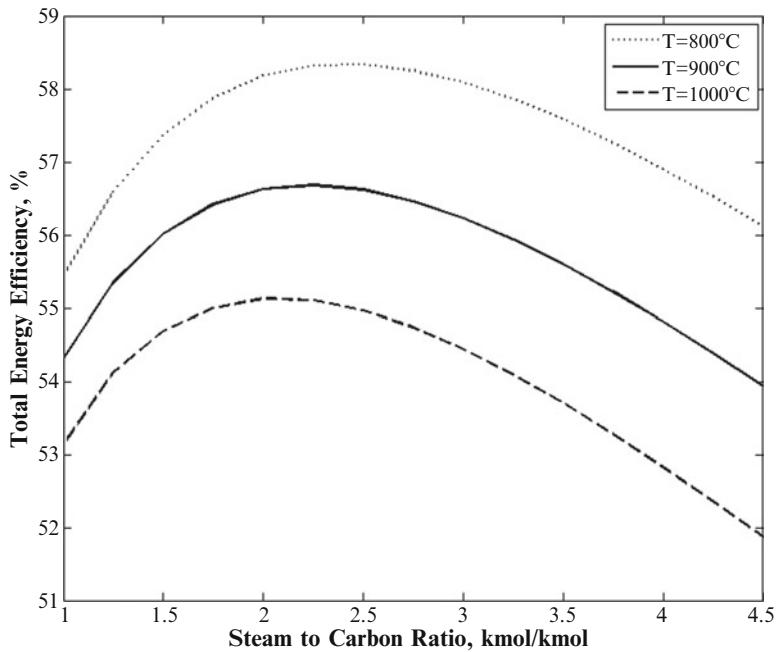
Fig. 41.11 Total exergy efficiency of sawdust gasification vs. steam-to-carbon ratio, for various gasifier temperatures

seen in Fig. 41.10. The gasification exergy efficiency exhibits a similar trend as the energy efficiency. However, the maximum value occurs at higher SC values. Higher values are achieved for efficiencies based on exergy compared to energy, because the exergy of heat is less than its energy. Since heat is an input to the gasification process, the denominator of the efficiency definition for exergy is less than that for energy.
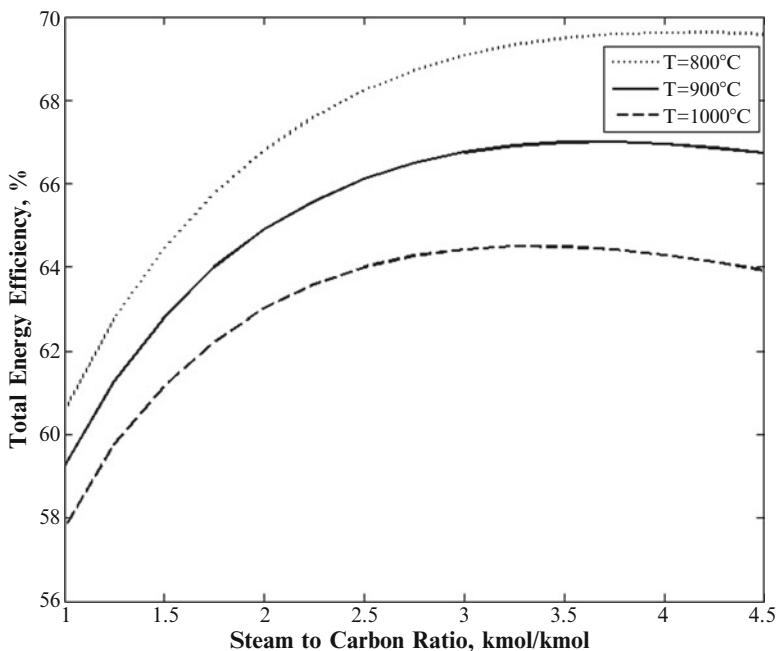
The SOFC-MGT power output varies as a result of the change in the syngas LHV, as do the total energy and exergy efficiencies of the integrated SOFC-MGT system with biomass gasification. These variations are illustrated in Figs. 41.12 and 41.13.

According to the results in Fig. 41.3, the molar fraction of both CO and CH_4 decrease with increasing steam-to-carbon ratio. These two constituents are the source of CO_2 production in the SOFC-MGT cycle. However, by introducing more steam into the gasifier, the rate of CO_2 production increases, which results in an overall increase in the CO_2 emission of the integrated SOFC-MGT cycle with biomass gasification (Fig. 41.14).
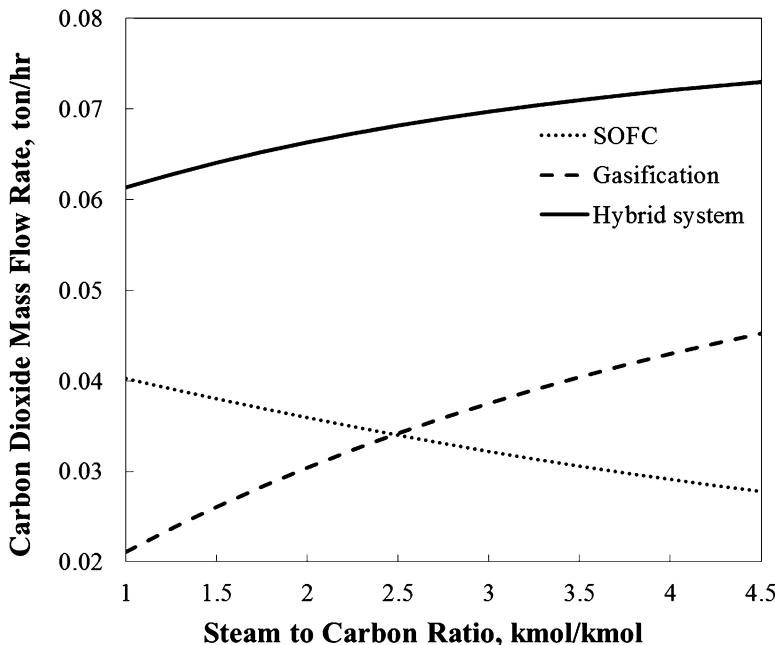
Figure 41.14 can also be interpreted based on the extent of carbon dioxide emission per unit of electricity generation. For SC = 2, the hybrid SOFC-MGT system generates 87.7 kW net electricity power. Figure 41.11 shows that the CO_2 emission is 0.065 ton/h, which corresponds to 741 g/kWh. This compares well with the CO_2 emission levels of conventional power generation plants (Table 41.2). Moreover, since the biomass can be obtained in more sustainable ways, the carbon emissions of the biomass integrated system are less than the nonrenewable-based power generation systems.

Fig. 41.12 Variation of total energy efficiency with SC for gasifier at various temperatures

Fig. 41.13 Variation of total exergy efficiency with SC for gasifier at various temperatures

Fig. 41.14 Variation of carbon dioxide emission with steam-to-carbon ratio

41.4   Brief Review of Some Renewable-Based Energy Integrated Systems

Integrated renewable-based energy systems are not limited to the two systems presented above. Other sources of renewable energy can be used to exploit their clean and sustainable characteristics. For example wind energy can be added to the systems above, especially in coastal areas where there is a continuous (but variable) wind. Geothermal heat pumps are able to supply a portion (albeit small) of the thermal demand of a house or a district. Alternatively, they can be used to preheat the heating medium to reduce fuel consumption and GHG emissions. Syed et al. [23] studied the effect of an integrated, residential solar PV-wind turbine system on energy conservation and decreasing GHG emissions. They considered the use of PV and wind power in supplying a part of electricity demand of some Canadian houses. Depending on house type and location, hot water and space heating may be provided by electric heating or a natural gas furnace. The integrated renewable energy system is capable of generating a great portion of the house's electricity demand, which leads to a significant decrease in the GHG reduction. Syed et al. [23] reported that the national Canadian GHG reduction can be decreased by 4.1–12.7 Mton/year. Thus, this approach in which a Canadian house

is equipped with such a technology can be a significant step toward achieving sustainability in Canada, in terms of environmental stewardship.
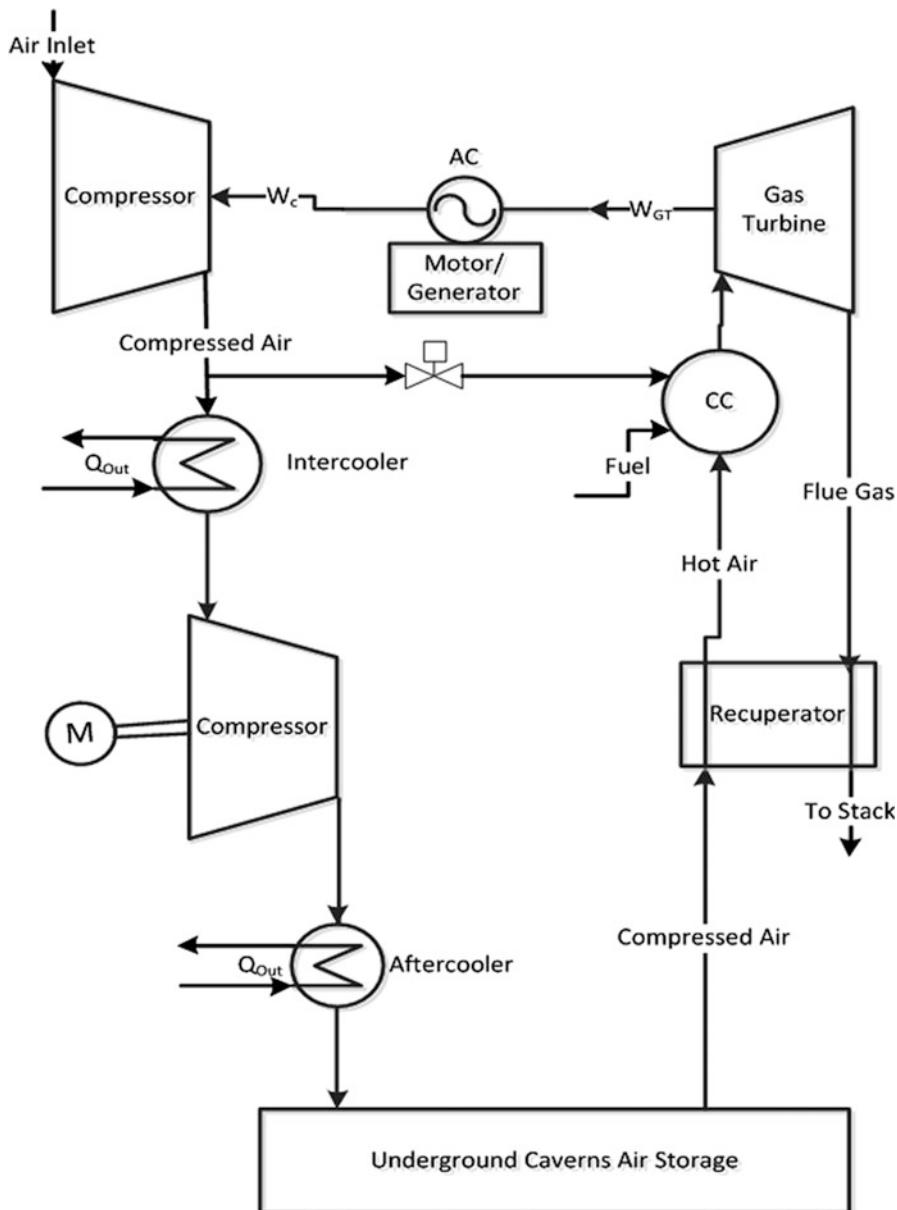
In another example of IRESs, Calderon et al. [24] analyzed the components of an actual test-bed hybrid photovoltaic-wind system with hydrogen storage, in terms of energy and exergy. The test-bed is installed in the School of Industrial Engineering at the University of Extremadura, Spain. The system component irreversibility rates and exergy efficiencies are reported. The exergy efficiencies are as follows: electrolyzer: 68 %, photovoltaic module: 8.39 %, and fuel cell: 35.9 %. The authors concluded that designing more efficient PV modules can increase the utilization of the solar renewable energy, leading to less GHG emissions, when electricity is generated by solar and wind rather than fossil fuels.

The intermittency behavior of renewable energy resources can be addressed in part by energy storage. Greenblatt et al. [25] investigated the competition between gas turbines and compressed air energy storage (CAES) systems for integration with a base-load wind turbine.

They aim to explore the economic feasibility of using gas turbines to avoid problems associated with the intermittency of wind energy. In one strategy they suggest the integration of the wind turbine(s) with a gas turbine cycle. The gas turbine covers the load during periods when wind energy cannot meet the demand. Energy storage is another strategy to be integrated with the wind turbine(s). Since CAES is economically viable in terms of large-capacity storage of energy, Greenblatt et al. suggest its integration with wind energy systems. The wind power output is fed to an electric motor, which is connected to the air compressor of the CAES system (see Fig. 41.15).
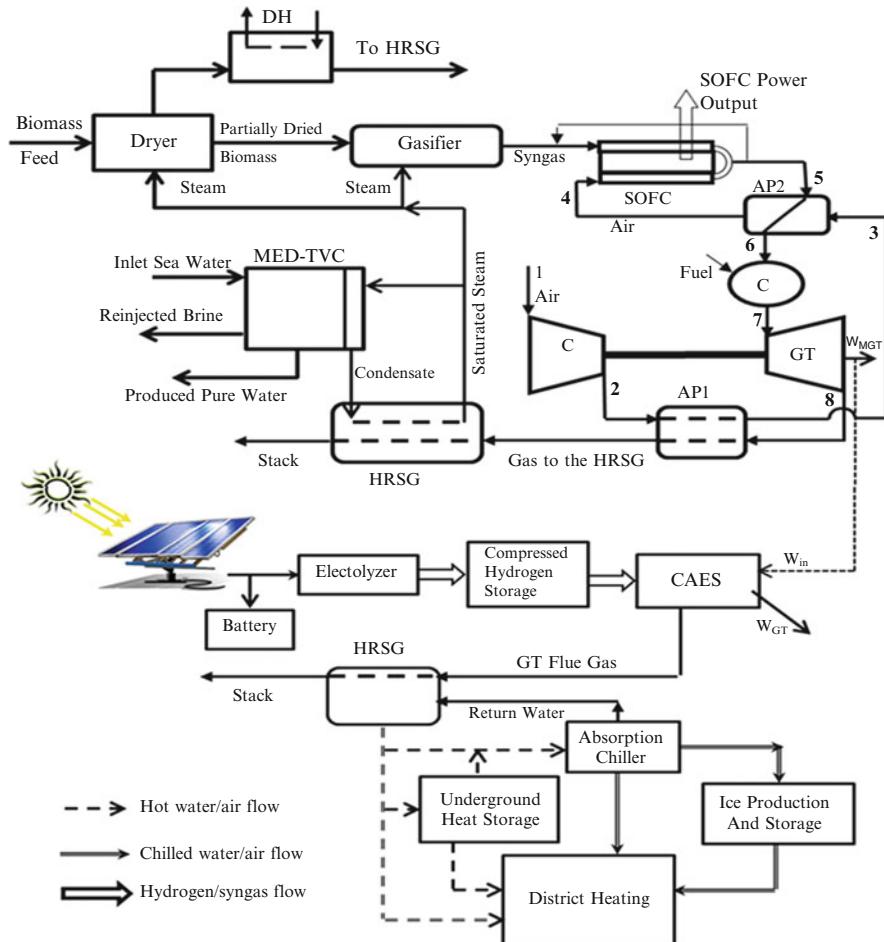
The DC power generated by the wind turbines is consumed by the electric motor that is connected to the air compressor, which compresses ambient air to an intermediate pressure. Medium-pressure, high-temperature air releases its heat to a coolant in the intercooler and undergoes another compression process in the booster compressor. The work input to the booster compressor is provided by the wind turbines or by the power grid. High-temperature, compressed air releases its thermal energy to a cooling medium in the aftercooler and is stored in underground caverns. Whenever high-quality electricity is required by the power grid, the high-pressure stored air is extracted from the CAES system, and fed to the combustion chamber (CC) of the gas turbine, in which compressed air is heated by the combustion of natural gas or syngas.

According to Calderon et al. [24] the estimated electrical round-trip efficiency would be in the range of 77–89 %. They also estimate the cost of electricity (COE) for different systems and the effect of the natural gas price. The optimal COE using the wind-CAES system is 6.5 ¢/kWh for case in which the natural gas price is $9.0/ GJ. For lesser prices of natural gas, combined cycle power plants exhibit the minimum cost of electricity generated. However, the primary advantage of the renewable wind-CAES system is the reduction in GHG emissions. With only 32 g/ kWh CO_2 emissions, the wind-CAES system emits one-fourth of the emissions from a natural gas combined power plants.

Fig. 41.15 Simplified schematic of compressed air energy storage system with its components

The SOFC-MGT cycle integrated with biomass gasification shown in Fig. 41.5 can take advantage of integration with other renewable energy resources and heat recovery technologies. There is a great need for drinking water in coastal areas, since most of these areas suffer from potable water shortages. Thermal desalination units can provide communities with healthy water, at reasonable prices. The energy

Fig. 41.16 Hybrid SOFC-micro gas turbine system with thermal desalination and energy storage options for coastal areas

requirement of thermal desalination systems can be met with any kind of available heat, e.g., waste heat from gas turbine exhaust gas. Hosseini et al. [21] proposed an integrated system containing a hybrid SOFC-MGT and a multi-effect desalination (MED) system. Along with power generation by the hybrid system, waste heat recovery from a micro gas turbine gives the opportunity to produce potable water.

In Fig. 41.16a schematic of the integrated system is shown [26]. To implement renewable energy resources, the integrated system is joined with a biomass gasification plant and a solar PV system. Energy storage options are included in the systems to enhance efficiency and power and heat reliability. The MGT flue gas (Point 8) is used to preheat the SOFC inlet air (AP1), and to produce saturated steam in the HRSG. The HRSG outlet steam enters the MED system in order to provide heat for pure water production, and to provide the gasification plant with the

required steam. During off-peak hours, the power output of the micro gas turbine is fed to the CAES system. While the gas turbine of the CAES system is in operation, it consumes the produced hydrogen in the solar PV-electrolyzer system as fuel. The gas turbine flue gas is fed to a heat recovery unit for enhanced energy utilization. The integrated system presented in Fig. 41.16 can supply a coastal area with electricity, drinking water, and thermal energy with the use of renewable energy resources. The development and implementation of such systems can reduce GHG emissions significantly.

41.5 Conclusions

Integrated renewable-based energy systems are developed with the purpose of reducing GHG emissions and mitigating global warming, and the role of IRESs in decreasing GHG emissions is reviewed here. Various types of renewable energy resources can be integrated in a system to provide the thermal and electrical energy of a house, a residential area, or a community. Also, the possibilities of implementation of these systems in residential and coastal areas are discussed by providing the results of energy and exergy analyses of two integrated systems, which utilize solar and biomass as the main sources of energy. The systems are compared with conventional power generation methods in terms of GHG emissions, demonstrating that the hybrid PV-FC system has zero carbon dioxide emissions during its operation while the integrated biomass-SOFC-MGT system emits less CO_2 than a fossil power plant. The integrated system configurations depend on the energy source and the demand profiles. Although these systems are not economically available today, several cases of their implementation are reported. Moreover, results of modeling and analyses of IRESs are presented in literature.

References

1. Boden TA, Marland G, Andres RJ (2010) Global, regional, and national fossil-fuel CO2 emissions. Carbon Dioxide Information Analysis Center, Oak Ridge National Laboratory, U.S. Department of Energy, Oak Ridge, TN, USA. doi:10.3334/CDIAC/00001_V2010
2. LeMar P (2002) Integrated energy systems (IES) for buildings: a market assessment. September 2002, Prepared by Resource Dynamics Corporation, Contract No. DE-AC05-00OR22725
3. Hosseini M, Rosen MA, Dincer I (2011) Hybrid solar-fuel cell CHP systems for residential applications. In: World engineering convention, Geneva, 4–9 Sept 2011
4. Hosseini M, Dincer I, Rosen MA (2013) Hybrid solar-fuel cell CHP systems for residential applications: energy and exergy analyses. J Power Sources 221:372–380
5. Hosseini M, Dincer I, Rosen MA (2012) Steam and air fed biomass gasification: comparisons based on energy and exergy. Int J Hydrogen Energy 37:16446–16452
6. Hosseini M, Dincer I, Rosen MA (2012) Thermodynamic analysis of a cycle integrating a solid oxide fuel cell and micro gas turbine with biomass gasification. 11th International conference on sustainable energy technologies (SET 2012), Vancouver, Canada, 2–5 Sept 2012

7. Hosseini M, Dincer I, Naterer GF, Rosen MA (2012) Thermodynamic analysis of filling compressed gaseous hydrogen storage tanks. Int J Hydrogen Energy 37:5063–5071
8. Gibson TL, Kelly NA (2008) Optimization of solar powered hydrogen production using photovoltaic electrolysis devices. Int J Hydrogen Energy 33:5931–5940
9. Largose J, Simoe MG, Miraoui A, Costerg P (2008) Energy cost analysis of a solar-hydrogen hybrid energy system for stand-aloneapplications. Int J Hydrogen Energy 33:2871–2879
10. Pregger T, Graf D, Krewitt W, Sattler C, Roeb M (2009) Prospects of solar thermal hydrogen production processes. Int J Hydrogen Energy 34:4256–4267
11. Hosseini M, Ziabasharhagh M (2010) Energy and exergy analysis of a residential SOFC-GT/absorption chiller system. Proc. ECOS 2010, 14–17 June, Lausanne, 5:411–418
12. Akkaya AV, Sahin B, Erdem HH (2008) An analysis of SOFC/GT CHP system based on exergetic performance criteria. Int J Hydrogen Energy 33:2566–2577
13. Hawkes AD, Aguiar P, Croxford B, Leach MA, Adjiman CS, Brandon NP (2007) Solid oxide fuel cell micro combined heat and power system operating strategy: options for provision of residential space and water heating. J Power Sources 164:260–271
14. Velumani S, Guzman CE, Peniche R, Vega R (2009) Proposal of a hybrid CHP system: SOFC/microturbine/absorption chiller. Int J Energy Research 34:1088–1095
15. Hartkopf VH, Archer D, Brahme R, Yin H (2003) A fuel cell based energy supply system for a multi-purpose building. 14th National conference of the Facility Management Association of Australia limited (FMA Australia), Sydney, 7–9 May, 2003
16. Paepe MD, Dherdt P, Mertens D (2006) Micro-CHP systems for residential applications. Energy Conversion and Management 47:3435–3446
17. Cohce MK, Dincer I, Rosen MA (2010) Thermodynamic analysis of hydrogen production from biomass gasification. Int J Hydrogen Energy 35:4970–4980
18. Abuadala A, Dincer I, Naterer GF (2010) Exergy analysis of hydrogen production from biomass gasification. Int J Hydrogen Energy 35:4981–4990
19. Basu P (2010) Design of biomass gasifiers. In: Biomass gasification and pyrolysis. Elsevier, Kidlington
20. Abudala A, Dincer I (2012) A review on biomass-based hydrogen production and potential applications. Int J Energy Res. doi:10.1002/er.1939
21. Hosseini M, Dincer I, Avval HB, Ahmadi P, Ziabasharhagh M (2011) Thermodynamic analysis of SOFC-MGT systems for desalination purposes. Int J Energy Res. doi:10.1002/er.1945
22. Colpan CO, Dincer I, Hamdullahpur F (2007) Thermodynamic modeling of direct internal reforming solid oxide fuel cells operating with syngas. Int J Hydrogen Energy 32:787–795
23. Syed AM, Fung AS, Ugursal VI, Taherian H (2009) Analysis of PV/wind potential in the Canadian residential sector, through high-resolution building energy simulation. Int J Energy Res 33:342–357
24. Calderon M, Calderon AJ, Ramiro A, Gonzalez JF, Gonzalez I (2011) Evaluation of a hybrid photovoltaic-wind system with hydrogen storage performance using exergy analysis. Int J Hydrogen Energy 36:5751–5762
25. Greenblatt JB, Succar S, Denkenberger DC, Williams RH, Socolow RH (2007) Baseload wind energy: modeling the competition between gas turbines and compressed air energy storage for supplemental generation. Energy Policy 35:1474–1492
26. Hosseini M, Dincer I, Rosen MA (2011) Investigation of energy storage options for sustainable energy systems, PhD candidacy exam report, University of Ontario Institute of Technology

Chapter 42
Exergetic and Environmental Impact Assessment of an Integrated System for Utilization of Excess Power from Thermal Power Plant

Tahir A.H. Ratlamwala, Ibrahim Dincer, and Bale V. Reddy

Abstract In this chapter, we propose an integrated system with electrolyzer, proton exchange membrane fuel cell and quadruple-effect absorption refrigeration system for power and cooling productions from the excess power produced by power plant. A parametric study is undertaken, and the effects of some operating parameters such as excess power, current density, and condenser load are investigated. It is found that increase in excess power results in higher power output but lower rate of cooling production. It is also found that increasing excess power decreases the overall energetic and exergetic utilization factors of the system and has negative effect on the environment.

Keywords Electrolyzer • Proton exchange membrane fuel cell • Exergy • Energy • Environmental impact • Efficiency • Excess power • Thermal power plant • Quadruple-effect absorption refrigeration system • Current density • Condenser load • Cooling • Energetic utilization factor • Exergetic utilization factor

Nomenclature

COP	Coefficient of performance
$\dot{En}$	Energy rate, kW
$\dot{Ex}$	Exergy rate, kW
$\dot{m}$	Mass flow rate, kg s^{-1}
$\dot{Q}$	Heat transfer rate, kW

T.A.H. Ratlamwala (✉) • I. Dincer • B.V. Reddy
Faculty of Engineering and Applied Science, University of Ontario Institute of Technology, 2000 Simcoe Street North, Oshawa, ON L1H 7K4, Canada
e-mail: tahir.ratlamwala@uoit.ca; Ibrahim.dincer@uoit.ca; bale.reddy@uoit.ca

T	Temperature, K
$\dot{W}$	Work rate, kW

Greek Letters

η	Efficiency
ε	Overall utilization factor
β	Constant

Subscripts

abs	Absorption system
A	Anode
C	Cathode
CHX	Condenser heat exchanger
con	Condenser
FC	Fuel cell
en	Energy
ex	Exergy
eva	Evaporator
H_2	Hydrogen
H_2O	Water
HTG	High-temperature generator
HHX	High-temperature heat exchanger
LHX	Low-temperature heat exchanger
LTG	Low-temperature generator
MTG	Medium-temperature generator
MHX	Medium-temperature heat exchanger
O	Oxygen
p	Pump
PP	Power plant
x	Concentration of ammonia–water
1...41	State numbers of
0	Ambient or reference condition

Acronyms

QEAS	Quadruple-effect absorption refrigeration system
PEMFC	Proton exchange membrane fuel cell
VHTG	Very-high-temperature generator
VHHX	Very-high-temperature heat exchanger

42.1 Introduction

Renewable energy is considered a key option for meeting future energy demands in a sustainable and environment-friendly manner. Due to ever-increasing levels of emission of greenhouse gases, countries and researchers around the world are looking forward to renewable energy-based systems. The excess energy produced by most of the power plants is dumped to the environment which adds to the problem of global warming.

Most of the power plants around the globe are not equipped with energy storage systems. The excess power produced by power plants during off-peak hours is not stored and is dumped into the environment. Storing this power and using it for peak hours can prove beneficial from both economics and environment point of view. Researchers are working to come up with the systems which can store this excess power in an environment-friendly manner. Some of the energy storage systems which are currently being researched on are pumped hydro and compressed air energy storage. These two systems are also being put to practical applications in very few power plants [1–3]. The benefit of these systems is that they can store huge power but the disbenefit is that they both are harmful to environment. For pumped hydro system huge land needs to be converted to the storage dam for water storage. For compressed air technology, the air compressed needs to be stored under high pressure inside the ground, hence affecting the composition under the ground.

Many researchers investigate the ways of improving the performance of the power plants. Peterson [4] introduced an idea of using heat pump and heat engine to store excess power from the grid as a latent heat. In this system, the storage process utilizes a boiling refrigerant at sub-ambient temperatures to freeze a latent heat storage material using electrically driven compressors. For recovering of the latent heat for electrical generation, vapor expansion and condensation processes are used which essentially reverses the storage process. Pandiyarajan et al. [5] conducted second-law analysis of diesel engine waste heat recovery systems and found out that recovering waste heat makes system more efficient and also increases the production capacity of the plant. Bal et al. [6] did the review of solar dryers with latent and sensible heat storage systems and found attractive results. Now the interest is shifting towards using hydrogen as the storage medium and energy carrier. As it is predicted by many researchers [7–10] that in future hydrogen will emerge as an energy carrier, it is important to study hydrogen as a power storage medium.
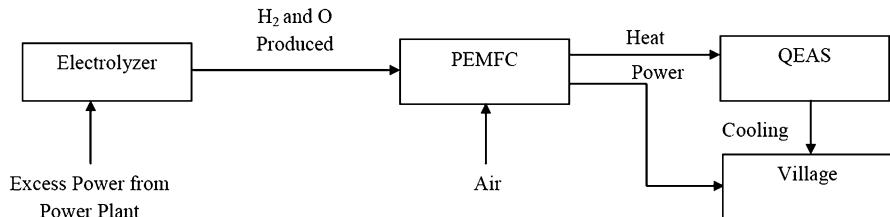
The common method of producing hydrogen using power is the water electrolyzer technology. Water electrolyzer technology is very well developed and has reached a mature level for separation of water molecule into hydrogen and oxygen molecule. In this system we use electrolyzer to produce hydrogen. The hydrogen produced is later used in proton exchange membrane fuel cell (PEMFC) to produce power and heat. Hydrogen as a fuel holds in itself all the capabilities of working as an alternative fuel which is environmentally friendly and sustainable at the same time. Hydrogen is expected to play a key role in the near future as an

energy carrier for sustainable development [11–14]. The use of hydrogen as an energy provider by using fuel cell holds a great potential due to higher efficiency, and eco-friendliness. Also, use of hydrogen as a fuel makes the energy generation process eco-friendly, because the by-product of this process is water. The use of hydrogen in fuel cells to generate electricity is efficient and clean with water as the only by-product [12, 13]. In the future, the role of hydrogen may become more important, as some researchers suggest that the world's energy systems may undergo a transition to an era in which the main energy carriers will be hydrogen [14–16]. All these benefits associated with PEMFC make it an attractive solution to the energy and environment crisis. These benefits also make it a good contender for the combined power and cooling production systems.
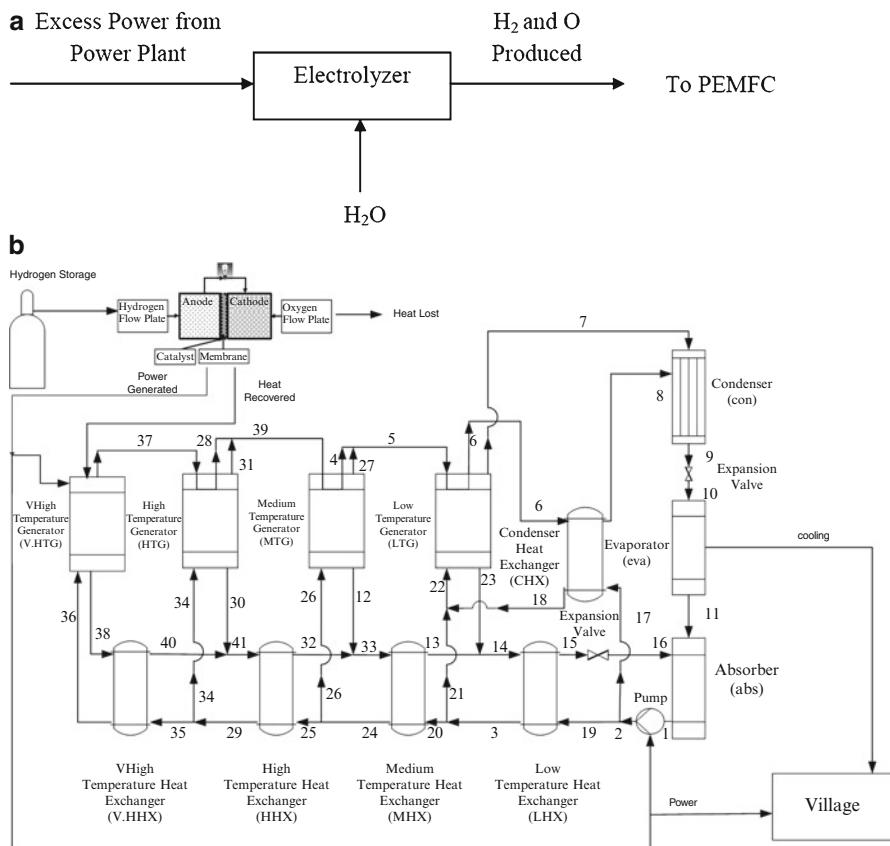
The heat produced by the PEMFC can be used as energy input to the absorption system to produce cooling instead of dumping it to the environment. Use of heat produced by PEMFC for further processes makes system more efficient and environmentally benign. In this chapter, we use heat generated by PEMFC for cooling production by using quadruple-effect absorption refrigeration system (QEAS). Absorption refrigeration systems appear to be a key solution to meet the cooling and heating requirement in an energy-efficient and eco-friendly way [16]. The major benefit of absorption system is that it requires no compressor to provide cooling; instead it works on low-grade energy such as heat generated by PEMFC. Most amount of work is being done on single- and double-effect absorption systems by researchers [17–23]. Several researchers [24–27] have undertaken studies to investigate the triple-effect absorption systems. Very few researchers such as Grossman and Zaltash [28] have studied QEAS using LiBr/H$_2$O solution using simulation software. So far, no researcher has studied QEAS using ammonia–water pair for cooling purposes through energy and exergy analyses. In this chapter, a comprehensive energy and exergy analysis of an integrated system, consisting of electrolyzer, PEMFC, and QEAS for power and cooling production is carried out. Its performance is extensively studied by various individual and integrated performance measuring criteria, namely, energetic and exergetic utilization factors, energetic and exergetic COPs, energy and exergy efficiency of the fuel cell, and amount of power and cooling produced. These performance measures are then compared for better illustration of the system for practical applications.

42.2   System Description

In this chapter, we study an integrated system which uses the excess power produced by power plant to provide power and cooling as shown in Fig. 42.1. The excess power produced by power plant is used to run electrolyzer as illustrated in Fig. 42.2a. In electrolyzer chemical bond of water molecule is broken by providing energy to produce hydrogen and oxygen. Hydrogen and oxygen produced by the electrolyzer are used to fuel PEMFC. In PEMFC hydrogen enters the cell from the anode side where it comes in contact with membrane electrode assembly (MEA). MEA is made

Fig. 42.1 Schematic of overall system

Fig. 42.2 (**a**) Schematic of electrolyzer. (**b**) Schematic of PEMFC integrated with QEAS

of nafion membrane and carbon cloth. MEA acts as a porous medium which only allows protons to pass through. Protons of hydrogen pass through to the cathode side while electrons go through the circuit to provide power before entering cathode plate. Oxygen is supplied to the cathode plate where it combines with protons and electrons of hydrogen to produce water as by-product. The schematic of PEMFC is shown in Fig. 42.2b. The power produced by PEMFC is used to supply power to the

pump of absorption system and to the village. The heat produced by the PEMFC is fed into the very-high-temperature generator (VHTG) of QEAS to produce cooling. In the VHTG strong solution coming from absorber at state 36 is being heated to leave the VHTG as a weak solution at state 38 and an ammonia–water vapor with high concentration at state 37 as shown in Fig. 42.2b. Weak solution coming out of the VHTG at state 38 then releases heat in the very-high-temperature heat exchanger (VHHX) and is combined with weak solution coming from the high-temperature generator (HTG) at state 30 to leave at state 41 as a weak solution. This weak solution from state 41 then gives out heat in high-temperature heat exchanger (HHX) and is combined with weak solution leaving the medium-temperature generator (MTG) at state 12 to leave at state 33. This weak solution at state 33 then gives out heat in the medium-temperature heat exchanger (MHX) and is combined with weak solution from state 23 to leave at state 14. This weak solution then enters the low-temperature heat exchanger (LHX) where it heats the strong solution coming from the solution pump at state 19. After losing heat, weak solution at state 15 enters the expansion valve where the pressure and temperature drop and the solution enters the absorber at state 16. The refrigerant vapor leaving the VHTG at state 37 then enters the HTG where it heats up the strong solution coming from the HHX at state 34 and leaves as ammonia–water vapor at state 28 and state 31. These two streams are combined and leave at state 39 to enter the MTG where it heats up the strong solution coming from the MHX at state 26 and leaves as ammonia–water vapor at state 4 and state 27. These two ammonia–water vapors are then combined and leave at state 5. Ammonia–water vapor at state 5 then enters the low-temperature generator (LTG), heats up the strong solution coming from state 22, and leaves as ammonia–water vapor at state 6 and state 7. State 7 goes directly into the condenser while state 6 is directed to the condenser heat exchanger (CHX) to lose heat to part of the liquid that is fed backward by the solution pump at state 17. That liquid gains heat and leaves the condenser at state 18. Ammonia–water vapor leaving CHX at state 8 enters the condenser (con) where it gives out heat and then leaves the condenser at state 9. This stream then passes through the expansion valve and leaves at state 10 to enter the evaporator (eva). In the evaporator, heat is being gained by the system and the heated mixture leaves at stat 11 to enter the absorber (abs). In the absorber all three streams mix together and release heat to leave at state 1 in liquid form to enter the pump. The cooling is provided by passing air through the evaporator of QEAS.

42.3   Energy and Exergy Analyses

In order to analyze the integrated system, mass, energy, and exergy balance equations are applied for the PEMFC and components of QEAS. Also, equations to calculate efficiency of the PEMFC, COPs of QEAS, and overall utilization factors are developed. All systems are assumed to be running under thermodynamic equilibrium and steady-state conditions. The heat losses and pressure drops in heat

exchangers and connecting piping system are considered negligible. The concentrations of strong and weak solution of ammonia–water vapor, condenser load, and evaporator temperature are assumed.

42.3.1 Electrolyzer

The amount of hydrogen produced by electrolyzer is calculated using

$$\eta_{electrolyzer} = \frac{\dot{m}_{H_2} \times HHV}{\dot{W}_{pp}} \tag{42.1}$$

where $\eta_{electrolyzer}$ is the efficiency of the electrolyzer which is assumed to be 56 % based on industrial standards. $\dot{m}_{H_2}$ is the mass flow rate of hydrogen, HHV is the higher heating value of hydrogen, and $\dot{W}_{pp}$ is the excess power produced by the power plant.

42.3.2 PEMFC

The power output per unit specific area of the fuel cell is given by

$$\dot{W}_{FC} = i \times [V_{rev} - v_{act} - v_{ohm} - v_{conc}] \tag{42.2}$$

where the reversible voltage is

$$V_{rev} = 1.229 - 8.5 \times 10^{-4}(T_{FC} - 298.15) + 4.3085 \times 10^{-5}$$
$$\times T_{FC} \left[\ln(p_{H_2}) + \frac{1}{2} \ln(p_{O_2}) \right]$$

The activation voltage at anode and cathode are given as

$$v_{act_{Anode}} = \frac{RT_{FC}}{\alpha_A nF} \ln\left(\frac{i}{i_o}\right) \tag{42.3a}$$

$$v_{act_{cathode}} = \frac{RT_{FC}}{\alpha_C nF} \ln\left(\frac{i}{i_o}\right) \tag{42.3b}$$

The ohmic voltage is

$$v_{ohmic} = iR_{ohmic} \tag{42.4}$$

where

$$R_{ohmic} = \frac{t_{mem}}{\sigma_{mem}}$$

$$\sigma_{mem} = (0.005139\lambda_{mem} - 0.00326) \exp\left[1268\left(\frac{1}{303} - \frac{1}{T_{FC}}\right)\right]$$

The membrane water content is calculated by

$$\lambda_{mem} = 0.043 + 17.81\, a_l - 39.85\, a_l^2 - 39.85\, a_l^3$$

where a_l represents water activity in the membrane and is expressed as follows:

$$a_l = x_{H,2,O}\left(\frac{P}{P_{sat}}\right)$$

The concentration overvoltage is defined as

$$v_{conc} = i\left(\beta_1 \frac{i}{i_{max}}\right) \tag{42.5}$$

The heat output of the cell which is fed into the HTG is calculated based on exergy balance and is given by

$$\dot{Q}_{FC} = \left\{ T_0\left[\sum (\dot{m} \times s)_{out} - \sum (\dot{m} \times s)_{in}\right] + \dot{W}_{FC} + (\dot{m} \times ex)_{H_2 out} \right.$$
$$\left. + (\dot{m} \times ex)_{H_2O,out} - (\dot{m} \times ex)_{H_2 in} - (\dot{m} \times ex)_{O_2 in} \right\}$$
$$\times \left(r_{HL} + (1 - r_{HL})\frac{T_0}{T_{FC}}\right)^{-1} \tag{42.6}$$

The energy and exergy efficiency of PEMFC are defined as

$$\eta_{FC,en} = 0.95 \times \frac{\dot{W}_{FC}}{i \times 1.25} \tag{42.7}$$

where 1.25 V represents the electromotive force relative to the lower heating value of hydrogen and 0.95 is the fuel utilization coefficient. This coefficient represents the ratio of the mass of fuel reacted in cell to the mass of fuel input to the cell. Therefore, Eq. (42.7) is derived for the lower heating value of hydrogen and can be found in literature [29]:

$$\eta_{FC,ex} = \frac{\dot{W}_{FC} + \dot{E}x_{th}}{\dot{E}x_{H_2}} \tag{42.8}$$

where

$$\dot{Ex}_{th} = \left(1 - \frac{T_o}{T_{FC}}\right)\dot{Q}_{FC} \text{ and}$$

$$\dot{Ex}_{H_2} = \dot{m}_{H_2}(ex^{PH} + ex^{CH})$$

Details on energy and exergy models of PEMFC can be found in the study done by Ratlamwala et al. [27].

42.3.3   QEAS Unit

The rate of heat to the VHTG of an absorption system is provided using geothermal water source and is calculated using

$$\dot{Q}_{VHTG} = \dot{Q}_{FC} \tag{42.9}$$

The mass balance equations for the ammonia–water mixture of VHTG are given as follows:

$$\dot{m}_{36}\, x_{36} = \dot{m}_{37}\, x_{37} + \dot{m}_{38}\, x_{38} \tag{42.10}$$

$$\dot{m}_{36} = \dot{m}_{37} + \dot{m}_{38} \tag{42.11}$$

In order to obtain the outlet conditions of the VHTG, the following equation is used:

$$\dot{m}_{36}\, h_{36} + \dot{Q}_{VHTG} = \dot{m}_{37}\, h_{37} + \dot{m}_{38}\, h_{38} \tag{42.12}$$

The exergy destruction in VHTG becomes

$$\dot{Ex}_{VHTG} = \dot{Ex}_{36} - \dot{Ex}_{38} - \dot{Ex}_{37} \tag{42.13}$$

where

$$\dot{Ex}_{37} = \dot{m}_{37}((h_{37} - h_0) - T_0(s_{37} - s_0)) \tag{42.14}$$

and the same relationship is employed for other states.
    The energy balance equation of evaporator is given below:

$$\dot{m}_{10}\, h_{10} + \dot{Q}_{eva} = \dot{m}_{11}\, h_{11} \tag{42.15}$$

The work done by the pump is calculated using the equation given below:

$$\dot{W}_p = \dot{m}_1(h_2 - h_1) \tag{42.16}$$

The energetic and exergetic COPs are found by

$$COP_{en} = \frac{\dot{Q}_{eva}}{\dot{Q}_{VHTG} + \dot{W}_P} \tag{42.17}$$

$$COP_{ex} = \frac{\dot{Ex}_{eva}}{\dot{Ex}_{VHTG} + \dot{W}_P} \tag{42.18}$$

where $\dot{Ex}_{eva}$ and $\dot{Ex}_{VHTG}$ are calculated on the same principle as that of $\dot{Ex}_{th}$ given in Eq. (42.8).

The overall energy and exergy utilization factors are calculated using

$$\varepsilon_{en} = \frac{\dot{Q}_{eva} + \dot{W}_{village}}{\dot{W}_{pp}} \tag{42.19}$$

$$\varepsilon_{ex} = \frac{\dot{Ex}_{eva} + \dot{W}_{village}}{\dot{W}_{pp}} \tag{42.20}$$

where $\dot{W}_{village}$ is the power supplied to village and is calculated by

$$\dot{W}_{village} = \dot{W}_{FC} - \dot{W}_p$$

The environmental impact factor is the positive effect of the system on exergy-based sustainability. By positive effect we mean to supply more desired exergy output, decrease the irreversibilities, and minimize the waste exergy outputs during the system operation. The reference value for this factor should be "zero" for better exergy-based sustainability and is defined as

$$f_{ei} = \frac{\dot{Ex}_{des,tot}}{\dot{W}_{pp}} \tag{42.21}$$

The environmental impact coefficient is related to the exergetic efficiency of the system. In ideal case its value should be one indicating that the system is working under ideal condition with no exergy destruction. This coefficient is defined as

$$C_{ei} = \frac{1}{\varepsilon_{ex}} \tag{42.22}$$

The environmental impact index is an important parameter to indicate whether or not the system damages the environment due to its unusable waste exergy output and exergy destruction. The smaller the value the better the system performance is. It is defined as

$$\theta_{ei} = f_{ei} \times C_{ei} \tag{42.23}$$

Environmental impact improvement indicates the environmental appropriateness of the system. In order to improve the environmental appropriateness of the system, its environmental impact index should be minimized to be closer to the best reference value. The higher value of environmental impact improvement means system is more useful for the environment and it is defined as

$$\theta_{eii} = \frac{1}{\theta_{ei}} \tag{42.24}$$

The exergetic stability factor is a function of the desired output, exergy destruction, and exergies by unused fuel. In this study it is assumed that all the fuel is utilized in the system. The best value of this factor should be close to "one." This factor is defined as

$$f_{es} = \frac{\dot{Ex}_{tot,out}}{\dot{Ex}_{tot,out} + \dot{Ex}_{des,tot}} \tag{42.25}$$
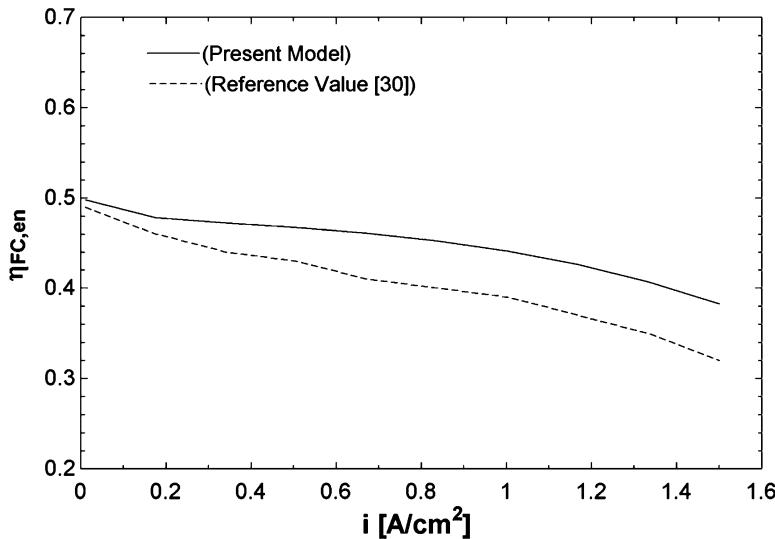
The exergetic sustainability index is defined as multiplication of environmental impact improvement index and exergetic stability factor of the system. The higher value of this index means better is the performance of the system from exergetic sustainability perspective. This index is defined as

$$\theta_{est} = f_{es} \times \theta_{eii} \tag{42.26}$$

The exergetic environmental impact assessment model is adapted from [15].

42.4   Results and Discussion

Due to such an unexpected hike in fossil fuel prices and emission of greenhouse gasses, it has become prominent to design energy systems that are eco-friendly, cost effective, and sustainable in order to serve the environment and the struggling economies throughout the world. In this chapter, we study an integrated electrolyzer, PEMFC, and QEAS system for provision of hydrogen, cooling, and power in a manner which can serve thermal energy storage. The power input to electrolyzer and PEMFC current density are varied in order to investigate their
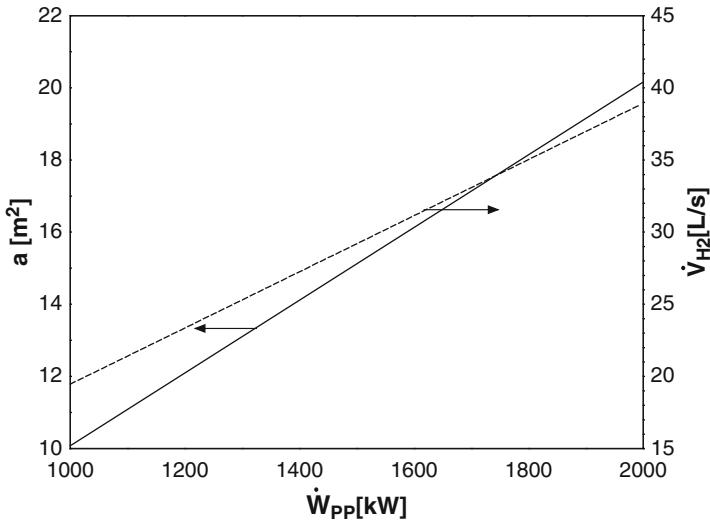
Fig. 42.3 Validation of PEMFC model with study conducted by Mert et al. [30]
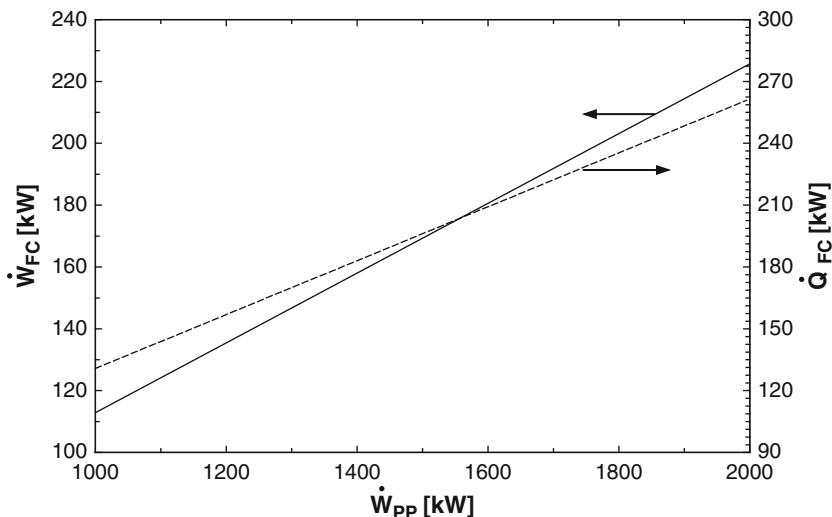
effects on the production of hydrogen, cooling, power, area of PEMFC, energetic and exergetic COPs, energetic and exergetic efficiencies of PEMFC, and overall energetic and exergetic utilization factors. In order to make sure that the system developed is working properly, model validation is carried out. The PEM fuel cell model is compared with the study done earlier by Mert et al. [30]. This comparison can be seen in Fig. 42.3. It is found that the efficiency distribution behaves in a similar manner when current density is increased with little difference in the values. This confirms the accuracy of the present model and encourages proceeding with the analysis.

42.4.1 *Effect of Excess Power Available from Power Plant*

Figure 42.4 shows how the area of PEMFC and amount of hydrogen produced vary with increase in the power input to the electrolyzer. Both the area of PEMFC and hydrogen produced are found to be varying from 10 to 20 m^2 and 19.5 to 38.9 L/s, respectively, with increase in input power from 1,000 to 2,000 kW. These results are obtained because as more power is supplied to the electrolyzer more hydrogen is produced. As the amount of hydrogen produced increases which is later fed into the PEMFC, the area of the PEMFC to cater this increase in hydrogen flow rate increases. It is of common understanding that a fixed area of PEMFC can handle certain amount of hydrogen flow and as the flow increases the area of the PEMFC has to increase in order to function properly without having degrading performance.
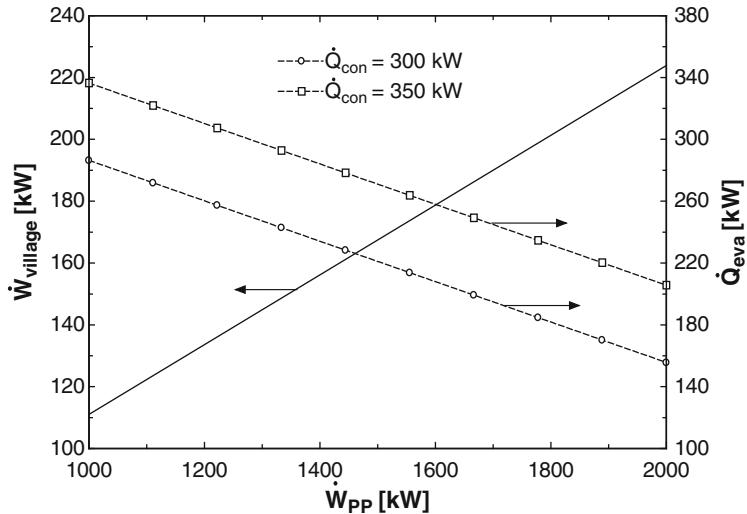
Fig. 42.4 Variation in area of PEMFC and hydrogen produced with increase in excess power from power plant

Fig. 42.5 Variation in power and rate of heat produced by PEMFC with increase in excess power from power plant

As the amount of hydrogen produced in electrolyzer increases the amount of power rate of useful heat produced by PEMFC increases as well. It is noticed that power and rate of useful heat produced increase from 112.9 to 225.7 kW and 130.7 to 261.5 kW, respectively, with increase in power input to the electrolyzer from the power plant as seen in Fig. 42.5. This behavior of PEMFC is very much expected as

Fig. 42.6 Variation in power and cooling supplied to village with increase in excess power from power plant

the increase in mass flow rate of hydrogen and increase in area of PEMFC are directly related and as when the area of PEMFC and mass flow rate of hydrogen increase the energy production capability of PEMFC also increases. Increase in energy produced by PEMFC results in increase in the power supplied to the village but decrease in the rate of cooling produced by the QEAS for specific cooling load as displayed in Fig. 42.6. The amount of power supplied to the village and the rate of cooling produced by QEAS vary from 111 to 223.9 kW and 336.4 to 155.6 kW, respectively, with increase in power supplied to the electrolyzer and for condenser load of 300 and 350 kW. The rise in power supplied to the village is directly related to the rise in power produced by the PEMFC. However, the rate of heat produced by PEMFC is supplied to the QEAS. For a fixed cooling load if the rate of heat supplied to the QEAS increases the performance of the QEAS decreases because the stream entering the evaporator is at higher temperature than what it would be if the rate of heat input to the QEAS is smaller. However, if the condenser load is increased for a fixed power input to the electrolyzer a rise in the rate of cooling produced is noticed. This rise is noticed because rise in condenser load means more heat is rejected in the condenser and therefore, stream entering the evaporator has the higher capability of carrying the heat from the conditioned space. This decrease in the rate of cooling production of QEAS with increase in power input to the electrolyzer results in decrease in the energetic and exergetic COPs of the QEAS as seen in Fig. 42.7. Both energetic and exergetic COPs vary from 2.54 to 0.59 and 1.28 to 0.15, respectively, with increase in power input to electrolyzer. It is also noticed that for a specific power input to the electrolyzer, increase in condenser load results in higher COPs, because increase in condenser load results in increase in the rate of cooling produced. Figure 42.8 summarizes the whole process in terms of overall energetic
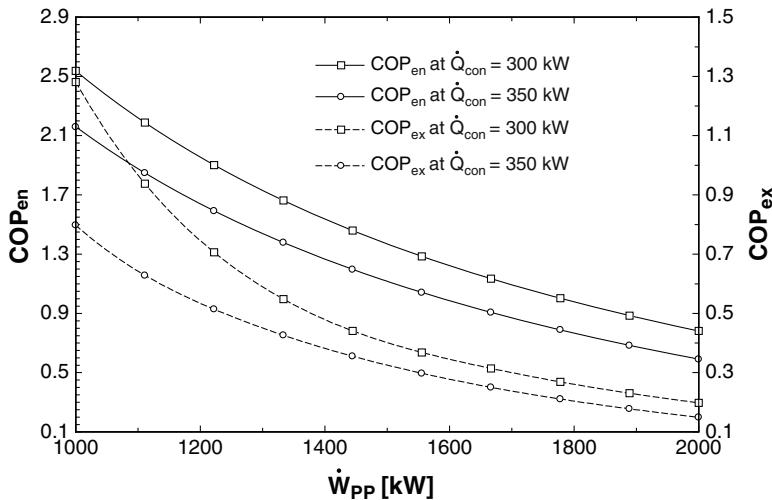
Fig. 42.7 Effect of increase in excess power from power plant on energetic and exergetic COPs
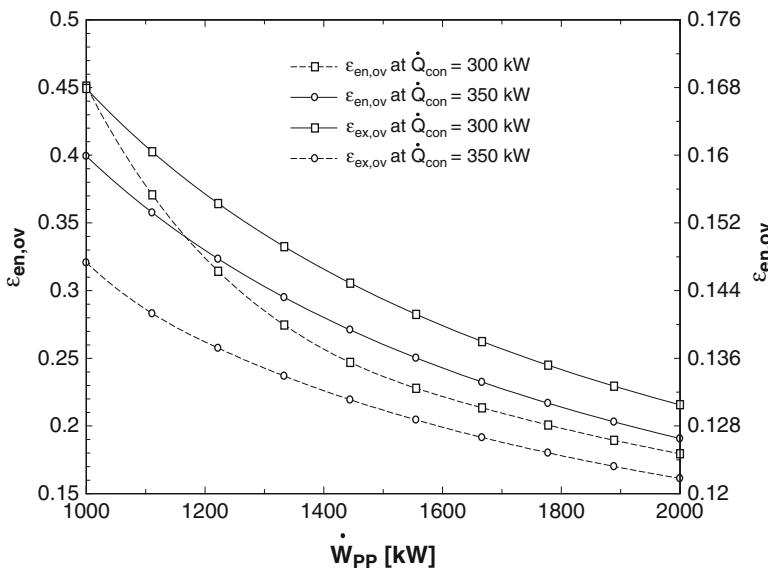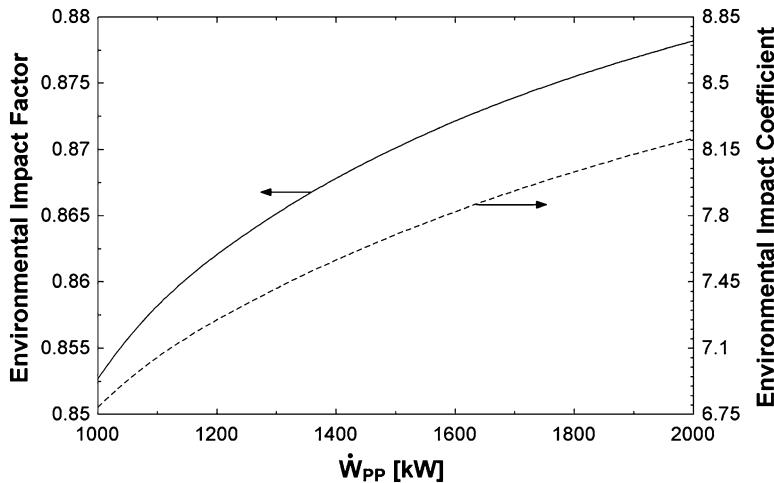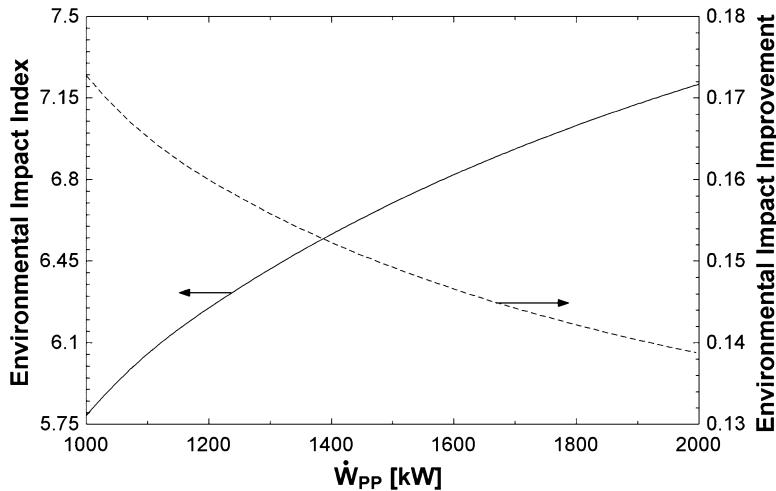
Fig. 42.8 Effect of increase in excess power from power plant on overall energetic and exergetic utilization factor

and exergetic utilization factors. It is seen in Fig. 42.8 that the overall energetic and exergetic performance of the system decreases with increase in the power input to the electrolyzer. Both the energetic and exergetic overall utilization factors are found to be varying from 0.45 to 0.19 and 0.19 to 0.12, respectively. This behavior
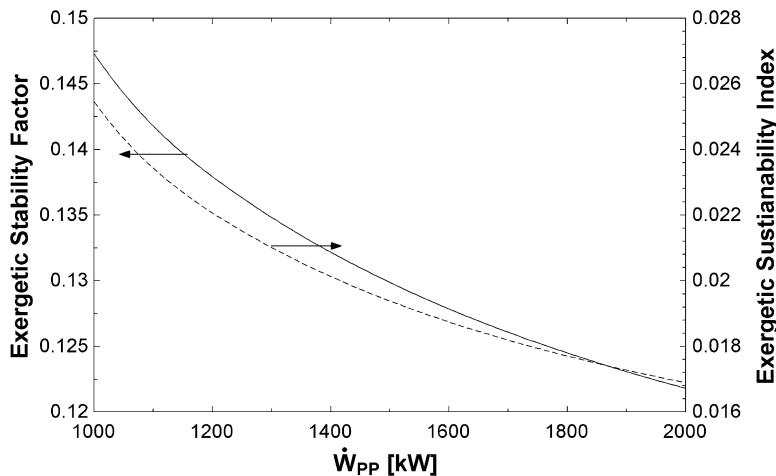
Fig. 42.9 Effect of increase in excess power on environmental impact factor and environmental impact coefficient

is noticed because the rate of cooling production plays a major role in the overall performance of the system. As the rate of cooling produced decreases with increase in power input the overall performance of the system also decreases. Figure 42.9 shows the effect of increase in excess power from power plant on the system environmental impact factor and environmental impact coefficient. Both the environmental impact factor and environmental impact coefficient are found to be increasing from 0.85 to 0.88 and 6.8 to 8.2, respectively, with increase in excess power from the power plant. The increase in excess power results in higher exergy destruction by the system, therefore increasing its impact on the environment in a negative manner. Figure 42.10 shows the effect of increase in excess power on environmental impact index and environmental impact improvement. The environmental impact index helps visualize the damages caused to the environment by the system due to its waste exergy output and exergy destruction and in ideal case this index should approach 0. The environmental impact improvement indicates the environmental appropriateness of the system and it is desirable to get this factor as high as possible. The environmental impact index is found to be increasing from 5.8 to 7.2 and the environmental impact improvement is found to be decreasing from 0.17 to 0.14. Figure 42.11 helps visualizing the impact of increase in excess power on exergetic stability factor and exergetic sustainability index. The exergetic stability factor helps us realize how much stable the system is from exergy perspective. The purpose of exergetic sustainability index is to show how much sustainable the system is from exergy perspective and it is desired to have high value of this index. The results show that increase in excess power has negative impact on the exergetic stability factor and the exergetic sustainability index and both the parameters are found to be decreasing from 0.15 to 0.12 and 0.025 to 0.017, respectively.
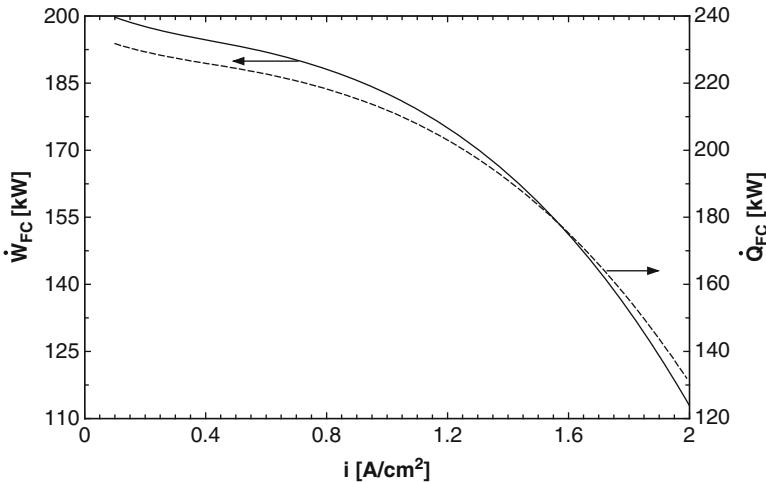
Fig. 42.10 Effect of increase in excess power on environmental impact index and environmental impact improvement

Fig. 42.11 Effect of increase in excess power on exergetic stability factor and exergetic sustainability index

42.4.2 *Effect of Current Density of PEMFC*

Current density of PEMFC is a very important parameter as the performance of the PEMFC is highly dependent on the current density. It is seen that increase in current density results in decrease in power and rate of heat output from PEMFC. The power and rate of heat produced by PEMFC are found to be decreasing from 199.7
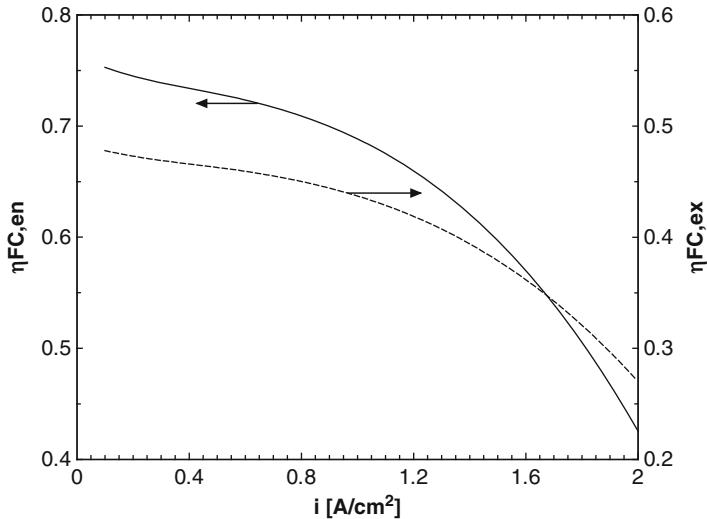
Fig. 42.12 Effect of increase in current density on power and rate of heat produced by PEMFC
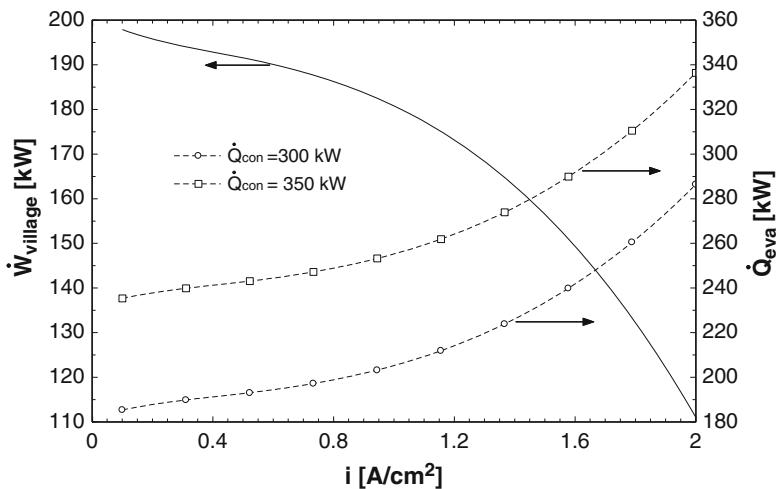
to 112.9 kW and 231.8 to 130.7 kW, respectively, with increase in current density and for a fixed power input to electrolyzer of 1,000 kW as shown in Fig. 42.12. This decrease in energy produced by PEMFC is noticed because increase in current density for a certain membrane area results in too much accumulation of current at one point which results in degrading performance of the PEMFC. Such an accumulation of current can be compared with accumulation of pressure at one point which results in degrading performance for better understanding.

As the energy produced by PEMFC decreases with increase in current density the energy and exergy efficiencies of PEMFC also decrease as shown in Fig. 42.13. Both energy and exergy efficiencies are found to be decreasing from 0.75 to 0.42 and 0.47 to 0.27, respectively, with increase in current density. This decrease in efficiencies is directly related to the production capability of PEMFC which decreases with increase in current density.

As the power and rate of heat produced by PEMFC decrease, the power supplied to the village decreases but the rate of cooling produced increases as shown in Fig. 42.14. The power and rate of cooling vary from 197.9 to 111 kW and 185.4 to 336.4 kW, respectively. The decrease in power supplied to the building is directly related to the power produced by PEMFC, but the rate of cooling produced by the QEAS is inversely related to the rate of heat produced by PEMFC. Decrease in the rate of heat provided to the QEAS for a certain condenser load results in higher rate of cooling production because with decrease in rate of heat input the temperature of the stream entering the evaporator decreases. As the temperature of stream entering evaporator decreases, its capability of carrying more cooling load increases and therefore, the rate of cooling produced by the QEAS increases. The increase in the rate of cooling with increase in current density is reflected on the energetic and

Fig. 42.13 Effect of increase in current density on energy and exergy efficiency of PEMFC

Fig. 42.14 Variation in power and rate of cooling supplied to village with increase in current density

exergetic COPs of the QEAS as seen in Fig. 42.15. Both energetic and exergetic COPs vary from 0.79 to 2.5 and 0.21 to 1.28, respectively, with increase in current density. This behavior is noticed because increase in current density results in higher rate of cooling production and, therefore, increase in the COPs. Figure 42.16 summarizes the overall performance of the system in terms of overall energetic and
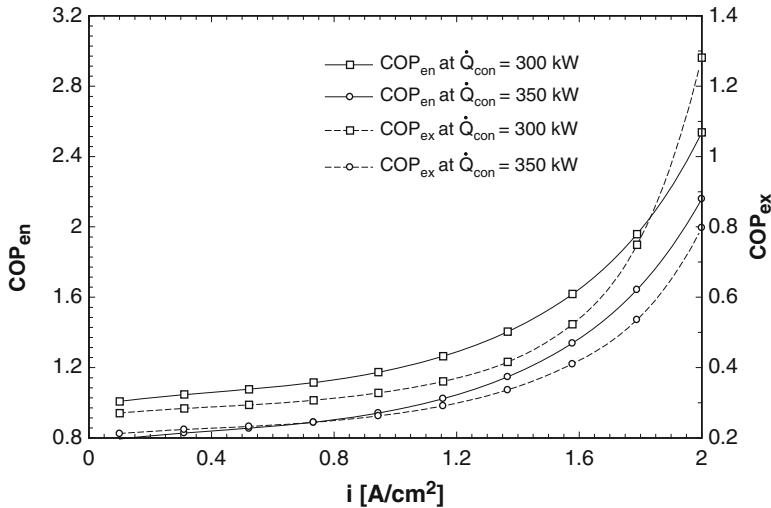
Fig. 42.15 Effect of increase in current density on energetic and exergetic COPs
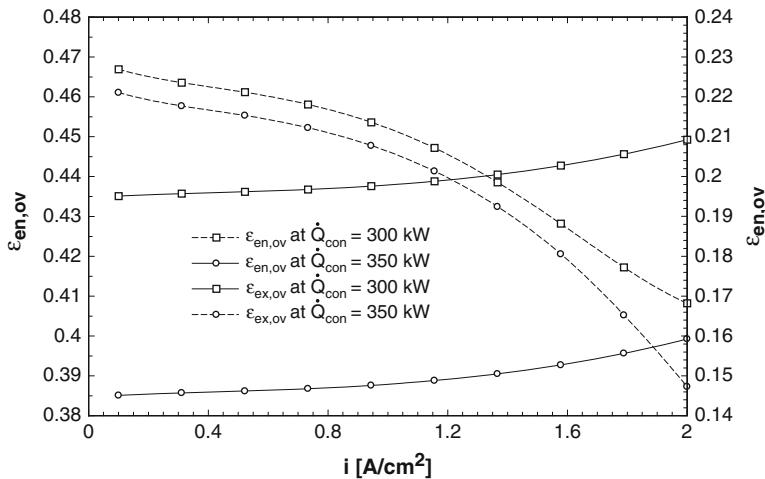
Fig. 42.16 Effect of increase in current density on overall energetic and exergetic utilization factor

exergetic utilization factors. Both the utilization factors are found to be varying from 0.38 to 0.45 and 0.22 to 0.14, respectively. These overall energetic and exergetic utilization factors are directly related to the power produced by PEMFC and the rate of cooling produced by the QEAS.

42.5   Conclusions

This chapter has presented an integrated system with electrolyzer, PEMFC and QEAS system for power and cooling productions using excess power supplied by power plant. In this regard, we have studied the effects of excess power available and current density of PEMFC on the rate of hydrogen produced, power supplied to the village, rate of heat produced, rate of cooling produced, energetic and exergetic efficiencies and COPs, and energetic and exergetic utilization factors. The results show that increase in available excess power results in higher area of PEMFC, higher power supplied to the village and lower rate of cooling production. Also, increase in excess power results in degrading performance of the QEAS and overall system. Increase in current density results in a lesser power supplied to the village and higher rate of cooling production, and hence in a better performance of the QEAS. The exergetic environmental impact assessment study concludes that rise in excess power is detrimental to the system as it leads to higher exergy destruction and higher impact on the environment. Furthermore, it shows that cogeneration systems utilizing renewable energy are environmentally friendly, efficient and cost effective for utilizing excess power produced by the power plant. The hydrogen produced in this system can be stored and later used for the production of power and cooling.

References

1. Nag PK (2001) Power plant technology, 2nd edn. Tata McGraW Hill, New Delhi
2. El-Wakil MM (2002) Power plant technology. McGraW Hill, New York
3. Sorensen HA (1983) Energy conversion systems. Wiley, New York
4. Peterson RB (2011) A concept for storing utility-scale electrical energy in the form of latent heat. Energy 36:6098–6109
5. Pandiyarajan V, Chinnappandian M, Raghavan V, Velraj R (2011) Second law analysis of a diesel engine waste heat recovery with a combined sensible and latent heat storage system. Energy Policy 39:6011–6020
6. Bal LM, Satya S, Naik SN, Meda V (2011) Review of solar dryers with latent heat storage systems for agriculture products. Renew Sustain Energy Rev 15:876–880
7. Yilmaz C, Kanoglu M, Bolatturk A, Gadalla M (2011) Economics of hydrogen production and liquefaction by geothermal energy. Int J Hydrogen Energy 37:2058–2069
8. Balta MT, Dincer I, Hepbasli A (2010) Geothermal-based hydrogen production using thermo-chemical and hybrid cycles: a review and analysis. Int J Energy Res 34:757–775
9. Kilkis B (2011) A lignite–geothermal hybrid power and hydrogen production plant for green cities and sustainable buildings. Int J Energy Res 35:138–145
10. Kanoglu M, Bolatturk A, Yilmaz C (2010) Thermodynamic analysis of models used in hydrogen production by geothermal energy. Int J Hydrogen Energy 35:8783–8791
11. Barelli L, Bidini G, Gallorini F, Ottaviano A (2010) Analysis of the operating conditions influence on PEM fuel cell performances by means of a novel semi-empirical model. Int J Hydrogen Energy 36:1–9
12. Ni M, Leung MKH, Leung DYC (2007) Parametric study of solid oxide fuel cell performance. Energy Convers Manage 18:1525–1535

13. Saeed A, Ali M, Mahrokh S (2010) Study of PEM fuel cell performance by electrochemical impedance spectroscopy. Int J Hydrogen Energy 35:9283–9290
14. Midilli A, Dincer I (2008) Hydrogen as a renewable and sustainable solution in reducing global fossil fuel consumption. Int J Hydrogen Energy 33:4209–4222
15. Midilli A, Dincer I (2009) Development of some exergetic parameters for PEM fuel cells for measuring environmental impact and sustainability. Int J Hydrogen Energy 34:3858–3872
16. Moriarty P, Honnery D (2009) Hydrogen's role in an uncertain energy future. Int J Hydrogen Energy 34:31–39
17. Dincer I, Dost S (1996) Energy analysis of an ammonia-water absorption refrigeration system. Energy Sources 18:727–733
18. ASHRAE (2006) ASHRAE handbook of refrigeration. American Society of Heating, Refrigerating and Air-Conditioning Engineers Inc., Atlanta, GA
19. Ataer ÖE, Gögüs Y (1991) Comparative study of irreversibilities in an aqua-ammonia absorption refrigeration system. Int J Refrig 14:86–92
20. Ziegler F, Kahn R, Summerer F, Alefeld G (1993) Multi-effect absorption chillers. Int J Refrig 16:301–311
21. Tozer R, Syed A, Maidment G (2005) Extended temperature–entropy (T–s) diagrams for aqueous lithium bromide absorption refrigeration cycles. Int J Refrig 28:689–697
22. Mateus T, Oliveira AC (2009) Energy and economic analysis of an integrated solar absorption cooling and heating system in different building types and climates. Appl Energy 86:949–957
23. Zhai XQ, Qu M, Li Y, Wang RZ (2011) A review for research and new design options of solar absorption cooling systems. Renew Sustain Energy Rev 15:4416–4423
24. Gomri R (2008) Thermodynamics evaluation of triple effect absorption chiller. Thermal Issues in Emerging Technologies ThETA '08, pp 245–250
25. Gadalla MA, Ratlamwala TAH, Dincer I (2010) Energy and exergy analysis of an integrated fuel cell and absorption cooling system. Int J Exergy 7:731–754
26. Ratlamwala TAH, Gadalla MA, Dincer I (2011) Performance assessment of an integrated PV/T and triple effect cooling system for hydrogen and cooling production. Int J Hydrogen Energy 36:11282–11291
27. Ratlamwala TAH, Gadalla MA, Dincer I (2011) Performance assessment of a combined PEM fuel cell and triple-effect absorption cooling system for cogeneration applications. Fuel Cells 11:413–423
28. Grossman G, Zaltash A (2001) ABSIM-modular simulation of advanced absorption systems. Int J Refrig 24:531–543
29. Larminie J, Dicks A (2000) Fuel cell systems explained, 2nd edn. Wiley, New York
30. Mert SO, Dincer I, Ozcelik Z (2007) Exergoeconomic analysis of a vehicular PEM fuel cell system. J Power Sources 165:244–252

Chapter 43
Exergy Analysis and Environmental Impact Assessment of a Geothermal Power Plant

Hadi Ganjehsarabi, Ibrahim Dincer, and Ali Gungor

Abstract Geothermal power plants are one of the environmentally benign systems among other types of power generation systems. In this chapter, the exergy efficiencies and exergy destruction rates are analyzed for the binary geothermal. In addition, greenhouse gas (GHG) emissions (in ton CO_2-eq/kWh) during operation as well as the sustainability index are determined under various operating conditions. For the case study presented here, it is shown that the Dora II binary geothermal power plant produces no GHG emissions during operation since no fossil fuels are burned. For the same production capacity, it helps reduce the emissions by 56 Mega Ton CO_2-eq/yr compared to a coal-fired power plant and 28 Mega Ton CO_2-eq/yr compared to a natural gas combined cycle power plant.

Keywords Environmental impact assessment • Exergy • Geothermal energy

H. Ganjehsarabi (✉)
Department of Mechanical Engineering, Faculty of Engineering, Ege University, Bornova, Izmir TR-35100, Turkey

Faculty of Engineering and Applied Science, University of Ontario Institute of Technology, 2000 Simcoe Street North, Oshawa, ON L1H 7K4, Canada
e-mail: Hadi.Ganjehsarabi@gmail.com

I. Dincer
Faculty of Engineering and Applied Science, University of Ontario Institute of Technology, 2000 Simcoe Street North, Oshawa, ON L1H 7K4, Canada
e-mail: Ibrahim.Dincer@uoit.ca

A. Gungor
Department of Mechanical Engineering, Faculty of Engineering, Ege University, Bornova, Izmir TR-35100, Turkey
e-mail: ali.gungor@ege.edu.tr

Nomenclature

D_p	Depletion number
e	Specific emission (kg CO_2-eq/kWh)
E	Emission (kg/kWh)
$\dot{E}x$	Exergy rate (kW)
h	Specific enthalpy (kJ/kg)
$\dot{m}$	Mass flow rate (kg/s)
P	Power (kW)
$\dot{Q}$	Heat transfer rate (kW)
T	Temperature (K or °C)
T_0	Ambient temperature (K or °C)
$\dot{W}$	Work rate (kW)

Greek Letters

η	Exergy efficiency

Subscripts

a	Air
av	Avoided
bat	Battery
cool	Coolant
en	Energy
ex	Exergy
g	Generation
geo	Geothermal fluid
n	n-Pentane
p	Pump
pre	Preheater
$turb$	Turbine
vap	Vaporizer

Acronyms

GHG	Greenhouse gas
GWP	Global warming potential
SI	Sustainability index

43.1 Introduction

The major source of greenhouse gas emissions (consisting of mainly carbondioxide as about 74%) is the combustion of fossil fuels which cause greenhouse effect. There is an urgent need to tackle with this global issue through potential solutions[1, 2]. The factors to consider for assessing the sustainable and environmentally benign energy systems are fossil fuel depletion along with pollutant emissions and global warming as discussed by Hammond [3]. The ways of reducing society's dependence on fossil fuels are reducing demand and promoting the use of alternative energy sources [4].

In the perspective of increasing the share of renewable energy in order to mitigate global warming issues and to respond to fossil resource depletion, the use of geothermal energy has gained interest. Geothermal energy is thermal energy generated and stored in the Earth. It is a widely adopted and effective energy source. In addition, it is used in order to generate electricity and for direct uses such as space heating and cooling, industrial processes, and greenhouse heating. The geothermal electrical capacity and direct use capacity for heating in the world were about 67,246 GWh_e/yr and 117,740 GWh_{th}/yr in 2010, respectively [5, 6]. As stated by the international energy agency in its roadmap for geothermal energy IEA (2011), by 2050 the geothermal power production should be increased to 1,400 TWh_e/yr, and the direct heating use to 1,600 TWh_{th}/yr [7]. A geothermal well can produce hot water (brine), wet steam (liquid–vapor mixture), dry steam (saturated steam), or superheated steam. Liquid-dominated systems are much more common than vapor-dominated systems and can be produced either as brine or as a brine–steam mixture, depending on the pressure maintained on the production system. If the pressure is reduced below the saturation pressure at that temperature, some of the brine will flash, and a two-phase mixture will result. If the pressure is maintained above the saturation pressure, the fluid will remain single phase [8, 9]. Among 100 geothermal resources that have been investigated, 10 % are vapor dominated, 60 % are liquid dominated, and 30 % are brine resources [10]. Most of the world's high-temperature geothermal resources have already been exploited for the generation of electricity.

The present study aims to assess the environmental impacts produced by geothermal power plants though they represent promising systems toward mitigation of GHG emissions and global warming. Also a case study is carried out in this chapter to exemplify the environmental impacts of these systems.

43.2 Types of Geothermal Power Generation System

Mainly, there are three types of geothermal power plant used in order to produce electricity from geothermal sources. The first type of geothermal power plant is dry steam plants. Dry steam power plants utilize straightforwardly steam which is piped from production wells to the plant, and then transmitted via pipelines directly to a steam turbine. For the first category of these systems, around 71 units have been reported to be under operation in August 2011 which contributes about 12 % of all
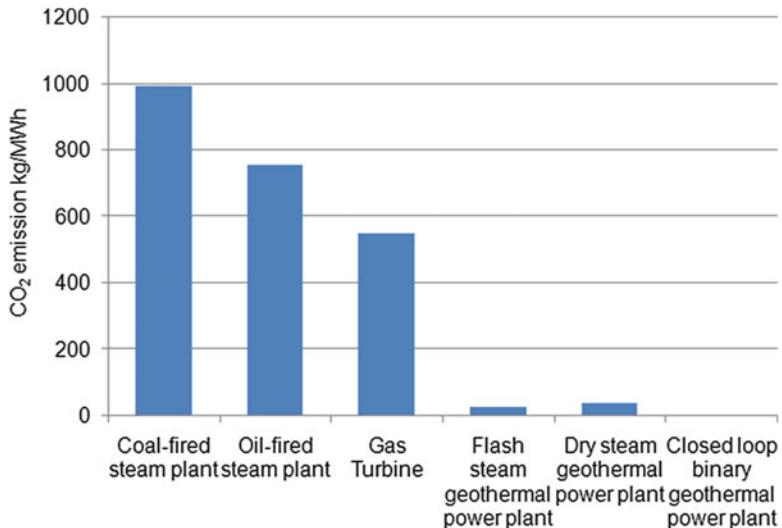
geothermal plants. The overall power produced by these generators accounts for 2,893 MW installed or about 27 % of the overall geothermal worldwide capacity [11]. The second type of geothermal power plants is the flash steam plants. Flash steam plants are used to produce power from liquid-dominated resources that are not hot enough to flash a significant proportion of the water to steam in surface equipment, either at one or two pressure stages (single-flash or double-flash plants). About 29 % of the overall geothermal plants are single-flash plants. Nearly 43 % of the total installed geothermal power capacity in the world is related to this type of geothermal. The produced power ranges from 3 to 117 MW while the average power rating is 27 MW per unit [11]. Binary cycle plants use the geothermal brine from liquid-dominated resources usually below 170 °C. These plants operate with a binary working fluid (isobutane, isopentane, freon, etc.) which has a low boiling temperature in a Rankine cycle. The working fluid is completely vaporized and usually super-heated by the geothermal heat in the vaporizer. The vapor expands in the turbine. It is then condensed in a water-cooled condenser or dry cooling tower before being pumped back to the vaporizer to complete the cycle. The binary plants are categorized among the most widely used type of binary plants and are more common than other types of geothermal power plants. The literature review shows that 235 units were in operation in August 2011 in over 15 countries with gross power production of 708 MW. Although they constitute 40 % of all geothermal units in operation, only 6.6 % of the total power is produced by this type of geothermal power plants [11].

43.3 Environmental Impact of Electricity Generation

All generation of electricity (including geothermal power) has a number of side effects. The degrees of each depend on the type of power generation, and geothermal energy causes these side effects in varying quantities. This includes, but is not limited to:

- Gas emission to the atmosphere
- Water pollution
- Solid emissions to the surface and the atmosphere
- Noise pollution
- Land usage
- Land subsidence
- Induced seismicity
- Induced landslides
- Water usage
- Disturbance of natural hydrothermal manifestations
- Disturbance of wildlife habitat and vegetation
- Alteration of natural views
- Catastrophic events

Although geothermal power plants offer considerably fewer of these side effects in lesser degree than fossil-fuel combustion power plants, some affect geothermal

Fig. 43.1 CO_2 emissions from various power plants (modified from ref. [12])

plants in a greater degree and thus technology is present to mitigate their effects as much as possible [11, 12].

43.3.1 Environmental Impacts of Geothermal Plants

Gaseous emissions from dry-steam and flash-steam geothermal power plants are from dissolved gases in geo-fluid. These so-called no-condensable gases (NCG) accumulate in the condenser. They could be removed upstream of the turbine, but commercial plants do not currently employ this technique. Because of this accumulation, back pressure on the turbine will increase and thus turbine power will reduce accordingly. The most common NCG found in geothermal steam are carbon dioxide (CO_2) and hydrogen sulfide (H_2S). There is also presence of methane, hydrogen, sulfur dioxide, and ammonia, usually in extremely low concentrations. NCG can be captured and removed, and be re-dissolved into waste brine [13]. Currently in the United States, there is no requirement to trap and remove CO_2, but H_2S is highly regulated due to toxicity at high concentrations. Fig. 43.1 shows a comparison of typical geothermal plants with other types of power plants [14].

The binary geothermal power plants do not emit any CO_2, and flash plants emit considerably less CO_2 than fossil fuel-powered plants. This remarkable CO_2 emission profile ensures that geothermal power plants will be excellently positioned if regulations covering CO_2 emission are ever introduced. Land usage by geothermal plants depends very much on individual factors surrounding a plant. These factors include the type of plant, the well field, access roads, and requirements for

buildings. The well fields can be large (up to 10 km^2 in size) and cover approximately 2 % of the total area required by a geothermal plant. Pipelines are used to transfer geo-fluid, and must be as short as possible to avoid heat loss with a network that follows service roads.

The water which is withdrawn from the deep underground reservoir is normally a hot water, mineral-rich and salty liquid. Part of the water in vapor form or flashed from the hot water is used to turn the turbine and therefore to generate the electricity. When the steam is extracted from the hot water, the remaining will be collected and then will be re-injected to the geothermal reservoir by deployed pumps. The re-injected water then will be heated up to the degree of initial condition. Other water-cooled systems have much more wasted water which can exceed to 50 % of the water to be evaporated to the atmosphere. The remaining 50 % is going to be re-circulated. The water consumption of binary power plants is minimum. Geothermal water is isolated in a geothermal facility, during production, and injected back into the geothermal reservoir. Thickly encased pipes are used to separate the water from the underground reservoir which makes the facility virtually free of water pollutants. To minimize the effects of re-injection of geothermal water to the wells, they are placed in deep underground place well below groundwater reservoirs. These considerations will cause a minimum impact of used water.

Other aspect of environmental impact of geothermal systems is the generated noise. First, the noise of drilling is an impact. Since it is a short-time effect which is prevailing during the operation phase of the power plant, the impact is categorized unimportant though the noise rarely exceeds 90 dB. Secondly, the noise initiates from discharging boreholes. The noise may exceed 120 dB. In the next phase where the geothermal power plant is under operation, the environment noise can be kept under 65 dB limits by using a noise muffler. The threshold noise follows the US Geological Survey for noise limit [15].

The major environmental issues for geothermal power plant are associated with groundwater use and contamination, with related concerns about induced seismicity or subsidence as a result of water injection and production. Issues of noise, safety, visual impacts, and land use associated with drilling and production operations are also important but fully manageable. As geothermal technology moves away from hydrothermal and more toward larger enhanced geothermal system (EGS) developments, it is likely that environmental impacts and risks will be further reduced relative to those associated with hydrothermal systems. For example, EGS plants should only rarely have a need for abatement of hydrogen sulfide (H_2S), ammonia (NH_3), and other chemical emissions [11].

43.4 System Descriptions

The Geothermal Power Plant Dora-II is located in the West of the village Salavatli, near the city of Aydin in Turkey. A flow diagram and the main characteristics of the "Dora II" geothermal power plant are illustrated in Fig. 43.2. The Aydin Sultanhisar-Salavatli geothermal field is a liquid-dominated reservoir. Electricity
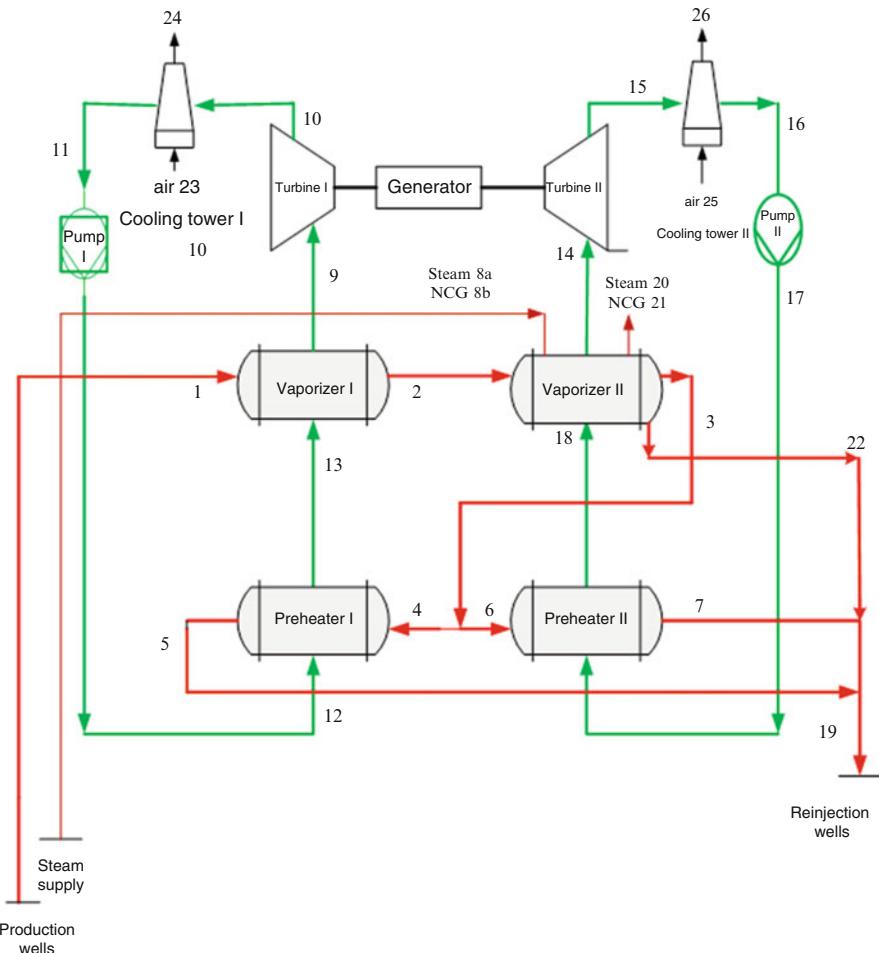
Fig. 43.2 Flow diagram of the "Dora II" geothermal power plant (modified from ref. 19)

is generated from the geothermal source at a temperature ranging from 78 to 170 °C. The employed organic Rankine cycle and binary technology were designed for the specific conditions of a wide variety of heat sources and therefore provide increased efficiency for the geothermal power plant. It is an outdoor installation that consists of a vaporizer/preheater, turbogenerator, cooling tower, feed pump, and controls. The hot brine is pumped from the production wells and directed to the generator through isolated transmission lines.

The thermal fluid is passed through a heat exchanger, and the heat from the fluid is transferred to a secondary fluid (n-pentane). The n-pentane is vaporized to generate electricity via two turbines, which are both connected to a power generator. After having passed the heat exchanger, the geothermal fluid drops to 83 °C and

is re-injected back to the reservoir via a re-injection well. The re-injection well is located right at the generation facility. The production cycle is closed due to complete re-injection of the geothermal brine into the reservoir. This system both serves to sustain the reservoir and avoids adverse environmental impacts [16].

43.4.1 System Analysis

In the following analysis, some assumptions are made such as that the operation of the geothermal power plant is considered in steady state. The turbines and pumps possess isentropic efficiencies, the geothermal fluid is treated as water, and air is taken as ideal gas.

43.4.2 Exergy Analysis

The exergy analysis of the process determines the exergy flows as a basis for the exergo-economic analysis and exergetic variables such as exergy destruction and exergy efficiency for a thermodynamic evaluation. The exergy destruction rate and exergy efficiency equations of the components are given in (Table 43.1).

Exergy analysis helps identify the irreversibilities in the stems and improve the efficiency of the system, since it quantifies the locations, types, and magnitudes of waste and losses. This leads to increased exergy efficiencies and reduced exergy losses (both waste exergy emission sand internal exergy consumption) in the system. In the analysis, by using general mass, energy, and exergy balance equations, the exergy destruction in each component of the DGPP is calculated. The overall exergetic efficiency for the DGPP can be calculated as follows:

$$\eta_{ex} = \frac{\dot{W}_{net}}{\dot{Ex}_{in}} \tag{43.1}$$

where $\dot{Ex}_{in}$ is the exergy of geothermal fluid as the exergy input to the system.

In order to improve environmental sustainability, it is important to minimize the environmental damage while using sustainable source of energy. Accordingly, a sustainability index (SI) is used to connect exergy and environmental impact [17]:

$$SI = \frac{1}{D_P} \tag{43.2}$$

Here, D_P is a depletion number, which is defined as the exergy destruction divided to exergy input.

Table 43.1 Expressions of exergy destruction rate and exergy efficiency for each component of the system

Component	Exergy destruction rate	Exergy efficiency
Turbine I	$\dot{E}x_{d,turb,I} = \dot{m}_n(ex_9 - ex_{10}) - \dot{W}_{turb,I}$	$\eta_{ex,turb_I} = \frac{\dot{W}_{turb,I}}{\dot{E}x_9 - \dot{E}x_{10}}$
Turbine II	$\dot{E}x_{d,turb,II} = \dot{m}_n(ex_{14} - ex_{15}) - \dot{W}_{turb,II}$	$\eta_{ex,turb_{II}} = \frac{\dot{W}_{turb,II}}{\dot{E}x_{14} - \dot{E}x_{15}}$
Vaporizer I	$\dot{E}x_{d,vap,I} = \dot{m}_n(ex_{13} - ex_9) + \dot{m}_{geo}(ex_1 - ex_2)$	$\eta_{ex,vap_I} = \frac{\dot{E}x_{13} - \dot{E}x_9}{\dot{E}x_1 - \dot{E}x_2}$
Vaporizer II	$\dot{E}x_{d,vap,II} = \dot{m}_n(ex_{18} - ex_{14}) + \dot{m}_{geo}(ex_2 - ex_3) + \dot{m}_{8a}ex_{8a}$ $+ \dot{m}_{8b}ex_{8b} - \dot{m}_{20}ex_{20} - \dot{m}_{21}ex_{21} - \dot{m}_{22}ex_{22}$	$\eta_{ex,vap_{II}} = \frac{\dot{m}_n(ex_{18} - ex_{14})}{\dot{E}x_2 - \dot{E}x_3 + \dot{E}x_{8a} + \dot{E}x_{8b} - \dot{E}x_{20} - \dot{E}x_{21} - \dot{E}x_{22}}$
Preheater I	$\dot{E}x_{d,pre_I} = \dot{m}_n(ex_{12} - ex_{13}) + \dot{m}_{geo}(ex_4 - ex_5)$	$\eta_{ex,pre_I} = \frac{\dot{E}x_{12} - \dot{E}x_{13}}{\dot{E}x_4 - \dot{E}x_5}$
Preheater II	$\dot{E}x_{d,pre_I} = \dot{m}_n(ex_{17} - ex_{18}) + \dot{m}_{geo}(ex_6 - ex_7)$	$\eta_{ex,pre_{II}} = \frac{\dot{E}x_{17} - \dot{E}x_{18}}{\dot{E}x_6 - \dot{E}x_7}$
Cooling tower I	$\dot{E}x_{d,cool_I} = \dot{m}_n(ex_{10} - ex_{11}) + \dot{m}_a(ex_{23} - ex_{24})$	$\eta_{ex,cool_I} = \frac{\dot{E}x_{10} - \dot{E}x_{11}}{\dot{E}x_{24} - \dot{E}x_{23}}$
Cooling tower II	$\dot{E}x_{d,cool_{II}} = \dot{m}_n(ex_{15} - ex_{16}) + \dot{m}_a(ex_{25} - ex_{26})$	$\eta_{ex,cool_{II}} = \frac{\dot{E}x_{15} - \dot{E}x_{16}}{\dot{E}x_{26} - \dot{E}x_{25}}$
Pump I	$\dot{E}x_{d,P,I} = \dot{m}_n(ex_{11} - ex_{12}) + \dot{W}_{P,I}$	$\eta_{ex,P_I} = \frac{\dot{E}x_{11} - \dot{E}x_{12}}{\dot{W}_{P,I}}$
Pump II	$\dot{E}x_{d,P_{II}} = \dot{m}_n(ex_{16} - ex_{17}) + \dot{W}_{P,II}$	$\eta_{ex,p_{II}} = \frac{\dot{E}x_{16} - \dot{E}x_{17}}{\dot{W}_{P,II}}$
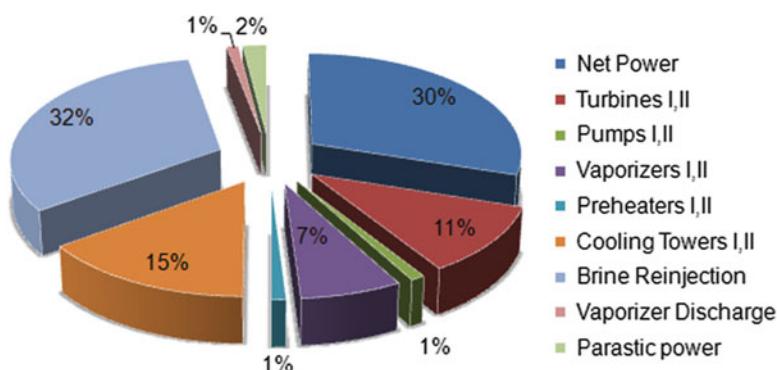
In the present analysis, the yearly avoided CO_2-equivalent emissions ($E_{co2,av}$) in (ton CO_2) are mainly the CO_2 emissions which are generated by conventional systems and can be calculated as follows:

$$E_{co_2,av} = P_g e_{co_2,p} \qquad (43.3)$$
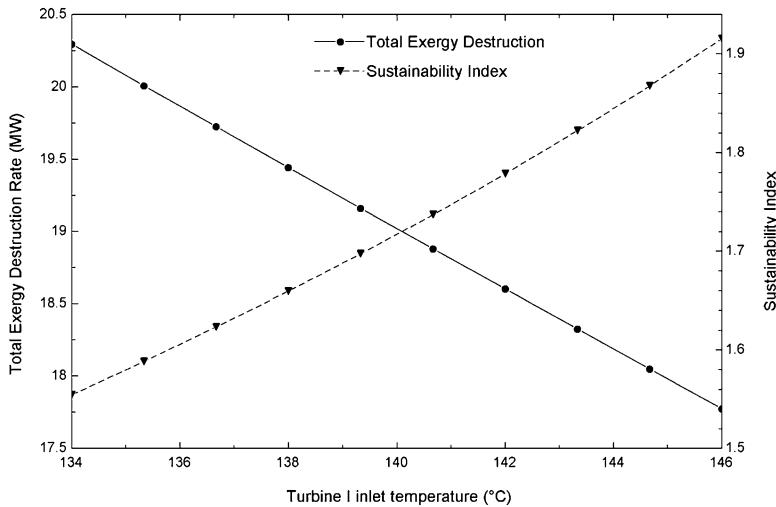
where P_g and $e_{CO2,P}$ are the power generation (kWh) and the specific CO_2 emissions of electricity production (kg CO_2-eq/kWh) from conventional systems. Moreover, an enviro-economic (environmental cost) analysis will also be conducted in order to evaluate the system's impact on the environment in terms of the amount of carbon dioxide released through the electricity consumption [18].

43.5   Results and Discussion
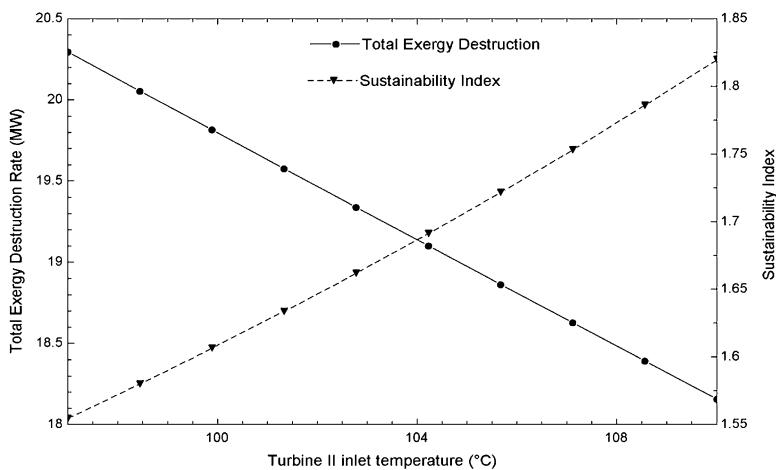
In this section, the results of thermodynamic modeling and environmental impact assessment of using a geothermal power plant are presented, including evaluation and discussion of the effects of various design parameters on the system performance. In this regard, energy and exergy rates were calculated for each state of Fig 43.2 by using actual operational data [19]. In order to determine the sites of exergy destruction, an exergy diagram is herewith shown in Fig. 43.3. The results show that 69 % of the exergy input to the plant is destroyed. The remaining 31 % is converted to power and 6.2 % of this power is used for parasitic load in the plant. In addition, brine re-injection is the most significant exergy destructor in the geothermal power plant. It is because of the relatively high temperature of brine that is re-injected back into the ground. It can be suggested that the re-injected brine can be used for district heating systems. This may be surveyed

Fig. 43.3 Exergy destruction diagram (given as the percentages of brine exergy input out of 32,120 kW)
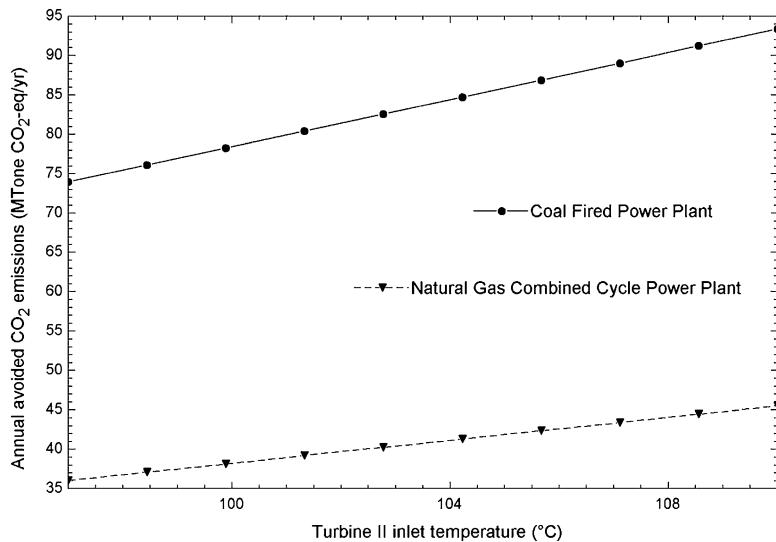
Fig. 43.4 Variations of total exergy destruction rate and sustainability index versus turbine I inlet temperature

Fig. 43.5 Variations of total exergy destruction rate and sustainability index versus turbine II inlet temperature

if there is a residential, commercial, or industrial district in a close distance to the power plant [20].

An increase in temperature of turbines leads to a tangible increase in the sustainability index and a decrease in the total exergy destruction. The variations of turbine I inlet temperature and turbine II inlet temperature are shown in Figs. 43.4 and 43.5 for comparison purposes.

Fig. 43.6 Variations of annual avoided CO_2 emission with turbine II inlet temperature for various cases

Figure 43.6 compares the annual avoided CO_2 emissions in natural gas combined power plant and coal-fired power plant. As seen in this figure, an increase in turbine inlet temperature leads to an increase in annual avoided CO_2 emissions at both plants. It means that an increase in fuel burnt in boiler will eventually result in an increase of CO_2 emissions. It is also seen that the amount of annual CO_2 of natural gas combined cycle is less than coal-fired power plant at a same power output emphasizing on the higher specific CO_2 emissions for the coal-fired power plant.

43.6 Conclusions

In this chapter, the Dora II binary geothermal power plant has been examined under some given operating conditions and compared to the other types of power generation system in terms of environmental impact. Based on the analysis and assessment, the following main conclusions are obtained:

- The largest exergy destruction rate takes place in brine re-injection as 10.3 MW. The second and third highest exergy destructions occur in cooling tower and turbine with 4.7 and 3.4 MW, respectively.
- The CO_2 emissions from geothermal power generation are much lower than those produced by power generation based on burning fossil fuels.
- The annual avoided CO_2 emissions associated with the Dora II binary geothermal power plant are 85 Mega Ton CO_2-eq/yr and 40 Mega Ton CO_2-eq/yr with regard to the production of the same services with a coal-fired power plant and natural combined gas cycle power plant for electricity, respectively.

References

1. Dincer I, Balta MT (2011) Potential thermochemical and hybrid cycles for nuclear-based hydrogen production. International Journal of Energy Research 35(2):123–137
2. Ahmed M, Dincer I (2011) A review on methanol crossover in direct methanol fuel cells: challenges and achievements. International Journal of Energy Research 35(14):1213–1228
3. Hammond GP (2000) Energy, environment and sustainable development: a UK perspective. Trans IChemE Part B Process Saf Environ Prot 78:304–323
4. Self SJ, Reddy BV, Rosen MA (2013) Geothermal heat pump systems: status review and comparison with other heating options. Appl Energ 101:341–348
5. Lund J, Bertani R (2010) Worldwide geothermal utilization 2010. In: Geothermal resources council transactions, vol 34, p 182–185
6. Gerber L, Maréchal F (2012) Enviroeconomic optimal configurations of geothermal energy conversion systems: application to the future construction of enhanced geothermal systems in Switzerland. Energy 45:908–923
7. IEA, Technology Roadmap (2011) Geothermal heat and power tech rep. International Energy Agency, Paris, France
8. White DE (1973) Characteristics of geothermal resources. In: Kruger P, Otte C (eds) Chap. 4 in Geothermal energy: resources, production, stimulation. Stanford University Press, Stanford, CA, pp 69–94
9. Barbier E (1997) Nature and technology of geothermal energy: A review. Renew Sustain Energy Rev 1(1-2):1–69
10. Hochstein MP (1990) Classification and assessment of geothermal resources. UNITAR/UNDP 305 Center on Small Energy Resources, Rome, Italy
11. DiPippo R (2012) Geothermal Power Plants, Principles, Applications, Case Studies and Environmental Impact, Third Edition. Butterworth-Heinemann
12. Tester JW, Anderson BJ, Batchelor AS, Blackwell DD, DiPippo R, Drake EM, Garnish J, Livesay B, Moore MC, Nichols K, Petty S, Toksoz MN, Veatch RW Jr (2006) The future of geothermal energy: impact of enhanced geothermal systems (EGS) on the United States in the 21st century, Massachusetts Institute of Technology, Cambridge, MA. http://geothermal.inel.gov
13. DiPippo R (1991) Geothermal energy: electricity generation and environmental impact. Energy Policy 19:798–807
14. Kagel A, Bates D, Gawell K (2005) A guide to geothermal energy and the environment. Geothermal Energy Association, Washington, D.C
15. Kristmannsdo´ttir H, Armannsson H (2003) Environmental aspects of geothermal energy utilization. Geothermics 32:451–461
16. Verification report of the DORA-II 9.5 MWE geothermal power plant project in Turkey, Swiss Carbon Value Ltd.
17. Baniasadi E, Dincer I, Naterer GF (2012) Exergy and environmental impact assessment of solar photoreactors for catalytic hydrogen production. Chem Eng J 213:330–337
18. Dincer I, Midilli A, Hepbasli A, Karakoc H (2008) Global warming: engineering solutions. Springer, NY
19. Ganjehsarabi H, Gungor A, Dincer I (2012) Exergetic performance analysis of Dora II geothermal power plant in Turkey. Energy 46:101–108
20. Kanoglu M (2002) Exergy analysis of a dual level binary geothermal power plant. Geothermics 31:709–724

Chapter 44
Exergy Analysis and Environmental Impact Assessment of Solar-Driven Heat Pump Drying Systems

Hasan Ozcan and Ibrahim Dincer

Abstract Exergy and sustainability analysis and environmental impact assessment of drying processes are performed for conventional and solar-driven two-stage evaporator heat pump drying systems. Some parametric studies are also undertaken to investigate the influence of environmental and system parameters on the overall efficiencies. Greenhouse gas (GHG) emissions, for electricity generation are comparatively evaluated under various options. Coal-based generation has the highest emissions for both conventional and solar-driven drying systems and lowest emissions are observed for nuclear and solar photovoltaic based electricity generation. The results show that solar thermal integration to the heat pump drying system brings an additional 32 gCO_2/kWh carbon dioxide emission due to production, transportation, maintenance, and disposal of the solar thermal system. However, GHG emissions from conventional HPD system are 20.4–34.1 % higher than those of solar-driven HPD system for different generation resources.

Keywords Environmental assessment • Exergy analysis • Efficiency • Drying systems • Heat pump • Renewable energy • Solar • Two-stage evaporation

Nomenclature

Cp	Specific heat (kJ/kg °C)
ex	Exergy rate (kW)
$\dot{E}x$	Exergy rate (kW)

H. Ozcan (✉) • I. Dincer
Faculty of Engineering and Applied Science, University of Ontario Institute of Technology, 2000 Simcoe Street North, Oshawa, ON, Canada L1H 7K4
e-mail: Hasan.Ozcan@uoit.ca; Ibrahim.Dincer@uoit.ca

h	Specific enthalpy heat convectivity (kJ/kg)—(W/m^2 K)
$\dot{m}$	Mass flow rate (kg/s or L/min)
Nu	Nusselt number
P	Pressure (kg/m s^2)
$\dot{Q}$	Heat transfer rate (kW)
s	Specific entropy (kJ/kg K)
T	Temperature (K or °C)
T_0	Ambient temperature (K or °C)
T_{SP}	Solar panel temperature (K or °C)
T_{SUN}	Sun temperature (K or °C)
U	Overall heat transfer coefficient for solar panels (W/m^2 K)
w	Specific humidity ratio (g water/kg air)
$\dot{W}$	Work rate or power (kW)

Greek Symbols

η	Energy efficiency
ψ	Exergy efficiency

Subscripts

a	Air
act	Actual
B	Blower
comp	Compressor
$cond$	Condenser
D	Destruction
dry	Dryer
en	Energy
ex	Exergy
r	Refrigerant
s	Isentropic
v	Water vapor
w	Water
p	Product

Acronyms

C-HPD	Conventional heat pump drying system
COP	Coefficients of performance
EES	Engineering equation solver

EIE	Environmental impact assessment
EV	Expansion valve
GHG	Greenhouse gas
GWP	Global warming potential
HP	Heat pump
HPD	Heat pump drying
HPE	High-pressure evaporator
LCA	Life cycle assessment
LPE	Low-pressure evaporator
ODP	Ozone depleting potential
SC	Sub-cooler
S-HPD	Solar heat pump drying system
SI	Sustainability index

44.1 Introduction

The main cause of global climate change is generally accepted to be growing emissions of greenhouse gases (GHGs) as a result of increased use of fossil fuels. Rising concerns about the effects of global warming and declining fossil fuel stocks have led to increased interest in renewable energy sources such as wind and solar energies [1, 2]. Several methods and analysis are performed by researchers and scientists to reduce the GHG emissions from energy- and material-intensive processes such as industrial and residential processes and transportation.

Drying processes are thermal applications used for various applications as food, wood, clothe drying, residential or industrial conditioning, etc. Drying industry utilizes large quantities of energy, making it one of the most energy-intensive industrial operations. The objective of a dryer is to supply the substance with more heat than is available under ambient conditions, thus sufficiently increasing the vapor pressure of the moisture held within the product to enhance moisture migration from within the product and significantly decreasing the relative humidity of the drying air so as to increase its moisture carrying capability and to ensure a sufficiently low-equilibrium moisture content [3, 4]. Exergy analysis can be used to assess and improve energy systems and can help better understand the benefits of utilizing green energy by providing more useful and meaningful information than energy provides. Exergy clearly identifies efficiency improvements and reductions in thermodynamic losses attributable to green technologies. Exergy can also identify better than energy the environmental benefits and economics of energy technologies. Thus, exergy has an important role to play in increasing utilization of green energy and technologies [5].

Solar energy is a promising renewable technology providing considerable thermodynamic and environmental advantages compared to conventional systems and considered to be the cleanest energy source available. Solar-driven energy systems decrease the GHG emissions, provide reclamation degraded lands, reduce
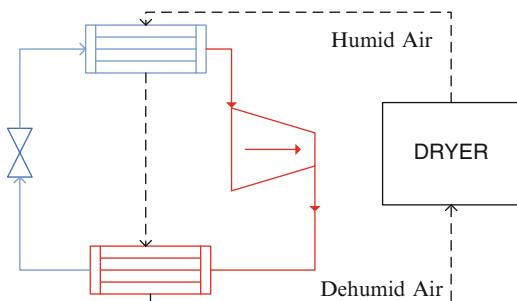
transmission lines of electricity grids, as well as improve socioeconomic parameters such as employment and energy supply security [6, 7]. Solar energy does not cause any emission when the system is running; however there is a considerable amount of emissions during the construction and transportation of solar systems. Several papers have been published to evaluate the environmental impact of solar thermal and solar photovoltaic systems using life cycle assessment (LCA) methodology, considering global warming potential (GWP), acidification, eutrophication of air and water and heavy metals, and cancerogenic factors [8].

In this study a solar-driven two-stage evaporation heat pump drying system is considered. Energy, exergy, sustainability analysis, and environmental impact assessment (EIA) are performed for various environmental and system parameters. Coal, fuel oil, natural gas, Canada mix (2008), nuclear, and solar photovoltaic energy sources are used as the electricity input for the overall system. The following objectives are aimed for this study:
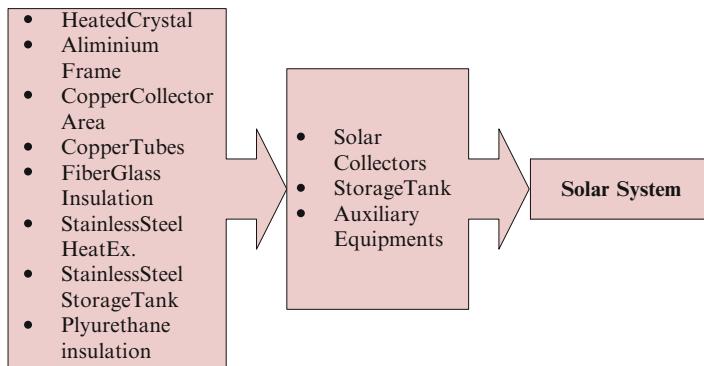
- Comprehensive energy and exergy analyses considering various environmental and system parameters.
- Sustainability and EIA to evaluate some parameters for better sustainability.
- A comparison of conventional and solar-driven system to show the impact of solar energy resource on the environment.

44.2 Heat Pump Drying Systems

The essential goal of drying processes is to produce dehumidified products to a desired value. Drying is one of the most energy-intensive processes and almost 15 % of industrial energy is utilized for drying applications [9, 10]. In developed countries 9–25 % of national energy is used for drying purposes such as wood, textile, and food product drying applications. Thus, it is necessary to utilize better and efficient technologies to reduce the energy consumption [10–13]. Heat pump drying systems are considered to be one of the most efficient thermal systems for drying purposes [14]. A simplified schematic representation of heat pump drying system is shown in Fig. 44.1.

Fig 44.1 Simplified representation of a conventional HPD system

Fig 44.2 Components of an air-type solar system (modified from ref. 8, 21)

Two-stage evaporation system provides two different airstreams with different temperature and humidity. Such a system would ensure the versatility of multiple drying chambers whereby two or more different products requiring different drying conditions can be dried with one heat pump system. Therefore, this system regulates the drying process better than one-stage evaporation heat pumps [15]. This two-stage evaporation is investigated by various researchers and they have concluded that two-stage evaporation heat pump units are superior to one-stage evaporation heat pumps in terms of performance and drying conditions [16–20].

Since it is obvious that solar-driven heat pump drying systems reduce the environmental impact, the life cycle of the solar units should be considered as there are embodied emissions from production and transportation of these units. When compared to fossil fuel electricity generation systems, renewable energy electricity is characterized by a greater share of total environmental impact attributable to fabrication and installation compared to the operation phase [21]. The solar system used in this study is an air-type flat-plate collector which is typical and commonly used for air and water heating. Specification of such system and approximated quantities of materials used for the production are evaluated from the data given in ref. 22. Components of air-type solar collector and relative impact of the system is also graphically represented in Figs. 44.1 and 44.2. This data proportionally changes due to the need for more solar collector area for drying systems [8, 23].
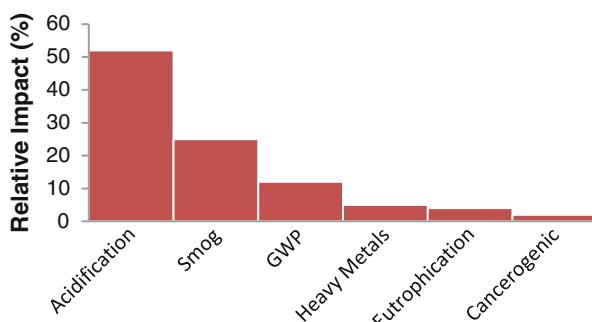
Solar and conventional systems include same components with the exception of solar heat pump drying unit including a solar heating unit in it. Thus, the life cycle and impact assessment for each component of the systems are not considered. Since the energetic and exergetic efficiencies of both C-HPD and S-HPD systems are different, there will be a slight difference between life cycles of the units and S-HPD has an additional emission due to solar system production. However, considering the power consumption of both systems S-HPD is more advantageous in terms of GHG emissions and thermodynamic efficiencies. These analyses are discussed and represented in next sections.

44.3   System Description
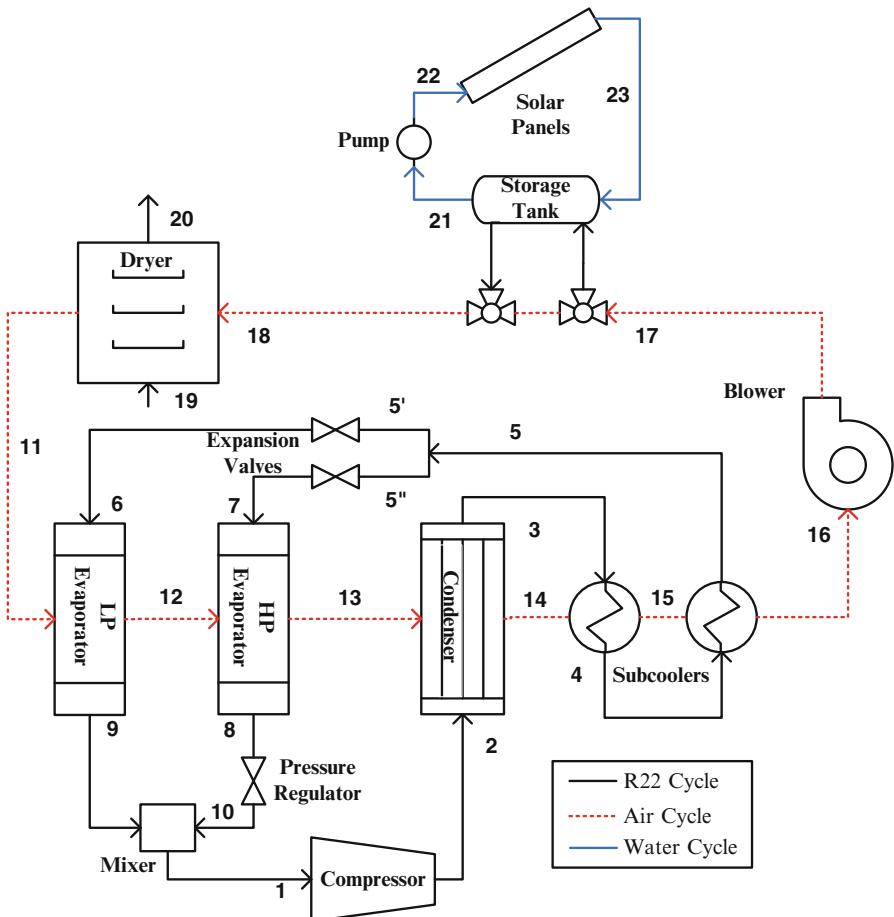
A schematic representation of proposed solar-driven heat pump drying system is
shown in Fig. 44.4. As mentioned in Sect. 44.2, multistage evaporation heat pump
systems show better energy and exergy efficiencies. Considered solar-driven heat
pump drying system is integrated to a two-stage high- and low-pressure evaporation
heat pump. Humid air enters to low-pressure evaporator and high-pressure evapo-
rator for dehumidification. Dehumidified air enters to condenser, sub-cooler 1, and
sub-cooler 2, respectively. Heated air is at a low temperature and not at the desired
conditions for the dryer input. Thus, air-type flat-plate solar collectors are
integrated to the system to obtain the desired temperature inlet to the dryer. For
the conventional system, it is assumed that the energy input from the solar
collectors is taken from electric grid and desired temperature input is improved
for the dryer. Two-stage evaporation heat pump unit is modified from ref. 15
(Fig. 44.4).

Heat pump system consists of a compressor, condenser, sub-cooling units, two
expansion valves, high- and low-pressure evaporators, back-pressure regulator
valve, and a mixer. R22 is used as refrigeration fluid. The refrigerant is at high
pressure in superheated region at condenser inlet. Assuming that the refrigerant is
totally condensed at the condenser, it extracts some heat to the air cycle with
sub-coolers. Cooled down fluid refrigerant expands with expansion valves into
two different pressures and gets into high- and low-pressure expansion valves.
Assuming that the refrigerant is totally evaporated, it is brought to the
low-pressure side of refrigerant with back-pressure regulator valve and two streams
are mixed in the mixing chamber.

During the analysis, each input is varied within certain ranges in order to
understand the effects of each parameter. Solar global radiation (S_t), refrigerant
and air mass flow rates, compressor isentropic efficiency (η_s), desired dryer input
temperature, ambient pressure (P_0) and temperature (T_0) and wind speed (v_0)
variation, specific humidity ratio (w), heat exchanger efficiencies (η_{hex}), and solar
system parameters have strong influences of component and overall system

Fig. 44.3 Relative impact of solar system production (modified from ref. 8)

Fig. 44.4 Schematic representation of solar-driven heat pump drying system (adapted from ref. 15)

efficiencies in terms of energy and exergy. Thus, some system parameters and their ranges are represented in Table 44.1. Effect of these parameters on efficiencies is graphically discussed in results and discussion section.

HCFC-22 refrigerant is a replacement for HCFC-12 refrigerant with lower ozone depletion potential (ODP). However, the chlorine atoms still deplete the ozone layer with reacting O_3 atoms. Natural hydrocarbons are promising replacements for ozone-depleting refrigerants with lower GWP but the higher flammability of these refrigerants is still an existing problem for large-scale heat pump systems. Considering the hazardous effects of natural refrigerants, HCFC-22 is selected to be the running fluid in the heat pump system [25]. A comprehensive mass, energy, exergy, and sustainability analysis and EIA of the solar-driven and conventional heat pump drying systems are represented in Sect. 4. Formulations for evaluating efficiencies, exergy destructions, and GHG emissions are also explained in detail.

Table 44.1 System property data and parameters (adapted from refs. [15], [24])

Property	Unit	Range of variation
Compressor isentropic efficiency (η_s)	(%)	90–95
Heat exchanger efficiency (η_{hex})	(%)	75–90
Specific heat of air (C_a)	(kJ/kg °C)	1.004
Specific heat of water (C_v)	(kJ/kg °C)	1.872
Sun temperature (T_{sun})	K	5,762
Ambient temperature (T_0)	K	285–300
Ambient pressure (P_0)	kPa	90–110
Global solar radiation (S_t)	kW/m^2	0.3–0.9
Ambient velocity (v)	m^2/s	0.2–0.5
Solar panel area	m^2	20–40
Refrigerant mass flow rate $\dot{m}_{ref}$	kg/s	0.05–0.07
Air mass flow rate $\dot{m}_a$	kg/s	0.4–0.5
Dryer input temperature	K	320–340
Working refrigerant	–	HCFC22
Humidity ratio (w)	g water/kg air	2–14

44.4 Thermodynamic Analyses

In this section, thermodynamic and environmental analysis of the HPD system is discussed in detail. Energy and exergy efficiencies, GHG emissions, and sustainability index are defined in terms of component-based balance equations for mass, energy, entropy, and exergy. The thermodynamic analysis and EIA are applied to the considered system and results are discussed in the next section. Following assumptions are made during the analysis [e.g., Eq. 44.4]:

- All processes through the system are of steady state and steady flow.
- Air is treated as ideal gas.
- Potential and kinetic energies of the overall system are negligibly small.
- Compressor is taken to be internally and externally reversible, and its isentropic efficiency is 95 %.
- No pressure drops and heat exchange during the components and piping.
- Temperature of sun is taken to be 5,762 K [24].
- Specific heats of air and water are constant during the process.

A general mass, energy, and entropy balance for the heat pump drying system is defined as follows:

$$\sum \dot{m}_{in} = \sum \dot{m}_o \tag{44.1}$$

$$\sum \dot{m}_i h_i = \sum \dot{m}_o h_o \tag{44.2}$$

$$\sum \dot{m}_i s_i + \dot{S}_{gen} = \sum \dot{m}_o s_o \tag{44.3}$$

$$\sum \dot{m}_i ex_i = \sum \dot{m}_o ex_o + \dot{Ex}_d + \dot{Ex}^Q \qquad (44.4)$$

where $\dot{m}$ is mass flow rate, h is enthalpy, s is entropy, and ex is exergy of the matter at the considered state. $\dot{S}_{gen}$, $\dot{Ex}_d$, and $\dot{Ex}^Q$ refer to entropy generation rate, exergy destruction rate, and thermal exergy rate of the stream, respectively. Subscripts i and o represent inputs and outputs. Thermal exergy rate and exergy of water, refrigerant, and air as well as exergy rate are defined as follows [4, 26]:

$$\dot{Ex}^Q = \left(1 - \frac{T_L}{T_H}\right) \cdot \dot{Q} \qquad (44.5)$$

$$ex_{w,r} = (h - h_0) - T_0(s - s_0) \qquad (44.6)$$

$$\begin{aligned} ex_a = (Cp, a + \omega Cp, v)T_0[(T/T_0) - 1 - \ln(T/T_0)] &+ (1 + 1.6078\omega)RaT_0 \ln(P/P_0) \\ + RaT_0\{(1 + 1.6078\omega) \ln[(1 + 1.6078\omega_0)/(1 + 1.6078\omega)] \\ + 1.6078\omega \ln(\omega/\omega_0)\} \end{aligned}$$

$$(44.7)$$

$$\dot{Ex} = \dot{m}(ex) \qquad (44.8)$$

where Cp_a, Cp_v, R_a, and w represent specific heats of air and water vapor, gas constant of air, and specific humidity ratio and subscript 0 represents ambient condition. The generalized energy and exergy efficiencies are defined as follows:

$$COP_{HP} = \frac{\dot{Q}_{evap}}{\dot{W}_{comp}} \qquad (44.9)$$

$$\eta = \frac{\dot{E}_{out}}{\dot{E}_{in}} \qquad (44.10)$$

$$\psi = \frac{\dot{Ex}_{useful}}{\dot{Ex}_{in}} \qquad (44.11)$$

Here, COP is coefficient of performance for the heat pump system, and η and ψ are energy and exergy efficiency of the overall system and components. Since the EIA is based on the exergy destructions and exergetic efficiencies of the system, these data are tabulated in Table 44.2. For the solar-driven heat pump unit, exergy of sun is considered as the input to the system. Energy and exergy definitions for the solar system are defined as follows [27]:

$$\dot{Ex}_{sun} = \left(1 - \frac{T_0}{T_{sun}}\right) \cdot S_t.A \qquad (44.12)$$

Table 44.2 Exergy efficiencies and exergy destructions of the system components

Part	Exergy efficiency	Exergy destruction rate
Compressor	$(\dot{E}x_{2,act} - \dot{E}x_1)/\dot{W}_{comp}$	$\dot{E}x_{D,comp} = T_0\dot{m}_r(s_{2,act} - s_1)$
Condenser	$(\dot{E}x_{14} - \dot{E}x_{13})/(\dot{E}x_2 - \dot{E}x_3)$	$\dot{E}x_{D,cond} = T_0[\dot{m}_r(s_2 - s_3) - \dot{m}_a(s_{14} - s_{13})]$
Sub-cooler I	$(\dot{E}x_{15} - \dot{E}x_{14})/(\dot{E}x_3 - \dot{E}x_4)$	$\dot{E}x_{D,SCI} = T_0[\dot{m}_r(s_3 - s_4) - \dot{m}_a(s_{15} - s_{14})]$
Sub-cooler II	$(\dot{E}x_{16} - \dot{E}x_{15})/(\dot{E}x_4 - \dot{E}x_5)$	$\dot{E}x_{D,SCII} = T_0[\dot{m}_r(s_4 - s_5) - \dot{m}_a(s_{16} - s_{15})]$
Evaporator (HP)	$(\dot{E}x_{12} - \dot{E}x_{13})/(\dot{E}x_7 - \dot{E}x_8)$	$\dot{E}x_{D,HPE} = T_0[\dot{m}_r(s_7 - s_8) - \dot{m}_a(s_{12} - s_{13})]$
Evaporator (LP)	$(\dot{E}x_{11} - \dot{E}x_{12})/(\dot{E}x_9 - \dot{E}x_6)$	$\dot{E}x_{D,LPE} = T_0[\dot{m}_r(s_9 - s_6) - \dot{m}_a(s_{11} - s_{12})]$
Expansion valve I	$(\dot{E}x_6/\dot{E}x_{5'})$	$\dot{E}x_{D,EVI} = T_0\dot{m}_r(s_6 - s_{5'})$
Expansion valve II	$(\dot{E}x_7/\dot{E}x_{5''})$	$\dot{E}x_{D,EVII} = T_0\dot{m}_r(s_7 - s_{5''})$
BP regulator valve	$(\dot{E}x_{10}/\dot{E}x_8)$	$\dot{E}x_{D,BPRV} = T_0\dot{m}_r(s_{10} - s_8)$
Mixer	$(\dot{E}x_1/(\dot{E}x_{10} + \dot{E}x_9)$	$\dot{E}x_{D,MIX} = T_0\dot{m}_r(s_1 - s_9 - s_{10})$
Blower	$(\dot{E}x_{17} - \dot{E}x_{16})/\dot{W}_{fan}$	$\dot{E}x_{D,B} = T_0\dot{m}_r(s_{17} - s_{16})$
Solar panels	$\dfrac{\dot{E}x_{out} + \left(1 - \frac{T_0}{T_{sp}}\right)\dot{Q}_{sp}}{\dot{E}x_{sun}}$	$\dot{E}x_{D,SP} = T_0\dot{m}_a(s_{18} - s_{17}) - \left(\frac{\dot{Q}_{Solar}}{T_{SP}}\right)$
Storage tank	$(\dot{E}x_{23} - \dot{E}x_{21})/(\dot{E}x_{18} - \dot{E}x_{17})$	$\dot{E}x_{D,ST} = T_0[\dot{m}_w(s_{23} - s_{21}) - \dot{m}_a(s_{18} - s_{17})]$
Solar pump	$(\dot{E}x_{22} - \dot{E}x_{21})/\dot{W}_{pump}$	$\dot{E}x_{D,P} = T_0\dot{m}_w(s_{22} - s_{21})$
Dryer	$(\dot{E}x_{20} - \dot{E}x_{19})/(\dot{E}x_{18} - \dot{E}x_{11})$	$\dot{E}x_{D,Dry} = T_0[\dot{m}_a(s_{20} - s_{19}) - \dot{m}_p(s_{18} - s_{11})]$
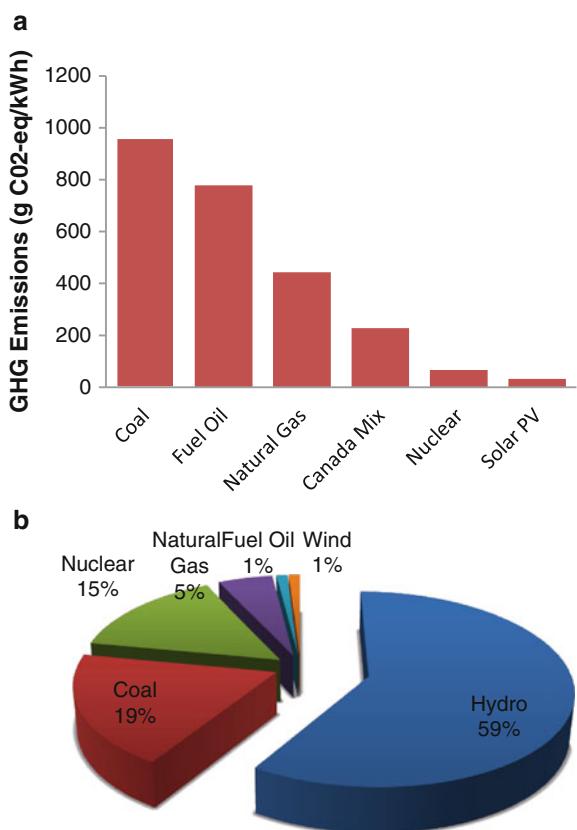
$$\psi_{sun} = \frac{\dot{E}x_{out} + \left(1 - \frac{T_0}{T_{sp}}\right)\dot{Q}_{sp}}{\dot{E}x_{sun}} \tag{44.13}$$

where A, S_t, and Q_{sp} indicate solar panel area, global solar radiation, and solar panel heat to air. Subscripts *sun* and *sp* represent sun and solar panels. Another way to understand the scope for improvement at the design stage as well as in the existing system is through the sustainability index (SI). Sustainability index is directly related to the exergy efficiency; thus sustainability should be considered together with exergy analysis. It shows how exergy methods are essential in improving performance that allows the society to benefit from it. As the sustainability index increases, it means better sustainability is obtained [3, 28]:

$$SI = \frac{1}{1 - \psi} \tag{44.14}$$

Exergy efficiencies and exergy destruction rates for every component of the solar-driven heat pump drying system are defined with the state points as mentioned in Table 44.2. Overall system efficiencies and sustainability of both conventional and solar-driven HPD systems are evaluated in terms of efficiency definitions given in Eqs. 44.10–44.14. Other tabulated exergy efficiency and exergy destruction rate definitions are obtained from mass, energy, entropy, and exergy analysis for each state point defined in system scheme. Exergy destructions are defined to be associated with the entropy generation of each component. This definition can be

Fig. 44.5 GHG emissions (**a**) from electricity generation resources and (**b**) Canadian grid mixture content (2008)

made with exergy balance equations by defining the difference between input and output exergy rates of streams in each component. Thermal exergy should also be included for both definitions as conducted for the entropy generation methodology.

A comparative assessment of these resources is performed in the results section and variation of GHG emissions with increasing exergy efficiency is graphically represented as well as the sustainability index in order to show the influence of thermodynamic performance of system on emission and sustainability.
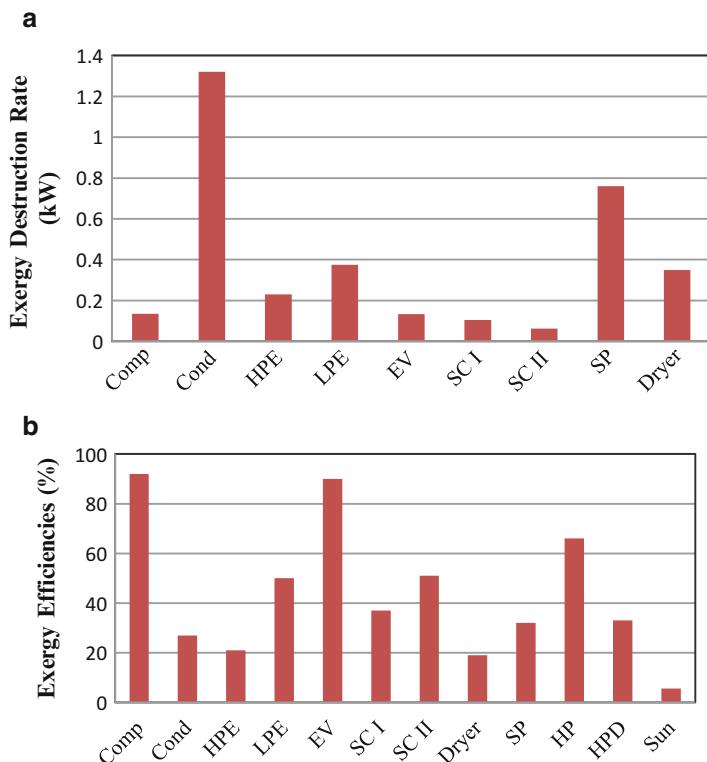
As for the EIA, GHG emissions, for electricity generation options are comparatively evaluated.

GHG emissions from considered power sources are represented in Fig. 44.5a, b. The emissions from these sources are 960, 778, 443, 228, 66, and 32 g CO_2-eq/kWh for coal, fuel oil, natural gas, Canada mix, nuclear, and solar PV, respectively [29–32]. Canadian grid consists of 59 % hydropower, 19 % coal, 15 % nuclear, 5 % natural gas, 1 % fuel oil, and 1 % wind. Since the total percentage of clean energy such as hydropower and nuclear has a higher percentage of 75 %, emissions from Canadian grid mixture are lower than that of coal, fuel oil, and natural gas by 76, 70, and 48 %, respectively. However, the emissions from Canadian grid mixture are

higher than those of nuclear and solar PV since it contains fossil fuel-based generation by 25 %. These emissions are related to the system power consumption and emissions for both solar-driven and conventional HPD systems are evaluated and discussed.

44.5 Results and Discussion

Thermodynamic analysis of the conventional and solar heat pump drying systems is performed using engineering equation solver (EES) software program and results are graphically represented [33]. Exergy destructions and exergy efficiencies of the components and overall system are shown in Fig. 44.6a, b. Among all components, the heat exchangers have the lowest exergy efficiencies with respect to the high temperature differences and resulting more entropy generation between the refrigerant and air. Based on the conducted analysis, the exergy destruction rates for the components are determined to be in the following descending order:
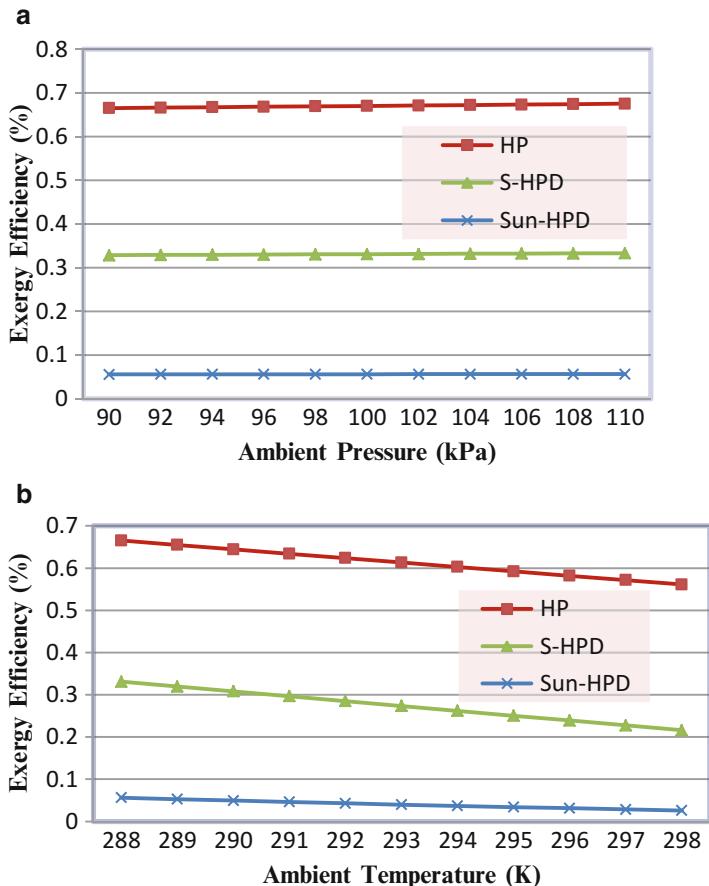
Fig. 44.6 Solar HPD: (**a**) Exergy destruction rates of components and (**b**) exergy efficiencies of components and overall system

compressor 0.135 kW, condenser 1.32 kW, sub-cooler I 0.105 kW, sub-cooler II 0.0625 kW, HP evaporator 0.229 kW, LP evaporator 0.3749, expansion valves 0.133 kW, solar panels 0.76 kW, and dryer 0.35 kW.
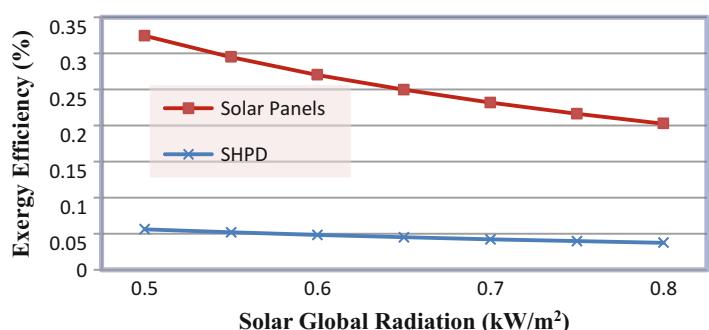
Since the compressor is assumed to be internally and externally reversible, it has one of the highest exergy efficiencies among all components by 92 %. Exergy efficiencies of system components are in the following order: condenser 27 %, HP evaporator 21 %, LP evaporator 50 %, expansion valves 90 %, sub-cooler I 37 %, sub-cooler II 51 %, and dryer 19 %. Exergy efficiency of the heat pump system is found to be 66 %. Exergy efficiency of S-HPD system is found to be 32.7 % for the baseline model. Considering the exergy of sun as the main input to solar collectors, total exergetic efficiency of the overall system is found to be 6 %. This low efficiency indicates that the solar energy cannot be used efficiently with the existing solar systems. Even if more efficient systems are commercially produced, solar exergy will always be superior due to the temperature of sun. In the analysis exergy efficiency of solar panels is considered instead of exergy of sun; however low efficiency from sun is to indicate that solar systems are still inefficient in terms of receiving energy from sun.

The ambient pressure and temperature variation effects on the exergy efficiency of heat pump system and overall heat pump drying system are shown in Fig. 44.7a, b. A pressure variation of 20 kPa increases overall efficiencies by 1.3–1.4 %. It is expected that higher ambient pressures will increase the exergy efficiency of the HPD system. However, the ambient pressure is generally constant and its effect on exergy efficiencies is almost negligible. Ambient temperature influences the system exergy more than that of ambient pressure. Considering 10 K of variation, solar heat pump drying exergy efficiency decreases by 36 %. The HPD system performance is better at lower ambient temperatures. It is expected that performance of the system will decrease in summers and increase in winters. However, cloudy nature of winters will decrease the solar radiation and solar HPD performance is dependent on this parameter and the ambient temperature as well. However, this conclusion is made considering Eq. 44.12. Solar systems provide higher amounts of energy in summer times, which is practically desired.

Solar global radiation effect on solar panel and overall exergy efficiencies are exhibited in Fig. 44.8. It is expected that solar radiation increase also increases the exergy efficiency; however the more the solar radiation is, the more the sun of exergy. Thus, since exergy of sun is denominator for the exergy efficiency of solar panels, exergy efficiency of solar panels in terms of sun temperature decreases by 37 % and overall exergy efficiency by 25 % with an increase of 0.3 kW/m^2 at solar global radiation. The best option for solar global radiation is found to be 0.5 kW/m^2 for the system. To increase the solar exergy received by sun, increasing the solar panel area is the best option. Solar panel area effect on the system overall exergy efficiency is represented by Fig. 44.9. Exergy efficiency associated with exergy of sun increases by 45.3 % with a variation of 20 m^2 solar panel area. Increasing solar panel area linearly increases the exergy efficiency; however, GHG emissions also increase since production of raw materials also increases. Optimum solar panel area

a

b

Fig. 44.7 Effect of environmental parameters on exergy efficiency: (**a**) Pressure and (**b**) temperature

Fig. 44.8 Effect of solar global radiation on total and solar panel exergy efficiency
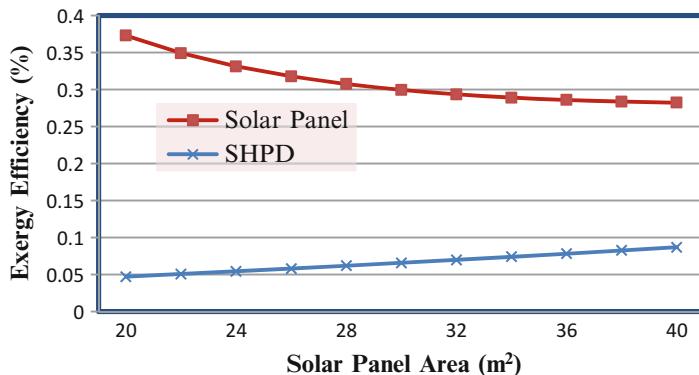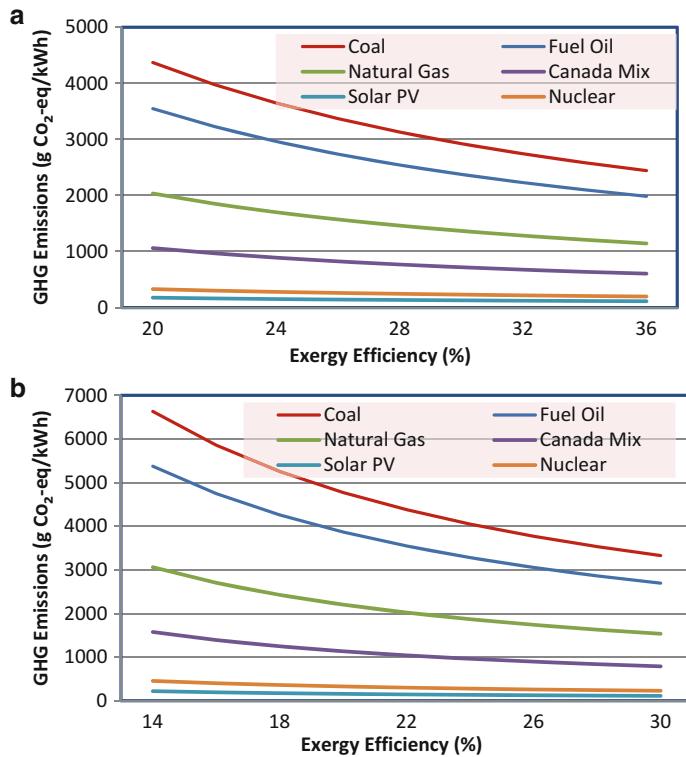
Fig. 44.9 Solar panel area effect on the solar panel and total exergy efficiency

for the existing S-HPD system is found to be 28 m^2. Solar panel area is calculated considering the desired dryer inlet temperature.

Another environmental parameter, wind speed, is also a varying environmental parameter influencing the solar panel performance by a decrease of up to 25 %. Heat convection coefficient is influenced by the Nusselt number and this dimensionless number is affected by the ambient velocity. This environmental parameter increases and decreases during the operation of the system and makes a slight effect on the overall exergy efficiency of the S-HPD system. Conventional HPD system is not influenced by solar global radiation, ambient velocity, and other solar parameters.

Corresponding indirect emissions and the sustainability indices are determined with respect to the system parameters of the solar and conventional heat pump drying systems. The sustainability index is a good indicator of how efficiently the resources are utilized in the solar-driven and conventional HPDs. Thus, it is therefore directly related to the exergy efficiencies and exergy destruction rates associated with each HPD systems. Moreover, the indirect GHG emissions are produced from electricity generation associated with the compressor, blower, and solar pump work. Fig. 44.10a, b represents the variation of GHG emissions from six different generation resources for the S-HPD and C-HPD systems. Exergy efficiency of S-HPD system varies in terms of mass flow rate of air and HCFC-22 and ambient parameters such as temperature, pressure, ambient velocity, and global solar radiation. These parameters can vary the total exergy efficiency of the system between 20 and 36 %. Considering this variation, emissions from coal, fuel oil, natural gas, Canadian grid mixture, nuclear, and solar PV decrease by 40–44 %. This significant decrease occurs only with a performance increase of 20 %. It is of crucial importance to phase out fossil fuel power production units to decrease emissions. Renewable resources as solar PV have even lower emissions from nuclear plants.

Table 44.3 represents the emissions for six generation resources for both solar-driven and conventional HPD systems for the baseline model. GHG emissions from solar panel LCC analysis are found to be 32 g CO2-eq/kWh for the solar-driven
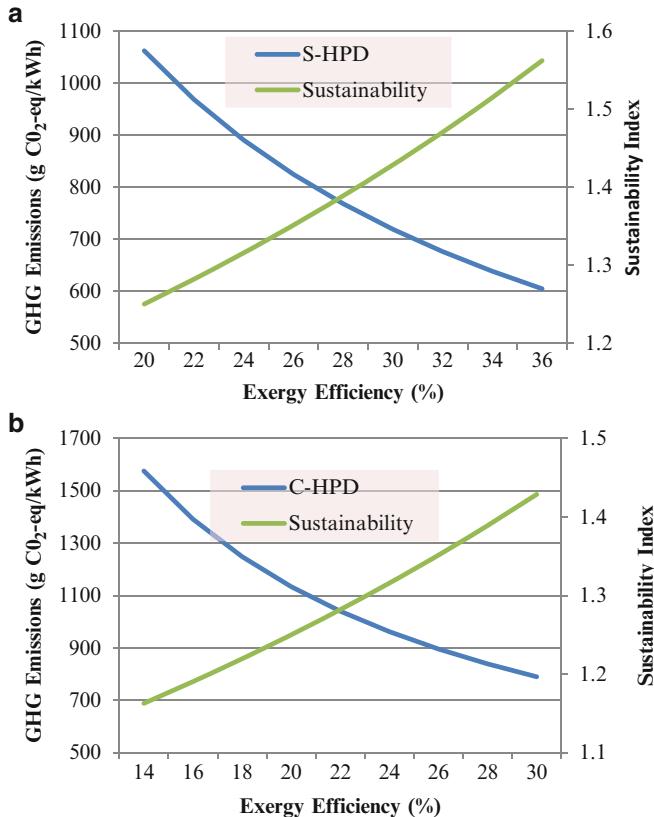
Fig. 44.10 GHG emissions: (**a**) Solar-driven HPD system and (**b**) conventional HPD system

Table 44.3 GHG emissions (gCO$_2$eq/kWh) from generation resources for the baseline model HPDs

Baseline model	Coal	Fuel oil	Natural gas	Canada mix	Nuclear	Solar PV
S-HPD	2,744	2229.85	1283.475	676.1	218.45	175.17
C-HPD	5,255	4258.9	2,425	1248.1	361.29	200.18

system. This evaluated value is also added to the total emissions. However, GHG emissions from conventional HPD system are 20.4–34.1 % higher than those of solar-driven HPD system for different generation resources. Highest emissions are from coal generation resource and lowest emissions are from nuclear and solar PV generation resources for both solar-driven and conventional HPD systems.

Considering the Canadian grid mixture, GHG emissions and sustainability index variation are given in Fig. 44.11. For the baseline models GHG emissions from Canadian grid are evaluated to be 676.1 and 1248.1 g CO$_2$eq/kWh for S-HPD and C-HPD and sustainability indices are 1.49 and 1.20, respectively. Exergy efficiencies of both systems are dependent on system and environmental parameters. Sustainability index of solar-driven HPD system is 19.2 % higher and GHG emissions are 45.8 % lower than the conventional HPD system.

Fig. 44.11 GHG emissions and sustainability index with respect to overall exergy efficiencies considering Canada electricity mixture: (**a**) Solar-driven HPD and (**b**) conventional HPD

Thermodynamic performance of drying systems and integration of renewable energy resources to such systems strongly influence the sustainability and GHG emissions. High-energy- and -exergy-efficient thermal system design and transition to environmentally friendly resources for power generation are of importance for sustainable development and lower GHG emissions.

44.6   Conclusions

In this chapter, energy, exergy, and sustainability analysis and EIA of drying processes are performed for conventional and solar-driven two-stage evaporator heat pump drying systems. Some parametric studies are also performed to designate the influence of environmental and system parameters on the overall efficiencies.

GHG emissions from different generation resources are also presented. The following findings are obtained from the analysis:

- Among all components, the heat exchangers have the lowest exergy efficiencies with respect to the high temperature differences and resulting more entropy generation between the refrigerant and air. Based on the conducted analysis, the exergy destruction rates for the components are determined to be in the following descending order: compressor 0.135 kW, condenser 1.32 kW, sub-cooler I 0.105 kW, sub-cooler II 0.0625 kW, HP evaporator 0.229 kW, LP evaporator 0.3749, expansion valves 0.133 kW, solar panels 0.76 kW, and dryer 0.35 kW.
- Exergy efficiency of S-HPD system is found to be 32.7 % for the baseline model. Considering the exergy of sun as the main input to solar collectors, total exergetic efficiency of the overall system is found to be 6 %. Exergy efficiency of the baseline conventional HPD system is 16.7 %. Exergy efficiency of the S-HPD system is 48.9 % higher than that of C-HPD system.
- GHG emissions from conventional HPD system are 11–34.1 % higher than those of solar-driven HPD system for different generation resources. Highest emissions are from coal generation resource and lowest emissions are from nuclear and solar PV generation resources for both solar-driven and conventional HPD systems.
- For the baseline models GHG emissions from Canadian grid are evaluated to be 676.1 and 1248.1 g CO_2eq/kWh for S-HPD and C-HPD and sustainability indices are 1.49 and 1.20, respectively. Exergy efficiencies of both systems are dependent on system and environmental parameters. Sustainability index of solar-driven HPD system is 19.2 % higher and GHG emissions are 45.8 % lower than the conventional HPD system considering Canadian grid mixture as the generation resource.
- Thermodynamic performance of drying systems and integration of renewable energy resources to such systems strongly influence the sustainability and GHG emissions. Design of efficient thermal systems and phase out of fossil fuels are of importance for a sustainable development.

References

1. Granovskii M, Dincer I, Rosen MA (2007) Greenhouse gas emissions reduction by use of wind and solar energies forhydrogen and electricity production: economic factors Int. J Hydrogen Energ 32:927–931
2. Wuebbles DJ, Atul KJ (2001) Concerns about climate change and the role of fossil fuel use. Fuel Process Technol 71:99–119
3. Dincer I (2011) Exergy as a potential tool for sustainable drying systems, Sus. Cities and Society 1:91–96
4. Dincer I, Rosen MA (2007) Exergy, energy environment and sustainable development, 2nd edn. Elsevier, Oxford, UK
5. Rosen MA, Dincer I, Kanoglu M (2008) Role of exergy in increasing efficiency and sustainabilityand reducing environmental impact. Energ Pol 36:128–137

6. Tsoutsos T, Frantzeskaki N, Gekas V (2005) Environmental impacts from the solar energy Technologies. Energ Pol 33:289–296
7. Various, Karapanagiotis N (Ed.) (2000) Environmental impacts from the use of solar energy technologies. THERMIE
8. KoroneosCJ NEA (2012) Life cycle environmental impact assessment of a solar water heater. J Clean Prod 37:154–161
9. Goh LJ, Othman MY, Mat S, Ruslan H, Sopian K (2011) Review of heat pump systems for drying application. Rene and SusEnr Rev 15:4788–4796
10. Sun L, Islam MR, Ho JC, Mujumdar AS (2005) A diffusion model for drying of a heat sensitive solid under multiple heat input modes. Bioresour Technol 96:1551–1560
11. Chua KJ, Mujumdar AS, Hawlader MNA, Chou SK, Ho JC (2001) Batch drying of banana pieces—effect of stepwise change in drying air temperature on drying kinetics and product color. Food Res Int 34:721–731
12. Ogura H, Yamamoto T, Otsubo Y, Ishida H, Kage H, Mujumdar AS (2005) A control strategy for chemical heat pump dryer. Dry Technol 23:1189–1203
13. Mujumdar AS (1987) Handbook of industrial drying, 2nd edn. Marcel Dekker, New York, USA
14. Mujumdar AS (2005) Handbook of industrial drying, vol 2. Marcel Dekker Inc, New York, NY, pp 1241–1272
15. Chua KJ, Chou SK (2005) A modular approach to study the performance of a two-stage heat pump system for drying. Appl Therm Eng 25:1363–1379
16. Li CJ, Su CC (2003) Experimental study of a series-connected two-evaporator refrigerating system with propane (R-290) as the refrigerant. Appl Therm Eng 23:1503–1514
17. Brundrett GW (1987) Handbook of dehumidification technology, vol 1. Butterworths, London, p 138
18. Rose RJ, Jung DS, Radermacher R (1992) Testing of domestic two-evaporator refrigerators withzeotropic refrigerant mixtures. ASHRAE Transaction 98:216–226
19. Jung DS, Radermacher R (1991) Performance simulation of a two-evaporator refrigerator–freezer charged with pure and mixed refrigeration. Int J Refrig 14:254–263
20. Simmons KE, Haider I, Radermacher R (1996) Independent compartment temperature control of Lorenz–Meutzner and modified Lorenz–Meutzner cycle refrigerators. ASHRAE Transaction 102:1085–1092
21. Brian Norton B, Eames PC, Lo SNG (1998) Full-energy-chain analysis of greenhouse gas emissions for solar thermal electric power generation systems. Renew Energ 15:131–136
22. Eco-Indicator 99: A damage oriented method for life cycle impact assessment (2000), Ministry of housing, spatial planning and environment. doi: http://www.pre-sustainability.com/down load/manuals/EI99_Manual.pdf
23. Kreith F, Kreider JF (1978) Principles of solar engineering. McGraw-Hill, New York
24. Akyuz E, Coskun C, Oktay Z, Dincer I (2012) A novel approach for estimation of photovoltaic exergy efficiency. Energy 44:1059–1066
25. Powell RL (2002) CFC phase out: have we met the challenge? J Flourine Chem 114:237–250
26. Wepfer WJ, Gaggioli RA (1980) Reference datums for available energy. Thermodynamics: second Law analysis, ACSSymposium series, vol 122. American Chemical Society, Washington, DC, pp 77–92
27. Kalogirou SA (2004) Solar thermal collectors and applications. Progr Energ Combust Sci 30:231–295
28. Hammond GP (2004) Engineering sustainability: thermodynamics, energy systems, and the environment. Int J Energ Res 28:613–639
29. Parliementary office of science and technology (2011) Carbon footprint of electricity generation. doi: http://www.parliament.uk/documents/post/postpn_383-carbon-footprint-electricity-generation.pdf
30. International energy Agency (2012) CO2 Emissions from fuel combustion highlights. doi: http://www.iea.org/co2highlights/co2highlights.pdf

31. National inventory report NIR (2010) Greenhouse gas sources and sinks in Canada, submission to UN framework convention on climate change Part 3, Canada, doi: http://unfccc.int/national_reports/annex_i_ghg_inventories/national_inventories_submissions/items/6598.php
32. Sovacool BK (2008) Valuing the greenhouse gas emissions from nuclear power: a critical survey. Energ Pol 36:2940–2953
33. Engineering equation solver (2009) version 8.176. F-Chart Software, Box 44042, Madison, WI, USA

Chapter 45
Regional Energy Planning Tool for Renewable Integrated Low-Energy District Heating Systems: Environmental Assessment

Hakan İbrahim Tol, Ibrahim Dincer, and Svend Svendsen

Abstract Low-energy district heating systems, operating at low temperature of 55 °C as supply and 25 °C as return, can be the energy solution as being the prevailing heating infrastructure in urban areas, considering future energy schemes aiming at increased exploitation of renewable energy sources together with low-energy houses in focus with intensified energy efficiency measures. Employing low-temperature operation allows the ease to exploit not only any type of heat source but also low-grade sources, i.e., renewable and industrial waste heat, which would otherwise be lost. In this chapter, a regional energy planning tool is described considered with various energy conversion systems based on renewable energy sources to be supplied to an integrated energy infrastructure involving a low-energy district heating, a district cooling, and an electricity grid. The developed tool is performed for two case studies, one being Greater Copenhagen Area and the other Greater Toronto Area, in accordance with various climate conditions and available resources in these locations, CO_2 emission savings obtained with up to 880 and 1,400 M tons, respectively.

Keywords Regional energy planning • Low-energy • Low temperature • District heating • Renewable energy • Integrated energy distribution • Renewable integrated low-energy district heating systems • Environmental assessment • Intensified energy efficiency measures • Low-grade sources • Industrial waste heat • Regional energy planning tool • Integrated energy infrastructure • Low-energy district

H.İ. Tol (✉) • S. Svendsen
Department of Civil Engineering, Technical University of Denmark, Brovej, Building 118, 2800 Kgs. Lyngby, Denmark
e-mail: hatol@byg.dtu.dk; ss@byg.dtu.dk

I. Dincer
Faculty of Engineering and Applied Science, University of Ontario Institute of Technology, 2000 Simcoe Street North, Oshawa, ON, Canada L1H 7K4
e-mail: Ibrahim.Dincer@uoit.ca

heating • District cooling • Electricity grid • Copenhagen • Toronto area • CO_2 emission savings

45.1   Introduction

As long-term energy solutions, energy supply systems based on renewable energy sources have been of considerable interest to policy makers due to such systems being more environmentally friendly than those of fossil fuels that lead to depletion [1, 2]. District heating has shown its weightiness as a sustainable solution to community-wide energy supply system due to its benefits of being energy efficient in urban scale, ease of connecting to any type of heat source, and improved comfort levels provided to houses even in cold climate conditions [3, 4]. Aims focused on reducing the residential heat consumptions, together with the increasing exploitation of renewable energy sources for providing heat, have led to a new concept of district heating systems with improved efficiency measures by means of low-temperature operation such as 55 °C in the case of supply and 25 °C in the case of return [5, 6]. Various advantages have been observed regarding low operating temperatures in district heating systems, such as (a) reduced heat loss from the network and the network equipment, (b) increased efficiency of generating heat at the production site, (c) ease of exploiting low-grade heat sources such as waste heat from industrial facilities which otherwise gets lost, and (d) improved indoor thermal comfort at the consumer site with lowered speeds of air circulation, prevented dehydration of air, and reduced risk of skin burns [6–9].

Hence, the intention of this research was directed to design an energy planning tool on the regional basis with focus being given to determining the capacities of renewable-based energy conversion systems to regional heat requirements, which involves space heating and domestic hot water production.

45.1.1   Background

It can be rewarding to provide adequate background information for a better understanding of both concepts with respect to (a) the developments presented regarding the field of low-energy district heating systems and (b) various emphases considered in the models of energy planning tools presented by some of the studies in this field.

Low-Energy District Heating Systems

A preliminary project in this field [5, 6] has presented the concept of low-temperature operation (50 °C as supply and 25 °C as return) in low-energy

district heating systems with detailed analysis, in particular, being performed with respect to (a) heat demand of low-energy houses, (b) substation configurations in proper to low-temperature operation, (c) twin-pipe utilization in the district heating network, and (d) socioeconomic assessment of employing low-energy district heating systems in comparison to alternative heating option considered with equipping an individual heat pump at each house located in the district. The observations regarding the case studies taken in this research showed that low-energy district heating systems are competitive in socioeconomic perspective compared to alternative heating systems. Several successful examples of employing low-energy district heating systems have been demonstrated in case projects in Lystrup, Denmark [10, 11]; in the SSE Greenwatt Way development project in Slough in the UK [12]; in the Drake Landing Solar Community project in Okotoks, Alberta, Canada [13]; and in Munich, Germany [14].

Various analyses have been performed in order to investigate the further improvements in employing low-energy district heating systems in addition to the benefits achieved by means of low-temperature operation. Torio [15] performed exergy analysis on low-energy systems involving heating and cooling, operating in low temperatures and high temperatures, respectively, in assessing exergy performance with different scopes such as in the levels of human thermal comfort, building, community, and heat source. Christiansen [11] and Brand [16] presented detailed description of substation configurations, equipped either with storage tank or without, both in proper with low-temperature operation. Tol and Svendsen [17, 18] addressed various aspects of designing low-energy district heating systems, details being given regarding (a) determination of pipe dimensioning methods; (b) comparative assessment of substation types, either equipped with storage tank or not; and (c) the effect of consumer behavior on the energy performance of the network layouts, either branched or looped.

Regional Energy Supply Planning

Lund et al. [19] assessed expansion scenarios of renewable-based district heating in urban and rural areas located at Denmark. Their results concluded in prevailing use of district heating systems in the urban areas to be considered as the future national energy supply scheme. However, the energy supply in the rural areas was found to be relied on individual heat pump systems for the purpose of heating. Sperling and Möller [20, 21] addressed that expending the network of district heating when considered together with improved residential energy performance improves the heat production efficiency. Østergaard and Lund [22] proposed a transition period for the Frederikshavn energy infrastructure—considering electricity, heat, and fuel required for industry and transportation system—to be based totally on renewable energy. Mathiesen [23] carried out a comparative analysis focused on exploiting biomass considered either in the heat sector or in the industrial sectors. The results highlighted using biomass in industrial sectors more than heating sector. Weber and

Shah [24] presented a communal energy supply tool DESDOP with respect to meeting two different energy requirements as heating and electricity.

45.1.2 Goal and Scope Definition
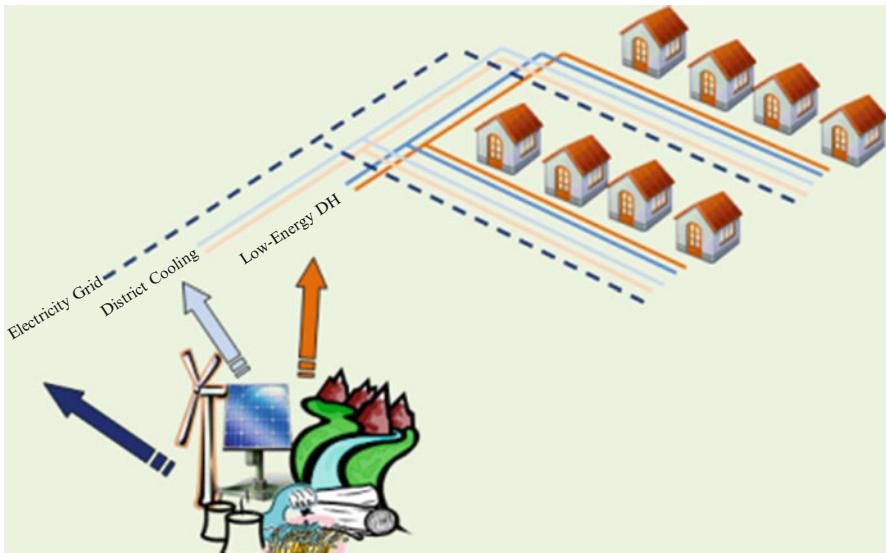
This chapter presents an energy planning tool focused on determining the capacities of energy conversion systems, each sourcing from different renewable energy source and/or having different energy generation configuration considered with single generation, co-generation, and tri-generation. The latter was considered due to the efficiency gains by means of multi-generation systems in which the waste heat from one energy generation, which would otherwise be lost, is utilized in the generation of another energy form(s) [1]. Hence the focus was extended to the consideration of other energy requirements such as electricity and cooling in addition to the heating requirement. Further consideration was directed to assess the satisfaction of the energy requirements on a monthly basis since the availability of certain renewable energy sources varies stochastically through an year period (such as solar and wind energy) as well as energy requirements, each showing distinct trend of variation [24].

45.2 System Description

The regional energy supply was considered with a city-wide integrated energy system taking account of a low-energy district heating system, an electricity grid, and a district cooling. The energy source of the integrated system can be multiple energy conversion systems, each based on different renewable energy source and/or having different generation technology (Fig. 45.1).

45.2.1 Low-Energy District Heating Networks

A low-energy district heating network is considered as the prevailing heating infrastructure, when it covers the whole neighboring urban settlements in a city/region due to its ease to connect any type of heat source. One of the successful examples of large-scale district heating systems can be illustrated by the Copenhagen district heating network which has the capacity to supply heat to 275,000 households [3]. Employing such city-wide district heating system in populated urban settlements brings the need for an energy planning scheme on the basis of infrastructure transformation with respect to new and existing settlements. New settlements can be easily employed with low-energy district heating systems. The design of the piping network, however, was considered with

Fig. 45.1 Simplified illustration of an integrated renewable supply

optimizing the piping network being aimed at minimizing the dimensions of each pipe segment until the pressure loss through each route reaches to the head lift provided by the main pump station [17]. The existing settlements employed with either conventional district heating systems operating in high temperature configuration or natural gas grid were considered to be replaced with low-energy district heating systems. The transition period for these settlements was considered with operational control philosophy involved with boosting of the supply temperature in the peak cold winter periods. This operational strategy allowed reduction of the pipe dimensions in the design stage of low-energy district heating systems in these locations. This is due to the over-sizing of the in-house radiator systems equipped in the old houses located at the existing settlements, which was obtained with reduced mass flow requirement in case the supply temperature is boosted [25, 26].

45.2.2 Integrated Energy Supply

The efficiency improvement measure that is possible with multi-generation facilities contributes to the necessity of integrating other energy requirements to be considered with low-energy district heating systems. Hence, in this chapter, the energy forms are considered with heating, electricity, and cooling, each being provided by means of a distribution network, i.e., heat supply via low-energy district heating system, electricity via electricity grid, and cooling via district cooling system, all of which considered as the residential requirements.

Large-scale distribution systems have the advantage of utilizing economy of scale that allows lowered specific investment costs (cost per unit nominal capacity) for the energy conversion systems when they are designed in large scales.

45.2.3 Renewable Energy Conversion Systems

Various energy conversion systems are considered in this chapter on the basis of having various renewable energy sources and/or different energy generation technologies. An extensive assessment of various energy conversion systems together with exergy analysis can be found in [27].

Solar Energy

Being used by the mankind for many millenniums, solar energy is still the most used energy source, not only being the energy source to produce the useable energy forms (such as heat and electricity) but also being the passive source required for the natural life and also with its passive heating on the earth. In this chapter the solar energy is considered to be exploited by the recent conventional energy conversion systems that are photovoltaic (PV) cells, hybrid PV and thermal (PV/T) cells, and solar collectors (SC) [28–30]. PV cells convert the solar photons to electricity energy, SC recover the accumulated thermal energy to heat energy, and hybrid PV/T cells produce electricity while the thermal energy accumulated on the cells being recovered to be used as useable output of heat energy. The solar energy is dependent on the sunlight with respect to its availability and insolation rate due to a substantial level of capacity factor regarding the nominal capacities of solar energy conversion systems.

Wind Energy

Having its earlier applications by means of windmills, wind energy is a prominent renewable energy source to be considered in the future energy supply solutions. The wind turbine technology makes use of harvesting the kinetic energy of wind in order to generate electricity. The electricity generation performance by the use of wind energy is dependent on various parameters regarding the weather conditions such as wind speed together with its regularity, wind direction, and flatness of the site area where it is employed [31]. Although wind turbine technology is the same for both onshore and offshore applications, excessive variation of the cost for energy generation from onshore wind turbines are observed due to varying land prices [32].

Geothermal Energy

The geothermal energy is the hot medium that exists in the depths of the earth, either in the form of hot water or in the form of steam, or mixture of both. The temperature gradient (the temperature change per depth below earth) of the geothermal energy shows variation according to the geological conditions of the location. The quality of the geothermal energy has a significant impact on determining the energy output to be generated and/or the technology of the energy conversion system [33]. Low-quality-level geothermal sources found in low temperatures of hot water below 80 °C can be exploited by direct utilization, as heat source for district heating systems. Direct utilization shall not be mixed with the direct connection which is used for the geothermal district heating systems in which geothermal water is circulated through the whole piping network while indirect connection makes use of heat exchangers to separate the piping networks, one being the piping network circulating the geothermal mean while the other being the district heating network circulation, another heat carrier medium. There are three different energy conversion systems commonly used on the basis of the quality level of the source. In the case the brine medium in the geothermal reservoir is obtained with vapor-dominated medium, the "dry steam" technology is considered, which circulates the steam extracted from the ground directly in its plant cycle. In the case of a geothermal source embodying liquid-dominated brine medium (above 80 °C) the "binary" technology is used, which makes use of the brine energy in vaporizing the binary working fluid having low boiling temperature to be circulated in its plant cycle. In the case of a geothermal source embodying brine medium with a mixture of liquid and vapor the "flash" technology is used, which separates the steam out of the mixture of brine and directly utilizes the extricated steam in its cycle [27, 34].

Despite it being economical and sustainable, geothermal energy has some limitations such as dependency on the geological conditions of the location together with the temperature gradient existing there, and the risk of reservoir cooling after a long period of usage in the situation of stagnant brine circulation.

The earth mass can also be utilized for storing the energy of hot water, its heat energy being generated by means of other renewable sources when excessive production more than consumption is possible. Borehole storage technology consisting of aggregated circulation holes can be referred as natural storage option despite being man-made [35]. Its application is commonly based on storing the excessive heat produced during summer period when the heat requirement is low and discharging the heat stored in the peak winter periods to be supplied to district heating network [36].

Biomass

Being obvious as the most mature renewable source due to its existence based on the discovery of fire, biomass fuel has been having recent interest by most as being the alternative solution instead of using coal when considered together with its

benefit of being found easily in the nature [37]. However, it should be noticed that the increasing demand on biomass by not only the heating sector but also other industrial sectors may cause a shortage of biomass supply. Biomass utilization can be considered as renewable when the biomass fuel is harvested from a farm (not a forest) in which the following biomass plants have to be grown sequentially. If not (if the consumption of biomass exceeds its production), then it could not be renewable any more [23, 38]. In the case of municipal solid waste (MSW), it cannot be considered as biomass and renewable unless the fossil fuel-based plastics are replaced with bio-based polymers [39].

In this chapter, biomass-based energy conversion technologies (being assumed to be totally renewable) are considered with three different technologies as MSW co-generation with incineration and with gasification, and as biomass tri-generation, their details being presented in [40–42].

Waste Heat Recovery

Despite its possibility of sourcing from fossil fuels, recovering of the waste heat (also called as surplus heat) from industrial facilities can be rewarding due to it being a savior for the waste heat that is easy to be utilized and gets lost if not recovered. Waste heat energy, if recovered in high qualities, is better to be utilized in the same industrial cycle. If it cannot be utilized in the industrial cycle then it should be considered to be exploited in the production of electricity (if found in high quality level) or in the production of heat to be supplied to district heating system or neighboring heating facility (if found in low quality level) [43, 44]. In this chapter, waste heat recovery technology is considered as heat recovery facilities in connection to medium- or low-scale industry refrigeration cycles (details given in [45]), the recovered heat being considered to be supplied to low-energy district heating system.

Large-scale hybrid heat pumps are also considered in this chapter. Hybrid heat pumps based on tri-generation technology were considered to be sourced by the waste heats from medium-scale industries, operating in tri-generation mode in summer periods and in co-generation mode in winter periods [46, 47].

Hydroelectricity

Hydroelectric plants are the efficient way of producing electricity allowing rapid response to spontaneous electricity requirements by means of taking advantage of the potential energy of the previously stored river water behind the dam. The electricity production of hydroelectric plants differs significantly between seasons, i.e., the peak production occurs in winter period that is significantly higher than summer period (in the northern sphere) [48]. On this basis, capacity factor was considered in the monthly basis for this technology. The hydro-energy plant technology is considered in small-scale applications in this chapter due to already overspreading existing large-scale applications on the available river sites.

Cooling Systems
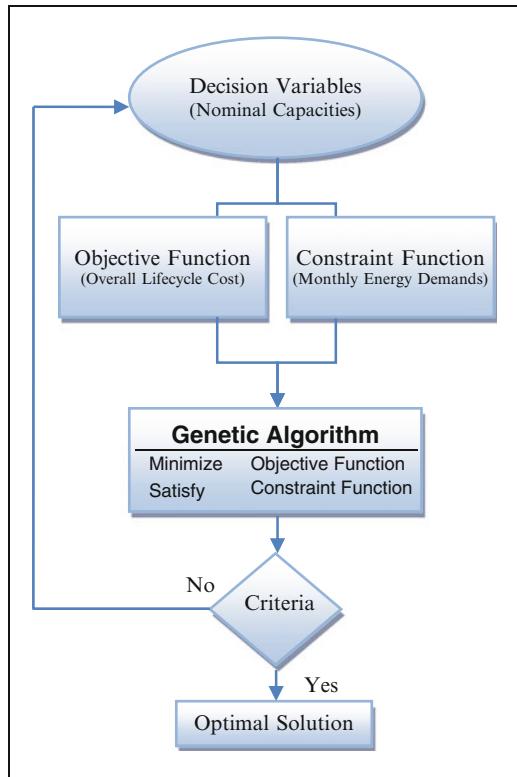
Being similar in the concept-manner with direct utilization of the geothermal energy in district heating systems, free cooling energy conversion systems become trendier as a source for the district cooling systems due to it being economical and having simpler technology compared to alternative cooling technologies. Associating free cooling with the direct utilization of geothermal is due to similar operations being observed between them. For example, in the case of free cooling, the passively cooled water mass existing in the depths of water bodies (such as sea, lake, and river) is being directly utilized as a cooling source for the district cooling network, as well as in the case of direct utilization of geothermal energy in which the brine medium is the heating source for district heating network [49, 50]. The variation in the temperature of water bodies has to be measured in order to assess the capacity factor for the use of free cooling. Hence the peak-period energy conversion technologies have to be considered in accordance with the variation of water temperature, especially for the summer period. The energy conversion systems for the peak cooling period are considered with compressor chillers which make use of electricity, and with absorption chiller which makes use of heat (recovered from industrial facilities); their details are given in the studies [51–53].

45.3   Energy Planning Considerations

The most important consideration in energy planning, above all, is estimating the energy requirements of the region (as the focus in this chapter on heat, electricity, and cooling) wisely, in particular considering the energy demands (of the regional houses) by taking account of the current demands together with their expected values in future and with the expected population growth. Another consideration has to be directed to the determination of the heat load (on the distribution network) by taking account of simultaneity factor that is based on the phenomenon that each consumer in a district does not consume energy at the same time nor at the same rate [54]. Energy losses from the DH network also have to be considered due to its considerable effect on the heat production site. However, in the case of employing a low-energy district heating system as the prevailing heating infrastructure at the region, heat saving is possible due to significant reductions of the heat loss from the network, thanks to the low-temperature operation [17]. The energy planning has to be based on an analysis formulated with evaluation of the energy requirements in shorter periods than an year period assessment. The reason behind this is the variable nature of most energy requirements together with the dissimilar variation of the renewable energy production [24].

After determining the most plausible energy requirements of the region in focus, it can be beneficial to use a regional energy planning tool that determines the nominal capacities of the energy conversion systems that exploit the locally

Fig. 45.2 Optimization
flow chart, as defined for the
energy planning tool

available renewable sources, considered with prevention of having over-
dimensioned energy conversion systems and also lack of security of supply.
Hence, an energy planning tool was modelled in this research work with an
optimization method involved with the genetic algorithm (details presented in
[55]). As shown in Fig. 45.2, the objective function of the optimization method in
question was formulated with minimization of the overall life cycle cost of the
entire regional energy conversion systems while an expression being modelled for
the constraint function as evaluation of monthly energy requirements.

In order to maintain a general basis as comparative degree for all of the energy
conversion systems, life cycle cost calculation was involved with various economic
considerations. The specific investment cost expression was derived by taking
account of the economy of scale for each energy conversion system [53]. The
reason behind this is to include the effect of the nominal capacity on the investment
cost for each energy conversion system. Salvage cost values were involved in the
economic calculations since each energy conversion system has quite different
lifetime and salvage value at the end of its lifetime. Due to the variation in the
lifetimes, a base period was considered for the net present value (NPV) method on
the account of the energy conversion technology with the shortest lifetime, and the
salvage costs of the energy conversion technologies are allocated accordingly.

(Further details are presented elsewhere [56]). Annual costs were considered with O&M cost for all technologies and, exceptionally, with also fuel cost for the case of biomass-based tri-generation system.

As a general impression, efficiency measures are not generally of any interest since there is no need to concern fuel costs when renewable energy sources are considered (except for biomass). However, the nominal capacity being determined in the design stage of an energy conversion system is significantly dependent on efficiency measures as well as the availability of the renewable source. Besides, the seasonal weather conditions can also affect the performance of the energy genera-tion to a lesser or a greater degree, dependent on the energy conversion system in focus. This seasonal effect was involved in the performance calculations by means of capacity factor considerations. The capacity factor was considered with monthly variation for the case of energy conversion systems, their renewable source varying significantly amongst months, while in the case of other energy conversion systems, the capacity factor accounted as same value for each month.
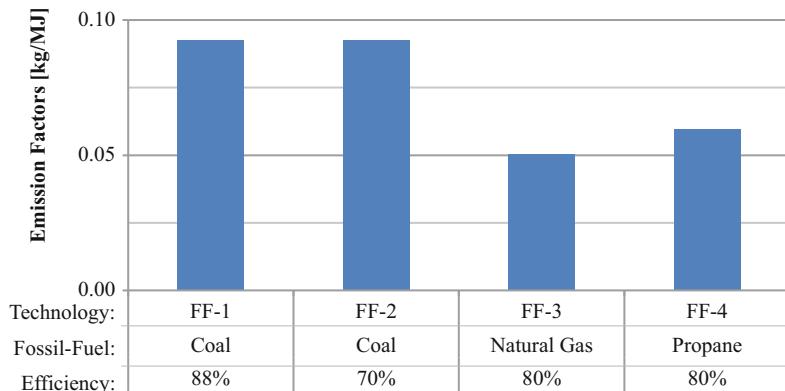
Heat supply was exclusively considered with long-term energy storage option in order to overcome the supply/demand mismatch amongst seasons due to the significant gap between the excessive heat energy produced in summer and the intensive heat demand in winter periods. The seasonal mismatch in terms of electricity was not considered in this study with long-term storage option due to limitations of the current technology.

45.4   Environmental Assessments

In this section, environmental issues regarding the use of renewable energy sources and the major savings compared to use of traditional fossil fuel-based energy conversion systems are described.

45.4.1   *Environmental Issues*

Renewable sources are known to be "green" due to their environmental impact being excessively low or nonexistent during their operation. However, some energy conversion systems have some minor impacts to environment either in their manu-facture or during their operation. For example, PV cells can be hazardous due to the materials used and/or the fossil fuels consumed during the manufacturing process [57]. One should note that during the drilling of the geothermal wells, underground gases can leak to the atmosphere and the waste geothermal medium, after its heat content utilized, should be re-injected back to the underground reservoir [58]. Onshore wind farms are known with the environmental issues as noise pollu-tion and as risk of killing the birds and bats during the operation [32]. In the incineration application of MSW, the fossil fuel-based plastic materials should be

Fig. 45.3 The emission factors and thermal efficiencies, as assumed for four different fossil fuel-based energy conversion systems, based on [61]

removed from the solid waste by means of recycling before the incineration [39]. The debate regarding the environmental effect of biomass is due to the risk of losing the soil nutrients, and soil erosion occurring due to rainfalls after harvesting of biomass farm [59]. Employing the free cooling technology should be considered with special attention about the temperature increment on the water body [60].

45.4.2 Emission Savings

Besides their minor environmental effects, utilizing renewable energy sources can save significant amount of emissions in comparison to the fossil fuel-based technologies. For the case the same amount of energy requirements were provided by them instead of renewable-based technologies, the emission impacts were assessed for four different traditional fossil fuel-based energy conversion technologies, being defined as (FF-1) coal-based back-pressure steam turbine with a thermal efficiency of 88 %, (FF-2) coal-based extraction-condensing steam turbine with a thermal efficiency of 70 %, (FF-3) natural gas-based gas turbine with a thermal efficiency of 80 %, and (FF-4) propane-based reciprocating engine with a thermal efficiency of 80 %, as shown in Fig. 45.3 [61].

45.5 Results

In this chapter, the developed energy planning method is applied on two case areas: the Greater Copenhagen Area (GCA) and the Greater Toronto Area (GTA), where the annual heating degree-hours being, respectively, 1,807 and 2,400 and the cooling degree-hours in summer season being, respectively, 30 and

Table 45.1 Optimal nominal capacities, as obtained for the case areas GCA and GTA

Color labels[a]	Renewable technology		Nominal capacity GCA	GTA	Units[b]
	PV cells		–	2.1e+7	m^2
	PV/T cells		4.0e+6	5.0e+4	m^2
	SC		5.0e+6	–	m^2
	Wind—onshore		1.1e+3	8.5e+2	MW
	Wind—offshore		1.0e+3	8.0e+2	MW
	Hydroelectric		–	1.0e+5	MW
	Geothermal direct		6.1e+2	4.3e+3	MW
	Charge	BTS	4.9e+5[c]	1.1e+6[c]	m^3
	Discharge				
	Waste heat—chillers		2.5e+4	8.0e+5	kW
	Hybrid heat pump		1.0e+3	1.1e+2	kW
	MSW—incineration		2.9e+6	5.3e+3	tpa
	MSW—gasification		3.0e+6	1.0e+6	tpa
	Biomass—tri-generation		5.5e+5	9.5e+5	tpa
	Free cooling		1.5e+2	5.4e+2	kW
	Absorption		4.2e+4	8.0e+4	kW
	Compressor chiller		1.1e+4	–	kW
	Overproduction[d]		–	–	–

[a]The color labels are used, as same, in Figs. 45.4 and 45.5
[b]The unit of each nominal capacity is given in the last column
[c]The nominal capacity of borehole storage while the color labels given for charge and discharge
[d]The overproduction refers to the excessive energy produced more than the demand, shown in black color in the figures
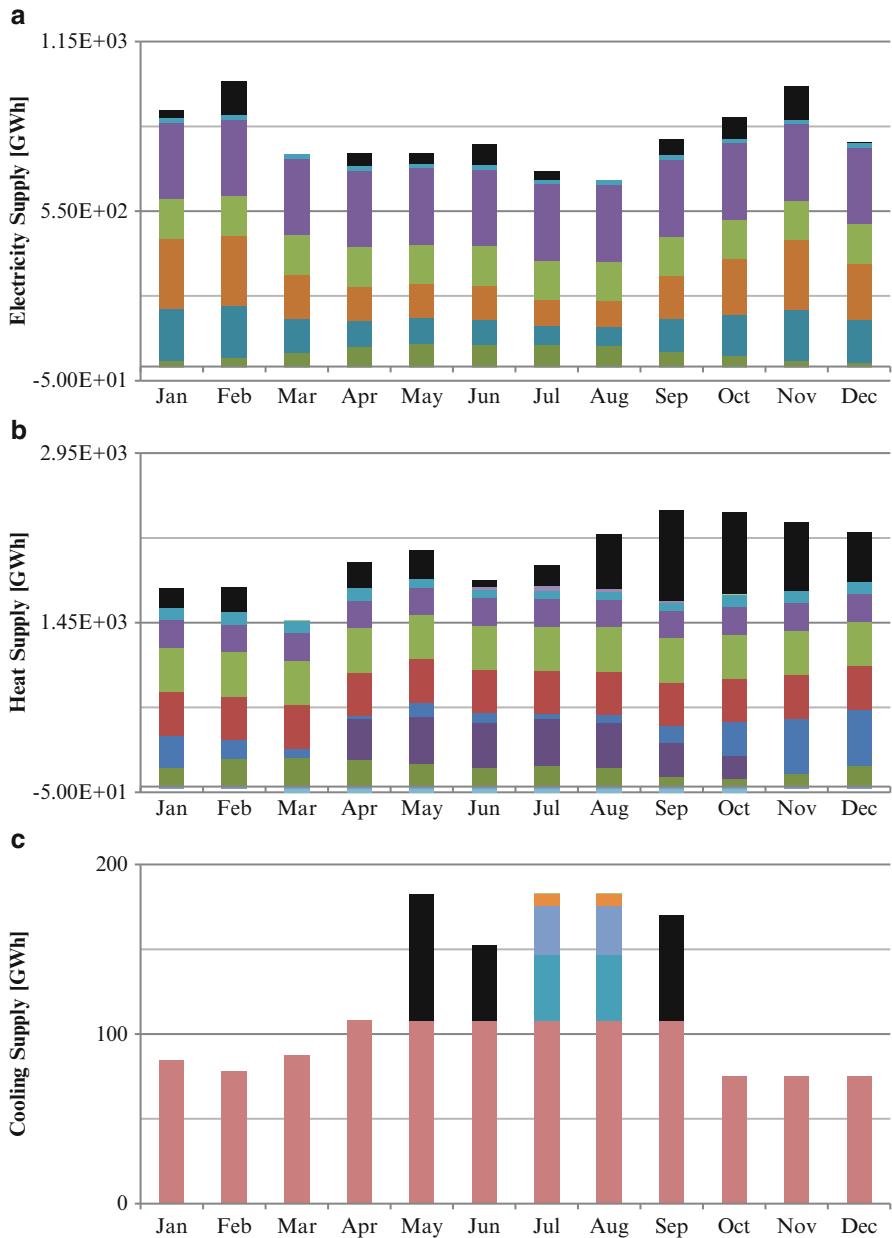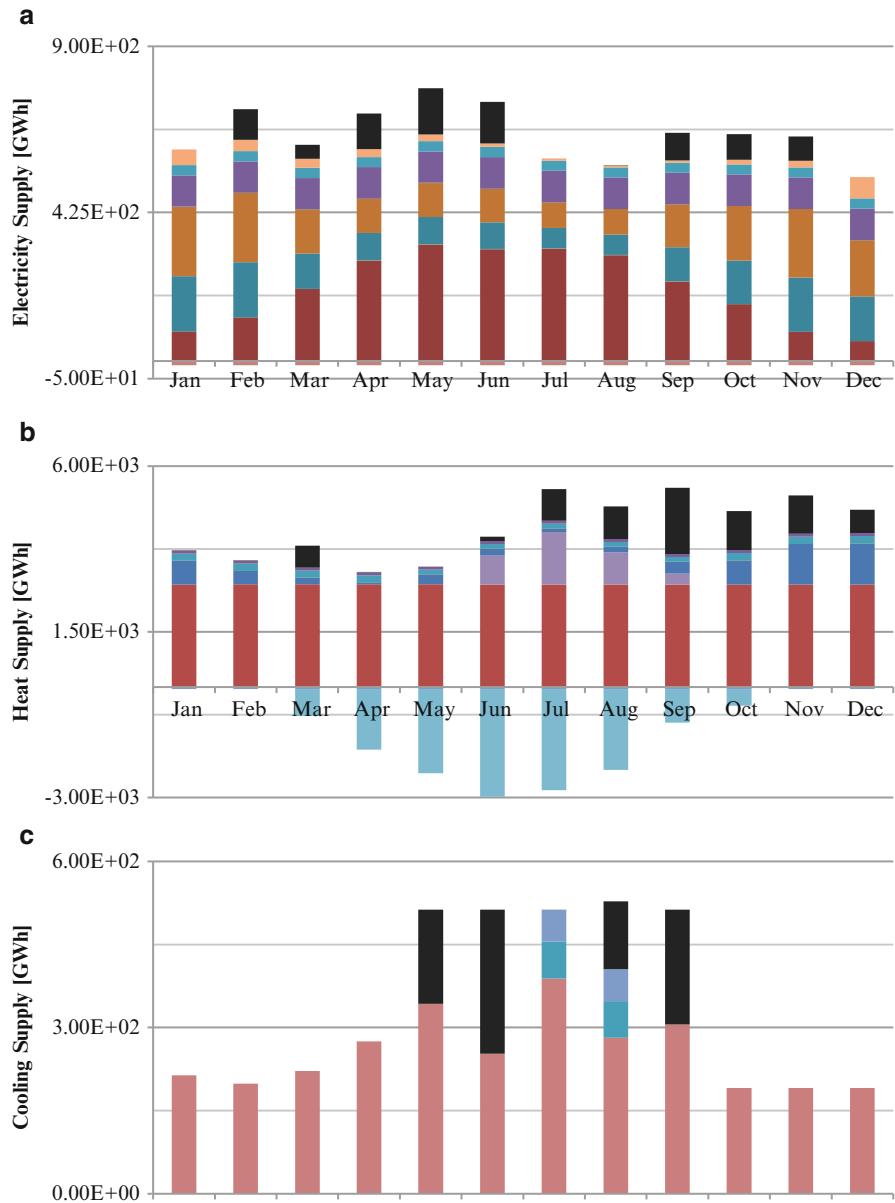
370, respectively (units in [°C-h]). Hydroelectric energy conversion system is not considered in GCA due to the absence of rivers in this location [3]. Biomass fuel prices are assumed to be 166 €/ton in the GCA case, whereas it is assumed to be 130 €/ton for GTA (due to the vast amount of land and biomass fuel), the values being derived from [62, 63]. Moreover, both case areas have the geothermal source with a temperature gradient of 30 °C/km [64, 65]. Table 45.1 shows the nominal capacities for each of the case areas GCA and GTA, obtained with overall life cycle costs of 19 and 24 B€ (billion euro), respectively.

The energy supplies by each of the energy conversion systems, their nominal capacities shown in Table 45.1, are given in terms of the energy requirement types—electricity, heating, and cooling, respectively, in subsections (a), (b), and (c)—in Fig. 45.4 for the case of GCA, and in Fig. 45.5 for the case of GTA.

The CO_2 emissions were observed with respect to the case in which the same amount of energy requirements were produced by means of fossil fuel-based energy conversion systems, as shown in Table 45.2.

Fig. 45.4 The energy supplies in terms of electricity, heat, and cooling, as obtained for GCA (see Table 45.1 for the labels)

Fig. 45.5 The energy supplies in terms of electricity, heat, and cooling, as obtained for GTA (see Table 45.1 for the labels)

Table 45.2 CO_2 emissions, as obtained for each of the four technologies based on fossil fuels

	Emissions (CO_2) [M tons]	
Technologies	GCA	GTA
FF-1	703	1,118
FF-2	883	1,406
FF-3	420	668
FF-4	499	794

45.6 Discussions

This chapter provides an energy planning method considered with solely renewable energy sources supplying various energy types via an integrated energy distribution network. The integrated distribution network considers low-energy district heating network, district cooling, and electricity grid, as the scope of this chapter. The optimal capacities of renewable energy conversion systems obtained exclude the existing renewable sources exploited in the case areas in question since a general method can be drawn for assessing the locally available renewable energy sources and in determination of the requiring energy conversion systems for any focused case. Integrated city-wide distribution networks allow having the advantage of economy of scale considering the investment cost of each energy conversion system. This can be the basis behind the relatively small difference observed between the overall life cycle costs of two difference case areas in question, as can be seen in Table 45.1. The relatively small increment at the life cycle cost for the case of GTA, for example, could be due to the economy-of-scale effect despite colder and hotter climate conditions enduring, respectively, in winters and in summers in the case of GTA than in the case of GCA. The climatic nature of a case area has its influence on the optimal solutions in two manners, one being its effect on the energy requirements and the other being the availability of the renewable energy sources together with the variation of energy generation rate through an year period by use of them.

The energy planning method in question can result with several solutions, each being obtained with another optimization run despite the same modelling of the case area employed. However each solution obtained could not necessarily be the optimal solution considering the security of supply and the overproduction of each energy form together with the overall life cycle cost. The solution involving a reasonable variety of renewable sources and having the minimum overall life cycle cost is considered as the optimal solution, which is observed with also the least degree of overproduction in most, as seen in Fig. 45.4 for GCA and in Fig. 45.5 for GTA. The saving of CO_2 emissions in comparison to the case of the same input values of energy requirements supplied by traditional fossil fuel-based energy conversion systems can be seen in Table 45.2, which can account significantly in the carbon emission reduction targets when considering only meeting the residential energy requirements.

45.7 Conclusions

This chapter presents a novel method for determining the optimal capacities of RE-based energy conversion systems in focus with handling different climatic conditions and satisfaction of the energy requirements of various types for different periods of the year. A number of general conclusions not yet taken up can be drawn. One is that employing a city-wide distribution network supplying the energy forms required for the case area in focus can be beneficial due to the reduced unit costs achieved by means of the large-scale application of energy conversion systems together with the efficiency improvements possible with multi-generation systems. In addition, the borehole storage option can be considered for balancing the mismatch of heat production to heat demand between different seasons in long-term periods. One can note that significant environmental benefits can be achieved in proper with the national emission reduction targets of most by use of the proposed optimization method in an urban district in which the residential buildings are planned to be in focus with improved efficiency measures and potentials of the local renewable energy sources being comprehensively assessed.

References

1. Dincer I, Zamfirescu C (2012) Renewable-energy-based multigeneration systems. Int J Energ Res 36:1403–1415
2. Lund H (2010) Renewable energy systems: the choice and modeling of 100 % renewable solutions. Elsevier Science & Technology, MA, USA
3. Lund H, Mathiesen BV (2009) Energy system analysis of 100 % renewable energy systems—the case of Denmark in years 2030 and 2050. Energy 34:524–531
4. Persson U, Werner S (2011) Heat distribution and the future competitiveness of district heating. Appl Energ 88:568–576
5. Olsen PK, Lambertsen H, Hummelshøj R, Bøhm B, Christiansen CH, Svendsen S et al (2008) A new low-temperature district heating system for low-energy buildings. In: The 11th international symposium on district heating and cooling, Reykjavik, Iceland, 31 Aug to 2 Sept 2008
6. Paulsen O, Fan J, Furbo S, Thorsen JE (2008) Consumer unit for low energy district heating net. In: The 11th international symposium on district heating and cooling, Reykjavik, Iceland, 31 Aug to 2 Sept 2008
7. Danfoss (N/A) 8 steps—control of heating system. http://www.heating.danfoss.com/Content/61078BB5-1E17-4CA2-AC498A7CAC2BA687_MNU17424997_SIT54.html. Accessed 10 Nov 2011
8. Foged M (1999) Low temperature operation, DBDH. http://www.dbdh.dk. Accessed 10 Jan 2011
9. Østergaard PA, Mathiesen BV, Möller B, Lund H (2010) A renewable energy scenario for Aalborg Municipality based on low-temperature geothermal heat, wind power and biomass. Energy 35:4892–4901

10. Thorsen JE, Christiansen CH, Brand M, Olesen PK, Larsen CT (2011) Experiences on low-temperature district heating in Lystrup—Denmark. In: Proceedings of the international conference on district energy international conference on district heating and cooling, Portorož, Slovenia, 20–22 Mar 2011

11. Christiansen CH, Worm J, Jørgensen H, Thorsen JE, Bennetsen J, Larsen CT et al (2011) Demonstration of low energy district heating system for low energy building in ringgårdens Afd. 34 in Lystrup (Demonstration af lavenergifjernvarme til lavenergibyggeri i boligforeningen ringgårdens afd. 34 i Lystrup). DEA, Århus, Denmark

12. Wiltshire R (2011) Low temperature district energy systems (2011) In: Proceedings of the urban energy conference, Debrecen, Hungary, 14–15 Oct 2011

13. Sibbitt B, Onno T, McClenahan D, Thronton J, Brunger A, Kokko J et al (2007) The drake landing solar community Project—early results. In: Canadian solar buildings conference, Canmet Energy Technology Centre, Calgary, 10–14 June 2007

14. Bodmann M, Mangold D, Nußbicker J, Raab S, Schenke A, Schmidt T (2006) Solar unterstützte Nahwärme und Langzeit-Wärmespeicher. Forschungsbericht zum BMWA/BMU-Vorhaben (Februar 2003 bis Mai 2005), Universitetät Stuttgart and Technische Universitetät Braunschweig, Stuttgart

15. Torio H, Schmidt D (2011) Low exergy systems for high-performance buildings and communities. ECBCS—Annex 49

16. Brand M, Thorsen JE, Svendsen S (2012) Numerical modelling and experimental measurements for a low-temperature district heating substation for instantaneous preparation of DHW with respect to service pipes. Energy 41:392–400

17. Tol Hİ, Svendsen S (2012) Improving the dimensioning of piping networks and network layouts in low-energy district heating systems connected to low-energy buildings: a case study in Roskilde, Denmark. Energy 38:276–290

18. Tol Hİ, Svendsen S (2012) A comparative study on substation types and network layouts in connection with low-energy district heating systems. Energ Convers Manag 64:551–561

19. Lund H, Möller B, Mathiesen BV, Dyrelund A (2010) The role of district heating in future renewable energy systems. Energy 35:1381–1390

20. Sperling K, Hvelplund F, Mathiesen BV (2011) Centralisation and decentralisation in strategic municipal energy planning in Denmark. Energy Policy 39:1338–1351

21. Sperling K, Möller B (2012) End-use energy savings and district heating expansion in a local renewable energy system—a short-term perspective. Appl Energ 92:831–842

22. Østergaard PA, Lund H (2011) A renewable energy system in Frederikshavn using low-temperature geothermal energy for district heating. Appl Energ 88:479–487

23. Mathiesen BV, Lund H, Connolly D (2012) Limiting biomass consumption for heating in 100 % renewable energy systems. Energy 48:160–168

24. Weber C, Shah N (2011) Optimisation based design of a district energy system for an eco-town in the United Kingdom. Energy 36:1292–1308

25. Tol Hİ, Svendsen S (2012) Optimal dimensioning of low-energy district heating networks with operational planning—case study for existing buildings. In: 11th international conference on sustainable energy technologies, Vancouver, Canada, 2–5 Sept 2012

26. Tol Hİ, Svendsen S (2012) Operational Planning of low-energy district heating systems connected to existing buildings. In: International Conference on Renewable Energy: Generation and Applications, Al-Ain, United Arab Emirates, 4–7 Mar 2012.

27. Hepbasli A (2008) A key review on exergetic analysis and assessment of renewable energy resources for a sustainable future. Renew Sustain Energy Rev 12:593–661

28. Bosanac M, Sørensen B, Katic I, Sørensen H, Nielsen B, Badran J (2003) Photovolta-ic/thermal solar collectors and their potential in Denmark. Danish Technological Institute, Novator Advanced Technology Consulting, and Esbensen Consulting Engineers Ltd., Denmark

29. Kalogirou SA (2004) Solar thermal collectors and applications. Progr Energ Combust Sci 30:231–295

30. Fisch MN, Guigas M, Dalenbäck JO (1998) A review of large-scale solar heating systems in Europe. Sol Energ 63:355–366
31. Burton T, Jenkins N, Sharpe D, Bossanyi E (2011) Wind Turbine Installations and Wind Farms. In: Wind Energy Handbook: John Wiley & Sons, Ltd 2011:525–564
32. Blanco MI (2009) The economics of wind energy. Renewable and sustainable energy re-views 13:1372–1382
33. Lee KC (2001) Classification of geothermal resources by exergy. Geothermics 30:431–442
34. Coskun C, Oktay Z, Dincer I (2011) Performance evaluations of a geothermal power plant. Appl Therm Eng 31:4074–4082
35. Kizilkan O, Dincer I (2012) Exergy analysis of borehole thermal energy storage system for building cooling applications. Energ Build 49:568–574
36. Chapuis S, Bernier M (2009) Seasonal storage of solar energy in borehole heat exchangers. In: Eleventh international IBPSA conference, 27–30 July 2009
37. Vallios I, Tsoutsos T, Papadakis G (2009) Design of biomass district heating systems. Biomass Bioenergy 33:659–678
38. O'Kelly G, Rahikainen A (2011) European biomass review—new comprehensive analysis and forecast of the European bioenergy sector. RISI
39. Wolf O, Crank M, Patel M, Marscheider-Weidemann F, Schleich J, Hüsing B et al (2005) Techno-economic feasibility of large-scale production of bio-based polymers in Europe. European Communities, Prague
40. Michalski ML (2006) Biomass, biogas and municipal waste as alternative energy sources for historical cities. Environ Prot Eng 1:41–49
41. Murphy JD, McKeogh E (2004) Technical, economic and environmental analysis of energy production from municipal solid waste. Renew Energy 29:1043–1057
42. Fruergaard T, Christensen TH, Astrup T (2010) Energy recovery from waste incineration: assessing the importance of district heating networks. Waste Manag 30:1264–1272
43. Bédard S (2012) Waste heat to power: a process integration perspective. CanmetENERGY, Devon
44. Johnson I, Choate WT (2008) Waste heat recovery: technology and opportunities in U.S. industry. BCS, Memphis
45. Baxter VD (2003) Advanced supermarket refrigeration/heat recovery systems - Final report volume 1 - Executive summary. IEA Annex 26
46. Lund H, Morten BB (2007) Large-scale heat pumps in sustainable energy systems: system and project perspectives. Therm Sci 11:143–152
47. Westerlund R, Chiba T, Åstrand LE (1987) Heat pumps for district heating applications. In: Zimmerman KH, Powell RH (eds) Heat pumps—prospects in heat pump technology and marketing. LEWIS PUBLISHERS, INC., Orlando, FL, pp 427–452
48. Pöttler R. Energy from hydropower—innovative and regenerative. http://www.ilf.com.pl/fileadmin/user_upload/publikationen/13_Energy_from_Hydropwer_Innovative_and_regenerative.pdf. Accessed 15 Dec 2012
49. Bøgeskov H (2012) KE Fjernkøling A/S (KE Cooling A/S). Københavns E. http://www.ke.dk/. Accessed 1 Dec 2012
50. Looney CM, Oney SK (2007) Seawater district cooling and lake source district cooling. Energ Eng 104:34–45
51. Bailer P, Pietrucha U (2006) District heating and district cooling with large centrifugal chiller—heat pumps. In: Proceedings of 10th international symposium on district heating and cooling, Hanover, Sept 2006
52. Dalin P, Ivancic A, Tvärne A, Penthor A, Martin B, Ricci F et al (2006) District cooling—cooling more with less. Euroheat Power 32
53. Werner S (2004) District heating and cooling. In: Cleveland CJ (ed) Encyclopedia of energy. Elsevier, New York, pp 841–848

54. Winter W, Haslauer T, Obernberger I (2001) Simultaneity surveys in district heating net-works: results and project experience (Untersuchungen zur Gleich-zeitigkeit in Nahwärmenetzen: Ergebnisse und Projekterfahrungen). Euroheat Power 30:42–47

55. Ghaebi H, Saidi MH, Ahmadi P (2012) Exergoeconomic optimization of a trigeneration system for heating, cooling and power production purpose based on TRR method and using evolutionary algorithm. Appl Therm Eng 36:113–125

56. Sundberg G, Karlsson BG (2000) Interaction effects in optimising a municipal energy system. Energy 25:877–891

57. Kammen DM (2004) Renewable energy, taxonomic overview. In: Cleveland CJ (ed) Encyclopedia of energy. Elsevier, New York, pp 385–412

58. Kaya E, Zarrouk SJ, O'Sullivan MJ (2011) Reinjection in geothermal fields: a review of worldwide experience. Renew Sustain Energy Rev 15:47–68

59. Patzek TW, Pimentel D (2005) Thermodynamics of energy production from biomass. Crit Rev Plant Sci 24:327–364

60. Eliadis C (2003) Deep lake water cooling – a renewable technology. Presented at electrical line, 26 May to 8 June 2003

61. Fuel emission coefficients (2012) EIA. http://www.eia.gov/oiaf/1605/emission_factors.html. Accessed 10 Aug 2012

62. Nikolaisen L (2012) Country report 2011 for Denmark. Danish Technological Institute - IEA bioenergy task 40

63. Oo A, Kelly J, Lalonde C (2012) Assessment of business case for purpose-grown biomass in Ontario. The Western University Research Park, Sarnia-Lambton Campus, 44

64. Magtengaard J, Mahler A (2010) Geothermal reserves and sustainability in the greater Copenhagen area. In: Proceedings World geothermal congress, Bali, Indonesia, 25–29 Apr 2010

65. Bristow D (2012) The business case for alternative energy technologies in Ontario. Civil Engineering, University of Toronto. http://www.trca.on.ca/dotAsset/51366.pdf. Accessed 6 June 2012

Chapter 46
Exergy Analysis and Environmental Impact Assessment of Using Various Refrigerants for Hybrid Electric Vehicle Thermal Management Systems

Halil S. Hamut, Ibrahim Dincer, and Greg F. Naterer

Abstract Thermal management systems (TMSs) are one of the key components of hybrid electric vehicles in terms of their impact on vehicle efficiency and performance, as well as the vehicle's environmental footprint. In this chapter, an environmental assessment of hybrid electric vehicle thermal management systems is developed with respect to various refrigerants such as R134a, R600 (butane), R600a (isobutane), R1234yf (tetrafluoropropene) and dimethyl ether (DME). The energetic and exergetic COPs along with exergy destruction rates are analyzed for the TMS using each refrigerant. Also, greenhouse gas (GHG) emissions (in g CO_2-eq/kWh) during operation and the sustainability index are determined under various system parameters, operating conditions, as well as carbon dioxide scenarios. Based on the results, all selected TMSs are determined to have higher energetic and exergetic COPs along with lower environmental impact than the baseline TMS (which uses R134a) except for the TMS using R1234yf. The highest efficiency and lowest environmental impact are achieved by TMS using DME with higher energetic and exergetic COPs (by 7.9 and 8.2 %, respectively) and lower GHG emissions (by 8.3 %) and higher sustainability index (by 3.3 %) than the baseline TMS.

H.S. Hamut (✉) • I. Dincer
Faculty of Engineering and Applied Science, University of Ontario Institute of Technology, 2000 Simcoe Street North, Oshawa, ON, Canada L1H 7K4
e-mail: Halil.Hamut@uoit.ca; Ibrahim.Dincer@uoit.ca

G.F. Naterer
Faculty of Engineering and Applied Science, Memorial University of Newfoundland, 240 Prince Phillip Drive, St. John's, NL, Canada A1B 3X5
e-mail: Gnaterer@mun.ca

Nomenclature

D	Diameter (m)
$\dot{E}x$	Exergy rate (kW)
f	Friction factor
h	Specific enthalpy (kJ/kg)
$\bar{h}$	Heat transfer coefficient (W/m^2 K)
k	Thermal conductivity (W/m $^\circ$C)
$\dot{m}$	Mass flow rate (kg/s or L/min)
P	Pressure (kg/m s^2)
Pr	Prandtl number
$\dot{Q}$	Heat transfer rate (kW)
Re	Reynolds number
s	Specific entropy (kJ/kg K)
T	Temperature (K or $^\circ$C)
T_0	Ambient temperature (K or $^\circ$C)
U	Overall heat transfer coefficient (W/m^2 K)
$\dot{W}$	Work rate or power (kW)

Greek Symbols

Δ	Change in variable
ψ	Exergy efficiency

Subscripts

act	Actual
bat	Battery
cool	Coolant
$c, cond$	Condenser
ch	Chiller
$comp$	Compressor
$crit$	Critical
D	Destruction
en	Energy
ex	Exergy
$e, evap$	Evaporator
g	Gas
ref	Refrigerant
s	Isentropic
txv	Thermal expansion valve
wg	Water/glycol mix

Acronyms

AACS	Automotive air conditioning system
A/C	Air conditioning
AC	Alternative current
DC	Direct current
CFC	Chlorofluorocarbon
CV	Conventional vehicle
COP	Coefficients of performance
DME	Dimethyl ether
EES	Engineering equation solver
EV	Electric vehicle
GHG	Greenhouse gas
GWP	Global warming potential
HEV	Hybrid electric vehicle
ICE	Internal combustion engine
LCA	Life cycle assessment
NBP	Normal boiling point
ODP	Ozone depleting potential
PCM	Phase change material
PHEV	Plug-in hybrid electric vehicle
TMS	Thermal management system
TXV	Thermal expansion valve
VOC	Volatile organic compound

46.1 Introduction

Most hybrid electric vehicles (HEVs) use electricity from the grid to power the thermal management system (TMS). The TMS has a significant role in reducing the associated GHG emissions compared to conventional vehicles. Even though these vehicles produce virtually zero GHG emissions in all-electric mode during operation, there may still be indirect emissions associated with the generation of electricity [1]. These emissions, especially under a high-carbon-derived electricity generation mix, can be significantly high (possibly even higher than conventional vehicles) and therefore methods of reducing this environmental footprint should be investigated.

One of the possible ways of mitigating the environmental footprint of the TMS is to use alternative refrigerants that can increase the TMS efficiency and reduce the corresponding environmental impact. Natural refrigerants, such as hydrocarbons, can be a suitable replacement since they have negligible global warming potential (GWP) and zero ozone depleting potential (ODP), as well as a significant role in increasing the TMS efficiency and reducing the indirect greenhouse gas (GHG) emissions from resources used for electricity generation. Hydrocarbons also have

various additional advantages such as availability, low cost, high miscibility with the conventional mineral oil, and compatibility with existing refrigerating systems. On the other hand, a drawback is potential flammability and safety hazards. Currently, these hydrocarbons are already utilized in a few established applications such as household refrigerators and small heat pump applications. It should be noted that R-744 (CO_2) is not considered among the major hydrocarbons even though it offers a number of desirable properties such as good availability, low toxicity, and low GWP and cost. It has a need for implementing a transcritical cycle and additional safety standards that require significant modifications to the baseline system based on its different thermophysical properties relative to R134a.

In addition, there are also certain other refrigerants that could be utilized in EV TMSs, such as R1234yf and DME, and therefore included in the study. Among the fluorinated propene isomers, R1234yf is one of the key candidates as an R134a replacement in automotive applications due to its ability to be used with compatible materials and oils, as well as low GWP (about 4) and low normal boiling temperatures with respect to R134a. Moreover, several studies have shown that the environmental performance of R1234yf can be lower than R134a in most cases [2]. However, it also has certain drawbacks such as additional costs, relative flammability, miscibility with oil, as well as stability problems in the presence of small amounts of water and air in the TMS. DME is another good candidate due to its nontoxic behavior during normal usage; it is widely available, is environmentally safe, has excellent material compatibility and better heat transfer properties, as well as has lower costs than R134a. The main drawback is its high flammability, which is about twice as high as the considered hydrocarbons.

46.2 Electric Vehicles

46.2.1 *Electric and Hybrid Electric Vehicles*
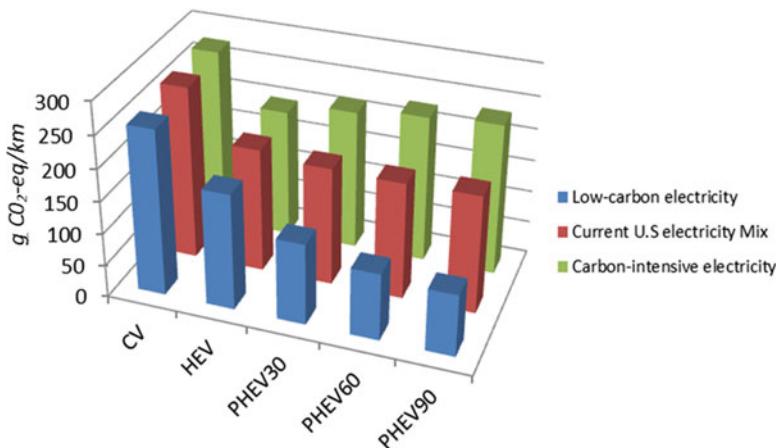
Electric and hybrid electric vehicles have significant advantages over conventional vehicles in terms of energy efficiency, energy source options, and corresponding environmental impact. Electric vehicles can be powered either directly from an external power station or through stored electricity (that is acquired originally from an external power source), and by an onboard electrical generator, such as an engine (in HEVs) [3]. Pure electric vehicles have the advantage of having full capacity withdrawn at each cycle, but they will have a limited range. HEVs on the other hand have significantly higher ranges, as well as the option of operating in electric-only mode, and therefore they are the main focus of this chapter.

HEVs take advantage of having two discrete power sources: usually primary is the heat engine (such as diesel or turbine, or a small-scale ICE) and the auxiliary power source is usually a battery. Their drivetrains are generally more fuel efficient than conventional vehicles since the auxiliary source either shares the power output

allowing the engine to operate mostly under efficient conditions such as high power for acceleration and battery recharging (dual mode) or furnishes and absorbs high and short bursts of current on demand (power assist). Moreover, in both architectures, the current is drawn from the power source for acceleration and hill-climbing and the energy from braking is charged back into the HEV battery for reuse which increases the overall efficiency of the HEVs [4]. In plug-in hybrid electric vehicles (PHEVs), a larger rechargeable storage battery that enables drawn power from the electricity grid is utilized instead of fossil fuel energy alone. Since the vehicle has an alternative energy unit and a battery that can be charged from the grid, the mass of the battery is significantly smaller than EVs, thus enabling the PHEVs to operate more efficiently in electric-only mode than similar EVs [5]. PHEV chargers must be lightweight, compact, and highly efficient in order to maximize the effectiveness of the electric energy from the grid. They are designed to use either inductive or conductive chargers. Inductive chargers have preexisting infrastructure and are intrinsically safer. Conductive chargers are lighter and more compact and allow bidirectional power, thus achieving higher efficiencies. By utilizing the stored multi-source electrical energy from the grid and stored chemical energy in the fuel tank together or separately, PHEVs can achieve even better driving performance, higher energy efficiencies, lower environmental impact, and lower cost than conventional HEVs, mainly depending on the driving behavior and energy mix of the electricity generation [6].

46.2.2 EV/HEV Emissions
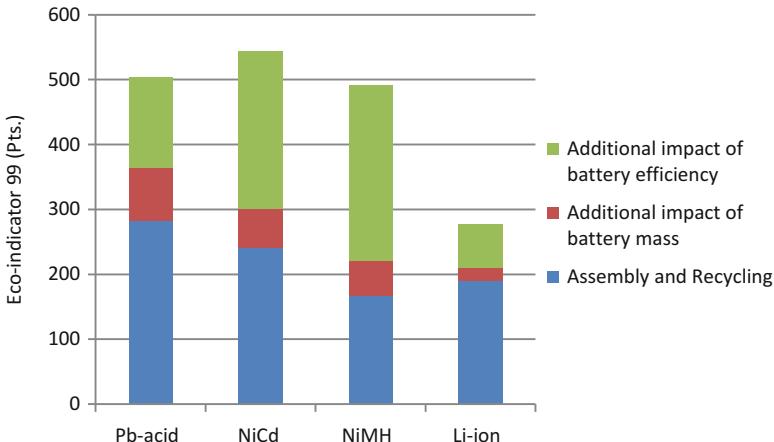
EVs, conventional HEVs, and PHEVs provide significant reduction in emissions compared to conventional vehicles (CVs) with ICEs while having competitive pricing due to government incentives, increasing oil prices, and high carbon taxes combined with low-carbon electricity generation [7]. The emissions of CVs increase significantly especially for short-distance travels due to the inefficiencies of the current emission control systems for gasoline vehicle cold starting [8]. It is estimated that vehicles traveling fewer than 50 km per day are responsible for more than 60 % of daily passenger vehicle kilometers travelled in the USA [9]. Powering this distance with electricity would reduce gasoline use significantly and yield a considerable reduction of emissions. Even when traveling with the use of gasoline in HEVs and PHEVs, the efficiency of the ICE is significantly higher than the ICE of CVs. However, the reduction in fuel and emissions depends primarily on the energy generation mix used to create the electricity. The balance of the 2006 US electricity mix is composed of coal (49 %), nuclear (20 %), natural gas (20 %), hydroelectric (7 %), renewable (3 %), and others (1 %) [10]. Therefore, for the US average GHG intensity of electricity, PHEVs can reduce the GHG emissions by 7–12 % compared to HEVs. This reduction is negligible under high-carbon scenarios and 30–47 % under the low-carbon scenarios. When PHEVs are compared against CVs, the reduction in GHG emissions is about 40 % for the average

Fig. 46.1 Life cycle GHG emission sensitivity of CVs, HEVs, PHEV30, and PHEV90 under different carbon intensity scenarios (adapted from [1])

scenarios, 32 % for high cases, and between 51 and 63 % for low-carbon-based scenarios. The detailed life cycle GHG emissions (g CO_2-eq/km) for CVs, HEVs, and PHEVs under various scenarios are shown in Fig. 46.1. The number after PHEV (PHEV30 or PHEV90) represents the all-electric range of the vehicle in km.

When the emissions for PHEVs are examined, the majority of emissions come from the operational stage as shown in Fig. 46.1. A large portion is due to the gasoline used for traveling, followed by electricity used for traveling based on the carbon intensity of the electricity generation source. When the emissions from the electric power increase significantly under a high-carbon scenario (coal-based generation capacity), the reduction in volatile organic compounds (VOCs) and CO are offset by a dramatic increase in SO_x and slight increase in particulate emissions (PM10). However, the total GHG emissions are still lower compared to CVs since the increase in upstream emissions has a lower magnitude than the decrease in tailpipe emissions [6]. The GHGs associated with most battery materials and production generate a relatively small portion of the emissions and account for 2–5 % of the life cycle emission from PHEVs [1]. Moreover, the GHG emissions from the vehicle end of life are not shown since they are relatively negligible [11]. The reduced fuel use and GHG emissions for PHEVs depend significantly on vehicle and battery characteristics, as well as the recharging frequency. Using PHEVs also has a significant impact on the operating costs of the vehicle. PHEVs in all-electric mode can reduce the gasoline consumption by half, by shifting 45–77 % of the miles from gasoline to electricity, which would reduce the operating costs assuming that the electricity cost per mile is significantly less than the gasoline cost [12]. Battery life also has a significant role on the cost associated with PHEVs since replacing the battery would increase the life cycle cost of a PHEV by between 33 and 84 % [13]. However, the overall cost savings would be based on the overall cost of the vehicle, range, and driving behavior, as well as economic incentives such as taxes on carbon emissions and gasoline.

Fig. 46.2 Environmental impact of the evaluated technologies based on Eco-indicator 99 (adapted from [16])

46.2.3   Effects of Battery on the EV/HEV Environmental Impact

Environmental impact also has a significant role in advancing the battery technologies based on customer behavior, regulatory limitations, and cost (carbon tax, government incentives). Even though the substitution of battery technologies with conventional energy sources in the transportation industry reduces the associated environmental impact, the content and magnitude of this impact depend heavily on the electricity mix, battery technologies, and operating conditions. Life cycle assessment (LCA) has been performed in order to assess the overall environmental impact of the different battery technologies in various stages of their life [14, 15]. The environmental impact of the study based on eco-indicator 99 under a European electricity mix can be seen in Fig. 46.2. It should be noted that the energy losses due to efficiencies of the battery as well as the mass of the battery have a significant impact on the environment.

Among the analyzed battery technologies, NiCd has the most environmental impact mainly due to the presence of the environmentally hazardous material cadmium. This is followed by lead-acid based on its energy storage capacity, rather than the chemical content of the battery. The high environmental impact during the production stage is reduced by the excess recyclability since this battery technology has been around the longest. However, since lead-acid has the lowest specific energy density among the analyzed batteries, it may require additional mass and/or multiple charging to cover the same range with other batteries, producing more environmental impact. NiMH has relatively lower impact than the previous batteries since it has a significantly higher energy density than lead-acid and better recyclability than NiCd. This environmental impact is only reduced further with

Li-ion [16] mostly since it can store two to three times more energy than NiMH in its lifetime and an order of magnitude less nickel and an insignificant amount of rare earth metals [17]. However, these predictions are very sensitive to the battery characteristics and even a 5 % change in battery efficiency can lead up to 23 % change in GWP and reduction of lifetime can increase the impact in all categories by up to 45 %.

In the environmental assessments, the impact associated with the operating phase is determined to contribute up to 40 % of the GWP and 27–45 % of eutrophication (based on the European electricity mix) [15]. However, this impact is very sensitive to the content of the electricity mix and would increase by 10–16 % for GWP and 10–29 % for particulate matter for the Chinese electricity mix. The remainder is associated with assembly and recycling, which is based on the emissions with respect to the energy and materials used to assemble the batteries as well as the likelihood of recycling.

Even though different battery technologies have varying characteristics, the battery performance for all of them depends heavily on the operating temperatures. Batteries operate efficiently over a narrow temperature range (20–45 °C for most commonly used batteries) and uniformity (usually less than 5 °C nonuniformity) which is generally difficult to maintain due to different ambient temperatures and operating conditions. Operating outside of the specified temperature range affects the round trip efficiency, charge acceptance, and power and energy capability of the battery [18]. Since the battery performance and efficiency directly affect the vehicle performance, such as range, power for acceleration, and fuel economy, as well as reliability, safety, and life cycle cost [19], considerable focus has been given on keeping the battery at ideal conditions. In order to achieve this objective, several types of TMSs are currently used in EVs and HEVs.

46.2.4 EV/HEV Thermal Management Systems

Thermal issues associated with EV and HEV battery packs and underhood electronics can significantly affect the performance and life cycle of the battery and the associated system. In order to keep the battery operating at the ideal parameter ranges, the discrepancy between the optimum and operating conditions of the batteries needs to be reduced significantly by implementing TMSs in EVs and HEVs. These systems are utilized to improve the battery efficiency, by keeping the battery temperature within desired ranges. Thus freezing and overheating of the electrochemical systems in the battery can be averted which can prevent any reduction in power capability and charge/discharge capacity and premature aging of the battery [19–21].

Most electric and hybrid electric vehicle TMSs consist of four different cycles to keep the associated components in their ideal temperate range in order to operate safely and efficiently. Even though the components and structure of these loops may vary from vehicle to vehicle, their purposes are usually the same, creating an

efficient and robust system that is not adversely affected by internal and ambient temperature variations. Generally, the overall vehicle thermal TMS is composed of the radiator coolant loop, power electronics coolant loop, drive unit coolant loop, and air-conditioning (A/C) and battery loop. A brief description of these loops is provided below.

Radiator Circuit

In the radiator loop, the engine is kept cool by the mixture of water and antifreeze pumped into the engine block to absorb the excess heat and draw it away from the crucial areas. When this superheated engine coolant leaves the engine block, it returns to the radiator. The radiator has a very large surface area through the internal chambers where the excess heat of the coolant is drawn out through the walls of the radiator. As the vehicle moves, the front of the radiator is also cooled by the ambient air flowing through the car's grill. The loop also includes a surge tank, a storage reservoir for providing extra water during brief drops in pressure, as well as to absorb sudden rises of pressure. Next, a coolant pump is used for moving the coolant back and forth to the radiator. When the ICE is off, the cooler heating control module is used to provide heat to the coolant. A portion of the heat in this loop is also transferred to the passenger cabin with help of the heater core.

Power Electronics Circuit

The power electronics coolant loop is mainly dedicated to cooling the battery charger and the power inverter module to ensure that the main underhood electronics do not overheat during usage. The power inverter module converts direct current (DC) from the high-voltage battery into three-phase alternating current (AC) motor drive signals for the motor generator units. The module is also responsible for converting AC to DC for charging operations during regenerative braking. In these operations, a large amount of heat is generated in the system. In order to prevent overheating, the loop incorporates a high-flow electric pump to create and control the coolant flow which passes through the plug-in battery charger assembly, the radiator, and the power inverter module before it flows back to the pump. This loop also includes a coolant pump for the circulation of the coolant and an air separator to ensure that the coolant does not have any air bubbles that would affect the cooling performance before traveling through the major electronic parts.

Drive Unit Circuit

The drive unit loop is designed to cool the two motor generator units and electronics within the drive unit transaxle that are used to propel the vehicle using electric power (in addition to generating electricity to maintain high-voltage battery state of

charge). It provides lubrication for the various associated parts. Significant heat is generated in these parts due to high-power levels during normal operation. The drive unit uses a system of pressurized automatic transmission fluid to cool the electronics in the loop, especially the motor generator units to prevent overheating [22].

A/C Circuit

Even though all of the circuits mentioned above have significant roles in enabling the vehicle to operate as robustly, efficiently, and safely as possible, in EVs and HEVs, a majority of the focus is given to A/C and battery cooling loops due to its direct effect on the battery performance, which has significant impact on the overall vehicle performance, safety, and cost. For this reason, various studies are conducted in this cooling loop to optimize their operating conditions of the associated components, the cabin and the battery. Thus, different cooling systems and configurations will be analyzed based on various criteria and operating conditions.

The main goal of the A/C cycle is to keep the battery pack at an optimum temperature range, based on the cycle life and performance trade-off, in a wide spectrum of climates and operating conditions as well as keeping even temperature distributions with minimal variations within cells while keeping the vehicle cabin at desired temperatures. Meanwhile, the system should also consider trade-offs between functionality, mass, volume, cost, maintenance, and safety [23].

Since the main focus will be the A/C and battery loops, they will be called the TMSs for the rest of the analysis. They will be categorized based on their objective (providing only cooling vs. cooling and heating), method (passive where only the ambient environment is used vs. active cooling where a built-in source is utilized for heating/cooling), and heat transfer medium (air distributed in series/parallel or liquid via direct/indirect contact) [23].

A passive cabin air cooling system utilizes the conditioned air to cool the battery in warm ambient conditions. It was used on early EV and HEV battery packs (Honda Insight, Toyota Prius, and Nissan Leaf) mainly due to cost, mass, and space considerations. This is a very effective cooling method for the battery at mild temperatures (10–30 °C) without the use of any active components designated for battery cooling. It is highly efficient since it uses the heat from the vehicle air conditioning. The ideal battery operating temperature (for Li-ion) is around 20 °C on the low end, which is highly compatible with the cabin temperature. However, air conditioning systems are limited by the cabin comfort levels and noise consideration, as well as dust and other contaminants that might get into the battery, especially when air is taken from outside. Certain precautions should be taken in this system to prevent toxic gases from entering the vehicle cabin at all situations. In independent air cooling, the cool air is drawn from a separate micro air conditioning unit (instead of the vehicle cabin) with the use of the available refrigerant. Even though this may provide more adequate cooling to the battery, the energy consumption as well as cost and

space requirements associated with installation of the blower and the micro air conditioning unit increase significantly [24]. The rate of heat transfer between the fluid and the battery module depends on various factors such as the thermal conductivity, viscosity, density, and velocity of the fluid. Cooling rates can be increased by optimizing the design of air channels; however it is limited by the packaging efficiency due to larger spacing between the cells. Air can flow through the channel in both serial and parallel fashions, depending on whether the airflow rate splits during the cooling process. In series cooling, the same air is exposed to the modules since the air enters from one end of the pack and leaves from the other. In parallel cooling however, the same airflow rate is split into equal portions where each portion flows over a single module. In general, parallel airflow provides a more uniform temperature distribution than series [25].

Refrigerant cooling is a compact way of cooling the battery, with more flexibility compared to a fan with ducts, by connecting the battery evaporator parallel to the evaporator in the cooling loop. Heat generated by the battery is transferred to the evaporating refrigerant. This system only requires two additional refrigerant lines, namely, suction and pressure lines. The battery evaporator uses some portion of the compressor output that was reserved for the air conditioning, and thus this might cause conflict in some conditions. However, the compressor work needed to cool the battery is usually considerably lower than the air conditioning evaporator need.

Liquid cooling utilizes the previous cooling method with the incorporation of an additional liquid cooling loop specifically for the battery that connects to the refrigerant. This additional cooling loop usually has water or a 50/50 water–glycol mixture and it is kept cool via different procedures depending on the cooling load and ambient conditions. The coolant can be cooled either by ambient air through the battery cooler (if the ambient temperature is low enough) or by transferring the heat to the refrigerant through the chiller. Both methods increase the efficiency of the system since the additional compressor work (that is used in refrigerant cooling) is no longer needed.

In addition, battery cooling can also be done with phase change material (PCM) integrated cooling systems. PCMs have significant advantages over the aforementioned TMSs due to their simple design, lightweight and compact size, safety, and relatively low cost, especially when the integration is considered from the outset and it is improved with the addition of aluminum foam and fins [26]. PCMs are capable of keeping the magnitude and uniformity of the cell temperatures under stressful operating conditions without the need of a complicated system or a fan power. Moreover, the heat transfer associated with adding PCMs to a cell can prevent the propagation of thermal runaway, when the cell temperature reaches critical levels. Furthermore, PCMs can be used to have both an active and a passive role (complementary/secondary) in thermal management of the battery packs which can reduce the complexity and cost of the system [27, 28].

46.3 System Description

46.3.1 System Configuration

HEV TMSs are significantly different systems with unique requirements with respect to their commercial and industrial counterparts such as conventional vehicle and residential building air conditioning systems. The TMS needs to handle significant thermal load variations and provide comfort under highly fluctuating conditions, as well as be compact and efficient, and last several years without any significant maintenance. Moreover, the airflow volume, velocity, and temperature must be adjustable over a wide range of ambient temperatures and drive cycles without having a significant impact on the all-electric vehicle performance characteristics. Furthermore, due to the limited time spent in the vehicles compared to buildings, along with the competing energy requirements between the cabin and the battery, the TMSs must be capable of conditioning the air in the passenger cabin quickly and quietly while keeping the vehicle components operating under ideal operating temperature ranges (especially the electric battery) to prolong their lifetime and increase the fuel efficiency and all-electric range. Thus, special attention needs to be given to HEV TMSs [29, 30].

A simplified TMS of an electric vehicle with liquid battery cooling is considered in Fig. 46.3. The system is composed of two loops, namely, a refrigerant and battery coolant loop. The refrigerant loop enables air conditioning of the vehicle cabin, while the coolant loop keeps the electric battery operating within its ideal temperature range. These two loops are connected via a chiller, which enables heat exchange
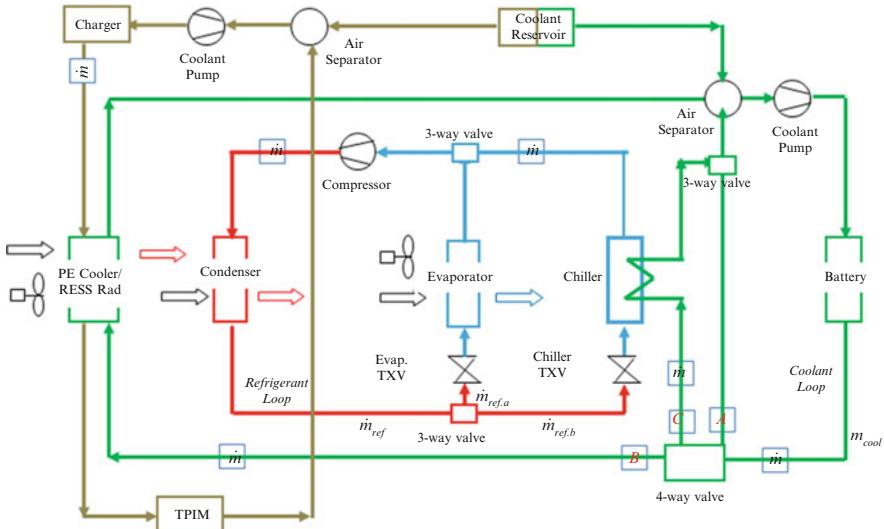
Fig. 46.3 Simplified representation of the hybrid electric vehicle thermal management system

among the loops to provide supercooling to the battery cooling as it passes through the chiller unit. This increases the efficiency of the system significantly since cooling via refrigeration circuit would consume more energy than operating the battery coolant circuit due to the need of the air compressor in the first case [24].

The TMS incorporates the advantages of both the air cooling and refrigerant-based cooling with the help of the additional battery cooler and chiller. The additional cooling loop is kept cool via different procedures depending on the cooling load and ambient conditions. If the battery coolant circuit has stable temperatures within the ideal range, then it bypasses the TMSs and only recirculates before getting pumped into the battery (Route A as shown in Fig. 46.3). This loop permits temperature stability by controlling cell temperatures through pump control. When the battery temperature is high and the ambient temperature is lower than the desired temperature of the battery, the ambient airflow in the battery cooler is used to keep this coolant circuit cool (Route B). If the battery temperature is significantly higher and the ambient temperature is higher than the desired battery temperature, then by operating the electric air conditioning compressor, R134a refrigerant will be throttled by the thermal expansion valve (TXV) to permit supercooling of the battery coolant as it passes through the chiller unit (Route C). This increases the efficiency of the system significantly since cooling via a cooling circuit would consume more energy than operating the battery coolant circuit due to the need of the air compressor in the first case [24].

The system includes three cooling media—an R134a refrigerant is used in the refrigerant cycle, water/glycol mixture of 50/50 by weight is used in the battery coolant cycle, and ambient air is utilized in the evaporator and condensers in the system. In the baseline model, ambient air conditions of 35 °C and 1 atm. are used to study the effects of the TMS on the battery. The refrigerant mass flow rates are determined from TXV correlations and the cooling capacity is calculated accordingly. For the baseline model, the temperature of the passenger cabin is set at 20 °C. Temperatures of 5 and 55 °C are used for evaporating and condensing temperatures along with 5 °C superheating and subcooling in the evaporator and condenser, respectively. The refrigerant mass flow rate in the chiller is determined with respect to the amount of battery heat transferred from the water/glycol mix in the coolant circuit to the refrigerant circuit via the chiller. In the refrigerant cycle, the refrigerant flow in the evaporator and chiller is combined in the system before it is compressed to the condenser. For the coolant circuit, the battery coolant temperature is assumed to be 19 °C before entering the battery, and the heat generated by the battery is assumed to be 0.35 kW on average, where the mass flow rate of the battery coolant is determined accordingly.

46.3.2   System Parameters

For the analysis, each input is varied within certain ranges in order to understand the effects of each parameter on the overall system for different refrigerants. These ranges were constructed based on the common standards in the literature along with

Table 46.1 Range of
parameters in the analysis

Parameter	Range of variation
Compressor speed (rev/min)	1,500–5,000
Compression ratio	1–5
Evaporating air temperature (°C)	0–15
Superheating temperature (°C)	0–12
Evaporator air mass flow rate (kg/s)	0.1–0.5
Cooling capacity (kW)	1–5
Condensing air temperature (°C)	40–55
Condenser air mass flow rate (kg/s)	0.1–0.5
Subcooling temperature (°C)	0–12

physical and economical limitations. In the refrigeration cycle, up to 12 °C of superheating and subcooling is utilized in order to improve the system efficiency. The evaporator and condenser air mass flow rates vary with respect to the vehicle speed and fan power. They are taken to be between 0.1 and 0.5 kg/s. Moreover, initially relatively high ambient temperatures are used in order to observe the effects of cooling on the electric battery under high temperatures, since hot weather conditions are a more significant concern than cold weather conditions due to the permanent effects of high temperatures on the battery performance as well as associated potential safety concerns. Furthermore, a cooling capacity of up to 5 kW is used in order to provide adequate cooling to the vehicle cabin under these ambient temperatures. The list of all parameters and their selected ranges can be observed in Table 46.1.

Moreover, since the use of R134a will be terminated in the near future by the European Community (due to the requirement of using refrigerants with GWP less than 150), the use of alternative refrigerants in the TMS is considered for the analysis [31]. One of the possible solutions to avoid R134a is the use of natural refrigerants, such as hydrocarbons, since they are environmentally benign with negligible GWP and zero ODP. They also have various additional advantages such as availability, low cost, high miscibility with conventional mineral oil, and compatibility with existing refrigerating systems. On the other hand, their main drawback is potential flammability and safety hazards. The characteristics of these refrigerants along with R134a can be seen in Table 46.2. In addition, there are also certain other refrigerants that could be utilized in EV TMSs, such as R1234yf and dimethyl ether (DME), and therefore included in the analysis. R1234yf is one of the major candidates as a replacement for R134a in automotive applications due to its ability to be used with compatible materials and oils as well as a low GWP and low normal boiling temperatures with respect to R134a. Moreover, DME is another good candidate due to being nontoxic, widely available, and environmentally safe and having excellent material compatibility and better heat transfer properties as well as lower costs than R134a. The main drawback is its high flammability, which is about twice as high as the other hydrocarbons.

Table 46.2 Characteristics of R134a and various alternative refrigerants [32–34]

Code	Chemical formula/ common name	NBP[a] (°C)	T_{crit} (°C)	P_{crit} (bar)	Latent heat (kJ/kg)	Lower flam. limit (vol.%)[b]	GWP
R134a	CH_2FCF_3	−42.1	96.7	42.5	216.8	Nonflammable	1,300
R290	C_3H_8/propane	−42.1	96.7	42.5	423.3	2.3–7.3	20
R600	C_4H_{10}/butane	−0.5	152.0	38.0	385.7	1.6–6.5	20
R600a	C_4H_{10}/isobutane	−11.7	134.7	36.4	364.2	1.8–8.4	20
R1234yf	$CF_3CF=CH_2$/ tetrafluoropropene	−29.0	95	33.8	175	6.2–13.3	4
RE170 (DME)	CH_3OCH_3/dimethyl ether	−24.7	126.9	53.7	410.2	3.4–17	<3–5

[a]Normal boling point (NBP) is at 101.325 kPa (°C)
[b]Explosive limits in air % by volume

46.4 Thermodynamic Analysis

In the analysis, the evaporator is divided into two-phase and superheated regions. The condenser is divided into desuperheated, two-phase, and subcooled regions. The heat transfer and pressure drop correlations associated with the evaporator and condenser are determined with respect to correlations in Table 46.3.

Based on the aforementioned model, correlations, and parameter ranges, a steady-state thermodynamic model was created with Engineering Equation Solver (EES) and REFPROP software [39, 40]. In order to create a consistent comparison between different refrigerants, the same cooling capacity (3 kW) and condensing and evaporating temperatures (55 and 5 °C, respectively), along with superheating and subcooling temperatures (5 °C), were used in each model. The parameters for the model with different refrigerants are shown in Table 46.4.

Once the properties are determined at each point in the system, the mass, energy, entropy, and exergy balance equations are used to calculate the exergy efficiency and exergy destruction rate of component irreversibilities in Table 46.5.

Based on the work input to the system (in terms of the compressor and pump) and the associated cooling load (with regard to the evaporator and the chiller) under the defined boundary conditions, the energetic and exergetic COPs of the TMS are also determined based on Eqs. (46.1a) and (46.1b) below [41, 42]:

$$COP_{en,system} = \frac{\dot{Q}_{evap} + \dot{Q}_{ch}}{\dot{W}_{comp} + \dot{W}_{pump}} \qquad (46.1a)$$

$$COP_{ex,system} = \frac{\dot{Ex}_{\dot{Q}_{evap}} + \dot{Ex}_{\dot{Q}_{ch}}}{\dot{W}_{comp} + \dot{W}_{pump}} \qquad (46.1b)$$

Furthermore, the GHG emissions associated with the TMS are calculated based on the electricity consumption of the TMS and the indirect emissions associated

Table 46.3 Heat transfer and pressure drop correlations for evaporator and condenser [35–38]

Part	$\bar{h}_{ref}$ correlation	ΔP_{ref} correlation
Evap. Cond.	$\bar{h}_{evap\ or\ cond} = \frac{k}{D_i} \cdot \frac{0.5f(Re-1000)Pr}{1+12.7(0.5f)^{0.5}\left(Pr^{\frac{2}{3}}-1\right)}$ $f = 0.054 + 2.3 \times 10^{-8}Re^{3/2}$ *for* $2300 < 4000$ $f = 1.28 \times 10^{-3} + 0.1143Re^{-0.311}$ *for* $4000 < 5 \times 10^6$	$\Delta P_{evap} = 6 \times 10^{-6}Re_g^{1.6387}\ for\ 4000e_g < 12000$ $\Delta P_{cond} = 6 \times 10^{-8}Re_g^2 + 0.0009\ Re_g$ $\quad - 6.049\ for\ 3000 < Re_g < 3 \times 10^4$

Table 46.4 Operating parameters of a standard EV TMS with various refrigerants at baseline conditions

Refrigerant	$\dot{m}_{ref,a}$ (kg/s) $\times 10^2$	$\dot{m}_{ref,b}$ (kg/s) $\times 10^2$	$\dot{W}_{comp}$ (kW)	x_{evap} (–)	$T_{sat,dis}$ (°C)	P_{dis} (kPa)	ΔP_{cond} (kPa)	ΔP_{evap} (kPa)
R134a	2.21	0.26	1.30	0.31	81.92	1,492	25.11	29.41
R290	1.18	0.14	1.27	0.32	77.93	1,907	24.60	32.97
R600	1.08	0.13	1.26	0.28	73.62	564.6	8.64	14.00
R600a	1.25	0.15	1.26	0.32	68.71	764.8	10.68	17.64
R1234yf	2.98	0.35	1.37	0.39	65.60	1,464	53.61	64.51
(DME)	0.92	0.11	1.21	0.25	95.33	1,297	6.28	13.25

Table 46.5 Exergy efficiencies and exergy destruction rates associated with each system component

Part	Exergy efficiency	Exergy destruction rate
Compressor	$(\dot{Ex}_{2,act} - \dot{Ex}_1)/\dot{W}_{comp}$	$\dot{Ex}_{D,comp} = T_0\dot{m}_r(s_2 - s_1)$
Condenser	$\dot{Ex}_{\dot{Q}_H}/(\dot{Ex}_2 - \dot{Ex}_3)$	$\dot{Ex}_{D,cond} = T_0[\dot{m}_c(s_{c2} - s_{c1}) - \dot{m}_r(s_2 - s_3)]$
Evaporator TXV	$\dot{Ex}_4/\dot{Ex}_{3'}$	$\dot{Ex}_{D,evap,TXV} = T_0\dot{m}_{r1}(s_4 - s_3)$
Chiller TXV	$\dot{Ex}_5/\dot{Ex}_{3'}$	$\dot{Ex}_{D,ch,TXV} = T_0\dot{m}_{r2}(s_5 - s_3)$
Evaporator	$\dot{Ex}_{\dot{Q}_L}/(\dot{Ex}_4 - \dot{Ex}_{1'})$	$\dot{Ex}_{D,evap} = T_0[\dot{m}_e(s_{e2} - s_{e1}) - \dot{m}_{r1}(s_4 - s_1)]$
Chiller	$\dot{Ex}_{\dot{Q}_{ch}}/(\dot{Ex}_5 - \dot{Ex}_{1''})$	$\dot{Ex}_{D,ch} = T_0[\dot{m}_{cool}(C_{wg}\ln(T_6/T_7)) - \dot{m}_{r2}(s_5 - s_1)]$
Pump	$(\dot{Ex}_{8,act} - \dot{Ex}_7)/\dot{W}_{pump}$	$\dot{Ex}_{D,pump} = T_0\dot{m}_{cool}(C_{wg}\ln(T_6/T_0))$
Battery	$\dot{Ex}_{\dot{Q}_{bat}}/(\dot{Ex}_6 - \dot{Ex}_8)$	$\dot{Ex}_{D,bat} = T_0\dot{m}_{cool}(C_{wg}\ln(T_6/T_8))$
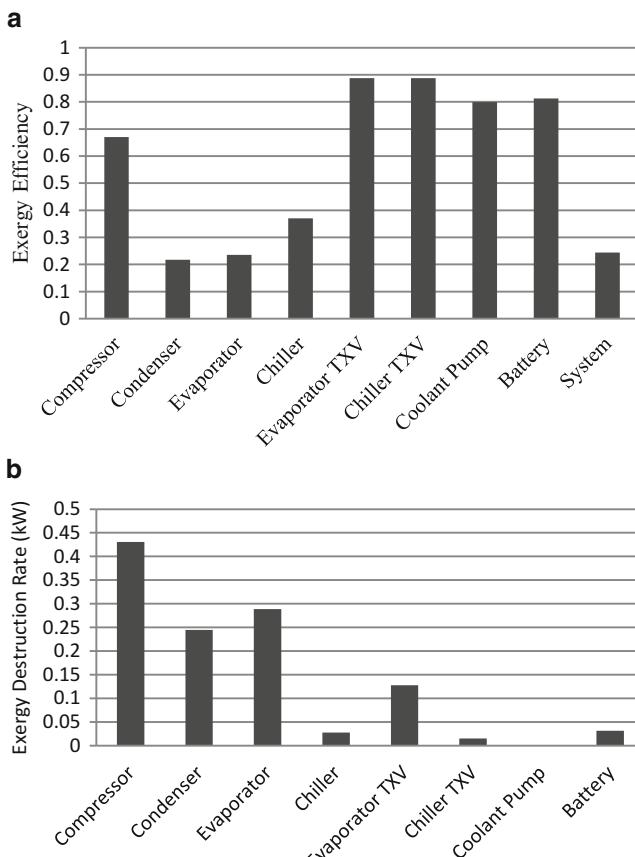
with the electricity production carbon intensity. Finally, the sustainability index is then determined as a measure of how the exergy efficiency affects sustainable development as shown in Eq. (46.2) below:

$$SI = \frac{1}{1 - \psi} \tag{46.2}$$

In the next section, sample results for a TMS with various refrigerants are presented and discussed, including TMS COPs along with the environmental impact and sustainability index.

46.5 Results and Discussion

A software code in EES was created to analyze a baseline model, with respect to the balance equations and system parameters provided. Based on the baseline analysis, the exergy efficiencies and exergy destruction rates associated with each component are provided in Fig. 46.4. Throughout the exergy analysis, the exergetic efficiency and exergy destruction rates are calculated for each component in the TMS. Among these components, the heat exchangers have the lowest exergy efficiencies with respect to the high temperature differences and phase change which results in more entropy generation between the refrigerant and coolants. In addition, based on the conducted analysis, the exergy destruction ratios for the components are determined to be in the following descending order: condenser (78.3 %), evaporator (75.2 %), chiller (56.8 %), compressor (31 %), electric battery (25 %), pump (20.1 %), and thermal expansion valves (11.2 %).

Fig. 46.4 Baseline model: (**a**) Exergy efficiency and (**b**) exergy destruction rate of each component in the refrigerant and coolant cycles
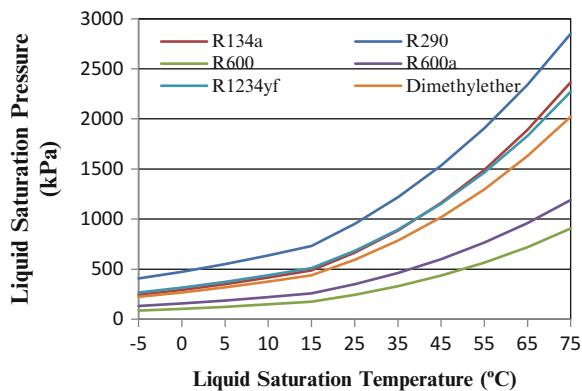
In the evaporator, the exergy losses are relatively high since (aside from the frictional losses) only part of the heat rejection occurs during the phase change process with large temperature differences between the working fluid in the evaporator and the vehicle cabin. Thus, reducing the mean temperature difference would reduce the exergy losses. One way of reducing the mean temperature difference is to increase the evaporator surface area; however, it should be weighed against the increase in the cost of installation [43].

The condenser is calculated to have a lower exergy efficiency than the evaporator and the chiller, mainly due to the relatively higher temperature difference between the condenser exit and ambient air (taken at 35 °C), when compared to the differences between the evaporator exit and vehicle cabin temperature as well as the refrigerant and coolant temperatures. Among the remaining components, the compressor has a relatively low exergy efficiency due to the high compression pressure ratio and change in temperature of the refrigerant passing through the compressor, which contributes to an increase in exergy destruction. The exergy loss in the compressor can be reduced by using a compressor with higher isentropic efficiencies. Moreover, since the compressor power is highly dependent on the inlet and outlet pressures, proper sealing inside the compressor, heat exchanger improvements (such as reducing ΔT), and implementation of multistage compression would reduce the exergy losses, thus reducing the compressor power.

Furthermore, since a part of the irreversibilities occurs with respect to the frictional losses inside the compressor, utilizing appropriate lubricating oil that is miscible with the refrigerant (such as polyolester oil for R-134a) would reduce the respective exergy losses. There is also significant research conducted [44, 45] on the effects of using additives with a high conductivity (certain lubricant-based nanofluids) in the refrigerant in order to improve the heat transfer rate, thus reducing the difference in the operating temperatures, which also reduced the exergy losses. However, proper care must be taken in the utilization of the lubricant in order to prevent the deposition of the lubricant in the evaporator wall. The interaction between the cooling and battery coolant cycles also helps in reducing the compressor requirements significantly. The transfer of excess heat from the battery coolant to the cooling cycle via the chiller helps allocate the thermal energy appropriately, since otherwise, the cooling cycle would need to supply the additional energy which uses a compressor. Therefore, further utilizing this interaction would also be beneficial. Moreover, irreversibilities in the system occur due to high temperature differences in heat exchangers, and therefore reducing these differences would reduce the associated irreversibilities [24].

The exergy efficiencies for the evaporator TXV and chiller TXV are higher (over 80 %) since the processes are isenthalpic and have little or no heat loss. Therefore the exergy losses occur mainly due to a pressure drop in the expansion valve. The exergy losses in these TXVs can be reduced by lowering (or subcooling) the temperature of the refrigerant exiting the condenser, which can be feasible by utilizing the refrigerant vapor exiting the evaporator [46, 47]. The coolant pump also has a relatively higher efficiency (81 %) since there is no significant heat loss from the pump.

Fig. 46.5 Liquid saturation
temperature vs. pressure for
various refrigerants with
respect to the evaporating
temperature
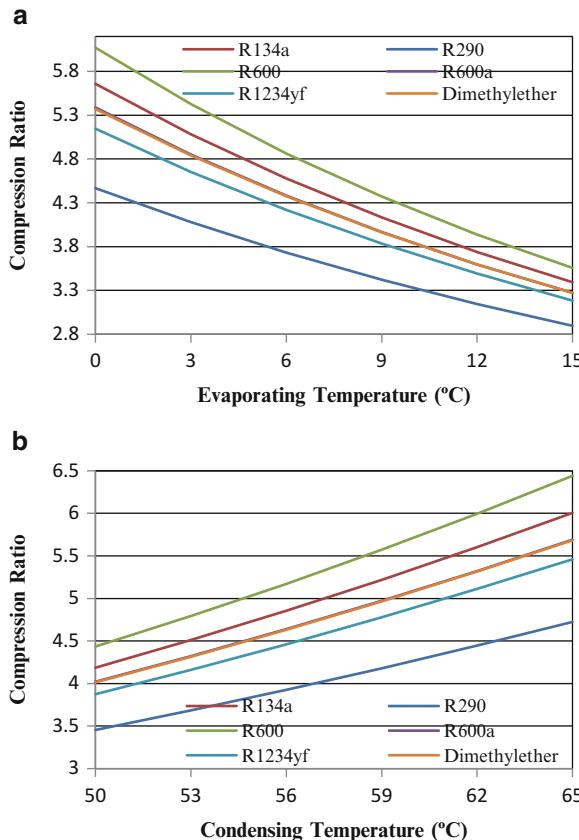
It should be noted that the battery is modeled as a system and thus the internal
efficiencies for the battery are not considered in this analysis. In this regard, the
battery has high efficiencies within the target operating temperature range (up to
50 °C). However, the associated efficiency would decrease significantly as the
battery is heated up beyond this range.

Moreover, parametric studies are conducted with respect to various refrigerants
using EES and REFPROP software. In order to have a consistent comparison
between these different refrigerants, the same cooling capacity (3 kW) and con-
densing and evaporating temperatures (55 and 5 °C, respectively), along with
superheating and subcooling temperatures (5 °C), are used in each model.

In order for a refrigerant to be a suitable replacement for R134a, its compressor
capacity should be similar to avoid a different size compressor in the cycle to
accommodate the difference in capacity. For this reason, the vaporization tempera-
ture of the liquid in the evaporator (which is the suction or the evaporating tempera-
ture) becomes one of the critical properties in considering a drop-in replacement
refrigerant for the TMS, since refrigerants with similar vapor pressure will evaporate
and condense at the same pressures. Thus, a refrigeration cycle designed with a
particularly high and low side pressure would perform comparably for two
refrigerants with comparable vapor pressures [48]. This would prevent a different
size compressor in the cycle, since the compressor size is decreased for fluids with
higher vapor pressure and increased for systems with higher vapor pressure in order
to provide the same cooling load. Moreover, since the expected capacities are
proportional to the vapor pressure, the saturation pressure and temperature of the
refrigerant alone would be good indicators of the compressor displacement volume
[49]. Thus, a convenient way to compare vapor pressure for multiple refrigerants is a
saturation temperature–pressure plot as shown in Fig. 46.5.

As shown in Fig. 46.5, R290, R1234yf, and DME have more compatible drop-in
replacements (with the least changes in compressor physical dimensions) based on
their compressor capacities, compared to R600 and R600a.
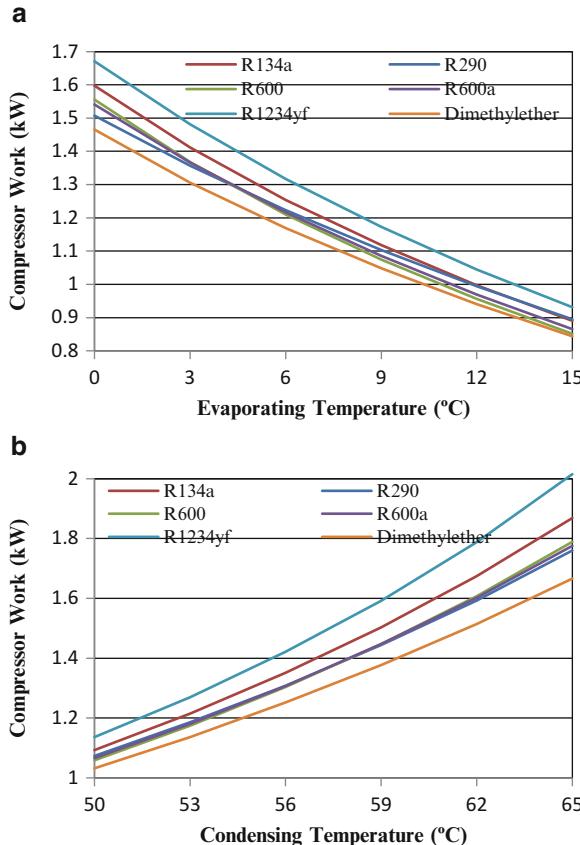
The compression ratio is also a useful parameter on which to predict the
volumetric performance of the compressor, since lower compression ratios can

Fig. 46.6 Compression ratio of the TMS with respect to (**a**) evaporating and (**b**) condensing temperatures using various refrigerants

reduce the amount of potential leakage, and therefore can be used to compare the performance of the TMS using various refrigerants. Figure 46.5 shows that TMSs using R-600, R600a, and R134a have higher compression ratios compared to the other systems. Systems utilizing R1234yf and DME exhibit the closest behavior to that of R134a with the compression ratio slightly lower than R134a system. Furthermore, the lowest compression ratio is achieved by TMS using R290, where it outperforms the system using R-134a up to 18 % depending on the condensing and evaporating temperatures.
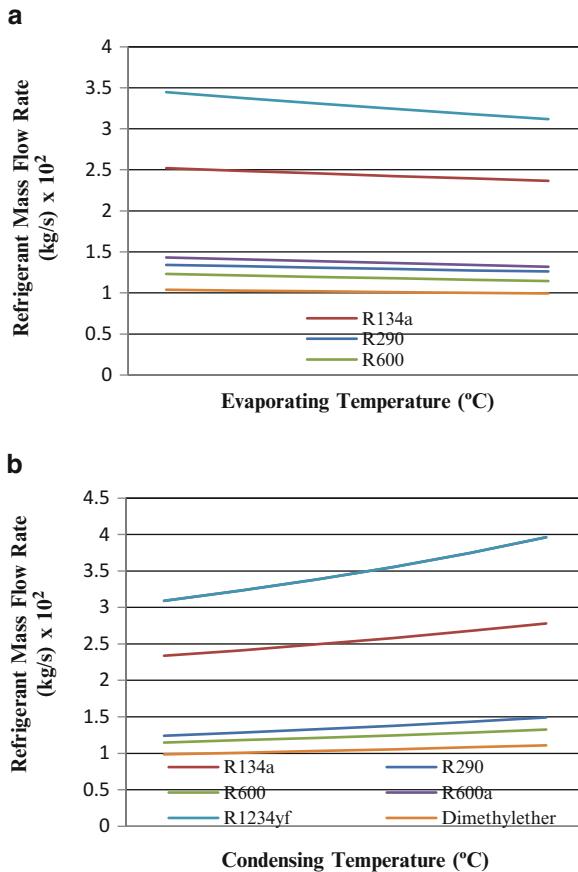
Moreover, the compressor work is also compared for the TMS using different refrigerants based on various evaporator and condenser temperatures, since it has a significant impact on the overall efficiency of the cycle. It can be seen that even though the TMS using R1234yf has a very low compression ratio among the refrigerants, it has the highest compressor work under baseline conditions due to its highest mass flow rate, as shown in Fig. 46.6a, b. On the other hand, the TMS

Fig. 46.7 Compressor work of the TMS with respect to (**a**) evaporating and (**b**) condensing temperatures using various refrigerants

using DME has the lowest compressor work due to having the lowest mass flow rate as well as a relatively low compression ratio under baseline conditions. The systems using the rest of the studied refrigerants are calculated to have similar but slightly less compressor work, compared to R134a, due to lower compression ratios and significantly lower mass flow rates in the system as shown in Figs. 46.6, 46.7, and 46.8.
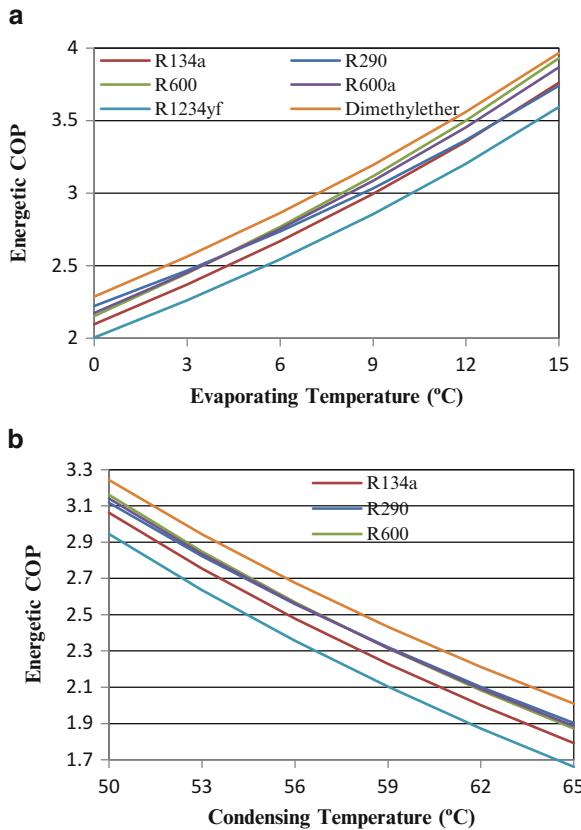
Moreover, since the energy consumption of the compressor is also proportional to the pressure ratio and refrigerant mass flow rate, the COP of the system also varies for the same cooling loads and different refrigerants. Among the TMS studied, all of the systems, except those using R1234yf, have lower exergy destruction rates and higher energetic and exergetic COPs compared to the baseline R134a system for the range of evaporating and condensing temperatures. TMS using DME has the highest energetic and exergetic efficiencies with 7.3 and 7.7 % higher than the baseline R134a system, respectively. However, due to the high flammability of

a

b

Fig. 46.8 Refrigerant mass flow rate with respect to (**a**) evaporating and (**b**) condensing temperatures using various refrigerants
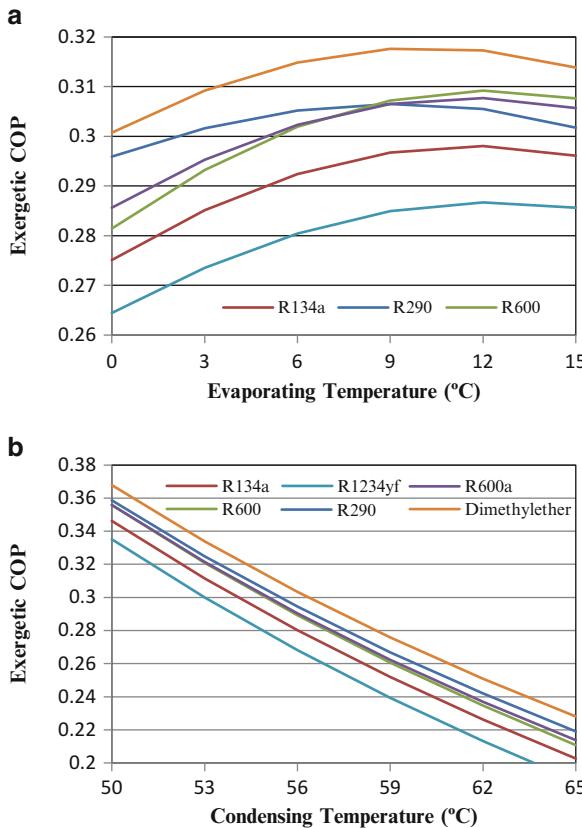
this substance, in order to reduce the associated safety concerns, a secondary loop should be implemented to the TMS, where the conventional evaporator is replaced by a secondary fluid heat exchanger, which transfers heat between the primary and secondary loops. Thus, the overall efficiency of the system using this refrigerant may decrease for more practical applications. The energetic and exergetic COPs and exergy destruction of TMS with respect to evaporating and condensing temperatures using various refrigerants can be observed from Figs. 46.9, 46.10, and 46.11, respectively.

Once the TMS COPs are calculated for various refrigerants, the corresponding indirect emissions and the sustainability indices are determined with respect to the system parameters of the baseline model. The sustainability index is a good indicator of how efficiently the resources are utilized in the TMS. Thus, it is therefore directly related to the exergetic COP and exergy destruction rates
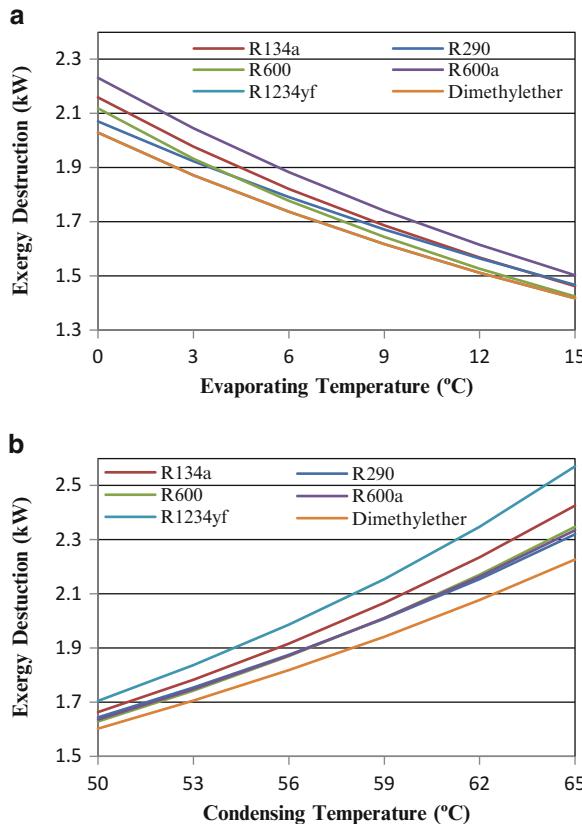
Fig. 46.9 Energetic COP of the TMS with respect to (**a**) evaporating and (**b**) condensing temperatures using various refrigerants

associated with each TMS. Moreover, the indirect GHG emissions are produced from electricity generation associated with the compressor and pump for the TMS. Figure 46.12 shows the GHG emissions and sustainability index with respect to the exergetic COP for the baseline TMS using R134a. As the efficiency of the baseline TMS is increased, the power input required for the TMS will decrease under the same cooling loads. Hence, the corresponding emissions will decrease and the sustainability index will increase. It should be noted that the emissions in Fig. 46.12a are determined based on the US average energy generation mix [50] and therefore the associated indirect emissions will be different under other energy generation cases with different carbon intensities. Figure 46.12b shows that the emissions produced from electricity generation almost double under a high-carbon scenario, such as with coal. This reduces significantly under a low-carbon scenario, where electricity is produced through a natural gas combined cycle.
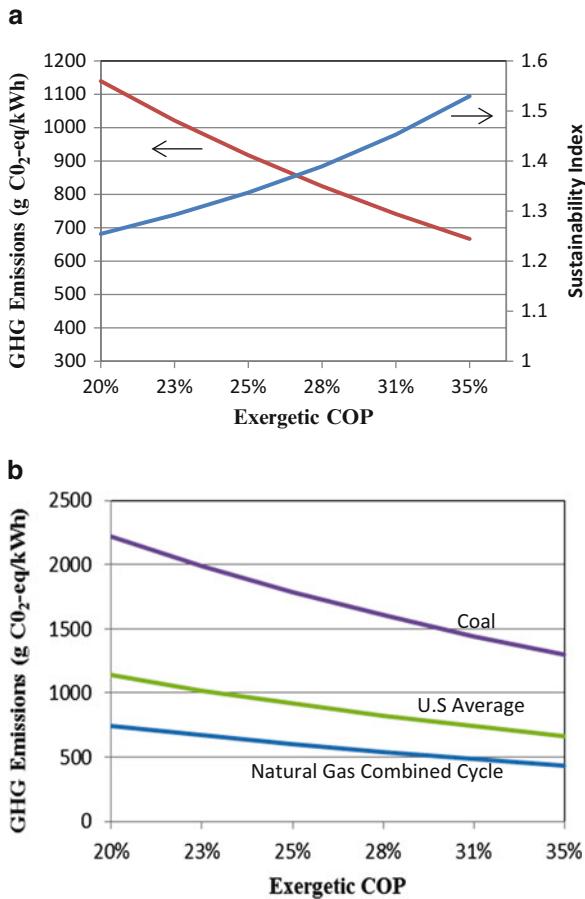
Fig. 46.10 Exergetic COP of the TMS with respect to (**a**) evaporating and (**b**) condensing temperatures using various refrigerants
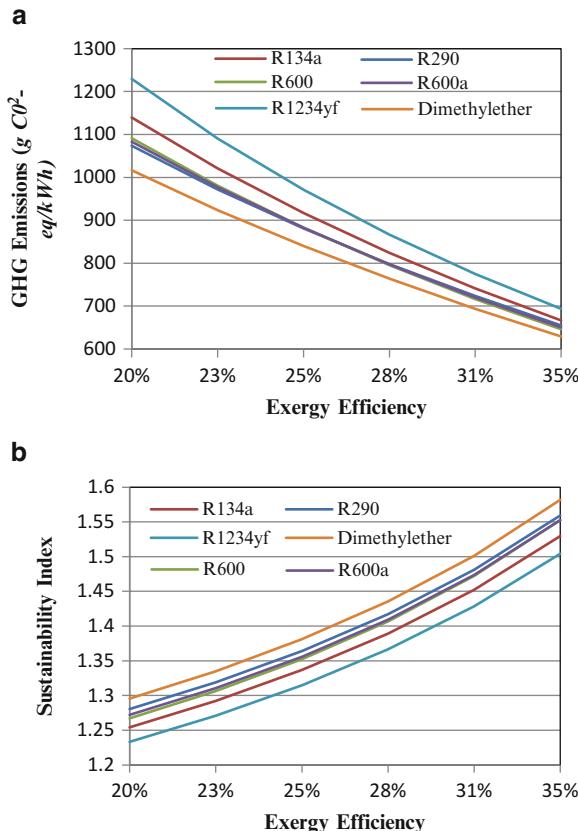
Moreover, the calculated baseline TMS GHG emissions and sustainability index are compared against TMSs using various refrigerants. Figure 46.13a, b shows that the TMS using R1234yf generates the highest indirect emissions and lowest sustainability index (6 and −1.6 % over the baseline TMS, respectively). The case with DME generates the lowest indirect emissions and highest sustainability index (−8.3 and 3.3 % over the baseline TMS, respectively), among the studied TMSs.

Fig. 46.11 Exergy destruction of the TMS with respect to (**a**) evaporating and (**b**) condensing temperatures using various refrigerants

Fig. 46.12 (**a**) GHG emissions and sustainability index with respect to baseline TMS exergetic COPs (**b**) under various carbon intensity of electricity generation

Fig. 46.13 (**a**) GHG emissions and (**b**) sustainability index with respect to exergetic COPs of the TMSs using various refrigerants

46.6 Conclusions

In this chapter, a TMS of an HEV composed of R134a refrigerant and 50/50 glycol mixture battery coolant circuits was examined under different operating conditions and compared against various alternative refrigerants such as R290 (propane), R600 (butane), R600a (isobutane), R1234yf (tetrafluoropropene), and DME, in terms of efficiency and environmental impact. Based on the analysis, the following main findings are obtained:

(a) The TMSs using R290, R600, and R600a were calculated to have similar energetic and exergetic COPs, which are slightly over the baseline TMS. The highest energetic and exergetic COPs are achieved by a TMS using DME (7.9 and 8.2 % higher than baseline, respectively), while the lowest energetic and

exergetic COPs are achieved by R1234yf (4.9 and 4.2 % less than baseline, respectively).

(b) All of the analyzed TMSs, except for the case using R1234yf, were calculated to have lower environmental impact and sustainability indices than the baseline TMS. However, the associated GHG emissions depend significantly on the electricity production mix and can be doubled for all refrigerants under high-carbon scenarios.

(c) The TMS using DME has the lowest GHG emissions (8.3 % lower than baseline) and highest sustainability index (3.3 % higher than baseline). However, due to the high flammability of this refrigerant, secondary loop systems should be added before calculating the overall system efficiency and environmental impact associated with the refrigerant.

References

1. Samaras C, Meisterling K (2008) Life cycle assessment of greenhouse gas emissions from plug-in hybrid vehicles: implications for policy. Environ Sci Technol 42:3170–3176
2. Koban M (2009) HFO-1234yf low GWP refrigerant LCCP analysis. In: Proceedings of SAE world congress, Detroit, MI, USA
3. Faiz A, Weaver CS, Walsh MP (1996) Air pollution from motor vehicles: standards and technologies for controlling emissions. World Bank Publications, Washington, DC
4. Nelson RF (2000) Power requirements for batteries in hybrid electric vehicles. J Power Sources 91:2–26
5. Doucette RT, McCulloch MD (2001) Modeling the prospects of plug-in hybrid electric vehicles to reduce CO_2 emissions. Appl Energy 88:2315–2323
6. Bradley TH, Frank AA (2009) Design, demonstrations and sustainability impact assessments for plug-in hybrid electric vehicles. Renew Sustain Energy Rev 13:115–128
7. Shiau CN, Samaras C, Hauffe R, Michalek JJ (2009) Impact of battery weight and charging patterns on the economic and environmental benefits of plug-in hybrid vehicles. Energy Policy 37:2653–2663
8. Ross M (1994) Automobile fuel consumption and emissions: effects of vehicle and driving characteristics. Annu Rev Environ Resour 19:75–112
9. National Household Travel Survey Data (2001) U.S. Department of Transportation, Federal Highway Administration. http://nhts.ornl.gov/download.shtml#2001
10. EIA (2008a) Annual energy review 2007. US Department of Energy. http://www.eia.doe.gov/emeu/aer/elect.htmlS
11. Schmidt WP, Dahlqvist E, Finkbeiner M, Krinke S, Lazzari S, Oschmann D, Pichon S, Thiel C (2004) Life cycle assessment of lightweight and end-of-life scenarios for generic compact class passenger vehicles. Int J Life Cycle Asses 9:405–416
12. Yeh S (2009) Reducing long-term transportation emissions: electricity as a low carbon fuel. Presentation at the EPRI conference, Long Beach, California
13. Wood E, Alexander M, Bradley TH (2011) Investigation of battery end-of-life conditions for plug-in hybrid electric vehicles. J Power Sources 196:5147–5154

14. Matheys J, Timmermans J-M, Van Mierlo J, Meyer S, Van den Bossche P (2009) Comparison of the environmental impact of 5 electric vehicle battery technologies using LCA. Int J Sustain Manuf 1:318–329
15. Majeau-Bettez G, Hawkins TR, Strømman AH (2011) Life cycle environmental assessment of lithium-ion and nickel metal hydride batteries for plug-in hybrid and battery electric vehicle. Environ Sci Technol 45:4548–4554
16. Bossche PV, Vergels F, Mierlo JV, Matheys J, Autenboer WV (2006) SUBAT: an assessment of sustainable battery technology. J Power Sources 162:913–919
17. Pesaran AA (2002) Battery thermal models for hybrid vehicle simulations. J Power Sources 110:377–382
18. Pesaran AA, Vlahinos A, Stuart T (2003) Cooling and preheating of batteries in hybrid electric vehicles. 6th ASME-JSME thermal engineering conference, Hawaii
19. Noboru S (2001) Thermal behavior analysis of lithium-ion batteries for electric and hybrid vehicles. J Power Sources 99:70–77
20. Pesaran AA, Kim G, Keyser M (2009) Integration issues of cells into battery packs for plug-in and hybrid electric vehicle. EVS 24 Stavanger, Norway
21. Kuper Ch, Hoh M, Houchin-Miller G, Fuhr J (2009) Thermal management of hybrid vehicle battery system. 24th International battery, hybrid and fuel cell electric vehicle conference and exhibition, Stavanger, Norway
22. GM-Volt LLC website. (2010) The Chevrolet volt cooling/heating systems explained. http://gm-volt.com/2010/12/09/the-chevrolet-volt-coolingheating-systems-explained. Accessed 10 Oct 2012
23. Pesaran AA (2001) Battery thermal management in EVs and HEVs: issues and solutions. Advanced automotive battery conference, Las Vegas, Nevada, USA
24. Behr GmbH & Co. KG, Press Official Website. (2009) Technical Press Day. http://www.behrgroup.com/Internet/behrcms_eng.nsf. Accessed 01 Oct 2012
25. Pesaran AA, Burch S, Keyser M (1999) An approach for designing thermal management systems for electric and hybrid vehicle battery packs. The Fourth Vehicle Thermal Management Systems Conference and Exhibition, London, UK
26. Khateeb SA, Farid MM, Selman JR, Al-Hallaj S (2004) Design and simulation of a lithium-ion battery with a phase change material thermal management system for an electric scooter. J Power Sources 128:292–307
27. Kizilel R, Lateefa A, Sabbah R, Farid MM, Selman JR, Al-Hallaj S (2008) Passive control of temperature excursion and uniformity in high-energy Li-ion battery packs at high current and ambient temperature. J Power Sources 183:370–375
28. Sabbah R, Kizilel R, Selman JR, Al-Hallaj S (2008) Passive thermal management system for plug-in hybrid and comparison with active cooling: limitation of temperature rise and uniformity of temperature distribution. ECS Trans 13:41–52
29. Jabardo JMS, Mamani WG, Ianekka MR (2002) Modeling and experimental evaluation of an automotive air conditioning system with a variable capacity compressor. Int J Refrig 25:1157–1172
30. Wang SW, Gu J, Dickson T, Dexter T, McGregor I (2005) Vapor quality and performance of an automotive air conditioning system. Exp Therm Fluid Sci 30:59–66
31. European Union (2006) Directive 2006/40/EC of the European parliament and of the Council of 17 May 2006. OJEU 161(12):1–4
32. Granrdy E (2001) Hydrocarbons as refrigerants—an overview. Int J Refrig 24:15–24
33. Wongwises S, Kamboon A, Orachon B (2006) Experimental investigation of hydrocarbon mixtures to replace HFC-134a in an automotive air conditioning system. Energy Convers Manage 47:1644–1659
34. Leck TJ (2009) Evaluation of HFO-1234yf as a potential replacement for R-134a in refrigeration applications. In: The proceedings of the 3rd IIR conference on thermophysical properties and transfer processes of refrigerants, Boulder, CO
35. Dittus SJ, Boelter LMK (1930) Heat Transfer in Automobile Radiators of the Tubular Type. University of California Publications in Engineering 2:443

36. Churchill SW, Chu HHS (1975) Correlating equations for laminar and turbulent free convection from a vertical plate. Int J Heat Mass Transf 18:1323–1329
37. Raman A (1995) Modelling of condenser, evaporators and refrigeration circuit in automobile air conditioning systems. PhD thesis, University of Valladolid, Vallodolid, Spain
38. Yoo SY, Lee DW (2009) Experimental study on performance of automotive air conditioning system using R-152a refrigerant. Int J Automot Technol 10:313–320
39. Engineering equation solver (2009) version 8.176. F-Chart Software, Box 44042, Madison, WI, USA
40. NIST (1998) NIST thermodynamic and transport properties of refrigerants and refrigerant mixtures-REFPROP Version 6.01. National Institute of Standards and Technology, Boulder, Colorado, USA
41. Hamut HS, Dincer I, Naterer GF (2011) Performance assessment of thermal management systems for electric and hybrid electric vehicles. Int J Energy Res. doi:10.1002/er.1951
42. Hamut HS, Dincer I, Naterer GF (2012) Exergy analysis of a TMS (thermal management system) for range extended EVs (electric vehicles). Energy. doi:10.10.16/j.energy.2011.12.041
43. Hepbasli A, Erbay Z, Icier F, Colak N, Hancioglu E (2009) A review of gas engine driven heat pumps (GEHPs) for residential and industrial applications. Renew Sustain Energy Rev 13:85–99
44. Lee CG, Cho SW, Hwang Y, Lee JK, Lee BC, Park JS, Jung JS (2007) Effects of nano-lubricants on the friction and wear characteristics at thrust slide bearing of scroll compressor. 22nd international congress of refrigeration, Beijing, China
45. Kedzierski MA, Gong M (2009) Effect of CuO nano-lubricant on R134a pool boiling heat transfer. Int J Refrig 32:791–799
46. Kumar S, Prevost M, Bugarel R (1989) Exergy analysis of a compression refrigeration system. Heat Recover Syst CHP 9:151–157
47. Arora A, Kaushik SC (2008) Theoretical analysis of a vapour compression refrigerant system with R502, R404a and R507a. Int J Refrig 31:998–1005
48. Reasor P, Aute V, Radermacher R (2010) Refrigerant R1234yf performance comparison investigation. International refrigeration air conditioning conference, Paper 1085
49. Kumar KS, Rajagopal K (2007) Computational and experimental investigation of low ODP and low GWP HCFC-123 and HC-290 refrigerant mixture alternate to CFC-12. Energy Convers Manage 48:3053–3062
50. Yang C, Maccarthy R (2009) Electricity grid: impacts of plug-in electric vehicle charging. Recent work. Institute of Transportation Studies, UC Davis, Davis, CA

Chapter 47
Green Building Approach in Turkish Aviation Sector

Isil Yazar, Emre Kiyak, and T. Hikmet Karakoc

Abstract Nowadays, the idea of green building is a very popular concept. With the increase in the number of unregulated buildings, unchecked usage of natural resources, global warming, and environmental pollution, our lives suffer from problems resulting from these reasons. Scientists focus their studies on decreasing energy needs or using renewable energy sources due to the increased value of energy and increases in energy requirements. In addition, the financial burden caused by energy requirements is another factor to consider. Furthermore, energy savings, more environmental system designs, and reduction of consumption costs become important issues. Due to this, certificates are devised with certain determined provisions. Around the world there are many certificates relating to green buildings, but there is no unique global certificate because of countries' different locations, geographical structures, resources, and so on. In Turkey, there is currently no green building certificate, but the Turkish Green Building Association, established in 2007, continues its studies into developing such a unique certificate.

In Turkey, green building studies have grown rapidly in the aviation sector. In this sector "Directorate General of Civil Aviation" awards companies "green airport" and "green aviation company" titles according to their environmental studies. In our study, we attempt to analyze green airport and green aviation

I. Yazar (✉)
Department of Mechatronics, Eskisehir Osmangazi University,
Industrial Zone, Eskisehir, Turkey
e-mail: iyazar@ogu.edu.tr

E. Kiyak
Department of Avionics, Faculty of Aeronautics and Astronautics,
Anadolu University, 26470 Eskisehir, Turkey
e-mail: ekiyak@anadolu.edu.tr

T.H. Karakoc
Department of Airframe and Powerplant Maintenance, Civil Aviation Research and
Application Center, Anadolu University, 26470 Eskisehir, Turkey
e-mail: hkarakoc@anadolu.edu.tr

company terms in respect of Turkish companies that have Green Company official titles. The introduction deals with the theoretical background concerning green building, green airport, green aviation company, and so on. The following section gives information about Turkish green aviation companies and their studies related to becoming green companies. In the conclusion section, the studies that have been conducted by aviation companies and problems of the processes are considered.

Keywords Green buildings • Green aviation • Green airports • Energy • Green certificates—licenses • Green building approach • Turkish aviation sector • Turkey • Green building certificate • Green licenses • Istanbul • Antalya • Vehicle efficiency • LEED • Transportation • Renewable

47.1 Introduction

Energy terms are used intensively in different areas of our lives. Transportation, communication, illumination, heating, and suchlike are typical examples of these. Failing in one of them causes problems and is waste of our time. Hence, it seems that a life without energy is impossible. Furthermore, energy policy plays a vital role in the mitigation of the impacts of global warming and the crisis of energy availability [1]. From this view, the usage of renewable energy strategies becomes an important point. It is vital for a nation's social and economic development [2]. Renewable energy strategies can make an important contribution to the economies of countries. Thus, it should be encouraged by governments and other authorities for more environmental and sustainable future [3]. Nowadays, there is growing awareness about the importance of energy and the number of studies about effective energy usage and renewable energy sources are on the increase. The term "green building" has entered the literature as a main title for all sectors concerned with this awareness.

Buildings are significant in terms of the economic and social developments of cities, as well as their environmental impact, because they are responsible for a large percentage of carbon emissions and use a considerable number of resources and energy [4, 5]. Green building is the practice of creating structures and using processes that are environmentally responsible and resource efficient throughout a building's lifetime from conception to design, construction, operation, maintenance, renovation, and deconstruction. This practice expands and complements the classical building design concerns of economy, utility, durability, and comfort. A green building is also known as a sustainable or high-performance building [6]. Green building movement can be seen in different sectors like medicine, transportation, agriculture, and so on. They are adopted in various approaches toward greening their activities by using certificate standards [7].

Individual countries have drawn attention to the importance of energy and have prepared their own policies concerning green buildings. GBC (Green Building Challenge), LEED (Leadership in Energy and Environmental Design), BREEAM

(Building Research Establishment Environmental Assessment Method), GREENSTAR (depends on LEED and BREEAM criteria), BEES (Building for Environmental and Economic Sustainability), SBtool (Sustainable Building Tool-Canada), ECO-QUANTUM (based on simulation model), ECOPROFILE, LCAid, and CASBEE are examples of standards and certificates issued around the world [8–12]. As we can see, there is no one unique global certificate because of countries' different location, geographical structures, resources, and so on [13]. In Turkey, there is currently no green building certificate, but the Turkish Green Building Association, established in 2007, has been continuing its studies into developing such a unique certificate [14].

International aviation is growing rapidly, resulting in a rise in aviation greenhouse gas emissions, and waste products [15]. To avoid this rise, the Directorate General of Civil Aviation prepares a program for the aviation sector. In Turkey, green building studies have grown rapidly in the aviation sector. In this sector "The Directorate General of Civil Aviation" awards aviation companies with "Green Airport" and "Green Aviation Company" titles according to their environmental studies.
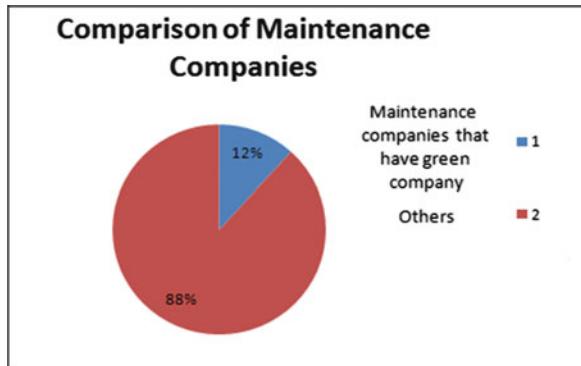
A Green Aviation Company is an environmental project developed by the Directorate General of Civil Aviation. If an aviation company fulfills the requirements of certain determined criteria, after audit it becomes a green aviation company in Turkey. In addition, if all aviation companies at an airport have a green aviation certificate, this airport is called a green airport in Turkey. Green aviation companies or green airports that have certificates get discounts from the Directorate General of Civil Aviation for other certificates of authority, and license, as well as for certificate renewals. Discounts are 20 % for green aviation companies individually and 50 % for green airport aviation companies [16]. In Turkey, the number of certificated aviation companies increases day by day, but there is no green airport yet. Basic facilities about being green aviation company and green airport are continued by the other aviation companies and airports.

47.2 General Requirements for Being Green Aviation Company
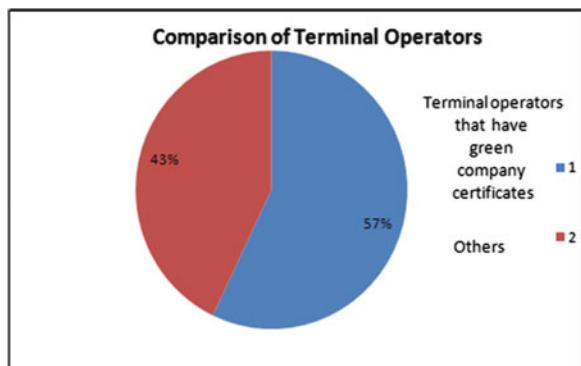
The following are some of the requirements to become a green aviation company in Turkey [17]:

- Companies should compile their environmental management system handbook. It must include goals, strategies, obligations, risk analyses procedures, waste management plans, responsibilities, and organizational knowledge of the company and so on.
- Exhaust emission measurement details and procedures, noise measurement details and procedures, other adjustment details (describing waste type, waste

Fig. 47.1 Comparison of
maintenance companies

Fig. 47.2 Comparison of
terminal operators
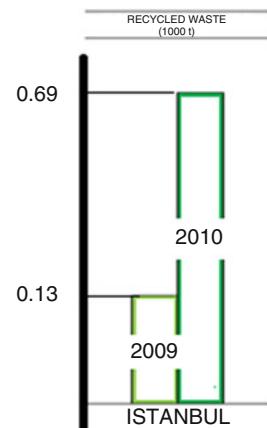
temporary storage place, waste transportation, waste disposal details and
procedures), and so on.

According to the June 2012 dated data, total certificated aviation company
number is 16.4 of 16 is from maintenance companies and another 4 of 16 is from
terminal operators. Total number of maintenance companies is 34 and total number
of terminal operators is 7 (Figs. 47.1, 47.2 and 47.3).

47.3 Green Airports and Aviation Companies in Turkey

- TAV Istanbul Terminal Operations Corporation
- Turkish Technic Incorporated
- ATM Airport Construction and Management Incorporated
- Fraport IC Ictas Antalya Airport Terminal Investment and Management
  Incorporation

Fig. 47.3 Percentage of
recycled waste

47.3.1   TAV Istanbul Terminal Operations Corporation

This is the operation responsible for the Istanbul Atatürk Airport International
Terminal. TAV Istanbul was the first green aviation company in Turkey. It was
awarded the green company title on 1 February 2010 [18].

Purpose of Applying Certificate

The purpose of applying for this certificate is to reduce their effects on the
environment. Furthermore, they aim to make staff aware of the effective use of
resources.

Submission Process

Initially, according to the certificate requirements, a multidisciplinary study group
is formed to try to achieve the certification needs. After the completion of the
studies, the company makes a submission to the Directorate General of Civil
Aviation. Finally, the company is audited under the responsibility of Directorate
General of Civil Aviation and receives the Green Company Certificate. They
establish their sustainability report after they hold the Green Company Certificate.

Alternation Process

Firstly, the company evaluates its current condition and prepares a report, making
plans with regard to the certificate requirements. The environmental strategy, goals,
and purposes of the company are updated due to the certification plans. It forms a

waste management plan that involves all aspects of the company. Environment–dimension–effect–risk analyses are carried out. Waste storage–transmission–disposal conditions are reviewed according to a waste management plan and formal requirements.

Storage conditions for domestic solid waste are reviewed and before the transmission process, domestic solid waste is stored temporarily at +4 °C. Plastic containers begin to be used instead of metal containers for collecting waste. Containers were labeled according to their contents. For waste recycling–disposal–transmission operations contracts are arranged with licensed firms. For recyclable waste (glass–plastic–chapter–metal and suchlike), triple decomposition boxes are started to be used. For other waste, decomposition at the point of origin is established. For dangerous waste (batteries, toners, cartridges, filters, and suchlike) appropriate collection containers are prepared and they are begun to be transported in licensed vehicles, finally being disposed of at licensed centers. Personnel are trained in environment consciousness and waste management by TAV academics.

Difficulties of Process

Personnel attitudes toward waste management have critical role during this process. At the start of the project, staffs are uninterested in the decomposition of waste at the point of origin. By trainings and awareness-raising campaigns, this problem is tried to solve.

47.3.2 Turkish Technic Incorporated

This is the technical maintenance responsible for Turkish Airlines [19].

Purpose of Applying Certificate

The purpose of applying for this certificate is to reduce their effects on the environment. They aim to make the staff more conscious of using resources effectively. In addition, their one another goal is to prepare an environment-friendly, developing system for upcoming generations.

Submission Process

Since 2006, the company has been checking audits concerning its environmental management certificate ISO 14001 studies. The company collects its studies as required for application and then submits the documentation to the Directorate

General of Civil Aviation. Eventually, the company is audited by the Director-ate General of Civil Aviation and achieves the Green Company Certificate.

Alternation Process

With the ISO 14001 Certification, their studies are monitored periodically. The company reviews its goal-realization conditions concerning environmental management every year. The HABOM Memorial Forest is constructed by the Turkish Technic Incorporated in support of the fight against carbon emissions and global climate changes. The organizational structure of the company is changed according to the certificate requirements. A new environmental management department is formed with two environmental engineers and a chemical engineer. They are responsible for controlling-coordinating environmental studies, requirements, and suchlike. Waste (except domestic waste) is grouped in green containers, red containers (dangerous chemical waste), and blue containers (recycled waste). These containers are transported by battery-operated vehicles to reduce the negative effects on the environment. Dangerous waste is stored in confined areas. Transmission of the waste is carried out by licensed vehicles. Vehicles are licensed by the Ministry of Environment and Urban Planning. Waste is disposed of by companies that are accredited by the same Ministry. Medical waste is transported in different containers to the municipality. Batteries are transported in different containers to responsible companies. Waste such as aircraft tires, cartridges, and toners are disposed of by licensed companies or recycled. According to a contract between GE and the Turkish Technic Incorporation, scrap aircraft material and components that are appropriate for recycling are sent to the company for recycling. Industrial waste water that is formed from different plants like paint, coating, and so on are stored and distilled in waste treatment plants and, after the distillation process, it rejoins the city water network.

Emission measurements are periodically carried out by the Ministry-accredited companies according to the regulations.

Noise level measurements are conducted by accredited companies periodically every year and noise maps are formed. For noisy departments, walls are coated with noise-absorbent panels so as to reduce noise levels. On the Web, a form is being prepared for proposals and complaints.

Instead of fuel-operated cars, battery-operated cars are used for material transfer operations. By the company, an emergency state handbook is prepared. It includes emergency state plans, rules, sanctions, and so on. In plants and hangars, risk analysis applications are carried out for new inputs. They are evaluated whether or not they have a dangerous effect on the environment, before becoming a member of the system. Every year on fifth of June (World Environment Day) certain activities such as tree planting and competitions that relate to the environment are organized by the company. Furthermore, with posters and announcements, staffs are encouraged to gain environmental responsibility. Staff undergoes in-service training triennially.

47.3.3 ATM Airport Construction and Management Incorporated

It is the operation responsible for Dalaman Airport International Terminal [20].

Purpose of Applying Certificate

In the short term, their purpose of application is to reduce harm caused to the environment systematically and, in the long term, to eradicate the harm completely. Furthermore, their plan is to make the staff be aware of the need to use resources effectively.

Submission Process

The certification process starts as soon as correspondence is received from the Directorate General of Civil Aviation. During 5 months, base studies are started and maintained. Finally, the company is audited by the Directorate General of Civil Aviation and receives the Green Company Certificate.

Alternation Process

In the alternation stage, dangerous waste is transported to disposal centers. In addition, personnel are trained in the efficient use of resources, decomposition of waste at the point of origin, as well as collection of dangerous waste with the cooperation of the Mugla Directorate of the environment and city planning, every year since 2010.

Difficulties of Process

At the end of this work, an important problem is found. The number of licensed dangerous waste storage, transmission, and disposal centers are insufficient for areas situated away from city centers.

47.3.4 Fraport IC Ictas Antalya Airport Terminal Investment and Management Incorporation

It is the operation responsible for Antalya Airport Terminal [21].

Purpose of Applying Certificate

Firstly, the Directorate General of Civil Aviation projects have a priority for company and so, company values the Directorate General of Civil Aviation projects. They have a parallel operation strategy with the Directorate General of Civil Aviation. Furthermore, the contents of this certificate (saving ecological equilibrium, preparing livable environment) are intersecting with its policy. They plan to utilize the incentive discounts. By this way, company aims to contribute to its economy.

Submission Process

Certification process starts in 2009. Base studies are maintained for 6 months. Finally, the company is audited by the Directorate General of Civil Aviation and receives the Green Company Certificate.

Alternation Process

Many innovations can be seen with the alternation process. There are some adjustments about measurement and evaluation systematic like quality of air and operation of waste treatment plant. Contracts are done about waste management and transmission and disposal of dangerous waste. Water–soil analysis is done properly. Organic waste is started to store regularly and so, recycling ratio is increased. In 2011, 1.950 ton materials are recycled. Staff becomes conscious. In 2011, 760 employees are educated about environmental responsibilities. Value of the company is increased. Energy saving is provided. It has positive effects to the general economy. Costs are decreased.

Difficulties of Process

Eventually, the process results show that the number of alternative co-operating companies is inadequate. For staff training, expended time interval is needed. Sometimes the formal regulations are not practical because of the step-by-step procedures. Suppliers are adapted to the subjects slowly. Their basic facilities level is not enough for the subjects.

47.4   Conclusions

Being a Green Airport Company provides many advantages to a company. The title increases the value of the company. The company also fulfills its legal responsibilities. In addition, it utilizes payment discounts concerning certificates of authority, licenses, certificate renewals, and so on. The common gain achieved by the

company is teamwork studies. Studies cause staff to become closer within the company. Staffs understand the team spirit and company spirit, and therefore they work more carefully and conscientiously. The last and the most important result is that the company becomes an environment-friendly structure reducing harmful negative effect to our lives. Furthermore, according to the feedback from the companies, it is understood that the most important problem that has been encountered relates to the inadequate number of licensed disposal centers and their inadequate capacities.

References

1. Saidur R, Islam MR, Rahim NA, Solangi KH (2010) A review on global wind energy policy. Renew Sustain Energy Rev 14:1744–1762
2. Jebaraj S, Iniyan S (2006) A review of energy models. Renew Sustain Energy Rev 10:281–311
3. Midilli A, Dincer I, Ay M (2006) Green energy strategies for sustainable development. Energy Policy 34:3623–3633
4. Burnett J (2007) City buildings-eco labels and shades of green. Landsc Urban Plann 83:29–38
5. Lacouture DC, Sefair JA, Flórez L, Medaglia AL (2009) Optimization model for the selection of the materials using a leed-based green building rating system in Colombia. Build Environ 44:1162–1170
6. U. S. Environmental Protection Agency (2012) Green Building http://www.epa.gov/greenbuilding/index.htm. Accessed 9 Aug 2012
7. Kibert C (2008) Sustainable construction: green building design and delivery. Wiley, UK
8. Dogru M (2012) Yesil Binaların Butuncul Enerji Verimliligi Yaklasimi Nedir? http://www.tesisat.com.tr/yayin/181/yesil-binalarin-butuncul-enerji-verimliligi-yaklasiminedir_4382.html. Accessed 9 Aug 2012
9. Ekobina Yesil Bina Danismanligi (2011) LEED Nedir? http://www.ekobina.com.tr/portfolio/leed-nedir. Accessed 9 Aug 2012
10. Erten D (2012) Turkiye Için Yesil Bina Sertifikasi ve Onerileri http://www.yesilbina.com/Turkiye-Icin-Yesil-Bina-Sertifikasi-ve-Onerileri_a363.html Accessed 9 Aug 2012
11. Green Building Council Australia (2012) Welcome to Green Building Council of Australia http://www.gbca.org.au/ Accessed 9 Aug 2012
12. Katz A (2012) LEED-certified building stock swells to two billion square feet worldwide http://www.usgbc.org/Docs/News/2billionsqft_Aug2012.pdf. Accessed 9 Aug 2012
13. Erten D, Henderson K, Kobas B (2009) Uluslararasi Yesil Bina Sertifikalarina Bir Bakis: Turkiye icin bir Yesil Bina Sertifikasi Olusturmak icin Yol Haritasi. Fifth international conference on construction in the 21st century
14. Cevre Dostu Yesil Binalar Dernegi (2011) Cevre Dostu Yesil Binalar Dernegi www.cedbik.org. Accessed 9 Aug 2012
15. Macintosh A, Wallace W (2009) International aviation emissions to 2025: can emissions be stabilized without restricting demand? Energy Policy 37:264–273

16. Sivil Havacilik Genel Mudurlugu (2009) Havaalanlarinda Devrim Proje: Yesil Havaalani (Green Airport) http://web.shgm.gov.tr/kurumsal.php?page=haberler&id=1&haber_id=755. Accessed 9 Aug 2012
17. Sivil Havacilik Genel Mudurlugu (2010) Yesil Havaalani Projesine Iliskin Yeni Duzenlemeler http://web.shgm.gov.tr/kurumsal.php?page=duyurular&id=1&haber_id=1508.   Accessed 9 Aug 2012
18. TAV Airports Holding Co. (2012) http://www.tav.aero/tr-TR/Sayfalar/default.aspx Accessed 9 Aug 2012
19. Turkish Technic Inc. (2012) http://www.turkishtechnic.com/. Accessed 9 Aug 2012
20. ATM Dalaman Airport (2012) http://www.atmairport.aero/. Accessed 9 Aug 2012
21. Fraport IC Ictas Antalya Havalimanı Terminal Yatirim ve Isletmeciligi A. S. (2012) http://www.aytport.com/tr/index_1.asp. Accessed 9 Aug 2012

Chapter 48
Assessment of Energy Efficiencies and Environmental Impacts of Railway and Bus Transportation Options

Mine Sertsoz, Sule Kusdogan, and Onder Altuntas

Abstract In this study, energy efficiency and environmental impacts of railway and bus transportation are applied in three steps. While comparison between railway system and bus transportation options is discussed in first and second steps, *indirect*, energy consumption changing of railway system with person number and gradient rate is studied in the last step, *direct*. Firstly, energy efficiency of railway systems is compared with bus transportation in urban transportation in Istanbul in terms of carbon dioxide (CO_2). Then, energy consumptions and cost analysis of both systems are evaluated by calculations on the basis of numerical data, received from certain organizations. And finally, they are compared in terms of the number of passengers and gradient rate energy consumptions by using SimuX simulation program. Preferring railway systems in transportation becomes more important because of best environment impacts (CO_2 per capita will decrease 244.6 g), energy cost (bus transportation is 2.66 times lower than railway systems), and energy efficiency (energy consumption with gradient value increases by 18.62 and with passenger number increases per capita by 3.63).

Nomenclature

CO_2	Carbon dioxide
EU	European Union

M. Sertsoz (✉) • S. Kusdogan • O. Altuntas
Anadolu University, Eskişehir, Turkey

IETT   Istanbul electric tramway and tunnel establishments
OECD   Organization for Economic Co-operation and Development
TEP   Ton equivalent petrol
UIC   International Union of Railways
UNCBD   United Nations Convention to Biologics Diversity
UNCCD   United Nations Convention to Combat Desertification
UNFCCC   United Nations Framework Convention to Climate Change

48.1   Introduction

One of the negative impacts of the industrial revolution, which began in the eighteenth century, is the environmental effects (the global temperature increase in atmosphere and in oceans, decreased longevity, increased mortality, etc.), and was observed since the end of the nineteenth century. At the end of the twentieth century, the sources of these negative environmental impacts have been examined and then many studies have been conducted on the measures for precaution, in many fields.

The reasons of environmental problems and the solutions to these problems, which passed local borders, were taken as agenda by the conference of United Nations Human and Environment Conference in Stockholm in 1972. 20 years after Stockholm Conference, United Nations Convention to Combat Desertification (UNCCD), United Nations Convention on Biological Diversity (UNCBD), and United Nations Framework Convention on Climate Change (UNFCCC) legalized concepts of "sustainable development."

Besides the other universal contracts, UNFCCC, accepted in 1994, is the most known contract that emerges radical transformation in order to prevent the greenhouse effects, based on human, energy, industry, transportation, agriculture, waste, and forestry. Kyoto Contract, which was accepted in 1997 and gained validity in 2005, supports strong and reformist sanctions to prevent climate changes [1].

Many studies have been applied in the transport sector. According to reports of Organization for Economic Co-operation and Development (OECD) countries, the share of the transport sector, in total energy demand, was 24 % in 1971, whereas this ratio is estimated to reach 37 % by 2020. For this reason, studies, conducted on energy efficiency and environmental impact issues in the transport industry, will be even more important [2].

To increase the consumption of energy per capita, developed with a measure of development of countries for many years, the efficient use of energy has been important. In the open literature about energy economics, the methods of Granger [3] and Sims [4] have been constantly used in the causality relationship analysis between energy consumption and economic growth. This relationship was firstly discussed by Kraft and Kraft [5], who demonstrated that this is a one-way causality from economic growth to energy consumption based on the US data for the

1947–1974 period. After this study, many researchers [6–13] have used the same methods in their studies.

In addition to the studies on energy economy, the studies have been guided to monitor and measure CO_2, caused by energy consumption. When CO_2 emission, varied with the total energy demand (the CO_2 share of the transport sector in total energy demand), was 19 % in 1971, this value is approximately estimated to reach 30 % by 2020 [2]. This result clearly shows the importance of the global warming and other environmental impact analyses.

Today, passenger capacity, affordability, and environmental impacts are important parameters in the determination of urban transportation vehicles. Selection of transportation systems, such as railway systems, is important in terms of energy efficiency and economic and environmental impact.

A study of Pietzsch [14], about passenger transportation, has indicated that the consumed energy in highways is 3 times and in airways 5.2 times higher than railways. According to a report issued by UIC (International Union of Railways), while a train travels 5 km, a car can travel 1.7 km and a plane can travel only 1.1 km, using 1 kWh of energy [15].

Different energy consumption for the same distance directly affects emissions, released into the environment. While the share of pollution caused by electric railways is 5 %, it is about 85 % for highways. An electric train emits 1 kg of CO_2 in 42 km of travel, while the same amount of CO_2 is emitted in 12 km by car and in 7 km by plane [15].
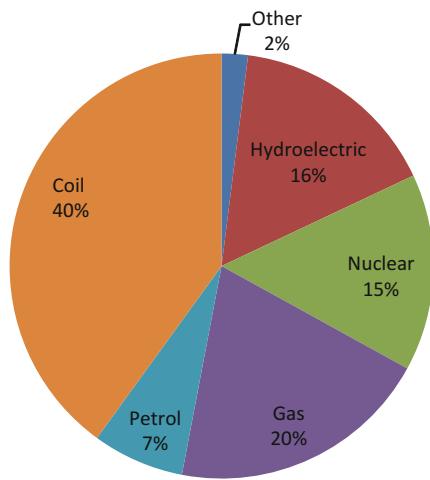
The energy efficiency in transportation is handled in three different approaches in this study. Firstly, railway and bus transportation systems are compared in terms of CO_2 emissions. (The example given here is the current transportation forms used in the city of Istanbul. Usage ratio of the land transport in Istanbul is 87.3 %; usage ratio of the railway transport is 10.17 %; and usage ratio of the sea transport is 2.53 % of total [16].) And then, railway and bus transportation systems are compared base on the type of fuel used currently in terms of per capita cost of transportation. Finally, the railway systems are compared in itself in terms of the energy efficiency by changing their certain parameters.

In this study, the mathematical calculations were performed by two steps: (a) the numerical data obtained from government institutions and (b) the digital data found through simulation. It is possible to compare bus transportation and railway system in terms of their environmental impact and costs—*indirectly*—energy efficiencies, and it is also possible to see the—*direct*—effect of certain energy consumption parameters on the energy efficiency.

48.2   Energy Efficiency

In the twenty-first century, the two indicators, concepts of energy efficiency (producing much) and less energy consumption (reducing the energy intensity), are used in the agenda (Fig. 48.1).

Fig. 48.1 Electrical energy
production proportions
according to sources
[modified from ref. 17]

Today, the oil and gas supply strategies are important milestones in both the development of countries and their foreign policies because of the increasingly strategic role of these resources as an energy source in world politics.

Despite all the efforts on the search and technology development for alternative energy sources, it is expected to increase energy demand. Increasing energy demand will largely be met by oil and natural gas again in the coming years, to scientific estimates.

In the last decades, while the worldwide oil reserves have been determined to be 156.7 billion tons, which will run out in 41 years, natural gas reserves have been determined to be 175.8 trillion m^3, which will run out in 67 years. So for today, depletion of oil and natural gas will be between 32 and 56 years, respectively [1].

While the world economy grows 3 % per year, the energy intensity decreases 1 % per year by means of the energy efficiency. If the average increase is 2 % per year in the world energy consumption, this value will reach 12.3 billion TEP in 2015 and 15.1 billion TEP in 2025.

The world oil demand is expected to increase by 1.6 % per year in the next 30-year period. And the most important factor is expected to increase transport demand because of this increase. Currently, 47 % of the total oil consumption is originated from the transport industry, and this ratio will reach to 55 % by 2030. About two of the three are expected to be originated from the non-OECD countries [1].

Because of increasing energy demand, more reserves should be found and trillions of dollars should be invested for usability of these resources. For instance, in 2001, the world production of conventional oil was 72 million barrels/day and it is estimated to be 120 million barrels/day in 2030. And also, the natural gas demand was 2.5 billion m^3 in 2000, and it is expected to be doubled to reach 5 trillion m^3 in 2030. And the average annual demand growth will be 2.4 % [1].

The primary energy supply has been 99,840 million TEP, and the primary energy production has been 26,779 million TEP in Turkey since 2006 and 73 % of its energy needs are met by imported energy. In 2006, total energy consumption of world was 11.4 billion TEP, and share of Turkey in this consumption was 0.8 %. Ninety-three percent of the crude oil demand and 97 % of the natural gas have been currently provided with imports. If the necessity is not supplied by local sources, these demand rates will increase to 99 and 100 %, respectively, in 2020 [1].

48.2.1 Perspective on Energy Efficiency of Turkey in the Transportation Sector

Passenger transportation is basically divided into three categories: highway, railroad, and airline. While these proportions are 95.5 % highway, 2.8 % railroad, and 1.7 % airline in Turkey [18], these are 44.5 % highway, 9.6 % railroad, and 6.6 % airline in the European Union (EU) [19]. There is a more balanced condition in passenger transportation in the EU than in Turkey.

To improve the energy efficiency in transportation, regulation has been published in 2008 by the Ministry of Transportation in the Official Gazette called "Principles and Procedures for Improving Energy Efficiency in Transport." This improvement can be held by mentioning the principles and procedures on establishment of the systems to reduce fuel consumption of motor vehicles, to increase the efficiency standards in vehicles, to promote the public transport, and to increase traffic flow.

This regulation deals with all kinds of transportation. Some transportation ways are mentioned according to population density. Specific duties can be assigned to municipalities for the use of public transport. It is stated in the first paragraph of Article 6 of this regulation "in Order to Reduce the Energy Consumption Down to Minimum in the Railway Transport, Priority is Given to the Electric Operation." The railway systems are mentioned here and it is referred to efficient use of electricity.

This regulation, the coordination of the subsystems with each other, is weak while the transportation subunits are under various ministries. And this causes late realization of the decisions on transportation. Center is created to provide coordination of these subunits or to assign all under the same ministry. In this way, the progress will be faster.

In recent years, countries searched clean energy in parallel with the increasing importance on energy efficiency and environmental pollution. And this has been reflected to the transportation sector in efforts to improve railway transport, and to search on the efficient use of energy in railway systems as well.

Turkey has made great progress with important projects on this issue, through the use of the railway system in both long-distance and local transport (for example, Ankara–Eskisehir High Speed Trains, Ankara–Konya High Speed Trains, the

Fig. 48.2 Technical information of ABB tram

Marmaray Project, Bursa Tram Line, Eskisehir Tram Line, and Kartal–Kadikoy Subway Line in Istanbul).

48.2.2 System Descriptions

The technical information of the vehicle, used in this study, is shown in Fig. 48.2. Passenger capacity was accepted as 280 because of standing passenger in this information.

This figure shows the tram's technical information which is used in this study. Its manufacturer company is ABB and it has been used in İstanbul Transportation. As for that the bus which is used for this study is Ikarus 260. Its passenger capacity is 102 and it consumes 35 l diesels per 100 km.

48.3 Methodology

48.3.1 CO_2 Emission Estimation Method

Energy industry, transport, and electricity consumption lead to emissions, originated from heating. This is increasing in total emissions.

The intelligent transport systems, developed by utilizing information and communication technologies for efficient use and better presentation of the transport system, can be used to contribute that improvement of air quality and environment, in parallel with the energy efficiency [20].

The increasing greenhouse gas emission, originated from the transport sector, is the main source of the energy sector. It is the only increasing sector in reality. The amount of CO_2 emissions of transport is 17 %, compared to other sectors [21]. In this context, this study will be conducted to reduce the share of transport and thus to reduce the amount of total CO_2. Because of this increasing amount, calculation is also important for the future.

- *Annual CO_2 propagation of İETT* = Annual diesel consumption of İETT × CO_2 propagation of diesel per liter
- *Annual CO_2 propagation of railway systems* = Annual energy consumption of railway systems × CO_2 propagation of coil per 1 kWh
- *CO_2 quantity per capita for IETT* = Annual CO_2 propagation of İETT/annual passenger numbers for IETT
- *CO_2 quantity per capita for railway systems* = Annual CO_2 propagation of railway systems/annual passenger number for railway systems

48.3.2   Cost Estimation Method

- *For Tram:*

  Total energy consumption = Energy consumption per km × length
  Total cost = Total energy consumption × cost per kWh
  Cost per capita = Total cost/person number

- *For City Bus:*

  Total fuel consumption = Fuel consumption per km × length
  Total cost = Total fuel consumption × cost per km
  Cost per capita = Total cost/person number

48.3.3   SimuX Method

SimuX software, developed by Turan Söylemez, was firstly used by Süleyman Açıkbaş on his PhD thesis. There are many aims of Simux (train performance, transformer sizing, catenary sufficing, etc.) and some aims of the SimuX are tram's energy consumption by changing gradients and number of passengers [22].

Modeling of the railways is very complex; that is why manually solving is almost impossible. Nowadays analysis, operating, and different factors are being solved by SimuX simulation program for railways.

48.4   Results and Discussion

48.4.1   *CO$_2$ Calculation Results and Discussion*

Table 48.1 shows the various electricity generation and their CO2 emissions according to some institutions. Average value in this table is these institutions' average CO$_2$ emissions.

Coil has the most and hydroelectricity has the least CO$_2$ emissions. Contrary to popular belief nuclear is the cleanest for environment after hydroelectricity.

But in this study only coil's CO$_2$ emission was used.

When we compare the data in 2009, the annual passengers who used railway systems were about 466 million [27] and the annual passengers who used Istanbul Electric Tramway and Tunnel Establishments (IETT) were about one billion [16]. In addition, the total annual energy consumed by railway systems was about 6 million kWh [27], where the annual diesel oil quantity consumed by IETT was about 98 million l [16]. The amount of CO$_2$ produced per liter of diesel oil was about 2.65 kg/l.

Calculation was made using Table 48.1 and the above numerical data and Table 48.2 was constituted. Table 48.2 shows CO$_2$ amounts for different forms of electricity generation of railway systems and only diesel for IETT.

According to CO$_2$ calculation results, the use of the railway system has the lowest value in terms of CO$_2$ emissions in each case. The amount of CO$_2$ per capita is decreasing by 244.6 g, even if the preferred fuel type is coal. It has been seen that the railway transport should be the priority in Turkey instead of the bus transport. For this case, the government needs to increase the railway transport by giving incentives to the private sector or by its own. The efficient use of energy seems quite logical in terms of the environmental pollution [28].

48.4.2   *Cost Calculation Results and Discussion*

Here, the energy consumption values found as a result of the simulation studies performed before on tram and the energy consumption values of city bus are compared in terms of the costs per capita. Some assumptions are listed as follows:

- Vehicles are traveling on a road with no gradients.
- Auxiliary energy consumption of the vehicles is zero.

Table 48.1   Amount of CO$_2$ emissions in kg/MWh according to the forms of electricity generation

	Coil	Gas	Solar PV	Nuclear	Wind	Hydroelectricity
CRIEPI, Japon [23]	990	653	59	21	37	18
Paul Scherr Inst. [24]	949	485	79	8	14	3
IAEA [25]	968	440	100	9–21	9–36	4–23
Vattenfall AB [26]	980	450	50	6	6	3
Average	971	507	72	12.5	20	10

Table 48.2 The amount of CO_2 per capita calculated by changing the transportation modes and the fuel types

CO_2 per capita by utilizing İETT (fuel: diesel)	257.5 g
CO_2 per capita by utilizing railway systems (fuel: electricity, resource: coil)	12.9 g
CO_2 per capita by utilizing railway systems (fuel: electricity, resource: gas)	0.9 g
CO_2 per capita by utilizing railway systems (fuel: electricity, resource: nuclear)	0.08 g
CO_2 per capita by utilizing railway systems (fuel: electricity, resource: wind)	0.2 g
CO_2 per capita by utilizing railway systems (fuel: electricity, resource: hydroelectricity)	0.04 g

Table 48.3 Gradient and energy consumptions (full capacity)

Gradient (%)	Energy consumptions (kWh/km)
−5	0.62
−4	1.03
−3	1.66
−2	2.41
−1	3.35
0	4.46
1	5.78
2	7.16
3	8.61
4	10.04
5	11.55

- Both vehicles are loaded to full capacity.
- They travel equal distances, which is 5,570 m.
- The energy consumption is zero at the waits at bus stations.

The passenger carrying capacity of city bus is 102 people, and the amount of diesel oil use is 0.035 l/km in the best conditions [29].

The passenger carrying capacity of tram is 280 people, and the preferred fuel type is coal.

The energy consumption of tram was found as 4.46 kWh/km held with SimuX, as listed in Table 48.3.

As a result of the analysis, while the cost of fuel per person for tram was calculated to be 1.71 kurus, this value was found to be 7.49 kurus for city bus. These results indicate that city bus is 4.38 times of higher cost than tram. (Since the costs of infrastructure and superstructure are covered by civil engineering, these could not be included in the calculation.) In addition, the maintenance cost for road is 4.4 times than that for the railroad [30]. Thus, tram is more suitable transportation system in both results—cost of fuel and maintenance.

48.4.3   SimuX Results and Discussion

While the gradient value increases from −5 to +5 %, the energy consumption value increases by 18.62 times. (The tram works at full capacity.)

Table 48.4 Passenger numbers' energy consumption efficiency when gradient is 0 %

Passenger number	Vehicle height	Energy consumption (kWh)	Energy consumption distinction (%)	Vehicle height distinction (%)
0	31,900	2.92		
50	35,400	3.21	9.93	11
100	38,900	3.5	19.86	22
150	42,400	3.8	30.1	33
200	45,900	4.1	40.4	44
250	49,400	4.39	50.3	55

As the weight of the vehicle, given in Table 48.4, increases by 11 % the energy consumption difference increases by 10 % approximately. This is because of Newton's second law of motion. This law shows us that as mass increases, force and energy consumption also increases (since our speed is constant always). The example gradient was 0 % here; however this ratio will always be the same. Thus, this simulation also confirms this law. The remarkable issue here is that if the number of passengers increases from 50 to 250 people in a tram, despite the increase in total energy consumption by 1.36 times, the energy consumption per capita is 3.63 times lower.

48.5 Concluding Remarks

The conclusions of the research and calculations are listed below:

- Even if coal is used as the fuel to generate electricity, the amount of CO_2 per capita will decrease by 244.6 g in IETT.
- As a result of the cost analysis, the cost of fuel for tram is 1.71 kurus per capita, while this value is 7.49 kurus for city bus, which is 4.38 times higher. Tram is more suitable transportation system in both results—cost of fuel and maintenance.
- While the gradient value decreases from 0 to −5 %, the energy consumption decreases by 8.2 times. Besides, the gradient value increases from 0 to 5 %, and the energy consumption increases by 2.6 times.
- While the gradient value increases from −5 to +5 %, that is, in ten units of increase in gradient, the energy consumption value increases by 18.62 times.
- While the number of passengers increases from 50 to 250 people in a tram, the total energy consumption increases by 1.36 times.
- And despite the number of passengers increased from 50 to 250 people in a tram, the energy consumption per capita is 3.63 times lower.

References

1. EİEİ Bina Enerji Yöneticileri Eğitimi Cilt 1 (2008)
2. Landwehr M, Marie-Lilliu C (2002) Transportation projections in OECD regions detailed report, İnternational energy agency
3. Granger CWJ (1969) Investigating causal relations by econometric models and cross spectral methods. Econometrica 37:424–438
4. Sims CA (1972) Money, income and causality. Am Econ Rev 62:540–552
5. Kraft J, Kraft A (1978) On the relationship between energy and GNP. J Energ Dev 3:401–403
6. Akarca AT, Long TV (1979) Energy and employment: a time series analysis of the causal relationship. Resour Energ 2:151–162
7. Akarca AT, Long TV (1980) On the relationship between energy and GNP: a re-examination. J Energ Dev 5:326–331
8. Yu ESH, Hwang BK (1984) The relationship between energy and GNP: further results. Energ Econ 6:186–190
9. Yu ESH, Choi JY (1985) The causal relationship between energy and GNP: an international comparison. J Energ Dev 10:249–272
10. Erol U, Yu ESH (1987) Time series analysis of the causal relationships between US energy and employment. Resour Energ 9:75–89
11. Erol U, Yu ESH (1989) Spectral analysis of the relationship between energy and income for industrialised countries. J Energ Dev 13:113–122
12. Yu ESH, Jin JC (1992) Cointegration tests of energy consumption, income and employment. Resour Energ 14:259–266
13. Asafu-Adjaye J (2000) The relationship between energy consumption, energy prices and economic growth: time series evidence from Asian developing countries. Energ Econ 22 (6):615–625
14. Pietzsch W (1979) Strassenplanung 3. Neuearbeitete und Erweiterte Auflage. Werner
15. Gökdağ M (2005) Kentsel Ulaşımda Karayolu ve Raylı Taşıma Sistemlerinin Bazı Önemli Faktörlere Göre Karşılaştırılması. Ulaşım ve Trafik Kongresi—Sergisi, Sayı:1 chapters: 394–400
16. http://www.İETT.gov.tr. Accessed 30 Aug 2012
17. IEA Key Energy Statics (2005)
18. Devlet Planlama Teşkilatı (2006)
19. Accardo L (2009) Energy saving onboard. Energy efficiency days France
20. Sussmann JM (2005) Perpesctives on intelligent transportation systems. Springer, New York
21. Kumbaroğlu G, Arıkan Y (2009) Türkiye'nin CO_2 Salımları Açık Toplum Vakfı, İstanbul
22. Açıkbaş S (2008) Çok Hatli Çok Araçli Rayli Sistemlerde Enerji Tasarrufuna Yönelik Sürüş Kontrolü, İTÜ
23. Energy Technology Life Cycle Analysis that Takes CO_2 Emission Reduction into Consideration (1995) Central Research Institute of Electric Power Industry annual research report, Japan
24. Doneset al R (2003) Greenhouse gas emissions from energy systems: comparison and overview, Paul Scherrer Institut Annual Report 2003, Annex IV (Table 2, page 38)
25. Spadaro JV et al (2000) Greenhouse gas emissions of electricity generation chains: assessing the difference, IAEA Bulletin 42/2/2000 (page 21)
26. Enviromental Product Decleration of Electricity from Torness Nuclear Power Station, British Energy (2005)
27. İstanbul Ulaşım a.ş. interviewed at 25 Sept 2012
28. Kuşdoğan Ş et al. (2012) Energy efficiency in rail systems and comparison between rail system in istanbul and bus transportation in terms of carbondioxide (CO_2) emission GCGW, İstanbul
29. tr.wikipedia.org/wiki/Ikarus_260. Accessed 15 Aug 2012
30. Öztürk T, Öztürk Z (2010) Istanbul İçin Kara Ulaşımı Üstyapı Maliyetlerine Bir Yaklaşım İMO Teknik Dergi. 330 Short Announcement. doi: 2012 5059-5064

Chapter 49
A Change in the Transportation Needs Today, a Better Future for Tomorrow: Climate Change Review

Leonard E.N. Ekpeni and Abdul-Ghani Olabi

Abstract No sooner than later, the world will be a living hell as a result of the now escalating transportation effects on our climate. The pressure is now growing towards their resultant effects to be totally eradicated in order to save our planet; otherwise, the stabilisation of these effects, global warming, greenhouse gas emission and degradation, will need to be sought after. The world all over is at it now in an effort to restore our climate, to save it from the effects of these catastrophes/ disasters.

On the proposition of the Kyoto Protocol in 1997, the main focus was to decrease greenhouse emissions of mainly six gases—carbon dioxide, methane, nitrous oxide, sulphur hexafluoride, hydrofluorocarbons and per fluorinated compounds (PFCs). And transport alone accounts for over 26 % of global CO_2 and has been regarded as one of the few industrial sectors wherein emissions are still on the increase; on this basis, researchers and policy makers are all at it to tackle the menace of climate changes through provision of sustainable transport.

This chapter focuses on the new and developed technologies like the renewable energy source, which will be an alternative to transport fuels to avoid the dependence on petroleum the after effects of which are damaging to the world climate, and may probably not be there forever to continue serving the world's ever-increasing population. While the long-term solutions are being sought, these alternatives will make do for now.

Keywords Kyoto Protocol • Global warming • Sustainable transport • Greenhouse gases • Climate change • Transportation • Greenhouse gas emission • Degradation • Catastrophes • Disaster • Carbon dioxide • Methane • Nitrous oxide • Sulphur hexafluoride • Hydro fluorocarbons • Per fluorinated compounds • Renewable energy source • Transport fuel

L.E.N. Ekpeni (✉) • A.-G. Olabi
Biofuel Research Group, School of Mechanical and Manufacturing Engineering, Dublin City University (DCU), Collins Avenue, Glasnevin, Dublin 9, Republic of Ireland
e-mail: leonardo55en@yahoo.com; leonard.ekpeni3@mail.dcu.ie; abdul.olabi@dcu.ie

Nomenclature

Chemical Formula

CO_2	Carbon dioxide
CH_4	Methane
PFCs	Perfluorocarbon
N_2O	Nitrous oxide
HFCs	Hydrofluorocarbons
$SF/_6$	Sulphur hexafluoride

Acronyms

GHGs	Greenhouse gases
MFT	Motor fuel taxes
Mtoe	Million tonne
NGO	Non-governmental organisations
PFCs	Per fluorinated compounds
RES	Renewable energy source

49.1   Introduction

Energy demand has been on the increase over the last decade due to the increasing demand of the world population particularly in the transport sector of the economy. As this demand increases, it tends also to increase the impact of the damaging effect on our climate. To this effect, fossil fuel utilisation has threatened the world economy in the areas of global climate change, world energy conflicts and energy source shortages [1]. The damaging effects of the fossil fuels to the world's climate through greenhouse gases (GHGs) have also now led to the researchers in finding an alternative solution to the limited supply of fossil fuels currently not meeting the much-needed demand [2] and this is predicted to near exhaustion within the next 50 years [3]. Since transportation is needed by this oil, its reliance for the movement of goods and services is inevitable as production and manufacturing activities revolve around it [4]. This therefore means that the ever-increasing fossil fuel consumption will result in the imminent petroleum production peak [5]. As transportation in the recent years has become an issue of great concern due to the damaging effect of fossil fuel use, the management of the health effects of climate change will require inputs from all sectors of government and civil society as well as the collaboration between many academic disciplines and new ways of international cooperation that have until now eluded us. A new advocacy is needed as soon as possible if not already in place so as to bring together governments, international agencies, non-governmental organisations (NGOs), communities and academics from all disciplines in adapting to the resultant effects on transport through the new advocacy [6].

To this effect, the development of alternative energy sources has become of paramount importance to the world as a result, and has led researchers in finding alternatives for energy use. It is imperative that the climate be preserved by changes that are in place. Movement towards seeking more sustainable production methods, waste minimisation, reduced air pollution, distributed energy generation, conservation of native forests, GHG emissions [7], and, most importantly, control over these GHG emissions led to an agreement being made with the overall pollution prevention targeted, hence the proposition Kyoto Protocol agreement [8].

In this chapter, focus is directed towards ways on reducing the emissions of CO_2 in the environment from the way we live and use transportation, as doing this will further help in saving the climate from global warming, depletion of the ozone layer, and other vices that tend to interfere with the proper environmental living by humans and by so doing, our good health will be restored.

49.2   Background: World Energy Conflicts

The discrepancy between energy and teaming population in the world has aggravated in the conflicts currently being experienced worldwide. The love for huge wealth particularly that generated from fossil fuels is on the other hand pushing the world leaders of these oil nations to continuously stick on to power when especially democracy is not being exercised in this country.

For over 50 years until now, the technological development in all sectors has improved and has changed the entire performance as well as the needs of the world including that of transportation. And these changes have been both positive and negative; for example, on the positive side, it has resulted in more stable and abundant food supply while on the negative side, it has continuously added to our environmental degradation, more dependence on fossil fuel as well as lowering of our energy efficiency which in other words added to the climate effects we are experiencing now [9]. As this fossil fuel has become the main source of the world's energy, it has also been seen as a means of increasing the world's conflict [10]. Through our current energy need, and luxury goods and services especially those needing the use of energy generated from fossil fuel has increased well long ago and as such, has also added to the damaging effect of climate. Conflict over the control of valuable oil supplies has been a persistent feature of international affairs since the beginning of the twentieth century and as oil has become more scarce and valuable; this has also increased the severity of its conflicts which has varied from one nation to another [11]. Since this product is extremely lucrative in terms of export particularly to the producing countries, they rely mainly on it as a major source of foreign revenue to them; for Nigeria, Saudi Arabia and Iran for example it accounts for 90–95, 90–95 and 80 %, respectively, of foreign revenue. Also, because whoever that controls the government of oil-producing states controls the allocation of oil revenues, these governments tend to stay in power in any way possible so as to still remain as benefactors to this product using means such as army rebellion, terrorism or coup d'etat [11]. Overcoming this dependence on fossil fuel means that there should be

alternative means as a basis for solving the current climate menace; otherwise, the competition for oil will remain a source of conflict so long as the demand for this fossil fuel rises faster than supply [11]; hence in consideration, renewable energy sources (RES) are now being looked at so as to preserve the climate and protect the environment. The negative effects of fossil fuel and other nonrenewable energy sources have continued to be surfacing and in the transportation industry, our current need for it has also shown a rise in the menaces that are resultant from such usage, like the GHGs, CO_2 emission, global warming, depletion of the ozone layers as well as other variances that are detrimental to human health and environment. However human activities are assumed to be responsible for almost all of the increase in GHGs in the atmosphere since the last 150 years wherein the largest source of GHG emissions from human activities, for example, in the United States, is from the burning of fossil fuels for electricity, heat and transportation [12] but on a greater scale, this can be reduced to the barest minimum through changing our ways of living and shifting from the nonrenewable to renewable energy sources.

49.2.1 Energy Source Shortages

Amidst the current energy crisis, it is of great concern to show that the energy supply source will not last for too long. The ever-growing population whose demand needs to be met and the shortage in the supply source are some reasons for this current situation. The environmental movement has been questioned of being the cause of the nation's energy crisis and the balancing of environment and energy factors will be essential in determining policies to meet the demand of the crisis.

And as predicted by Dr. M. King Hubbert of Shell Oil in 1956, that US oil production would peak in 1970; this was disregarded by most oil experts and in furtherance to this [13], asserts it that in 2005, oil production stopped growing, and the price of crude oil shot upward from $45 per barrel to $140 per barrel, we hit "peak oil" otherwise known as the "Hubbert's peak," a geological limitation to the supply of oil in the ground and with no additional supplies, a bidding war resulted in 2005 over the remaining oil in the ground. The eminent consequence of this is the high prices of oil which on the other hand increase the prices of food as modern agriculture is an energy-intensive business [13]. The oil shortage will not only cause energy crisis in nations across the globe as it is being experienced now but also cause the oil reserves being depleted and that again will make the price to rise sharply because of its nearing exhaustion and as such the demand of the population cannot be met.

Apart from the effects on our climate and health resulting from its use, the way of life needs to be adjusted to suit the current energy need through alternative energy use of RES. This alternative has been considered necessary as the implications from these shortages need to be addressed regardless of whether it lasts another 40, 60 or 80 years as it is certain now that the resource is dwindling and that competition over it will become more intense. As it is acclaimed now any factors that threaten fossil fuel stability will result in the price rise and will, in alternative, threaten investments as well [14].

In another development, in guiding against this shortage of energy source the best possible way is the minimisation of the associated risk [15] and despite the best efforts to prevent a supply crisis, this cannot be totally prevented as one can still occur. In cases like these, energy security thinking dictates minimising the impact of the crisis on national security and economic welfare. Also strategic stockpiles, which are often owned and managed by the government, is one of the most effective ways to deal with a supply disruption crisis and/or a price shock. Although this has not been used yet as in the case of shortages they are thought to be essential in the minimisation of price impact during a crisis situation.

49.2.2   Renewable Energy Source Scenario

As the world's climate is changing through the negative effects of GHG, global warming and bio degradation, efforts are required to have all these corrected through RES. Not only now but also in time to come this will play a major role in the world's climate revival as it has been tagged, the power for a sustainable future.

This has been categorised into three parts: renewable resources, nuclear resources and fossil fuels [16]. Renewable energy studies is the most exciting aspect in that it is inherently positive as it offers the possibility of solutions to some of the society's most difficult problems [16, 17].

49.3   Global Climate Change

Twenty-first century's climate change (CC) is now unequivocal [18] and has become a dominant issue that has arguably been thought of, and the earth's climate has changed over the years due to the warming and cooling of the cloud as depicted in [19, 20], which are termed as primary concerns for humanity in the twenty-first century as they may affect health through different pathways; typical examples are as a result of vector-borne diseases, increased floods and droughts and increased frequency and intensity of heat waves, to mention a few.

Maintaining the atmospheric new equilibrium means that there will be changes to its compositions which will ultimately require balance in the achievement of the global climate change.
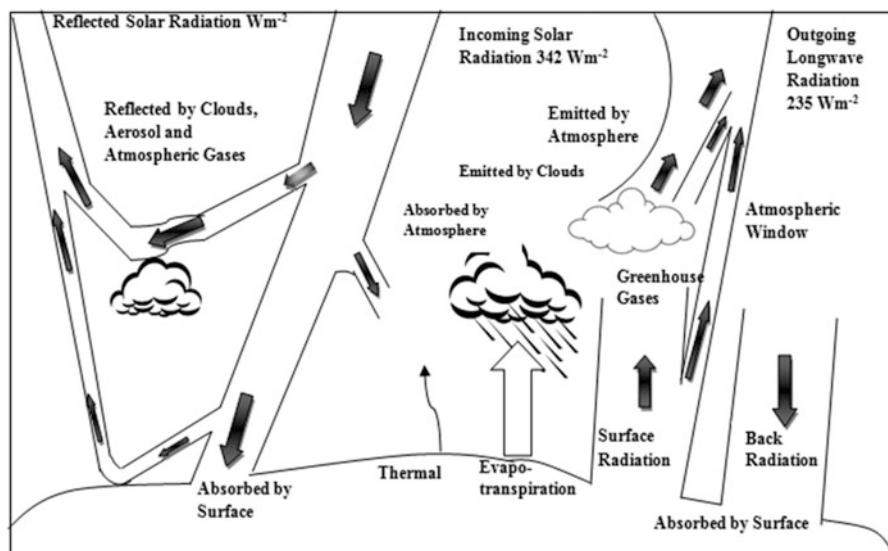
Since this has become a global problem, it therefore also requires a global response that embraces the interests and needs of all countries [21]. The world no longer sees it as an environmental problem alone, instead as an economic, trade and security issue which has increasingly dominated global and national policies as its impacts have become more severe.

It has also been considered as the potentially most important environmental problem that concerns energy, either greenhouse effect or global warming [21, 22].

Global warming is referred to as the measured increase in the average temperature of the earth, caused by the build-up of some GHGs in the atmosphere which has

Greenhouse Gases	Main Sources
Carbon Dioxide (CO_2)	Fossil fuel combustion (e.g. Road transport, energy industries, other industries, residential, commercial and public sector), forest clearing
Methane (CH_4)	Agriculture, landfill, gas leakage, coal mines
Nitrous oxide (N_2O)	Agriculture, industrial processes, road transport, other
Perfluorocarbons (PFCs)	Industry (e.g Aluminium production, semi-conductor industry)
HydroFluoroCarbons (HFCs)	Refrigeration gases, industry (as perfluorocarbons)
Sulphur hexafluoride (SF/6)	Electrical transmissions and distribution systems, circuit breakers, magnesium production

Fig. 49.1 Greenhouse basketed under the Kyoto Protocol and their main generators as modified from [18]

Fig. 49.2 Annual earth estimate and global mean energy balance; energy is transferred to the atmosphere via warming the air in contact with surface through long-wave radiation which is absorbed by clouds and GHG as modified from [12]

accumulated over time from the land use changes and fossil fuel combustion continually [23]. Figure 49.1 above depicts the GHGs under the Kyoto Protocol and their main generators as source. The first three have been estimated to account for 50, 18 and 6 %, respectively, of the global warming effect arising from human activities [18]. Just to note that GHG from the air transport has been exempted from the protocol (Figs. 49.2, 49.3 and 49.4).
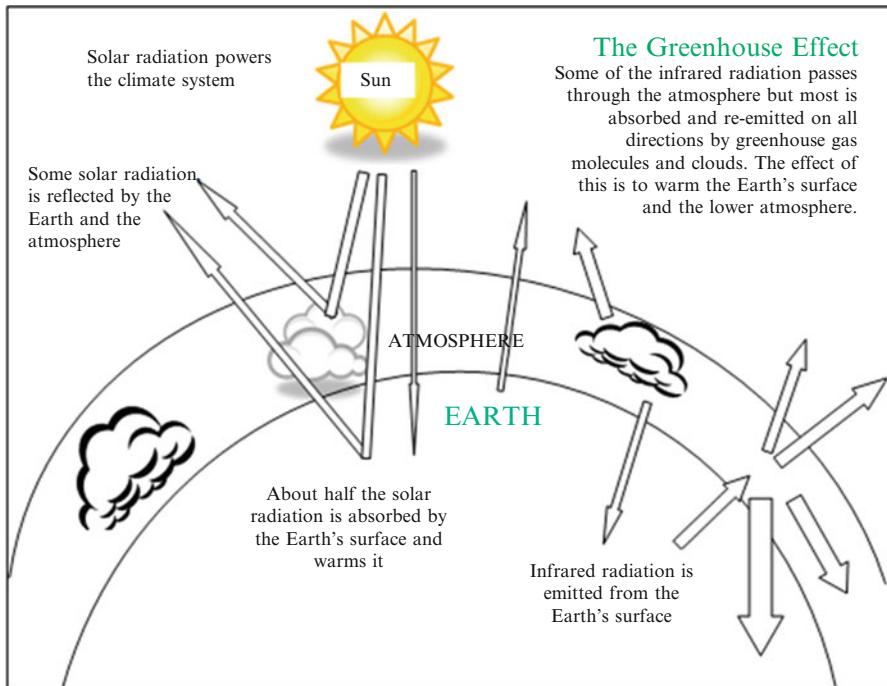
Fig. 49.3 Natural greenhouse effect with an idealised model as modified from [12]
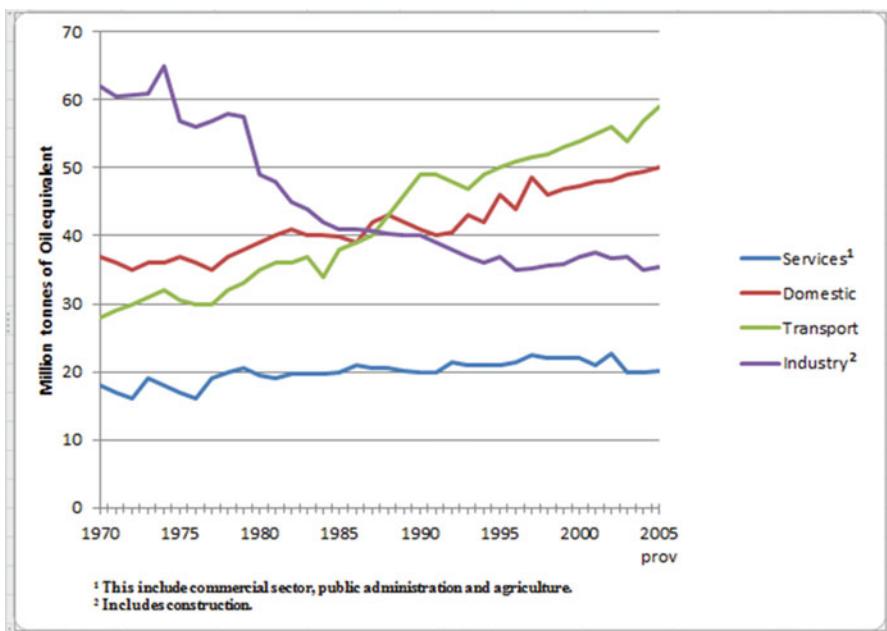
Fig. 49.4 UK energy sectoral consumption as modified from [25]

49.4   Transportation Roles in the Society

When the Kyoto Protocol was proposed in 1997, transportation was considered as the key sector that needed to be tackled. This was to have GHG emissions down; the figure shows that percentage level of the 1990 level to 2008 level has been up by 47.5 % for CO_2 worldwide [21]. The reason behind this increment is oil being the dominant fuel source for transport movement accounting for over 84 % of the total energy use by the transport sector. For example in the UK alone, the transport industry has also seen a dramatic change with figures climbing 47 % from 28.1 million tonne (Mtoe) in 1970 to 59.7 Mtoe in 2006 [24]. The population and the increase in consumer goods available have led to an increase in road haulage and personal transport needs.

This overdependence on oil makes transport a major GHG contributor and still one of the industries where emissions are still on the rise [25].
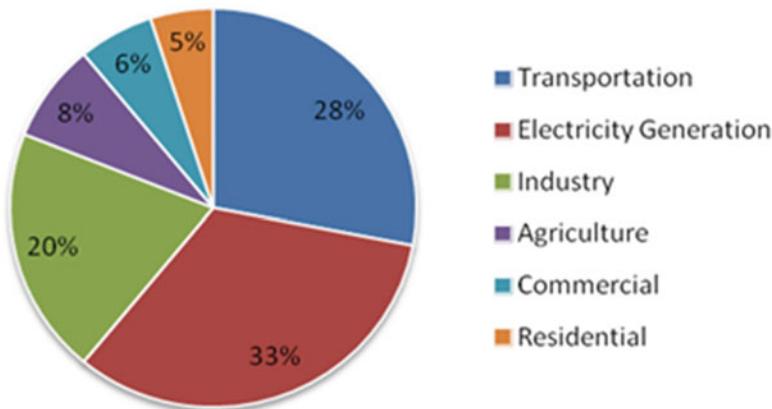
The impact of transport on the global climate is not limited to vehicle emissions as the production and distribution of fuel from oil, a "wells-to-wheels" approach, produce significant amounts of GHG in it [26].

Figure 49.5 below indicates the energy use by end user wherein transport accounts for more as compared to others in the sectors, from 28,174 in 1970 to 59,780 in 2006 for UK data.

Also in the United States from Fig. 49.6, the transportation sector accounts directly for 28 % of the total GHG emissions in 2006, hence making that sector the second largest source of GHG emissions, while electricity generation taking the lead at 34 %. Almost 97 % of transportation GHG emissions results as direct combustion of fossil fuels, as the remaining are due to CO_2 from electricity (for rail) and hydrofluorocarbons (HFCs) emitted from vehicle air conditioners and refrigerated transport, as shown in Fig. 49.6 [27].

				Thousand tonnes of oil equivalent	
	Industry	Transport	Domestic	Other final users	All final users
1970	62,333	28,174	36,884	18586	145,977
1975	55,444	30,885	37,062	17,360	140,751
1980	48,291	35,541	39,841	18,721	142,394
1985	41,702	38,500	42,062	19,603	141,867
1990	38,660	48,635	40,756	19,218	147,268
1995	36,276	50,238	42,691	21,179	150,384
2000	35,352	55,461	46,851	21,547	159,211
2005	33,555	59,062	47,161	20,315	160,093
2006	32,561	59,780	45,563	19,888	157,792

Fig. 49.5 Final energy use by end user as modified from [25]

Fig. 49.6 Percentage of GHG emission in the United States, 2006 (all gases in Teragram [Tg] CO_2) as modified from [27]
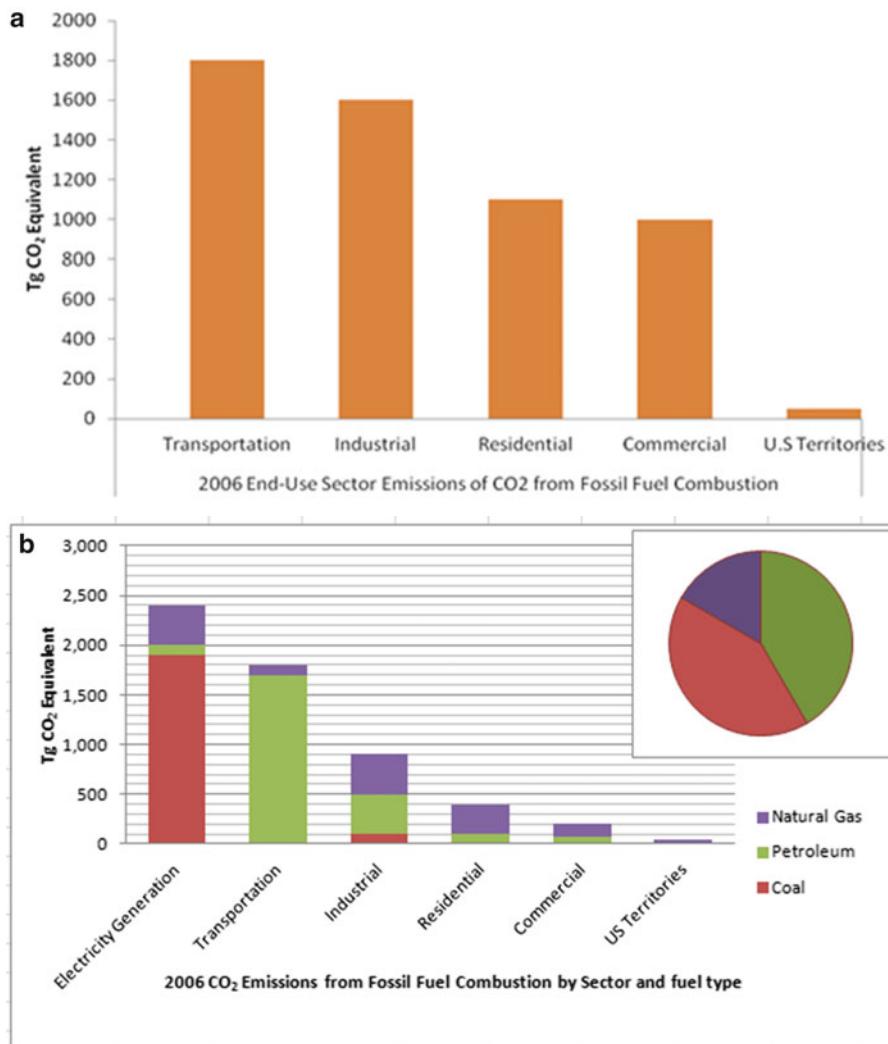
The end-use emissions of CO_2 depicted in Fig. 49.7a, b indicate that the energy consumed in the transportation activities came from petroleum products, while more than 60 % of the emissions resulted in gasoline consumption for personal vehicle use [27].

The remaining are thought to be from heavy-duty vehicles and jet fuel in aircraft. It is estimated that transportation accounts for 28 % of emission of the GHG in the United States and 26 % worldwide.

Transportation sectors generally are experiencing expansion and there is also a general trend that considers the modes that are experiencing the most growth to be the most polluting. Air transports show the highest among all transport modes (motor car, aviation, road freight, rail, ship, walking and cycling) [28]. Motor cars and aviation are favoured mode of transportation. This has resulted in the actual energy consumption and CO_2 emissions from aviation significantly more damaging than the others despite the fact that they appear to be lower when compared to those of motor cars; but on the other hand, aviation is the biggest contributor to climate change. It is environmentally damaging than the CO_2 emission figures that are presumed, because other GHGs are being released straight into the upper atmosphere, where the localised effects can be more damaging than the effects of just CO_2 only [29].

49.4.1   Transport Mitigations

The world's value for material wealth has led to the present infrastructure not being able to curtail with the large increases in the number of vehicles and as such, congestion is now becoming an ever-increasing problem in so many towns and cities of the world. This has contributed not only to the air pollution and CO_2

Fig. 49.7 (**a**) End-use sector emissions of CO_2 from fossil fuel combustion as modified from [27]. (**b**) CO_2 emissions from fossil fuel combustion by sector and fuel type as modified from [27]

emissions but also to a great significant economic consequence [21]. To tackle this menace of reducing the damaging effect of CO_2 emission from our road, there must be shift of car ownership to the use of public transports as this will reduce the number of vehicles on the road. For the effectiveness of this measure, policies need to be put in place like offsetting the affordability of car possession via indirect tax implementations or having to increase parking charges at some destinations or fuel tax levies [30].

Aviation on its own poses a greater problem when compared to other transportation means in that it emits the gases like CO_2 and nitrous oxide directly into

troposphere and stratosphere. Although the emission impact will vary as it is dependent on where the aircraft is flying the NOx emission in the troposphere upper layer results in more ozone for radiative forcing than the same quantity released at the surface because some gases have an increased effect at altitude [31].

For the road freight, its growth has become an environmental and economic burden in terms of GHG emissions. About 45 % of transportation energy used in freight can be cut down by half through technological advancement of the developed and well-improved fuel efficiency [32].
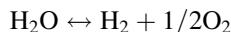
Cycling and walking is overall the best to the environment in terms of saving our climate; this is zero carbon emission and environmentally friendly. This should be encouraged at all levels not only for climate sake but also for the good health of every individual and for this to be properly considered, every local authority, school and business even within family cycle should consider "soft" transport policy measures to encourage these [33]; but for longer journey, other alternatives should be sought.

49.5 New Generation/Developed Technologies

49.5.1 Fuel Cell

Towards the technological advancement to save the climate, fuel cell has been developed. This uses hydrogen as its fuel for powering vehicle. And as a sustainable energy supply with little or no hydrocarbons use, it is preferred to fossil fuels because it is a clean and environmentally friendly fuel which produces water instead of GHG when combusted [1]. Though some methods of producing hydrogen generate GHG, there are methods to capture and sequester the CO_2 that is generated [34].

The most suitable source of hydrogen production is water because it is clean, renewable and abundant [2]. Water dissociates into oxygen and hydrogen at high temperatures through the reaction below:

$$H_2O \leftrightarrow H_2 + 1/2O_2$$

49.5.2 Biofuel

This is otherwise known as the sustainable fuel with no effect of CO_2 to the environment. It works by recycling the natural occurring products such as the conventional crops, bioethanol from sugarcane and biodiesel from vegetable oils; this usually delivers a 10–90 % reduction on a well-to-wheels or crop-to-car basis when compared to conventional fuels like gasoline and diesel [34]. Apart from the reduction of CO_2 emission into the atmosphere, the use of non-intensively farmed crops or waste enhances the GHG emission savings, thereby increasing the overall availability of potential and production cost improvement.

49.5.3 Battery-Powered Electric Vehicle/Hybrid

This is the zero emission of CO_2 at source and provides the advantages of electric propulsion by requiring fuel cell, that is, the energy management system being used in the optimisation of the fuel economy of both engines since electric and combustion engines work better under different driving conditions.

49.5.4 Carbon Tax and Audit (Carbon Footprint)

This is a means towards reducing CO_2 of every individual contribution to the environment also known as the footprint and its audit is the first step towards this development of carbon strategy. And as most nations have implemented these, particularly in the EU, Japan, United States and Canada, it reduces CO_2 emissions in two ways: by increasing the prices of fossil fuels—this in a way will encourage more efficient use of energy through stimulating the development of zero-emission technologies and, on the other hand, by changing the relative prices—this will encourage a proper shift in consumption from coal and oil to cleaner burning natural gases which are environmentally friendly. As compared to motor fuel taxes (MFT), carbon tax has a number of advantages:

- This is less regressive as compared to MFT.
- It promotes global and local environmental quality while revenues are being raised.
- Shifting from the single-fuel energy taxes towards carbon tax implies that a required level of revenue can be raised at a lower tax rate [35].

And trading of emissions across all sectors of the economy addresses this by allowing emitters to purchase carbon offsets from businesses that are able to lower their own emissions below their allocation. On this basis, it will be a considerable idea to design a climate policy that would tap all possible avenues to limit net CO2 emissions. For example, offsetting emissions by storing carbon in soils, forests and other forms of biomass in the United States will have the potential in offsetting about 10–20 % of the US emissions in the next 10–15 years from now at relatively low cost [36].

49.6 Conclusion

The reduction of CO_2 emissions will never cease to be of major concern for as long as fossil fuels are still the main form of energy usage across the globe. The way forward is the implementation of these new-generation and developed technologies as explained above which will gradually take over fossil fuel and nuclear energy. It would be impossible to unite the entire world to tackle the issue of climate change/

global warming because only a fraction of the entire world accepts the threat that it poses. In a gradual process, the shift of direction from fossil fuel and nuclear energy to alternative energy source (RES) will become acceptable by all and sundry. In the meantime, it will require people in authority to enforce any actions that are required for its implementation. As the world is in the midst and continuation of a period of drastic change four decades after the oil crises of the 1970s, everything from new information technologies to the rise of genetic engineering and the breakdown of traditional social structures are reshaping modern economies and lifestyles at an unprecedented pace [37] including the improvement of transportation and transportation systems over the period till date. Also in the implementation and further improvement of these ideas and plans, it should be borne in mind that certain changes should be in proper place to improve the overall efficiencies and goals towards making this a huge success.

Some or parts of these changes are as follows: technological change, which includes incremental technologies so as to make vehicles more technically efficient than they are today and at the same time lessen their fuel consumption/distance travelled: these will to a greater extent significantly reduce transport CO_2 emissions over short to medium term though the term of transportation usage and improvement of transport need as to quality and CO_2 emission has drastically reduced as compared to what it was 15–20 years ago. In essence, these technologies will further make transport systems and infrastructure more efficient, through reducing the need for vehicle travel to more efficient routing if the need be for it to be used as well as better in use fuel efficiency and mode switching; and new lower carbon fuels and fuels lower in GHGs on a well-to-wheels basis [38]. Development and improvement of hybrid cars and design of lower CO_2 emission aircraft has also become part towards this global issue of energy-efficient and sustainable development. As zero-emission vehicles continue to exist, this will be a history of alternative petroleum vehicles, which will continue to meet the needs of the people and, as a result, reduce the overdependence on fossil fuel usage. These aircraft engines are expected to cut fuel consumption compared by 15 %, lower emissions of NOx and reduce the noise footprint by 75 % [39].

Also to consider in terms of change is the behavioural change; this tends to contribute greatly to the reduction of CO_2 emissions or saving energy through the framework of improving city living or its quality of life and as a result estimating the potential contribution of integrated pricing; this will be through pricing of road use decrees promulgated and enforced by the appropriate authorities; they will be in charge with calculating the national road user charging scheme, and others to consider in the behavioural change will be soft factors and land use planning in reducing travel [40].

However, the potentials for carbon rationing should never be dismissed; as this is a system wherein tradable CO_2 emission permits would have several effects on the overall well-being and climatic change of the environment through free yearly allocated CO_2 budget given to individuals, and through the optimisation of their travel patterns within the budget will assist in improving the emission of CO_2 and GHGs released.

On the general view in this study, the overall success of the change in the transportation needs today so as to result in a better future for tomorrow lies in the creation of awareness to all and sundry across the globe through proper communication channel and dissemination of information by way of education in different languages to the over seven billion population across the globe while efforts are still being made and researches carried out to devise more meaningful ways in tackling this global menace.

References

1. Kothari R, Tyagi VV, Pathak A (2010) Waste-to-energy: a way from renewable energy sources to sustainable. Renew Sustain Energ Rev 14:3164–3170
2. Park CY, Lee TH, Doris SE, Balachandran U (2010) Hydrogen production from fossil and renewable sources using oxygen transport membrane. Hydrogen Energ 35:4103–4110
3. Oman H (2003) Energy sources for the world's post petroleum era. IEEE Aero Electron Syst 18:35–39
4. Isife CT (2010) Energy crisis and sustainable development in Nigeria. Sustain Hum Dev Rev 2 (2):67–77
5. Duncan RC, Youngquist W (1999) Encircling the peak of world oil production. Nat Resour Res 8:219–232
6. Costello A et al (2009) Managing the health effects of climate change. Lancet and University College London Institute for global health commission. Lancet 373:1693–1733
7. Sim REH (2003) Bioenergy to mitigate for climate change and meet the needs of society, the economy and the environment. Mitig Adapt Strat Glob Chang 8:349–370
8. Nielsen JBH, Seadi TA, Popiel PO (2009) The future of anaerobic digestion and biogas utilization. Bioresour Technol 100:5478–5484
9. Giampietro M, Pimentel D (1993) the tightening conflict: population, energy use, and the ecology of agriculture. http://www.npg.org/forum_series/tightening_conflict.htm. Accessed 12 Dec 2012
10. Barnett C (2006) Oil, conflict and the future of global energy supplies. http://www.globalresearch.ca/oil-conflict-and-the-future-of-global-energy-supplies/1781. Accessed 12 Dec 2012
11. Klare MT (2004) Blood and oil: the dangers and consequences of America's growing petroleum dependency. http://www.hampshire.edu/academics/22172.htm. Accessed 12 Dec 2012
12. IPCC (2007) Summary for policymakers. In: Solomon S, Qin D, Manning M, Chen Z, Marquis M, Averyt KB, Tignor M, Miller HL (eds) Climate change 2007: the physical science basis. contribution of working group I to the fourth assessment report of the intergovernmental panel on climate change. Cambridge University Press, Cambridge, United Kingdom and New York, NY, USA. http://www.epa.gov/climatechange/ghgemissions/sources.html. Accessed 10 Dec 2012
13. Deffeyes KS (2001) Hubbert's peak: the impending world oil shortage. Princeton University Press, NJ, USA
14. Perovic J, Mockli D (2006) Energy security: oil shortages and their implications. CSS Analyses in security policy. 1:2. CSS An ETH Center. http://www.css.ethz.ch/publications/pdfs/CSS-Analyses-2.pdf. Accessed 12 December 2012

15. Hippel DV, Suzuki T, Williams JH, Savage T, Hayes P (2011) Energy security and sustainability in Northeast Asia. Energy Policy 39:6719–6730
16. Demirbas A (2000) Recent advances in biomass conversion technologies. Energ Educ Sci Tech 6:19–40
17. Boyle G (1996) Renewable energy: power for a sustainable future. Oxford University Press, Oxford, UK
18. UNFFCCC (2003) Accessed 8 Mar 2012
19. IPPC (2007) www.int/resource/docs/publications/unitingonclimate_eng.pdf. Accessed 11 Mar 2012
20. Tingem M, Rivington M (2009) Adaptation for crop agriculture to climate change in Cameroun: turning on the heat. Mitig Adapt Strat Glob Chang 14:153–168
21. Chapman L (2007) Transport and climate change: a review. Transport Geogr 15:354–367
22. Panwar NL, Kaushik SC, Kothari S (2011) Role of renewable energy sources in environmental protection: a review. Renew Sustain Energ Rev 15:1513–1524
23. Weubles DJ, Jain AK (2001) Concerns about climate change and the role of fossil fuel use. Fuel Process Tech 71:99–119
24. Defra (2007) www.defra.gov.uk/environment/climatechange/uk. Accessed 22 Mar 2012
25. WBCSD (2001) World Business Council for Sustainable Development. Mobility 2001: World mobility at the end of the twentieth century and its sustainability. www.wbcsdmobility.org. Accessed 1 Apr 2012
26. Weiss MA, Heywood JB, Drake EM, Schafer A, AuYeung FF (2000) On the road in 2020—a life cycle analysis of new automobile technologies. Energy Laboratory, MIT, Cambridge
27. www.epa.gov/climatechange/emissions/downloads/08CR.pdf. Accessed 7 Apr 2012
28. Lenzen M, Dey C, Hamilton C (2003) Climate change. In: Henser DA, Button KJ (eds) Handbooks in transport 4: handbook of transport and the environment. Elsevier, Oxford, pp 37–60
29. Cairns S, Newson C (2006) Predict and decide. Aviation, climate change and UK policy. Environmental Change Institute, Oxford, p 122
30. IEA (International Energy Agency) (2000) Transportation energy. www.iea.org. Accessed 18 Apr 2012
31. Penner JE, Lister DH, Griggs DJ, Dokken DJ, McFarland F (1999) IPCC special report: aviation and the global atmosphere. Cambridge University Press, UK, 373
32. IMO (International Maritime Organisation) (2000) Prevention of air pollution from ships, consideration of an IMO strategy for greenhouse gases reduction: MEPC 45/8/3, NY
33. Cairns S, Sloman L, Newson C, Anable J, Kirkbride A, Goodwin P (2004) Smarter choices: changing the way we travel, Department of Transport
34. www.Biofuels_Fact_Sheetonrenewableenergy.pdf. Accessed 14 Apr 2012
35. Muller F, Hoerner JA (1994) Greening state energy taxes: carbon taxes for revenue and the environment. pace environmental law review. 12 Pace Envtl L Rev 5. (www.digitalcommons.pace.edu/pelr/vol12/iss1/2)
36. Chameides W, Oppenheimers M (2007) Climate change: carbon trading over taxes. Policy forum. Science 315. www.sciencemag.org
37. Lenssen N, Flavin C (1996) Sustainable energy for tomorrow's world: the case for an optimistic view of the future. Energy Policy 24(9):769–781
38. IEA (International Energy Agency) (2004) Transportation energy. www.iea.org. Accessed 10 June 2012
39. http://www.aviationbenefitsbeyondborders.org/environmental-efficiency/case-studies/new-engines-offer-ever-lower-fuel-burn-and-emissions. Accessed 11 June 2012
40. Hickman R, Banister D (2005) towards a 60 % reduction in UK transport carbon dioxide emissions: a scenario building and backcasting approach. Sustainable transport and land use. ECEEE 2005 summer study—what works & who delivers?

Chapter 50
Emission Analysis of a Commercial Aircraft for Different Ranges

Hakan Aydın, Onder Turan, T. Hikmet Karakoc, and Adnan Midilli

Abstract In this chapter the lower take off cycle and total flight fuel consumptions and emissions of B737-400 commercial aircraft for selected routes are being calculated and evaluated for specified flight parameters. For case studies Eskisehir–Istanbul, Trabzon–Istanbul, and Ankara–London flights are selected as short-, medium-, and long-range flights with having 350, 980, and 3,270 km flight distances. The primary emissions released to environment are CO_2, CH_4, N_2O, NO_x, CO, and SO_2. During Ankara–London flight with aircraft maximum takeoff weight operation (68,040 kg), B737-400 consumes 12,660 kg fuel and as a result 40,000 kg of CO_2, 1.296 kg of CH_4, 1.62 kg of N_2O, 116.7 kg of NO_x, 211.5 kg of CO, and 12.66 kg of SO_2 are emitted into environment.

Keywords Green aircraft • Emission • Propulsion • Greenhouse gases • Emission analysis • LTO cycle • Flight • Istanbul • Ankara • London • Eskisehir • Trabzon • Transportation

Nomenclature

IPCC	Aviation and the global atmosphere
Kt	Knot, nautical mile/h
LTO	Lower takeoff

H. Aydın (✉)
TEI, Eskişehir, Turkey

O. Turan • T.H. Karakoc
Anadolu University, Eskişehir, Turkey

A. Midilli
Recep Tayyip Erdoğan University, Rize, Turkey

MTOW	Maximum takeoff weight, kg
LW	Landing weight, kg
PL	Payload, kg
TOW	Takeoff weight, kg

50.1 Introduction

The main objective pursue in this chapter is to reveal the hazardous emissions exhausted to environment from commercial aircraft and to emphasize the society, aircraft, and engine manufacturer to improve the efficiencies in order to decrease the emission rates. For case studies, a widely used medium-range commercial aircraft (B737-400) is selected and its operation in short-, medium-, and long-distanced flights for various takeoff weights are theoretically investigated per aircraft performance data. In this regard, Eskisehir–Istanbul, Trabzon–Istanbul, and Ankara–London routes are selected as short-, medium-, and long-distanced flight case studies having 350, 980, and 3,270 km flight distances. The flight analyses are executed based on flight parameters for ISA condition, climb speed at 280 Kt/0.74 Mach, cruise speed at Mach 0.78, cruise level at 31,000 ft, and descent speed at 250 Kt/0.74 Mach. The fuel consumptions for each part of flight phase including lower take off (LTO) cycle are found out per aircraft takeoff weight. The emissions are obtained for both LTO cycle and complete flight, and the results are presented in tables. The primary emissions released to environment are CO_2, CH_4, N_2O, NO_x, CO, and SO_2. About 12,660 kg fuel is consumed during B737-400's Ankara–London flight at 68,040 kg takeoff weight operation and also approximately 40,000 kg of CO_2, 1.296 kg of CH_4, 1.62 kg of N_2O, 116.7 kg of NO_x, 211.5 kg of CO, and 12.66 kg of SO_2 are emitted into environment during complete flight.

The negative effects of exhaust emissions on environment from commercial and military aircraft have been focused in the recent years. Despite the gradual increase of oil prices in last decades, the aviation industry continues to grow and this trend is expected to continue in years to come. Though there is continuous improvement in fuel efficiency of the new engines and aircraft, the expected growth in air traffic implies that this emission source in the future will increase in importance [1]. Passenger traffic on scheduled airlines increased by 60 % in the past 10 years and forecasts indicate a 5 % per year growth rate for the next 10–15 years [2].

In this chapter B737-400 aircraft fuel consumptions and emissions are being calculated and evaluated per B737-400 performance manual for selected flight parameters and flight routes with respect to aircraft takeoff weights [3, 4]. The flight and LTO cycle emissions and fuel consumptions are presumed per B737-400 emission rates listed in Table 50.1 [2]. The results are listed in Tables 50.2, 50.3, and 50.4.

Table 50.1 B737-400 commercial aircraft LTO cycle emissions (kg) [2]

CO_2	CH_4	N_2O	NO_x	CO	SO_2	LTO
2,480	0.08	0.1	7.19	13.03	0.78	780

Table 50.2 B737-400 Eskisehir–Istanbul LTO cycle and flight emissions (kg) [2]

	TOW	Payload	CO_2	Fuel cons.	CO	NO_x	SO_2	N_2O	CH_4
LTO cycle	41,360	2,265	2,003	630	10.53	5.81	0.63	0.081	0.065
	58,100	18,664	2,380	750	12.50	6.89	0.75	0.096	0.077
Total flight	41,360	2,265	5,372	1,700	28.40	15.60	1.70	0.22	0.170
	58,100	18,664	6,310	1,997	33.30	18.40	2.00	0.25	0.20

Table 50.3 B737-400 Trabzon–Istanbul LTO cycle and flight emissions (kg) [2]

	TOW	Payload	CO_2	Fuel cons.	CO	NO_x	SO_2	N_2O	CH_4
LTO cycle	43,300	2,265	2,067	650	10.86	5.99	0.65	0.08	0.067
	60,200	18,530	2,448	770	12.86	7.1	0.77	0.1	0.079
Total flight	43,300	2,265	11,092	3,510	58.64	32.35	3.51	0.45	0.359
	60,200	18,530	13,098	4,145	69.24	38.2	4.14	0.53	0.424
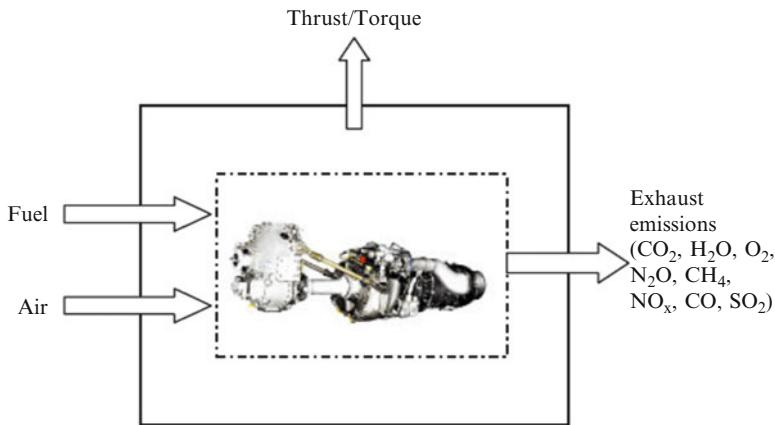
Table 50.4 B737-400 Ankara–London LTO cycle and flight emissions (kg) [2]

	TOW	Payload	CO_2	Fuel cons.	CO	NO_x	SO_2	N_2O	CH_4
LTO cycle	50,470	2,265	2,210	695	11.61	6.41	0.7	0.09	0.07
	68,040	17,420	2,591	815	13.61	7.51	0.82	0.1	0.08
Total flight	50,470	2,265	32,722	10,355	173	95.45	10.25	1.33	1.06
	68,040	17,420	40,000	12,660	211.5	116.7	12.66	1.62	1.296

50.2   Background

Air transportation is a significant source of pollution that impacts both local air quality and the global climate. Air transportation-sourced emissions are carbon dioxide (CO_2), water vapor (H_2O), nitrogen oxides (NO_x), unburned hydrocarbons (HC), carbon monoxide (CO), sulfur oxides (SO_x), and particulates. Local air quality is affected, for example, by CO and NO_x which are precursors of tropospheric ozone, a toxic compound. Furthermore, NO_xs are a key ingredient of smog and acid rain, which aggravates asthma and affects forests and wildlife, respectively. On the other hand, tropospheric ozone as well as CO_2 are greenhouse gases which contribute to global climate change [5, 6].

The aviation sector consumes approximately 13 % of the total fossil fuel used in transportation, which corresponds to roughly 2–3 % of the total fossil fuels used worldwide [2]. In the European Union, greenhouse gas emissions from aviation increased by 87 % between 1990 and 2006 [7].

Fig. 50.1 Mass, energy, and emission flows of aircraft engine (modified from [4])

As a result, the aviation sector is increasingly becoming an important source of GHGs and its impact on local air quality and global climate change is expected to increase in the future. IPCC's medium-range estimate forecasts that by 2050 the global aviation industry, including aircraft emissions, will emit about 3 % of global carbon dioxide and about 5 % of the potential warming effect of all global human-generated emissions [8].

Figure 50.1 shows the primary exhaust emissions from aircraft engine. Carbon dioxide is direct result of fuel burn. For every gallon of jet fuel burned, about 21 lb of carbon dioxide is emitted. Reducing the amount of fuel burned, therefore, also reduces the amount of carbon dioxide emitted. Water vapor emissions and certain atmospheric temperature and humidity conditions can lead to the formation of contrails, a cloudlike trail of condensed water vapor, and can induce the creation of cirrus clouds. Both contrails and cirrus clouds are believed to have a warming effect on the earth's atmosphere. Aircraft also emit other pollutants that affect local air quality.

50.3 Methodology and Analysis

In this chapter the following steps are performed:
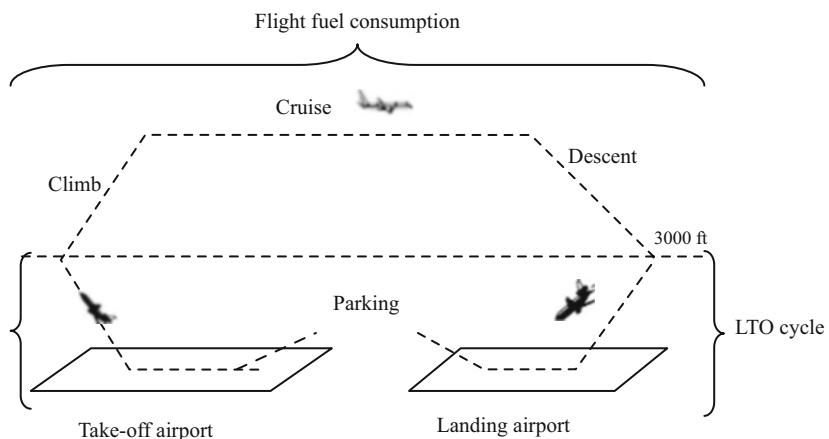
1. Selection of aircraft and flight routes.
   B737-400 commercial aircraft and Eskisehir–Istanbul, Trabzon–Istanbul, and Ankara–London flight routes are selected for case studies.
2. Calculation of flight parameters:
   Flight parameters (e.g., fuel consumptions, flight time) are calculated for short-, medium-, and long-range operation of B737-400 commercial aircraft per aircraft performance data.

3. Calculation of LTO cycle and total flight fuel consumptions for all case studies.
4. Calculation of LTO cycle and total flight emissions:
   LTO cycle and total flight emissions for all case studies are derived per B737-400 emission rates [2]. The results are presented in Tables 50.2, 50.3, and 50.4.

50.4 Emissions

Table 50.1 presents the LTO cycle fuel consumption and emissions for B737-400 commercial aircraft. These rates will be used as reference for both LTO cycle and total flight emission calculations. As seen in Table 50.1, CO_2 is most weighted emission emitted into environment and 2,480 kg of CO_2 is produced as of 780 kg LTO cycle fuel consumption. However, only 80 g of CH_4 is generated during LTO cycle.

In this chapter flight emissions will be classified into two categories for LTO (landing/takeoff) cycle and total flight emissions. LTO cycle emission contains all activities near the airport that take place below the altitude of 3,000 ft (1,000 m). This includes taxi-in and out, takeoff, climb-out, and approach-landing [1]. The total flight emission includes all emissions emitted into environment during complete flight that contains LTO cycle, climb and descent above 3,000 ft, and cruise flights. LTO cycle and total flight sections are shown in Fig. 50.2.

Fig. 50.2 Total flight and LTO cycle (modified from [1])

50.5   Results and Discussion

B737-400 fuel consumptions of complete flights and LTO cycle are calculated for accepted flight parameters for short-, medium-, and long-range flight case operations with the help of B737-400 climb, cruise, and descent performance curves [3]. The calculated LTO cycle and complete fuel consumption values are presented in Tables 50.2, 50.3, and 50.4. Having had the fuel consumptions, LTO cycle and total flight emissions for all investigated flight cases are then obtained per referenced LTO cycle emission rates specified in Table 50.1. B737-400 flight and LTO cycle emissions for selected flight parameters are also presented in Tables 50.2, 50.3, and 50.4 for Eskisehir–Istanbul, Trabzon–Istanbul, and Ankara–London flight cases.

50.5.1   *B737-400 Eskisehir–Istanbul Short-Range Flight Emissions*

For short-range flight case Eskisehir–Istanbul is selected which has 350 km flight distance. The LTO cycle and total flight fuel consumptions along with the emissions are obtained for two calculated B737-400 aircraft TOW as 41,360 kg and as 58,100 kg. TOW with 41,360 kg enables 2,265 kg of payload (25 passengers) transportation and 58,100 kg takeoff weight is limited max. takeoff weight for this flight case that 18,644 kg of payload can be transported. In short-distanced flights the aircraft cannot generally take off with max. takeoff weight (MTOW) due to max. landing weight (MLW) limitation; that is the case for B737-400 in Eskisehir–Istanbul operation. These two specified takeoff weights and flight parameters for all investigated flight cases are calculated by using B737-400 operational manual performance curves [3]. B737-400 Eskisehir–Istanbul flight path LTO cycle and total flight emissions are listed in Table 50.2 which are calculated per emission index presented in Table 50.1 [2].

Regarding LTO cycle emission rates as noted 2,380 kg of CO_2 is emitted into atmosphere as a result of 750 kg LTO cycle fuel consumption for 58,100 kg TOW and about 7 kg of NO_x is emitted. Looking at the total flight emissions, flight fuel consumption and CO_2 emissions are recorded as 1,997 and 6,310 kg, respectively, for 58,100 kg takeoff weight operation. Meanwhile, CH_4 is emitted as only 0.2 kg which is the least amount among the emissions.

50.5.2   B737-400 Trabzon–Istanbul Medium-Range Flight Emissions

Trabzon–Istanbul having 981 km flight distance is selected as medium-range flight case for B737-400. Similarly, the emissions are calculated for two flight cases with 43,300 and 60,200 kg of takeoff weights. Obtained LTO cycle and total flight emissions are listed in Table 50.3. Regarding the LTO cycle the minimum emission is CH_4 as 67–79 g per TOW. CO emission changes around 11–13 kg. At maximum payload (18,530 kg) flight operation case the CO_2 emission is about 13,100 kg.

50.5.3   B737-400 Ankara–London Long-Range Flight Emissions

Ankara–London flight with 3,270 km flight distance is a long-range flight case for B737-400 commercial aircraft. In this chapter LTO cycle and total flight emissions are calculated for 50,470 and 68,040 kg of takeoff weights. With longer flight distance the fuel consumption increases accordingly. 68,040 kg is MTOW for B737-400 and 17,240 kg payload is transported in this flight.

Total flight CO and N_2O emissions reach to 211 and 1.6 kg, respectively, for 68,040 kg of TOW. The total flight fuel consumption changes around 10.3–12.6 tons per TOW. In about 40,000 kg of emission rate for 68,040 kg of TOW, CO_2 is the most weighted emission. Table 50.4 presents the LTO cycle, total flight fuel consumptions, and exhaust emissions per aircraft TOW.

50.6   Conclusion

Among the emissions released from B737-400, CO_2 and CO have the greater influence on the global atmosphere. It is noticed that the LTO emissions do not change much for all the investigated cases since LTO cycle includes only the flight path below 3,000 ft; hence flight distance does not make any contribution on the LTO cycle emission. On contrary the total flight emissions increase significantly in long-distanced flights due to higher fuel consumption. This chapter highlights the significant amount of emissions released to environment as a consequence of air transport.

The primary emissions from aircraft engines are CO_2, CH_4, N_2O, NO_x, CO, and SO_2 which have hazardous impact on the environment. LTO cycle fuel consumption of B737-400 for MTOW (68,040 kg) in Ankara–London flight is computed as 815 kg. Besides 2,591 kg of CO_2, 13.6 kg of CO, 7.5 kg of NO_x, 0.82 kg SO_2, 0.1 kg of N_2O, and 0.08 kg of CH_4 are emitted into environment. The total flight fuel consumption is found as 12,660 kg which leads to formation of 40,000 kg CO_2

emission. The released emissions CO, NO_x, SO_2, N_2O, and CH_4 are obtained as 211, 116, 12.6, 1.6, ad 1.3 kg in B737-400 Ankara–London flight for MTOW operation. Having tens of thousands of civil and military airplane flying in the world every day, the negative impact of emissions into environment is getting more and more severe and needs to be get controlled. It is required that these emissions should be decreased as much as possible. Although the aircraft and their engines' efficiency get better thanks to technological improvements, the emissions from aviation and their hazardous effects in the world will continue to increase as a result of the upcoming air traffic. In addition to engine and airframe efficiency improvement efforts the sustainable fuel energy sources as an alternate to classical fossil fuels should be supported as remedy.

References

1. Kristin R, Niels K, Steve S, and Karen T (2000) Aircraft emissions. Energy Sector: 93–102
2. IPCC Aviation and the Global Atmosphere (2006) IPCC Guidelines for National Greenhouse Gas Inventories. Website http://www.ipcc-nggip.iges.or.jp/public/2006gl/
3. BOEING 737-400 (1988) Operation Manual Enroute Climb 280/.74 ISA, Integrated Range Mach 0.78 Cruise and 0.74 M/250 KIAS Descent performances Tables
4. Aydin H (2012) Development of exergetic sustainability indicators of commercial aircraft. Ph.D. Thesis, Natural and Applied Science, Anadolu University, Eskisehir, Turkey
5. IPCC (1999) Aviation and the Global Atmosphere. Cambridge University Press, Cambridge
6. Bruno M, Kenneth M, John-Paul C (2008) Constraints in aviation infrastructure and surface aircraft emissions. Massachusetts Institute of Technology, Cambridge, MA, Retrieved 2008-01-02
7. EU (2006) Climate change: commission proposes bringing air transport into EU, IP/06/1862
8. US GAO (2009) Aviation and climate change: aircraft emissions expected to grow, but technological and operational improvements and government policies can help control emissions, GAO-09-554

Chapter 51
Effect of Cavitation in Ships on the Environment

Munir Suner and Onur Birdal

Abstract Ships are the most important transport tools worldwide in respect to their huge cargo carrying capacities and enabling the connections between distant lands. Although shipping transportation is the most economic transportation mode, there could be large amount of operational costs as a result of hard conditions of these environment. Ship's hull, propeller, machineries, and equipment work in contact with liquid flows. As it is well known, cavitation is one of the main reasons of material fatigue and corrosion, which occurs due to decreasing of the pressure below the saturation pressure of the liquid. The prevention of cavitation on propeller, on rudder, in pumps, in pipes, and in fittings such as valves and elbows leads to lower depreciation costs of the equipment. Also cavitation-based damages could detain the ships from their sail, leading to crucial costs for the shipping companies. Thus cavitation reduction methods should be determined and implemented. In this study, the effect of cavitation on total energy loss and damage on world seas and maritime transportation are presented.

Keywords Cavitation • Emissions • Efficiency • Environment • Propeller • Pump • Ship • System valve • Cargo • Shipping transportation • Hull • Material fatigue • Corrosion • Saturation pressure of the liquid • Depreciation • Energy loss • Maritime transportation

M. Suner (✉) • O. Birdal
Istanbul Technical University, Turkey
e-mail: msuner@itu.edu.tr; onurbirdal@hotmail.com

51.1   Introduction

Oceans and seas have been the most widely utilized areas by men throughout the history of mankind because transportation of freight via both blue water and inland waterways has always been the most essential issue while people are engaged in the businesses of transportation of the goods which they need [1].

As it has been known, CO_2 emissions depend on fossil fuel consumption. Generally, the energy used in ships is originated from fossil fuel [2–6]. It has been estimated by scientist that the energy source life is 50–60 years. Every single ton of oil consumption produces 3.14 tons of CO_2. Approximately, 3 % of energy consumption in the world is done by the ships. According to IMO 2009 [7] report, through the international shipping, ships produce 823 million tons (2.7 % of world's anthropogenic CO_2 emissions), and from domestic and fishing ships (ships above 100 GT) 1,019 million tons of CO_2, which was 3.3 % of world's anthropogenic CO_2 emissions that year. More than 35 % of the energy losses in the ships are a result of the mechanical energy losses and 10–20 % of these losses are due to cavitations [8–10].

As stated before to meet energy demand this will result in the use of more use of energy fossil fuel. As a result of the burning of fossil fuel new emissions to damage surrounding will arise; thereby maximum burning will cause CO_2 to emerge. The other emission gasses are NO_x, which pollute environment. Their effect on environment is enormous, and are hard to control. The realization of them depends on heat of the cylinder of the engine. They arise as a result of the oxygen molecules in the air, which they burn. Where the temperature is high in the cylinder they emerge when the mix with air is in enough concentration. Another compound to emerge is SO_x, which depends on the amount of sulfur in the fuel. It is known to be poisonous and a reason for acid rain. Apart from these, these pollutants cause CO and some solid particles.

Innumerable sorts of sea vessels such as passenger ships, dry cargo ships, and chemical tankers sail all around the world to carry all sorts of goods to meet the demands of people. Depending on the utilization purposes of those sea vessels, their piping systems, fittings, and forms of their connecting links differ from each other significantly. Transportation of approximately 90 % of the merchandise launched on the world trade markets is put into practice by means of merchant ships [11].

Those cavitation problems that can be observed in merchant ships occur owing to some errors which originate from operational misconduct and some mistakes made regarding their equipment. The problems of cavitation often result in substantial amount of increase in equipment costs because cavitation decreases the efficiency and productivity within the systems of sea vessels due to the scourge in equipment and ship components. Although the amount of loss such problems cause in the long run is quite essential, sufficient precautions are not usually taken. Not many sources and findings have been encountered while conducting researches in this respect [12].

The study conducted by S.D. Sharma and others in 2003 [13] helps us a lot to understand the commencement of cavitation seen on propellers, measurement of

the sound of cavitation, the number of cavitation, geometry of propellers, and cavitation of turbulence better with those findings they obtained [14, 15].

During the survey conducted in 2010, resistance rates of cast iron and other metals to cavitation were studied and the findings were compared with the resistance measurement rates of carbon steel [16].

In another survey conducted by X. Y. Li and others in 2004 [17, 18], the usage of copper–manganese and aluminum alloys which were exposed to cavitation was studied in the welding method used while repairing the propellers of vessels.

In a research conducted in 2005, the cavitation and its different kinds which occur in the rudder tillers of ships owing to the speed of propellers which increases in proportional to the rate of acceleration of ships while sailing in full speed have been observed and studied [19].

In this study, the problems caused by cavitation which occurs in ships and also how and where the cavitation accrues, the effects on general operation, as well as the precautions to be taken to avoid the negative consequences of such cases are considered thoroughly.

51.2 Theory

51.2.1 Definition and Calculation of Cavitation

As known, cavitation occurs while fluidal substance flows somewhere if the pressure of the liquid decreases to a level much lower than steam pressure. Liquid vaporizes and the particles of gas and minerals in the liquid creates some bubbles during the flow of liquid. Later those bubbles explode when they arrive at high-pressured areas due to being closely pressed together and such cycles repeat themselves over and over again. This incident is called cavitation. They damage the surfaces they touch, cause abrasion, and scour around and create the effects of vibration. Such incidents occur merely in fluids and may result in great harm and loss in ships.

Consequently, the efficiency of the system decreases, costs of operating ships increase significantly, and finally the whole system becomes inactive. Cavitation appears in different ways in respect to its formation.

When Bernoulli's theorem is applied (as in the case of Eq. 51.1) to this matter, the relationship of pressure–speed between two points can easily be observed. As long as the speed increases, the static pressure decreases as a result of which the risk of cavitation goes up:

$$\frac{\rho}{2}v_1^2 + \rho g h_1 + P_1 = \frac{\rho}{2}v_2^2 + \rho g h_2 + P_2 \tag{51.1}$$

Cavitation appears where and when the static pressure of the fluid at a certain point is equal to the pressure of steam and much lower. Since linear velocity

increases as long as the rated speed or gyre increases in propellers, the dynamic pressure increases and therefore, the risk of cavitation will also increase:

$$P_m = e \quad \text{cavitation starts}$$

$$P_m < e \quad \text{cavitation exists}$$

$$P_m > e \quad \text{cavitation does not exist}$$

$$\frac{P_\infty - P_M}{\frac{\rho}{2} v_\infty^2} = 1 - \left(\frac{v_M^2}{v_\infty^2}\right) = \frac{\Delta P}{q} \tag{51.2}$$

$$\frac{\Delta P}{q} = \sigma \tag{51.3}$$
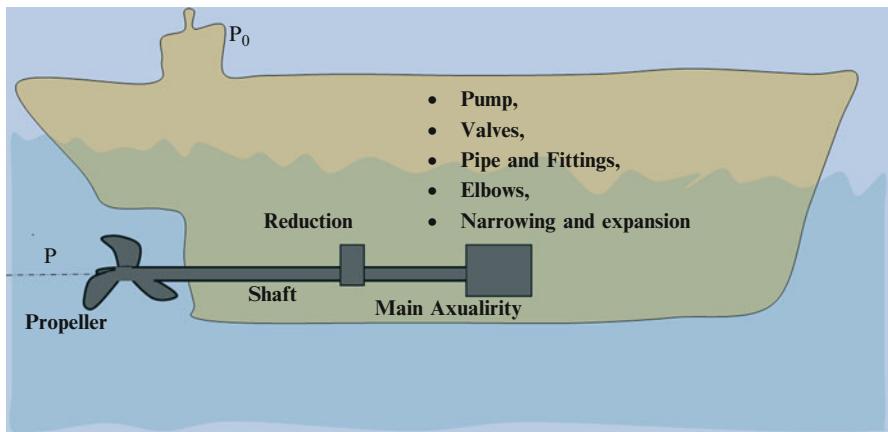
It is necessary to be aware of those factors which cause cavitation so as to avoid cavitation. Local pressure, depth, pressure of evaporation, density, heat, velocity, and mass flow rate are primary factors which create and boost cavitation.

51.3 Cavitation in Vessel Components

The main engine and the propeller which are connected together with a shaft enable the sea vessel to float and move away. Other systems comprise auxiliary ship machines and piping systems. These piping systems contain 10 various kinds of pumps and approximately 100 different kinds of valves. Any sort of defect, failure, and malfunction likely to occur within these systems may not only decrease productivity of the system itself, but it may also affect the whole system. Cavitation that can be observed in ships is one of the significant reasons to cause decrease of efficiency and productivity. Cavitation is seen on propellers which are one of the most essential components to enable ships to move and also during the phases of shrinks, contractions, and expansion within the valves and pumps in the piping systems which are also some other essential components of ships. Those various ship components on which cavitation is seen will be dealt with separately in different sections. Those components which are likely to be exposed to cavitation are illustrated in Fig. 51.1.
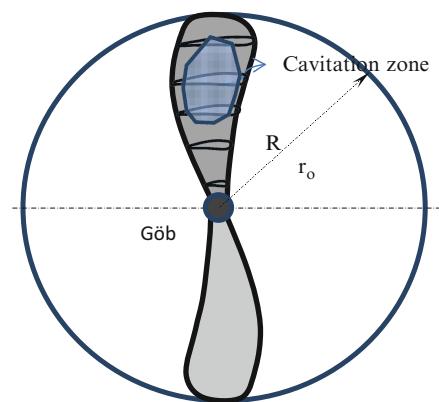
51.3.1 Propellers

As it is known, sea vessels are provided with impulse by means of a major machine which is composed of either a diesel engine or a steam turbine. One of the most essential components of a ship is the propeller or the impeller. Any hazardous impact and damage likely to accrue on the propeller will directly affect the

Fig. 51.1 Main components of a sea vessel and its systems which are likely to be exposed to cavitation

Fig. 51.2 The blade cross section of a propeller of a ship
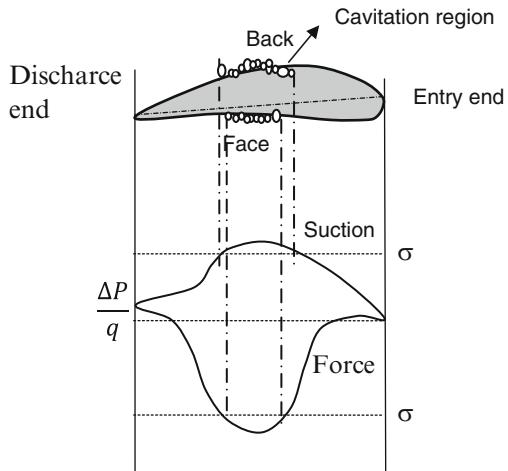
efficiency of a sea vessel. The distribution of pressure around the propeller of a ship is very important because the angle of attack of the blade of a propeller affects the distribution of pressure. The geometry of the propeller must be modified accordingly in case it changes. That is to say, according to the formula, $r_0 \leq r \leq R$, the hub of the propeller blade must be as small as possible (Figs. 51.2 and 51.3).

Cavitation occurs on the end, face, back plate, and root of blades of propellers which provide ships with impulse to move. The blades are the most essential parts of propellers.

Cavitation in Propellers

The cavitation which accrues on propellers can be classified into two different ways depending on their location and physical appearance when they occur (Fig. 51.4).
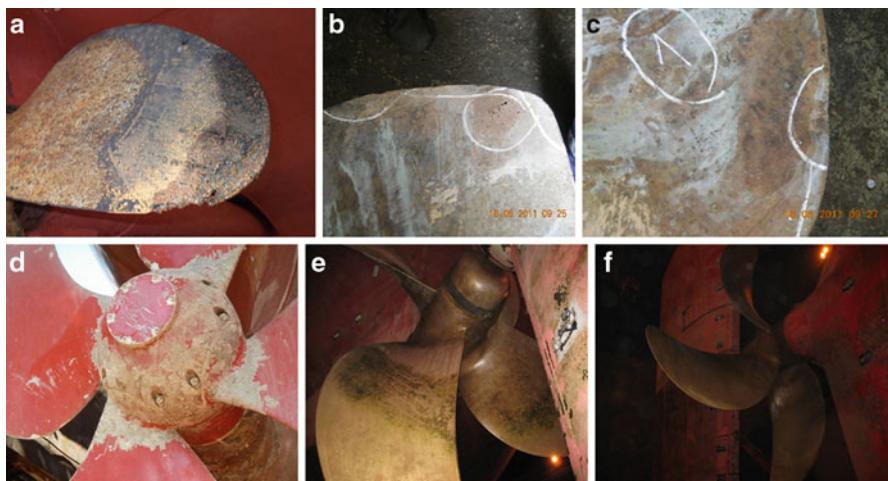
Fig. 51.3 Pressure
distribution around the cross
section

Fig. 51.4 FiA screw
sample

The cavitation which occurs in propeller changes depending on the geometry of blade cross section. They are in the forms of wing cross section, moon cross section, segmental cross section, and shuttle cross section. As it is seen in Fig. 51.3, the value to be obtained from the equation $\frac{\Delta P}{q}$ is a non-dimensional coefficient and is larger than the number of cavitation; in that case, the incident of cavitation begins and it can be observed. The cavitation which occurs in propeller changes depending on the geometry of blade cross section. They are in the forms of wing cross section, moon cross section, segmental cross section, and shuttle cross section. As it is seen in Fig. 51.3, the value to be obtained from the equation $\frac{\Delta P}{q}$ is a non-dimensional coefficient and is larger than the number of cavitation; in that case, the incident of cavitation begins and it can be observed (Fig. 51.5).

Fig. 51.5 Various areas exposed to cavitation on propellers. (The propeller photographs were taken from ÇınDemir Shipyard and Tersan Shipyard in March 2012 (**a**, **d**–**f**), in June 2009 (**b**, **c**))

Prevention of Cavitation on Propellers

The activity of reducing the cavitation observed in propellers to the lowest level or suppressing it completely can be achieved by manufacturing the propellers properly and operating the sea vessels accurately. The simplest practice to achieve to handle the problem of cavitation is to make the propeller run in places where the pressure of the fluid is much higher. This can be accomplished by increasing the vessel draught after evacuating the ballast water of the sea vessel when the ship is empty and adjusting the vessel trim to the poop/stern of the sea vessel. Thus, it will be possible to reduce the risk of cavitation for the ship by maintaining the pressure of the liquid in areas where the propeller of the ship runs much higher than the pressure of steam. While a ship is sailing away normally, the outer casing and the propeller of the ship are exposed to all sorts of dirt and pollution constantly owing to sea creatures. This sort of pollution on propellers causes decline of efficiency, proficiency, as well as cavitation. Both the propeller and the outer casing of the ship under the water must be examined from time to time and if it is necessary, all sorts of dirt and pollution must be cleaned off in order to avoid cavitation which occurs due to pollution of the propeller.

It is also possible to protect both the outer casing of the ships and their propellers by benefitting from some special designs to avoid cavitation during the phases of ship construction procedures. Besides, some small steering fins as many as the number of propeller blades must be used on the hub of the propeller so as to make them stand in a certain angle in order to protect the ship from the cavitation of hub vortex. Therefore, those small steering fins will protect the ship from the vortex likely to occur around the hub of the propeller.

In order to avoid root cavitation that can be seen around propellers, some holes must be drilled so that they are located in the same position of those cross sections near the root starting from the pressure side to the suction side. The vortexes which occur around the root can be avoided in this way.

Finally, some retarding nozzles are used on propellers in order to avoid cavitation. The retarding nozzles decrease the power of water currents coming to the propeller but increase the pressure on the propeller itself. Thus, the risk of cavitation declines. One disadvantage of those nozzles is that they decrease the efficiency of propellers a little bit.

51.3.2   Pumps

Those systems which facilitate the transfer of liquids from one place to another are called pumps. The plunger pumps are utilized in bilge piping system, in the fuel pumps within the cycle of diesel engines but those diaphragm pumps are used as the chemical dosage pumps of boilers. Those rotating pumps widely used in ships and in the cycles where they are utilized are gear pumps in oil and fuel cycles, lobe pumps, screw pumps within the cycles of oil, clay and bilge piping, vane-type pumps, and plunger pumps that are used in hydraulic systems. The most common types of pumps used in ships are centrifugal pumps.

Cavitation in Pumps

Cavitation is most widely seen in centrifugal pumps due to three reasons. The working principle of centrifugal pumps is to enable the fluid flow into the pump with the help of vacuum which occurs on the hub of the propeller. If the pressure of the liquid goes below the level of steaming during this vacuuming activity, the propeller accelerates the sucked liquid while sending the liquid to the cycle. Meanwhile, as it was stated earlier, if the pressure decreases while the speed is increasing according to the Bernoulli's law, it results in turbulence and those turbulences which accrue around cause decrease of pressure at those places where they occur. Also cavitation causes wear. Contaminated fluid is released as a result of wear of metal parts (Fig. 51.6).

How to Avoid Cavitation in Pumps

Principally ENPY must be increased in order to avoid cavitation seen in pumps. The suction cycle must be kept clean in order to achieve this because ENYP decreases as the cycle losses increase owing to the pollution of suction cycle. This can be accomplished by turning up the valve in the suction cycle completely, reducing those losses within the suction cycle, increasing the diameter of the suction cycle,

Fig. 51.6 An impeller exposed to suction cavitation. (The impeller photographs, viewed were taken in April 2012 at Tersan Shipyard)
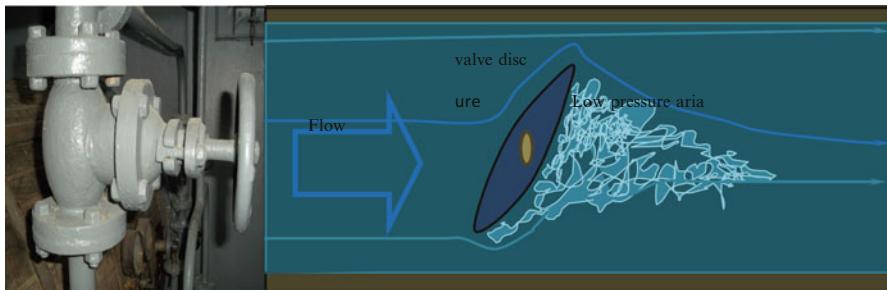
Fig. 51.7 Main structure of a valve and its components. (The valve photographs viewed were taken in March 2012 at Tersan Shipyard)

and reducing the height of suction. Besides, the mass flow rate cavitation of return must be adjusted accurately and properly.

51.3.3   Valves

Valves are components which are used in order to adjust the direction, mass flow rate, and pressure of those fluids that flow in the cycles of fitting systems. Valves are some of the most significant components of cycles. The geometrical shapes of valves are the most important factors that affect cavitation. Cavitation accrues depending on the geometrical forms and speed and that is why sufficient amount of knowledge should be obtained about the inner structures of valves (Fig. 51.7).

There are various kinds of valves depending on their geometrical shapes and components in their structure. The most widely used types of valves in ships are explained here. Among one of the most essential components of valves located within the fitting systems of ships is valves. Tens of different fitting cycles exist in ships and approximately 100 different kinds of valves occur in those piping systems. Sluice valves, globe valves, global valves, butterfly valves, conical valves, and snifter valves or bucket valves are the most common types of valves used in ships. The geometrical shapes, running pressures, and the sort of fluids to be used are the basic factors to affect cavitation here.

Fig. 51.8 The low-pressure region that occurs behind the valve disc

51.3.4 Cavitation in Valves

In valves, cavitation causes loud noises, extreme vibrations, wearing out, fatigue, and decrease of efficiency and productivity. That is why it is necessary to stop vibration somehow. Preventing the actualization of cavitation is achieved in two phases and the first phase commences during the construction process. That is why selecting the right sorts of valves is very important and it requires keeping in mind those calculations of cavitation while providing ships with valve equipment. Proper operation is as essential as the selection of accurate types of valves for their effective functions. Those calculations performed by those manufacturer companies and information offered in their manuals should be utilized correctly. The cavitation in valves usually actualizes while turning on those valves at low levels and during the phases of turning off the valves because a sort of low-pressure region occurs behind the valve discs as it results in cavitation (Fig. 51.8).

When low pressure occurs, the pressure of the fluid decreases, the fluid starts to vaporize, and some bubbles appear. When those bubbles touch the metal surfaces, they blow up and as a result of these series of explosions cavitation actualizes. Once it is understood that a valve has started running with cavitation, an analysis of cavitation test should be applied and the level of progress of the cavitation must be measured or calculated. Thus, it will be possible to prevent the progress of cavitation towards further phases. Cavitation occurs in valves in three steps. The first step is the starting point of cavitation. It may be possible to hear the slight explosion noises of those bubbles as a result of the initial activities of cavitation formation. Cavitation does not cause any damage on the valve and its system at this stage. However, it results in wearing out and dynamic fatigue of the material in the long run. The second step starts when cavitation begins to harm the valve. Some noises and vibration which accrue may be observed at this step. The third step starts when the amount of cavitation boosts and wears out the valve intensively and shortens the functional life-span of the valve. Valves continue running by making excessive amount of noise and vibration. While conducting the analysis of tests, the cavitation structure of the valve is calculated and the obtained outcome is compared with those values provided by the manufacturer.

Calculation of Cavitation in Valves

While performing the analysis of tests in valves, the equation of cavitation figures is calculated according to the number of 4:

$$\sigma = \frac{P_u - P_v}{P_v - P_d} \tag{51.4}$$

σ: cavitation figure of the valve
P_d: the rate of pressure after the valve disc of the fluid (Pa.)
P_v: the rate of steaming pressure at the current temperature of the fluid (Pa.)
P_u: the rate of pressure before the valve disc of the fluid (Pa.)

As it can be seen in the equation, the bigger the cavitation figure gets, the less the possibility of cavitation. Generally the cavitation figure is 2.5 when cavitation begins:

$$C_v = \frac{Q}{\sqrt{\Delta P}} \tag{51.5}$$
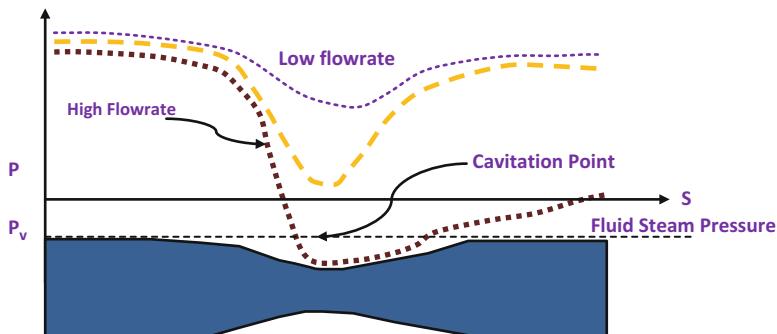
It is essential to determine the lowest level of turning on points of valves in order to maintain conditions to make the valves operate without any cavitation and also to make sure not to go below these proportional rates.

Prevention of Cavitation in Valves

The pressure of the fluid declines to its lowest level right after the valve disc. Later it rises again after it comes out of the valve and when it goes into the cycle. If more than one valve is used in a serial connection system, this sudden decline of pressure is divided into respective valves and thus the decrease of pressure in valves much lower than the steaming pressure is prevented. The bigger the cavitation figure gets, the lower the risk of cavitation decreases. As it can be seen in Eq. 51.4, the pressure of the fluid flowing out of the valve can be increased in order to increase the figure of cavitation. In order to create this situation, back/counterpressure should be created to increase the pressure at the exit of the valve (P_d) at the place where sonar will be utilized and thus the figure of cavitation will get bigger. Another method of preventing the damages of cavitation is to use valves coated with durable materials. Although it is the most practical method to prevent cavitation, it is costly.

51.3.5   Cavitation in Pipe Bends/Elbows, Expansions, and Contractions

Bends are screwed/threaded or welded fitting connection components bearing 90 or 45° angles at their pipe connecting parts. Pipe bends or elbows are the most widely used pipe joints. The fact that diameters of pipes and fittings at certain places

Fig. 51.9 Flow rate–cavitation relationship

Fig. 51.10 Cavitation in fittings and in 90 and 180° elbows. (The elbow photographs viewed were taken in March 2012 at ÇanDemir Shipyard)

decrease in pipe bends and elbows as a result of narrowing or contracting in pipe elbows especially in orifices and orifice nozzles causes decrease of pressure with the acceleration of velocity of liquid. The decrease of pressure causes the pressure of the fluid go down much lower than the steam pressure and this case results in cavitation. That is why pipes and pipe elbows must be used very carefully in such systems. Usage of pipe elbows should be avoided as much as possible because narrowing and contractions of pipes and elbows increase the mass flow rates of fluids, which causes much faster pressure decrease.

As seen in Fig. 51.9 as long as the mass flow rate of the liquid increases, the difference of pressure at the point where narrowing and contraction occurs also goes up and the pressure of the fluid decreases towards the level of steam pressure. Meanwhile, cavitation begins to accrue. Those air bubbles that occur at narrowing parts of elbows or pipes create cavitation because the number of these bobbles boosts at high mass flow rates although very few air bubbles occur at the beginning as seen in Fig. 51.10.

Bends or pipe elbows may be in various angles, especially in those elbows with 90° and much larger angles cause local losses at sudden curves as a result of which the problem of the likelihood of turbulence increase comes out and the risk of cavitation rises here.

Fig. 51.11 Cavitation on vertical side of ship. (The vertical side photographs viewed were taken in May 2012 from M/V Sismik-1)

Besides, at places where the logic of siphon is valid, sudden pressure change is likely to appear at the peak points of the system when the pressure goes to the lowest levels and this is the case if pressure rises suddenly when cavitation is inevitable.

As the sudden pressure decrease is likely to occur at high levels at steep cornered elbows, again similar problems may arise. An example of this event is seen in Fig. 51.11. That is why smaller angled elbows must be used because there is less cycle loss in elbows with smaller angles. The important thing to consider here is to prevent the pressure from going down to the level of steam pressure. Sometimes some small fins are used in fittings and pipe elbows to get rid of this problem.

51.4   General Conclusions and Suggestions

As a conclusion, we may say that higher cavitation will lead to higher energy losses and fuel consumption. This increase in energy losses and fuel consumption will lead to higher CO_2 emissions, which results in temperature increases. Increase of CO_2 will be % 0.1155 (3.3 × 0.035 × 0.1). If cavitation is prevented, it decreases consumption of fuel % 60 and this is approximately % CO_2 0.040425, and the other emission gases will also decrease.

Cavitation will lead to depreciation of the systems, which lead to the wear of the materials. The worn materials will pollute the water and lead to toxicity.

The cavitation leads to early depletion of parts of the systems, and this results in the production of the same materials again and again.

Cavitation causes vibration and noise pollution. This leads to deterioration of vibration calibration of electronic systems on board. Cavitation causes a decrease in human motivation, and it also threatens the health of people working on board.

A ship is a highly complex structure composed of several propellers, bow and aft thrusters, many pumps (30–100), hundreds of valves, hundreds of fittings and elbows, and several other hull and machinery parts; and therefore, massive energy

losses occur in all of these parts and furthermore these parts also depreciate and hold corrosion due to the above-summarized cavitation effects. During the operation of the ships and during their construction, hydrocarbon products are extensively used and furthermore massive emissions are produced, which greatly damage the environment. In this context prevention of cavitation will both decrease the depreciation in these parts and furthermore greatly eliminate corrosion effects, which overall will decrease the emissions to the air and help the mankind to preserve the natural resources of the earth.

- Cavitation may cause losses of mechanical energy up to 15–20 % in total. This is a considerable amount of cost for business management.
- Cavitation causes wearing out and even makes those materials impossible to benefit from.
- Cavitation causes dynamic fatigue, extra management cost, and loss of materials.
- Due to decrease of efficiency of propellers, the speed of the ship is affected negatively.
- Cavitation results in decrease of mass flow rate in pumps, wearing out at wings as well as narrowing expanding in valves and elbows. As a result of this, quite risky explosions and leakage may occur in fitting systems.
- Avoiding the realization of big losses caused by cavitation is a must.
- If the staff of the ship is not aware of such risks, they may use wrong parts such as valves, elbows, and connection parts and this may increase the possibility of cavitation. To avoid this, the staff must be provided with enough knowledge on such matters. Of course, this will enable the ship owners to make big profits in the long run.
- Those parts which are likely to decrease the efficiency of ships and cause leakage must be replaced with new ones immediately. This is impact of cavitation on business management expenses.

Task of preventing cavitation at site commences while selecting the right sort of equipment during the process of ship construction. Naturally it is more expensive to use materials which are strong enough to avoid cavitation in ships. However, in the long run it is more beneficial to use better quality equipment while constructing the ship because all those parts and equipment which work properly and do not cause any cavitation will definitely decrease the expenses of running that ship. Therefore, running the ship will cost less in the long run. To illustrate, an expensive valve can be used for many years without causing any problem if it is of the best quality. Assuming that a valve is worn out in a few years' time due to cavitation, it will decrease the productivity and the efficiency of the whole system and of course such valves must be replaced frequently and this will result in some extra cost for the management. Besides, repairing or replacing such equipment which malfunction will take time and create costly expenses and delays at delivering freight on time. There are thousands of parts and components used while building ships and this shows how big problems the staffs of ships have to face and deal with.

Some special designs should be made in order to avoid cavitation in ships before constructing ships. It is also possible to protect both the outer casing of the ships and their propellers by benefitting from some special designs to avoid cavitation during the phases of ship construction procedures. Besides, some small steering fins as many as the number of propeller blades must be used on the hub of the propeller so as to make them stand in a certain angle in order to protect the ship from the cavitation of hub vortex. Therefore, those small steering fins will protect the ship from the vortex likely to occur around the hub of the propeller. In order to avoid root cavitation that can be seen around propellers, some holes must be drilled so that they are located in the same position of those cross sections near the root starting from the pressure side to the suction side. The vortexes which occur around the root can be avoided in this way. Finally, some retarding nozzles are used on propellers in order to avoid cavitation. The retarding nozzles decrease the power of water currents coming to the propeller but increase the pressure on the propeller itself. Thus, the risk of cavitation declines. One disadvantage of those nozzles is that they decrease the efficiency of propellers a little bit. In order to reduce the cavitation at the lowest levels seen around propellers, the propeller must be made to operate in deeper levels of water than the water surface. To facilitate this, the trim of the vessel should be set towards the stern of the ship and the vessel draught should be increased. Besides, the underwater parts of the ship should be checked and when it is necessary, it should be cleaned properly. Especially the levels of turbulence should be reduced. Since decreasing the gyre/rotation speed will decrease the velocity and it prevents the absolute pressure from going much lower than certain values, this is one of those precautions to be considered.

The suction cycle should be kept clean, the height of suction should be reduced, the diameter of the suction cycle should be increased, the losses within the suction cycle should be reduced, the turbulence should be decreased, and the valve in the suction cycle should be turned on completely. Besides the mass flow rate of the fluid must be adjusted accurately.

One of those cavitation methods used in valves is to utilize more than one valve in a serial system. One of the most significant precautions is to select and fix the right sort of valve. Apart from this, another valve to reduce the amount of flowing liquid into the system should be used at the exit section. All those equipment aforesaid should be selected properly in order to reduce the risk of cavitation in valves.

While trying to avoid the actualization of cavitation in elbows of pipes, utmost care should be taken to select the right sorts of elbows with definite angles to the fitting system. Using steeply curved elbows, sudden curves and expansions should be avoided. Turbulence should be considered thoroughly and parts with convenient cross-sectional areas should be used. Besides, using wings or fins in some fitting elbows affects cavitation positively. There should be definite conical angles at expansions and narrowing and those conical angles should be minimized under provided circumstances.

References

1. Crowe CT, Elger DF, Roberson JA, Williams BC (2009) Engineering fluid. Mechanics, 9th edn. Wiley, New York
2. Ric EG (1958) The mechanism of cavitation. Wear 2(2):97–106
3. Seol H, Suh J-C, Lee S (2005) Development of hybrid method for the prediction of underwater propeller noise. J Sound Vib 288(1–2):345–360
4. Hermann R (1989) Life prediction methods for constrained grain boundary cavitation. Int J Press Vessels Piping 39(1–2):119–134
5. Carlton J (2007) Marine propellers and propulsion. Butterworth-Heinemann, Oxford, UK
6. ICCT (The International Council on Clean Transportation) (2007) Air pollution and greenhouse gas emissions from ocean-going ships. The International Council on Clean Transportation, Washington, DC
7. IMO (International Maritime Organization) (2009) Prevention of air pollution from ships. Second IMO GHG study. International Maritime Organization, London
8. International Maritime Organization (2009) Study on greenhouse gas emissions from ships. London, UK
9. Matveev KI (2003) On the limiting parameters of artificial cavitation. Ocean Eng 30 (9):1179–1190
10. Kafalı K (1980) Gemi Direncive Sevk Sistemleri. ITU, Istanbul
11. Güner M, Kükner A, Baykal MA (1999) Gemi Pervanelerive Sevk Sistemleri. İTÜ Kütüphanesi, Sayfa, pp 44–63
12. Chern M-J, Wang C-C, Ma C-H (2007) Performance test and flow visualization of ballvalve. Exp Therm Fluid Sci 31(6):505–512
13. Sharma SD, Mani K, Arakeri VH (2003) Cavitation noise studies on marine propellers. Departments of Mechanical and Civil Engineering, Indian Institute of Science, Bangalore, India
14. Aydın SS (2004) Lecture Notes on Cavitation, Kocaeli Unversity, Turkey
15. Shin HR, Changmin L, Hee BL, Jungkeun O (2010) Rudder gap cavitation fundamental understanding and its suppression devices. Department of Naval Architecture & Ocean Engineering, Research Institute of Marine Systems Engineering, Seoul National University, Republic of Korea
16. Hattori S, Kitagawa T (2010) Analysis of cavitation erosion resistance of cast iron and nonferrous metals based on database and comparison with carbon steel data. Graduate School of Engineering, University of Fukui, Japan
17. Tullis JP (1989) Hydraulics of pipelines pumps, valves, cavitation, transients. Wiley, New York
18. Li XY, Yan YG, Ma L, Xu ZM, Li JG (2004) Cavitation erosion and corrosion behavior of copper–manganese–aluminum alloy weldment. State Key Lab for Marine Corrosion and Protection, Luoyang Ship Materials Research Institute Qingdao Branch, PR China
19. Hu YT, Qin S, Ting H, Katherine WF, Qing J (2005) Asymmetric oscillation of cavitation bubbles in a microvessel and its implications upon mechanisms of clinical vessel injury in shock-wave lithotripsy. Int J Non Linear Mech 40(2–3):341–350

Internet Resources

http://www.aaaco.com/products/positive_diagrams.html
http://tariqhafez.blogspot.com/2010_10_10_archive.html
http://www.spiraxsarco.com/resources/steam-engineering-tutorials/pipeline-ancillaries/isolation-valves-linear movement.asp
http://www.valmatic.com/pdfs/Cavitation%20in%20Valves_7-22-08.pdf
http://www.engineeringtoolbox.com/control-valves-cavitation-d_490.html
http://pompaakademisi.com/index.php?option=com_content&view=article&id=74:pa124&catid=44:pa-kat-temel- kavramlar&Itemid=1/
http://www.scribd.com/doc/16325824/Cavitation-in-Centrifugal-Pump-Pictures
http://hyperphysics.phy-astr.gsu.edu/hbase/kinetic/watvap.html
http://www.chengfluid.com/crv%C2%AE
http://www.waterworld.com/index/display/article-display/6464587063/articles/waterworld/volume-26/issue-6/departments/pump-tips___techniques/how-to_avoid_damage.html
http://www.mhi.co.jp/en/products/detail/fixed_pitch_propellers.html
http://www.chengfluid.com/crv%C2%AE
http://www.waterworld.com/index/display/article-display/6464587063/articles/waterworld/volume-26/issue-6/departments/pump-tips___techniques/how-to_avoid_damage.html
http://www.mhi.co.jp/en/products/detail/fixed_pitch_propellers.html

Chapter 52
Effective Ship Ballast Water Treatment System Management

Levent Bilgili, Kaan Ünlügençoğlu, and Uğur Buğra Çelebi

Abstract Shipping runs the major part of world trade. Using ballast water is the most common way to stabilize a ship after loading and unloading the cargo. Taking ballast water after unloading the cargo would increase the ship's weight. Therefore draught of the ship increases to the level before unloading. Increased draught may be required for proper propeller immersion or any other function. Similarly, ballast water discharging after loading would decrease the draught and thus, the total resistance would reduce. Ballast water is also used by submarines to submerge and emerge as the sole way.

Besides its great effect on ship stability, ballast water causes an important problem. While a ship loads ballast water from any sea, it also loads some endemic species to its tanks. When the ballast water is being discharged, these species are moved into another ecology in which they may behave as invasive species. These species may have a great effect on the local ecological system. Besides, discharging ballast water in different water mass may cause the moving of some solid or liquid harmful materials.

By Marine Environment Protection Committee, International Maritime Organization has studied on this issue. Besides, ballast water systems are being regulated by national and international rules.

To provide these effects some new technologies are being developed such as new and more effective filters. In this chapter, the importance of ballast water treatment systems and new technologies is investigated and presented. Treatment systems, their effects on water issues, and the costs and benefits of the systems are mainly focused.

Keywords Marine environment • Ballast water • Ballast water management • Ballast water operation • Marine pollution

L. Bilgili (✉) • K. Ünlügençoğlu • U.B. Çelebi
Yildiz Technical University
e-mail: leventbilgili1661@gmail.com

Nomenclature

Acronyms

BWE	Ballast water exchange
BWM	Ballast water management
BWPS	Ballast water performance standard
EU	European union
IMO	International maritime organization
MEPC	Marine environment protection committee
MTB	Marine testing board
OOE	Open-ocean exchange
USA	United States of America
USD	United States Dollar
UV	Ultraviolet

52.1 Introduction
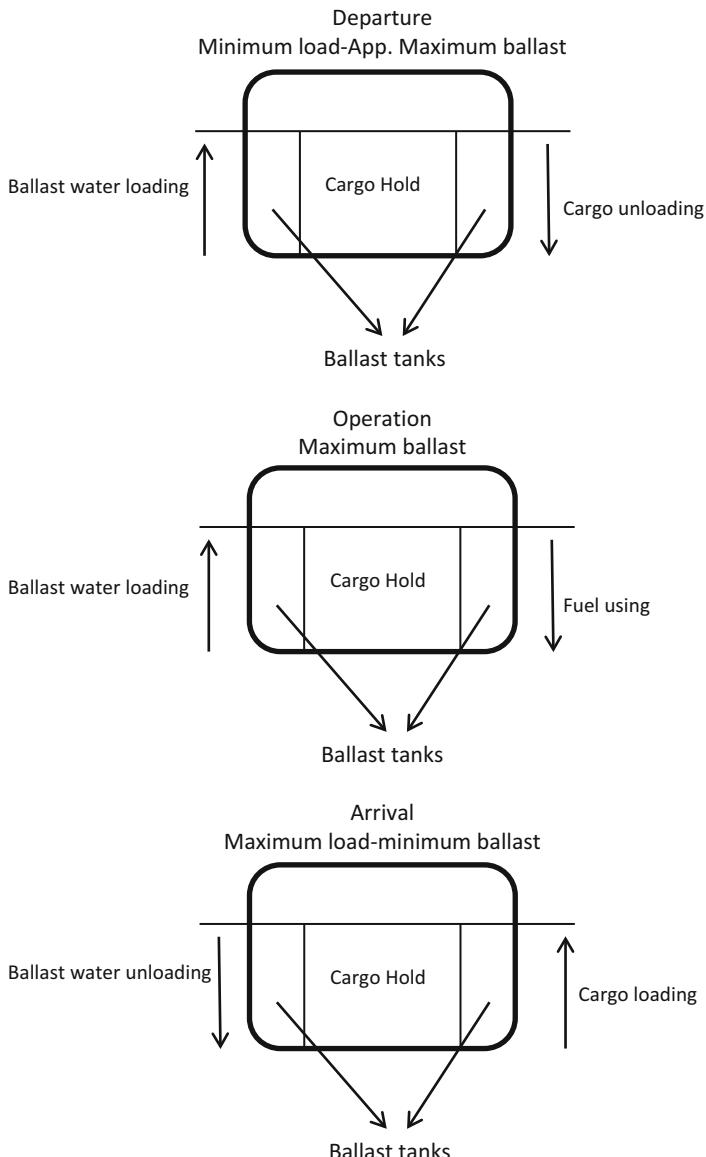
Ship stability is one of the main problems that naval architectures must solve. Stability is so important that it has an effect on ship's safety at sea and at port—during loading and unloading—and especially when an accident occurs.

The ballast water has many functions for ships such as submerging the propeller, providing the adequate stability, helping the propulsion, and maneuvering and reducing the stresses on ship.

Using ballast water is the most common way to provide the adequate stability. During cruising, due to using fuel, the ship becomes lighter and thus the value of draught decreases. Lower draught may cause lack of stability due to the changes on the center of buoyancy and center of gravity. To prevent this risk, ballast water is taken to the ballast tanks to supersede the fuel used. Filling the port-side and starboard-side ballast tanks with different amounts of water can prevent capsizing in extraordinary conditions. Ballast water is also used by submarines to submerge and emerge.

Although it has a vital part for ship stability, ballast water has a bad effect for especially marine environment, at the same time. During loading ballast, some endemic species are also taken with water. When the ballast is discharged, these organisms are moved into another ecology in which they behave as invasive species and they may cause harm to human health, ecosystem, and economy.

The ballast water operation for a ship is illustrated in Fig. 52.1.

Fig. 52.1 Ballast water operation

The unintentional introduction of nonnative species via ships' ballast water has been well documented and in response to this problem the International Maritime Organization (IMO) and Marine Environment Protection Committee (MEPC) have worked for several years on an International Convention for the Control and Management of Ships' Ballast Water and Sediments [1].

In the recent studies, apart from harmful effects such as consequences of shipping disasters, shipping activity exerts other negative influences on the environment: e.g., sea pollution through the discharges of oily water and sewage water from vessels; air pollution from exhaust gases emitted from the vessel's machinery; pollution of water and marine organisms from toxic protective underwater hull coatings; and ballast water discharging causes a very harmful effect to the environment due to the translocation of harmful organisms and pathogens [2].

Ships also transfer organisms that are associated with the hulls and other underwater surfaces. As with ballast water, a diverse range of organisms has been described from the hulls of ships. Organisms attach to the underwater surfaces of vessels while in port, and can colonize other ships or harbor infrastructure at subsequent ports of call. A first step in assessing the potential risk of invasions associated with shipping is to characterize the magnitude of ship arrivals, the volume of ballast water delivery, and the origin (sources) for both arrivals and ballast [3]. Ballast-mediated bioinvasions into freshwater, estuarine, and marine habitats have altered the structure of host ecosystems and have caused a significant economic losses [4].

Economic losses are caused by the expenditure spent to prevent the harmful effects by translocation of the invasive species by using or retrofitting the filters, to abolish the organisms once they are translocated. Besides, invasive species are the reason of death of the species that have economic benefits. Keeping the vessel's hull clean is another reason for the economic loss.

A wide variety of organisms that are transported in ballast water in ocean trade vessels may establish themselves in new environments when discharged from the ship and alter or impact the receiving ecosystems. Invasive marine species are one of the greatest threats to the world's oceans. The total amount of ballast water unloaded from ships in international trade was estimated to be 2,200 Mton in 2000. Untreated ballast water discharged by ships in national trade is estimated to be 1,300 Mton, resulting in global annual amount of 3,500 Mton [5]. In addition, it is estimated that approximately 3,000–4,000 species are moved into another ecosystem by ballast water [6]. The USA receives more than 79 million metric tons of ballast water from overseas each year, and over 10 billion metric tons of ballast are transferred annually across the world [7]. According to a study, the total annual economic cost of invasive species to the USA is $137 billion [8].

Besides the effects on economic issues and marine ecosystem, ballast water movement may create an important impact on global warming and climate change.

Recent studies show that moss oxygen production could cause ice ages throughout history. While ancient moss started to spread on land, they absorbed CO_2 from the atmosphere and produced some minerals that could dissolve the rocks they were growing on. As a result, the rocks reacted with the atmospheric CO_2 and formed new carbonate rocks in the ocean. These new formed rocks weathered phosphorus and iron to the ocean and this supported the increasing quantities of nutrients and, as a result, algal blooms. An ice age may take place due to Earth's surface's CO_2 absorption may cause cooling on land and atmosphere [9].

As a result of the ballast water movement, some species can move and settle in some ecosystems where they behave as invasive species and they can damage the

endemic algae population. If the amount of CO_2 absorption increases in parallel with the algae and moss population, fewer amounts of algae mean more CO_2. In these conditions, it can be estimated that ballast water movement has an indirect effect on global warming and climate change due to the positive effects on the CO_2 increasing rates.

On the other hand, some other researches show that if warming rates keep on increasing, the survival rates of organisms in ballast water and ships' hull will increase, as well [10].

Since the ballast water indicates a big problem for both economic and environmental issues, national and international organizations have made some regulations.

The IMO's proposed regulation of discharged ballast water has brought several issues to the forefront. Recent studies have been done about the development of an independent, international Marine Testing Board (MTB), funded by ship owners, regulators, and interested parties with the endorsement of national and international regulatory bodies and environmental organizations for (1) the development of standardized international performance protocols, (2) field testing, and (3) certification of ballast water treatment technologies. The proposed MTB is a process to expedite the implementation of international standards and regulations, and the subsequent testing, certification, and regulatory approval of new ballast water treatment technologies [11].

On this issue, recent studies were carried out before the IMO standard was agreed, so only a broad indication of whether the results achieved the standard was given. The aim of the Convention is to reduce the risk of introducing nonnative species and, in order to achieve this, ballast water treatment standard will be phased in over time based on the age and size of vessels [12].

52.2 Investigations on Ballast Water Treatment System Management

Ballast water treatment is an issue that concerns to prevent translocation of the harmful and invasive organisms during loading and unloading of ballast water. Open-ocean exchange (OOE) is a basic ballast water management method that uses a very simple way, discharging the water taken at harbor to the ocean and taking the ocean water instead. An acceptable and successful treatment needs to prevent harmful organisms from ballast water while discharged water must be nontoxic. The system must be economic, as well.

Ballast water management is a complex issue raising the challenge of merging international regulations, ship technical solutions, and ecological conservation. International regulations by nature take a relatively long time to enter into force; hence regional and national regulations tend to be developed to meet more local demands. Such developments are of major concern to the shipping industry, which must operate across different jurisdictions. Ecological awareness that forms the public opinion now demands measures to reduce the risk of invasive species introductions [5].

A well-organized and appropriate ballast water management system, which depends on the route and the form of the ship, may reduce the amount of the ballast water. Ballast water operation should not be done in the shallow and still waters due to the population density of the organisms.

52.2.1 Ballast Water Treatment Systems

A number of approaches or technologies for treatment of ballast water have been considered or evaluated including thermal techniques, deoxygenation, ultraviolet irradiation and filtration/separation, and advanced oxidation techniques [13]. Other methodologies involve also chemical treatments (biocides), which are an attractive alternative due to their potential for destroying a wide range of organisms and relatively easy applicability to existing and future vessels. However, most of the biocides were developed for drinking water or sewage treatments instead of salt water applications. Therefore efficacy of these biocides in ballast waters has to be addressed [14].

Invasions via ballast are limited by the survivorship of organisms during passage. Ballast management today relies primarily on OOE of ballast water. The flushing of ballast tanks that contain estuarine or coastal water with oceanic water is widely believed to significantly reduce the risk of bioinvasions by physical displacement and by biocidal effects [4].

Besides OOE, a non-technological method, which has begun to set some standards about ballast water for IMO, there are few treatment systems developed and under development. High-temperature heat treatment is one of the effective methods that is used and discussed for a long time.

It is also important that OOE is not always biologically effective and is not always possible to perform due to ship safety and operational issues involved. These operational considerations and safety aspects indicate that a portion of the ballast water transported annually will have to be treated by other methods or discharged as untreated ballast water. Slamming and tank sloshing increase the risk of causing structural damage to the vessel. From an economical viewpoint, the global ballast water amount discharged into open sea is estimated to be around 2,788 Mton and this represents an annual treatment cost of USD 40–60 million [5].

The heat treatment of ballast water has been widely advocated as a possible treatment regime based on theoretical and laboratory/small-scale trials. Various methods of heating the ballast water on board vessels have been used previously. There are concerns over the physical impacts of dealing with large volumes of heated water, the energy costs of heating the water, and the possible environmental impacts of hot water discharge. There are also additional concerns over the engineering implications of storing large volumes of heated water in ballast tanks [1].

Ozone has been used as a disinfectant in drinking water since the late 1800s. It is also applied in wastewater treatment as an oxidant and disinfectant and its use is increasing. In some recent studies, the use of ozone for ballast water treatment was

investigated on a laboratory scale. Due to the requirements that the treatment system must be environment friendly, economic, and applicable, the goal when using biocides such as ozone is to use a minimum concentration for the removal of organisms in the ballast tank and to have the toxicity decay to a minimum level during the voyage before ballast is discharged [7]. According to a recent experimental study, the ozone-based ballast water treatment system provides a 99 % reduction in the amount of zooplankton [8].

Deoxygenation is a different and useful method to kill the organisms in ballast water. In a recent experimental study, zooplankton abundance decreased in all the tanks during the trial with a rate of 40–65 % per day. Phytoplankton amount also tended to decrease [12].

In recent studies, the physical processes associated with removing ballast tank contamination by continuous flushing is examined [15].

Sonication is another method to kill the organisms. Although it is proved that ultrasound systems kill the bacteria and zooplankton, the applicability is unclear [13]. In recent studies it was shown that ultrasound technique was able to kill less than 40 % of zooplankton. Besides, the cost of the system was unacceptably high [16]. In a different study, the system's operating frequency was approximately 19 kHz and the percentage of success was around 90 % [13].

In a previous study, an innovative filtration technology, using waste-tire-made crumb rubber as filter media, was developed to remove indigenous organisms from ballast water. Compared with conventional granular media filters crumb rubber filters weigh less. However, crumb rubber filtration alone did not achieve the target removal of invasive species proposed by the IMO. Experiment results show that this filtration system has removed 54–84 % of phytoplankton and 46–72 % of zooplankton. The results changed according to the dosage of coagulant [17]. According to a different study that uses chemical and biocides to treat ballast water, killing rate could be raised up to >90 % [14].

Translocation of invasive species via ballast water is an international issue. Thus, besides national and local restrictions, organizations such as IMO have brought stricter rules about carrying ballast water.

Ballast water exchange can reduce the risk of invasions, the practice of which is subject to ship safety limitations. Mechanical separation techniques including filtration and cyclonic separation are ineffective against sediment bacteria and viruses. Heat treatment, ultraviolet (UV) radiation, and electric pulse applications are physical treatments with no chemical doses, but their disinfection efficiencies are claimed to be limited. Chemical treatments using chlorine, chlorine dioxide, or hydrogen peroxide are effective disinfectants; however, the undesirable by-products produced are of health concern. Ozonation is a convenient method for ballast water treatment as no chemicals need to be stored on board or made available at ports for ships to use. Nevertheless, some microorganisms have shown high resistance to ozonated seawater [18].

In a recent study, the various methods have been compared for their success for eliminating the different types of organisms that have different sizes. Ballast exchange and filtration methods are the best solutions for treating almost all

Table 52.1 Planned phase in of the Convention standards regarding ballast water exchange (Regulation D-1) and the more stringent ballast water performance standard (Regulation D-2) [modified from [20]]

Ships built	BW capacity [m^3]	2009	2010	2011	2012	2013	2014	2015	2016
<2009	1,500–5,000	D1–D2					D2		
<2009	<1,500; >5,000	D1–D2							D2
≥2009	<5,000	D2							
≥2009; <2012	>5,000	D1–D2							D2
≥2012	>5,000				D2				

organisms that can be carried by ballast water. Chemical solutions are not effective for the organisms which are relatively large. Using heat is only effective for the relatively large organism such as fishes. UV light technique is only effective for microscopic organisms such as planktons, larvae, and bacteria [19].

52.2.2   Regulations on Ballast Water Treatment

As a first effort, the International Guidelines for Preventing the Introduction of Unwanted Aquatic Organisms and Pathogens from Ships Ballast Water and Sediment Discharges were adopted at the 31st Session of MEPC in July 1991. It became clear shortly thereafter that species' movements in ballast water cannot be completely prevented and it was agreed that work on this matter should be continued at IMO to minimize the transfer of organisms in ballast water. As a consequence, the Guidelines for the Control and Management of Ships' Ballast Water to Minimize the Transfer of Harmful Aquatic Organisms and Pathogens were adopted by Resolution A.868 (20) [20].

Some recent studies focused on the ballast water management (BWM) issue in European seas in light of the European Union (EU) Maritime Policy and EU Marine Strategy. The lack of effective BWM tools means that this issue remains a challenge. The Convention introduces two different protective regimes as a sequential implementation: 1. Ballast Water Exchange (BWE) Standard (regulation D-1) requiring ships to exchange a minimum of 95 % ballast water volume; 2. Ballast Water Performance Standard (BWPS) (Regulation D-2) requires that the ballast water discharged has the number of viable organisms below the specified limits [2].

In Table 52.1, standards regarding ballast water exchange and ballast water performance are presented. Standards are set according to the ships' building date and ballast water capacity.

The BWPS as outlined in Regulation D-2 stipulates that ships meeting the requirements of the Convention must discharge:

– Less than ten viable organisms per cubic meter greater than or equal to 50 μm in minimum dimension.
– Less than ten viable organisms per ml less than 50 μm in minimum dimension and greater than or equal to 10 μm in minimum dimension [20].

The newly adopted International Ballast Water Convention sets maximum concentrations of ten viable organisms per m^3 for organisms larger than 50 μm and ten viable organisms per ml for organisms larger than 10 μm and less than 50 μm in the minimum dimension [17].

If there is no ballast water treatment system, MEPC suggests the exchange of the ballast water at sea to reduce the risk. Convention indicates that BWE must be carried out when the ship is at least 200 nm far from the nearest coast and in water at least 200 m in depth. The areas in which exchanging is allowed must be monitored frequently for the possibility of invasive effects. The ballast water treatment systems must be examined strictly for approval. Both land-based and ship-board tests must be taken.

52.3 Conclusions

Due to the stability problems, ballast water seems to be a vital part of ships. Using ballast water is the most common way to stabilize a ship after loading and discharging the cargo. Besides its great effect on ship stability, ballast water causes an important problem. Every sea or big water mass has a different habitat and ecological system. While a ship loads ballast water from any sea, it also loads some endemic species to its tanks. When the ballast water is being discharged to provide the required stability, these species are moved into another ecology in which they behave as invasive species. Once they are moved, it would be an important problem to get rid of them. These species may have a great effect on the local ecological system. Besides, discharging ballast water in different water mass may cause the moving of some solid or liquid harmful materials.

Ballast water treatment systems may be effective solutions for translocation of invasive species. Local and international organizations have some important works on this issue. IMO brought some strict rules and regulations. While new problems occur, MEPC adopts new resolutions for solution. Due to invasive species' proved impact on economic losses, shipping companies developed new technologies for ballast water treatment systems.

Although these actions have an important effect on reducing the harmful effects of ballast water translocation, future of the shipping industry is in need of new and devastating ideas such as ballast water-free ships.

References

1. Badia GQ, McCollin T, Kjell DJ, Vourdachas A, Gill ME, Mesbahi E, Frid CLJ (2008) On board short time high-temperature heat treatment of ballast water: a field trial under operational conditions. Mar Pollut Bull 56:127–135
2. David M, Gollasch S (2008) EU shipping in the dawn of managing the ballast water issue. Mar Pollut Bull 56:1966–1972

3. McGee S, Piorkowski R, Ruiz G (2006) Analysis of recent vessel arrivals and ballast water discharge in Alaska: toward assessing ship-mediated invasion risk. Mar Pollut Bull 52:1634–1645
4. Hülsmann N, Galil BS (2001) The effects of freshwater flushing on marine heterotrophic protists-implications for ballast water management. Mar Pollut Bull 42:1082–1086
5. Endresen Ø, Behrens HL, Brynestad S, Andersen AB, Skjong R (2004) Challenges in global ballast water management. Mar Pollut Bull 48:615–623
6. Göktürk D (2005) İstanbul Limanlarında Balast Suyu Örneklemeleri, M.Sc. Thesis, in Turkish
7. Perrins JC, Cooper WJ, Leeuwen HJ, Herwig RP (2006) Ozonation of seawater from different locations: formations and decay of total residual oxidant-implications for ballast water treatment. Mar Pollut Bull 52:1023–1033
8. Wright DA, Gensemer RW, Mitchelmore CL, Stubblefield WA, Genderen E, Dawson R, Dawson CEO, Bearr JS, Mueller RA, Cooper WJ (2010) Shipboard trials of an ozone-based ballast water treatment system. Mar Pollut Bull 60:1571–1583
9. Lenton TM (2012) First plants cooled the Ordovician. Nat Geosci 5:86–89
10. Pyke CR, Thomas R, Porter RD, Hellmann JJ, Dukes JS, Lodge DM, Chavarria G (2008) Current practices and future opportunities for policy on climate change and invasive species. Conserv Biol 22(3):585–592
11. Champ MA (2002) Marine testing board for certification of ballast water treatment technologies. Mar Pollut Bull 44:1327–1335
12. McCollin T, Badia GQ, Josefsen KD, Gill ME, Mesbahi E, Frid CLJ (2007) Ship board testing of a deoxygenation ballast water treatment. Mar Pollut Bull 54:1170–1178
13. Holm ER, Stamper DM, Brizzolara RA, Barnes L, Deamer N, Burkholder JM (2008) Sonication of bacteria, phytoplankton and zooplankton: application to treatment of ballast water. Mar Pollut Bull 56:1201–1208
14. Carbona SL, Frösen SV, Masson D, Sassi J, Pineau S, Lehtiniemi M, Corroler D (2010) Efficacy and environmental acceptability of two ballast water treatment chemicals and an alkylamine based-biocide. Sci Total Environ 409:247–255
15. Eames I, Landeryou M, Grieg A, Snellings J (2008) Continuous flushing of contaminants from ballast water tanks. Mar Pollut Bull 56:250–260
16. Mesbahi E (2004) Latest results from testing seven different Technologies under the EU MARTOB project—where do we stand now? In: Matheickal JT, Raaymakers S (eds.) Proceedings of 2nd international ballast water treatment R&D symposium, IMO London. GloBallast Monograph Series No. 15. International Maritime Organization, London, 21–23 July 2003, pp 210–230
17. Tang Z, Butkus MA, Xie YF (2009) Enhanced performance of crumb rubber filtration for ballast water treatment. Chemosphere 74:1396–1399
18. Wu D, You H, Zhang R, Chen C, Lee DJ (2011) Ballast water treatment using UV/Ag-TiO$_2$ + O$_3$ advanced oxidation process with Escherichia coli and Vibrio alginolyticus as indicator microorganisms. Chem Eng J 174:714–718
19. Chase, C., C. Reilly and J. Pederson, Ph.D. (2012) Marine bioinvasions fact sheet: Ballast water treatment options. http://massbay.mit.edu/resources/pdf/ballast-treat.pdf
20. Gollasch S, David M, Voigt M, Dragsund E, Hewitt C, Fukuyo Y (2007) Critical review of the IMO international convention on the management of ships' ballast water and sediments. Harmful Algae 6:585–600

Chapter 53
Coal as a Component of Sustainable Energy Portfolio

Muhammad A.A. Khan and Ali Muhtaroğlu

Abstract Sustainable production and use of energy is currently a critical problem area for the world. The emissions from fossil fuels have valid environmental concern as reported by various scientific studies. This chapter reviews the geographical distribution of world coal reserves at the year-end 2010, and provides an overview of the opportunities for this most carbon-intensive fuel to be exploited in an environmentally benign way. Clean coal technologies (CCTs) are studied for both coal production and use. The potential of the CCTs is evaluated by focusing on five top coal producers of the world. Two of the examined producers are from the developed world, i.e., the United States and Australia. The remaining three are the developing countries, China, India, and South Africa. The status of the CCTs is outlined in the context of ongoing projects, and future prospects. Evidence for sustainable development capacity is provided with respect to "the three pillars of sustainable development," i.e., economic development, social well-being, and environmental sustainability. Economic appeal of coal-based energy is also demonstrated through comparative analysis against various other fuel options. The study concludes that unlike popular belief, production and use of coal can be relatively clean. Immediate deployment of CCTs can enable coal to remain in world energy mix at least until the end of this century. Incorporating the new and advanced technologies to coal production and use can reduce its emissions close to zero level in not-too-distant future.

Keywords Sustainable energy • Clean coal technologies • Sustainable development

M.A.A. Khan (✉)
Sustainable Environment and Energy System, Middle East Technical University, Northern Cyprus Campus, Kalkanlı, Güzelyurt, Mersin 10, Turkey
e-mail: tanazhar88@hotmail.com

A. Muhtaroğlu
Electrical and Electronics Engineering Department, Middle East Technical University, Northern Cyprus Campus, Kalkanlı, Güzelyurt, Mersin 10, Turkey
e-mail: amuhtar@metu.edu.tr

Acronyms

BP	British petroleum
CBM	Coal bed methane
CCS	CO_2 capture and storage
CMM	Coal mine methane
DTI	Department of trade and industry, London
IEA	International energy agency
IGCC	Integrated gasification combined cycle
NMA	National mining association
USEPA	United States Environmental Protection Agency
WCA	World Coal Association
WCI	World Coal Institute
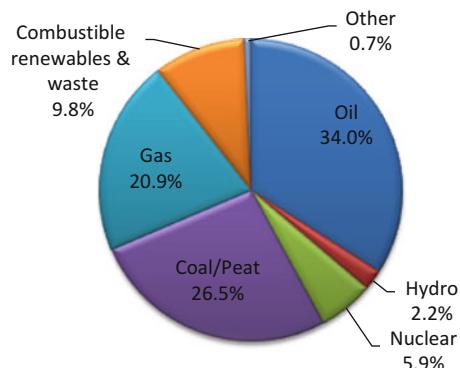
53.1 Introduction

Coal is considered to be the oldest fossil fuel used by mankind. It stands second with its 26.5 % share in world's primary energy as shown in Fig. 53.1 [1]. One reason of using coal is its vast geographical distribution across the world. However, accurate estimation of coal reserves is found to be a tricky exercise owing to the fact that data quality of these reserves is poor both on global and national levels. It is true that coal is abundant, affordable, safe and secure, and easy to transport and store, but it is also the most carbon-intensive fuel for electricity, and poses technological challenges when considered in the context of sustainable global growth.

It is observed that energy demand has grown strongly and will continue to increase, mainly in developing countries where energy is needed in economic growth and poverty alleviation. Renewable energy utilization is growing at a fast pace, but still represents only a small proportion of the world energy mix due to high cost, whereas coal has been heavily consumed for centuries. The price per unit energy from coal is relatively lower and more stable than other fuels. This is one of the main reasons coal has remained the fuel of choice for electricity generation at global level and is likely to remain so for several decades. Regardless of the well-recognized fact that coal is an environmentally harmful energy source due to CO_2 emissions 1.3 times more than oil and 1.7 times more than gas, the consumption of coal is expected to rise by 1.9 % per year between now and 2030 [2]. Almost three-quarters of the coal produced are used in fueling power or cement plants. Steel industry also utilizes it as a vital resource in production.

The use of fossil fuels in a sustainable manner is in debate for several years. In particular, coal's environmental impact always remains a key concern as one of the major contributors to climate change and global warming. Much work is already done over the last two decades to reduce the environmental impacts of coal, and research in this area is under way for making it part of a sustainable energy portfolio.

Fig. 53.1 Fuel shares of total primary energy supply in 2007 ~12 Gtoe (source: modified from [1])
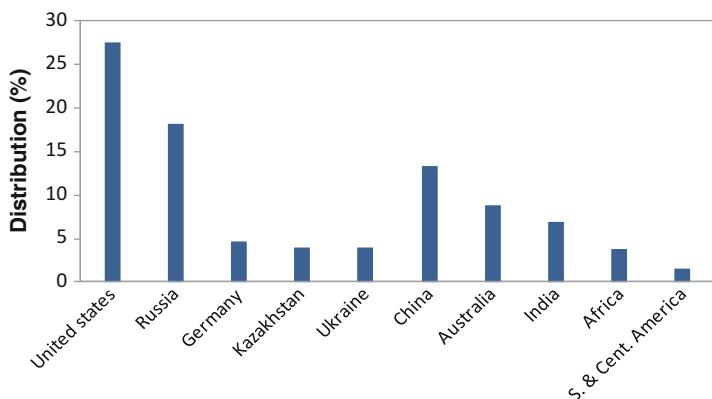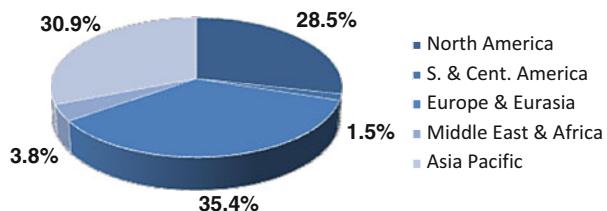
In this study, the sustainable development of coal is investigated. Five major coal-producing countries are selected for analysis, two from the developed (the United States and Australia) and the other three from the developing (China, South Africa, India) block of the world. An assessment of the global coal reserves is done based on the data collected by British Petroleum (BP) at the year-end 2010. Clean coal technologies (CCTs) are then briefly introduced, followed by a detailed discussion on the role of these technologies in coal production and use, their present status, and future prospects. The evidence of coal's sustainable development is provided in light of the three pillars of sustainability, namely, economic development, social well-being, and environmental sustainability. A comparative analysis is presented to demonstrate the economic appeal of coal-based energy compared to other fuel sources. Conclusions and recommendations are summarized at the end of the chapter.

53.2   Background: World Coal Reserves
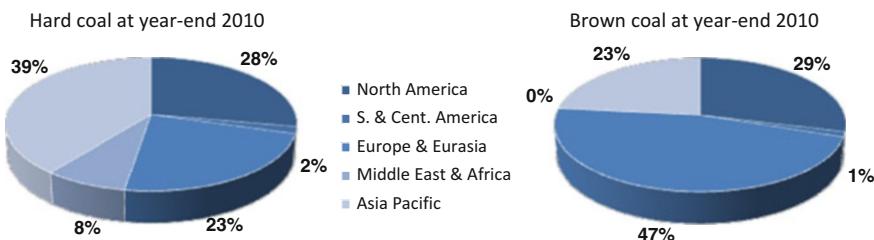
Proved coal reserves at year-end 2010 are estimated at 860 billion tons (Gt), which represents about 118 years of production at the current rate. When compared with the estimates published in 2008, these numbers are 34 Gt and 4 years higher [3].

According to BP statistical review of world energy, the proved reserves are distributed in five regions of the world, namely, Europe and Eurasia, Asia Pacific, North America, the Middle East and Africa, and South and Central America as shown in Fig. 53.2 [4]. However, it is evident from the figure that world reserves for coal are concentrated in thirds. One-third is located in Europe and Eurasia (35.4 %), dominated by Russia (18.2 %), to which Germany (4.7 %), Kazakhstan (3.9 %), and Ukraine (3.9 %) can be added; one-third is located in Asia Pacific (30.9 %), where the reserves in China (13.3 %) alone are almost equal to the sum of reserves in India (7 %) and Australia (8.9 %); and one-third is located in North America (28.5 %), dominated by the United States (27.6 %). The Middle East and Africa represent less

Fig. 53.2 Distribution of
proved reserves in 2010
(source: modified from [4])

Fig. 53.3 World distribution of recoverable coal reserves at year-end 2010

Fig. 53.4 Distribution of world coal reserves according to hard coal and brown coal

than 5 % of the total, with the bulk of coal wealth in South Africa. South and Central America holds only 1.5 % of world reserves. A detailed distribution of major reserves is shown in Fig. 53.3.

The total of 860 billion tons (Gt) breaks down into 405 Gt of hard coal (anthracite and bituminous coal) and 455 Gt of brown coal (subbituminous coal and lignite). The main application of hard coal is in the steel industry and power generation whereas brown coal is normally used as onsite fuel. With this classification of coal, the reserves are distributed in the world as shown in Fig. 53.4.

Clearly, Asia Pacific contains 39 % of hard coal, dominated by China (15.3 %), and Europe and Eurasia contains 47 % of brown coal, dominated by Russia

(23.6 %). North America shares equal amount of hard and brown coal (~28 %), and the Middle East and Africa area has hard coal (8 %) only. South and Central America area has 2 and 1 % of hard coal and brown coal, respectively.

53.3 Clean Coal Technologies

CCTs enable improvements in coal's performance as an energy source, and at the same time reduce its environmental impacts. These technologies contribute to different stages of coal production and use which may include extraction, preparation, storage, transportation, and use in power stations, steel mills, and other industrial applications. The following sections discuss the sustainable practices associated with coal production and use in detail.

53.3.1 Clean Coal Technologies in Coal Production

Coal is normally extracted by two different types of mining: "surface or open cast mining" and "underground or deep mining." The type of mining is selected based on the geology of the coal deposit. These processes cause harm to land, surface water, groundwater, and even air quality [5]. The impact can however be reduced through CCTs. Some of these techniques are already adapted in different parts of the world, and many of them are still in research and development phase.

For the purpose of this study, two broad areas of CCT in production are studied: (a) advanced coal preparation and cleaning techniques, and (b) coal mine methane (CMM).

Advanced Coal Preparation and Cleaning Techniques

The coal is extracted from mines with a rich content of mineral matter. It needs to be separated from these minerals for its proper functioning and end use. Normally the sequence of processes adapted for this purpose consists of coal pretreatment, cleaning, sizing and classification, dewatering and tailing treatments, and water clarification [6]. These processes result in high-quality processed coal that can be used commercially without environmental constraints. The plants fired by this coal in general have better environmental performance in terms of reduced SO_2, CO_2, and particulate emissions. The amount of combustion ash can also be decreased using these techniques.

Coal cleaning processes are usually categorized by the size of coal. According to technology status report of cleaner coal technology program [6], coal can be divided into coarse coal (>25 mm), small coal (25–3 mm), fine coal (<3 mm),

Table 53.1 Coal cleaning processes

Coal type	Cleaning process
Coarse coal	Dense medium separation
	Jig washing
Small coal	Jig washing
	Dense medium cyclone
Fine coal	Spiral concentration
	Teeter-bed separation
Ultrafine coal	Froth floatation

and ultrafine coal (<0.15 mm). The processes of cleaning different types of coal are listed in Table 53.1.

DTI London [6], under the cleaner coal technology program, categorizes the international markets for coal preparation and cleaning technologies as:

– Industrialized nations such as the United States, the UK, Australia, Germany, and South Africa, in which various coal preparation and cleaning techniques are in operation and are further researched by institutions and manufacturers.
– Nations in transition and development such as China, Ukraine, Kazakhstan, and Russia, in which lack of capital is a major constraint in technological advancement and indigenously developed tools with minimal processing are used for coal preparation and cleaning.

The fraction of extracted coal which is processed and cleaned varies from region to region. Similarly, the process and technology employed depend upon the type of coal available for cleaning. Table 53.2 summarizes the cleaning processes for the selected coal-producing countries. It is observed that by using these processes, power plants today emit 90 % less pollutant (SO_2, CO_2, particulates, and mercury) compared to plants in 1970s. Moreover, regulated emissions from coal-based power generation have decreased to nearly 40 % since 1970s, while the use of coal has tripled over the same time [7].

Coal Mine Methane

Methane can be extracted from coal seams that never experience mining, in which case it is called coal bed methane (CBM). Methane can also be extracted during and after the coal mining process, and referred to as CMM. CMM is simultaneously considered a mining hazard, a greenhouse gas, and a possible energy source [8].

According to International Anthropogenic Methane Emissions [9], underground coal mines liberate an estimated 29 to 41 $\times$ 10^9 m^3 of methane annually, of which less than 2.3 $\times$ 10^9 m^3 are used as fuel. There are several reasons to practice methane extraction during and after coal mining. In the first place, it increases mine safety. Fatalities and ventilation requirements can be reduced with improved working efficiency in less time. Another important reason is that it supports global sustainability. It is a clean fuel as compared to coal because it produces only half the

Table 53.2 Coal preparation and cleaning technologies (source of data: [6])

Country	Coal preparation and cleaning techniques
Australia	64 Plants in 1998, capacity >600 t/h
	Main technologies include
	1. Dense medium (DM) separation
	2. Teeter-bed separation
	3. Column floatation for fine coal
China	1,570 small coal preparation plants, capacity <3,000 t/a
	73 coal preparation plants >1.5 Mt/a
	Main technology used is jig washing
India	Total 24 coal preparation plants
	Main technologies include
	1. Dense medium (DM) separation
	2. Dense medium (DM) cyclone
South Africa	58 coal-processing plants in 1996
	Main technologies include
	1. Dense medium (DM) cyclones
	2. Spiral concentrators since mid 1980s
	3. Froth floatation
USA	Main technologies include
	1. Dense medium (DM) cyclone (more than 50 %)
	2. Jig washing
	3. Froth floatation and spiral concentrators for fine coal
	4. Column floatation for recovery and cleaning of ultrafine coal

Note: t/h and t/a in Table 53.2 refer to tons per hour and tons per annum, respectively

amount of CO_2 as compared to coal combustion on an energy equivalent basis, with no SO_2 and particulate emissions [10].

The selected countries for this study are among the top sources of CMM. Table 53.3 summarizes the amount of methane liberated annually by underground mining activities, the recovered amount, and its primary use. It can be observed that China is the primary source of CMM with 14 to 24×10^9 m^3 of methane, but the United States recovers more of the extracted methane than China, i.e., 700×10^6 m^3. India releases the least amongst all, but has potential for CMM. Some projects are in research and development phase in India, such as Moonidih and Sudamdih in Jharia Coalfields, and National Coal Company's CMM project.

53.3.2 *Clean Coal Technologies in Coal Use*

CCTs also play a significant role in efficient coal use. The sustainable use of coal is discussed under two categories in this study: (a) clean fuels from coal and (b) CO_2 capture and storage.

Table 53.3 CMM potential (source of data: [10])

Country	CMM potential
Australia	594 to 1,162 $\times$ 10^6 m^3 of methane are liberated
	70 to 122 $\times$ 10^6 m^3 of methane are recovered
	Primary use: Electricity generation
China	14 to 24 $\times$ 10^9 m^3 of methane are liberated
	561 $\times$ 10^6 m^3 of methane are recovered
	Primary uses
	1. Heating and cooking at mine facilities and nearby residences
	2. Used by the glass and plastic industry
	3. Power generation
India	576 $\times$ 10^6 m^3 of methane are liberated
	No coal mine methane recovery programs are in place
South Africa	1.1 $\times$ 10^6 m^3 of methane are liberated
	Normally exploration is done not for the purpose of methane recovery
USA	4.2 $\times$ 10^9 m^3 of methane are liberated
	0.7 $\times$ 10^9 m^3 of methane are recovered
	Usually sale to gas distributors to earn profit

Clean Fuels from Coal

Coal can be used sustainably by minimizing its direct combustion in the atmosphere. Coal has the potential to be converted into liquid and gaseous fuels, the combustion of which yields less pollutants than the combustion of coal itself. The conversion of coal into liquid fuels enables many countries to reduce their oil imports and at the same time reduce its environmental impacts. Coal-to-liquid conversion is found to be more promising compared to coal-to-gas conversions due to the cost and transportation issues associated with it.

Coal Liquefaction

Coal can be readily converted into a variety of liquid fuels which in turn offer a host of advantages. For example the liquid fuel derivatives of coal are ultra-clean, sulfur-free products, are low in aromatic hydrocarbons (such as benzene), and reduce vehicle emissions such as oxides of nitrogen, particulate matter, volatile organic compounds, and carbon monoxide [11]. One example of these fuels is dimethyl ether (DME). It is a domestic fuel, noncarcinogenic, and nontoxic to handle, and emits fewer amounts of carbon monoxide and hydrocarbons to the atmosphere. Some of the coal liquefaction projects from the countries under discussion are highlighted in Table 53.4.

Table 53.4 Coal liquefaction projects (source of data: [11])
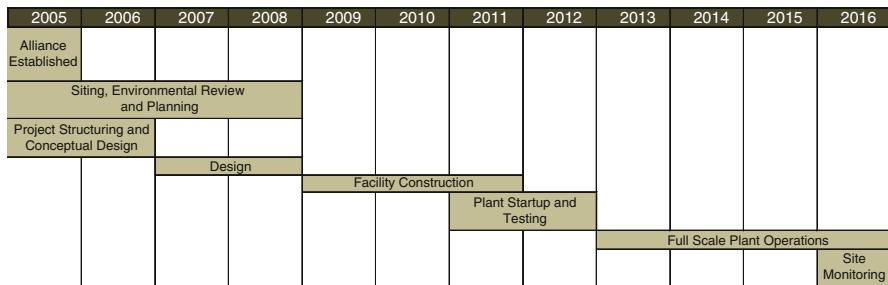
Country	Coal liquefaction projects
Australia	Monash Energy Project
	Capacity: 62,000 bbl/day
	Products: Coal-derived diesel and other liquids
	Expected year of operation: 2010
	Location: SE Australia
China	Shenhua Energy Group Project
	Capacity: 50,000 bbl/day
	Products: Jet fuel, gasoline, and diesel fuels
	In operation since 2007
	Location: North China's inner Mongolia autonomous region
India	No coal-to-liquid (CTL) projects have been formally proposed yet but its high-ash, low-quality coals well suited to conversion
South Africa	Sasol CTL Project (I, II and III)
	Capacity: 112,000 bbl/day
	Products: Coal-derived fuels for vehicles and commercial jets
	In operation since 1955
	Location: Sasolburg and Secunda
USA	DKRW Energy's CTL Project
	Capacity: 11,000 bbl/day and expected to rise by 40,000 bbl/day
	Products: Various fuels—primarily diesel
	Location: Medicine Bow, Wyoming

Coal Gasification

Coal gasification can provide an affordable energy supply with high efficiencies and near-zero pollutants. Normally, coal is converted to gas using integrated gasification combined cycle (IGCC). An IGCC plant uses up to 40 % less water, and 90 % of mercury emissions can be captured compared to conventional plants. Emissions of oxides of nitrogen (NOx) are reduced by at least a third, sulfur oxides (SOx) by more than two-thirds, and particulates down to almost zero [12].

An IGCC plant does not use conventional natural gas as fuel. Instead, it uses a synthetic gas produced via gasification of another feedstock which is normally coal or petroleum residuals. The IGCC plant breaks down the coal into its chemical constituents such as carbon monoxide (CO), hydrogen (H_2), and some other gaseous compounds, instead of burning it directly. The CO is converted to CO_2 and can be captured if there is a provision of doing so, but for conventional coal-fired plants, it is always emitted to atmosphere. The resulting gas is called synthetic gas (or syngas), consists mostly of hydrogen, and is used in power generation. Syngas possesses the ability of polygeneration, i.e., it can produce commercial by-products such as methanol, ammonia/fertilizer, hydrogen, and substitute natural gas [13].

IGCC is relatively a new technology, and different projects are in research and development phase. One of such projects is FutureGen, USA. This project claims to

Fig. 53.5 FutureGen time line (source: modified from [12])

be the world's first coal-fueled near-zero emission power plant. According to World Coal Institute [12], the project will use coal gasification technology with combined cycle electricity generation and CO_2 storage. It is expected that the plant will be economically feasible by producing low-cost electricity and hydrogen from coal with almost zero emissions. A detailed time line of FutureGen is presented in Fig. 53.5.

CO_2 Capture and Storage

The amount of CO_2 is continuously increasing in the atmosphere due to energy production and use. According to World Energy Outlook [14], the global energy-related CO_2 emissions will be 57 % higher in 2030 than in 2005. In this alarming situation, CO_2 capture and storage is the only technology which seems capable of mitigating the greenhouse gas emissions, especially CO_2 emissions from large-scale fossil-fueled plants. Coal-fired plants can significantly reduce their emission by integrating CCS. This integration can be done in three ways, namely, pre-combustion, post-combustion, and oxyfuel combustion.

Pre-combustion capture involves gasification of coal prior to combustion as discussed earlier in sect. 3.2.1.2. The resulting CO_2 is then compressed into a supercritical fluid so that it can be transported for geological storage. Post-combustion involves separation of CO_2 from exhaust gases resulting from coal combustion. For oxyfueling the combustion of coal is carried out in an oxygen-rich environment, rather than air, without allowing nitrogen to enter into the combustion chamber. The resulting stream of CO_2 can easily be captured, compressed, and stored. However, this technique is still in the demonstration phase.

The coal producers are now working to incorporate CCS in their coal-fired plants. The current status along with future prospects of CCS is discussed for the five countries under consideration and the projects which are in development phase are briefly summarized in Table 53.5.

Table 53.5 CO_2 capture and storage projects (source of data: [14])

Country	CO_2 capture and storage projects	

Australia	1. ZeroGen Project
	  Location: Brisbane, Queensland
	  Capture method: Pre-combustion
	  Expected year of operation: 2017
		2. FutureGas Project
		  Location: South Australia
		  Capture method: Post-gasification
		  Expected year of operation: 2016

China	1. China–Australia Collaboration
	  Location: Huaneng, Beijing
	  Capture method: Post-combustion
		2. China–Japan Collaboration
		  Location: Heilongjiang, NE—China
		  Capture method: Post-combustion

India	Indian CO_2 sequestration Applied Research Network is established in 2007 No current project	
South Africa	South African center for Carbon Capture and Storage established in 2009 South Africa emits over 400 million tons of CO_2/year It is estimated that 60 % of these emissions can be captured	

USA	1. FutureGen Project
	  Location: Meredosia, Illinois
	  Capture method: Pre-combustion
	  Expected year of operation: 2012
		2. Texas Clean Energy Project (TCEP)
		  Location: West of Odessa, Texas
		  Capture method: Pre-combustion
		  Expected year of operation: 2014

53.4 Coal and Sustainable Development

The extraordinary dependence of world on coal brings about the need of sustainability in its use. Sustainable development is a broad concept, and is founded on three pillars—economic development, social well-being, and environmental sustainability. Coal has an active participation in all three pillars and much work is in progress to exploit it in a more sustainable manner.

53.4.1 Economic Development

Coal is a major contributor in world's economy. According to World Coal Association [15], coal produces 41 % of world's electricity, which is double compared to its competitors, gas and hydro, and it is also used in 70 % of world's steel production today. Coal mining is done in over 50 countries and this industry employs around seven million people, 90 % of which are in developing countries [16]. Moreover, developing countries are found to be export oriented in the coal industry which helps them to earn foreign hard currency while saving in import costs. World Coal Association estimates that coal generates around $7 billion per annum in export revenues for developing countries and saves them $60 billion or more in energy import costs every year.

53.4.2 Social Well-Being

Adequate energy access to all is a global challenge today. According to World Energy Outlook [17], 1.6 billion people in developing countries do not have electricity and around 2.4 billion people rely on primitive biomass fuel for cooking and heating. Coal offers some solutions to these problems. For example, in China over the past 15 years, around 700 million people are served by coal-based electrification. The electricity production in China is raised by 1,000 TWh, 84 % of which is coal fired. Besides electrification, coal industries run on workforce from local communities in which they operate. These companies emphasize education and skill development programs. They contribute to school needs, or help administrators of the area by developing some management programs. An educated and skilled local community helps in attracting further investment and thus sustains the people even after mine closure.
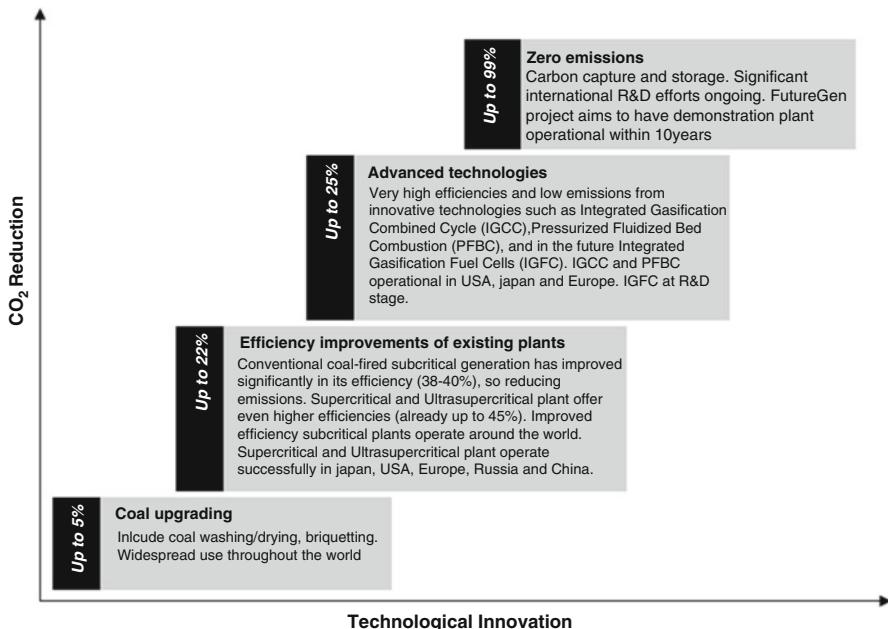
53.4.3 Environmental Sustainability

The coal industry realizes that its extraordinary consumption may degrade the environment, and therefore measures are taken to improve the coal's environmental performance steadily. Power plant builders are now capable of working at an efficiency level beyond 40 % and are further trying to achieve 50 %. The greenhouse gas emissions can be expected to be lower by 10–20 % by operating power plants at these enhanced efficiencies. In its report "The role of coal as an energy source," WCI narrated that the United States has reduced its sulfur emissions by 3 % every year since 1980 despite rising coal use, and Germany has also reduced its NOx and particulate emissions by over 80 % since 1980s [16].

   Figure 53.6 clearly demonstrates the movement of coal in sustainable energy portfolio. It can be observed that the technological advancements can reduce the CO_2 emissions from coal up to 99 %. As discussed earlier, some of the CCTs are already incorporated in coal production and use, and are able to reduce about 25 % of CO_2 emissions. However, significant research and development in newer CCTs is ongoing. It is expected that the advanced carbon capture and storage projects will be operational in around 10 years from now which can reduce the CO_2 emissions by ~99 %.

53.5 Economic Appeal of Coal-Based Energy

An important factor that keeps coal in the global energy portfolio is its superiority in providing a stable cost for electricity generation compared to other fuels. A comparative analysis is done by Morgan et al. to identify the most cost-effective form of energy production among nuclear, coal, natural gas, wind, solar, and hydro
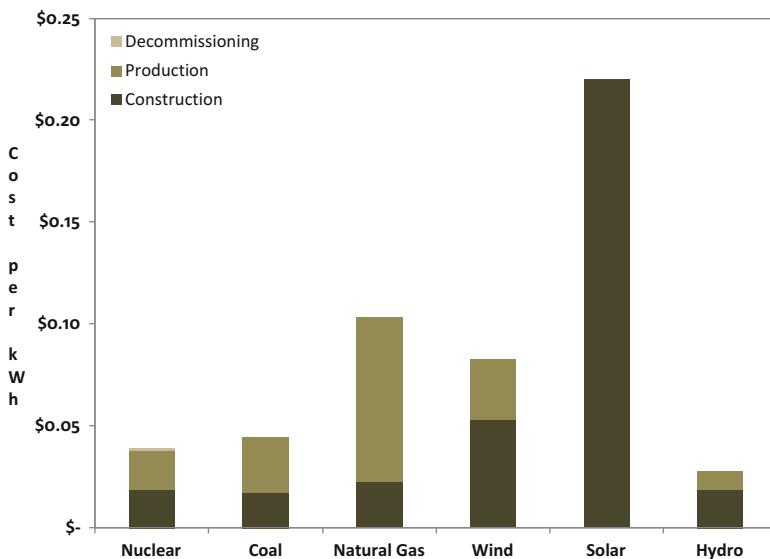
Fig. 53.6 Coal-fired route to CO_2 reduction (source: modified from [15])

[18]. Construction, production, and decommissioning costs (where necessary) are taken into account. The results of the analysis are shown in Fig. 53.7. Although hydroelectric is found to be most cost effective with 30 cents/kWh, it has some geographical and environmental limitations such as biodiversity impact and relocation of people. Coal and nuclear are nearly equal with 40 cents/kWh, but nuclear production has certain decommissioning cost and risks. Therefore, coal production and utilization using CCTs can be the most attractive option for energy generation since all other sources such as natural gas, wind, and solar have high cost per kWh.

53.6   Conclusions and Recommendations

The future global energy portfolio will include widespread use of coal as a primary energy source. The sustainability issues associated with this energy source are discussed in this chapter. The sustainable practices in both developed and developing countries are analyzed. The key conclusions and recommendations from this study are as follows:

- Coal plays an important role in sustainable energy systems for the foreseeable future due to plenty of advantages associated with it. CCTs are needed to be deployed immediately both in developed and developing world if coal is to remain in the global energy portfolio for later part of the century.

Fig. 53.7 Cost of electricity production per kWh (source: modified from [18])

- The techniques, such as coal preparation and cleaning, CMM, and coal-derived clean fuels, are already employed in different countries, and more advanced technologies like IGCC with carbon capture and storage (CCS) are under development to be operational in a couple of years.
- More improvements are required in environmental performance of the coal. Although improved coal technologies provide increased efficiency with reduced emissions to date, accelerated technological advancements can lead to near-zero emissions. An example of such a technology is FutureGen which was expected to be in operation by 2012.
- Coal has a great contribution in the three pillars of sustainable development. This development could be more effective by establishing well-defined policies specific to each pillar.

References

1. IEA (2009) Key energy statistics 2009. International Energy Agency, Paris
2. IEA (2009) World energy outlook 2009. International Energy Agency, Paris
3. BP (2009) BP statistical review of world energy, June 2009. British Petroleum, London
4. BP (2011) BP statistical review of world energy, June 2011. British Petroleum, London
5. Keating M (2001) Cradle to grave: the environmental impacts from coal, vol 1. Spectrum printing and graphics, Boston, MA, Clean Air Task Force
6. DTI (2001) "Coal Preparation", Cleaner coal technology program. Department of Trade and Industry, London. http://webarchive.nationalarchives.gov.uk/+/http://www.berr.gov.uk/files/file19296.pdf. Accessed 28 Nov 2011

7. NMA (2000) Clean coal technologies. National Mining Association. http://www.nma.org/ccs/cct.asp. Accessed 30 Nov
8. USEPA (2009) Coal mine methane recovery: a primer. United States Environmental Protection Agency, Philadelphia, PA, EPA-430-R-09-013
9. USEPA (1994) International anthropogenic methane emissions: estimates for 1990. United States Environmental Protection Agency, Philadelphia, PA, EPA-230-R-93-010
10. Bibler CJ, Marshall JS, Pilcher RC (1998) Status of worldwide coal mine methane emissions and use. Int J Coal Geol 35:283–310
11. WCI (2006) Coal: liquid fuels. World Coal Institute, United Kingdom, p 20
12. WCI (2007) Coal: delivering sustainable developments. World Coal Institute, United Kingdom, p 5
13. Walker R (2011) Coal gasification: power over pollution. Living Energy 4:40
14. IEA (2008) CO_2 capture and storage: a key carbon abatement option. International Energy Agency, Paris. ISBN 978-92-64-04140-0
15. WCA Uses of coal. World Coal Association. http://www.worldcoal.org/coal/uses-of-coal/. Accessed 04 Dec 2011
16. WCI (2003) The role of coal as an energy source. World Coal Institute: United Kingdom, p 7
17. IEA (2002) World energy outlook 2002. International Energy Agency OECD/IEA, Paris, pp 32–33
18. Morgan J (2010) Comparing energy costs of nuclear, coal, gas, wind and solar. Nucl Fissionary. http://nuclearfissionary.com/2010/04/02/comparing-energy-costs-of-nuclear-coal-gas-wind-and-solar/. Accessed 17 Dec 2011

Chapter 54
Adsorption Capacity, Towards Carbon Dioxide, of a Chemically Activated Coal

Abdelhamid Addoun, Larbi Temdrara, and Aissa Khelifi

Abstract The chemical activation of a low-rank coal by alkaline hydroxides and carbonates, successively, carries the formation of activated carbons characterized by a very developed porous texture and highly microporous. Indeed, the microporous volume can reach the value of 0.63 cm^3 g^{-1} and the pore size distribution, deduced from the technique of immersionnal calorimetry into liquids of increasing molecular dimensions, shows that the average diameter of these pores is of the order of 0.7 nm. This distribution is perfectly suitable to the adsorption of the carbon dioxide at room temperature so that the adsorption capacities, at this temperature, of the prepared activated charcoals towards this greenhouse gas are very important (0.68 g/g, i.e., 0.68 ton/ton). Otherwise, the obtained results show that the alkaline hydroxides are more effective than the corresponding carbonates.

Keywords Activation • Adsorption • Immersional calorimetry • Greenhouse gas • Adsorption capacity • Carbon dioxide • Chemically activated coal • Chemical activation • Alkaline hydroxides • Carbonates

Nomenclature

CO	Carbon monoxide
CO_2	Carbon dioxide
c	Constant
E_0	Characteristic energy, J/mol
GHG	Greenhouse gas

A. Addoun (✉) • A. Khelifi
Faculté de Chimie, USTHB, BP 32, El-Alia, 16111 Bab-Ezzouar, Alger, Algérie
e-mail: addboudz@yahoo.fr; khelifiaissa@yahoo.fr

L. Temdrara
Faculté des Sciences, Université de Chlef, Chlef 02000, Algérie
e-mail: temlarbi@yahoo.fr

HCl   Hydrochloric acid
h_i Specific enthalpy of immersion, mJ/m^2
K_2CO_3 Potassium carbonate
KOH   Potassium hydroxide
Lm   Minimal width of the pore, nm
Me   Low-rank coal
N_2 Nitrogen gas
ppm   Parts per million
S_{CO_2} Dubinin and Radushkevich (DR) apparent specific area, m^2/g
Se   External surface, m^2/g
S_{N_2} Brunauer, Emmett, and Teller (BET) specific area, m^2/g
Tc   Critical temperature, °C
TPD   Temperature-programmed desorption
Vm   Molar volume, cm^3/mol
W(L)   Micropore volume filled, cm^3/g
W_0 Total micropore volume, cm^3/g

Greek Letters

α Thermal expansion coefficient, K^{-1}
β Affinity coefficient
-ΔH   Enthalpy of immersion, J/g
ϕ Pore diameter, nm

54.1   Introduction

As it is widely known, activated carbons are used for the removal of pollutants from drinking water or wastewater and from air. The use of these materials as adsorbents of inorganic and organic pollutants is due to their unique versatility resulting from their high surface area, porous structure, high adsorption capacity, and surface chemical nature, which can be appropriately modified by physical and chemical treatments to enhance the extent of a given adsorption process [1]. It is known that phenol is the most frequently occurring contaminant in industrial wastewaters.

Preparative methods for porous carbons are conventionally classified into physical and chemical activation. The former is carried out in two heat treatment steps: carbonization in an inert gas up to a given temperature followed by activation in an oxidant gas. The latter is carried out in a single heat treatment step in the presence of an added chemical. Among the activating agents, one cites the phosphoric acid which is one of the commonly used agents for the activation of various precursors [2–6]. The formation of highly microporous carbons by pyrolysis of various types of precursors (lignites, green cokes, coals) in the presence of potassium and sodium hydroxides and carbonates is now well documented [7–10]. Alkaline and carbonate hydroxides were also used in the chemical activation of coals [8, 11]. Considering

their very developed microporous texture, the activated carbons would retain no negligible amounts of carbon dioxide whose critical temperature is relatively high (31 °C). On the one hand, carbon dioxide plays a crucial role in the cycle of life, including providing the necessary carbon for plants to produce organic food, balancing the heat radiation of the earth, balancing the calcium carbonates in soils and oceans, and buffering water and soils. On the other, it is admitted that the rising CO_2 levels are degrading the environment and damaging global ecosystems; the residence time of this greenhouse gas (GHG) in the atmosphere lasts around 100 years [12].

Otherwise, as world population rises, human-induced environmental pressures mount. By some measures, one of the pressing environmental issues is global climate change related to the rise of atmospheric concentrations of CO_2 and other GHG [13]. Scientists know that carbon dioxide is warming the atmosphere, which in turn is causing sea level to rise, and that the CO_2 adsorbed by the oceans is acidifying the water [14]. World CO_2 emissions from fuel combustion account for about 70 % of GHG emissions and 80 % of the total CO_2 emission [15]. The emission of CO_2 in the energy sector is expected to grow from 29 billion metric tons in 2006 to 40.6 billion metric tons in 2030. Coal share in the world CO_2 emission is also expected to grow from 42 % in 2006 to 45 % in 2030 [16].

The concentration of atmospheric carbon dioxide since preindustrial times has increased from about 280 parts per million (ppm) to over 380 ppm [14, 17]. The rate change climbs about two molecules every year [14]. The case for attributing the recent global warming to human activities rests on the following undisputed scientific facts [17]. Carbon dioxide is a GHG that warms the atmosphere. Independent measurements demonstrate that the increased CO_2 in the atmosphere comes from burning fossil fuels and forests. Since preindustrial times, global average temperatures have increased by about 0.7 °C, with about half of the warming occurring over the past few decades [17]. Therefore, the environmental changes, due to human activities, require fast actions to reduce the harmful effect to the environment and to prevent further damage to the global climate system.

The purpose of the present work is to investigate further the development of the microporous texture of a heat-treated coal in the presence of alkaline hydroxides and carbonates and to compare the adsorption properties of the resulting charcoals, towards the carbon dioxide, a GHG.

54.2 Theoretical

The enthalpy of immersion of a microporous carbon is given by the relation [18]

$$- \Delta H_i \left(J.g^{-1} \right)_{mi} = \frac{\beta E_0 W_0 (1 + \alpha T) \sqrt{\pi}}{2 V_m} \tag{54.1}$$

Table 54.1 Properties of the organic liquids used as molecular probes

	V_m (cm^3 mol^{-1})	β	α (10^{-3} K^{-1})	L (nm)
Carbon dioxide (CO_2)	–	0.35	–	0.28
Benzene (C_6H_6)	88.90	1.00	1.24	0.41
Cyclohexane (C_6H_{12})	108.00	1.04	0.95	0.54
Carbon tetrachloride (CCl_4)	96.50	1.05	1.22	0.63
α-Pinène ($C_{10}H_{16}$)	158.80	1.70	1.02	0.80
Perchlorocyclopentadiene(C_5Cl_6)	159.50	1.90	1.17	0.88

where β, E_0, W_0, α, V_m, and T being the affinity coefficient of the given liquid, the characteristic energy of the solid, the total volume of the micropores accessible to the adsorbate, the thermal expansion coefficient and the molar volume of the liquid filling the micropore system and the temperature of the experiment, respectively.

The contribution of the wetting of the external surface, S_e, is h_iS_e, where h_i represents the specific enthalpy of immersion of the open surface. The experimental enthalpy of immersion is therefore

$$- \Delta H_i(\exp) = \frac{\beta E_0 W_0 (1 + \alpha T) \sqrt{\pi}}{2V_m} - h_i S_e \qquad (54.2)$$

and it follows that for a liquid acting as a molecular probe, the micropore volume W(L) filled is given by

$$W(L) = \frac{-[\Delta H_i(\exp) - h_i S_e].2V_m}{\beta E_0 \sqrt{\pi}(1 + \alpha T)} \qquad (54.3)$$

Table 54.1 lists the essential data of a series of organic liquids and CO_2 used as molecular probes. These data are taken from literature [19–22].

Otherwise, the theoretical pore size distributions are calculated from the equation

$$\frac{dW}{d\phi} = -2W_0 c(\phi - Lm). \exp\left[-c(\phi - Lm)^2\right] \qquad (54.4)$$

deduced from

$$W = W_0 \exp\left[-c(\phi - Lm)^2\right] \qquad (54.5)$$

where c, ϕ, and Lm being a constant, the pore diameter, and the minimal width of the pore, respectively.

54.3   Experimental

A low-rank coal Me (volatile matter: 32.4 % daf; ash: 3.4 %) was ground with alkaline hydroxide KOH and carbonate K_2CO_3, successively. The rate is defined as the ratio, r, of the adjuvant weight (hydroxide or carbonate alkaline) on the weight coal. Untreated, alkaline hydroxide-treated and carbonate-treated coal samples were carbonized in a stream of nitrogen (6 l h^{-1}) at a heating rate of 5 K min^{-1} up to 1,073 K and maintained for 1 h at this temperature. After carbonization, the alkaline salts were removed by refluxing in diluted HCl and the char was then washed with distilled water until the silver nitrate-negative test was obtained and finally oven-dried at 383 K during 4 h and kept in hermetic bottles to protect them from air and humidity. The untreated pyrolyzed coal, the hydroxide-treated and pyrolyzed coal, and the carbonate-treated and pyrolyzed coal are noted as Me (r = 0.0), Me-KOH (r = 0.5, 1 or 2.2), and Me-K_2CO_3 (r = 0.5 or 1.2), where Me designates the coal.

Adsorption isotherms of N_2 at 77 K and CO_2 at 293 K were determined using a volumetric apparatus (Micromeritics ASAP 2010). The surface and pore characteristics of the carbons were determined by measurement of the BET specific area, S_{N_2}, obtained from N_2 adsorption and the Dubinin–Radushkevich micropore volume and surface, W_0 and S_{CO_2}, deduced from adsorption of CO_2 at 293 K.

The cross-sectional area for the N_2 molecule was taken as 0.162 nm^2. The retained characteristics of the carbon dioxide, at 273 K, are as follows: saturated vapor pressure 34.40 MPa, cross-sectional area 0.18 nm^2, and density of adsorbed phase 1.038 g ml^{-1} [23].

The TPD method was used to determine the amounts of CO and CO_2 evolved upon heating under a flow of nitrogen up to 800 °C; a quadrupolar mass spectrometer was used to analyze the gases evolved during TPD.
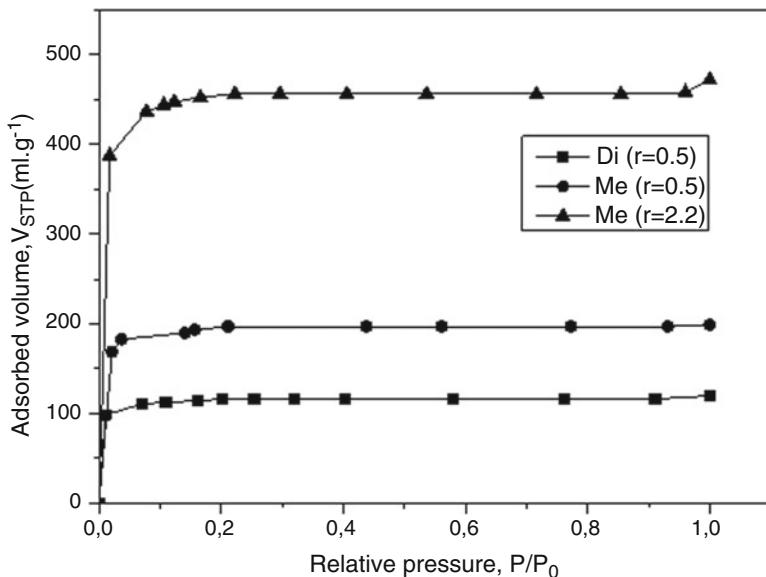
The enthalpies of immersion were determined at 293 K with a calorimeter of the Calvet type (Setaram MS 70), described previously by Stoeckli and Kraehenbuehl [24]. The liquids (HPLC grade, from Aldrich) were used in this study.

54.4   Results and Discussion
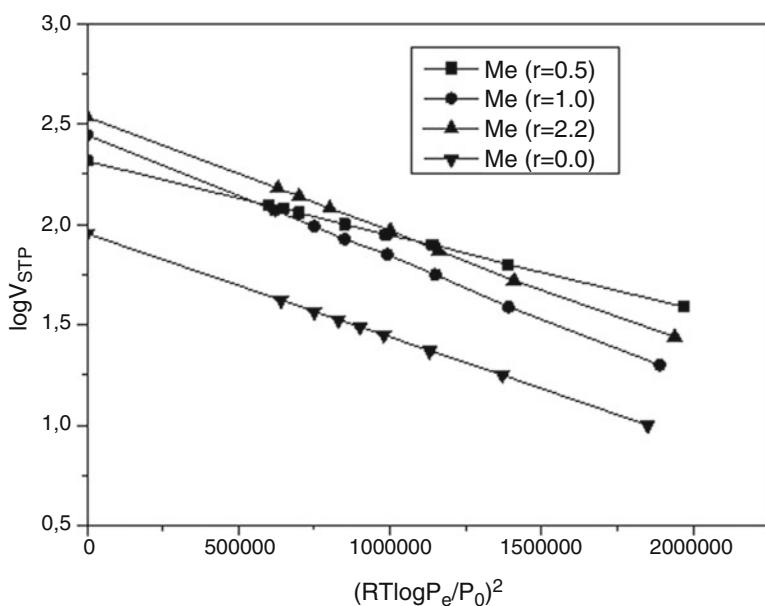
54.4.1   Porous Texture

The nitrogen adsorption isotherms at 77 K of the carbonized impregnated coals Di-KOH and Me-KOH are shown in Fig. 54.1 and those of the carbonized nonimpregnated coal Me (r = 0.0) and the carbonized impregnated coals Me-KOH and Me-K_2CO_3 in Figs. 54.2 and 54.3, respectively.
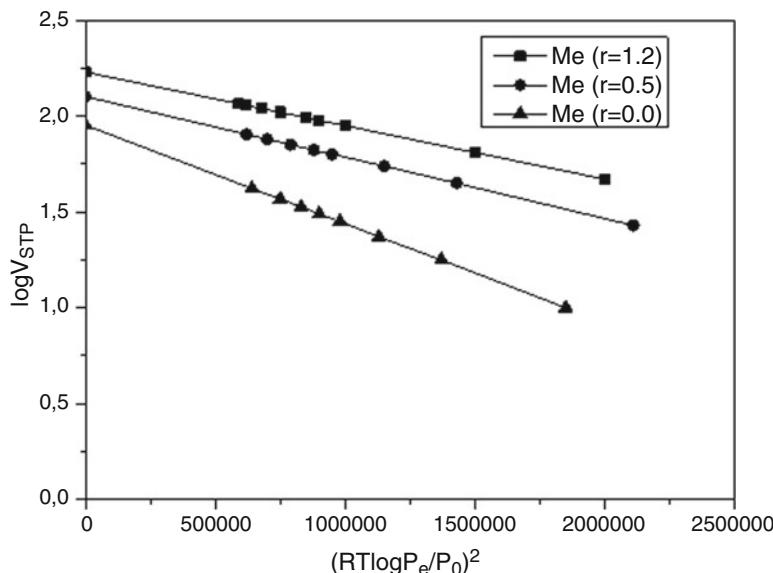
The values of the BET specific surface area, S_{N_2}, and the micropore volume and the micropore surface, W_0 and S_{CO_2}, are given in Table 54.2.

Fig. 54.1 Nitrogen adsorption isotherms, at 77 K, of the carbonized impregnated coals Di-KOH and Me-KOH

Fig. 54.2 Carbon dioxide adsorption isotherms at 273 K, in Dubinin's coordinates, of the carbonized nonimpregnated coal Me (r = 0.0) and the impregnated coal Me-KOH

Fig. 54.3 Carbon dioxide adsorption isotherms at 273 K, in Dubinin's coordinates, of the carbonized nonimpregnated coal Me (r = 0.0) and impregnated coal Me-K_2CO_3
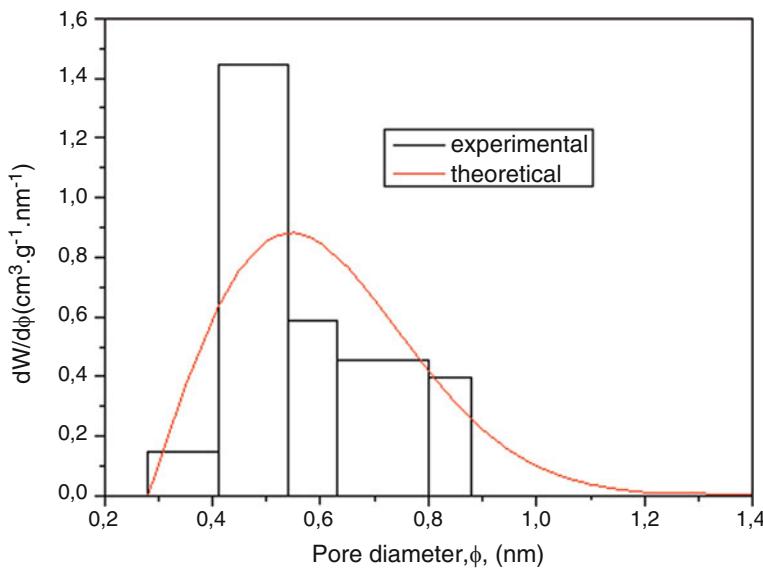
Table 54.2 BET specific surface area, S_{N_2}; micropore volume, W_0; and Dubinin specific micropore surface area, S_{CO_2}

	S_{N_2}—BET (m^2/g)	W_0 (cm^3/g)	S_{CO_2}—DR (m^2/g)
Me (r = 0.0)	0.5	0.17	436
Me-KOH (r = 0.5)	703	0.39	1,002
Me-KOH (r = 1.0)	Nd	0.528	1,352
Me-KOH (r = 2.2)	1,554	0.650	1,661
Me-K_2CO_3 (r = 0.5)	Nd	0.2405	615
Me-K_2CO_3 (r = 1.2)	Nd	0.322	823
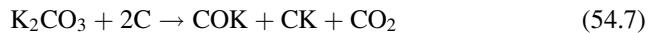
It is seen that the alkaline hydroxide is more effective than the corresponding carbonate. Otherwise, in the case of KOH, W_0 reaches considerably larger values. Thus for KOH content of 2.2 (r = 2.2), a highly activated carbon is obtained since their BET and Dubinin specific surface areas, S_{N_2} and S_{CO_2}, are of the order of 1,550 and 1,660 m^2 g^{-1}, respectively. Furthermore, an enlargement of the micropore size simultaneously occurs along with the increase of the pore volume [20]. Hence, it appears that upon carbonization of this coal in the presence of KOH, an activation process also takes place. These observations can be explained as follows [8]:

– *Dispersion step*:

$$2KOH+ > CH_2 \rightarrow K_2CO_3 + K_2O + 3H_2 \tag{54.6}$$

Fig. 54.4 Histogram of the micropore volumes for Me-KOH (r = 0.5)

$$K_2CO_3 + 2C \rightarrow COK + CK + CO_2 \tag{54.7}$$

– *Activation step*:

$$K_2O + C \rightarrow 2K + CO \tag{54.8}$$

$$K_2CO_3 + 2C \rightarrow 2K + 3CO \tag{54.9}$$

Indeed, the larger the amount of KOH or K_2CO_3, the larger the activation process will be. Moreover, KOH is more effective than K_2CO_3.

54.4.2 Pore Size Distribution

The histograms of the micropore volumes, W, are shown in Figs. 54.4, 54.5, and 54.6. They were calculated from the enthalpies of immersion by using Eq. (54.3). Considering the sample obtained after carbonizing of the coal Me, it appears that in the absence of KOH, the micropore volume is rather low. Moreover, the microporous texture of this carbon is not accessible to benzene, indicating the presence of very narrow pores of less than 0.41 nm in size. On the other hand, after carbonization in the presence of KOH (r = 0.5), one obtains a significant micropore volume. For this sample, the nitrogen adsorption isotherm is of type I (Fig. 54.1), the sign of
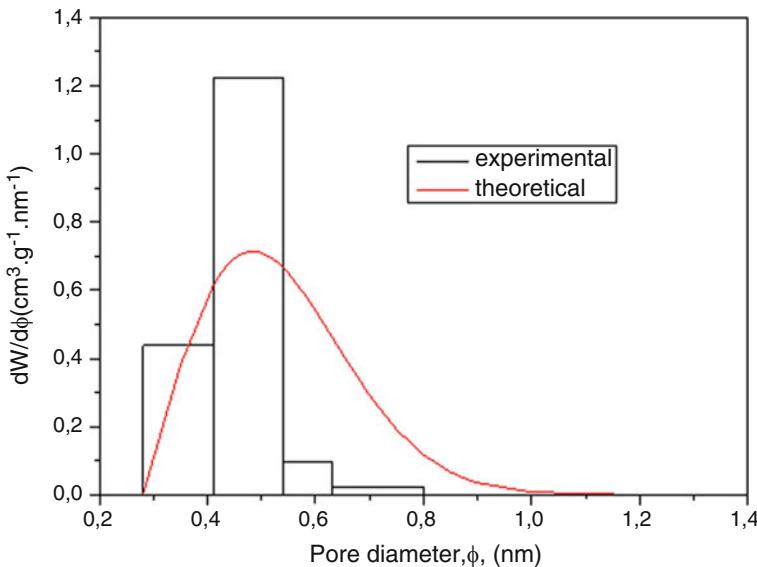
Fig. 54.5 Histogram of the micropore volumes for Me-K$_2$CO$_3$ (r = 0.5)
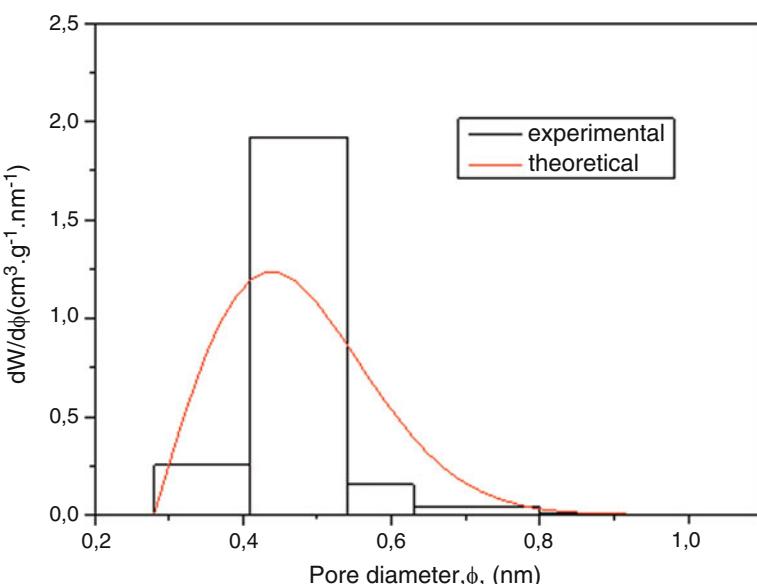
Fig. 54.6 Histogram of the micropore volumes for Me-K$_2$CO$_3$ (r = 1.2)

Table 54.3 Adsorbed amounts of CO_2 by activated carbons
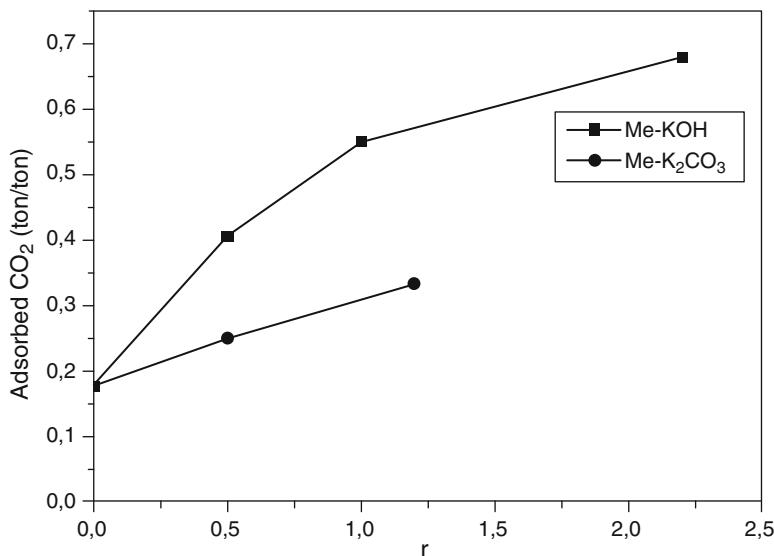
	W_0 (cm^3/g)	Adsorbed amount of CO_2 (g/g)
Me (r = 0.0)	0.17	0.177
Me-KOH (r = 0.5)	0.39	0.405
Me-KOH (r = 1.0)	0.528	0.550
Me-KOH (r = 2.2)	0.650	0.680
Me-K$_2$CO$_3$ (r = 0.5)	0.2405	0.250
Me-K$_2$CO$_3$ (r = 1.2)	0.322	0.334

a microporous texture with no appreciable external (non-microporous) surface area. Figures 54.4, 54.5, and 54.6 show the micropore distributions resulting from the volumes W(L) accessible to the different molecular probes. These volumes were calculated from the enthalpies of immersion, by using Eq. (54.3) with S_e = 0. There appears to be a widening of the micropore system, since molecules as large as C_5Cl_6 can penetrate to some extent into the porous texture. Otherwise, by increasing the amount of KOH, r, to 2.2, the micropore volume of the resulting sample, Me-KOH (r = 2.2), will become even higher and correspond to a well-activated carbon. In this case, immersion calorimetry indicates that the micropores are completely accessible to C_5Cl_6, the largest molecule of the series. This result illustrates the activation process occurring during carbonization of coal in the presence of KOH.

54.4.3 Amounts of Adsorbed CO_2

On the basis of combined adsorption and immersion techniques, and for strongly activated carbons, the initial adsorption stage corresponded essentially to secondary filling, i.e., to adsorption on the walls of wide pores followed by their gradual filling [25]. Thus, assuming the density of adsorbed phase of CO_2 equal to 1.038 g ml^{-1}, the adsorbed amounts by the prepared activated carbons can be calculated; they are shown in Table 54.3 and in Fig. 54.7.

One notices that the adsorbed quantities of CO_2 can reach important values. Indeed, the activated carbon Me-KOH (r = 2.2), which corresponds to a well-activated carbon because of its high micropore volume and its wide micropore diameter, can adsorb until 0.68 g/g, i.e., 0.68 ton/ton. At 293 K, the kinetic energy of CO_2 molecules is sufficient to overcome the potential barrier of the constrictions in the micropores [26]. Therefore, in our case, the coal Me treated by potassium hydroxide can be an excellent precursor for the production of activated carbons to trap and to store carbon dioxide.

Fig. 54.7 Adsorbed amount of CO_2 by activated carbons Me-KOH and Me-K_2CO_3

54.5   Conclusion

From these results it appears that potassium hydroxide is more effective than the corresponding carbonate and the larger the amount of KOH or K_2CO_3, the larger the activation process will be. Indeed, the most developed and the widest porosity is obtained with the KOH-activating agent. Otherwise, one notices that the adsorption capacities, at room temperature, of the prepared activated charcoals towards the carbon dioxide, a GHG, can reach high values (0.68 g g^{-1}, i.e., 0.68 ton/ton). Therefore, the coal Me can be an excellent precursor for the production of activated carbons for trapping and storage of carbon dioxide, the harmful effects and damages of which caused to environment have been known and proven.

References

1. Yun CH, Park YH, Park CR (2001) Effects of pre-carbonization on porosity development of activated carbons from rice straw. Carbon 39:559–567
2. Jagtoyen M, Thwaites M, Stencel J, McEnaney B, Derbyshire F (1992) Adsorbent carbon synthesis from coals by phosphoric acid activation. Carbon 30(7):1089–1096
3. Hayashi J, Kazehaya A, Muroyama K, Watkinson AP (2000) Preparation of activated carbon from lignin by chemical activation. Carbon 38:1873–1878

4. Suarez-Garcia F, Martinez-Alonso A, Tascon JMD (2004) Activated carbon fibers from Nomex by chemical activation with phosphoric acid. Carbon 42:1419–1426
5. Molina-Sabio M, Rodriguez-Reinoso F (2004) Role of chemical activation in the development of carbon porosity. Colloid Surface A 241:15–25
6. Gomez-Serrano V, Cuerda-Correa EM, Fernandez-Gonzalez MC (2005) Preparation of activated carbons from chestnut wood by phosphoric acid-chemical activation; study of microporosity and fractal dimension. Mater Lett 59:846–853
7. Marsh H, Yan DS, O'Grady TM, Wennerberg A (1984) Formation of active carbons from cokes using potassium hydroxide. Carbon 22(6):603–611
8. Ehrburger P, Addoun A, Addoun F, Donnet JB (1986) Carbonization of coals in the presence of alkaline hydroxides and carbonates: formation of activated carbons. Fuel 65(10):1447–1449
9. Verheyen V, Rathbone R, Jagtoyen M, Derbyshire F (1995) Activated extrutades by oxidation and KOH activation of bituminous coal. Carbon 33(6):763–772
10. Lillo-Rodenas MA, Lozano-Castello D, Cazorla-Amoros D, Linares-Solano A (2001) Preparation of activated carbons from Spanish anthracite. II. Activation by NaOH. Carbon 39:751–759
11. Addoun A, Dentzer J, Ehrburger P (2002) Porosity of carbons obtained by chemical activation: effect of the nature of the alkaline carbonates. Carbon 40:1140–1143
12. Hammond GP (2000) Energy, environment and sustainable development: a UK perspective. Trans I Chem E B Process Saf Environ Protect 78:304–323
13. Eshel G, Martin PA (2006) Diet, energy and global warming. Earth Interact 10:1
14. Socolow RH (2005) Can we bury global warming? Sci Am 293:49–55
15. Metz B, Davidson O, Bosch PR, Dave R, Meyer LA (eds) (2007) Climate change: mitigation of climate change. Cambridge University Press, Cambridge
16. Energy Information Administration (2009) Office of integrated analysis and forecasting. U.S. Department of Energy, International Energy Outlook, EIA, Washington, DC
17. Wang J, Chameides B (2007) Are humans responsible for global warming? Review of the facts. Environmental Defence, New York
18. Stoeckli HF, Kraehenbuehl F (1984) The external surface of microporous carbons, derived from adsorption and immersion studies. Carbon 22(3):297–299
19. Kipling JJ, Wilson RB (1960) Adsorption properties of polymer carbons. Part1. comparative data. Trans Faraday Soc 56:557–561
20. Kraehenbuehl F, Stoeckli HF, Addoun A, Ehrburger P, Donnet JB (1986) The use of immersion calorimetry in the determination of micropore distribution of carbons in the course of activation. Carbon 24(4):483–488
21. Adams LB, Boucher EA, Everett DH (1970) Adsorption of organic vapors by sara-fibre and powders. Carbon 8:761–772
22. Ainscough AN, Dolimore D, Heal GR (1973) The adsorption characteristics of polyvinylidene chloride carbon. Carbon 11:189–197
23. Garido J, Linares-Solano A, Martin Martinez JM, Molina-Sabio M, Rodriguez-Reinoso F, Torregrosa R (1987) Use of nitrogen vs. carbon dioxide in the characterization of activated carbons. Langmuir 3(1):76–81
24. Stoeckli HF, Kraehenbuehl F (1981) The enthalpies of immersion of active carbons, in relation to the Dubinin theory for the volume filling of micropores. Carbon 19:353–356
25. Stoeckli HF (1993) Dubinin's theory for the volume filling of micropores: an historical approach. Adsorp Sci Technol 10:3–16
26. Marsh H, Wynne-Jones WFK (1964) The surface properties of carbon. I. The effect of activated diffusion in the determination of surface area. Carbon 1:269–279

Chapter 55
Integrated Coal Power Plant and Cu–Cl Water Splitting Cycle for Greenhouse Gases Reduction

Calin Zamfirescu, Ibrahim Dincer, and Greg F. Naterer

Abstract In this chapter, a pulverized coal-fired power plant is integrated with a hydrogen-producing Copper–Chlorine (Cu–Cl) thermochemical cycle for emission reduction of greenhouse gases and cogeneration of hydrogen and electricity. A new furnace design is developed wherein low pressure steam at 900 K is generated as well as high pressure steam at 800 K. The low pressure steam is used to transfer heat to the Cu–Cl cycle for the endothermic high temperature reactors of hydrolysis and thermolysis. The chapter analyzes the system integration and performance in terms of efficiency and carbon dioxide emissions per unit of generated hydrogen. The specific carbon emissions are compared with a gasification system and with an integrated system of a nuclear supercritical water cooled reactor (SCWR) and Cu–Cl cycle. Although the SCWR system has a lower carbon footprint, the coal-based hydrogen system is thermodynamically more efficient. Also, the hydrogen generation efficiency with an integrated coal power plant and Cu–Cl cycle is compared to hydrogen production from coal gasification. It is found that the integrated system is less efficient but has more than 50 % less carbon footprint.

Keywords Emission reduction • Coal-fired power plant • Cu–Cl water splitting plant • Integrated system • Hydrogen production

C. Zamfirescu (✉) • I. Dincer
Faculty of Engineering and Applied Science, University of Ontario Institute of Technology, 2000 Simcoe Street North, Oshawa, ON, Canada L1H 7K4
e-mail: Calin.Zamfirescu@uoit.ca; Ibrahim.Dincer@uoit.ca

G.F. Naterer
Faculty of Engineering and Applied Science, Memorial University of Newfoundland, 240 Prince Phillip Drive, St. John's, NL, Canada A1B 3X9
e-mail: GNaterer@mun.ca

Nomenclature

Bi	Biot number
c_p	Specific heat, J/kgK
ex	Specific exergy, kJ/kg
$\dot{E}$	Energy rate, kW
$\dot{Ex}$	Exergy rate, kW
EF	Emission factor, kg CO_2/GJ
f	Dimensionless factor
Fo	Fourier number
GCV	Gross calorific value, MJ/kg
h	Specific enthalpy, kJ/kmol
H	Total enthalpy, kJ
HHV	Higher heating value, MJ/kg or MJ/mol
k	Thermal conductivity, W/mK
$\dot{m}$	Mass flow rate, kg/s
n	Molar fraction
NCV	Net calorific value, MJ/kg
Q	Heat flux, kJ
$\dot{Q}$	Heat flux rate, kW
Pr	Prandtl number
r	Radius, m
Re	Reynolds number
REF	Relative emission factor
S	Entropy, kJ/K
T	Temperature, K
w	Weight fraction
$\dot{W}$	Work rate, kW

Greek Letters

α	Heat transfer coefficient, W/m^{2}K
η	Energy efficiency (coal utilization fraction)
ε	Emissivity
ν	Stoichiometric number
ψ	Exergy efficiency
θ	Excess temperature, K
σ	Stefan–Boltzmann constant

Subscripts

0	Reference state
A	Ash
c	Convection
C	Fixed carbon
cal	Calandria
d	Destroyed
daf	Dry, ash-free basis
g	Gas
i	Index, or input
ign	Ignition
k	Index
M	Moisture
o	Output
P	Products
r	Radiation
R	Reactants
ref	Reference case
VM	Volatile matter

Superscripts

0	Standard state
ch	Chemical

55.1   Introduction

Coal is the most abundant among the fossil fuel resources. The world energy supply depends highly on coal combustion although the associated carbon dioxide emissions to the atmosphere by flue gas stacks contribute majorly to environmental pollution and global warming. Coal-fired power plants are mature technologies and they are used in nearly every country of the world.

In the past few decades, significant efforts have been made in the scientific and technical community towards improvement of coal-fired power plants for enhancing their efficiency and reducing their specific carbon emissions. Exergy analysis has been widely adopted in recent years as an important method of identifying irreversibility losses and efficiency improvement possibilities. Several case studies of exergy methods in fossil fuel based energy systems are described by Dincer and Rosen in Ref. [1]. The most significant exergy losses occur in the coal-fired steam generator. As indicated by a case study by Regulagadda et al. in Ref. [2], the exergy destruction in the steam generator of a coal-fired power plant represents over 85 %

of the total exergy destruction. In another example it is analyzed the coal-fired power plant from Nanticoke (Ontario) and found that the exergy destruction in the boiler represents close to 80 % of the total exergy destruction [3]. Sengupta et al. analyzed in Ref. [4] a 210 MW coal-fired power plant and concluded that the exergy destruction in the steam generator is over 60 %.

The high level of exergy destruction in the coal-fired boiler occurs because there is a large temperature difference between flue gas temperature profile and the temperature of water and steam along the heat transfer surface. As reported in [5] for a pulverized coal-fired furnace, the maximum flue gas temperature occurs just above the upper level burner which normally is about ¼ of the furnace height; this temperature could be around 1,500 K. The temperature decreases to 1,000 K at the highest point of the combustion channel, while the stack gas temperature is around 450 K. On the other hand, water is supplied to the combustion channel at a pressure of about 16 MPa and ~500 K. By heat addition, superheated steam is generated at ~800 K; the saturation temperature is ~620 K. The average pipe wall temperature of coal-fired burners across the boiling section is ~650 K [6].

In general, a gas-solid reaction such as a combustion process of coal powder is difficult to analyze. The combustion process is highly influenced by coal rank, its moisture content, and its ash content. According to the so-called coal rank, which expresses the geological maturity of coal, there are four categories of coal: lignite, sub-bituminous, bituminous, and anthracite. A review of heating value correlations and chemical exergy correlations and specific emissions for coal as a function of the rank is given in [7]. The gross calorific value of coal varies from 13 MJ/kg to ~34 MJ/kg; chemical exergy (which is sensitive to moisture content) varies from about 5 MJ/kg to ~25 MJ/kg; and the specific GHG emissions of coal combustion are in the range of 70–140 kg CO_2 equivalent per GJ on a net calorific value basis.

Note that two main combustion technologies are used currently for coal-based power plants, namely, those of pulverized coal boilers and fluidized bed boilers. Although the two technologies are different in regard to transport phenomena, the transient heat and mass transfer from a combusting coal particle to the surroundings are relatively similar in both cases.

The combustion process of coal particles involves drying, devolatilization, and chemical reactions. There is intense heat transfer between the solid particle—which is consumed during the reaction—and its surroundings. The heat transfer occurs by combined conduction, convection, and radiation. The main modeling assumptions are similar to those identified in a previous study [8]:

• Internal heat generation due to chemical reaction occurs at a constant rate.
• The thermo-physical properties of coal remain constant during the process.
• The coal particle is assumed spherical.
• The heat transfer is radial and one-dimensional.
• Just before pulverization, the particle has a uniform temperature distribution.

Pulverized coal-fired furnaces are crucial to the utility industry. Typically, pulverized coal-fired furnaces comprise a coal mill which grinds coal to form small powder-like particles conveyed with primary air to the pulverization point

where ignition occurs and bulk combustion air (preheated to ~600 K) is supplied. The combustion process occurs within seconds [9]. Thereafter, thermal energy of the hot flue gases is transferred to water and steam mainly by radiation heat exchange, whereas water and steam flow through a complex network of pipes which forms a large heat transfer surface area. Many design parameters are important to obtain a high efficiency of this type of furnace, namely, coal particle size distribution, rate of reaction of the devolatilization and oxidation processes, temperature evolution of coal particle, gas phase velocity, temperature of primary and secondary air, and other factors [10].

A dimensionless parameter (N_{com}) that describes the ignition process in pulverized coal-fired burners was discussed in Ref. [10]. This parameter represents the ratio between excess temperature at the ignition and initial temperatures. The excess temperature represents the difference between the ignition temperature and the initial coal particle temperature. The operating range is identified where N_{com} in the range of 1.1–1.8. After ignition, the coal temperature increases due to oxidation while hot flue gases are generated.

A method to improve the coal-fired boiler efficiency is to use coal gasification as a first step and then combustion of the produced syngas in a second step. A case study was presented by Dincer and Zamfirescu Ref. [11] where it was shown that by applying gasification, the LMTD (log-mean temperature difference in the furnace) can be substantially reduced. The carbon footprint of power plants can be reduced by using oxyfuel combustion as a method to facilitate carbon dioxide separation from flue gases. A review of carbon capture methods with oxyfuel combustion in energy systems was presented in Ref. [12].

This chapter presents a new method to enhance the coal-fired boiler efficiency by system integration with a Cu–Cl cycle for water splitting and hydrogen generation. Instead of generating electricity only, in the new approach, the coal-fired power plant works synergistically with a Cu–Cl chlorine water splitting plant to ultimately produce electricity and hydrogen with reduced GHG (greenhouse gas) emissions.

The Cu–Cl water splitting cycle is currently being investigated in several research centers around the world especially with a focus on nuclear based hydrogen production. A recent review on the Cu–Cl cycle and its development was presented in Refs. [13–15]. Particular attention is given to the integration of a Supercritical Water Reactor (SCWR) with a Cu–Cl cycle and steam Rankine cycle. The Cu–Cl cycle has two thermochemical reactors (for $CuCl_2$ hydrolysis and $CuO·CuCl_2$ thermolysis) and one electrochemical cell for hydrogen production by CuCl chlorination with HCl. All intermediate chemical compounds are recycled, while only water is consumed and oxygen and hydrogen are generated.

In the first part of this chapter, some necessary background information is given on the design and modeling of coal-fired furnaces, pulverized coal combustion process, and Cu–Cl water splitting plant. Subsequently, the integrated system and furnace concept proposed herein are described in detail. Further, the analysis and modeling aspects are discussed. The results section has three parts including: (1) furnace assessment, (2) integrated system efficiency and carbon footprint, and (3) emission comparison of the system with a nuclear based Cu–Cl water splitting plant. Point (3) represents the main focus of the chapter.

55.2 Background

Thermodynamic design and analysis of coal-fired power plants involve the prediction of thermal properties of coals including their calorific values, chemical exergy, and specific emissions. This type of general analysis provides information on maximum system efficiency and the minimum (theoretically possible) emissions per unit of power production; information which is crucial as a starting point of design and feasibility study.

The design of coal furnaces requires correlations for estimating the thermodynamic properties of products from coal combustion. The combustion process of coal starts by a physical–chemical process of devolatilization during which the volatile matter is released from solid material during heating. Devolatilization is an initial stage of a pyrolysis process. At the same time, tar is produced by distillation of organic compounds such as hydrocarbons from coal (which are a combination of aromatic and aliphatic chains). The solid material remaining after devolatilization and tar release is denoted as char.

The gross calorific value of coal can be correlated with the coal composition from proximate analysis according to the recent correlation [16]:

$$GCV = 0.35w_C + 0.33w_{VM} - 0.11w_M - 0.03w_A$$

where w represents the weight fraction and C, VM, M, A are subscripts indicating fixed carbon, volatile matter, moisture, and ash content, respectively. Based on the GCV, the net calorific value of coal can be determined provided that the weight fraction of hydrogen is known from the ultimate analysis. The following correlation shows how NCV can be estimated [17]:

$$NCV = GCV(1 - w_M) - 2.444w_M - 21.839w_H(1 - w_M)$$

Although coal can be approximated as a carbon–hydrogen blend in view of determining its specific entropy and chemical exergy, more elaborate predictive methods are available. The ultimate analysis of coal is required in order to predict the specific entropy according to Eisemann et al. [18] based on the following four factors:

$$f_1 = \frac{n_{H_2}}{n_{CN}}, \quad f_2 = \frac{n_{O_2}}{n_{CN}}, \quad f_3 = \frac{n_{N_2}}{n_{CN}}, \quad f_4 = \frac{n_S}{n_{CN}}, n_{CN} = n_C + n_{N_2}$$

where n represents the molar fraction of a chemical element among H_2, O_2, N_2, S. The correlation for specific entropy is expressed as follows:

$$s_{daf}^0 = 37.165 - 31.477e^{-0.564682f_1} + 20.1145f_2 + 54.3111f_3 + 44.6712f_4$$

where s_{daf}^0 is the specific entropy of coal in kJ/kg.K on a dry, ash-free basis at standard pressure and temperature conditions. The chemical exergy of coal can be

calculated based on s_{daf}^0 and GCV according to the equation proposed by Kaygususzin Ref. [19] as follows:

$$ex_{daf}^{ch} = GCV - T_0 \left(s_{daf}^0 + f_1 s_{O_2} - n_C s_{CO_2} - \frac{1}{2} n_{H_2} s_{H_2O} - n_S s_{SO_2} - \frac{1}{2} n_S s_{N_2} \right)$$
$$+ n_C\ ex_{CO_2}^{ch} + \frac{1}{2} n_{H_2}\ ex_{H_2O}^{ch} + n_S\ ex_{SO_2}^{ch} + \frac{1}{2} n_{N_2}\ ex_{N_2}^{ch} - f_2\ ex_{O_2}^{ch}$$

where ex_{daf}^{ch} represents the chemical exergy of coal on a dry, ash free basis, expressed in the same units as GCV, MJ/kg. The chemical exergy of coal on an as-received basis—also called wet basis—can be estimated as a function of ex_{daf}^{ch}, ash and moisture content according to the equation given in [20], namely:

$$ex^{ch} = (1 - w_M - w_A)ex_{daf}^{ch} + \frac{w_M}{M_{H_2O}} ex_{H_2O}^{ch}$$

where M_{H_2O} and $ex_{H_2O}^{ch}$ are the molecular mass and chemical exergy of water, respectively.

In a coal-fired power plant, it is important to determine the quantity of emitted GHG per unit of power produced. The ratio between the stoichiometric quantity obtained at coal combustion and the chemical exergy of coal can be used to estimate the minimum emissions which are obtained in the extreme case when the plant operates at the Carnot efficiency and ideal combustion process. This emission factor can be expressed with the following equation:

$$EF = \frac{44}{12} \frac{w_C}{ex^{ch}}$$

where 44 kg/kmol and 12 kg/kmol are the molecular masses of carbon dioxide and carbon, respectively.

The heat transfer from coal particles involves the heat conduction equation according to:

$$\frac{\partial^2 \theta}{\partial r^2} + \frac{2}{r} \frac{\partial \theta}{\partial r} + \frac{q'''}{k_c} = \frac{1}{a} \frac{\partial \theta}{\partial t}$$

where $\theta = T(r) - T$ is the excess temperature defined based on the local particle temperature $T(r)$ at the radial coordinate r and the initial particle temperature T_i; also, q''' is the heat generation due to the chemical reaction, k_c is the thermal conductivity of coal, and a is the thermal diffusivity of coal. The following boundary conditions exist at any local radius r, particle periphery ($r = R$), and time t:

$$\theta(r, 0) = 0, \quad \partial\theta(0, t)/\partial r = 0, \quad \text{and} \quad k[\partial\theta(R, t)/\partial r] + \alpha\theta(R, t) = 0$$

where α is the apparent heat transfer coefficient which includes the effects of forced convection from spherical particles and thermal radiation.

Table 55.1 Main processes of the copper–chlorine (Cu–Cl) water splitting cycle

Process	Chemical equation	T (K)	ΔH
Electrochlorination	E: $2CuCl(aq) + 2HCl(aq) \rightarrow H_2(g) + 2CuCl_2(aq)$	350	52.3[*]
Dehydration	T: $CuCl_2(aq) + nH_2O(l) \rightarrow CuCl_2 \cdot mH_2O(s)$ $+ (n - m)H_2O, n > 7.5$	473	122.2
Hydrolysis	T: $2CuCl_2 \cdot nH_2O(s) + H_2O(g) \rightarrow CuO \cdot CuCl_2(s)$ $+ 2HCl(g) + nH_2O(g), n = 0 - 4$	650	181.8
Thermolysis	T: $CuO \cdot CuCl_2(s) \rightarrow 2CuCl(l) + 0.5O_2(g)$	800	149.4

Note: E electrochemical step, T thermochemical step, ΔH reaction enthalpy or Gibbs energy ([*]) in kJ/mol H_2
Source: Ref. [21]

In the heat conduction equation, the thermal diffusivity of coal is calculated based on the relation $a = k_c/(\rho_c\, c_{p,c})$ where—as indicated in Ref. [8]—the thermal conductivity and specific heat of coal can be estimated as a function of temperature by
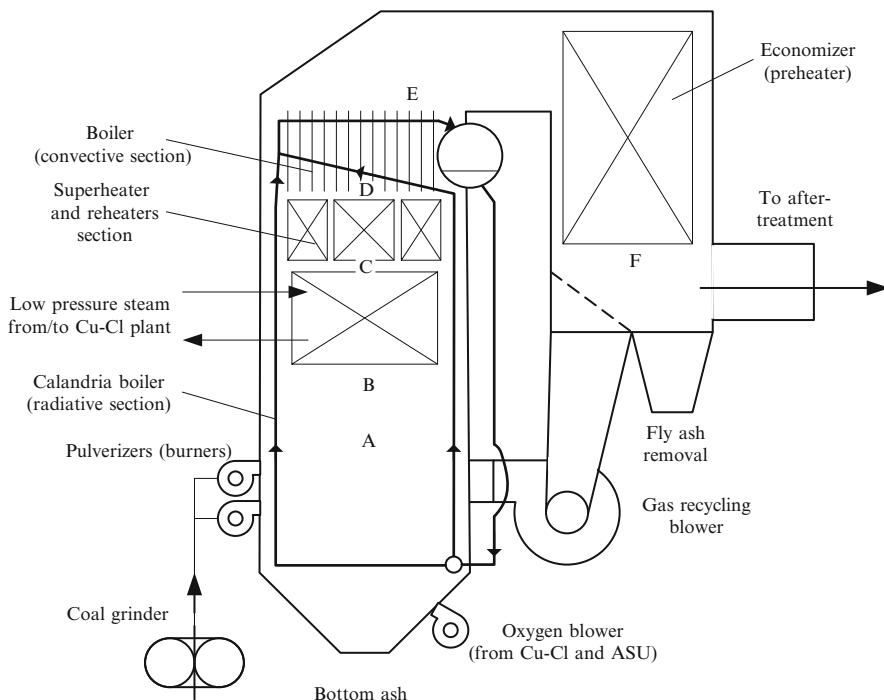
$$
\begin{cases}
k_c = 0.19 + 2.5 \times 10^{-4} \times (T - 300), & \left[\text{W/mK}\right] \\
c_{p,c} = 1.15 + 2.03 \times 10^{-3} \times (T - 300) - 1.55 \times 10^{-6} \times (T - 300)^2, & \left[\text{J/kgK}\right]
\end{cases}
$$

The analytical solution of the transient heat transfer equation was reported by Kilic et al. in Ref. [8] and can be expressed in a series form such as $\theta(t) = 1 - \sum [\prod A_{ij}(Fo,Bi,\alpha)]$ where each term of the series is a product of A_{ij} coefficients and each coefficient depends on various parameters such as the Fourier number (Fo), Biot number (Bi), and the apparent heat transfer coefficient (α).

The Cu–Cl cycle for water splitting consists of a number of physical and chemical reaction steps that are performed in a loop. There are many variants of this cycle, but the one adopted for the analysis in this chapter is presented in Table 55.1. This table shows the cycle steps with the associated temperature and the required energy input. Energy is provided both as heat and electricity. The amount of thermal and electrical energy required to generate one mole of hydrogen using this cycle is shown. Accordingly, one needs ~150 kJ/mol of heat at over 820 K, ~182 kJ/mol at a temperature over 670 K, ~123 kJ at a temperature over ~500 K, and ~53 kJ/mol of electrical energy.

55.3 Integrated System and Furnace Description

A modified furnace concept with pulverized coal is introduced as a main component of an integrated system that couples a steam Rankine power plant with a Cu–Cl water splitting cycle to the same source of energy. A low pressure steam reheater is the first heat exchanger in the flue gas stream.
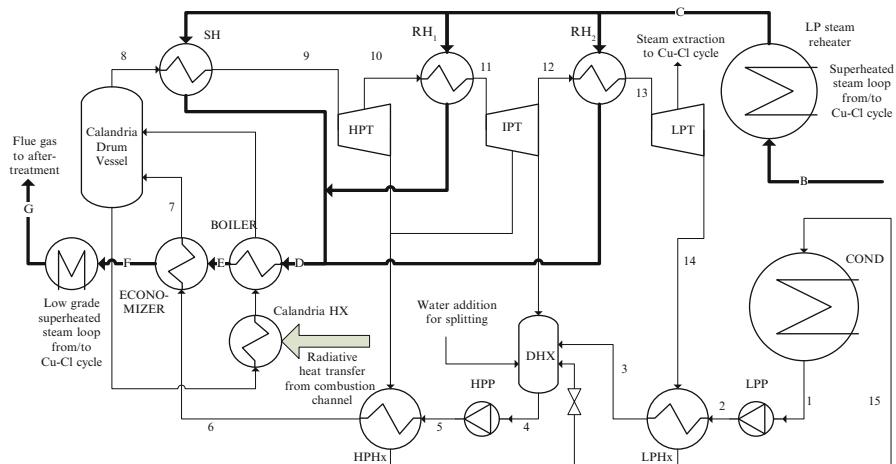
Fig. 55.1 Pulverized coal furnace for integrated copper–chlorine water splitting plant with steam Rankine power plant

The integrated system functions as follows:

- Heat of flue gases is transferred to the water preheater, boiler, superheater, and reheaters of the steam Rankine plant; simultaneously heat of the flue gases is transferred to a low pressure steam reheater that conveys thermal energy to the Cu–Cl plant. A new coal-fired furnace concept with a better temperature profile match between hot and cold streams is introduced.
- The Cu–Cl plant generates hydrogen and oxygen from water and the hydrogen is stored in a compressed form, while oxygen is used to conduct an oxyfuel combustion process with pulverized coal. In order to fulfill the need of oxidant, additional oxygen is generated from air using an air separation unit (ASU).
- The steam Rankine cycle generates power in which a part is supplied to the electrochemical reaction within the Cu–Cl cycle.
- Since oxyfuel combustion is applied, the oxygen supply rate can be adjusted such that a very limited amount of oxygen is present in the stack gases, which is composed of mainly carbon dioxide and steam. The stack gas is therefore partially recirculated and partially cooled to condense water and capture carbon dioxide.

Figure 55.1 illustrates the coal-fired furnace concept which integrates the Rankine power plant with Cu–Cl water splitting plant. Coal is pulverized at the lower

Fig. 55.2 Integrated system of coal-fired power plant with a Cu–Cl water splitting cycle for hydrogen production (only the power plant and heat supply system to the Cu–Cl cycle are represented; *bold lines* represent a flue gas stream flow corresponding to Fig. 55.1)

part of the furnace where it devolatilizes and ignites in an oxidative atmosphere. The average temperature of gases at the lower part of the furnace (below point A in the figure) is typically around 650–700 K. A calandria boiler system with pipes at the lower half of the furnace is installed. Heat transfer by radiation occurs between the hot gases and the pipes (with boiling water) placed at the channel periphery. In the first part of the combustion process, the volatiles are oxidized while the temperature of coal particle increases. Subsequently, carbon oxidizes and the flue gas temperature increases further. This process occurs approximately between locations A and B in the figure. In point B, coal particles are completely consumed and the flue gas temperature reaches its maximum value (around 1,200 K).
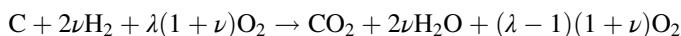
Between states B and C (see Fig. 55.2), hot flue gas exchanges heat by convection and radiation with low pressure steam in a heat exchanger linked to the heat supply circuit for the Cu–Cl cycle. In this heat exchanger, superheated steam is reheated from 800 to 900 K. In the path of flue gases, it follows two reheaters and the superheater of the steam Rankine power plant. In point D, the flue gas temperature reaches about 950 K. Furthermore, heat is transferred to the last segment of boiler (states D–E in the figure); note that state E at 820–850 K corresponds to the pinch point. It follows the economizer after which the flue gas temperature decreases to about 550 K. A part of the combustion gases—comprising mainly carbon dioxide, steam, and oxygen—is recirculated back to the combustion zone. The other part passes to the after-treatment section where gases are cleaned, particulate matter is extracted, further cooling water is condensed and carbon dioxide is captured.

Figure 55.2 represents the integrated system of a coal-fired power plant with a Cu–Cl cycle for hydrogen production. The heat generated by the combustion

process is transferred via multiple heat exchangers to the working fluid of the steam Rankine plant and to the Cu–Cl water splitting cycle. Radiative heat transfer exists at the bottom part of the furnace (until the maximum flue gas temperature point, B, in Fig. 55.1) between the hot gas and walls flanked with calandria pipes where forced convection boiling occurs. This process is represented in the diagram from Fig. 55.2 by the "Calandria HX." Furthermore, hot flue gases in state B (see Fig. 55.2) pass through the low pressure steam reheater and then are diverted to the superheating heat exchanger (SH) and the reheater heat exchangers (RH1 and RH2), connected in parallel at the hot stream side. Next the flue gas is directed to the boiler (D–E) and then the economizer (E–F). The lowest grade heat recovered at the economizer section (F–G) of the furnace is transferred to the dehydration process within the Cu–Cl cycle. The steam generated in the low pressure superheater is transported to the Cu–Cl cycle for heating purposes; this is a secondary steam circuit. Steam for water splitting purposes is extracted from the low pressure turbine (LPT) of the power plant. In order to maintain the working fluid balance within the Rankine plant, fresh water is supplied to the direct contact heat exchanger (DHX) in the same amount as it is extracted as steam from the LPT. The component labels in Fig. 55.2 are as follows: COND—condenser, LPP—low pressure pump, LPHx—low pressure heat exchanger (preheater), DHX—direct contact heat exchanger (and deaerator), HPP—high pressure pump, HPHx—high pressure heat exchanger (preheater), SH—superheater, RH—reheater, HPT—high pressure turbine, IPT—intermediate pressure turbine, LPT—low pressure turbine.

55.4   System Analysis and Modeling

As a first step of system analysis, thermodynamic modeling can be applied, based on several assumptions. The crucial component of the system is the pulverized coal furnace which generates thermal energy for both the power plant and water splitting plant. The oxyfuel combustion of coal can be modeled by the following equation, namely:

$$C + 2\nu H_2 + \lambda(1 + \nu)O_2 \rightarrow CO_2 + 2\nu H_2O + (\lambda - 1)(1 + \nu)O_2$$

where ν represents a stoichiometric number accounting for the hydrogen content of coal. It is assumed that coal is modeled with sufficient accuracy for the purpose of this study as a substance comprising only coal and hydrogen.

In the above equation, the excess oxidant for combustion is denoted with λ. During the combustion process, volatile matter emanates from the pulverized coal particle and ignites. The particle temperature increases until a level when carbon combustion initiates and further the particle is consumed due to the oxidation process occurring with a continuous emanation of hot flue gases. During all processes, heat is exchanged via radiation with the colder walls of the furnace at

the bottom side. The walls are lined with calandria tubes where water boils in forced convection. Therefore, the energy balance of the combustion process is:

$$H_R = H_P + Q_{ign}$$

where $H_{R,P}$ represents the total enthalpy of reactants and flue gases, respectively and Q_{ign} is the total heat transfer by radiation from hot coal particles and hot combustion gases to the calandria pipes. The enthalpy of the reactants is expressed in the following manner for one mole of carbon combusted:

$$H_R = h_C + 2\nu h_{H_2} + \lambda(1 - \nu)h_{O_2} + y[h_{CO_2} + 2\nu h_{H_2O} + (\lambda - 1)(1 + \nu)h_{O_2}]$$

where h represents the molar specific enthalpy and y is the recycling fraction of combustion gases. Note that the y fraction of combustion gases from the state indicated with F in Figs. 55.1 and 55.2 is recycled and reinjected back to the combustion chamber. The recycling fraction of gases comprises oxygen which enters in the combustion reaction with volatiles and coal; the other part of recycled gases has the role of a heat transfer medium and an adjusting mechanism of the flue gas temperature. If the recycling fraction is high, the flue gas temperature is lower, and vice versa. The enthalpy of products is expressed by:

$$H_P = h_{CO_2} + 2\nu h_{H_2O} + (\lambda - 1)(1 + \nu)h_{O_2}$$

Note that the enthalpy of products (H_P) is calculated for the highest temperature of flue gases (state B), whereas the enthalpy of recycled gases (which is the term $y[...]$ in the equation for H_R given above) is calculated for a lower temperature, corresponding to state E. The heat exchange by radiation during the combustion phase is determined by:

$$\dot{Q}_{ign} = \alpha_r A_{cal}(\overline{T}_g - \overline{T}_{cal})$$

where A_{cal} is the heat transfer area of calandria tubes, $\overline{T}_{cal}$ represents the average temperature of calandria tubes, $\overline{T}_g$ is the average temperature of hot gases during the ignition period and α_r is the linearized coefficient at heat transfer by radiation, defined by

$$\alpha_r = \sigma\varepsilon(\overline{T}_g + \overline{T}_{cal})(\overline{T}_g^2 + \overline{T}_{cal}^2)$$

Here, σ is the Stefan–Boltzmann constant and ε is the emissivity of tubes surface. In the above equation, the shape factor of heat transfer by radiation is assumed to unity, due to the large cross-sectional opening of the furnace at its bottom side.

As stated previously, this chapter focuses on pulverized coal-fired boilers and their integration with thermochemical water splitting systems. The heat transfer

coefficient can be expressed as the sum of heat transfer by convection and by radiation, $\alpha = \alpha_c + \alpha_r$, where, as shown in Ref. [8], the convective component can be calculated with

$$\alpha_c = \frac{k_g}{2r} \times \left(2 + 0.6 \ Re^{05} \ Pr^{1.3}\right)$$

whereas the heat transfer from radiation in its linearized form is calculated with an equation which is similar to that given above for heat transfer coefficient by radiation, where ε is the emissivity of coal and the temperatures are that of the coal particle surface and the average temperature of surrounding gases. In the equation for convective heat transfer coefficient, k_g is the thermal conductivity of the gaseous phase surrounding the coal particle (combustion gases), and Re and Pr are the Reynolds and Prandtl numbers calculated for the average properties of combustion gases.

All processes of the integrated system are modeled by steady-state operation. Energy, entropy, and exergy as well and mass balance equations are written for each system component and the overall assembly. For any component "i" enclosed in a control volume, these equations involve the inlet (subscript i) and outlet (subscript o) mass flow rates $(\dot{m})$, heat transfer rates $\left(\dot{Q}\right)$ to (subscript i) and from (subscript o) the system, work production rate $\left(\dot{W}\right)$, entropy generation rate $\left(\dot{S}_{gen}\right)$, exergy rate $\left(\dot{Ex}$ at inlet and outlet$\right)$, exergy destruction rate $\left(\dot{Ex}_d\right)$, the corresponding process temperature (T), and the temperature of the reference environment (T_0). The following set of equations can be written for each system component:

$$\begin{cases} \sum_i \dot{m}_i = \sum_o \dot{m}_o \\ \sum_i \dot{E}_i + \dot{Q} = \sum_o \dot{E}_o + \dot{W} \\ \sum_i S_i + \sum_i \left(\frac{\dot{Q}}{T}\right)_i + \dot{S}_{gen} = \sum_o S_o + \sum_o \left(\frac{\dot{Q}}{T}\right)_o \\ \sum_i \dot{Ex}_i + \sum_k \left(1 - \frac{T_0}{T_k}\right)\dot{Q}_k = \sum_o \dot{Ex}_o + \dot{W} + \sum_o \dot{Ex}_d \end{cases}$$

Based on energy analysis of the system, the fuel utilization efficiency (η) can be introduced, while based on exergy analysis, the exergy efficiency (ψ) can be defined. These system assessment parameters are defined by

$$\begin{cases} \eta = \dfrac{\dot{W} + \dot{m}_{H_2} \times HHV_{H_2}}{\dot{m}_{coal} \times HHV_{coal}} \\[3mm] \psi = \dfrac{\dot{W} + \dot{m}_{H_2} \times ex^{ch}_{H_2}}{\dot{m}_{coal} \times ex^{ch}_{coal}} \end{cases}$$

where, as already mentioned above, it is assumed that coal is modeled as a compound formed of carbon and hydrogen, therefore $HHV_{coal} = h_C + 2\nu \times HHV_{H_2}$ and h_C is the formation enthalpy of coal (graphite), and ex^{ch} represents the molar specific chemical exergy.

55.5   Results and Discussion

The first part of the results refers to the furnace design. A computer code has been written to solve simultaneously the energy balance equations and heat transfer equations for the combustion zone. The result this simulation code is the flue gas temperature at point B and the heat transfer rate from hot gases to the calandria system at furnace bottom $\dot{Q}_{ign}$. The main assumed parameters for modeling are summarized in Table 55.2. The variation of flue gas temperature (T_{fg}) with oxidant excess ratio (λ) is presented in Fig. 55.3 for three cases of stack gas recycling fraction. Reasonable values of (λ) of 5–20 correspond to flue gas of 1,100–1,300 K.

Figure 55.3 superimposes the profile of partial pressure of oxygen in stack gases (P_{O_2}) which also corresponds to molar concentration. Very low oxidant concentration in flue gases is obtained for high recycling ratios. A recycling ratio of 0.9 is selected with an oxidant excess ratio of 3 in order to obtain a good utilization factor of oxygen corresponding to a concentration in stack gases of less than 6 % and flue gas temperature of around 1,200 K.
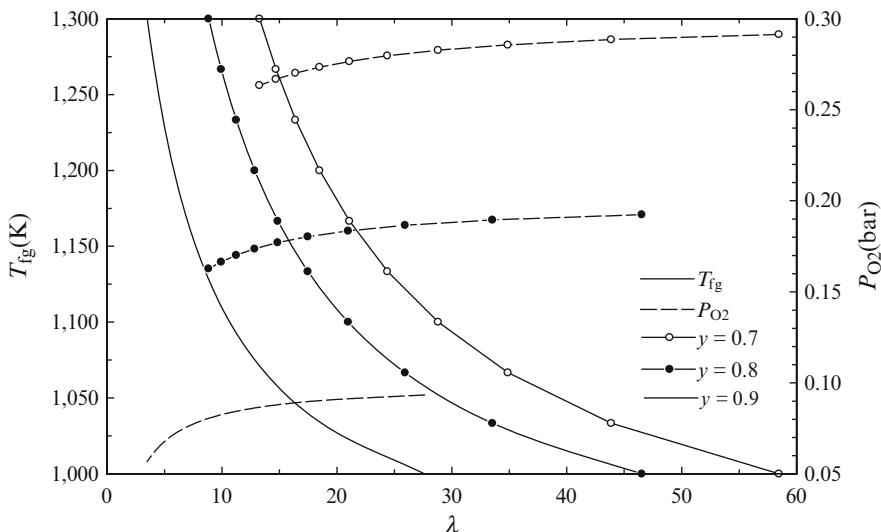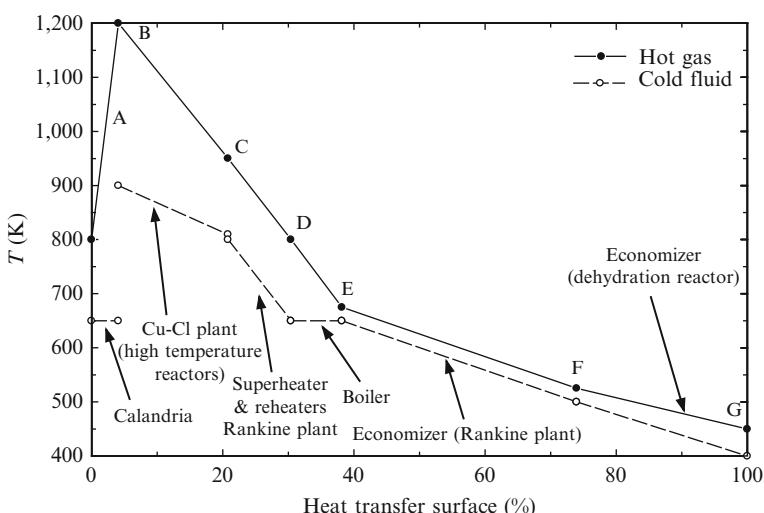
The next result studies the temperature vs. heat transfer surface diagram of the modified coal-fired furnace. This diagram has been obtained by determining heat transfer coefficients for each zone. Starting from the furnace bottom, the following heat transfer processes occur:

- Pulverized coal combustion and radiative heat transfer occur to the calandria tubes. As mentioned above, there is a first phase of this process of coal devolatilization (process before point A) followed by carbon combustion (A–B). The estimated heat transfer via thermal radiation is 200 W/m^{2}K which corresponds as an order of magnitude to the past study by Kilic et al. [8].
- B–C radiative and convective heat transfer to the low pressure steam, which transports heat to the high temperature reactors of the Cu–Cl plant.
- C–D radiative and convective heat transfer to the reheaters and superheater of the steam Rankine plant.
- D–E radiative and convective heat transfer to the boiler.
- E–F convective heat transfer to the water preheater.
- F–G convective heat transfer to low pressure steam to transport heat to the dehydration reactor of the Cu–Cl plant.

The next result refers to exergy and energy analysis of the integrated system for hydrogen and power production. The Rankine cycle is modeled based on mass, energy, entropy, and exergy balances. The level of temperatures of the working fluid at the furnace is obtained from the diagram in Fig. 55.4. Table 55.3 shows the

Table 55.2 Assumed parameters for simulations

Molar fraction H:C for coal (2ν)	2
Thermal conductivity of gases (k_g)	0.05 W/mK
Prandtl number (Pr)	0.7
Emissivity of coal (ε)	0.93
Density of coal (ρ_c)	1,080 kg/m^3
Particle inlet temperature (T_i)	300 K
Thermal diffusivity of coal particle (a)	1.9×10^{-7} m^2/s

Fig. 55.3 Flue gas temperature and partial pressure in stack gases as a function of oxidant excess ratio (λ)

Fig. 55.4 Temperature vs. heat transfer surface diagram for the modified coal-fired furnace

Table 55.3 Thermodynamic parameters of state points of integrated system (Fig. 55.2)
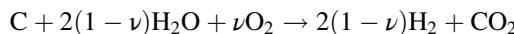
State	1	2	3	4	5
T (°C)	40.0	40.4	209.9	239.8	244.1
P (kPa)	7.4	3,424	3,424	3,424	15,893
h (kJ/kg)	167.5	172.4	897.6	1,036	1,058
s (kJ/kgK)	0.57	0.57	2.42	2.70	2.71
State	6	7	8	9	10
T (°C)	226.9	346.9	346.9	526.9	247.3
P (kPa)	15,893	15,893	15,893	15,893	1,231
h (kJ/kg)	978.7	1,645	2,584	3,375	2,927
s (kJ/kgK)	2.56	3.74	5.25	6.40	6.80
State	11	12	13	14	15
T (°C)	526.9	280.6	526.9	283.1	40
P (kPa)	1,231	95.31	95.31	7.4	7.4
h (kJ/kg)	3,535	3,035	3,546	3,043	2,573
s (kJ/kgK)	7.74	8.17	8.93	9.36	8.25

Note: specific values are given with respect to the mass of the working fluid in the Rankine cycle
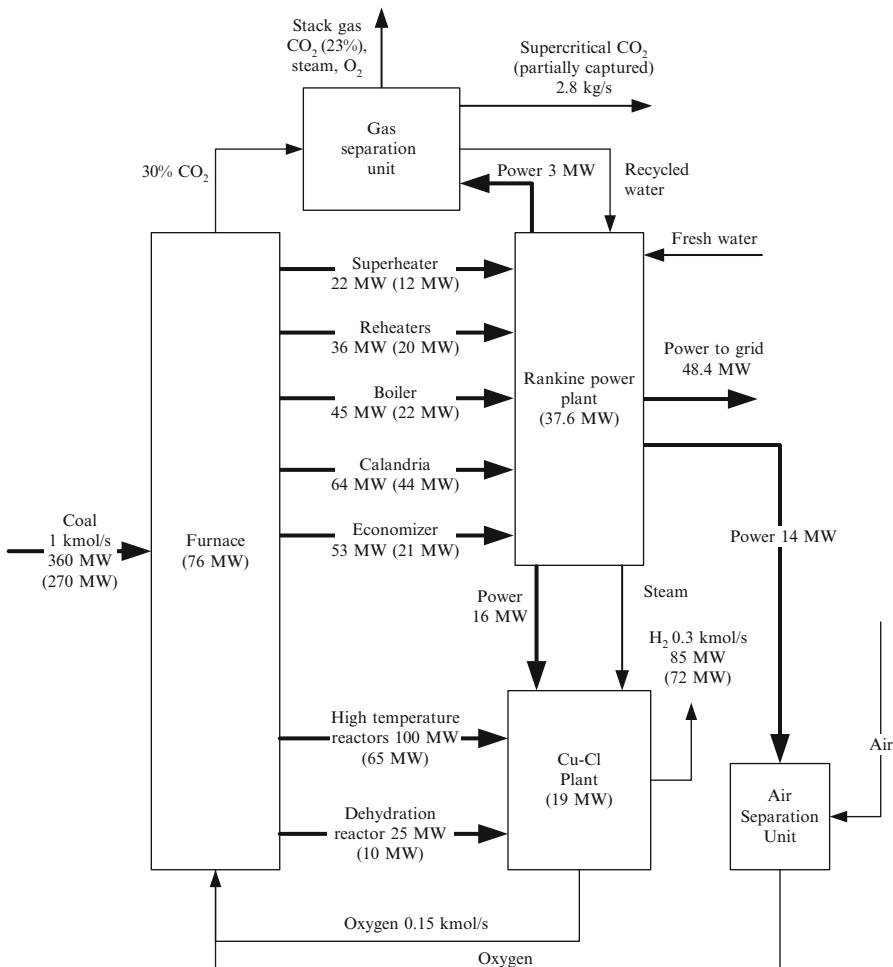
indicated parameters for each state point represented in the system diagram from Fig. 55.2. The results of the thermodynamic analysis of the integrated system are presented in Fig. 55.5.

As indicated in Fig. 55.5, the flow rate of coal is assumed to be 1 kmol/s; in the conditions considered here, it yields an exergy destruction in the furnace of 76 MW and the furnace operates with 71 % exergy efficiency. The exergy destruction in the Rankine plant is 37.6 MW while its energy efficiency is 37 % and the exergy efficiency is 68 %. The exergy efficiency of the Cu–Cl plant is estimated to be 79 % provided that 50 % of the heat is recovered inside the cycle, and the rejected heat has very low grade.

The carbon emissions of the integrated system are 84 g CO_2 emitted per MW of exergy generated (of which 60 % represents hydrogen product and 40 % represents electricity to the grid). In other words, the carbon emissions can be expressed as 50 g CO_2 emitted per MW of exergy in hydrogen produced, or 6 kg CO_2 emitted per kg of produced hydrogen. This amount can be compared with the carbon dioxide emissions of coal gasification. An autothermal coal gasification process uses energy from the coal combustion in order to extract hydrogen from water. The process can be described by the following overall chemical equation:

$$C + 2(1 - \nu)H_2O + \nu O_2 \rightarrow 2(1 - \nu)H_2 + CO_2$$

In it is assumed—conservatively, for determining the CO_2 emissions—that coal can be modeled as carbon. By setting the reaction enthalpy of Eq. (55.10) to zero and solving for the stoichiometric number, ν, which must take values between 0 and 0.5, one obtain $\nu = 0.31$s, therefore 1.38 moles of hydrogen must be produced for one mole of carbon in an autothermal coal gasification process. It follows that carbon dioxide emissions of a coal gasification plant are at least higher
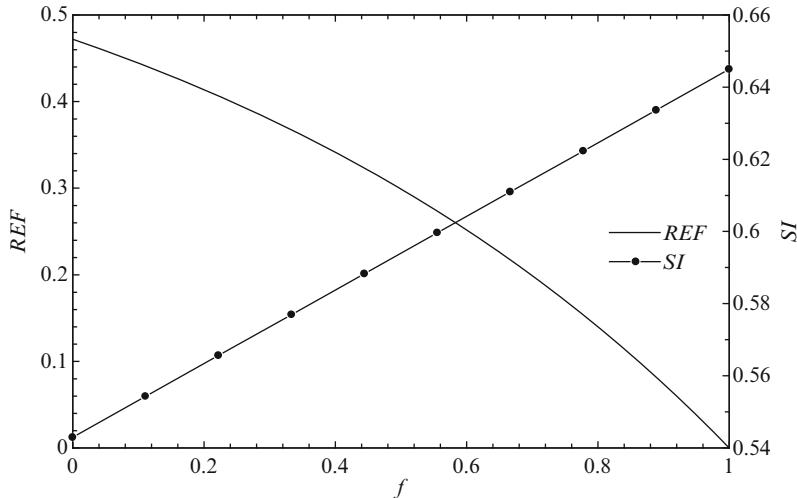
Fig. 55.5 Thermodynamic energy and exergy analysis of the integrated coal-fired plant for hydrogen and power production (note: figures in the parentheses represent exergy)

than 16 kg CO_2 per kg H_2. This figure represents a reference value for estimation of the carbon mitigation potential of other coal-fired hydrogen production systems such as those considered in this chapter.

We denote in this chapter the GHG emissions per unit of hydrogen generated as emission factor EF. As stated, the reference value of the emission factor is EF_{ref} = 16 kg CO_2 per kg H_2. We further introduce the relative GHG emissions factor (REF) according to the following definition equation

$$REF = EF / EF_{ref}$$

where EF represents carbon dioxide emissions per kg of hydrogen production.
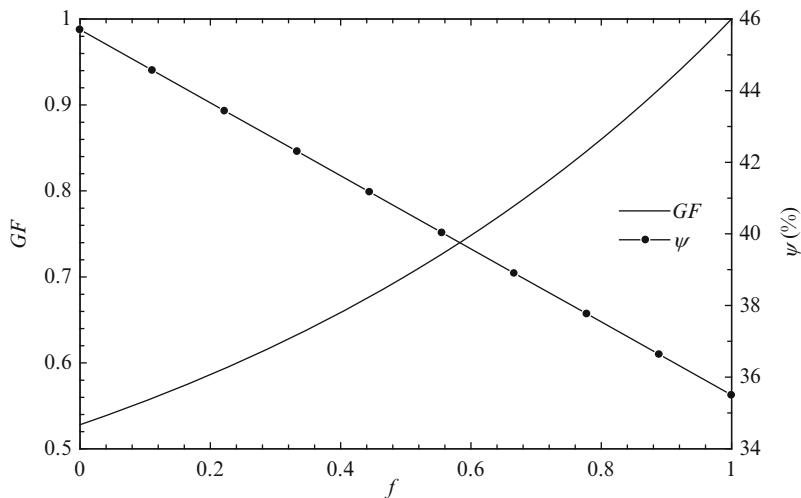
Fig. 55.6 Variation of carbon emissions relative to coal gasification and sustainability index with CO_2 capture fraction (f) for the integrated coal-fired system for hydrogen production
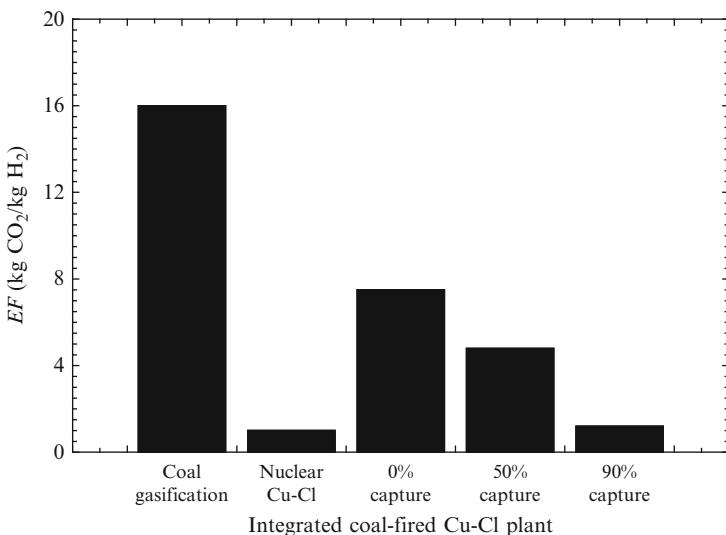
Based on the definition equation for *REF* and the thermodynamic model of the integrated system, the graph from Fig. 55.6 is obtained, where the carbon mitigation potential and the sustainability index are plotted against the carbon dioxide capture fraction (f). The sustainability index (*SI*) was introduced in a past paper of Dincer and Rosen [22]. The CO_2 capture fraction is varied from 0 to 1, where 0 represents a "no capture" case while 1 represents the case when all CO_2 is captured from the stack gas. When CO_2 is captured, there is an energy penalty on net production of electricity, while the production of hydrogen is not influenced.

It can be observed from Fig. 55.6 that the sustainability index of the system improves by more than 10 % when carbon is captured completely. A similar plot as Fig. 55.6 is shown in Fig. 55.7, where the "greenization factor" and exergy efficiency of the integrated system are plotted against carbon capture fraction. The greenization factor has been introduced in past work by Dincer and Zamfirescu [11] and it can be defined as $GF = 1 - REF$. It can be shown that the exergy efficiency penalty due to carbon capture is slightly higher than 10 % while the greenization factor improves by about 0.5 units. This implies that the integrated system without carbon dioxide capture is 50 % greener than the reference system of coal gasification for hydrogen production.

The last result is a comparative assessment of nuclear based and coal-fired production of hydrogen and coal with an integrated system including the Cu–Cl water splitting cycle. The environmental impact of nuclear based hydrogen production with a Cu–Cl water splitting cycle has been studied in detail by Ozbilen et al. [23]. According to these past studies, it appears that the global warming potential of the system is on the order of 10^9 kg CO_2, for a plant with 125 t H_2 production per day. This estimate is based on a life cycle assessment. The upper bound of carbon

Fig. 55.7 Greenization factor and exergy efficiency of integrated system as a function of carbon capture ratio

Fig. 55.8 Emissions comparison of two integrated hydrogen production systems based on Cu–Cl water splitting cycle (note: reference coal gasification system is in the plot)

emissions of the system is slightly below 1 kg CO_2 per kg of H_2 produced. This estimate considers the indirect emissions related to the nuclear power plant since no direct carbon dioxide pollution is produced at these facilities. In the plot of Fig. 55.8, comparisons are shown for the emissions of the reference coal gasification plant, the

nuclear based Cu–Cl integrated plant and the coal-fired integrated plant for hydrogen and power generation. Even without carbon capture, a coal-fired integrated plant is better from a pollution point of view than the coal gasification system. When carbon capture is applied, the coal-fired integrated system approaches (with respect to pollution mitigation) the nuclear based system which is the most environmentally benign.

55.6   Conclusions

In this chapter, a new integrated system including a Cu–Cl water splitting plant, a steam Rankine power plant, an air separation unit, and a carbon dioxide carbon unit is presented. The source of energy is derived from coal and the source of hydrogen is water. A new coal-fired furnace is conceptually designed which implements oxyfuel combustion. The furnace has additional heat exchange units with respect to a coal-fired system, such that high temperature heat is transferred to the Cu–Cl plant. The following specific conclusions can be drawn from this chapter.

- Flue gas recirculation is beneficial for heat transfer purposes within the furnace and as a source of recycled oxygen. A recirculation fraction of the order of 0.8–0.9 can be used.
- By placing additional high temperature heat exchangers in the furnace, such as low pressure steam reheaters and an additional economizer with low pressure steam, the temperature profile of fluids that exchange heat is matched better with respect to common furnaces, and thus the exergy efficiency of the furnace reaches ~70 %.
- Carbon emissions are reduced by at least 50 % with respect to the reference case of coal gasification when the novel integrated system is used.
- If carbon capture is applied, there is an exergy efficiency penalty, which, as a function of the carbon capture fraction, can reach up to 12 %.
- The sustainability index and greenization factor improve substantially when carbon capture is applied.
- With respect to a nuclear based integrated system and a Cu–Cl cycle, the coal-fired system emits roughly seven times more greenhouse gases. This figure is reduced substantially if carbon capture is applied.

This chapter presents a thermodynamic analysis and heat transfer modeling of the coal-fired furnace that generates superheated steam at low pressure for Cu–Cl plant and, simultaneously, supplies heat to a steam Rankine power plant. The results are promising to encourage more detailed studies with respect to system design and optimization, efficiency, and pollution assessment.

References

1. Dincer I, Rosen MA. Exergy: energy. Environment and Sustainable Development. New York: Elsevier; 2007.
2. Regualgadda P, Dincer I, Naterer GF. Exergy analysis of a thermal power plant with measured boiler and turbine losses. Appl Therm Eng. 2010;30:970–6.
3. Rosen MA. Energy- and exergy-based comparison of coal-fired and nuclear steam power plants. Exergy Int J. 2001;1:180–92.
4. Sengupta S, Datta A, Duttagupta S. Exergy analysis of a coal-based 210 MW thermal plant. Int J Energ Res. 2007;31:14–28.
5. Chu J-Z, Shieh S-S, Jang S-S, Chien C-I, Wan H-P, Ko H-H. Constrained optimization of combustion in a simulated coal-fired boiler using artificial neural network model and information analysis. Fuel. 2003;82:693–703.
6. Zheng S, Luo Z, Zhang X, Zhou H. Distributed parameters modeling for evaporation system in a once-through coal-fired twin-furnace boiler. Int J Therm Sci. 2011;50:2496–505.
7. Dincer I, Zamfirescu C. Sustainable energy systems and applications. New York: Springer; 2011.
8. Kilic YA, Kahveci N, Dincer I, Bardakci T. An experimental and theoretical investigation of transient heat transfer between a spherical coal particle and air medium during devolatilization. Int Commun Heat Mass Transf. 1993;20:711–20.
9. Singer JG. Combustion fossil power. A reference book on fuel burning and steam generation. New York: Combustion Engineering Power System Group; 1991.
10. Xu M, He X, Azevedo JLT, Garvalho MG. Flexibility using CFD results and simplified heat transfer model for pulverized coal-fired boilers. Int J Energ Res. 2000;24:1161–9.
11. Dincer I, Zamfirescu C. Potential options to greenize energy systems. Energy. 2012;46:5–15.
12. Habib MA, Badr HM, Ahmed SF, Ben-Mansour R, Mezghani K, Imashuku S, Ia O' GJ, Shao-Horn Y, Mancini ND, Mitsos A, Kirchen P, Ghoneim AF. A review of recent developments in carbon capture utilizing oxy-fuel combustion in conventional and ion transport membrane systems. Int J Energ Res. 2011;35:909–22.
13. Naterer GF, Suppiah S, Stolberg L, Lewis M, Ferrandon M, Wang Z, Dincer I, Gabriel K, Rosen MA, Secnik E, Easton EB, Trevani L, Pioro I, Tremaine P, Lvov S, Jiang J, Rizvi G, Ikeda BM, Luf L, Kaye M, Smith WR, Mostaghimi J, Spekkens P, Fowler M, Avsec J. Clean hydrogen production with the Cu-Cl cycle – progress of international consortium, I: experimental unit operations. Intl J Hydrogen Energ. 2011;36:15472–85.
14. Naterer GF, Suppiah S, Stolberg L, Lewis M, Ferrandon M, Wang Z, Dincer I, Gabriel K, Rosen MA, Secnik E, Easton EB, Trevani L, Pioro I, Tremaine P, Lvov S, Jiang J, Rizvi G, Ikeda BM, Luf L, Kaye M, Smith WR, Mostaghimi J, Spekkens P, Fowler M, Avsec J. Clean hydrogen production with the Cu-Cl cycle – progress of international consortium, II: simulations, thermochemical data and materials. Intl J Hydrogen Energ. 2011;36:15486–501.
15. Naterer GF, Dincer I, Zamfirescu C (2013) Hydrogen production from nuclear energy. Springer: New York.
16. Majumder AK, Jain R, Banerjee P, Baewal JP. Development of a new proximate analysis based correlation to predict calorific value of coal. Fuel. 2008;87:3077–81.
17. Van Loo S, Koopejan J. The handbook of biomass combustion and co-firing. Sterling, VA: Earthscan; 2008.
18. Eiserman W, Johnson P, Conger WI. Estimating thermodynamic properties of coal, char, tar, and ash. Fuel Process Technol. 1980;3:39–53.
19. Kaygusuz K. Chemical exergy of some coals in Turkey. Energ Source A. 2009;31:299–307.
20. Bilgen S, Kaygusuz K. The calculation of the chemical exergies of coal-based fuels by using the higher heating values. Appl Energ. 2008;85:776–85.

21. Wang Z, Naterer GF, Gabriel KS, Secnik E, Gravelsins R, Daggupati V. Thermal design of a solar hydrogen plant with a copper-chlorine cycle and molten salt energy storage. Intl J Hydrogen Energ. 2011;36:11258–72.
22. Dincer I, Rosen MA. Thermodynamic aspects of renewables and sustainable development. Rene Sus Energ Rev. 2005;9:169–189
23. Ozbilen A, DIncer I, Rosen MA. Environmental evaluation of hydrogen production via thermochemical water splitting using the Cu-Cl cycle: A parametric study. Int J Hydro Energ. 2011;36:9514–9528

Chapter 56
Potential Methods for Converting Coal into Gasification Products for Reduced Global Warming

Jale Gülen

Abstract Turkey has huge lignite reserves although they have high ash, sulfur, and volatile matter. The direct usage of this fossil fuel has disadvantages such as fouling, acid rains, greenhouse gases (GHGs), etc. Greenhouse gases are the principal factor for global warming and climate change. Some gasification processes can be applied for turning coal into valuable products such as water gas, producer gas or synthetic natural gas. The undesired parts of coal that cause the pollution in the environment can be removed for increasing the fuel quality. This can be managed by physical and chemical methods or both of them.

In this chapter, some gasification processes, the comparisons among them, the characteristics affecting gasification and gasification products are mentioned. Also, the demineralization application of Nallıhan lignite is presented. The undesired parts of it such as sulfur and mineral matter are removed by chemical treatments. For this purpose, the coal samples were stirred with 5 % 50 ml H_2O_2 for 20 min. They were washed with distilled water and dried at 105 °C in the oven. Later, these dried samples were stirred with 5 % 50 ml methanol solution. The same procedure was applied for 5 % 50 ml CH_3COOH solution after applying for 5 % 50 ml H_2O_2 solution. The ash, sulfur and demineralized parts are determined. Some spectra such as FTIR are also taken to observe the chemical process effects in Nallıhan lignite.

J. Gülen (✉)
Yildiz Technical University, Istanbul, Turkey

Nomenclature

O–C	Oxygen–Carbon
C–H	Carbon–Hydrogen
CO	Carbon monoxide
CO_2	Carbon dioxide
N_2	Nitrogen
NO_x	Nitrogen oxides
N_2O	Nitrous oxide
H_2	Hydrogen
S	Sulfur
SO_x	Sulfuroxides
CH_4	Methane
CFC	Chlorofluorocarbon
PAN	Peroxyacetylbitrate
GHGs	Greenhouse gases
H_2O_2	Hydrogen peroxide
CH_3COOH	Acetic acid
HF	Hydrofluoric acid
HNO_3	Hydronitrate acid
HCl	Hydrocloride acid
NaOH	Sodium hydroxide

Acronyms

ASTM	American Standard Testing Materials
CFD	Computational Fluid Dynamics
FTIR	Fourier Transform Infrared Spectroscopy
IGT-U	Institute Gas Technology (Des Plaines, IL)(single stage, fluidized bed gasifier)

56.1 Introduction

The risk of climate change due to emissions of carbon dioxide from fossil fuels is considered to be the main environmental threat from some energy systems. Other environmental problems are acidification and dispersion of metals originating from fossil fuels [1]. Fossil fuels supply about 75 % of the total primary energy use in the world. Shreshtha and Timilsina (1996, 1997) have studied CO_2, SO_2, and NO_x emissions in the power sectors for selected Asian economics [2, 3]. As the coal quality deteriorates, the greenhouse emission index increases [4]. The issue of global warning is becoming a major and unavoidable element of world energy policy. About 29 billion tons of CO_2 that including 23 billion from fossil fuel burning and industry are released into the atmosphere annually by human activities [5].

Coal is one of fossil fuel and known to be derived from decayed plants. Coalification is the process by which deposited plant that made up mainly lignin and cellulose is gradually converted into coal under the effects of pressure and heat. As the process proceeds, the carbon content of coal increases. The increase in carbon content is accompanied by a decrease in hydrogen, oxygen, moisture, volatile matter, and porosity. The increase of carbon content is also accompanied by condensation of the aromatic rings [6].

Coal is a complex mixture of strong aromatic bonds linked each other by straight weak bonds. The weakly bonded structures split off under the effect of average high temperatures. This is the devolatization stage. Gasification stages take place in later stages. A lot of studies have been done on gasification.

Harris and Roberts [7] studied the gasification behavior of Australian coals at high temperature and pressure. The experimental values of pressure and temperature are 2 MPa and 1,773 K. The effects of O–C ratio, residence time, and coal type are the parameters investigated. They found that at higher conversion levels, the effect of coal type on product gas composition were more apparent than at lower conversion levels. Harris and Roberts [8] studied the kinetic study of coal char gasification reactions at high pressure. Langmuir–Hinshelwood rate equation is used. The analysis is well established with up to 0.1 MPa of the reactant. Hla et al. [9] studied the CFD modelling for an entrained flow gasification reactor using intrinsic kinetic data. The model provides detailed information on temperatures, reaction rates, gas composition, and carbon conversion. A series of numerical simulation have been performed for the gasification of a range of Australian bituminious coals under different operating conditions (reactor temperature, O–C ratio). The results found are consistent with the experimental data. Stanczyk et al. [10] studied the gasification of lignite and hard coal with air and oxygen enriched air in a pilot scale ex situ reactor for underground gasification. They found that optimum oxygen air ratios have produced valuable gas production. Wu et al. [11] studied the Chinese coal gasification at 900–1,200 °C in steam medium. The temperature effects the pyrolysis yield. They found that chemical reactions have controlled the process instead of diffusion. Zaporowski [12] studied the energy conversion processes in gas steam power plants. He took into account several parameters such as coal gasification technology, coal type, gasifying medium, fuel desulfurization technology, and gas turbine design on the efficiency of electric energy generation. Bhitto et al. reviewed underground coal gasification (UCG). As compared with conventional mining and surface gasification, UCG promises lower capital/operating costs and other advantages such as no human labor underground. It has the potential to be linked with carbon capture and sequestration. The increasing demand for energy, depletion of oil and gas resources, and threat of global climate change have lead to growing interest in UCG. The potential for UCG converts low grade, inaccessible coal resources into valuable gaseous products. They mentioned the operating parameters on UCG such as physical characteristics of feedstock, process chemistry, gasifier design, and operating conditions [13]. Liu and Niksa studied the char gasification at elevated pressures from 0.02 to 3 MPa's for 28 coal samples ranging from lignite to

anthracite. The process parameters are CO_2 and steam mole percentages from 0 to 100 %, CO and H_2 levels to 50 %, gas temperatures from 800 to 1,500 °C. They also studied the gasification mechanism that based on carbon burn out kinetics [14]. Ghani et al. presented an improved, comprehensive, one-dimensional model for combustion and gasification of coal in fixed beds. The effects of the devolatilization, oxidation and gasification submodels on the model predictions are discussed. The product gas compositions predicted via various gas phase chemistry are shown. The effects of five model parameters and one operational variable on the predictions of the model are also presented [15]. Irfan et al. presented a brief about coal gasifection in CO_2 atm. Different factors are studied over the coal gasification with CO_2 such as coal rank, pressure, temperature, gas composition, catalyst and the minerals present inside the coal, heating rate, particle size, and diverse reaction types. Moreover this paper reviews the kinetics and reaction rate equations (Arrhenius and Langmuir–Hinshelwood types for coal-char gasification both in the reaction kinetic control region (low temperature) and at both low and high pressures [16]. Fermoso et al. studied the co-gasification of coal with biomass and petroleum coke. The effects of the main operation variables (temperature, pressure, and gasifying agent compositions on gas production and other process parameters such as carbon conversion, cold gas efficiency, and high heating value, during the steam–oxygen gasification of a bituminious coal are studied. They found that temperature and oxygen concentration were the most influential parameters during the gasification process [17]. Wang et al. proposed the addition of $Ca(OH)_2$ in the char preparation for K_2CO_3-catalyzed steam gasification of coal char. They found that the $Ca(OH)_2$-added char had higher reactivity for the catalytic gasification than the raw char [18]. Zhang et al. proposed a new concept in catalytic coal gasification. The use of crude vinegars (CVs) derived from different lignocellulosic biomass resources is described for the recovery and reuse of calcium in coal gasification. CVs are found to be capable of reclaiming calcium from gasification residue and of improving the catalytic activity of the indigeneous crystalline calcite in bituminious coal as in situ catalyst [19].

As can be seen in the literature, several chemicals can be applied for increasing the process yield. The chemicals are also very effective for decreasing the undesired parts of coal. The industrialized countries are responsible for air pollution, ozone depletion, carbon emission, green gas effects, etc. Energy must be used efficiently in developing countries. There is a need to make major changes in the production and usage of energy. Some national and international programs are taken into account for this reason [20].

Turkey is an energy importing country. More than half of the energy requirement has been supplied by imports. Turkish energy policy is concentrated on the natural gas supply and coal [21]. Turkey has huge lignite reserves although most of them is low quality. They have high moisture content, high ash and sulfur amounts. The proven lignite reserves are 8 billion tones, and the estimated possible reserves are 30 billion tones [22].

Air pollution is becoming a great environmental concern in Turkey. Air pollution from energy utilization in the country is due to the combustion of fossil fuels [23]. Coal mining has a direct impact on the environment, affecting land and

causing subsidence, as well as producing mine waste that must be managed. Coal combustion produces several types of emissions that adversely affect the environment, particularly ground-level air quality. Concern for the environment has in the past and will in the future contribute to policies that affect the consumption of coal and other fossil fuels. The main emissions from coal combustion are sulfur dioxide (SO_2), nitrogen oxides (NO_x), particulates, and carbon dioxide (CO_2) [24, 25].

In an expanding global economy still dependent on fossil fuels for 85 % of its energy needs, reducing the releases in order to stabilize atmospheric CO_2 is an extreme task. At the present time, coal is responsible for 30–40 % of world CO_2 emissions from fossil fuels. SO_2 and NO_x contribute to acid rain.

Currently, it is estimated that CO_2 contributes about 50 % to the antropogenic greenhouse effect. In addition to CO_2, several other gases, e.g., CH_4, CFCs, halons (hydrocarbons containing halogens), N_2O, SO_2, ozone, peroxyacetylnitrate (PAN) produced by the industrial and domestic activities, leading to GHGs, can also contribute to this effect, resulting in a rise in the Earth's temperature [26, 27].

Mineral matter content effects the fossil quality and causes many problems in the utilization stage such as combustion, gasification, liquefaction, carbonization, etc. [28]. Demineralization treatments increase the coal quality from the points of reducing these undesired parts and also, global warming effect. Chemical cleaning is expensive but more effective to fine distributed and bound minerals in the coal body [29]. Chemical cleaning of coal with alkali and acid solutions has highly effective in reducing significant amounts of ash forming minerals and undesired parts of coal such as sulfur [30]. In the demineralization process some solutions such as acidic, basic, some solutions like H_2O_2 and combination of these are used [31–33].

Steel and Patrick tried HF and HF followed HNO_3 acid for the mineral matter of high volaltile UK coal. The ash level is decreased from 7.9 to 2.6 % and from 2.8 to 0.6 % with HF and HF plus HNO_3, respectively [34]. Mukherjee and Borthakur leached the mineral matter of Assam coal with 16 % NaOH and then HCl addition at 90 °C. They managed to reduce 50 % of ash and 10 % of organic sulfur amounts in Assam coal [35]. Wang et al. studied the $Ca(OH)_2$ leaching of Hunter Valley coal. After the treatment, some clay was fairly removed by demineralization, other clay and quartz appeared to be less reactive [36]. Wu and Steel demineralized a UK bituminious coal using HF and ferric ions. In the first stage, hydrofluoric acid (HF) at 65 °C was used and mainly Al and Si minerals were removed. Subsequent leaching by ferric ions decreases the pyrite and fluorides formed during the HF leaching. They manage to decrease the mercury and sulfur contents by 40 % and 20 % after two stage leaching, respectively [37]. Ishihara et al. experienced the four different coals that obtained Argonne premium coal sample bank. Mineral matters in coal were removed by HCl or HCl/HF treatments. Alkali metals and a part of pyrite were removed by HCl solution. SiO_2 and Al_2O_3 were removed only by HCl/HF applications. They studied the efficiency of hydrogen transfer of coal on the demineralized body. Their results showed that iron species from pyrite may catalyze the hydrogen reaction with H_2 gas [38]. Demirbaş studied to decrease sulfur in six lignites and three coal samples. Froth flotation method is very effective for removal of pyritic sulfur from coal and lignites. He compared the sulfur removal

yield with alkali desulfurization and oxidesulfurization methods [39]. Jorjani et al. compared the demineralization yield with microwave irradiation pretreatment and sequential leaching with HF followed by HNO_3. The ash content ranged 22–78 and 22–82 % after two stage treatments [40]. Ambedkar et al. investigated the utilization of ultrasound for de-ashing and de-sulfurization of Girald mine, Rajastham Indian coals. They used three reagents HCl, HNO_3, and H_2O_2 with ultrasound. They searched the effect of several pretreatments such as reagent concentration, sonication time, coal particle size, and coal concentration [41].

The present chapter reports coal gasification processes, comparison of them and gasification products. The demineralization application of Turkish coal is shown by the successive treatments of H_2O_2 plus methanol and H_2O_2 plus acetic acid on the Nallıhan lignite body.

56.2 Coal Gasification Products

Utilization of coal in energy and chemical industries becomes more and more important due to the rapid decrease of petroleum resource and also increase of crude oil. Coal gasification is a kind of clean technology for high effective usage of coal and is widely used in coal gas supply, ammonia synthesis industry, power plants, and other industries [42, 43].

In the gasification reactions, the carbon in the coal body reacts with air or oxygen and several intermediate or end products are produced according to the effects of process condition and process type. The gasification products are shown at below (Fig. 56.1).

	Reactant gas	Product gas	Composition	Usage
COAL	Air and steam	Poducer gas (Low Btu)	CO, H_2, CH_4, N_2	Industrial fuel
	Air and high pressure steam	Producer gas (Low Btu)	CO, H_2, CH_4 (higher concent.), N_2	Power generation
	Oxygen and steam	Water gas (Synt. gas) (Medium Btu)	CO,H_2, N_2 (low concent.)	Ammonia synt., metanol synt., Fischer Tropsch synt., Hydrogen recovery, Carbonization, Ore reduction, CO recovery
	Oxygen and high pressure steam	Town gas (Medium Btu)	H_2, CH_4, N_2 (low concent.)	Supplementary coke gas and domestic gas
		Synthetic natural gas (High Btu)	CH_4, N_2 (low concent.)	Supplementary natural gas

Fig. 56.1 Coal gasification products (modified from [6])

Coal gasification processes can be classified according to their energy content per unit volume as low, medium, and high calorific classes. The heating values are 7.5 MJ/m^3, 7.5–15 MJ/m^3, and 37 MJ/m^3, respectively.

Low calorific gas is preferred in small scale applications. Power can be generated by gas turbines using low calorific gas. Medium calorific gases can be used for heating a synthesis gas converted into high calorific gas. High calorific gas can be used for any purpose. There are special names for gas mixtures with certain compositions [44].

(a) Producer Gas: This is low calorific gas obtained classical gasifier upon reacting of air instead of oxygen to the fuel bed. The composition is 28 % CO, 55 % N_2, 12 % H_2, and 5 % CH_4 plus CO_2 of 4.6–6.7 MJ/m^3 heating value.
(b) Water Gas: It is produced by reacting of large amounts of steam to the fuel bed of gasifier. The composition is roughly 50 % H_2, 40 % CO plus N_2 and CO_2. The heating value is in the range of 10–12.5 MJ/m^3.
(c) Town Gas: This is a medium calorific gas. The composition is 55 % H_2, 27 % CH_4, 6 % CO, 10 % N_2, 2 % CO_2. The heating value is in the range of 16.7–20 MJ/m^3.
(d) Synthetic Natural Gas: This is methane obtained from the reaction of CO or C with hydrogen. The heating value can be depended on methane concentration.

56.3 Factors Affecting the Gasification Properties of Coals

The coal properties have high effect on the efficiency of the gasification reactors. These are moisture, ash, volatile matter, caking, fixed carbon, and ash fusion temperature [45].

(a) Moisture: This content decreases with coal rank. The high moisture content causes to the clogging of the particles. The coal must be predried in order not to forming aglomeration.
(b) Ash: It is the noncombustible part of coal. It must be at minimum in all processes.
(c) Volatile matter: This content varies 5–50 % according to the coal rank. High volatile matter content has the positive effect for supplying the gaseous products from fossil fuels.
(d) Fixed carbon: The physical and chemical characteristics of coal play a role in the efficiency of the gasification process. Chemically reactive carbon can involve gasification reactions easily.
(e) Ash fusion temperature: Maximum operating temperature is limited by the fusion temperature of the ash formed. If the ash is to be removed in the form of slag, then the ash fusion temperature has to be exceeded. In this case, the viscosity of slag ash and temperature must be considered.
(f) Size distribution: The size distribution of coal particles is related to the design of the gasifier.

56.4   Gasification Reactors
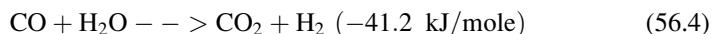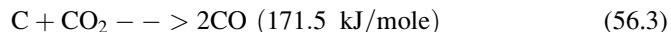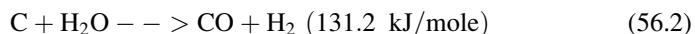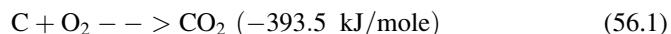
Coal gasification is the process of producing coal gas. The conversion of solid fuel into a gaseous fuel is important because of arising some problems of fossils such as transportation, environmental pollution, etc. For gasification of coal, the following reactors can be used.

Fixed bed, fluidized bed, entrained flow, molten bath.

(a) Fixed Bed Gasifier:

The bed of solid reactant coal remains static as the reactive gas moves through the reactor. The reacting gases air and/or oxygen and steam pass through the bed in cocurrent or countercurrent flow to the incoming coal feed. Cocurrent flow is the preferred scheme. Coal is supplied from the top of the gasifier, the residue and ash, or slag ash are removed from the lower end. There are several stages in the reactor such as drying (devolatilization), gasification (reduction), and combustion (ash). The temperatures are 370–$600°C$, 600–$920°C$ and 920–$1,400°C$, respectively.

These are the reactions that are seen.

$$C + O_2 --> CO_2 \; (-393.5 \; kJ/mole) \tag{56.1}$$

$$C + H_2O --> CO + H_2 \; (131.2 \; kJ/mole) \tag{56.2}$$

$$C + CO_2 --> 2CO \; (171.5 \; kJ/mole) \tag{56.3}$$

$$CO + H_2O --> CO_2 + H_2 \; (-41.2 \; kJ/mole) \tag{56.4}$$

If the production of synthetic natural gas is desired, the methane forming reaction should be promoted by operating under high pressure.

$$C + 2H_2 --> CH_4 \; (-74.9 \; kJ/mole) \tag{56.5}$$
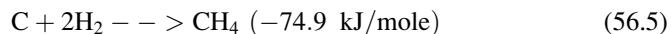
Figure 56.2 shows the fixed bed gasifier.
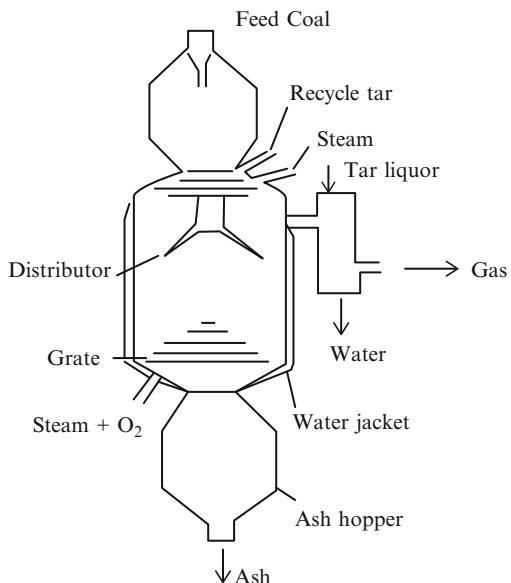
There are various industrial applications of fixed bed gasifiers. Lurgi and British gas council/Lurgi applications are the examples of this process.

(b) Fluidized Bed Gasifiers
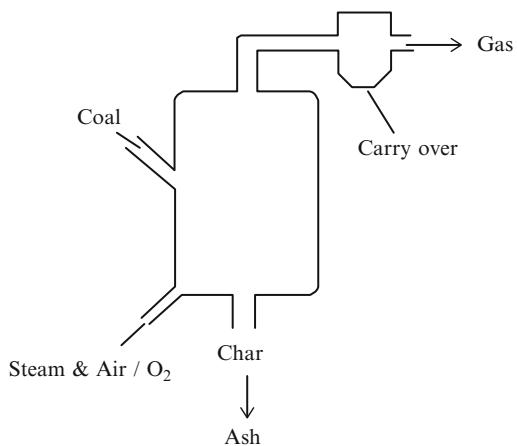
The fuel bed is fluidized by the agitating action of incoming reactant gases. The coal undergoes rapid devolatization, followed by gasification reactions upon introduction to the gasifier. This type of gasifier limits the size of the coal particles because of fluidizing small particles. This unit has higher coal input rates than fixed bed. The exit temperature of the reactor is roughly the same as that of fixed bed. Heat exchange units are utilized for avoiding heat losses. Fluidized bed reactor is shown in Fig. 56.3.

The examples of fluidized bed gasifiers are Winkler, Westinghause, CO_2 acceptor, and IGT-U processes.

Fig. 56.2 Fixed bed reactor
(modified from [6] and [46])
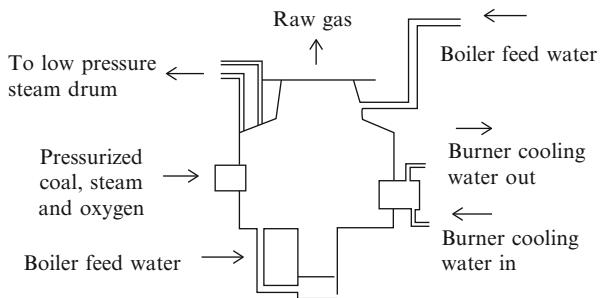
Fig. 56.3 Fluidized bed
reactor (modified from [6])
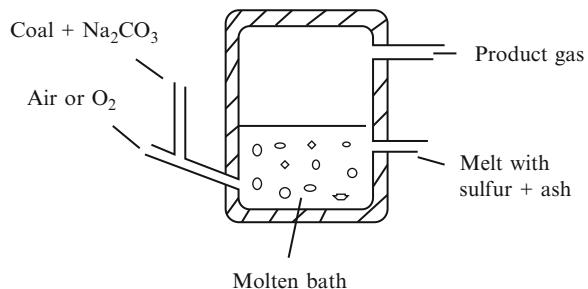
(c) Entrained Flow Gasifiers

The coal particles are carried or entrained by the reactant gases. The mixture of
coal particles and reactant gases is fed into the gasifier at high velocities through
one or more burners or nozzles. The reaction takes place in the suspension of
coal particles and gaseous reactants. The residence time is very short. The size
of particles is very small. The entrained flow type reactor is given in Fig. 56.4.
Four well-known applications of the entrained flow gasification are Koppers
Totzek entrained flow gasification, Shell-Koppers entrained flow gasification,
Texaco entrained flow gasification, and Foster Wheeler entrained flow gasifica-
tion systems.

Fig. 56.4 Entrained flow gasifier (modified from [6])

Fig. 56.5 Molten bath gasifier (modified from [6, 47])

(d) Molten Bath Gasifier

Crushed coal, steam air and/or oxygen are injected into a bath molten salt, iron, or coal ash. Coal dissolves in the melt. 900 °C and above temperatures are required to maintain the bath molten depending on the nature of the melt. This high temperature levels favor high reaction rates. Molten bath gasifier is seen in Fig. 56.5.

There are a number of applications of the molten bath gasification. Three of them are Rockwell international molten bath gasification, Atgas molten bath gasification, and Rummel single shaft molten bath gasification systems.

56.5 Gasifier Characteristics

A comparative summary about the gasifiers used is given in Table 56.1 below.

56.6 A Demineralization Application

A demineralization experiment was applied on Nallıhan lignite for increasing the fuel quality. It was grinded to 0.250 mikrons. 4 g Nallıhan lignite was stirred with 5 % 50 ml H_2O_2 at the room temperature for 20 min. Later, the sample was filtered through the blue ribbon filter, washed with distilled water and dried in the oven at 105 °C.

Table 56.1 The comparatives of the reactors (adapted from [6] and [48])

	Fixed Bed	Fluidized Bed	Entrained Flow	Molten Bath
Capacity	Lowest, due to the limited gas flow	High due to low residence times but limited by particle entrainment at high gas velocities	Highest capacity per unit volume	Determined by melt entrainment in product gas at high flow rates
Complexity	Internal moving parts require high precision in design and manufacture	No internal moving parts but design of distributor is critical	Design of combuster nozzles and heat recovery is critical in the presence of molten slag	Bath circulation and cleanup of product gas and molten medium are complicated
Feed Coal Type	Caking coals normally introduce problems; agitation of the bed may be necessary	Caking coals may require pretreatments	All types may be used	All types are handled
Handling	Sized coal is required; fines must be handled seperately	Sized coal is not essential, but fines may need to be removed to prevent elutration or flow instability	Pulverizing and drying of surface moisture are required; fines are not rejected	No limitation
Product Gas	Contains tar and oil, phenols, ammonia, a small amount of dust	Low tars and phenols, uniform composition but high carry over of ash and char	No tars and phenols but ash, char and sensible heat must be recovered for improved efficiency	Bath retains both ash and sulfur, contains no tars and phenols at high temperatures and requires no cooling
Ash Removal	Ash contains very little carbon due to high conversion	Gravitational segregation of ash, high carbon in ash	Produces inert slagged ash with low carbon content, high sensible heat	Must be seperated from melt, has moderately high carbon content and sensible heat
Temperature	Has to be kept below the fusion point of ash, temperature gradient in bed provides high thermal efficiency	Operation at lower temperatures possible	Highest temperature of four classes	Melt at gasifier temperature may be highly corrosive to refractory

Table 56.2 Proximate analysis of Nallıhan lignite

Sulfur (%)	8.58
Ash (%)	17.79
Moisture (%)	9.79
Volatile matter (%)	18.28
Fixed carbon (%)	63.93
Calorific value (kJ/Kg)	20,370

Table 56.3 Sulfur removal % values of Nallıhan lignite after treated with chemicals

Nallıhan	H_2O_2	Decrease in S (%)	S Removal %
Methanol	6.04	2.54	29.60
CH_3COOH	6.27	2.31	26.92

Table 56.4 Demineralization values of Nallıhan lignite after treated with chemicals

Nallıhan	H_2O_2	Ash removal (%)	Demineralization %
Methanol	9.69	8.1	45.53
CH_3COOH	10.38	7.41	41.65

Table 56.5 Calorific values of Nallıhan lignite after treated with chemicals

Nallıhan	H_2O_2 (J/g)	Variation in calorific value (%)
Methanol	23,071.84	13.26
CH_3COOH	22,843.98	12.15

This dried sample was stirred with 5 % 50 ml methanol for 20 min, filtered, washed with distilled water, and dried in the oven at 105 °C. The sulfur and mineral matter removal experiments are done on this dried sample. The same procedure is repeated with the experiments done with CH_3COOH. The proximate values of Nallıhan lignite are given in Table 56.2.

The sulfur values of Nallıhan lignite after treated with chemicals are shown in Table 56.3. This test is done according to ASTM Standards. Desrease in sulfur values and sulfur removal % are calculated from the point of chemicals effectiveness. Table 56.4 shows the variation of Nallıhan lignite demineralization values at the final effect of chemicals. The calculations are shown at below. Table 56.5 shows the variation of calorific values of coals being effected with chemicals. The increase in calorific values is given at the bottom of Table 56.5.

Decrease in S% = 8.58 − 6.04 = 2.54

$$\text{S Removal } \% = \frac{2.54}{8.58} x100 = 29.60$$

Ash removal % = 17.79 − 9.69 = 8.1

$$\text{Demineralization } \% = \frac{8.1}{17.79} x100 = 45.53$$

$$\text{Variation in calorific value } \% = \frac{23071.84 − 20370}{20370} = 13.26$$

56.6.1   FTIR Spectra

Figure 56.6 shows the FTIR spectrum of Nallıhan lignite. The spectrum is drawn at 450–4,000 cm^{-1} wave numbers. The bond properties of peaks were given at the following.
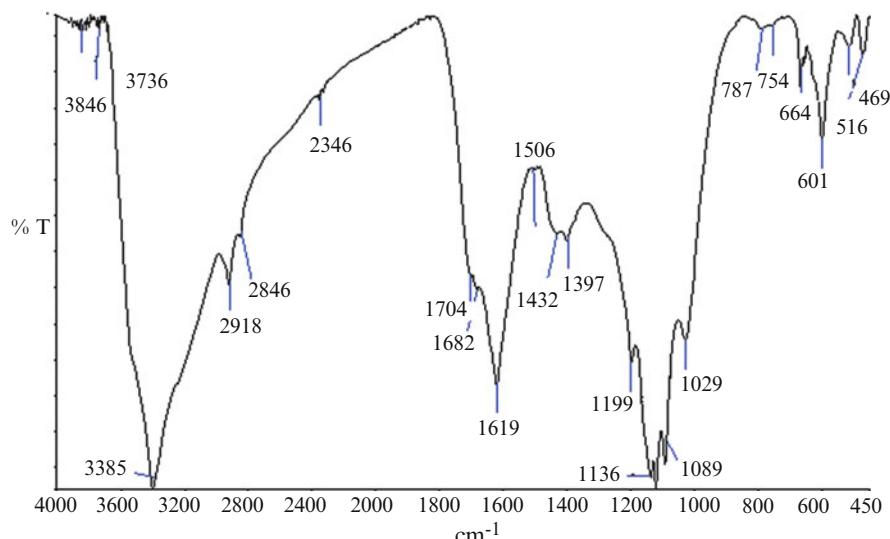
469, 516, 601, 664, 754, 787 → Mineral matter
1,089, 1,136 → C-O stretching
1,432, 1,397 → C=C and C=O stretching
1,619, 1,682, 1,704 → Asymetric symetric carboxyl groups
2,918, 2,846 → Aliphatic C-H groups

The FTIR spectrum of Nallıhan lignite after treated with H_2O_2 plus methanol is shown in Fig. 56.7. The bond structures of the body are given at below.
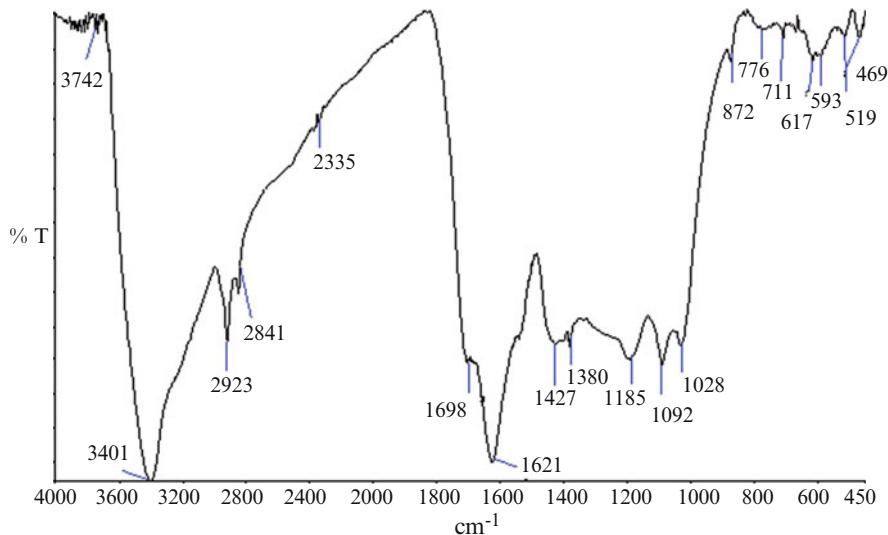
469, 519, 593, 617, 711, 776, 872 → Mineral matter
1,028, 1,092, 1,185 → C-O stretching
1,380, 1,427, 1,621, 1,698 → Asymetric symetric carboxyl groups
2,841, 2,923, 3,401 → Aliphatic C-H groups

FTIR spectrum of Nallıhan coal treated with H_2O_2 plus acetic acid is given in Fig. 56.8. The peak groups are defined at below.
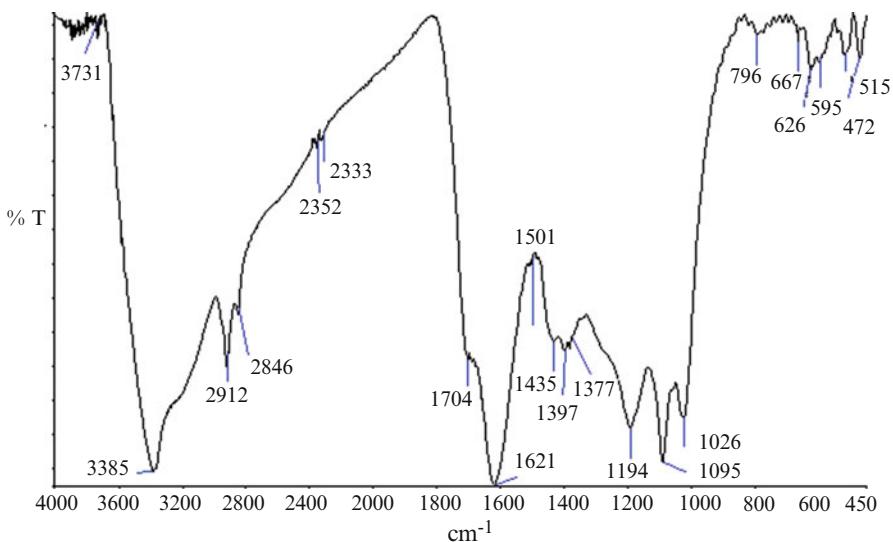
472, 515, 595, 626, 667, 796 → Mineral matter
1,026, 1,095, 1,194 → C-O stretching
1,377, 1,397, 1,435, 1,621, 1,704 → Asymetric symetric carboksyl groups
2,846, 2,912, 3,385 → Aliphatic C-H groups

Fig. 56.6 FTIR spectrum of Nallıhan coal

Fig. 56.7 FTIR spectrum of Nallıhan coal treated with H_2O_2 plus methanol

Fig. 56.8 FTIR spectrum of Nallıhan coal treated with H_2O_2 plus acetic acid

56.7 Results and Discussion

Energy can be termed as a prime factor in the development process of any country. World population is expected to double by the end of twenty-first century. There is a strong positive correlation between energy production/consumption and economic development/scientific progress [49]. Table 56.6 shows the energy

Table 56.6 Concentrated energy sources and their usage forms (adapted from [49])

Source	Usage
Coal	Electric generation, heating, power plants, heavy industry and chemicals
Oil	Engine fuel, transportation, power plants, heavy industry, heating, chemicals
Gas	Electric generation, domestic heating, power plants and chemicals
Uranium	Nuclear reactor, electric generation, nuclear power central

Table 56.7 Sustainability of primary world energy sources (adapted from [49])

Energy sources	Sustainability
Historic energy sources	Simple technologies using renewable resources: solar energy, hydropower, wind power, wood
Today's energy sources	Advanced technologies using premium energy resources such as oil, coal, natural gas, nuclear
Future energy sources	High tech generators using renewable resources: solar energy, geothermal, hydropower, wind power, biomass

sources and usage of them. Table 56.7 shows the primary world energy sources sustainabilities.

States have played a leading role in protecting the environment by reducing emissions of greenhouse gases (GHGs). State emissions are significant on a global scale. CO_2 and CO are main greenhouse gases associated with global warming. Table 56.8 presents the pollutants and hazards involved, as welll as the cause and effect linkage between energy activities, pollutants, and environmental effects [20]. Table 56.9 is given to provide a schme of the pollutants and their environmental impacts [27] Table 56.10 show the substances emitted from coal, petroleum and natural gas [20]

Increasing atmospheric concentrations of greenhouse geses are increasing the manner in which these gases trap heat radiated from the Earth's surface, thereby raising the surface temperature of the Earth. The Earth surface temperature has increased about 0.6 °C over the last century, and as a consequence sea level is estimated to have risen by perhaps 20 cm [51]. Such changes can have wide ranging effects on human activities all over the world. Most scientist agree that there is a cause effect relationship between the observed emission of greenhouse gases and global warming. Many sciemtist predict that if atmospheric concentrations of greeenhouse gases continue to increase, as present trends in fossil fuel consumption suggest will ooccur, the Earth's temperature may increase in the next century by another 2 °C and perhaps by up to 4 °C. If this prediction is realized, sea level could rise between 30 and 60 cm before the end of the twenty-first century [51].

Global warming has many potential environmental impacts, including effects on agriculture production, forests, water resources, coastal areas, and species and natural areas [52]. Warmer temperatures can lead to more intense rainfall and flooding in some areas and with more frequent droughtlike conditions in other areas. Forest areas could be seriously affected. As temperatures increase, the composition of a forest could change, with warmer climate varieties moving into

Table 56.8 Importance of energy activities in the generation of air pollutants (adapted from [50])

Pollutant	Man-made as % of total	Energy activities		Contributions as % of energy related releases
		As % of total	As % of manmade	
SO_2	45[a]	40[a]	90[a]	80[b] coal combustion, 20[b] oil combustion
NO_x	75[a]	64[a]	85[a]	51[b] transport, 49[b] stationary sources
CO	50[a]	15–25[a]	30–50[a]	75[b] transport, 25[b] combustion in stationary sources
Lead	100[a]	90[a]	90[b]	80[c] transport, 20[c] combustion in stationary sources
PM	11.4[a]	4.5[a]	40[b]	17[b] transport, 5[b] electric utilities, 12[b] wood combustion
VOC	5[b]	2.8[a]	55[b]	15[b] oil industry, 10[b] gas industry, 75[b] mobile sources
Radionuclides	10[a]	2.5[a]	25[a]	25[c] mining and uranium milling, 75[c] nuclear power and coal combustion
CO_2	4[d]	2.2–3.2[a]	55–80[a]	15[b] natural gas, 45[b] oil, 40[b] solid fuels
N_2O	37–58[a]	24–43[a]	65–75[a]	60–75[a] fossil fuel combustion, 25–40[a] biomass burning
CH_4	60[a]	9–24[a]	15–40[a]	20–40[a] natural gas losses, 30–50[a] biomass burning

[a]Global estimates
[b]Estimates for OECD countries
[c]Estimates for the United States
[d]Global estimates of contribution of anthropogenic CO_2 to increase in CO_2 concentrations and to global warming is much larger

Table 56.9 Essential gaseous pollutants and their impacts (adapted from [26])

Gaseous pollutant	Greenhouse effect	Stratospheric ozone depletion	Acid precipitation	Smog
Carbonmonoxide (CO)				
Carbondioxide (CO_2)	+	+/−		
Methane (CH_4)	+	+/−		
Nitric oxide (NO) and Nitrogen dioxide (NO_2)		+/−	+	+
Nitrous oxide (N_2O)	+	+/−		
Sulfur dioxide (SO_2)	−−	−		
Chlorofluorocarbons (CFCs)	+	+		
Ozone (O_3)	+			+

(where + stands for positive contribution, and − stands for variation with conditions and chemistry, may not be a general contributor.)

traditionally colder climate areas. Forest health and productivity could be impacted. Coastal areas are predicted to undergo erosion of beaches, inundation of coastal lands and increased costs to protect coastal communities. There will be a decreasing vailiability of fresh water for irrigation and other essential issues. Current rates of sea level rise are expected to increase two to five times due to both thermal

Table 56.10 Substances emitted from coal, petroleum, and natural gas sources (adapted from [26])

Substance	Coal	Petroleum	Natural gas
CO_2	x	x	x
CO	x	x	
NO_x	x	x	x
SO_2	x	x	
CH_4	x	x	x
HCl	x		

expansion of the oceans and the partial melting of mountain glaciers and polar ice caps. Changes in temperature and water availability could decimate nonintensively managed ecosystems, such as forests, rivers and wetlands.

Human health is also impacted by global climate change [52]. This includes increases in weather related mortality, infectious diseases and air quality respiratory illnesses. Small increases in average temperatures can increase the spread of diseases like malaria and dengue fever and lead to a significant rise in the number of extreme heat waves. Elderly people are particularly vulnerable to heat stress. Heat waves could also aggravate local air quality problems, which pose threats to young children and asthmatics. Such consequences could jeopardize the survival of entire population.

56.8   Conclusions

Alternative energy technologies are being disseminated in many countries with an objective to reduce the uses of traditional and commercial energy sources. These technologies convert local resources to usable energy forms. For each country, the choice between the various available options is strongly dependent on the local conditions [49].

Coal is a combustible, sedimentary rock. It is composed of heterogeneous components which have different physical and chemical properties. Gasification is a promising way for producing several components from this solid fossil fuel. All types of coal can be gasified. The gasifier design, operation and performance can be chosen according to the coal properties.

Coal gasification has emerged as a clean and effective way for the production of which can be used for power or heat generation or as a synthetic precursor. A good understanding of the char reactivity makes it possible to improve gasifier design and efficiency.

A distinction of the factors affecting char gasification can be made according to whether they are only related the intrinsic chemical characteristics of the char or they can be related to the physical structure of the coal or to the environment in which it goes through chemical reactions (combustion or gasification). In this way, the first are said to represent the char reactivity and the second are related to the respective reaction rates [53].

With the gasification processes, some valuable components can be obtained such as hydrogen. It is used as an intermediate for the synthesis of chemicals or hydrogen

can be used as an energy carrier itself. As can be seen from Table 56.9, many gaseous pollutants play an important role from the point of greenhouse effect and staratospheric ozone depletion such as CO_2, CH_4, N_2O, and CFCs. CO and CO_2 emissions of man made (Table 56.8) range as 30–50 % and 55–80 %, respectively. Gasification plants are also the best solution to capture CO_2 compared to other coal based alternatives. It can be used for the production of several chemicals after separating from the syngas [54].

A demineralization application was given from the point of showing the effects of the medium on the product quality [55]. An oxidative and acidic mediums are applied for decreasing sulfur and mineral matter of Nallıhan lignite. 29.60 % and 26.92 % sulfur removal are performed for H_2O_2 plus methanol (A) and H_2O_2 plus acetic acid (B), respectively. H_2O_2 plus methanol is more effective for sulfur and ash removal than H_2O_2 plus acetic acid. The ash ratios are found as 46 % (45.53) and 42 % (41.65) for A and B, respectively. The calorific values of lignites treated with these chemicals are determined as 23,071.84 J/g and 22,843.98 J/g for A and B, respectively. The chemicals are increased the calorific values as 13 % and 12 % for A and B process, respectively.

References

1. Johansson J, Lundqvist U (1999) Estimating Swedish biomass energy supply. Biomass Bioenerg 17:85–93
2. Shreshtha RM, Timilsina GR (1996) Factors affecting CO_2 intensities of power sector in Asia: a divisia decomposition analysis. Energ Econ 18:283–292
3. Shreshtha RM, Timilsina GR (1997) SO_2 intensities intensities of power sector in Asia: effects of generation mix and fuel intensity changes. Energ Econ 19:355–362
4. Bhatt MS (2000) Energy efficiency and green house emission burden from coal-fired electric power plants. A case study of the indian power sector. Energ Source 22:611–623
5. IPCC (2001) Climate change (2001): the scientific basis. Contribution of the working group I to the third assesment report of the intergovernmental panel on climate change. Cambridge University Press, Cambridge
6. Ünal S, Pişkin S, Williams A (1994) Coal gasification in coal resources, properties, utilization, pollution, Chap. 26, Orhan Kural, Özgün AŞ (eds.) Ozgun AS. Istanbul, Turkey.
7. Roberts DG, Harris DJ (2006) The kinetic study of coal char gasification reactions at high pressure. Energy Fuel 20:2314–2320
8. Harris RJ, Roberts DG (2006) The gasification behaviour of Australian coal at high temperature and pressure. Fuel 85(2):134–142
9. Hla SS, Harris DJ, Roberts DG (2006) CFD modelling for an entrained flow gasification reactor using measured intrinsic kinetic data, Fifth international conference on CFD in the process industries CSIRO, Melbourne, Australia, 13–15 December 2006
10. Stanczyk K, Homanies N, Smolinski A, Swiadrowski J, Kapusta K, Wiatowski M, Grabowski J, Rogut J (2011) Gasification of lignite and hard coal with air and oxygen enriched air in a pilot scale ex situ reactor for underground gasification. Fuel 90:1953–1962
11. Wu S, Gu J, Li L, Wu V, Gao J (2006) The reactivity and kinetics of Yanzhou coal char from elevated pyrolysis temperatures during gasification in steam at 900-1200 °C. IchemE. Institution of chemical engineers. Trans I Chem E B Process Safe Environ Protect 84 (B6):420–428

12. Zaporowski B (2003) Analysis of energy conversion processes in gas steam power plants integrated with coal gasification. Appl Energ 74:297–304
13. Bhitto AW, Bazmi AA, Zahedi G (2013) Underground coal gasification: from fundamentals to applications. Progr Energ Combust Sci 39:189–214
14. Liu GS, Niksa S (2004) Coal conversion submodels for design appplications at elevated pressures. Part II. Char gasification. Progr Energ Combust Sci 30:679–717
15. Ghani MU, Radulovic P, Smooth LD (1996) An improved model for fixed bed combustion and gasification: sensitivity analysis and applications. Fuel 75:1213–1226
16. Irfan MF, Usman MR, Kusakabe K (2011) Coal gasification in CO_2 atmosphere and its kinetics since 1948: a brief review. Energy 36:12–40
17. Fermoso J, Arias B, Plaza MG, Pevida C, Rubiera F, Pis JJ, Garcia-Pena F, Casero P (2009) High pressure co-gasification of coal with biomass and petroleum coke. Fuel Process Technol 90:926–932
18. Wang J, Yao Y, Cao J, Jiang M (2010) Enhanced catalysis of K_2CO_3 for steam gasification of coal char by using $Ca(OH)_2$ in char preparation. Fuel 89:310–317
19. Zhang Y, Ashizawa M, Kajitani S, Hara S (2010) A new approach to catalytic coal gasification: the recovery and reuse of calcium using biomass derived crude vinegars. Fuel 89:917–922
20. Dinçer I (1998) Energy and environmental impacts: present and future perspectives. Energ Source 20:427–453
21. Kaygusuz K (1999) Energy and water potential of the southeastern anatolia project (GAP). Energ Source 21:913–922
22. Kaygusuz K (1999) Energy situation, future developments, energy saving and energy efficiency in Turkey. Energ Source 21:405–416
23. Tasdemiroglu E (1994) Environmental damage due to thermal power generation in Turkey. Energy 19(12):1235–1244
24. EIA (2002) Energy Information Administration, ınternational energy outlook 2002, pp. 69–89
25. Hepbaslı A (2004) Coal as as energy source in Turkey. Energ Source 26:55–63
26. Speight JG (1996) Environmental technology handbook. Taylor Francis, Washington, DC
27. Dincer I (2001) Environmental issues: I-Energy utilization. Energ Source 23:69–81
28. Shirazi AR, Börtin O, Eklund L, Lindquist O (1995) The impact of mineral matter in coal on its combustion: a new approach to the determination of the calorific value of coal. Fuel 74(2):247–251
29. Wang ZY, Tomita A (1998) Removal of mineral matter from some Australian coals by Ca$(OH)_2$/HCl leaching. Fuel 77:1747–1753
30. Mukherjee S (2003) Demineralization and desulfurization of high sulfur Assam coal with alkali treatment. Energy Fuel 17:559–564
31. Kumar M, Shankari RH (2000) Removal of ash from Indian Assam coking coal using sodium hydroxide and acid solutions. Energ Source 22:187–196
32. Karaca H, Önal Y (2003) Demineralization of lignites by single and successive pretreatment. Fuel 82:1517–1532
33. Gulen J, Doymaz I, Toprak S, Pişkin S (2005) Removal of mineral matter from Silopi Harput asphaltite by various acid treatment. Energ Source 2:1457–1464
34. Steel KM, Patrick SW (2001) The production of ultra clean coal by chemical demineralization. Fuel 80:2019–2023
35. Mukherjee S, Borthakur PC (2001) Chemical demineralization/desulphurization of high sulphur coal using sodium hydroxide and acid solutions. Fuel 80:2037–2040
36. Wang J, Tomita A, Taylor GH, Gerald J, Fitz D (1997) Microscopic observation of coal demineralization by $Ca(OH)_2$ leaching. Fuel 76:369–374
37. Wu Z, Steel KM (2007) Demineralization of a UK bituminious coal using HF and ferric ions. Fuel 26:2194–2200
38. Ishihara A, Sutrisna IP, Finahari I, Qian EW, Kabe T (2004) Effect of demineralization on hydrogen transfer of coal with tritiated gaseous hydrogen. Fuel Process Technol 85:887–903

39. Demirbaş A (2002) Demineralization and desulfurization of coals via column froth flotation and different methods. Energ Conver Manag 43:885–895
40. Jorjani E, Ghasemi Chapi H, Tayebi Khorami M (2011) Ultra clean coal production by microwave irradiation pretreatment and sequential leaching with HF followed by HNO_3. Fuel 92:1898–1904
41. Ambedkar B, Chintala TN, Nagarajan R, Jayanti S (2011) Feasibility of using ultrasound-assisted process for sulfur and ash removal from coal. Chem Eng Process 50:236–246
42. Perry N (1981) Coal gasification process. Noyes Data Corporation, Park Ridge
43. Gai H, Jiang Y, Qian Y, Kraslawsk A (2008) Conceptual design and retrofitting of coal gasification waste water treatment process. Chem Eng J 138:84–94
44. Telli K (1984) Fuels and combustion, Akdeniz Üni., Isparta, Publication no: 17, (Yakıtlar ve Yanma - in Türkish).
45. Hebden D, Stroud HJF (1981) Coal gasification processes. In: Elliot MA (ed) Chemistry of coal utilization, second supplemantory volume. New York, NY, Wiley Interscience
46. Hartman HF, Belk JP, Reagan DE (1978) Low Btu gasification processes. Oak Ridge National Laboratory, Springfield, VA, US Department of energy
47. Botts WV, Kohl AL, Thrilling CA (1976) Low Btu gasification of coal by atomics international molten process. Proceedings of eleventh intersociety energy conversion engineeering conference, Washington, DC
48. Nowacki P (1981) Coal gasification processes. Noyes Data Corporation, Park Ridge, NJ
49. Demirbaş A, Demirbaş A, Demirbaş H (2004) Global energy sources, energy usage and future developments. Energ Source 26:191–204
50. IEA, International Energy Agency (1989) Energy and environment: policy overview. IEA, Paris
51. Colonbo U (1992) Development and the global environment. In: Hollander JM (ed) The energy-environment connection. Island Press, Washington, DC, pp 3–14
52. IPPC (2007) Intergovernmental panel on climate change, climate change 2007. Synthesis report, November 17, 2007
53. Molina A, Mondragon F (1998) Reactivity of coal gasification with steam and CO_2. Fuel 77(15):1831–1839
54. Collot AG (2006) Matching gasification technologies to coal properties. Int J Coal Geol 65:191–212
55. Gülen J (2007) Mineral matter identification in Nallıhan lignite by leaching with mineral acids. Energ Source 29:231–237

Chapter 57
Experimental and Theoretical Analysis of Evapotranspiration in Green Roof Systems

Harisha Karanam, William Retzlaff, Susan Morgan, and Serdar Celik

Abstract This study focuses on the water loss of green roof systems due to evapotranspiration, which is the combination of evaporation and transpiration processes. Water loss through evapotranspiration increases the capacity of a green roof to intercept additional stormwater during the following rain event and keep it out of the municipal stormwater system. Hence it is important that amount of water loss through a green roof, with known plant and growth medium properties and climate conditions, can be quantified. A theoretical model based on energy equation is used and MATLAB is employed in solving the equations due to the complexity of the problem. Relevant heat transfer equations with appropriate thermophysical properties of materials are used. Values obtained from the theoretical analysis are compared with experimental values that were gathered via a field project in which different green roof samples were tested for 2.5 years in terms of their weight under wet and dry seasonal conditions. The results from the theoretical model are found to be in close agreement with the experimental measurements, which is encouraging for predicting water loss of green roof systems in different geographic locations with known climate conditions.

Nomenclature

A	Area, m^2
C	Bulk transfer coefficient
c_p	Specific heat, J/kgK
H	Sensible heat flux, W/m^2
h	Enthalpy, J/kg
I	Solar radiation, W/m^2

H. Karanam (✉) • W. Retzlaff • S. Morgan • S. Celik
Southern Illinois University, Edwardsville, IL 62026, USA
e-mail: nkarana@siue.edu; wretzla@siue.edu; smorgan@siue.edu; scelik@siue.edu

K   Thermal conductivity, W/mK
L   Latent heat flux, W/m^2
LAI   Leaf area index
m   Mass, kg
P   Volume, m^3
Q   Mixing ratio
r''   Surface wetness factor
S   Solar peak hours, h/day
T   Temperature, K
W   Wind speed, m/s
Z   Height, m

Greek Symbols

α   Surface albedo
Δ   Net change
ε   Emissivity
ρ   Density, kg/m^3
σ   Amount of foliage covered

Subscripts

A   Air
dir   Direct
evap   Evaporation
f   Foliage
g   Growth medium
sat   Saturation

57.1   Introduction

Green roofs play a major role by providing benefits such as maintaining lower temperatures inside the building, reducing stormwater runoff, mediating heat island effect, improving environmental quality, increasing the lifespan of roofing membranes, and acting as an acoustic insulator. Among these benefits, stormwater runoff is the main advantage that especially the municipalities and city authorities focus on. Due to retention of rain water above the roof, the sewer systems are not loaded fully during heavy rain events. This prevents possible floods that can cause significant damage in large cities.

While retention of stormwater above the roof can be an advantage in terms of preventing flood events, the added weight of water kept above the roof can introduce some risks to the buildings, especially those which are in earthquake zones. Hence a clear understanding of amount of water coming to the roof and leaving the roof is necessary. Water adds weight on top a roof either due to precipitation or irrigation. Some amount of this water goes to the sewer through drainage, while some amount is stored within the plant canopy and growth medium layers of a green roof. There is also a portion of water that is returned back to the atmosphere through evapotranspiration which is the combined processes of evaporation from the plants and the soil, and transpiration from the plant canopy. Evapotranspiration for a green roof is important as it reduces again the added weight of water on green roofs, eliminating or reducing the heavy weight risk of these roof systems.

Numerous studies on stormwater management using green roofs exist in literature. An experimental study [1] deals with the storm water management for three different roof designs including conventional type, medium design type and extensive green roof, over a period of one year. Performance of a green roof system during winter and dry seasons are studied to evaluate seasonal influence of the system for different designs. It is observed that the medium only and extensive green roofs reduced storm water runoff identically during winter rainy seasons whereas during summer seasons the extensive green roof retains more rainfall. As expected, as the growth medium gets more saturated with rainfall, stormwater retention decreases proportionally. Several studies have demonstrated that stormwater retention has its peak value when the growth medium is dry [2–4]. The amount of moisture in the growth media used in an experimental study [5] employs a 14 cm-deep growth medium composed primarily with expanded shale, perlite, and coconut husks. It has demonstrated that 0.1 cm of moisture can be retained by the green roof when there is 25 % moisture by volume in the growth media. When moisture by volume in the growth media is 15 %, approximately 0.5 cm of stormwater can be retained before runoff from the green roof begins. A review conducted on the performance of quantity and quality of storm water runoff from a green roof system presents information about different factors controlling runoff [6]. The different factors affecting stormwater runoff including green roof properties such as slope, vegetation, moisture properties of growth medium, weather, season, etc. are discussed and also the quality of stormwater with the minerals and other materials are considered. Another experimental analysis [7] examines the differences in quality and quantity of different green roof designs. It is observed that there are significant variations in concentrations of total phosphorus and nitrogen levels between green roofs having different plant and growth media. For the evaluation of effect of stormwater runoff, its quantity, and its quality of dissolved nutrients and metals from an extensive green roof system, rain water runoff is collected for precipitation analysis [8]. According to this study, the green roof retains 51.4 % of precipitation during the experiments which is 34 % more than the predicted value obtained from the calibration equation. Richter's thesis study [9] analyzes atmospheric water

loss from modular green roof systems with varying growth media and plant types. Karanam [10] compares experimental results to theoretically obtained water loss from green roof systems by modifying the models suggested in literature [11, 12].

In this chapter, theoretical and experimental studies are compared for verification purposes. Results from the experimental study performed at the Southern Illinois University Edwardsville campus [9] are compared to the theoretical model developed [11, 12].The recorded output of the experimental work includes amount of water loss from the green roofs by means of evapotranspiration. The theoretical model is modified based on the conditions of the experimental setup, climate, and system properties. The model accounts for significant parameters affecting evapotranspiration such as solar irradiance, fractional plant coverage, leaf area index, stomatal resistance, wind speed, moisture content, and growth medium depth. Due to the complex nature of the problem, MATLAB is used to solve for the loss of water from the green roof systems.
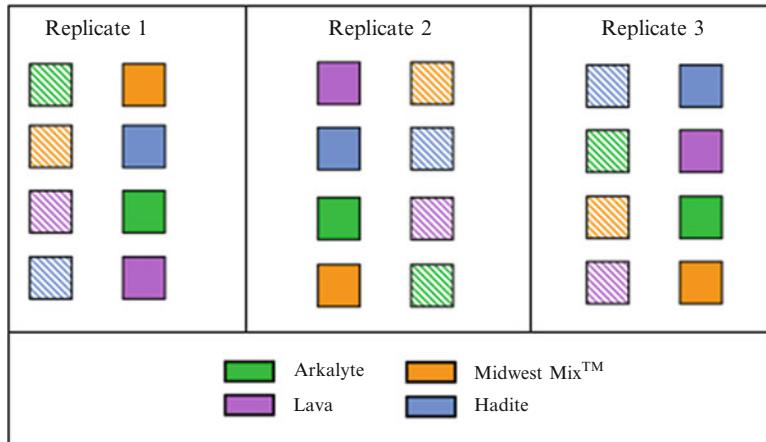
57.2 Background

A research conducted by Richter [9] deals with the effects of atmospheric water loss from two dissimilar modular green roof systems (Green Paks^{TM} and Green Roof Blocks^{TM}), having different drainage layers, growth medium (Arkalyte-expanded clay, Haydite-expanded slate, Lava, and Midwest Mix^{TM}) and plant species combinations (*Sedum kamtschaticum* and *Sedum spurium*). Fractional plant coverage for the modular green roof systems are evaluated using a modified dot grid method from the data measured on specific days throughout the study. A one-way ANOVA technique was used to compare percent roof coverage and total storm water loss from vegetation, growth media, and drainage layer direction using the data collected from the experimental analysis (Fig. 57.1).
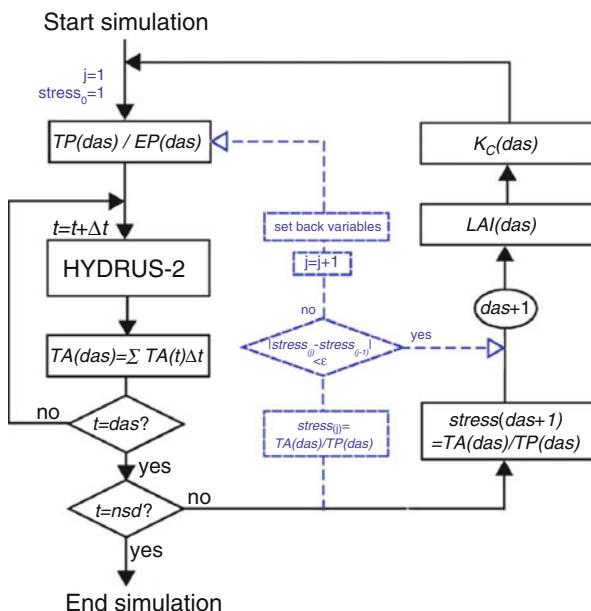
In a thesis study by Feller [13], evapotranspiration from an extensive green roof system is analyzed. Experimental data is compared to some predictive correlations such as Penman equation and Penman–Monteith equation to evaluate evapotranspiration. The study reveals that both equations yield close results to experimentally obtained values. The theory on water uptake in plants is also crucial as evapotranspiration amount is related to the water coming from the roots.

In another study [14], 2D subsurface flow model, HYDRUS-2, is coupled with an analytical solution of the zero-inertia surface flow equations to account for the water uptake (Fig. 57.2).

The irrigation system is considered as a dynamic system comprised with the crop, soil surface, and the soil body. This crop module simulates transport of water to, from, and within the system by computing daily average of evaporation, transpiration, and the leaf area index (LAI).
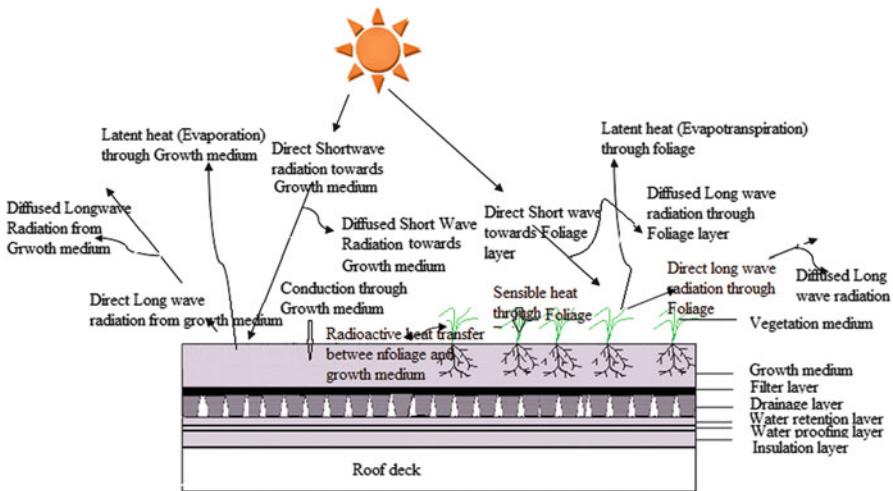
Fig. 57.1 Green roof blocks oriented in a completely randomized design (Source: Modified from [9])

Fig. 57.2 Schematic of the coupling of HYDRUS-2 and the crop model (Source: Modified from [14])

57.3 Theoretical Analysis

Laws of conservation of mass and energy are employed for deriving an equation that will lead to amount of water loss from the green roofs due to evapotranspiration phenomenon. Based on conservation of mass, amount of water coming to the

Fig. 57.3 Conservation of energy on a green roof system

roof system should equal to the amount of water leaving the roof and stored in the green roof system.

$$P' + I'\frac{dT_g}{dZ} = ET + D' + \Delta M_s \tag{57.1}$$

In Eq. (57.1); P' is the volume flow rate of precipitation entering the system, I' the rate of water supplied to green roof through sprinkler (irrigation), ET' is the rate of water loss due to evapotranspiration, D' is the rate of drainage, and ΔM_s is the amount of water stored in the growth medium per unit time.

Conservation of energy equation accounts for all means of solar radiation, sensible heat fluxes, and latent heat fluxes. Figure 57.3 lists all heat transfer mechanisms that the vegetation and the growth medium are experiencing, along with a sketch of green roof layers.

Simplified energy equations developed for both the foliage and growth medium layer are given in Eq. (57.2) and Eq. (57.3), respectively:

$$\Delta I_s + \Delta I_l + Q + H_f + L_f + P_f = 0 \tag{57.2}$$

$$\Delta I_s + \Delta I_l - Q + H_g + L_g + P_g + K\frac{dT_g}{dZ} = 0 \tag{57.3}$$

In the above equations; ΔI_s and ΔI_l represent the shortwave and longwave radiations. Q is the radiation exchange between the foliage and the growth medium. It is same in magnitude, however negative due to the direction in the two equations. Here, growth medium temperature is considered to be higher than that of foliage

temperature, hence the negative sign for Q in Eq. (57.3). H, L, and P are the sensible, latent, and precipitation heat fluxes, respectively. The last term in Eq. (57.3) gives the conduction heat flux through the growth medium. Eqs. (57.4–57.8) give the shortwave and longwave radiation fluxes to/from the foliage, radiation heat flux from the growth medium to the plant canopy, and sensible and latent heat fluxes to/from the foliage layer, respectively [12]. Precipitation heat flux is assumed to be zero for the foliage layer.

$$\Delta I_{sf} = \sigma_f \left(1 - \alpha_f\right) I_{s\downarrow}^{dir} \tag{57.4}$$

$$\Delta I_{lf} = \epsilon_f \sigma_f I_{lf\downarrow}^{direct} - \epsilon_f \sigma_f \sigma T_f^4 \tag{57.5}$$

$$Q = \frac{\sigma_f \sigma \epsilon_f \epsilon_g}{\epsilon_1} \left(T_g^4 - T_f^4\right) \tag{57.6}$$

$$H_f = \left(1.1 LAI \rho_{af} C_{p,a} W_{af} C_f\right)\left(T_{af} - T_f\right) \tag{57.7}$$

$$L_f = l_f LAI \rho_{af} C_f W_{af} r''\left(q_{af} - q_{f,sat}\right) \tag{57.8}$$

Similar set of equations are given for the growth medium:

$$I_{sg} = (1 - \sigma_f)\left(1 - \alpha_g\right) I_s^{\downarrow} \tag{57.9}$$

$$\Delta I_g = (1 - \sigma_f)\left(\epsilon_g I_1^{\downarrow} - \epsilon_g \sigma T_g^4\right) \tag{57.10}$$

$$H_g = \rho_{ag} C_{p,a} C_{hg} W_{af}\left(T_{af} - T_g\right) \tag{57.11}$$

$$L_g = C_{e,g} l_g W_{af\,ag}\left(q_{af} - q_g\right) \tag{57.12}$$

$$P_g = -Y_p [P_r - I + D] C_p T_p \tag{57.13}$$

In Eqs. (57.4–57.13), the symbols σ, α, ρ, LAI, W, C, r″, Y, I, and D denote fractional plant coverage, albedo, density, leaf area index, wind speed, bulk heat transfer coefficient, surface wetness factor, precipitate density, irrigation rate, and drainage rate, respectively.

Evapotranspiration occurs due to latent heat flux through the foliage and the growth medium layers. Hence, total amount of latent heat transfer rate per unit surface area of green roof system should be calculated using Eq. (57.8) and Eq. (57.12). Total latent heat flux is:

$$L = L_f + L_g \tag{57.14}$$

where L_f and L_g are latent heat flux values (W/m^2) through the foliage and growth media, respectively. As this is the instantaneous latent heat flux based on the azimuthal angle of the sun used in the solar radiation calculations, an overall latent heat flux value should be calculated by integrating the instantaneous values over the day time when the sun is up. Using solar peak hour values (S, hour/day), overall latent heat flux can be obtained:

$$L_{overall} = L \; S \qquad (57.15)$$

Once the total latent heat flux throughout the day is calculated, daily mass of water leaving the green roof can be obtained using Eq. (57.16):

$$L = \frac{L_{overall} A}{h_{evp}} \qquad (57.16)$$

where A is the surface area of the green roof (m^2), and h_{evap} is the enthalpy of vaporization of water (J/kg).

57.4 Results

Daily water loss of green roof systems is experimentally tested on a research site at Southern Illinois University Edwardsville campus. Recorded values for one set of days are presented in Table 57.1. Weight data of green roof samples are collected for four days, the samples being fully saturated on the first day. Table 57.2 lists the amount of water loss for different growth media during the first 24 hours of the experimentation [10]. First day is used in the theoretical analysis for simplicity as the system is known to be fully saturated.

These weight loss values are compared with the calculated weight loss values. In the theoretical model, one major problem is finding the leaf area index (LAI) value for the samples. As determination of LAI is a complex problem, a reverse engineering method is used. Data from one of the other experimental day sets (June 29–30, 2009) are used to solve backwards for the LAI value for each growth medium so that the theoretical and experimental water loss amounts can perfectly agree. Table 57.3 lists the experimental and theoretical values along with percent error for illustrating the accuracy of the model and the assumptions. As can be seen in the table, theoretical findings are in close agreement with the experimental results (2.33–8.54 % error range).

In addition to comparison of theoretical and experimental results, identification of the significant parameters on water loss from green roof systems is also performed. Among approximately 12 independent variables, wind speed and leaf area index are found to be the dominant ones affecting the water loss. Also, to have an idea about the effect of growth medium depth, this parameter is also observed.

Table 57.1 Experimental daily weight data in kg/m^2

Replicate	Growth medium	7/15/2008	7/16/2008	7/17/2008	7/18/2008
1	Haydite	88.1	84.3	82.3	80.8
	Arkalyte	90.5	86.2	82.9	81
	Lava	82.7	78.9	76.1	73.7
2	Lava	89.7	84.7	80.9	78.2
	Haydite	97.5	94.2	91.9	90
	Arkalyte	95.3	92	90.2	88.7
3	Haydite	83.7	81.8	80.3	79.5
	Lava	81	78.2	76.5	75.3
	Arkalyte	89.7	86.4	84.5	83.3

Table 57.2 Weight loss data (kg/m^2) for the first day of being fully saturated

Replicate	Growth medium	7/15–7/16
1	Haydite	3.8
	Arkalyte	4.3
	Lava	3.8
2	Lava	5
	Haydite	3.3
	Arkalyte	3.3
3	Haydite	1.9
	Lava	2.8
	Arkalyte	3.3
Average of reps	Haydite	3
	Lava	3.6
	Arkalyte	3.9

Table 57.3 Comparison of experimental and theoretical weight loss results

Growth medium	LAI	Plant coverage (σ_f)	Experimental (kg/m^2 day)	Theoretical (kg/m^2 day)	% Error
Haydite	0.905 σ_f	0.65	3	2.93	2.33
Arkalyte	0.9 σ_f	0.72	3.6	3.32	8.54
Lava	1.635 σ_f	0.68	3.9	3.74	3.36

Change in the amount of water loss due to evapotranspiration with changing wind speed, leaf area index, and growth medium depth are given in Figs. 57.4, 57.5, and 57.6, respectively.

Wind speed does not seem to have an effect on water loss until about 0.8 m/s. Although the expectation is that the heat flux would increase with increasing wind speed, resulting in increased evapotranspiration losses; as wind speed goes above 0.8 m/s, water loss is decreasing. This is due to the closing of stomata at high wind speeds.
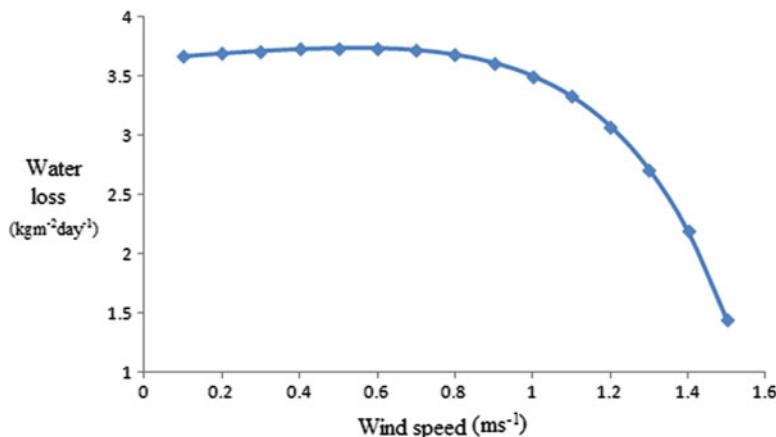
Fig. 57.4 Water loss vs. wind speed for lava
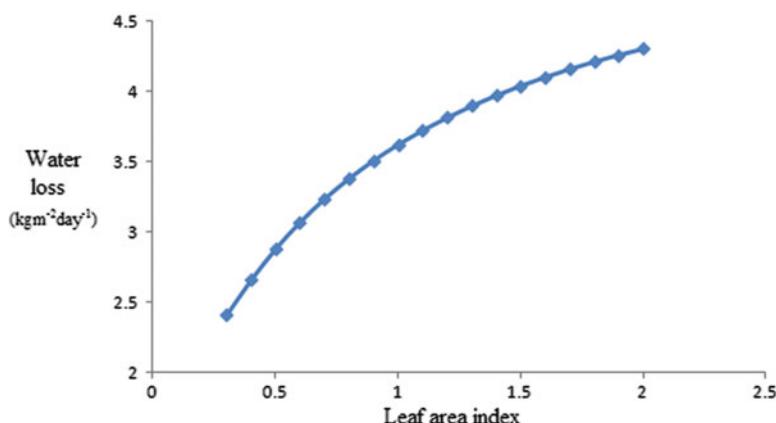
Fig. 57.5 Water loss vs. leaf area index for lava

Once the sedum plants sense increased air flow, they close their stomata resulting in increased stomatal resistance. Increase in leaf area index (LAI) results in increased water loss from the green roof system. This can be explained by higher transpiration rates due to increased leaf surface area. It should be noted that fractional plant coverage (σ_f) was kept constant while changing the LAI values (more layers of leaves with same amount of shading on the green roof surface). Water loss is observed to be slightly decreasing as the growth medium depth increased from 5 to 20 cm. This is due to decreasing effect of solar radiation through the growth medium from the surface to the bottom.
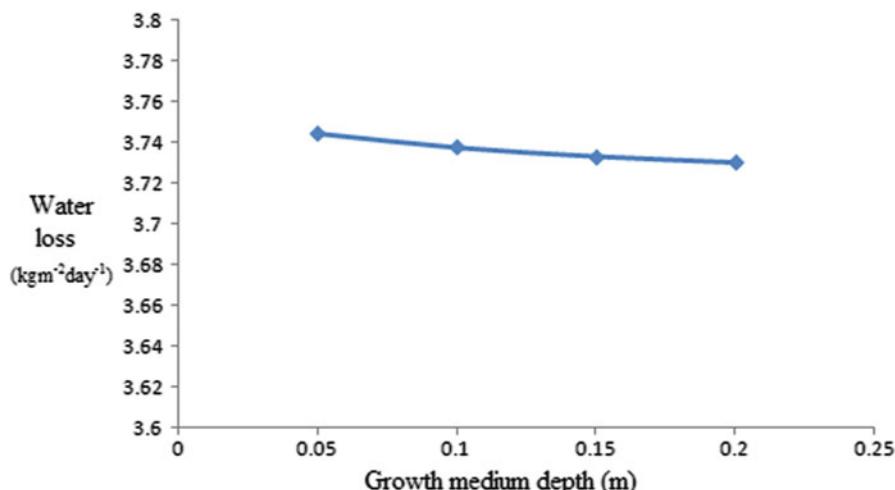
Fig. 57.6 Water loss vs. growth medium depth for lava

57.5   Conclusion

An existing heat transfer model in literature is modified and implemented in MATLAB to determine the amount of water loss by means of evapotranspiration. Validation of the model is tested through an experimental work conducted on SIUE campus. Analysis is performed on three different growth media: haydite, arkalyte, and lava, all planted with *Sedum spurium*. Input values used in the analyses are obtained from several sources such as experimental studies, literature, and online databases providing weather history data and thermophysical properties of materials used. As determination of leaf area index (LAI) is a complex problem, a deductive engineering approach is employed. Data from one of the experimental day sets is used to solve backwards for the LAI value for each growth medium. Obtained LAI values are used for the other two sets of days to verify the model. Theoretical results are found to be in close agreement with the experimental data having an error range of 2.33–8.54 %. Possible sources of error are approximations in plant and growth medium properties, climate data including instantaneous wind speed and sky clearness, and determination of leaf area index. The modified model can be very useful in predicting water loss from green roof systems for safer building and site designs.

References

1. Schroll E, Lambrinos J, Righetti T, Sandrock D (2011) The role of vegetation in regulating stormwater runoff from green roofs in a winter rainfall climate. Ecol Eng 37:595–600
2. Bengtsson L (2005) Peak flows from thin sedum-moss roof. Nord Hydrol 36:269–80

3. Monterusso MA, Rowe DB, Rugh CL, Russell DK (2004) Runoff water quantity and quality from green roof systems. Acta Hort 639:369–73

4. Villareal EL, Semadeni-Davies A, Bengtsson L (2004) Inner city stormwater control using a combination of best management practices. Ecol Eng 22:279–98

5. Bliss DJ, Neufeld RD, Ries RJ (2009) Storm water runoff mitigation using a green roof. Environl Eng Sci 26(2):407–17

6. Berndtsson JC (2010) Green roof performance towards management of runoff water quantity and quality: a review. Ecol Eng 36:351–60

7. Stanford RL, Yu SL, Ruifen L, Field R, Tafuri AN, Luo L, Deng Y (2011) Performance evaluation of different green roof designs - Chengdu, China. Low impact development symposium. Philadelphia, PA, 25–28 Sept 2011.

8. Gregoire BG, Clausen JC (2011) Effect of a modular extensive green roof on storm water runoff and water quality. Ecol Eng 37:963–9

9. Richter L (2010) Stormwater loss through evapotranspiration from green roof systems. Master's Thesis. Southern Illinois University Edwardsville.

10. Karanam NH (2012) Analysis of water loss by evapotranspiration from green roof systems. Master's Thesis. Southern Illinois University Edwardsville.

11. Frankenstein S, Koenig GG (2004) Fast all-season soil strength. Technical report TR-04-25. US Army Engineer Research and Development Center, Hanover, NH.

12. Sailor DJ (2008) A green roof model for building energy simulation programs. Energ Buildings 40:1466–78

13. Feller MM (2011) Quantifying evapotranspiration in green infrastructure: a green roof case study. Master's Thesis. Villanova University.

14. Wohling T, Schmitz GH (2007) Physically based coupled model for simulating 1D surface – 2D subsurface flow and water uptake in irrigation furrows: model development. J Irrig Drain E-ASCE 133:538–47

Chapter 58
New Parameters for Reduction of Heating-Based Greenhouse Gas Emissions: A Case Study

Can Coskun, Mustafa Ertürk, Zuhal Oktay, and Ibrahim Dincer

Abstract In this study, the effect of indoor temperature for heating on reduction of carbon dioxide emissions in Turkey is studied under various conditions. Two new parameters are introduced, namely, carbon dioxide emission reduction effect (CO_2 RE) and carbon dioxide emission reduction rate (CO_2RR). The potential heating degree-hour values for Turkey are used in conjunction with the potential average outdoor temperature distribution of the country to calculate/arrive at values for the two new parameters. The average outdoor temperature distributions for Turkey are calculated using this approach. In order to estimate the potential average outdoor temperature distributions and the respective heating degree-hour values, the effects of population and outdoor temperature distribution for each city are considered and included here for comparison purposes. The results show that heating-based carbon dioxide emissions may be decreased by 111 % and 5.6 % for 18 °C and 28 °C indoor design temperatures, respectively. It is considered that these two potential parameters may prove valuable tools for local authorities in identifying cities with significant potential for reductions in carbon dioxide emissions caused by residential heating applications.

C. Coskun (✉) • Z. Oktay
Energy Systems Engineering Department, Faculty of Engineering, Recep Tayyip Erdoğan University, Rize, Turkey
e-mail: dr.can.coskun@gmail.com; zuhal.oktay@gmail.com

M. Ertürk
Mechanical Engineering Department, Faculty of Engineering, Balikesir University, 10110 Balikesir, Turkey
e-mail: merturk@balikesir.edu.tr

I. Dincer
Faculty of Engineering and Applied Science, University of Ontario Institute of Technology (UOIT), 2000 Simcoe St. N., Oshawa, ON, Canada L1H 7K4
e-mail: ibrahim.dincer@uoit.ca

Nomenclature

CAHDH	Country average degree hour values, °C-hours
CO₂RE	Carbon dioxide emission reduction effect, %
CO₂RR	Carbon dioxide emission reduction rate, %
HDH	Heating degree-hours, °C-hours
P	Population

Subscripts

DT	Desired indoor temperature (°C)
RT	Reference indoor temperature (°C)

58.1   Introduction

In the twenty-first century, some of the most significant problems for mankind are climate change, high energy demand, waste management, high water consumption, land management, the conservation of ecosystems, the conservation of endangered species, and issues of public health [1].

Among these, the problem of high demand for energy requires the utilization of different energy sources. It is well known that there is a strong relation between the use of some energy sources, such as fossil fuels, and climate change. Burning of hydrocarbons emits greenhouse gases into the atmosphere, primarily in the form of carbon dioxide, CO_2. Now widely accepted as a greenhouse gas, CO_2 has detrimental impacts on both human health and the global climate. Stabilizing the carbon dioxide-induced components of climate change is an important challenge in the utilization of energy sources [2]. Carbon concentration is predicted to increase to 750 ppm by the end of the century, while the global goal is to keep its concentration at 350 ppm.

Global climate change, it is now generally believed, derives largely from CO_2 emissions, and manifests itself in a range of serious environmental issues such as a 0.6 degree rise in average global surface temperature in the last 100 years, an increase of the global average surface temperature over the last century, a rise in the temperature of the lowest 8 km of the atmosphere, a significant decrease in snow and ice cover, and a general rise in global sea levels and ocean temperatures

[2]. The rapid bulid-up of these problems serves only to make the need for new methods of control and prevention more urgent. Radical changes are required both in the way we use fossil fuels and also in our utilization of energy systems. It is obvious that continued use of fossil fuels at current or increasing rates will have a detrimental impact on the global climate. Stabilization of the amount of fossil fuels used requires effort to reduce energy demand. It also requires new developments in the utilization of primary energy sources which do not emit carbon dioxide into the atmosphere [3].

Revision of indoor temperatures in living areas can reduce heating energy demand and thereby help to reduce heating-related greenhouse gas emissions. Several studies have been undertaken to analyze outdoor temperatures by using degree-hour/day values in order to predict energy requirements for the heating and cooling of buildings [4–8]. Haas et al. [9] investigated the impact of consumer behavior on residential energy demand for space heating in Austria. He states that the thermal quality of buildings, consumer behaviour, heating degree days and building type all have a significant effect on residential energy demand. The result of this investigation provides evidence of a rebound-effect of about 15–30 % due to building retrofit. This leads to the conclusion that energy savings achieved in practice (and consequently the reduction in CO_2 emissions) due to energy conservation measures will be lower than those calculated in engineering conservation studies.

In this study, the effect of variations in indoor heating temperatures on the reduction of CO_2 emissions is examined, and a range of cases are presented for analysis and comparison purposes.

58.2   Development of New Parameters

In this study, two new parameters are introduced to the literature-CO_2 emission reduction effect (CO_2RE) and CO_2 emission reduction rate (CO_2RR). CO_2RE, and are correlated for each city of the country on CO_2 emission reduction by varying the indoor heating temperature. In fact, CO_2RE is a combination of the total degree-hour value and the population of a city and can be defined as follows:

$$CO_2RE_{city} = \frac{100 \cdot (HDH_{DT} - HDH_{RT}) \cdot P_{city}}{P_{country} \cdot HDH_{RT}} \qquad (58.1)$$

where, HDH_{DT} and HDH_{RT} represent the heating degree-hours for desired and indoor temperature; P_{city} and $P_{country}$ are the populations of the city and country considered in the study; and DT and RT represent the desired and reference indoor temperature, respectively.

The other parameter, CO_2 emission reduction rate, shows the contribution of a city to the total effect and can be obtained as follows:

$$CO_2RR_{city} = \frac{100 \cdot CO_2RE_{city}}{CO_2RE_{Tot,city}} \tag{58.2}$$

where, $CO_2RE_{Tot,city}$ indicates the total CO_2 emission reduction effect for all cities in the studied country and can be obtained by

$$CO_2RE_{Tot,city} = \sum \left[CO_2RE_{city,1} + ... + CO_2RE_{city,n} \right] \tag{58.3}$$

This calculation method can be extended to evaluate the contribution of each individual country to overall co_2 emission reduction across the world. For this purpose, the population density-based average heating degree hours for each country should be calculated. In this regard, CO_2 emission reduction rate for a country can be obtained by

$$CO_2RE_{country} = \frac{100 \cdot (CAHDH_{DT} - CAHDH_{RT}) \cdot P_{country}}{P_{world} \cdot CAHDH_{RT}} \tag{58.4}$$

where, $P_{country}$ and P_{world} indicate the population of the country and the world, respectively. The country average degree hour values ($CAHDH_{RT}$) can be calculated for any reference indoor temperature by the following equation:

$$CAHDH_{RT} = \sum \left[HDH_{city,1}^{RT} \cdot \frac{P_{city,1}}{P_{country}} + ... + HDH_{city,n}^{RT} \cdot \frac{P_{city,n}}{P_{country}} \right] \tag{58.5}$$

Note that the population density-based average heating degree hours for Turkey is determined by the following equation:

$$CAHDH_{Turkey}(RT) = 170.85 \cdot 0.97656^{RT} \cdot RT^{2.099} \tag{58.6}$$

The CO_2 emission reduction rate for a country ($CO_2RR_{country}$) and country total CO_2 emission reduction effect ($CO_2RE_{Tot,city}$) can be obtained by using the following equations:

$$CO_2RR_{country} = \frac{100 \cdot CO_2RE_{country}}{CO_2RE_{Tot,country}} \tag{58.7}$$

$$CO_2RE_{Tot,country} = \sum \left[CO_2RE_{country,1} + ... + CO_2RE_{country,n} \right] \tag{58.8}$$

58.3   Results and Discussion

In order to illustrate how to use Eqs. (58.1)–(58.3), two new parameters proposed in this study are calculated for a case study which is carried out for the city of Istanbul. The CO_2 reduction effect for Istanbul by decreasing the reference indoor temperature from 24 to 23 °C can be calculated as

$$CO_2RE_{Istambul} = \frac{100 \cdot (HDH_{23°C} - HDH_{24°C}) \cdot P_{Istambul}}{P_{Turkey} \cdot HDH_{24°C}}$$

$$CO_2RE_{Istambul} = \frac{100 \cdot (67522 - 72528) \cdot (13624240)}{(74724269) \cdot (72528)} = -1.258$$

As seen from the result, there is a 1.258 % decrease in total CO_2 emission in Turkey if the reference indoor temperature in Istanbul is lowered by 1 °C. For this case, CO_2 reduction rate of Istanbul can be calculated as follows:

$$CO_2RR_{Istambul} = \frac{100 \cdot CO_2RE_{Istambul}}{\sum CO_2RE_{city,n}} = \frac{100 \cdot (-1.258)}{(-6.644)} = 18.93$$
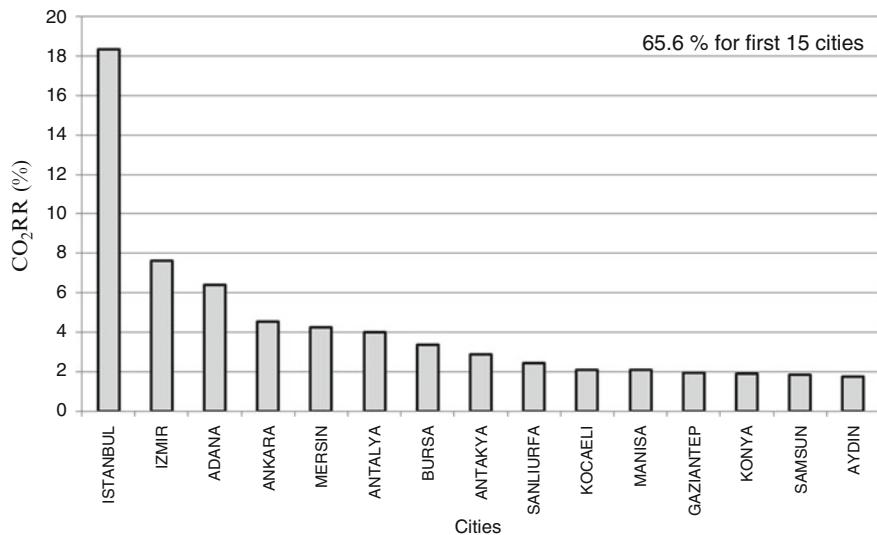
The result points out that the contribution of Istanbul within Turkey on decreasing the heating based CO_2 emission when the reference indoor temperature is lowered by 1 °C is 18.93 %. Similar to this, the average CO_2RR for each city in Turkey was calculated for 18–28 °C reference indoor temperatures and given in Table 58.1. Meanwhile, the 15 cities with highest CO_2RR values are given in Fig. 58.1. These cities are Istanbul, Izmir, Adana, Ankara, Mersin, Antalya, Bursa, Antakya, Şanlıurfa, Kocaeli, Manisa, Gaziantep, Konya, Samsun, and Aydın. As seen in the figure, these cities have 65.6 % contribution to the total CO_2RR. It should be noted that ordering in these cities is not directly related to their population.

It is apparent that outdoor temperature distribution is another factor effecting both CO_2RR and CO_2RE. Annual outdoor temperature distribution for each city in Turkey was determined and used to calculate the average annual outdoor temperature distribution for Turkey. Here, the reference is taken as the population of each city. Average outdoor temperature distribution for Turkey was calculated and given in Fig. 58.2.
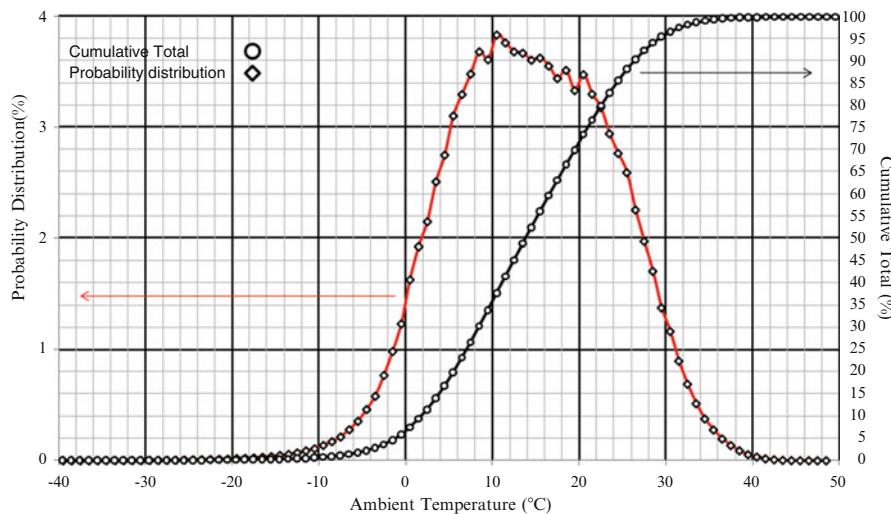
Furthermore, the population density-based average heating degree hours for Turkey is calculated by using average outdoor temperature distribution and given in Fig. 58.3. The effect of variation in indoor temperature between 18 and 28 °C on the heating-based CO_2 emission is investigated and given in Table 58.2. As can be seen from Table 58.2, the heating-based CO_2 emission reduction for 1 °C indoor temperature difference changes between 5.3 % and 9.3 % respectively.

Table 58.1 Average CO$_2$ reduction rate of each city in Turkey
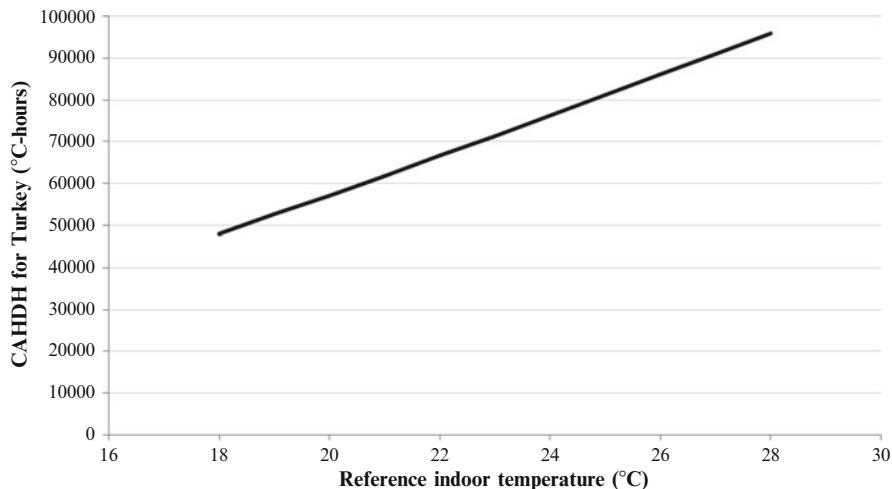
No	City	CO_2RR (%)	No	City	CO_2RR (%)
1	İstanbul	18.355	41	Erzurum	0.502
2	İzmir	7.634	42	Çorum	0.494
3	Adana	6.407	43	Rize	0.478
4	Ankara	4.536	44	Edirne	0.447
5	Mersin	4.261	45	Isparta	0.444
6	Antalya	4.034	46	Yozgat	0.425
7	Bursa	3.351	47	Kırklareli	0.395
8	Antakya	2.865	48	Amasya	0.382
9	Şanlıurfa	2.464	49	Düzce	0.379
10	Kocaeli	2.120	50	Siirt	0.376
11	Manisa	2.105	51	Aksaray	0.372
12	Gaziantep	1.957	52	Uşak	0.370
13	Konya	1.896	53	Kastamonu	0.327
14	Samsun	1.877	54	Kırıkkale	0.308
15	Aydın	1.750	55	Muş	0.306
16	Diyarbakır	1.749	56	Sinop	0.300
17	K.Maraş	1.492	57	Burdur	0.285
18	Balıkesir	1.486	58	Yalova	0.277
19	Denizli	1.278	59	Nevşehir	0.265
20	Sakarya	1.187	60	Bitlis	0.261
21	Trabzon	1.186	61	Bolu	0.260
22	Ordu	1.083	62	Karabük	0.251
23	Kayseri	1.048	63	Ağrı	0.239
24	Muğla	0.997	64	Bilecik	0.231
25	Tekirdağ	0.988	65	Karaman	0.228
26	Mardin	0.981	66	Bingöl	0.224
27	Osmaniye	0.946	67	Bartın	0.223
28	Zonguldak	0.863	68	Kırşehir	0.217
29	Adıyaman	0.850	69	Hakkâri	0.203
30	Van	0.821	70	Artvin	0.203
31	Malatya	0.777	71	Kars	0.197
32	Eskişehir	0.751	72	Kilis	0.191
33	Çanakkale	0.720	73	Erzincan	0.191
34	Afyon	0.690	74	Iğdır	0.172
35	Tokat	0.688	75	Çankırı	0.160
36	Giresun	0.661	76	Gümüşhane	0.113
37	Batman	0.608	77	Tunceli	0.081
38	Kütahya	0.569	78	Ardahan	0.065
39	Elazığ	0.548	79	Bayburt	0.053
40	Sivas	0.527			

Fig. 58.1 CO$_2$ emission reduction rates for 15 cities in Turkey

Fig. 58.2 Average outdoor temperature distributions for Turkey

Fig. 58.3 Population density-based average heating degree hours for Turkey

58.4 Conclusions

The comfort conditions required by users have a considerable effect on residential energy use for heating and consequently for levels of heating-based CO_2 emissions. It is important to study the feasibility of decreasing indoor reference temperatures around the world if significant CO_2 emission reductions are to be achieved. Two new parameters proposed in this study, CO_2 RE and CO_2 RR, should be utilized to determine priority cities for pilot applications. For instant, heating-based CO_2 emission can be decreased 7.1 % for Turkey when indoor reference temperature decreases from 23 to 22 °C. Several significant outcomes of this study are highlighted below:

- This is the first study to investigate the effect of CO_2 reduction by changing the indoor reference temperature for Turkey.
- Two new parameters are introduced to the literature, namely, CO_2 emission reduction effect and CO_2 emission reduction rate.
- These new parameters are very useful tools in identifying key target cities for heating-based CO_2 emission reduction.

Table 58.2 Percentage effect of variation of inside comfort temperature on the heating-based CO_2 emission for Turkey

Desired Temperature (°C)	Indoor temperature (°C)										
	18	19	20	21	22	23	24	25	26	27	28
18	0.0	−9.3	−17.1	−23.6	−29.3	−34.1	−38.4	−42.2	−45.4	−48.4	−51.0
19	10.3	0.0	−8.6	−15.9	−22.2	−27.6	−32.3	−36.5	−40.1	−43.3	−46.2
20	20.9	9.5	0.0	−8.1	−15.0	−20.9	−26.1	−30.6	−34.6	−38.2	−41.3
21	31.8	19.3	8.8	0.0	−7.5	−14.0	−19.7	−24.7	−29.0	−32.9	−36.4
22	42.8	29.2	17.8	8.2	0.0	−7.1	−13.2	−18.6	−23.3	−27.5	−31.3
23	54.0	39.2	26.9	16.5	7.6	0.0	−6.6	−12.5	−17.6	−22.1	−26.2
24	65.3	49.4	36.1	24.9	15.4	7.2	0.0	−6.3	−11.8	−16.6	−21.0
25	76.9	59.8	45.5	33.5	23.2	14.4	6.8	0.0	−5.8	−11.1	−15.8
26	88.3	70.0	54.8	41.9	31.0	21.6	13.4	6.2	0.0	−5.6	−10.6
27	99.9	80.4	64.2	50.5	38.9	28.9	20.2	12.5	5.9	0.0	−5.3
28	111.6	90.9	73.7	59.2	46.8	36.2	27.0	18.9	11.9	5.6	0.0

References

1. http://webecoist.momtastic.com/2008/08/18/most-important-environmental-issues-of-today/. Accessed Mar, 2012
2. Energy and nanotechnology: strategy for the future conference report 2005. http://www.rice.edu/energy/publications/docs/NanoReportFeb2005.pdf. Accessed Mar, 2012
3. Hoffert M (2005) Global warming and fuel choices. Energy and nanotechnology: strategy for the future conference report 2005. http://www.rice.edu/energy/publications/docs/NanoReportFeb2005.pdf. Accessed Mar, 2012
4. Oktay Z, Coskun C, Dincer I (2011) A new approach for predicting cooling degree hours and energy requirements in buildings. Energy 36:4855–4863
5. Coskun C (2010) A novel approach to degree-hour calculation: indoor and outdoor reference temperature based degree-hour calculation. Energy 35:2455–2460
6. Sarak H, Satman A (2001) The degree-day method to estimate the residential heating natural gas consumption in Turkey: a case study. Energy 28:929–939
7. Duryamaz A, Kadıoglu M, Sen Z (2000) An application of the degree-hours method to estimate the residential heating energy requirement and fuel consumption in Istanbul. Energy 25:1245–1256
8. Satman A, Yalcinkaya N (1999) Heating and cooling degree-hours for Turkey. Energy 24 (10):833–840
9. Haas R, Auer H, Biermayr P (1998) The impact of consumer behavior on residential energy demand for space heating. Energ Build 27:195–205

Chapter 59
Environmental Impact Assessment of Building Energy Systems

M. Tolga Balta, Ibrahim Dincer, and Arif Hepbasli

Abstract This chapter deals with energy/exergy and environmental analyses of a low exergy heating system. A building with a volume of about 392 m^3 and a floor area of 140 m^2 is presented as a case study. For this building, four different heating options are investigated, namely, (1) electric boiler, (2) ground heat pump system, (3) standard boiler, and (4) solar collector. In this regard, an energy and exergy analysis is employed to assess their performances and compare them through energy and exergy efficiencies. Also, CO_2, NO_x, SO_2 emissions of the considered systems are determined and compared with each other. Overall exergy efficiencies of the heating systems are found to be 4.0, 10.1, 7.6, and 35.7 %. CO_2, NO_x, SO_2 emissions rate per year (kg emission/year) calculated for considered cases as 10,726.32, 4,224.17, 3,737.56, and 337.67, 11.14, 4.39, 3.40, and 3.35, and 116.34, 45.82, 3.68, and 3.66, respectively. The lowest environmental impact is provided by case 4.

M.T. Balta (✉)
Department of Mechanical Engineering, Faculty of Engineering, Aksaray University, 68100 Aksaray, Turkey
e-mail: mustafatolgabalta@aksaray.edu.tr

I. Dincer
Faculty of Engineering and Applied Science, University of Ontario Institute of Technology, 2000 Simcoe Street North, Oshawa, ON, Canada L1H 7K4
e-mail: Ibrahim.Dincer@uoit.ca

A. Hepbasli
Department of Energy Systems Engineering, Faculty of Engineering, Yaşar University, Bornova, 35100 Izmir, Turkey
e-mail: arif.hepbasli@yasar.edu.tr
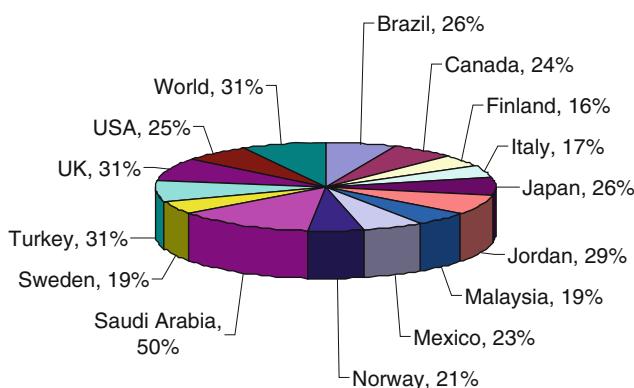
59.1 Introduction

Global consumption of primary energy to provide space heating/cooling, lighting, and other building-related energy services grew up due to growth in population, urbanization, and industrialization. These appliances are the main parts of the energy consumption in buildings, which is one of the main parts of the total energy consumption in most countries. Worldwide energy consumption by HVAC equipment in buildings ranges 16–50 % of total energy consumption, depending on the countries and their sectoral energy use patterns, as shown in Fig. 59.1. More than half of this energy is typically used for heating [1].

Today's building energy systems are based mainly on fossil fuels, which are both non-renewable, and also the major cause of global climate change. Global utilization of fossil fuels for energy demand is resulting with not only to global warming, but also to such environmental concerns as air pollution to climate change, forest destruction, and emission of radioactive substances, etc. These issues must be taken into consideration simultaneously if humanity is to achieve a bright energy future with minimal environmental impacts. Much evidence exists, which suggests that the future will be negatively impacted if humans keep degrading the environment [2].

In recent years, how to build sustainable buildings has been one of the prime concerns. Many scientists propose a large variety of solutions. One of the important solutions is efficient use of resources, which is a significant contributor to any sustainable plan for meeting growing energy demands and reducing GHG emissions. In this regard, solutions based on sustainable energy technologies are a key aspect for the future generations. Local initiatives and many researchers have been conducted on to develop new methodologies to analyze the energy systems of the buildings.

In the residential sector, most of the energy is used for maintaining the room temperatures at about 20 °C. In most cases energy demand of the buildings is

Fig. 59.1 Worldwide residential energy consumption (adapted from Ref. [3])

supplied by high quality energy sources, such as fossil fuels or using electricity [4, 5]. However, fossil fuels and low efficient equipment are still extensively used in many developing and some developed countries, particularly for HVAC applications. Therefore, energy utilization in an efficient way for space heating and cooling is very important for the development of the energy systems. The main energy items used in buildings are building envelope, HVAC equipment, and energy consuming devices and appliances. The efficiency of all these energy systems can be improved by implementing various measures and switching to energy efficient equipment.

The aim of this chapter is to study how to make buildings energetically sustainable. Exergy is a suitable scientific concept for optimizing the building energy systems, towards sustainable development. To enhance the understanding of the nature of energy flows in systems, one can use the concept of exergy, in addition to the energy conservation principle [6]. In fact, exergy is a long forgotten concept in building and HVAC technology so much so that energy balances are made by the first law of thermodynamics, which states that energy is neither destroyed nor created under this conservation law [6–8]. Simply, exergy can be defined as potential or quality of energy. Therefore, exergy analysis is very essential in improving efficiency that allows society to maximize the benefits.

The low exergy approach is one of these approaches, which may be used in sustainable building design. The scope of this approach is the main object to constitute a sustainable built environment. Low exergy heating and cooling systems use low valued energy also easily obtained by sustainable energy sources (e.g., by using heat pumps, solar collectors, etc.), instead of high valued energy [9].

The main objective of this chapter is to perform an energy, exergy, and environmental analyses of four heating options [(1) electric boiler, (2) ground heat pump water-water, (3) standard boiler and (4) solar collector] which are driven by renewable and fossil-fuel sources for a building and compare their thermodynamic performances through energy and exergy efficiencies and environmental performances through CO_2, NO_x, and SO_2 emissions of the systems.
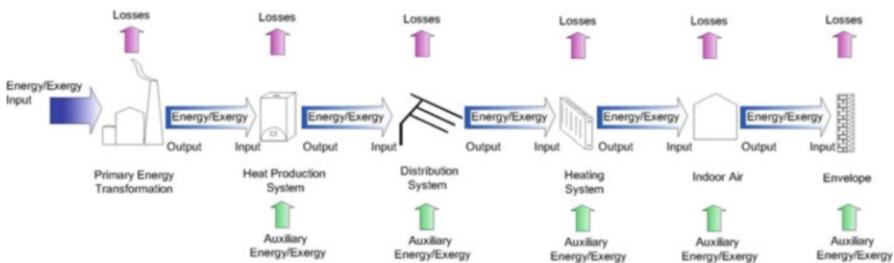
59.2 System Description

In this chapter, a building with a volume of 392 m^3 and a net floor area of 140 m^2 is considered to be located in the city of Aksaray in Turkey. The indoor and exterior air temperatures are taken as 20 °C and −15 °C, respectively. The construction materials locally manufactured consist of two layers of horizontal bricks, in between which the insulation material is placed, reinforced concrete floors with a square cement floor tiles and sand/cement mixture plastering on the other interior surfaces. Some specifications of the building listed in Table 59.1. Nevertheless, for this study, insulation, in accordance with the current Turkish building standard [10], in walls and ceiling as well as window shading was considered.

Table 59.1 Some specifications of building

Description	Value	Building part	U (W/m² K)
Volume	392 m³	Exterior walls	0.77[a]
Floor area	144 m²	Door	2.91[a]
Window area	19.38 m²	Window	2.60[a]
Ceiling height	2.8 m	Floors to ground	0.42[a]

[a]Adapted from Ref. [11]

Fig. 59.2 Energy and exergy flows from primary energy transformation to the environment (modified from Refs. [6, 7])

For the heating applications of the considered building, four different options are studied. The energy and exergy flows from primary energy transformation to the environment are shown in Fig. 59.2, while Table 59.2 gives some necessary data of these heat production systems.

Additionally, for all cases of heating systems, the radiators have the inlet and outlet temperatures of 55 °C and 45 °C with a heat loss/efficiency of 0.95, respectively. The distribution systems of all cases are considered with a heat loss of about 18 % and a temperature drop of 5 K.

59.3 Analyses

The methodology and relations used are based on a pre-design analysis tool, which was essentially produced during the ongoing work for the International Energy Agency (IEA), the Energy Conservation in Buildings and Community Systems (ECBCS) Programme Annex 37 [13].

In the first step, the general project data and boundary conditions are checked out. V and A_N are the internal volume of the building and the net floor area, respectively. T_o is the outdoor temperature and T_i is the indoor temperature under the design conditions. The outdoor temperature is taken as the reference temperature T_{ref} for analysis purposes. The heat loss through the building envelope can be divided into two groups, namely, (1) The total transmission heat loss rate, (2) the ventilation heat losses rate.

Table 59.2 Some necessary data of the studied heat production systems [6]

Case No	Heat production system	Efficiency/ COP [-]	Primary energy factor of source F_P [-]	Quality factor of source $F_{q,S}$ [-]	Maximum supply temperature $T_{S,max}$ [°C]	Auxiliary energy $P_{aux,HP}$ [W/kW$_{heat}$]	Auxiliary energy $P_{aux,HP,const}$ [W]	Part. Env. energy F_{renew} [-]
1	Electric boiler	0.98	3.00	1.00	100	0.02	–	–
2	Ground heat pump-water/water	2.32[a]	3.00	1.00	55[a]	2.00	–	1.32[a]
3	Standard boiler	0.80	1.30	0.95	90	1.80	20	–
4	Solar collector-flat plate	0.70	–	0.23	80	0.01	–	1.00

[a]Adapted from Ref. [12]

Table 59.3 Heat demand rate of the building

Heat demand rate	Heat losses rate	Heat demand rate
	Transmission + Ventilation	Solar + Occupants + Equipments + Lighting
	$\dot{Q}_T + \dot{Q}_V$	$\dot{Q}_S + \dot{Q}_O + \dot{Q}_e + \dot{Q}_l$

The sum of heat gains through the building envelope can be divided into four groups, they are (1) the solar heat gain rate, (2) the internal heat gains from occupants, (3) the internal heat gains from equipments, (4) other uses of electricity, such as for artificial lighting and ventilation.

All heat flows, heat losses via the envelope, and internal gains, occurring inside the building have to be summed up to create the following energy balance, which refers to the first law of thermodynamics and are given in Table 59.3.

Here, the heat demand rate is usually expressed in a specific number in order to be able to compare different buildings with each other:

$$\dot{Q}''_h = \dot{Q}_h / A_N, \tag{59.1}$$

For the energy source in the primary energy transformation given parameters, F_p and $F_{q,s}$ are the figures of the primary energy factor and the quality factor of the energy source, respectively. F_R is a fraction factor for the environmental and listed in Table 59.2. The quality factors and exergy load rate of the each sub-system are given in Table 59.4.

$$T_{heat} = \frac{T_{in} - T_{ret}}{\ln\left(\frac{T_{in} - T_i}{T_{ret} - T_i}\right)} \cdot \frac{1}{2} + T_i, \tag{59.2}$$

where T_{in} and T_{ret} are inlet and return temperatures of the heater while the heater surface temperature is the absolute temperature in K.

$$T'_{heat} = T_{heat} + 273.15K, \tag{59.3}$$

The thermal efficiency of the distribution system is calculated by

$$\eta_{dis} = 0.98 . f_{HPP} . f_{ins} . f_{dt} . f_{td}, \tag{59.4}$$

where f values are taken from Ref. [6] and listed in Table 59.5.

By keeping the derivation of the exergy demand rate of the heating system as calculated from

$$\Delta \dot{Ex}_{HS} = \frac{(\dot{Q}_h + \dot{Q}_{loss,HS})}{(T_{in} - T_{ret})} \left\{ (T_{in} - T_{ret}) - T_{ref} . \ln\left(\frac{T_{in}}{T_{ret}}\right) \right\}, \tag{59.5}$$

The exergy demand rate of the distribution system becomes

Table 59.4 Quality factor, heat loss rate, and exergy load rate of the sub-systems

	Quality factor F_q [-]	Heat loss rate $\dot{Q}_{loss}$ [kW]	Exergy load rate $\dot{Ex}$ [kW]
Room air	$F_{q,air} = 1 - \frac{T_o}{T_i}$	$\dot{Q}_T + \dot{Q}_V$	$\dot{Ex}_{air} = F_{q,air} \cdot \dot{Q}_h$
Heater	$F_{q,heat} = 1 - \frac{T_{ref}}{T_{heat}}$	–	$\dot{Ex}_{heat} = F_{q,heat} \cdot \dot{Q}_h$
Heating system	–	$\dot{Q}_{loss,HS} = \dot{Q}_h \cdot \left(\frac{1}{\eta_{HS}} - 1\right)$	$\dot{Ex}_{HS} = \dot{Ex}_{heat} + \Delta\dot{Ex}_{HS}$
Distribution system	–	$\dot{Q}_{loss,dis} = (\dot{Q}_h + \dot{Q}_{loss,HS}) \cdot \left(\frac{1}{\eta_{dis}} - 1\right)$	$\dot{Ex}_{dis} = \dot{Ex}_{HS} + \Delta\dot{Ex}_{dis}$
Heat production system	Given in Table 59.2	$\dot{Q}_{HP} = (\dot{Q}_h + \dot{Q}_{loss,HS} + \dot{Q}_{loss,dis}) \cdot (1 - F_S) \cdot \frac{1}{\eta_{HP}}$	$\dot{Ex}_{HP} = \dot{Q}_{HP} \cdot F_{q,S}$

Table 59.5 Values of f_i parameters, adapted from [6]

Criteria		Parameter f_i
Position of the heat production system (f_{HPP})	Inside envelope	1.00[a]
	Outside envelope	0.90
Insulation (f_{ins})	No insulation	0.70
	Bad insulation	0.90
	Good insulation	1.00[a]
Mean design temperature (f_{dt})	Low (<35 °C)	1.00
	Middle (35 °C < f_{dt} < 50 °C)	0.95
	High (>50 °C)	0.90[a]
Design temperature drop (f_{td})	Low (<5 K)	0.98
	Middle (5 K < f_{td} < 10 K)	0.99[a]
	High (>10 K)	1.00

[a]Selected for this study

$$\Delta\dot{E}x_{dis} = \frac{\dot{Q}_{loss,dis}}{\Delta T_{dis}}\left\{T_{dis} - T_{ref}.\ln\left(\frac{T_{dis}}{T_{dis} - \Delta T_{dis}}\right)\right\}, \tag{59.6}$$

where the inlet temperature of the distribution system is the mean design temperature T_{dis} and the return temperature is the design temperature minus the temperature drop ΔT_{dis} (not: used here as absolute temperatures in K):

Efficiencies of heat production systems are given in Table 59.2. The demand values on auxiliary energy or electricity of the distribution system and heat production system are given in more detail in [6, 14].

As a second step, the exergy load rate of other building service appliances, such as lighting and ventilation, is taken into consideration and, in this case, named "plant."

$$\dot{E}x_{plant} = (P_l + P_V).F_{q,el}, \tag{59.7}$$

The overall energy and exergy load rates of the building are expressed in the required primary energy and exergy input rates. For the fossil or non-renewable part of the primary energy, the result becomes

$$\dot{E}_{p,tot} = \dot{Q}_{HP}.F_P + \sum P.F_{p,el}, \tag{59.8}$$

where F_p is the primary energy factor and is given in Table 59.2 for the studied heat production systems.

If the heat production system utilizes a renewable energy source or extracts heat from the environment, as heat pumps or solar collectors do, the additional renewable energy load rate is estimated by

$$\dot{E}_R = \dot{Q}_{HP}.F_R + \dot{E}_{env}, \tag{59.9}$$

The total exergy load rate of the building becomes

$$\dot{Ex}_{tot} = \dot{Q}_{HP}.F_p.F_{q,s} + \sum P.F_{p,el} + \dot{E}_R.F_{q,R}, \tag{59.10}$$

Note that the relations used in this study are summarized while it has been explained in more detail in [6, 14].

59.3.1   Performance Assessment

The total energy efficiency of the system, η_{sys} (%), is expressed as follows:

$$\eta_{sys} = \frac{\dot{E}_{building}}{\dot{E}_{tot}}, \tag{59.11}$$

The total exergy efficiency of the system, ψ_{sys} (%), is defined as follows:

$$\psi_{sys} = \frac{\dot{Ex}_{building}}{\dot{Ex}_{tot}}, \tag{59.12}$$

The exergy flexibility factor, F_{flex} is calculated by

$$F_{flex} = \frac{\dot{Ex}_{HS}}{\dot{Ex}_{tot}}, \tag{59.13}$$

59.3.2   Environmental Impact Assessment

The building sector, constituting 30–40 % of the society's total energy demand as well as roughly 1/3 of the total CO_2 emission, has been identified as one of the main factors of greenhouse gas emissions [15]. It should be noted that, every energy generation, conversion, transmission and use are the primary driver of greenhouse gas (GHG) emissions and global warming. Nowadays, environmental damage resulting from the excessively use of non-renewable energy resources, such as CO_2 emission from combustion of fossil fuels, is due to the drastically increased GHG emissions. The atmospheric concentration levels are now much higher than what it was at the beginning of the industrial revolution. So, estimating the GHG emission is important to do an environmental assessment.

Table 59.6 Estimates of average greenhouse gas and criteria pollutant emissions (adapted from [16, 17])

Resource	CO_2 emissions (g/kW h)	NO_x emissions (g/kW h)	SO_2 emissions (g/kW h)
Coal	346.67	0.36	3.76
Natural gas	200.94	0.18	0.0009
Renewable energy	0.00	0.00	0.00

The electrical energy demand of the building considered here is produced from coal. So, electric energy consumption is an important point to estimate GHG emissions of the system. Table 59.6 shows the values used to estimate the mean coefficient of CO_2, NO_x, SO_2 emissions per kW h consumed. These values were used to obtain the emissions produced in the heating of the considered building.

So, environmental assessment of the system is performed based on the values for estimated GHG emission and the systems' energy consumption in a working period as follows [18]:

$$x_{emission} = \frac{(y_{emission}).\dot{W}_{consume}.t_{working}}{10^3},$$
(59.14)

where "$x_{emission}$" is emission releasing in a year (kg/year), "$y_{emission}$" is emission value for resource, "$\dot{W}_{consume}$" is the consumed power of system and "$t_{working}$" is working hours of the system in a year (1,000 h/year).

59.4   Results and Discussion

The total transmission loss rates and ventilation heat loss rates are calculated to be 8,159 W and 551 W, respectively. Heat gain rates from solar, internal and other uses are obtained to be 136 W, 698 W, and 240 W, respectively. Using these data, the heat demand rate and the specific heat demand rate of the building are calculated as 7,636 W and 54.55 W/m^2, respectively.

Energy flows in the subsystems are calculated and given in Table 59.7. For the four cases considered in this study, the system requires the primary energy rates between 30,941 and 974 W in order to supply a total of 7,636 W to the building. Also, the renewable energy rates included in cases 2 and 4 are calculated as 6,071 W and 13,984 W, respectively.

The total exergy demand rate is determined based on the methodology as followed in the energy demand calculation, but with exergy analysis. Similarly we considered the same operating conditions for each component. The largest exergy demand rate is calculated for the primary energy transformation of case 1 as 30,941 W. Also, as can be seen in Table 59.8, the smallest exergy demand rate for the primary energy transformation is 974 W for case 4.

Table 59.7 Energy flows in the subsystems of studied cases

Studied cases	Input (W)	After primary energy transformation (W)	After heat production system (W)	After distribution (W)	After heating system (W)	After room (W)	After envelope (W)
Case 1	30,941	10,313	9,873	8,038	7,636	8,711	8,711
Case 2	12,185	4,061	9,873	8,038	7,636	8,711	8,711
Case 3	16,994	12,598	9,873	8,038	7,636	8,711	8,711
Case 4	974	14,309	9,873	8,038	7,636	8,711	8,711

Table 59.8 Exergy flows in the subsystems of studied cases

Studied cases	Input (W)	After primary energy transformation (W)	After heat production system (W)	After distribution (W)	After heating system (W)	After room (W)	After envelope (W)
Case 1	30,941	10,229	3,277	2,852	1,236	1,040	0
Case 2	12,185	3,958	3,277	2,852	1,236	1,040	0
Case 3	16,198	11,865	3,277	2,852	1,236	1,040	0
Case 4	974	3,457	3,277	2,852	1,236	1,040	0

According to the energy and exergy analyses results, the overall energy and exergy efficiencies of the studied heating systems are calculated to be (energy demand building/total energy input) 24.6 %, 41.8 %, 44.9 %, 51.0 %, and (exergy demand building/total exergy input) 4.0 %, 10.1 %, 7.6 %, and 35.7 % for Cases 1 through 4, respectively.

Electric boiler has the lowest energy and exergy efficiencies as expected. In this study, exergy efficiencies of non-renewable heating options are lower than those of the renewable heating options. In this case, the solar collector heating system has the highest exergy efficiency than that of others because most of the required energy is supplied by solar.

In the environmental impact assessment, CO_2, NO_x and SO_2 emissions rate per year (kg emission/year) calculated for the considered cases as 10,726.32, 4,224.17, 3,737.56, and 337.67, 11.14, 4.39, 3.40, and 3.35 and 116.34, 45.82, 3.68, and 3.66, respectively. The lowest environmental impact appears to be case 4.

59.5 Conclusions

In this chapter, energy/exergy and environmental analysis methods are applied to four heating options for a building with a volume of 392 m^3 and a net floor area of 140 m^2. Their performances are also compared through energy/exergy efficiencies and CO_2 emissions. The main conclusions drawn from the results of the present study may be listed as follows:

- The energy demand rate of the building is 7,636 W. The total exergy demand rates of the systems studied are 30,941 W for case 1, 12,185 W for case 2, 16,198 W for case 3, and 974 W for case 4. And also, the renewable energy rates for cases 2 and 4 are calculated as 6,071 W and 13,984 W, respectively.
- The total energy and exergy efficiencies of the considered heating systems are found to be 24.6 %, 41.8 %, 44.9 %, and 51.0 %, and 4.0 %, 10.1 %, 7.6 %, and 35.7 % respectively.
- The exergy flexibility factor values for four cases with an electric boiler, a ground heat pump water-water, a standard boiler and a solar collector heating system are determined as 0.088, 0.225, 0.169, and 0.790, respectively.
- CO_2 emissions of the considered systems are calculated to be $CO_{2,case1} > CO_{2,case2} > CO_{2,case3} > CO_{2,case4}$.
- NO_x emissions of the considered systems are calculated to be $NO_{x,case1} > NO_{x,case2} > NO_{x,case3} > NO_{x,case4}$.
- SO_2 emissions of the considered systems are calculated to be $SO_{2,case1} > SO_{2,case2} > SO_{2,case3} > SO_{2,case4}$.
- Case 4 provides the best environmental performance with the lowest amount of emissions.

References

1. IEA (2004) Oil crises and climate challenges: 30 years of energy use in IEA countries. International Energy Agency, Available from http://iea.org/textbase/nppdf/free/2004/30years.pdf of subordinate document. Accessed 15 May 2009
2. Dincer I, Ozgener L, Hepbasli A (2007) Geothermal energy resources. In: Capehart BL (ed) Encyclopedia of energy engineering and technology, vol 1. CRC Press, Boca Raton, FL, pp 744–752
3. Saidur R, Masjuki HH, Jamaluddin MY (2007) An application of energy and exergy analysis in residential sector of Malaysia. Energy Policy 35:1050–1063
4. International Energy Agency (2002) ECBCS 2002, Energy conservation in buildings and community service programme, http://www.ecbcs.org Accessed 9 Jan 2008
5. Baehr HD (1980) Zur Thermodynamik des Heizens. II. Prima renergieeinsparung durch Anergienutzung. Brennstoff-Warme-Kraft, Germany 32(2):47–57
6. Schmidt D (2003) Design of low exergy buildings-method and a pre-design tool. Int J Low Energ Sustain Build 3:1–47
7. Balta MT, Dincer I, Hepbasli A (2010) Performance and sustainability assessment of energy options for building HVAC applications. Energ Build 42(8):1320–1328
8. Schmidt D, Juusela MA (2004) Low-exergy systems for heating and cooling of buildings. In: Proceedings of the 21st conference on passive and low energy architecture, Eindhoven, The Netherlands, 19–22 September, 2004
9. Balta MT, Dincer I, Hepbasli A (2011) Development of sustainable energy options for buildings in a sustainable society. Sustain Cit Soc 1(2):72–80
10. TS 825 (1998) Turkish Standard, Heat Insulation Rules in Buildings
11. Karakoc TH (2001) Calculating the central heating system, Demirdokum, Publication no. 1, 3rd edn (in Turkish).

12. Hepbasli A, Balta MT (2007) A study on modeling and performance assessment of a heat pump system for utilizing low temperature geothermal resources in buildings. Build Environ 42:3747–3756
13. IEA, Low exergy heating and cooling of buildings–Annex 37 from Available from http://www.vtt.fi/rte/projects/annex37/Index.htm of subordinate document. Accessed 15 May 2009
14. Hepbasli A (2012) Low exergy heating and cooling systems for sustainable buildings and societies. Renew Sustain Energy Rev 16:73–104
15. Li Z (2006) A new life cycle impact assessment approach for buildings. Build Environ 41:1414–1422
16. Ordonez J, Modi V (2011) Optimizing CO2 emissions from heating and cooling and from the materials used in residential buildings, depending on their geometric characteristics. Build Environ 46:2161–2169
17. The National Team for Climate Change the State of Qatar, (2002) Major environmental, economic and methodological considerations to promote the utilization of NG as a cleaner or less GHG emitting energy source for the 21th century, Subsidiary Body for Scientific and Technological Advice, 5–14 June 2002 Available from http://unfccc.int/resource/docs/2002/sbsta/misc03.pdf of subordinate document. Accessed 25 Nov 2012.
18. Sovacool BK (2008) Valuing the greenhouse gas emissions from nuclear power: a critical survey. Energy Policy 36:2940–2953

Chapter 60
Environmental Impact Assessment of Various Energy Storage Options for Buildings

Hakan Caliskan, Ibrahim Dincer, and Arif Hepbasli

Abstract The thermochemical, sensible (aquifer) and latent TES systems are modeled and analyzed using energy, exergy, and enviroeconomic analysis methods under various environment temperatures while sustainability and environmental impact assessments are made. The environment (dead state) temperatures considered are 8, 9, and 10 °C, respectively. Among the TES systems, the hot well of the aquifer TES has maximum energy and exergy efficiency values of 94.12 % and 88.78 % at a dead state temperature of 8 °C. Furthermore, the most sustainable TES system is found to be the aquifer TES. On the other hand, this combined TES system causes maximum 1,864.07 kgCO_2/month emissions at 10 °C environment temperature. So, the total CO_2 emission values are directly proportional to the environment temperature. The total enviroeconomic values are also directly proportional to the environment temperatures. For this system, a maximum of $27.029 CO_2 emission is released per month at 10 °C environment temperature. So, these kinds of systems become more enviroeconomic at low environment temperatures.

H. Caliskan (✉)
Department of Mechanical Engineering, Faculty of Engineering,
Usak University, 64200 Usak, Turkey
e-mail: hakan.caliskan@usak.edu.tr

I. Dincer
Faculty of Engineering and Applied Science, University of Ontario Institute of Technology,
2000 Simcoe Street North, Oshawa, ON, Canada L1H 7K4
e-mail: Ibrahim.Dincer@uoit.ca
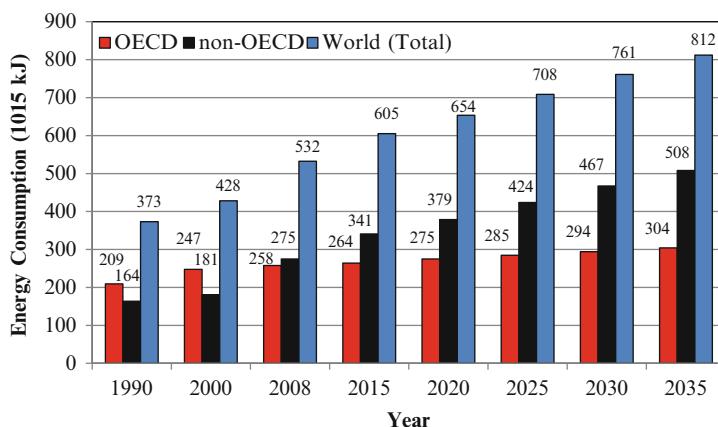
A. Hepbasli
Department of Energy Systems Engineering, Faculty of Engineering, Yaşar University,
Bornova, 35100 Izmir, Turkey
e-mail: arif.hepbasli@yasar.edu.tr

60.1 Introduction
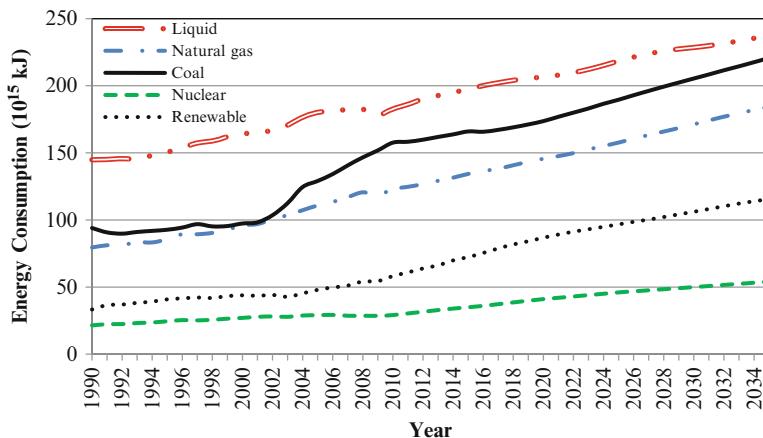
Energy consumption in the world is expected to rise from 532.5×10^{15} kJ in 2008 to 812.1×10^{15} kJ in 2035 according to International Energy Agency (IEA), with an increase of 53 %. It is seen that total energy consumptions of the Organisation for Economic Co-operation and Development (OECD) countries are less than that of non-OECD countries [1]. The energy consumption between 1990 and 2035 world-wide is shown in Fig. 60.1.

Energy is also considered as a key input to economic development. It is not completely neutral with respect to the environment. So, energy includes sustainable development and environmental impact. The reasons of the environmental issues are generally related to generation, transformation and utilization of energy. Energy takes a role about environmental concerns such as air, water and maritime pollution, radiation, waste disposal, climate change, ozone depletion, etc. [2]. The energy consumption according to energetic fuel types between 1990 and 2035 in the world is illustrated in Fig. 60.2.
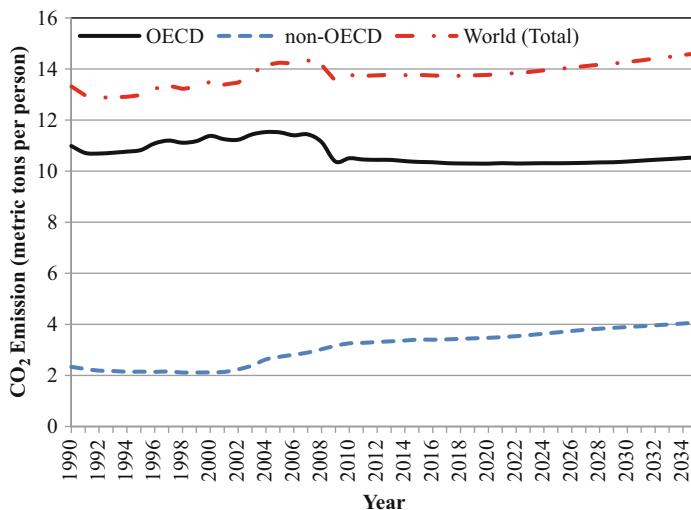
Especially, the climate change is a biggest issue for politicians and publics. Concerns related to the economic and environmental aspects of energy have been growing. According to International Energy Agency, energy-related CO_2 emissions in the world are projected to rise from 30.2 billion metric tons in 2008 to 43.2 billion metric tons in 2035. This increase in CO_2 is about 43 % and most of it occurs in the developing non-OECD countries due to their policies, such as continued heavy reliance on fossil fuels for strong economic growth. CO_2 emissions per capita in OECD economies are more than those in non-OECD economies. OECD countries have high level of fossil fuel use due to their high income. So, their CO_2 emissions per capita have higher levels [1]. The CO_2 emissions per capita between 1990 and 2035 in the world are shown in Fig. 60.3.

Fig. 60.1 Energy consumption between 1990 and 2035 in the world (Adapted from Ref. [1])

Fig. 60.2 Energy consumption according to energetic fuel types between 1990 and 2035 in the world (Adapted from Ref. [1])

Fig. 60.3 CO_2 emissions per capita between 1990 and 2035 in the world (Adapted from Ref. [1])

In recent years, most of the thermodynamics systems are designed under consideration of the combine of thermodynamics, environmental impacts and cost accounting disciplines. Theoretical or empirical studies of the economic effects of environmental policies around the world are generally known as Enviroeconomic. Particular issues include the costs and benefits of alternative environmental policies to deal with air pollution, water quality, toxic substances, solid waste, greenhouse gases (e.g. CO_2), and global warming [3].

Until the end of the twentieth century, environmental issues were seen the major problems and especially air pollution and climate change are still the potential problems. Until the early 1990s, the interaction between the environmental impact and energy utilization became more manifest. Then, it is considered that impact of energy resource utilization on the environment is best addressed by regarding exergy. A system's exergy is described as the maximum shaft work which obtained by the composite of the system and a specified reference environment. It is assumed that the reference environment infinite, in equilibrium, and to enclose other systems. Here, exergy is a property of both the reference environment and system [4].
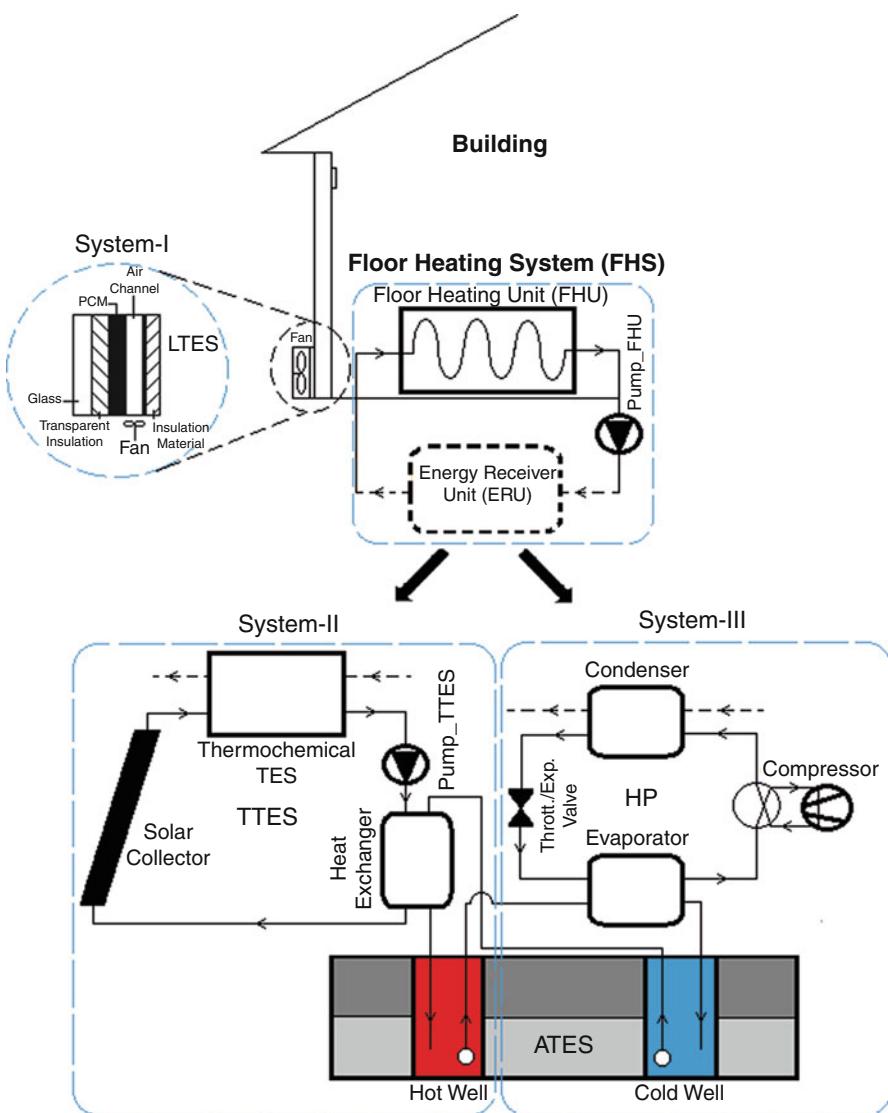
Also, the technologies in progress can ensure efficiency, energy security, and environmental quality. Thermal energy storage (TES) is a hopeful technique. TESs may reduce the energy consumption, thereby conserving indigenous fossil fuels and reducing costly imports of energy resources. TES systems are generally three types as sensible, latent and thermochemical. In sensible TES systems, liquid (or solid) is heated without phase change, considering its heat capacity and temperature change. The medium's temperature changing is used for sensible TES. Latent TES (LTES) systems use phase change heat at a constant temperature for liquid–solid or solid-solid phases. It is associated with a phase change of a material and generally used with Phase Change Material (PCM). Furthermore, in thermochemical TES (TTES) systems, large quantities of chemical energy is absorbed or released due to shifting of equilibrium by changing temperature and pressure [5].

60.2 Systems Description

The latent, thermochemical and sensible TES systems are studied and named as Systems I, II, and III, respectively. Thermochemical and sensible (Aquifer TES-ATES) TES systems are working with floor heating system (FHS) in the building while latent TES system (PCM) is working with room air and building envelope. It is assumed that heating demand of the house is approximately 16 kW (depending on the assembled TES system) and environment temperatures are changing between 8 and 10 °C. The schematic layout of the system is illustrated in Fig. 60.4 and system data and assumptions are listed in Table 60.1.

In System-I, façade construction design is used to store the heat of solar radiation. The absorber plate of the system is a kind of n-paraffin and waxes type PCM (RT-27). System components of the LTES are a glass, a transparent insulation material, a PCM, an air channel, a fan and inner insulation material. The PCM absorbs the solar radiation energy passing through glass and transparent insulation material. This stored energy is used to heat the air entering the channel and then the air sent to the room by fan.

In System-II, endothermic reaction occurs and thermal energy is absorbed from energy sources during the charging process of the TTES. So, two different materials occur from the thermochemical material and thus the required energy is obtained by

Fig. 60.4 Schematic layout of the system (Adapted from Refs. [5, 6])

reaction heat. Two dissociated materials are stored during the storing process. In the discharging process two dissociated materials combined together with exothermic reaction and some of the energy is recovered from the fraction of the energy which is released during the reaction. The water is heated in the solar collector and the thermochemical material takes the heat from the hot water and operates the charging reaction (dehydration) of the chemical process. The charging reaction is "$SrBr_2 \cdot 6 H_2O + Heat \rightarrow SrBr_2 \cdot H_2O + 5H_2O$." Then the water enters the heat exchanger

Table 60.1 System data and assumptions made

System-I

Volume of the PCM (m³)	4.01	Temperature of ATES water at HE inlet (°C)	13
Utilization time of the PCM (h)	7.22		25
Glass area of the PCM-envelope (m²)	58.8	Temperature of ATES water at HE outlet (°C)	3,732
Solar radiation rate (W/m²)	800		68
Temperature of glass interior surface (°C)	16	Reaction enthalpy of TTES (kJ/kgH₂O)	47.5
	28	Inlet temperature of TTES water (°C)	0.4778
Melting temperature of PCM (°C)	41	Outlet temperature of TTES water (°C)	34
Final temperature of PCM (°C)	1.8	Mass flow rate of FHS water (TTES discharging) (kg/s)	25
Specific heat of solid PCM (kJ/kg°C)	2.4		25
Specific heat of liquid PCM (kJ/kg°C)	184	Temperature of FHS water at input at TTES (°C)	25
	0.14741		25
Melting heat of PCM (kJ/kg)		Temperature of FHS water at output at TTES (°C)	25
Mass flow rate of air (kg/s)			24
		Standard temperature of TTES (°C)	
		Charging temperature of the hot well of ATES (°C)	
		Discharging temperature of the hot well of ATES (°C)	

Temperature of input air (°C)	11	*System-III*	
Pressure of LTES input and output air (kPa)	101.325	Charging temperature of the cold well of ATES (°C)	14
	23.5		13
Temperature of LTES output air (°C)	0.00407	Discharging temperature of the cold well of ATES (°C)	0.0876
Humidity ratio of air at LTES input (kg$_m$/kg$_{da}$)	0.00654		−4
	50	Mass flow rate of R-134a for HP (kg/s)	252.85
Mole fraction ratio of air at LTES input (-)	0.00814	Temperature of R-134a at evaporator input and output (°C)	0.25
	0.01308		1
Humidity ratio of air at LTES output (kg$_m$/kg$_{da}$)	45	Pressure of R-134a at evaporator inlet and outlet (kPa)	24
	6,000		14
Mole fraction ratio of air at LTES outlet (-)	10	Degree of dryness at evaporator inlet (-)	0.85
	101.325	Degree of dryness at evaporator outlet (-)	35.82
Relative humidity of air at LTES outlet (%)	0.00381	Temperature of ATES water at evaporator inlet (°C)	800
	0.00612	Temperature of ATES water at evaporator outlet (°C)	>1
Temperature of sun (K)		Mechanical and electrical efficiencies of compressor (-)	
Dead state (environment) temperature (°C)		Temperature of R-134a at compressor outlet (°C)	
Dead state pressure (kPa)		Pressure of R-134a at compressor outlet (kPa)	
Humidity ratio of air at dead state (kg$_m$/kg$_{da}$)		Degree of dryness at evaporator outlet (-)	
Mole fraction ratio of air at dead state (-)			

System-II		Temperature of R-134a at compressor outlet (°C)	42.85
Mass flow rate of TTES (charging) water (kg/s)	0.4715		815.89
	40.42	Pressure of R-134a at compressor outlet (kPa)	>1
Temperature of water at solar collector inlet (°C)	68		32
	70	Degree of dryness at evaporator outlet (-)	815.89
Temperature of water at solar collector outlet (°C)	47.5	Temperature of R-134a at thrott./exp. valve inlet (°C)	0

Table 60.1 (continued)

Total solar collector area (m²)		Pressure of R-134a at thrott./exp. valve inlet (kPa)	
Temperature of TTES water at pump inlet (°C)		Degree of dryness at thrott./exp. valve inlet (-)	
Mechanical and electrical efficiencies of compressor (-)	0.85	*FHS*	
Temperature of TTES water at HE inlet (°C)	48.5	Mechanical and electrical efficiencies of compressor (-)	0.85
Temperature of TTES water at HE outlet (°C)	40.42	Temperature of FHS water at pump inlet (°C)	25
Mass flow rate of ATES water (kg/s)	0.3177	Temperature of FHS water at pump outlet (°C)	26

Source: [5, 6]

through TTES and pump. At the same time, the ATES water is pumped from the cold well to the hot well. Also, the TTES system water leaves the heat exchanger and enters to the solar collector to complete the cycle. On the other hand, the discharging process occurs while the FHS water enters the TTES. So, the discharging reaction (hydration) happens as "$SrBr_2 \cdot H_2O + 5H_2O \rightarrow SrBr_2 \cdot 6H_2O + Heat$."

If System-II is not sufficient due to environmental causes (solar radiation) or the hot well of ATES is completed, System II is closed and System-III is operated with charging process. In System-III, the ATES water is pumped when needed from the hot well to the cold well through the evaporator of the heat pump. At the same time, R-134a flows in the heat pump unit through evaporator, compressor, condenser, and valve. Finally, the necessary heat energy of the FHS is taken from the TTES of System-II or the condenser of System-III. The switch of the systems is operated through the flow control unit of the FHS. Furthermore, the necessary electricity for the fan, the compressor and the pumps is taken from "coal fired power station," which is the major source of the CO_2 emissions contributing to the global warming [5, 6].

60.3   Analysis

60.3.1   Energy Analysis

System-I: LTES + Fan

Energy Analysis of the LTES Charging Process

The energy balance of the LTES charging process is given as follows:

$$\dot{En}_{solar,LTES\_c} = \dot{En}_{acc,LTES\_c} + \dot{En}_{loss,LTES\_c} \tag{60.1}$$

where $\dot{E}n_{solar,LTES\_c}$, $\dot{E}n_{acc,LTES\_c}$, and $\dot{E}n_{loss,LTES\_c}$ are the solar energy input rate, the accumulated energy rate, and the energy loss rate of the LTES charging process, respectively.

The solar energy input rate to the LTES charging process, $\dot{E}n_{solar,LTES\_c}$ is expressed by

$$\dot{E}n_{solar,LTES\_c} = I_T A_{glass} \tag{60.2}$$

where I_T is the solar radiation and A_{glass} is the glass area on the building envelope.

The accumulated energy rate (or received heat) of the LTES charging process, $\dot{E}n_{acc,LTES\_c}$ is determined to be

$$\dot{E}n_{acc,LTES\_c} = \left\{ m_{PCM} \left[c_{p,s} \left(T_{PCM,m} - T_{glass,in} \right) + q_t + c_{p,l} \left(T_{PCM,final} - T_{PCM,m} \right) \right] \right\} / t_{PCM} \tag{60.3}$$

where m_{PCM} is the mass rate of the PCM, $c_{p,s}$ is the specific heat of solid PCM, $c_{p,l}$ is the specific heat of liquid PCM, $T_{PCM,m}$ is the phase change (melting) temperature of PCM, $T_{glass,in}$ is the interior surface temperature of glass on the building envelope, $T_{PCM,final}$ is the PCM final temperature at the end of the process, q_t is the melting heat of the PCM, and t_{PCM} is the utilization time of the PCM during the process.

The energy loss rate of the LTES charging process, $\dot{E}n_{loss,LTES\_c}$, can be found from the energy balance equation of the LTES charging process as follows:

$$\dot{E}n_{loss,LTES\_c} = \dot{E}n_{solar,LTES\_c} - \dot{E}n_{acc,LTES\_c} \tag{60.4}$$

The energy efficiency of the LTES charging process, η_{LTES_c} is calculated from

$$\eta_{LTES\_c} = \frac{Accumulated\ energy\ rate}{Solar\ energy\ input\ rate} = \frac{\dot{E}n_{acc,LTES\_c}}{\dot{E}n_{solar,LTES\_c}} \tag{60.5}$$

Energy Analysis of the LTES Discharging Process

The energy balance of the LTES discharging process is written as

$$\dot{E}n_{acc,LTES\_d} = \Delta \dot{E}n_{received,LTES\_d} + \dot{E}n_{loss,LTES\_d} \tag{60.6}$$

where $\dot{E}n_{acc,LTES\_d}$, $\Delta \dot{E}n_{received,LTES\_d}$, and $\dot{E}n_{loss,LTES\_d}$ are the accumulated energy rate, the net received energy rate, and the energy loss rate of the LTES discharging process, respectively.

The accumulated energy rate (heat stored in PCM) of the LTES discharging process, $\dot{E}n_{acc,LTES\_d}$ is equal to the accumulated energy rate of the charging process, $\dot{E}n_{acc,LTES\_c}$ as follows:

$$
\begin{aligned}
\dot{E}n_{acc,LTES\_d} &= \dot{E}n_{acc,LTES\_c} \\
&= \dot{m}_{PCM} \left[c_{p,s} \left(T_{PCM,m} - T_{glass,in} \right) + q_t + c_{p,l} \left(T_{PCM,end} - T_{PCM,m} \right) \right]
\end{aligned}
$$
(60.7)

Net received energy rate of the LTES discharging process, $\Delta \dot{E}n_{received,LTES\_d}$ is the difference between the output and input energy rates of the air, as given below:

$$
\Delta \dot{E}n_{received,LTES\_d} = \dot{E}n_{air,out,LTES\_d} - \dot{E}n_{air,in,LTES\_d}
$$
(60.8)

where $\dot{E}n_{air,out,LTES\_d}$ and $\dot{E}n_{air,in,LTES\_d}$ are the output and input energy rates of the air used in the LTES discharging process, respectively, as follows:

$$
\dot{E}n_{air,out,LTES\_d} = \dot{m}_{air} \, h_{air,out,LTES\_d}
$$
(60.9)

and

$$
\dot{E}n_{air,in,LTES\_d} = \dot{m}_{air} \, h_{air,in,LTES\_d}
$$
(60.10)

where $\dot{m}_{air}$, $h_{air,in,LTES\_d}$, and $h_{air,out,LTES\_d}$ are the mass flow rate of air, the enthalpy of the input air, and the enthalpy of the output air used in the LTES discharging process, respectively.

The energy loss rate of the LTES discharging process, $\dot{E}n_{loss,LTES\_d}$, is determined from the following energy balance equation.

$$
\dot{E}n_{loss,LTES\_d} = \dot{E}n_{acc,LTES\_d} - \Delta \dot{E}n_{received,LTES\_d}
$$
(60.11)

The energy efficiency of the LTES discharging process, η_{LTES_d} can be calculated by the relation

$$
\eta_{LTES\_d} = \frac{Received \, energy \, rate}{Accumulated \, energy \, rate} = \frac{\dot{E}n_{received,LTES\_d}}{\dot{E}n_{acc,LTES\_d}}
$$
(60.12)

Energy Analysis of the Fan

The energy balance of the fan is expressed in the rate form as

$$
\dot{W}_{fan} = \dot{E}n_{air,out,fan} - \dot{E}n_{air,in,fan}
$$
(60.13)

where $\dot{W}_{fan}$ is the fan power. Also, $\dot{E}n_{air,in,fan}$ and $\dot{E}n_{air,out,fan}$ are the energy input and output rates of the air used in the fan, respectively, as follows:

$$\dot{E}n_{air,in,fan} = \dot{m}_{air}\, h_{air,in,fan} \tag{60.14}$$

and

$$\dot{E}n_{air,out,fan} = \dot{m}_{air}\, h_{air,out,fan} \tag{60.15}$$

where $\dot{m}_{air}$, $h_{air,in,fan}$ and $h_{air,out,fan}$ are the mass flow rate of the air, the enthalpy of the input air and the enthalpy of the output air used in the fan, respectively.

System-II: TTES + Solar Collector + HE + Pump + Hot Well of ATES

Energy Analysis of the TTES Charging (Dehydration) Process

The charging reaction of the TTES (dehydration) is "$SrBr_2 \cdot 6H_2O + Heat \rightarrow SrBr_2 \cdot H_2O + 5H_2O$." So, the energy balance of the TTES charging process is given as follows:

$$\Delta\dot{E}n_{flow,TTES\_c} = \sum H_{reaction,TTES\_c} + \dot{E}n_{loss,TTES\_c} \tag{60.16}$$

where $\Delta\dot{E}n_{flow,TTES\_c}$, $\sum H_{reaction,TTES\_c}$ and $\dot{E}n_{loss,TTES\_c}$ are the net energy flow rate, the total energy rate of the reaction and the energy loss rate of the TTES charging process, respectively.

The net energy flow rate of the TTES charging process, $\Delta\dot{E}n_{flow,TTES\_c}$ is difference between the energy input and output rates of the water used in the TTES charging process as

$$\Delta\dot{E}n_{flow,TTES\_c} = \dot{E}n_{water,in,TTES\_c} - \dot{E}n_{water,out,TTES\_c} \tag{60.17}$$

with

$$\dot{E}n_{water,in,TTES\_c} = \dot{m}_{TTES\_c}\, h_{water,in,TTES\_c} \tag{60.18}$$

and

$$\dot{E}n_{water,out,TTES\_c} = \dot{m}_{TTES\_c}\, h_{water,out,TTES\_c} \tag{60.19}$$

where $\dot{E}n_{water,in,TTES\_c}$ and $\dot{E}n_{water,out,TTES\_c}$ are the energy input and output rates of the water used in the TTES charging process while $\dot{m}_{TTES\_c}$, $h_{water,in,TTES\_c}$ and $h_{water,out,TTES\_c}$ are the mass flow rate of the water, the enthalpy of the input water

and the enthalpy of the output water used in the TTES charging process, respectively.

The total energy rate of the reaction (or reaction energy rate) of the TTES charging process, $\sum H_{reaction,TTES\_c}$ is calculated to be

$$\sum H_{reaction,TTES\_c} = n_{product,TTES\_c}\, \Delta H_{reaction}\, \dot{m}_{product,TTES\_c} \tag{60.20}$$

where $n_{product,TTES\_c}$, $\Delta H_{reaction}$, and $\dot{m}_{product,TTES\_c}$ are the mole number of the product H_2O, the reaction enthalpy rate, and the mass flow rate of the product used in the TTES charging process, respectively.

The energy loss rate of the TTES charging process, $\dot{En}_{loss,TTES\_c}$ is determined from the energy balance equation of the TTES charging process as follows:

$$\dot{En}_{loss,TTES\_c} = \Delta\dot{En}_{flow,TTES\_c} - \sum H_{reaction,TTES\_c} \tag{60.21}$$

The energy efficiency of the TTES charging process, η_{TTES_c} is expressed as

$$\eta_{TTES\_c} = \frac{\sum H_{reaction,TTES\_c}}{\Delta\dot{En}_{flow,TTES\_c}} \tag{60.22}$$

Energy Analysis of the TTES Discharging (Hydration) Process

The discharging reaction of the TTES (hydration) is "$SrBr_2 \cdot H_2O + 5H_2O \rightarrow SrBr_2 \cdot 6H_2O + Heat$." In this regard, energy balance of the TTES discharging process is written to be

$$\sum H_{reaction,TTES\_d} = \Delta\dot{En}_{flow,TTES\_d} + \dot{En}_{loss,TTES\_d} \tag{60.23}$$

where $\sum H_{reaction,TTES\_d}$, $\Delta\dot{En}_{flow,TTES\_d}$, and $\dot{En}_{loss,TTES\_d}$ are the total energy rate of the reaction, the net energy flow rate, and the energy loss rate of the TTES discharging process, respectively.

The total energy rate of the reaction of the TTES discharging process, $\sum H_{reaction,TTES\_d}$ is equal to the total energy rate of the reaction of the TTES charging process, $\sum H_{reaction,TTES\_c}$ as follows:

$$\begin{aligned} \sum H_{reaction,TTES\_d} &= \sum H_{reaction,TTES\_c} \\ &= n_{product,TTES\_c}\, \Delta H_{reaction}\, \dot{m}_{product,TTES\_c} \end{aligned} \tag{60.24}$$

The net energy flow rate of the TTES discharging process (also known as heat transfer rate between TTES and FHS), $\Delta\dot{En}_{flow,TTES\_d}$ is the difference between the energy input and output rates of the water used in the TTES discharging process and is given by

$$\Delta \dot{E}n_{flow,TTES\_d} = \dot{E}n_{water,out,TTES\_d} - \dot{E}n_{water,in,TTES\_d} \tag{60.25}$$

where $\dot{E}n_{water,in,TTES\_d}$ and $\dot{E}n_{water,out,TTES\_d}$ are the energy input and output rates of the water used in the TTES discharging process, respectively, as follows:

$$\dot{E}n_{water,in,TTES\_d} = \dot{m}_{TTES\_d}\, h_{water,in,TTES\_d} \tag{60.26}$$

and

$$\dot{E}n_{water,out,TTES\_d} = \dot{m}_{TTES\_d}\, h_{water,out,TTES\_d} \tag{60.27}$$

where $\dot{m}_{TTES\_d}$, $h_{water,in,TTES\_d}$ and $h_{water,out,TTES\_d}$ is the mass flow rate of the water (also equal to the mass flow rate of the FHS water "$\dot{m}_{FHS}$"), the enthalpy of the input water and the enthalpy of the output water used in the TTES discharging process, respectively (Heat transfer of TTES discharging process used for FHS).

The energy loss rate of the TTES discharging process, $\dot{E}n_{loss,TTES\_d}$ is calculated from the energy balance equation of the TTES discharging process as

$$\dot{E}n_{loss,TTES\_d} = \sum H_{reaction,TTES\_d} - \Delta \dot{E}n_{flow,TTES\_d} \tag{60.28}$$

The energy efficiency of the TTES discharging process, η_{TTES_d} is expressed as

$$\eta_{TTES\_d} = \frac{\Delta \dot{E}n_{flow,TTES\_d}}{\sum H_{reaction,TTES\_d}} \tag{60.29}$$

The overall energy efficiency of TTES, $\eta_{TTES\_overall}$ can be calculated as follows:

$$\eta_{TTES\_overall} = \frac{\Delta \dot{E}n_{flow,TTES\_d}}{\Delta \dot{E}n_{flow,TTES\_c}} \tag{60.30}$$

Energy Analysis of the Solar Collector

The energy balance of the solar collector is written as

$$\dot{E}n_{solar,collector} = \Delta \dot{E}n_{flow,collector} + \dot{E}n_{loss,collector} \tag{60.31}$$

where $\dot{E}n_{solar,collector}$, $\Delta \dot{E}n_{flow,collector}$, and $\dot{E}n_{loss,collector}$ are the solar energy rate, the net energy flow rate, and the energy loss rate of the solar collector, respectively.

The solar energy rate of the solar collector, $\dot{E}n_{solar,collector}$ is expressed as

$$\dot{E}n_{solar,collector} = I_T\, A_{collector} \tag{60.32}$$

where I_T is the solar radiation and $A_{collector}$ is the area of the solar collector.

The net energy flow rate of the solar collector, $\Delta \dot{E}n_{flow,collector}$ is the difference between the energy input and the output rates of the water used in the solar collector.

$$\Delta \dot{E}n_{flow,collector} = \dot{E}n_{water,out,collector} - \dot{E}n_{water,in,collector} \qquad (60.33)$$

where $\dot{E}n_{water,in,collector}$ and $\dot{E}n_{water,out,collector}$ are the energy input and the output rates of the water used in the solar collector, respectively as

$$\dot{E}n_{water,in,collector} = \dot{m}_{TTES\_c} \, h_{water,in,collector} \qquad (60.34)$$

and

$$\dot{E}n_{water,out,collector} = \dot{m}_{TTES\_c} \, h_{water,out,collector} \qquad (60.35)$$

where $\dot{m}_{TTES\_c}$, $h_{water,in,collector}$ and $h_{water,out,collector}$ are the mass flow rate of the water ($\dot{m}_{collector} = \dot{m}_{TTES\_c}$), the enthalpy of the input water and the enthalpy of the output water used in the solar collector, respectively.

The energy loss rate of the solar collector, $\dot{E}n_{loss,collector}$ is determined from the balance equation of the solar collector as follows:

$$\dot{E}n_{loss,collector} = \dot{E}n_{solar,collector} - \Delta \dot{E}n_{flow,collector} \qquad (60.36)$$

The energy efficiency of the solar collector, $\eta_{collector}$ is computed from

$$\eta_{collector} = \frac{\Delta \dot{E}n_{flow,collector}}{\dot{E}n_{solar,collector}} \qquad (60.37)$$

Energy Analysis of the HE

The energy balance of the HE between the TTES unit and the hot well of the ATES is given by

$$\dot{E}n_{TTES\_c,in,HE} + \dot{E}n_{ATES\_hw\_c,in,HE} = \dot{E}n_{TTES\_c,out,HE} + \dot{E}n_{ATES\_hw\_c,out,HE} \qquad (60.38)$$

where $\dot{E}n_{TTES\_c,in,HE}$ and $\dot{E}n_{TTES\_c,out,HE}$ are the energy input and the output flow rates of the heat exchanger due to the charging process of the TTES (the water used in TTES), respectively. Also, $\dot{E}n_{ATES\_hw\_c,in,HE}$ and $\dot{E}n_{ATES\_hw\_c,out,HE}$ are the energy input and output flow rates of the heat exchanger due to the charging process of the hot well of ATES (the water used in ATES), respectively. These rates can be calculated as follows:

$$\dot{E}n_{TTES\_c,in,HE} = \dot{m}_{TTES\_c} \, h_{TTES\_c,in,HE} \qquad (60.39)$$

$$\dot{En}_{TTES\_c,out,HE} = \dot{m}_{TTES\_c}\, h_{TTES\_c,out,HE} \tag{60.40}$$

$$\dot{En}_{ATES\_hw\_c,in,HE} = \dot{m}_{ATES}\, h_{ATES\_hw\_c,in,HE} \tag{60.41}$$

$$\dot{En}_{ATES\_hw\_c,out,HE} = \dot{m}_{ATES}\, h_{ATES\_hw\_c,out,HE} \tag{60.42}$$

where $\dot{m}_{TTES\_c}$, $h_{TTES\_c,in,HE}$ and $h_{TTES\_c,out,HE}$ are the mass flow rate of the TTES water, the enthalpy of the input and output TTES water of the HE due to the charging process of the TTES while $\dot{m}_{ATES}$, $h_{ATES\_hw\_c,in,HE}$ and $h_{ATES\_hw\_c,out,HE}$ are the mass flow rate of the ATES water, the enthalpy of the input and output ATES water of the HE due to the charging process of the hot well of ATES, respectively.

The heat transfer rate of the HE (between TTES and ATES units), $\dot{Q}_{ht,HE}$ is calculated by

$$\dot{Q}_{ht,HE} = \dot{En}_{ATES\_hw\_c,out,HE} - \dot{En}_{ATES\_hw\_c,in,HE}$$
$$= \dot{En}_{TTES\_c,in,HE} - \dot{En}_{TTES\_c,out,HE} \tag{60.43}$$

Energy Analysis of the Pump (Used with TTES)

The energy balance of the pump used with TTES is given as follows:

$$\dot{W}_{TTES\_pump,t} = \dot{En}_{TTES\_pump,out} - \dot{En}_{TTES\_pump,in} \tag{60.44}$$

where $\dot{W}_{TTES\_pump,t}$ is the theoretical power of the pump used with TTES, $\dot{En}_{TTES\_pump,out}$ and $\dot{En}_{TTES\_pump,in}$ are energy output and energy input flow rates of the pump used with TTES, respectively as follows:

$$\dot{En}_{TTES\_pump,out} = \dot{m}_{TTES\_c}\, h_{TTES\_pump,out} \tag{60.45}$$

and

$$\dot{En}_{TTES\_pump,in} = \dot{m}_{TTES\_c}\, h_{TTES\_pump,in} \tag{60.46}$$

where $h_{TTES\_pump,out}$ and $h_{TTES\_pump,in}$ are enthalpy of output and input water of the pump used with TTES, respectively.

Also, the mechanical power of the pump used with TTES, $\dot{W}_{TTES\_pump,m}$ can be calculated from

$$\dot{W}_{TTES\_pump,m} = \frac{\dot{W}_{TTES\_pump,t}}{\eta_{TTES\_pump,m}\, \eta_{TTES\_pump,el}} \tag{60.47}$$

where $\eta_{TTES\_pump,m}$ and $\eta_{TTES\_pump,el}$ are the mechanical and electrical efficiencies of the pump used with TTES, respectively.

The energy loss rate of the pump used with TTES, $\dot{En}_{loss,TTES\_pump}$ is difference between the mechanical and theoretical powers of the pump used with TTES and is given by

$$\dot{En}_{loss,TTES\_pump} = \dot{W}_{TTES\_pump,m} - \dot{W}_{TTES\_pump,t} \qquad (60.48)$$

Energy Analysis of the Hot Well of ATES

The energy balance of the hot well of ATES are written as follows:

$$\dot{En}_{c\_ATES\_hw} = \dot{En}_{d\_ATES\_hw} + \dot{En}_{loss\_ATES\_hw} \qquad (60.49)$$

where $\dot{En}_{c,ATES\_hw}$, $\dot{En}_{d,ATES\_hw}$, and $\dot{En}_{loss,ATES\_hw}$ are the charging energy rate, the discharging energy rate, and the energy loss rate of the hot well of ATES, respectively.

The charging energy rate of the hot well of ATES, $\dot{En}_{c,ATES\_hw}$ is expressed by

$$\dot{En}_{c,ATES\_hw} = \dot{m}_{ATES}\, c_{p,ATES}\left(T_{c,ATES\_hw} - T_0\right) \qquad (60.50)$$

where $\dot{m}_{ATES}$ is the mass flow rate of water used in the ATES, $c_{p,ATES}$ is the specific heat of water, $T_{c,ATES\_hw}$ is the charging temperature of the water used in the hot well of ATES and T_0 is the environment temperature (also equal to dead state temperature).

The discharging energy rate of the hot well of ATES, $\dot{En}_{d,ATES\_hw}$ is determined from

$$\dot{En}_{d,ATES\_hw} = \dot{m}_{ATES}\, c_{p,ATES}\left(T_{d,ATES\_hw} - T_0\right) \qquad (60.51)$$

where $T_{d,ATES\_hw}$ is the discharging temperature of the water used in the hot well of ATES.

The energy loss rate of the hot well of ATES, $\dot{En}_{loss,ATES\_hw}$ is obtained from the balance equation of the hot well of ATES as follows:

$$\dot{En}_{loss\_ATES\_hw} = \dot{En}_{c\_ATES\_hw} - \dot{En}_{d\_ATES\_hw} \qquad (60.52)$$

The energy efficiency of the hot well of ATES, η_{ATES_hw} is defined as

$$\eta_{ATES\_hw} = \frac{\dot{En}_{d\_ATES\_hw}}{\dot{En}_{c\_ATES\_hw}} \qquad (60.53)$$

System-III: Cold Well of ATES + HP

Energy Analysis of the Cold Well of ATES

The energy balance of the cold well of ATES is given as follows:

$$\dot{En}_{c\_ATES\_cw} = \dot{En}_{d\_ATES\_cw} + \dot{En}_{loss\_ATES\_cw} \tag{60.54}$$

where $\dot{En}_{c\_ATES\_cw}$, $\dot{En}_{d,ATES\_cw}$, and $\dot{En}_{loss,ATES\_cw}$ are the charging energy rate, the discharging energy rate, and the energy loss rate of the cold well of ATES, respectively.

The charging energy rate of the cold well of ATES $\dot{En}_{c,ATES\_cw}$ is determined by

$$\dot{En}_{c,ATES\_cw} = \dot{m}_{ATES}\, c_{p,ATES}\left(T_{c,ATES\_cw} - T_0\right) \tag{60.55}$$

where $\dot{m}_{ATES}$ is the mass flow rate of water used in the ATES, $c_{p,ATES}$ is the specific heat of water, $T_{c,ATES\_cw}$ is the charging temperature of water used in the cold well of ATES and T_0 is the environment temperature.

The discharging energy rate of the cold well of ATES, $\dot{En}_{d,ATES\_cw}$ is calculated from

$$\dot{En}_{d,ATES\_cw} = \dot{m}_{ATES}\, c_{p,ATES}\left(T_{d,ATES\_cw} - T_0\right) \tag{60.56}$$

where $T_{d,ATES\_cw}$ is discharging temperature of water used in the cold well of ATES.

The energy loss rate of the cold well of ATES, $\dot{En}_{loss,ATES\_cw}$ is obtained from balance equation of the cold well of ATES to be

$$\dot{En}_{loss\_ATES\_cw} = \dot{En}_{c\_ATES\_cw} - \dot{En}_{d\_ATES\_cw} \tag{60.57}$$

The energy efficiency of the hot well of ATES, η_{ATES_cw} is written as follows:

$$\eta_{ATES\_cw} = \frac{\dot{En}_{d\_ATES\_cw}}{\dot{En}_{c\_ATES\_cw}} \tag{60.58}$$

Energy Analysis of the HP

The HP unit consists of evaporator, compressor, condenser and throttling/expansion valve. The energy balance of the evaporator is expressed to be

$$\dot{En}_{HP\_evap,in} + \dot{En}_{ATES\_cw\_c,in,evap} = \dot{En}_{HP\_evap,out} + \dot{En}_{ATES\_cw\_c,out,evap} \tag{60.59}$$

where $\dot{En}_{HP\_evap,in}$ and $\dot{En}_{HP\_evap,out}$ are the energy input and output flow rates of the evaporator due to HP fluid R-134a, respectively. "$\dot{En}_{ATES\_cw\_c,in,evap}$ and

$\dot{En}_{ATES\_cw\_c,out,evap}$" are the energy input and output flow rates of the evaporator due to charging process of the cold well of ATES water, respectively. These parameters are obtained as follows:

$$\dot{En}_{HP\_evap,in} = \dot{m}_{HP}\, h_{HP\_evap,in} \tag{60.60}$$

and

$$\dot{En}_{HP\_evap,out} = \dot{m}_{HP}\, h_{HP\_evap,out} \tag{60.61}$$

and

$$\dot{En}_{ATES\_cw\_c,in,evap} = \dot{m}_{ATES}\, h_{ATES\_cw\_c,in,evap} \tag{60.62}$$

and

$$\dot{En}_{ATES\_cw\_c,out,evap} = \dot{m}_{ATES}\, h_{ATES\_cw\_c,out,evap} \tag{60.63}$$

where $\dot{m}_{HP}$, $h_{HP\_evap,in}$ and $h_{HP\_evap,out}$ are the mass flow rate of R-134a used in the HP, and the enthalpy of input and output fluid (R-134a) of the evaporator, respectively. Also, where $\dot{m}_{ATES}$, $h_{ATES\_cw\_c,in,evap}$ and $h_{ATES\_cw\_c,out,evap}$ are the mass flow rate of ATES water, and the enthalpy of input and output ATES water of the evaporator due to charging process of the cold well of ATES, respectively.

The heat transfer rate of the evaporator (between ATES unit and evaporator of HP), $\dot{Q}_{ht,evap}$ is calculated to be

$$\dot{Q}_{ht,evap} = \dot{En}_{ATES\_cw\_c,in,evap} - \dot{En}_{ATES\_cw\_c,out,evap}$$
$$= \dot{En}_{HP\_evap,out} - \dot{En}_{HP\_evap,in} \tag{60.64}$$

The energy balance of the compressor is given as

$$\dot{W}_{HP\_comp,t} = \dot{En}_{HP\_comp,out} - \dot{En}_{HP\_comp,in} \tag{60.65}$$

where $\dot{W}_{HP\_comp,t}$ is the theoretical compressor power. Also $\dot{En}_{HP\_comp,out}$ and $\dot{En}_{HP\_comp,in}$ are the energy output and input flow rates of the compressor, respectively as follows:

$$\dot{En}_{HP\_comp,out} = \dot{m}_{HP}\, h_{HP\_comp,out} \tag{60.66}$$

and

$$\dot{En}_{HP\_comp,in} = \dot{m}_{HP}\, h_{HP\_comp,in} \tag{60.67}$$

where $h_{HP\_comp,out}$ and $h_{HP\_comp,in}$ are enthalpy of output and input fluids (R-134a) of the compressor, respectively.

Also, the mechanical compressor power $\dot{W}_{HP\_comp,m}$ can be calculated by

$$\dot{W}_{HP\_comp,m} = \frac{\dot{W}_{HP\_comp,t}}{\eta_{comp,m}\,\eta_{comp,el}} \qquad (60.68)$$

where $\eta_{comp,m}$ and $\eta_{comp,el}$ are the mechanical and electrical efficiencies of the compressor, respectively.

The energy loss rate of the compressor $\dot{En}_{loss,HP\_comp}$ occurs between the mechanical and theoretical compressor powers as follows:

$$\dot{En}_{loss,HP\_comp} = \dot{W}_{HP\_comp,m} - \dot{W}_{HP\_comp,t} \qquad (60.69)$$

The energy balance of the condenser is given to be

$$\dot{En}_{HP\_cond,in} + \dot{En}_{FHS,in,cond} = \dot{En}_{HP\_cond,out} + \dot{En}_{FHS,out,cond} \qquad (60.70)$$

where $\dot{En}_{HP\_cond,in}$ and $\dot{En}_{HP\_cond,out}$ are the energy input and output flow rates of the condenser due to HP fluid (R-134a), respectively. Also, $\dot{En}_{FHS,in,cond}$ and $\dot{En}_{FHS,out,cond}$ are the energy input and output flow rates of the condenser due to FHS water, respectively. These parameters can be determined as follows:

$$\dot{En}_{HP\_cond,in} = \dot{m}_{HP}\,h_{HP\_cond,in} \qquad (60.71)$$

and

$$\dot{En}_{HP\_cond,out} = \dot{m}_{HP}\,h_{HP\_cond,out} \qquad (60.72)$$

and

$$\dot{En}_{FHS,in,cond} = \dot{m}_{FHS}\,h_{FHS,in,cond} \qquad (60.73)$$

and

$$\dot{En}_{FHS,out,cond} = \dot{m}_{FHS}\,h_{FHS,out,cond} \qquad (60.74)$$

where $\dot{m}_{HP}$, $h_{HP\_cond,in}$ and $h_{HP\_cond,out}$ are the mass flow rate of R-134a used in the HP, and the enthalpy of the input and output fluids (R-134a) of the condenser, respectively. Also, where $\dot{m}_{FHS}$, $h_{FHS,in,cond}$ and $h_{FHS,out,cond}$ are the mass flow rate of the FHS water, and the enthalpy of input and output FHS water of the condenser, respectively.

The heat transfer rate of the condenser (between condenser of HP and energy receiver unit (ERU) of FHS), $\dot{Q}_{ht,cond}$ is calculated to be

$$\dot{Q}_{ht,cond} = \dot{En}_{FHS,out,cond} - \dot{En}_{FHS,in,cond} = \dot{En}_{HP\_cond,in} - \dot{En}_{HP\_cond,out} \qquad (60.75)$$

The energy balance of the throttling/expansion valve is written as follows:

$$\dot{E}n_{HP\_thrott,in} = \dot{E}n_{HP\_thrott,out} \tag{60.75}$$

where $\dot{E}n_{HP\_thrott,in}$ and $\dot{E}n_{HP\_thrott,out}$ are the energy input and output flow rates of the throttling/expansion valve due to HP fluid (R-134a), respectively as follows:

$$\dot{E}n_{HP\_thrott,in} = \dot{m}_{HP} \, h_{HP\_thrott,in} \tag{60.77}$$

and

$$\dot{E}n_{HP\_thrott,out} = \dot{m}_{HP} \, h_{HP\_thrott,out} \tag{60.78}$$

where $\dot{m}_{HP}$, $h_{HP\_thrott,in}$ and $h_{HP\_thrott,out}$ are the mass flow rate of R-134a used in the HP, and the enthalpies of the input and output fluids (R-134a) of the throttling/expansion valve, respectively.

The COP of the HP, COP_{HP} is obtained from;

$$COP_{HP} = \frac{\dot{Q}_{ht,cond}}{\dot{W}_{HP\_comp,m}} = \frac{\dot{E}n_{FHS,out,cond} - \dot{E}n_{FHS,in,cond}}{\dot{W}_{HP\_comp,m}}$$

$$= \frac{\dot{E}n_{HP\_cond,in} - \dot{E}n_{HP\_cond,out}}{\dot{W}_{HP\_comp,m}} \tag{60.79}$$

FHS: FHU + Pump + ERU

Energy Analysis of the FHU

The energy balance of the FHU is written as follows:

$$\dot{Q}_{FHU\_ht} = \dot{E}n_{FHU\_in} - \dot{E}n_{FHU\_out} \tag{60.80}$$

where $\dot{Q}_{FHU\_ht}$ is the energy transfer rate from the FHU (also known as heat transfer rate from FHS to the building). Also, $\dot{E}n_{FHU\_in}$ and $\dot{E}n_{FHU\_out}$ are the energy input and output rates of the FHU, respectively. These parameters can be expressed as

$$\dot{E}n_{FHU\_in} = \dot{m}_{FHS} \, h_{FHU\_in} \tag{60.81}$$

and

$$\dot{E}n_{FHU\_out} = \dot{m}_{FHS} \, h_{FHU\_out} \tag{60.82}$$

where $\dot{m}_{FHS}$, h_{FHU_in} and h_{FHU_out} are the mass flow rate of the water used in the FHS, and the enthalpies of the input and output water of the FHU, respectively.

Energy Analysis of the Pump (Used with FHU)

The energy balance of the pump used with FHU can be written as

$$\dot{W}_{FHU\_pump,t} = \dot{En}_{FHU\_pump,out} - \dot{En}_{FHU\_pump,in} \qquad (60.83)$$

where $\dot{W}_{FHU\_pump,t}$ is the theoretical power of the pump used with FHU. Also $\dot{En}_{FHU\_pump,out}$ and $\dot{En}_{FHU\_pump,in}$ are the energy output and input flow rates of the pump used with FHU, respectively as follows:

$$\dot{En}_{FHU\_pump,out} = \dot{m}_{FHU}\, h_{FHU\_pump,out} \qquad (60.84)$$

and

$$\dot{En}_{FHU\_pump,in} = \dot{m}_{FHU}\, h_{FHU\_pump,in} \qquad (60.85)$$

where $h_{FHU\_pump,out}$ and $h_{FHU\_pump,in}$ are the enthalpies of the output and input water of the pump used with FHU, respectively.

Also, the mechanical power of the pump used with FHU, $\dot{W}_{FHU\_pump,m}$ is obtained from

$$\dot{W}_{FHU\_pump,m} = \frac{\dot{W}_{FHU\_pump,t}}{\eta_{FHU\_pump,m}\, \eta_{FHU\_pump,el}} \qquad (60.86)$$

where $\eta_{FHU\_pump,m}$ and $\eta_{FHU\_pump,el}$ are the mechanical and electrical efficiencies of the pump used with FHU, respectively.

The energy loss rate of the pump used with FHU, $\dot{En}_{loss,FHU\_pump}$ is difference between mechanical and theoretical powers of the pump used with TTES to be

$$\dot{En}_{loss,FHU\_pump} = \dot{W}_{FHU\_pump,m} - \dot{W}_{FHU\_pump,t} \qquad (60.87)$$

Energy Analysis of the ERU

The ERU of FHS is operated with the System-II and/or System-III. If it is operated with System-II, the ERU rate of FHS is written as follows:

$$\dot{En}_{FHS,ERU} = \Delta\dot{En}_{flow,TTES\_d} = \dot{En}_{water,out,TTES\_d} - \dot{En}_{water,in,TTES\_d} \qquad (60.88)$$

or

$$\dot{En}_{FHS,ERU} = \Delta\dot{En}_{flow,TTES\_d} = \dot{m}_{TTES\_d}\left(h_{water,out,TTES\_d} - h_{water,in,TTES\_d}\right) \qquad (60.89)$$

If the ERU of FHS is used with System-III, the ERU rate of FHS is determined to be

$$\dot{E}n_{FHS,ERU} = \dot{Q}_{ht,cond} = \dot{E}n_{FHS,out,cond} - \dot{E}n_{FHS,in,cond}$$
$$= \dot{E}n_{HP\_cond,in} - \dot{E}n_{HP\_cond,out} \tag{60.90}$$

or

$$\dot{E}n_{FHS,ERU} = \dot{m}_{FHS} \left(h_{FHS,out,cond} - h_{FHS,in,cond} \right)$$
$$= \dot{m}_{HP} \left(h_{HP\_cond,in} - h_{HP\_cond,out} \right) \tag{60.91}$$

The COP of the HP and FHS, COP_{HP+FHS} can be calculated from

$$COP_{HP+FHS} = \frac{\dot{E}n_{FHS,ERU}}{\dot{W}_{HP\_comp,m} + \dot{W}_{FHU\_pump,m}} = \frac{\dot{Q}_{ht,cond}}{\dot{W}_{HP\_comp,m} + \dot{W}_{FHU\_pump,m}} \tag{60.92}$$

or

$$COP_{HP+FHS} = \frac{\dot{E}n_{FHS,out,cond} - \dot{E}n_{FHS,in,cond}}{\dot{W}_{HP\_comp,m} + \dot{W}_{FHU\_pump,m}}$$
$$= \frac{\dot{E}n_{HP\_cond,in} - \dot{E}n_{HP\_cond,out}}{\dot{W}_{HP\_comp,m} + \dot{W}_{FHU\_pump,m}} \tag{60.93}$$

60.3.2 Exergy Analysis

System-I: LTES + Fan

Exergy Analysis of the LTES Charging Process

The exergy balance of the LTES charging process is written as follows:

$$\dot{E}x_{solar,LTES\_c} = \dot{E}x_{acc,LTES\_c} + \dot{E}x_{loss,LTES\_c} + \dot{E}x_{dest,LTES\_c} \tag{60.94}$$

where $\dot{E}x_{solar,LTES\_c}$, $\dot{E}x_{acc,LTES\_c}$, $\dot{E}x_{loss,LTES\_c}$, and $\dot{E}x_{dest,LTES\_c}$ are the solar exergy input rate, the accumulated exergy rate, the exergy loss rate, and the exergy destruction rate of the LTES charging process, respectively.

The solar exergy input rate of the LTES charging process, $\dot{E}x_{solar,LTES\_c}$ is obtained from

$$\dot{E}x_{solar,LTES\_c} = I_T A_{glass} \left[1 + \frac{1}{3} \left(\frac{T_0}{T_{sun}} \right)^4 - \frac{4}{3} \left(\frac{T_0}{T_{sun}} \right) \right] \tag{60.95}$$

where T_0 is the dead state temperature (equal to environment temperature) and T_{sun} is the sun temperature.

The accumulated exergy rate of the LTES charging process, $\dot{Ex}_{acc,LTES\_c}$ is given as

$$
\begin{aligned}
\dot{Ex}_{acc,LTES\_c} = \Bigg\{ & m_{PCM}\, c_{p,s} \left[(T_{PCM,m} - T_{glass,in}) - T_0\, \ln\left(\frac{T_{PCM,m}}{T_{glass,in}}\right) \right] \\
& + m_{PCM}\, q_t \left(1 - \frac{T_0}{T_{PCM,m}} \right) \\
& + m_{PCM}\, c_{p,l} \left[(T_{PCM,final} - T_{PCM,m}) - T_0\, \ln\left(\frac{T_{PCM,final}}{T_{PCM,m}}\right) \right] \Bigg\} / t_{PCM}
\end{aligned}
\tag{60.96}
$$

The exergy loss rate of the LTES charging process, $\dot{Ex}_{loss,LTES\_c}$ can be determined as follows:

$$
\dot{Ex}_{loss,LTES\_c} = \dot{En}_{loss,LTES\_c} \left(1 - \frac{T_0}{T_{PCM,m}} \right)
\tag{60.97}
$$

The exergy destruction rate of the LTES charging process, $\dot{Ex}_{dest,LTES\_c}$ is obtained from exergy balance equation of the LTES charging process:

$$
\dot{Ex}_{dest,LTES\_c} = \dot{Ex}_{solar,LTES\_c} - \dot{Ex}_{acc,LTES\_c} - \dot{Ex}_{loss,LTES\_c}
\tag{60.98}
$$

The exergy efficiency of the LTES charging process, ψ_{LTES_c} is calculated to be

$$
\psi_{LTES\_c} = \frac{Accumulated\ exergy\ rate}{Solar\ exergy\ input\ rate} = \frac{\dot{Ex}_{acc,LTES\_c}}{\dot{Ex}_{solar,LTES\_c}}
\tag{60.99}
$$

Exergy Analysis of the LTES Discharging Process

The exergy balance of the LTES discharging process is given as

$$
\dot{Ex}_{acc,LTES\_d} = \Delta\dot{Ex}_{received,LTES\_d} + \dot{Ex}_{loss,LTES\_d} + \dot{Ex}_{dest,LTES\_d}
\tag{60.100}
$$

where $\dot{Ex}_{acc,LTES\_d}$, $\Delta\dot{Ex}_{received,LTES\_d}$, $\dot{Ex}_{loss,LTES\_d}$, and $\dot{Ex}_{dest,LTES\_d}$ are the accumulated exergy rate, the net received exergy rate, the exergy loss rate, and the exergy destruction rate of the LTES discharging process, respectively.

The accumulated exergy rate of the LTES discharging process, $\dot{Ex}_{acc,LTES\_d}$ is equal to accumulated exergy rate of the charging process $\dot{Ex}_{acc,LTES\_c}$ as follows:

$$
\begin{aligned}
\dot{Ex}_{acc,LTES\_d} &= \dot{Ex}_{acc,LTES\_c} \\
&= \dot{m}_{PCM}\, c_{p,s} \left[(T_{PCM,m} - T_{glass,in}) - T_0 \, \ln\left(\frac{T_{PCM,m}}{T_{glass,in}} \right) \right] \\
&\quad + \dot{m}_{PCM}\, q_t \left(1 - \frac{T_0}{T_{PCM,m}} \right) \\
&\quad + \dot{m}_{PCM}\, c_{p,l} \left[(T_{PCM,final} - T_{PCM,m}) - T_0 \, \ln\left(\frac{T_{PCM,final}}{T_{PCM,m}} \right) \right]
\end{aligned}
\tag{60.101}
$$

The net received exergy rate of the LTES discharging process, $\Delta \dot{En}_{received,LTES\_d}$ is the difference of output and input exergy rates of air as

$$
\Delta \dot{Ex}_{received,LTES\_d} = \dot{Ex}_{air,out,LTES\_d} - \dot{Ex}_{air,in,LTES\_d}
\tag{60.102}
$$

where $\dot{Ex}_{air,out,LTES\_d}$ and $\dot{Ex}_{air,in,LTES\_d}$ are the output and input exergy rates of the air used in the LTES discharging process, respectively as follows:

$$
\begin{aligned}
\dot{Ex}_{air,out,LTES\_d} &= \dot{m}_{air} \left(c_{p,a} + \omega_{air,out,LTES\_d}\, c_{p,v} \right) T_0 \left(\frac{T_{air,out,LTES\_d}}{T_0} \right) \\
&\quad + \dot{m}_{air} \left(1 + \bar{\omega}_{air,out,LTES\_d} \right) R_a T_0 \, \ln\left(\frac{P_{air,out,LTES\_d}}{P_0} \right) \\
&\quad + \dot{m}_{air} R_a T_0 \left[\left(1 + \bar{\omega}_{air,out,LTES\_d} \right) \ln\left(\frac{1 + \bar{\omega}_0}{1 + \bar{\omega}_{air,out,LTES\_d}} \right) \right] \\
&\quad + \dot{m}_{air} R_a T_0 \left[\bar{\omega}_{air,out,LTES\_d} \ln\left(\frac{\bar{\omega}_{air,out,LTES\_d}}{\bar{\omega}_0} \right) \right]
\end{aligned}
\tag{60.103}
$$

and

$$
\begin{aligned}
\dot{Ex}_{air,in,LTES\_d} &= \dot{m}_{air} \left(c_{p,a} + \omega_{air,in,LTES\_d}\, c_{p,v} \right) T_0 \left(\frac{T_{air,in,LTES\_d}}{T_0} \right) \\
&\quad + \dot{m}_{air} \left(1 + \bar{\omega}_{air,in,LTES\_d} \right) R_a T_0 \, \ln\left(\frac{P_{air,in,LTES\_d}}{P_0} \right) \\
&\quad + \dot{m}_{air} R_a T_0 \left[\left(1 + \bar{\omega}_{air,in,LTES\_d} \right) \ln\left(\frac{1 + \bar{\omega}_0}{1 + \bar{\omega}_{air,in,LTES\_d}} \right) \right] \\
&\quad + \dot{m}_{air} R_a T_0 \left[\bar{\omega}_{air,in} \ln\left(\frac{\bar{\omega}_{air,in,LTES\_d}}{\bar{\omega}_0} \right) \right]
\end{aligned}
\tag{60.104}
$$

where $\omega_{air,in,LTES\_d}$, $T_{air,in,LTES\_d}$, $\bar{\omega}_{air,in,LTES\_d}$, and $P_{air,in,LTES\_d}$ are the humidity ratio of the air at input, temperature of input air, the mole fraction ratio of the air at input, and the pressure of the air at input of the LTES discharging process, respectively. Also, $\omega_{air,out,LTES\_d}$, $T_{air,out,LTES\_d}$, $\bar{\omega}_{air,out,LTES\_d}$, and $P_{air,out,LTES\_d}$ are the humidity ratio of the air at output, the temperature of the output air, the mole fraction ratio of the air at output, and the pressure of the air at output of the LTES discharging process, respectively. Furthermore, $c_{p,v}$ is the specific heat of the water vapor, $\bar{\omega}_0$ is the humidity ratio of the air at dead state, P_0 is the dead state pressure (equal to environment pressure), and R_a is the general gas constant of the air.

The exergy loss rate of the LTES discharging process, $\dot{Ex}_{loss,LTES\_d}$ is found from

$$\dot{Ex}_{loss,LTES\_d} = \dot{En}_{loss,LTES\_d}\left(1 - \frac{T_0}{T_{PCM,m}}\right) \tag{60.105}$$

The exergy destruction rate of the LTES discharging process, $\dot{Ex}_{dest,LTES\_d}$ is determined to be

$$\dot{Ex}_{dest,LTES\_d} = \dot{Ex}_{acc,LTES\_d} - \Delta\dot{Ex}_{received,LTES\_d} - \dot{Ex}_{loss,LTES\_d} \tag{60.106}$$

The exergy efficiency of the LTES discharging process, ψ_{LTES_d} is expressed as

$$\psi_{LTES\_d} = \frac{Received\ exergy\ rate}{Accumulated\ exergy\ rate} = \frac{\dot{Ex}_{received,LTES\_d}}{\dot{Ex}_{acc,LTES\_d}} \tag{60.107}$$

Exergy Analysis of the Fan

The energy balance of the fan is written to be;

$$\dot{Ex}_{air,in,fan} + \dot{Ex}_{w,fan} = \dot{Ex}_{air,out,fan} + \dot{Ex}_{dest,fan} \tag{60.108}$$

where $\dot{Ex}_{w,fan}$ is the exergetic fan power. Also, $\dot{Ex}_{air,in,fan}$, $\dot{Ex}_{air,out,fan}$, and $\dot{Ex}_{dest,fan}$ are the exergy input, the exergy output, and the exergy destruction rates of the air used in the fan, respectively as follows:

$$\dot{Ex}_{air,in,fan} = \dot{m}_{air}\left(c_{p,a} + \omega_{air,in,fan}\,c_{p,v}\right)T_0\left(\frac{T_{air,in,fan}}{T_0}\right)$$
$$+ \dot{m}_{air}\left(1 + \bar{\omega}_{air,in,fan}\right)R_a\,T_0\,\ln\left(\frac{P_{air,in,fan}}{P_0}\right)$$
$$+ \dot{m}_{air}\,R_a\,T_0\left[\left(1 + \bar{\omega}_{air,in,fan}\right)\ln\left(\frac{1+\bar{\omega}_0}{1+\bar{\omega}_{air,in,fan}}\right) + \bar{\omega}_{air,in}\ln\left(\frac{\bar{\omega}_{air,in,fan}}{\bar{\omega}_0}\right)\right] \tag{60.109}$$

and

$$
\begin{aligned}
\dot{Ex}_{air,out,fan} = {} & \dot{m}_{air}\left(c_{p,a} + \omega_{air,out,fan}\, c_{p,v}\right) T_0 \left(\frac{T_{air,out,fan}}{T_0}\right) \\
& + \dot{m}_{air}\left(1 + \bar{\omega}_{air,out,fan}\right) R_a T_0 \ln\left(\frac{P_{air,out,fan}}{P_0}\right) \\
& + \dot{m}_{air} R_a T_0 \left[\left(1 + \bar{\omega}_{air,out,fan}\right) \ln\left(\frac{1 + \bar{\omega}_0}{1 + \bar{\omega}_{air,out,fan}}\right)\right] \\
& + \dot{m}_{air} R_a T_0 \left[\bar{\omega}_{air,out,LTES\_d} \ln\left(\frac{\bar{\omega}_{air,out,fan}}{\bar{\omega}_0}\right)\right]
\end{aligned}
\tag{60.110}
$$

where $\omega_{air,in,fan}$, $T_{air,in,fan}$, $\bar{\omega}_{air,in,fan}$ and $P_{air,in,fan}$ are the humidity ratio of the air at input, the temperature of the input air, the mole fraction ratio of the air at input, and the pressure of the air at input of the fan, respectively. Also, $\omega_{air,out,fan}$, $T_{air,out,fan}$, $\bar{\omega}_{air,out,fan}$, and $P_{air,out,fan}$ are the humidity ratio of the air at output, the temperature of the output air, the mole fraction ratio of the air at output, and the pressure of the air at output of the fan, respectively.

Also, the exergy destruction of the fan, $\dot{Ex}_{dest,fan}$ can be calculated from the exergy balance equation as

$$
\dot{Ex}_{dest,fan} = \dot{Ex}_{air,in,fan} + \dot{Ex}_{w,fan} - \dot{Ex}_{air,out,fan}
\tag{60.111}
$$

The exergy efficiency of the fan, ψ_{fan} is expressed to be

$$
\psi_{fan} = \frac{\dot{Ex}_{air,out,fan} - \dot{Ex}_{air,in,fan}}{\dot{Ex}_{w,fan}}
\tag{60.112}
$$

System-II: TTES + Solar Collector + HE + Pump + Hot Well of ATES

Exergy Analysis of the TTES Charging (Dehydration) Process

The exergy balance of the TTES charging process is written to be

$$
\Delta\dot{Ex}_{flow,TTES\_c} = \sum \dot{Ex}_{reaction,TTES\_c} + \dot{Ex}_{loss,TTES\_c} + \dot{Ex}_{dest,TTES\_c}
\tag{60.113}
$$

where $\Delta\dot{Ex}_{flow,TTES\_c}$, $\sum\dot{Ex}_{reaction,TTES\_c}$, $\dot{Ex}_{loss,TTES\_c}$, and $\dot{Ex}_{dest,TTES\_c}$ are the net exergy flow rate, the total exergy rate of reaction, the exergy loss rate, and the exergy destruction rate of the TTES charging process, respectively.

The net exergy flow rate of the TTES charging process, $\Delta\dot{Ex}_{flow,TTES\_c}$ is the difference of the exergy input and output rates of the water used in the TTES charging process to be

$$\Delta \dot{E}x_{flow,TTES\_c} = \dot{E}x_{water,in,TTES\_c} - \dot{E}x_{water,out,TTES\_c} \qquad (60.114)$$

where $\dot{E}x_{water,in,TTES\_c}$ and $\dot{E}x_{water,out,TTES\_c}$ are the exergy input and output rates of the water used in the TTES charging process, respectively as

$$\dot{E}x_{water,in,TTES\_c} = \dot{m}_{TTES\_c} \left[\left(h_{water,in,TTES\_c} - h_{water,st,TTES} \right) \\ - T_{st} \left(s_{water,in,TTES\_c} - s_{water,0,TTES} \right) \right] \qquad (60.115)$$

and

$$\dot{E}x_{water,out,TTES\_c} = \dot{m}_{TTES\_c} \left[\left(h_{water,out,TTES\_c} - h_{water,0,TTES} \right) \\ - T_{st} \left(s_{water,out,TTES\_c} - s_{water,0,TTES} \right) \right] \qquad (60.116)$$

where T_{st} is the standard temperature of the TTES system. Also, $s_{water,in,TTES\_c}$ and $s_{water,out,TTES\_c}$ are the entropy of the input and output water used in the TTES charging process. Furthermore, $h_{water,0,TTES}$ and $s_{water,0,TTES}$ are the enthalpy and entropy of the water at standard condition used in the TTES charging process, respectively.

In the exergy analysis of the TTES system, standard temperature and pressure values are used instead of dead state conditions because standard chemical exergy (related with Gibbs energy formation) of reaction is calculated in standard temperature and pressure to calculate total exergy rate of the reaction of TTES. So, they are taken into account for the rest of the exergetic calculation of TTES for reliability of the system.

The total exergy rate of reaction (or reaction exergy rate) of the TTES charging process $\sum \dot{E}x_{reaction,TTES\_c}$ is calculated as follows:

$$\sum \dot{E}x_{reaction,TTES\_c} = \dot{E}x_{product,reaction,TTES\_c} - \dot{E}x_{reac\tan t,reaction,TTES\_c} \\ = \left[\left(N_{SrBr_2H_2O(l)} \, ex_{ch_{SrBr_2H_2O(l)}} \right) + \left(N_{H_2O(g)} \, ex_{ch_{H_2O(g)}} \right) \right] \\ - \left[N_{SrBr_26H_2O(l)} \, ex_{ch_{SrBr_26H_2O(l)}} \right] \qquad (60.117)$$

where N and $ex_{ch,n}$ are the molar flow rate and the standard chemical exergy of the products and reactants, respectively.

The standard chemical exergy $ex_{ch,n}$ is found from

$$ex_{ch,n} = \sum \Delta G_f + \sum_e n_e \, ex_{ch_{n_e}} \qquad (60.118)$$

where ΔG_f is the Gibbs energy formation, n_e is the amount of element, and $ex_{ch_{n_e}}$ is the standard chemical exergy of the related element.

The exergy loss rate of the TTES charging process, $\dot{Ex}_{loss,TTES\_c}$ is found by

$$\dot{Ex}_{loss,TTES\_c} = \dot{En}_{loss,TTES\_c}\left(1 - \frac{T_{st}}{T_{av,TTES\_c}}\right) \tag{60.119}$$

where $T_{av,TTES\_c}$ is the average temperature of the TTES charging process as follows:

$$T_{av,TTES\_c} = \frac{T_{water,in,TTES\_c} + T_{water,out,TTES\_c}}{2} \tag{60.120}$$

where $T_{water,in,TTES\_c}$ and $T_{water,out,TTES\_c}$ are the water input and output temperatures of the TTES charging process.

The exergy destruction rate of the TTES charging process, $\dot{Ex}_{dest,TTES\_c}$ is calculated from the exergy balance equation to be

$$\dot{Ex}_{dest,TTES\_c} = \Delta\dot{Ex}_{flow,TTES\_c} - \sum\dot{Ex}_{reaction,TTES\_c} - \dot{Ex}_{loss,TTES\_c} \tag{60.121}$$

The exergy efficiency of the TTES charging process, ψ_{TTES_c} is expressed as

$$\psi_{TTES\_c} = \frac{\sum\dot{Ex}_{reaction,TTES\_c}}{\Delta\dot{Ex}_{flow,TTES\_c}} \tag{60.122}$$

Exergy Analysis of the TTES Discharging (Hydration) Process

The exergy balance of the TTES discharging process is given by

$$\sum\dot{Ex}_{reaction,TTES\_d} = \Delta\dot{Ex}_{flow,TTES\_d} + \dot{Ex}_{loss,TTES\_d} + \dot{Ex}_{dest,TTES\_d} \tag{60.123}$$

where $\sum\dot{Ex}_{reaction,TTES\_d}$, $\Delta\dot{Ex}_{flow,TTES\_d}$, $\dot{Ex}_{loss,TTES\_d}$, and $\dot{Ex}_{dest,TTES\_d}$ are the total exergy rate of the reaction, the net exergy flow rate, the exergy loss rate, and the exergy destruction rate of the TTES discharging process, respectively.

The total exergy rate of the reaction of TTES discharging process $\sum\dot{Ex}_{reaction,TTES\_d}$ is equal to the total exergy rate of the reaction of TTES charging process $\sum\dot{Ex}_{reaction,TTES\_c}$ as

$$\sum\dot{Ex}_{reaction,TTES\_d} = \sum\dot{Ex}_{reaction,TTES\_c} \tag{60.124}$$

The net exergy flow rate of the TTES discharging process, $\Delta\dot{Ex}_{flow,TTES\_d}$ is the difference of exergy input and output rates of the water used in the TTES discharging process to be

$$\Delta\dot{Ex}_{flow,TTES\_d} = \dot{Ex}_{water,out,TTES\_d} - \dot{Ex}_{water,in,TTES\_d} \tag{60.125}$$

where $\dot{E}x_{water,in,TTES\_d}$ and $\dot{E}x_{water,out,TTES\_d}$ are the energy input and output rates of the water used in the TTES discharging process, respectively as follows:

$$
\dot{E}x_{water,in,TTES\_d} = \dot{m}_{TTES\_d} \left[\left(h_{water,in,TTES\_d} - h_{water,st,TTES} \right) \\ - T_{st} \left(s_{water,in,TTES\_d} - s_{water,st,TTES} \right) \right] \tag{60.126}
$$

and

$$
\dot{E}x_{water,out,TTES\_d} = \dot{m}_{TTES\_d} \left(h_{water,out,TTES\_d} - h_{water,st,TTES} \right) \\ - \dot{m}_{TTES\_d} T_{st} \left(s_{water,out,TTES\_d} - s_{water,st,TTES} \right) \tag{60.127}
$$

where $s_{water,in,TTES\_d}$ and $s_{water,out,TTES\_d}$ are the entropy of input and output water used in the TTES charging process, respectively.

The exergy loss rate of the TTES discharging process, $\dot{E}x_{loss,TTES\_d}$ is calculated from

$$
\dot{E}x_{loss,TTES\_d} = \dot{E}n_{loss,TTES\_d} \left(1 - \frac{T_{st}}{T_{av,TTES\_d}} \right) \tag{60.128}
$$

where "$T_{av,TTES\_d}$" is average temperature of the TTES discharging process to be

$$
T_{av,TTES\_d} = \frac{T_{water,in,TTES\_d} + T_{water,out,TTES\_d}}{2} \tag{60.129}
$$

where $T_{water,in,TTES\_d}$ and $T_{water,out,TTES\_d}$ are the water input and output temperatures of the TTES discharging process.

The exergy destruction rate of the TTES discharging process, $\dot{E}x_{dest,TTES\_d}$ is obtained from the exergy balance equation as

$$
\dot{E}x_{dest,TTES\_d} = \sum \dot{E}x_{reaction,TTES\_d} - \Delta\dot{E}x_{flow,TTES\_d} - \dot{E}x_{loss,TTES\_d} \tag{60.130}
$$

The exergy efficiency of the TTES discharging process, ψ_{TTES_d} is expressed as

$$
\psi_{TTES\_d} = \frac{\Delta\dot{E}x_{flow,TTES\_d}}{\sum \dot{E}x_{reaction,TTES\_d}} \tag{60.131}
$$

The overall exergy efficiency of the TTES, $\psi_{TTES\_overall}$ can be calculated by

$$
\psi_{TTES\_overall} = \frac{\Delta\dot{E}x_{flow,TTES\_d}}{\Delta\dot{E}x_{flow,TTES\_c}} \tag{60.132}
$$

Exergy Analysis of the Solar Collector

The exergy balance of the solar collector is expressed as

$$\dot{Ex}_{solar,collector} = \Delta\dot{Ex}_{flow,collector} + \dot{Ex}_{loss,collector} + \dot{Ex}_{dest,collector} \qquad (60.133)$$

where $\dot{Ex}_{solar,collector}$, $\Delta\dot{Ex}_{flow,collector}$, $\dot{Ex}_{loss,collector}$, and $\dot{Ex}_{dest,collector}$ are the solar exergy rate, the net exergy flow rate, the exergy loss rate, and the exergy destruction rate of the solar collector, respectively.

The solar exergy rate of the solar collector, $\dot{Ex}_{solar,collector}$ is written to be

$$\dot{Ex}_{solar,collector} = I_T A_{collector} \left[1 + \frac{1}{3}\left(\frac{T_0}{T_{sun}}\right)^4 - \frac{4}{3}\left(\frac{T_0}{T_{sun}}\right) \right] \qquad (60.134)$$

The net exergy flow rate of the solar collector, $\Delta\dot{Ex}_{flow,collector}$ is the difference of the energy input and output rates of the water used in the solar collector.

$$\Delta\dot{Ex}_{flow,collector} = \dot{Ex}_{water,out,collector} - \dot{Ex}_{water,in,collector} \qquad (60.135)$$

where $\dot{Ex}_{water,in,collector}$ and $\dot{Ex}_{water,out,collector}$ are the exergy input and output rates of the water used in the solar collector, respectively as follows:

$$\dot{Ex}_{water,in,collector} = \dot{m}_{TTES\_c}\left(h_{water,in,collector} - h_{water,0,collector}\right) \\ - \dot{m}_{TTES\_c} T_0\left(s_{water,in,collector} - s_{water,0,collector}\right) \qquad (60.136)$$

and

$$\dot{Ex}_{water,out,collector} = \dot{m}_{TTES\_c}\left(h_{water,out,collector} - h_{water,0,collector}\right) \\ - \dot{m}_{TTES\_c} T_0\left(s_{water,out,collector} - s_{water,0,collector}\right) \qquad (60.137)$$

where $h_{water,0,collector}$ and $s_{water,0,collector}$ are the enthalpy and entropy of the water at the dead state condition, respectively.

The exergy loss rate of the solar collector, $\dot{Ex}_{loss,collector}$ is found to be

$$\dot{Ex}_{loss,collector} = \dot{En}_{loss,collector}\left(1 - \frac{T_0}{T_{av,collector}}\right) \qquad (60.137)$$

where $T_{av,collector}$ is the average temperature of the collector as

$$T_{av,collector} = \frac{T_{in,collector} + T_{out,collector}}{2} \qquad (60.139)$$

where $T_{in,collector}$ and $T_{out,collector}$ are the water input and output temperatures of the collector.

The exergy destruction rate of the solar collector, $\dot{E}x_{dest,collector}$, is determined from the exergy balance equation as follows:

$$\dot{E}x_{dest,collector} = \dot{E}x_{solar,collector} - \Delta\dot{E}x_{flow,collector} - \dot{E}x_{loss,collector} \qquad (60.140)$$

The exergy efficiency of the solar collector, $\psi_{collector}$ is computed to be

$$\psi_{collector} = \frac{\Delta\dot{E}x_{flow,collector}}{\dot{E}x_{solar,collector}} \qquad (60.141)$$

Exergy Analysis of the HE

The exergy balance of the HE between the TTES unit and hot well of the ATES is written as

$$\sum \dot{E}x_{in,HE} = \sum \dot{E}x_{out,HE} + \dot{E}x_{dest,HE} \qquad (60.142)$$

where $\sum \dot{E}x_{in,HE}$, $\sum \dot{E}x_{out,HE}$, and $\dot{E}x_{dest,HE}$ are the total exergy input rate, the total exergy output rate, and the exergy destruction rate of the HE, respectively.

The total exergy input rate of the HE can be express to be

$$\sum \dot{E}x_{in,HE} = \dot{E}x_{TTES\_c,in,HE} + \dot{E}x_{ATES\_hw\_c,in,HE} \qquad (60.143)$$

where $\dot{E}x_{TTES\_c,in,HE}$ is the exergy input flow rate of the heat exchanger due to the charging process of TTES (water used in TTES), and $\dot{E}x_{ATES\_hw\_c,in,HE}$ is the exergy input flow rate of the HE due to the charging process of the hot well of ATES (water used in ATES). These parameters are calculated as follows:

$$\dot{E}x_{TTES\_c,in,HE} = \dot{m}_{TTES\_c} \left[\left(h_{TTES\_c,in,HE} - h_{water,0,HE} \right) \right. \\ \left. - T_0 \left(s_{TTES\_c,in,HE} - s_{water,0,HE} \right) \right] \qquad (60.144)$$

and

$$\dot{E}x_{ATES\_hw\_c,in,HE} = \dot{m}_{ATES} \left[\left(h_{ATES\_hw\_c,in,HE} - h_{water,0,HE} \right) \right. \\ \left. - T_0 \left(s_{ATES\_hw\_c,in,HE} - s_{water,0,HE} \right) \right] \qquad (60.145)$$

where $h_{water,0,HE}$ and $s_{water,0,HE}$ are the enthalpy and entropy of the water at the dead state condition, respectively.

The total exergy output rate of the HE is determined as

$$\sum \dot{E}x_{out,HE} = \dot{E}x_{TTES\_c,out,HE} + \dot{E}x_{ATES\_hw\_c,out,HE} \qquad (60.146)$$

where $\dot{E}x_{TTES\_c,out,HE}$ is the exergy output flow rate of the HE due to the charging process of TTES, and $\dot{E}x_{ATES\_hw\_c,out,HE}$ is the exergy output flow rate of the heat exchanger due to the charging process of the hot well of ATES. These parameters can be computed as follows:

$$\dot{E}x_{TTES\_c,out,HE} = \dot{m}_{TTES\_c} \left[\left(h_{TTES\_c,out,HE} - h_{water,0,HE} \right) \\ - T_0 \left(s_{TTES\_c,out,HE} - s_{water,0,HE} \right) \right] \qquad (60.147)$$

and

$$\dot{E}x_{ATES\_hw\_c,out,HE} = \dot{m}_{ATES} \left(h_{ATES\_hw\_c,out,HE} - h_{water,0,HE} \right) \\ - \dot{m}_{ATES} T_0 \left(s_{ATES\_hw\_c,out,HE} - s_{water,0,HE} \right) \qquad (60.148)$$

The exergy destruction rate of the HE, $\dot{E}x_{dest,HE}$ is found from

$$\dot{E}x_{dest,HE} = \sum \dot{E}x_{in,HE} - \sum \dot{E}x_{out,HE} \qquad (60.149)$$

The exergy efficiency of the HE, ψ_{HE} is written as

$$\psi_{HE} = \frac{\dot{E}x_{ATES\_hw\_c,out,HE} - \dot{E}x_{ATES\_hw\_c,in,HE}}{\dot{E}x_{TTES\_c,in,HE} - \dot{E}x_{TTES\_c,out,HE}} \qquad (60.150)$$

Exergy Analysis of the Pump (Used with TTES)

The exergy balance of the pump used with TTES is given to be

$$\dot{E}x_{TTES\_pump,in} + \dot{E}x_{w,TTES\_pump,m} = \dot{E}x_{TTES\_pump,out} + \dot{E}x_{TTES\_pump,dest} \qquad (60.151)$$

where $\dot{E}x_{TTES\_pump,in}$, $\dot{E}x_{TTES\_pump,out}$, $\dot{E}x_{w,TTES\_pump,m}$, and $\dot{E}x_{TTES\_pump,dest}$ are the exergy input flow rate, the exergy output flow rate, the exergetic power, and the exergy destruction rate of the pump used with the TTES, respectively as follows:

$$\dot{E}x_{TTES\_pump,in} = \dot{m}_{TTES\_c} \left[\left(h_{TTES\_pump,in} - h_{TTES\_pump,0} \right) \\ - T_0 \left(s_{TTES\_pump,in} - s_{TTES\_pump,0} \right) \right] \qquad (60.152)$$

and

$$\dot{E}x_{TTES\_pump,out} = \dot{m}_{TTES\_c} \left[\left(h_{TTES\_pump,out} - h_{TTES\_pump,0} \right) \\ - T_0 \left(s_{TTES\_pump,out} - s_{TTES\_pump,0} \right) \right] \qquad (60.153)$$

and

$$\dot{Ex}_{w,TTES\_pump,m} = \dot{W}_{TTES\_pump,m} \qquad (60.154)$$

and

$$\dot{Ex}_{TTES\_pump,dest} = \dot{Ex}_{TTES\_pump,in} + \dot{Ex}_{w,TTES\_pump,m} - \dot{Ex}_{TTES\_pump,out} \qquad (60.155)$$

where $h_{TTES\_pump,0}$ and $s_{TTES\_pump,0}$ are the enthalpy and entropy of the water at the dead state condition, respectively.

The exergy efficiency of the pump used with the TTES, ψ_{TTES_pump} is written as

$$\psi_{TTES\_pump} = \frac{\dot{Ex}_{TTES\_pump,out} - \dot{Ex}_{TTES\_pump,in}}{\dot{Ex}_{w,TTES\_pump,m}} \qquad (60.156)$$

Exergy Analysis of the Hot Well of ATES

The exergy balance of the hot well of ATES can be given as follows:

$$\dot{Ex}_{c\_ATES\_hw} = \dot{Ex}_{d\_ATES\_hw} + \dot{Ex}_{dest\_ATES\_hw} \qquad (60.157)$$

where $\dot{Ex}_{c,ATES\_hw}$, $\dot{Ex}_{d,ATES\_hw}$, and $\dot{Ex}_{loss,ATES\_hw}$ are the charging exergy rate, the discharging exergy rate, and the exergy loss rate of the hot well of ATES, respectively.

The charging exergy rate of the hot well of ATES, $\dot{Ex}_{c,ATES\_hw}$ is determined by

$$\dot{Ex}_{c,ATES\_hw} = \dot{En}_{c,ATES\_hw} - \dot{m}_{ATES}\, c_{p,ATES}\, T_0 \ln\left(\frac{T_{c,ATES\_hw}}{T_0}\right) \qquad (60.158)$$

The discharging exergy rate of the hot well of ATES, $\dot{Ex}_{d,ATES\_hw}$ is calculated as

$$\dot{Ex}_{d,ATES\_hw} = \dot{En}_{d,ATES\_hw} - \dot{m}_{ATES}\, c_{p,ATES}\, T_0 \ln\left(\frac{T_{d,ATES\_hw}}{T_0}\right) \qquad (60.159)$$

The exergy destruction rate of the hot well of ATES, $\dot{Ex}_{loss,ATES\_hw}$ is obtained from the exergetic balance equation as follows:

$$\dot{Ex}_{dest\_ATES\_hw} = \dot{Ex}_{c\_ATES\_hw} - \dot{Ex}_{d\_ATES\_hw} \qquad (60.160)$$

The exergy efficiency of the hot well of ATES, ψ_{ATES_hw} is computed from

$$\psi_{ATES\_hw} = \frac{\dot{Ex}_{d\_ATES\_hw}}{\dot{Ex}_{c\_ATES\_hw}} \qquad (60.161)$$

System-III: Cold Well of ATES + HP

Exergy Analysis of the Cold Well of ATES

The exergy balance of the cold well of ATES can be written as follows:

$$\dot{Ex}_{c\_ATES\_cw} = \dot{Ex}_{d\_ATES\_cw} + \dot{Ex}_{dest\_ATES\_cw} \tag{60.162}$$

where $\dot{Ex}_{c,ATES\_cw}$, $\dot{Ex}_{d,ATES\_cw}$, and $\dot{Ex}_{loss,ATES\_cw}$ are the charging exergy rate, the discharging exergy rate, and the exergy loss rate of the cold well of ATES, respectively.

The charging exergy rate of the cold well of ATES, $\dot{Ex}_{c,ATES\_cw}$ is calculated by

$$\dot{Ex}_{c,ATES\_cw} = \dot{En}_{c,ATES\_cw} - \dot{m}_{ATES}\, c_{p,ATES}\, T_0 \ln\left(\frac{T_{c,ATES\_cw}}{T_0}\right) \tag{60.163}$$

The discharging exergy rate of the cold well of ATES, $\dot{Ex}_{d,ATES\_cw}$ is computed to be

$$\dot{Ex}_{d,ATES\_cw} = \dot{En}_{d,ATES\_cw} - \dot{m}_{ATES}\, c_{p,ATES}\, T_0 \ln\left(\frac{T_{d,ATES\_cw}}{T_0}\right) \tag{60.164}$$

The exergy destruction rate of the cold well of ATES, $\dot{Ex}_{loss,ATES\_cw}$ is determined from the exergy balance equation as follows:

$$\dot{Ex}_{dest\_ATES\_cw} = \dot{Ex}_{c\_ATES\_cw} - \dot{Ex}_{d\_ATES\_cw} \tag{60.165}$$

The exergy efficiency of the cold well of ATES, ψ_{ATES_cw} is given by

$$\eta_{ATES\_cw} = \frac{\dot{Ex}_{d\_ATES\_cw}}{\dot{Ex}_{c\_ATES\_cw}} \tag{60.166}$$

Energy Analysis of the HP

The exergy balance of the evaporator is written as

$$\sum \dot{Ex}_{in,evap} = \sum \dot{Ex}_{out,evap} + \dot{Ex}_{dest,evap} \tag{60.167}$$

where $\sum \dot{Ex}_{in,evap}$, $\sum \dot{Ex}_{out,evap}$, and $\dot{Ex}_{dest,evap}$ are the total exergy input rate, the total exergy output rate, and the exergy destruction rate of the evaporator, respectively.

The total exergy input rate of the evaporator, $\sum \dot{E}x_{in,evap}$ can be determined from

$$\sum \dot{E}x_{in,evap} = \dot{E}x_{HP\_evap,in} + \dot{E}x_{ATES\_cw\_c,in,evap} \qquad (60.168)$$

where $\dot{E}x_{HP\_evap,in}$ is the exergy input flow rate of the evaporator due to the HP fluid R-134a, and $\dot{E}x_{ATES\_cw\_c,in,evap}$ is the exergy input flow rate of the evaporator due to the charging process of the cold well of ATES water. These parameters are expressed as follows:

$$\dot{E}x_{HP\_evap,in} = \dot{m}_{HP} \left[\left(h_{HP\_evap,in} - h_{HP\_evap,0} \right) - T_0 \left(s_{HP\_evap,in} - s_{HP\_evap,0} \right) \right]$$
$$(60.169)$$

and

$$\dot{E}x_{ATES\_cw\_c,in,evap} = \dot{m}_{ATES} \left(h_{ATES\_cw\_c,in,evap} - h_{ATES\_cw\_c,0,evap} \right)$$
$$- \dot{m}_{ATES} T_0 \left(s_{ATES\_cw\_c,in,evap} - s_{ATES\_cw\_c,0,evap} \right) \qquad (60.170)$$

where $h_{ATES\_cw\_c,0,evap}$ and $s_{ATES\_cw\_c,0,evap}$ are the enthalpy and entropy of the water at the dead state condition, respectively. Also, $h_{HP\_evap,0}$ and $s_{HP\_evap,0}$ are the enthalpy and entropy of the R-134a at the dead state condition, respectively.

The total exergy output rate of the evaporator, $\sum \dot{E}x_{out,evap}$ is determined as

$$\sum \dot{E}x_{out,evap} = \dot{E}x_{HP\_evap,out} + \dot{E}x_{ATES\_cw\_c,out,evap} \qquad (60.171)$$

where $\dot{E}x_{HP\_evap,out}$ is the exergy output flow rate of the evaporator due to the HP fluid R-134a, and $\dot{E}x_{ATES\_cw\_c,out,evap}$ is the exergy output flow rate of the evaporator due to the charging process of the cold well of ATES water. These parameters can be written as follows:

$$\dot{E}x_{HP\_evap,out} = \dot{m}_{HP} \left[\left(h_{HP\_evap,out} - h_{HP\_evap,0} \right) - T_0 \left(s_{HP\_evap,out} - s_{HP\_evap,0} \right) \right]$$
$$(60.172)$$

and

$$\dot{E}x_{ATES\_cw\_c,out,evap} = \dot{m}_{ATES} \left(h_{ATES\_cw\_c,out,evap} - h_{ATES\_cw\_c,0,evap} \right)$$
$$- \dot{m}_{ATES} T_0 \left(s_{ATES\_cw\_c,out,evap} - s_{ATES\_cw\_c,0,evap} \right) \qquad (60.173)$$

The exergy destruction rate of the evaporator, $\dot{E}x_{dest,evap}$ is computed by

$$\dot{E}x_{dest,evap} = \sum \dot{E}x_{in,evap} - \sum \dot{E}x_{out,evap} \qquad (60.174)$$

The exergy efficiency of the evaporator, ψ_{evap} is written as

$$\psi_{evap} = \frac{\dot{Ex}_{ATES\_cw\_c,in,evap} - \dot{Ex}_{ATES\_cw\_c,out,evap}}{\dot{Ex}_{HP\_evap,in} - \dot{Ex}_{HP\_evap,out}} \tag{60.175}$$

The exergy balance of the compressor is given to be

$$\dot{Ex}_{HP\_comp,in} + \dot{Ex}_{HP\_comp,w,m} = \dot{Ex}_{HP\_comp,out} + \dot{Ex}_{HP\_comp,dest} \tag{60.176}$$

where $\dot{Ex}_{HP\_comp,in}$, $\dot{Ex}_{HP\_comp,out}$, $\dot{Ex}_{HP\_comp,w,m}$, and $\dot{Ex}_{HP\_comp,dest}$ are the exergy input flow rate, the exergy output flow rate, the exergetic power, and the exergy destruction rate of the compressor, respectively as follows:

$$\dot{Ex}_{HP\_comp,in} = \dot{m}_{HP}\left[\left(h_{HP\_comp,in} - h_{HP\_comp,0}\right) - T_0\left(s_{HP\_comp,in} - s_{HP\_comp,0}\right)\right] \tag{60.177}$$

and

$$\dot{Ex}_{HP\_comp,out} = \dot{m}_{HP}\left[\left(h_{HP\_comp,out} - h_{HP\_comp,0}\right) - T_0\left(s_{HP\_comp,out} - s_{HP\_comp,0}\right)\right] \tag{60.178}$$

where $h_{HP\_comp,0}$ and $s_{HP\_comp,0}$ are the enthalpy and entropy of the R-134a at dead state condition, respectively.

The exergetic power of the compressor, $\dot{Ex}_{HP\_comp,w,m}$ is equal to mechanical compressor power $\dot{W}_{HP\_comp,m}$ as

$$\dot{Ex}_{HP\_comp,w,m} = \dot{W}_{HP\_comp,m} \tag{60.179}$$

The exergy destruction rate of the compressor, $\dot{Ex}_{HP\_comp,dest}$ can be determined to be

$$\dot{Ex}_{HP\_comp,dest} = \dot{Ex}_{HP\_comp,in} + \dot{Ex}_{HP\_comp,w,m} - \dot{Ex}_{HP\_comp,out} \tag{60.180}$$

The exergy efficiency of the compressor, ψ_{comp} is given as

$$\psi_{comp} = \frac{\dot{Ex}_{HP\_comp,out} - \dot{Ex}_{HP\_comp,in}}{\dot{Ex}_{HP\_comp,w,m}} \tag{60.181}$$

The exergy balance of the condenser is written to be

$$\sum \dot{Ex}_{in,cond} = \sum \dot{Ex}_{out,cond} + \dot{Ex}_{dest,cond} \tag{60.182}$$

where $\sum \dot{E}x_{in,cond}$, $\sum \dot{E}x_{out,cond}$, and $\dot{E}x_{dest,cond}$ are the total exergy input rate, the total exergy output rate, and the exergy destruction rate of the condenser, respectively.

The total exergy input rate of the condenser, $\sum \dot{E}x_{in,cond}$ can be obtained from

$$\sum \dot{E}x_{in,cond} = \dot{E}x_{HP\_cond,in} + \dot{E}x_{FHS,in,cond} \tag{60.183}$$

where $\dot{E}x_{HP\_cond,in}$ is the exergy input flow rate of the condenser due to the HP fluid R-134a, and $\dot{E}x_{FHS,in,cond}$ is the exergy input flow rate of the condenser due to the FHS water. These parameters are given as follows:

$$\dot{E}x_{HP\_cond,in} = \dot{m}_{HP} \left[\left(h_{HP\_cond,in} - h_{HP\_cond,0} \right) - T_0 \left(s_{HP\_cond,in} - s_{HP\_cond,0} \right) \right] \tag{60.184}$$

and

$$\dot{E}x_{FHS,in,cond} = \dot{m}_{FHS} \left[\left(h_{FHS,in,cond} - h_{FHS,0,cond} \right) - T_0 \left(s_{FHS,in,cond} - s_{FHS,0,cond} \right) \right] \tag{60.185}$$

where $h_{FHS,0,cond}$ and $s_{FHS,0,cond}$ are the enthalpy and entropy of the water at the dead state condition, respectively. Also, $h_{HP\_cond,0}$ and $s_{HP\_cond,0}$ are the enthalpy and entropy of the R-134a at the dead state condition, respectively.

The total exergy output rate of the condenser $\sum \dot{E}x_{out,cond}$ is computed to be

$$\sum \dot{E}x_{out,cond} = \dot{E}x_{HP\_cond,out} + \dot{E}x_{FHS,out,cond} \tag{60.186}$$

where $\dot{E}x_{HP\_cond,out}$ is the exergy output flow rate of the condenser due to the HP fluid R-134a, and $\dot{E}x_{FHS,out,cond}$ is the exergy output flow rate of the evaporator due to the FHS water. These parameters can be obtained as follows:

$$\dot{E}x_{HP\_cond,out} = \dot{m}_{HP} \left[\left(h_{HP\_cond,out} - h_{HP\_cond,0} \right) - T_0 \left(s_{HP\_cond,out} - s_{HP\_cond,0} \right) \right] \tag{60.187}$$

and

$$\dot{E}x_{FHS,out,cond} = \dot{m}_{FHS} \left[\left(h_{FHS,out,cond} - h_{FHS,0,cond} \right) - T_0 \left(s_{FHS,out,cond} - s_{FHS,0,cond} \right) \right] \tag{60.188}$$

The exergy destruction rate of the condenser, $\dot{E}x_{dest,cond}$ is expressed by

$$\dot{E}x_{dest,cond} = \sum \dot{E}x_{in,cond} - \sum \dot{E}x_{out,cond} \tag{60.189}$$

The exergy efficiency of the condenser, ψ_{cond} is determined as

$$\psi_{cond} = \frac{\dot{Ex}_{FHS,out,cond} - \dot{Ex}_{FHS,in,cond}}{\dot{Ex}_{HP\_cond,in} - \dot{Ex}_{HP\_cond,out}} \qquad (60.190)$$

The exergy balance of the throttling/expansion valve is given to be

$$\dot{Ex}_{HP\_thrott,in} = \dot{Ex}_{HP\_thrott,in} + \dot{Ex}_{HP\_thrott,dest} \qquad (60.191)$$

where $\dot{Ex}_{HP\_thrott,in}$, $\dot{Ex}_{HP\_thrott,in}$ and $\dot{Ex}_{HP\_thrott,dest}$ are the exergy input flow rate, the exergy output flow rate, and the exergy destruction rate of the throttling/expansion valve due to the HP fluid R-134a, respectively as follows:

$$\dot{Ex}_{HP\_thrott,in} = \dot{m}_{HP} \left[\left(h_{HP\_thrott,in} - h_{HP\_thrott,0} \right) - T_0 \left(s_{HP\_thrott,in} - s_{HP\_thrott,0} \right) \right]$$
$$(60.192)$$

and

$$\dot{Ex}_{HP\_thrott,out} = \dot{m}_{HP} \left[\left(h_{HP\_thrott,out} - h_{HP\_thrott,0} \right) - T_0 \left(s_{HP\_thrott,out} - s_{HP\_thrott,0} \right) \right]$$
$$(60.193)$$

where $h_{HP\_thrott,0}$ and $s_{HP\_thrott,0}$ are the enthalpy and entropy of the R-134a at the dead state condition, respectively.

The exergy destruction rate of the throttling/expansion valve, $\dot{Ex}_{HP\_thrott,dest}$ can be calculated from

$$\dot{Ex}_{HP\_thrott,dest} = \dot{Ex}_{HP\_thrott,in} - \dot{Ex}_{HP\_thrott,in} \qquad (60.194)$$

The exergy efficiency of the throttling/expansion valve, ψ_{thrott} is determined as

$$\psi_{thrott} = \frac{\dot{Ex}_{HP\_thrott,in}}{\dot{Ex}_{HP\_thrott,in}} \qquad (60.195)$$

The exergetic COP of the HP, $COP_{ex_{HP}}$ is obtained from

$$COP_{ex_{HP}} = COP_{HP} \left(1 - \frac{T_0}{T_{av,HP}} \right) \qquad (60.196)$$

where $T_{av,HP}$ is the average temperature of the HP working between the cold and hot sources as follows:

$$T_{av,HP} = \frac{T_{av,HP,cold\,source} + T_{av,HP,hot\,source}}{2} \qquad (60.197)$$

where $T_{av,HP,cold\,source}$ and $T_{av,HP,hot\,source}$ are the average temperatures of the cold and hot sources of the HP, respectively.

FHS: FHU + Pump + ERU

Exergy Analysis of the FHU

The exergy balance of the FHU is given to be

$$\dot{E}x_{FHU\_in} = \dot{E}x_{FHU\_out} + \dot{E}x_{FHU\_ht} + \dot{E}x_{FHU\_dest} \tag{60.198}$$

where $\dot{E}x_{FHU\_in}$, $\dot{E}x_{FHU\_out}$, $\dot{E}x_{FHU\_ht}$, and $\dot{E}x_{FHU\_dest}$ are the exergy transfer rate (from the FHU to building), the exergy input rate, the exergy output rate, and the exergy destruction rate of the FHU, respectively. These parameters are determined as follows:

$$\dot{E}x_{FHU\_in} = \dot{m}_{FHS} \left[(h_{FHU\_in} - h_{FHU\_0}) - T_0(s_{FHU\_in} - s_{FHU\_0}) \right] \tag{60.199}$$

and

$$\dot{E}x_{FHU\_out} = \dot{m}_{FHS} \left[(h_{FHU\_out} - h_{FHU\_0}) - T_0(s_{FHU\_out} - s_{FHU\_0}) \right] \tag{60.200}$$

where h_{FHU_0} and s_{FHU_0} are the enthalpy and entropy of the FHS water at the dead state condition, respectively.

The exergy transfer rate of the FHU, $\dot{E}x_{FHU\_ht}$ is computed from

$$\dot{E}x_{FHU\_ht} = \dot{Q}_{FHU\_ht} \left(1 - \frac{T_0}{T_{av,FHS}} \right) \tag{60.201}$$

where $T_{av,FHS}$ is the average temperature of the FHU as follows:

$$T_{av,FHS} = \frac{T_{FHU\_in} + T_{FHU\_out}}{2} \tag{60.202}$$

where T_{FHU_in} and T_{FHU_out} are the input and output temperatures of the FHU.

The exergy destruction of the FHU, $\dot{E}x_{FHU\_dest}$ can be determined as

$$\dot{E}x_{FHU\_dest} = \dot{E}x_{FHU\_in} - \dot{E}x_{FHU\_out} - \dot{E}x_{FHU\_ht} \tag{60.203}$$

The exergy efficiency of the FHU, ψ_{FHU} is determined as

$$\psi_{FHU} = \frac{\dot{E}x_{FHU\_ht}}{\dot{E}x_{FHU\_in} - \dot{E}x_{FHU\_out}} \tag{60.204}$$

Exergy Analysis of the Pump (Used with FHU)

The exergy balance of the pump used with TTES is written as

$$\dot{Ex}_{FHU\_pump,in} + \dot{Ex}_{w,FHU\_pump,m} = \dot{Ex}_{FHU\_pump,out} + \dot{Ex}_{FHU\_pump,dest} \quad (60.205)$$

where $\dot{Ex}_{FHU\_pump,in}$, $\dot{Ex}_{w,FHU\_pump,m}$, $\dot{Ex}_{FHU\_pump,out}$, and $\dot{Ex}_{FHU\_pump,dest}$ are he exergy input flow rate, the exergy output flow rate, the exergetic power, and the exergy destruction rate of the pump used with the FHU, respectively as follows:

$$\dot{Ex}_{FHU\_pump,in} = \dot{m}_{FHU} \left[\left(h_{FHU\_pump,in} - h_{FHU\_pump,0} \right) \right.$$
$$\left. - T_0 \left(s_{FHU\_pump,in} - s_{FHU\_pump,0} \right) \right] \quad (60.206)$$

and

$$\dot{Ex}_{FHU\_pump,out} = \dot{m}_{FHU} \left[\left(h_{FHU\_pump,out} - h_{FHU\_pump,0} \right) \right.$$
$$\left. - T_0 \left(s_{FHU\_pump,out} - s_{FHU\_pump,0} \right) \right] \quad (60.207)$$

and

$$\dot{Ex}_{w,FHU\_pump,m} = \dot{W}_{FHU\_pump,m} \quad (60.208)$$

and

$$\dot{Ex}_{FHU\_pump,dest} = \dot{Ex}_{FHU\_pump,in} + \dot{Ex}_{w,FHU\_pump,m} - \dot{Ex}_{FHU\_pump,out} \quad (60.209)$$

where $h_{FHU\_pump,0}$ and $s_{FHU\_pump,0}$ are the enthalpy and entropy of the water at the dead state condition, respectively.

The exergy efficiency of the pump used with FHU, ψ_{FHU_pump} is found from

$$\psi_{FHU\_pump} = \frac{\dot{Ex}_{FHU\_pump,out} - \dot{Ex}_{FHU\_pump,in}}{\dot{Ex}_{w,FHU\_pump,m}} \quad (60.210)$$

Exergy Analysis of the ERU

If the ERU is used with System-II, the exergetic ERU rate of the FHS is written to be:

$$\dot{Ex}_{FHS,ERU} = \Delta\dot{Ex}_{flow,TTES\_d} = \dot{Ex}_{water,out,TTES\_d} - \dot{Ex}_{water,in,TTES\_d} \quad (60.211)$$

If the ERU of FHS is operated with System-III, the exergetic ERU rate of the FHS is obtained from

$$\dot{Ex}_{FHS,ERU} = \dot{Ex}_{FHS,out,cond} - \dot{Ex}_{FHS,in,cond} = \dot{Ex}_{HP\_cond,in} - \dot{Ex}_{HP\_cond,out} \quad (60.212)$$

The exergetic COP of the HP and FHS, $COP_{ex_{HP+FHS}}$ can be calculated by

$$COP_{ex_{HP+FHS}} = COP_{HP+FHS}\left(1 - \frac{T_0}{T_{av,HP+FHS}}\right) \quad (60.213)$$

where $T_{av,HP+FHS}$ is the average temperature of the combined HP and FHS system as follows:

$$T_{av,HP+FHS} = \frac{T_{av,HP+FHS,cold\,source} + T_{av,HP+FHS,hot\,source}}{2} \quad (60.214)$$

where $T_{av,HP+FHS,cold\,source}$ and $T_{av,HP+FHS,hot\,source}$ are the average temperatures of the cold and hot sources of the combined HP and FHS system, respectively.

60.3.3 Sustainability Assessment

Sustainability is called as a key to solve ecological, economic, and developmental problems. Also, it is developed into a blueprint for reconciling economic and ecological necessities. Sustainable development requires using the resources efficiently. In this regard, exergy is important in improving efficiency. More efficient usage of the resources results to contribute to development over a longer period of time [7]. Sustainability analysis is associated with *SI* parameter, and it is a function of exergy efficiency (Ψ) as follows [4]:

$$SI = \frac{1}{1 - \Psi} \quad (60.215)$$

60.3.4 Environmental Impact Assessment

Utilization of energy may cause global warming, ozone depletion, climate change, acid rain, etc. Greenhouse gases (GHGs) play an important role to cause the most environmental effect. The CO_2 releasing in the utilization of energy resources has the major GHG effect. In this regard, GHG calculation is essential to make an environmental assessment [3].

The system considered here has various units of equipment working with electricity. It is considered that the fan, the compressor and the pumps take the necessary electricity from the "coal fired power station," which produces electricity usually for the public utilization. The coal-fired power station causes an environmental damage because of its GHGs releasing. The CO_2 emissions are released from the station

Table 60.2 GHG emissions based on life cycle estimation for electricity generators

Method	Configuration	Estimate (gCO_2/kW h)
Biogas	Anaerobic digestion	11
Biomass	Forest wood reciprocating engine	27
Biomass	Waste wood steam turbine	31
Biomass	Short rotation forestry reciprocating engine	41
Biomass	Forest wood Co-combustion with hard coal	14
Biomass	Forest wood steam turbine	22
Biomass	Short rotation forestry Co-combustion with hard coal	23
Coal	Various generator types with scrubbing	960
Coal	Various generator types without scrubbing	1,050
Diesel	Various generator and turbine types	778
Fuel Cell	Hydrogen from gas reforming	664
Heavy oil	Various generator and turbine types	778
Natural gas	Various combined cycle turbines	443
Nuclear	Various reactor types	66

Source: [8]

due to the electricity generation to meet the buildings' electricity demands. So, the negative impacts on climate change, acid rain, and ozone depletion may increase during the energy consumption. Thus, the CO_2 emission releasing in a specific period of time is calculated.

The GHG emissions based on life cycle estimation for electricity generators are listed in Table 60.2. Coal-fired power stations have CO_2 emission value of "960 gCO_2/kW h" including life cycle estimates. The environmental analysis of the system can be applied basing on the electricity consumption and CO_2 emission rate in a given time as follows:

$$x_{CO_2} = \frac{(y_{CO_2}) \, \dot{W}_{consume} \, t_{working}}{10^3} \tag{60.216}$$

where x_{CO_2} is the CO_2 emission (kgCO_2/month), y_{CO_2} is the CO_2 emission value for the coal-fired electricity generator (960 gCO_2/kW h), $\dot{W}_{consume}$ is the consumed power of the related system component (kW), and $t_{working}$ is the working hours of the related system component in a period of time (h/month) [3, 8].

60.3.5 Enviroeconomic Analysis

Enviroeconomic analysis can be also named as environmental cost analysis, and it bases on carbon price (CO_2) and released carbon quantity. Determination of the carbon price is one of the major methods to reduce greenhouse gas emissions. The carbon price is an approach imposing a cost on the emission of greenhouse gases which cause global warming. Paying a price for CO_2 released into the atmosphere is a way of motivating people and countries to reduce carbon emissions

[3]. It also provides an incentive to invest and deploy renewable energy technology that does not emit carbon to the atmosphere. Also, the pricing method would also act as a disincentive for electricity generators to use relatively more polluting coal, gas and oil fired stations [9]. The international carbon price is between 13 $/tCO$_2$ and 16 $/tCO$_2$ for the low and high pledge scenario [10]. So, this value can be taken on average to be 14.5 $/tCO$_2$. Thus, the enviroeconomic analysis, basing on the CO$_2$ releasing and CO$_2$ emission price, is written as follows:

$$C_{CO_2} = (c_{CO_2}) (x_{CO_2}) \qquad (60.217)$$
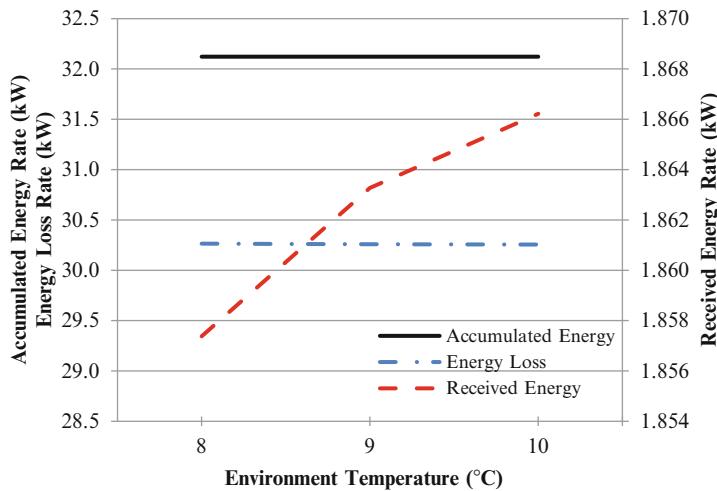
where C_{CO_2} is the environmental cost parameter, which is based on the environmental analysis (CO$_2$ emission price in a given time) ($/month), c_{CO_2} is the CO$_2$ emission price per tCO$_2$ (14.5 $/tCO$_2$), and x_{CO_2} is the CO$_2$ emission releasing in a given time (tCO$_2$/month).

60.4 Results and Discussion
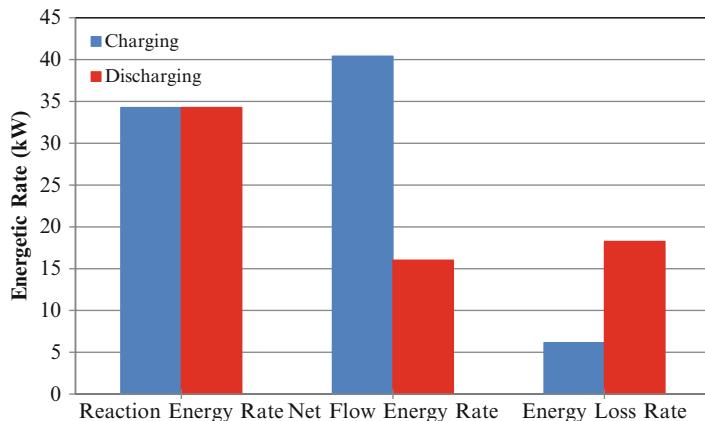
The three types of TES systems are investigated along with energy, exergy, and environmental analyses, also sustainability and environmental impact assessments are applied. Various environmental temperatures are considered as 8, 9, and 10 °C. In the energy analysis, the charging process of the LTES system is not affected by the environment temperature variation. The temperature, specific heat, and mass flow rate are constant during the phase changing of the PCM, and solar energy input rate is associated with the solar radiation and panel area. The solar energy input rate is found to be 47.041 kW, and 31.715 % of it is lost. So, 14.919 kW accumulated energy rate is obtained with an efficiency of 68.285 %.

The air temperatures are different at the inlet and outlet of the air channel. So, only energy of the air changes with different environment conditions. The maximum and minimum received energy rates of the discharging process of the LTES system are found to be 1.866 kW and 1.857 kW at 10 °C and 8 °C environment temperatures, respectively. Also, the maximum and minimum energy lose rates of the discharging process of the LTES system are calculated as 30.265 kW and 30.256 kW at 8 °C and 10 °C environment temperatures while the maximum and minimum energy efficiencies of the discharging process of the LTES system are determined to be 5.81 % and 5.782 % at 10 °C and 8 °C environment temperatures, respectively. The energy analysis results of the discharging process of the LTES system are shown in Fig. 60.5.

The TTES system is not affected from the various environment temperatures due to its calculation at a standard temperature (due to Gibbs energy formation). In the charging process of the TTES system, the net flow energy rate is calculated as 40.408 kW, and 15.196 % of it is lost, so 34.267 kW reaction energy rate occurs. The reaction energy rate is constant and in the discharging process of the TTES
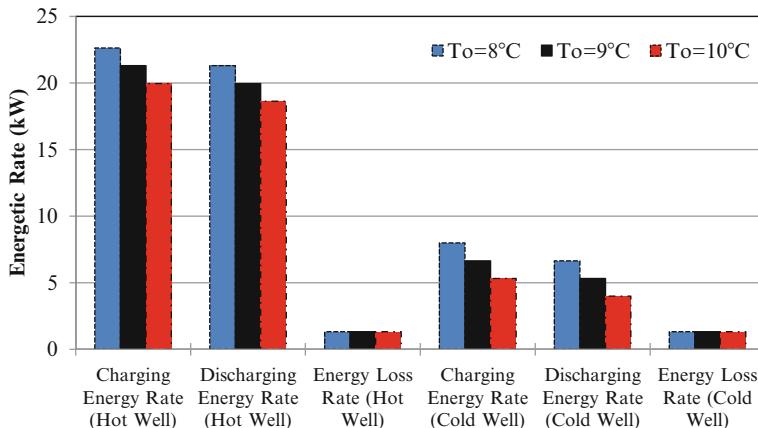
Fig. 60.5 Energy analysis results of the discharging process of the LTES system (Adapted from Ref. [5])
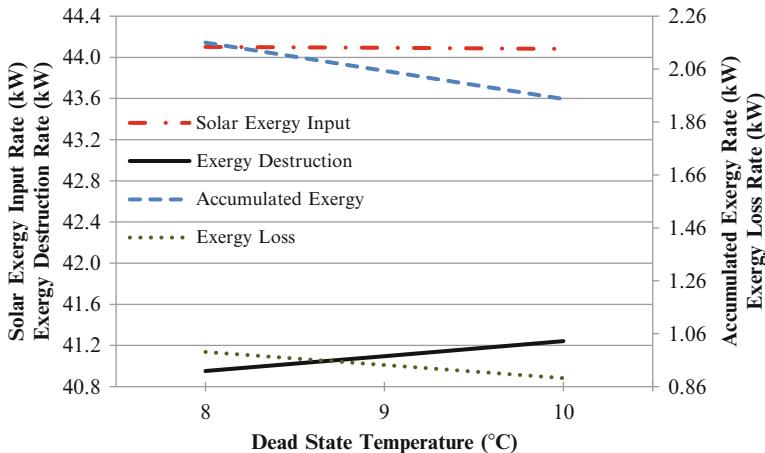
Fig. 60.6 Energy analysis results of the TTES system [5]

system, 53.286 % of the reaction energy is lost, so 16.007 kW net flow energy rate is obtained. If the both of the charging and discharging processes of the TTES are considered, the overall energy efficiency of the TTES system is determined as 39.615 %. The energy analysis results of the TTES system are given in Fig. 60.6.

In the hot well of the ATES system, the maximum values are obtained at 8 °C environment temperature. At this temperature, the charging and the discharging energy rates found as 22.631 kW and 21.3 kW, respectively. Furthermore, the maximum charging energy rate, the discharging energy rate, and the energy efficiency of the cold well of the ATES system are found to be 7.987 kW, 6.656 kW,

Fig. 60.7 Energy analysis results of the ATES system [5]
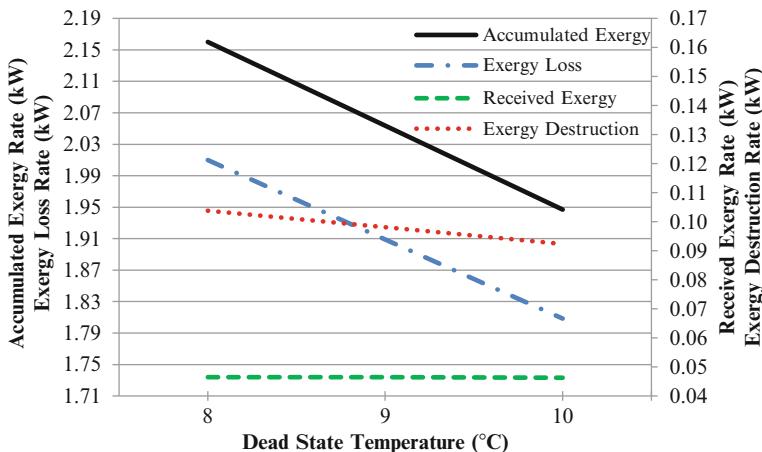
Fig. 60.8 Exergy analysis results of the charging process of the LTES system [5]
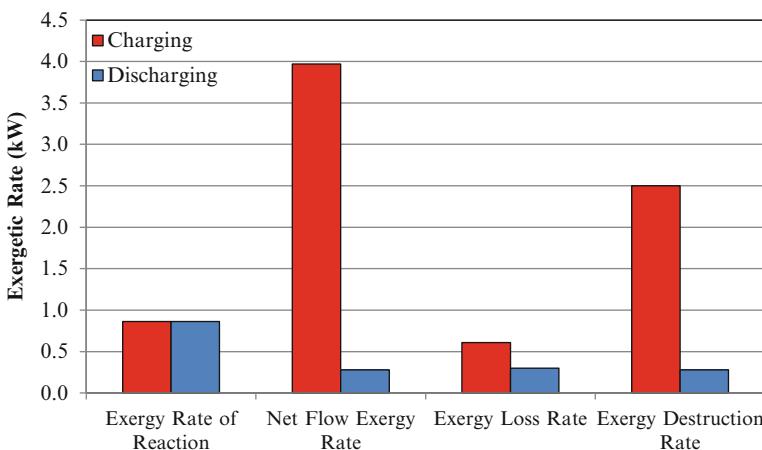
and 83.333 % at 8 °C environment temperature. The minimum values are obtained at 10 °C environment temperature for both of the wells. The energy analysis results of the ATES system is illustrated in Fig. 60.7.

The exergy analysis results of the charging process of the LTES system are given in Fig. 60.8. The maximum solar exergy input rate, the accumulated exergy rate, and the exergy loss rate of the charging process of the LTES system are calculated as 44.102 kW, 2.16 kW, and 0.991 kW at 8 °C dead state temperature, respectively. Only the maximum exergy destruction rate of the charging process of the LTES system is found to be 41.242 kW at 10 °C dead state temperatures,

The exergy analysis results of the discharging process of the LTES system are shown in Fig. 60.9. The maximum accumulated exergy rate, the exergy loss rate,

Fig. 60.9 Exergy analysis results of the discharging process of the LTES system [5]
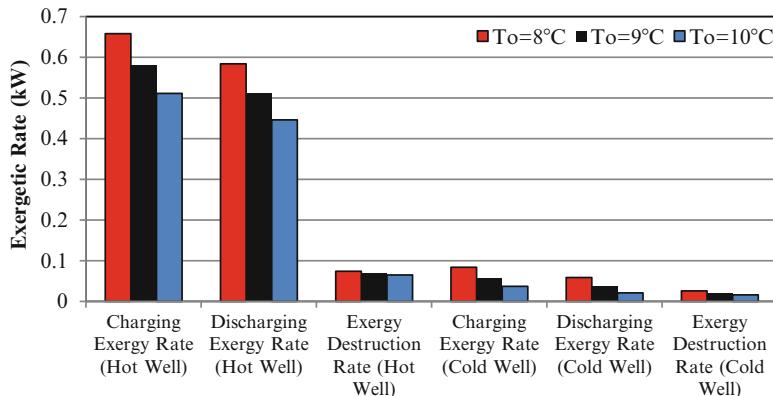
Fig. 60.10 Exergy analysis results of the TTES system [5]
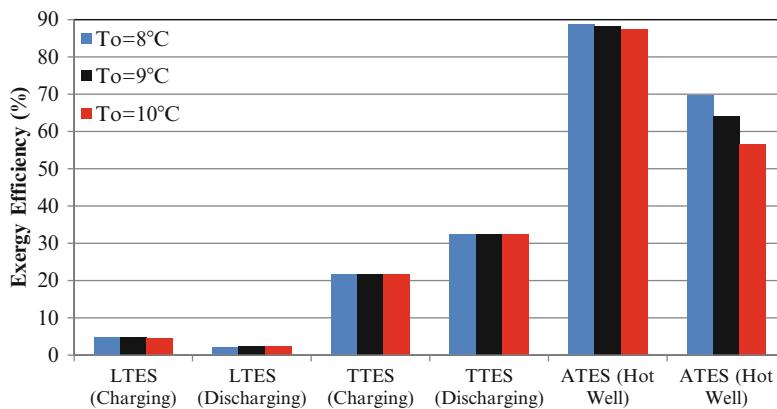
the exergy destruction rate, and the received exergy rate of the discharging process of the LTES system are found to be 2.160 kW, 2.01 kW, 0.104 kW, and 0.0465 kW at 8 °C dead state temperature, respectively.

The exergy rate of reaction is constant as 0.861 kW in the TTES system. In the charging process of the TTES system, the net flow exergy rate, the exergy loss rate, and the exergy destruction rate are determined as 3.970 kW, 0.608 kW, and 2.501 kW, respectively while in the discharging process the corresponding values are found as 0.279 kW, 0.301 kW, and 0.281 kW. The exergy analysis results of the TTES system are given in Fig. 60.10.

The exergy analysis results of the sensible TES system are illustrated in Fig. 60.11. In the hot well of the ATES system, the maximum charging exergy

Fig. 60.11 Exergy analysis results of the sensible TES system [5]

Fig. 60.12 Exergy efficiencies of the all TES systems [5]

rate, the discharging exergy rate, and the exergy destruction rate are determined to be 0.658 kW, 0.584 kW, and 0.074 kW at 8 °C dead state temperature, respectively. Furthermore, the maximum charging exergy rate, the discharging exergy rate, and the exergy destruction rate of the cold well of the ATES system are calculated as 0.084 kW, 0.058 kW, and 0.026 kW at 8 °C dead state temperature, respectively.

The exergy efficiencies of the all TES systems are shown in Fig. 60.12, while the efficiencies of the all system components are tabulated in Table 60.3. The maximum and minimum energy efficiencies of the discharging process of the LTES system are determined to be 5.81 % and 5.782 % at 10 °C and 8 °C environment temperatures, respectively, while the energy efficiency of the charging process of the LTES system is calculated as 68.285 %. In the charging process of the TTES system, the energy efficiency is estimated as 84.804 %, while the corresponding efficiency is computed to be 46.714 % in the discharging process. If the both
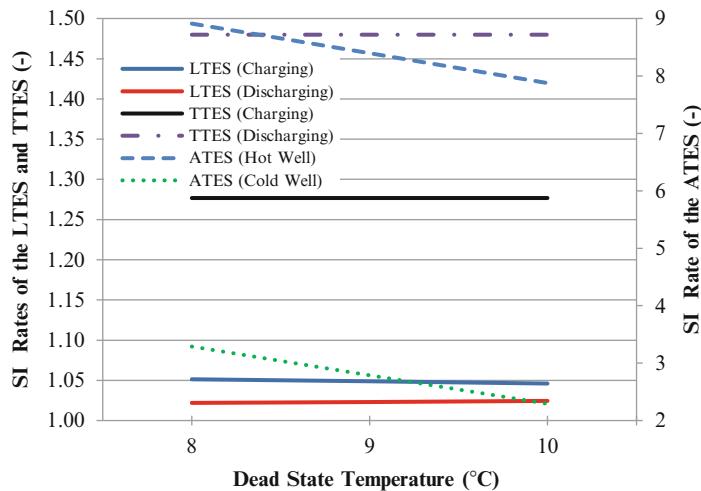
Table 60.3 Efficiencies of the all system components

Component	Dead state temperature (°C)			Average
	8	9	10	
Energy efficiency (%)				
LTES-Charging	68.29	68.29	68.29	68.29
LTES-Discharging	5.78	5.80	5.81	5.80
Solar Collector	97.16	97.16	97.16	97.16
TTES-Charging	84.80	84.80	84.80	84.80
TTES-Discharging	46.71	46.71	46.71	46.71
TTES-Overall	39.61	39.61	39.61	39.61
ATES-Hot Well	94.12	93.75	93.33	93.73
ATES-Cold Well	83.33	80.00	75.00	79.44
Exergy efficiency (%)				
LTES-Charging	4.90	4.66	4.42	4.66
LTES-Discharging	2.15	2.26	2.38	2.26
Fan	0.1793	0.1779	0.1732	0.1769
Solar Collector	14.61	14.30	13.98	14.30
Heat Exchanger	32.23	30.07	27.79	30.03
TTES-Charging	21.69	21.69	21.69	21.69
TTES-Discharging	32.43	32.43	32.43	32.43
TTES-Overall	7.03	7.03	7.03	7.03
ATES-Hot Well	88.78	88.09	87.31	88.06
ATES-Cold Well	69.61	64.15	56.38	63.38
Evaporator	84.27	70.68	59.04	71.33
Compressor	58.37	58.32	58.27	58.32
Thrott./Exp. Valve	88.21	88.45	88.64	88.43
Condenser	91.46	91.06	90.63	91.05
Floor Heating Unit	98.28	98.20	98.10	98.19
Pump FHS	4.54	4.30	4.06	4.30
Pump TTES	7.84	7.61	7.38	7.61
Pump ATES-HW	7.27	7.04	6.81	7.04
Pump ATES-CW	0.81	0.56	0.31	0.56

Source: [5, 6]

charging and discharging processes of the TTES system are considered, the overall energy efficiency of it is found to be 39.615 %. Also, in the hot well of the ATES system, the maximum energy efficiency is determined to be 94.118 % at 8 °C environment temperature while the minimum rate is obtained as 93.333 % at 10 °C environment temperature. In the cold well of the ATES the maximum energy efficiency is found to be 83.333 % at 8 °C environment temperature, while minimum rate is calculated as 75 % at 10 °C environment temperature.

The maximum exergy efficiency of the charging process of the LTES system is found as 4.898 % at 8 °C dead state temperature, while the minimum one is calculated to be 4.417 % at 10 °C dead state temperature. Also, the maximum exergy efficiency of the discharging process of the LTES system is determined as 2.378 % at 10 °C dead state temperature. The exergy efficiency of the charging and discharging processes of the TTES system are computed as 21.686 % and

Fig. 60.13 Sustainability analysis results of the TES systems [5]

32.428 %, respectively, while the overall exergy efficiency of the TTES system is calculated to be 7.032 %. In the hot and cold wells of the ATES system, the maximum exergy efficiencies are found as 88.782 % and 69.607 % at 8 °C dead state temperature, respectively.

The sustainability analysis results of the TES systems are given in Fig. 60.13. It is found that the maximum sustainable TES system is ATES system, while minimum one is LTES system. The maximum SI rate is determined to be 8.914 for the hot well of ATES at 8 °C dead state temperature. Also, the minimum SI rate is calculated as 1.022 for the discharging processes of LTES at 8 °C dead state temperature.
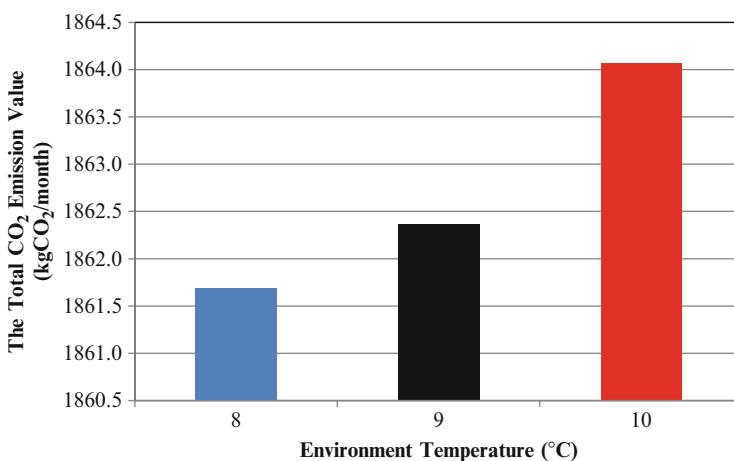
The total CO_2 emission values released from the coal-fired power station due to the operation of the electrical devices (pumps, fan and compressor) are found to be 1,861.694 kgCO$_2$/month, 1,862.373 kgCO$_2$/month, and 1,864.072 kgCO$_2$/month at 8 °C, 9 °C, and 10 °C environment temperatures, respectively. The CO_2 emission value released from the coal-fired power station due to the electricity production is 0.96 kgCO$_2$/kWh. Also, the fan and the Pump_FHS are worked 240 h in a month while the compressor, the pumps are operated 120 h monthly. The fan power changes due to variable air flows. In this regard, the consumed fan power are found as 0.237 kW, 0.240 kW, and 0.248 kW at 8 °C, 9 °C, and 10 °C environment temperatures, respectively. On the other hand, the consumed powers of the compressor and the pumps are calculated to be 3.761 kW, 2.676 kW, 2.778 kW, 1.856 kW, and 1.838 kW, respectively. The environmental analysis results are shown in Table 60.4, while the variations of the total CO_2 emission values of the system are given in Fig. 60.14.

The total enviroeconomic (environmental cost) values are found to be 26.995 $/month, 27.004 $/month, and 27.029 $/month at 8 °C, 9 °C, and 10 °C

Table 60.4 Environmental analysis results (kgCO$_2$/month)

Component	Environment temperature (°C)		
	8	9	10
Fan	54.681	55.360	57.059
Compressor	433.260	433.260	433.260
Pump_TTES	308.234	308.234	308.234
Pump_FHS	639.985	639.985	639.985
Pump_ ATES-HW	213.780	213.780	213.780
Pump_ ATES-CW	211.754	211.754	211.754
Total	1,861.694	1,862.373	1,864.072

Source: [5]

Fig. 60.14 Variations of the total CO$_2$ emission values of the system [5]

Table 60.5 Enviroeconomic analysis results ($/month)

Component	Environment temperature (°C)			
	8	9	10	Average
Fan	0.793	0.803	0.827	0.808
Compressor	6.282	6.282	6.282	6.282
Pump_TTES	4.469	4.469	4.469	4.469
Pump_FHS	9.280	9.280	9.280	9.280
Pump_ATES-HW	3.100	3.100	3.100	3.100
Pump_ATES-CW	3.070	3.070	3.070	3.070
Total	26.995	27.004	27.029	27.009

environment temperatures, respectively. Approximately CO$_2$ emission cost of 27.009 $ is lost per month by releasing. Among the components, the pump of the FHS causes the maximum CO$_2$ emission cost as 9.280 $/month, while the corresponding cost of the fan is minimum as 0.793 $/month at 8 °C environment temperature. The enviroeconomic analysis results are shown in Table 60.5.

60.5   Conclusions

The thermochemical, sensible (aquifer) and latent TES systems are modeled and assessed using energy, exergy, and enviroeconomic analyses along with sustainability and environmental impact assessments under various environment temperatures. The following main conclusions can be drawn:

- The heating load of the buildings can be received efficiently from the combination of the various TES systems, such as latent, sensible, and thermochemical options.
- Sensible TES systems are more efficiently than other TES methods for this kind of system. The exergy efficiency of the ATES is inversely proportional to the environment (dead state) temperature due to constant mass flow rate and specific heat of the water. So, only the environment temperature is responsible for this variation.
- Thermochemical TES systems' efficiencies may be lower than sensible types due to their standard temperature specification. They are not affected by the environment temperature variations because of the definition of the Gibbs energy formation.
- Latent TES system in this process is assembled as low capacity. Because only decreasing of the heating load of the building is expected from LTES. It can be seen that PCM supported building façade successfully decreases the necessary heating load of the building under various environment temperatures.
- Sensible TES system (ATES) is the most sustainable TES method due to its high efficiency. The sustainability of the ATES system is inversely proportional to the environment temperature.
- Among the electrical devices of the process, the fan causes the minimum CO_2 releasing from the coal-fired power station. So, it is the most environmental system component and its CO_2 emission values are directly proportional to the environment temperature. Furthermore, the pump of the FHS is the worst environmental component in the process. Because, it causes the maximum CO_2 value the releasing of 639.985 kg per month. Also, the total CO_2 emission values are directly proportional to the environment temperature. Because the CO_2 emission values of the other components are not affected by various environment temperatures.
- The total enviroeconomic values changes with various environment temperatures. It is directly proportional to the environment temperatures. For this system, maximum 27.029 \$ CO_2 emission is released per month at 10 °C environment temperature. So, these kinds of systems are more enviroeconomic at low environment temperatures.

References

1. IEA (2011) International energy outlook 2011. In: U.S. International Energy Administration. Available from www.eia.gov/forecasts/ieo/pdf/0484(2011).pdf
2. Dincer I (2002) The role of exergy in energy policy making. Energy Policy 30:137–149

 3. Caliskan H, Dincer I, Hepbasli A (2012) Exergoeconomic, enviroeconomic and sustainability analyses of a novel air cooler. Energ Build 55:747–756
 4. Dincer I, Rosen MA (2007) Exergy, Energy, Environment and Sustainable Development. Elsevier, Oxford
 5. Caliskan H, Dincer I, Hepbasli A (2012) Thermodynamic analyses and assessments of various thermal energy storage systems for buildings. Energ Conver Manag 62:109–122
 6. Caliskan H, Dincer I, Hepbasli A (2012) Energy and exergy analyses of combined thermo-chemical and sensible thermal energy storage systems for building heating applications. Energ Build 48:103–111
 7. Rosen MA, Dincer I, Kanoglu M (2008) Role of exergy in increasing efficiency and sustainability and reducing environmental impact. Energy Policy 36:128–137
 8. Sovacool BK (2008) Valuing the greenhouse gas emissions from nuclear power: a critical survey. Energy Policy 36:2950–2963
 9. GGW (2012) Carbon price. In: Global greenhouse warming. Available from http://www.global-greenhouse-warming.com/carbon-price.html
10. Den Elzen MGJ, Hof AF, Beltran AM, Grassi G, Roelfsema M, van Ruijven B, van Vliet J, van Vuuren DP (2011) The copenhagen accord: abatement costs and carbon prices resulting from the submissions. Environ Sci Pol 14:28–39

Chapter 61
Comparative Environmental Impact Assessment of Residential HVAC Systems

Nader Javani, Fadi Abraham, Ibrahim Dincer, and Marc A. Rosen

Abstract Residential energy use represents a considerable fraction of the total energy consumption in a region. Therefore, there is an increasing focus on reducing energy use and related greenhouse gas (GHG) emissions by improving the energy efficiency of building envelopes and major household appliances. The residential sector can benefit from the application of environmental impact assessment methods like life cycle assessment (LCA), which can be used to evaluate the environmental impacts of building materials, appliances, and heating, ventilation, and air conditioning (HVAC) units. Results of such assessments can identify and target important areas for improvement, to achieve optimal benefits. In this chapter, two residential HVAC systems in Canada are compared using the ReCiPe method. The systems are evaluated against a number of important environmental impact indicators. The results show that heat pumps present a good option for reducing household energy consumption and GHG emissions. Furthermore, areas for improvement are identified and suggestions are provided which aim at increasing residential energy efficiency and reducing related GHG emissions.

Keywords Efficiency • Environmental assessment • Greenhouse Gas • Heat Pump • Residential sector

Nomenclature

I_m	Midpoint impact category
h	Specific enthalpy (kJ/kg)
k	Thermal conductivity (W/m C)

N. Javani (✉) • F. Abraham • I. Dincer • M.A. Rosen
Faculty of Engineering and Applied Science, University of Ontario Institute of Technology,
2000 Simcoe Street North, Oshawa, ON, Canada L1H 7K4
e-mail: Nader.javani@uoit.ca; Fadi.abrahamr@uoit.ca; Ibrahim.Dincer@uoit.ca;
Marc.Rosen@uoit.ca

$\dot{Q}$ Heat transfer rate (kW)
Q_{mi} Characterization factor
R   Thermal Resistance (m^2.K/W)
T   Temperature (K or °C)
U   Overall heat transfer coefficient (W/m^2 K)

Subscripts

crit   Critical
en   Energy
g   Gas
i   Inventory

Acronyms

AFUE   Annual fuel utilization efficiency
A/C   Air conditioning
GHG   Greenhouse gas
GWP   Global warming potential
HVAC   Heating, ventilation, and air conditioning
LCA   Life cycle assessment
ODP   Ozone depleting potential
PCM   Phase change material
VOC   Volatile organic compound

61.1   Introduction

Residential greenhouse gas (GHG) emissions constitute 15 % of the total GHG emissions in Canada despite improvements in the energy efficiency of building materials, appliances, and heating, ventilating, and air conditioning (HVAC) systems [1]. This is mainly due to the steady increase of the average house size over the past few years, and is fostering improvements in energy efficiency in residential buildings. Various mature technologies for residential heating and cooling applications exist for consumers. Typically, the choice of technology is influenced by a number of factors such as: energy efficiency, initial investment, payback period, and reliability. In recent years the government of Ontario, the largest province in Canada, began efforts at raising public awareness about global warming and greenhouse gas emissions, and introduced various incentive programs to promote energy-efficient appliances and energy conservation practices [2].

The environmental impact of residential buildings has been investigated previously, including studies on key aspects such as embodied energy in construction

materials, maintenance and operational energy usage. A study commissioned by the Canada Mortgage and House Corporation (CMHC) found that the building foundation and exterior envelope account for 40 % of the initial embodied energy of building systems, while 74 % of the overall life cycle energy use of the building is consumed during the operation phase [3]. Kassab et al. estimated the embodied energy of a modern, energy efficient house with a floor area of 310 m^2 located in Montreal, Canada as 2,280 MJ/m^2 [4]. Several other studies address similar themes for various locations and weather conditions around the world [5–7].

Fewer studies have shed light on residential HVAC applications. The environmental impact of hot water and forced air heating systems has been evaluated for a house located in Quebec, Canada [8]. The concepts of expanded cumulative exergy consumption (ECExC) and embodied energy were used as indicators of the environmental impact of the systems, and the authors concluded that the hot water heating system has the lowest ECExC. Another study compared a vapor compression unit and desiccant cooling device using EPS2000 method [9], and found that the energy consumed during the operation phase was the dominant contributor to the environmental impact of both systems. An ABB EU 2000 air handling unit also has been analyzed with respect to nine environmental impact categories and nine resource depletion categories [10]. Areas for improvement were identified such as increasing efficiency and avoiding galvanizing unit surfaces. The Eco-indicator 95 method has been applied to examine the environmental impact of the manufacturing stages and processes for three residential heating systems [11]: convection system, floor heating system, and radiator unit with pipes. The results of the study showed that the radiator unit has the highest environmental impact followed by the floor heating and the convection system, respectively.

In the present study, a comparative environmental impact assessment of two HVAC systems for a house located in Toronto, Ontario is performed, to improve understanding of the benefits of the options. The two systems considered are: (1) hot-air furnace combined with an air-conditioning unit, and (2) air-to-air heat pump unit. The ReCiPe method [12] is used to assess the environmental impact of the systems, and serves as a tool to assist home owners and builders in making informed decisions when purchasing or installing residential HVAC equipment.

61.2   System Description

61.2.1   Features of Residential Buildings

A typical modern detached house is selected for analysis. The total living space of the two-story building is 185 m^2 (2,000 sq. ft). The main floor comprises the kitchen, the family room, and the laundry area, while the second floor includes bedrooms and bathrooms. A two-car garage is attached to the house and considered to be part of the building envelope. Furthermore, the area of the basement is equal to

Table 61.1 Thermal resistance of building components (adapted from [14])

Building component	Thermal resistance [m^2 K/W]
Ceiling with roof space	7.00
Roof (no roof space)	5.00
Wall	3.35
Foundation wall	2.12
Concrete floor/slab	1.41
Window (fixed)	0.63
Glass door (sliding)	0.30
Exterior door	0.63

the area of the main floor [13]. The hot water heater and the HVAC equipment are located in the basement. The air distribution system consists of non-insulated galvanized metal ducts properly sized to handle the required volumetric air flow rates. The construction of the house conforms to the Ontario Building Code and the municipal code of Toronto [14, 15]. Because of the airtight construction of the house, natural air infiltration is taken to be 1.5 air changes per hour (ACH) at 50 Pa. The thermal resistances of the building components are listed in Table 61.1.

Additionally, the following assumptions are made in this study:

1. The front of the house faces East
2. The house is occupied by a family of four (two adults and two children)
3. The internal heat gain from occupants and appliances accounts for 15 % of the total energy supplied to the house
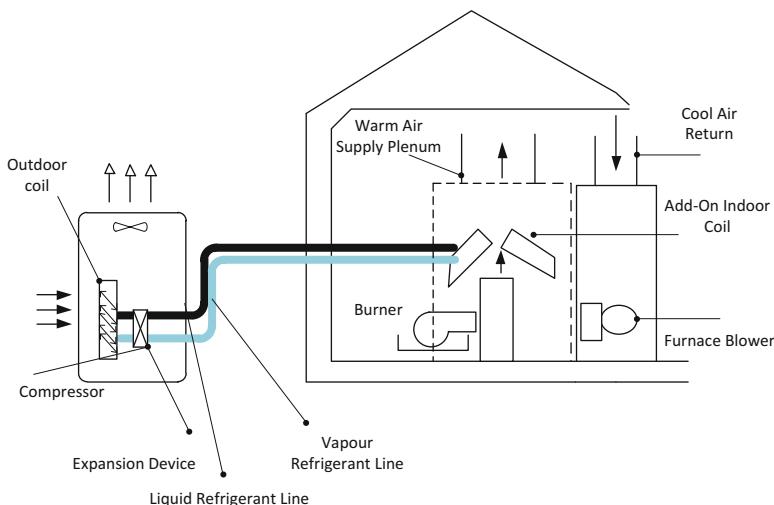
61.2.2 HVAC Equipment and System Boundaries

A regional study conducted by Natural Resources Canada (NRC) revealed that 76 % of households in the province of Ontario use a hot-air furnace (HAF) as the main heating system, mainly because affordability and availability in developed communities make natural gas the preferred fuel choice [16]. For summer cooling, window-type air conditioning units are available in a variety of sizes, but add-on central air conditioning (AC) units are usually more popular. Different heating systems and their market share in Canada have been listed in Table 61.2. The combination of HAF/AC shown in Fig. 61.1 forms the boundary of system "A" in this study.
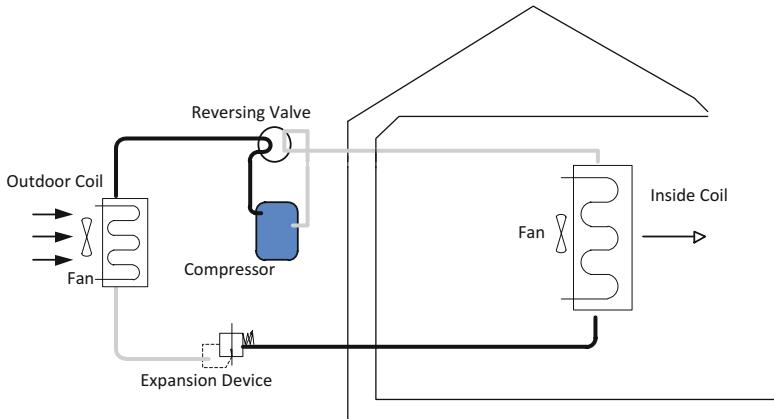
Alternatively, a heat pump (HP) can replace the HAF/AC combination system, with the advantage that such a device can provide heating during winter and cooling during summer (dual mode). This is achieved using a reversing valve contained within the heat pump which allows for switching the direction of the refrigerant thus changing the mode of operation [16]. The heat pump is designated as system "B" with a system boundary as reflected in Fig. 61.2.

Table 61.2 Market share of various heating systems in Canada (adapted from [16])

Region	Heating system	Market share [%]
Atlantic	Electric baseboard	33
Quebec	Electric baseboard	61
Ontario	Hot-air furnace	76
Prairies	Hot-air furnace	82
British Columbia	Hot-air furnace	50

Fig. 61.1 Boundary definition of HAF/AC system (System "A") (Modified from [16])

Fig. 61.2 Boundary definition of heat pump (HP) system (System "B") (Modified from [16])

Table 61.3 Rated capacities and efficiencies of subsystems (adapted from [18])

System	Subsystem	Capacity [kW]	Efficiency
A	HAF	19.35	AFUE = 93 %
	AC	7.00	SEER = 14
B	HP	17.60	SEER = 14
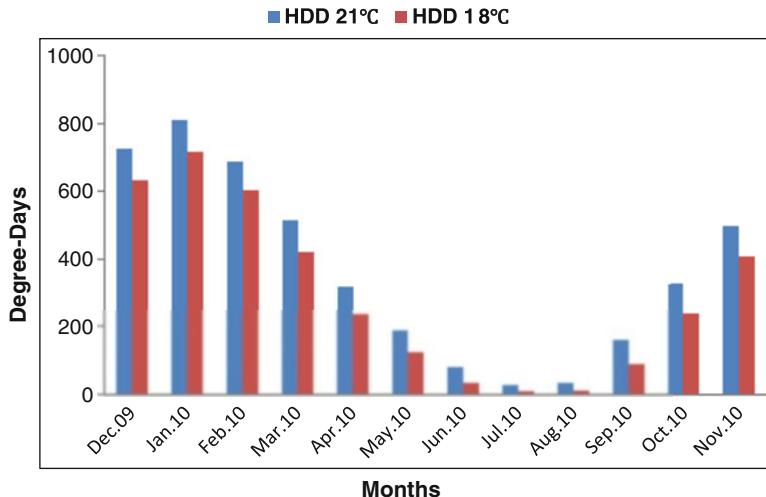
Table 61.4 Compositions and weights of materials for subsystems

Subsystem	Material	Weight [kg]
Furnace	Cold-rolled steel	36.21
	Galvanized steel	14.17
	Aluminum	7.08
	Copper	–
	Total	63.95
Air-conditioner	Cold-rolled steel	33.79
	Galvanized steel	15.16
	Aluminum	7.36
	Copper	7.36
	Total	63.68
Heat pump	Cold-rolled steel	84.84
	Galvanized steel	26.88
	Aluminum	5.88
	Copper	8.40
	Total	126.00
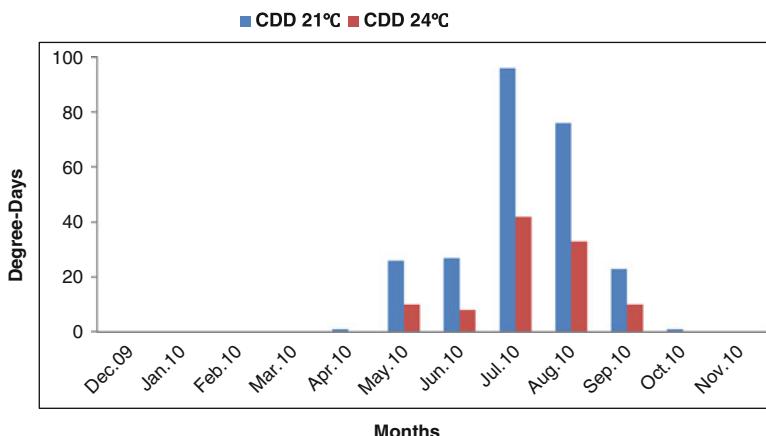
The program HOT2000 and the CSA standard (CAN/CSA F280) are used to size HVAC equipment [17]. The capacities of the systems are determined as shown in Table 61.3. To determine component distributions, compositions, and relative weights, units manufactured by Lennox International are selected. The units used for the base case study are energy-star rated and certified by the Air-Conditioning and Refrigeration Institute (ARI), and their capacities and efficiencies are listed in Table 61.3 [18]. The electronic components of the units are neglected in order to simplify this analysis without unreasonably compromising accuracy. Table 61.4 lists the material compositions and weights.

61.2.3 Weather Characteristics

Toronto is located in southern Ontario on the north shoreline of Lake Ontario. The lake serves to moderate the city's weather and renders it somewhat mild for Canada. The Degree-Days (DD) method provides a simplified representation of the historical weather data pertaining to a specific area or region. For this study, weather data are obtained from the weather station at Toronto's Pearson International Airport (CYYZ), located about 20 km northwest of Toronto city center [19]. The heating degree-days (HDD) and cooling degree-days (CDD) for Toronto are depicted in

Fig. 61.3 Heating Degree-Days (HDD) for the city of Toronto for a typical year

Fig. 61.4 Cooling Degree-Days (CDD) for the city of Toronto for a typical year

Figs. 61.3 and 61.4, respectively. The significant heating loads in comparison to the cooling loads can be clearly construed from the figures. A software application developed by CanmetENERGY (HOT2000) was used to estimate the heating and cooling requirements and to calculate the energy consumption of the residential building under study.

Data such as the building design characteristics, specifications of construction materials, number and type of appliances as well as internal heat gains can be specified by a user in detail. The current version of the software (version 10.51) has a great deal of flexibility that allows for the examination of multiple scenarios and comparative studies [20], which are presented in subsequent sections.

61.3 Methodology: ReCiPe Method
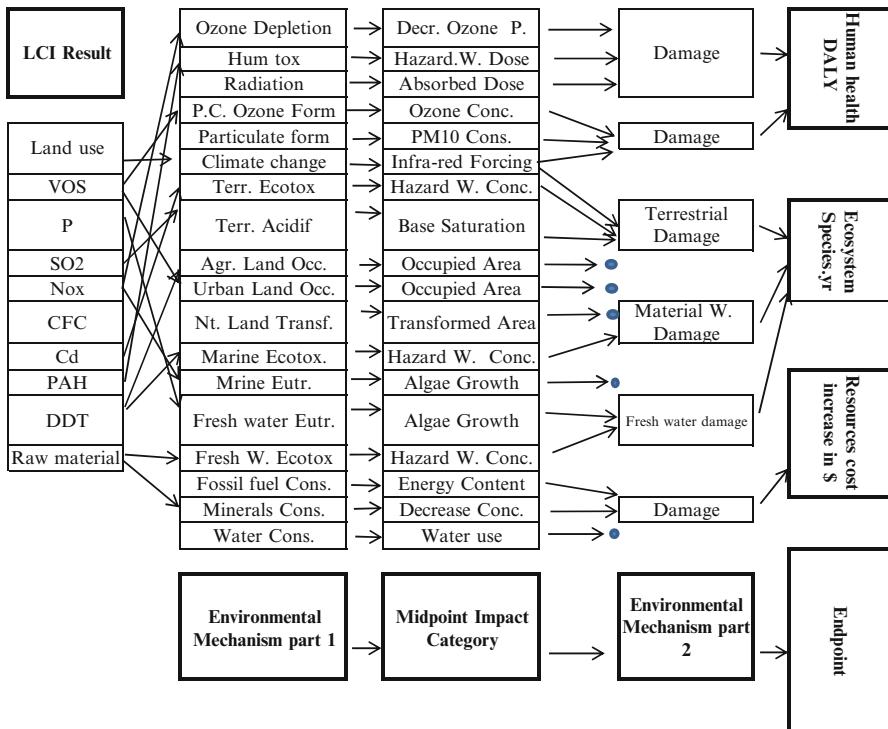
Since the inception of life-cycle assessment (LCA), efforts have been dedicated to improving the method. The International Standards Organization introduced the framework of LCA under the ISO 14040 series which aims at standardizing the process at an international level [12]. Various LCA methods based on ISO standards have been developed over the years. Although there are some differences among these methods in terms of determining the impact factors of various processes and substance, the majority of the methods follow the scheme of midpoint and endpoint evaluation indicators. The ReCiPe method uses midpoint indicators with environmental mechanisms like acidification, climate change, and ecotoxicity and endpoint indicators like human health and resource depletion [12].

Some researchers believe that there should be a harmonization between these two groups of indicators and consequently attempt to develop models with a harmonized structure [12, 21]. Some of the methods convert environmental hazardous substances and the effects of resource depletion to the midpoint level while other methods relate them to more generalized impacts at the endpoint level. Life cycle impact (LCI), midpoint and endpoint indicators are shown in Fig. 61.5, from left to right, respectively. Eighteen impact categories for midpoint level are considered in this method. These midpoint impact indicators can be linked to the endpoint level through environmental mechanisms. The endpoints are: (1) damage to human health (HH), (2) damage to ecosystem diversity (ED), and (3) damage to resource availability (RA).

It is useful to apply global rather than regional impacts since some environmental mechanisms are limited regionally in scope and can be ignored in a comprehensive list of mechanisms. Mechanisms like acidification, eutrophication, photochemical ozone formation, toxicity, wastewater and land use are dependent on regional conditions. This method is also suitable for developed countries. The impact categories are considered as design tools for sustainable engineering and policy making. Therefore, the endpoint level is selected based on important protection issues: human health, ecosystem quality, and availability of resources.

61.3.1 *Impact Categories for Midpoint and Endpoint levels*

For midpoints, the equivalent impact of different substances is shown in Table 61.5. Substances obtained from the life cycle inventory are categorized by their equivalent impact on the midpoint indicators. For example, CO_2 is generally agreed to be responsible for climate change and other substances may be expressed by their equivalent of CO_2, to show their effect on climate change. Although endpoints assign score points to each system, they are not considered since the midpoint can be normalized to show the relative environmental impact of the systems under investigation.

Fig. 61.5 Relationship between LCI, and midpoint and endpoint levels. (Modified from [12])

61.3.2   Midpoint Level in ReCiPe Method

For the midpoint level, this method uses the following relation:

$$I_m = \sum_{i}^{n} Q_{mi} m_i$$

Here, m_i is the amount of considered intervention i, like the amount of CFC-11 released to atmosphere for ozone depletion impacts. Q_{mi} is a factor that connects midpoint impact category m to the intervention of i (Characterization Factor), and I_m represents midpoint impact category obtained for intervention i

Referring to ReCiPe database, there are three classifications in developing the impacts: (1) Individualist (I) as short-term time frame, (2) Hierarchist (H), and (3) Egalitarian (E) which uses a long-term schedule with a more conservative approach. In this study, we selected the Hierarchist class that uses 100 years as a time-frame of impact. As some researchers show, 50 years is rather more realistic, but the ReCiPe method does not consider such time frame [22].

Table 61.5 Midpoint, endpoint categories and characterization factors [12]

	Characterization factor name	Unit	Abbreviation
Midpoint Impact	Global warming potential	kg (CO_2 to air)	GWP
	Ozone depletion potential	kg (CFC-115 to air)	ODP
	Terrestrial acidification potential	kg (SO_2 to air)	TAP
	Freshwater eutrophication potential	kg (P to freshwater)	FEP
	Marine eutrophication potential	kg (N to freshwater)	MEP
	Human toxicity potential	kg (14DCB to urban air)	HTP
	Photochemical oxidant formation potential	kg (NMVOC6 to air)	POFP
	Particulate matter formation potential	kg (PM10 to air)	PMFP
	Terrestrial ecotoxicity potential	kg (14DCB to industrial soil)	TETP
	Freshwater ecotoxicity potential	kg (14DCB to freshwater)	FETP
	Marine ecotoxicity potential	kg (14-DCB7 to marine water)	METP
	Ionizing radiation potential	kg (U235 to air)	IRP
	Agricultural land occupation potential	$m^2 \times$ year (agricultural land)	ALOP
	Urban land occupation potential	$m^2 \times$ year (urban land)	ULOP
	Natural land transformation potential	m^2 (natural land)	NLTP
	Water depletion potential	m^3 (water)	WDP
	Mineral depletion potential	kg (Fe)	MDP
	Fossil depletion potential	kg (oil)	FDP
Endpoint Impact	Indicator Name	Impact Category Name	Unit
	Damage to human health	Damage to human health	Year
	Loss of species during a year	Damage to ecosystem diversity	Year
	Increased cost	Damage to resource availability	$

61.3.3   Life Cycle Inventory Assessment (LCIA)

After identifying the material composition of the HVAC units, a life cycle inventory is constructed using the materials database provided by the National Renewable Energy Laboratory (NREL) [23]. The NREL database provides individual "cradle-to-gate" accounting of the energy and material inputs and outputs relative to the production of materials and substances. While populating and analyzing specific inventories, it came to our attention that some emissions to nature were assigned negative values. No clarification is provided in the NREL inventory user manual, so we assume there is a net gain (positive impact) resulting from such emissions; however, these values are not considered in our final results. The NREL database is not comprehensive and does not contain information regarding the production of copper tubing. Consequently, the copper life cycle inventory is

obtained from the European Copper Institute [24]. Although the inventory resources and methods of preparations are potentially different, this represents the best available information for this study. Note that LCA software is not used in this study. Instead, all relevant inventories are manually processed to develop a better understanding of the environmental impact assessment stage.

61.3.4 Assumptions and Limitations
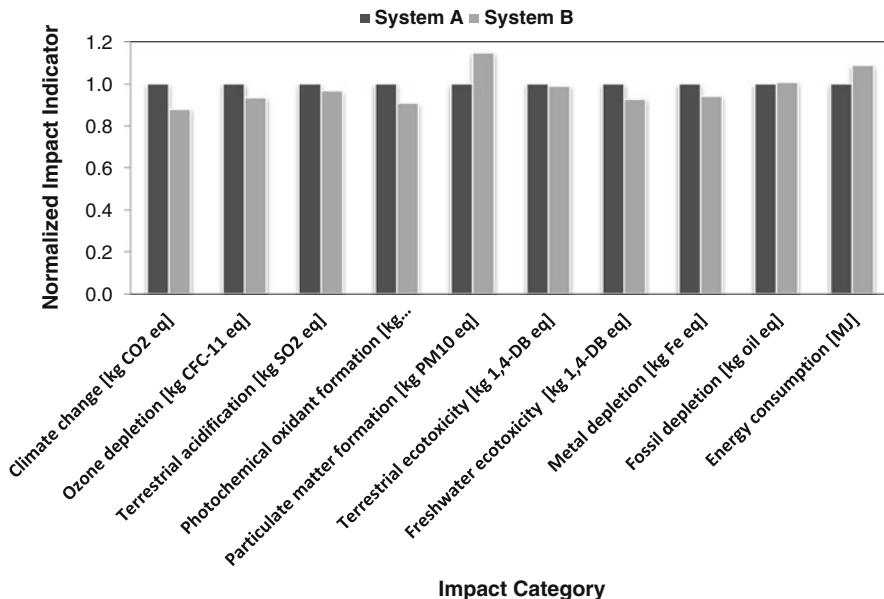
All life cycle assessment methods have inherent limitations which may differ from one method to another [22]. The following assumptions and limitations are invoked in the current study:

1. Due to the lack of reliable data, only the energy consumption is considered for the manufacturing stage for the units.
2. Maintenance, reduction in system efficiency, and waste disposal are neglected since these factors are assumed comparable for both systems.
3. Environmental impact results are influenced by operating conditions.
4. The electricity generation profile in a given region remains the same for the duration of the study.
5. At the stage of production of raw materials, the ratio of scrap–virgin materials is 52:48, 31:69, 30:70, and 50:50 for aluminum, cold rolled steel, galvanized steel, and copper, respectively.
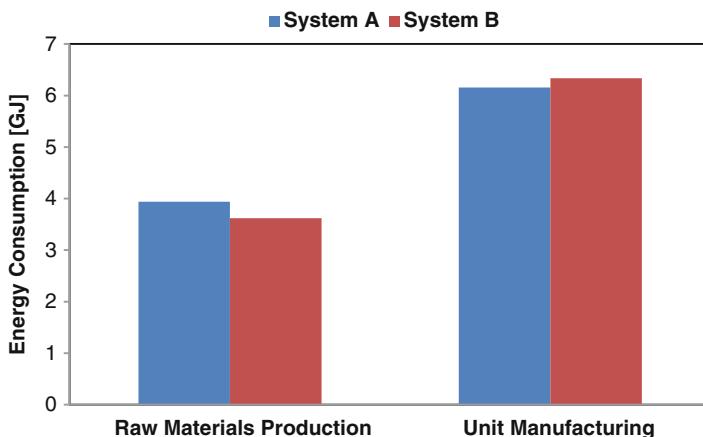
61.4 Results and Discussion

The impact assessment is divided over the three life stages of the HVAC devices: production of metals from raw materials, manufacturing/assembly of HVAC units, and operation. Using the midpoint factors from the ReCiPe method, the impact of raw materials production for each system is depicted in Fig. 61.6. The results are normalized by selecting system "A" as the reference system. In general, the environmental impact of system "A" is similar to that of system "B." This result is primarily dictated by the large amount of raw materials required by system "B," which has a total mass of 140 kg in comparison to the combined mass of system "A" (64 kg for HAF and 71 kg for AC).

HVAC units are manufactured using proprietary processes. An extensive search for the environmental impact of such processes yielded unreliable data. However, Yang et al. were able to estimate the energy consumption during the manufacturing stage using the manufacturing cost of the respective unit which is approximately equal to 1.8 MJ/$ [8, 25]. The cost of each unit was then estimated to be equal to $1400, $2000, and $3500 for the AC, HAF, and HP, respectively [26]. Figure 61.7 shows the energy consumption during the production of raw materials
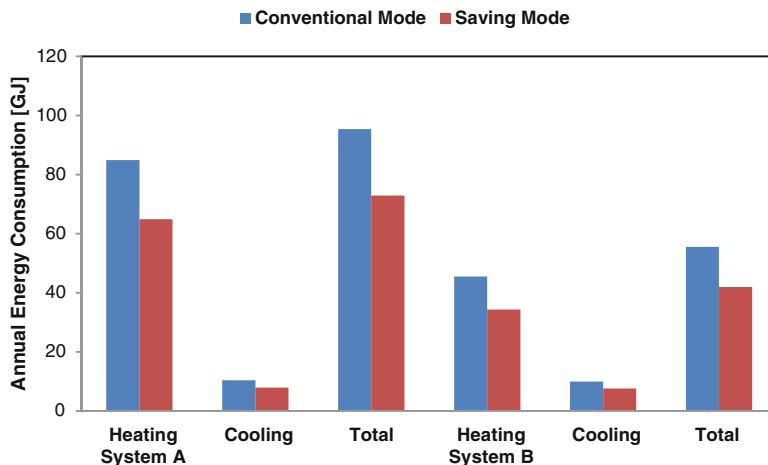
Fig. 61.6 Normalized impact of the production of raw materials for both systems

Fig. 61.7 Energy consumption during the raw material production and manufacturing

along with the estimated consumption of energy during the manufacturing stage. Although the energy consumption of both systems is comparable in both stages, the consumption during the manufacturing stage appears to be about 50 % higher. The uncertainty associated with the method of estimating the energy consumption during manufacturing may have contributed to the final values.
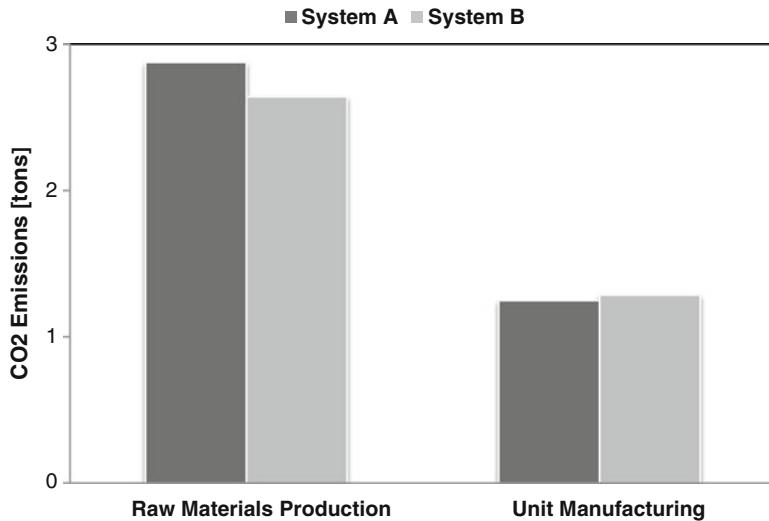
Fig. 61.8 Annual energy consumption for systems
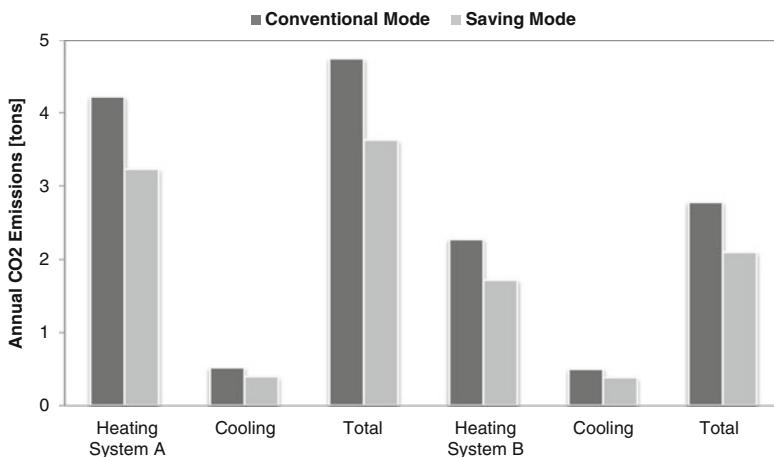
The operational life of the system represents the longest life stage. These systems may last between 15 and 25 years depending on a number of factors like initial quality, operating environment and maintenance. Two operating modes are considered to evaluate their impact on the energy consumption during the heating and cooling seasons. The conventional mode assumes that the thermostat heating and cooling set points are equal to 21 °C. The saving mode assumes that some ventilation cooling may be achieved during mild weather by opening the house windows while lower heating requirements may be met by reducing the setting temperature on the thermostat. Accordingly, the thermostat heating and cooling set points are 18 °C and 24 °C, respectively.

The annual energy consumption is depicted in Fig. 61.8 which compares both systems and reflects the benefit on the saving mode of operation. The reduction of energy consumption amounts to 5–25 % using the saving mode. Furthermore, 30–40 % of additional energy savings may be realized during the heating season by using the heat pump while minimal energy saving is achieved during the cooling season due to the comparable energy efficiency of the air-conditioning unit and the heat pump (cooling mode).

Greenhouse gas emissions are an important aspect in assessing the environmental impact of the systems under consideration. Carbon dioxide is considered to be a major greenhouse gas, so much effort is being expended to mitigate its production and release to the environment [27]. The impact assessment performed on the stage of raw materials production takes into account CO_2 release and its effects on climate change as depicted in Fig. 61.6. However, the CO_2 emissions during the unit manufacturing stage may be estimated by assuming that the units are manufactured at Lennox facilities in Texas, USA (Lennox Headquarters) and that electricity is the primary fuel used during the process. The CO_2 emission factor for

Fig. 61.9 CO_2 emissions during the raw material and unit manufacturing stages

Fig. 61.10 Annual CO_2 emissions

electricity produced in the State of Texas is 0.73 ton_{CO2}/MWh [28]. The CO_2 emissions based on the energy consumption only (effects of chemical emissions are not considered) are shown in Fig. 61.9.

On the other hand, the operation phase of the systems occurs in Ontario, Canada which has CO_2 emission factors of 0.18 ton_{CO2}/MWh and 0.0497 ton_{CO2}/GJ for electricity and natural gas consumption respectively [29, 30]. The annual CO_2 emissions during the operation phase are reflected in Fig. 61.10. By comparing

Figs. 61.9 and 61.10, it can be seen that emissions during the annual operation phase are higher than those during the production of raw materials and unit manufacturing combined. The results also show that there is an environmental benefit from using the heat pump system for heating and cooling throughout the year.

61.5   Conclusions

A comparative life cycle assessment of two residential HVAC systems is demonstrated. LCA methods normally consider a set of assumptions which can highly influence the final outcome of the assessment. Our results show that weather characteristics and geographic location can heavily impact the environmental assessment of residential HVAC systems since their performances and efficiencies are weather dependent. A sensitivity analysis may be incorporated within the LCA to address the effects of uncertainty associated with various input data and life cycle inventories on the final results. While using heat pumps for heating and cooling may yield energy savings and reductions in greenhouse gas emissions, financial savings are difficult to realize by the end user. This is mainly due to the higher specific cost of electricity (per unit energy) compared to natural gas, which leads to long payback periods if a heat pump is to be selected for use. Some financial factors such as inflation rate, interest rate, and rise of commodity prices can also alter the LCA outcome and the benefits of using one system over the other. Further research and development is merited to improve the energy efficiency of building envelops, materials, and major home appliances, and local governments should consider endorsing energy-efficient appliances through incentive programs and end-user education.

References

1. Office of energy efficiency website. Energy efficiency trends in Canada, overview—Residential energy use and GHG emissions, 1990 to 2007, http://oee.nrcan.gc.ca/publications/statistics/trends09/chapter3.cfm?attr=0. Accessed Sept 2012
2. Office of energy efficiency Website. Eco-energy retrofit—homes grants. http://oee.nrcan.gc.ca/residential/personal/grants.cfm?attr=0. Accessed Sept 2010
3. Canada mortgage and housing corporation website, compendium of research on the conservation co-op building. https://www03.cmhc-schl.gc.ca/catalog. Accessed Nov 2011
4. Kassab M (2002) Improving the energy performance of houses in Montreal using the life-cycle analysis. MASc thesis, Department of Building, Civil, and Environmental Engineering, Concordia University, Montreal, Canada
5. Adalberth K (1997) Energy use during the life cycle of buildings: examples. Build Environ 32(4):321–329
6. Mithraratne N, Vale B (2004) Life cycle analysis model for New Zealand houses. Build Environ 39:483–492

7. Blanchard S, Reppe P (1998) Life cycle analysis of a residential home in Michigan. Master thesis, School of Natural Resources and Environment, University of Michigan
8. Yang L (2008) Comparison of environmental impacts of two residential heating systems. Build Environ 43(6):1072–1081
9. Heikkila K (2004) Environmental impact assessment using a weighting method for alternative air-conditioning systems. Build Environ 39(10):1133–1140
10. Legarth JB (2000) A screening level life cycle assessment of the ABB EU 2000 air handling unit. Int J Life Cycle Assess 5(1):47–58
11. Prek M (2004) Environmental impact and life cycle assessment of heating and air conditioning systems, a simplified case study. Energy Buildings 36(10):1021–1027
12. Goedkoop MJ, Heijungs R, Huijbregts M, De Schryver A, Struijs J, Van Zelm R (2009) ReCiPe 2008, A life cycle impact assessment method which comprises harmonized category indicators at the midpoint and the endpoint level; First edition Report I: Characterisation. http://www.lcia-recipe.net. Accessed Sept 2012
13. Luvian homes Website. Building for generations. http://luvianhomes.com/main.php. Accessed Dec 2010
14. Ministry of municipal affairs and housing Website. Ontario's Building Code 2006. Accessed Sept 2011
15. City of Toronto Website. Toronto Municipal Code. http://www.toronto.ca/legdocs/municode/1184_363.pdf. Accessed Sept 2011
16. Natural Resources Canada website. Survey of Household Energy Use: Summary Report, 05. http://oee.nrcan.gc.ca/Publications/statistics/sheu-summary/pdf/sheusummary.Pdf. Accessed Nov 2010
17. Canadian standards association/national standard of Canada, CAN/CSA F280-12, 280-M90. Determining the Required Capacity of Residential Space Heating and Cooling Appliances. Edition: 3rd, 30-Mar-2012 ISBN: 9781554918035
18. Lennox Residential HVAC Systems. Lennox International Web. http://www.lennox.com. Accessed 28 Nov 2010
19. 2012 BizEE Software Limited website. Heating and Cooling Degree Days—Free Worldwide Data Calculation. http://www.degreedays.net. Accessed Oct 2012
20. Natural resources Canada Website. HOT2000—CanmetENERGY, http://canmetenergy-canmetenergie.nrcan-rncan.gc.ca/eng/software_tools/hot2000.html. Accessed Sept 2012
21. Zamagni A (2008) Critical review of the current research needs and limitations related to ISO-LCA Practice, Rep. No. 037075. Italy: CALCAS
22. Graedel TE, Allenby BR (2010) Industrial ecology and sustainable engineering. International Edition, Pearson Education
23. National renewable energy laboratory (NREL) Website. NREL: U.S. Life Cycle Inventory Database. http://www.nrel.gov/lci. Accessed Dec 2011
24. European copper institute website, life cycle assessment of copper products. www.copper-life-cycle.de. Accessed Dec 2011
25. Statistics Canada. CANSIM tables 304-0014 and 128-0006. http://cansim2.statcan.ca/cgi-win. Accessed 2009
26. NS Heating & Cooling, Inc. Website. NSHVAC. http://nshvac.com. Accessed Dec 2010
27. Mitchell JFB (1989) The greenhouse effect and climate change. Rev Geophys Space Phys 27 (1):115–139
28. US department of energy Website. electricity emission factors, voluntary reporting of greenhouse gases program. 31 July 2010. http://www.eia.doe.gov/oiaf/1605/pdf/Appendix%20F_r071023.pdf. Accessed Dec 2010
29. Canadian standards association. Greenhouse gas emission factors. Canadian GHG Registries. http://www.ghgregistries.ca/challenge/index_e.cfm. Accessed Dec 2010
30. Natural Resources Canada. Guide for computing CO_2 emissions related to energy use. http://canmetenergy-canmetenergie.nrcan-rncan.gc.ca/fichier.php/codectec/En/2001-66/2001-66e.pdf. Accessed Dec 2010

Chapter 62
Comparative Assessment of Costs and CO_2 Emissions for Various Residential Energy Options

Sinan Ozlu, Ibrahim Dincer, and Greg F. Naterer

Abstract In this chapter, the heating and hot water demands of a North American residence are assessed and compared. Five specific systems are analyzed: ground and air source heat pumps, stand-alone PV, PV–fuel cell hybrid, and a wind turbine–fuel cell hybrid system. They are compared with traditional sources of energy such as natural gas, coal, and fuel oil. From the results, although renewable sources have no CO_2 emissions, heat pump systems have significant cost advantages over the other systems.

Keywords Heat pump • PV • Fuel cell • Wind energy • Residential energy • Natural gas • Coal • Fuel oil • CO_2 emissions • North American residence • Ground source heat pumps • Air source heat pump • Wind turbine • Hybrid system

62.1 Introduction

Sustainability in the building sector requires a major effort to reduce energy demand, improve energy efficiency, and increase the share of renewable energy sources. The improvement of fenestration, heat insulation and air tightness in the building envelope also has importance. Various options exist on the supply side for the combined provision of home electricity, heating and the integration of renewable energies [1]. Renewable energy sources (solar, wind, etc.) are gaining more

S. Ozlu (✉) • I. Dincer
Faculty of Engineering and Applied Science, University of Ontario Institute
of Technology (UOIT), Oshawa, ON, Canada
e-mail: sinan.ozlu@uoit.ca; Ibrahim.Dincer@uoit.ca

G.F. Naterer
University of Ontario Institute of Technology, Oshawa, ON, Canada

Memorial University of Newfoundland, St. John's, NL, Canada
e-mail: gnaterer@mun.ca

attention as alternatives to conventional fossil fuel sources, due to diminishing fuel sources, as well as environmental pollution and global warming problems [2].

The solar photovoltaic (PV) cell is one of the most significant and rapidly growing renewable energy technologies. During the last decade, PV applications have increased and extended to industrial use in some countries. The clean, renewable, and reliable PV systems have attracted growing attention from political and business decision makers [3]. Wind energy is also among the world's most significant and rapidly growing renewable energy sources. Recent technological developments have significantly reduced wind energy costs to economically attractive levels in many locations. Wind energy farms, consequently, are considered a key alternative energy source in many jurisdictions [4]. Though still in early stages of adoption, fuel cell systems are becoming a focus of interest due to their potential for high efficiency, low emissions, and low noise. Fuel cells normally operate on hydrogen, but can also be used with natural gas or other fuels by external or internal reforming.

In this chapter, comparisons of the carbon dioxide emissions and the costs of various residential energy options are performed. Different residential energy sources for heat demand are considered.
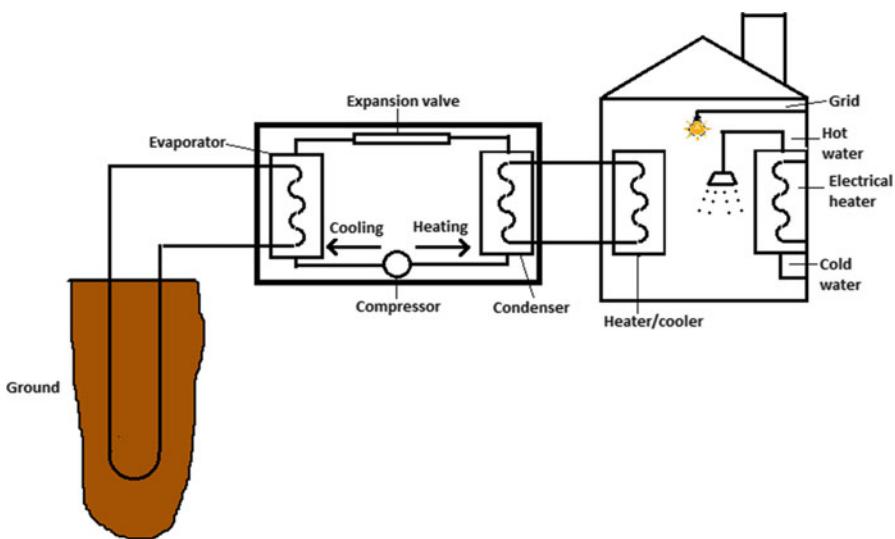
62.2 System Description

Five residential energy systems will be compared in this section. The first two systems are widely used and grid dependent. The other three systems are innovative alternatives and grid independent. The comparison will be made between traditional and promising systems [5].
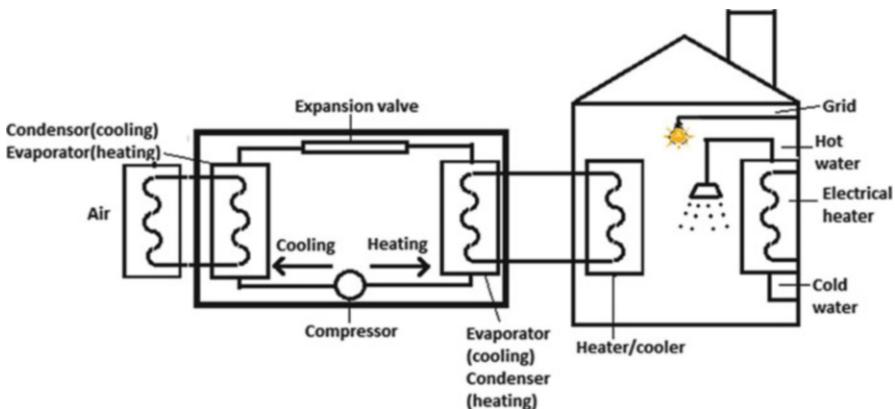
62.2.1 Grid: Ground Source Heat Pump—Electrical Water Heater

In the cooling cycle, as shown in Fig. 62.1, refrigerant vapor exits the compressor at a temperature in the range of 50–60 °C, which is warmer than the ground. As a result, it spontaneously loses heat when it enters the condenser, causing it to condense. The refrigerant leaves the condenser as a liquid, still under high pressure. The expansion valve allows through just as much refrigerant liquid as can be completely vaporized by the indoor coil. The pressure drop through the expansion valve vaporizes some refrigerant and lowers its temperature to 4–10 °C. In the evaporator, it absorbs heat, which vaporizes the rest of the refrigerant liquid. The low-pressure refrigerant vapor leaves the evaporator and returns to the compressor, where the cycle begins again.

In the heating cycle, as shown in Fig. 62.1, the refrigerant releases its latent heat to the room. It is then expanded and vaporized in the ground coil, where it gains latent heat from the ground. The refrigerant vapor then returns to the compressor where the cycle begins again. The hot water is supplied to the home by the electric heater. Electric water heaters supply hot water for household use in many homes.

Fig. 62.1 System1: Ground source heat pump and the electrical heater

Fig. 62.2 System 2: Air source heat pump—electrical heater system

62.2.2 Grid: Air Source Heat Pump—Electric Furnace System

The system is shown in Fig. 62.2. Using electricity as its energy source, heat pumps are used for either heating or cooling of the homes by transferring heat between two reservoirs. In the warmer months, the heat pump acts like an air conditioner, removing heat from the air inside the home and transferring it outside. During

colder months, heat from outdoor air is extracted and transferred to the interior of the home. The working fluid, in its gaseous state, is pressurized and circulated through the system by a compressor. On the discharge side of the compressor, the hot and pressurized vapor is cooled in a heat exchanger, within the condenser, until it condenses into a high pressure, moderate temperature liquid. The condensed refrigerant then passes through a pressure-lowering device called a metering device like an expansion valve, capillary tube, or possibly a work-extracting device such as a turbine. The low pressure, liquid refrigerant leaving the expansion device enters another heat exchanger, the evaporator, in which the fluid absorbs heat and boils. The refrigerant then returns to the compressor and the cycle is repeated.

The submerged electric resistance heating elements in water heaters are very efficient, providing about 99 % of the available heat to the surrounding water. In the heating cycle, the refrigerant is brought back to the heat pump unit inside the house. It then passes through the refrigerant-filled primary heat exchanger for ground water or antifreeze mixture systems. In direct-expansion systems, the refrigerant enters the compressor directly, with no intermediate heat exchanger.
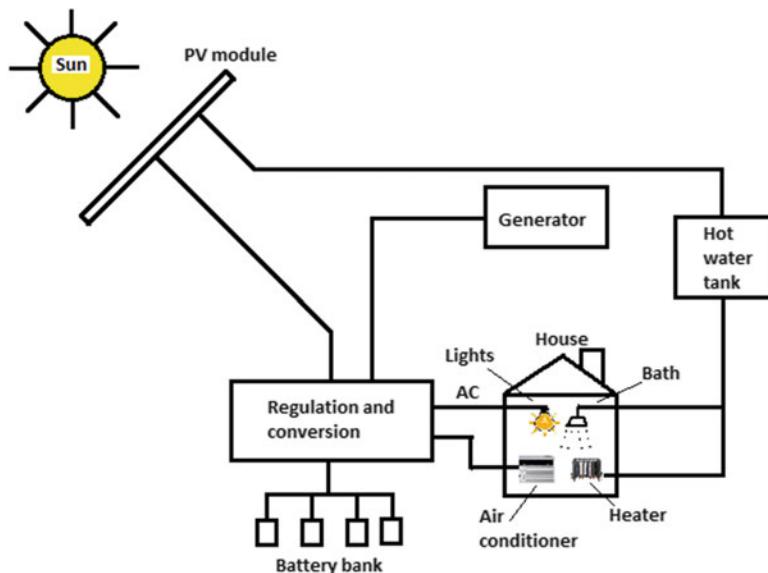
The heat is transferred to the refrigerant, which boils to become a low-temperature vapor. Then the antifreeze mixture or refrigerant is pumped back out to the underground piping system to be heated again. The reversing valve sends the refrigerant vapor to the compressor. The vapor is then compressed and heated.

Finally, the reversing valve sends the now-hot gas to the condenser coil, where it releases heat. Air is blown across the coil, heated, and then forced through the ducting system to heat the home. After releasing its heat, the refrigerant passes through the expansion device, where its temperature and pressure are dropped further before it returns to the first heat exchanger, or to the ground in a direct-expansion system, to begin the cycle again.

The cooling cycle is the reverse of the heating cycle. The direction of the refrigerant flow is changed by the reversing valve. The refrigerant absorbs heat from the house air and transfers it directly in direct-expansion systems or an anti-freeze mixture. The heat is then pumped outside, into the underground piping. Some of this excess heat can be used to preheat domestic hot water. In addition to the air source heat pump, an electric water heater is used to supply hot water to the house.

62.2.3 PV System

The system is shown in Fig. 62.3. A stand-alone PV system is not connected to any electricity grids. The system is solely responsible for powering any loads connected to it. This type of system is common in remote locations where an electricity grid is not available or too costly for connection. It consists of at least a solar panel, charge controller, rechargeable batteries, inverter, hot water system and various loads. The rechargeable battery stores electricity produced by the solar panels. The charge controller acts as an intelligent central unit where solar panel, batteries and various DC loads are connected and monitored. An inverter is added to allow AC

Fig. 62.3 System 3: PV System
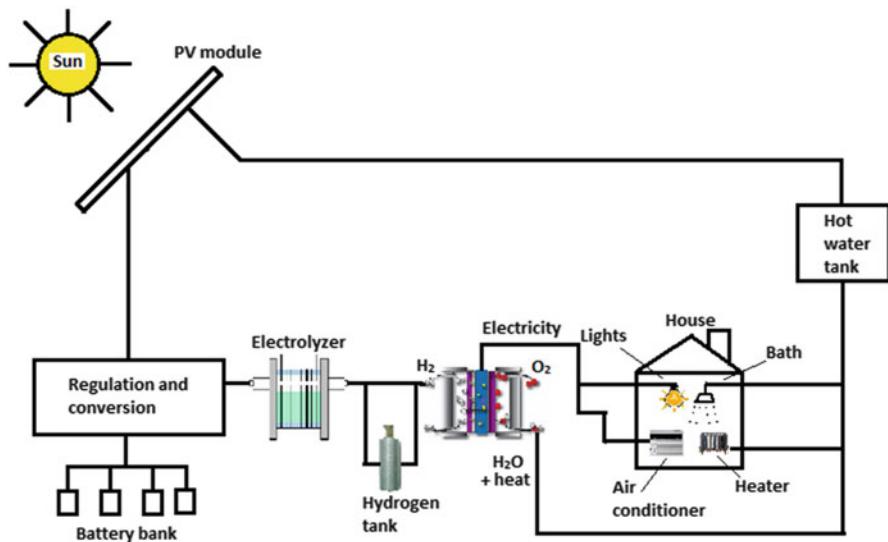
appliances and loads to be used too. Also, a generator is used as a backup energy during the night.

62.2.4   PV: Fuel Cell Hybrid System
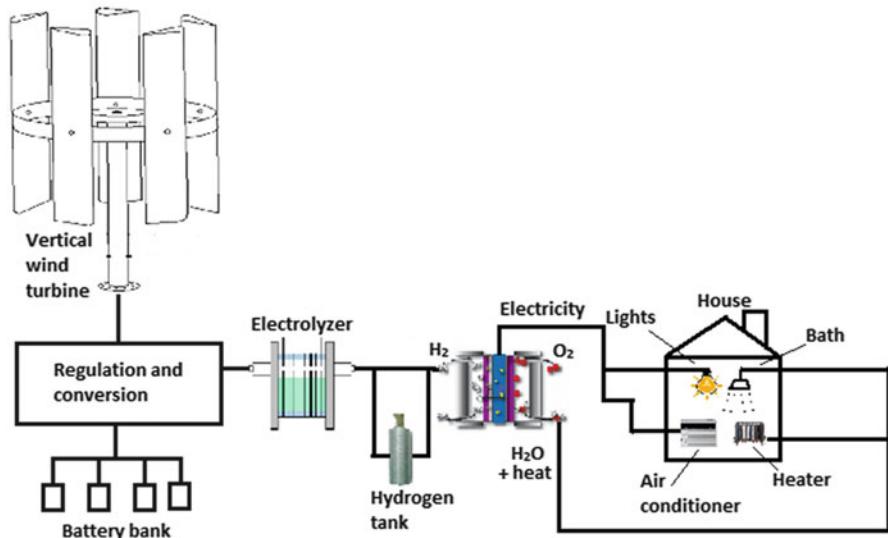
The hybrid system consists of photovoltaic panels and fuel cells designed for a residence to supply electrical demand. DC voltage obtained by photovoltaic panels has been stored in batteries with charge regulators. The voltage has been used in an electrolysis unit which will generate hydrogen used by a fuel cell, as shown in Fig. 62.4. Hydrogen obtained by electrolysis is stored in hydrogen tanks. DC voltage from a fuel cell is converted to AC voltage and electrical demand of the residence is supplied. Excess heat from the fuel cell is used to heat the house. An electrical air conditioner is used to cool the house during the summer.

62.2.5   Wind Turbine: Fuel Cell Hybrid System

A wind energy/fuel cell hybrid is very similar to a PV/fuel cell hybrid system except it uses wind energy as the main source to supply the fuel cell instead of using PV. The system consists of a wind turbine and fuel cells designed for a residence to supply electrical demand. DC voltage obtained by a wind turbine has been stored in batteries

Fig. 62.4 System 4: PV–fuel cell hybrid system

Fig. 62.5 System 5: Wind turbine—fuel cell hybrid system

with charge regulators. The voltage has been used in an electrolysis unit which will generate hydrogen used by fuel cell, as shown in Fig. 62.5. Hydrogen obtained by electrolysis is stored in hydrogen tanks. DC voltage obtained from the fuel cell is converted to AC voltage and electrical demand of the residence is supplied. Excess

heat from the fuel cell is used to heat the house. An electrical air conditioner is used to cool the house during the summer.

Vertical-axis wind turbines (VAWTs) are an emerging development. VAWTs have rotor blades that spin parallel to the ground, so that they can operate anywhere without having to account for the wind direction. This allows locations with volatile wind directions to be viable locations for VAWTs. Because of the axis orientation, the gearbox and generator can be placed near the ground, eliminating the need for a high tower.

Advantages of VAWT's over Horizontal-Axis Wind Turbines (HAWTs) are numerous. Since VAWTs can have rotor blades close to the ground, they are easier to install compared to HAWTs that often require the rotor blades to be at a high altitude depending on the blade length. For the same reason, VAWTs are easier to maintain since most of them are installed near the ground. HAWTs should also be checked constantly so that it faces against the wind, unlike VAWTs which require less maintenance. Automatic yaw-adjustment mechanisms have eliminated this need of constant maintenance on HAWTs. HAWTs require a tower that can erect the rotor blades to a high enough location that would maximize wind speeds, while VAWTs would require guy cables to ensure that the machine remains stable. HAWTs require lesser land space compared to VAWTs since tower bases occupy minimal space while the need for guy cables for VAWTs would entail occupying a much larger land area.

62.3 Results and Discussion

62.3.1 CO$_2$ Emissions

Typical medium gas consumption in the UK is 16,500 kW h/year, while in the USA, it is 16,000 kW h/year (for heating 12,000 kW h/year, hot water 3,000 kW h/year, and cooking 1,000 kW h/year). The CO$_2$ emissions for typical resident energy sources are shown in Table 62.1. The emission of CO$_2$ if these sources are used is shown in Table 62.2.

Natural gas emits 1.65 times less CO$_2$ than coal, 1.4 times less than fuel oil, and 4.3 times less than electricity. Ground or air source heat pumps use electricity as the source. However, as their coefficients of performance (COP) are high enough, they emit much less CO$_2$ than pure electricity source. The COP of the heat pumps depend on the heat source and the destination temperatures. When the temperature difference between them decreases, the COP increases, and vice versa.
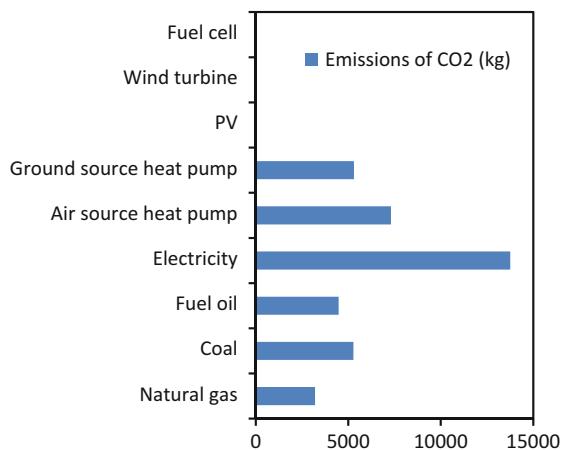
Table 62.1 CO$_2$ emissions for typical resident energy sources

Sources	Emissions in kgCO$_2$/kW h
Natural gas	0.20
Coal	0.33
Fuel oil	0.28
Electricity	0.86

Table 62.2 Emissions of CO_2 for various sources

Fuel	Emissions in kgCO_2
Natural gas	3,200
Coal	5,280
Fuel oil	4,480
Electricity	13,760

Fig. 62.6 CO_2 emissions of selected sources per year

As a reference if the ground is assumed as 10 °C, and the destination temperature is 65 °C for radiator or domestic hot water, the typical COP for the ground source heat pump is 2.9. This means when 1 unit of electricity is used, 2 units of energy are received. For an average USA home, 12,000 kW h is consumed for heating, 3,000 kW h for hot water, plus 1,000 kW h for cooking. A COP of 2.9 reduces electricity usage to 4,138 kW h for heating. If electricity is used for hot water and cooking, the total electricity consumption would be 8,138 kW h. This makes 6,999 kg CO_2 emission.

If a high efficiency air source heat pump is used when air is at 0 °C, for the same destination as above (65 °C for radiator or domestic hot water), the typical COP is 2. By a similar approach as above, the CO_2 emission is 8,600 kg. A comparison of the results is shown in Fig. 62.6.

62.3.2 Costs

Previous work by Ozlu et al. [5] showed that a ground source heat pump is the cheapest solution in the short and long term (Fig. 62.7). Adding to these systems natural gas, coal, fuel oil heating and updating the prices gives the results in Fig. 62.8. It shows that renewable systems are still high in price even after 20 years of operating life. Coal is the cheapest solution for heating and hot water.
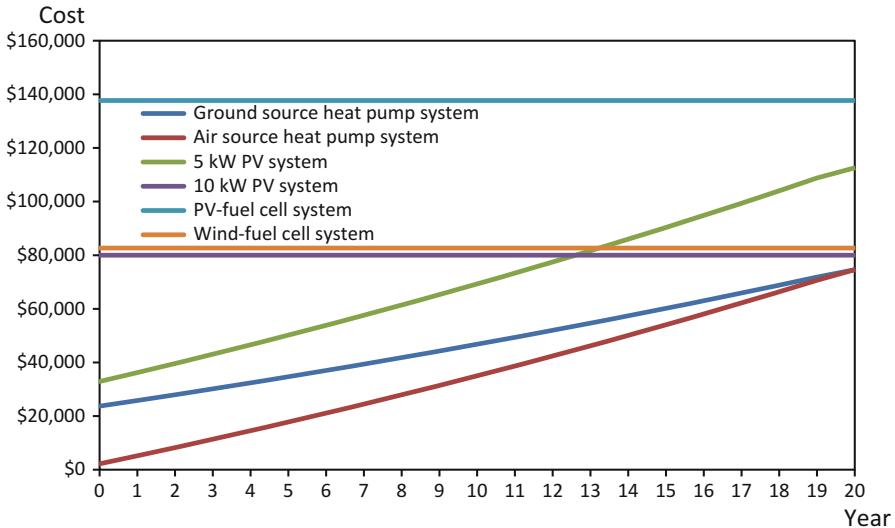
Fig. 62.7 20 year cost span of various systems
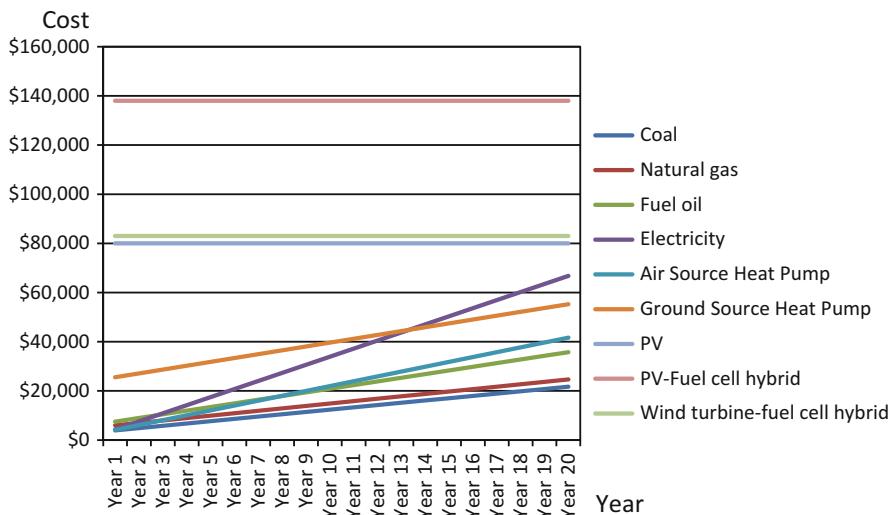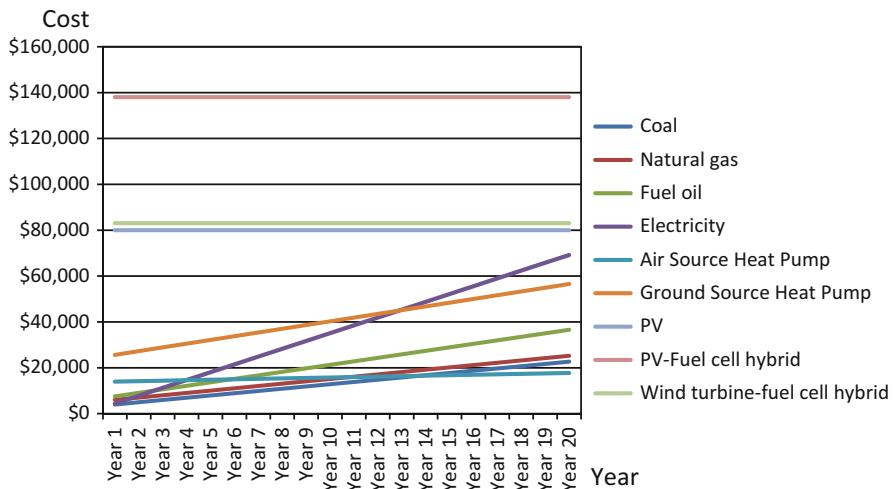
Fig. 62.8 Initial and fuel costs of various systems

62.3.3   Prices and Carbon Dioxide Emissions Combined

Carbon emissions trading is a form of emission trading that specifically targets carbon dioxide (calculated in tons of carbon dioxide equivalent or tCO_2e) and it currently constitutes the bulk of emissions trading. This form of permit trading is a common method countries utilize in order to meet their obligations specified by the

Fig. 62.9 Combination of prices and CO_2 emissions

Kyoto Protocol, namely, the reduction of carbon emissions in an attempt to reduce (mitigate) future climate change.

Currently there are six exchanges trading in UNFCCC related carbon credits: the Chicago Climate Exchange (until 2010), European Climate Exchange, NASDAQ OMX Commodities Europe, PowerNext, Commodity Exchange Bratislava, and the European Energy Exchange.

The price of carbon emissions is 6.8 euro/ton or $8.84/ton. In the previous chapters, the price of the residence fuels and their carbon emissions were examined. Combining them with a price of $8.84/ton of carbon emissions, the results in Fig. 62.9 are achieved. The figure doesn't change significantly as the current price of CO_2 emissions is low compared to the past. If the price of CO_2 emissions will be higher and renewable source systems costs will be lower, then they could be comparable.

62.4 Conclusions

In this chapter, CO_2 emissions and prices for traditional energy sources such as electricity, natural gas, coal, fuel oil and renewable sources such as PV, wind turbine, fuel cell are compared. Heat pumps are also considered as they are widely used. As a result, renewable sources have no CO_2 emissions, while natural gas emits less than others and then ground source heat pump, air source heat pump, fuel oil, coal, and electricity in order. When the prices are compared, the renewable sources are still relatively expensive even when the costs of CO_2 emissions are added. The main disadvantage of the renewable sources is their cost. When they will be widely used, the cost will decrease.

References

1. Dorer V, Weber R, Weber A (2005) Performance assessment of fuel cell micro-cogeneration systems for residential buildings. Energ Build 37:1132–1146
2. El-Shatter TF, Eskandar MN, El-Hagry MT (2002) Hybrid PV/fuel cell system design and simulation. Renew Energy 27:479–485
3. Sahin AD, Dincer I, Rosen MA (2007) Thermodynamic analysis of solar photovoltaic cell systems. Sol Energ Mater Sol Cell 91:153–159
4. Sahin AD, Dincer I, Rosen MA (2006) Thermodynamic analysis of wind energy. Int J Energ Res 30:553–566
5. Ozlu S, Dincer I, Naterer GF (2012) Comparative assessment of residential energy options in Ontario, Canada. Energ Build 55:674–684

Index